ACTA METALLURGICA

VOLUME 1 1953

Author Index to Volume I

(References with (L) are to Letters to the Editor)

Title Index to Volume I

(References with (L) are to Letters to the Editor)

ACTA METALLURGICA

A new journal should be founded only if a real need exists. If the need is merely for more pages of conventional material for an established audience it is far better to increase the size of present journals than to start a new one. A new journal should create a new grouping of readers; it should serve as a medium of expression for a new combination of authors; and it should serve as a focus for the integration of types of knowledge the relation of which is newly perceived. The volume of scientific literature related to metallurgy is already so vast that those suggesting the addition of yet another publication must clearly see that it will contribute significantly to professional maturity and not just divert material from the older journals.

The realignment of knowledge is a sign of progress, with new fields continually crystallizing and receiving professional approval. For various purposes and at various times the same areas of knowledge will be differently grouped, and it is the opinion of the founders of this journal that a partial regrouping is now taking place in metallurgy. *Acta Metallurgica* will deal with the whole science of metals: it will draw upon the basic sciences of physics and chemistry on the one hand and upon the science to be inferred from metallurgical practice on the other, with considerable dipping into other applied sciences and the characteristics of other materials where these will assist the understanding of metals. The application of established knowledge to industrial problems is the right and proper field for the metallurgical societies themselves and is admirably covered by their established publications.

The metallurgist, part scientist, part artisan, and part manager, is placed where many fields of knowledge and intuitive skill merge. In the past he has been more concerned with the application of knowledge than with its advancement or rigorous formulation. He has, nevertheless, frequently been required to develop the science of his materials and has made many contributions to the understanding of chemical and physical principles. Now, however, metallurgy is too broad to be encompassed by a single human mind: it is essential to enlist the interest of the "pure" scientists, under whatever name, and to increase the number of metallurgists whose connections with production and managerial problems are partially sacrificed in order that they may be more concerned with physics and physical chemistry as a framework for useful metallurgical advance. Even now much of the literature of a research metallurgist is to be found in the professional journals of the physicist and chemist and he can no longer depend on the metallurgical journals alone. Similarly, the solid-state physicist and the physical chemist have shown an increasing interest in metallurgical journals. This situation exists in all major countries doing scientific research, yet the bulk of such specialized publications in any one country hardly justifies a special journal; an international journal, therefore, seems particularly appropriate. Though such a journal has been discussed for many years on both sides of the Atlantic, it remained only an idea until Dr. John H. Hollomon and Dr. John Chipman supplied the necessary energy of activation, and the American Society for Metals the necessary initial funds.

The journal cannot constitute the whole professional reading of a metallurgist or other scientist concerned with metals; indeed, it will have failed if it does, for its purpose is to break down, rather than to encourage specialization. It will be a catastrophe if the scientific metallurgist loses touch with his more practical colleagues, or if the solid-state physicist ceases to be interested in the broad field of physics. It is hoped that the new journal will serve, not to force us all into one mold, but rather to cultivate the benefits of diversity. Contact with neighboring sciences, and with one's own field as seen from the viewpoint of another country, cannot help but prove stimulating.

"*Acta Met*," as it will doubtless come to be called familiarly, is off to a good start; it has some excellent papers lined up for early issues, and an admirable source of readers in the wide membership of its sponsoring and cooperating societies. Its progress will depend on the degree to which it continues to meet the changing needs of the future.

CYRIL STANLEY SMITH
Chairman, Board of Governors

Institute for the Study of Metals
University of Chicago
November, 1952

AN ABNORMAL AFTER-EFFECT IN METALS*

CHARLES S. BARRETT†

A metal wire that has been subjected to plastic flow in torsion generally untwists at a rate such that equal strains occur in equal intervals of log time. It was found that this is true with single crystal and polycrystalline wires of iron and of zinc, both when coated with oxide films and when freshly cleaned of oxide. But the normal after-effect following plastic twisting of these wires is replaced by an abnormal after-effect (twisting instead of untwisting), which occurs as a transient, when an etchant is suddenly applied to an oxide-coated wire that has been twisted.

The transient reversal of the after-effect was predicted on the basis that adherent oxide films on metals act as barriers to the movement of dislocations. When a wire is twisted, dislocations pile up beneath the oxide-metal interface; these escape through the surface when acid is applied. An after-effect in the normal direction but with a reduced rate follows the transient effect and is also accounted for by dislocations escaping that had previously been piled up beneath the surface.

UNE REPERCUSSION ANORMALE DANS LES METAUX

Un fil métallique soumis à l'écoulement plastique par torsion, se détord à une vitesse telle que des contraintes égales ont lieu à des intervalles égaux du log de temps.

Il a été constaté que cela est vrai pour des fils monocristallins et polycristallins, dans les deux cas immédiatement après avoir enlevé la couche d'oxyde dont ils étaient préalablement couverts. Mais à la répercussion normale se substitue une répercussion transitoire, anormale (continuation de la torsion au lieu d'une détorsion) qui a lieu quand un réactif d'attaque est appliqué subitement à un fil tordu, couvert d'une couche d'oxyde.

Le renversement transitoire de la répercussion a été prédit sur le fondement que les couches d'oxyde qui adhèrent au métal, empêchent le mouvement des dislocations. Lors de la torsion d'un fil, les dislocations s'entassent en- dessous du joint métal-oxyde et s'échappent par la surface, quand on applique un acide. Une répercussion normale, mais à une vitesse réduite, suit le phénomène transitoire, ceci est aussi expliqué par l'échappement des dislocations qui ont été préalablement accumulées sous la surface.

EIN ANOMALER NACHWIRKUNGSEFFEKT IN METALLEN

Ein Metalldraht, der in Torsian plastisch verformt wurde, entspannt sich im allgemeinen mit einer solchen Geschwindigkeit, dass gleiche Verzerrungen in gleichen Log-Zeit Intervallen auftreten. Das trifft auf Einkristalle und auf polykristalline Drähte von Eisen und Zink zu, sowohl wenn diese mit einem Oxydfilm überzogen sind, als auch wenn sie frisch von Oxyd gereinigt sind. Aber an Stelle des normalen Nachwirkungseffekts der plastischen Verdrillung dieser Drähte tritt ein anomaler Nachwirkungseffekt (weitere Verdrillung statt Entspannung) als ein Übergangsstadium auf, wenn ein gedrillter Oxyd bedeckter Draht plötzlich geätzt wird.

Die vorübergehende Umkehr des Nachwirkungseffekts wurde auf Grund der Tatsache, dass haftende Oxydfilme auf Metallen Hindernisse für die Bewegung von Versetzungen ("dislocations") sind, vorausgesagt. Wenn ein Draht verdrillt wird, dann häufen sich die Versetzungen ("dislocations") unter der Grenzfläche Oxyd-Metall. Sie entweichen durch die Oberfläche wenn mit Säure geätzt wird. Ein Nachwirkungseffekt in normaler Richtung aber mit verminderter Geschwindigkeit folgt dem Übergangseffekt. Auch er kann durch das Entweichen der vorher unter der Oberfläche aufgehäuften Versetzungen erklärt werden.

Many experiments have recently shown that crystals are strengthened by the presence of thin adherent surface layers. Oxide films of the order of 10^{-5} cm. thick have been observed to increase the flow stress of cadmium crystals to more than twice the normal value (Roscoe [1]; Cottrell and Gibbons [2]); marked strengthening has also been observed from oxide films on crystals of zinc (Harper and Cottrell [3]) and silver (Andrade and Henderson [4]) and from electrodeposited copper layers on zinc crystals (Pickus and Parker [5]); hydroxide films on cadmium crystals cause measurable amounts of hardening (Andrade and Randall [6]; Menter and Hall [7]) even with thicknesses as small as 10^{-7}cm. (Phillips and Thompson [8]). Similar strengthening has been noted in creep tests of polycrystalline nickel, although it was not observed in tests on polycrystalline zinc (Pickus and Parker [5]; Andrade and Randall [6]) or polycrystalline cadmium (Phillips and Thompson [8]; Andrade and Randall [6]). That surface conditions affect plastic behaviour of crystals is also evident metallographically: extremely fine slip bands are seen on oxide-free and strain-free surfaces of crystals after slight plastic extension whereas heavier, more widely spaced bands are seen in areas subjected to mechanical polishing (Brown and Honeycombe [9]), abrasion, or oxidation (Paxton, Adams and Massalski [10]).

The explanation of these effects is not clear, as will be seen from the discussions in the references cited above and others (Kuhlmann [11]; Fisher [12]). It may be argued, on the one hand, that plastic flow starts in the interior and encounters a greater barrier upon reaching the surface if the surface is oxidised, coated with an adherent layer, or abraded, than if the surface is clean and undistorted.

*Received August 11, 1952.

†Visiting Professor at the University of Birmingham during the time devoted to this work; Professor, Institute for the Study of Metals, University of Chicago.

2

In one alternate theory it has been suggested by Fisher [12] that just beneath an adherent surface layer is a zone where deformation is initiated more easily than at interior points, and that the effect of a surface layer is to strengthen this zone and thus to inhibit the onset of slip.

It was suggested by Cottrell [13] that if the theory of dislocations piling up beneath a surface layer is correct, it should be possible to allow them to remain for a time after the applied load is released, and then upon sudden removal of the surface film they should escape to the surface. The escape process would be identified by an after-effect of abnormal character, reversed in sign from the normal after-effect. The experiments reported below were successful in disclosing this effect, and accordingly lend support to this hypothesis. The experiments also confirmed earlier observations that a Bauschinger effect and a normal after-effect can be detected in single crystals (Sachs and Shoji [14]; Held [15]).

Materials and Methods

The tests were conducted by twisting wires quickly (in 2 to 4 seconds), releasing them, and measuring the after-effects by reflecting a beam of light from a mirror attached to the free end of the wire. The tests were conducted at room temperature (15–18°C) and all liquids were brought to room temperature before being applied to the wires. The wires were prepared as follows:

A. Polycrystalline wires of zinc roughly 1 mm. in diameter were prepared by extruding a billet of "spectroscopically pure" zinc, supplied by the National Smelting Company, having the following spectrographic analysis: Pb 0.0001 per cent, Cd < 0.0001 per cent, Cu < 0.0001 per cent, Fe $<$ 0.0005 per cent, Sn < 0.0005 per cent. The billet was melted in glass after evacuating and admitting a little argon.

B. The same zinc was melted in an atmosphere of nitrogen with nitrogen bubbling through the melt for 30 minutes, a treatment that has been found adequate to produce a yield point in tensile tests of the crystals. Extruded wires were sealed into silica tubes of 1.5 mm. inside diameter, evacuated, degassed, and sealed off with 2/3 atmosphere pressure of argon to reduce volatilization. Single crystals were grown by moving the solid-liquid interface along the wires (in bundles of four).

C. Crystals of lesser purity (99.99 per cent) zinc of "Crown Special" grade were grown from the melt in silica tubes without contact with nitrogen.

D. Mild steel containing S, 0.04 per cent; Mn, 0.3 per cent; Si, trace, was decarburized in wet hydrogen by heating 0.080 in. diameter wires 18 hours at 700°C. These specimens were used in the polycrystalline form, in which the average grain diameter was approximately one-thirtieth the diameter of the wire; this wire exhibited no yield point in tensile tests.

E. Mild steel treated as in *D* above was made into single crystals containing small amounts of carbon by the following treatment: after stretching 3 per cent the wires were annealed 4 days at 870°C in wet hydrogen, carburized slightly by heating $\frac{1}{4}$ hour in a heptane-dry hydrogen mixture, then homogenized by heating 5 days at 670°C in vacuum. The carbon content was estimated to be 0.002–0.003; it was sufficient to produce a yield point when crystals of the batch were tested in tension.

In preliminary tests the oxide layers were removed during the test by dripping an etchant over the wire. In the later tests reported here the wires were immersed in a flowing water bath throughout the test, with the water being displaced by the etching solution when removal of the oxide was desired. In some experiments the acid bath was continued to the end, in others it was changed back to water when its sudden effects had ceased. The continuous immersion technique was adopted in order to avoid the effects observed when oxidized specimens are first immersed in certain liquids (Harper and Cottrell [3]; Rehbinder, Lichtman and Maslenikov [16]; Andrade and Randall [6]).

Results

As with other relaxation effects, the untwisting of a wire that has been previously twisted would be expected to follow the law of equal strain increments in equal intervals of the logarithm of elapsed time after the twisting, except for periods near zero time and infinite time (Kuhlmann [18]; Zener [17]). Accordingly, the data from the present experiments were plotted as curves of strain *vs.* log time, and as anticipated, the portions of the curves governed by the normal after-effect are linear.

Typical after-effect curves for single crystals of zinc are reproduced in Figure 1. The crystals were made from Material C above (99.99 per cent zinc). They were covered with the original oxide film that had been produced when the crystals were grown. Curve *A* is for a crystal having an orientation such that the basal plane was 7 degrees from the axis of the wire, and a slip direction, [11$\bar{2}$0], was 23.5 degrees from the axis. A segment 15 mm. long, 1.0 mm. in diameter was twisted 60 degrees while

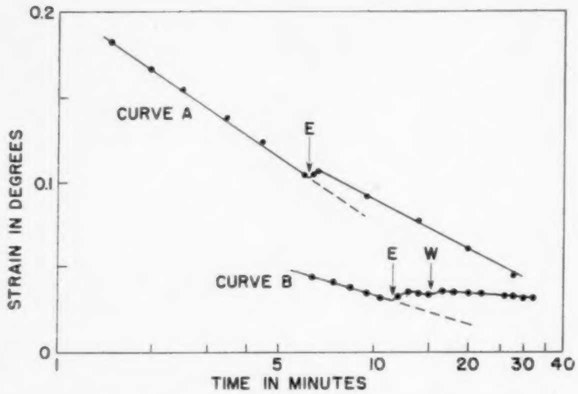

FIGURE 1. Torsional after-effect curves for single crystals of zinc. Water was replaced by etchant at points indicated by E, and this was continued to the end of the test in curve A, but was replaced by water at W in curve B.

immersed in water; the normal after-effect was allowed to proceed for 6 minutes, then the water was displaced by an etchant consisting of 1 part HCl in 9 parts water, at the time indicated by point E on curve A. A transient strain then occurred that twisted the wire in the direction of the original twisting, opposite to the normal after-effect. The reversed motion continued for about 40 seconds, at which time the wire was twisted 0.008 degrees more than it would have been if the normal untwisting had continued. This represents about 5 per cent of the strain at the torsional elastic limit. (Since there was a strong Bauschinger effect after this experiment, the elastic limits in both directions of twisting were determined and the average of these was taken; each value represented the twist that would leave the minimum detectable permanent set, about 0.0015 degree.

With the specimen still immersed in the etchant, the transient died out and was replaced by an after-effect in the normal direction (untwisting). This, however, was at a reduced rate, the curve in Figure 1 having a lesser slope than before. If this later part of curve A is displaced about 4 minutes to the right throughout its length its slope becomes equal to that of the first part; this equivalent time displacement is a convenient description of the change of slope which accompanied the removal of the oxide film.

Curve B, Figure 1, shows the results of a test with another zinc crystal of the same purity, prepared similarly but with a different orientation. It was given a 40 degree twist followed a minute or so later by a further 20 degree twist. The crystal was 20 mm. long, 1 mm. in diameter and had its original oxide film. The normal after-effect was nearly stopped by the removal of the oxide film at the time indicated by E on curve B and did not return to normal when the etchant (again 10 per cent HCl) was replaced by water, at the time W, although in this particular test there seemed to be a slight irregularity here.

Various additional tests were made on single crystals that confirmed the features mentioned. In tests of crystals that had been held in a steam bath at 100°C for an hour, a treatment that had been found adequate to produce a surface layer with marked hardening effects in tensile experiments (Harper and Cottrell [3]), it was found that there were similar reverse after-effects when etched and a subsequent slowing of the normal after-effect—in some cases a reduction of the rate to nearly zero. In several tests the etchant was left around the specimen only during the time the reverse transient lasted, and was then replaced by water; when the water was again replaced by the etchant there were no transient effects produced. This indicated that the initial attack on the surface layer caused the changes, and eliminated the possibility that thermal transients or viscosity changes could have been responsible. Crystals of Material B appeared to behave similarly to those of Material A.

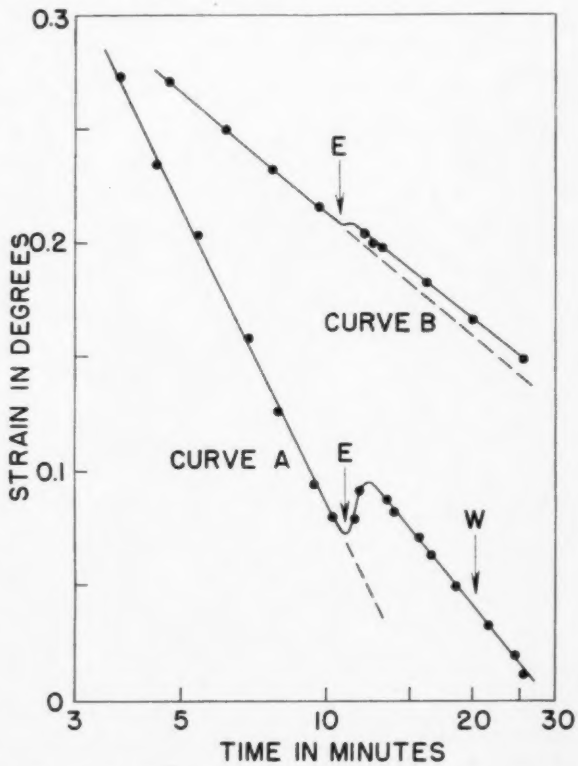

FIGURE 2. Curves for polycrystalline zinc. Curve A, zinc of 99.99 per cent purity, containing nitrogen. Etchant applied at E, replaced by water at W. Curve B, zinc of 99.999 per cent purity, melted without contact with nitrogen. Etchant applied at E.

Curve *A*, Figure 2, is a typical curve for polycrystalline zinc of 99.99 per cent purity ("Crown Special" grade). The specimen, 12 mm. long, 1 mm. in diameter, had been subjected to steam for 2 hours. After immersion in water at 16°C it was twisted 40 degrees. The normal untwisting was interrupted by replacing the water by 10 per cent HCl after 11 minutes, which caused a twist of about 0.04 degree back from the position that would have been obtained without etching (a twist equal to about 15 per cent of the strain at the elastic limit). The transient lasted less than 2 minutes and was replaced by a slow after-effect in the normal direction. The change of rate was equivalent to a displacement of the curve to the right by 9 minutes of arc. When the etchant was later replaced by water no transient was observed. Additional tests with polycrystalline samples of this purity need not be discussed in detail as they produced qualitatively similar results and confirmed the general conclusions already stated. Control tests in which the etchant was later reapplied showed no transient effects.

Curve *B*, Figure 2, gives the results of a test of polycrystalline zinc of 99.999 per cent purity melted without contact with nitrogen (Material A). A 2 hour treatment in steam preceded the test. The specimen was 24 mm. long, 1.4 mm. in diameter, and was twisted 30 degrees. Although the changes introduced by the etching were small, they were of the same nature as those obtained with the less pure specimens. Since etching times, temperatures, oxide thicknesses, and specimen dimensions varied in the different tests, the exact magnitudes of the effects are not of significance.

Several tests were conducted in which the etchant was applied much later. This had the effect of reducing the magnitude of the reverse after-effect. For example a polycrystalline specimen of the high purity zinc (Material A) etched after 140 minutes showed no reversed motion. The slope of the curve subsequent to etching, however, was less (equivalent to a 50 minute displacement along the time axis).

Tests were made using iron crystals (Material E), 20 to 30 mm. long, electropolished, then oxidized in air until covered with an oxide film showing blue temper colours. The technique used was similar to that described above except that dilute nitric acid was used as the etchant. Transients were observed both in the forward direction (untwisting) in some tests, and in the reverse direction in others. As the largest forward motion occurred with an etchant containing 10 per cent HNO_3 and smaller or reversed motion was obtained when concentrations of 5 to $2\frac{1}{2}$ per cent were used, it was concluded that heating or other effects might be entering during the etching period. A test with $\frac{1}{2}$ per cent HNO_3 on a specimen containing two crystals each about 1 cm. long is plotted as curve *A*, Figure 3. A definite reverse effect

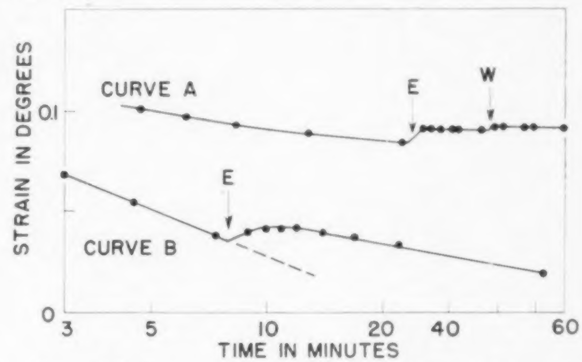

FIGURE 3. Curves for decarburized mild steel. Curve *A*, large crystals with sufficient carbon introduced to give a yield point in tensile tests. Etched with ½ per cent nitric acid in water, at *E*; etchant replaced by water at *W*. Curve *B*, polycrystalline sample, decarburized, showing no yield point in tensile tests. Etched with ½ per cent nitric acid in water at *E*.

is evident. When the experiment was repeated 30 minutes later as a control experiment with the surface in the etched condition, the transient was absent. The reverse after-effect was confirmed with another large-grained specimen. In every case when an etchant (either strong or weak) had removed an oxide the normal after-effect continued at a lowered rate.

In similar tests on polycrystalline iron (Material D) etched with $\frac{1}{2}$ per cent HNO_3 in water, a reduced slope in the curves was obtained after etching, and reversed after-effects were clearly observed, as is illustrated by curve *B*, Figure 3. In the experiment illustrated by this curve a wire approximately 30 mm. long was oxidized to a brown temper colour and twisted 360 degrees while immersed in water. The etchant caused a reversed motion equal in magnitude to about 6 per cent of the strain corresponding to the torsional yield point in the annealed state, and the slope of the curve after etching was about half the former slope. These effects were absent in an immediate repetition of the test starting with the wire in the etched condition.

Discussion

The results of oxide removal (excluding those obtained with too rapid etching, where heating was suspected) were qualitatively the same for each of these samples, which included samples that normally

show a yield point and samples that do not; also high purity, low purity, hexagonal, and body-centred cubic specimens in single crystal form and in polycrystalline form.

The effects of oxide removal were such as could be fully accounted for by assuming that dislocations pile up beneath an oxide layer and escape when this is removed or loosened. During the initial straining, according to this theory, the piling up continues until either the back stress due to the pile counteracts the applied stress and stops the generation or the approach of further dislocations, or until the stress concentration at the front of the pile "punches through" the barrier, permitting the dislocations to escape from the metal. Upon release of the load the dislocations that have left the metal contribute to the permanent deformation, but those that have remained in the pile tend to repel each other and separate by moving back toward their point of origin, thereby causing the normal after-effect. Sudden removal of the oxide layer permits some to escape through the surface. This escape begins very quickly, in accord with the theory that the dislocations pile up very close to a barrier, but as the stress field of those behind is relaxed, the rate rapidly diminishes. Those escaping through the freshly cleaned surface are moving in the same direction as they moved when the original twist was given to the wire, thus the effect of their motion is to twist rather than untwist the wire, and if enough escape per second to overbalance the effect of those moving away from the pile in the opposite direction, there will be a reverse after-effect temporarily interrupting the normal untwisting. With fewer escaping there may be almost an exact balance, as is observed in some experiments, and with still fewer there will be merely a decrease of the normal rate of untwisting.

If the removal of oxide is delayed long after the initial straining, the internal process of redistribution will have relieved the stress of the dislocation pile and few dislocations will be forced to escape through the freshly cleaned surface. This accounts for the lesser transients in the delayed etching experiments. That some still escape, however, is seen by the lower rates after etching and is expected by the theory since the driving force, while lower, is of the same nature as before.

Figure 4 is a sketch illustrating the theory. Potentially active slip planes in a torsion specimen are indicated, with slip blocked at point A by a surface layer, causing dislocation rings to pile up up beneath the surface. The stress field around the

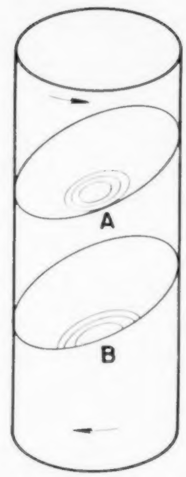

FIGURE 4. Illustrating dislocation rings formed in torsion, piling up beneath a surface layer at A, and penetrating to the surface at B.

slipped region forces reversed flow in the slip band and causes the normal after-effect, the dislocation rings shrinking in size in the process. After etching, a slip band appears at the surface where one side of the dislocation rings pass out of the metal, as indicated at B, contributing to the strain in the direction opposite to the normal after-effect and relieving some of the microscopic residual stresses.

An alternative theory for the effect of adherent surface layers has been proposed by Fisher [12]. A Frank-Read dislocation generator located so that both of its anchor points are embedded in the interior of a crystal should require higher stresses to become active in generating concentric dislocation rings than a source of the same length that has one end in the crystal and the other at the surface. In the latter case an imaged anchor point exists outside of the crystal at a distance from the interior point (which is the *effective* length of the source), that is twice the distance of the interior point from the surface. If the *actual* lengths of embedded sources and of sources near the surface are assumed to be about equal on the average, then the stress required to activate the surface sources would average about half that required to activate embedded sources, since the stresses vary inversely as the length of the dislocation between effective anchor points. This theory suggests that slip should be initiated at the surface of a crystal and that layers on the surface might strengthen the crystal up to a maximum of about a factor of two, as actually observed in some creep tests and tensile tests.

This alternative theory is not adequate, we feel, to explain the present results. Frank-Read sources at

the surface that become operative when the surface layer is suddenly removed should be responsible for both forward and backward after-effects in roughly equal amounts. Those located inside the piled up dislocation rings would aid the normal after-effect, those outside the rings but within their stress field would aid the abnormal after-effect.

Acknowledgements

The author wishes to thank Professor A. H. Cottrell for his suggestions and interest, and Messrs. G. W. Ardley, R. L. Bell, M. J. Dumbleton, and H. W. Paxton for the single crystals and polycrystalline wires used. He is also most grateful to Professor D. Hanson, the University of Birmingham, Professor Cyril S. Smith, and the Institute for the Study of Metals, University of Chicago, for the arrangements that made this work possible at the University of Birmingham.

This work was supported in part by Contract N6-ori-20, Task Order 4.

References

1. Roscoe, R. Phil. Mag., **21** (1936) 399.
2. Cottrell, A. H. and Gibbons, D. F. Nature, **162** (1948) 488.
3. Harper, S. and Cottrell, A. H. Proc. Phys. Soc. London, **B63** (1950) 331.
4. Andrade, E. N. da C. and Henderson, C. Phil. Trans. Roy. Soc. London, **244** (1951) 177.
5. Pickus, M. R. and Parker, E. R. Trans. A.I.M.E., **191** (1951) 792.
6. Andrade, E. N. da C. and Randall, R. F. Y. Nature, **162** (1948) 890; Proc. Phys. Soc. London, **B65** (1952) 445.
7. Menter, J. M. and Hall, E. O. Nature, **165** (1950) 611.
8. Phillips, D. J. and Thompson, N. Proc. Phys. Soc. London, **B63** (1950) 839.
9. Brown, A. F. and Honeycombe, R. W. K. Phil. Mag., [7] **42** (1951) 1146.
10. Paxton, H. W., Adams, M. A. and Massalski, T. B. Phil. Mag., [7] **43** (1952) 257.
11. Kuhlmann, D. Proc. Phys. Soc. London, **A64** (1951) 140.
12. Fisher, J. C. J. Metals, **4** (1952) 531.
13. Cottrell, A. H. Private communication (1951).
14. Sachs, G. and Shoji, H. Zeit. Phys., **45** (1927) 776 (brass crystals in torsion).
15. Held, H. Zeit. Metallkunde, **32** (1940) 201 (zinc crystals).
16. Rehbinder, P., Lichtman, V. I., and Maslenikov, V. M. C.R. Acad. Sci. U.R.S.S., [2] **32** (1941) 125.
17. Zener, C. In "Cold Working of Metals" (Cleveland, Ohio, Am. Soc. Metals, 1949).
18. Kuhlmann, D. Zeit. Phys., **124** (1947) 468.

THEORY OF CATALYSIS OF NUCLEATION BY SURFACE PATCHES*

DAVID TURNBULL†

By hypothesizing a plausible distribution of units for crystal nucleation with respect to size, and that the size of the units may be of the order of the critical size for growth of a nucleus into a supercooled liquid, the multiplicity in crystal nucleation frequency sometimes observed for the isothermal solidification of small droplets is accounted for with the use of no more than two fundamental frequencies. The theory satisfactorily explains the athermal nucleation of crystals for the solidification of small mercury droplets that have "HgX" patches on their surface.

THEORIE DE L'ACTION CATALYTIQUE DES CONCENTRATIONS A LA SURFACE SUR LA GERMINATION

La multiplicité dans les fréquences de germination parfois observée lors de la solidification isotherme de petites gouttelettes est expliqueé en employant une fréquence fondamentale seulement; ceci en supposant une distribution plausible des unités pour la germination des cristaux en rapport avec les dimensions, et que les dimensions des unités sont de l'ordre des dimensions critiques nécessaires pour la croissance d'un germe dans un liquide surfondu. Cette théorie explique d'une façon satisfaisante la germination athermique des cristaux pour la solidification de petites gouttelettes de mercure, dont la surface est couverte de concentrations de "HgX".

DIE THEORIE DER KEIMBILDUNGSKATALYSE DURCH OBERFLÄCHENFLECKEN

Es wird als Hypothese eine plausible Grössenverteilung von Bereichen der Keimbildung vorgeschlagen. Es wird weiterhin angenommen, dass die Dimensionen dieser Bereiche von der gleichen Grössenordnung wie die kritische Grösse für das Wachstum eines Keimes in eine unterkühlte Flüssigkeit sind. Dann lässt sich die Multiplizität der Keimbildungsfrequenz, die manchmal bei der isothermen Erstarrung kleiner Tröpfchen beobachtet wird, unter Benutzung von nur zwei elementaren Frequenzen erklären. Die Theorie erklärt zufriedenstellend die nicht-thermische Kristallkeimbildung bei der Erstarrung kleiner Quecksilbertröpfchen, die "HgX" Flecken auf ihrer Oberfläche haben.

Introduction

Recently the kinetics of solidification of small droplets of mercury [1] and tin [2] coated with various surface films were investigated. Isothermal data for certain mercury droplet dispersions coated with a given film were well described by a single nucleation frequency (I)/area or volume. However, the isothermal data on oxide-coated tin droplets and on mercury droplets having "HgX" patches (HgX, a strong catalyst for the formation of mercury crystal nuclei, is a decomposition product of certain mercury carboxylates) seemed to require a multiplicity of I values for their description. Although various explanations for this multiplicity, all presupposing heterogeneous nucleation, were considered [1; 2], none were fully developed.

In an earlier note [3] a new theory for the multiplicity in I was proposed. In this paper we shall give a more complete development of the theory and compare its predictions with experience.

Theory

The potency, P, of the surface of a substance in catalyzing the formation of crystal nuclei has been characterized by the contact angle θ made by the nucleus on the flat catalyst surface in contact with supercooled liquid. The less is θ, the greater is P, and we may set $P \propto 1/\theta$. The angle θ is determined by the structure and chemistry of the catalyzing surface. Suppose that the crystal embryos have the form of spherical caps on the relatively flat catalyst surface. In order to survive as a crystal nucleus on the surface, these embryos must have attained a critical radius, r^*_s, given by [4]:

(1) $$r^*_s = -2\sigma \sin\theta/\Delta F_v$$

where ΔF_v = free energy per volume for the liquid→crystal transition when both phases have an infinite volume-to-surface ratio, and σ is the interfacial energy between liquid and crystal phases. The radius, r^*, of the crystallization nucleus that forms in the body of the supercooled liquid without the aid of any catalytic surface is equal to or larger than r^*_s and given by:

(2) $$r^* = -2\,\sigma/\Delta F_v.$$

When the linear dimension R of the catalyzing surface exceeds r^* any nucleus on this surface with a radius exceeding r^*_s becomes a *transformation nucleus*, that is, it grows on the surface to a dimension exceeding r^* and thence into the body of the supercooled liquid. However when $R < r^*$, crystal nuclei with $r \gg r^*_s$ formed on the catalyst surface do not become transformation nuclei except by fluctuations‡ that increase the radius of the aggregate of catalyst particle plus crystal to r^*.

In earlier publications [4; 1] we have developed the theory of catalysis of nucleation by catalytic

*Received August 8, 1952.
†General Electric Research Laboratory, The Knolls, Schenectady, New York.

‡Reiss [5] and Pound and La Mer [2] have discussed the theory for this process.

units having radii greatly in excess of r^*. We now consider the catalysis of nucleation by bodies whose radii are of the same order of magnitude as r^*. It will be supposed, for simplicity, that these bodies (we shall hereafter call them patches) are all characterized by a single value of θ and that their number is proportional to the surface area of the liquid.†

Let n_A be the number of patches per unit area with radius $\geqslant R$. We assume a continuous distribution of n_A with respect to R, as follows:

$$n_A = f(R) \tag{3}$$

If θ_p is the contact angle made by a crystal nucleus on a patch the critical radius r^*_p for nucleation on the surface of the patch is given by:

$$r^*_p = -2\,\sigma \sin \theta_p / \Delta F_v. \tag{4}$$

A crystal nucleated on the patch surface grows to the patch boundary but it will not, in general, become a transformation nucleus unless $R > r^*_s$ or r^*.

To a good approximation:

$$\Delta F_v = \Delta S_v\, \Delta T \tag{5}$$

where ΔS_v is the entropy of transition/volume and ΔT is the supercooling. The number of patches (n_A^*)/area capable of serving as transformation nuclei is found by substituting r^* or r^*_s in equation (3). From equations (1), (2), (3) and (5), it follows that the dependence of n_A^* on ΔT is

$$n_A^* = f(-2\,\sigma/\Delta S_v\, \Delta T) \tag{6}$$

or

$$n_A^* = f(-2\,\sigma \sin \theta/\Delta S_v\, \Delta T). \tag{7}$$

Let I_p be the frequency of nucleation/area of patch. Then the nucleation frequency (c)/patch is

$$c = I_p/a_p \tag{8}$$

where a_p is the area of the patch.

Now consider a collection of supercooled liquid droplets of diameter D. The average number of patches (m)/droplet capable of serving as transformation nuclei is given by:

$$m = n_A^*\,(\pi D^2). \tag{9}$$

c will be very strongly dependent upon temperature so that there is a very narrow temperature range in which it changes from an imperceptible to a perceptible value. For some systems m will be very much larger than unity when c becomes perceptible and the nucleation frequency/droplet for droplets of uniform size will be constant. However, there is a large probability that, for some systems, c becomes perceptible when m is of the order of unity or less. Under these circumstances, the number of patches/droplet that can serve as transformation nuclei is far from uniform and a substantial fraction of droplets will contain no supercritical patches.

Let x be the fraction of a liquid sample, consisting of uniform droplets, solidified in time t. To obtain $x = f(t)$ for m of the order unity or less, a derivation due to Kimball is directly applicable. Kimball [6] assumed that all catalytic units (average m/droplet) are equally effective and that they are distributed among the droplets according to Poisson's distribution law. With these assumptions he obtained for constant ΔT:

$$x = 1 - \exp\{-m[1 - \exp(-ct)]\}. \tag{10}$$

All supercritical patches are not equally effective as nucleation catalysts since their areas are different. Actually, however, the temperature range for which the rate of nucleation is measured is very small and the variation in r^* or r^*_s is correspondingly small (e.g., 5 to 10 per cent). Hence it may be assumed, with fair accuracy, that all supercritical patches have the same area so that equation (10) satisfactorily describes the isothermal dependence of x on t for the solidification of a collection of uniform droplets containing on the average m supercritical patches/droplet. As $t \to \infty$, x approaches a limiting value, $x_a < 1$ given by:

$$x_a = 1 - \exp(-m). \tag{11}$$

The fraction of droplets containing no supercritical patches is therefore $1 - x_a$. To obtain a more convenient relation for analysis we derive from (10):

$$dx/(1 - x)\,dt = f = cm \exp(-ct) \tag{12}$$

and

$$\ln f = \ln(cm) - ct. \tag{13}$$

Suppose that instead of a uniform droplet diameter we have a distribution of diameters such that at time t the fraction of droplets of diameter D that have not solidified is x_D. When $t = 0$, $x_D = x_D^0$ and D' is defined by:

$$\tfrac{1}{2} = \int_0^{D'} x_D^0 dD. \tag{14}$$

Equation (12) becomes:

$$f = \{cm'[F(t, D)]/(1 - x)D'^2\}\exp(-ct) \tag{15}$$

where

†The theory to be developed is easily extended to the case where the number of patches is proportional to the liquid volume.

$$F(t, D) = \int_0^\infty x_D D^2 dD, \tag{16}$$

$$m' = \left[\int_0^\infty x_D{}^0 D^2 dD \right] \Big/ D'^2 \tag{17}$$

and

$$\int_0^\infty x_D dD = 1 - x. \tag{18}$$

x_a is now given by:

$$x_a = 1 - \int_0^\infty x_D{}^0 \exp[-m'(D/D')^2] dD. \tag{19}$$

Although our theory and the earlier one due to Kimball give formally identical expressions for the isothermal dependence of x on t, there are important differences in the predictions of the two theories. As described by Pound and La Mer, Kimball's theory seems to require that m be indepedent of ΔT, while our theory requires that m increase with ΔT, according to equations (6) and (9). According to Kimball's theory, x will be perceived to approach an asymptote x_a substantially less than unity and perceptibly greater than zero only for systems in which (approximately) $0.01 < m < 3$ where m is the number of catalyst units/droplet characterized by the smallest θ value. Our theory predicts that $0 < x_a < 1$ if $0 \leqslant m < 3$ (approximately) when c becomes perceptible. Therefore, Kimball's theory seems to predict that the perception of $0 < x_a < 1$ should be a very improbable occurrence while our theory predicts that such perception should be possible in a fair number of instances.

Comparison of Theory and Experience

Mercury Droplets Infected with HgX Patches

Mercury droplets coated with mercury laurate or mercury stearate become infected in time with patches of a decomposition product, HgX (believed to be mercury oxide formed by hydrolysis of the carboxylates), that is a very powerful catalyst for the formation of mercury crystal nuclei. Transformation nuclei formed rapidly from these patches at only 2–4° supercooling. The fraction x of droplets solidified quickly approached an asymptote $x_a < 1$ almost as soon as the droplets reached bath temperature so that the essential features of the transformation were described by $x_a = f(\Delta T)$, where x_a increases with increasing ΔT. This type of transformation in which time does not enter into the description is called "athermal" and has been recognized in crystalline media [7] and designated the "athermal martensite transformation."

The interpretation of these results is that c is perceptible and in fact very large, at a value of ΔT which corresponds to a value of m that is essentially zero. When supercooling is increased sufficiently to make x_a perceptible ($m > 0.02$ approximately) all the patches are already covered with crystalline mercury. Thus the potential transformation nuclei are fully formed before any transformation is perceptible. These potential nuclei become active transformation nuclei immediately when ΔT is increased sufficiently to make r^* (or r^*_s) $= R$.

Because of the athermal nature of the transformation, c cannot be determined but n_A can be evaluated quite accurately from x_a. The value of $n_A{}^*$ calculated from the earlier data [1] (sample A) is approximately given by:

$$n_A{}^* = a \exp(\beta \Delta T) \tag{20}$$

where a and β are constants. Combining equations (2), (5) and (6) we have

$$n_A = a \exp[b/R] \tag{21}$$

where $b = -2\sigma\beta/\Delta S_v$.

The droplets of sample A were 100 per cent infected with HgX patches. In certain other samples a substantial fraction of the droplets were not infected at all. Therefore, it is concluded that the

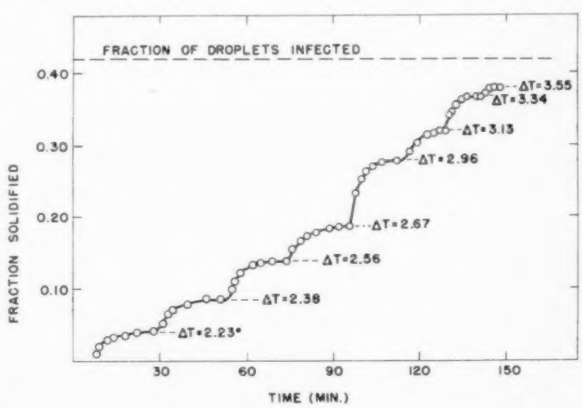

FIGURE 1. Fraction of mercury droplets solidified with successively increasing supercooling. 42 per cent of the droplets are infected with HgX patches. (Sample B).

patch sizes must be distributed about some most probable value $R = R_m$ and that equation (21) does not give a complete description of the distribution. In order to obtain such a description $x_a = f(\Delta T)$ was measured on a sample (B) in which 42 per cent of the droplets were infected with HgX. In this experiment† the sample was maintained at a cons-

†This experiment was performed by Mr. W. A. Rocco of this laboratory.

tant temperature until $x \rightarrow x_a$ then cooled to a slightly lower temperature and again held until $x \rightarrow x_a$. This procedure was repeated until nearly all of the infected droplets had solidified. The results are shown in Figure 1.

The values of x_a obtained from these data were substituted into equation (11) to obtain m. $n_A{}^*$ was calculated† from equation (9) with $D = D' = 4.0 \times 10^{-4}$cm. $R = r^*$ corresponding to these $n_A{}^*$ values was calculated from equations (2) and (5) using the value of σ calculated from earlier results [1]. n_A is plotted against R and ΔT in Figure 2.

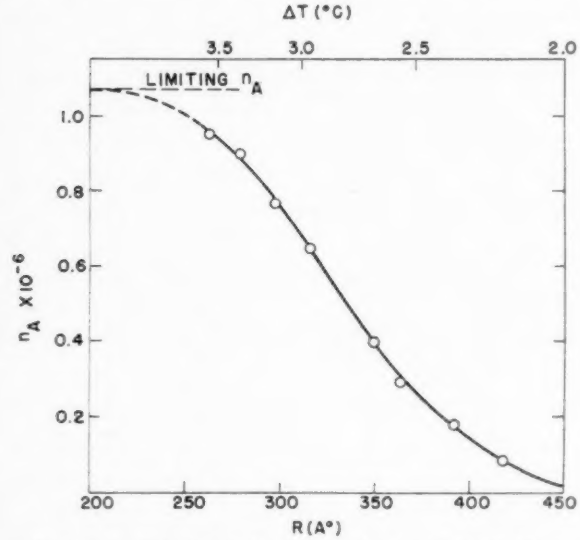

FIGURE 2. Calculated size distribution curve for HgX patches on mercury droplets of sample B.

$n_A = f(R)$ is a sigmoidal relation that is fairly symmetrical around $R = R_m$. The slope of $n_A = f(R)$ is satisfactorily described by:

$$(22) \quad dn_A/dR = (7.7 \times 10^{11}) \exp[-1.8 \times 10^{12}(R - R_m)^2]\text{cm}^{-3}$$

where $R_m = 3.3 \times 10^{-6}$cm. and $n_A = 5.3 \times 10^5$ cm.$^{-2}$ at $R = R_m$. The range of patch radii, 250 to 450Å, seems plausible.

Solidification of Tin Droplets Coated with Tin Oxide

Pound and La Mer [2] established that the major fraction of nuclei for the solidification of oxide-coated tin droplets formed isothermally. The rate determining step is the formation of a tin nucleus on a supercritical patch (thermal nucleation). Crystalline tin may also coat subcritical patches but these cannot serve as transformation nuclei. Therefore, it follows that the solidification rate at a given temperature, T_1, and extent of transformation x will be more rapid when the sample is quenched to T_1 after having been held at a temperature a few tenths of a degree above T_1 than if the sample is quenched to T_1 from above the melting temperature.

Pound and La Mer [2] established that two of their isotherms could be described approximately by the Kimball equation (10) with m increasing with ΔT. They gave no explanation for the dependence of m on ΔT. According to equation (13), ln f should be a linear function of t. We have measured f between $x = 0.3$ and $x = 0.7$ for the four of Pound and La Mer's isotherms corresponding to the greatest supercooling and the droplet size distribution corresponding to $D' = 3.75$ microns (D between 2.5 and 5.0 microns). Figures 3, 4, 5, and 6 show ln f

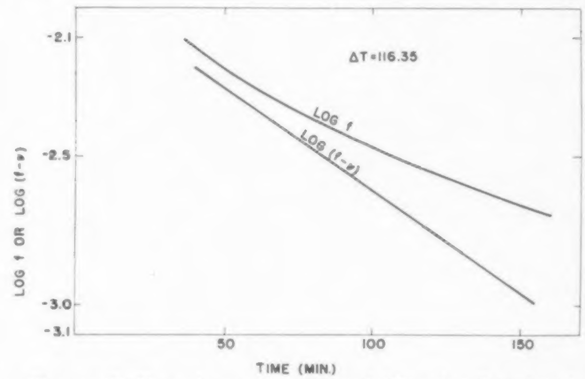

FIGURE 3. Test of equations (18) and (20) using Pound and La Mer's data on the solidification of oxide-coated tin droplets ($\Delta T = 116.35$).

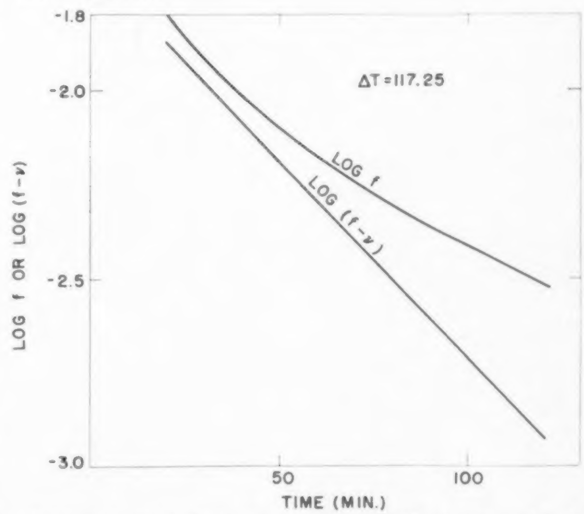

FIGURE 4. Test of equations (18) and (20) using Pound and La Mer's data on the solidification of oxide-coated tin droplets ($\Delta T = 117.25$).

†It was established from the droplet size distribution that m values calculated from equations (11) and (19) did not differ to an important extent.

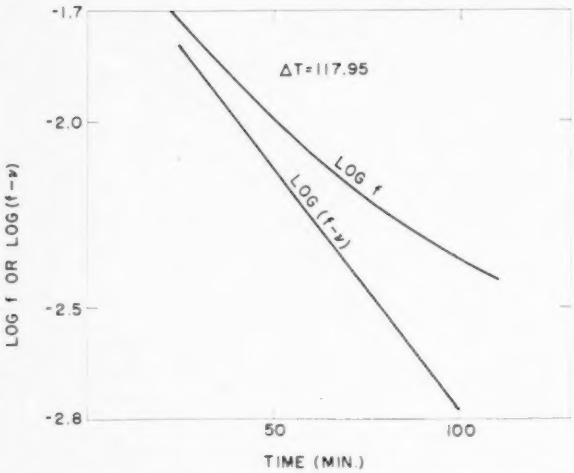

FIGURE 5. Test of equations (18) and (20) using Pound and La Mer's data on the solidification of oxide coated tin droplets ($\Delta T = 117.95$).

as a function of t for each of the four ΔT values. In all cases f and hence the transformation rate dx/dt, tends to be larger at the longer times than predicted by the Kimball equation. The existing non-uniformity of droplet size would cause f to fall off more sharply with time (see equation (15)) than predicted by the Kimball equation.

However, these results and the theory are easily reconciled by taking into account the auxiliary

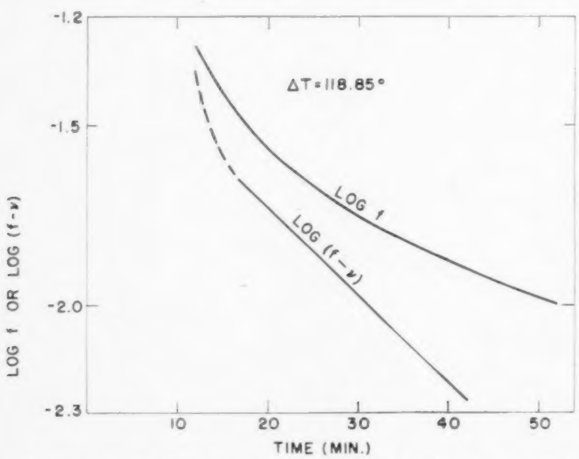

FIGURE 6. Test of equations (18) and (20) using Pound and La Mer's data on the solidification of oxide-coated tin droplets ($\Delta T = 118.85$).

steady nucleation process suggested by Pound and La Mer. Let the frequency of the auxiliary nucleation be ν per droplet; then

$$f = cm \exp(-ct) + \nu \tag{23}$$

and

$$\ln(f - \nu) = \ln(cm) - ct. \tag{24}$$

By proper selection of ν a good straight-line relation between ln $(f - \nu)$ and t is obtained for each of the four values of ΔT. These relations are shown in Figures 3, 4, 5 and 6.

Thus each of Pound and La Mer's isotherms can be satisfactorily described by three parameters c, m, and ν, each of which is a function of ΔT and droplet size. m is the number of supercritical patches per droplet. c is given by equation (8) and is the frequency of forming a tin nucleus on a patch. ν is a steady nucleation frequency per droplet that may correspond to the frequency of homogeneous nucleation or possibly to the heterogeneous nucleation frequency per area of inactive surface.

The values of c, ν, and m that describe Pound and La Mer's data are summarized in Table I. The un-

TABLE 1

NUMERICAL VALUES OF CONSTANTS THAT DESCRIBE POUND AND LA MER'S DATA

ΔT(°C)	m	c (sec^{-1})	ν (sec^{-1})
107.65	0.090		
110.85	0.20		
113.85	0.40		
116.35	0.74	2.64×10^{-4}	1.67×10^{-5}
117.25	0.87	4.05×10^{-4}	3.00×10^{-5}
117.95	1.10	5.00×10^{-4}	4.24×10^{-5}
118.85	1.08	9.5×10^{-4}	11.6×10^{-5}

certainty in each value is of the order of $\pm$ 10 per cent. There is an additional uncertainty due to the neglect of the non-uniformity of the droplet size. It is hoped that this uncertainty is minimized by the evaluation of f in the vicinity of $x = 0.5$ ($x = 0.3$ to $x = 0.7$) for all four isotherms. Also listed in the table are m values calculated from x_a for the three isotherms corresponding to the smallest ΔT's. This calculation is approximately valid since the contribution of ν to the rate is less the less is ΔT.

Pound and La Mer's isothermal results for four different droplet size distributions indicate that m is proportional to droplet area [2].† Values of $n_A{}^* = m/\pi D'^2$ were calculated from the m values listed in Table I, which correspond to $D' = 3.75 \times 10^{-4}$ cm. As a function of ΔT, $n_A{}^*$ is satisfactorily described by equation (20) with $a = 1.41 \times 10^{-6}$ cm^{-2} and $\beta = 0.238$°K^{-1}. a and β were calculated from the constants of the straight line obtained by plotting log $n_A{}^*$ against ΔT (see Fig. 7). From equation (21) and the value of σ estimated by Pound and La Mer

†This fact was established independently by F. C. Frank.

we obtain the following expression for n_A:

(25) $n_A = 1.41 \times 10^{-6} \exp[3.14 \times 10^{-6}/R] cm^{-2}$.

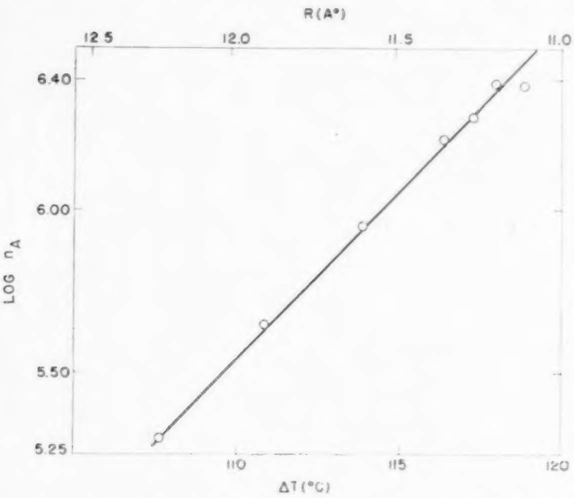

FIGURE 7. Calculated size distribution curve for the patches that catalyzed the formation of tin crystal nuclei in Pound and La Mer's sample.

Log c and log ν are plotted against $1/(\Delta F_v)^2T$, where ΔF_v is expressed in ergs/c.c., in Figure 8. c is described by the equation:

(26) $c = 10^{11\pm6} \exp[-1.74 \times 10^6/(\Delta F_v)^2kT]$,

and ν by:

(27) $\nu = 10^{17\pm6} \exp[-2.60 \times 10^6/(\Delta F_v)^2kT]$.

Now the area of a patch of critical size is of the order of 10^{-13} cm^2, hence I_p the frequency of nucleation per cm^2 of patch is (see equation (8)):

(28) $I_p = K_s \exp[-1.74 \times 10^6/(\Delta F_v)^2kT]$

where $K_s = 10^{24\pm6}$ cm^{-2} sec^{-1}. This value of K_s is in fair agreement with the value $10^{27.5}$ cm^{-2} sec^{-1} predicted by the theory of heterogeneous nucleation [1].

ν might be interpreted as the frequency of homogeneous nucleation or the frequency of heterogeneous nucleation on an inactive surface. If we assume homogeneous nucleation:

(29) $\nu/v_D' = I = K_v \exp[-2.60 \times 10^6/(\Delta F_v)^2kT]$

where I = nucleation frequency per volume and v_D' is the volume of a droplet of diameter $D' = 3.75 \times 10^{-4}$cm. To describe the data on this basis $K_v = 10^{27\pm6}$ cm^{-2} sec^{-1}, a value in poor agreement with $K_v = 10^{36}$ predicted by the theory of homogeneous nucleation [1].

Assuming heterogeneous nucleation on the inactive surface of the droplet we obtain:

(30) $\nu/a_D' = I_s = K_s \exp[-2.60 \times 10^6/(\Delta F_v)^2kT]$

where I_s is the nucleation frequency per area of inactive surface and a_D' is the area of the droplet of diameter D'. K_s is found to be $10^{23.4\pm6}$ cm^{-2} sec^{-1} in fair agreement with the value $10^{27.5}$ predicted by the theory of heterogeneous nucleation.

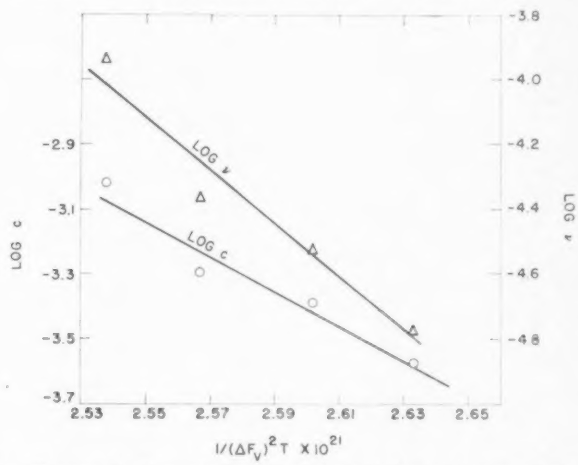

FIGURE 8. Dependence of ν and c, for the nucleation of tin crystals in Pound and La Mer's sample, upon supercooling.

Crystallization of Small Water Droplets

Dorsch and Hacker [8] have measured the initial freezing temperature, T_i, of water droplets as a function of their diameter D and found that T_i decreased with decreasing D. In order to explain these results Levine [9] postulated that a variety of types of units that catalyze ice nucleation ordinarily exist in water, each variety characterized by a particular ΔT corresponding to the initiation of freezing. Let n_v be the number of units/volume that initiate freezing at a supercooling of ΔT or less. Levine showed that the dependence of T_i on D is satisfactorily described by assuming n_v proportional to exp $(\beta\Delta T)$.† He gives no theory for the increase of n_v with ΔT.

One possible interpretation for the dependance of n_v on ΔT in the freezing of water is that nucleation is effected by patches characterized by a single θ and a size distribution function of the form $n_v = a$ exp (b/R). However, Dorsch and Hacker made no

†The formal analogy between Levine's statistical theory for the initiation of freezing and Weibull's [10] (see also Fisher and Hollomon [11]) theory for the stress specimen-size relationship in brittle fracture is noteworthy. According to Griffith [12] brittle fracture is initiated by microcracks. The larger the radius, r, of the crack the less is the fracture stress. Weibull showed that the experimental stress-size relationship can be explained on the assumption that $n_A = a$ exp (b/r) where n_A is the number of microcracks per area having a radius $\geqslant r$.

quantitative measurements on the time dependence of solidification of the droplets as a function of D and ΔT. It is possible, therefore, that the catalytic units responsible for solidification in their experiments were supercritical at all values of ΔT. The dependence of n_v on ΔT, deduced from their results, can be accounted for on the assumption of a statistical distribution of catalyst units with respect to the contact angle, $\theta[n_v = f(\theta)]$ such that the number per volume, n_v, characterized by a contact $< \theta$ increases with increasing θ.

The temperature coefficient of the rate of nucleation I_s on a particular catalyst surface is very large so that I_s changes from an imperceptible value to a magnitude too large to measure over 2–3° temperature range. Hence to a gross approximation a catalyst unit characterized by a given θ may also be characterized by a particular value of ΔT.

Conclusions

The multiplicity in crystal nucleation frequency that has been observed for the solidification of small droplets is readily accounted for by the patch nucleation theory with the use of no more than two fundamental nucleation frequencies for a given dispersion at a given temperature. It is shown that the data are described by plausible distributions of patches with size. Also the theory satisfactorily explains the athermal formation of crystal nuclei in solidification processes.

Although the existing data are accounted for on the assumption that the patches are distributed over the droplet surface, the surfaces of very small particles suspended in the droplet might under certain circumstances constitute the patches. Formally the theory is analogous for suspended particles and patches in the droplet surface.

Acknowledgement

The author is pleased to acknowledge valuable discusssions with E. W. Hart in developing the content of this paper.

References

1. Turnbull, D. J. Chem. Phys., **20** (1952) 411.
2. Pound, G. M. and La Mer, V. K. J. Amer. Chem. Soc., **74** (1952) 2323.
3. Turnbull, D. J. Chem. Phys., **20** (1952) 1327.
4. Turnbull, D. J. Chem. Phys., **18** (1950) 198.
5. Reiss, H. J. Chem. Phys., **18** (1950) 529.
6. Kimball, G. E. Private communication to Pound and La Mer [2].
7. Fisher, J. C., Hollomon, J. H., and Turnbull, D. Trans. A.I.M.E., **185** (1949) 691.
8. Dorsch, R. G. and Hacker, P. T. Nat. Advisory Comm. Aeronaut. Repts. Tech. Mem. Notes (1950) 2142.
9. Levine, J. Nat. Advisory Comm. Aeronaut. Repts. Tech. Mem. Notes (1950) 2234.
10. Weibull, W. Roy. Swed. Inst. Eng. Research, No. 151 (1939).
11. Fisher, J. C. and Hollomon, J. H. Metals. Tech., **14** (1947), no. 5.
12. Griffith, A. A. Phil. Trans. Roy. Soc., **221A** (1921) 163.

MARTENSITE*

F. C. FRANK †

In discussing the martensite transformation, it is advantageous to adopt a face-centered tetragonal unit cell for martensite. The empirical observations about lattice orientation suggest that each close-packed plane of the α-phase meets a close-packed plane of the γ-phase edge on in the surface of contact, and that in the Kurdjumov-Sachs case this meeting occurs in close-packed rows. Assuming this, and using the known lattice parameters, one may calculate the lattice orientation and habit plane, both agreeing with observation within experimental error. This picture of the surface of contact automatically demands the presence of a grid of screw dislocations, parallel to the common close-packed rows. The motion of these dislocations generates Bowles' invisible shear.

MARTENSITE

Il est avantageux d'adopter dans la discussion de la transformation martensitique, une maille tétragonale à faces centrées. Les observations empiriques concernant l'orientation du réseau, font croire, que chaque plan compact de la phase α rencontre un plan compact de la phase γ suivant l'arrête dans la surface de contact, et que dans le cas de Kurdjumov-Sachs cette rencontre a lieu suivant des rangées compactes. En admettant ceci et en employant les paramètres de réseau connus, il est possible de calculer l'orientation du réseau et le "habit plane," tous les deux étant, à l'erreur expérimentale près, en accord avec les observations. Cette représentation de la surface de contact entraine automatiquement la nécessité de la présence d'un réseau de dislocations hélicoïdales (screw dislocations) parallèles à la rangée compacte commune. Le mouvement de ces dislocations engendre le cisaillement invisible de Bowles.

MARTENSIT

Es ist vorteilhaft, die flächenzentrierte, tetragonale Elementarzelle des Martensits der Diskussion der Martensit Transformation zu Grunde zu legen. Die empirischen Beobachtungen der Gitterorientierungen deuten darauf hin, dass jede dichtest besetzte Gitterebene der α-Phase kantenweise auf eine dichtest besetzte Gitterebene der γ-Phase in der Berührungsfläche trifft, und dass im Kurdjumov-Sachs Fall dieses Zusammentreffen entlang dichtest besetzter Gittergraden erfolgt. Unter dieser Annahme und mit den bekannten Gitterkonstanten kann man die Orientierung des Gitters und die Habitus-Ebenen berechnen. Beide Berechnungen stimmen mit den Beobachtungen im Rahmen der experimentellen Fehlergrenzen überein. Dieses Bild einer Berührungsfläche verlangt automatisch die Anwesenheit eines Gitters von Schraubenversetzungen das den gemeinsamen dichtest besetzten Gittergraden parallel ist. Die Bewegung dieser Versetzungen führt zu Bowles' Scherung.

1. Introduction

Despite much good work upon it, the martensite problem is not yet solved. Apart from the direct analysis of experimental observations (no mean achievement, incidentally) the culmination of previous studies (Bain [1]; Kurdjumov and Sachs [2]; Greninger and Troiano [3]; Jaswon and Wheeler [4]; Bowles [5]) gives answers to partial questions such as: "Given an observed relative orientation of old and new lattices in the transformation, what property distinguishes the observed habit plane?" or "Given the observed lattice orientation, what system of probable movements will bring it about; and can these be separated into those producing the observed mass motions, and others occurring invisibly?" We may reasonably wish to answer the question: "Given the lattice constants of α and γ phases, what determines the natural habit, motions, and resulting orientation when the transformation occurs?" This paper makes some progress towards that goal.

2. The Lattice Description of Martensite

Martensite is customarily described in terms of a body-centered tetragonal unit cell, for the excellent reason that it is closely related to body-centered cubic α-iron. However, when it is tetragonal, we shall lose nothing by adopting another unit cell and describing it as face-centered tetragonal: when we are considering its formation from austenite it may be profitable to emphasize its relationship to face-centered cubic γ-iron. The relationship between the two unit cells, and the standard axes we shall adopt, are shown in Figure 1. In the body-centered

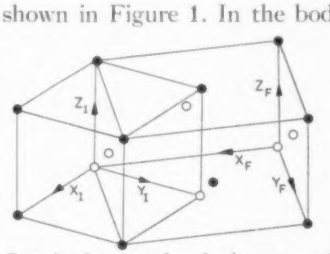

FIGURE 1. Standard axes for body-centered tetragonal lattice, $(c/a)_I = K$, = face-centered tetragonal lattice, $(c/a)_F = K/\sqrt{2}$

description (for which we use the conventional suffix I) we have $(c/a)_I$ varying linearly with carbon content from 1 at zero carbon to 1.08 at 1.75 wt. per cent carbon. In the face-centered description (suffix F) we have $(c/a)_F$ varying from $\sqrt{\tfrac{1}{2}} = 0.707$ . . . to $1.08\sqrt{\tfrac{1}{2}} = 0.763$ . . . .

We may usefully tabulate conversion formulas from one system of reference to the other. With the

*Received August 5, 1952.

†The H. H. Wills Physical Laboratory, University of Bristol, England.

axes standardized as in Figure 1, the vectors

$$(1, 0, 0)_I = (\tfrac{1}{2}, \tfrac{1}{2}, 0)_F$$
$$(0, 1, 0)_I = (-\tfrac{1}{2}, \tfrac{1}{2}, 0)_F \qquad (1)$$
$$(0, 0, 1)_I = (0, 0, 1)_F$$

Hence for transformations of *points* or *directions:*

$$(2) \qquad \begin{pmatrix} x \\ y \\ z \end{pmatrix}_F = \tfrac{1}{2}\begin{pmatrix} x - y \\ x + y \\ 2z \end{pmatrix}_I = \tfrac{1}{2}\begin{pmatrix} 1 & \bar{1} & 0 \\ 1 & 1 & 0 \\ 0 & 0 & 2 \end{pmatrix}\begin{pmatrix} x \\ y \\ z \end{pmatrix}_I$$

The reciprocal transformation to this one is

$$(3) \qquad \begin{pmatrix} x \\ y \\ z \end{pmatrix}_I = \begin{pmatrix} x + y \\ -x + y \\ z \end{pmatrix}_F = \begin{pmatrix} 1 & 1 & 0 \\ \bar{1} & 1 & 0 \\ 0 & 0 & 1 \end{pmatrix}\begin{pmatrix} x \\ y \\ z \end{pmatrix}_F$$

The equation of a plane $(h\,k\,l)_I$ is

$$(4) \qquad h\,x_I + k\,y_I + l\,z_I = D$$

that is,

$$(5) \qquad (h - k)x_F + (h + k)y_F + l\,z_F = D.$$

Thus for transformations of *planes*

$$(6) \qquad \begin{pmatrix} h \\ k \\ l \end{pmatrix}_F = \begin{pmatrix} h - k \\ h + k \\ l \end{pmatrix}_I = \begin{pmatrix} 1 & \bar{1} & 0 \\ 1 & 1 & 0 \\ 0 & 0 & 1 \end{pmatrix}\begin{pmatrix} h \\ k \\ l \end{pmatrix}_I$$

and the reciprocal of this transformation is

$$(7) \qquad \begin{pmatrix} h \\ k \\ l \end{pmatrix}_I = \tfrac{1}{2}\begin{pmatrix} h + k \\ -h + k \\ 2l \end{pmatrix}_F = \tfrac{1}{2}\begin{pmatrix} 1 & 1 & 0 \\ \bar{1} & 1 & 0 \\ 0 & 0 & 2 \end{pmatrix}\begin{pmatrix} h \\ k \\ l \end{pmatrix}_F$$

3. Empirical Martensite Orientations

The observed martensite orientations (summarized by Bowles and Barrett [7]) when expressed in terms of the face-centered α-lattice, assume particularly simple forms

Fe–C, (0.5–1.4 wt. per cent C); the Kurdjumov-Sachs relationship:

$$(111)_\gamma \parallel (111)_{\alpha F};\ [01\bar{1}]_\gamma \parallel [01\bar{1}]_{\alpha F}$$

associated habit plane $\{522\}_\gamma$; presumed $(522)_\gamma$

Fe-C (1.4–1.8 wt. per cent C):

Unknown orientation: habit $\{925\}_\gamma$ approx.

Fe-Ni (27–34 wt. per cent Ni); the Nishiyama relationship:

$$(111)_\gamma \parallel (111)_{\alpha F};\ [11\bar{2}]_\gamma \parallel [11\bar{2}]_{\alpha F}$$

Habit $\{925\}_\gamma$ approx.

Fe–Ni–C (22 wt. per cent Ni, 0.8 wt. per cent C): an intermediate relationship found by Greninger and Troiano:

$$(111)_\gamma \parallel (111)_{\alpha F} \qquad \text{(within } 1°)$$
$$[5, 12, \overline{17}]_\gamma \parallel [5, 12, \overline{17}]_{\alpha F}$$

(if expressed in integers, presumably irrational) Habit $(15, 3, 10)_\gamma$ (if expressed in integers, presumably irrational).

The habit planes are only known in general indices except in Greninger and Troiano's example. They polished a section parallel to the thin martensite plate, and determined orientations by X-ray diffraction. (15, 3, 10) is 5° away from (925). The presumption of (522) for the Kurdjumov-Sachs case corresponds to a conclusion of Jaswon and Wheeler. This conclusion was based on the postulate of homogeneous deformation, but we shall see that it survives revision of this postulate.

Our chosen standard variants of the general lattice relationships, expressed in the customary form, are

Kurdjumov-Sachs:

$$(111)_\gamma \parallel (101)_{\alpha I};\ [01\bar{1}]_\gamma \parallel [11\bar{1}]_{\alpha I}$$

Nishiyama:

$$(111)_\gamma \parallel (101)_{\alpha I};\ [11\bar{2}]_\gamma \parallel [10\bar{1}]_{\alpha I}$$

Jaswon and Wheeler chose a different standard variant of the Kurdjumov-Sachs relationship, with the same planes, but with $[1\bar{1}0]_\gamma \parallel [11\bar{1}]_{\alpha I}$; that is, $[1\bar{1}0]_\gamma \parallel [01\bar{1}]_{\alpha F}$. This is an inelegant choice: it is obviously desirable to have the z-axis in γ correspond to the z-axis in α (which is a unique axis for carbon steels). We shall therefore not follow it. The Jaswon-Wheeler standard orientation may be converted into ours by a cyclic permutation of the γ-indices. $[1\bar{1}0]_\gamma$ (J.-W.) becomes $[01\bar{1}]_\gamma$ (this paper): $(225)_\gamma$ (J.-W.) becomes $(522)_\gamma$ (this paper): the point transformation

$$(8) \qquad \begin{pmatrix} x \\ y \\ z \end{pmatrix}_I = \begin{pmatrix} 1 & 1 & 0 \\ \bar{1} & 1 & 0 \\ 0 & 0 & 1 \end{pmatrix}\begin{pmatrix} x \\ y \\ z \end{pmatrix}_F \qquad \text{(this paper)}$$

becomes

$$(9) \qquad \begin{pmatrix} x \\ y \\ z \end{pmatrix}_I = \begin{pmatrix} 1 & 0 & 1 \\ 1 & 0 & \bar{1} \\ 0 & 1 & 0 \end{pmatrix}\begin{pmatrix} x \\ y \\ z \end{pmatrix}_F \qquad \text{(J.-W.).}$$

In the latter we recognize Jaswon and Wheeler's matrix τ.

4. The Hypotheses of Bain and of Jawson and Wheeler

Jaswon and Wheeler derived their matrix τ from the hypothesis that the old lattice changes into the new, in its observed (Kurdjumov-Sachs) orientation, with minimal relative motion of atoms in small regions.* Bowles has also verified the same result for the Nishiyama orientation. We see that it simply signifies that atoms of the face-centered cubic γ-lattice become *corresponding* atoms of the face-

*The final qualification is a necessary one, as we shall see presently.

centered tetragonal α-lattice. This was Bain's hypothesis, though he chanced to adopt the alternative description of γ-iron as body-centered tetragonal ($c/a = \sqrt{2}$) becoming body-centered cubic (or body-centered tetragonal with a smaller axial ratio) on transformation. Bain omitted to contemplate lattice rotations, and supposed that in each piece of martensite there were sub-microscopic regions "upset" along the x, y, and z axes in equal numbers. Determination of the orientations disposed of this hypothesis.

It is clear that when a plate undergoes a homogeneous uniaxial compression on an axis oblique to its plane, it may be made to fit approximately into its original space by a rotation, such that the normal to the plate moves away from the axis of compression, so that the plate is once more parallel to its original plane. Jaswon and Wheeler verified (as their second main conclusion) that the homogeneous deformation comprising a uniaxial compression which converts the old lattice into the new one, and the rotation which brings it into the observed (Kurdjumov-Sachs) orientation, brings the transformed (522) plane (actually the (4.9, 2, 2) plane) parallel to its old orientation. The corresponding result is not found for the Nishiyama orientation.

We have said that uniaxial compression coupled with the requisite rotation allows the transformed plate to fit *approximately* into its original space. It cannot do so exactly. For when a sphere undergoes uniaxial compression into a spheroid, (with accompanying transverse extension, since there is little change in volume) all diametral sections become ellipses, except one which becomes an expanded circle; and the major axis of all of them exceeds the original diameter. A moderate change in the thickness of a plate is elastically tolerable, but an increase in width is not, unless the plate cuts into the surrounding material. If it did this, it would protrude at free surfaces, or break the continuity of previously existing scratches. It does neither of these things, and we infer that additional deformations must occur.

A satisfying feature of Bain's "upsetting" of the lattice along the z-axis, noted by Jaswon and Wheeler, is that it brings carbon atoms immediately into their proper positions in the tetragonal martensite: for all 8-coordinated interstices, in which the carbon atoms reside, become 2-coordinated interstices, with nearest neighbours along the z-axis. This property will be preserved if there is additional deformation by slip (but not by twinning). The non-rotating property of a plane (say, the 522 plane) will be preserved if atomic motions in the additional deformation are all parallel to this plane.

5. Lattice Conformity: The Kurdjumov-Sachs Orientation

The characteristics of the martensite transformation very clearly indicate an orderly transfer of atoms from the one arrangement to the other, in rapidly succeeding planes. This requires the two lattices to meet in a uniform manner over the surface of contact.

A curious feature, common to the three observed martensite lattice relationships, is the parallelism of close-packed planes, $(111)_F$, which are nevertheless not habit planes. Since they are evidently connected in some way, it is a natural supposition that they meet edge to edge in the surface of contact. The suggestion is supported by the fact that in the two simpler relationships the parallel directions are important atom rows in these planes; which, moreover, lie in the habit plane, exactly, for the Kurdjumov-Sachs relationship ($[01\bar{1}]$ in (522)) and very nearly for the Nishiyama relationship ($[11\bar{2}]$ in (925)). However, this is impossible if the lattice relationships are precisely as stated, because the $(111)_{\alpha F}$ and $(111)_\gamma$ interplanar spacings are not equal. They differ by 1.63 per cent in iron, and from about 0.5 to 2 per cent in the various steels we have mentioned, being in each case smaller in the α-phase. There is a simple way out of this difficulty, which is to have the close-packed planes in the two lattices not exactly parallel, but bent through a small angle ψ where they cross the surface of contact. If this surface makes an angle ϕ with the $(111)_\gamma$ plane, and t_γ, t_α are the interplanar spacings, we have

$$(10) \qquad \frac{t_\alpha}{t_\gamma} = \frac{\sin(\phi - \psi)}{\sin \phi} = \cos\psi - \cot\phi \cdot \sin\psi$$

or, assuming ψ is small,

$$(11) \qquad \psi = (1 - t_\alpha/t_\gamma)\tan\phi.$$

Values of t are calculated from the lattice parameters by the formula

$$(12) \qquad t = c_F/(1 + 2\,c_F^2/a_F^2)^{\frac{1}{2}}.$$

For ϕ we may take 25° (the angle between $(522)_\gamma$ and $(111)_\gamma$) or 28° (the angle between $(15, 3, 10)_\gamma$ or $(925)_\gamma$ and $(111)_\gamma$), so that tan ϕ is about $\frac{1}{2}$. The required deviation ψ, a rotation by less than 1° of the $(111)_{\alpha F}$ pole, away from $(111)_\gamma$, towards the pole of the habit plane, would generally escape notice. Greninger and Troiano actually report a deviation of about 1° in approximately the required direction. This exceeds the deviation calculated

from the lattice constants, which is 0.3°. The proposed slight modification of the lattice relationships is so reasonable that we shall assume it to be correct hereafter.

Evidently the requirement of congruence of close-packed planes in the contact surface will not uniquely determine ϕ though it forbids values near to 90°. We shall next consider the congruence of close-packed rows. In the Kurdjumov-Sachs relationship these are parallel to each other and to the habit plane. It appears a probable requirement that these rows in the contact surface should conform to both lattices, or change from conformity with one to conformity with the other by a merely longitudinal displacement.

On examining projections (Figures 2 and 3) of the face-centered cubic and body-centered cubic lattices

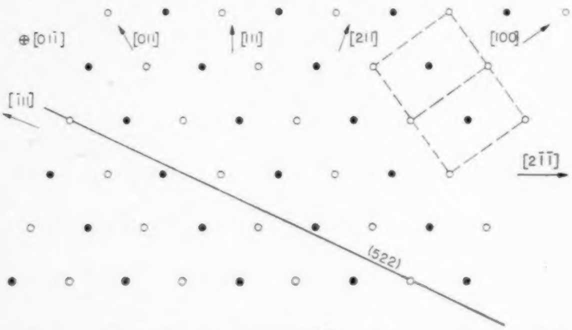

FIGURE 2. Projection along $[01\bar{1}]_F$ of face-centered cubic lattice.

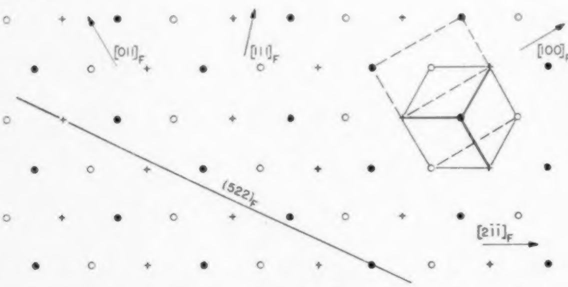

FIGURE 3. Projection along $[01\bar{1}]_F$ ($= [11\bar{1}]_f$) of body-centered cubic lattice: indices refer to face-centered description.

along their close-packed $[01\bar{1}]_F$ rows, without paying attention to the positions of atoms on these rows, we observe an array of equilateral triangles in the latter, and a closely similar array in the former, in which however each triangle has one angle of $70\frac{1}{2}°$ and two of $54\frac{3}{4}°$. The two projections differ essentially by a shear of $1/\sqrt{32}$ on the $(111)_F$ plane, an increase (by 6 to 7 per cent for the various steels) in the lateral spacing between $[01\bar{1}]_F$ rows in $(111)_F$ planes, and the small decrease in interplanar spacing which we have already dealt with. With a suitable obliquity of the contact surface between the two lattices, the change in lateral spacing between rows will just provide the requisite shear. Approximately, the suitable obliquity is given by

$$\tan \phi = \frac{\text{lateral contraction}}{\text{shear}} = 0.07\sqrt{32}$$
$$= \tan 21.6°.$$

When carbon is present, and the body-centered α-lattice is tetragonal, its projection along the close-packed rows is no longer an array of equilateral triangles but is intermediate in shape between Figure 2 and Figure 3. The requisite shear is thereby reduced, and ϕ is increased. This is offset by some decrease in the lateral contraction, so that for 1 per cent carbon ϕ increases to about 24°. The angle between $(522)_\gamma$ and $(111)_\gamma$ is 25.2°. Thus by postulating coincidence of $(111)_F$ planes and $(01\bar{1})_F$ rows in the contact surface, we predict what are substantially the observed lattice relationship and habit plane of martensite in this kind of steel. The approximate mode of calculation adopted here suffices to explain the principle. A more exact but less transparent treatment is given in section 7.

We now have to bring atoms in the $[01\bar{1}]$ rows into their correct positions along these rows. We meet an immediate difficulty, that the interatomic distances in these rows are not identical in the two lattices. They differ by the same amount, 1 or 2 per cent, as the interplanar spacings. There is no simple avoidance of this except to suppose that during the transformation this strain is taken elastically, and subsequently adjusted by plastic deformation. This is compatible with all the observations of minor slip and twinning accompanying the transformation, and will account for the large hysteresis in the reverse transformation. Moreover, the inception of this plastic deformation will probably bring the growth of the individual martensite plate to an end and sharp cessation of growth is one of the notable observed facts. If this is the case we ought not to have made our previous calculations with the lattice constants of martensite in equilibrium, but those of martensite stretched elastically 1 per cent in the $[01\bar{1}]$ direction (this figure being appropriate to 1 per cent carbon steel). Assuming for want of better information that martensite behaves approximately like an isotropic body with Poisson's ratio 1/3, the consequence will be a further decrease in interplanar spacing and in lateral spacing between $[01\bar{1}]$ rows by 1/3 per cent, so that ψ is increased by about 0.1° and ϕ by about 1°. Agreement with observation is thus improved. We assume therefore that the

$[01\bar{1}]$ rows preserve their length during the main transformation; but they require longitudinal displacement to bring the atoms into their proper positions in the new (slightly stretched) lattice.

Using the word "depth" to signify position along the $[01\bar{1}]_F$ direction, and measuring depth in interatomic spacings for such rows, we may note that all atoms in an $(011)_F$ plane of either lattice are at the same depth, modulo 1, but taken in successive (011) planes in the [011] direction they are at depths

$$0\ \tfrac{1}{2}\ 0\ \tfrac{1}{2}\ 0\ \tfrac{1}{2}\ 0\ \tfrac{1}{2}\ 0\ \tfrac{1}{2}\ 0\ \tfrac{1}{2}\ \ldots, \text{mod } 1,$$

in the γ-lattice, but

$$0\ \tfrac{2}{3}\ \tfrac{1}{3}\ 0\ \tfrac{2}{3}\ \tfrac{1}{3}\ 0\ \tfrac{2}{3}\ \tfrac{1}{3}\ 0\ \tfrac{2}{3}\ \tfrac{1}{3}\ \ldots, \text{mod } 1,$$

in the α-lattice. Formally a homogeneous shear depressing the successive planes by

$$0\quad 1/6\quad 2/6\quad 3/6\quad 4/6\quad 5/6\quad 6/6\quad 7/6\quad 8/6\quad 9/6\quad 10/6\quad 11/6\ldots$$

brings them into these positions: but this, involving large displacements in planes remote from the origin is not an acceptable kind of motion. Depressing them by

$$0\quad 1/6\quad 2/6\quad 3/6\quad -2/6\quad -1/6\quad 0\quad 1/6\quad 2/6\quad 3/6\quad -2/6\quad -1/6\ldots$$

is acceptable. This may be analysed into a uniform downward translation of 1/12, which would escape every method of observation, and a system of shears in stacks of six successive planes, thus:

$$-1/12\quad 1/12\quad 3/12\quad 5/12\quad -5/12\quad -3/12\quad -1/12\quad 1/12\quad 3/12\quad 5/12\quad -5/12\quad -3/12\ldots$$

These displacements are effected by a parallel grid of screw dislocations, lying along $[01\bar{1}]$ directions in the contact surface, and travelling in the direction [100] between every sixth pair of $(011)_F$ planes as shown in Figure 4. The slip direction is a normal one for either γ or α lattices. The slip plane is not a usual one in the γ-lattice, but is in α (it is $(\bar{1}12)_{\alpha I}$). The continuity of dislocation lines is preserved by uniting them with opposite screw dislocations on the other side of the plate, by short lengths of edge dislocation at its edges. These make up the "tilt boundary" between the relatively rotated but coherent lattices at these edges. At other edges of the plate new dislocation loops must be successively created as the plate expands. The way in which stresses at the edge of the plate suffice for the creation of further dislocation loops as required may be treated after the manner of Frank and Stroh's treatment of kink-bands [8].

There is a twin of our chosen standard martensite orientation in which the depth sequence in $(011)_{\alpha F}$ planes is

$$0\ \tfrac{1}{3}\ \tfrac{2}{3}\ 0\ \tfrac{1}{3}\ \tfrac{2}{3}\ 0\ \ldots, \text{mod } 1.$$

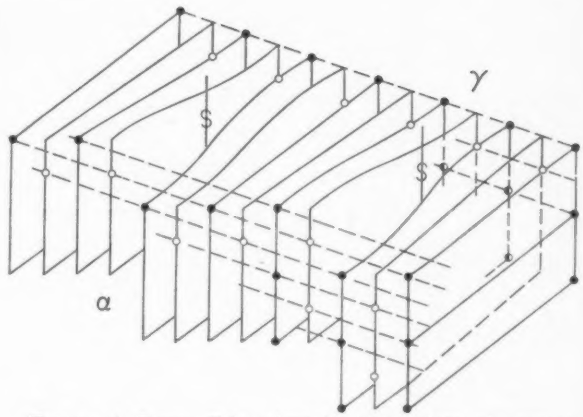

FIGURE 4. Screw dislocations in the surface of contact between γ and α lattices (Kurdjumov-Sachs relationship).

The vertical sheets are $(011)_F$ planes (a slight bend at the surface of contact is omitted from the diagram). Their upper edges are $[100]_F$ rows and their vertical edges $[01\bar{1}]_F$. The dislocation lines and their Burgers vectors are parallel to $[01\bar{1}]_F$. The front and back surfaces are $(100)_F$ planes. Filled (and half-filled) circles represent atoms in these planes while open circles represent the mid-points between atoms in $[100]_F$ rows. The upper surface, an $(01\bar{1})_F$ plane in γ becomes a staircase of these planes in α.

The necessary displacements for this are produced by dislocations of opposite sign.

6. Comparison with Bowles' Conclusions

We may now compare our results with those of Bowles. He worked from the phenomenological data, taking some clues from the atomic lattice properties, and sought an analysis into likely deformations which would produce the observed results. We have worked from the lattice properties, taking some clues from the observations, and have arrived at an essentially identical conclusion, our introduction of the angle ψ being the chief source of minor differences. He arrived at a "first distortion" with atomic motions in direction $[\bar{1}\bar{1}2]_A$, with undistorted plane $(225)_A$, and a "second distortion" (which is invisible) with atomic motions in direction $[11\bar{1}]_M$ and undistorted plane $(112)_M$. In our notation and standard orientation, these are $[2\bar{1}\bar{1}]_\gamma$, $(522)_\gamma$ and $[01\bar{1}]_{\alpha F}$, $(011)_{\alpha F}$. The first corresponds to our shear on $(111)_F$ planes, accompanied by change in lateral spacing: the second to our heterogeneous shear generated by motion of $[01\bar{1}]_F$ screw dislocations on $[011]_F$ planes. A notable difference is that in our mode of description we do not have to specify this motion as occurring *second*, and in the α-lattice: rather we visualize the dislocations moving in the transformation front, and the deformations occurring simultaneously.

The distinction between first and second deformations is one rendered necessary when deformations are combined by matrix methods, referred to fixed

coordinates: this does not mean that it is a physically necessary distinction.

7. Calculation of the Habit Plane of a Coherent Transformation from the Lattice Parameters

Let two lattices denoted by the suffices 1, 2 meet in the contact plane C, so that certain rows of the family R, lying in C, belong to both lattices. All rows R_1, R_2 are therefore parallel. Let P_1, P_2 be corresponding families of planes, such that every m^{th} P_1 plane meets every m^{th} P_2 plane edge to edge in one of the common rows R. Let Q_1, Q_2 be a second family of corresponding planes, such that every n^{th} Q_1 plane meets every n^{th} Q_2 plane edge to edge in the same common rows R. Figure 5 shows a projection

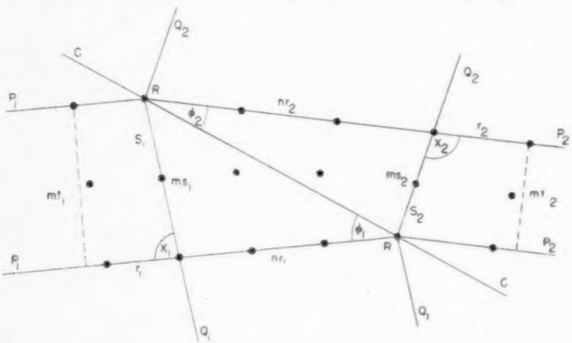

FIGURE 5

of the two lattices along R. Planes P_1 make angles ϕ_1, with the plane C, and angles χ_1 with planes Q_1. r_1, s_1, are the spacings between rows R_1 in P_1 and Q_1 respectively. The spacing between successive planes P_1 is

(13) $$t_1 = s_1 \sin\chi_1$$

The corresponding definitions and formula apply also with suffix 2 throughout.

Now we have the following equations

(14) $$\frac{nr_1 \sin\chi_1}{\sin(\chi_1 - \phi_1)} = \frac{ms_1 \sin\chi_1}{\sin\phi_1} = \frac{nr_2 \sin\chi_2}{\sin(\chi_2 - \phi_2)} = \frac{ms_2 \sin\chi_2}{\sin\phi_2}.$$

Eliminating n and m, and using (13) gives us two equations for the two unknowns ϕ_1 and ϕ_2:

(15) $$t_1/\sin\phi_1 = t_2/\sin\phi_2$$

and

(16) $$r_1 \sin\chi_1/\sin(\chi_1 - \phi_1) = r_2 \sin\chi_2/\sin(\chi_2 - \phi_2)$$

which may be combined to give an alternative second equation

(17) $$\frac{r_1/t_1}{\cot\phi_1 - \cot\chi_1} = \frac{r_2/t_2}{\cot\phi_2 - \cot\chi_2}.$$

A particular combination of r, t and χ values may or may not allow a choice of ϕ_1 and ϕ_2 which satisfies these equations; e.g. in the simple case

$$\chi_1 = \chi_2 = 90°$$

we have the pair of equations (15) and

(18) $$r_1/\cos\phi_1 = r_2/\cos\phi_2.$$

Then the equations can always be satisfied if, and only if, $(r_2/r_1 - 1)$ and $(t_2/t_1 - 1)$ are of opposite sign.

In the special case of face-centered tetragonal lattices, applicable to the γ–α transformation in steel, when we identify the planes P as $(111)_F$, the planes Q as $(100)_F$ and the rows R as $[01\bar{1}]_F$ we have

(19) $$\tan\chi = (1 + a^2/c^2)^{\frac{1}{2}}$$

(20) $$t = c(1 + 2c^2/a^2)^{-\frac{1}{2}}$$

(21) $$r = \tfrac{1}{2}a(1 + 2c^2/a^2)^{\frac{1}{2}}\,(1 + c^2/a^2)^{-\frac{1}{2}}$$

or

(22) $$r \sin\chi = \tfrac{1}{2}a.$$

These lattice parameters are those of the face-centered description: i.e. for the α-phase

$$c_{\alpha F} = c_{\alpha I}$$

$$a_{\alpha F} = \sqrt{2}\, a_{\alpha I}$$

For γ-iron, $a_{\gamma F} = 3.562$A, $(c/a)_{\gamma F} = 1$
With 1.8 wt. per cent C, $a_{\gamma F} = 3.632$A, $(c/a)_{\gamma F} = 1$
For α-iron, $c_{\alpha F} = 2.860$A, $(c/a)_{\alpha F} = 1/\sqrt{2}$
With 1.8 wt. per cent C, $c_{\alpha F} = 3.080$A, $(c/a)_{\alpha F} = 1.082/\sqrt{2}$

For intermediate carbon contents, linear interpolation of the parameters suffices within experimental error.

8. Remaining Questions

This investigation is not yet completed. We may mention here the questions which remain to be asked, and the lines along which we may hope to answer them.

First, can the other observed martensite orientations and habits be interpreted along similar lines? At the time of writing it appears probable that the Greninger-Troiano relationship can be given an essentially similar interpretation. This involves dislocations intersecting the $(111)_F$ plane, which produces a geometrical situation less easy to analyze completely. No similar interpretation of the Nishiyama relationship has yet been found.

Since in the steels, the martensitic transformation can go in alternative ways, depending on alloy

composition and on temperature, we ought to find what determines the choice which is made. This is presumably determined at the nucleation of a martensitic plate. The important parameters governing nucleation are the magnitudes of volume- and surface-free energy. The former is influenced by the elastic strain which we have found to be present. This is a function of lattice parameters and therefore of composition. With regard to surface energy we have two separate considerations.

In the first place, we recognize that dislocations are present in the boundary. They will contribute a substantial proportion of the boundary energy, and this can be calculated to some degree of approximation. This part of the boundary energy will not be very sensitive to alloy composition, but will be different for different martensite orientations. A second part of the boundary energy, more sensitive to alloy composition, arises as follows. The habit plane determined by the principles set forth above is in general irrational; its orientation is a continuous function of lattice parameters. When the contact is on this plane the long-range stresses are minimized, but there may be substantial local stresses of alternating sign due to local misfit in the boundary. For certain compositions the contact surface determined in this way will approximate to a rational plane which minimizes these local stresses, so producing a minimum in the surface-free energy, and favoring the nucleation of martensite plates in the corresponding orientation.

Finally, it will be of interest to apply a similar analysis to martensitic transformation in other metals. It is worth mentioning that the task will be greatly simplified if, along with the determination of a lattice orientation, the determination of the corresponding habit plane, not merely in general indices, is available.

This study was made during a stay at the General Electric Research Laboratory in Schenectady during the summer of 1951, and would not have been carried out without the stimulus of conversation with John Fisher and other members of that very lively research group.

References

1. Bain, E. C. Trans. A.I.M.E., **70** (1924) 25.
2. Kurdjumov, G. and Sachs, G. Zeits. Phys., **64** (1930) 325.
3. Greninger, A. B. and Troiano, A. R. Trans. A.I.M.E., **140** (1940) 307; **185** (1949) 590.
4. Jaswon, M. A. and Wheeler, J. A. Acta Cryst., **1** (1948) 216.
5. Bowles, J. S. Acta Cryst., **4** (1951) 162.
6. Nishiyama, Z. Sci. Rep. Tôhoku Univ., **23** (1934) 638.
7. Bowles, J. S. and Barrett, C. S. Progress in Metal Physics, 3. Edited by B. Chalmers (London, Pergamon Press, 1952).
8. Frank, F. C. and Stroh, A. Proc. Phys. Soc. London, **65B** (1952) 811.

X-RAY LINE BROADENING FROM FILED ALUMINIUM AND WOLFRAM*

G. K. WILLIAMSON† and W. H. HALL†

Methods of analysis previously used in the interpretation of line broadening are discussed and are shown to be inadequate; more reliable methods being outlined. An analysis of published results using one of these methods suggests that the observed effects can be attributed to simultaneous small particle size and strain broadening. Measurements of the changes in intensity distribution have been made, using a Geiger counter spectrometer, in the spectra of cold worked aluminium and wolfram. The line breadths may be attributed to simultaneous small particle size and strain broadening, the latter predominating, particularly at the higher Bragg angles, and it is shown that the observed effects are produced by dislocations or some similar structural fault. The observed rise in the breadths of the high angle lines from annealed materials suggests that some dislocations remain after annealing. Fourier analysis of the line shapes in general merely confirm the results of the analysis of the line breadths, but in the case of the recovered specimens it suggests that the dislocations form into walls ("polygonization").

L'ELARGISSEMENT DES RAIES DE RAYONS X OBTENUES DES LIMAILLES D'ALUMINIUM ET DE TUNGSTENE

Les méthodes utilisées auparavant dans l'interprétation de l'élargissement des raies sont discutées et il est montré qu'elles sont inadéquates; des méthodes plus correctes sont indiquées. L'examen des résultats publiés, obtenus au moyen d'une des ces méthodes, fait croire que les effets observés peuvent être attribués en même temps à la petitesse des particules et à l'élargissement dû à la déformation. Les variations de la distribution d'intensité dans les spectres d'aluminium et de tungstène ont été mesurées au moyen d'un spectromètre à compteur Geiger. Les largeurs des raies peuvent être attribuées simultanément à la petitesse des particules et à l'élargissement dû à la déformation, cette dernière étant la plus importante, surtout aux plus grands angles de Bragg, il est aussi démontré que les effets observés sont dûs aux dislocations ou à un autre défaut structural, similaire. L'augmentation observée dans la largeur des raies à grand angle obtenues des matériaux recuits, fait croire, qu'une partie des dislocations reste après recuit. L'analyse de Fourier de la forme des raies confirme en général les résultats d'analyse de la largeur des raies, mais dans le cas des échantillons qui ont subi un recuit de restauration, cela conduit plutôt à la conclusion que les dislocations se rangent en plans (polygonisation).

DIE VERBREITERUNG DER ROENTGENINTERFERENZLINIEN VON ALUMINIUM- UND WOLFRAMSPAENEN

Die analytischen Methoden, die bisher zur Auswertung von Messungen der Linienverbreiterung von Röntgeninterferenzen benutzt wurden, werden diskutiert. Es wird gezeigt, dass sie unzureichend sind, und zuverlässige Methoden werden beschrieben. Analysiert man die in der Literatur veröffentlichten Daten nach einer dieser Methoden, so scheint die beobachtete Verbreiterung sowohl auf den Effekt der kleinen Teilchengrösse als auch auf innere Spannungen zurück zu gehen. Veränderungen in der Intensitätsverteilung der Feinstrukturdiagramme von kaltbearbeitetem Aluminium und Wolfram wurden mit Hilfe eines Zählrohr-Spektronometers gemessen. Die Linienverbreiterung kann auf die gleichzeitig vorhandenen Effekte kleiner Teilchengrösse und innerer Spannungen zurückgeführt werden; der Einfluss der Spannungen überwiegt, vor allem bei grossen Reflexionswinkeln. Es wird gezeigt, dass die beobachteten Effekte durch Versetzungen ("dislocations") oder ähnliche Kristallbaufehler hervorgerufen werden. Die beobachtete Verbreiterung der Linien grosser Reflexionswinkel in geglühten Materialien deutet darauf hin, dass nach der Glühung noch einige Versetzungen ("dislocations") im Material zurückbleiben. Fourieranalyse der allgemeinen Linienform bestätigt nur die Resultate der Analyse der Linienverbreiterung. Allein bei erholten Proben deutet sie darauf hin, dass sich die Versetzungen ("dislocations") zu Wänden zusammenschliessen ("Polygonisation").

Introduction

The cold working or plastic deformation of metals has been shown to produce appreciable changes in the intensity distribution of diffracted X-rays. The most prominent of these effects are changes in line shape and in integrated intensity, and previous workers have usually confined their studies to one or other of these topics. Changes in integrated intensity have been studied and discussed by Hall and Williamson [1] and it is the object of this paper to interpret, discuss and correlate the changes in line shape with the simultaneous measurements of integrated intensity reported previously.

Previous work suggests that the broadening is produced by either lattice strains alone, or by lattice strains and small particle size simultaneously. Stokes and Wilson [2] have shown that if the integral breadth of the strain distribution is ξ the corresponding spectral integral line breadth‡ β_s due to strains is

$$(1) \qquad \beta_s = 2\xi \tan \theta$$

where θ is the Bragg angle, a relation deduced by many earlier workers. In terms of the reciprocal lattice the effect of lattice strain is to broaden the reciprocal lattice points to a breadth β_s^* which varies linearly with the distance from the origin,

*Received August 12, 1952.

†Department of Metallurgy, University of Birmingham, England.

‡Spectral breadths are usually measured in terms of the dispersion χ (a scale of 2θ).

d^*, thus, since $\beta^* = \beta \cos \theta/\lambda$ and $d^* = 2 \sin \theta/\lambda$

$$\beta_s^* = \xi d^* \tag{2}$$

(Lipson [3]).

Particle size broadening has been shown by many investigators to obey the relation

$$\beta_P = \lambda/t \cos \theta \tag{3}$$

where λ is the X-ray wavelength, and t is a mean linear dimension of the particle defined by Stokes and Wilson [2], and has been called the apparent particle size by Jones [4]. The reciprocal lattice breadth β_P^* is a constant independent of d^* and equal to $1/t$.

Correction for experimental broadening necessarily introduced by imperfections of the camera and recording device have been discussed in detail by Jones [4]. Stokes and Wilson [2], Schull [5] and Stokes [6] have suggested and described Fourier methods of correction which require no *a priori* assumptions of experimental and broadening function line shapes.

Previous Work

Since the first report of line broadening by van Arkel [7] most of the published work has been held to support the view that broadening is due to randomly directed, slowly varying internal lattice strains. Wood [8; 9], Haworth [10], Brindley and Ridley [11], Brindley [12], Smith and Stickley [13], Stokes, Pascoe and Lipson [14], Megaw and Stokes [15] have used similar methods of interpretation in supporting the "strain" hypothesis. For example, Smith and Stickley [13] found that the physical broadening (i.e. the measured breadth corrected for experimental broadening) from wolfram was linear with tan θ (equation (1) for lattice strain effects) showing no dependence on wavelength (equation (3) for particle size broadening). The same results plotted against sec θ (equation (3)) indicated a negative value of β when λ sec θ was zero, a physically meaningless result.

For α-brass Smith and Stickley were able to resolve the variation in the apparent strain 2ξ with the indices of reflection in terms of the elastic anisotropy of brass. They suggested that $\xi/2$ should have an order of magnitude U/E, where U is the tensile strength and E Young's modulus, and found good agreement between these two values.

Further evidence in favour of the lattice strain theory, differing in the method of interpretation from the above, is that advanced by Warren and Averbach [16; 17]. They studied the changes in line shape rather than changes in line breadth and concluded that line broadening is due to lattice strains, which are not constant over distances greater than about 10 atomic diameters.

Evidence supporting the contention that some of the broadening is due to particle size is generally less convincing. Dehlinger and Kochendörfer [18] attempted some separation between particle size and strain effects by attributing the low angle broadening to small particle size. Bragg [19; 20] related the strength of metals to their apparent particle size and found good agreement between the observed values and those calculated from the data of Wood [21; 22], and Wood and Rachinger [23] have reported some dependence of the observed broadening upon wavelength, in agreement with equation (3).

Discussion of the Theories of Line Broadening

Any complete theory of line broadening must relate the cause of line broadening to the existing theories of work-hardening and plastic deformation, explain the apparent anomalies between the two conflicting interpretations just reviewed, and relate the line broadening to the changes in integrated intensity produced by cold work.

One useful approach is to consider a spectrum in which both strain and small particle size broadening occur simultaneously, to calculate the variation of the total broadening β with θ, and to apply the tan θ and sec θ criteria as used by previous workers supporting the strain hypothesis. In Figure 1, the

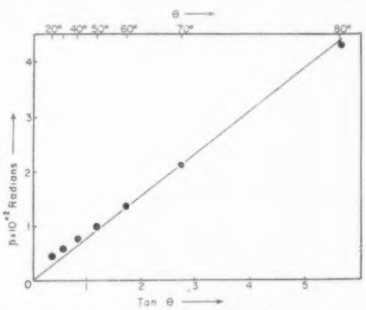

FIGURE 1. A plot of the physical broadening β due to simultaneous small particle size and strain broadening against tan θ. The calculated points correspond closely to a straight line through the origin despite the presence of appreciable particle size broadening.

values of β calculated for typical values of $t/\lambda = 250$, $2\xi = 0.5$ per cent, and on the assumption that the breadths are additive is plotted against tan θ. The plot is linear within a small margin of error, the greatest discrepancy being apparent below $\theta = \chi/2 = 30°$ where experimental accuracy is usually low. The plot of β against sec θ (Figure 2) shows that the

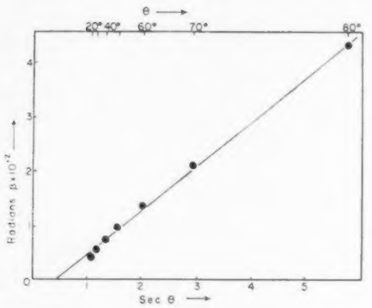

FIGURE 2. A plot of the physical broadening β due to simultaneous small particle size and strain broadening against sec θ. Any reasonable line through the calculated points gives a negative intercept.

high angle points correspond fairly closely to a straight line having a negative intercept at sec $\theta = 0$. Thus Figures 1 and 2 correspond closely to those previously reported experimental results which have been held to support the strain theory, although they have been calculated on the assumption that appreciable small particle size broadening exists in the spectrum; the tan θ and sec θ plots cannot therefore be regarded as satisfactory criteria in the interpretation of line broadening.

The interpretation of results obtained with many wavelengths may also be misleading since θ and λ are not independent variables.

In general β is given approximately by

$$\beta = 2\xi \tan \theta + \lambda/t \cos \theta, \tag{4}$$

and on substituting from the Bragg Law for λ then

$$\beta = (2\xi + 2d/t) \tan \theta \tag{5}$$

and the breadth is a linear function of tan θ *for any one reflection* (hkl) irrespective of the nature of the broadening (the values of 2ξ and $2d/t$ are dependent on the indices of reflection). This too is in agreement with the reported work (e.g. Brindley and Ridley, Smith and Stickley).

The interpretation in terms of small particle effects has been criticized by Stokes, Pascoe and Lipson [14] and by Stokes and Lipson [24] and also appears to be in doubt.

Hall [25] proposed a method of interpretation allowing some separation of particle size broadening and strain broadening. The method consists essentially in plotting the breadth of the reciprocal lattice points against their distance from the origin. Small particle size alone then gives a horizontal plot with an intercept $1/t$, and strain gives a line through the origin slope, ξ, if the strain distribution is isotropic.

The composite broadening produced by simultaneous small particle size and strain depends to some extent on the broadening functions of the separate effects. If both broadening functions are Cauchy curves (of the form $1/(1 + k^2x^2)$) then the breadths are additive and the plot is linear with slope ξ and intercept $1/t$ (curve a, Fig. 3). If the broadening

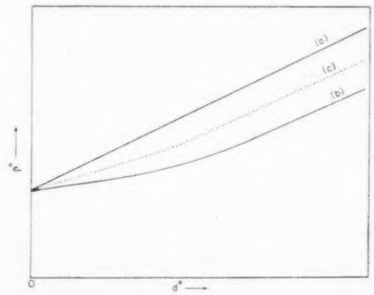

FIGURE 3. A plot of β^* ($= \beta \cos \theta/\lambda$) due to simultaneous small particle size and strain broadening against d^* ($= 2 \sin \theta/\lambda$). Curve (a) is obtained if the broadening functions are of the Cauchy type whilst curve (b) is that obtained if the functions are Gaussians. The dotted curve (c) represents an intermediate case discussed in the text.

functions are Gaussians, the squares of the breadths are additive and the graph is curved, being asymptotic to a line of slope ξ curving upwards near the origin to an intercept $1/t$, (curve b, Fig. 3). Since the curvature is dependent on the exact forms of the line shapes and broadening functions assumed, it is preferable to calculate the type of variation expected from various models. Such a calculation for a randomly strained crystal is discussed below, and it is of interest to note that Wilson [26] has generalised his calculation on diffraction by bent lammelae to show that there is a similar gradual transition from pure particle size broadening at $d^* = 0$ to strain broadening for large values of d^*.

Warren and Averbach [17] have shown that the strains and particle size of a sample can be deduced from the Fourier coefficients A_n of the broadening function and the breadth of the reciprocal lattice broadening function is given by

$$\beta^* = a_3^* \Big/ \sum_{-\infty}^{+\infty} A_n \tag{6}$$

It follows that it is possible to obtain the variation of the breadth throughout the reciprocal lattice by calculating the Fourier coefficients for a particular model. It is convenient to obtain Warren and Averbach's A_n by folding the coefficients due to particle size P_n with the corresponding coefficients due to internal strains, S_n. By choosing new axes any reflection can be made the *ool* reflection from planes of fundamental spacing a_3. If cells along columns perpendicular to the reflecting plane suffer displace-

ments which have a Gaussian distribution such that the mean square displacement for cells na_3 apart is $\langle Z_n^2 \rangle_{av.}$, then

$$S_n = \exp(-2\pi^2 l^2 \langle Z_n^2 \rangle_{av.}) \tag{7}$$

(Warren and Averbach, [17, equation 14]).

The term P_n is the ratio of the number of cells n spacings apart to the total number of cells, and thus for a crystal of length N_3 perpendicular to the reflecting planes

$$P_n = (N_3 - n)/N_3. \tag{8}$$

Thus the coefficient A_n due to both small particle size and internal strains is

$$A_n = (1 - n/N_3)\exp(-2\pi^2 l^2 \langle Z_n^2 \rangle_{av.}) \tag{9}$$

Quite generalized arguments show that as l approaches zero the strain component approaches unity and the breadth approaches pure particle size broadening

$$\beta^* \rightarrow \left(a_3 \sum_{-N_3}^{+N_3} 1 - n/N_3\right)^{-1} = \frac{1}{t}. \tag{10}$$

At large values of l, P_n becomes virtually constant compared to the rapid variation in S_n and the high angle broadening approximates to pure strain broadening. More particularly, if the strain varies slowly within the crystal then $\langle Z_n^2 \rangle_{av.} = n^2\bar{\eta}^2$ where $\bar{\eta}^2$ is the mean square strain and, when $l^2\bar{\eta}^2$ is small,

$$A_n \simeq (1 - n/N_3)(1 - 2\pi^2 l^2 \bar{\eta}^2 n^2) \tag{11}$$

whence

$$\sum A_n \simeq N_3(1 - \pi^2 l^2 \bar{\eta}^2/3) \tag{12}$$

and

$$\beta^* \simeq 1/t(1 - \pi^2 l^2 \bar{\eta}^2/3). \tag{13}$$

Hence to the extent that the approximation holds the plot of β^* against d^* (which equals la_3^*) intersects $d^* = 0$ at $1/t$ and curves away from the horizontal line representing particle size very rapidly with increasing d^*.

For a crystal in which $l^2\bar{\eta}^2$ is large,

$$\sum A_n = (1/l\sqrt{2\pi\bar{\eta}^2}) - (1/N_3 2\pi^2 l^2 \bar{\eta}^2) \tag{14}$$

and

$$\beta^* \backsim (d^*\sqrt{2\pi\bar{\eta}^2}) + (1/\pi t). \tag{15}$$

Thus for large values of $\bar{\eta}^2$ or d^* this approximates to $\beta^* = d^* \sqrt{(2\pi\bar{\eta}^2)}$ i.e. $\beta_x = 2\sqrt{(2\pi\bar{\eta}^2)} \tan\theta$ which may be compared with equation (1) for strain broadening in which $\xi = \sqrt{(2\pi\bar{\eta}^2)}$. This result coincides with curve b, Figure 3, deduced by a more qualitative discussion. The strain distribution appears to lie between the two extremes of Cauchy and Gaussian functions and a general curve such as Figure 3c is probable. The use of a linear extrapolation from measurements at high angles only, results in correct values of the lattice strain for all cases but values of particle size which may be too large by a factor in the range 1 to π.

Hall [25] analysed much of the published data using a plot of β^* against $d^*/2$ using a linear extrapolation and found a positive intercept for all cases excepting that of martensite, the particle sizes ranging about a value of 10^{-5}cm. A similar value has also been reported by Mazur [27] and by Krainer [28] for martensite. The slopes (and hence the mean strains) increased generally with the hardness of the metals.

An interpretation attributing broadening to simultaneous particle size and strain effects seems to correlate most of the published results, and, as will be shown later, this is in good accord with the current dislocation theory of deformation. Since the method used by Hall involves a long extrapolation from the experimental points further measurements have been made using an improved experimental technique in order that a more certain correlation of the observed effects with the dislocation theory can be made.

Aluminium and wolfram have been chosen for study, since they are both approximately elastically isotropic. These two metals also approximate to the extremes of hardness normally encountered in metals, aluminium being one of the softest metals and wolfram one of the hardest, and it may be possible to determine the influence of hardness on the changes observed.

Preparation of Specimens

All specimens used in these experiments were prepared by hand filing, followed by sieving through a 350 mesh per inch sieve.

Four samples of aluminium were prepared, two from a sample of high purity aluminium greater than 99.99 per cent pure, and two from a sample of commercially pure aluminium (approximately 99.7 per cent Al), using a "smooth" file. Filings of both purities annealed in vacuo (less than 10^{-2} cm. mercury) at 500°C for 25 minutes, but as the line breadths from both were found to be identical only the spectrum of the high purity sample was examined in detail.

Three specimens of wolfram were prepared from a bar 99.9 per cent pure supplied by the Tungsten

Manufacturing Co. After sieving, the filings were shown by analysis to contain less than 0.4 per cent of iron. Two samples were annealed in vacuo, one for 50 minutes at 1150°C and the other for 3 hours at 1300°C.

The Experimental Method

The results were obtained using a Geiger counter spectrometer and the experimental methods previously described [1], the measurements of line shape being carried out simultaneously with those of the changes in intensity previously reported. Measurements were made of the reflected intensity, using a scaling unit, at specific angular settings of the Geiger counter in order to avoid the distortion introduced by the use of a counting-rate meter [29]. The "count" was recorded on the scaling unit, not for a constant time, but for an arbitrary monochromatic X-ray output from the X-ray set as measured on a second monitoring counter and was corrected for counting losses (Hall and Williamson [30]). Frequent checks on the stability of the monitoring were made and although a long term drift of $\pm$ 2 per cent was observed, the drift of less than 1 per cent during the measurement of any one line would introduce a distortion less than uncertainty due to statistical scatter on the results; monochromatized copper K_α radiation generated at 50 K.V. peak and 10 M.A. has been used throughout.

Integral line breadths were obtained by graphical resolution of the line shapes [31] to obtain the sum of the α_1 and α_2 peak intensities, Simpson's rule being used to determine the integrated intensity. The resolved line shapes coincided with Cauchy functions within experimental error and thus the observed breadth is simply the sum of the required physical breadth and the experimental breadth.

Line Broadening Results for Aluminium

The values of the line breadths observed in the spectra from the three aluminium specimens are shown in Figure 4 in which $N = h^2 + k^2 + l^2$ and the breadth B_χ is expressed in minutes of arc in χ. Two features are noticeable: first, the very low value of the broadening in the cold worked, high purity specimen compared to that in the commercially pure specimen, and secondly, the rapid rise in the broadening at high angles in the annealed specimen. This latter effect is due to physical broadening, since Alexander [32] has shown that the form of the experimental broadening is that shown dotted in Figure 4. Particle sizes as small as 5×10^{-5} cm. are inadequate to explain this broadening and it appears that lattice strains exist even in the annealed state.

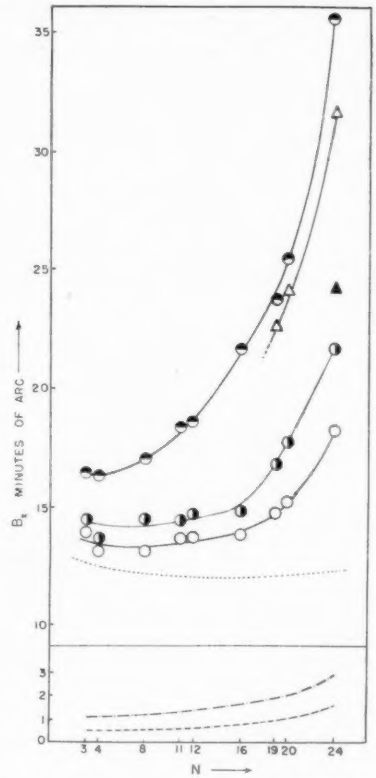

FIGURE 4. The line breadths β_χ for the aluminium spectra plotted against $N = h^2 + k^2 + l^2$. ○ from the high purity annealed sample; ◑ from the high purity filed sample; ◓ from the commercial purity filed sample; △ from the slowly mechanically filed high purity sample; ▲ from the high purity samples rapidly filed under liquid air; . . . . . . the predicted form of the experimental broadening; — — — — physical broadening produced by a particle size of 10^{-4} cm; • — • — • — physical broadening produced by a particle size of 5×10^{-5} cm.

An estimation of the experimental broadening must be made before the results can be interpreted, since no direct measure is possible. The divergence of the X-rays has been restricted to 2° and the experimental broadening is approximately symmetrical about $\chi = 90°$. A constant experimental breadth has therefore been chosen for two lines equidistant from $\chi = 90°$ (in Fig. 5, lines 3 and 24), such that the reciprocal lattice broadening indicates a particle size of 0.8×10^{-4} cm. for the annealed state, a value which is of the correct order of magnitude [33]. Both cold worked specimens have smaller particle sizes a value of 4×10^{-5} cm. being indicated for both purities on Figure 5.

The values of β^* for the other lines, calculated for the same assumed experimental breadth of 12′, lie on a smooth curve and indicate the lack of anisotropy in the broadening. The assumption of symmetrical experimental broadening and Cauchy line shapes, tends to reduce the slope of the reciprocal

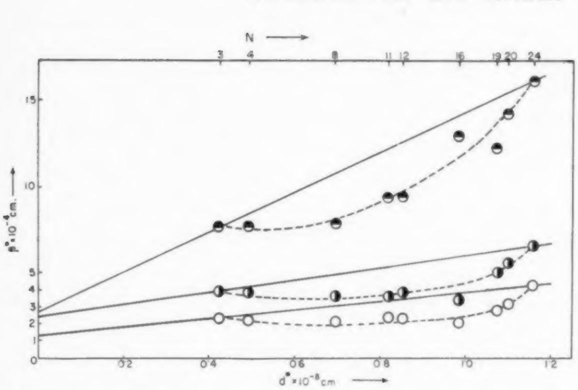

FIGURE 5. The interpretation of the line broadening in the aluminium spectra in which β^* is plotted against d^* assuming an experimental breadth of 12 mins. of arc. Symbols as for Figure 4.

lattice broadening so that the values of the lattice strain breadths of 0.025 per cent for annealed aluminium, 0.045 per cent for filed high purity, and 0.14 per cent for filed commercial purity are minimum and not absolute values.

The different impurity content of the two filed specimens is probably responsible for the differences in the strain breadths since both received the same cold working treatment, the impurities retarding or preventing the recovery of the commercial specimen. No difference in line broadening could be detected in the high purity sample examined $\frac{1}{2}$ hour, and 350 hours after filing and this suggests that the recovery, if any, occurred at the instantaneous high temperature generated during filing. Further high purity samples were examined in which this instantaneous temperature rise was restricted, either by filing very slowly with a lightly loaded file so that the heat generated was dissipated very rapidly, or by filing under liquid air. Both these methods gave increased broadening as shown in Figure 4, the slowly filed sample having a broadening little different from that of the commercially pure specimen, confirming that the difference is due to instantaneous recovery on filing.

Discussion of Results for Aluminium

The effect of recovery on the value of the breadths is of great interest in view of the simultaneous measurements of the changes in integrated intensity and background level [1]. In these experiments cold work was observed to produce a uniform reduction in the intensities of each reflection (after a corrrection for extinction which is also affected by cold work) and a corresponding rise in the background level. The intensities of the lines and the background level were not affected by recovery, within the limits of experimental accuracy. Since the background rise was substantially constant over the entire spectrum very large atomic displacements of the order of up to half a spacing must be responsible. These two results together provide a very critical test for any theory of cold work, since the very high short range strains responsible for the increase in background intensity and the decrease in line intensity must be more stable at the high temperature produced during filing than the small long range strains responsible for the increase in line breadths. The simple random lattice strain theory is inadequate for this reason since the greater the strain the less should be its stability; on recovery the background would be expected to change first, and not the line broadening as observed. The only satisfactory explanation is that some metastable fault exists which produces the high short range strains and persists even after the dissipation of the smaller long range strains.

Two types of lattice fault which would conform to the stringent requirements of the experimental data are the screw and edge dislocations, which are stable in so far as they can only be removed from the lattice by movements to a free boundary or by mutual annihilation of two dislocations of opposite sign. A detailed discussion of the dislocation theory is beyond the scope of this paper and excellent reviews exist (see for example Burgers [34], and Cottrell [35]).

From the dislocation models produced by Bragg and Nye [36] for a bubble raft, and by Bilby [37] in ball models it can be seen that dislocations cause a bending of the lattice in their immediate neighbourhood so that coherent X-ray reflection will not occur over regions much greater than the dislocation separation. The study of specific heat, plasticity, and magnetic properties suggests that cold working increases the dislocation density to a limiting value of approximately 10^{12} lines per cm^2 in the fully cold worked state. For a random distribution of dislocations these figures correspond to average distances between neighbouring dislocation lines of 10^{-6} cm. for the cold worked state, values which are in good agreement with those reported by Wood [21]. Each dislocation is surrounded by a slowly varying strain field, and thus a material containing dislocations will show both strain broadening and particle size broadening, the greater the density of dislocations, the greater in general being the broadening due to both causes. Annealed metals may be expected to show some strain broadening as observed (since they are generally assumed to contain of the order of 10^8 dislocations per cm^2), although this is

very small and must have passed unnoticed in most experiments.

The actual value of the breadths from the cold worked metal will be very much influenced by recovery, which has been discussed by Koehler [38], Burgers [34], Cahn [39] and Guinier and Tenevin [40]. Although the mechanism of recovery is not fully understood it seems certain that it involves the migration of the dislocations into walls, similar to grain boundaries. It has been shown that such a mechanism can reduce the strain energy of the lattice. Recovery is thus dependent on the mobility of the dislocations and is greater for soft metals than for hard ones, and can be reduced by the presence of impurities (e.g. Cottrell and Churchman [41], and Bilby [42]). Thus the differences in strain found by Hall when interpreting previous results may be due either to the production of different dislocation densities by different method of working, or to different degrees of recovery, but in the present results they are due entirely to recovery.

In addition to the reduction in strain energy on recovery, reduction in particle size broadening is to be expected since reflection will be coherent over distances of the same order as the separation of polygonised boundaries. The small change observed in aluminium suggests that extensive polygonisation had occurred in the commercial purity specimen.

Thus the results from aluminium would agree with the predictions of the dislocation theory, the commercial purity aluminium having a higher strain energy (as indicated by the breadths) than the high purity aluminium because of the action of the impurities in restricting the movement of the dislocations. Any alternative theory of the changes would have to be based on a different type of metastable fault and would thus not be significantly different.

Line Broadening Results from Wolfram

The measured line breadths from the spectra from the three samples of wolfram are shown in Figure 6. The increase in the breadths from the annealed sample at high angles is very marked, partly because of the reduced experimental breadth in this particular series of experiments and partly because wolfram line 16 occurs at a higher angle than aluminium line 24. Thus the existence of a definite physical broadening in the annealed metal is more apparent than in the study of aluminium, though a subsidiary experiment on an annealed aluminium specimen showed that the breadth of line 24 coincided

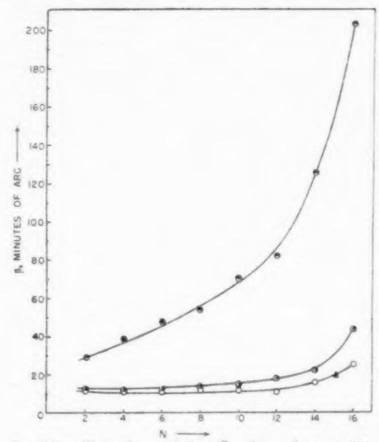

FIGURE 6. The line breadths β_x for the wolfram spectra plotted against N. ○ from the sample annealed at 1300°C; ◑ from the sample recovered at 1150°C; ◓ from the sample examined as filed; ▲ subsidiary measurement of aluminium line 24.

with the curve through the breadths from the annealed wolfram.

The breadths from the specimen heated at 1150°C are only slightly greater than those from the annealed specimen and indicate that very extensive recovery has taken place from the high values of the breadths given by the cold worked specimen. Measurements of the background level showed that both the cold worked specimen and that heated at 1150°C gave similar background levels, which were significantly higher than that from the specimen annealed at 1300°C, indicating that the former had recovered and the latter had recrystallised.

A plot of β^* against d^* is shown in Figure 7, using a similar method of analysis to that used for aluminium. The analysis has been carried out for the recovered and annealed samples by assuming a constant breadth of 10 minutes of arc for line 2 and for a point midway between lines 14 and 16, posi-

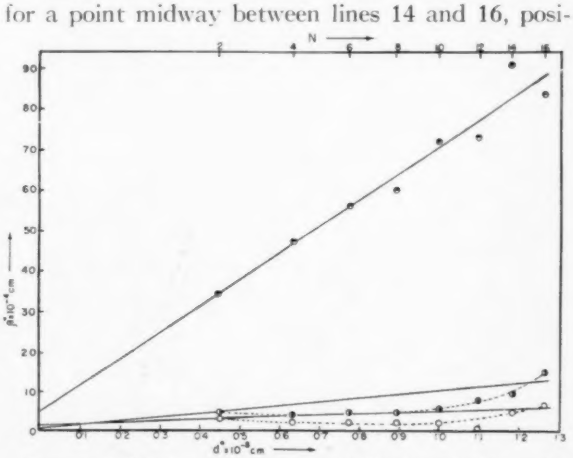

FIGURE 7. The interpretation of the line broadening in the wolfram spectra. Symbols as in Figure 6.

tions which are approximately equidistant from $\chi = 90°$. The plot which represents the annealed sample then has an intercept corresponding to 10^{-4} cm. and a small slope corresponding to a strain breadth 0.03 per cent. The intercept for the recovered metal indicates a similar particle size to that in the annealed state and a greater apparent strain having a value of approximately 0.1 per cent. This result suggests that if the postulated mechanism of recovery is correct, the separation of the walls of dislocations in the recovered state in this particular specimen is of the same order of magnitude as the separation of dislocations in the annealed state. The cold worked sample shows much greater particle size broadening, indicating a particle size of the order of 2×10^{-5} cm, and a much greater value of the strain breadth of 0.62 per cent.

Thus the results from wolfram support the dislocation theory of deformation as closely as do those from aluminium, the only appreciable difference in the two sets of results being the greater strain and particle size broadening of the cold worked wolfram. The observed fractional rises in the background intensity from the two metals coincide fairly closely and indicate that the dislocation densities in both cold worked specimens are approximately equal. However, since the observed strains in the two metals differ so greatly, it is apparent that appreciable recovery must have occurred even in the commercially pure aluminium specimen. Such an interpretation is reasonable since the mobility of dislocations is a function of both the impurity content and the atomic mobility, which will in turn be a function of the melting point. Thus dislocations in the aluminium (melting point 933°A) will be more mobile at the temperature produced during filing ($\sim$ 600°A) than in wolfram (melting point approximately 3700°A).

Fourier Analysis of the Line Shapes

Interpretation of the Fourier coefficients has been carried out by the method of Warren and Averbach [17]. This method is unsuitable for determining particle sizes as large as 10^{-5} cm. occurring simultaneously with strain since errors in the analysis due to numerical summation and slight errors in placing the peak of the line reduce the reliable accuracy of the coefficients to three figures, leaving the value of particle size indeterminate.

An interesting feature of the plots of A_n versus n shown in Figure 8 for aluminium is that the values of A_n from line 24 do not decrease as rapidly as do those from line 4, at low values of n. Since the coefficients

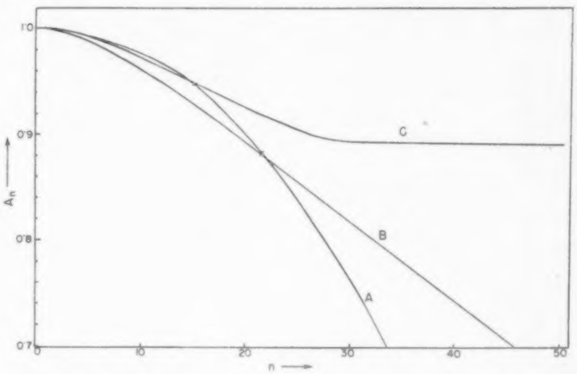

FIGURE 8. The Fourier coefficients of the broadening functions of some lines in the aluminium spectra. The curves have been drawn through the experimental points obtained at values of n = 0, 1, 2, 3, 4, 5, 10, 30, 40, and 50. A for line 24, B for line 4, from the filed commercially pure sample; C for line 4 from the filed high purity sample.

are given by the $\langle \cos 2\pi l Z_n \rangle_{av.}$ where Z_n is the displacement between two points n cells apart they should decrease more rapidly for line 24, than for line 4. This apparent anomaly can be readily explained if it is assumed that the annealed specimen produces broadened lines, particularly at high Bragg angles.

The values of $\sqrt{\bar{Z}_n^2}$ for line 4 from the two purities of aluminium are plotted in Figure 9. The

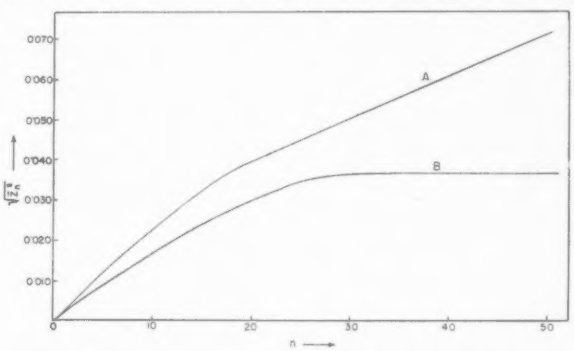

FIGURE 9. The variation of $\sqrt{\bar{Z}_n^2}$ with n for line 4 aluminium. The curves have been fitted to experimental points at the same values of n as in Figure 8. A for the commercially pure sample; B from the high purity sample.

curve for the commercially pure specimen has the form previously reported by Warren and Averbach for α-brass which they interpret as showing that the strains are not constant over regions of greater than about 10 spacings. The plot for the high purity specimen however is unusual in that the value of $\sqrt{\bar{Z}_n^2}$ becomes constant above values of n = 30. Similar results, shown in Figure 10 have been obtained from wolfram. This result is surprising because a truly random arrangement of strains would result in a curve continuing to rise smoothly towards a

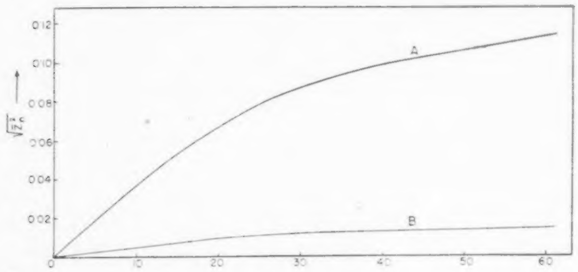

FIGURE 10. The variation of $\sqrt{\bar{Z}_n{}^2}$ with n for line 14 wolfram. The curves have been fitted to the experimental points at the same values of n as in Figure 8. A from the as filed sample; B from the sample recovered at 1150°C.

value of $\frac{1}{2}$ and thus the strains must take up some regular arrangement. This constancy implies that, to a good approximation, the regions of strain cannot extend for distances greater than 30 spacings. If this were not so the values of $\sqrt{\bar{Z}_n{}^2}$ would continue to increase beyond $n = 30$. If dislocations are accepted as causing the diffraction effects studied then this process would correspond to polygonization, and the walls of strain would bound the regions of coherent reflection. Thus the condition of the recovered specimen may be represented schematically as in Figure 11, in which walls of strain occur

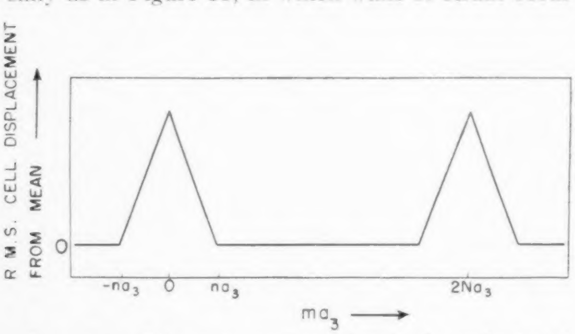

FIGURE 11. Schematic representation of the variation of the root mean square displacement of the cells with distance in recovered metals.

$2N$ spacings apart, and $2m$ spacings wide. To calculate the average absolute or mean square strains for all pairs of cells n spacings apart, three terms must be considered:

(a) the displacement between cells in the wall, for values of $n < m$, $(m - n)$ cells exist having a displacement $Z_n \sim n\epsilon$ where ϵ is the strain in the wall, and for values of $n > m$ the contribution of this term is zero.

(b) the displacement between cells, one of which is in the strain free region and the other in the strained region. For values of $n < m$, $(n - 1)$ such combinations exist for each wall and have values $\epsilon, 2\epsilon, 3\epsilon, \ldots, (n-1)\epsilon$, whereas for values of $n > m$ $(m - 1)$ such combinations exist having values $\epsilon, 2\epsilon, 3\epsilon, \ldots, (m-1)\epsilon$.

(c) the additional displacement if slight strains occur in the so-called strain free region.

Neglecting the contribution from (c) the mean strain for $n < m$ is given approximately by:

$$(16)\ \sqrt{\bar{Z}_n{}^2} \sim \bar{Z}_n = \frac{(m-n)(n\epsilon) + \sum_{j=0}^{j=n} (j-1)\epsilon}{N}$$

and for $n > m$,

$$(17)\qquad \bar{Z}_n = \frac{0 + \sum_{j=0}^{j=m} (j-1)\epsilon}{N} = \text{constant.}$$

Thus $\bar{Z}_n$ gradually increases until at a value $n = m$ it becomes a constant. The width of the walls is thus about 30 atoms in both the aluminium and the wolfram. This analysis confirms the postulated mechanism of recovery, that the dislocations migrate into walls surrounding relatively large strain free regions. The analysis, however, throws some doubt on the usual interpretation of the A_n versus n plots, that the strains are non-uniform over distances greater than 10 spacings; a possibly more correct interpretation is that in certain regions the strains change appreciably over the distance of 10 spacings.

The surprising feature of the plots from the cold worked samples is their general similarity, despite the large recovery of the commercially pure aluminium, and it appears that this method of analysis is not sensitive to recovery until the recovery is almost complete.

Conclusions

The changes in line profile with cold work have been correlated with the changes in intensity and it is shown that some lattice defects such as dislocations must be present in the cold worked state. The presence of broadening in the spectra of the annealed metals indicates that a smaller density of dislocations persists even after annealing. The differences in the apparent strains between the aluminium and wolfram spectra may be interpreted entirely in terms of the instantaneous recovery without necessitating either a different mechanism or dislocation density. Fourier analysis of the line shapes, confirms the above interpretations and indicates that the postulated mechanisms of recovery, namely, the migration of the dislocation into walls, is correct, at least for the later stages of recovery.

The above interpretation, however, is basically dependent on the observed changes in background

level measured in the spectra of aluminium and wolfram, and although the theory is expected to apply generally the lack of experimental evidence as to the nature of the intensity changes in the spectra of other materials makes this uncertain.

Acknowledgements

It is a pleasure to acknowledge the encouragement given to us by Professor D. Hanson, Director of the Department of Metallurgy. Generous financial assistance has been received from the Department of Scientific and Industrial Research, and this paper is published by permission of the Director of the National Physical Laboratory. A summary of this work was given at the Second International Congress of Crystallography, Stockholm, 1951.

References

1. Hall, W. H. and Williamson, G. K. Proc. Phys. Soc. **64B** (1951) 937, 946.
2. Stokes, A. R. and Wilson, A. J. C. Proc. Camb. Phil. Soc., **40** (1944) 197; Proc. Phys. Soc., **56** (1944) 174.
3. Lipson, H. Symposium on Internal Stresses in Metals and Alloys (London, Institute of Metals, 1948), 35.
4. Jones, F. W. Proc. Roy. Soc., **A166** (1938) 16.
5. Schull, C. O. Phys. Rev., **70** (1946) 697.
6. Stokes, A. R. Proc. Phys. Soc., **61** (1948) 382.
7. van Arkel, E. A. Physica, **5** (1925) 208.
8. Wood, W. A. Phil. Mag., **14** (1932) 636.
9. Wood, W. A. Phil. Mag., **19** (1935) 219.
10. Haworth, F. E. Phys. Rev., **52** (1937) 613.
11. Brindley, G. W. and Ridley, P. Proc. Phys. Soc., **50** (1939) 432, 501.
12. Brindley, G. W. Proc. Phys. Soc., **52** (1940) 117.
13. Smith, C. S. and Stickley, E. E. Phys. Rev., **64** (1943) 191.
14. Stokes, A. R., Pascoe, K. J., and Lipson, H. Nature (London), **151** (1943) 137.
15. Megaw, H. D. and Stokes, A. R. J. Inst. Met., **71** (1945) 279.
16. Averbach, B. L. and Warren, B. E. J. Appl. Phys., **20** (1949) 885.
17. Warren, B. E. and Averbach, B. L. J. Appl. Phys., **21** (1950) 595.
18. Dehlinger, U. and Kochendörfer, A. Z. Metallkunde, **31** (1939) 231.
19. Bragg, W. L. Nature (London), **149** (1942) 511.
20. Bragg, W. L. Proc. Camb. Phil. Soc., **45** (1949) 125.
21. Wood, W. A. Proc. Roy. Soc., **A172** (1939) 231.
22. Wood, W. A. Nature (London), **151** (1943) 558.
23. Wood, W. A. and Rachinger, W. A. J. Inst. Met., **75** (1949) 571.
24. Stokes, A. R. and Lipson, H. Nature (London), **163** (1949) 871.
25. Hall, W. H. Proc. Phys. Soc., **A62** (1949) 741.
26. Wilson, A. J. C. Acta Cryst., **2** (1949) 220.
27. Mazur, J. Nature (London), **164** (1949) 358.
28. Krainer, H. Arch. Eisenhuttenw., **22** (1951) 53.
29. Wainwright, C. Brit. J. Appl. Phys., **2** (1951) 157.
30. Hall, W. H. and Williamson, G. K. J. Sci. Inst., **29** (1952) 132.
31. Rachinger, W. A. J. Sci. Inst., **25** (1948) 254.
32. Alexander, L. J. Appl. Phys., **21** (1950) 126.
33. Hirsch, P. B. and Kellar, J. N. Proc. Phys. Soc., **64B** (1951) 369.
34. Burgers, W. G. Proc. Roy. Acad. Sci. Amsterdam, **50** (1947) 452.
35. Cottrell, A. H. Progress in Metal Physics, **1** (1949) 77.
36. Bragg, W. L. and Nye, J. F. Proc. Roy. Soc. **A190** (1947) 474.
37. Bilby, B. A. J. Inst. Met., **76** (1950) 613.
38. Koehler, J. S. Phys. Rev., **60** (1941) 397.
39. Cahn, R. W. Progress in Metal Physics, **2** (1951) 151.
40. Guinier, A. and Tenevin, J. Progress in Metal Physics, **2** (1951) 177.
41. Cottrell, A. H. and Churchman, A. T. J. Iron and Steel Inst., **162** (1949) 271.
42. Bilby, B. A. Proc. Phys. Soc., **A63** (1950) 191.

APPLICATION OF NUCLEATION THEORY TO ISOTHERMAL MARTENSITE*

J. C. FISHER†

A previously described extension of classical nucleation theory is shown to agree quantitatively with experimental observations of isothermal martensite formation in an iron-nickel-manganese alloy. The martensite transformation in this alloy is described in terms of the nucleation and rapid growth of thin plates, nucleation being the rate-limiting process.

L'APPLICATION DE LA THÉORIE CLASSIQUE DE LA GERMINATION À LA MARTENSITE ISOTHERME

L'extension de la théorie classique de la germination décrite précédemment, paraît être en accord quantitatif avec les observations expérimentales de la formation isotherme de la martensite dans un alliage de fer-nickel-manganèse. La transformation martensitique dans cet alliage est décrite comme germination et croissance rapide de minces paillettes; cette germination constitue le facteur limitant la vitesse.

DIE ANWENDUNG DER KEIMBILDUNGSTHEORIE AUF DIE ISOTHERME MARTENSIT TRANSFORMATION

Es wird gezeigt, dass eine früher beschriebene Ausdehnung der klassischen Keimbildungstheorie quantitativ mit den experimentellen Beobachtungen an isothermer Martensit Bildung in einer Eisen-Nickel-Mangan Legierung übereinstimmt. Die Martensit Transformation in dieser Legierung wird an Hand von Keimbildung und schnellem Keimwachstum dünner Plättchen beschrieben, wobei die Keimbildung die Reaktionsgeschwindigkeit bestimmt.

Introduction

Completely isothermal formation of martensite has been reported by Cech and Hollomon. They state that the transformation rate is limited by the rate of nucleation; and not by growth, which is very rapid. This report gives a quantative description of isothermal martensite nucleation using a previously described extension of classical nucleation theory.

Theory

A simple extension of classical nucleation theory to martensite-type transformations considers the shape of the nucleus to be lenticular, with radius r and thickness δ, and includes the strain energy of the plate and surrounding parent phase [1]. According to this view, the free energy of formation of a martensite nucleus is made up of three terms; a surface free energy term, a volume free energy term, and a strain energy term:

$$\Delta f = 2\pi r^2\sigma + (\pi r^2\delta/2)\Delta f_v + \theta\pi r\delta^2. \tag{1}$$

In this expression, σ is the interfacial free energy per unit area of austenite-martensite interface, Δf_v is the free energy change per unit volume accompanying the austenite to martensite transformation in the absence of strain energy, and the coefficient θ depends upon the elastic constants of the parent phase and the shear angle of the martensite plate.

The saddle-point value of Δf can be found by differentiating with respect to r and δ and equating to zero. It is the free energy of formation of a critical size nucleus,

$$\Delta f^* = 8192\ \pi\theta^2\sigma^3/27\ \Delta f_v^4. \tag{2}$$

In an alloy for which composition fluctuations are unimportant in the nucleation of martensite (in contrast to iron-carbon alloys where fluctuations in carbon content largely control nucleation), the rate of homogeneous nucleation of martensite plates is

$$\dot{n} = (N/V)\nu \exp(-\Delta f^*/kT) \tag{3}$$

nuclei per cubic centimeter per second, where N is Avogadro's number, V the molar volume, ν an atomic frequency.

Equation (3) predicts a maximum in the rate of nucleation at the temperature where $d\dot{n}/dT = 0$, or where

$$(4T/\Delta f_v)\, d\,\Delta f_v/dT + 1 = 0. \tag{4}$$

According to Jones and Pumphrey [2], the free energy change upon transforming the γ phase to the α phase of an iron-nickel alloy is

$$\Delta F = C\Delta H + 1.25(1 - C)\Delta F_{Fe} \tag{5}$$

calories per mole where C is the atomic fraction of nickel, ΔF_{Fe} is the free energy change upon transforming one mole of γ iron to α iron, and ΔH is 2500 cal/mole. According to equations (4) and (5), and using the values of ΔF_{Fe} tabulated by Fisher [3], the maximum rate of martensite nucleation in a 26 per cent nickel, 74 per cent iron alloy occurs at 147°K = − 126°C.

Cech and Hollomon [4] have studied the isothermal formation of martensite in a 23 per cent Ni, 4 per cent Mn, 73 per cent Fe alloy for which the free energy changes are substantially the same as for a 26 per cent Ni, 74 per cent Fe alloy. They find a family of C-curves representing varying fractions of austenite transformed to martensite, with the most

*Received August 14, 1952.

†General Electric Research Laboratory, The Knolls, Schenectady, New York.

rapid transformation rate at about $-128°C$, within $2°C$ of the calculated temperature. This observation strongly supports their statement that isothermal transformation in this alloy is the direct result of isothermal nucleation.

The martensite nucleation rates can be estimated from the isothermal transformation curves given by Cech and Hollomon, if it is assumed that martensite plates compartmentalize the austenite, so that the nth plate to form transforms a constant fraction f of $(1/n)$th of the remaining untransformed volume. Starting with a unit volume of austenite, let V be the volume transformed to martensite. Then

$$dV/dn = f(1 - V)/n. \tag{6}$$

Solving,

$$f \ln(n/n_0) = -\ln(1 - V) \tag{7}$$

where n_0 is the number of plates per unit volume present at the beginning of transformation. n_0 is essentially the number of austenite grains per unit volume. For a constant rate of nucleation, then, the effective number of nuclei (n_0 + the true number) is

$$n = n_0 + \int_0^t \dot{n}(1 - V)\, dt. \tag{8}$$

Substituting this value in equation (7) and solving for V, the relationship between volume transformed and time is

$$V = 1 - [1 + (1 + f)\dot{n}t/n_0]^{-f/(1+f)}. \tag{9}$$

This equation, fitted to an experimental curve, gives f and $\dot{n}/n_0$. When the grain size is known, $\dot{n}$ itself can be obtained.

Estimation of Experimental Nucleation Rates

Cech and Hollomon give curves at thirteen different temperatures for the volume fraction of isothermal martensite V as a function of time t. Each of these was fit as well as possible with equation (9), treating f and $\dot{n}/n_0$ as disposable parameters. Figures 1–3 show typical experimental data points and fitted curves, one for the highest temperature investigated, $-79°C$, one for the lowest, $-196°C$, and one for the temperature of most rapid transformation, $-128°C$. Figure 4 gives the best values of f and $\dot{n}/n_0$ determined in this way for all thirteen curves.

Ideally, one would hope to find the values of f in Figure 4 all the same, or at most varying slowly and uniformly with temperature; and to find the major portion of the temperature variation of V accounted for by changes in $\dot{n}/n_0$. This hope was not entirely realized, the values of f varying from 0.014 to 0.069, a factor of about 5, and showing a maximum at about $-110°C$. Values of $\dot{n}/n_0$ showed much more variation, however, ranging from 0.034 at $-196°C$ to 2.36 at $-128°C$, a factor of about 70, with a sharp maximum at $-128°C$.

Except for the two highest temperatures, where the original data were least reproducible, the values of f all are in the neighbourhood of 0.05, indicating that each martensite plate transforms about 5 per cent of the partitioned volume in which it is nucleated. Variations in the values of f calculated by the use of equation (9) probably should be expected; for, among other things, the influence of the stress field around a previously formed martensite plate in stimulating more rapid nucleation in its neighbourhood [5] has been neglected. In spite of the fact that f did not turn out to be constant, it is likely that the corresponding values of $\dot{n}/n_0$ are approximately correct.

Since the mean number of austenite grains per unit volume in the alloy was about 56,000 grains per cubic centimeter [4], the nucleation rate is given by the relationship

$$\dot{n} = 56{,}000(\dot{n}/n_0). \tag{10}$$

Figure 5 gives $\log \dot{n}$ versus T for $\dot{n}$ calculated in this way from the values of $\dot{n}/n_0$ in Figure 4.

Comparison with Experiment

Equation (4) has given the first opportunity for a comparison of theory and experiment. The temperature of maximum nucleation rate calculated therefrom was found to be within $2°C$ of the experimental temperature of $-128°C$, a striking agreement.

Another test of the nucleation theory is whether or not the nucleation rate given by equation (3) fits the data in Figure 5, which gives the nucleation rate as a function of temperature. This test is not entirely satisfactory, for the data in Figure 5 are not direct experimental results but have been derived therefrom by a somewhat oversimplified model of the partition of austenite by martensite plates.

Rewriting equation (3), the theoretical nucleation rate is

$$\dot{n} = 10^{36}\exp[-8192\pi(\theta^2\sigma^3)/27\Delta f_v^4 kT] \tag{3a}$$

nuclei per cc per sec. The coefficient 10^{36} is the product of $(N/V) = 6(10)^{23}/7\ \text{cc}^{-1}$ and $\nu \approx 10^{13}\ \text{sec}^{-1}$. The only unknown quantity is $\theta^2\sigma^3$, as Δf_v can be computed from equation (5).

The value of $\theta^2\sigma^3$ required to give the observed nucleation rates by calculation from equation (3a) is $5.85(10)^{22}$, in fair agreement with the value $2.9\ (10)^{23}$

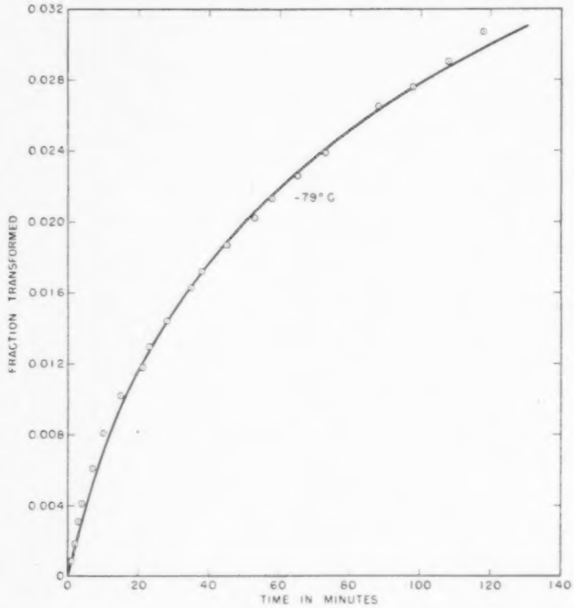

FIGURE 1. Formation of isothermal martensite in an iron-nickel-manganese alloy. Fraction transformed as a function of time at $-79°C$, according to Cech and Hollomon [4]. Curve calculated from equation (9).

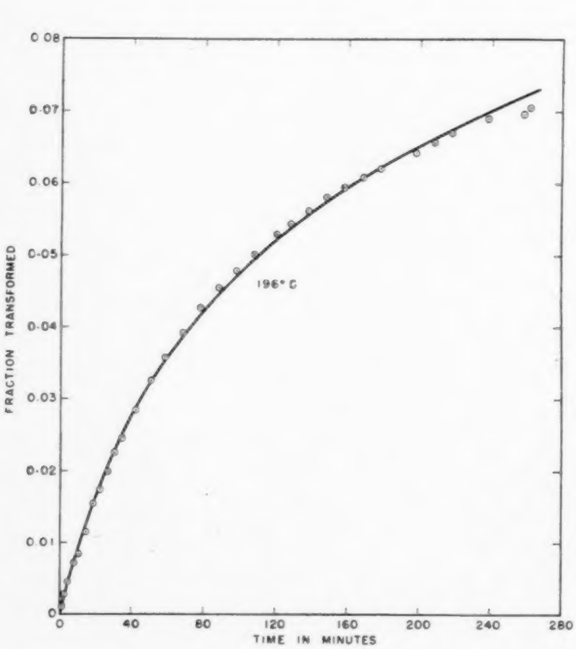

FIGURE 2. Formation of isothermal martensite in an iron-nickel-manganese alloy. Fraction transformed as a function of time at $-196°C$, according to Cech and Hollomon [4]. Curve calculated from equation (9).

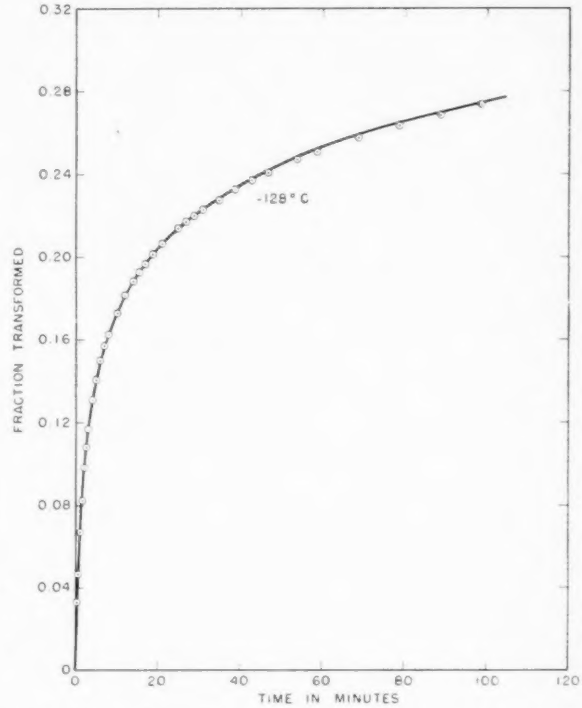

FIGURE 3. Formation of isothermal martensite in an iron-nickel-manganese alloy. Fraction transformed as a function of time at $-128°C$, according to Cech and Hollomon [4]. Curve calculated from equation (9).

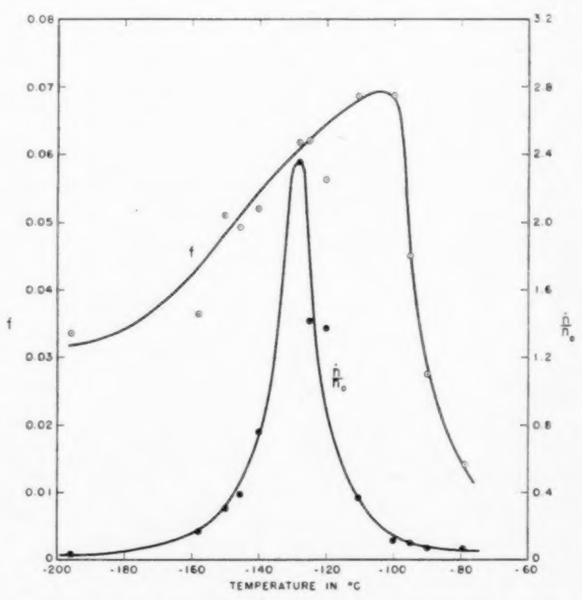

FIGURE 4. Best values of f and $\dot{n}/n_0$ as functions of temperature for isothermal martensite nucleation, found by fitting equation (9) to isothermal transformation data as in Figures 1–3.

previously calculated for iron-carbon-3 per cent chromium steels [1]. The factor of five difference is not unreasonable in that it can be produced by a 30 per cent change in each of θ and σ. Taking the value $5.85(10)^{22}$ for $\theta^2\sigma^3$, the nucleation rates for

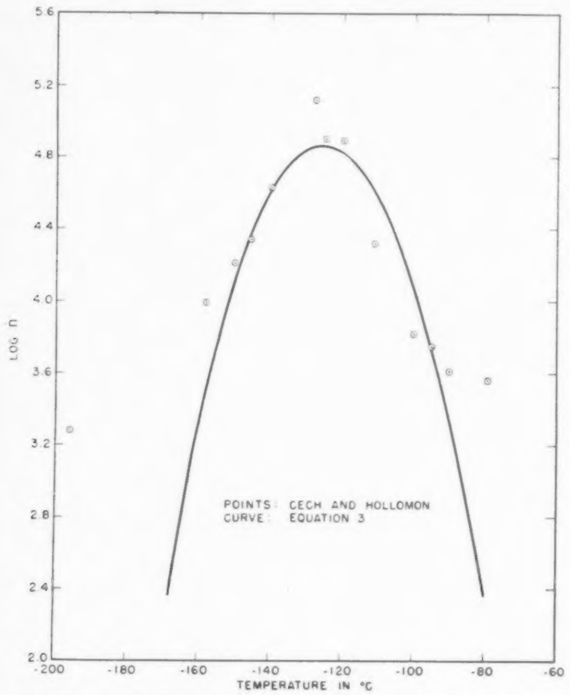

FIGURE 5. Comparison of nucleation rates taken from Figure 4 (points) and calculated from equation (3a) (curve).

isothermal martensite nucleation were calculated and are compared with those derived from Cech and Hollomon's data in Figure 5.

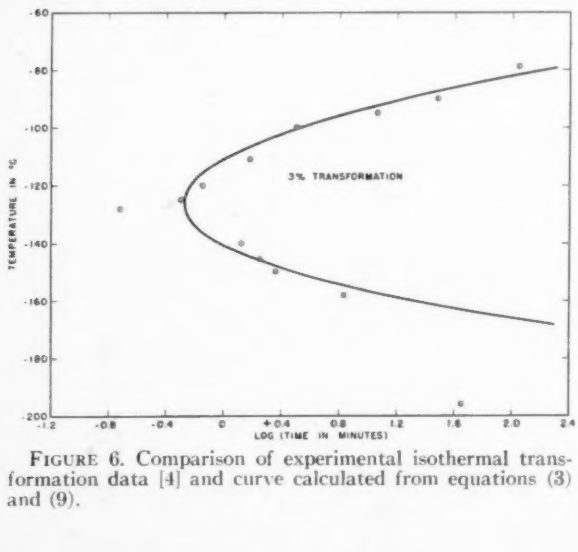

FIGURE 6. Comparison of experimental isothermal transformation data [4] and curve calculated from equations (3) and (9).

A comparison of calculated and experimental C-curves can be made by assuming that each martensite plate transforms a constant fraction of the austenite volume in which it finds itself. Taking $f = 0.05$ for this fraction, and using equations (3) or (3a) and (9), a C-curve was calculated for 3 per cent transformation. It is compared with the experimental curve in Figure 6.

Summary

Cech and Hollomon have reported an isothermal martensite transformation in an iron-nickel-manganese alloy. They state that the transformation proceeds by isothermal nucleation and rapid growth of martensite plates, so that the rate-limiting step is nucleation. New nuclei are required to continue the transformation, for a martensite plate does not grow beyond the austenite region in which it is nucleated.

Using a simple extension of classical nucleation theory to include the effects of elastic strain energy, it has been shown that the experimental data on the isothermal formation of martensite can be accounted for quantitatively. In the process of making this comparison, the rate of nucleation of martensite plates per unit volume of untransformed martensite was deduced by assuming that martensite plates compartmentalize the austenite as they form, restricting the volume in which they can nucleate.

The only unknown quantity in the expression for the absolute nucleation rate for martensite is $\theta^2\sigma^3$, a function of the elastic constants of austenite, the shear angle of the martensite, and the austenite-martensite interfacial free energy. When $\theta^2\sigma^3$ is set equal to $5.85(10)^{22}$ in c.g.s. units, the agreement shown in Figures 5 and 6 is obtained. The value of $\theta^2\sigma^3$ calculated earlier from the influence of carbon content on M_s temperatures in a series of 3 per cent chromium steels is within a factor of 5 of this value, a reasonable agreement in view of the dissimilarity of the materials.

References

1. FISHER, J. C., HOLLOMON, J. H., and TURNBULL, D. Trans. A.I.M.E., **185** (1949) 691.
2. JONES, F. W. and PUMPHREY, W. I. J. Iron and Steel Inst., **163** (1949) 121.
3. FISHER, J. C. Trans. A.I.M.E., **185** (1949) 688.
4. CECH, R. E. and HOLLOMON, J. H. To be published in Trans. A.I.M.E.
5. MACHLIN, E. S. and COHEN, M. Trans. A.I.M.E., **191** (1951) 746.

THERMAL STABILIZATION OF AUSTENITE IN IRON-CARBON-NICKEL ALLOYS*

E. R. MORGAN† and T. KO‡

The thermal stabilization of austenite above and below M_s during cooling and during isothermal holding has been investigated. It has been found that M_s is depressed by stabilization above M_s and the effect is reflected in an increase in the amount of retained austentite when the steel is slowly quenched to a reference temperature. The amount of martensite lost during stabilization may be recovered by sufficient further cooling. A mechanism of stabilization based on the concept of an increase in the resistance to martensite formation has been suggested. In nickel steels, this increase could be caused by the formation of a Cottrell atmosphere around dislocations.

LA STABILISATION THERMIQUE DE L'AUSTENITE DANS LES ALLIAGES FER-CARBONE-NICKEL

La stabilisation thermique de l'austenite a été investiguée au-dessous et au-dessus de M_s lors du refroidissement et lors du maintien isotherme. Il a été constaté que M_s est abaissé par stabilisation au-dessus de M_s et l'effet se manifeste par un accroissement de la quantité d'austenite retenue quand l'acier est lentement trempé jusqu'à une température de référence. La quantité de martensite perdue pendant la stabilisation, peut être récupérée en refroidissant suffisamment par après. Un mécanisme de stabilisation basé sur le concept d'un accroissement de la résistance à la formation de la martensite a été proposé. Dans les aciers au nickel, cet accroissement pourrait être causé par la formation d'un "nuage" (atmosphère) de Cottrell autour des dislocations.

THERMISCHE STABILISIERUNGEN VON AUSTENIT IN EISEN-KOHLENSTOFF-NICKEL LEGIERUNGEN

Die thermische Stabilisierung von Austenit wird oberhalb und unterhalb M_s (d.i. die Temperatur, bei der die Martensit-Transformation während des Abkühlungsvorganges beginnt) während der Abkühlung und während isothermer Halteperioden untersucht. Es stellte sich heraus, dass M_s durch Stabilisierung oberhalb von M_s herabgedrückt wird; dieser Effekt zeigt sich in einem Anwachsen der Menge des verbleibenden Austenits, wenn der Stahl langsam auf eine Bezugstemperatur abgeschreckt wird. Der Martensit, der während der Stabilisierung verloren geht, kann durch hinreichende weitere Kühlung zurückgewonnen werden. Ein Mechanismus für die Stabilisierung, der auf der Vorstellung eines Anwachsens des Widerstandes gegen die Martensit Formation basiert, wird vorgeschlagen. Dieses Anwachsen kann in Nickelstählen zur Bildung von Cottrell-Bereichen um die Versetzungen ("Dislocations") hervorgerufen werden.

1. INTRODUCTION

It has long been known that the progress of the austenite-martensite transformation can be influenced by the rate of cooling. For instance, Mathews [1] showed that oil-hardening steels contain more retained austenite when oil-quenched than when water-quenched. It has also been observed that if the cooling through the martensitic range is interrupted and the steel held isothermally for a certain period, the transformation does not necessarily resume immediately when cooling is continued but only after a certain temperature lag, which may result in a loss of martensite when the steel is quenched to a fixed reference temperature. This phenomenon, first reported by Gulyaev [2], is known as "stabilization of austenite." However, the term "thermal stabilization" is to be preferred in order to differentiate between this effect and the retarding effect of plastic deformation on the martensitic transformation, which may be called "mechanical stabilization."

Degree of thermal stabilization can be expressed in two ways:* (i) in terms of the increase, δ, in the amount of retained austenite when the steel is quenched to a reference temperature [3]; and (ii) in terms of the difference, θ, between the temperature at which cooling is interrupted and that, T_s, at which the martensitic transformation recommences when cooling is resumed [4].

The extent of stabilization, when the amount of prior transformation is constant, has been found to increase progressively with time for tool steels [5], high alloy [2; 6], low alloy [7] and plain carbon steels [8–10].

The rate of stabilization increases with increasing temperature [6; 11]. However, when the effect of temperature on the degree of stabilization is considered, then for a given steel, holding at different temperatures introduces the complexity of different amounts of prior transformation. This complication has led the two principal investigations on stabilization to yield conflicting results [3; 4].

Petrosyan [4] indicated that stabilization occurred throughout the transformation range, and that the amount of stabilization, in terms of θ, increased with decreasing holding temperature for a fixed time, passed through a maximum, then a minimum, and

*Received August 8, 1952.

†Department of Metallurgy, University of Birmingham, England. Now at Scientific Laboratory, Ford Motor Company, Dearborn, Michigan, U.S.A.

‡Department of Metallurgy, University of Birmingham, England.

*The notation used in this paper is summarized in Table I.

finally rose sharply with further decreasing temperature. This is in contrast with Harris and Cohen's finding [3] that θ increases continuously with decreasing temperature.

TABLE I
NOTATION

$M\%$	Percentage martensite
$M\%$ (Brine, oil or Hg)	Percentage martensite after brine, oil or mercury quenching.
M_o	The temperature at which austenite and martensite are in thermodynamic equilibrium.
M_s	The temperature at which the martensitic transformation begins during cooling.
M_s (Brine, oil or Hg)	The temperature at which the martensitic transformation begins during brine, oil or mercury quenching.
S_o	The temperature above which stabilization does not occur.
σ_s	The holding temperature above which isothermal stabilization is not detected.
T_a	The austenitizing temperature.
T_h	The temperature of isothermal holding.
T_r	The reference temperature.
T_s	The temperature at which the martensitic transformation resumes after isothermal stabilization.
δ	The degree of isothermal stabilization in terms of the loss of martensite.
θ	The degree of isothermal stabilization in terms of the temperature lag before the martensitic transformation resumes, i.e. $T - T_s$, where T is the temperature at which the cooling was interrupted for isothermal stabilization.

For a series of four steels containing 1.1 per cent of carbon and various amounts of chromium or nickel up to 5.5 per cent, Harris and Cohen [3] found that the maximum amount of stabilization was given by:

$$\delta_{\max} = \text{constant} \,.\, (\sigma_s - T_h),$$

where T_h is the holding temperature and σ_s is a temperature above which no stabilization was detected, and

$$\sigma_s = 0.57\ (M_s) + 26°\text{F}.$$

Depression of part of the martensitic transformation range has also been observed for iron-nickel alloys [12; 13] when the quench was interrupted and the temperature held constant. Partial transformation in the lower bainite range, above M_s, has been found [11; 14–19] to lower M_s although in at least one case [16] parameter measurements suggested that there was no compositional change in the austenite. Moreover a lowering of M_s was found following holding for periods after the isothermal bainite transformation had ceased [15]. High chromium high carbon alloys have been found to be particularly sensitive to cooling rates [20] and in certain cases M_s was depressed by reducing the cooling rate from the austenitizing temperature.

2. EXPERIMENTAL PROCEDURE

2.1 Materials Used

A series of alloys containing from 0.9 to 1.3 per cent carbon and 0 to 10 per cent nickel have been investigated. All alloys except a commercial carbon steel were melted under argon from electrolytic iron, carbonyl nickel and carbon. Chemical analyses indicated that there was no longitudinal segregation in the chill-cast ingots and the radial segregation was removed by subsequent homogenization. The compositions of the alloys are shown in Table II. The alloys contained a small amount of impurity, and a typical analysis is: 0.04 per cent Mn, 0.07 per cent Si, 0.020 per cent S and 0.020 per cent P.

TABLE II
CHEMICAL ANALYSES OF MATERIALS USED

Alloy	Per cent C	Per cent Ni
10C	1.01	Trace
10C1N	1.01	1.28
10C2N	0.92	2.66
10C5N	1.08	5.04
10C10N	0.98	9.92
12C2N	1.26	2.00
13C5N	1.32	4.72
Carbon Steel	1.07	0.12

The ingots homogenized for eight hours at 1100°C (2010°F) under argon and nickel plated, were forged (4:1 reduction), and the central portions of the bars were further homogenized at 1150°C (2100°F) until test samples showed no signs of heterogeneity. The bars were ground between each stage. After annealing at 475°C (887°F) for 18 hours, they were ground to 0.5 in. diameter and machined to 0.125 in. discs. These discs were stored in a dessicator to prevent surface rusting. The use of flat specimens ensured that the section examined, which was parallel to the flat surface, was free from such stress and temperature gradients as would have been produced in a cylindrical specimen.

2.2 Austenitizing and Quenching

A high austenitizing temperature was used, as results obtained by Sheehan, Julien and Troiano [21] indicate that in certain alloys of the present type there is a possibility of graphitization during

the anneal before machining. In order to avoid either carburization or decarburization of specimens, austenitizing was carried out in a modified salt bath, which was neutral to 1.1 per cent alloys at 1100°C (2010°F). All the specimens were austenitized at this temperature.

The specimens were suitably mounted on a wire to avoid contamination and lowered into the quenching media in a horizontal position. The equipment was so arranged that the transference of specimens from the austenitizing furnace to the quenching bath and from the quenching bath to the tempering bath could be made in less than 2 seconds. The specimens were retained in the quenching medium for 10 seconds beyond the time required to reach steady temperature in that medium. For quenching below 0°C the maximum quenching rate was obtained by quenching into brine at 0°C followed immediately by refrigeration.

Cooling rates in all the media were determined at selected temperatures by means of a standard specimen on to which were welded thermocouple elements, one on each flat side of the specimen. For measurement of the quenching rate in mercury, an insulated alumel wire was sealed into the specimen while a chromel wire was welded to one flat face. The cooling curves for brine showed that there was a difference of 1/40 second in the respective times required to cool through the range 400–350°C in these two arrangements.

Figure 1 illustrates, for saturated brine, the effect of raising the quenching bath temperature upon the quenching efficiency when the temperature of the medium is raised from 23°C (73.4°F). There is a marked falling off above 66°C (150.8°F). This effect, as will be seen later, is reflected in the progress of the martensitic transformation as determined by quenching into brine. Similar quenching curves are

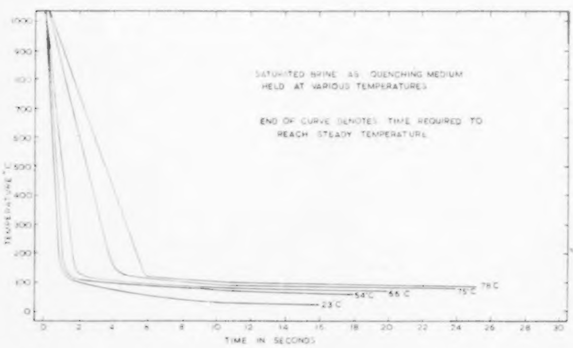

FIGURE 1. The effect of raising the quenching bath temperature upon the cooling rate of 0.500 in. diameter 0.125 in. thick steel discs quenched from 1100°C (2012°F) into brine.

shown in Figure 2 where mercury is the quenching medium. In this case there is a smooth change in the quenching efficiency of mercury as the bath temperature is raised.

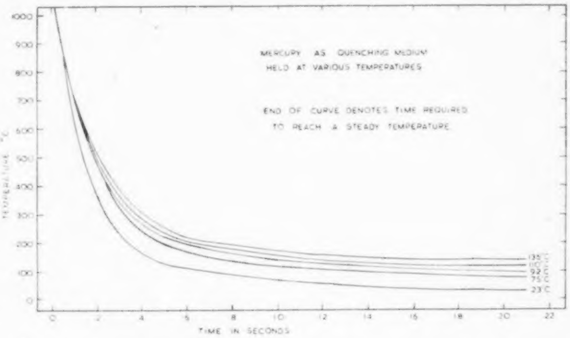

FIGURE 2. The effect of raising the quenching bath temperature upon the cooling rate of 0.500 in. diameter 0.125 in. thick steel discs quenched from 1100°C (2012°F) into mercury.

2.3 Estimation of the Amount of Martensite

The individual specimens were examined for macroscopic heterogeneity and for carburization or decarburization at the edges after heat-treatment. The actual surface examined was exposed by the removal of 0.025 in. from one flat surface. No specimen was accepted if it showed any heterogeneity.

The amount of martensite was estimated by counting after tempering for 30 seconds at 300°C (572°F), a time and temperature established as satisfactory for the present alloys. Specimens in a few series were tempered at other temperatures, as indicated on the diagrams. The reproducibility from specimen to specimen was of the order of ± 1.5 per cent martensite. All results for individual specimens had a 95 per cent probability of an error not more than ± 1.5 per cent. The etchant used was 4 per cent nital with the addition of 1 per cent cetyl dimethyl benzyl ammonium chloride.

3. EXPERIMENTAL RESULTS

3.1 Transformation Curves

Curves indicating the progress of transformation (M–T curves) are given in Figures 3 to 10 inclusive. These show that:

(i) For the alloys studied except 10C10N and 13C5N, M_s is dependent upon the quenching medium used, an indication that the rate of cooling through the austenitic range must have an effect upon the martensitic transformation.

(ii) For a given alloy the results from an individual quenching medium lie on a smooth curve, but the curves for the different media do not coincide.

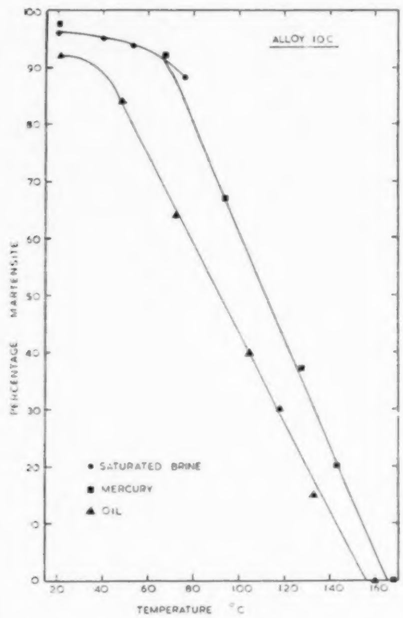

FIGURE 3. Martensite transformation curves for 1.0 per cent carbon-iron alloy.

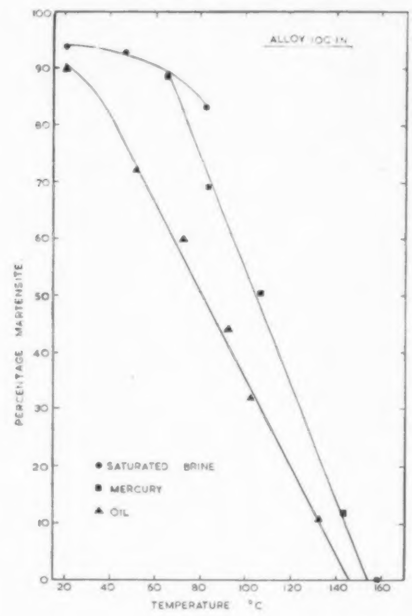

FIGURE 4. Martensite transformation curves for 1.0 per cent carbon 1.3 per cent nickel-iron alloy.

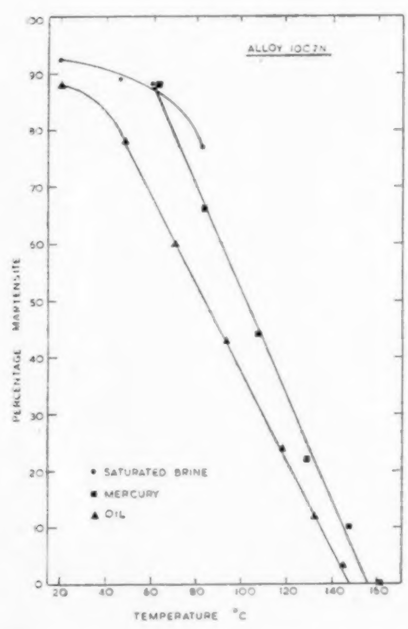

FIGURE 5. Martensite transformation curves for 0.9 per cent carbon 2.7 per cent nickel-iron alloy.

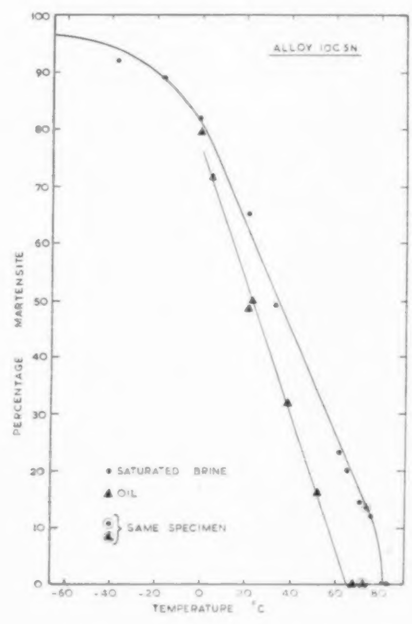

FIGURE 6. Martensite transformation curves for 1.1 per cent carbon 5 per cent nickel-iron alloy.

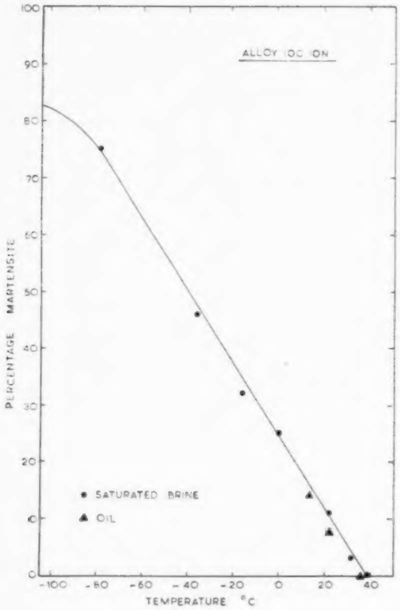

FIGURE 7. Martensite transformation curves for 1.0 per cent carbon 10 per cent nickel-iron alloy.

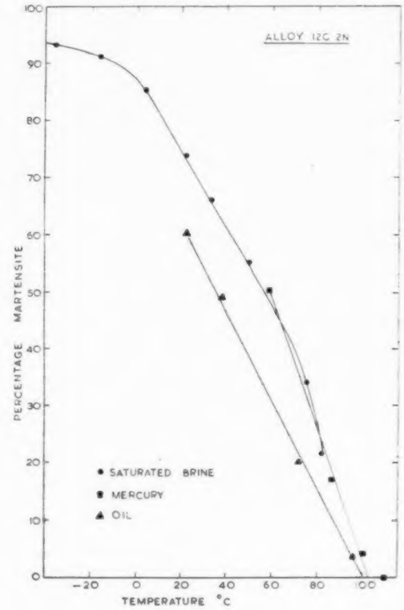

FIGURE 8. Martensite transformation curves for 1.3 per cent carbon 2 per cent nickel-iron alloy.

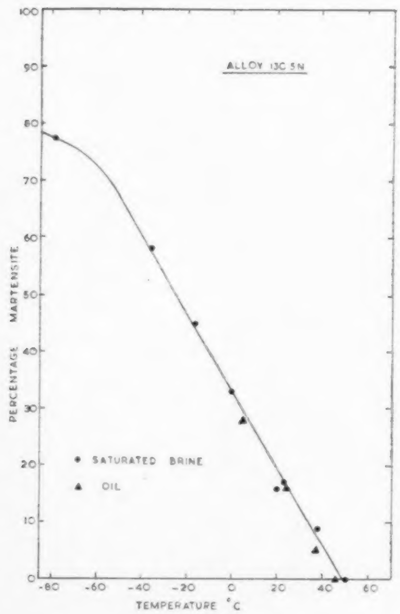

FIGURE 9. Martensite transformation curves for 1.3 per cent carbon 4.7 per cent nickel-iron alloy.

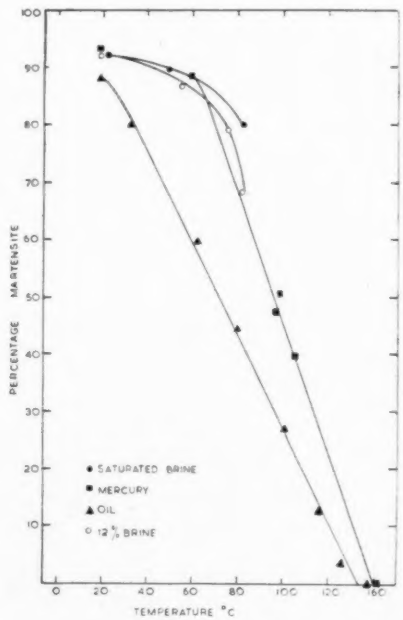

FIGURE 10. Martensite transformation curves for 1.1 per cent carbon steel (0.4 per cent Mn, 0.1 per cent Ni).

However, the amount of martensite in the mercury-quenched specimens approached that in brine-quenched specimens when the temperature of the quenching medium was sufficiently low.

(iii) The amount of martensite formed in both mercury- and oil-quenched specimens is linearly related to temperature from M_s to about 70 per cent of martensite, except in the case of the mercury-quenched alloy 12C2N (Fig. 8) for which the curve is linear up to about 50 per cent martensite. In the case of brine quenching there is a divergence from linearity above 70°C (158°F) which becomes more marked as the temperature rises, undoubtedly owing to the rapid lowering of the quenching power of the brine. There is no evidence of departure from linearity of the M–T curves near M_s, as reported by many other workers who used commercial steels.

(iv) The M–T curves tail off at martensite contents higher than 85 per cent, and the transformation is not complete at − 195°C (− 315°F). The amount of retained austenite at this temperature varies from about two per cent for alloy 10C to 17 per cent for alloy 13C5N.

The fact that there is a depression of M_s during oil quenching, compared with the M_s for a more rapid quench, was verified in the following manner: A specimen of alloy 10C5N was quenched in oil to 72°C (161.6°F), which lies between M_s (oil) and M_s (brine). Examination after tempering showed no dark martensite. When this *same* specimen was re-austenitized and brine-quenched to 74°C (165.2° F) it contained 14 per cent of martensite, a value corresponding to that of a specimen used only once.

Grange [22] has pointed out that tailing-off of the M–T curves near M_s increases with increasing banding and is smaller with laboratory melts where care has been taken to reduce the segregation. During the preparation of alloys for the present work, special precautions were taken to minimize the segregation of alloying elements and this probably accounts for the resultant M–T curves being linear from M_s.

Alloy 10C2N has a mixed grain size, as shown in Figure 11, the majority of the grains conforming to the range ASTM No. 5 to 6, but there are occasional large grains which have an effective size of ASTM No. 0 to − 1. The cause of the formation of the mixed grain size is not clear. Actual counting showed that the grain size had no effect upon the progress of the transformation. Grange and Stewart [23], who determined the M_s of a 0.65 per cent carbon steel, also found that grain size variation, within the range ASTM No. 6 to 2, had no effect on the progress of the martensitic transformation.

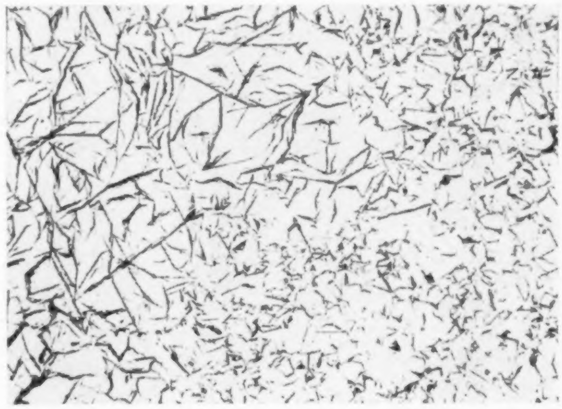

FIGURE 11. Specimen of alloy 10C2N austenitized at 1100°C (2012°F) and mercury quenched to 129°C (264°F). × 60.

3.2 Thermal Stabilization

3.21 *Thermal Stabilization above M_s*

The observation that the M_s temperatures in these alloys depend on the quenching medium used indicates that certain changes which take place during quenching affect the martensitic transformation. This difference in M_s must contribute significantly towards the difference in retained austenite in the brine- and oil-quenched specimens.

Moreover, the present M–T curves produced by quenching into different media were not parallel, and the difference was largest at about 70°C (158°F). The decreasing divergence below 70°C (158°F) can be partly accounted for in alloys 10C, 10C1N, 10C2N, and the carbon steel, by the non-linearity of the M–T curves at high martensite contents. However, in alloys 10C5N and 12C2N there is still a decrease in divergence below 70°C (158°F), whereas had significant stabilization during quenching been occurring below M_s as suggested by Harris and Cohen [3], the divergence would be expected to increase as the quenching temperature decreased, so long as the linear portions only of the curves were considered. This suggests that the difference between the amounts of retained austenite found after oil and water quenching to the same temperature is due mainly to an effect occurring above M_s. If this is so, the difference between the rates of cooling produced by quenching into oil and brine must be a maximum when the quenching media are held at approximately 70°C (158°F). Comparison of the cooling curves in Figure 12 shows that there is a marked difference between the cooling rates pro-

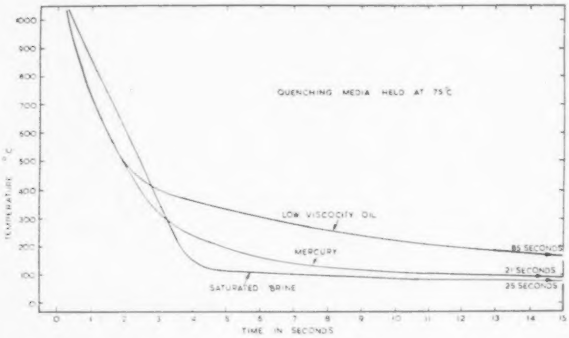

FIGURE 12. Cooling curves of a steel specimen 0.500 in. diameter and 0.125 in. thick in saturated brine, mercury and oil at 75°C (167°F).

duced by brine and oil quenching into the respective media held at 75°C (167°F). Moreover, comparison of the cooling curves for brine and mercury held at 75°C (167°F) shows that the cooling rate achieved by quenching into brine is the greater only below approximately 650°C (1200°F). Consequently, as quenching into brine held at 75°C (167°F) produces more martensite than quenching into mercury held at the same temperature (Figs. 4, 5 and 8) the process of stabilization must occur below 650°C (1200°F).

(i) *Effects of cooling rate above M_s.* The effects of varying the cooling rate above M_s on the amount of retained austenite were investigated by quenching specimens at various rates through different ranges. The results are shown in Tables III and IV.

TABLE III
(Specimens tempered at 300°C (572°F) for 30 seconds)

Alloy	Reference temperature	Per cent martensite	Cooling procedure
10C5N $M_s \sim 80$°C	73°C (163.4°F)	12	Mercury-quenched to 110°C (230°F) and held for 65 min. before brine quenching to 73°C
	72°C	14	Direct saturated brine quench
Carbon Steel $M_s \sim 140$°C	20°C (68°F)	88	Salt - quenched to 155°C (311°F) and air-cooled to 20°C
	20°C	88	Direct oil quench
	20°C	87	Salt-quenched to 155°C and brine-quenched to 20°C

These results clearly show that stabilization was occurring rapidly between 405°C (761°F) and 310°C (590°F) because the amount of stabilization is independent of the cooling rate above the first temperature, and only slightly dependent below 310°C (590°F). This means that there is a temperature, S_0, above which stabilization cannot occur. It lies between 310°C (590°F) and 405°C (761°F) for the alloy 10C5N. The progress of transformation below M_s was virtually independent of cooling rate below 155°C (311°F) in the carbon steel.

TABLE IV
ALLOY 10C5N
Reference temperature 22°C (71.6°F)

Per cent martensite	Cooling procedure
	Quenched into lead bath at 405°C (761°F) held 30 seconds and then
60	(*a*) brine-quenched to reference temperature
51	(*b*) oil-quenched to reference temperature
47	(*c*) air-cooled to reference temperature
	Quenched into lead–tin eutectic alloy at 310°C (590°F) held 30 seconds and then
52	(*a*) brine-quenched to reference temperature
50	(*b*) oil-quenched to reference temperature
47	(*c*) air-cooled to reference temperature
	Quenched into lead–tin eutectic alloy at 200°C (392°F) and held 15 minutes and then
51	(*a*) brine-quenched to reference temperature
50	(*b*) oil-quenched to reference temperature
52	Quenched into lead–tin eutectic alloy at 200°C (392°F) held 30 seconds and then brine-quenched to reference temperature
60	Brine-quenched to reference temperature
50	Oil-quenched to reference temperature

(ii) *Isothermal stabilization above M_s.* It was thus shown that the depression of M_s was due to a stabilization effect which occurred below 405°C (761°F). The rate of this process was then measured by holding specimens of alloy 10C5N isothermally at different temperatures. Since the previous results and cooling curves had shown that complete stabilization would occur during slow direct quenching to these holding temperatures, the specimens were quenched to a lower temperature and immediately heated to the required holding temperatures.

Specimens of alloy 10C5N were mercury-quenched to 120°C (248°F) and immediately raised to 202°C (395.6°F) and 280°C (536°F) ± 2°C (4°F), for periods of between 0 and 195 minutes and then quenched in brine to a reference temperature of 75°C (167°F). Measurement of the holding period was begun at the time at which the specimen was estimated to be at steady temperature as shown by cooling curves.

The results are given in Figures 13 and 14, and it is evident that the depression of M_s, calculated from the amount of martensite lost at the reference temperature due to the isothermal holding, in-

creases with increasing time. For alloy 12C2N similar tests showed that a 4°C (7°F) depression in M_s could be achieved in 20 minutes at 200°C (392°F) and further holding up to 65 minutes did not produce any significant further depression.

Accurate measurements of activation energy for stabilization are in progress; preliminary estimates yield an approximate value of 30,000 cal. per mole. Consequently if this process is occurring at temperatures up to 400°C (752°F) it will occur at the rates given below:

Temperature °C	°F	Time required for 6°C (11°F) depression of M_s of alloy 10C5N
280	536	38 seconds
300	572	14
325	617	4.6
350	662	1.6
375	707	0.6
400	752	0.25

From Figures 13 and 14, it is apparent that the rate of stabilization depends upon the amount of stabilization that has already occurred, the process becoming slower as it progresses. In alloy 10C5N, the maximum difference between the amounts of martensite produced in brine and oil quenching is of the order of 20 per cent (depression of 20°C or 36°F). The data given above for the time required to give a 6°C (11°F) depression of M_s apply to the later portions of the process; it is to be expected that the full 20 per cent stabilization occurs in less than three times the values quoted for the 6°C depression. Comparison with the times required for oil- and brine-quenched specimens to pass through the various ranges of temperature indicates that the stabilization must have begun in the temperature range 375° to 400°C (707°-752°F). The 20 per cent loss of martensite is the integrated result of stabilization during quenching. The values plotted in Figures 13 and 14 thus represent the continuation of the stabilization which had already occurred during initial mercury quenching before the temperature was raised for isothermal stabilization tests.

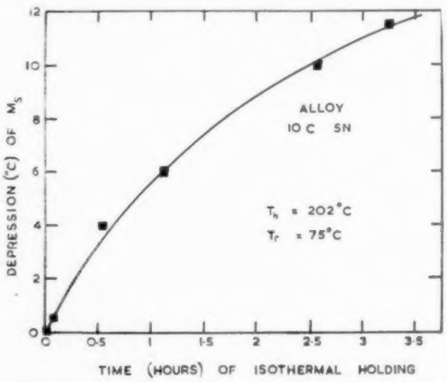

FIGURE 13. Isothermal stabilization of alloy 10C5N at 202°C (395.6°F).

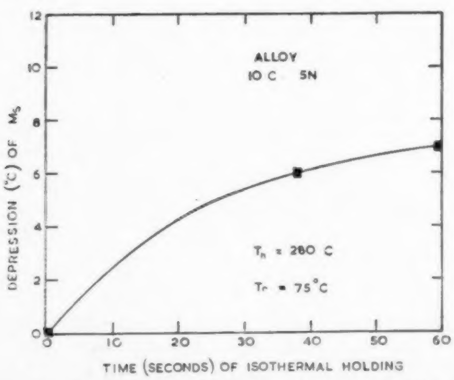

Figure 14. Isothermal stabilization of alloy 10C5N at 280°C (536°F).

3.22 *Isothermal stabilization below M_s*

Although the experiments described in the previous sections clearly show that the difference in the amount of martensite at a given temperature in the martensitic range is due mainly to a process taking place above M_s, stabilization can still occur if the steel is held below M_s for a sufficient time. Investigations were, therefore, made into this phenomenon.

(i) *Carbon steel, alloys* 10C5N, 12C2N. When the carbon steel was quenched to different holding temperatures between 130°C (266°F) and 20°C (68°F), isothermally held for 30 minutes, and then brine-quenched to a reference temperature of 20°C (68°F), no stabilization was observed until a certain temperature σ_s was reached. The amount of austenite stabilized increased with decreasing holding temperature to a maximum and then decreased again when the normal M–T curve was intercepted. The curve is similar to those given by Harris and Cohen [3] (their Fig. 9). However, when the amounts of martensite were examined at a reference temperature of − 193°C (− 315°F), no difference was observed between the specimens. In other words, the effect of stabilization between σ_s (for T_r = 20°C) and 20°C had been completely removed by further cooling to − 193°C (− 315°F).

Results obtained with a series of reference temperatures for a given holding temperature are shown in Figures 15 and 16. Figure 15 shows that, after quenching in 12 per cent brine to 70°C (158°F) and holding there for 30 minutes, the remaining austenite

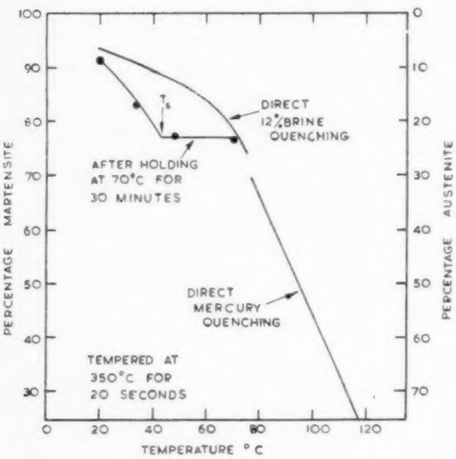

FIGURE 15. Martensite transformation curves for carbon steel during normal quenching and after holding at 70°C (158°F) for 30 minutes.

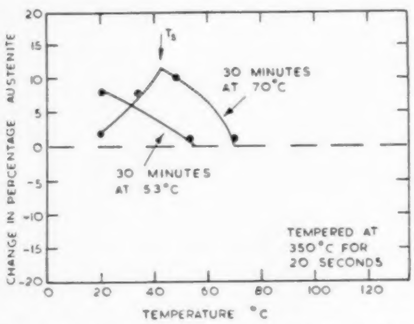

FIGURE 16. Amounts of austenite stabilized in carbon steel at different reference temperatures after isothermal holding for 30 minutes at 70°C (158°F) and 53°C (127.4°F).

was completely stabilized until it was cooled to 43°C (109°F). When cooled below this temperature the austenite continued to transform but at a rate which was greater than that shown by the M–T curve obtained from direct quenching in 12 per cent brine, until at the reference temperature of 20°C (68°F), the effect of stabilization had almost been removed. That the effect of stabilization can be completely removed has also been observed in Krupp steels with more than 0.9 per cent carbon [24]. Thus it is evident that the amount of stabilization observed depends upon the reference temperature used; so does the temperature σ_s above which no stabilization is observed at a given reference temperature. Figure 16 in which the effect of holding at 70°C (158°F) is shown, together with that for a holding temperature of 53°C (127.4°F), illustrates the fact that the temperature at which the maximum amount of stabilization is observed is affected by the holding temperature. Similar results were obtained with specimens of the carbon steel quenched into saturated brine, and with alloys 10C5N and 10C2N (Figs. 17–20).

For a determination of the rate of stabilization below M_s it is necessary to maintain a constant martensite content, as it is known that stabilization depends on the degree of prior martensitic transformation [3].

Specimens of alloy 10C5N were, therefore, first brine-quenched to 43°C (109.4°F) which produced 37 per cent of martensite. They were then isothermally stabilized for different periods at 43°C (109.4°F) or 74°C (165.2°F) before quenching to 22°C (71.6°F). A reference temperature of 22°C was selected because this had been shown to be low enough to allow up to 20 per cent stabilization to be measured and yet high enough to prevent the transformation below T_s from removing an observable effect. The maximum increase of retained austenite is limited to 20 per cent by the choice of reference temperature. Before the maximum amount is reached, the degree of stabilization increases with

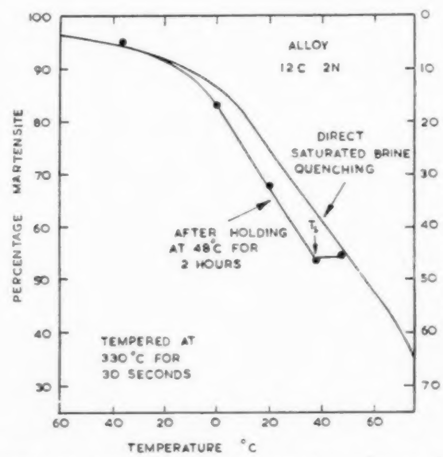

FIGURE 17. Martensite transformation curves for alloy 12C2N during normal quenching and after holding at 48°C (118.4°F).

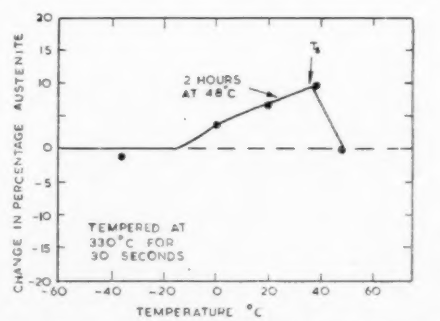

FIGURE 18. Amounts of austenite stabilized in alloy 12C2N at different reference temperatures after isothermal holding for 2 hours at 48°C (118.4°F).

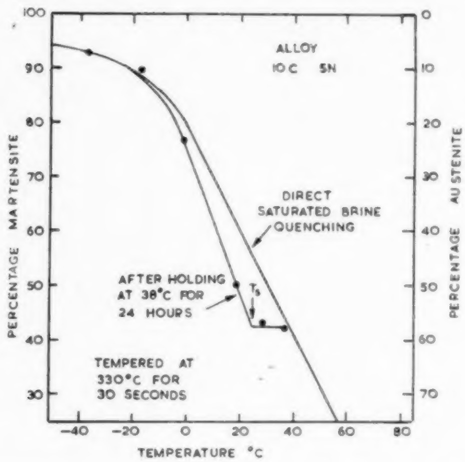

FIGURE 19. Martensite transformation curves for alloy 10C5N during normal quenching and after holding at 37°C (100.4°F) for 24 hours.

increasing time, the time required for it to reach a value of 12 per cent being one minute and 75 minutes at 74°C (165.2°F) and 43°C (109.4°F) respectively. At 74°C (165.2°F), 2 minutes were required to give 20 per cent stabilization.

(ii) *Alloy* 13C5N. Specimens of alloy 13C5N were brine quenched to 50°C (122°F) and held for 0.5 to 24 hours before cooling to the reference temperature of 22°C (71.6°F). In no case was there observable stabilization.

Harris and Cohen [3] had suggested that isothermal stabilization could occur only if the steel was first cooled below σ_s before holding. Accordingly, specimens were quenched to 2°C (35.6°F) (σ_s, in Harris and Cohen's equation, is 36°C or 96.8°F) and then held at temperatures above and below 36°C. The amounts of austenite stabilized at a reference temperature of − 36°C (− 32.8°F) were as follows:

Holding temperature		Holding time	Austenite stabilized at −36°C
°C	°F	Minutes	per cent
49	120.2	23	2
25	77.0	120	0

There was apparently no significant isothermal stabilization in alloy 13C5N after such treatment. It is unlikely that the austenite had been completely removed at the reference temperature; in view of the fact that there was also little difference between M_s (brine) and M_s (oil) for these alloys, it was possible that only a small amount of isothermal stabilization could be observed, at least when the martensite content was below 30 per cent.

The present findings agree with Harris and

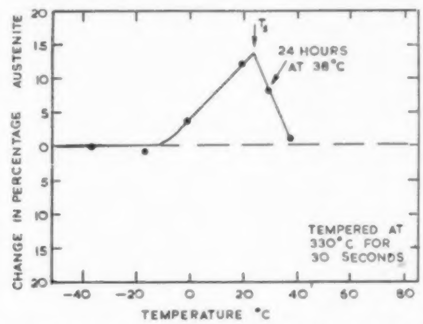

FIGURE 20. Amounts of austenite stabilized in alloy 12C2N at different reference temperatures after isothermal holding for 24 hours at 38°C (100.4°F).

Cohen's [3] conclusion that there is a holding temperature, σ_s, above which stabilization cannot be observed under a given experimental condition. It is evident, however, that σ_s varies with experimental conditions and has little significance. Indeed, Petrosyan [4] has found that stabilization can occur at all temperatures below M_s.

There are several causes which can lead to the observation of a σ_s:

(*a*) It has been shown that the effect of stabilization can be removed by sufficient further cooling. Thus, if the reference temperature is sufficiently low, the effect of stabilization will not be observed.

(*b*) Stabilization of austenite is slow at temperatures below 150°C, unless an appreciable amount of martensite is present. For a fixed time of isothermal holding, the amount of stabilization near M_s, if this is low, may be small and unobservable under certain experimental conditions.

(*c*) It has been found that unless the proper temperature and time have been chosen, tempering may lead to the formation of bainite at the austenite-martensite interface. Thus any small stabilization effects near M_s, such as those recorded by Petrosyan [4], might be obscured by tempering.

4. DISCUSSION

Stabilization occurs by affecting the progress of transformation; some process takes place in the austenite during ageing which influences either the nucleation or the growth of martensite crystals on further cooling. The temperature dependence of the progress of the martensitic transformations is a characteristic of the process, and no satisfactory explanation has yet been advanced. That an explanation of the phenomenon of stabilization must be an integral part of any theory of martensitic transformation has long been pointed out by Troiano [25].

The following theories of stabilization have been previously proposed:

(i) Stress relaxation theory. Various authors [26–28] have proposed that isothermal stabilization occurs by relaxation of stresses. Orowan suggested [29] that the stresses around one martensite plate assist in the formation of other plates in the vicinity. Such relaxation would probably cause stabilization in those alloys, such as In-Tl [30], in which martensitic transformation proceeds by alternating shears. However, in austenite, martensite plates do not always form in the vicinity of previous plates, so that stabilization would not be expected to prevent completely the subsequent transformation.

(ii) Composition change theory. Fisher, Hollomon and Turnbull [31] suggest that austenite regions of statistically low carbon content, at the austenitizing temperature, act as nuclei at M_s when they are retained during the quench. Fisher [32] suggests that stabilization may be due to a migration of carbon from the carbon poor regions, now in the form of ferrite, to the surrounding austenite, thereby lowering the temperature at which the austenite can transform. This theory is unacceptable for the following reasons: (*a*) A stabilization effect of as much as 20°C depression in M_s has been observed in a 1.0 per cent carbon alloy. This depression would be equivalent to an increase of about 0.1 per cent carbon in the austenite. Results obtained in investigations on bainite formation show no indication that there was any change in composition of this magnitude prior to the formation of bainite. (*b*) It should not be possible to remove the effect of stabilization if this was due to an increase in the carbon content of austenite. Furthermore, the slope of the M–T curves should be smaller than that of the unstabilized austenite. These are contrary to the present observations.

(iii) Exhaustion of nuclei theory. Most of the recent theories of martensite transformation [31–35] depict that the temperature dependence of athermal martensite formation is the consequence of exhaustion of nuclei, which have a statistical distribution in size. Each nucleus grows to full length controlled by the boundaries of the austenitic regions and to a thickness determined by strain considerations. The stabilization could be due to some effect upon the nuclei of martensite plates either by relaxation [35] or by a redistribution of embryos due to statistical fluctuations [34]. The second possibility is unlikely because it has been found that there is an upper limit for stabilization, S_0, and Cohen and his coworkers (36) have also shown that the progress of martensite transformation in a nickel-iron is insensitive to the prequenching temperature in the austenite range.

The progress of martensitic transformation is not *necessarily* controlled by the exhaustion of nuclei, as can be seen from the following considerations:

(*a*) In the case of an Au-Cd alloy containing 47.5 atomic per cent of Cd (27), the transformation from a single crystal of the high temperature phase to a single crystal of the low temperature phase occurs by the movement of a single interface and is temperature dependent. Stabilization has been observed in this single-interface transformation.

(*b*) Kurdjumov and his coworker [37] have reported that, in a Cu-Al-Ni alloy, the martensitic transformation was reversible without any hysteresis in the martensitic range, and a different set of martensite crystals was obtained only when the alloy had been reheated to above M_s and cooled.

(*c*) When both coarse and fine grains are present, it is to be expected from the exhaustion theory that the same number of nuclei will be available, so that, as the plates in the small grains are shorter and thinner, less martensite should form. According to Fisher and his coworkers [31] a difference of about 15 per cent is expected when the austenitic grain size varies from ASTM No. 6 to No. 0. In fact, the same volume percentage of martensite ($\pm$ 1.5 per cent) has been obtained at the same temperature in the present work, and there is no indication in the literature that austenite grains of vastly different sizes give appreciably different amounts of martensite, although M_s may be slightly affected owing to the additional constraint in fine-grained materials.

An alternative point of view which is qualitatively satisfactory and worthy of consideration is that the progress of the transformation is partly controlled by the resistance offered by the matrix to the growth of the new crystals.

This resistance is important in the case of shear transformations in which the rate of growth is relatively high so that thermal agitation plays a less important part in overcoming the resistance. A more detailed description of this concept will be given elsewhere; it is sufficient to mention here the following points. The growth of martensite can be viewed as taking place by the movement of an interface consisting of a set of fractional dislocations [38]. The movement of these dislocations will be impeded by the presence of obstacles, such as other dislocations in the parent phase. When plastic

deformation takes place in the austenite during the formation of martensite, more dislocations will be generated, and additional driving force must be provided before more martensite can form. This offers an explanation for the temperature dependence of the transformation and also for the phenomenon of mechanical stabilization.

The thermal stabilization can then be caused by an increase in the resistance of austenite to the growth of martensite due to the formation of carbon clusters during slow quenching or during isothermal holding. The suggestion that carbon may be responsible for stabilization in steels is consistent with the preliminary estimate of the activation energy for stabilization. The present value of about 30,000 cal. per mole is of the same order of magnitude as the value of the activation energy for the diffusion of carbon in austenite free from martensite.

The carbon grouping could occur anywhere within the matrix austenite. In steels which contain no carbide-forming elements, it is more likely that it occurs at dislocations by forming Cottrell atmospheres. If this is correct, the time required for stabilization to take place should be that required for carbon atoms to move a distance greater than that between carbon atoms but smaller than that between dislocations. The diffusion constant A_0 and activation energy Q for carbon diffusion at 5 atomic per cent carbon have been given by Wells, Batz and Mehl [39] as 0.1 $cm^2/sec.$ and 30,000 cal. per mole respectively. If it is assumed that these data remain valid in the temperature range 200–400°C (390–750°F), the length of diffusion path at these temperatures can be estimated. At 280°C (536°F), $D \sim 10^{-13} cm^2/sec.$, the time required for stabilization is of the order of 100 seconds, therefore $x = \sqrt{(Dt)}$ or 10^{-5} to 10^{-6}cm., which seems of the right order of magnitude required by the mechanism.

The formation of a Cottrell atmosphere around dislocations will not result in a permanent loss of martensite. On cooling to T_s, after holding at T_h and producing isothermal stabilization, the driving force for the transformation will have increased sufficiently to overcome the extra resistance and the first martensite plates will form. The formation of these plates will result in plastic deformation of the austenite matrix and some of the dislocations will be moved away from their anchoring carbon groups. As long as rapid cooling is continued, these released dislocations will remain free. The lower resistance together with the increased driving force will enable the resumed transformation to proceed at a greater rate, and the effect of stabilization will eventually be removed.

The concentration of carbon atoms in a dislocation will decrease with increasing temperature until at the temperature S_0 it becomes so small that stabilization cannot occur. The temperature S_0 should be higher, the higher the carbon content. Thus in the present alloys of higher nickel and carbon contents, there should be a marked increase in the rate of stabilization during quenching owing to an increase in S_0 and in the rate of diffusion of carbon in the presence of nickel [40]. This offers a possible explanation for the fact that M_s (brine) and M_s (oil) are similar in the alloy 10C10N and 13C5N, because M_s (brine) will represent a markedly depressed M_s. Furthermore, since the completeness of an atmosphere will increase with decreasing temperature, the maximum degree of stabilization will also increase with decreasing temperature, although this maximum effect may not be obtained by a limited time of ageing at low temperatures owing to the low rate of diffusion.*

5. SUMMARY AND CONCLUSIONS

The phenomenon of stabilization of austenite during continuous cooling and during isothermal holding above and below M_s has been studied. Using specially selected homogeneous materials, it has been shown that, for steels containing about 1 per cent carbon and 0–5 per cent nickel:

(i) Stabilization of austenite occurs during isothermal holding above and below M_s. The rate of stabilization varies with the composition of the austenite, increases with increasing temperature and is greatly increased by the presence of martensite.

(ii) The stabilization above M_s causes a depression of M_s and increases the amount of austenite at a reference temperature near M_s.

(iii) The difference in the amounts of retained austenite in a steel quenched at various rates is chiefly due to stabilization above M_s during quenching.

(iv) The amount of martensite lost due to athermal and isothermal stabilization can be recovered by quenching to a sufficiently low temperature.

It is suggested that stabilization is caused by an increase in the resistance of austenite to martensite

Note added in proof. Further work carried out by one of the authors (T.K.) and his coworkers indicates that some other factors can be involved in addition to the carbon and nickel contents in preventing the observation of stabilization above M_s.

formation, and that this increase is mainly due to the formation of Cottrell atmospheres around dislocations.

6. ACKNOWLEDGEMENTS

The research was carried out in the Metallurgy Department of the University of Birmingham, under the direction of Professor D. Hanson, Director of the Departments of Metallurgy and Industrial Metallurgy, to whom the authors' gratitude is due for his interest, encouragement and advice. The authors' thanks are also due to Professor C. S. Barrett of Chicago, and Professor A. H. Cottrell and Mr. F. R. N. Nabarro of Birmingham for helpful discussions. The investigation has been supported by British Timken Ltd., and the authors are indebted to Messrs. D. McNicoll, J. H. Evans, J. Mills and R. Treen of this firm for innumerable works facilities and to other members of staff for their co-operation. Thanks are due to Mr. H. W. G. Hignett of The Mond Nickel Co. Ltd., for the supply of nickel. Messrs. B. Edmondson, and S. G. Glover have given considerable help in the experimental work.

REFERENCES

1. Mathews, J. A. Trans. Amer. Soc. Steel Treating, **8** (1925) 565.
2. Gulyaev, A. P. Metallurg, **14** (1939) 64.
3. Harris, W. J., Jr. and Cohen, M. Trans. Amer. Inst. Min. Met. Eng., **180** (1949) 447.
4. Petrosyan, P. P. Dok. Akad. Nauk SSSR., **59** (1948) 6.
5. Fletcher, S. G. and Cohen, M. Trans. Amer. Soc. Metals, **34** (1945) 216.
6. Gordon, P. and Cohen, M. Trans. Amer. Soc. Metals, **30** (1942) 569.
7. Scheil, E. Z. Anorg. Allg. Chem., **183** (1929) 98.
8. Nielsen, H. P. and Dowdell, R. L. Trans. Amer. Soc. Metals, **22** (1934) 810.
9. Shteinberg, S. S. and Zyuzin, V. I. Metallurg, **11** (1936) 3.
10. Tammann, G. and Scheil, E. Z. Anorg. Allg. Chem., **157** (1926) 1.
11. Fletcher, S. G., Averbach, B. L., and Cohen, M. Trans. Amer. Soc. Metals, **40** (1948) 703.
12. Forster, F. and Scheil, E. Z. Metallkunde, **28** (1936) 245.
13. Jones, F. W. and Pumphrey, W. I. J. Iron Steel Inst., **163** (1949) 121.
14. Lyman, T. and Troiano, A. R. Trans. Amer. Soc. Metals, **37** (1946) 402.
15. Gulyaev, A. P. Metallurg, **15** (1940) 43.
16. Lyman, T. and Troiano, A. R. Trans. Amer. Inst. Min. Met. Eng., **162** (1945) 196.
17. Gordon, P., Cohen, M., and Rose, R. S. Trans. Amer. Soc. Metals, **31** (1943) 161.
18. Troiano, A. R. Trans. Amer. Soc. Metals, **41** (1949) 1093.
19. Shteinberg, S. S. and Zyuzin, V. I. Arch. Eisenhüttenw., **7** (1934) 537.
20. Klier, E. P. and Troiano, A. R. Trans. Amer. Inst. Min. Met. Eng., **162** (1945) 175.
21. Sheehan, J. P., Julien, C. A., and Troiano, A. R. Trans. Amer. Soc. Metals, **41** (1949) 1165.
22. Grange, R. A. (Discussion to a paper by R. T. Howard, Jr. and M. Cohen) Trans. Amer. Inst. Min. Met. Eng., **176** (1948) 397.
23. Grange, R. A. and Stewart, H. M. Trans. Amer. Inst. Min. Met. Eng., **167** (1946) 467.
24. Otte, H. M. and Ko, T. To be published in J. Iron Steel Inst., **173** (1953) January.
25. Troiano, A. R. (Discussion to a paper by C. Zener) Trans. Amer. Inst. Min. Met. Eng., **167** (1946) 550.
26. Hollomon, J. H., Jaffe, L. D., and Buffum, D. C. J. Appl. Phys., **18** (1947) 780.
27. Chang, L. C. and Read, T. A. Trans. Amer. Inst. Min. Met. Eng., **189** (1951) 47.
28. Barrett, C. S. Discussion to [11].
29. Orowan, E. Symposium on Internal Stresses in Metals and Alloys (London, Institute of Metals, 1948), p. 47.
30. Bowles, J. S., Barrett, C. S., and Guttmann, L. Trans. Amer. Inst. Min. Met. Eng., **188** (1950) 1478.
31. Fisher, J. S., Holloman, J. H., Turnbull, D. Trans. Amer. Inst. Min. Met. Eng., **185** (1949) 691.
32. Fisher, J. C. Thermodynamics in Physical Metallurgy (Cleveland, Amer. Soc. Metals, 1950) p. 201.
33. Kurdjumov, G. V. Z. Tek. Fiz., **18** (1948) 999. Also Dok. Akad. Nauk SSSR., **60** (1948) 1543.
34. Cohen, M. Trans. Amer. Soc. Metals, **41** (1949) 35.
35. Cohen, M., Machlin, E. S., Paranjpe, V. G. Thermodynamics in Physical Metallurgy (Cleveland, Amer. Soc. Metals, 1950), p. 242.
36. Cohen, M. and Machlin, E. S. Trans. Amer. Inst. Min. Met. Eng., **189** (1951) 746.
37. Kurdjumov, G. V. and Khandros, L. G. Dok. Akad. Nauk SSSR., **66** (1949) 211.
38. Barrett, C. S. In "Phase Transformation in Solids" (New York, Wiley, 1950), p. 343.
39. Wells, C., Batz, W., and Mehl, R. F. Trans. Amer. Inst. Min. Met. Eng., **188** (1950) 553.
40. Wells, C. and Mehl, R. F. Trans. Amer. Inst. Min. Met. Eng., **140** (1940) 279.

PLASTIC DEFORMATION OF ALPHA-URANIUM; TWINNING AND SLIP*

R. W. CAHN†

Data on the crystallography of twinning, slip and kinking in α-uranium are reported. In default of single crystals, very coarse grained uranium was used for the experiments, in conjunction with a new design of X-ray camera. The techniques, some of them new, used for finding the slip, twinning and kink band planes, the slip directions and the directions and magnitudes of the twinning shears are fully set out. A discussion follows of the observed intersections of twins and their application to the confirmation of twin directions. The principal slip plane is (010), the slip direction [100], and the kink bands are normal to [100]. {110} is a subsidiary slip plane. The twinning elements found are tabulated. One of the four observed twin types is of the "second kind" (i.e. with an irrational twinning plane and rational twinning direction); it is the only one of its kind hitherto observed in a metal. Observations on the influence of the temperature on slip and twinning, on the effect of annealing on twins and on the pseudo-cleavage sometimes associated with twins, are set forth. The observations are discussed in relation to the crystal structure of uranium; in particular, the probable atomic motions in twinning are derived graphically.

LA DÉFORMATION PLASTIQUE DE L'URANIUM ALPHA

Des resultats sur la cristallographie du maclage, glissement et kinking dans l'uranium α sont données. A défaut de monocristaux, de l'uranium à très gros grain, en même temps qu'un appareil à rayons X de nouvelle conception ont été employés dans ces essais. Les techniques (dont certaines sont nouvelles) employées pour découvrir les plans de glissement et les directions et grandeurs des cisaillements de maclage sont complètement décrites. Une discussion des intersections observées des macles et leur application pour confirmer les directions de maclage suit. Le plan principal de glissement est (010), la direction de glissement [100], et les bandes de kinking sont normales à [100]. {110} est un plan de glissement auxiliaire. Les éléments de maclage trouvés, sont indiqués. Un des quatre types de macle trouvés, est de seconde espèce (second kind) c'est-à-dire avec un plan irrationnel de macle et une direction de macle rationnelle; c'est le seul dans son genre qui ait été constaté jusqu'à présent dans un métal. Des observations sont faites sur l'influence de la température sur le glissement et le maclage, sur l'effet du recuit sur les macles et sur le pseudoclivage qui est parfois associé avec le maclage. Les observations sont discutées en relation avec la structure cristalline de l'uranium; en particulier, le mouvement probable des atomes lors du maclage est déterminé graphiquement.

PLASTISCHE VERFORMUNG VON ALPHA-URAN

Die Kristallographie der Zwillingsbildung, der Gleitung und des "Kinking" wird beschrieben. Da keine Einkristalle zur Verfügung standen, wurde sehr grobkristallines Uran für diese Versuche benutzt, in denen auch eine neu-entwickelte Röntgenkamera Verwendung fand. Die Methoden, einige davon neu, die zur Bestimmung der Gleit- und Zwillingselementen und der "Kink" Bänder angewandt wurden, werden in Einzelheiten beschrieben. Anschliessend wird der experimentell beobachtete Schnitt der Zwillingskristalle und seine Anwendung zur Bestimmung der Zwillingsachsen diskutiert. Die Hauptgleitebene ist (010), die Gleitrichtung [100] und die Kinkbänder sind senkrecht zu [100]. Die Zwillingsebenen und -achsen sind zusammengestellt. Einer der vier beobachteten Zwillinge ist zweiter Art (d.h.mit einer irrationalen Zwillingsebene und einer rationalen Zwillingsachse). Dies ist der bisher einzige Fall von Zwillingen zweiter Art in Metallen. Es werden Beobachtungen berichtet über den Einfluss der Temperatur auf die Gleitung und Zwillingsbildung, den Einfluss von Glühbehandlung auf Zwillingskristalle und über die Pseudospaltung, die manchmal mit der Zwillingsbildung verbunden ist. Die Beobachtungen werden in Beziehung zur Kristallstruktur des Urans diskutiert, und die wahrscheinliche Bewegung der Atome während der Zwillingsbildung wird graphisch abgeleitet.

TWINNING AND SLIP IN α-URANIUM

Introduction

After decades of research, the crystallographic mechanisms of the deformation of metals are now fairly well understood. Experiments have, however, been largely restricted to structures of high symmetry—cubic, hexagonal and trigonal; even so, the difference in plastic behaviour of metals belonging to the different structural types is one of the least understood aspects of the subject. For this reason, much interest attaches to the crystallographic nature of deformation in a metal of unusual symmetry and structure. α-uranium, the allotropic form of the metal stable up to 670°C, is such a metal, and this paper gives an account of a study of its deformation crystallography. No attention was given to the other allotropic forms of uranium, because in the pure metal these cannot be stabilised at room temperature. Recently Holden [1] has published a study of slip in the intermediate form, β-uranium, which was stabilised by alloying with chromium.

The structure of α-uranium was determined by Jacob and Warren [2], who used powder patterns, and confirmed by Lukesh [3] by the rotating crystal method. During the present work all Laue photographs of uranium crystals were satisfactorily

*Received August 15, 1952.

†Atomic Energy Research Establishment, Harwell, England. Now at the Department of Metallurgy, University of Birmingham, England.

interpreted on the basis of the unit cell determined by the other workers. The symmetry is centrosymmetric orthorhombic, with $a = 2.852$, $b = 5.865$ and $c = 4.945$ A.U. The atoms are at $0y\frac{1}{4}$; $0 - y\frac{3}{4}$; $\frac{1}{2}, y + \frac{1}{2}, \frac{1}{4}$; $\frac{1}{2}, \frac{1}{2} - y, \frac{3}{4}$, where $y = 0.105 \pm 0.005$. The structure has been discussed from a crystal chemical standpoint by Tucker [4], who shows that all the available evidence implies that the binding of the atoms is partly covalent. The structure may be regarded as consisting of "giant molecules," corrugated sheets of atoms bound together by covalent bonds. The sheets are held together by metallic forces. Interatomic distances within a sheet are about 15 per cent smaller than those between nearest neighbours in adjacent sheets. The structure is shown in Figure 1.

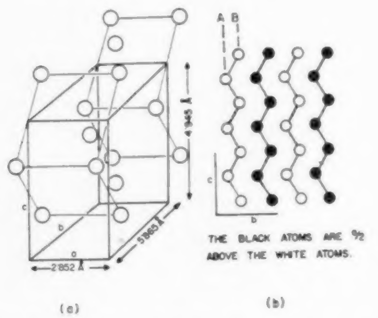

FIGURE 1. The crystal structure of α-uranium.

Twinning

Twinning plays an important part in the deformation of uranium. Several different types of twin were found, including a type with a twinning *plane* which does not have rational* indices, and another with an irrational twinning *direction*. With the idea of showing how such twins are crystallographically possible, and so that the methods used for determining the twinning elements shall be clear, a section on the formal crystallographic theory of twinning follows. The terminology adopted is that in normal use by mineralogists, except that the term "compound twin" has been newly coined.

Figure 2*a* represents a sphere cut from a single crystal. K_1 is the *twinning* or *composition plane*, η_1 is the *direction of shear*. Any point above K_1 moves parallel to η_1 through a distance proportional to its own height above K_1. The *magnitude of shear s* is defined as the distance through which a point at distance unity from K_1 moves; it is always such that each atomic plane parallel to K_1 moves relative to the neighbouring plane through a distance which is considerably less than the repeat distance along η_1. There is one central section of the sphere, apart from K_1, which remains circular *after* twinning. This is the *second circular section* K_2, and the angle 2ϕ it makes with K_1 is an alternative measure of the shear. After twinning, K_2 still makes an angle 2ϕ with K_1. The plane including η_1 and normal to K_1 is called the *plane of shear*. The line of intersection of K_2 with the plane of shear is given the symbol η_2.

An essential point about twinning is that the symmetry and structure of the crystal is the same after twinning as it is beforehand. It is easily shown that the shape and size of the *unit cell* will be unchanged if it is possible to find three non-coplanar rational lattice vectors in the untwinned crystal which retain the same lengths and mutual angles after twinning. Now all vectors which remain unchanged in length lie either in the twinning plane K_1 or in the second circular section K_2. Any vector in K_2 will make the same angle with the plane K_1 after twinning as it did before, but only the vector η_2 will make the same angle, before and after twinning, with *any selected vector lying in* K_1. The same thing applies to η_1 and any vector lying in K_2. To satisfy the condition that the shape and size of the unit cell shall be unchanged by twinning, we have two possibilities: (1) η_2 and K_1 are rational (η_1 and K_2 being irrational). Then we can always select two rational vectors lying in K_1 (because there are an infinite number of rational vectors in a rational plane), and these, together with η_2, will constitute our three invariant rational vectors. (2) η_1 and K_2 are rational (η_2 and K_1 being irrational), in which case the invariant directions would be η_1 and any two rational directions lying in K_2. These two cases are illustrated in Figures 2*b* and 2*c*. P, Q, R are the invariant vectors before twinning, P′, Q′, R′ their position after twinning. In case (1) the orientations of the invariant directions before and after twinning are related by reflection in K_1 as mirror-plane (or by a rotation of 180° about the normal to K_1). In case (2), the mirror-plane relating orientation of parent and twin is normal to η_1. Alternatively in this case the orientation of the twin is obtained from that of the parent by a rotation of 180° about η_1 as axis. This is equivalent to the mirror-plane description for all centrosymmetric crystals. The two kinds of twin described under (1) and (2) are known, respectively, as *twins of the first and second kinds*.

It is possible for K_1, K_2, η_1 and η_2 all to have rational indices, and this is the more probable, the

*A rational direction or plane is one which is denoted by integral Miller indices. In structural terms, a rational direction is parallel to a row of atoms, and a rational plane is parallel to a sheet of atoms.

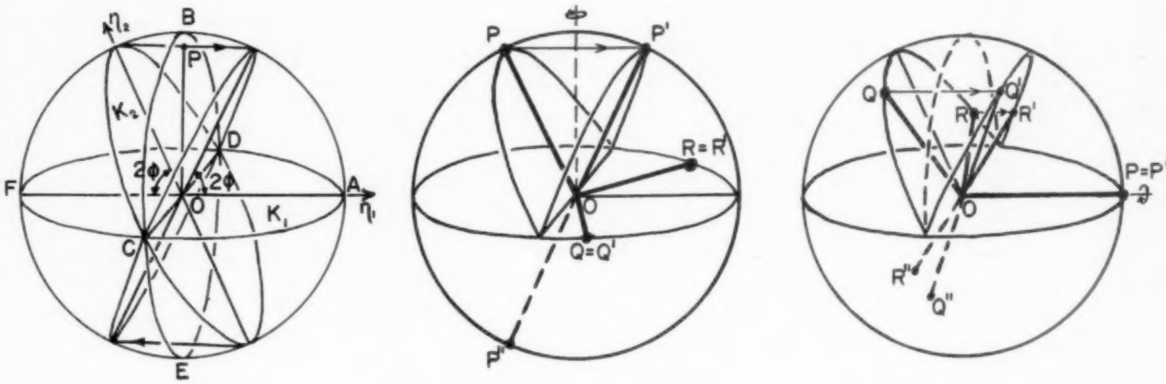

(*a*)
Length OP = Unity
$s = 2 \cdot OP \cdot \cot 2\phi$
$= 2 \cot 2\phi$

(*b*)
Twin of first kind
$\angle QOR = \angle Q'OR'$
$\angle POQ = \angle P''OQ'$
$\angle POR = \angle P''OR'$
K_1, η_2 rational

(*c*)
Twin of second kind
$\angle QOR = \angle Q'OR'$
$\angle POQ = \angle P'OQ''$
$\angle POR = \angle P'OR''$
K_2, η_1 rational

FIGURE 2. Elements of a twin.

higher the crystal symmetry. The twins in cubic, hexagonal and trigonal metals are in fact all *compound twins* of this kind, with all four elements rational. However, twins of the first and second kinds are common in salts and minerals of orthorhombic or lower symmetry, and, as we shall see, they occur in uranium. In minerals, it is common to find *reciprocal twins*; that is, K_1 and η_2 of a twin of the first kind are found to have the same indices as K_2 and η_1, respectively, of a twin of the second kind in the same substance. This is also found in uranium.

It should be clearly noted that the condition, that the shape and size of the unit cell should remain unchanged by twinning, is not strictly equivalent to the condition that the crystal structure should not change. This disparity results in the necessity for small positional adjustments by individual atoms after twinning. We shall return to this important point later.

With the model we have been considering, the whole upper hemisphere is supposed to shear at once. What happens in practice is not this, but a gradual growth of the twin. This takes place by a steady migration of the K_1 plane, making the twin, which starts as a thin lamina, progressively thicker. Only a few atomic layers are shearing at any instant. Actual twins are nearly always in the form of thin lamellae. Where these are parallel-sided, both bounding surfaces are parallel to K_1. Where they are lens-shaped, or *lenticular*, they have grown on either side of an initial lamina parallel to K_1, the successive layers gradually decreasing in area as they grow.

Experimental Methods

Making the Specimens

It would have been desirable to use single crystals for this study, but it was not found possible to make them both large, and perfect structurally. In consequence coarse-grained polycrystalline samples had to be used, with grains usually 2 mm. or less across. Figure 3 shows a portion of such a specimen after macro-etching. These samples were made by recrystallization. Details of the method used are to be given in another paper.

Determining the Orientation

The grains in these samples yielded perfect back-reflection Laue photographs, with very sharp spots, showing the orientation to be strictly uniform. Because of the small grain-size, however, it was difficult to identify under the microscope grains of which Laue photographs had been taken. The method followed at first, of selecting large grains on a macro-etched specimen, taking Laue photographs of these, and then repolishing the specimen for examination in polarized light, proved unsatisfactory as it could not be predicted in advance which grains would reveal the most interesting features under the microscope.

To meet the difficulty, a special X-ray camera was designed, which made it possible to select a grain, or particular region thereof, under the polarising microscope, and then to direct an X-ray beam of small cross-section at the same area, with an accuracy of positioning of about 0.01 mm. The instrument was made to precision standards and orienta-

tions derived by its use were generally accurate to 1°. An account of the instrument is being published elsewhere [5].

Preparation and Examination of Specimens

The specimens used were mostly of rectangular section. In some cases the central portion was polished on all four surfaces to allow individual grains to be examined on two surfaces at right angles, Figure 3 shows two such grains on a macro-etched specimen, prior to repolishing. In other cases only one surface was polished. The polished specimens were either stretched (generally by 1–2 per cent overall), or compressed after removing the shoulders (the compression might be as great as 10 per cent). The specimens were sometimes examined immediately, sometimes after repolishing. In all cases polishing was completed by an electrolytic method. Details of several baths which were used, and of the appropriate conditions, have been given by Mott and Haines [6]. The best results were obtained with the sulphuric acid–phosphoric acid bath. It was necessary to polish fairly deeply, otherwise twins due to the preceding abrasion by emery paper remained visible. The sections were not etched, but always examined in polarised light, which revealed grains and twins very clearly by a difference of colour. The inclusions visible in many of the photomicrographs consist of uranium oxide.

Experimental Results

Twins

Twins were formed in uranium by several methods: (1) heating and cooling; (2) deformation (extension, compression, bending); (3) abrasion.

The reason for the ready formation of twins by heating and cooling is to be found in the great anistropy of thermal expansion of uranium. The principal coefficients of expansion, over the range 25–650°C, are 28, -1.5 and 22×10^6 per °C. In polycrystalline metal this anisotropy leads to large stresses in the grains as the temperature changes, and these stresses are relieved by twinning (and by slip). This process of "thermal fatigue" has been demonstrated in other anisotropic metals by Boas and Honeycombe [7]. Cooling once from the temperature of recrystallization was enough to generate twins in many grains. Figure 5*a* shows such a one, exceptionally heavily twinned.

Deformation at room temperature always leads to twins accompanied in some suitably oriented grains by visible slip markings. The most notable feature of the twins is their extreme thinness. It was rare to find twins more than 10μ thick. Even with continued deformation, the twins do not thicken but their number increases. This may be seen from Figure 5*b*, made of a region close to a sawcut. Here some adjacent twins have begun to join up. Figures 6*a* and 6*b* show a portion of a tensile specimen before and after a slight extension. Here twinning and slip both take part.

The twins usually had the appearance of parallel-sided plates, rather like Neumann bands in iron. In regions where two systems of twins had operated simultaneously, the lamellae were prevented from spreading, and short lens-shaped twin traces resulted. Figure 7 shows an instance of this.

One other point regarding the appearance of the twins is of importance. In one and the same grain there are often twin traces following many different directions. The largest number of directions found in one grain was ten; nine directions may be distinguished in Figure 8. Now, in the orthorhombic system there are only four planes of the general form $\{hkl\}$. The observation just mentioned therefore showed that at least three distinct types of twinning (K_1) plane must operate in uranium.

Slip

Slip lines were always formed on some grains when a specimen was deformed. It was also possible to generate them by thermal cycling. Two characteristic features were observed. The slip lines were always very fine at room temperature, and when there were many slip lines, they were extremely close together (about 1μ spacing). The other feature was the presence of cross slip, i.e. a localised change of the slip plane. These points are well brought out in Figure 9, made at high magnification from a grain in which there had been an exceptionally large amount of slip. In a thermally cycled sample, where much of the slip must have occurred at elevated temperature, the slip was coarser and noticeably wavy (implying that there was very much cross slip on a fine scale). Figure 10 was made from a sample cycled 55 times between 20°C and 630°C.

Through the kind co-operation of Miss S. Vernon-Smith, of the British Non-Ferrous Metals Research Association, several electron micrographs of slip lines on uranium were obtained, the formvar replica technique being employed throughout. Two of these micrographs are reproduced. Figure 11 shows cross slip and emphasises the irregularity of the cross slip segments, which are often zigzagged on an extremely fine scale (cf. the writer's observations on aluminium [8]). Figure 12 shows an extreme case of the

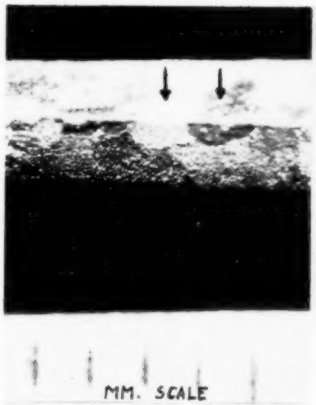

3

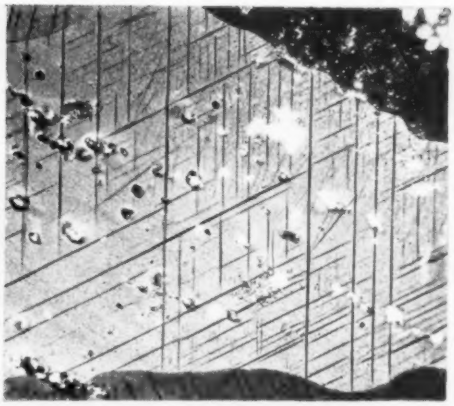

5a

5b

6a

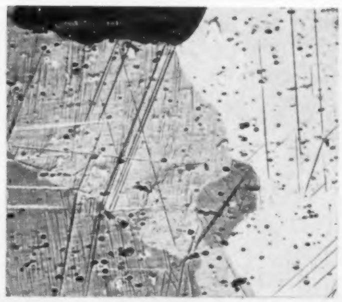

6b

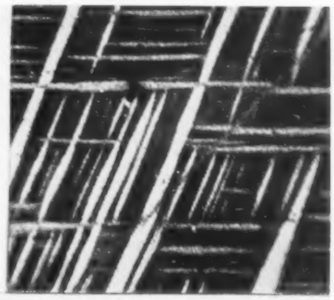

7

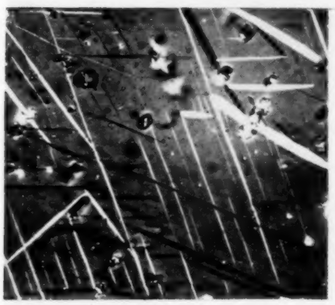

8

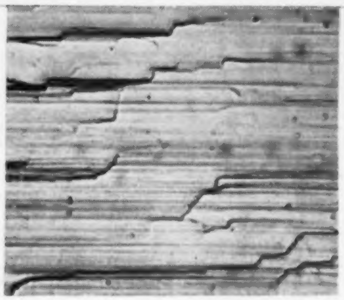

9

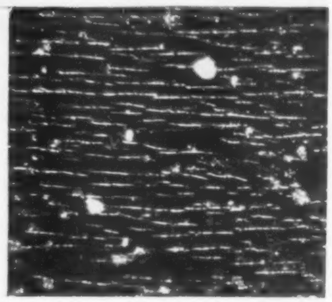

10

PLATE I. Figure 3—Two grains used for the "two-surface" method. Figure *5a*—Twins due to cooling stresses. 200×. Figure *5b*—Intense twinning near a sawcut. 150×. Figure *6a*—Grains in an undeformed specimen (twins are due to thermal stresses). 65×. Figure *6b*—Same field, after extension to fracture (repolished before extension). 65×. Figure 7—(130) and ($1\bar{3}0$) twins due to compression. 1200×. Figure 8—Multiple twinning in deformed grain. 300×. Figure 9—(010) slip lines, with cross slips, on stretched specimen. 1800×. Figure 10—Slip lines on a sample cycled 55 times between 20°C and 635°C. 300×.


11


12


13


14


15

17

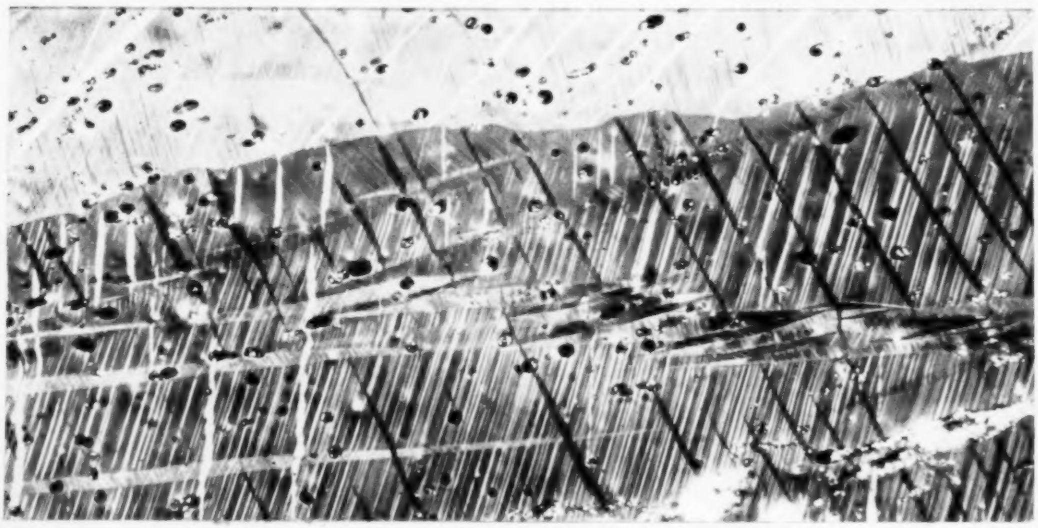
16

PLATE II. Figure 11—Cross slip. (Electron micrograph from formvar replica.) 10000×. Figure 12—A twin and fine slip lines (Electron micrograph from formvar replica.) 7000×. Figure 13—Slip lines in corner of a grain in a compressed specimen. 540×. Figure 14—(010) slip lines passing through a kink band. 680×. Figure 15—Kink bands in stretched specimen (repolished after stretching). 230×. Figure 17—Fine twins due to cooling stresses. 190×. Figure 16—Multiple kink bands and twins in a severely bent specimen (repolished after bending). 200×.

18

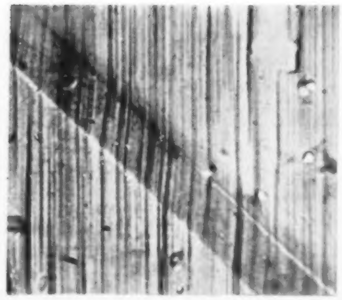

21

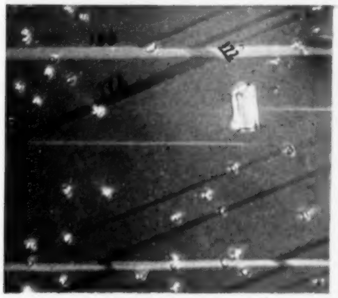

24a

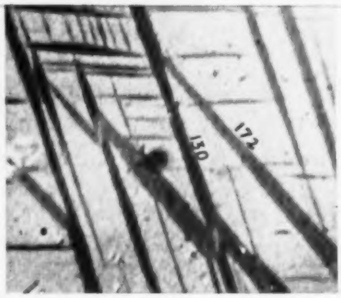

24b

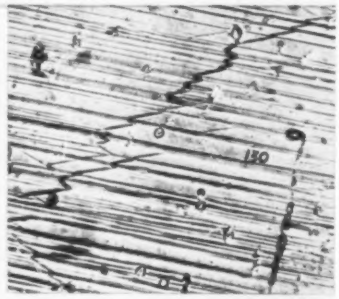

24c

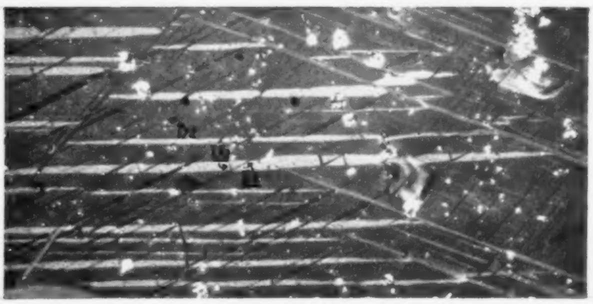

24d

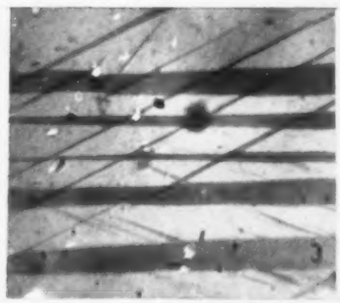

24e

PLATE III. Figure 18—As Figure 17, after removal of 0.0024 cm. thickness of metal. 190×. Figure 21—(010) slip lines passing through a (121) twin. 1800×. Figure 24*a*—Twin intersections (172) and (130). 1000×. Figure 24*b*—Twin intersections (172) and (130). 1200×. Figure 24*c*—Twin intersections (free surface) (172), (172), and (130). 240×. Figure 24*d*—Twin intersections (172) and (172). 500× Figure 24*e*—Twin intersections (172) and (172). 1200×.

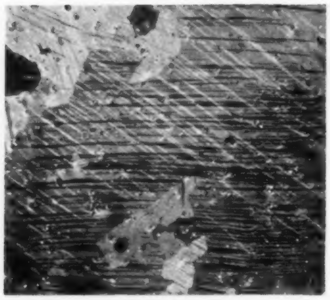

24f

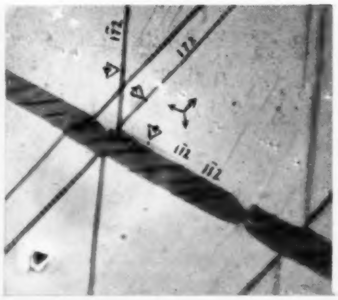

24g

26

27

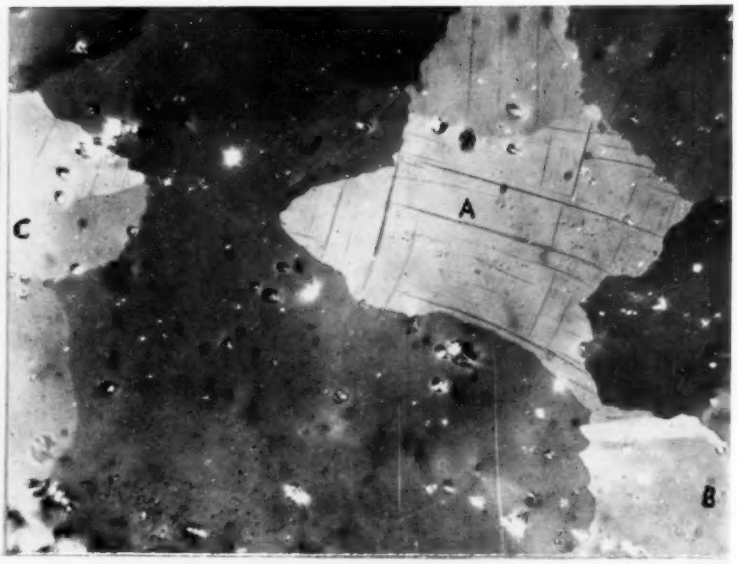

28a

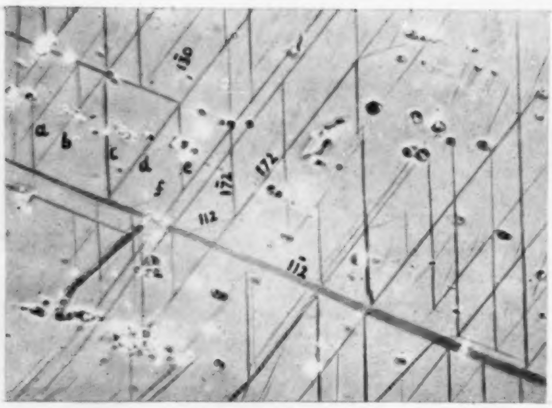

25a

25b

PLATE IV. Figure 24*f*—Twin intersections (172) and (172). 450×. Figure 24*g*—Triple twin intersections. (Abnormal intersection at left.) 1050×. Figure 26—Section under a Brinell impression made at room temperature. 140×. Figure 27—Section under a Brinell impression made at 550°C. 140×. Figure 28—As Figure 27 (higher magnification). 270×. Figure 25*a*—"Bouncing twins." 200×. Figure 25*b*—Same grain, repolished. (Detail) 600×.

very close spacing and fineness of the slip lines. It is noteworthy that none of the micrographs furnished any evidence for a fine lamellar substructure within strong slip bands, such as exists in aluminium.

In a few cases a set of very faint slip lines entirely devoid of cross slip were detected *in addition* to the stronger family showing cross slip. In one instance two such faint families were present. This suggested that two distinct slip systems operated, one being predominant, and this was later confirmed by detailed analysis. Figure 13 shows a set of the minor slip lines. The predominant system operated also here, but as the slip direction is almost parallel to the plane of section, the corresponding slip lines do not appear particularly strong.

Kinking

In grains in which there was a good deal of slip, there were often bands, looking rather like twins, but considerably thicker, and of slightly variable direction in any one grain. The surface was often tilted through a considerable angle in these bands. Slip lines were often seen to traverse these bands with a small, discontinuous change of direction, and the angle through which they were bent often varied at different places along a band. (This is never the case where slip lines traverse a twin). An example is shown in Figure 14. When a specimen containing such bands was sectioned and repolished, the bands were still visible in polarised light. It was noticed that the colour of the bands in polarised light was only slightly different from that of the parent grain, and this was true of all bands and for all settings of the rotating stage. This proved that the bands differed only slightly in orientation from the parent grain.

Figure 15 shows bands in a grain repolished after extension. The white lines, deflected within the bands, are twins. The characteristic double arrowheads (with two distinct colourings, and therefore with two orientations) at the tips of two of the bands should be noted, as well as the gradual fading away of the bands, again showing them to have an orientation varying from point to point. Figure 16 shows a group of well defined bands in a specimen which was strongly bent and then repolished.

The orientation of the planes of these bands was determined, and it was found that they were always *nearly* perpendicular to the slip direction of the predominant slip system (for details of the determinations, see below). This is a characteristic of the *kink bands* studied in recent years by various investigators [8–11]. They are generated, in single crystals of zinc or cadmium, when an axial compressive force is applied to a crystal rod the axis of which is approximately parallel to the slip direction. With this form of stressing, twinning cannot (in these metals) relieve the stress. The slip planes collapse, as it were, so that the crystal becomes divided into regions, often wedge-shaped, in which the slip direction is inclined at various angles to the compression direction. The result is of course to shorten the crystal.

It was found by analysis of the twin crystallography that the situation in uranium is similar to that described for zinc and cadmium, in that a compression parallel to the predominant slip direction cannot be relieved by any of the possible twinning systems (excepting one which appeared very rarely and was therefore presumed to form only with great difficulty). The second, minor slip system which sometimes operated also appeared to have a high critical stress. It is evident that under such conditions of stressing the crystal is obliged to deform by kinking. We shall return to this later.

Kink bands were found, not only in compressed specimens, but also in stretched coarse-grained samples. In these cases, however, where an analysis was made the slip direction proved to make a large angle with the axis of tension, so that the kink bands were evidently formed as a consequence of the transverse compressive stresses exerted by neighbouring grains. The result of kinking was to reduce the transverse dimension of the specimen. Grains which were favourably oriented for slip in tension showed much slip but no kink bands (e.g. the grain of Figure 9).

The "double arrowhead" appearance referred to above, in connection with Figure 15, is simply due to the genesis of two bands simultaneously, one being tilted one way and one the other. One band only develops, the other remains embryonic. Occasionally whole bands were seen in one crystal in which the lattice was tilted opposite ways. Instances of this occur in Figure 16.

Crystallography of Twins

Determination of K_1

To define a twin completely, it is necessary to know the indices either of K_1 and η_2, or of K_2 and η_1, according as the twin is of the first or second kind. In practice K_1 is always determined, because this is the easiest to find experimentally. When we are concerned with a twin of the second kind, K_1 will not have rational indices.

(i) *Two surface method.* K_1 is the plane to which the thin twin lamellae are parallel. To determine it, the usual way (the "two-surface method") is to polish two flat surfaces on a single crystal containing a family of lamellae, and to measure the directions of the traces of the lamellae on each surface. The orientation of the crystal is determined by X-rays, the angle between the surfaces is measured, and there is then sufficient information to plot the pole of K_1 on the stereographic projection of the crystal. The situation is complicated if there are several families of twins, for it is then necessary to pair off the several sets of traces on each surface correctly. It is more awkward still if only small grains are available. Both these complications had to be faced in the present experiments. In consequence, it was only possible to carry out a few determinations of this nature. Samples of the type shown in Figure 3 were used. The K_1 plane of one of the types of twin was determined in this way, and found to be $\{130\}$.

(ii) *Pole locus method.* To determine the K_1 planes of the remaining types of twins, another method was used. A large number of grains which were sectioned by a single surface only were examined; each of the grains chosen contained several families of twins. The orientations of these grains, many of which were quite small, were determined by means of the X-ray camera mentioned earlier. Since the X-ray pattern exhibits some asterism and requires a long exposure (and moreover becomes very difficult to interpret) if a grain has been at all strongly deformed, preference was given to samples twinned by cooling stresses, or by a slight deformation only. For each grain a stereogram was plotted with the normal to the plane of section at the centre. For each set of parallel twin traces, a great circle, passing through the centre of the projection, was drawn. This great circle, a straight line on the projection, was drawn perpendicular to the direction of the twin traces. It follows that the *pole* of the twin plane to which the lamellae were parallel must lie somewhere on the great circle. For this reason such great circles are referred to as *pole loci*.

Numerous pole loci were drawn on the stereograms of the various grains examined, and these were then all plotted together on a stereogram in standard orientation (i.e. one with (001) at the centre). To achieve this, it was only necessary to rotate each stereogram together with the great circles, about the appropriate axis, so that it came into the standard orientation. The pole loci were then all redrawn so as to lie entirely within one unit triangle of the standard stereogram (i.e. one quadrant of the projection). This follows Bowles' [12] practice.

The pole loci mostly passed close to one or other of a number of points on the standard stereogram. Thus numerous loci passed close to the pole of (130), confirming the indices of the first type of twin which had already been identified by the two-surface method. In this way the second type of twin was found to have $\{112\}$ for composition plane.

This still left a large number of loci unaccounted for, almost all of which congregated in the vicinity of the pole (172). Now there is a well-established

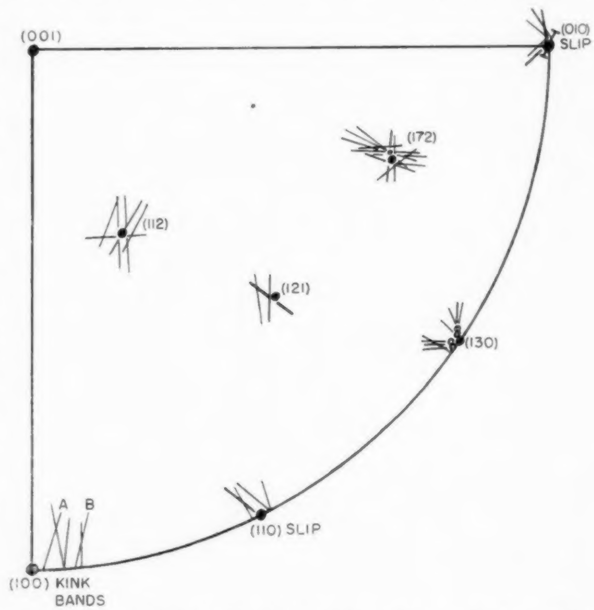

FIGURE 4. Coincidences of pole loci for twins, slip lines and kink bands.

empirical rule regarding twinning, that all rational elements have indices consisting of *small* integers. (172) hardly obeys this rule, so the probability was that the twins in question were of the second kind, with an irrational K_1 plane close to (172).* Of the nine remaining traces, three passed close to a pole of the form $\{121\}$, and further examination of one of these twins on the assumption that $\{121\}$ was the correct attribution yielded reasonable results (see below). Thus the method of pole loci has identified four K_1 planes: $\{130\}$, $\{112\}$, $\{121\}$ and an irrational plane close to $\{172\}$. Of these, $\{121\}$ must be regarded as being only insecurely established.

Figure 4 shows one quadrant of the stereographic projection of uranium in standard position, with a

*For conciseness these twins will be referred to simply as $\{172\}$ twins, though this is not strictly accurate.

number of pole loci drawn in. Only short lengths of the loci are included to avoid confusion. The open circles near the (130) pole represent poles as determined by the two surface method. The true position of K_1 for the twins of the second kind, as determined from later experiments, is indicated near the pole of (172). (The pole of (172) is indicated by a small dot, the correct position of K_1 by a large one.) On the same stereogram the pole loci for the slip planes and plane of the kink bands are included also. Only a proportion of the observed loci are included, to avoid overcrowding.

(iii) *Self-consistency method.* It was desirable to check the indices of the K_1 planes of the {112} and {172} types in some way. (The {130} planes had already been cross-checked by the two-surface method, while the {121} twins were only observed in two grains which had been destroyed before it was realised that they contained twins of unusual indices.) The following way was found: A grain (Figure 17) was selected which contained eight different sets of twin traces. (Some of these are too faint to show clearly on the photograph.) The stereographic projection of the grain, obtained from a Laue photograph, is shown in Figure 19 in the

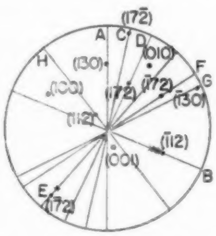

FIGURE 19. Stereogram of grain, showing pole loci (in mirror image to match Figures 17 and 18).

correct orientation, with the pole locus for each set of twin traces drawn in. It will be noticed that the planes (130) and (17$\bar{2}$), corresponding, according to the provisional attribution of indices, to twin families G and C respectively in Figure 17, are almost perpendicular to the plane of the specimen surface. It was therefore easy to use individual traces of these families as reference planes passing right through the grain. A point such as "a", where a C trace and a G trace intersect, was taken as origin, and the position of particular traces belonging to the other families were measured on the photomicrograph relative to the point "a". About 0.02 mm. of specimen surface was then removed by grinding on fine emery and repolishing, and a fresh photograph taken (Figure 18). The configuration of traces had of course changed, but many individual traces present in Figure 17 were still recognizable in Figure 18, since the thickness of metal removed was small. The exact thickness of metal removed was computed by measuring the change in position of a particular A trace relative to the reference point "a". From a knowledge of the thickness of metal removed, and the change of configuration, it was possible to determine the inclination of traces B and E to the plane of the section. The results of three separate determinations, using different traces of the B family, and of one determination for the E family, are entered on the stereogram; it will be seen that, within the error of experiment, the assignment of indices is proved to be self-consistent.

This experiment has been described in some detail, because the method should be of general applicability in checking complicated twin or Widmanstätten patterns, if some reasonable provisional guess can be made of the indices concerned. It would be possible, though laborious, to check a number of possible alternatives. It is an advantage, but by no means essential, for two of the twins, or Widmanstätten plates, to be perpendicular to the plane of section.

Determination of K_2, η_1, η_2, s

The method always adopted by mineralogists to determine these elements is to make optical goniometric measurements of the rotation of the various natural faces of a crystal where these are intersected by a twin. There are in effect two unknowns, namely the direction of shear η_1 and the magnitude of shear s. It is sufficient to measure the rotations on two non-parallel faces to determine these two unknowns. Knowing K_1, η_1, and s, we can calculate K_2 and η_2 (either of which in any particular case may or may not be rational).

This method was not used a great deal, because of the poor optical quality of the electrolytically polished surface. Because of this, the twin lamellae were too narrow to give a recognizable reflection of their own on an ordinary optical goniometer. A simple goniometric arrangement was built for use in conjunction with a microscope used at very low N.A. By this means a rough value for the rotation of the surface in a twin lamella could be obtained. The method was used as a check only.

{130} *twins.* Here we can simplify our task by making use of the known symmetry properties of the uranium structure. There is a plane of symmetry normal to (130), namely (001). From this we can deduce that η_1 must coincide with the intersection of (130) and (001), that is, the direction [3$\bar{1}$0]. If

this were not so, (001) would no longer be a symmetry plane in the twinned parts of a grain, and this would violate the fundamental requirement that the crystal symmetry be unchanged by twinning. We still have to find the indices of K_2 or η_2. (We know that all four elements are rational, because both K_1 and η_1 are, and that K_2 must be of the form $(h\bar{k}0)$.) Now with very few exceptions among known crystals, s is small, so that the angle between K_1 and K_2 is usually greater than 80° and always greater than 70°. The only planes of form $(h\bar{k}0)$ and of low indices for which this is true are $(1\bar{1}0)$ and $(1\bar{2}0)$. The angle 2ϕ (Figure 2*a*) is 81° 30′ if we take $K_2 = (1\bar{1}0)$, and 82° 14′ if $K_2 = (1\bar{2}0)$. It was considered almost certain that one of these planes was the correct one, but an appeal to experiment was necessary to decide between them. The goniometric method, though rough, was suitable for this purpose. A crystal with two well-developed sets of twins parallel to (130) and $(1\bar{3}0)$ was chosen, and the best value for the angle of tilt determined as $8 \pm 3°$ for (130), and $11 \pm 3°$ for $(1\bar{3}0)$. The calculated angles of tilt, on the assumption that $K_2 = (1\bar{1}0)$ and (110) respectively, were 8° and $11\frac{1}{2}°$ respectively, and the sense of the rotation in each case was consistent with this assumption, but not with the alternative.

Thus we have $K_1 = (130)$, $\eta_1 = [\bar{3}10]$, $K_2 = (1\bar{1}0)$ and hence $\eta_2 = [110]$. By calculation $2\phi = 81°\ 30'$, and hence $s = 2 \cot 2\phi = 0.299$.

"{172}" *twins*. The first requirement here was again to determine the shear direction η_1. Because of the high indices of K_1, the hypothesis was adopted that these were twins of the second kind, i.e. twins with rational η_1 and K_2 and irrational η_2 and K_1.

A stereogram was drawn on which was plotted the most probable position of the pole of K_1 as determined by the pole locus method, surrounded by a generous circle of confidence of radius $1\frac{1}{2}°$. A band was then defined by two bounding curves such that any direction falling within the band would lie in K_1 for some position of the true pole of K_1 within the circle of confidence (Figure 20). This band contains the poles of all directions which might be the shear direction η_1. All directions, with indices involving no number higher than 5, which lie within the band, were also plotted on the stereogram. Of these directions, three have indices involving no number higher than 3, namely, [201], $[\bar{1}\bar{1}3]$, and $[\bar{3}\bar{1}2]$. In the first instance only these three directions were considered.

In deciding which of the directions in the band is the true direction, it helps to remember that as we are dealing with a twin of the second kind, the pole

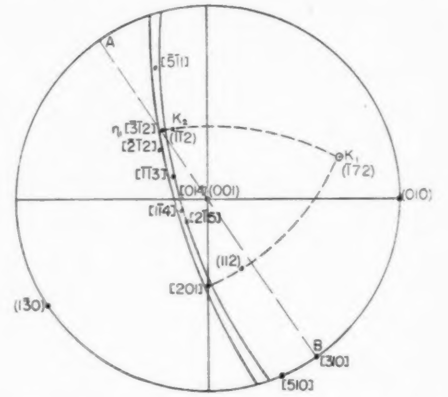

FIGURE 20. Determination of η_1 of (172) twins.

of K_2 (which must be a plane of rational and low indices) must lie on the great circle connecting the pole of η_1, with the pole of K_1; moreover the pole of K_2 must lie fairly close to η_1 (within 20° at the outside) else the corresponding shear is impossibly great. On this criterion, it was found that either [201] or $[\bar{3}\bar{1}2]$ might be the twinning direction. If [201] is correct, then $K_2 = (112)$; if $[\bar{3}\bar{1}2]$ is correct, then $K_2 = (\bar{1}\bar{1}2)$. This will be clear from Figure 20. $[\bar{1}\bar{1}3]$, and the other possible directions of higher indices, are excluded for lack of a possible rational K_2 plane to go with them.

The two possibilities, then, are the following: (1) $\eta_1 = [\bar{3}\bar{1}2]$, $K_2 = (\bar{1}\bar{1}2)$, $2\phi = 83°30'$, $s = 0.228$;* and (2) $\eta_1 = [201]$, $K_2 = (112)$, $2\phi = 70°\ 40'$, $s = 0.702$.

Fortunately a simple experimental test makes possible an unambiguous decision between the alternatives. For a twin of the second kind, the orientations of parent and twin are related by a rotation of 180° about η_1 as axis. Consider alternative (1). The four possible twins (i.e. those with $K_2 = (112)$, $(1\bar{1}2)$, and $(\bar{1}\bar{1}2)$ in one and the same grain, would all have different orientations, because all have different shear directions (namely [312], $[3\bar{1}2]$, $[\bar{3}12]$ and $[\bar{3}\bar{1}2]$ respectively). With alternative (2), however, the four twins would have only two different orientations between them, since the twins with $K_2 = (112)$ and $(1\bar{1}2)$ would both have $\eta_1 = [201]$, while the other pair would both have $\eta_1 = [\bar{2}01]$. Now in all cases examined where two *or more* twins of this type occurred, they all had different orientations as revealed by polarised light and the rotating stage. For instance, Figure 24*d* shows a pair of twin families which on alternative (2)

*The values $2\phi = 83°30'$ and $s = 0.228$ were obtained after careful checking and supersede erroneous values published elsewhere (83°55′ and 0.213) [13].

should have the same orientation, but in fact have not.

The conclusion that ⟨312⟩ is the correct shear direction was reinforced by a goniometric check. A family of well-formed "{172}" twins was examined in the way described earlier, and a tilt of $9 \pm 4°$ observed. The calculated tilt was 10°, in the observed sense.

Calculation shows that the exact position of K_1 is about 1° removed from {172}; it is marked in Figure 4 as a large dot.

A basically different kind of check was also applied, and confirmed the assignment of indices. This, the method of twin intersections, will be described when

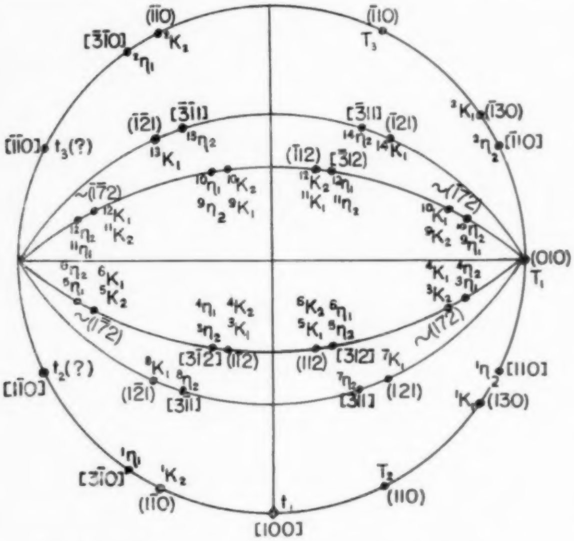

FIGURE 22. Slip and twinning elements in α-uranium.

we have discussed the remaining types of twins. Finally, ⟨312⟩ was confirmed as slip direction from the fact that the plane normal to it was the mirror plane relating parent and twin orientations (see p. 60).

{112} *twins*. From the fact that {112} is the K_2 plane for the preceding type of twin, it appeared probable that the {112} twins are reciprocal to that type (see p. 51). On this basis we should have $K_1 = (112)$, $\eta_2 = [312]$, $2\phi = 83°30'$, and $s = 0.228$.

{112} twins were found comparatively rarely, and were usually very small. For this reason none were found suitable for goniometric analysis. However, a different method of check was found. In two specimens which were examined after deformation, slip lines were found crossing a (112) twin with a small deflection as in Figure 33. The slip lines in the twin were not situated symmetrically with respect to the twinning plane. As we are concerned with a twins of the first kind (K_1 rational and acting as mirror plane) we can conclude from this that slip *preceded* twinning. The observed angular deflection of the slip lines was therefore compared with the deflection computed by stereographic construction on the basis of the assumed η_2 indices. The observed and computed deviation were 11° and $8\frac{3}{4}°$, respectively, in the one case, and 8° and $6\frac{3}{4}°$, respectively, in the other. The sense of deflection was correct in each case. This is strong evidence for the correctness of the proposed indices.

Here again, the method of twin intersections gave indirect confirmation of the assignment of indices (v.i.).

{121} *twins*. It is to be noted again that the attribution of {121} to the K_1 of certain twins rests on only three pole loci. One of these loci was derived from a well-developed family of twins in a grain with well-marked slip lines (Figure 21). The deviation of the slip lines was again used to distinguish between possible alternatives for η_2. An examination of the possible η_2 directions which would give reasonable values for the magnitude of shear showed that ⟨211⟩, ⟨311⟩ and ⟨321⟩ were candidates. A very careful graphical determination of the theoretical angle of deviation of the slip lines in the twin band suggested that ⟨311⟩ is the correct η_2. The theoretical deviation was $6 \pm \frac{1}{4}°$, the observed deviation, $5\frac{3}{4} \pm \frac{1}{4}°$; the sense of deviation was correct. In view of this excellent agreement, it seems justifiable to regard the identity of this type of twin as established, though further experimental verification would be welcome. In particular, the possibility that the twin is of the second kind cannot be excluded.

TABLE I

TWINNING ELEMENTS IN URANIUM

("X" signifies absence of rational indices)

Type no.	K_1	K_2	η_1	η_2	2ϕ	s	Kind
1	(130)	$(1\bar{1}0)$	$[3\bar{1}0]$	[110]	81°30′	0.299	Compound
2	X approx. $(1\bar{7}2)$	(112)	[312]	X	83°30′	0.228	2nd
3	(112)	X approx. $(1\bar{7}2)$	X	[312]	83°30′	0.228	1st
4	(121)	X	X	[311]	80°40′	0.329	1st

For this type, provisionally, $K_1 = (121)$, $\eta_2 = [311]$, $2\phi = 80°4'$, $s = 0.329$.

All the twinning elements derived in the preceding paragraphs are entered in a stereographic projection, Figure 22. The superfix attached to each K and η is intended to show which K's and η's belong together. The twins are numbered from 1 to 14.

Concerning the six twin traces that remain unaccounted for, the author prefers to believe that they were due to spurious markings on the specimen surfaces. This is quite possible, for sometimes only a single short trace of a particular direction was seen on the whole surface of a grain.

Details of the four types of twins are assembled in Table I.

Twin Intersections

It has been found possible to confirm the elements of twinning derived in the preceding paragraphs by a study of intersecting pairs of twins. By "twin intersection" is meant a situation where one twin passes right through another, rather than tapering to a point and starting afresh on the other side (as is the case, for example, in Figure 7). Examples of such intersections were frequently observed, and some are shown in Figure 24 *a–f*. The indices of the intersecting twins are indicated in the photographs, putting, as before, (172) as an approximation to the twinning plane of the type 2 twins. We shall show now in what way such intersections provide evidence about the elements of twinning.

Consider a twin lamella A intersecting another, B, which was formed prior to A (Figure 23). The

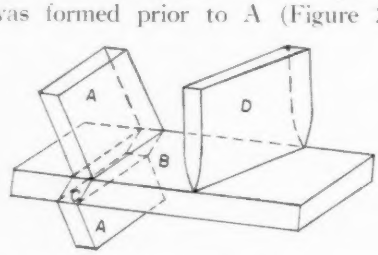

FIGURE 23. Intersecting and non-intersecting twins.

intersection is itself a twin in relation to B, and we shall call it C. We shall call A the *crossing twin*, B the *crossed twin*, and C the *secondary* twin. Such an intersection is only possible if the following two conditions are satisfied:

1. The traces of A and of C in the K_1 plane of B must be parallel to each other.

2. The direction and magnitude of shear (i.e. η_1 and s) must be identical in A and C. In addition the *sense* of shear must be the same in A and C. This proviso is explained in Appendix I.

If (1) were not satisfied, A and C could not join up with each other, along the composition (K_1) plane of B, and if (2) were not satisfied, the *displacements* caused by the twinning operations in A and C would not match, and the tremendous strain set up in the neighbourhood on account of this would prevent C from developing beyond a minute nucleus. If both conditions are not satisfied simultaneously, the impinging twin should stop short as shown at D in the figure. See Appendix I for a fuller discussion of these conditions.

The circumstances under which these conditions are satisfied are straightforward if the *crossed* twin, B, is of the first kind (K_1 and η_2 rational). It is only required that η_1 of the *crossing* twin A shall be parallel to the intersection of A and B. This is explained in Appendix I. It may be mentioned that intersections of this kind have been observed between appropriate pairs of Neumann bands in iron by Smith, Dee and Young **[14]**, and both conditions were satisfied. (This is very strong evidence that Neumann bands in iron are indeed deformation twins, a point on which there has been protracted controversy.)

When the *crossed* twin B is of the second kind (K_2 and η_1 rational) the situation is more complicated, and a general analysis is given in Appendix I. Here we shall simply accept the conclusion reached in the Appendix and analyse the experimentally observed intersections of their basis.

Twin intersections observed. Two main types of intersection were found. In each case they appeared to take place very easily, in the sense that there appeared to be no tendency for the crossing twins in question to stop short of the other family of twins.

(i) (172) or $(\bar{1}\bar{7}2)$ crossing (130); $(\bar{1}72)$ or $(1\bar{7}2)$ crossing $(1\bar{3}0)$ (Figures 24*a*, *b*, *c*).

Consider first (172) or $(\bar{1}\bar{7}2)$ crossing (130). Here the crossed twin B is of the first kind, with K_{1B} = (130). The required condition is that η_{1A} be parallel to K_{1B}. Now η_{1A} = $[3\bar{1}2]$ or $[\bar{3}12]$, for the (172) or $(\bar{1}\bar{7}2)$ twins respectively. These directions are both exactly parallel to (130), as is easily seen by reference to Figure 22, and the required condition is thus satisfied. The argument for the other trio of twins is exactly similar. No instance of (172) or $(\bar{1}\bar{7}2)$ crossing $(1\bar{3}0)$ was ever found. This kind of intersection furnishes confirmation for the correctness of the indices assigned for the shear direction of the {172} type twins. If in Figure 20 we plot a locus AB of all directions which lie in the $(1\bar{3}0)$ plane, its intersection with the confidence band containing the possible positions of η_1 for the $(\bar{1}\bar{7}2)$ twin will give the correct position for η_1, because only if η_1 lies somewhere on AB can the observed intersection of $(\bar{1}72)$ and $(1\bar{3}0)$ be accounted for.

(ii) (172) crossing $(1\bar{7}2)$; $(\bar{1}72)$ crossing $(\bar{1}\bar{7}2)$. This was the type of twin intersection most commonly observed, and was found wherever the appropriate twins occurred at all plentifully. In fields such

as those shown in Figure 24*d*, the two families of twins seem entirely oblivious, as it were, of each other's presence. This impression is due to the striking fact that the crossing twin is not deflected in direction where it passes through the other twin, though with appropriate stage settings, crossing, crossed and secondary twins all have different colours (and therefore different orientations). Because of the lack of deviation, there is generally no means of distinguishing between the crossed and crossing twins.

As is shown in the appendix, no intersection is possible under any circumstances between two twins of the second kind if both crossing and secondary twins have the same indices. It was necessary to see whether the intersection could be explained on the assumption that they have different indices and this proved to be possible. The crystallography of these intersections is complex, and its exposition has been relegated to Appendix II.

In principle $(\bar{1}12)$ twins should be able to cross $(\bar{1}72)$ twins (but not vice versa!) without deflection in an exactly analogous manner. (Here the secondary twin would have indices $(1\bar{7}2)$.) In fact this has not been observed, presumably because {112} type twins occur rarely and no opportunity for such intersection occurred in any of the grains examined.

An exhaustive analysis showed that no other pair of twins satisfies the necessary conditions exactly, though in a few cases they are roughly satisfied. The corresponding intersections were not, however, observed. In a very few cases only, intersections were observed between pairs of twins, of which at least one was always very thin, which did not satisfy the conditions. An instance is shown in Figure 24*g*, where a (172) twin crosses a $(1\bar{1}2)$ twin. Evidently the strains engendered by such intersections are so high that they can only be accommodated when one of the twins is very thin.

Bouncing twins. Figure 25*a* shows a configuration which was repeatedly observed. Here a large $(1\bar{1}2)$ twin cuts right across a grain and acts as an obstacle, since no other twin can normally intersect it. Several (172) twins impinge upon it, and at the points of contact, the local strain is partly relieved by a (172) twin which starts from the same point. Sometimes this starts a whole avalanche of twins, bouncing to and fro between two parallel $(1\bar{1}2)$ twin lamellae; the set a, b, c, d, e, f at the top of Figure 25*a* is a case in point. A view of this region at higher magnification (after repolishing) is shown in Figure 25*b*. (Figure 24*g* shows another part of the same grain).

This configuration is only possible because the (172) and $(1\bar{7}2)$ twins can cross each other freely, and because the K_1 planes (172), $(1\bar{7}2)$ and $(1\bar{1}2)$ are almost exactly cozonal. This explains why such "bouncing" is ***possible*** but not why it actually happens. It is thought that this is due to the fact that a $(1\bar{1}2)$ twin is virtually impenetrable to either a (172) or a $(1\bar{7}2)$ twin. When a (172) twin impinges on a $(1\bar{1}2)$ twin, the resultant shear (indicated in Figure 24*g* and roughly parallel to the plane of the photograph) must somehow be accommodated at the point of impingement. This is normally achieved by a tapering of the impinging twin (cf. Figure 7). Here this does not happen, and instead a $(1\bar{7}2)$ twin bounces back producing a fresh shear as indicated. The resultant of the two shears is roughly parallel to the η_1 direction of the $(1\bar{1}2)$ twin (which is also approximately in the plane of the photograph). Often this resultant appears to be cancelled by a third shear effected by a thickening of the $(1\bar{1}2)$ twin on one side of the point of impingement. This is well brought out by Figure 24*g*. This figure also illustrates another consequence of impingement of this kind, namely, the appearance of a similar configuration of twins exactly opposite the first.

Other Observations Relating to Twinning

Effect of Temperature on Twinning

Investigations of twinning in other metals has repeatedly shown that twinning becomes less important, or even gives way completely to slip, as the temperature of deformation is raised. Experiments on this point were undertaken with uranium.

It was not possible to stretch tensile specimens at elevated temperatures, as would have been preferred, since no provision was available for this to be done in a protective atmosphere. An existing apparatus for hot Brinell testing in argon was therefore used instead. Coarse-grained specimens were used, and impressions were made by a steel ball, 5 mm. diameter, at temperatures ranging from room temperature to 630°C. Loads were chosen so as to produce impressions of approximately equal diameter (about 1.5 mm.) in each specimen. The specimens were subsequently sectioned transversely through the impression. The sections were deeply ground on fine emery and deeply polished, to obviate any spurious sources of deformation.

Specimens deformed at room temperature and at 300°C had twinned profusely. A specimen deformed at 450°C was devoid of twins except for some isolated clusters in one grain. Specimens deformed at 550°C and 630°C were entirely devoid of twinning.

The few, thin twins due to cooling stresses are ignored in this statement; they could easily be distinguished from the thicker twins produced by the Brinell ball where these were present. Figures 26–28 are representative photomicrographs.

The conclusion from this series of experiments is that somewhere between 300°C and 450°C, twinning is almost entirely superseded by slip. The peculiarities of slip at higher temperatures will be discussed later.

Some experiments were also done with an apparatus in which twinning during heating and cooling is followed by amplifying the "cry" of the individual twins and projecting the signals on to an oscilloscope screen. Twinning due to thermal fatigue seems to be absent above about 350°C, and even below this temperature it occurs only on the cooling cycle. The explanation of this is not known at present, but it may well be basically similar to the theory put forward by Burke and Turkalo [15] to account for "thermal ratcheting" in zinc bicrystals. It is noteworthy that, on cooling from a high temperature, the first twins to form (between 350°C and 300°C approximately) are also the largest, if amplitude of sound is taken as a measure of twin size.

These two independent methods taken together indicate that twinning is largely superseded by slip round about 350°C.

Effect of Annealing on Deformation Twins

The experiments to be described were purely exploratory, and the observations should be evaluated with this in mind. The effects found are interesting enough to merit further experiments.

A few coarse-grained specimens which had been lightly deformed in tension or compression, were annealed in vacuo for periods varying from one day to several days at 630°C. The specimens were examined in polarised light after repolishing. In a number of grains there were signs of (1) swelling of twins, and (2) lengthwise absorption of twins by the parent. Instances of these phenomena are illustrated in Figures 29–32. The fields shown in Figures 29 and 30 were examined most fully.

The configuration shown in Figure 29*a* was attained by an anneal of 16 hours at 630°C. Further annealing had very little effect. Laue photographs were taken with a 0.1 mm. beam at the locations indicated by the inked circles. The orientations of parent and twin are shown in the stereogram, Figure 29*b*. The mirror plane relating these orientations was found by construction, and is inserted together with its pole. The pole locus corresponding to the trace of the twin plane is also included. From the stereogram we see that the twin is of type 2 (a twin of the second kind), with $K_1 \sim (1\bar{7}2)$ and $\eta_1 = [31\bar{2}]$. (This pair of Laue photographs furnished yet further evidence for the correctness of the twinning elements, and incidentally verifies for the

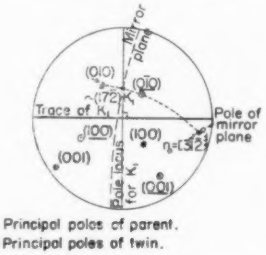

FIGURE 29*b*. Annealed twin configuration, $(1\bar{7}2)$ type (to match Figure 29*a*).

first time that in a twin of the second kind η_1 is the rotation axis giving the twin orientation.)

Figure 30*a* gives the appearance of another field in the same specimen after 16 hours at 630°C. Figure 30*b* shows the same field after an additional 6 hours at 645°C; after the second anneal the surface was repolished electrolytically for a few seconds only, to avoid taking off much metal. With one minor exception, all the twins which have been affected at all by the second anneal have become partly or entirely absorbed by the white matrix. The twins differ from ordinary deformation twins, partly in being very parallel-sided, but particularly in being blunt-ended instead of tapering. In the left-hand bottom corner are some pairs of twins joined at their middles, a configuration characteristic of annealing twins [16]. (The whole of Figure 29*a* is a single complex of this type.) Laue photographs were taken of the white grain in Figure 30, and of the large neighbouring black grain which from its colouration was judged to have the same orientation as the twins (this also follows from the way the twins merge smoothly with the black grain). The two grains were almost exactly in twin relationship according to a $(1\bar{7}2)$ plane parallel to the traces seen; the corresponding η_1 was again the rotation axis. The small discrepancy is probably due to the black grain having *grown from a twin*, but in some remote, slightly bent, part of the white grain. It was striking that the Laue photograph from the white grain had more asterism than that from the black. It would be interesting to know whether the lattice of the white grain gets rid of distortion in the places where a black twin is absorbed by it. If this is so, we have a close analogy to the phenomenon which has been called "strain-induced grain growth" [17].

Figure 31, from another specimen, shows that (130) twins are also liable to become absorbed from their ends, as evidenced by some blunt-ended twins which no longer abut on other twins (compare this photograph with Figure 7).

No study of recrystallization in uranium has been carried out, but it does seem justifiable to say that some recrystallized grains must be the product of enormously swollen twins. The large black grains in Figures 29 and 30 are strong evidence for this; so is the twin "caught in the act" in Figure 32.

One other effect of annealing was sometimes observed. When a specimen was deformed, sealed up in vacuo without repolishing, and annealed, thermal etching effects appeared at some of the twins. Figure 33 shows an example. It is not known whether a sample repolished before annealing would show the effect, which is presumably due to elastic strains associated with the twins. These would affect surface mobility or the vapour pressure.

Cleavage

Fracture of coarse-grained specimens under tension generally produced a dull irregular surface. Rarely, small cleavage facets were seen on one grain in the cross-section. The facets reflected light over an angular range of 2–3°. In an attempt to determine the indices of the cleavage plane, Laue photographs were taken with the X-ray beam incident normally on a cleavage facet. This method failed, however, for the surface was so intensely strained that there were no recognizable Laue spots; fragments of Debye-Scherrer rings took their place. The numerous striations visible on the cleavage facets (an example is shown in Figure 34) suggested that the strain was associated with intensive twinning near the cleavage.

Sections through several cleavages of this sort showed thick twins near, and running parallel to the trace of the cleavage. In one case it was possible to interpret a Laue photograph taken of a cleaved grain some distance from the cleavage, and thus to identify the plane of cleavage as (172). Evidently we have to do, not with a true cleavage, but with what mineralogists call a "parting."

This kind of parting is more common than was once thought. It occurs with great perfection in calcite [18]. This has been confirmed by the author, and it was found that the parted surface was goniometrically more perfect than any true cleavage plane. Twin-parting has been reported to occur in stretched zinc crystals [19] when the twin bands were "few in number and far apart." It has recently been studied in several alloys (Zapffe, private communication). Recent work has shown that cleavage often occurs at, or more often very close to, Neumann bands in silicon iron [20]. A remarkable feature in the case of uranium is that the plane of parting is irrational.

Crystallography of Slip and Kinking

The Slip Elements

The method used to find the slip planes was that of the pole locus, already described in connection with twinning. By this means the two slip planes were found to be {010} and {110}, the former being far the more prevalent. Pole loci used in the determination are assembled in Figure 4. The short H-shaped marking through the (010) pole refers to a single determination which was made by the two-surface method.

The slip direction associated with the (010) plane was determined by making use of the cross slip which occurs together with the ordinary slip. The short cross slips seen on many grains (Figure 9 shows an example) are caused by localized slip on a number of planes which are all parallel to a common slip direction [8]. Consequently, the angular deviation of the cross slip traces from the main slip traces is the greater, the larger the angle at which the slip direction is inclined to the (flat) specimen surface. When the slip direction is almost parallel to the surface, the slip lines are faint and the cross slips cannot be distinguished because their traces are almost parallel to the main slip traces. By comparing the appearance of slip lines on a number of grains of known orientation, bearing this in mind, it was found that the slip direction must be within 10–20° of [100]. Since slip directions are almost always found to be the closest-packed lattice vector, and [100] is this vector in uranium, it was evident that the slip direction must in fact be [100]. Figure 9 was made of a grain in which [100] made an angle of 65° with the surface, while this angle was only a few degrees in the case of the grains shown in Figures 13 and 14.

No satisfactory way of establishing the slip direction of the {110} slip was found; this was a pity, since this knowledge would be of some theoretical interest. The closest-packed direction in the (110) plane is [1$\bar{1}$2], with [1$\bar{1}$0] a close second. The method used for the predominant slip was of course inapplicable here, as there was no cross slip. From a consideration of the relative intensity of the {110} slip lines in the few grains of different orientations where they were visible, it was tentatively concluded that ⟨110⟩ was the slip direction.

The Kink Bands

The orientations of the planes of the kink bands were determined by the pole–locus method, and the results are entered on Figure 4. The bands were all *approximately* normal to [100], but, if we make the assumption, reasonable in view of the mechanism of kinking, that the correct point to take on each pole locus is at its intersection with the [100]-[010] great circle, the positions of the poles of the planes of the bands were all displaced by a small, variable angle towards [010]. This displacement was greater for bands in which the slip lines were more deviated. Thus A and B in Figure 4 are pole loci from two bands in the same grain, B corresponding to the "stronger" band. Now according to the usual model of kinking, the orientations inside and outside the bands are related by a rotation of a few degrees about an axis lying in the slip plane and normal to the slip direction; here this axis is [001]. The systematic deviation of the plane of the kink bands from being normal to [100] therefore suggest that instead of being exactly normal to the slip direction, this plane bisects the slip directions inside and outside the bands. This would indeed be expected, and it is in agreement with observations on zinc and cadmium [9; 10].

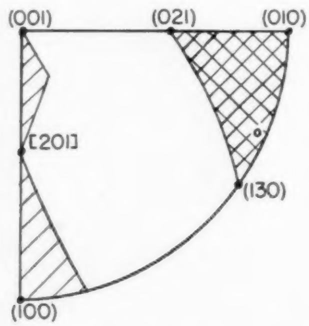

FIGURE 35. Relation of twinning to direction of stressing (twins on {121} have been left out of account).

It was suggested on p. 53 that the comparative readiness with which uranium undergoes kinking should be attributed to the inability of twinning to relieve compressive stresses in certain directions. Some such explanation must evidently be sought for the occurrence of kinking in a substance which disposes of three slip planes and 14 twinning planes. Referring to Figure 2*a*, the formation of a lamellar twin causes contraction only for directions emerging in quadrants AECD or BFCD of the sphere. Accordingly the regions on the standard stereogram of uranium were marked which would be contracted by lamellar twinning on each of the various possible twins, with the exception of the four {121} type twins; these were omitted from consideration as this type of twin only formed with great difficulty. It turned out that none of the other twins would cause contraction for compression directions lying within the area singly hatched in Figure 35. All directions lying in this area make fairly small angles with the predominant slip plane, (010), and if the direction also makes a fairly small angle with the slip direction [100] (say anywhere within the broader, bottom half of the "hour-glass") the conditions are ideal for kinking. The only alternatives would be either slip on (110) or $(1\bar{1}0)$ or else twinning on one of the (121) type twins. These must both require high stresses for their inception, in view of their rarity, and kinking is evidently easier.

It was found that there was also an area such that *tensile* stresses along directions lying within it could not be relieved by twinning (other than by a {121} twin). This area is doubly hatched in Figure 35. It is noteworthy that a large grain in a stretched specimen, oriented so that the axis of tension came at the point, just inside the double-hatched area, marked by an open circle, underwent (010) slip only and no twinning, apart from some well-formed wide {121} twins and a very few narrow {172} twins. This was the grain illustrated in Figures 9 and 21.

Calnan and Clews [21] have used considerations of this sort to account for the textures found in rolled uranium.

It would be interesting to study the behaviour of *single* crystals of certain orientations, in the light of these special areas on the stereogram. In particular, single crystals should be *compressed* parallel to directions lying in the central, narrower half of the "hour-glass" area in Figure 35 as close as possible to [001]. This would exclude kinking of the (010) slip planes, and also slip on (110), if $[1\bar{1}0]$ is indeed the slip direction of the latter. The only feasible deformation mechanism would then be twinning on {121}. Since the resistance to this is high and no form of slip is possible, the strength of the crystal to such compression should be extraordinarily high. Again, a crystal *stretched* approximately along [010] should be very strong, since it could only deform by slip on (110) or twinning on (121). By an obvious extension of these arguments, polycrystalline rods with a strong fibre texture should be very resistant to compression if the fibre axis is [001], and resistant to tension if it is [010].

Effect of Temperature on Slip and Kinking

Raising the temperature of deformation caused the (010) slip lines to become somewhat more widely spaced and thicker, and the amount of cross slip to increase so much that the slip lines become wavy (Figure 10). The coarsening of slip with increasing temperature is common among metals, generally, and the accompanying increase of cross slip is paralleled by a similar effect in aluminium [8].

Some information on slip at high temperatures was also derived from the sectioned specimens in which Brinell impressions had been made at various temperatures. Figures 26–28 were made from two of these sections; Figures 27 and 28 are from the specimen tested at 550°C, at two magnifications. In Figure 28, several grains vary markedly in orientation from point to point. The large grain A reveals this by the curvature of the twin lamellae while the grains B and C happen to be oriented in such a way that the small orientation differences show as differences of colour between several sharply defined bands. This suggests that the grains have become divided into separate kink bands or "cells." (Just such behaviour has been observed in hot-worked polycrystalline zinc [22].) Another striking feature of Figures 27 and 28 is the irregularity of the grain boundaries. It is certain that there had been no recrystallization. The time at temperature had been too short, and the deformed structure graded insensibly into the undeformed regions of the specimen. An examination of grains B and C, particularly the former, will show that the boundary irregularities seem to be associated with the individual kink bands. The orientation variation and ragged boundaries were observed to a lesser extent in a specimen thermally cycled between room temperature and 630°C, and a Laue photograph of a grain in this specimen had spots subdivided into many specks, characteristic of a polygonized specimen. It makes little difference whether we attribute the effects just described to kinking or to polygonization. The two are closely similar phenomena. In the one case dislocation groups move under stress alone, in the other, under that of high temperature alone; here we have an instance where both act together. That stress and high temperature reinforce each other in fragmenting the structure, we know from the work of Greenough, Bateman and Smith [23], to mention no others. Again, a recent study of the deformation of beryllium [24; 33] has shown very similar behaviour. With temperatures of deformation above about 400°C, twinning ceases, and deformed grains are twisted in such a way that separate bands are visible under polarised light.

One can only speculate why the observed small movements of grain boundaries should occur under the influence of kinking. It may be that when a kink band or cell has been formed, it is denuded of dislocations (except those constituting its boundaries) and so becomes more perfect, and this would give the band a tendency to grow at the expense of a less perfect, because still distorted, neighbouring grain. At the intersection of the boundary of the kink band with the grain boundary the latter is effectively pinned down; this is particularly clearly seen at the top left of grain B.

Discussion

The present investigation was undertaken because of the unique crystal structure of α-uranium. Our main preoccupation in assessing the results will be to relate them to the crystal structure.

The experiments carried out on twinning served to determine the macroscopic features of twinning in uranium. They do not tell everything about the microscopic aspect of the process, the actual paths taken by the atoms as a twin develops. This can only be studied by drawing a suitable projection of the crystal structure, seeing where the atoms start and where they finish, and trying to work out the simplest way for them to get from one set of positions to the other. This will be done for type 1 and type 2 twins.

The Slip Systems

It has been found for other metals that the slip direction is always parallel to the direction of closest packing in the crystal lattice. The only exception to this rule is tin. Here the closest-packed direction, $\langle 001 \rangle$, is certainly the most common, but $\langle 011 \rangle$ occurs also. We shall return to this exception. Among metals in general, while the slip plane is usually the most close-packed plane, this is not invariably so. We need only call to mind the alternative slip planes, $\{110\}$, $\{112\}$ and $\{123\}$, operating in some body-centred cubic metals. Again, the existence of cross slip in a number of metals is itself a demonstration of the comparative latitude in choice of the slip plane. The constancy of the slip direction is not surprising, as this direction coincides with the Burgers vector of the dislocations producing slip. This vector is immutable, but with the exercise of some ingenuity various mechanisms can be worked out for deflection of a dislocation to another plane.

(010) is the closest-packed plane only if we take

pairs of neighbouring sheets together, giving densely packed corrugated sheets; these are the "giant molecules" referred to earlier and seen in projection in Figure 1*b*. If we were to consider A and B (Figure 1*b*) as separate sheets of atoms, the packing density would be low. It is reasonable to consider the giant molecules as a unit since they are held together internally by covalent bonds. When there is slip according to (010) [100], the corrugated sheets simply slip over each other along the line of corrugations.

The minor slip system with $\{110\}$ as slip plane has still to be examined. The closest-packed directions in the (110) plane are $[1\bar{1}2]$ and $[1\bar{1}0]$, in that order. From stereographic analysis the very tentative conclusion was drawn that $[1\bar{1}0]$ was the active slip direction. On a projection of the (110) plane it can be seen that, while the $[1\bar{1}0]$ direction is simply a straight line of atoms regularly spaced at 3.3 A.U., the atoms in the $[1\bar{1}2]$ direction form a gentle zigzag with a *mean* spacing, projected along the direction, of 2.95 A.U. Thus $[1\bar{1}2]$ would be preferred as being most close packed, while $[1\bar{1}0]$ would be preferred as not being puckered. If our attribution is right, it would appear that straightness of atom rows is more important than closeness of spacing. Comparison with tin is instructive here. The most common slip direction is $\langle 001 \rangle$, and this is both straight and closest packed. Occasionally $\langle 011 \rangle$ is also found to operate. The packing density here is almost identical with that along $\langle 001 \rangle$, but the atoms lie on a puckered line.

It is interesting to speculate why slip on $\{110\}$ operates so rarely and so very weakly that the slip lines are scarcely visible. It appears probable that this is simply because slip or any plane other than (010) involves the disruption of the "giant molecules" and consequently the disruption of covalent bonds. These bonds are not so strong as in metalloids such as silicon, or slip would certainly be quite impossible on any but the (010) plane.

Atom Movements in Uranium Twinning

In the elementary crystallographic treatment of twinning given in the introduction we were concerned only with the movements of the crystal axis; the restrictions imposed on the possible choice of twinning elements were due to the requirement that the shape and size of the unit cell should be unchanged by the twinning operation. The motions of the atoms themselves depend entirely on their positions within the unit cell and will not coincide with the simple twinning shear unless all the atoms are actually situated at the points of the space lattice (and not always even then). This is the case for body-centered cubic metals, including iron, which is known to twin, and here the atoms have only to execute the exact twinning shear to arrive at their final positions. In all other substances capable of twinning, some of the atoms occupy non-special positions in the unit cell, defined by one or more parameters. For the hexagonal metals this applies to half the atoms, and the same is true for uranium. The atoms of these substances will not, then, be brought to their final positions by the twinning shear but will have to undergo additional adjustments, all rather smaller than the mean interatomic distance, to find their correct places in the twinned lattice. The only way open to one to determine these adjustments is to draw a projection of the crystal on the plane of shear (i.e. the plane including η_1 and normal to K_1), to draw the trace of the twinning plane K_1 across the projection and to move all atoms on one side of K_1 by the correct twinning shear. Then it is only necessary to adjust each sheared atom to the nearest correct position with respect to the twinned lattice, which is derived from the parent lattice by means of the appropriate symmetry relation (i.e. either K_1, or else the plane normal to η_1, serving as symmetry plane). This sort of analysis has been carried out by Mathewson [25] for zinc, and by Barrett [26] for magnesium. It is important to realise that the size of these individual atomic adjustments will depend upon just where we draw the trace of the composition plane in relation to the unit cells of the untwinned part of the crystal. In making the drawings, the position of the twinning plane can be chosen, by trial and error, either (1) to minimize the *mean* distance of adjustment of the atoms, or else (2) to make all the atoms move as nearly as possible the same distance, or else (3) to allow a proportion of the atoms to fall into place without requiring any adjustments at all. It turns out that the positions of K_1 which satisfy these three conditions do not differ much from each other.

Projection for Type 1 *Twins* ($K_1 = (130)$, $\eta_1 = [3\bar{1}0]$, $K_2 = (1\bar{1}0)$, $\eta_2 = [110]$)

Figure 36*a* is the projection in the plane of shear which is (001). The black atoms are in the plane of projection, the white ones $c/2$ above it, then the pattern repeats. The dots to the right of the K_1 composition plane indicate the positions occupied by the atoms before twinning, and are simply a continuation of the lattice on the left of the composition plane. The crosses indicate the positions to which

the atoms move in executing the twinning shear, while the circles indicate the final position of the atoms, these being determined simply by reflecting the parent lattice in K_1 as mirror plane. The arrows from each spot indicate the presumed actual atomic motions, obtained by vector addition of the twinning shear and subsequent adjustment. It should be noted that all adjustment vectors are parallel to the

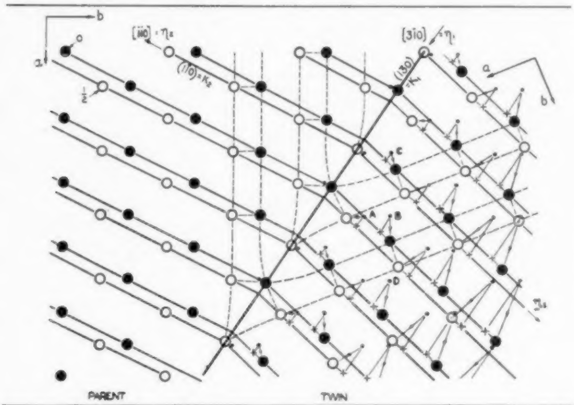

FIGURE 36*a*. Atom movements, (130) twin.

plane of shear. The position of the composition plane was chosen so that all atoms have to adjust their position through about the same distance. (If the composition plane is moved 0.25 A.U. to the left, the black atoms would require no adjustments, but the white atoms would need large adjustments; if the plane is moved 0.25 A.U. to the right, the reverse obtains. The *mean* distance of adjustment is approximately the same in all three cases.) All atoms in the immediate vicinity of the composition plane are in abnormal positions; this remains true wherever the composition plane is placed. In the drawing, atoms a little way to the left or right of the composition plane have been moved slightly so as to coincide with the plane; in this way they conform as closely as possible to both parent and twin lattices, but exactly to neither. The immediate vicinity of the composition plane must therefore be the seat of considerable stresses.

It is instructive to see what happens to the covalently bound sheets, or "giant molecules," during twinning. Two such sheets are indicated in both parent and twin by dotted lines joining covalently bound atoms. Consider the atoms A, B, C, and D before twinning. B is bound to A, C, D and to the atom at a distance *c* below A. On twinning the atoms move as shown by the arrows, and as a result B is no longer bound to any of the other four. This is true whichever group of atoms we consider, from which it follows that twinning completely breaks up the old covalent bonds and causes bonds to be established between new pairs of atoms. From this it again follows that the bonding cannot be very strong.

Projection for Type 2 Twins ($K_1 = (172)$, $K_2 = (1\bar{1}2)$, $\eta_1 = [3\bar{1}2]$)

It is not worthwhile to study both type 2 and type 3 twins, for these are reciprocal to each other. Johnsen [20] has shown theoretically that if one type of twin is capable of forming by pure shear (i.e. without any subsequent atomic adjustments) then the same is true of its reciprocal type. It seems a reasonable extension that the magnitude of adjustments, in the case of a twin where these are required, will be about the same for it as for its reciprocal twin. Type 2 was preferred for examination as atomic movements have not previously been examined for a twin of the second kind.

Here the plane of shear is irrational, but as may be seen from Figure 36*b*, it is extremely close to $(\bar{2}03)$, while this plane in turn is almost precisely normal to $[\bar{2}01]$. It was thus considered a justifiable approximation to project the lattice along $[\bar{2}01]$ and to treat the resulting projection as being in the plane of shear. This has been done in Figure 36*b*. As we go along the $[\bar{2}01]$ direction, there are fourteen layers of atoms before the pattern repeats. These layers, numbered 1′–14′, are indicated in the projection by the symbols listed at the bottom right of the figure. To avoid confusing the diagram, the following procedure was adopted. The positions to which the atoms move by executing the exact twinning shear are found in the upper half of the projection of the plane of shear, by geometrical construction. These positions are indicated by dots. The projection comprising part of the parent lattice and also the dots just mentioned, is then translated bodily along the η_1 direction and drawn afresh. The numbering along η_1 is merely intended to facilitate the identification of corresponding points. The twinned lattice is also drawn in, using the plane normal to η_1 as mirror plane, as is proper for a twin of the second kind. The adjustment required to move each spot to the nearest lattice position is then inserted.

The exact position of the composition plane has been chosen this time so as to cause one in four of the atoms to fall into place without the need for adjustment. It was found that to a good approximation this also gave the smallest mean distance of adjustment for all the atoms; actually for this type of twin the position of the composition plane is not

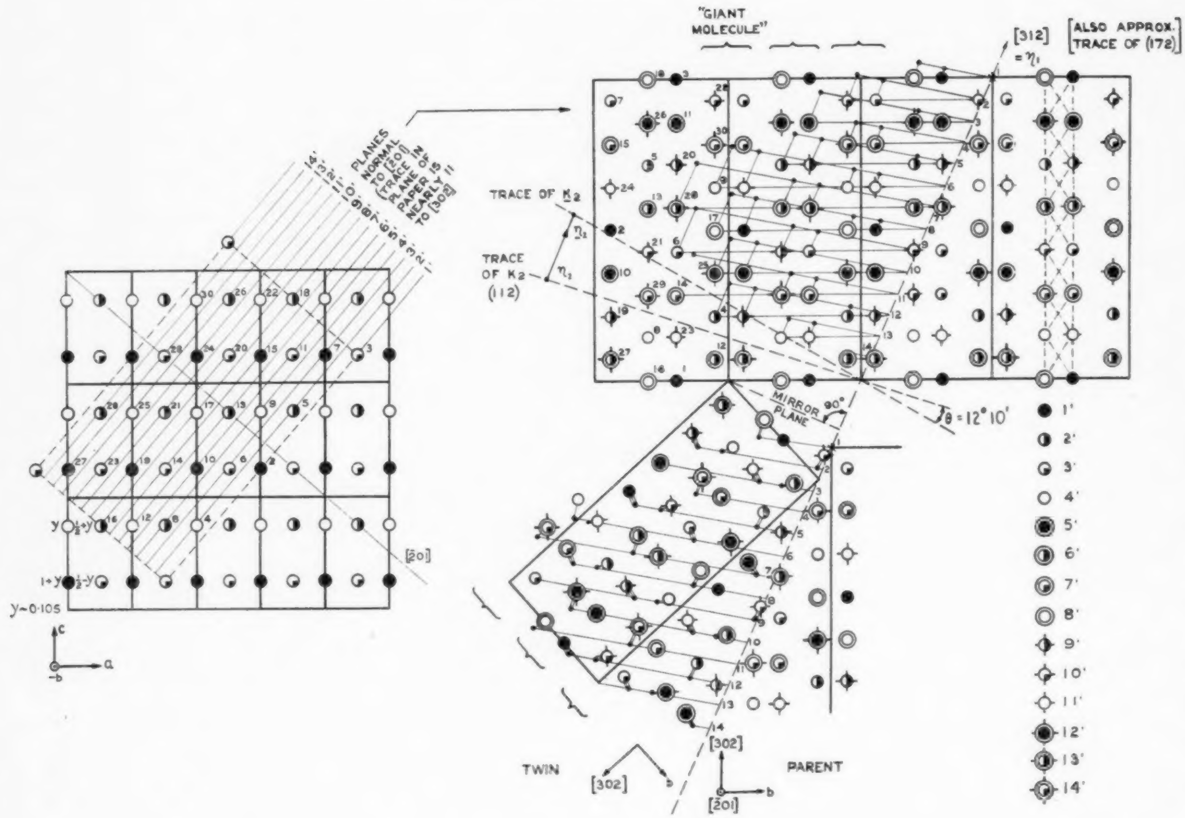

FIGURE 36*b*. Atom movements, (172) twin.

at all critical. For the purpose of the drawing, all atoms to the left of the composition plane have been made to conform strictly to the twinned lattice, no attempt being made to move them to compromise positions. We find that the adjustments are not all in the plane of shear. One quarter of the atoms move up one layer (0.55 A.U. above the plane of shear), one quarter move in the plane of shear, and one quarter move down one layer. The three kinds of atom are indicated respectively by single, double and treble tie-lines joining them to the corresponding dots. The remaining quarter of the atoms undergo no adjustments, *ex hypothesi*. Adjustments out of the plane of shear have not been found in the analysis of twins in other metals.

A detailed examination showed that the structural distortion in the vicinity of the composition plane is slight, less in the aggregate than for the {130} twins. Some of the atoms (those in layer 9′) are in fact a perfect fit in both the parent and the twinned lattice. This is remarkable since the two lattices are not related by reflection across K_1 and in general one would expect to find considerable distortion of the structure near the composition plane of a twin of the second kind.

The behaviour of the giant molecules was again investigated. One of these, with its bonds, is indicated near the top right of the figure, in the parent. To save crowding the drawing it is not included in the twinned lattice. It turned out that half the bonds only are broken, i.e., each atom remains bonded to two of its four initial closest neighbours after twinning.

Type 4 *twins* (K_1 = (121), η_2 = [311])

No projection was made for this type of twin, as its identity had not been established beyond all doubt. It is, however, striking that here again the plane of shear is very close to a rational plane. It is estimated to be within 4′ of $(\bar{1}03)$, and perpendicular to $[\bar{1}01]$ to the same approximation. (This is due to the pseudo-hexagonality of the structure about the *b* axis.) It is noteworthy that for all four types of twins, the plane of shear, and the lattice direction normal to it, are coincident with or very close to rational lattice elements.

The Choice of Twinning Elements

It is hoped that the present observations may contribute to answering the question: What properties of a crystal determine the indices of the operative twinning elements, and whether twinning occurs at all?

It is fruitless at the present stage of our knowledge to do more than to make some empirical generalizations, which should provide a touch-stone for the validity of any general answer to the question (such as may perhaps be hoped for by an extension of the dislocation treatment applied to twinning in iron by Cottrell and Bilby [27]). The following generalizations can be made with fair confidence:

1. Whether a twin is of the first or second kind, or compound, the plane of shear and the normal to it are simple rational elements or very close to being so. This is based on an examination of a compilation of all known species of mechanical twin [28], together with the data for uranium. Only two minerals were found for which the divergence was more than a few minutes of arc. It remains to be seen what the theoretical significance of this generalization is.

2. The shear is always quite small. The largest known is that in iron. The angle 2ϕ between K_1 and K_2 never differs from 90° by more than 20°. It is noticeable that substances like iron and uranium, and many minerals, with relatively large shears, produce only thin twin lamellae, while metals like tin and bismuth which have small shears, produce thick ones. Perhaps this correlation is significant, and twins for which $2\phi < 70°$ could never grow beyond submicroscopic dimensions.

3. There is some evidence that the elastic anisotropy plays a part in determining the choice of elements [29]. No data are available at present for checking this for uranium.

Effect of Annealing on Mechanical Twins

The evidence presented above shows that twin lamellae in uranium can either swell or else be absorbed by the matrix. Absorption of twins on annealing has also been reported to occur in iron [30], zinc [31], bismuth [32], beryllium [33] and sodium nitrate [34]. All twins are eventually absorbed completely in beryllium. Swelling of twins sometimes occurs in iron [30; 35] and zinc [31]. There is evidence that swelling of a twin requires that the matrix should have been further strained in slip after the twin was formed, which would leave the twin with less strain energy than the matrix. This is in line with the absence of twin swelling in beryllium, which can only slip with great difficulty at room temperature. The analogy between twin absorption and strain-induced grain boundary migration, pointed out earlier, then applies also to the swelling of twins. Whether absorption or swelling occurs is determined by the relative states of strain of twin and matrix. These may vary greatly from point to point in a grain and here we may find the explanation for the occurrence of both absorptions and swelling in a single grain of uranium (cf. Figure 30). These processes deserve more systematic study.

Acknowledgements

My grateful thanks are due first of all to Messrs. B. W. Mott, H. R. Haines, L. Kent and S. D. Ford, who placed at my disposal their skill and knowledge in the electrolytic polishing of uranium and in preparing photomicrographs in polarised light. Without their help this work could not have been carried out. I am obliged to Mr. W. Munro for carrying out on an apparatus of his design the experiments on hot deformation of uranium, and to Miss S. Vernon-Smith of the B.N.F.M.R.A., who took great pains over the electron micrography of slip lines in uranium. To Dr. H. M. Finniston I owe a debt of gratitude for his consistent encouragement throughout the course of this work. This paper is published by permission of the Director, A.E.R.E.

APPENDIX I

Conditions for Two Twin Lamellae to Intersect Each Other

The nomenclature and basic conditions have been explained on p. 58 and in Figure 23. The conditions are:

1. The traces of the crossing (A) and the secondary (C) twins in the planes of the crossed twin (B) must be parallel.

2. The direction (η_1) and magnitude (s) of shear must be identical in the crossing and secondary twins. Also the sense of shear must be the same (this is explained below).

We divide the possible cases according as the crossed twin B is of the first or second kind. It is assumed, except where otherwise stated, that the indices of C (taken relative to the crystal axes inside B) are the same as the indices of A (relative to the axes in the parent grain). This implies that the orientations of A and C are related by reflection in K_1 (for twins of the first kind), or by a 180° rotation about η_1 (for twins of the second kind).

Case (i). *The Crossed Twin* (B) *is of the First Kind*

Figure 37*a* is a stereographic projection of the parent grain with the pole of the twinning plane of B ($= K_{1B}$) at the centre. Let K_{1A} be the pole of the twinning plane of A. Then K_{1C}, the pole of the twinning plane of C, is located as shown. The traces of K_{1A} and K_{1C} in K_{1B} are both parallel to XY. Condition 1 is therefore satisfied for any combination of A and B, whatever their indices.

If the shear direction of A (η_{1A}) lies in K_{1B}, as drawn, then η_{1C} will coincide with η_{1A}; moreover, since *ex hypothesi* A and C have the same indices,

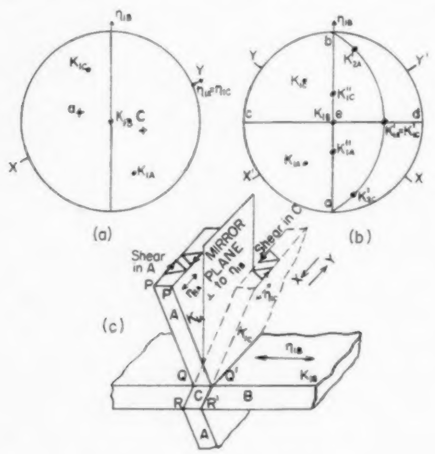

FIGURE 37. Conditions for twin intersections.

they are the same type of twin and therefore have the same value of s. Consequently condition 2 above is satisfied. If η_{1A} were anywhere else, for instance at a in Figure 37*a*, then η_{1C} (at c in the figure) would not be parallel to η_{1A} and the intersection would consequently not be possible.

At first sight it would appear that if the twinning plane and shear direction of A were both normal to K_{1B}, an intersection would be possible. This special case is illusory, however, because the sense of shear is reversed in the secondary twin if its composition plane moves in the same sense as does that of the crossing twin during their joint development (as must surely be the case).

We find, then, that when B is a twin of the first kind, and independently of the nature or indices of A, *the condition for an intersection to be possible is that* η_{1A} *is parallel to* K_{1B}.

Case (ii). *The Crossed Twin* (B) *is of the Second Kind*

Figure 37*b* is a projection as in the previous case. For an arbitrary position of K_{1A}, we obtain K_{1C} by rotation about η_{1B} (which is equivalent to reflection in a plane normal to η_{1B}). K_{1A} and K_{1C} intersect K_{1B} along traces parallel to, say, XY and X′Y′ respectively, in the general case, and condition 1 is evidently not satisfied. If, however, the pole of K_{1A} lies anywhere along the great circle *ced* (e.g. at K'_{1A}), then the traces of K'_{1A} and K'_{1C} in K_{1B} are both parallel to *ab* and therefore to each other. Similarly, if K_{1A} lies anywhere along the great circle *aeb* (e.g. at K''_{1A}), then the traces of K''_{1A} and K''_{1C} in K_{1B} are both parallel to *cd* and therefore to each other.

We shall examine condition 2 for the two distinct cases just mentioned.

(a) Poles of K_{1A} and K_{1C} lying on great circle *ced*. At first sight condition (2) is satisfied if η_{1A} is parallel to η_{1B}, because then η_{1C} will also be parallel to η_{1B}. However, the same objection applies as above, that the sense of shear will be reversed, and no intersection is possible.

(b) Poles of K_{1A} and K_{1C} lying on *aeb*. At first sight condition (2) is satisfied if η_{1A} is parallel to *cd*. Again, however, the same objection applies, and no intersection is possible.

Thus no intersection is possible at all, at least if A and C have the same indices. To make the objection regarding reversed shears clearer, K_2 poles have been inserted in Figure 37*b* for case (a) above. If an intersection were possible, not only would K'_{1A} and K'_{1C} coincide, but K'_{2A} and K'_{2C} would also. Figure 37*c*, which shows in perspective the situation for case *b*, is also intended to clarify this point. If twin A starts as a thin lamina coinciding with PQ, then C will be a lamina along QR. A must grow by the process of one of its two boundary planes moving parallel to itself, say till it reaches P′Q′. Then C would have to develop in the same way, till one of its boundaries reached Q′R′. But in the process, the parent crystal to the right of P′Q′ is sheared in the sense X, while twin B to the right of Q′R′ is sheared in the sense Y. This means that C cannot develop beyond the stage of a very thin lamella.

It remains to consider what happens when the indices of A and C are different. The important point here is that *in general* the condition that the magnitude of shear must be the same in A and C, will not be satisfied in this case. The only exceptions to this are (i) when A and C are twins of different indices but the same type, e.g. (*hkl*) and ($h\bar{k}l$), or (ii) when A and C belong to reciprocal twin types. Where these exceptions occur, it is in principle possible to have a situation where the objection about reversed sense of shear does not apply and an intersection may occur. Just such a situation in fact turns up in the

case of $\{172\}$ and $\{112\}$ type twins in uranium (see pp. 58-59). However, this is nothing short of an extraordinary coincidence and it may be doubted whether anything like it will be found in any other substance.

APPENDIX II

Crystallography of $(\bar{1}72)$–$(\bar{1}72)$ Twin Intersections

The key to these intersections is to be found in Figure 24*d*. Here $(\bar{1}72)$ twins are crossing $(\bar{1}72)$ twins (in this instance we can distinguish which are the crossing twins). It will be noticed that at a number of intersections, a $(\bar{1}72)$ twin splits into two separate secondary twins where it abuts on a broad $(\bar{1}72)$ twin. This was found in no other grain, but is quite distinct here. Stereographic analysis showed that, of the two secondary twins, the one which is deflected with respect to $(\bar{1}72)$ is $(\underline{\bar{1}72})$. (Underlined indices are referred to the crystal axes *within the crossed twin*.) The undeflected secondary twin, on the other hand, proved to have indices $(\underline{\bar{1}12})$. (Both these indices were obtained by drawing pole loci for the secondary twins on a stereogram showing the orientation of the lattice in the *crossed twin*.) Thus, in the usual case of an undeflected secondary twin in these intersections, the secondary twin has different indices from the crossing twin. At first sight this would seem to be incompatible with our two conditions, but detailed analysis (Appendix I) shows this is not so.

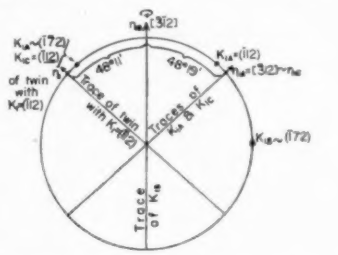

FIGURE 38. Stereogram to illustrate $(\bar{1}72)$-$(\bar{1}72)$ intersections. K_{1A} & K_{1C} and η_{1A} & η_{1C} respectively, coincide within 8′ of arc. The common plane of shear is in the plane of the paper.

Figure 38 presents the situation. The stereogram is projected so that the *plane of shear* (cf. p. 50) of the crossed twin ($K_1 = (\bar{1}72)$) lies in the plane of the page. The *poles* of $(\bar{1}72)$ and $(\bar{1}12)$, and the direction $[\bar{3}12]$, which are also drawn in, lie in the plane of shear of the crossing twin ($K_1 = (\bar{1}72)$). The important point here is that the two planes of shear coincide within about 1° (see Figure 22), so that to a close approximation it is permissible to place all these poles and directions on the primitive circle of the stereograms. The other important point is that the angles $(\bar{1}72)$–$[\bar{3}12]$ and $(\bar{1}12)$–$[\bar{3}12]$, are found by calculation to be almost exactly equal (respectively 48°19′ and 48°11′). From these facts it follows, as is made clear in Figure 38, that η_{1A} ($= [\bar{3}12]$) and η_1 of a twin which has $K_1 = (\bar{1}12)$ make practically equal, but opposite, angles with $[\bar{3}12]$.

The intersection we are discussing has indices thus: $K_{1A} = (\bar{1}72)$, $K_{1B} = (\bar{1}72)$, $\eta_{1B} = [\bar{3}12]$, $K_{1C} = (\underline{\bar{1}12})$, $\eta_{1A} = [\bar{3}12]$, η_{1C} irrational. To obtain the position of η_{1C}, we rotate η_1 of the $(\bar{1}12)$ twin through 180° about $[\bar{3}12]$ as axis (because the crossed twin is of the second kind and this is its shear direction). Then we find that η_{1C} and η_{1A} coincide within a few minutes of arc. The stereogram shows that, to a close approximation, (1) the traces of K_{1A} and K_{1C} in K_{1B} are parallel (and normal to the plane of the projection), (2) η_{1A} and η_{1C} are parallel, (3) the shear is the same (exactly) in twins A and C, because they are reciprocal to each other, (4) the sense of shear is the same in A and C. In addition K_{1A} and K_{1C} are very nearly parallel, which agrees with observation. All the conditions necessary for a twin intersection are thus satisfied, in spite of the fact that crossing and secondary twins have different indices.

REFERENCES

1. HOLDEN, A. N. Acta Cryst., **5** (1952) 145.
2. JACOB, C. W. and WARREN, B. E. J. Amer. Chem. Soc., **59** (1937) 2588.
3. LUKESH, J. S. Acta Cryst., **2** (1949) 420.
4. TUCKER, C. W. Trans. Amer. Soc. Metals, **42** (1950) 762.
5. CAHN, R. W. J. Sci. Instr. (in the press).
6. MOTT, B. W. and HAINES, H. R. Metallurgia, **43** (1951) 255.
7. BOAS, W. and HONEYCOMBE, R. W. K. Proc. Roy. Soc., **A186** (1946) 57.
8. CAHN, R. W. J. Inst. Met., **79** (1951) 129.
9. OROWAN, E. Nature, **149** (1942) 643.
10. HESS, J. B. and BARRETT, C. S. Trans. Amer. Inst. Min. Met. Eng., **185** (1949) 599.
11. JILLSON, D. C. Trans. Amer. Inst. Min. Met. Eng., **188** (1950) 100.
12. BOWLES, J. S. Trans. Amer. Inst. Min. Met. Eng., **191** (1951) 44.
13. CAHN, R. W. Acta Cryst., **4** (1951) 470.
14. SMITH, S. W. J., DEE, A. A., and YOUNG, J. Proc. Roy. Soc., **A121** (1928) 477.
15. BURKE, J. E. and TURKALO, A. M. J. Metals, **4** (1952) 651.
16. RATHENAU, G. W. and BAAS, G. Physica, **17** (1951) 117.
17. BECK, P. A. and SPERRY, P. R. J. Appl. Phys., **21** (1950) 150.
18. BREZINA, A. Verh. Geol. Reichsanstalt Wien (1880), p. 45.

19. DAVIDENKOV, N. N., KOLESNIKOV, A. F., and FEDOROV, K. N. Zh. Eksp. Teor. Fiz. (U.S.S.R.), **3** (1933) 350.
20. TIPPER, C. F. and SULLIVAN, A. M. Trans. Amer. Soc. Met., **43** (1951) 906.
21. CALNAN, E. A. and CLEWS, C. J. B. Phil. Mag., **43** (1952) 93.
22. RAMSEY, J. A. J. Inst. Met., **80** (1951) 167.
23. GREENOUGH, G. B., BATEMAN, C. M., and SMITH, E. M. J. Inst. Met., **80** (1952) 545.
24. KAUFMANN, A. R., GORDON, P., and LILLIE, D. W. Trans. Amer. Soc. Metals, **42** (1950) 785.
25. MATHEWSON, C. H. Trans. Amer. Inst. Min. Met. Eng., **78** (1928) 7.
26. BARRETT, C.S. In "Cold Working of Metals" (Amer. Soc. Metals, 1949), p. 81.
27. COTTRELL, A. H. and BILBY, B. A. Phil. Mag., **42** (1951) 573.
28. TERTSCH, H. Die Festigkeitserscheinungen der Metalle (Vienna, 1949), p. 56.
29. STEPANOV, A. V. Zh. Eksp. Teor. Fiz. (U.S.S.R.), **17** (1947) 713.
30. KRIVOBOK, N. V. Amer. Inst. Min. Met. Eng. Preprint No. 1557--E (1926).
31. MATHEWSON, C. H. and PHILLIPS, A. J. Trans. Amer. Inst. Min. Met. Eng., (1927) 143.
32. GINDIN, E. A. and STARTSYEV, V. E. Zh. Eksp. Teor. Fiz. (U.S.S.R.), **20** (1950) 738.
33. HAUSNER, H. H. and PINTO, N. P. Trans. Amer. Soc. Metals, **43** (1951) 1152.
34. GARBER, R. Zh. Eksp. Teor. Fiz. (U.S.S.R.), **17** (1947) 63.
35. PFEIL, L. B. Carnegie Schol. Mem. of the Iron and Steel Inst., **15** (1926) 319; **16** (1927) 153.

A NOTE ON TWINNING IN ALPHA-URANIUM*

F. C. FRANK†

The crystal structure of α-uranium resembles that of zinc but has lower symmetry. Comparison of the two helps to classify the twinning modes of the more complex case. The lowering of the symmetry gives rise to new twinning modes in two ways: because the reciprocals of some of the zinc modes become distinct twinning modes of the second kind; and by the operation of Mallard's law, according to which each lost symmetry plane may become a twinning plane. Most, perhaps all, of the twinning modes of uranium are thus accounted for. Among reciprocal pairs of modes, the twinning of the second kind seems to be the easier: the reason for this is discussed.

LE MACLAGE DANS L'URANIUM ALPHA

La structure cristalline de l'uranium α ressemble à celle du zinc, mais a une moins haute symétrie. La comparaison des deux aide à la classification des modes de maclage de ce cas qui est plus complexe. L'abaissement de la symétrie donne lieu à de nouveaux modes de maclage pour deux raisons: premièrement parce que les réseaux réciproques de certains modes dans le zinc deviennent des modes de maclage distincts de seconde espèce, deuxièmement parce que suivant la loi de Mallard, chaque plan de symétrie qui cesse d'en être un, après l'abaissement de celle-ci, peut devenir un plan de maclage. C'est ce qui explique la plupart et peut-être même tous les modes de maclage dans l'uranium. Parmi les paires réciproques des modes, le maclage de seconde espèce paraît être le plus facile; la raison de ce phénomène est discutée.

ZWILLINGSBILDUNG IM ALPHA-URAN

Die Kristallstruktur des α-Urans ist der des Zinks ähnlich, hat jedoch niedrigere Symmetrie. Der Vergleich der beiden Strukturen hilft die Zwillingselemente in dem komplizierten Fall zusammenzustellen. Die Erniedrigung der Symmetrie gibt aus zwei Gründen Anlass zu neuen Zwillingselementen. Erstens werden die Reziproken einiger Zwillingselemente zu definierten Zwillingselementen zweiter Art. Zweitens ist Mallard's Gesetz anwendbar, wonach jede beim Übergang zu niedrigerer Symmetrie "verlorne" Symmetrie-Ebene zur Zwillingsebene wird. Vergleicht man reziproke Elementpaare, so scheint die Bildung von Zwillingen zweiter Art leichter zu erfolgen. Die Gründe werden diskutiert.

Introduction

Cahn [1] has determined the twinning modes of α-uranium. The purpose of this note is to compare them with those of zinc, since there is a certain resemblance between the two lattices. To prepare the ground for this, the next three sections are devoted firstly to a comparison of the crystal structures, and secondly to a discussion of reciprocal shears and twinning modes, differing somewhat from previous treatments.

Crystal Structure

The crystal structure of α-uranium is approximately described as deformed close-packed-hexagonal. In the orthorhombic cell of α-uranium we have

$$a : b : c = 1 : 2.06 : 1.73$$

with atoms at

$$(0, 0, 0) \quad (\tfrac{1}{2}, \tfrac{1}{2}, 0)$$
$$(0, 0.21, \tfrac{1}{2}) \quad (\tfrac{1}{2}, \tfrac{1}{2} + 0.21, \tfrac{1}{2})$$

while in the orthorhombic cell of the typical hexagonal metal zinc we have

$$a : b : c = 1 : \sqrt{3} : 1.86$$

with atoms at

$$(0, 0, 0) \quad (\tfrac{1}{2}, \tfrac{1}{2}, 0)$$
$$(0, \tfrac{1}{3}, \tfrac{1}{2}) \quad (\tfrac{1}{2}, \tfrac{1}{2} + \tfrac{1}{3}, \tfrac{1}{2})$$

Thus α-uranium differs from zinc mainly by an expansion along the b-axis of the orthorhombic cell. This lowers the symmetry, for whereas we can take any of three orthorhombic cells for zinc, with axes rotated successively through 120°, only one of these is orthorhombic in α-uranium, and the other two are monoclinic.

Reciprocal Shears

A general shear of given magnitude (incorporating an arbitrary amount of rotation) transforms a sphere into an ellipsoid of the same volume and with one principal axis equal to the diameter of the sphere. This ellipsoid has just two diametral cross-sections which are circles of the same diameter as the sphere. Thus there are just two planes which remain undistorted (though, in general, rotated) as a result of the shear. Let us call these k_1, k_2 in the original body, k_1', k_2' in the body after shear. If 2ϕ is the smaller dihedral angle‡ between k_1 and k_2, the effect of the shear is to change this angle to $(\pi - 2\phi)$ so that the smaller dihedral angle between k_1' and k_2' is 2ϕ as before. ϕ is related to the magnitude of the shear, s, by the equation

$$s = 2 \cot 2\phi = \cot \phi - \tan \phi.$$

‡The reader unfamiliar with the subject may wonder why the factor 2 is introduced here. The best answer is that the shear transforms a certain rectangular parallelipiped into a similar "reciprocated" one, the edges p, q, r becoming q, p, r respectively. The ratio q/p is tan ϕ.

*Received August 13, 1952.

†The H. H. Wills Physical Laboratory, University of Bristol, England.

Varying the incorporated rotation, the general shear may be reduced to a simple shear in two alternative ways, so that either k_1' remains coplanar with k_1 or k_2' remains coplanar with k_2. In these cases we introduce new designations K_1 and K_2 for the undistorted planes. Either

$$K_1 = k_1 = k_1', \ K_2 = k_2, \ K_2' = k_2';$$

$$\text{or } K_1 = k_2 = k_2', \ K_2 = k_1, \ K_2' = k_1'.$$

Mineralogists, discussing deformation twinning, are accustomed to call two simple shears, related to each other in this manner, *reciprocal*.

In either case the rotation of the second undistorted plane is $(\pi - 4\phi)$.

Twinning Shears

We have been discussing homogeneous shears of bodies in general. We now consider such shears applied to crystal lattices. We shall suppose that the direction, λ, common to k_1 and k_2 undergoes no rotation. The plane normal to it is called the *plane of shear, S*. Two crystal lattices are equivalent if there is equality between the lengths and mutual angles of three independent pairs of lattice vectors, one from each lattice. Now, since the two undistorted planes make the same angles with each other before and after shear, it follows that *if two independent lattice vectors lie in one of them (say k_1) and a third on the intersection of the other (k_2) with the plane of shear, then the shear will regenerate an equivalent lattice.* This is called a twinning shear.

The lattice vectors concerned need not be the primitive generating vectors of the lattice: but the higher their indices in the primitive reference system, the larger the number of atoms in the unit cell they define, and the larger the proportion of atoms which must undergo inhomogeneous motions to come to an equivalent crystal structure. Such inhomogeneous motions are unavoidably associated with twinning shears in some crystal lattices, i.e., those with more than one atom per primitive unit cell.

When the specified conditions are fulfilled, k_1 is a rational plane; k_2 need not be.

Now let the associated rotation be chosen, *first*, in such a way that the shear is a simple shear with the unrotated plane $K_1 = k_1 = k_1'$. This is said to be a twinning shear *of the first kind*. Then the lattice vector γ, lying in the intersection of k_2 with S becomes γ' after the shear, and $-\gamma'$ together with two lattice vectors lying in K_1 define a unit cell which corresponds to the original one reflected in K_1. So that K_1 is a reflection plane between parent and twin. *Secondly*, let the associated rotation be chosen so that the shear is a simple shear with the unrotated plane $K_1 = k_2 = k_2'$. The second orientation differs from the first by a rotation $\pi = 4\phi$. There is therefore a mirror plane between the two lattices, containing λ and making an angle $\frac{1}{2}\pi - 2\phi$ with K_1: i.e., making an angle $\frac{1}{2}\pi$ with $K_2 = k_1$. Now, in the general case that $K_1 = k_2$ is irrational, we are said to have a *twin of the second kind*. In either case K_1, the unrotated plane, is the habit plane of the twinning mode.

We have already defined a sufficient number of twinning elements for a full specification: however it is also convenient to make use of η_1, the intersection of K_1 with S, and η_2, the intersection of K_2 with S. For a twin of the first kind η_2 corresponds to γ above, and is rational. Any pair with different suffixes chosen from K_1, K_2, η_1, η_2 serve to define the situation. Alternatively one may use K_1, η_1 and s (or ϕ). For a twin of the first kind K_1 and η_2 are rational: for a twin of the second kind K_2 and η_1 are rational. If three of these elements are rational, it can be shown that the fourth is also.

It may be noted that we have synthesized the theory of deformation twinning, rather than analysed it. That is to say we have constructed a twinning deformation of a fairly general kind, but we have not shown that every twinning deformation must conform to the system defined. This criticism applies to all treatment of deformation twinning known to the writer. It seems very difficult to prove necessity as well as sufficiency, when inhomogeneous atom movements have to be tolerated. Nevertheless the system defined above appears to cover all known kinds of deformation twinning, and the lattice vectors involved in defining the system are in fact always of relatively low index.

Comparison of the Twinning Modes of Zinc and Alpha-Uranium

The twinning modes of zinc are 6 in number, and all equivalent. In orthorhombic coordinates they are:

K_1	K_2	η_1	η_2
(011)	$(01\bar{1})$	$[01\bar{1}]$	$[011]$
$(01\bar{1})$	(011)	$[011]$	$[01\bar{1}]$
(112)	$(11\bar{2})$	$[31\bar{2}]$	$[312]$
$(11\bar{2})$	(112)	$[312]$	$[31\bar{2}]$
$(1\bar{1}2)$	$(1\bar{1}\bar{2})$	$[3\bar{1}\bar{2}]$	$[3\bar{1}2]$
$(1\bar{1}\bar{2})$	$(1\bar{1}2)$	$[3\bar{1}2]$	$[3\bar{1}\bar{2}]$

Successive pairs of these are reciprocal to each other.

When the symmetry is lowered in going to the α-uranium lattice, only the first two of these remain a reciprocal pair. The reciprocals of the other four become a distinct new set of twinning modes

equivalent to each other but distinct from the rest. They are now of the second kind. The lowering of the symmetry also introduces another possible (and probable) twinning mode, arising from the loss of symmetry planes, in accordance with "Mallard's law" [2]. There are four planes of reflection symmetry in zinc, one basal and three axial: (001), (100), (130) and $(1\bar{3}0)$ in orthorhombic coordinates. In α-uranium the first two are still symmetry planes, but the second two are planes of pseudo-symmetry which may be expected to function as twinning planes. Their reciprocals are also distinct, and thus able to furnish two more twinning modes. We could anticipate hypothetically 14 twinning modes in α-uranium, of 5 distinct types.

We may tabulate them:

K_1	K_2	η_1	η_2	multiplicity
(011)	$(01\bar{1})$	$[01\bar{1}]$	[011]	2
(112)	*	*	[312]	4
*	(112)	[312]	*	4
(130)	$(1\bar{1}0)$	$[3\bar{1}0]$	[110]	2
(110)	$(1\bar{3}0)$	$[1\bar{1}0]$	[310]	2

Asterisks signify irrational indices.

The modes actually observed in α-uranium correspond only in part to these. They are:

K_1	K_2	η_1	η_2	multiplicity
(112)	"$(1\bar{7}2)$"	"$[3\bar{7}2]$"	[312]	4
"$(1\bar{7}2)$"	(112)	[312]	"$[3\bar{7}2]$"	4
(130)	$(1\bar{1}0)$	$[3\bar{1}0]$	[110]	2
(121)	"$(1\bar{4}1)$"	"$[3\bar{2}1]$"	[311]	4

Symbols shown thus, "[ ]", signify approximations to irrational indices. Thus in fact three of the anticipated five types are found. Two are missing, and another which we did not anticipate is found. This one, (121), occurs only rarely. Having found it, we could anticipate its reciprocal, but this is also missing. The missing types, with habit planes (011) (110) and "(141)" are not necessarily all absent since Cahn found 6 twin traces which could not be accounted for in terms of the four identified types.

The absence of the (011) type is explicable owing to the large shear it would involve, namely

$$b/c - c/b = 0.35$$

compared with the shears of its observed pseudo-equivalents, the (112) and "(172)" types, 0.228. The shear of the (121) mode, 0.329, is also fairly large, and this may sufficiently explain its rarity, and the apparent absence of its reciprocal. On the other hand the (130) mode (with shear 0.299) is fairly common, and the failure to find its reciprocal seems to require another explanation.

Perhaps the most interesting observation we can make is that, of the reciprocal pair with twinning planes (112) and "$(1\bar{7}2)$", it is the latter which predominates, while of the hypothetical pair with twinning planes (110) and (130) it is only the one with higher indices which is observed. It suggests the possibility that boundaries between twins may be relatively immobile when they correspond to close-packed planes in deformation processes as they are known to be in solid recrystallization processes. The case of the (121) twins seems to make an exception, but it is too rare (3 observed examples) to establish a strong statistical case.

It is quite possible that a rule of this kind may apply in metals, without having been noticed before, since few thorough studies of twinning have been made in metals of low symmetry: and, as we have noticed in the case of zinc, the effect of higher symmetry is to group the twinning shears into reciprocal pairs with equivalent rational twinning planes.

The alternative rule suggested by Cahn derives from noticing that the irrational planes of shear S and directions λ common to the two undistorted planes, are closely approximated with simple rational indices. These facts, together with the approximate rationality of the habit planes, actually result simultaneously from the fact that in α-uranium c/a chances to be very close to $\sqrt{3}$. The suggestion is that it is the approximate simple rationality of one or other of these which facilitates twinning. Tabulating S and λ for the observed, and anticipated unobserved, twinning types of α-uranium, we have

Habit planes		S	λ
$\underline{(112)}$,	"$\underline{(1\bar{7}2)}$"	"$(20\bar{3})$"	"$[20\bar{1}]$"
$\underline{(130)}$,	$(1\bar{1}0)$	(001)	[001]
$\underline{(121)}$,	"$(1\bar{4}1)$"	"$(10\bar{3})$"	"$[10\bar{1}]$"
(011),	(011)	(100)	[100]

The underlined examples are those which have been observed. The rule is obeyed by all but scarcely helps to discriminate between the various types, and evidently cannot contribute to distinguishing between the relative facilities of a reciprocal pair of shears. In physical significance, the two alternative rules would appear to focus attention on the nucleation and propagation of twins. Rational, or nearly rational, habit planes, of low index, would commonly give rise to relatively low surface energy at the contact, and so possibly facilitate nucleation. At the same time, by increasing the distance between

successive equivalent locations of the contact plane, displaced parallel to itself, they may hinder the propagation of twinning. It will therefore be interesting to see whether either of these rules can be found to hold in other metals of low symmetry. It will also be interesting to ascertain whether any of the missing anticipated modes of twinning can be established in α-uranium.

Dr. Cahn contributes two comments to the foregoing. First that the (121) twinning mode is not established with complete certainty, and two of the three twin traces which he attributed to (121) twins are actually more accurately compatible with the habit plane (110). The anticipation of "(141)" twinning is of course dependent on the assumed reality of the (121) mode. Secondly, that there is some support for the rule that for a pair of reciprocal shears, the plane of higher index is the preferred habit plane, in the behaviour of tin and bismuth.

References

1. CAHN, R. W. Acta Crystallographica, **4** (1951) 470; Acta Met., **1** (1953) 49; and private communications.
2. FRIEDEL, G. Leçons de cristallographie (Paris, Berger-Levrault, 1926), p. 436.

FREQUENCY OF ANNEALING TWINS IN COPPER CRYSTALS GROWN BY RECRYSTALLIZATION*

W. G. BURGERS, J. C. MEIJS, and T. J. TIEDEMA†

The present paper describes experiments set up to show that the frequency of annealing twins in recrystallized metals depends on the orientation relationship between growing crystal and matrix texture. It is shown in particular that growth of a crystal in a "bent" strip, in which the above-mentioned relationship is altered, may influence the number of its twins. The results obtained can be understood on the assumption that a twin-formation is easiest if a growing crystal encounters a lattice domain in the matrix, which lies closer to its twin-orientation than to its own orientation.

LA FRÉQUENCE DES MACLES DE RECUIT DANS DES CRISTAUX DE CUIVRE PRODUITS PAR RECRISTALLISATION

Cet article décrit des essais établis en vue de montrer que la fréquence des macles de recuit dans des métaux recristallisés dépend de la relation entre l'orientation du cristal en croissance et de la matrice. En particulier, il est montré que la croissance d'un cristal dans un morceau de feuillard plié, c'est-à-dire quand la relation mentionnée ci-dessus est modifiée, peut conduire à une modification du nombre de macles. Les résultats obtenus peuvent être compris, si on admet que la formation des macles est la plus facile, lorsque le cristal en croissance rencontre dans la matrice une région de réseau dont l'orientation se rapproche plus de l'orientation de la macle que de celle du cristal lui-même.

DIE HÄUFIGKEIT DES AUFTRETENS VON REKRISTALLISATIONS-ZWILLINGEN IN KUPFERKRISTALLEN, DIE IM REKRISTALLISATIONSVERFAHREN GEZÜCHTET WURDEN

Die vorliegende Arbeit beschreibt Experimente, die angestellt wurden um zu zeigen, dass die Häufigkeit des Auftretens von Rekristallisations-Zwillingen in rekristallisierten Metallen von der Orientierung des wachsenden Kristalls in Bezug auf die Textur des Gefüges abhängt. Speziell wird gezeigt, dass Wachstum eines Kristalles in einem "gebogenen" Metallband ("bent" strip) in dem die oben erwähnte Beziehung der Kristallorientierungen durch das Biegen geändert wird, auch die Anzahl der Zwillinge ändern kann. Die experimentellen Resultate lassen sich unter der Annahme verstehen, dass die Zwillingsbildung dann am leichtesten von statten geht, wenn der wachsende Kristall auf ein Kristallgitter im Gefüge stösst, das der Zwillingsorientierung näher liegt als der eigenen.

Introduction

Recently considerable thought has been given to the formation of annealing twins in crystals of face-centered cubic metals grown by recrystallization. Various causes for the formation of such twins are suggested of which we mention:

1. The conception of Maddin, Mathewson and Hibbard [1]: annealing twins in face-centered cubic metals may arise from preformed nuclei which can be described as twin faults produced by the first movement of a two-stage slip process.

2. The assumption of Fullman and Fisher [2]: annealing twins form during grain-growth as a result of a decrease in the interfacial free energy of grain boundaries that would not be achieved in the absence of twinning.

3. The growth fault hypothesis of Burke [3]: annealing twins are produced by accidents of growth.

4. The stimulation process proposed by Burgers [4] [5]. In this case the assumption is made that growth of a "stimulated" crystal starts at the moment that an already growing "stimulating" crystal comes into contact with its nucleus, which is supposed to be a lattice region of the original matrix. In connection with the observed precise twin relationship existing between both crystals [6] it was thought possible that, on such encounter, diminution of dislocations at the plane of contact by mutual annihilation of dislocations of opposite sign (opposite sense in the case of screw dislocations) might cause a release of strain energy in the contacted lattice domain, which thus might be transformed into an active nucleus itself.

For the present it is very difficult to decide which one of the four mechanisms mentioned above is correct. It may even be quite possible that more than one mechanism accounts for the formation of annealing twins.

Burgers [7; 8] had already pointed out that, according to the suggestion mentioned under (3) and (4), and perhaps also under (2)— for which Fullman and Fisher [2] ascertained a dependence of twin abundance on texture—one might expect the frequency of twinning to depend upon the orientation relationship between growing crystal and matrix texture. In fact with regard to (2) and (3) it is likely that either the conditions at the grain boundaries which cause twinning or the number of growth faults are influenced by this orientation

*Received September 19, 1952.

†Laboratory for Physical Chemistry, Technical University, Delft, Holland. T. J. Tiedema is Associate worker of the Dutch Foundation for Fundamental Research (F.O.M.-T.N.O.).

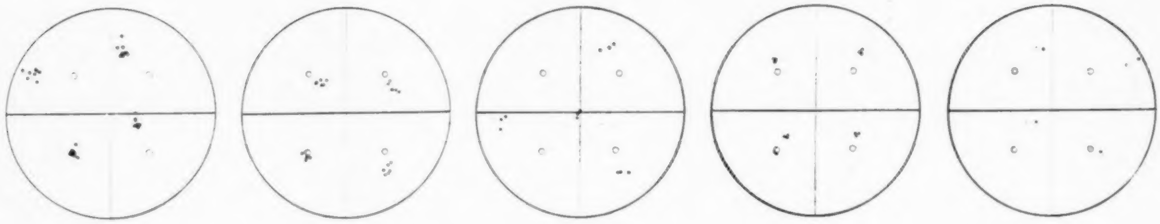

2 4 5 7 9

PLATE II. Stereographic projections of the octahedral poles of copper crystals grown in cubic texture sheet. The octahedral poles of the cubic orientation are indicated by large open circles. Figure 2—Eight crystals having the orientation as mentioned under Figure 1. Figure 4—Six crystals having almost the same orientation as crystal *A* of Figure 3. Figure 5—Three crystals having nearly the same orientation as crystal *B* of Figure 3. Figure 7—Three crystals containing wedge-shaped twins with the same orientation as the crystal of Figure 6. Figure 9—Orientation of the crystal of Figure 8. ● orientation of that part of the crystal showing a few twins. ○ orientation of the part showing numerous twins.

relationship, whereas in the case of (4) the number of lattice regions in such positions that they can be "stimulated" to exact twins by the growing crystal certainly depends on the texture of the matrix.

That twin abundance actually depends on such factors is supported by the occurrence of large differences in twinning frequency between various crystals grown in copper plate by secondary recrystallization [9]; and also by the fact that the abundance of "stimulated crystals" in primarily recrystallized aluminium plates is considerably different for various test-pieces [6]. The purpose of the present investigation was to make a further test of the influence of the orientation relationship between growing crystal and matrix texture: (1) by studying the frequency of twinning in crystals which possess different orientations with respect to the primary texture and (2) by using the method of growing a crystal "round the corner" as applied by Tiedema [10] for the preparation of aluminium crystals with a definite orientation with regard to the surface directions of the test-piece [11]. By this method the orientation relationship between growing crystal and matrix texture is changed during recrystallization by means of a bent in the test-piece. On the basis of the foregoing we may expect that owing to this change in orientation relationship the number of twins will be different at both sides of the bend.

Experimental Procedure

Cold rolled copper sheet of a thickness of 0.2 mm. and a rolling degree of 97 per cent was used in our experiments. From this sheet strips are cut with a length of about 15 cm. and a width of 1 cm. (longitudinal direction of strip coincides with rolling direction of sheet). The strips are annealed by passing them through a furnace at a rate of 3 cm/min. at a temperature of 850°C.* This produces a material with a fairly sharp cubic texture (spreading about 10°).

This material is converted into single crystals either by passing the strips immediately through the same furnace at a rate of 3 cm/hr. at a temperature of 930°C or by stretching the strips plastically by 2 per cent and then passing them through the furnace at the same rate and temperature.

To change the orientation relationship between growing crystal and primary texture during recrystallization, part of the strip is bent with a radius of 5 cm. over a certain angle before the second annealing is applied.

Results

A large number of crystals were investigated. They show many appearances of annealing twins and it is for the moment not possible to correlate all results. The following facts are, however, definitely established:

(*a*) If a crystal shows twins, in by far the most cases observed the twin plane is that (111)-plane of the growing crystal which is most nearly parallel to a (111)-plane of the cubic texture (if not, then a (111)-plane is chosen which is more perpendicular to the surface of the foil†).

(*b*) Crystals with an orientation which can be derived from the cubic texture by approximately a [111]-rotation over 30° contain many twins. An example is given in Figure 1 (natural size); Figure 2 shows in stereographic projection the positions of eight crystals having this orientation.

(*c*) Crystals with an orientation which can be derived from the cubic texture by approximately a [111]-rotation over not more than about 15° show none or only a few twins. This is demonstrated by

*All annealings are carried out in an atmosphere of dry nitrogen.

†This is also frequently observed in large crystals grown by secondary recrystallization in nickel-iron foil with cubic texture (Burgers, Hdb.d.Metallphysik (1941), III 2, pp. 378, 383; Custers and Rathenau, Philips Res. Rep. **4** (1949) 241).

FIGURE 1

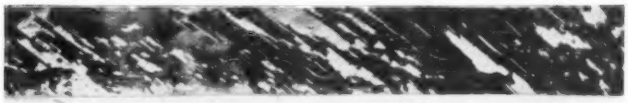

FIGURE 3

FIGURE 6

FIGURE 8

FIGURE 10

PLATE I. Recrystallized copper crystals containing twins. All crystals about natural size. FIGURE 1—Crystal with an orientation which can be derived approximately from the cubic texture by a [111]-rotation over 30°. FIGURE 3—Crystal *A* has an orientation which can be derived approximately from the cubic texture by a [111]-rotation over 15° and shows no twins at all. Crystal *B* is a twin of crystal *A* and has a (111)-plane almost parallel to the surface of the foil. This crystal shows many twins. FIGURE 6—Crystal containing wedge-shaped twins. FIGURE 8—Bent crystal with a different number of twins at both sides of the bend which is at the right-hand side of the crystal. FIGURE 10—Boundary between two partners of a wedge-shaped twin. Magnification 300×.

crystal A of Figure 3. Figure 4 again gives a stereographic projection of the orientations of six such crystals.

(*d*) Many twins are observed in crystals with a (111)-plane nearly parallel to the surface of the foil. These special crystals differ naturally largely in orientation from the cubic texture, but appear to be twins to the crystals mentioned under (*c*). Crystal B of Figure 3 is an example. The orientation relationship between three such crystals and the primary matrix is given by Figure 5.

(*e*) Whereas most twins have straight parallel-sided boundaries, "wedge-shaped" twins occur in a few crystals, and these crystals have all nearly the same orientation. Figure 6 shows an image of a crystal containing these wedge-shaped twins; Figure 7 gives a stereographic projection of their orientations.

(*f*) In using the method of growing a definite crystal "round the corner" it is observed in several cases that the frequency of twinning is different "before" and "after" the bend. This is demonstrated by Figures 8 and 9. Figure 8 gives an image of such a crystal, the bent region being seen at the right. Figure 9 shows the orientation relationship between the crystal and the cubic texture before and after the bend. The dependence is apparently such that there are more twins in that part of the crystal for which a (111)-plane is more nearly parallel to a (111)-plane of the cubic texture.

If, however, the original crystal does not possess a (111)-pole close to a (111)-pole of the cubic texture, the frequency of twinning does not differ very much at both sides of the bend. In this case it is practically impossible to decide whether the orientation of the crystal has become more favourable for twinning or not. For this reason these crystals have been left out of consideration.

Discussion

A possible explanation of the observed phenomena might be the following. Starting from the statement by Bowles and Boas [12] (see also Cook and Richards [13] and Burke [3])that growth takes place most rapidly on the (111)-planes of the growing crystal and especially on that (111)-plane which differs only by a rotation about its normal from that in the primary texture, it is understandable that twins are usually formed on this (111)-plane. This is true at least for the crystals mentioned under (*b*) and (*c*). With this in view, the following mechanism may account for the formation of twins during recrystallization. During their growth, crystals as mentioned under (*b*) and (*c*) meet numerous lattice regions which possess a (111)-plane (nearly) parallel to a (111)-plane of the growing crystal. Depending on the scatter of the primary texture such lattice regions may lie closer to the twin orientation than to the orientation of the growing crystal. We assume that under these conditions it is easier for the crystal to assimilate this lattice domain in twin orientation, and, on continued growth of crystal and domain, to start a twin.*

We shall now consider the experimental results presented in the foregoing section under (*b*)-(*f*) from this point of view.

In the case of the 30°-[111]-rotated crystals (case *b*) a twin of such a crystal would have a symmetrical orientation with regard to the cubic texture, as it can be derived from the mother crystal by a 60°-[111]-rotation. Consequently only a weak scatter of the cubic texture over about 5° in a direction "opposite" to that of the growing crystal is needed to fulfil the above-mentioned condition necessary for twinning. As a result twinning will occur frequently and so these crystals consist for practically half their volume of rather small twins (see Figure 1).

Reasoning along the same lines, the 15°-[111]-rotated crystals (case *c*) need an "opposite" scatter in the primary texture of at least 20° about [111] for the formation of twins. As lattice parts deviating so much from the cubic texture will be rather rare and, if present, may deviate in any direction—so that as a rule that (111)-plane of the growing crystal, which is (nearly)parallel to the cubic texture, will *not* be parallel to one of the (111)-planes of this deviating lattice block—none or only a few twins can occur in these crystals (Figure 3A). The possibility must be kept in mind, however, that another (111)-plane of the growing crystal is parallel to a (111)-plane of the deviating lattice region so that twinning can occur on this plane. Indeed it is observed that the 15°-[111]-rotated crystals sometimes twin on a (111)-plane which deviates about 15° from the cubic texture.

We now proceed to the crystals mentioned under (*d*), which have a (111)-plane nearly parallel to the surface of the foil. As stated there, the orientation of these crystals is such that at least one of their twin-orientations lies relatively close (within about 15 to 20°) to the cube-texture. Thus such crystals, during their growth, will meet numerous lattice

*An analogous view is brought forward by Barrett (Trans. A.I.M.E. **188** (1950), 123), from which we quote: "Evidence is increasing that annealing twins can originate when a growing grain encounters material in twin or near-twin relationship to the orientation of the growing grain."

blocks which have an orientation "closer" to their twins than to themselves, and which therefore can be assimilated as twins. Consequently they must contain many twins, as is demonstrated by Figure 3B.

The crystals with wedge-shaped twins mentioned under (*e*) (Figures 6 and 7) appeared to have such orientations that all four (111)-planes deviate approximately an equal amount from the (111)-planes of the cubic texture. As a result all four (111)-planes are equally favourable for growth. Microscopic examination of the boundary between both partners of such a twin reveals that it consists of small "steps" which are bounded by (111)-planes of the mother crystal, which started its growth first (see Figure 10). This supports the idea that the crystals grow on (111)-planes and this special type of growth may account for the shape of the twins. Perhaps in this case the twins can grow sideways according to the mechanism discussed by Ratheneau and Baas [14]. It is, however, a fact that the shape of the twins must be directly connected with the texture. This is also confirmed by observations on aluminium where in a quasi-isotropic material the twins do not show parallel boundaries in contrast with a material with a pronounced texture in which straight parallel-sided twin lamellae can occur [15].

Finally, coming to point (*f*), from the foregoing it is directly understandable that in the bent strip shown in Figure 8 many twins occur in that part of the crystal for which a (111)-plane is more parallel to a (111)-plane of the texture as the orientation of this part (∘ in Figure 9) is the same as that of the crystals of group (*b*).

Conclusions

The experimental results and in particular the result mentioned under (*f*) confirm once more that twinning in recrystallized materials is not a property of the metal as such, but connected with the texture in which the crystals grow.

On the basis of our experiments it is impossible to discriminate between growth fault and stimulation. The experiment proposed by Burke [16] gives no information about whether growth faults or stimulation give rise to twinning, as it has been found that the direction of the (111)-plane in the point-shaped crystals observed in aluminium is not reproducible in any way [6]. Perhaps the experiments described in this paper reduce both possibilities to the same original cause.

We agree with Burke's [3] conclusion that the mechanical nucleation theory is not able to explain the formation of all kinds of annealing twins found in copper crystals obtained by recrystallization.

Acknowledgement

One of the authors (J.C.M.) wishes to thank the Delfts Hogeschoolfonds for financial support, which enabled him to take part in the above research.

References

1. Maddin, R., Mathewson, C. H., and Hibbard, W. R. Trans. A.I.M.E., **185** (1949) 655.
2. Fullman, R. L. and Fisher, J. C. J. Appl. Phys., **22** (1951) 1350.
3. Burke, J. E. Trans. A.I.M.E., **188** (1950) 1324.
4. Burgers, W. G. Proc. Kon. Ned. Akad. Wet., **50** (1947) 858.
5. Burgers, W. G. Physica, **15** (1949) 92.
6. May, W. Thesis, Delft, 1950.
7. Burgers, W. G. J. Metals, **3** (1951) 1069.
8. Burgers, W. G. Neuvième Conseil Solvay de Physique, L'Etat Solide (Bruxelles, 1952), p. 73.
9. Kronberg, M. L. and Wilson, F. H. Trans. A.I.M.E., **185** (1949) 501.
10. Tiedema, T. J. Acta Cryst., **2** (1949) 261.
11. Dunn, C. G. Metals Trans., **187** (1949) 72.
12. Bowles, J. S. and Boas, W. J. Inst. Metals, **74** (1948) 501.
13. Cook, M. and Richards, T. Ll. J. Inst. Metals, **66** (1940) 1.
14. Rathenau, G. W. and Baas, G. Physica, **17** (1951) 117.
15. Burgers, W. G., and Dalitz, V. Ch. Proc. Kon. Ned. Akad. Wet., **52** (1949) 623.
16. Burke, J. E. J. Metals., **3** (1951) 1068.

ÉTUDE DE LA TENSION CAPILLAIRE D'UN JOINT DANS UN MÉTAL, EN FONCTION DE L'ORIENTATION DES GRAINS QU'IL SÉPARE*

J. FRIEDEL, B. D. CULLITY et C. CRUSSARD†

La tension interfaciale entre deux grains est mesurée, en valeur relative, dans une plaquette d'aluminium, par la méthode classique des points triples. Nous étudions sa variation en fonction de l'orientation du joint par rapport aux deux cristaux qu'il sépare et obtenons les résultats suivants: Un joint entre deux grains d'orientation quelconque (joint « banal ») a une tension à peu près constante; un joint entre deux grains dont les réseaux admettent un plan de symétrie possède une tension plus faible; celle-ci diminue encore quand le joint se trouve dans le plan de symétrie et s'annule pratiquement quand les grains sont parallèles ou en macle spinelle. Dans une deuxième partie, nous proposons un nouveau mode de calcul de l'énergie superficielle et de l'énergie interfaciale. Dans ce calcul, assez approximatif, on suppose que les deux cristaux, complètement rigides, établissent des liaisons interatomiques à travers le joint. Par une hypothèse simple, on passe de l'énergie interfaciale à l'énergie libre, c'est-à-dire la tension capillaire. Les calculs ont été faits pour l'aluminium, le cuivre, le fer γ et le fer α; pour l'aluminium, les résultats sont en bon accord, en valeur relative, avec les résultats expérimentaux de la première partie.

STUDY OF THE SURFACE TENSION OF A GRAINBOUNDARY IN A METAL AS A FUNCTION OF THE ORIENTATION OF THE TWO GRAINS WHICH THE BOUNDARY SEPARATES

The interfacial tension between two grains of an aluminum disk is measured in relative values by the classical method of the three way corner. We have studied the variation of the interfacial tension as a function of the orientation of the grainboundary with respect to the two neighbouring crystals and we obtained the following results: a grainboundary between two crystals of any orientation whatsoever has a nearly constant interfacial tension. A boundary between two grains whose crystal lattices have a common plane of symmetry has a lower interfacial tension, which decreases still further if the plane of the boundary is the plane of symmetry and which practically disappears when the grains are parallel or in spinelle twin orientation.

In a second part we suggest a new method of calculating the interfacial energy. In this rather approximative calculation it is supposed that the two completely rigid crystals establish interatomic relations across the grainboundary. By a simple hypothesis one goes from the interfacial energy to the free energy, that is the surface tension. Calculations were carried out for aluminum, copper, α-iron and γ-iron. The results for Al are in good agreement with the relative values obtained in the experiments of Part I.

UNTERSUCHUNG DER OBERFLAECHENSPANNUNG EINER KORNGRENZE IN EINEM METALL ALS FUNKTION DER KRISTALLOGRAPHISCHEN ORIENTIERUNG DER NACHBARKRISTALLE

Die relativen Werte der Grenzflächenspannung zwischen zwei Kristalliten in einem Aluminiumplättchen wurden nach der klassischen Methode des Dreiwinkelpunktes gemessen. Wir untersuchten die Variation der Grenzflächenspannung als Funktion der Orientierung der Korngrenze bezogen auf die beiden Nachbarkristallite und erhielten die folgenden Resultate: Eine Korngrenze zwischen zwei Kristalliten beliebiger Orientierung hat eine fast konstante Grenzflächenspannung. Eine Korngrenze zwischen zwei Kristalliten, deren Kristallgitter eine gemeinsame Symmetrie-Ebene besitzen, hat eine geringere Grenzflächenspannung. Diese verringert sich noch weiter, wenn die Korngrenze selbst die Symmetrie-Ebene ist und ist praktisch gleich null, wenn die Kristallite parallel oder Spinellzwillinge sind. Im zweiten Teil wird eine neue Rechenmethode zur Ermittlung der Oberflächen- und Grenzflächenenergie vorgeschlagen. In der—angenäherten—Berechnung wird angenommen, dass die beiden völlig starren Kristallite über die Korngrenze hinweg auf einander interatomar einwirken. Mit Hilfe einer einfachen Hypothese kam man von der Grenzflächenergie zur freien Energie, d.h. zur Oberflächenspannung. Berechnungen wurden für Aluminium, Kupfer, α-Eisen und γ-Eisen durchgeführt. Die Resultate für Aluminium stimmen gut mit den—als relative Werte anfallenden—experimentellen Resultaten überein, die im Teil I beschrieben sind.

I. INTRODUCTION

La tension capillaire des joints intergranulaires des métaux a fait l'objet récemment de nombreuses études, tant expérimentales que théoriques. Nous ne nous proposons pas ici de discuter l'ensemble de la question, ni de citer tous ces travaux, mais seulement de présenter quelques études expérimentales qui complètent nos connaissances sur ce sujet, ainsi qu'un mode ce calcul nouveau.

Lorsqu'un métal subit un recuit prolongé à haute température, on observe une *croissance des grains*; dont la principale cause semble être la tension capillaire des joints — ou tension interfaciale [1]; cette tension détermine aussi la forme que prennent les grains. Dans l'espace, le facteur qui gouverne la croissance des grains est le déplacement des points quadruples, rencontre de quatre interfaces séparant quatre grains [2]. Dans le cas de tôles minces, ce facteur se simplifie, car nous verrons que les joints deviennent sensiblement normaux au plan de la tôle (sauf quelques exceptions significatives, que nous analyserons); dans ces conditions, on est ramené à

*Reçu 9 juillet 1952.

†Centre de recherches métallurgiques, l'École nationale supérieure des mines, Paris.

un problème plan, et le facteur essentiel est le déplacement des points triples communs à 3 grains.

Si le recuit est assez poussé pour qu'on puisse atteindre un équilibre, on admet en général que les angles aux points triples (dans l'espace angles dièdres à une arête triple commune à trois grains A, B, et C, soit θ_A, θ_B, θ_C) permettent de déterminer *en valeur relative* les tensions interfaciales par l'équation d'équilibre simple

$$\frac{\gamma_{BC}}{\sin\theta_A} = \frac{\gamma_{CA}}{\sin\theta_B} = \frac{\gamma_{AB}}{\sin\theta_C}. \tag{1}$$

On a critiqué l'emploi de cette formule dans le cas où la tension interfaciale dépend de l'orientation du joint par rapport au couple de grains qu'il sépare. Herring a proposé une formule plus complète (citée par C. S. Smith [3]) obtenue en cherchant le minimum de l'énergie interfaciale totale lorsque certaines liaisons sont respectées. Cette formule s'applique très bien dans certains cas, par exemple dans les expériences de Dunn [4] dans lesquelles les 3 joints sont assujettis à passer chacun par un point fixe.

Mais dans le cas de la croissance générale des grains, l'emploi de la formule de Herring ne semble pas justifié; et voici pourquoi : le véritable minimum de l'énergie correspondrait au cas où un cristal envahirait toute la masse; mais ce sont des considérations cinétiques de croissance qui expliquent que l'on atteigne un *équilibre apparent* (métastable) lorsque les grains sont tous à peu près hexagonaux (cas des tôles minces). Cet état ne correspond pas à un minimum de l'énergie interfaciale totale par rapport à un déplacement arbitraire des points triples. Pour définir cet état comme minimum, il faut s'imposer des liaisons, c'est-à-dire se fixer une loi de déplacement des joints et points triples. C'est dans l'observation seulement que l'on peut trouver la loi qui intervient en fait. Or voici ce que l'on observe, comme nous le montrerons plus loin : au début du recuit, les points triples tendent rapidement vers une configuration d'équilibre local, et les joints se courbent; dans cette phase, l'application de la formule de Herring serait à peu près justifiée encore qu'il faudrait tenir compte des variations de courbure des joints. Mais quand on pousse le recuit, on voit que les joints tendent à devenir droits, c'est-à-dire tendent à leur tour vers une forme d'équilibre (à part certaines exceptions). Vers la fin du recuit, les joints se déplacent à peu près parallèlement à eux-mêmes, en changeant peu d'orientation. Dans ces conditions, si on admet que l'énergie est à peu près stationnaire, on voit aisément que c'est la formule (1) qui s'applique aux points triples.

Nos principaux résultats expérimentaux reposent sur une mesure de l'orientation relative de couples de grains séparés par un joint, sur une observation de la position du joint de chaque couple, et accessoirement de leur forme, et enfin sur une mesure des angles aux points triples.

Du point de vue théorique, les opinions oscillent entre deux conceptions : celle qui consiste à décrire un joint (dans un métal *pur*) comme un réseau de dislocations [5; 6; 7; 8]. D'autres au contraire considèrent un joint comme une surface formée de zônes où les réseaux des deux joints se raccordent, avec distorsion, séparées par des zônes lacunaires [9; 10]. Il semble à l'heure actuelle que l'on s'accorde [3] pour admettre que lorsque la désorientation* entre les réseaux est faible, le premier modèle, par dislocations, décrive bien l'état des choses; pour les fortes désorientations, le modèle lacunaire est préférable. Entre les deux existerait un domaine de transition où l'un et l'autre mode de description sont à peu près équivalents; cette zône se placerait vers des désorientations de l'ordre de 5 à 10°, pour des métaux à structure compacte, mais sans doute moins pour d'autres métaux, comme l'étain [11].

Du point de vue quantitatif, la première conception a donné lieu à divers calculs qui permettent d'évaluer l'*énergie* interfaciale [7; 8]. La seconde conception n'a pas encore été développée quantitativement; c'est ce que nous essayons de faire dans la deuxième partie de cette note. La théorie que nous développerons sur ce point est sujette à des limitations, que nous signalerons en temps utile; malgré cela, elle semble, en assez bon accord avec l'expérience.

Lorsque l'on veut confronter la théorie et l'expérience, il faut bien remarquer que celle-ci mesure l'*énergie libre* interfaciale, alors que celle-là donne simplement l'énergie. Pour passer de là à l'énergie libre, il faut faire intervenir l'entropie interfaciale, qui se compose de deux termes : une entropie de position (des défauts, dislocations ou lacunes, composant le joint) et un accroissement d'entropie de vibration des atomes du joint due à l'accroissement de leurs degrés liberté†. Ces termes d'entropie sont difficiles à évaluer dans le calcul basé sur les dislocations, plus faciles dans le calcul que nous proposons dans la suite. Mais la remarque suivante permet une évaluation approchée de l'énergie libre

*Nous appelons désorientation entre deux réseaux la plus petite rotation pouvant amener les réseaux en coïncidence.

†Ces termes d'entropie sont en relation avec l'accroissement de la vitesse d'autodiffusion du métal le long du joint [12] lui-même en relation avec la viscosité des joints.

Il serait plus rigoureux, mais plus compliqué de faire intervenir un système d'ondes « capillaires » supplémentaires, comme le fait L. Brillouin pour les surfaces libres.

interfaciale : certains auteurs [9; 12] ont montré qu'on pouvait assimiler les couches atomiques formant le joint à un liquide en surfusion*. On peut donc, en première approximation, admettre que l'énergie libre de la couche de passage constituant le joint devient égale à celle du reste de métal au point de fusion (point vérifié récemment par Huzuki); autrement dit l'énergie libre interfaciale, ou tension capillaire des joints, s'annule au point de fusion. Comme, dans ce raisonnement, nous avons négligé la tension capillaire à l'interface solide-liquide, du reste faible, au point de fusion l'annulation n'est pas complète. Cette propriété distingue la tension interfaciale de la tension superficielle qui, elle, suit la loi d'Eötvos et s'annule à une température beaucoup plus élevée, voisine de la température critique [13].

II. RÉSULTATS EXPÉRIMENTAUX

A. Matériel et mesures

Nous avons utilisé une tôle de 210 × 120 × 1 mm. d'Al raffiné (0,0025 Fe; 0,0025 Si; 0,004 Cu) et fortement laminé (88%) à partir d'une ébauche présentant une texture cubique généralisée. La tôle a été chauffée 1 H. à 310° au four à air. Une éprouvette de 60 × 20 × 1 mm. y est découpée, et recuite à 640°C au four à résistance, successivement pendant 1, puis 8 et enfin 7 jours. Les états correspondants sont notés 0, I, II, et III. Entre deux recuits, on attaque légèrement à l'acide pour voir le grain, puis l'on polit électrolytiquement pour éviter les dépressions superficielles dues à l'attaque des joints qui risqueraient d'entraver le déplacement de ceux-ci. L'épaisseur finale est 0,8 mm.

La direction des *joints* sur les deux faces de la tôle a été déterminée au microscope (grossissement 1000). La précision de la lecture est de l'ordre de 1° sur les parties rectilignes de joint, un peu moins bonne aux points triples dans beaucoup de cas (< 3°) par suite de la courbure. Sauf quelques exceptions, le joint a pu être considéré comme normal au plan de laminage, à la précision des mesures près (< 5°)†. Sur l'angle dièdre, l'erreur qui en résulte est négligeable.

L'orientation des *grains* a été déterminée par clichés Laue en retour, avec un diaphragme fin qui nécessite des poses de deux heures. La précision des mesures est alors uniquement limitée par un certain jeu dans le support; elle peut être évaluée à 2°. On a étudié ainsi 26 grains dans l'état I et 47 grains dans l'état II. Cette méthode est assez laborieuse et nous l'avons remplacée, pour l'étude des relations entre la direction des joints et l'orientation des grains, par une méthode un peu moins précise mais beaucoup plus rapide, utilisant les figures d'attaque. Après polissage et courte attaque (20 à 40 sec.) dans l'eau régale fluorée refroidie à − 15°, on observe en général de petits losanges. Deux côtés, très rectilignes si l'attaque est brève, sont nets et parallèles aux traces de deux directions (100), les deux autres délimitent une sorte d'escalier dont les marches très nettes sous un éclairage convenable, sont parallèles à la troisième trace (100). On a souvent des figures en pentagones. Pour restituer l'orientation du cube à partir de ses trois traces, sur le plan de laminage, nous utilisons un diagramme donnant, en projection stéréographique, le lieu de l'arête du dièdre droit dont les traces sur le plan de laminge font un angle 2α donné. Un calcul simple montre que ce sont des quartiques bicirculaires d'équation polaire (ρ, ϕ) :

$$\rho^2 - 2\frac{\cos 2\phi}{\cos 2\alpha}\rho^2 + 1 = 0. \tag{2}$$

Nous avons tracé l'abaque correspondant, pour des valeurs de α échelonnées de 5° en 5°. En projection stéréographique, chaque arête [100] de la figure de corrosion se trouve à l'intersection du lieu correspondant à l'un des angles α mesuré entre deux côtés de la figure avec la perpendiculaire menée par l'origine au troisième côté. La précision totale des lectures est d'environ 3°. Nous avons vérifié la méthode sur des grains orientés aux rayons X. Ce procédé permet d'orienter facilement en une journée une cinquantaine de grains. Avec un grossissement 1000, nous avons étudié sans difficulté une tôle de grain moyen $\simeq$ 0,02 mm., où le procédé par les rayons X est inapplicable.

B. Résultats Généraux

Les recuits à 640° donnent, dès l'état I, un grain qui traverse l'épaisseur de l'éprouvette et un diamètre voisin du diamètre définitif (1,4 mm., soit près du double de l'épaisseur). L'*équilibre* des points triples est à peu près réalisé, les joints arrivant normalement à la surface extérieure et les joints entre trois grains contigus se rencontrant à environ 120° les uns des autres. Les joints sont cependant assez contournés et ne prennent une courbure régulière que dans l'état II. L'aspect dans l'état III est identique à l'état II. Seuls se sont déplacés

*Un liquide en surfusion peut être en équilibre avec le solide correspondant, à condition de se trouver dans un état de pression négative, qui en abaisse le potentiel thermodynamique (ici, il faut prendre l'énergie utilisable ou potentiel de Gibbs, $U - TS + PV$). L'origine possible d'une telle « traction complète » a été suggérée par C. S. Smith [3].

†La direction des joints dans l'épaisseur de la tôle a été mesurée en photographiant les deux faces de la tôle rigoureusement avec le même agrandissement, et en superposant les clichés obtenus, les bords de la tôle étant découpés bien droits.

trois points triples qui, on peut le montrer, étaient hors d'équilibre. Un gros grain apparait dans l'état II; il absorbe environ la moitié de l'éprouvette et englobe un petit cristal insulaire d'orientation à peu près parallèle, ce qui est conforme aux observations de Lacombe [14].

L'étude des orientations cristallines aux rayons X et par la micrographie met nettement en évidence l'existence de deux *textures* :

— une texture cubique, d'importance décroissante au cours du recuit;

— une texture « Z » analogue à l'orientation observée par Rathenau sur les ferronickels [15], par Kronberg et Wilson sur le cuivre [16] et Beck sur l'aluminium [17], et qui s'obtient à partir de la texture cubique par rotation d'environ 40° autour d'un axe [111]. Dans cette texture, les pôles [100], ramenés au même quadrant par les symétries du laminage (plans normaux au plan de laminage et parallèles respectivement à la direction du laminage et à la direction transverse), se répartissent sur un arc qui part de la texture cubique et tourne autour d'un axe [111]. La position terminale la plus fréquente, est voisine de la macle (321) par rapport à la texture cubique (fig. 1).

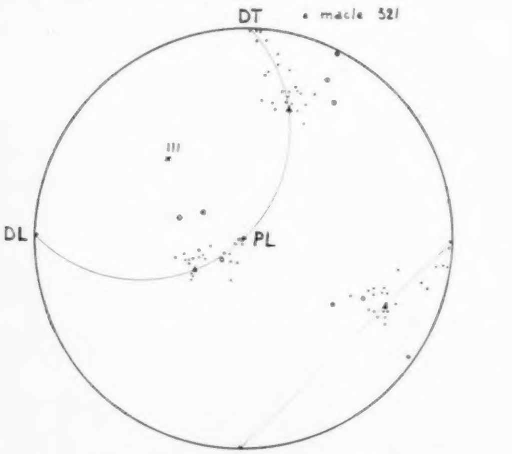

FIGURE 1. Texture de recristallisation. Dans la projection stéréographique des pôles (100), PL est la normale au plan de laminage; DL la direction du laminage; et DT la direction transverse. On a marqué la zône des pôles déduits de la texture cubique par rotation autour d'un axe (111), et les pôles de la macle (321) (triangles). Trois cristaux nettement en dehors de la texture générale sont marqués par des points plus gros.

L'existence de ces textures explique que beaucoup de cristaux, *même non jointifs*, sont approximativement parallèles : sur 325 couples examinés dans l'état I, 28, soit 8%, ont entre eux une désorientation inférieure à 8°. Une répartition au hasard des orientations cristallines donnerait une proportion de 0,4% (Tableau I).

TABLEAU I

Limite supérieure de la probabilité pour que deux cristaux cubiques pris au hasard soient maclés (*hkl*) à $\omega°$ près. ω est l'angle de la rotation minima qu'il faut imprimer à l'un des cristaux pour faire coïncider les plans de macle (*hkl*) des deux cristaux.

plan de macle	ω		
hkl	$\leqslant 2°$	$\leqslant 4°$	$\leqslant 8°$
100	0,007%	0,053%	0,43%
111	0,005	0,036	0,29
hhl ou *hkk*	< 0,014	< 0,11	< 0,88
h k 0	0,027	0,22	1,8
h k l	0,027	0,22	1,8

TABLEAU II

Fréquence des couples de cristaux maclés (*h,k,l*) à $\omega°$ près (dans état I, recuit 1 j. à 650°).

plan de macle	ω					
	couples quelconques			cristaux voisins		
hkl	$\leqslant 2°$	$\leqslant 4°$	$\leqslant 8°$	$\leqslant 2°$	$\leqslant 4°$	$\leqslant 8°$
111	0,3%	1,2%	2,4%	0%	0%	6%
221	0,3			0	0	0
441	0,3			0	0	0
321	0,9	2,2		0	4	8
632	0,9			0	0	0

Beaucoup de cristaux jointifs présentent entre eux un plan de symétrie d'ordre élevé : 30% à 4° près (fig. 2)*. Ce fait, noté pour la recristallisation du fer par Homes et Maquestiau, est dû à la symétrie élevée du système cubique. Il ne saurait s'expliquer par une influence réciproque entre grains voisins. En effet parmi les grains présentant entre eux un plan de symétrie approché *simple* (100) ou (110) — c'est-à-dire grains quasi parallèles, (321), (631), la fréquence des relations de macle entre grains *non* voisins, qui dépasse largement celle due au hasard, dépasse aussi celle des grains jointifs (Tableau II).

*Deux réseaux quelconques peuvent être amenés en coïncidence par rotation autour d'axes commun à ces deux réseaux; dans le cas général, il y a 24 axes de rotation pour des cristaux cubiques. L'existence d'un (ou plusieurs) plans de symétrie pour les deux réseaux est un cas particulier [18]. Le plus simple dans ce cas, pour décrire l'orientation relative des deux cristaux, est de les considérer comme *macles* par rapport au plan de symétrie. La macle envisagée ici est une macle par *mériédrie réticulaire*, au sens que les cristallographes donnent à ce nom (si la symétrie est approchée, c'est une *pseudo-mériédrie*). Ce cas étant très fréquent dans les métaux recristallisés, la description des orientations relatives par macle est très commode; c'est elle que nous utiliserons ici.

Cette fréquence est donc due à l'existence même des textures, et au fait que les mécanismes de recristallisation et croissance favorisent des orientations en relation de macle.

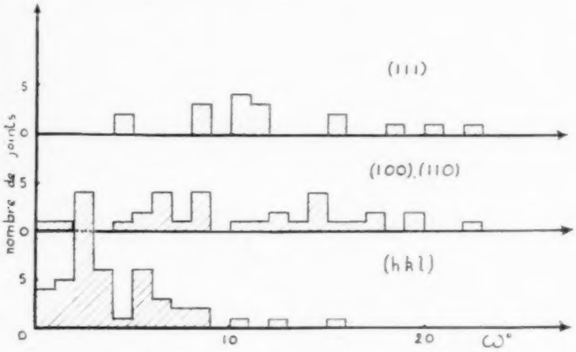

FIGURE 2. Répartition des joints correspondant à une macle à ω près (ω = désorientation ou approximation de la macle), pour la macle spinelle (111), le parallélisme (100, 110) et les autres macles (321, 631, etc.).

C. Joints

Nous avons cherché s'il y avait une relation entre la position du joint et l'orientation du grain. Admettant qu'une position observée fréquemment après recuit prolongé, correspond à un minimum de la tension capillaire de joint, on peut en déduire des renseignements qualitatifs sur cette grandeur.

Les mesures portent, dans l'état III, sur des parties importantes de joint, rectilignes ou quasirectilignes. Nous avons étudié les couples de grains en macle approchée (plan de macle (*hkl*)) en fonction de l'approximation de la macle, ω ($\omega/2$ est l'angle dont il faut faire tourner chaque cristal pour que leurs plans de macle (*hkl*) coïncident). Nous nous sommes limités à $\omega < 20°$. A ce degré d'approximation, presque tous les couples de grains sont des macles approchées; mais cette méthode permet de grouper ces couples en familles; en effet, la présence des textures donne une forte proportion de grains à peu près parallèles ou en macle simple, ce qui permet une étude statistique.

D'une façon générale, il existe une tendance pour le joint à se placer dans le plan de symétrie, comme le prouve les figures 3, 4 et 6 qui donne la densité de répartition des joints en fonction de leur écart en position avec le plan de symétrie. Mais on peut raffiner cette étude en faisant intervenir la nature du plan de symétrie, et la valeur de (*hkl*).

1. *Grains quasi-parallèles* (fig. 3)

(*a*) Pour les très faibles désorientations ($\omega < 5$ à $7°$) la position du joint (donnée par l'angle α qu'il fait avec le plan de macle, ici (100) ou (110) à volonté) semble assez quelconque*.

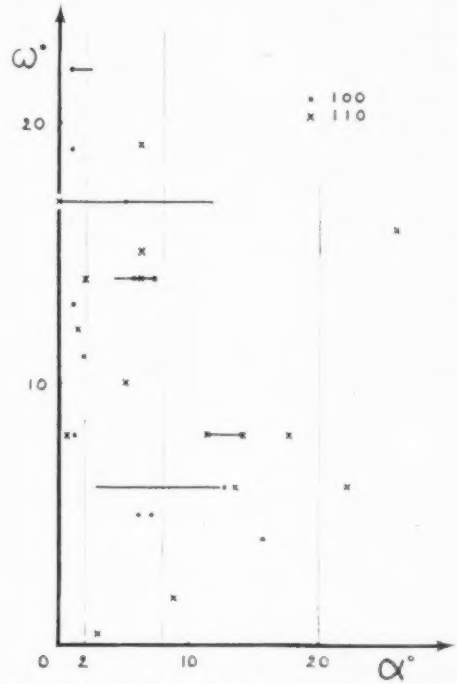

FIGURE 3. Angle α du joint avec le plan de symétrie voisin de (100) ou (110) pour deux grains à peu près parallèles possédant une désorientation ω. Les traits continus correspondant à des joints courbes.

(*b*) Pour des désorientations plus fortes ($7 < \omega < 20°$), le joint est souvent parallèle aux plans (100) ou (110). Ces deux plans apparaissent avec la même fréquence. C'est presque toujours, parmi les solutions possibles, le plan le plus voisin de la normale à la tôle qui est occupé, les exceptions concernant les petites portions de joints joignant deux points triples voisins (faible énergie totale mise en jeu). Parfois deux moitiés du joint occupent des positions voisines (100) et (110), formant ainsi un angle voisin de 45° (6 exemples).

Le joint présente donc un minimum net d'énergie quand il est en (100) ou (110) indifféremment, pour des grains de désorientation $7 < \omega < 20°$. Le gain d'énergie est alors suffisant pour l'amener, si besoin est, à faire des coudes. Pour $\omega < 7°$, la position du joint est indifférente; nous verrons que l'énergie semble être alors faible dans tous les cas.

2. *Grains en macle spinelle approchée* (fig. 4)

Les mêmes phénomènes s'observent, un peu moins marqués. Le joint présente un minimum d'énergie en (111) pour $7 < \omega < 20°$; ce minimum est

*Dans les cristaux polygonisés, deux sous-grains voisins sont presque parallèles et sont effectivement séparés par une sorte de joint souvent contourné et différent du plan de symétrie des 2 réseaux. Ces résultats ne semblent pas en accord avec les conséquences du modèle « dislocations ».

plus ouvert que dans le cas précédent, ce qui correspond à un maximum moins aigu sur la courbe des fréquences (fig. 5). Notons que, quand deux grains sont en macle spinelle, il y a deux plans de symétrie possible : (111) et (211). Dans ce cas, nous n'avons noté *qu'une seule fois* un joint voisin de (112). Ceci s'explique si l'énergie d'un joint de symétrie (112) est supérieure à celle d'un

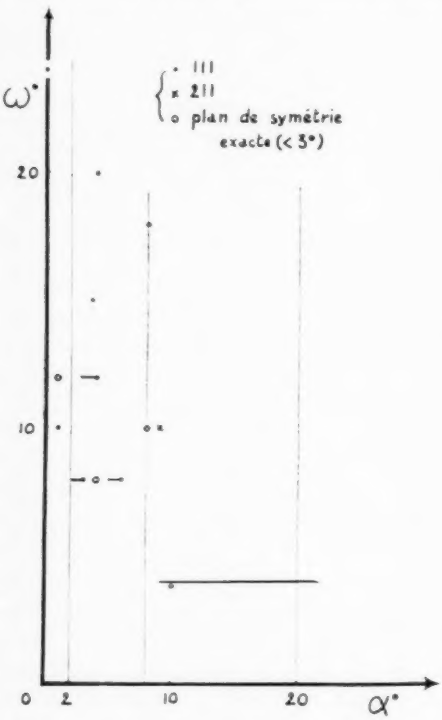

Figure 4. Angle α du joint avec le plan de symétrie voisin de (111) ou (211) pour deux grains à peu près en macle spinelle, avec une désorientation ω. Un seul joint est près d'un plan (211). Une symétrie exacte importe peu.

joint voisin de (111) même pour une désorientation notable. Les mesures sur les points triples (section D) confirment ce résultat*.

3. *Autres couples de grains symétriques* (fig. 6)

La corrélation entre le joint et le plan de symétrie est moins forte encore. Elle est plus nette pour les faibles désorientations ($3 < \omega < 8$).

4. Enfin les joints « banaux » ont une direction quelconque par rapport aux grains et sont normaux au plan de la tôle.

D. Points Triples (Etat III)

La mesure des angles que font entre eux les trois joints permet de calculer leurs tensions en valeurs relatives [1] et de préciser certaines « attirances » que les résultats précédents suggèrent.

(*a*) Quand deux grains ont une orientation relative quelconque (pas de plan de symétrie approchée) on a ce que nous avons appelé un joint banal. ***Tous les joints banaux semblent avoir la même énergie.*** Ainsi un point triple entre trois de ces joints (A,B,C) donne les rapports :

$$\frac{A/B}{1{,}0} = \frac{B/C}{1{,}0} = \frac{C/A\dagger}{0{,}97}.$$

(*b*) En comparant les joints de couples symétriques (à moins de 4° près) à des *joints communs*

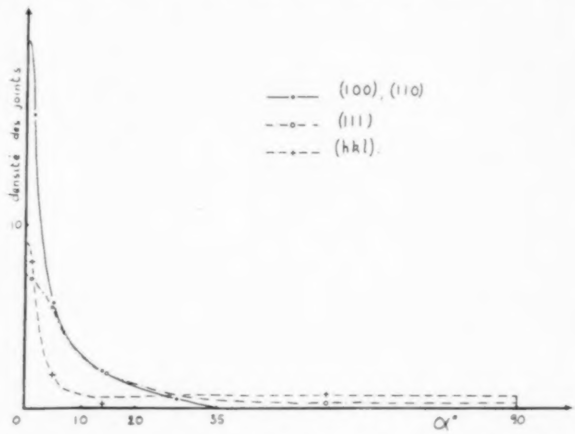

Figure 5. Fréquence des joints en fonction de leur angle α avec un plan de symétrie pour des couples de grains parallèles, en macle spinelle ou en macle quelconque.

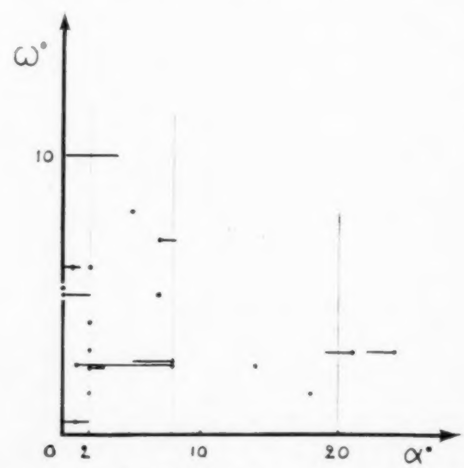

Figure 6. Angle α des joints avec un plan de symétrie pour deux grains à peu près en macle, avec une désorientation ω.

*La même remarque a été faite par Dunn et Lionetti [4; 20] sur les macles (112) et (111) du ferro silicium; on est alors dans le système cubique centré, et les rôles des deux plans sont inversés.

†C/A admet en réalité un plan de symétrie à forte désorientation.

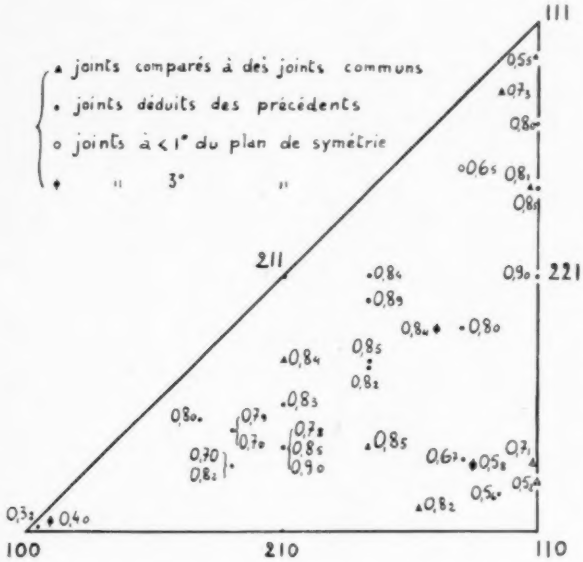

FIGURE 7. Valeur relative de la tension capillaire de joints voisins d'un plan de symétrie (h, k, l). La tension d'un joint banal est prise pour unité.

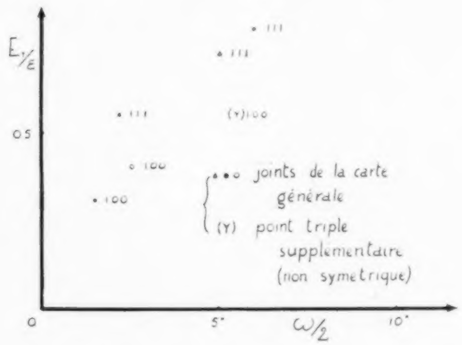

FIGURE 8. Comparaison des tensions capillaires pour des joints entre grains à peu près parallèles (**100**) et à peu près en macle spinelle (**111**), en fonction de la désorientation ω. La tension du joint banal est prise pour unité. (Points de la carte fig. 7.)

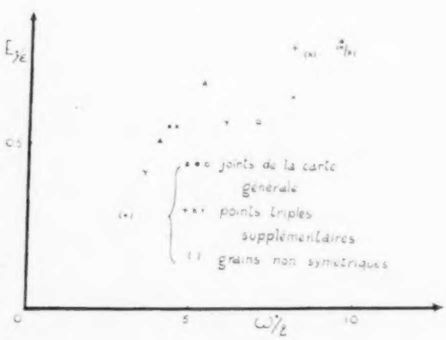

FIGURE 9. Autres mesures de tensions pour des joints entre grains presque parallèles, en fonction de la désorientation ω La tension du joint banal est prise pour unité.

(*d'énergie prise égale à l'unité*), puis en les comparant entre eux, on obtient une série de valeurs relatives, que nous avons reproduites sur la figure 7, où chaque point représente le pôle du plan de symétrie approchée correspondant. Nous avons porté toutes les valeurs calculées, et la dispersion est très acceptable.

On note trois minima voisins de 0 (100, 110 et 111), et une sorte de plateau à énergie constante voisine de 0,85, qui s'abaisse brusquement au voisinage de ces minima.

Pour ces symétries assez exactes, la position du joint est sans influence, sauf s'il est à moins de 10° du plan de symétrie, auquel cas l'énergie est réduite dans des proportions allant jusqu'à 15% semble-t-il (cas correspondant aux maximums de fréquence de la figure 5).

E. Voisinage des orientations* (100), (110), (111) (Etats II et III)

La présence des textures explique, comme nous l'avons vu, l'existence de nombreux joints voisins de ces trois orientations et permet de préciser les valeurs des tensions interfaciales correspondantes.

Nous avons reporté sur les figures 8,9 les valeurs obtenues, en fonction de la désorientation ω définie comme a la section C. Nous avons ajouté les valeurs relatives tirées de points triples entre cristaux quasi parallèles où certains couples n'admettent pas de plan de symétrie (à 4° près); dans ce cas ω a sa définition ordinaire d'angle de rotation. Ainsi, pour les faibles désorientations ω, la tension semble croître de façon continue avec ω à partir de 0, en accord avec les résultats obtenus par les autres auteurs. L'existence d'un plan de symétrie et la présence du joint dans ce plan jouent un rôle réduit. La croissance semble plus rapide près de (111) que près de (100) et (110).

F. Conclusions

(*a*) L'énergie des *joints banaux*, est très sensiblement constante, et prise comme unité.

(*b*) Quand le joint est *dans un plan de symétrie* (à quelques degrés près), l'énergie présente 3 minima à peu près nuls (100), (110) et (111) creusés dans un plateau d'énergie constante voisine de 0,75. Les minima (100), (110) sont plus évasés que (111). Leur départ correspond à 0,6 pour 10° de désorientation.

(*c*) Quand le joint est *hors du plan de symétrie*, le plateau est relevé à 0,85.

*Il s'agit de l'orientation du plan de symétrie, suivant la convention adoptée au paragraphe précédent.

(*d*) Quand la *symétrie n'est qu'approximative*, l'énergie se rapproche encore plus de celle du joint banal, sauf près des minima, où elle tend vers 0 comme précédemment.

(*e*) Quand dans le cas (*d*), *le joint est exactement dans le plan de symétrie approché*, il possède une énergie plus faible qu'en (*d*), sauf, pour les faibles désorientations ($\omega < 7°$) au voisinage des symétries approchées (100), (110) ou (111); dans ce cas, l'énergie semble indépendante de la position du joint.

Ces conclusions sont évidemment seulement valables pour des joints ayant subi de longs recuits.

III. CALCUL DES ÉNERGIES SUPERFICIELLES ET INTERFACIALES

A. Principe

Nous supposons que l'énergie interne d'un atome métallique dans un cristal peut se décomposer en autant d'éléments qu'il y a d'atomes voisins (« energies de liaisons »), en se limitant aux 12 plus proches voisins pour les structures compactes; et aux 8 proches et 6 seconds voisins dans le système cubique centré. Nous supposons aussi que l'introduction d'une surface libre ne modifie pas la position des atomes dans un cristal, mais supprime simplement les liaisons avec la partie enlevée; de même, qu'un joint modifie seulement les liaisons interatomiques qu'il traverse.

Dans ce calcul, on suppose le métal rigoureusement pur, et on ne tient pas compte des atomes étrangers qui peuvent se concentrer à la surface ou dans un joint, bien qu'en réalité ces impuretés aient une grande influence sur la tension capillaire [24; 25].

Soit ϵ l'énergie d'une liaison. L'atome entouré de n voisins aura, s'il est détaché du réseau, une énergie supplémentaire $E = n\epsilon$ (énergie de sublimation). Nous avons utilisé les valeurs de E données par Mott [21] et Seitz [22]. La variation de E avec la distance interatomique a été calculée théoriquement par Fuchs pour le cuivre [23]. Nous avons utilisé la méthode plus expérimentale développée par Mott et Jones [21], pour l'Al et le Fe.

Pour les métaux cubiques centrés, il faut répartir l'énergie E entre les 8 liaisons « primaires » à distance d_1 (énergie ϵ_1) et les 6 liaisons « secondaires » à distance d_2 (ϵ_2) de façon à rendre $E = 8\epsilon_1 + 6\epsilon_2$ minimum, avec la condition $d_1/d_2 = \sqrt{3}/2$. On a ainsi :

$$\frac{d\epsilon_2}{dd_2} = x\frac{d\epsilon_1}{dd_1}, \text{ avec } x = -\frac{8}{6}\frac{\sqrt{3}}{2} = -1,16. \tag{3}$$

Avec la courbe choisie pour le fer, on trouve, si d est la distance correspondant au minimum de ϵ:

$$d_1 = 0,97d \quad \epsilon_1 = 0,99\epsilon$$
$$d_2 = 1,13d \quad \epsilon_2 = 0,78\epsilon$$

et $E = 12,5\epsilon$ par atome. Ce mode de calcul donne un ordre de grandeur raisonnable pour la variation de distance interatomique dans la transformation α–γ, en supposant constante la distance d du minimum.

Nos hypothèses sont sujettes à deux critiques :

1. L'énergie du réseau ne peut être rigoureusement divisée en un certain nombre de liaisons, du fait que les actions interatomiques ne sont pas centrales.

2. Il faudrait tenir compte de la déformation élastique des cristaux au voisinage de la surface libre ou du joint.

Nous verrons qu'en fait les énergies obtenues par cette méthode semblent trop fortes, l'erreur étant probablement de l'ordre de 10–20% pour les énergies superficielles. Le calcul semble cependant rendre compte qualitativement de la variation de l'énergie superficielle ou interfaciale avec l'orientation.

B. Énergies superficielles

En supposant la surface parallèle à un plan (h,k,l), ($h \geqslant k \geqslant l$), ce qui est toujours approximativement vérifié, les distances des atomes à la surface, sont multiples entiers de l'équidistance des plans (h,k,l). On peut ainsi faire le décompte des liaisons coupées. Nous ne reproduisons pas le détail de ce calcul qui donne, pour l'énergie des liaisons coupées, par unité de surface:

$$E_s = (h+k+l)(h^2+k^2+l^2)^{-\frac{1}{2}}\epsilon d^{-2} \quad \text{pour le réseau cubique simple}$$

$$E_s = 4(2h+l)(h^2+k^2+l^2)^{-\frac{1}{2}}\epsilon d^{-2} \quad \text{pour le réseau CFC.} \tag{4}$$

$$E_s = 2(h+k+l)(h^2+k^2+l^2)^{-\frac{1}{2}} \cdot (\epsilon_1+\epsilon_2)d^2 \quad \text{si } h \leqslant k+l$$

ou

$$E_s = [2h\epsilon_1 + (h+k+l)\epsilon_2] \cdot (h^2+k^2+l^2)^{-\frac{1}{2}}d^{-2} \quad \text{si } h \geqslant k+l$$

pour le systéme CC

où d est le paramètre cristallin.

Ces formules donnent pour valeur *moyenne*:

$$E_s \simeq 2.600 \text{ e/mm}^2 \text{ pour le cuivre}$$
$$E_s \simeq 1.700 \text{ e/mm}^2 \text{ pour l'aluminium}$$

soit environ, par atome, le quart de l'énergie de cohésion [13]. Les mesures expérimentales sont rares; elles découlent de mesures de la tension superficielle faites près du point de fusion, avec une influence de la température assez mal déterminée. La comparaison est donc difficile. Cependant pour le cuivre, les mesures d'Udin, Shaler et Wulff [26] en bon accord avec celles de Bailey et Watkins [27],

correspondent à une énergie superficielle de $\simeq 2.400$ e/cm², donc peu inférieure à la valeur calculée. Un calcul de Huang et Willie [28] donne d'autre part 2.180 e/cm².

Nous voyons aussi que l'énergie superficielle varie de façon *continue* avec l'orientation $(h\ k\ l)$. Ses minima devraient correspondre, si on admet la loi de Wulff [29], aux faces les plus fréquentes dans la croissance du métal en présence de sa vapeur. Les cristaux d'argent (CFC) obtenus par condensation sous vide présentent effectivement les faces 111 [30]*.

C. Énergies interfaciales

Nous nous limiterons au cas de macles par mériédrie réticulaire où le joint se trouve dans le plan de symétrie des deux cristaux. C'est là, nous l'avons vu, un cas très fréquent, celui que nous avons étudié avec le plus de détails. Sans entrer dans le détail du calcul des énergies de macle, nous en donnerons un aperçu, puis nous analyserons les résultats que nous comparerons avec nos mesures relatives sur les tensions de joint et les résultats de divers auteurs.

Lorsque la symétrie des deux cristaux de la macle n'est qu'approchée, il semble que le meilleur moyen

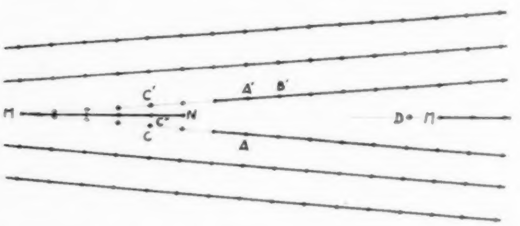

FIGURE 10. Schéma d'une macle $(h,1,0)$ par mériédrie réticulaire dans le système cubique simple.

de décrire l'interface soit de superposer à la macle décrite ci-dessous quelques dislocations. Ce n'est là qu'une hypothèse, car nous ne disposons pas de résultats expérimentaux assez précis pour trancher la question.

1. *Calcul des énergies de macle*

Nous supposons donc que le joint est un plan de macle, qui constitue un plan de symétrie pour les deux réseaux des cristaux contigus; ces réseaux ont en commun les atomes situés dans le plan de macle (cf. fig. 10), qui appartiennent au *réseau multiple* commun aux deux cristaux. La figure 10 a été dessinée dans le cas d'une macle $(h, 1, 0)$ d'un système cubique simple, et ressemble un peu à une dislocation; cette simplification, destinée à faciliter les explications, ne nuit en rien à la généralité du raisonnement. On suppose, comme précédemment, les deux cristaux non perturbés par la présence du joint. Les atomes tels que A ont alors un certain nombre de liaisons coupées par le plan de macle. Ils se trouvent enface d'atomes A'B' avec lesquels ils peuvent établir des liaisons plus ou moins distendues ou comprimées, que nous avons calculées en supposant que chaque liaison varie en fonction de la distance interatomique de la même façon que l'énergie de sublimation (cf. section III, A). Nous n'avons pas tenu compte des liaisons trop distendues, et nous nous sommes arrêtés lorsque la liaison était étendue de plus de 15% dans le système CFC et 20% dans le système CC.

En ce qui concerne les liaisons comprimées, telles que celles des atomes C voisins de M (fig. 10), nous avons adopté une autre règle de calcul : à cause de l'asymétrie de la courbe potentiel-distance interatomique, l'énergie de la liaison comprimée devient vite très forte. L'énergie totale du système diminue alors si l'un des atomes, C', est enlevé. On peut se demander si l'atome C ne vient pas en C'', dans le plan de macle. Nous avons fait le calcul dans l'une et l'autre hypothèse (atomes en C ou en C''); c'est le deuxième cas (C'') qui est le plus général. Pour les métaux « durs » cependant (Fe), la différence d'énergie est faible, et dans certains cas C est la position la plus stable. On ne peut pas, par contre, introduire des atomes supplémentaires tels que D dans le plan de macle sans augmenter l'énergie totale.

Dans le schéma final, les discontinuités des plans atomiques sont disposées comme dans les schémas de dislocations utilisés par Burgers [5] et Van der Merwe [8], avec cette différence qu'une « dislocation » N (fig. 10) n'est pas forcément à égale distance des deux voisines telles que M. Dans le cas particulier de la figure 10 ces « dislocations » sont des lignes s'étendant perpendiculairement au plan de la figure; mais *dans le cas général ce seront des zônes lacunaires isolées*.

Nous avons tenu compte, dans ces conditions, de toutes les liaisons normales, distendues ou comprimées, que permettait la géométrie, même si leur nombre dépassait un peu la coordinence du métal. Nous avons obtenu ainsi les énergies suivantes, *exprimées en unités* ϵd^{-2}:

*La loi de Wulff coïncide, pour nos calculs, avec la loi de Bravais–G. Friedel–Donnay [31; 32], tout au moins pour les plans les plus denses: 100 pour le système cubique simple; 110 pour le système cubique centré; 111 pour le système cubique à faces centrées.

TABLEAU III

CUBIQUE FACE CENTRÉ

			Cu				Al				Feγ	
hkl	p	E_a	$\sim E_b$	$\sim E_c$	E'_c	$E_a + E_b + E'_c$	$- E_b$	$- E_c$	$- E'_c$	$E_a + E_b + E'_c$	E	E'
100	0	0	0	0	0	0	0	0	0	0	0	0
110	0	2,8	+ 2.8	0	0	0	+ 2,8	0	0	0	0	0
111	0	0	0	0	0	0	0	0	0	0	0	0
210	1	12,6	+ 1,15	3,2	5,45	6,0	1,15	3,35	6,75	4,7	$\underline{9,9}$	12,85
211	1	11,2	+ 1,35	2,2	5,85	4	1,35	2,95	6,4	3,05	7,8	$\underline{7,3}$
221	1(2)	11,9(11,9)	1,05 (0,8)	4,6	6,6	(4,5)	1,2(0,8)	4,75	(7,35)	(3,75)	(7,9)	$\underline{7,75}$
310	1(2)	12,8(14)	0,85(0,85)	4,45	(7,45)	(5,7)	1,05(0,8)	4,6	9,3	(3,9)	(9,1)	$\underline{6,5}$
311	0(1)	4,8(12)	0,85	0	0,8	3,15	1,25	0	1,3	2,25	$\underline{(10,4)}$	(17,45)
320	1(2)	12,3(14,6)	1,1(0,85)	4,8	(8,6)	(5,15)	0,25(0,9)	5,05	(8,9)	(4,8)	$\underline{9,2}$	10,35
321	2	14	0,85	4,75	7	6,15	0,9	4,95	7,9	5,2	13,3	$\underline{7,4}$
322	2	12,5	0,95	3,25	6,15	5,4	0,95	3,35	6,65	4,9	8,1	$\underline{7,15}$
331	1	10,8	1,1	0	4,4	5,3	1,1	0	5,25	4,45	$\underline{9,5}$	18,5
332	2(3)	12,6(12,6)	0,45(0,6)	3	(7)	(5,0)	(0,7)	(3,1)	(7,6)	(4,3)	(9,1)	$\underline{7,45}$
410	2	13,4	0,95	4	7,45	5,05	0,95	4,2	8,2	4,25	8,0	$\underline{6,7}$
411	2	13,2	0,95	4	7,25	5,05	0,95	4,15	8,0	4,25	$\underline{7,9}$	7,9
421	2(3)	14,1(15,8)	0,75	4,5	8,05	5,25	0,8(0,65)	4,8	(11,15)	(4,0)	9,0	$\underline{6,95}$

TABLEAU IV

CUBIQUE CENTRÉ: Fe α

hkl	p	E_a	$- E_b$	$- E_c$	$E_a + E_b + E_c$
100	0	1,6	1,6	0	0
110	0	0	0	0	0
111	1	10,45	0,45	1,8	8,2
210	1	8,15	0,9	1,85	5,4
211	0	4,6	0,75	0	3,8
221	2	10,65	0,5	1,85	8,3
310	1	8,2	0,25	1,2	6,8
311	2	9,55	0,6	2,7	6,2
321	2	9	0,5	2,1	6,4
321	1	8	0,65	3,1	4,3
322	3	10,4	0,4	2,8	7,2
331	3	9,8	0,45	1,9	7,4
332	1	8,3	0,75	2,65	4,9
410	3	10,15	0,4	1,8	7,9
411	1	8,4	0,7	2,45	5,3
421	3	9,55	0,45	3,4	5,7

Dans ces tableaux, p est le nombre de plans cristallins contenant des atomes C′ supprimés; les nombres entre parenthèses correspondent à des cas analogues, où l'on peut choisir une autre valeur de p mise entre parenthèse. E_a est l'énergie des liaisons coupées; elle a la même valeur pour tous les métaux CFC; pour le fer α, elle se compose de deux termes représentant l'action des premiers et seconds voisins. E_b est l'énergie de liaison des couples d'atomes symétriques, tels que A et A′ de la figure 10. E_c et E'_c sont les énergies de liaison des atomes n'ayant pas de symétrique, quand ils restent en place et quand ils viennent dans le plan de symétrie respectivement.

Pour obtenir l'énergie interfaciale E, il faut soustraire de E_a les valeurs absolues des énergies E_b et E_c (ou E'_c) qui représentent des liaisons rétablies. On voit que, pour les métaux « mous », les énergies des liaisons rétablies $E_b + E_c$ diminuent beaucoup l'énergie totale. Signalons pour l'Al et le Cu le cas de la macle (311) où aucun atome n'est enlevé ($p = 0$). L'énergie totale présente en ce point une valeur un peu plus faible que pour les plans ($h\ k\ l$) voisins.

Pour savoir si les atomes C restent en place ou viennent dans le plan de macle, il faut comparer E_c à E_c'; si $E_c' > E_c$ les atomes viennent dans le plan de macle. C'est le cas pour le cuivre et l'aluminium. Pour le fer γ, c'est le cas aussi pour la moitié des plans environ, mais pour les autres, c'est l'inverse; nous n'avons indiqué sur le tableau que les deux énergies interfaciales totales $E = E_a + E_b + E_c$ et $E' = E_a + E_b + E_c'$ en soulignant la plus faible des deux. Pour le fer α, comme le calcul de E'

VOL. 1 1953

est très long, nous nous sommes contentés de calculer E; par analogie avec le cas du fer γ, on peut penser que E' ne s'en écarte pas beaucoup.

Notons enfin que la macle (211) du fer α a une valeur faible mais non nulle, tandis que la macle spinelle (111) des métaux CFC a une énergie nulle dans notre approximation, l'énergie réelle étant certainement très faible [33].

Nous nous sommes limités à un petit nombre de plans : pour les indices plus élevés, les termes de distorsion deviennent prépondérants, surtout pour l'Al et le Cu, et enlèvent toute précision au résultat. Nos mesures sur l'Al (cf. partie II) et celles des auteurs déjà cités [4; 11] semblent montrer que l'énergie de macle varie de façon continue avec l'indice du plan. Il est donc probable que les distorsions réalisent automatiquement l'interpolation entre les valeurs que nous avons calculées. Nous avons dressé des cartes approximatives à l'aide de ces valeurs (fig. 11, 12, 13, 14).

2. *Tensions interfaciales. Valeurs moyennes. Anisotropie*

Avant d'interpréter nos résultats, il est nécessaire de pouvoir passer de l'énergie interfaciale à l'énergie libre de joint qui correspond à la tension mesurée. Nous avons indiqué dans l'introduction les raisons d'admettre que l'énergie libre interfaciale s'annule presque, à la température de fusion T_f; ces raisons s'appliquent très bien dans notre modèle de joint, qui est du type « lacunaire ». D'autre part, il est naturel d'admettre que cette énergie libre, ou tension interfaciale, γ_s, varie en fonction de la température comme le fait la tension superficielle, c'est-à-dire linéairement (loi d'Eötvos). On peut donc écrire, en négligeant tout effet possible d'anisotropie sur l'entropie :

$$\gamma_s = E_s\left(1 - \frac{T}{T_f'}\right) \tag{5}$$

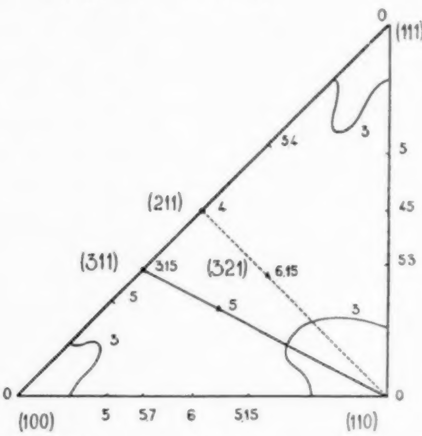

FIGURE 11. Diagramme des énergies de macle (h, k, l) calculées pour le cuivre (en unités ϵd^{-2}).

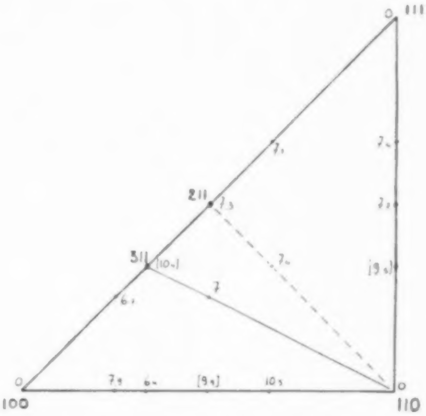

FIGURE 13. Diagramme des énergies de macle (h, k, l) calculées pour le fer γ (en unités ϵd^{-2}).

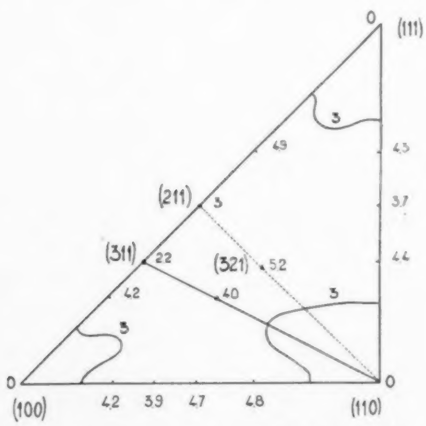

FIGURE 12. Diagramme des énergies de macle (h, k, l) calculées pour l'aluminium (en unités ϵd^{-2}).

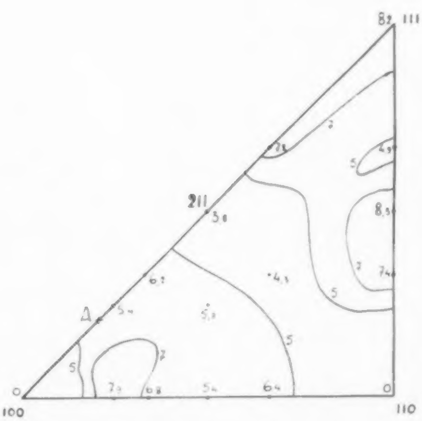

FIGURE 14. Diagramme des énergies de macle (h, k, l) calculées pour le fer α (en unités ϵd^{-2}).

où T_f' représente une température légèrement supérieure à la temperature de fusion T_f.

Examinons successivement les métaux CFC et le fer α.

(*a*) *Métaux CFC.* Le Cu, l'Al et le Fe γ (fig. 11, 12 et 13) présentent des variations analogues : 3 minima nuls (100, 110, 111) séparés par un plateau central présentant, pour le cuivre et l'aluminium, une faible dépression en (311).

Les figures 11, 12 et 13 donnent pour la valeur de E_s du *joint banal**:

$5\epsilon d^{-2} \times (0{,}8)^{-1} \simeq 6{,}2\epsilon d^{-2}$ pour le cuivre soit 2,000 e/cm²

$4{,}2\epsilon d^{-2} \times (0{,}8)^{-1} \simeq 5{,}2\epsilon d^{-2}$ pour l'aluminium soit 1,100 e/cm²

$7\epsilon d^{-2} \times (0{,}8)^{-1} \simeq 8{,}7\epsilon d^{-2}$ pour le fer, soit 5,100 e/cm²

La comparaison avec les maigres résultats expérimentaux obtenus jusqu'ici est délicate, du fait de la validité douteuse de l'équation (5). Les mesures de Bailey et Watkins sur le cuivre [27] donnent 640

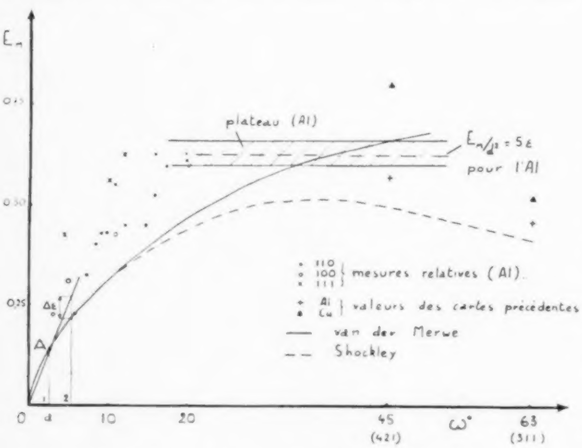

FIGURE 15. Comparaison des énergies de macle calculées (pour Al et Cu) et des tensions mesurées (pour Al) au voisinage des minima et dans la zône (h, k, $\frac{1}{2}$ $(h - k)$). On a choisi la valeur de l'énergie du plateau de façon à obtenir le meilleur accord.

e/cm² à 850°C†; Van Vlack [35] obtient 850 e/cm² pour le fer γ à 1105°C. L'équation (5) donnerait, avec nos valeurs de E_s, des valeurs de γ_s un peu supérieures à 350 e/cm² pour le cuivre, et 1220 e/cm² pour le fer γ aux mêmes températures.

Quant aux valeurs relatives des tensions interfaciales déduites de nos mesures, et représentées sur la figure 7, on voit qu'elles concordent assez bien avec les valeurs calculées de la figure 12. On notera la maximum aux environs de (321), que donnent le calcul et l'expérience. Près des minima (100), (110) et (111), les corrections dues aux distorsions élastiques deviennent prépondérantes, et le calcul perd toute précision. Pour la zône ($2h$, $2k$, $h - k$) des joints formés par des dislocations-coins (points représentatifs sur la ligne reliant 110 à 311), l'accord est bon pour l'aluminium, moins bon pour le cuivre (fig. 15); pour cette même zône, les calculs de Shockley [7] et Van der Merwe [8] donnent des courbes tracées sur la même figure 15, et qui encadrent les valeurs expérimentales pour les fortes

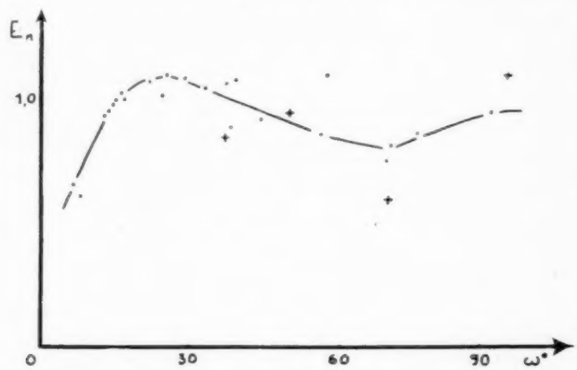

FIGURE 16. Comparaison des mesures de tensions pour le FeSi avec nos calculs d'énergie, dans la zône (h, k, k); les croix représentent les points donnés par nos calculs.

désorientations, mais semblent passer au-dessous, pour les faibles désorientations.

L'accord de nos calculs avec l'expérience est donc au moins aussi satisfaisant que celui des autres théories.

(*b*) *Fer α.* Pour ce métal (fig. 14), la variation de la tension interfaciale semble caractérisée par deux régions de sommets (410 à 311, 221 à 111) qui séparent deux zônes déprimées (100 et 110 à 211). L'énergie est nulle en (110) et faible en (211).

L'énergie moyenne semble un peu trop forte. Nous pouvons prendre (fig. 14) pour énergie moyenne *de macle* $6\epsilon d^{-2}$, soit 3.350e/cm²; ceci donne environ 800e/cm² pour la tension à 1105°C. Les mesures de Van Vlack (*loc. cit.*) donnent à cette température 725 à 765e/cm², pour un acier au silicium.

La *zône des macles* (*hkk*) a été explorée par Dunn et ses collaborateurs [20] pour le FeSi. Nous comparons leurs résultats et nos calculs (fig. 16). Le premier maximum de cette courbe, qui correspond à un point A sur la figure 14, est sans doute dû à la proximité du « sommet » 410 voisin (voir ligne de niveau $E_s/\epsilon d^{-2} = 7$), bien que nous n'ayons calculé aucun point à cet endroit. L'accord est donc satisfaisant.

*En admettant que les énergies de macle sur le plateau et de joint banal sont dans le rapport 0,8 (cf. II).

†Greenough [34] obtient, dans le cas de l'argent à 900; des valeurs plus faibles, de l'ordre de 300 e/cm².

Le minimum (211) correspond au plan de macle observé effectivement, comme (111) pour Al et Cu. Notons aussi que la zône déprimée (110)–(211) est celle des plans de plus grande densité réticulaire. Elle correspond aux directions de plans de glissement du fer α, comme (111) est celle relative aux métaux CFC.

Là encore, l'accord entre nos calculs et l'expérience est satisfaisant.

IV. RÉSUMÉ ET CONCLUSION

La morphologie des grains d'un métal recuit longtemps à haute température donne des renseignements sur la tension capillaire des joints (énergie libre interfaciale). Nous avons étudié dans cet esprit une tôle d'aluminium recuite au total 16 jours à 640°C. Les grains obtenus ont un diamètre moyen égal au double de l'épaisseur de la tôle, et les joints qui les séparent sont normaux à la tôle. Dans ces conditions, nous avons montré que la mesure des angles aux points triples donne directement les tensions interfaciales, en valeur relative.

Au cours du recuit à 640°, on observe que l'équilibre se réalise d'abord aux points triples, les joints restant contournés ou courbés. Ce n'est qu'au bout de quelques jours que les joints deviennent droits. C'est donc le déplacement des points triples qui gouverne le processus de croissance du grain.

Les orientations du grain observé ne sont pas réparties au hasard, mais se rangent dans deux textures : texture cubique, et texture Z, obtenue à partir de la précédente par une rotation autour d'un axe [111], approximativement. La présence de ces textures explique qu'il existe une proportion anormalement forte de grains quasi parallèles, ou de grains dont les réseaux possèdent un plan de symétrie simple, même si les grains ne sont pas jointifs.

Pour des couples de grains jointifs possédant un plan de symétrie approché, la position du joint par rapport au plan de symétrie est assez indifférente lorsque la symétrie est assez exacte, mais lorsque la symétrie est moins exacte, le joint est très souvent parallèle au plan de symétrie, comme si cette position correspondait à un minimum d'énergie.

Les mesures d'angles aux points triples permettent de préciser ces tensions interfaciales, en valeur relative. On trouve que :

— pour un *joint banal* (séparément deux grains d'orientation quelconque, sans plan de symétrie), la tension garde à peu près toujours la même valeur, que nous prenons pour *unité*.

— pour un joint séparant deux grains symétriques, mais non parallèle au plan de symétrie, la tension est de l'ordre de 0,85 (entre 0,85 et l'unité lorsque la symétrie n'est qu'approchée).

— Lorsque le joint est dans le plan de symétrie, la tension tombe à 0,75.

— Lorsque les grains sont approximativement symétriques par rapport à un plan (100), (110) ou (111), la tension tombe à des valeurs encore plus basses, et tend vers 0; elle vaut 0,6 pour une désorientation de 10°. La tension est toujours plus faible lorsque le joint est dans le plan de symétrie; il arrive dans ce cas que l'on observe des joints coudés, formés de portions (100) et (110) se raccordant avec un très petit arrondi. Cependant, pour, de trés faibles désorientations (quelques degrés), la position du joint semble indifférente.

Toutes ces observations permettent de dresser une carte des tensions interfaciales (en valeur relative par rapport à celle du joint « banal »), chaque couple de grain étant repéré par le plan de symétrie de leurs réseaux (fig. 7).

Du point de vue théorique, il semble que la description des joints comme parois de dislocations ne soit pas très satisfaisante pour des désorientations fortes. Nous avons cherché un mode de calcul qui permette d'évaluer les tensions interfaciales pour les couples de grains possédant un plan de symétrie, exacte ou approchée, qui sont trés nombreux. Cette symétrie correspond à ce que les cristallographes appellent *macle par mériédrie* (*ou pseudomériédrie*) *réticulaire* [19]. Pour calculer cette énergie de macle, nous avons opéré comme suit :

Admettons que l'énergie d'un atome de cristal métallique puisse se décomposer en « énergies de liaison » avec ses voisins (12 dans le système cubique à face centrée, 14 dans le système cubique centré, dont 8 fortes, et 6 faibles). Cette hypothèse est un peu artificielle; mais nous avons vérifié que pour le calcul de la *tension superficielle* (en évaluant le nombre de liaisons coupées par unité de surface), on obtient des valeurs en bon accord avec les mesures expérimentales, ce qui justifie l'hypothèse.

Pour les macles par mériédrie réticulaire, nous avons appliqué la même hypothèse, et compté les liaisons coupées, distendues, ou comprimées. Le calcul de l'*énergie interfaciale* par cette méthode est long, mais ne présente pas de difficulté spéciale. Nous l'avons effectué pour Al, Cu, Fe γ et Fe α. On passe de là à la *tension interfaciale* en supposant que l'entropie interfaciale est constante, et telle que la tension interfaciale s'annule presque au point de fusion, ce qui semble raissonable. Les tensions ainsi calculées sont en accord satisfaisant avec les valeurs

expérimentales, notamment avec les valeurs relatives que nous avons mesurées pour l'aluminium.

Lorsque la symétrie n'est pas exacte, il faut supposer que l'on rajoute quelques dislocations ou distorsions; de même lorsque le joint n'est pas dans le plan de symétrie. De ce fait la tension doit être plus élevée, comme l'ont montré nos mesures; mais nous n'avons pas calculé cet effet.

Ce mode de calcul, qui néglige les distorsions au voisinage du joint et suppose que les atomes restent aux nœuds du réseau (sauf un petit nombre pour lesquels nous avons supposé des déplacements) peut sembler un peu rigide; la réalité serait plus floue. Néanmoins, sauf pour les grains presque parallèles ou presque en macle spinelle, elle donne des résultats mieux en accord avec l'expérience, que celle de Shockley et Read, pour l'aluminium, et aussi satisfaisant pour le cuivre.

Ceci montre qu'il est difficile de choisir une théorie, d'après des expériences de précision forcément limitée. C'est plutôt par des conséquences indirectes que l'on pourra se faire une opinion, en étudiant des phénomènes tels que le fluage visqueux aux joints, la migration des joints (l'un de nous a observé ailleurs un cas où la macle par mériédrie entre deux grains voisins était évidente [37] et commandait le mode de déplacement du joint), diffusion le long des joints, frottement interne, attraction des impuretés, aux joints, etc. Remarquons à ce sujet que, pour le fer α, notre théorie permet d'expliquer la position des plans de macle.

Le modèle de joints que nous suggérons peut jeter des lumières nouvelles sur le rôle de l'énergie et de la mobilité des joints dans la formation des textures de recristallisation. En particulier, la macle (321) correspond aux relations d'orientation que Beck invoque pour expliquer les textures des métaux cubiques à faces centrées, et qui, d'après lui, correspondent à un maximum de mobilité des joints. Nos résultats prouvent que maximum de mobilité et maximum de tension interfaciale vont de pair.

Bibliographie

1. Smith, C. S. Trans. A.I.M.E., **175** (1948) 15.
2. Smith, C. S. Congr. A.S.M., Oct. 1951, Preprint no. 37.
3. Smith, C. S. C. R. du Congr. Internat. de Physique Solvay, Sept. 1951.
4. Dunn, C. G. et Lionetti, F. Trans. A.I.M.E., **185** (1949) 125.
5. Burgers, J. M. Proc. Phys. Soc., **52** (1940) 23.
6. Bragg, W. L. Proc. Phys. Soc., **52** (1940) 54.
7. Read, W. T. et Schockley, W. Phys. Rev., **78** (1950) 275.
8. Van der Merwe. Proc. Phys. Soc., **63** (1950) 616.
9. Mott, N. F. Proc. Phys. Soc., **60** (1948) 391.
10. T'ing Sui Ke. J. Appl. Phys., **20** (1949) 274.
11. Aust, K. T. et Chalmers, B. Proc. Roy. Soc., **A201** (1950) 210.
12. T'ing Sui Ke. Phys. Rev., **75** (1948) 267.
13. Friedel, J. et Crussard, C. J. Chim. phys., **47** (1950) 733.
14. Lacombe, P. et Berghezan, A. Mét. et Corrosion, **24** (1949) 1.
15. Rathenau, G. W. et Custers, J. F. H. Philips Res. Rep., **4** (1949) 241.
16. Kronberg, M. L. et Wilson, F. H. Trans. A.I.M.E., **185** (1949) 501.
17. Beck, P. A. Trans. A.I.M.E., **185** (1949) 627.
18. Lalœuf, A. et Crussard, C. Rev. Metallurgie, **48** (1951) 461.
19. Friedel, G. Leçons de Cristallographie (Nancy, Berger-Levrault, 1926), p. 444.
20. Dunn, C. G., Daniels, F. W., et Bolton, M. J. J. Metals, **2** (1950) 1245.
21. Mott, N. F. et Jones, H. Theory of Metals and Alloys (1936), p. 23.
22. Seitz, F. Theory of Solids (New York, McGraw-Hill, 1940), p. 3.
23. Fuchs, K. Proc. Roy. Soc., **A151** (1935) 585.
24. Crussard, C. Mét. et Corrosion, **25** (1950) 203.
25. Turnbull, D. J. Metals, **3** (1951) 661.
26. Udin, H. J. Metals, **3** (1951) 63.
27. Bailey, G. L. C. et Watkins, H. C. Proc. Phys. Soc., **63B** (1950) 350.
28. Huang, K. et Wyllie, G. Proc. Phys. Soc., **351A** (1949) 180.
29. Wulff, C. Z. Kryst., **34** (1901) 449.
30. Andrade, E. N. et Martinale, J. G. Phil. Trans. Roy. Soc. **235A** (1936) 69.
31. Friedel, G. Leçons de Cristallographie (Nancy, Berger-Levrault, 1926), pp. 128, 253.
32. Donnay, J. D. H. et Harker, D. American Mineralogist, **22** (1937) 600.
33. Fullman, R. L. J. Appl. Phys., **22** (1951) 448.
34. Greenough, A. P. et King, R. J. Inst. Met., **79** (1951) 415.
35. Van Vlack, L. H. J. Metals, **3** (1951) 251.
36. Gurney, G. Proc. Phys. Soc., **62** (1949) 639.
37. Wyon, G. et Crussard, C. Rev. Métallurgie, **48** (1951) 121.

THE SOLUBILITY OF OXYGEN IN GAMMA IRON*

J. A. KITCHENER,† J. O'M. BOCKRIS,† MOLLY GLEISER, and J. W. EVANS

Measurements have been made of the uptake of oxygen from a controlled CO–CO_2 gas mixture by thin strips of high-purity iron foil heated to 1325–1423°C by means of an electric current. The oxygen absorbed by the foil was determined by deoxidation with pure hydrogen at 1275°C, the water formed being frozen out and subsequently vaporized and measured manometrically in a small volume.

High-purity irons from three different sources led to a result of 0.003 ± 0.003 per cent by weight for the maximum oxygen content of gamma iron in equilibrium with ferrous oxide. It has been shown, however, theoretically and practically, that traces of impurities such as Mn, Si, Cr, Al, which are always present, may lead to uptake of oxygen by formation of oxidation products at grain boundaries. The evidence is consistent with a true solubility in ideally pure iron of even less than 0.001 per cent.

Metals which dissolve appreciable amounts of oxygen (Ag, Zr, Ti, V) do so interstitially; the vanishingly small solubility of oxygen in iron (and copper) can be ascribed to an unfavourable radius ratio, the octahedral holes being unable to accommodate oxygen atoms. The mechanism of diffusion of oxygen in iron is probably intergranular.

LA SOLUBILITE DE L'OXYGENE DANS LE FER GAMMA

Des mesures ont été prises de la soustraction d'oxygène d'un mélange controlé de gaz CO–CO_2, par des morceaux de mince feuillard de fer de haute pureté, chauffé à 1325–1423°C au moyen d'un courant électrique. La quantité d'oxygène absorbé par le feuillard a été déterminée par désoxydation avec de l'hydrogène pur à 1275°C, l'eau formée ayant été congelée, ensuite évaporée et mesurée manométriquement dans un petit volume.

Des fers de haute pureté provenant de trois sources différentes, ont donné 0.003 ± 0.003 pour cent en poids comme teneur maximum d'oxygène dans le fer gamma en équilibre avec l'oxyde ferreux. Il a été cependant montré, théoriquement et pratiquement, que des traces d'impuretés telles que Mn, Si, Cr, Al, et qui sont toujours présentes, peuvent conduire à une soustraction d'oxygène par formation de produits d'oxydation aux joints intercristallins. Ces considérations sont compatibles avec une vraie solubilité dans du fer idéalement pur, de moins même que 0.001 pour cent.

Les métaux qui dissolvent des quantités appréciables d'oxygène (Ag, Zr, Ti, V) le font intersticiellement; l'extrêmement faible solubilité de l'oxygène dans le fer (et le cuivre) peut être attribuée à un rapport défavorable des rayons, les trous octaèdraux ne pouvant pas loger les atomes d'oxygène. Le mécanisme de diffusion de l'oxygène dans le fer est probablement intergranulaire.

DIE LÖSLICHKEIT VON SAUERSTOFF IN GAMMA-EISEN

Die Aufnahme von Sauerstoff aus bekannten CO–CO_2 Gasgemischen durch Reinsteisenfolien, die auf 1325–1423°C erhitzt waren, wurde gemessen. Der an der Folie absorbierte Sauerstoff wurde durch Desoxydieren in reinem Wasserstoff bei 1275°C bestimmt; das gebildete Wasser wurde ausgefroren, wieder verdampft und manometrisch im kleinen Volumen gemessen.

Reinsteisen aus drei verschiedenen Bezugsquellen ergab als maximalen Sauerstoffgehalt des Gamma-Eisens im Gleichgewicht mit Ferro-oxyd 0,003 Gewichtsprozent. Es wurde jedoch theoretisch und experimentell gezeigt, dass Spuren von Verunreinigungen wie Mn, Si, Cr, Al die immer vorhanden sind, zur Sauerstoffaufnahme durch Bildung von Oxydationsprodukten an den Korngrenzen Anlass geben können. Dieses Beobachtungsmaterial ist im Einklang mit der wahren Löslichkeit von weniger als 0,001% in ideal reinem Eisen.

Metalle, die grössere Mengen Sauerstoff aufnehmen (wie Ag, Zr, Ti, V) lagern diesen in das Kristallgitter ein. Die verschwindend kleine Löslichkeit des Sauerstoffs in Eisen (und Kupfer) kann auf das ungünstige Radien-Verhältnis zurückgeführt werden, wobei die Löcher des Oktäders nicht in der Lage sind, die Sauerstoffatome unterzubringen. Die Diffusion von Sauerstoff im Eisen erfolgt wahrscheinlich entlang der Korngrenzen.

VOL. 1 1953

Introduction

It has frequently been suggested that numerous mechanical properties, the corrosion behaviour, and the metallographic structure of iron and steel are influenced by the presence of oxygen in solid solution in iron [1]. Consequently, many attempts have been made to determine the so-called "solubility of oxygen" in solid iron, but the results have been highly discordant, ranging from as high as 5 per cent [2] or 6–7 per cent [3] down to 0.003–0.006 per cent [4] for temperatures in the neighbourhood of 1000°C.‡ Probably the principal causes of disagreement between the results have been (*a*) failure to achieve equilibrium between the solid phases present, and (*b*) the presence of impurities in the iron used; only one of the previous workers [4] has given proper attention to this vital point.

The term "solubility of oxygen" means the maximum amount of oxygen that can be taken up by iron before a separate oxide phase is formed, i.e., at the limit of the Fe phase field. The problem is complicated by the phase transitions of iron (α–γ at 910°C, γ–δ at 1400°), and by the fact that at different temperatures different oxide phases are in equilibrium with solid iron, namely, below 500°C Fe_3O_4; from 560° to 1371°C the oxide phase is solid

*Received June 20, 1952.

†Department of Inorganic and Physical Chemistry, Imperial College, London, S.W.7.

‡A critical survey of previous work has been given elsewhere [5].

"wüstite" (non-stoichiometric FeO); from 1371° to 1528° liquid oxide containing 22.6–22.8 per cent oxygen; and from 1528° to 1539° liquid iron containing 0 to 0.16 per cent oxygen. At each of these phase changes there should be either a sharp change or a change of slope in the "solubility" line for the oxygen content of iron saturated with the appropriate phase.

However, even the order of magnitude of the solubility has not yet been established for any part of the range. The object of the present work was to decide whether any detectable amount of oxygen can go into true solution in solid iron.

This is of theoretical as well as technological interest as at the present time gas–metal interactions are still little understood, and it is impossible to predict with any confidence whether a gas such as oxygen can enter a given metallic lattice as atoms or ions, substitutionally or interstitially. Oxygen is known to diffuse at a measurable rate into a piece of iron at about 1000°C and many *liquid* metals and some solid metals, e.g. titanium, zirconium, and vanadium, undoubtedly dissolve considerable amounts of oxygen (or oxide), even up to 40 atomic per cent. Appreciable solubilities have been found for oxygen at pressures from 10–80 cm. in silver over the range 200–800°C [6]. On the other hand, work on copper [7] has revealed the importance of traces of impurities; whereas copper of 99.99 per cent purity showed an oxygen solubility of 0.012 per cent, the value was reduced to 0.008 per cent when copper of 99.999 per cent was used. This effect was traced to the separation of particles of oxides of impurity metals which have a greater affinity for oxygen than copper has (the so-called "internal oxidation" effect). The same effect must doubtless be anticipated with iron, and this fact has not previously been recognised. Consequently, the present work has been done with iron of very high purity, and attention has been paid to the influence of residual traces of impurities which are present even after the most extensive purification has been carried out.

The principle of the method adopted was to bring thin iron foil to equilibrium with a controlled gas mixture of either H_2–H_2O or CO–CO_2, the composition of the mixture being chosen to maintain an effective partial pressure of oxygen slightly smaller than that required to form wüstite (FeO). The small amounts of hydrogen or carbon dissolved simultaneously are unlikely to have a significant effect on the uptake of oxygen. The oxygen uptake by the iron from this gas mixture was then measured, and from a knowledge of the Fe–FeO equilibrium it was possible to calculate how much oxygen would have been absorbed by iron in equilibrium with FeO, assuming Sievert's Law to hold for oxygen in solid iron, as it does for liquid iron.

Experimental

Methods

Three distinct methods have been used, but for brevity the first two (which gave essential practical information but not quantitatively acceptable results) will be described only briefly [8].

In *Method A*, the changes of weight of thin iron foil heated in a molybdenum-wound vertical alumina tube furnace in (*a*) hydrogen, (*b*) hydrogen-steam mixtures, and (*c*) dry hydrogen, were followed with a sensitivity of 0.01 per cent. Approximate values of an apparent diffusion coefficient were obtained from the kinetics. Reduction in hydrogen at 1250°C is particularly suitable for removing dissolved oxygen from iron since impurities such as SiO_2 and Al_2O_3 are not reduced.

Method B was similar to Method A except that CO–CO_2 mixtures were used instead of H_2–H_2O, and the oxygen content was determined by reducing the sample with dry hydrogen *in situ* and collecting the water formed in Nesbitt absorption tubes containing anhydrone, which were then weighed. The "blank" from the furnace tube could be reduced to 2–3 mgm. of H_2O per hour, and since up to 100 gm. of iron could be used, the limit of sensitivity was about 0.005 per cent.

The principal information resulting from the experiments which were carried out by methods A and B may conveniently be summarised at this point, since it conditioned the design of the final method of determination. The following points were established: (1) At temperatures below 900°C the changes were too slow for equilibrium to be reached in many hours even with iron foil of only 2/1000 inch thick. This would account for the gross discrepancies between the results of various workers who have attempted to equilibrate iron with iron oxide in the lower temperature range. (2) At 1000°C the solubility cannot exceed 0.01 per cent oxygen. (3) At higher temperatures, especially near 1400°C, measurable amounts of oxygen were taken up by the iron, e.g., 0.05 per cent at about 1375°C and 0.12 per cent at 1465°C, but, at the same time, the iron was being progressively contaminated by material derived from the refractory tube. For example, the 1465°C sample had originally 0.014 per cent silicon, but after some hours in the hot tube it was found to contain 0.097 per cent Si on the outer

layer of foil and 0.033 per cent Si in the central core. The reaction by which silicon in iron causes the uptake of oxygen in a form reducible by hydrogen will be discussed later. Probably silicon was extracted from the alumina refractory (in which it is always present, at least in traces) by reduction to the volatile suboxide, SiO. (4) Slightly impure iron foils showed a very high "apparent solubility" for oxygen compared with high-purity iron. (5) High-purity iron foil to which 0.06 per cent manganese was added (by evaporation in vacuum followed by annealing) showed an enhanced oxygen uptake which would agree roughly with the amount expected by internal oxidation on the assumption that an ideal solid solution of FeO–MnO is produced under the conditions of the experiment.

It is evident that, to be satisfactory, a method must satisfy the following conditions: (*a*) It must be sensitive to better than 0.01 per cent. (*b*) It must entirely exclude hot refractories or other possible sources of contamination. (*c*) A detailed analysis of the iron for all significant impurities present to the extent of 0.001 per cent or more is essential. If such impurities exist, their influence must be carefully considered, since otherwise an apparent solubility may not correspond to true homogeneous solution. These conditions were satisfied by Method C.

VOL. 1 1953

Final Method C. A strip of high-purity iron foil about 5 inches long, ½ inch wide and 2–4 thousandths of an inch thick was heated by passage of an electric current through it, while it was subjected to a controlled atmosphere in an all-glass vacuum apparatus. The strip was first reduced with pure dry hydrogen, and then heated for various periods in $CO–CO_2$ gas mixtures to produce dissolved oxygen but not iron oxide. The $CO–CO_2$ mixture was then replaced by dry hydrogen again, and any oxygen present in the iron was thereby removed as water vapour which was condensed out in a liquid air trap. Finally, the trap was isolated and the amount of water was determined by evaporating it into a small measured volume in which its pressure could be determined.

The water-vapour method of determining oxygen in metal, which is due to Baker [9], is potentially very sensitive: in theory 0.0004 per cent oxygen could be detected with a 1 gm. sample of iron in the present apparatus. In practice, however, the sensitivity was limited by irreproducibility of the "blank" arising from desorption of water vapour from the walls of the apparatus. However, it was estimated that the final readings had a probable error of only about ± 0.002 per cent oxygen.

Apparatus

Figure 1 is a diagram of the "Pyrex" vacuum apparatus used. R is the reaction vessel, containing the sample of iron foil *Fe*, which was heated via heavy copper leads (*Cu*) and tungsten seals (W). J is a large flanged joint by which the assembly could be inserted or removed. TR is the trap in which water could be condensed (see below): it was subsequently evaporated into the section of apparatus between T_1 and T_2, its presence being read by the mercury manometer, M. B is a bulb which could be used to enlarge the volume of this section in case the water vapour pressure proved too high for accurate measurement in the smaller volume [9].

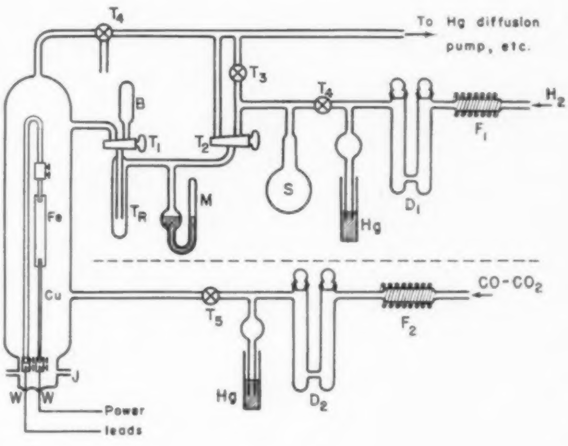

FIGURE 1

Gases

Hydrogen from a cylinder was passed slowly over palladised asbestos at 400°C, dried by anhydrone (D_1) and stored at atmospheric pressure in the bulb S ready for admission to the sample. Trace impurities not removed by this treatment are not significant.

$CO–CO_2$ mixtures were specially prepared in cylinders by the British Oxygen Company; they were analysed and found to contain 10.2 and 14.6 per cent CO_2 by volume respectively, giving CO_2/CO ratios of 0.114 and 0.175. These ratios were selected to correspond to 1/2 to 2/3 of the critical CO_2/CO ratio which would be required to form FeO in the range 1200–1500°C. For this data the results of Darken and Gurry [10] were employed; for example, at 1224°C the critical ratio corresponding to the Fe–FeO equilibrium was found to be 0.315, and at 1493° it was 0.199. The only significant impurity in the gas mixture was a trace of oxygen; this was converted to CO_2 by passing the gases over palladised

asbestos at 400°C, and followed by drying with anhydrone.

The $CO-CO_2$ mixtures used would introduce a certain amount of carbon into the iron. Calculations based on the work of Smith [11] showed that the amount introduced with gases at 1 atm. would be less than 0.02 per cent C but to keep it even lower the mixture was used at 0.1 atm. pressure, which would reduce the carbon uptake but would not influence the oxygen absorption. The carbon taken up under the conditions used would amount to about 0.005 per cent. This would not complicate the determination of oxygen in the iron by hydrogen reduction [12]—if large quantities of carbon are present a proportion of the oxygen is evolved as CO instead of H_2O.

The Iron Samples

High-purity iron from several sources has been used, and attention given to the trace impurities present. In each case the samples of iron were rolled to foil by Messrs. Johnson Matthey, with special care to avoid contamination.

Iron A was a particular batch of "sponge iron" of high purity prepared by Messrs. Johnson Matthey for the British Iron and Steel Research Association.

Iron N was a high-purity iron prepared for the British Iron and Steel Research Association (code "AH") by the National Physical Laboratory.

Iron U was a high-purity iron from the U.S. Bureau of Standards, manufactured during the well known researches of Cleaves [13].

Irons X, Y and Z were three high-purity iron made at the National Physical Laboratory and similar to N, but containing deliberately added alloys; namely X had 2.89 per cent Mn, Y 0.18 per cent Mn, and Z 0.013 per cent Si.

Iron A was rolled to 2/1000″, and the remainder to 4/1000″ thick. Strips about ½″ wide and as uniform as possible were cut for use. The analyses of these irons according to the suppliers are given in Table 1. The figures are approximate only.

TABLE 1

PERCENTAGE OF IMPURITIES DETECTED

Sample	C	Si	Mn	S	P	Ni	Cr	Cu	Al
A†	.02	.014	< .01	.006	.004	.08	.0035	.01	—
N	.003	.003	.004	.005	.001	.01	.001	.006	.001
U*	< .001	.001	—	.002	< .0005	—	—	< .002	—
X	.0046	.002	2.89	.004	< .001	.006	.001	.006	.001
Y	.0035	.007	.18	.009	< .001	.006	.002	.007	< .001
Z	.004	.013	.0024	.009	< .001	.007	.002	.006	< .001

†Mo < .002, V < .002, Co < .005.

*None of 47 other elements could be identified in the arc spectrum.

Heating and Temperature Measurement

The iron strip was mounted between copper electrodes; copper was used because it would not be oxidised in the $CO-CO_2$ mixtures used and it could not dissolve significant amounts of oxygen under the conditions of the experiment [7]. The strip was heated by passage of an a.c. current supplied by a variable auto-transformer, the external leads being cooled by a stream of air. This method of heating the iron was essential to avoid contamination from hot refractories, and, although the temperature of the strip was slightly lower at the edges than in the centre, and considerably lower near the ends owing to conduction, there was a substantially uniform zone 4 inch long over which the temperature did not vary by more than 20°. The arrangement could be used with $CO-CO_2$ mixtures because the thermodynamics of the reaction $Fe + CO_2 = FeO + CO$ show that a mixture which is not oxidising at the highest temperature of the strip will not be oxidising at lower temperatures (e.g., near the electrode connections). (This would not be true with H_2-H_2O mixtures.) Consequently, the only deficiencies of the strip heating method for the present purpose were (*a*) that it would give slightly low results since a small proportion of the strip (estimated by colour as 10 per cent of the total area) would be at lower temperatures at which the rate is slow; (*b*) it was found that temperatures much above 1400°C could not be maintained for long as the strip rapidly developed a "hot spot" and burnt out. Because of this limitation of the strip-heating method, the present work has been restricted to the region of the γ-phase of iron.

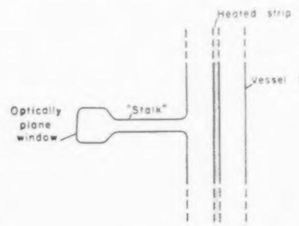

FIGURE 2

Temperatures were measured by sighting a disappearing filament optical pyrometer on the centre of the strip. To avoid condensation of iron on the window, the latter was made to project from the vessel *R* on a tube of narrow bore (see Fig. 2), which acted as a trap for iron vapour. Since a heated iron strip is not a "black body," a correction was applied to allow for the emissivity coefficient; Burgess [14] and his co-workers have given a value

of 0.39 ± 0.01 for the emissivity of pure, smooth iron in the temperature range 1000–1500°C. A correction amounting to about 15°C was also necessary to allow for the measured absorption by the Pyrex glass window. The pyrometer had been calibrated at the National Physical Laboratory.

Procedure

A strip of one of the high-purity iron foils was cut, carefully cleaned, weighed, and mounted in the copper electrodes and then assembled in the vessel *R*. The whole apparatus was then evacuated with a mercury condensation pump.

The next step was to deoxidise the iron completely. The bulb *S* was filled with purified hydrogen to a pressure of 1 atm. T_2 was then cautiously opened, to build up a pressure of about 50 mm. of hydrogen in vessel *R*, as indicated on the manometer *M*. The iron strip was heated by gradually increasing the current through it until, in about 2 minutes, the temperature reached about 1250°C which was then maintained for 10 minutes. After this preliminary deoxidation in hydrogen the current was switched off and the iron strip cooled in a few seconds. The hydrogen (containing a trace of water vapour) was pumped off through T_4. This deoxidation procedure was repeated but the water formed was now condensed in trap *TR* by means of liquid nitrogen, the hydrogen being pumped slowly off via T_1 and T_2. This method of collecting the water formed was found necessary as it was not possible to rely on diffusion alone to transport water vapour from *R* to *TR* (as in the method of Baker). The effectiveness of the procedure was checked by admitting into *R* a small amount of water vapour (measured by the pressure it exerted in the measuring volume) with a stream of hydrogen from *S*. This was then removed in the manner described above, the water being recondensed in *TR* and measured again. The accuracy was better than 90 per cent, which was adequate for the present purpose. The measurement of the amount of ice condensed in *TR* was effected by warming *TR* with tepid water, then allowing it to reach room temperature (measured) and finally measuring the movement of the manometer with a short-focus vernier microscope reading to 0.02 mm. From this pressure the amount of water (and hence oxygen) was easily calculated, knowing the volume of the apparatus between T_1 and T_2 (previously calculated before assembly of the complete apparatus). After measurement, the water was pumped away via T_2.

The above procedure for deoxidising the specimen was repeated several times until the amount of water collected had fallen to a low, constant value (the "deoxidising blank") which usually corresponded to about 0.004 per cent oxygen on the weight of the sample taken. The specimen then resembled platinum in appearance.

It was assumed that the specimen was now fully reduced, at least as far as FeO was concerned. (Oxides of any impurities not reduced by this treatment are therefore deliberately excluded from the determination.)

The next stage was to bring iron strip to equilibrium with the prepared CO–CO_2 mixture; this was introduced via T_5 to give a pressure of about 100 mm. The iron strip was heated to the required temperature in the mixture for a measured time (e.g., 10 minutes), and the current was then switched off to quench the equilibrium. Because the composition of the mixture would not permit formation of FeO, the iron remained perfectly clean and bright under this treatment. The CO–CO_2 mixture was pumped off.

The final stage was the determination of the oxygen absorbed by the iron from the CO–CO_2 atmosphere. This was carried out with pure hydrogen at 50 mm. pressure at 1250°C exactly as described for deoxidising the iron, the water vapour being condensed and measured as before. In practically all cases the first 10 minutes' heating sufficed to remove all the oxygen, and subsequent treatments yielded the constant "deoxidising blank."

To ascertain whether the time of heating in CO–CO_2 was long enough to allow equilibrium to be reached, the treatment in the gas mixture was repeated for increasing periods of time until no further increase in the oxygen absorbed was observed.

Precautions

(*a*) After a number of repeated heatings of a specimen had been made the results gradually became less reproducible. Apparently, this was caused by irreversible sorption of water vapour on the thin film of iron which gradually accumulated on the cool glass walls of vessel *R*. To obviate this trouble the strip was replaced after 8–10 runs and the inside walls of *R* were thoroughly cleaned with dilute HCl solution, rinsed with acetone, and dried with hot air. After such treatment the water vapour recovery from *R* was restored to the value mentioned above.

(*b*) It was considered that in this apparatus thermal segregation of the CO–CO_2 mixture would be negligible, but as a precaution several runs were carried out with a streaming instead of static

CO–CO_2 mixture. The results were unchanged.

(*c*) The "deoxidising blank" obtained from the procedure described above arose from traces of water or oxygen in the hydrogen and from water desorbed from the walls of the glass apparatus. With the precautions mentioned, it reached a constant, low value, and therefore did not seriously reduce the accuracy of the determination. However, this did not give the true "blank" which would ideally be obtained by carrying through all the stages without the presence of the iron specimen. In particular, it was necessary to ascertain if any water was taken up from the CO–CO_2 mixture by the vessel *R*. Unfortunately, the conditions of heating during the gas treatment period could not be exactly paralleled without heating the filament, but to approximate to the same conditions as closely as possible *R* was carefully heated on the outside for 10 minutes with a hand blow-lamp until the walls were heated to about the same extent as they reached by radiation from the filament during the main run with iron. The "probable blank" determined in this way was 0.9 mm. of water vapour in the measuring volume as compared with 0.5 mm. for the "deoxidising blank," and this factor contributed the largest source of uncertainty in the final results.

Results

To illustrate the method of measurement, Table 2 gives a typical record of readings obtained for one specimen.

TABLE 2

Record of a Typical Determination

Heating Period	Gas used	Time (min.)	Temp. (°C)	Pressure of H_2O collected (in mm. Hg)
1. Preliminary deoxidation	H_2(50 mm.)	10	1282	—
2. Second deoxidation	"	"	"	1.04
3. "Deoxidising blank"	"	"	"	0.50
4. "	"	"	"	0.52
5. Oxygen uptake period	CO-CO_2(100 mm.)	20	1365	—
6. Analysis run	H_2 (50 mm.)	10	1282	1.54
7. "Deoxidising blank"	"	"	"	0.54

Other data: Wt. of specimen (iron 'A') 0.620 g. Room temp. 17°C. CO_2–CO ratio 0.171. "Probable blank" = 0.90 mm. Hence, pressure of H_2O due to oxygen absorbed by specimen = 1.54 − 0.90 = 0.64 mm., which corresponds to 0.040 mg. of oxygen per mm. pressure.

∴ *oxygen absorbed by iron at* 1365°C = 0.004%.

The oxygen absorbed by the iron was thus small (0.004 per cent) although just significantly greater than the "blank."

A number of runs were made with the different irons and at several temperatures, and the final values obtained (calculated as for the example recorded in Table 2) are summarised in Table 3.

TABLE 3

Summary of Final Results with High-Purity Irons

(Oxygen absorbed from mixture with CO_2–CO = 0.171)

Iron used	Temperature (°C ± 20°)	Gas	Wt. per cent oxygen absorbed (±0.002)
A	1325	S	0.004*
	1365	S	0.004
	1412	S	0.004
N	1330	S	0.002
	1423	S	0.002
U	1330	S	0.002*
	1350	Str.	0.002
	1423	Str.	0.002
Z	1330	S	0.002
	1412	S	0.002

S = static gas mixture at 100 mm. pressure

Str. = streaming at mean linear flow rate of 1 cm./sec.

* = Mean of two determinations

Table 4 summarises the results obtained with iron-manganese alloys X and Y.

Accuracy

The probable uncertainty was estimated as ± 0.002 per cent. The consistency of the final results for different runs and different irons is satisfactory evidence that there were no large random errors unrecognized, and the results with alloy Y showed that when an appreciable uptake of oxygen (in the second decimal place) occurred, it could be measured satisfactorily.

TABLE 4

Summary of Results with Iron-Manganese Alloys

Alloy	Temperature (°C ± 20°)	CO_2/CO ratio	Per cent oxygen absorbed (±0.005)
X (2.89% Mn)	1330	0.171	0.1
Y (0.18% Mn)	1330	0.114	0.034
"	1412	0.114	0.030
"	1330	0.171	0.050
"	1412	0.171	0.041

(CO-CO_2 mixture static at 100 mm. pressure)

Discussion

In spite of the high values which have sometimes been reported for the solubility of oxygen in iron,* the lowest values appear more likely to be correct on the following grounds. (1) The solubility of *liquid* oxide in *liquid* iron is now fairly well established; at 1528° the limiting solubility is about 0.16 per cent oxygen. The solubility in solid δ-iron must be *less* than this value. (2) The maximum lowering of the freezing point of iron in equilibrium with liquid iron oxide is $10° \pm 1°C$ [15]. Applying the van t'Hoff equation for equilibrium between a dilute liquid solution and a solid solution,

$$N_2(\text{liquid}) - N_2(\text{solid}) = \frac{\Delta H\, \Delta T}{RT_m^2}$$

(where ΔH = heat of fusion, ΔT = lowering of melting point, T_m = melting point of pure solid, N_2 = atom fraction of solute). The heat of fusion of iron is about 3.6 kcal and the melting point is 1539°C. Hence one obtains for the maximum oxygen content of solid δ-iron 0 ± 0.016 per cent at 1528°C. The solubility in γ-iron would probably be smaller than in δ- (or α-) iron, judging by the behaviour of hydrogen and nitrogen, and by the fact that δ-iron is a slightly more open structure than γ-iron. (3) Incidentally to their study of the carbon dissolved by iron from CO–CO_2 mixtures, Dünwald and Wagner [16] concluded that the oxygen solubility could not exceed 0.01 per cent at 800°C. (4) Sloman [4] was able to detect by refined metallographic methods the presence of particles of oxide in high purity iron cooled from the liquid state and containing only 0.006 per cent oxygen, whereas no inclusion could be seen when the oxygen content was 0.003 per cent. These observations suggest that between 0.003 and 0.006 per cent of oxygen can exist in solution, but unfortunately the temperature for which this result applies is in doubt.

The apparent solubility in high-purity gamma iron. The results in Table 3 show that 3 out of 4 high-purity irons were found to absorb 0.002 ± 0.002 per cent by weight oxygen at temperatures varying from 1330°C to 1423°C while the fourth (A) gave 0.004 ± 0.002 per cent. Clearly, the lower values are the more significant as measures of the behaviour of pure iron.

There was no significant difference at different temperatures or with the three different irons N, U, and Z, the impurity contents of which differ (Table 1). The value 0.002 ± 0.002 per cent is therefore taken as representative of the highest-purity iron in the gamma range. This is the amount of oxygen apparently dissolved from a mixture of CO_2–CO ratio 0.171. Applying Sievert's Law for a mean temperature in the middle of the γ-range leads to a theoretical limiting solubility for iron in equilibrium with FeO of 0.003 ± 0.003 per cent by weight.

Significance. The value given above is lower than any previously recorded. It is consistent with the evidence, already mentioned, from the freezing point depression and from the metallographic work of Sloman.

It remains to consider, however, whether 0.003 per cent should be accepted as the true solubility of oxygen in gamma iron. It should be emphasized that (*a*) the present results were obtained with very high purity irons, but all the samples contained impurities exceeding 0.003 per cent, and (*b*) the experimental uncertainties allow the possibility that, even with these irons, the solubility could be less than 0.001 per cent, i.e., experimentally immeasurable with any iron obtainable. The fact that the oxygen uptake observed was independent of temperature supports the view that it did not represent true solubility of oxygen in iron.

These very low results are not necessarily incompatible with the evidence that oxygen will diffuse through ordinary iron. In the absence of any clear mechanism for entry of oxygen into the iron lattice (see below), an estimation of the order of magnitude of volume diffusion through iron cannot be made, but penetration of oxide along grain-boundaries seems a much more likely mechanism. Grain-boundary diffusion is known to occur in many metals with a lower activation energy than volume diffusion [17]. This possibility has not been examined in the iron–oxygen system.

Influence of traces of alloying elements. The present work has shown conclusively that slightly impure iron can absorb appreciable quantities of oxygen at oxygen activities where no oxide of iron can form. There is no doubt that this oxygen forms oxide "inclusions" of elements which have a higher affinity for oxygen than has iron ("internal oxidation"). The maximum amount of oxygen that could be taken up can be calculated from thermodynamic data if the probable oxidation products are known.

Several different cases may be distinguished:

(*a*) The free energy of formation of the oxide of the impurity is smaller than that for iron (e.g., NiO). In this case the alloying element will be inert and will have no influence on the oxygen absorption. Thus, the relatively high content

*See note added in proof, p. 101.

of Ni in iron A (0.08 per cent) has no significant effect.

(*b*) The impurity forms a pure oxide, not reducible by hydrogen at 1250°C. Such an element would undergo internal oxidation, but would not influence the measured oxidation absorption when that is measured by hydrogen reduction.

(*c*) The impurity forms a compound with FeO, for example, $FeO–Cr_2O_3$ (chromite), $FeO.Al_2O_3$ (hercynite), $2FeO.SiO_2$ (fayalite) $FeO.V_2O_3$. Such a compound could influence the apparent solubility since the FeO component would be reduced by hydrogen although the other component oxide would not.

(*d*) The impurity oxide forms a solid solution with FeO. This is probably the case with manganese, which forms FeO–MnO solutions. On reduction the oxygen would be recovered partially, but MnO is only slowly reduced.

It can be shown from the reaction isotherm that with a given $CO–CO_2$ mixture there is a critical concentration for each active impurity below which it would not undergo internal oxidation [8]. With Si, V, Ti, Al, etc., this critical concentration is so low that any detectable amount of the element present can be considered potentially available for internal oxidation.

With manganese, however, assuming ideality, the critical concentration is found to range from 0.018 to 0.054 per cent for the conditions used in the present experiments. Consequently, the manganese present in irons A, N, and Z would not react whereas that in X and Y could do so. It was apparent that a separate oxide phase did form, as it could be seen as a dull film with alloy X which under the microscope showed small crystals. Further, the amount of oxygen absorbed by alloy Y (Table 4) was of the right order of magnitude for that expected if FeO–MnO solid solutions were formed: the values are about half the theoretical maxima, but this is almost certainly due to the slowness of reduction of MnO by hydrogen.

Silicon is a significant impurity in all the irons used, ranging from 0.001 per cent in U to 0.014 per cent in A. Theoretically this could result in oxygen absorptions of 0.001 per cent to 0.016 per cent respectively. It is probable that the slightly high value obtained with A (0.004 per cent) is due to its higher level of impurities, but evidently at very low concentrations impurities such as silicon do not readily react to form the thermodynamically permissible phases. Probably nucleation is difficult when such minute quantities of oxidation product have to be formed at grain boundaries.

Conclusions

The solubility of oxygen in gamma iron has been measured as 0.003 ± 0.003 per cent, but the experimental evidence would be entirely compatible with an experimentally immeasurable value (<0.001 per cent) for absolutely pure iron, since all available irons contain impurities which could in theory account for the bulk of the small "apparent solubility." It is clear that true solubility is quite negligible for all practical purposes, but the absorption of oxygen by the process of internal oxidation of impurities is certain to be significant in all kinds of iron and steel used in practice.

The structural reason for the very low solubility of oxygen in iron is almost certainly a steric one. If oxygen in contact with iron is postulated to become O^{--}, this ion is certainly too large to enter the γ-iron lattice either interstitially or substitutionally, as the radius of the metallic iron in the gamma lattice is 1.26 Å; the octahedral holes are therefore $0.59 \times 1.26 = 0.74$ Å, whereas the radius of the O^{--} ion is 1.36 Å. On the other hand, Barrer [18] has suggested that in the known interstitial solid solutions of oxygen in silver, zirconium, titanium, and vanadium, the oxygen/metal radius ratios are compatible with interstitial solution (namely, 0.56, 0.50, 0.55, 0.60) if it is assumed that oxygen atoms occupy octahedral sites with a coordination number of 6 (radius 0.803 Å). This same radius, however, is still too large for oxygen to dissolve interstitially in iron or copper (radius ratio 0.63). The size factor therefore accounts for the vanishingly small solubility of oxygen in these metals. These conclusions suggest that the diffusion of oxygen in iron is probably intergranular.

Acknowledgements

We thank Dr. N. P. Allen of the National Physical Laboratory, Dr. Cleaves of the U.S. Bureau of Standards, and the British Iron and Steel Research Association for the specimens of high-purity iron employed in this work. We also thank the British Iron and Steel Research Association for research bursaries awarded to M. G. and J. W. E., and we are indebted to Dr. F. D. Richardson, Dr. J. Pearson and Mr. H. A. Sloman for valuable discussions.

References

1. See Briggs, C. W. Metallurgy of Steel Castings (New York, McGraw-Hill, 1946), p. 127, for a list of such claims.
2. Eastman, E. D. and Evans, R. M. J. Amer. Chem. Soc., **46** (1924) 888.
3. Matsubara, A. Z. anorg. Chem., **124** (1922) 39.
4. Sloman, H. A. J. Iron Steel Inst., **143** (1941) 295.
5. Evans, J. W. Ph.D. thesis, University of London (1951).

VOL
1
195

6. Steacie, E. W. R. and Johnson, F. M. G. Proc. Roy. Soc., **A112** (1926) 542.
7. Rhines, F. N. and Mathewson, C. H. Trans. A.I.M.E., **111** (1934) 337. Phillips, A. and Skinner, E. N. *Ibid.*, **143** (1941) 301 (T.P. 1280).
8. See Ph.D. theses, London, Gleiser, Molly and Evans, J. W. (1949, 1951).
9. Baker, W. A. Metallurgica, **40** (1949) 188.
10. Darken, L. S. and Gurry, R. W. J. Amer. Chem. Soc., **67** (1945) 1398; **68** (1946) 798.
11. Smith, R. P. J. Amer. Chem. Soc., **68** (1946) 1163.
12. Compare Peterson, H. Arch. für Eisenhüttenw., **3** (1929-30) 459.
13. Cleaves, H. E. J. U.S. Bur. Standards, **18** (1937) R.P. 996; **23** (1939) R.P. 1226.
14. Burgess, E. K. and Waltenburg, R. G. U.S. Bur. Standards Bulletin 11 (1915) 591.
15. Chipman, F. and Marshall, S. J. Amer. Chem. Soc., **62** (1940) 299.
16. Dünwald, H. and Wagner, C. Z. anorg. Chem., **199** (1931) 321.
17. See, for example, Metals Reference Book, C. J. Smithells, Ed. (London, Butterworth, 1949).
18. Barrer, R. M. Faraday Soc. Discussion, **4** (1948) 68.

Note Added in Proof

Dr. J. Pearson has informed the authors of some new work done by the metallographic method, which was reported at a recent meeting of La Societé Francaise de Métallurgie. The results for γ-iron were 0.029 per cent at 937°, 0.036 per cent at 950°, and 0.077 per cent at 1000° C. Such values, if not due to internal oxidation of impurities, must represent an entirely different phenomenon from that studied by the gas–metal equilibrium method described here. When massive iron is heated in contact with wüstite, it is to be expected that a film of oxide would spread, at temperatures far below its melting point, over the surface of the individual grains, and possibly also into the "sub-boundaries" and other imperfections that are known to exist in real metals (cf. Guinier, in "Imperfections in Nearly Perfect Crystals" (Ed. Shockley), John Wiley, 1952). This oxide film will be invisible (even to the electron microscope) and will therefore give a spurious "solubility" which will increase with rise of temperature owing to increased spreading pressure. This interpretation could be confirmed by parallel work on single crystals.

It follows, therefore, that the metallographic method will give high results, and is inherently unsuitable for studying homogeneous, thermodynamic solubility in metals for which other evidence indicates a very low true solubility.

LETTER TO THE EDITOR

Similar Glide Processes in Ionic and Metallic Crystals*

In a recent extensive study of the plastic deformation of single crystals of sodium chloride [1], certain features of the mechanism of deformation were observed which accounted for the particular shape of the strain-hardening curves. Use of the Schlieren technique [2] showed that deformation occurs at room temperature by a process of simple slip, similar to that in metals, on the (110) plane in the [110] direction, and not mainly or entirely by kinking as suggested by Orowan [3]. In the early stages of the deformation, where the mechanism is comparable with that of metal crystals, two basic types of strain-hardening curve were found, and using both the photo-elastic method of investigation, and the Schlieren technique, it was possible to account for the two types of curve.

On analysis, one type of curve was found to be accurately parabolic in shape and deformation occurred throughout by simultaneous slip on two mutually perpendicular systems. For systems of plane dislocations, intersecting at 90° as in this case, Heidenreich and Shockley [4] have shown that the shear stress required to move the one through the other is of the same order as the shear stress required to move dislocations of opposite sign past each other on nearby slip planes. An analogy can be drawn between this interpenetrant type of slip, where the number of slip planes increases in each system, and the square array of dislocations of opposite sign, pictured by Taylor [5] in his original dislocation theory of work-hardening. He showed that the shape of the hardening curve depended on the shape of the array built up during deformation, and for a square array he predicted a parabolic curve. In simultaneous double glide of the type found in sodium chloride, the stress centres are built up on a nearly square array of interpenetrating glide systems, and a parabolic curve is observed.

The second type of curve breaks sharply away below the parabola and becomes almost linear, as did the curves of Theile [6], and in this case the break in the curve coincided with the appearance of kink facets, and the cessation of glide on one of the two equally favoured systems. In sodium chloride, the planes of the inactive system become the kink planes because they are normal to the active system, and their spacing remains virtually constant throughout the deformation. The spacing of the glide planes of the active system decreases linearly with strain, and this, together with the experimentally observed constant amount of slip on each plane, accounts for the linear period of the strain-hardening curve.

To summarise, when sodium chloride deforms by double glide, that is by the simultaneous operation of two mutually perpendicular glide systems, a parabolic strain-hardening curve is found; whereas single glide gives an almost linear curve lying below that for double glide.

It is interesting to compare these strain-hardening curves with those of metallic single crystals where the deformation mechanism is supposedly the same. Crystals of the hexagonal metals of suitable orientation deform by means of a single glide system on the basal plane, with a linear strain-hardening curve up to 400 per cent extension, while the Laue spots remain sharp without the appearance of asterism. Furthermore, Röhm and Kochendörfer [7] have shown that when tested under conditions approximating to pure shear, where the end restraints were no longer effective, the hardening curve of single crystals of aluminium was linear, rather than parabolic, and asterisms were absent. The significant feature of their method of testing was that the ends of the specimen were free to rotate, during the deformation. While this eliminates the end restraints, a more important effect is that the crystal retains its original orientation with respect to the axis of straining. In normal tensile testing, the active glide system rotates towards the axis of straining during deformation, until another system is as favourably orientated and multiple glide can theoretically occur. In the pure shear experiments this rotation is eliminated, and glide on the single active system continues throughout the test. These two cases of a single glide system producing linear strain-hardening are comparable with the equivalent case of single glide in sodium chloride.

In the more general case of the deformation of face-centred cubic crystals by normal testing techniques, the shape of the hardening curve should be determined by the initial orientation of the crystal. There are twelve slip systems of the type (111) [110], and it can be seen that with the tension axis near the cube axis eight systems can operate; with the tension axis near [111] there are six possible systems, and near [110] four systems. With the crystal close to these orientations, multiple glide on two or more systems should occur from the beginning of deformation. The type of interaction to be

*Received October 2, 1952.

expected has been calculated by Lomer [8] who has shown that dislocations on different glide systems in the face-centred cubic lattice will attract one another, and combine to form a sessile dislocation which should influence the rate of hardening. The experimental evidence of Masing and Raffelsieper [9] on single crystals of superpure aluminium confirms this theoretical prediction. Single crystals having orientations near the [100] and [111] axis showed a steeply rising curve, which was more pronounced the closer the orientation was to the axes. A specimen which has the largest possible rotation and extension on a single glide system, before the onset of double glide, showed a linear curve lying below those for multiple glide, and specimens of intermediate orientation had a correspondingly shorter linear hardening period. A very recent paper by Lücke and Lange [10] provides further experimental confirmation of the effect of the initial orientation on the shape of the strain-hardening curve with pure materials. Their work is an extension of that of Masing and Raffelsieper on superpure aluminium to higher degrees of deformation, and their results are in good agreement with the earlier work. The increased rate of hardening observed where the glide systems interact may be compared directly with the parabolic hardening due to double glide in sodium chloride.

A full account of the work on sodium chloride is being prepared for publication, and I wish to thank the Director, Atomic Energy Research Establishment, Harwell, for permission to publish these extracts from A.E.R.E. Report M/R 883.

P. L. PRATT

Atomic Energy Research Establishment
Harwell, England

References

1. PRATT, P. L. Ph.D. thesis, Cambridge University, 1951.
2. LOMER, W. M. and PRATT, P. L. J. Inst. Metals, **80** (1952) 409.
3. OROWAN, E. Nature, **149** (1952) 643.
4. HEIDENREICH, R. D. and SHOCKLEY, W. Bristol Conference, Strength of Solids, 1948.
5. TAYLOR, G. I. Proc. Roy. Soc., **145** (1934) 362.
6. THEILE, W. Z. Physik, **75** (1932) 763.
7. RÖHM, E. and KOCHENDÖRFER, A. Z. Metallk., **41** (1950) 265.
8. LOMER, W. M. Phil. Mag., **42** (1951) 1327.
9. MASING, G. and RAFFELSIEPER, J. Z. Metallk., **41** (1950) 65.
10. LÜCKE, K. and LANGE, H. Z. Metallk., **43** (1952).

BOOK REVIEWS

Imperfections in Nearly Perfect Crystals. Edited by W. Shockley, J. H. Hollomon, R. Maurer, and F. Seitz. New York: John Wiley and Sons, Inc.; London: Chapman and Hall, Ltd. 1952. Pp. xii + 490. $7.50, £3.

In October, 1950 a conference was held at Pocono Manor, Pennsylvania, under the sponsorship of the U.S. National Research Council, to discuss the nature and properties of crystal imperfections. An outcome of the conference is the publication of this book, assembled by an editorial committee led by W. Shockley from the papers and discussions that were presented there.

The highly stimulating title, which reminds us that a crystal imperfection can be defined precisely if and only if it is surrounded by "good" crystal, and at the same time hints that the best way to study these imperfections experimentally is to work with nearly perfect crystals, presents a challenge which the authors of the seventeen articles in the book are not slow to take up. The first article, "Imperfections in Nearly Perfect Crystals: A Synthesis," by F. Seitz, is a monumental work in which the author's exceptionally wide knowledge of all kinds of crystal imperfections is directed towards the creation of a unified and all-embracing picture of the imperfect crystal. Perhaps this aim was a little too bold, and the task is at present an impossible one, for we do not at the moment possess a homogeneous theory capable of generating, from a single basic principle, information about all the various imperfections. Even so, the reader will find this authoritative survey of phonons, electron holes, excitons, vacant sites and interstitial atoms, foreign atoms, dislocations—and even such birds of passage as neutrons, photons, and charged radiations—most valuable and interesting.

Provided one is content to deal with only the geometrical properties of imperfections a unified treatment may be possible, and the ideal tool for this is topology, since the persistence of crystal imperfections through purely elastic deformations corresponds precisely with that of topological features during topological transformations. One can imagine that the topology of crystal imperfections may soon become a favourite subject in the pure mathematics seminar. Dislocations are ideally suited for this kind of treatment, as W. T. Read and W. Shockley show so clearly in their article "On the Geometry of Dislocations," which deals with such topics as the definition of a nearly perfect crystal, the concept of the Burgers circuit, and the kinematic properties of dislocations. The applications of topology are not limited to dislocations and, in his article "Interphase Interfaces," C. S. Smith shows how topological arguments can be used to discuss the manner in which lattices with different structures, orientations, and spacings can be joined together at an interface. These ideas may be important in connection with diffusionless transformations, a subject that is discussed from a more experimental standpoint by C. S. Barrett in his article "Imperfections from Transformation and Deformation." The author's development of an X-ray technique for the detection and analysis of stacking faults is a particularly important contribution.

Also important is another X-ray method described by B. E. Warren and B. L. Averbach in their article "X-Ray Diffraction Studies of Cold Work in Metals," which contains a very clear account of the Fourier analysis of reflections from cold-worked metal, an analysis which, as W. T. Read and W. Shockley point out in their discussion of the paper, goes far to prove that the cold-worked state consists of a substantially uniform distribution of dislocations. In his review of "Experimental Information on Slip Lines," W. T. Read presents the interesting spectacle of a theoretical physicist giving the most straightforward of accounts of experimental facts, and refusing completely to be drawn regarding their theoretical implications. This paper is a useful introduction to the article by N. F. Mott, "Mechanical Strength and Creep in Metals," which describes recent theories, mainly developed in England, of hardening in solid solutions, of the yield phenomenon, and of exhaustion creep. A new and simplified calculation of alloy hardening, which gives a result different from that of the earlier theory, is a valuable feature of the paper. A further analysis of solid solution hardening is made by J. S. Koehler in his paper "The Influence of Dislocations and Impurities on the Damping and Elastic Constants of Metal Single Crystals." This describes an original piece of work by the author on the motion of edge dislocations, which are pinned down by occasional solute atoms, under the action of a periodic external stress. Some discrepancies appear when the theory is compared with experimental measurements on copper, and the suggestion is made that

the distribution of solute atoms may not be random in practice, some segregation to dislocations or precipitation having taken place.

These are the only two papers dealing specifically with the mechanical strength of imperfect crystals, and one might perhaps wish for more on this important branch of the subject. By contrast, the topics of diffusion and crystal boundaries are discussed very thoroughly in a series of papers. On the experimental side the articles by R. G. Breckenridge on "Relaxation Effects in Ionic Crystals," and L. Apker and E. Taft, on "Studies of Alkali Halides by Photoelectric Methods," go far towards clarifying the complex interactions that take place between electrons, vacant sites, and foreign atoms in these crystals. On the theoretical side, J. Bardeen and C. Herring in an article "Diffusion in Alloys and the Kirkendall Effect" give a very thorough thermodynamic treatment of diffusion in binary alloys, which uses two diffusion coefficients, one for each component, and make an interesting deduction about the relation between radioactive and chemical diffusion coefficients. The article by C. Zener on "Theory of Diffusion" contains a brilliant assortment of new ideas, including an explanation of why the heat of activation is measured correctly experimentally even when it varies with temperature, and arguments to justify diffusion mechanisms other than that involving the movement of vacant sites.

The papers on crystal boundaries dovetail into one another neatly. That by C. S. Smith has already been mentioned. Writing on "Surface and Interfacial Tensions of Single-Phase Solids," J. C. Fisher and C. G. Dunn present a most valuable tabulation of experimental data and discuss critically the main methods for measuring these quantities. This experimental work is of course vital to the theory which W. T. Read and W. Shockley develop in their article "Dislocation Models of Grain Boundaries." Besides giving a new and simple derivation of their famous energy formula, they show that the absolute value of the boundary energy for copper, as given by dislocation theory, is within 15 per cent of the experimental value. Finally, A. Guinier's account of "Substructures in Crystals" is an excellent survey of the recent investigations in which the French school has played such a distinguished part, while the articles by B. Chalmers on "The Properties and Effects of Grain Boundaries" and R. Smoluchowski on "Movement and Diffusion Phenomena in Grain Boundaries" provide very useful accounts of the properties of large-angle boundaries, especially their mobility.

It is a well-known fact, in these days of superabundant scientific publications, that one cannot possibly afford the time to read original work unless it happens to strike at the centre of one's own interests. Many solutions have been sought to this problem. Textbooks do not succeed here, partly because they have another job to do, while monographs are usually as time-consuming as the original papers. Single reviews are useful, but generally cover either only a part of the field of interest, or all of it at an insufficiently advanced level. The present solution, to publish a set of articles by experts, mostly at a level between that of a review and an original paper, and tightly disciplined by a commanding title, is an excellent one.

A. H. Cottrell

Diffusion in Solids, Liquids, Gases. By W. Jost. New York: Academic Press Inc. 1952. Pp. 558. $12.00. (In English.)

Over the past twenty-five years the topic of diffusion, particularly in solids, has received great stimulus from carefully written survey volumes. Unlike the situation in many other fields, the quality of the reviews in the field of diffusion has been sufficiently high that the publications have had a strong tendency to consolidate the topic. Perhaps this is the result of the fact that the subject has had the attention of an excellent group of physical chemists immersed in the best European traditions in thermodynamics. In any case, the reviewers have usually subordinated any personal biases they might possess to the subject—an attitude that is lacking in a number of fields of interest to those concerned with the development of solid state theory.

The present book, written by an investigator who has had long experience in the field, is another volume in the sequence of good surveys. Those of us who read Jost's *Diffusion und chemische Reaktion in festen Stoffen* (Leipzig-Dresden, 1937) so avidly in the mid-thirties, for all the stimulation it offered, have looked forward to this book and have not found it disappointing. The new volume is much more concentrated in some respects: the topic of diffusion has grown so large that the writer has felt it advisable to restrict his attention primarily to it rather than to include much detail concerning chemical reactions in solids. However, he calls attention to other books by authors such as Cohn,

Fricke, Hüttig and Hedvall in the fields touched only lightly. By way of compensation, he has added important chapters on diffusion in liquid and gaseous systems and on thermal diffusion.

Perhaps the range of topics treated in the volume is indicated best by listing the chapter headings:

I. The Fundamental Laws of Diffusion
II. Disorder in Crystals
III. Theory of Diffusion in Solids
IV. Electrolytic Conduction and Diffusion in Ionic Crystals
V. Diffusion in Metals and Non-Polar Crystals
VI. Solubility in Solids
VII. Permeation and Diffusion of Gases in Solids
VIII. Mobility of Ions in Solid and Molten Metals and Alloys
IX. Surface Reactions of Metals, Formation of Protective Layers and Related Reactions
X. Diffusion in Gases
XI. Diffusion in Liquids
XII. Thermal Diffusion

The author has attempted successfully to combine in each chapter both the specialized and generalized features of the topic, thereby making the book useful to the experienced investigator who desires a standardized treatment of the topic, to the amateur who desires a general survey of the topic, and to the student who desires to learn the fundamentals in a thorough-going professional way. A person in any one of these categories will find the volume highly profitable.

In perusing the pages the reviewer found it exceedingly difficult to discover items which might form the basis of any adverse comments on those subjects with which he is familiar. The only serious omissions he could discover were on topics which are undergoing rapid changes as a result of research carried out in the last two years. Such lapses are impossible to avoid in a rapidly developing field and the writer has cut them to a minimum, first, by revising the text until the manuscript went to proof and, second, by including an addendum at the end of the book which contains a chapter by chapter presentation of important papers which appeared after it was no longer possible to revise the manuscript. Among papers which fall in this category are those dealing with grain boundary diffusion in metals, repetitions of the older measurements of Seith and his co-workers (e.g. antimony in silver) for which new D_0 values and activation energies have been obtained, and Zener's theory of D_0. From one point of view the existence of topics and papers of this kind indicates only that the field is an exciting one at the present stage of development and that the volume will have an important place within this development.

The terminal chapter on thermal diffusion in solids represents one of the first good reviews of this topic in English during recent years of which the reviewer is aware. Again, the reviewer feels that Jost has done an important service to the field of diffusion by presenting this topic from the general viewpoint adopted in the volume.

To summarize: the reviewer finds it very easy to give a strong recommendation for this volume for it represents another landmark in the development of the subject of diffusion. Anyone interested in the topic will find it exceedingly valuable to have at hand, both for general reading and as a handy reference book for the extensive research that has been carried out in the field.

F. SEITZ

SOME CURRENT PAPERS IN OTHER JOURNALS

Boletim da Associação Brasileira de Metais, Vol. 8

No. 28, 1952

The Soderberg electrodes and their influence on the design of electric reduction furnaces. Dr. M. O. Sem.

Foundry paints. Eng. Carlos Dias Brosch.

Generalities on the diffusion phenomenon. Eng. Dr. Luiz C. Corrêa da Silva.

The electrolytic zinc plant, Companhia Brasileira de Zinco, Utinga, São Paulo, and the problems of zinc production in Brazil. Eng. Dr. Francisco Somló.

Elimination of low contents of arsenic and antimony in lead by a modification of the Harris process. Eng. Tharcisio D. de Souza Santos.

Preliminary study on the kinetics of the modified Harris process for the elimination of low contents of arsenic and antimony in dezincified lead. Eng. Tharcisio D. de Souza Santos.

Preliminary note on the formation of an alloy of high content in zinc and silver, by liquation of Parkes crusts. Eng. Tharcisio D. de Souza Santos.

Experiments on the distillation of zinc-silver alloys of low lead content, in cast iron retorts under vacuum. Eng. Tharcisio D. de Souza Santos, Eng. Dr. Luiz C. Correa da Silva and Engdo. José Martini.

No. 29, 1952

Metallurgy as a factor of development of a nation. Eng. José Ermirio de Moraes. (8th Annual Lecture.)

Some recent progresses in lead refining metallurgy. Eng. Tharcisio D. de Souza Santos. (8th Annual Scientific Lecture.)

Estimate of iron ore reserves in Brazil. Prof. Dr. Luciano Jacques de Moraes.

Instituto del Hierro Y del Acero, Año 5

Número 4, Octubre-Diciembre, 1952

Emple e influencia de la electricidad en el desarrollo de los procesos metalúrgicos. Otto Barth.

Estudio de la nitruración de aceros. Lamberto A. Rubio Felipe.

Influencia de las inclusiones no metálicas sobre la calidad de los aceros nacionales. Justo Ferrer Flotats.

Determinación del tamano de grano austenítico de los aceros. Por la Sección Local de Aplicaciones Industriales de los Productos Siderúrgicos en Barcelona. del I.H.A.

Coloquio sobre la producción de arrabio. Georg Bulle.

Sobre la determinación potenciométrica del molibdeno en aceros. Fernando Burriel Marti y Ramón Suarez Acosta.

La "cifra de pérdidas" en los aceros al silicio: Influencia de la estructura, de los tratamientos mecánicos y térmicos y de algunos otros factores. (II parte). Miguel de P. Andres Sanz.

Investigaciones internacionales sobre el horno bajo. Por el Comité Directivo Del Comité Internacional de Investigaciones del Horno Bajo.

Examen de las teorías modernas de laminación desde el punto de vista práctico. (continuación). N. H. Polakowky. Extracto de "Sheet Metal Industries" Octubre, 1951.

Influencia del cromado electrolítico sobre el límite de fatiga de los aceros empleados en aeronáutica. Hugh L. Logan. Extracto de Revue de Métallurgie, Marzo, 1951.

Aceros para temple a la llama; por inducción y por inmersión. Hermann Voss. Extracto del Stahl und Eisen, 27 Septiembre, 1951.

Número Especial, Octubre, 1952

Obtensión de arrabio en los hornos eléctricos de reducción. Hermann Walde.

Estudio de algunos minerales españoles desde el punto de vista de su composición química. Manuel Salis Martinez, Luis Barron del Real, José de Figueras y Figueras y Emilio Charro Sanchez.

Algunas consideraciones acerca del comportamiento de los materiales metálicos a bajas temperaturas. Manuel Torrado Varela.

Cincuenta años de progreso en siderurgia (1900–1950). Georges Delbart.

Número Especial, Noviembre, 1952

La estabilización de la austenita por envejecimiento. Andre Michel.

Instalación de control térmico para un horno alto y la interpretación de los resultados obtenidos. Heinz Berg.

Estudio sobre la resistencia estática de la fundición de hierro. José Navarro Alcacer.

Pulido electrolítico. I. bibliografía (año 1931 a 1950). José Antonio Boned Sopena y José M Bermudez de Castro.

Metalurgia de los materiales magnéticos. Ramón de Lucas y Enrique Yuste.

La fase α del sistema hierro-carbono. Francisco Munoz del Corral.

Journal of Applied Physics, Vol. 23

October, 1952 (Partial Contents)

The effect of internal strains on linear expansion, x-ray lattice constant and density of crystals. P. H. Miller, Jr., and B. R. Russell.

Phase changes in silver-tin amalgams (letter). J. C. Moffett, G. Ryge, and A. G. Barker.

Journal of the Chemical Society

November, 1952 (Partial Contents)

Some structural properties of α-MnO_2 containing NH_4^+, K^+, Na^+, Ca^{++}, and Ba^{++} ions. K. H. Maxwell, G. Butler and H. R. Thirsk.

Some aspects of the solution chemistry of zirconium. B. A. J. Lister and (Miss) L. A. McDonald.

Separation of the lanthanons by ion exchange. A comparison of eluants. R. C. Vickery.

December, 1952 (Partial Contents)

A study of the supercooling of drops of some molecular liquids. D. G. Thomas and L. A. K. Staveley.

Studies on bond type in certain cobalt complexes. Part III. The polarographic reduction of some cobalt inner-complex compounds. J. R. Urwin and B. West.

The effects of crystal fields on the properties of transition-metal ions. L. E. Orgel.

A new reagent for the determination of antimony. R. Belcher and D. Gibbons.
The separation of the lanthanons with the aid of ethylenediaminetetra-acetic acid ("Enta Acid"). Part IV. Sodium lanthanon sulphate precipitation from sodium lanthanon enta solution. J. K. Marsh.
The magnetic susceptibility of urania-thoria solid solutions. J. K. Dawson and M. W. Lister.

Journal of the Institute of Metals, Vol. 81

November, 1952
Twenty-third autumn lecture: On the foot-hills of the plastic range. H. W. Swift.
The embrittlement of copper-antimony alloys at low temperatures. D. McLean.
The gold-platinum system. A. S. Darling, R. A. Mintern, and J. C. Chaston.
Crystal slip in aluminium during creep. D. McLean.
The viscosity of aluminium and binary aluminium alloys. W. R. D. Jones and W. L. Bartlett.
Plastic deformation of coarse-grained aluminium. (Mrs.) V. M. Urie and H. L. Wain.
Direct examination of solid surfaces using a commercial electron microscope in reflection. J. W. Menter.

December, 1952
A study of order-disorder and precipitation phenomena in nickel-chromium alloys. A. Taylor and K. G. Hinton.
Deformation of magnesium at various rates and temperatures. J. W. Suiter and W. A. Wood.
The effect of certain solute elements on the recrystallization of copper. V. A. Phillips and Arthur Phillips.
Equilibrium relations at 460° C. in aluminium-rich alloys containing 0–7% copper, 0–7% magnesium, and 1.2% silicon. H. J. Axon.
The sub-grain structure in aluminium deformed at elevated temperatures. J. A. Ramsay.
An example of strain-relief in powder specimens. J. Gordon Parr.

January, 1953
High-temperature oxidation characteristics of a group of oxidation-resistant copper-base alloys. J. P. Dennison and A. Preece.
A method of determining orientations in aluminium single crystals and polycrystalline aggregates. G. E. G. Tucker and P. C. Murphy.
Creep at 250° and 300° C. of some magnesium alloys containing cerium. G. A. Mellor and R. W. Ridley.
New values of the coefficient of equivalence for manganese, iron, cobalt, and nickel in copper-zinc alloys. J. B. Haworth.
The effect of minor additions on the age-hardening properties of a high-purity lead-antimony alloy. L. M. T. Hopkin and C. J. Thwaites.
The effect of cold work on the microstructure and corrosion-resistance of aluminium–5% magnesium alloys containing 0–1% zinc. P. Brenner and G. J. Metcalfe.

Journal of the Iron and Steel Institute

November, 1952 (Partial Contents)
A thermal and microscopic study of the iron-carbon-silicon system. J. E. Hilliard and W. S. Owen.
Speed-dependent variables in cold strip rolling. R. B. Sims and D. F. Arthur.
Studies in the deoxidation of iron; deoxidation by silicon. E. Ll. Evans and H. A. Sloman.
Effect of quench ageing on strain ageing in iron. A. H. Cottrell and G. M. Leak.
The formation of bainite. T. Ko and S. A. Cottrell.

Journal of the Mechanics and Physics of Solids, Vol. 1

No. 1, October, 1952
Plastic instability under plane stress. H. W. Swift.
On discontinuous plastic states, with special reference to localized necking in thin sheets. R. Hill.
Calculations on the influence of friction and die geometry in sheet drawing. A. P. Green and R. Hill.
Rheology of metals at elevated temperatures. A. E. Johnson and N. E. Frost.
The time laws of creep. A. H. Cottrell.
The yield phenomenon in polycrystalline mild steel. W. M. Lomer.

Journal of Metals, Vol. 4

No. 11, November, 1952 (Partial Contents)
Electrolytic zinc plant at Monsanto, Ill. T. I. Moore and L. A. Painter.
An aid for making stereographic plots when working with cubic crystals. Colman Goldberg.
Sampling of liquid steel for dissolved oxygen. G. F. Hutt, G. R. Bailey, and J. H. Richards.

No. 12, December, 1952 (Partial Contents)
Production of spiegeleisen from open hearth slag in an experimental blast furnace. R. C. Buehl and M. B. Royer.
Production of high manganese slags by selective oxidation of spiegeleisen. M. B. Royer and R. C. Buehl.
Lead blast furnace gas handling and dust collection. R. Bainbridge.
Liquidus surface of the Fe-S-O system. D. C. Hilty and W. Crafts.
Determination of oxygen in iron in the presence of sulphur by the vacuum-fusion method. H. L. Hamner and R. M. Fowler.
Nature of the line markings in titanium and alpha titanium alloys. C. M. Craighead, G. A. Lenning and R. I. Jaffee.
Thermodynamic properties of solid nickel-gold alloys. L. L. Seigle, M. Cohen and B. L. Averbach.
Microconstituents in chromium base chromium-iron-molybdenum alloys and their behavior with heat treatment. J. R. Hammond, A. B. Westerman and H. C. Cross.
Effect of a prequench on the martensite reaction in tool steel. J. A. Gilman.
Relative diffusion rates of zinc and copper in alpha brass. R. W. Balluffi and B. H. Alexander.
Modifications of an X-ray method for the measurement of retained austenite concentrations in hardened steels. K. E. Beu.
Increase of high magnetostriction by magnetic anneal. H. E. Stauss and G. Sandoz.
Structure and crystallography of second order twins in copper. M. Sharp and C. G. Dunn.

Physical Review, Vol. 88

November, 1952 (Partial Contents)

The scattering of slow neutrons in polycrystalline media. R. W. GURNEY.

Electron diffraction from small crystals. C. R. BERRY.

Revue de Métallurgie, 49e Année

Numéro 10, octobre, 1952

Influence du phosphore présent dans les rontes à graphite sphéroïdal. M. GRANDPIERRE et H. DE BOUVIER.

Étude de la structure et des propriétés de la pellicule de protoxyde de fer formée sur la surface du fer de très haute pureté. R. COLLONGUES et G. CHAUDRON.

Nouvelles recherches microcinématographiques sur la déformation et la rupture de l'acier. G. A. HOMÈS et J. GOUZOU.

Contrôle des alliages légers par radiographie. Sur quelques difficultés d'interprétation des clichés. G. GAUTHIER et M. RENOUARD.

La transformation ordre-désordre dans les alliages ternaires. E. JOSSO.

Quelques caractéristiques du mecanisme du frittage. G. C. KUCZYNSKI.

Détermination de quelques éléments peu abondants dans les minerais de fer de Lorraine. J. AUBRY, G. TURPIN et G. LAPLACE.

Recherches internationales sur le bas fourneau. Comité Directeur du Comité International de Recherches sur le Bas Fourneau.

Étude hydrodynamique sur modèles réduits et à l'échelle grandeur nature des mouvements du bain au convertisseur de fonte. P. LEROY.

Numéro 11, novembre, 1952

Les aliages industriels à base d'aluminium. J. HÉRENGUEL.

L'industrie du cobalt dans le Haut-Katanga. G. DESBRIÈRE.

Les déformations localisées en traction simple et leurs rôles dans la formation de la striction. P. BASTIEN, A. POPOFF et P. AZOU.

Observations sur la tenue en atmosphère marine d'alliages légers et d'assemblages hétérogènes. A. GUILHAUDIS.

Contribution à l'étude des métaux pyrophoriques. L'oxydation du cérium et de l'uranium (première partie). J. LORIERS.

Fonctionnement des fours métallurgiques de réduction en "marche sans air." L. POTTECHER.

Contribution à la stabilisation de l'austénite. J. PLATEAU, J. DUFLOT et CH. CRUSSARD.

Transactions of the Indian Institute of Metals, Vol. 5

Developments in blast furnace design. S. K. NANAVATI and P. K. CHATTERJEE.

Pig iron smelting without metallurgical coke. W. E. KREBS and D. JAGAT RAM.

Study of exogenous inclusions in bottom poured acid steel. N. R. KRISHNASWAMY.

Methods of wire production. Mr. K. V. AIYER.

Effect of titanium in steel. PARVEZ MEHTA.

Transformations in steels—isothermal and during continuous cooling. Dr. G. P. CONTRACTOR and Dr. V. G. PARANJPE.

Bainite reactions in steels. Dr. V. G. PARANJPE and D. D. KAUSHAL.

Equilibrium relations in iron-nitrogen system. V. G. PARANJPE and MORRIS COHEN.

The structure of cold worked steels. E. G. RAMACHANDRAN.

Interaction of hydrogen with white cast iron. P. C. GHOSH and B. CHATTERJEE.

Theories of graphite formation in modular cast iron. M. N. PARTHASARATHI, B. S. SRIKANTIAH, and B. R. NIJHAWAN.

Hardness and work-hardenability of metals and alloys. G. P. CHATTERJEE.

Rate of work-hardening of some aluminium-copper alloys. G. P. CHATTERJEE, K. C. SHOME, and R. GANGULY.

Sintering characteristics of iron-zinc powder blends. A. A. KRISHNAN.

Development of a new self-coated corrosion resistant porous body. A. A. KRISHNAN.

The influence of wear products in accelerating wear. M. S. MITRA and L. R. VAIDYANATHAN.

Studies on pin-holes in aluminium. G. P. CHATTERJEE, K. C. SHOME, and R. GANGULY.

Recovery of copper from scraps. T. BANERJEE and D. S. TANDON.

A NEW METHOD FOR DETERMINING THE HEAT OF ACTIVATION FOR RELAXATION PROCESSES*

C. WERT and J. MARX†

A straight line relationship is shown between the heat of activation of a relaxation process and the temperature at which the maximum relaxation occurs. The utility of this relationship is pointed out as being the following: (1) a quick way of finding the heat of activation from a single measurement, (2) a means of helping to locate the position of a relaxation peak if its activation energy is known roughly from some other measurement, (3) an aid in analyzing mathematically the factors which describe a given phenomena.

UNE NOUVELLE MÉTHODE POUR LA DÉTERMINATION DE LA CHALEUR D'ACTIVATION DANS LES PROCESSUS DE RELAXATION

Il est montré, qu'une relation linéaire existe entre la chaleur d'activation du processus de relaxation et la température à laquelle a lieu le maximum de relaxation. L'utilité de cette relation est due au fait qu'elle fournit: (1) un moyen rapide de trouver la chaleur d'activation d'après une seule mesure, (2) un moyen de localiser la position d'un maximum de relaxation, si son énergie d'activation est connue approximativement comme résultat de quelque autre mesure, (3) une aide dans l'analyse mathématique des facteurs qui décrivent un phénomène donné.

EINE NEUE METHODE ZUR BESTIMMUNG DER AKTIVIERUNGSWÄRME VON RELAXATIONSVORGÄNGEN

Es wird gezeigt, dass ein linearer Zusammenhang zwischen der Aktivierungswärme eines Relaxationsvorganges und der Temperatur, bei der dieser Vorgang von statten geht, besteht. Der praktische Wert dieser Beziehung besteht in folgendem: Sie gibt (1) einen schnellen Weg, die Aktivierungswärme aus einer einzigen Messung zu ermitteln, (2) eine Methode, die Lage eines Relaxationsmaximums zu finden, wenn der ungefähre Wert der Aktivierungsenergie aus anderen Messungen bekannt ist, und (3) ein Hilfsmittel, die verschiedenen Faktoren, die einen bestimmten Effekt ausmachen, mathematisch zu analysieren.

Introduction

There have been reported in the literature some ten or more relaxation peaks in metals. With the exception of those due to flow of heat, they are probably all caused in one way or another by local diffusion of atoms. It would be desirable, both for the better understanding of the relaxations and for the greater ease of finding new relaxations, to systematize the data wherever possible. One instance of a useful arrangement of some of the data is given in this paper.

Data and Analysis

For some time we have been aware that for a given frequency the position of a relaxation peak in temperature is higher the higher the heat of activation of the relaxation. This seemed to hold true for all types of relaxations which depend on temperature exponentially in $1/T$. Indeed, if a plot be made of all the data now available, the relationship between activation energy and T is seen to be much more than a trend. In Figure 1, data are shown at 1 c.p.s. and 37 kc. for all relaxation peaks in the literature or otherwise known to the authors. The points for 1 c.p.s. (which are up to this time much more numerous for any other frequency) show pretty clearly that a straight line relationship exists between the activation energy, ΔH, and the temperature of the peak. Furthermore, this line comes close to passing through the origin. The two points for 37 kc. also define a straight line passing close to the origin.

Two pieces of data which fit poorly on these curves are data for grain boundary relaxation in α-brass and grain boundary relaxation in α-iron. The first, point K in Figure 1, is some 4 kilocalories too low. The second, the grain boundary peak in α-iron is some 35 kilocalories too high. This peak, which Kê found at 760°K at one cycle, has a ΔH, as indicated by this curve, of about 50 kg-cal/mol., compared to the 85 kg-cal/mol. which he measured. It is not impossible that the discrepancy may represent an error in measurement, and we intend to recheck this point as soon as possible.

If the empirical relationship indicated in Figure 1 is substantiated, even for a single type of relaxation process, it should prove quite useful in future measurements. From it one could apparently estimate the heat of activation rather closely by observing a single relaxation peak at some commonly used measuring frequency, probably with an accuracy of 5 per cent or better. This procedure may prove to be as accurate as the commonly employed method of observing the temperature shift of the

*Received September 11, 1952.
†Department of Mining and Metallurgical Engineering, University of Illinois, Urbana, Illinois.

relaxation maxima with a change in measuring frequency. The device should be employed with caution, of course, since the particular relaxation investigated may show a real deviation from this relationship.

These data, shown in Figure 1, indicate a remarkable similarity in the relaxation processes. This

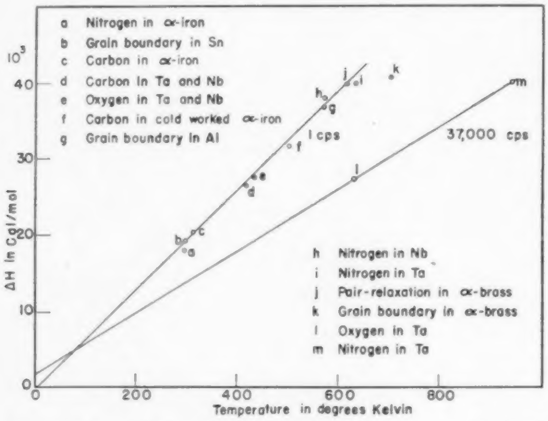

FIGURE 1. The heat of activation of a relaxation is plotted as a function of the temperature at which the peak relaxation occurs. All the data are taken from the literature or from our own data (to be published).

might be expected for a particular type of relaxation, such as interstitial migration in b.c.c. lattices, but it is surprising to find it existing between the various relaxations, some of which involve substitutional diffusion in close packed lattices.

A theoretical basis for the relationship is readily obtained for a given model. Using the migration of interstitials in b.c.c. lattices as an example, we can say that the mean time-of-stay (τ) of an interstitial atom in a given position is determined by the condition

$$(1) \qquad \frac{1}{\tau} = n\nu \exp(\Delta S/R) \exp(-\Delta H/Rt) .$$

Here n is the number of elementary diffusion paths (4 in this case), ν is the interstitial atomic frequency, ΔS is the entropy of activation, and ΔH the heat of activation. ν might be expected to vary somewhat for different alloy systems, but not by more than a factor of two. This variation, for the present calculation, is overwhelmed by the exponential terms, and nothing of significance is lost by taking the best average value of ν as 1.2×10^{13} c.p.s. τ is related to the relaxation time τ_r by the expression

$$(2) \qquad \tau = 3/2\tau_r = (3/2)\,(1/2\pi f_m) ,$$

where f_m is the frequency of the applied stress, or the measuring frequency, employed at the temperature at which the internal friction maxima is observed. From this analysis it follows that

$$(3) \qquad \Delta H = RT \ln(\nu/f_m) + T\Delta S .$$

The linear relationship shown by the data in Figure 1 then appears to indicate that the entropy changes are approximately the same for all the processes which fit the curve. In Figure 2 this equation is plotted (dashed lines) for several values of ΔS, with the experimental curve (solid line) included for reference. In view of the arbitrary choice of atomic frequency ν, the entropy changes cannot be regarded as of great significance except on an order of magnitude basis. Experiment and theory in this case

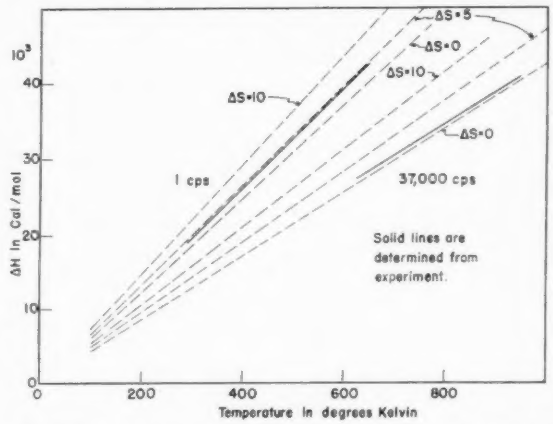

FIGURE 2. ΔH as a function of T for various values of ΔS.

indicate an entropy increase of more than one and less than five cal/mol-degree.

The theory of absolute reaction rates, as developed by Eyring and others, may also be applied to the processes described here. The resulting expression for ΔH is obtained by merely substituting kT/h for the atomic frequency constant ν in equation (3). This yields

$$(4) \qquad \Delta H = RT \ln(kT/hf_m) + T\Delta S .$$

Over the temperature range 100°K to 1000°K the curvature of this quantity is so slight that it can be made to fit the data of Figure 1 about as well as the straight line. Above 1200°K, however, equation (4) departs noticeably from linearity. It is suggested that measurement of some of the larger activation energy phenomena at increased frequencies will yield relaxation peaks above 1200°K and thus serve to distinguish between equations (3) and (4). Relaxation phenomena below 100°K might similarly serve to discriminate.

The ΔS values agree in magnitude with those obtained by other measurements for the migration

of interstitial impurities in b.c.c. lattices. The interpretation of grain boundary and substitutional pair relaxations is more difficult because the mechanism is not as well defined. However, both equations (3) and (4), together with the empirical curve of Figure 1, seem to accommodate these relaxations despite the differing mechanisms.

This work was supported by the Office of Ordnance Research.

Note Added in Proof

Dr. L. Jaffee has pointed out that the activation energy for the grain boundary relaxation in α-iron has been measured by Mr. W. West to be 51 Kcal/mol. [Trans. A.I.M.E., **167** (1946) 192]. This value fits well the curve in Figure 1, if we presume Kê's value of peak position to be correct.

THE ENERGY STORED DURING THE COLD WORKING OF A GOLD-SILVER ALLOY*

M. B. BEVER† and L. B. TICKNOR‡

Strips of an alloy of 75 wt. per cent gold and 25 wt. per cent silver were cold worked by rolling. The stored energy was released by dissolution of the samples in liquid tin and found calorimetrically by comparison with annealed samples. The total energy expended in rolling was determined from a stress-strain diagram applicable to the rolling process.

The stored energy increases with the strain, but shows a tendency toward saturation at high strains. The ratio of the stored energy to the total energy expended decreases at high strains.

L'ÉNERGIE ACCUMULÉE PENDANT L'ÉCROUISSAGE D'UN ALLIAGE OR-ARGENT

D'étroites lamelles d'un alliage de 75 pour cent en poids d'or et de 25 pour cent en poids d'argent, ont été écrouis par laminage. L'énergie accumulée a été libérée par dissolution des échantillons recuits. L'énergie totale dépensée lors du laminage a été déterminée d'un diagramme tension-déformation applicable au laminage.

L'énergie accumulée augmente avec la déformation, mais montre une tendance à la saturation aux grandes déformations. Le rapport de l'énergie accumulée à l'énergie totale dépensée diminue quand les déformations deviennent importantes.

DIE WÄHREND DER KALTBEARBEITUNG EINER GOLD-SILBER-LEGIERUNG GESPEICHERTE ENERGIE

Bänder einer Legierung von 75 Gew. prozent Gold und 25 Gew. prozent Silber wurden durch Walzen kalt verformt. Die aufgespeicherte Energie wurde durch Auflösen der Proben in flüssigem Zinn frei gemacht und kalorimetrisch durch Vergleich mit geglühten Proben bestimmt. Die gesamte während des Walzens aufgewandte Energie wurde aus der auf den Walzvorgang anwendbaren Verzerrungs-Spannungs-Kurve bestimmt.

Die aufgespeicherte Energie wächst mit wachsender Verzerrung, zeigt jedoch eine deutliche Tendenz zur Absättigung bei grossen Verzerrungen. Das Verhältnis der aufgespeicherten Energie zur gesamten aufgewandten Energie nimmt bei grösseren Verzerrungen ab.

Introduction

A metal retains part of the energy expended during plastic deformation, if the deformation is carried out in the temperature range of cold working. This stored energy, sometimes referred to as the latent energy of cold work, manifests itself by the increased solution potential of cold worked metal and by its tendency toward recovery and recrystallization. Measurements of the energy stored by metals during cold working under various conditions have been published, but extensive and systematic investigations are still needed for a better understanding of the energetics of cold working. This subject is of special interest because it may contribute to the interpretation of the mechanism of deformation and of strain hardening in terms of the dislocation theory. Correlation of X-ray diffraction measurements on cold worked metals with detailed data on the energy stored by them is also very desirable.

Review of Previous Work

The methods by which the energy stored during cold working has been measured fall into two categories: simultaneous methods and two-step methods. In the simultaneous methods, the energy expended in the deformation process and the energy dissipated as heat are measured directly and the difference is regarded as the retained energy. In the two-step methods, the metal is first deformed, with or without measurement of the total energy expended, and the stored energy is then evolved and measured; this evolution of the stored energy may be induced by annealing or may be incidental to a process such as dissolution.

In the earliest experiments by a simultaneous method, Hort [1] carried out tensile tests in a calorimeter; he determined the total work expended from the stress-strain curve and the heat dissipated from calorimetric measurements. Farren and Taylor [2] made tensile tests and measured the temperature rise of the specimens under nearly adiabatic conditions without the use of a calorimeter vessel. The same principle was employed by Masima and Sachs [3] in a few exploratory experiments. Rosenhain and Stott [4] placed a wire drawing die in a calorimeter; they encountered difficulties in their mechanical and calorimetric measurements. Maier and Anderson [5] also made energy measurements on the wire drawing process in a calorimeter. In order to produce large amounts of total work, Taylor and Quinney [6] used

*Received September 26, 1952.

†Department of Metallurgy, Massachusetts Institute of Technology.

‡Division of Industrial Cooperation, Massachusetts Institute of Technology.

torsion and compression; initially they determined the heat dissipated by measuring the adiabatic temperature rise of the specimen, but later they used a calorimeter into which the specimen was dropped immediately after working. Simultaneous measurements are also involved in the work of Epifanov and Rebinder [7], who determined an energy balance for a metal cutting process and arrived at a value for the energy retained by the chips. Mention should be made of calorimetric measurements during mechanical tests carried out by Giraud [8], which led to excessively high results, presumably because of a faulty calorimetric technique.

A distinct group among the applications of the two-step method consists of experiments in which the retained energy of cold work is evolved by annealing. Sato [9] cold worked specimens by torsion and obtained differential heating curves for cold worked and annealed samples; his method is accurate if the rate of heat transfer from specimens of the same shape is independent of the nature of the material and of accidental differences in manipulation. Quinney and Taylor [10] questioned this assumption and developed a method of thermal analysis involving only the assumption that the heat transfer remains unchanged in two successive heatings of a single specimen. They made two runs for each cold worked sample; in the first the stored energy was released and the second run served as a standard. The specimens, which had been worked in torsion, were heated internally. Suzuki [11] determined stored energies of cold work from heat capacity measurements on specimens strained in compression and on an annealed specimen. Bockstiegel and Lücke [12] used three different experimental arrangements to obtain heating curves for very highly deformed thin copper wires. Welber [13] reported the use of a refined application of the method of Quinney and Taylor.

Methods other than annealing have been used for evolving the stored energy. Smith [14] measured the heat of solution of annealed and cold worked samples in an aqueous solvent. In this method which was also used by France [15] the retained energy is superimposed on the ordinary heat of solution and is found as the difference between the heat effects of dissolving cold worked and annealed samples. In Smith's work this difference was only about one per cent of the heat effects measured. Koref and Wolff [16] concluded that the stored energy in cold worked tungsten could not be measured by a heat of solution method and van Liempt [17] came to the same conclusion for a method based on the differences in the heats of combustion of cold worked and annealed tungsten.

Differences in electrochemical potentials of cold worked and annealed metals measured by Spring [18] were evaluated by Desch [19], who questioned the accuracy of the resulting energy values. The literature also contains several reports of attempts to find a difference in the heat capacities of cold worked and annealed metal samples; these attempts produced negative or inconclusive results [20; 21; 22].

Some conclusions can be drawn concerning the merits of the methods which have been used for determining the energy stored during cold working. Since the stored energy is usually less than 10 per cent of the total energy expended in the deformation, all simultaneous methods attempt to measure a quantity which is the difference between two relatively much larger quantities. This inherent limitation casts considerable doubt on the advisability of further work by simultaneous methods. Among the two-step methods, evolution of the stored energy by annealing has probably given the best results to date. This method depends on the difference between the heating curves of a cold worked and an annealed sample, which may introduce some extraneous effects. This method becomes more difficult with small or finely subdivided samples; it seems doubtful whether the method can be modified so as to allow measurements starting below room temperature. The two-step methods which are based on the difference in the heat of solution and similar thermochemical measurements have in the past been used with heat effects which were large and thus the quantity to be measured was a small difference of large quantities. It will be shown, however, that this feature is not inherent in these methods. Finally, measurements of differences in electrical potential between cold worked and annealed samples seem to be without promise for measuring the stored energy of cold work.

The correlation of published results is complicated by the fact that different investigators used different metals and cold worked them by various processes and to varying degrees. The published results for copper, which has been investigated most often, are collated in Table I as an example. Most of the published results for other metals are of the order of 1–2 cal/gram, which amounts to approximately 10 per cent of the work done.

Sato [9] and Taylor and Quinney [6] found that the stored energy as a function of the amount of cold work in copper tends to a maximum or saturation

value. The results of Suzuki [11], which cover true strains up to a value of 0.9, do not show such a trend.

A review of the measurements of the stored energy of cold work has been published by Burgers [23]. The literature also contains speculative accounts of this subject [24; 25; 26]. The stored energy has been interpreted in terms of the dislocation theory [27] and of X-ray evidence [28; 29; 30].

TABLE I

MEASURED VALUES OF THE ENERGY STORED BY COPPER DURING COLD WORKING

Investigators	Method of Working	Work done (cal/gram)	Stored energy (cal/gram)	Per cent stored
Farren	Extension		0.076	9.5
and Taylor			0.52	8.0
Smith			10.5	
Sato	Torsion	4.2	0.18	
		18.1	0.32	
Rosenhain and Stott	Wire drawing	7.4	0.23	3.1
Maier and Anderson	Wire drawing		0.23	10 ±
Taylor	Torsion	0.2	0.02	10.0
and Quinney		14.1	1.15	
Quinney	Torsion	4.6		7.0
and Taylor		5.6	0.5	9.0
Suzuki	Compression		(0.05)	30.0
			(0.8)	13.0
Bockstiegel	Wire drawing		2.7	
and Lücke	Torsion		1.0	
Welber	Torsion	8.2		2.8
		11.9		3.4

Note. Some of the values listed required conversion to the basis of this table. Where two values are quoted, they are the lowest and highest values reported by the investigators. The value of Maier and Anderson is an average.

Experimental Procedure

The method used to obtain the results reported here is essentially the same as that previously announced by the authors [31]. This method involves a calorimetric determination of the heat effect associated with the dissolution of annealed and cold worked specimens in a liquid metallic solvent. The use of a metal as solvent eliminates several of the difficulties encountered with aqueous solvents, such as some side reactions and volatilization, but the major advantage results from the small heat of solution in most metallic systems. The method does not necessitate the evaluation of the heats of solution, but is based only on the difference in the total heat effects associated with bringing cold worked and annealed solute samples from a reference temperature to the dissolved state. This heat effect is the sum of the heat of solution and the difference in heat contents of the solute at the reference temperature and at the temperature of the solution, and in the following it will be referred to as the "heat effect." In favorable cases, this heat effect is very small and the contribution due to the stored energy of cold work is a large part of the measured quantity.

Since calorimetry becomes more difficult and less accurate with increasing temperature, it is desirable to use low-melting metals as solvents. The solubility of the solute, however, must be great enough so that an adequate amount of sample can be added. In the experiments reported here liquid tin was chosen as the solvent. Heat of solution measurements had shown that the dissolution of gold in tin is exothermic and that of silver endothermic. An alloy of 75 wt. per cent gold and 25 wt. per cent silver was found to have a heat of solution in tin at 240°C which is approximately equal to the heat necessary to bring the alloy from 0°C to 240°C; the over-all heat effect of an addition of the alloy to tin, therefore, was very small.

The equipment previously used for the measurement of heats of solution of group IB metals in tin [32] was used with minor modifications and only a brief description will be given here. The isothermal calorimeter consisted of a long-necked glass Dewar flask immersed in a constant-temperature salt bath. The neck admitted thermocouple leads and a stirrer and also allowed the introduction of solute samples under vacuum. When necessary, a confining atmosphere of argon was employed. The solute samples were held at 0°C before injection into the liquid tin. The temperature of the salt was regulated to ± 0.02°C; the temperature of the tin under steady conditions varied less than 0.01°C. During a run the temperature of the metal bath was read to about 0.005°C.

The gold-silver alloy was obtained in the form of strip, 0.6 inch wide and 0.030 inch thick, and was rolled with a large number of passes through rolls of $2\frac{1}{4}$ inch diameter with palm oil as a lubricant. The width-to-thickness ratio of the original strip was chosen as twenty-to-one so as to reduce lateral spread during rolling. The maximum spread observed was about 0.05 inch or less than 10 per cent. Thus the decrease in thickness was converted mostly into an increase in length. After rolling, the

metal was cleaned and cut into pieces of convenient size. A portion of the sample was then annealed.

In each run 500 grams of tin were used and annealed and cold worked samples were added in succession; an addition of tungsten was made for calibration. In each of Runs 25–29, three 4-gram additions of annealed metal and three 4-gram additions of cold worked metal were made alternately. In each of Runs 30, 31 and 33 a single 12-gram addition of annealed metal and a single 12-gram addition of cold worked metal were made. The temperature of the tin was close to 240°C and all results were corrected to that temperature.

Following the injection of a sample, the thermocouple e.m.f. was read as a function of time. When the alloy entered the metal bath, the temperature dropped because of the heat required for raising the alloy from 0°C to 240°C. Then the temperature rose again owing to the exothermic dissolution of the alloy. The maximum temperature change occurred about 15 seconds after insertion of the sample and was from $\frac{1}{2}$ to $1\frac{1}{2}$°C depending on the size of the sample. The time required for complete dissolution was about one minute. After dissolution of the alloy the temperature change was usually less than 0.1°C. The calorimeter then began its slow exponential return to the original temperature.

The heat effect of each addition was calculated in the manner previously described [32], but it was not necessary to calculate the heat of solution. The stored energy of cold work was obtained directly from the heat effects resulting from additions of annealed and cold worked samples. Each value of the retained energy reported here was based on measurements made in a single run instead of in two runs as in the preliminary work [31].

The heat effect for adding samples in the same physical condition in the dilute range covered was found to be a linear function of the composition of the resulting solution, provided all samples were of equal size. For each of the five Runs 25–29, two straight lines could be drawn through the three annealed and the three cold worked additions, respectively. The slopes of these ten lines were obtained by the method of least squares; the values averaged − 36 with an average deviation of 3.5. Since these slopes should have the same value, the average value of − 36 cal/g-atom per at. per cent of solute was used with the three points belonging to each line. The retained energy of cold working for a run was obtained from the vertical distance between the line for the annealed and the line for the cold worked additions. In Runs 30, 31 and 33 each of the two lines was obtained from the value of a single addition of 12 grams and the average slope of − 36 cal/g-atom per at. per cent of solute.

The Evaluation of the Total Energy Expended

The total energy expended in deforming a specimen can be determined from the area under a stress-strain curve. Ford [33] has shown that a stress-strain diagram applicable to the rolling process can be constructed from tensile tests on specimens of strip which have previously been rolled to varying degrees. The yield stress for the rolling of metal without lateral spread has been estimated to be 15 per cent larger than that obtained in tensile tests [33].

Tensile tests were made on pieces of rectangular cross section cut from the central third of rolled strip. These test specimens were about 0.18 in. wide and their thickness varied from 0.0024 in. to 0.0145 in.; the length between gauge marks was about 2 in. A small hand-operated tensile machine and a strain ring fitted with strain gauges were used; the extensions were followed with a cathetometer. It was observed that necking did not occur until just prior to fracture. The true tensile stress was obtained upon the assumption that the total volume of the metal did not change during the test. The true tensile strain was calculated as the natural logarithm of the length divided by the initial length, $\ln(l/l_0)$. The stress-strain curves for various specimens of rolled strip are shown in Figure 1. The tests were

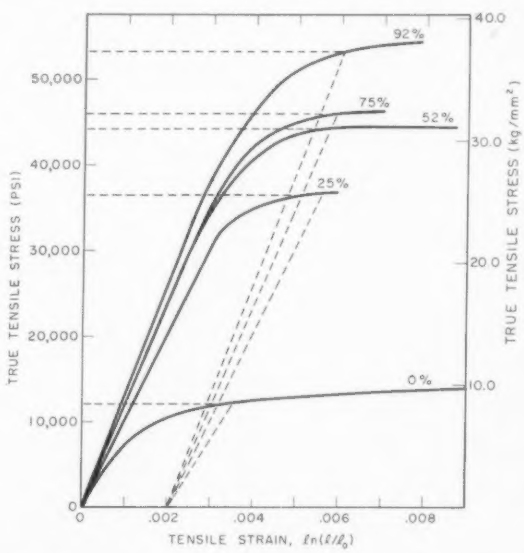

FIGURE 1. Stress-strain curves in tension for specimens previously reduced by rolling. Figures on curves indicate percentage reductions. 0.2 per cent offset lines are indicated by dotted lines.

carried to fracture except for the specimen which had not been rolled. The stress for the 0.2 per cent offset (inelastic elongation) was adopted as the yield stress.

Ford assumes that the rolling strain and the tensile strain are additive. On this approximate basis, the total strain of a tensile specimen which has been reduced previously by rolling from thickness t_0 to t is expressed as

$$\text{total strain} = \ln(t_0/t) + \ln(l/l_0)$$

If the tensile stress is plotted against this total strain for each specimen and a curve drawn through the values of the yield stress, the resulting curve, shown in Figure 2, is the approximate yield stress in

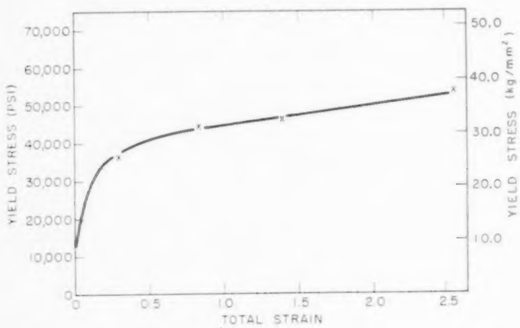

FIGURE 2. Yield stress in tension vs. total strain.

tension for the metal as a function of its total deformation by rolling and extension. The initial part of this curve is obtained from the values of the tensile stress for the specimen which was not rolled.

TABLE II

MEASURED VALUES OF STORED ENERGY OF COLD WORKING

Run No.	Percent reduction in thickness	Rolling strain	Rolling energy (cal/g-atom)	Stored energy (cal/g-atom)	Per cent energy stored
29	16	0.171	74	3	4.1
33	27	0.313	175	9	5.1
27	37.7	0.474	300	15	5.0
28	56.6	0.834	585	29	5.0
31	65.6	1.065	770	20	2.6
25	75	1.386	1040	21	2.0
26	92	2.526	2010	27	1.3
*30	83	1.790	1410	43	3.0

*Defective rolls.

The areas under this curve were found for the rolling strains specified in Table II and the resulting values were increased by 15 per cent as mentioned above; these data are given in Table II as the total energy of rolling in calories per gram-atom. This method of evaluating the energy expended gives values which can be expected to be accurate within 10 per cent.

Discussion of Results

The values of the stored energy of cold work and other pertinent data are given in Table II. In Figure 3 the stored energy is plotted as a function of the extent of deformation.

The points for individual additions in Runs 25–29 deviated by 7 cal/g-atom on the average from the average lines used for finding the stored energy.

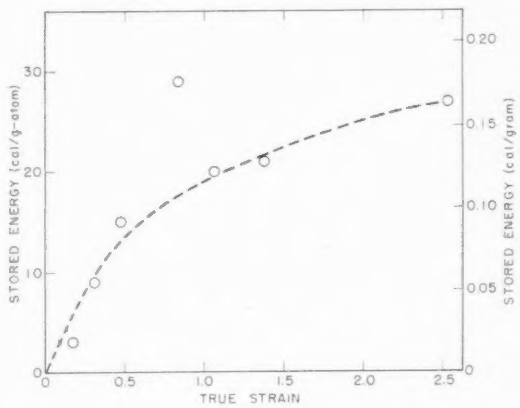

FIGURE 3. Energy stored during cold working vs. strain.

The potentiometer was read to the nearest 0.5 microvolt, equivalent to an uncertainty in the energy value of $\pm$ 8 cal/g-atom. A total uncertainty of $\pm$ 10 cal/g-atom may be assigned to these values. In Runs 30, 31 and 33 each addition was three times as large as in the previous five runs and the uncertainty due to the potentiometer reading was reduced to one-third; this reduction in the uncertainty, however, was offset by the reduction in the number of readings and an uncertainty of $\pm$ 10 cal/g-atom is again assigned. In considering the sources of error, it is important to recognize that by adding cold worked and annealed samples in a single run rather than in two separate runs, the effects of accidental variations between runs were eliminated.

The surface of the rolls had been damaged prior to Run 30. This caused a greater localized strain than measured by reduction in thickness. The rolls were replaced before Run 31.

Run 24, which is not included in Table II, differed from the other runs principally in the manner of rolling. Alloy wire of 0.032 in. diameter was cooled in liquid nitrogen between passes through the rolls. The energy of cold working retained by this sample was measured as 65 cal/g-atom. This increase in the

energy stored during cold work with decreasing temperature may be expected.

The values reported here may also be compared with the preliminary measurements reported previously [31], which had been made on the same alloy without determining the extent of deformation. The average of these previous measurements was 46 cal/g-atom; this high value may be attributed to the severe deformation involved in rolling a wire into flat strip.

The variation of the stored energy with the extent of deformation is of special interest. In Figure 3, in which the retained energy is plotted as a function of true strain, a tendency to level off is evident. Correspondingly, in Table II the value of the energy stored as a percentage of the work done, although at first almost constant at 4–5 per cent, decreases markedly at large strains. These results indicate that the stored energy is approaching a maximum or saturation value.

In addition to the values of stored energy, the experiments also yielded values of the heat of solution of the annealed gold-silver alloy in tin at infinite dilution and 240°C, which are listed in Table III. These values give an average of − 1326 cal/g-atom added, and a standard deviation of 11 cal/g-atom, compared to a value of − 1320 cal/g-atom previously reported on the basis of different measurements [32]. It should be noted that the variation in the values of the heat of solution, which are based on different runs, are not a measure of the uncertainty of the stored energy determinations. The new average heat of solution and the average slope already discussed yield the following equation for the integral heat of solution of the alloy at 240°C:

$$\Delta H = -1326 - 18x$$

where ΔH is in cal/g-atom of alloy added and x is the composition of the resulting solution expressed in at. per cent of alloy.

In an evaluation of the method of determining the stored energy of cold working by dissolution in a metallic solvent, important limitations are evident. For some metals no suitable solvents are available; in other solute-solvent combinations the heat effect may be too large for satisfactory accuracy. Also the method requires thin specimens for a sufficiently fast rate of dissolution. Among the advantages is the possibility of attaining considerable accuracy under favorable conditions. In some applications it may be desirable to use small quantities of samples as permitted by this method; the suitability of fine samples can also be an advantage as, for example, when working with metal chips. The method also probably lends itself to energy measurements starting at sub-atmospheric temperatures on samples cold worked at such temperatures. Finally, the method can be adapted to other latent energy measurements and thus promises to be of fairly general applicability.

TABLE III

HEAT OF SOLUTION OF ALLOY IN TIN AT INFINITE DILUTION AND 240°C

Run No.	ΔH cal/g-atom
25	− 1316
26	− 1342
27	− 1324
28	− 1313
29	− 1325
30	− 1317
31	− 1328
33	− 1345
Average	− 1326
Standard deviation	11

Summary

An alloy containing 75 wt. per cent gold and 25 wt. per cent silver was cold worked by rolling samples of strip. The energy stored in these samples was determined calorimetrically as the difference in the small heat effects associated with bringing cold worked and annealed samples of the alloy from 0°C into solution in liquid tin at 240°C. The values of the energy ranged from 3 cal/g-atom (0.02 cal/g. of alloy) for a strain of 0.17 to 27 cal/g-atom (0.16 cal/g.) for a strain of 2.53. One measurement was also made on a sample of wire which had been rolled severely at sub-atmospheric temperature; a value of the stored energy of 65 cal/g-atom (0.40 cal/g.) was found.

A stress-strain diagram for rolling was derived from tensile tests on strips that had previously been rolled to various amounts. The total plastic strain energy expended in rolling was found from this diagram. The measured values of the stored energy were expressed as fractions of this total energy. These fractions ranged from 4–5 per cent for small strains to 2 per cent or less for large strains. The results suggest an approach with increasing strains to a maximum or saturation value of the stored energy.

The experiments also yielded values of the heat of solution of the alloy containing 75 wt. per cent

gold and 25 wt. per cent silver in tin at 240°C. Eight determinations gave an average of -1326 cal/g-atom of alloy with a standard deviation of 11 cal/g-atom as the heat of solution of the alloy at infinite dilution in liquid tin at 240°C; the integral heat of solution as a function of the composition x in at. per cent of the alloy in the resulting solution in tin was $\Delta H = -1326 - 18x$.

Acknowledgments

The authors wish to acknowledge their great indebtedness to Professors John Chipman and Carl Wagner. Sincere thanks are also due to Professors W. A. Backofen and E. R. Marshall. The assistance of P. A. Clarkin and F. X. Spinelli in carrying out some of the tensile tests is gratefully acknowledged. The work was performed under Contract No. AT-30-GEN-1002 with the AEC.

References

1. Hort, H. Z. Ver. Deut. Ing., **50** (1906) 1831; Mitt. Forsch. Geb. Ing., **41** (1907) 1.
2. Farren, W. S. and Taylor, G. I. Proc. Roy. Soc. (London), **107A** (1925) 422.
3. Masima, M. and Sachs, G. Z. Physik, **56** (1929) 394.
4. Rosenhain, W. and Stott, V. H. Proc. Roy. Soc. (London), **140A** (1933) 9.
5. Maier, C. G. and Anderson, C. T. J. Chem. Phys., **2** (1934) 513.
6. Taylor, G. I. and Quinney, H. Proc. Roy. Soc. (London), **143A** (1934) 307.
7. Epifanov, G. I. and Rebinder, P. A. Dokl. Akad. Nauk SSSR, **66** (1949) 653.
8. Giraud, R. Rev. Mét., **25** (1928) 347.
9. Sato, S. Sci. Rep. Tôhoku Imp. Univ., **20** (1931) 140.
10. Quinney, H. and Taylor, G. I. Proc. Roy. Soc. (London), **163A** (1937) 157.
11. Suzuki, T. Sci. Rep. Res. Inst. Tôhoku Univ., **1A** (1949) 193.
12. Bockstiegel, G. and Lücke, K. Z. f. Metallkunde, **42** (1951) 225.
13. Welber, B. Phys. Rev., **87** (1952) 211A.
14. Smith, C. J. Proc. Roy. Soc. (London), **125A** (1929) 619.
15. France, R. W. Trans. Faraday Soc., **30** (1934) 450.
16. Koref, F. and Wolff, H. Z. Electrochem., **28** (1922) 477.
17. van Liempt, J. A. M. Z. anorg. allg. Chem., **129** (1923) 263.
18. Spring, W. Bull. Acad. Roy. Belg., **41** (1903) 1066.
19. Desch, C. H. Proc. Roy. Soc. (London), **125A** (1929) 628.
20. Levin, M. and Schottky, H. Ferrum, **10** (1913) 193.
21. Chappell, C. and Levin, M. Ferrum, **10** (1913) 271.
22. Gaudino, M. Rend. Accad. Sci. fis. mat. Napoli, **35** (1930) 204.
23. Burgers, W. G. in G. Masing, *Handbuch der Metallphysik* (Akademische Verlagsgesellschaft, Leipzig, 1941), III, 2, p. 96 ff.
24. Mazzoleni, F. Met. Ital., **33** (1941) 390, 423; *ibid.*, **34** (1942) 348.
25. Podszus, E. Z. f. Metallkunde, **41** (1950) 23.
26. Russel, T. F. J. Iron and Steel Inst., **57** (1923) 497.
27. Koehler, J. S. Phys. Rev., **59** (1941) 943A; *ibid.*, **60** (1941) 397; Amer. J. Phys., **10** (1942) 275.
28. Seitz, F. and Read, T. A. J. Appl. Phys., **12** (1941) 100, 170, 470, 538.
29. Haworth, F. E. Phys. Rev., **52** (1937) 613.
30. Masing, G. Z. f. Metallkunde, **35** (1943) 56.
31. Bever, M. B. and Ticknor, L. B. J. Appl. Phys., **22** (1951) 1297.
32. Ticknor, L. B. and Bever, M. B. J. Metals, **4** (1952) 941.
33. Ford, H. Sheet Metal Industries, **26** (1949) 2109.

ACTIVATION ENERGIES AND DIFFUSION COEFFICIENTS OF OXYGEN AND NITROGEN IN NIOBIUM AND TANTALUM*

C. Y. ANG†

With the use of the torsional pendulum method of internal friction measurement, the heats of activation for diffusion of O_2 and N_2 in Nb were found to be 27.6 and 38.6 Kcal/mol., respectively. For O_2 and N_2 in Ta the corresponding values of 27.3 and 39.8 Kcal/mol. were determined by the low frequency method coupled with a new high frequency technique.

The theoretical diffusion coefficient curves for these systems were obtained from the relationship between heats of activation and the calculated diffusion coefficient constants. An agreement, closer than before, between the experimental and theoretical values of entropy of activation was obtained from an analysis of this thermodynamic property important in the theory of D_0.

LES ÉNERGIES D'ACTIVATION ET LES COEFFICIENTS DE DIFFUSION DE L'OXYGÈNE ET DE L'AZOTE DANS LE NIOBIUM ET LE TANTALE

En employant la méthode du pendule de torsion, la même que celle utilisée dans les mesures de frottement interne, il a été trouvé, que les chaleurs d'activation pour la diffusion de l' O_2 et le N_2 dans le Nb étaient respectivement de 27,6 et 38,6 Kcal/mol. Pour l' O_2 et le N_2 dans le Ta les valeurs correspondantes de 27,3 et 39,8 Kcal/mol ont été déterminées par la méthode de basse fréquence jointe à une nouvelle technique de haute fréquence.

Les courbes théoriques des coefficients de diffusion pour ces systèmes ont été obtenues de la relation entre les chaleurs d'activation et les constantes de coefficients de diffusion calculées. Un meilleur accord qu'avant, entre les valeurs expérimentale et théorique de l'entropie d'activation a été obtenu de l'analyse de cette propriété thermodynamique importante dans la théorie de D_0.

AKTIVIERUNGSENERGIEN UND DIFFUSIONSKOEFFIZIENTEN VON SAURSTOFF UND STICKSTOFF IN NIOB UND TANTAL

Die Aktivierungswärme von Diffusion von O_2 und H_2 in Nb wurden zu 27,6 Kcal/mol. und 28,6 Kcal/mol. aus Messungen der inneren Reibung mit Hilfe eines Torsionspendels bestimmt. Die entsprechenden Werte für O_2 und H_2 in Ta wurden mit der Niederfrequenzmethode und einer neu entwickelten Hochfrequenzmethode zu 27,3 und 39,8 Kcal/mol. bestimmt.

Die theoretische Kurve der Diffusionskoeffizienten wurde für diese Systeme aus der Beziehung zwischen den Aktivierungswärmen und den berechneten Konstanten der Diffusionskoeffizienten gewonnen.

Eine Analyse der Aktivierungsentropie führte zu einer besser als bisher gefundenen Übereinstimmung der theoretischen und experimentellen Werte dieser für die Theorie der D_0 wichtigen thermodynamischen Eigenschaft.

Introduction

The anelasticity of interstitial atoms in b.c.c. lattices offers a convenient way of measuring diffusion coefficients of these atoms. These coefficients are usually expressed in terms of a constant, D_0, and a heat of activation ΔH, by the relationship

$$D = D_0\, e^{-\Delta H/RT}. \tag{1}$$

It is possible to get values of ΔH accurate to 5 per cent by using the earlier technique described in numerous articles [1; 2]. But such accuracy is not sufficient when one wishes to test Zener's theory for D_0 [3] because the calculated values of this constant would have a spread of about a factor of 5. With great care, however, and with the use of a wide range in the frequency of measurement, the inaccuracy in ΔH may be cut to about one per cent with a resulting inaccuracy in D_0 by a factor of less than 2. This paper presents new experimental data on diffusion of O_2 and N_2 in Nb and Ta, and calculated values of ΔH and D_0, together with a brief analysis of the entropies of activation for these systems.

Experimental Procedure and Data

The measurements of the diffusion coefficients of O_2 and N_2 in Nb were made using a conventional torsional pendulum with the specimen in the form of a wire. This specimen had been heated for 10 minutes at 1500°C in an atmosphere of NH_3 at 15″ of Hg, and then for 3 minutes at 2000°C in a vacuum of approximately 10^{-4} mm. of Hg before quenching in vacuo. The positions in temperature of the peaks for these two impurities were determined at two frequencies. These data are presented in Figure 1. Using the expression

$$\Delta H = \frac{R \ln (f_2/f_1)}{1/T_1 - 1/T_2}, \tag{2}$$

the heats of activation are calculated to be 27,600 and 38,600 cal/mol. for O_2 and N_2, respectively. These values are believed to be accurate to 2 per cent.

In the case of O_2 and N_2 in Ta, the measurements of their diffusion coefficients were made by a com-

*Received October 27, 1952.

†Department of Mining and Metallurgical Engineering, University of Illinois, Urbana, Illinois.

bination of the above method and a new high frequency technique. The low frequency measurement was made at 1.433 c.p.s. with the peaks occurring at 155°C and 360°C for O_2 and N_2, respectively. The high frequency measurement

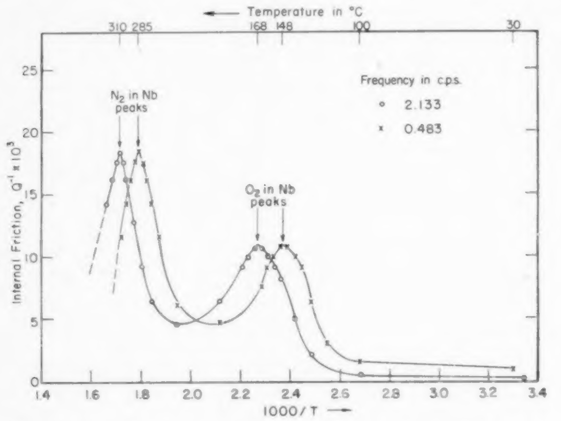

FIGURE 1. Internal friction curves for Nb containing O_2 and N_2.

(described in the following paragraph) was carried out at a frequency of 37,000 c.p.s., and in this case the O_2 peak occurred at 355°C, whereas the N_2 peak was observed to be at 662°C.

The technique of this high frequency method will be described in detail in a paper now being written by J. Marx and G. Baker. In brief, it consists of using a quartz resonator to excite longitudinal oscillations in a Ta sample. The frequency and damping are measured by associated electrical measuring equipment. Instead of the solid metal rod commonly used in this method a Ta foil rolled into a compact pencil-like rod of a proper length was used as specimen. The advantage of using this type of specimen over the solid rod lies in the greater ease of heat treatment for the loading of O_2 and N_2. The Ta foil used here had been annealed for 4 hours at 850°C in a vacuum of 10^{-6} mm. of Hg.

The values of ΔH computed in this case are 27,300 and 39,800 cal/mol. for O_2 and N_2, respectively. Here, an accuracy of about one per cent is realized because of the wide range in frequency of measurements.

Calculation of Diffusion Coefficients

Geometrically, interstitial diffusion in cubic lattices is simple and has been discussed in detail earlier [3]. The diffusion coefficient for the interstitial atoms in a b.c.c. lattice may be expressed as

$$D = \pi a^2 f / 18 , \tag{3}$$

where a is the lattice parameter and f is the frequency at which the internal friction is a maximum. Equating equations (1) and (3) one arrives at an expression for D_0 as follows:

$$D_0 = 0.1745\, a^2 f e^{\Delta H / RT_f}, \tag{4}$$

where T_f is the temperature at which the internal friction peak occurs when the frequency of oscillation is f.

The values of D_0 for O_2 and N_2 in Nb and Ta, computed from our values of ΔH, are given in Table I, and they are considered to be accurate to

TABLE I

DIFFUSION DATA FOR INTERSTITIAL ATOMS IN BCC LATTICES

System	C in α-Fe	N_2 in α-Fe	C in Ta	N_2 in Ta	O_2 in Ta	C in Nb	N_2 in Nb	O_2 in Nb
D_0 (cm./sec.)	.020	.030	.015	.012	.019	.015	.098	.015
$\nu(10^{13}$/sec.)*	1.30	1.15	1.31	1.48	1.15	1.31	1.45	1.15
β†	.43	.43	.40	.40	.40	.40	.40	.40
ΔH (Kcal/mol.)	20.10	18.20	27.00	39.80	27.30	27.00	38.60	27.60
$\Delta S/R$ (Theor.)	2.38	2.16	1.65	2.44	1.67	2.01	2.87	2.06
$\Delta S/R$ (Exp.)	2.41	0.64	1.84	1.53	2.21	1.84	3.62	1.95

*This vibration frequency is calculated from the expression [3]

$$\nu = (E/2m\lambda^2)^{\frac{1}{2}}$$

where E is the heat of activation in ergs, m is the mass of the interstitial atom, and λ is the distance between the interstitial positions, or, in b.c.c. lattice, $\frac{1}{2}$ the lattice parameter.

†Value for Nb has not been determined but is assumed to be the same as that for Ta since the two elements have many similar properties.

within a factor of 2. The diffusion coefficient curves for the four sets of data, drawn according to equation (1), are presented in Figure 2. One thing which is

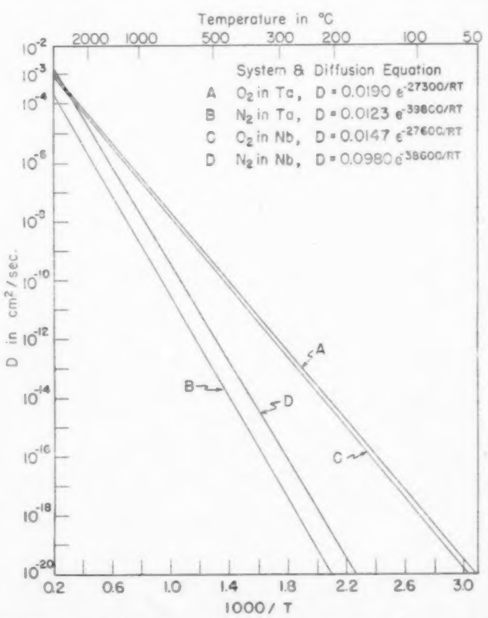

FIGURE 2. Diffusion coefficient curves for O_2 and N_2 in Nb and Ta.

rather striking is that all values of D_0 presented in Table I are about the same to within a factor of 2, except the values for N_2 in α-Fe and N_2 in Nb.

Analysis of the Entropy of Activation

From these experimental values of D_0, one may calculate the entropy of activation ΔS, for atomic diffusion in b.c.c. lattices, by applying Zener's condition

$$D_0 = (1/6)\ (a^2\ \nu\ e^{\Delta S/R}), \tag{5}$$

where ν is the frequency of oscillation of the solute atom in the interstitial site. This atomic frequency

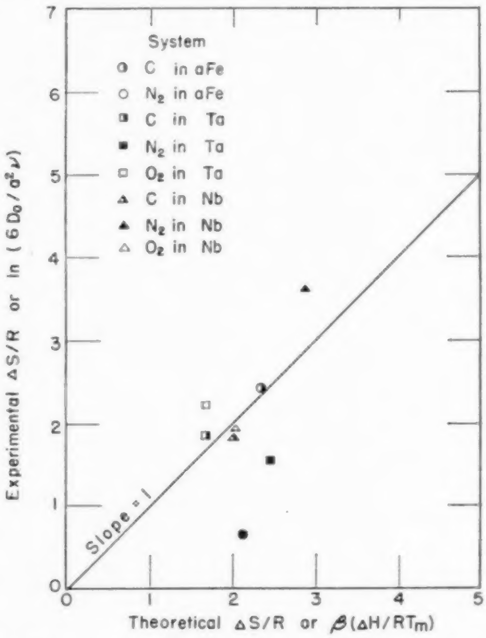

FIGURE 3. Theoretical $\Delta S/R$ *versus* experimental $\Delta S/R$.

varies only slightly, never more than a factor of 2, for different alloy systems. Since it is obvious from equation (5) that the main uncertainty in the value of D_0 lies in the exponential quantity, the importance of this entropy of activation cannot be neglected.

If one assumes that all the energy of activation goes into straining the lattice, then the entropy of activation may also be obtained from the theoretical approximation

$$\Delta S = \beta(\Delta H/T_m), \tag{6}$$

where T_m is the melting temperature of the metal and β is a quantity which has different values for different materials.

Following the argument presented by Wert in his article on atomic diffusion, and taking some of his data [2; 4], a revised plot of experimental against theoretical values of $\Delta S/R$ is shown in Figure 3. All the essential data relevant to the subject matter of this paper and to this plot in particular are tabulated in Table I. It is apparent that better values of D_0 have produced a closer agreement between experimental and theoretical values of $\Delta S/R$ than that in the earlier presentation.

Acknowledgment

The author wishes to express gratitude to Dr. J. Marx and Mr. G. Baker for the permission to use their relaxation data on O_2 and N_2 in Ta at high frequency. Thanks are especially due Dr. C. Wert for reviewing this manuscript and offering valuable suggestions.

This work was supported by the Office of Ordnance Research.

References

1. Kê, T. S. Phys. Rev., **74** (1948) 9.
2. Wert, C. Phys. Rev., **79** (1950) 601.
3. Wert, C. and Zener, C. Phys. Rev., **76** (1949) 1169.
4. Wert, C. J. Appl. Phys., **21** (1950) 1196.

YIELD POINTS IN ALUMINIUM ALLOY SINGLE CRYSTALS*

R. E. SMALLMAN,† G. K. WILLIAMSON,† and G. ARDLEY‡

Experiments have been made to compare the tensile behaviour of some aluminium alloy single crystals which contained copper, zinc, or hydrogen, with that of superpure aluminium crystals. Sharp yield points were observed in all the alloys when tested at liquid air temperature, but the superpure crystals showed no capacity for producing a yield point. These results are discussed from the standpoint of the dislocation theory of the yield point.

LES LIMITES D'ÉCOULEMENT DANS DES MONOCRISTAUX D'ALLIAGES D'ALUMINIUM

Des essais ont été faits en vue de comparer le comportement lors de la traction, de monocristaux d'alliages d'aluminium contenant du cuivre et du zinc ou de l'hydrogène, avec des cristaux d'aluminium très pur. Des limites d'écoulement bien prononcées furent observées dans tous les alliages essayés à la température de l'air liquide, alors que les cristaux d'aluminium très pur n'ont montré aucune tendance à la formation d'une limite d'écoulement. Ces résultats sont discutés en prenant comme base la théorie des dislocations de la limite d'écoulement.

ELASTIZITÄTSGRENZE IN EINKRISTALLEN VON ALUMINIUMLEGIERUNGEN

Experimente wurden unternommen um das Verhalten unter Zug von Einkristallen von Aluminiumlegierungen, die Kupfer, Zink oder Wasserstoff enthalten, mit Reinstaluminiumeinkristallen zu vergleichen. Alle Legierungen zeigten bei der Temperatur der flüssigen Luft scharfe Elastizitätsgrenzen, während das Reinstaluminium keine Fähigkeit zur Herausbildung einer deutlichen Elastizitätsgrenze zeigte. Diese Ergebnisse werden vom Standpunkt der Versetzungstheorie der Elastizitätsgrenze diskutiert.

Introduction

The presence of a yield point in body centred cubic metals containing small quantities of interstitial solute elements is well known, the best examples being polycrystalline iron containing carbon and nitrogen [1] and iron single crystals [2; 3; 4]. Polycrystalline molybdenum containing nitrogen also shows a yield point [5; 6].

These phenomena have been explained by the dislocation theory [7; 8; 9; 10] in which it is assumed that solute atoms having appreciable misfit in the lattice condense into dislocations because of an elastic interaction with them. The stress required to pull the dislocations away from these "atmospheres" is greater than that required for subsequent movement of the dislocations, so that a fall in applied stress occurs at the start of plastic flow.

In close-packed hexagonal metals an interstitial solute atom produces a non-spherically symmetrical distortion which is capable of interacting with both edge and screw dislocations, and yield points have been observed in cadmium [11] and in zinc [12] crystals which contained nitrogen. The absence of well-established yield points in face centred cubic metals has been attributed to the approximately symmetrical distortion produced by both substitutional and interstitial solute atoms; as a result pure screw dislocations may not be anchored by solute atoms in this lattice. Cottrell [13], however, has pointed out that the dissociation of a pure screw dislocation into partials [14] must always produce a substantial edge component in at least one member of the pair created by the dissociation. The locking of this component by the solute atmosphere necessarily locks the other member of the pair because of the elastic coupling between them. Thus yield points may be possible in face centred cubic alloys, although they may not be very pronounced. Irregularities in stress-strain curves resembling such yield phenomena have in fact often been noticed [15; 16; 17] and a clearly defined yield point (characterized by a fall in stress on first test, by the absence of any yield on an immediate retest, and by the return after appropriate strain ageing) has been observed by Ardley and Cottrell [18] in single crystals of α-brass.

The purpose of this paper is to present some new evidence for yield points in single crystals of certain aluminium alloys.

Experimental Procedure

Specimens were prepared from superpure aluminium both unalloyed and from alloys of it with additions of either 0.21 wt % copper, 2.49 wt % zinc, or 0.005 wt % (0.135 atomic %) hydrogen, and from a sample of commercially pure aluminium. The superpure aluminium (> 99.99%), the major impurities of which were silicon (< 0.003%) and iron (< 0.003%) and the pure zinc (> 99.999%)

*Received November 10, 1952.
†Department of Metallurgy, University of Birmingham, England.
‡Department of Metallurgy, University of Birmingham, England. Now at the General Electric Co., Schenectady, New York, U.S.A.

used in making the aluminium-zinc alloy were kindly donated by the British Aluminium Co. and the National Smelting Co. while the oxygen-free high-conductivity electrolytic copper (99.99%) used in making the aluminium-copper alloy was kindly supplied by I.C.I. Metals Ltd. The hydrogen addition was made by bubbling steam for 30 minutes through molten superpure aluminium held at 750°C in a pure alumina crucible. The commercially pure aluminium (99.7%) donated by Richard Thomas and Baldwin Co., contained iron (0.14%) and silicon (0.11%) as major impurities together with traces (< 0.005%) of copper, manganese, and titanium.

The ingots were rolled to 1 mm. thickness and annealed after every 50 per cent reduction in area. Specimens were milled from the strip with a 2 in. gauge length, 0.3 in. wide increasing on 5/16 in. radii to shoulders $\frac{3}{4}$ in. long and $\frac{1}{2}$ in. wide. Single crystals were produced by the strain anneal method [19], the entire gauge length and a large part of the shoulders being converted to a single crystal. The orientations were determined by the X-ray Laue method.

Tensile loading experiments were made with a hard machine of the Polanyi [20] type in which specimens were extended at a strain rate of 10^{-5} sec^{-1} by means of hooks which engaged grips clamped on the shoulders of the specimen. Prior to testing, every specimen was given a small initial strain to ensure perfect alignment. In order to maintain this alignment strain ageing was carried out *in situ*, i.e. while the specimen remained mounted in the machine under a nominal load of about 200 gm. This precaution is vital in examining crystals in which the yield point is weakly developed.

The criteria adopted in these experiments as being indicative of the presence of a yield point were as follows:

(*a*) a fall in load at the beginning of plastic deformation,

(*b*) the absence of this fall on immediate retesting,

(*c*) the return of the fall in load after a suitable ageing treatment.

Only crystals which consistently satisfied these requirements were recorded as having shown the yield phenomena.

Yield Points in Aluminium Alloys

Initially the tests were made at room temperature, but no yield points were observed in any crystals under these circumstances. Accordingly all of the subsequent tests were made at lower temperatures.

Stress-strain curves typical of those obtained for commercially pure aluminium crystals tested at liquid air temperature, are shown in Figure 1. A definite drop in load was observed first after strain ageing for $1\frac{1}{2}$ hours at 100°C (Curve *C*) and this was absent on immediate reloading, (curve *d*). Strain ageing resulted in another fall in load, again absent on retesting (curves *e* and *f*, *g* and *h*) thus satisfying

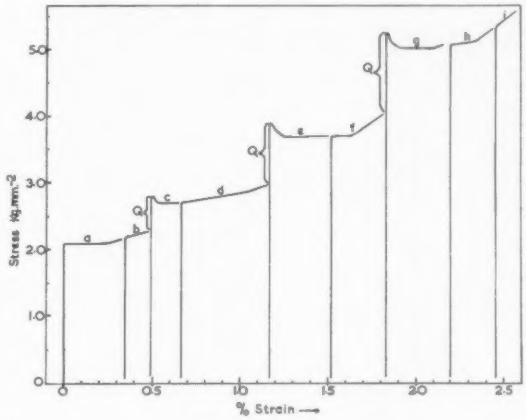

FIGURE 1. Typical stress-strain curves for commercially pure crystals tested at liquid air temperature: (*a*) after ageing 16 hours at 18°C, (*b*) immediate retest, (*c*) after ageing $1\frac{1}{2}$ hours at 100°C, (*d*) immediate retest, (*e*) after ageing $1\frac{1}{2}$ hours at 100°C, (*f*) immediate retest, (*g*) after ageing $2\frac{1}{2}$ hours at 100°C, (*h*) immediate retest, (*i*) immediate retest.

the three criteria for a yield point. The large degree of strain age hardening *Q* (curves, *b-c*, *d-e*, *f-g*) is a real effect since unloading in the absence of strain ageing produces no additional hardening (curves *a-b*, *c-d*, *e-f*, *g-h*). There is a smooth transition from the yield elongation to the underlying work hardening curve on which the yield point effects are superimposed. Unloading during either the yield extension curves (*c-d*, *e-f*, *g-h*) or during normal work hardening (curves *a-b*, *h-i*) produces no discontinuity on further testing. The extended plastic flow suggestive of a yield point after strain ageing for 16 hours at 18°C may not be taken as certain evidence of a yield point since the first criterion of yielding is not satisfied.

A summary of the effects of various strain ageing treatments on commercially pure crystals is given in Table I and it will be seen that given sufficient time yield points are always produced at ageing temperatures at or below 100°C.

A similar series of curves obtained with an aluminium zinc alloy crystal is shown in Figure 2. Here again, when testing at liquid air temperature the three necessary criteria for a yield point are satisfied reproducibly. The strain age hardening accompanying the yield point is however not so

large as in the commercially pure specimens. This may be due to the smaller misfit in the aluminium lattice of the zinc atom compared with iron or silicon atoms. In substitutional solutions the misfit is defined by the parameter ϵ, where $r_a = r(1 + \epsilon)$, r_a being the radius of the solute atom and r is that of the solvent atom [21]. Values of ϵ for copper and zinc in aluminium are 0.122 and 0.014 respectively [22]. This latter misfit should also result in a small value of the critical temperature above which the heat motion is strong enough to prevent substantial condensation of solute atoms on dislocations. The data of Table I indicates that this critical temperature is between 18°C and 50°C since ageing at or above 50°C fails to produce manifestations of yield phenomena whereas these may be obtained by ageing at 18°C if this is done for a time long enough for the necessary diffusion to occur.

TABLE I

SUMMARY OF STRAIN AGEING TREATMENTS AND THEIR EFFECT ON THE YIELD POINT OF ALUMINIUM ALLOY SINGLE CRYSTALS

Specimen	Temperature of test	Ageing Treatment		Yield Point
		Temp. (°C)	Time (hours)	
Commercially pure aluminium	Liquid air	18	1, 16	No
			17	Yes
		50	$\frac{2}{3}$	No
			$2\frac{1}{2}$	Yes
		100	$\frac{2}{3}$, $\frac{3}{4}$, $1\frac{1}{2}$, $2\frac{1}{2}$	Yes
Aluminium zinc	Liquid air	18	16, 24	No
			30, 40, 48	
			72, 108	Yes
		50	15	No
		75	4, 10	No
		100	3	No
Aluminium copper	− 50°C	18	16	No
		70	1	No
		100	1	No
	Liquid air	75	2	No
		100	$\frac{1}{2}$	No
			$\frac{3}{4}$, 1, $1\frac{1}{2}$, 2, 3, 11	Yes
		130	2	Yes
Aluminium hydrogen	18°C	18	$\frac{1}{2}$, 16, 26	No
		100	$\frac{1}{4}$, $\frac{1}{2}$	No
		200	$\frac{1}{2}$	No
	− 77°C	−77	1	No
		60	$\frac{2}{3}$	No
	Liquid air	18	1/6	No
			$\frac{1}{2}$, 1, $2\frac{1}{4}$, 16, 42	Yes
		100	$\frac{1}{4}$	No
			$\frac{1}{2}$	Yes
		−183	$2\frac{1}{2}$	No
Superpure 99.99% aluminium	18°C	18	1, 16	No
		80	2	No
	Liquid air	18	$\frac{1}{2}$, $1\frac{1}{4}$, 15, 24, 50	No
		50	$\frac{1}{2}$, $1\frac{1}{2}$	No
		75	$\frac{1}{2}$	No
		100—50	10° per hour	No
		100	2	No

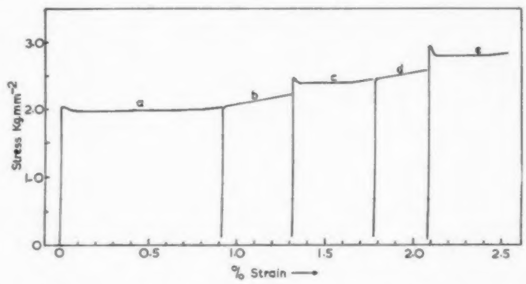

FIGURE 2. Typical stress-strain curves for the aluminium-zinc alloy crystals tested at liquid air temperature: (*a*) after ageing 40 hours at 18°C, (*b*) immediate retest, (*c*) after ageing 30 hours at 18°C, (*d*) immediate retest, (*e*) after ageing 72 hours at 18°C.

A typical set of stress-strain curves from an aluminium copper alloy crystal is shown in Figure 3. Here again the three criteria are satisfied and a definite yield point exists, although again the strain age hardening is smaller than in commercially pure crystals. The strain ageing data of Table I indicate that the critical temperature lies above 400°K, which is in agreement with theory [7] in so far as the misfit of a copper atom in the aluminium lattice ($\epsilon = 0.122$) is much greater than that of zinc ($\epsilon = 0.014$).

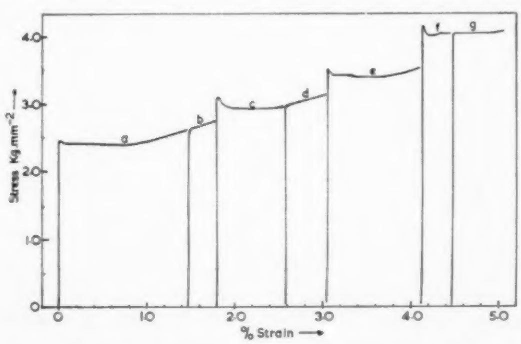

FIGURE 3. Typical stress-strain curves for the aluminium-copper alloy crystals tested at liquid air temperature: (*a*) after 2 hours at 100°C, (*b*) immediate retest, (*c*) after $1\frac{1}{2}$ hours at 100°C, (*d*) immediate retest, (*e*) after 2 hours at 100°C, (*f*) after 11 hours at 100°C, (*g*) immediate retest.

Definite yield points were also observed in the aluminium-hydrogen alloy crystals as shown in Figure 4, but these were weak and the strain age hardening was small. This weakness is probably due to the low strains produced by the hydrogen atoms

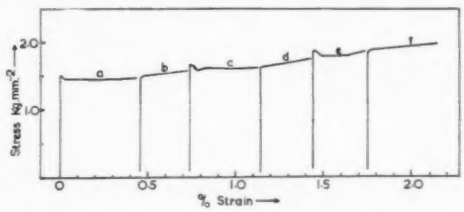

FIGURE 4. Typical stress-strain curves for the aluminium-hydrogen alloy crystals tested at liquid air temperatures: (*a*) after ageing for 1 hour at 18°C, (*b*) immediate retest, (*c*) after ageing 42 hours at 18°C, (*d*) immediate retest, (*e*) after ageing ½ hour at 18°C, (*f*) after ageing ¼ hour at 100°C.

(an interstitial hole 1.3 Å diameter exists in the centre of the structure cell in aluminium) but it may also be due to loss or segregation of hydrogen during the preparation of the crystal. An attempt was made to introduce hydrogen into a superpure crystal by annealing in wet hydrogen for two days at 630°C, but this specimen gave no evidence of yield phenomena.

Superpure crystals were tested extensively in control experiments and the typical curves of Figure 5, together with the data given in Table I, show clearly that the pure metal has no capacity for a yield point. Some slight recovery of the elastic

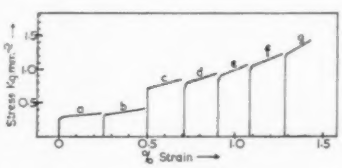

FIGURE 5. Typical stress-strain curves for superpure aluminium crystals: (*a*) tested at 18°C after ageing for 1 hour at 18°C, (*b*) tested at 18°C after ageing for 2 hours at 80°C, (*c*) tested at liquid air temperature after ageing for 2 hours at 100°C, (*d*) tested at liquid air temperature after ageing for 1½ hours at 50°C, (*e*) tested at liqiud air temperature after ageing for 15 hours at 18°C, (*f*) tested at liquid air temperature after ageing at 100°C, cooling at 10° per hour, to 50°C, (*g*) tested at liquid air temperature after ageing for 50 hours at 18°C.

limit occurs (Fig. 5) even after these small strains during heating above room temperature, though similar effects were absent in the alloys.

Summary and Discussion

Yield points have been observed in single crystals of commercially pure aluminium and in binary alloys of superpure aluminium containing 0.21 wt % copper, 2.49 wt % zinc, and 0.005 wt % (0.135 atomic %) hydrogen, whereas superpure aluminium crystals give no yield phenomena.

A new feature of the present results is that yield points are produced by the presence of solute atoms (copper and zinc) which are known to cause lattice contraction in aluminium [22]. For carbon and nitrogen in iron, on the other hand, the solute atoms cause lattice expansion. The results are consistent with the dislocation theory, which admits locking of dislocations by solute atoms that either contract or expand the lattice.

Much larger quantities of substitutional alloying elements are necessary to produce yield points than in, say, body centred cubic iron where less than 0.003 per cent carbon suffices. This is partly because the alloying elements in the present case have a smaller degree of misfit and partly because the distortion they produce is almost spherically symmetrical, so that they are able to interact only with the hydrostatic component of the pure and partial edge dislocations.

In order to display the yield points as clearly as possible during these experiments, certain precautions were taken; in particular, the use of a hard testing machine, testing at low temperatures, and care to obtain and maintain axial alignment, the latter by the maintenance of a small load during the whole sequence of tests. The absence of these precautions in earlier investigations may account for the previous lack of evidence for a definite yield point in these aluminium alloys.

Acknowledgements

We wish to thank Professor D. Hanson and the University of Birmingham for providing facilities and financial support, and Professor A. H. Cottrell for his interest, encouragement, and valuable discussions.

References

1. LOW, J. E. and GENSAMER, M. Trans. A.I.M.E., **156** (1944) 207.
2. COTTRELL, A. H. and CHURCHMAN, A. T. J. Metals, **1** (1949) 899.
3. COTTRELL, A. H. and CHURCHMAN, A. T. Nature (London), **167** (1951) 943.
4. HOLDEN, A. N. J. Metals, **4** (1952) 182.
5. TURY, P. and KRAUSZ, S. Nature (London), **138** (1936) 331.
6. TURY, P. and KRAUSZ, S. Nature (London), **139** (1937) 30.
7. COTTRELL, A. H. In "Report on the Strength of Solids" (London, Physical Society, 1948), p. 30.
8. NABARRO, F. R. N. In "Report on the Strength of Solids" (London, Physical Society, 1948), p. 38.

9. Cottrell, A. H. and Bilby, B. A. Proc. Phys. Soc., **A62** (1949) 49.
10. Cottrell, A. H. Report of the 9th Solvay Conference (1952) 487.
11. Cottrell, A. H. and Gibbons, D. F. Nature (London), **162** (1948) 488.
12. Wain, H. L. and Cottrell, A. H. Proc. Phys. Soc. **B63** (1950) 339.
13. Cottrell, A. H. Dislocations and Plastic Flow in Crystals (Oxford University Press), to be published.
14. Heidenreich, R. D. and Shockley, W. In "Report on the Strength of Solids" (London, Physical Society, 1948), p. 57.
15. Edwards, C. A., Phillips, D. L., and Liu, Y. H. J. Iron Steel Inst., **147** (1943) 145.
16. McReynolds, A. W. Trans. A.I.M.E., **185** (1949) 30.
17. Lubahn, J. D. Trans. Amer. Soc. Metals, **44** (1952) 643.
18. Ardley, G. W. and Cottrell, A. H. Submitted for publication.
19. Williamson, G. K. and Smallman, R. E. Submitted for publication.
20. Polanyi, M. Z. tech. Phys., **6** (1925) 121.
21. Cottrell, A. H. Progress in Metal Physics, **1** (1949) 77.
22. Axon, H. J. and Hume-Rothery, W. Proc. Roy. Soc., **A193** (1948) 1.

ANELASTIC MEASUREMENT OF ATOMIC MOBILITY UNDER NON-EQUILIBRIUM CONDITIONS*

A. S. NOWICK† and R. J. SLADEK‡

The anelastic method for the measurement of atomic mobility in substitutional solid solutions, which has been applied previously to the study of silver-zinc solid solutions under equilibrium conditions, is now used to measure mobility in these same alloys after quenching-in of an excess of vacancies. From the variation of the initial relaxation time with temperature of measurement, it is possible to separate the composite "activation energy" for atomic movement into the heat of formation of a vacancy and the heat of activation for the movement of a vacancy. In the case of a 70-30 silver-zinc alloy the values obtained are 11.8 kcal/mole for the heat of formation, and 19.7 kcal/mole for the heat of activation associated with a vacancy. The mole fraction of vacancies that are frozen in by quenching from 400°C, calculated from the experimental results, is 5×10^{-4}; the corresponding "freezing-in" temperature is probably about 300°C. The early part of the vacancy decay curve represents an approximately exponential time decay; in the later part of this curve the rate of disappearance of vacancies is very much diminished. The effect of cold working is to increase the rate of vacancy decay.

A lower limit is estimated for the number of jumps of a vacancy before its annihilation; this value is consistent with the concept that dislocations act as sinks for vacancies.

LA MESURE ANÉLASTIQUE DE LA MOBILITÉ DES ATOMES DANS DES CONDITIONS OÙ L'ÉQUILIBRE N'EST PAS ÉTABLI

La méthode anélastique de mesure de la mobilité des atomes dans les solutions solides de substitution, qui a été appliquée antérieurement à l'étude des solutions solides argent-zinc dans des conditions d'équilibre, est maintenant utilisée pour la mesure de la mobilité dans ces mêmes alliages, après avoir retenu un excès de lacunes réticulaires par trempe. En se basant sur les variations du temps initial de relaxation avec la température à laquelle s'effectue la mesure, il est possible de séparer l'énergie d'activation composée, du mouvement atomique, en chaleur de formation d'une lacune et en chaleur d'activation du déplacement d'une lacune. Dans le cas d'un alliage argent-zinc 70-30 les valeurs suivantes ont été obtenues: 11,8 kcal/mole pour la chaleur de formation et 19,7 kcal/mole pour la chaleur d'activation associée au déplacement de la lacune. La fraction moléculaire de lacunes retenues par trempe en partant d'une température de 400°C, calculée d'après les résultats expérimentaux, est de 5×10^{-4}; la température correspondante de "congélation" des lacunes est probablement d'environ 300°C. La première partie de la courbe de la vitesse de disparition des lacunes en fonction du temps, représente une loi approximativement exponentielle; ensuite la vitesse de disparition des lacunes diminue très sensiblement. L'effet de l'écrouissage est d'accroître la vitesse de disparition des lacunes.

La limite inférieure du nombre de sauts d'une lacune avant sa disparition a été estimée; cette valeur est en accord avec le concept, que les lacunes se perdent dans des dislocations.

ANELASTISCHE MESSUNGEN DER ATOMAREN BEWEGLICHKEIT UNTER GLEICHGEWICHTSFERNEN BEDINGUNGEN

Die anelastische Methode zur Messung der atomaren Beweglichkeit in Substitutionsmischkristallen fester Lösungen, die früher zur Untersuchung von festen Silber-Zink Lösungen unter Gleichgewichtsbedingungen benutzt wurde, wird jetzt zur Messung der atomaren Beweglichkeit in der gleichen Legierung, in die nun jedoch ein Überschuss an Leerstellen durch Abschrecken eingebaut worden war, angewandt. Es ist möglich aus der beobachteten Veränderung der ursprünglichen Relaxationszeit mit der Messungstemperatur die gesamte "Aktivierungsenergie" der atomaren Bewegung in die Bildungswärme einer Leerstelle und die Aktivierungswärme der Bewegung der Leerstelle zu zerlegen. Im Falle einer 70-30 Silber-Zink Legierung wurden die folgenden Werte erhalten: 11.8 Kcal/mol für die Bildungswärme und 19.7 Kcal/mol für die Aktivierungswärme einer Leerstelle. Der Prozentsatz (in Molprozent) der durch Abschrecken bei 400°C eingefrorenen Leerstellen wurde aus den experimentellen Ergebnissen zu 5×10^{-4} berechnet. Die entsprechende "Einfrierungstemperatur" ist etwa 300°C. Der Anfang der Abklingkurve der Leerstellen folgt ungefähr einer exponentiellen Zeit-Abklingskurve, im weiteren Verlauf geht jedoch die Geschwindigkeit des Verschwindens der Leerstellen sehr stark zurück. Die Geschwindigkeit, mit der die Leerstellen verschwinden, wird durch Kaltbearbeitung vergrössert.

Die untere Grenze der Zahl der Sprünge, die eine Leerstelle ausführt bevor sie verschwindet, wird geschätzt. Dieser Wert steht im Einklang mit der Vorstellung, dass Leerstellen durch Versetzungen ("dislocation") abfliessen können.

Introduction

It is now generally agreed that atomic mobility or diffusion in metals, at least in the close-packed structures, occurs principally by means of vacancies. Other mechanisms have been considered and eliminated, either because they predict that the two components of a binary solid solution diffuse at the same rate and therefore are unable to explain the Kirkendall experiments [1; 2], or because theoretical calculation shows that the "activation energy" associated with the mechanism is much higher than

*Received November 13, 1952.

†Hammond Laboratory, Yale University, New Haven, Conn., U.S.A.

‡Institute for the Study of Metals, University of Chicago, U.S.A.

experimentally obtained values. The direct interchange and "ring" mechanisms [3] fall into the former category, while the possibility of diffusion by means of atoms in interstitial lattice sites is eliminated for the latter reason [4]. The vacancy mechanism is capable of explaining the movement of inert markers during diffusion experiments (the "Kirkendall effect") and, in the case of self-diffusion in copper, for which detailed theoretical calculations have been carried out, the "activation energy" calculated on the basis of the vacancy mechanism is in reasonably good agreement with experiment [4; 5].

If the vacancy interpretation is correct, it should be possible to obtain a non-equilibrium concentration of vacancies at low temperatures by sufficiently rapid quenching from a higher temperature, i.e., to "freeze in" a non-equilibrium excess of vacancies. A specimen containing such frozen-in vacancies should show an abnormally high diffusion rate at low temperatures. Unfortunately, the time required for a diffusion experiment at any temperature is considerably greater than the time for vacancies to attain equilibrium at that temperature. Stated differently: in order that measurable diffusion occur within a reasonable amount of time, it is necessary that the measurements be carried out at a temperature so high that vacancy equilibrium is attained almost instantly. Thus, diffusion experiments cannot be used to observe the presence of non-equilibrium concentrations of vacancies.

In a recent paper [6] (henceforth to be designated as I) it is shown that many of the limitations of conventional diffusion experiments can be overcome by the use of the anelastic properties of certain solid solutions to study atomic mobility at comparatively low temperatures. This method is based upon the measurement of the relaxation time associated with a process of stress-induced ordering in an initially disordered solid solution. The measured relaxation time, which may be obtained from elastic after-effect experiments, is of the same order of magnitude as the mean time between atomic jumps. The theory of the anelasticity resulting from stress-induced ordering is described in I, and the method is applied to an extensive investigation of atomic mobility, under equilibrium conditions, in silver-rich solid solutions of the silver-zinc system. The fact that this method permits measurements of atomic mobility at low temperatures suggests its application to the study of the same alloys under non-equilibrium conditions, i.e., after the quenching-in of an excess of vacancies. Preliminary experiments of this type have already been reported [7]; it was shown that the relaxation time at 50°C for a silver-zinc solid solution was decreased by a factor greater than 10^4 as a result of quenching the specimen from a high temperature. It is the purpose of the present paper to extend these preliminary experiments.

The theory section of this paper contains an analysis showing which quantities may be obtained from relaxation measurements under non-equilibrium conditions. In the presentation of the experimental work, the evidence which shows that the measured effects are truly the result of an increased atomic mobility, and not some other effect of quenching, is first discussed. A quantitative study of the effect of quenching conditions, of prior cold working, and of the temperature and time of measurement on the relaxation time is then presented. From the variation of the initial relaxation time with temperature, it becomes possible to separate the composite "activation energy" for atomic movement into the heat of formation of a vacancy and the heat of activation for its movement.

Throughout this paper the term "vacancy" will be used loosely, to represent the type of imperfection which is responsible for atomic movement and which can be frozen in by rapid quenching. These experiments do not, of course, identify these imperfections as vacancies. Thus, although Frenkel defects (interstitialcies) have been eliminated on the basis of evidence already discussed, pairs of vacancies or other multiple vacancies are not ruled out and may actually play a significant role in diffusion.

Theory

The application of stress to a binary solid solution may result in an atomic redistribution, leading to a non-randomness in the relative arrangements of the two component atoms, and thereby acting to relieve the applied stress. This process is called stress-induced ordering, and the time of relaxation for the process is designated by τ. Let us denote by Γ_τ the atom jump frequency that controls the relaxation process. (In I, it is shown that if the two components of the solid solution differ markedly in their jump rates, then Γ_τ is essentially the jump frequency of the slower moving component.) This jump frequency is, for a vacancy mechanism, the product of the probability that a neighbor of a given atom is vacant and the probability per second for that atom to jump into a given vacant neighboring site. If c is the atom fraction of vacancies present in the lattice, the first of these probabilities is zc, where z is the number of nearest neighbors, while the second is given by a standard rate formula [8], so that

$$\Gamma_r = zc(\nu e^{-\Delta G_j/RT}), \tag{1}$$

where ν is the atomic vibration frequency and ΔG_j the increase in free energy of the lattice when an atom neighboring a vacancy is brought from its normal lattice position into the saddle point position associated with the jump into the vacant lattice site. The quantity ΔG_j may be separated, in the usual way, into an enthalpy and entropy term,

$$\Delta G_j = \Delta H_j - T\Delta S_j\,, \tag{2}$$

where ΔH_j is the height of the potential barrier associated with the jump and ΔS_j is the entropy of activation. It is shown in I that the relation between τ and Γ_r is

$$\tau^{-1} = \alpha\Gamma_r\,, \tag{3}$$

where α is a numerical constant whose value is about 0.4. By combining equations (1), (2), and (3), we obtain

$$\tau^{-1} = z\alpha\nu c e^{\Delta S_j/R}\, e^{-\Delta H_j/RT}. \tag{4}$$

If vacancies are present in equilibrium quantities, their concentration is given by $\bar{c}$, where

$$\bar{c} = e^{-\Delta G_f/RT} = e^{\Delta S_f/R}\, e^{-\Delta H_f/RT}, \tag{5}$$

where ΔG_f, ΔH_f and ΔS_f are, respectively, the free energy, enthalpy and entropy of formation of a lattice vacancy (or per mole of vacancies at infinite dilution). When equations (4) and (5) are combined, an expression is obtained for the time of relaxation under equilibrium conditions, $\bar{\tau}$, of the form*

$$\bar{\tau}^{-1} = \bar{\tau}_0^{-1}\, e^{-H_r/RT}, \tag{6}$$

where the apparent "activation energy for relaxation," H_r, is a composite quantity given by

$$H_r = \Delta H_j + \Delta H_f\,, \tag{7}$$

while the quantity $\bar{\tau}_0$ obeys the equation

$$\bar{\tau}_0^{-1} = z\alpha\nu e^{\Delta S_r/R};\ (\Delta S_r = \Delta S_j + \Delta S_f). \tag{8}$$

The quantities H_r and $\bar{\tau}_0$ obtained for a series of silver-zinc alloys are reported in I.

Equation (4) is applicable more generally than to the case where vacancies are present in equilibrium amounts. Suppose, for example, that an excess of vacancies is frozen in by quenching and that this vacancy excess decays with time such that

$$c = c(0)\, e^{-t/\theta}, \tag{9}$$

*The bar was not used over the symbol τ in I, since all measurements reported represented equilibrium conditions.

where $c(0)$ is the concentration of vacancies frozen into the alloy and θ may be called the *decay time*. Equation (9) implies that as $t \to \infty$, c approaches zero rather than the proper equilibrium vacancy concentration, but this equation may be very nearly correct when $c(0) \gg \bar{c}$ at the temperature of measurement. If c is a function of time, the quantity τ (equation 4) will also vary with time. If we designate the initial value of the relaxation time by $\tau(0)$, then this quantity is given by (4) with $c(0)$ substituted for c. If the quenching procedure can be duplicated as often as desired, so that $c(0)$ is always the same, values of $\tau(0)$ may be obtained as a function of the temperature of measurement. When these values are plotted on a logarithmic scale against T^{-1}, a straight line is obtained whose slope gives the quantity ΔH_j, and whose intercept is

$$- \log \tau_0(0) = \log (z\alpha\nu) + \log c(0) + \Delta S_j/2.3R. \tag{10}$$

From this equation, the frozen-in vacancy concentration, $c(0)$, may be obtained if reasonable values are inserted for ν and ΔS_j.

Another significant quantity may be calculated when $c(0)$ is known. This is the *freezing-in temperature*, T_F, defined by the equation

$$c(0) = e^{\Delta S_f/R}\, e^{-\Delta H_f/RT_F}. \tag{11}$$

The temperature T_F is, therefore, the temperature at which the equilibrium concentration of vacancies is equal to the frozen-in concentration, $c(0)$. It should be noted that (11) applies to a relatively high temperature, T_F, as compared to the lower temperatures at which the measurements are made. Inasmuch as the composite activation energy H_r and entropy ΔS_r are somewhat temperature-dependent (as shown by the experiments reported in I, where a plot of log $\bar{\tau}$ against T^{-1} does not give exactly a straight line), the values of ΔS_f and ΔH_f to be used in equation (11) are not precisely those calculated from the low-temperature measurements, but must be corrected for their temperature dependence.

Let us return now to the variation of the non-equilibrium concentration of vacancies, c, with time after quenching, at a given temperature of measurement. From equation (4) it is clear that for a given specimen and temperature, τ^{-1} is at any instant proportional to c, so that

$$\frac{\tau^{-1}(t)}{\tau^{-1}(0)} = \frac{c(t)}{c(0)}\,. \tag{12}$$

Thus, by an experimental determination of the quantity τ as a function of the time, for the quenched specimen, the relative variation of the vacancy concentration with time (the *vacancy decay curve*) may be obtained. If this curve should obey equation (9), the decay time, θ, may then be obtained. Clearly, the quantity $c/c(0)$ will fall off more rapidly with time the higher the temperature of measurement, due to the more rapid vacancy movement. In fact, it seems reasonable to expect that vacancy movement at a low temperature is simply a slow-motion version of the movement at a higher temperature. Consequently, we anticipate that $c/c(0)$ depends on time and temperature only through the mean number of jumps that a single vacancy will make in time t at the given temperature. The quantity $c/c(0)$ is, therefore, a function only of the product $te^{-\Delta H_J/RT}$. It should then be possible to obtain the same decay curve for all temperatures if $\tau^{-1}/\tau^{-1}(0)$ is plotted against this product, instead of against the time itself. More conveniently, we may plot $\tau^{-1}/\tau^{-1}(0)$ against a time corrected to a reference temperature T_1, i.e., the *corrected time*, t', is given by

$$t' = t \exp\left[-\frac{\Delta H_J}{R}\left(\frac{1}{T} - \frac{1}{T_1}\right)\right]. \tag{13}$$

Specimens and Experimental Method

The preparation of the silver-zinc wire specimens of various compositions for the torsional measurements is described in I. The specimens are .032 inch in diameter and 10 inches long. Most of the measurements reported herein apply to a specimen containing 30.2 atomic per cent zinc, unless otherwise stated. Preliminary experiments also include measurements on a 33.5 atomic per cent zinc specimen, a composition that had not been used in the earlier equilibrium experiments reported in I.

The quenching procedure is as follows. A specimen attached to a long steel wire support is introduced into a vertical tubular furnace (usually at 400°C) through which dry nitrogen is passed. After an appropriate annealing time, it is quenched into the desired solution at room temperature. A long rubber band in tension pulls the specimen down into the quenching solution. The solutions used are water, 0.5 per cent KOH and 10 per cent $CaCl_2$.

After quenching, the specimen is mounted between pin vises as in the earlier equilibrium measurements, and placed into the measuring furnace at the desired temperature. Successive elastic after-effect measurements are made to determine how the time of relaxation changes with time at a given temperature of measurement. For each measurement, the wire is twisted for an appropriate time, and, following its release, the anelastic strain is measured as a function of time. In each case the time of twist of the wire before measurement is of the order of the time of relaxation. The zero value for the total time at the measuring temperature is taken as the time at which the specimen is introduced into the measuring furnace. The small error due to the time required for the specimen to come to temperature is not significant in these measurements.

The precision in the measurement of the time of relaxation, or rather of the time to inflection τ_i (see the next section) is $\pm$ 10 per cent. The temperature is usually maintained constant to $\pm \frac{1}{2}$°C.

Determination of the Relaxation Time

In the case that a single time of relaxation is operative, the anelastic strain obeys the equation

$$\dot{\epsilon} = -\epsilon/\tau \tag{14}$$

whose solution is a simple exponential function, with relaxation time τ. It was shown, in I, that the relaxation due to stress-induced ordering does not deviate greatly from this simple behavior. The value of τ may then be obtained from a measurement of the elastic after-effect, either from the time for the anelastic strain to fall to $1/e$ of its initial value, or from the time from the start of the run to the inflection point in a plot of strain against log t. The latter quantity we will designate as τ_i, or the *time to inflection*. Under equilibrium conditions, when τ is a constant, these two methods are very nearly equivalent (i.e., $\tau_i = \tau$), but the latter one is preferred [6] because it does not require a knowledge of the final position of the specimen when relaxation is complete.

In the present experiments the situation is complicated by the fact that τ is a function of time. Clearly, if τ varies so slowly with time that it changes little during the measurement of one relaxation curve, the same methods may be used to determine τ as when this quantity is independent of time. The quantity τ_i may then be taken equal to the value of τ at a total time measured from the introduction of the specimen into the measuring furnace to the midpoint of the relaxation curve. However, if τ varies appreciably over the course of one relaxation curve, it is readily shown that the time for the anelastic strain to fall to $1/e$ of its initial value is no longer equal to τ_i. Assume that the variation of τ with total time, t, is given by $\tau = \tau(0)$

$e^{t/\theta}$, corresponding to equation (9). (Even if this assumption is not correct over relatively long times, it will probably be a good approximation over the time required for one measurement.) When the inflection point, τ_i, for the curve of ϵ against log t is calculated, we find that

$$\tau_i^{-1} - \theta^{-1} = \tau^{-1}(t) \tag{15}$$

where t is the total time, from the insertion of the specimen into the furnace to the inflection point of the ϵ–log t curve, and θ is the decay time defined by equation (9). Thus, when $\theta \gg \tau_i$, we have $\tau_i = \tau(t)$, as anticipated earlier. When τ_i is of the same order of magnitude as θ, equation (15) should be used to obtain the relaxation time, τ. In general, it will be more convenient in most cases to give the uncorrected and directly measured values, τ_i, in the presentation of the experimental results. In any calculation where the corrected τ-values are required, however, cognizance is taken of equation (15).

Results and Discussion

Preliminary Measurements

The effect of quenching a 70-30 silver-zinc alloy from 400°C to room temperature is to produce initial relaxation times which are small enough to be measured in the temperature range 70° to 35°C. Corresponding relaxation times after quenching run from about 100 to 2500 sec. for this range. The equivalent equilibrium values for the same temperature range, as obtained by extrapolation of the data obtained under equilibrium conditions in I, are from 5×10^5 to 10^8 sec. Specimens that are furnace-cooled in place of the quench show no relaxation effects in reasonable lengths of time and are therefore assumed to be more nearly in equilibrium than the quenched specimens. This very large decrease in the relaxation time after quenching has been attributed [7] to the freezing in of non-equilibrium numbers of vacancies, resulting in more rapid atomic mobility, as anticipated from equation (4). There are, however, two interpretations, other than the presence of a non-equilibrium concentration of imperfections, which might explain the observed phenomena. The first of these is the possibility that the quenching has frozen into the material a different state of short range order from that which should be present at low temperatures, and that the existence of this condition results in a more rapid atomic mobility. This assumption should imply that, under equilibrium conditions of measurement, τ-values at low temperatures should become abnormally high as compared to values obtained by extrapolation from higher temperatures. Actually, the equilibrium measurements reported in I show that, on the contrary, the plot of log $\bar{\tau}$ against T^{-1} curves in such a way that low temperature values are lower than those obtainable from a straight line. Furthermore, if the attainment of equilibrium were a matter of a change in a condition of short-range order, the decay time θ should be about equal to the initial relaxation time. Instead, we will see that the decay time is many times greater than $\tau(0)$.

An alternative explanation is that quenching stresses are responsible for the relaxation effects after quenching. This suggestion may be doubted immediately since the wires used are so fine that such stresses will be very small; furthermore, the effects of the quench disappear even below 50°C if sufficient time is allowed. In addition, the magnitude of the relaxation effects in the quenched 30 per cent zinc alloy is of the same order as that obtained under equilibrium conditions for this alloy; equivalent effects from internal stresses are only obtainable through very severe cold working [9]. To illustrate this point more quantitatively, we may make use of the fact demonstrated in I, that the magnitude of the equilibrium relaxation effects, as given by the relaxation strength, Δ_M, in torsion is strongly a function of zinc concentration; it falls off rapidly as the zinc concentration of the silver-zinc alloys is decreased. Thus, the second column of Table I shows the values of Δ_M at 230°C for different alloys, as obtained from the equilibrium measurements.

TABLE I

RELAXATION STRENGTHS FOR VARIOUS SILVER-ZINC ALLOYS AS MEASURED UNDER EQUILIBRIUM AND NON-EQUILIBRIUM CONDITIONS

Atomic per cent Zn	Δ_M at 230°C	Δ_M at 60°C
24.2	0.09	0.14
30.2	0.14	0.23
33.5	0.17	0.31

The data for the same quantity at 60°C are obtained from measurements on the same specimens after quenching and are somewhat less reliable than the values in the second column (the probable error of the low temperature values is ± 0.03). The low temperature values of Δ_M are higher than the values at 230°C, in accordance with the approximate inverse temperature dependence of this quantity [10]. It is clear, however, that when this temperature dependence is taken into account, the values of Δ_M as measured under equilibrium and non-

equilibrium conditions are in good agreement. If the low temperature effects were a consequence of quenching stresses, it would be quite coincidental if the plastic properties of these alloys ran so nearly parallel to the magnitude of the anelasticity resulting from stress-induced ordering. It therefore seems as if the atomic mobility is truly increased as a result of quenching, which means that imperfections are frozen into the lattice.

Preliminary measurements will now be discussed which show the effect of the quenching temperature on the time to inflection, τ_i, directly after quenching a 30 per cent zinc alloy into water at room temperature. All measurements are made at the same temperature, 49°C. The quenching temperature is in the range 250 to 450°C. For temperatures below 250°C, the relaxation time at 49°C is too long to be measured conveniently; quenching temperatures above 450°C are avoided to prevent damage to the specimen due to the evaporation of zinc. If most of the vacancies present under equilibrium conditions at the quenching temperature were frozen in by the quench, or, expressed differently, if the freezing-in temperature is, in each case, very close to the quenching temperature, we may expect that the concentration of trapped vacancies is given by equation (5), where T is the quenching temperature. The quantity ΔH_f could then be determined, approximately, from the slope of a plot of log τ_i against T^{-1}. On the other hand, if the attainment of equilibrium is very rapid in the vicinity of the quenching temperature, the freezing-in temperature will be somewhat lower. Under these conditions, the

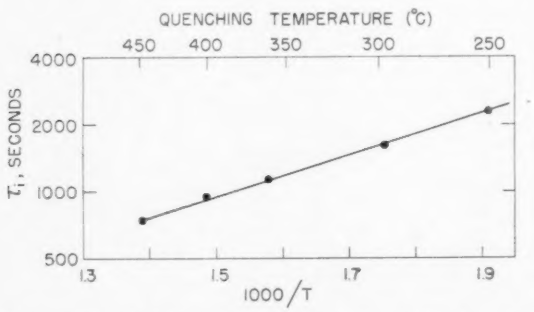

FIGURE 1. Variation of initial time-to-inflection with quenching temperature, for a 70-30 silver-zinc specimen quenched into water. Temperature of measurement, 49°C.

quantity τ_i will vary with quenching temperature more slowly than $e^{\Delta H_f/RT}$. Figure 1 shows the results of these quenching experiments; the slope of the best straight line corresponds to an energy of 4.3 kcal/mole. Since the quantity H_τ is about 32 kcal/mole for this alloy, it is very unlikely that this slope represents ΔH_f, i.e., that the heat of formation of a vacancy is such a small part of the composite "activation energy" (see equation (7)). Other results will be presented later which substantiate this conclusion. It therefore seems that we are not quenching in vacancies very efficiently from these temperatures, i.e., the freezing-in temperature is substantially below the quenching temperature. Under these conditions one would expect that the data of Figure 1 should level off at the higher temperatures more sharply than in the figure. One reason for this apparent failure of the curve to become completely flat at higher temperatures, in the range of values shown, is that the rate of quenching through the critical temperature range is probably greater the greater the quenching temperature; for high quenching temperatures the specimen is more likely to enter the quenching solution before it has cooled through the critical range. Actually, the linearity of Figure 1 over the range shown may be somewhat fortuitous since these preliminary data are not as precise as the other measurements reported herein. In particular the two end points of the curve are the least reliable; the 450°C point may be abnormally low as a result of accidental careless handling of the specimen which occurred in the case of that measurement.

In all measurements to be described throughout the remainder of this paper, the quenching temperature is 400°C. This temperature is high enough to take advantage of the increase in the initial rate of atomic mobility with quenching temperature, as illustrated by Figure 1, but at the same time is not so high that vaporization of zinc becomes serious.

It is found that the initial value of τ_i is independent of the annealing time at the quenching temperature in the range of times from 2 to 45 minutes. This result is in agreement with the anticipated rapid attainment of equilibrium at the quenching temperature.

The effect of the quenching solution is examined by a comparison of the initial values of τ_i at a given temperature, after quenching into water, 0.5 per cent KOH, and 10 per cent $CaCl_2$ solutions. The latter two solutions seem to decrease the initial value of τ_i by 20 or 25 per cent below the value obtained by quenching into water. In all remaining experiments the $CaCl_2$ solution is used.

Effect of Cold Working

Measurements of τ_i as a function of time at 59°C, following a quench from 400°C, are shown in Figure 2(A) for the 30 per cent zinc alloy. This curve is

typical of the decay curves that may be obtained from this alloy after quenching, showing the exponential behavior described by equation (9) only at the start. When the curve is extrapolated to zero time, an initial value, $\tau_i(0)$, equal to 270 seconds is obtained, corresponding to the freshly quenched specimen.

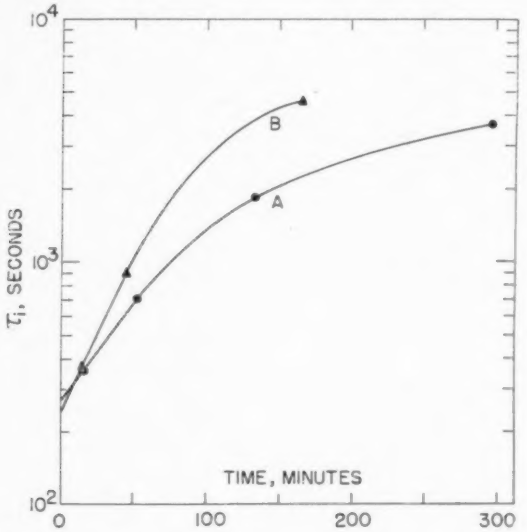

FIGURE 2. Variation of the time-to-inflection with total time at the measuring temperature (59°C) after quenching from 400°C. The two curves are: (A) specimen well annealed; (B) the same specimen slightly cold worked before quenching.

There has been much speculation about the possibility that dislocations act as sinks for vacancies [11; 12] and, therefore, aid in the attainment of equilibrium. If these ideas are correct, we would anticipate that the rate of disappearance of vacancies and, therefore, the rate at which τ_i increases with time will be strongly structure sensitive. To test this hypothesis, it is desirable to obtain the decay curve for a cold-worked specimen. If this cold working is carried out after quenching, the possible generation of vacancies [12] by the motion of dislocations during plastic flow may complicate matters. On the other hand, if cold working occurs before the quench, the anneal at 400°C may remove the excess dislocations introduced into the material. The procedure actually used is as follows. The specimen is cold worked before quenching by straining it 1.0 per cent in tension. It is then inserted into the furnace at 400°C for 30 seconds and quenched after this period. The attainment of equilibrium by vacancies should be almost instantaneous at 400°C; it is therefore expected that such a short anneal time will not affect the concentration of frozen-in vacancies (as already indicated by the preliminary measurements). On the other hand, in such a short time, the annealing out of the effects of the cold work will be minimized. A series of measurements of τ_i (again at 59°C) as a function of time for such a cold-worked specimen is given in Figure 2(B); the rate of approach to equilibrium is indeed more rapid than in the earlier series of runs. The intercepts at zero time, τ_i (0), in the two cases are almost the same and, in fact, when these values are converted to τ according to equation (15), the two values of $\tau(0)$ are equal to 280 sec. within experimental error. It therefore appears that whereas the rate of decay of vacancies is a highly structure-sensitive property, the frozen-in vacancy concentration, $c(0)$, is not. To further check the results of Figure 2, the same specimen after run B is annealed at 400°C for 45 minutes and then quenched. The subsequent run coincides with curve A within experimental error. When the same specimen is again elongated 1.0 per cent and the 30 second anneal and quench repeated, data close to curve B are again obtained.

Temperature Dependence of $\tau_i(0)$

A series of runs at different temperatures, each similar to that of Figure 2(A), was carried out on a well-annealed 70-30 silver-zinc specimen, under constant quenching conditions. In each case an extrapolation to $t = 0$ yields $\tau_i(0)$. As shown in the theory section, the quantity $\tau(0)$ should vary with temperature as exp $(\Delta H_j/RT)$. This same variation also applies to the quantity $\tau_i(0)$, without the correction of equation (15), since the decay time, θ, should be proportional to the same exponential factor. The range of measurement is 36–67°C, because at higher temperatures vacancy decay is so rapid that precise extrapolation of the decay curve becomes difficult, while below 35°C the relaxation becomes too slow and even a single initial value of τ_i is too large to measure. The results are presented in Figure 3. Some of the points shown in this figure are the average of two or three determinations at the same temperature. The precision of these results shows that the quenching operation, and therefore the value of $c(0)$, is quite reproducible. The quantity ΔH_j calculated from Figure 3 is 19.7 kcal/mole, estimated as accurate to $\pm$ 0.5 kcal/mole, while from the intercept the value log $\tau_0(0) = -10.48$ is obtained.

If we now combine these results of the quenching experiments with the earlier equilibrium measurements reported in I for the same (70-30) alloy, some of the computations indicated in the theory section can be made. As mentioned earlier, the equilibrium

measurements show that H_r and $\bar{\tau}_0$ are somewhat dependent on temperature. The values of these quantities required for the present computations are not the average values over the entire temperature range of measurement which were presented in I,

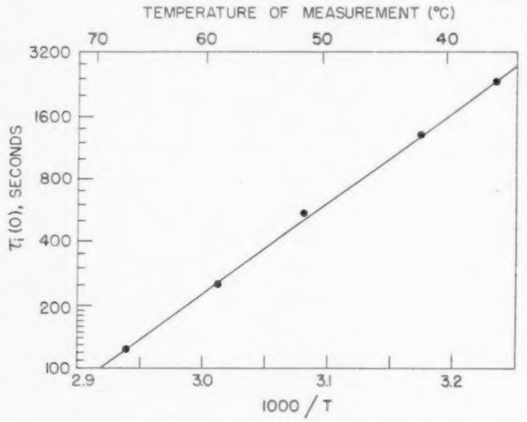

FIGURE 3. The initial time-to-inflection as a function of the temperature of measurement, for a 70-30 silver-zinc specimen quenched from 400°C into a calcium chloride solution. From the slope of the straight line the value ΔH_j = 19.7 kcal/mole is obtained.

but the low temperature values. These are listed in Table II together with the results of the non-equilibrium measurements. The heat of formation

TABLE II

PRINCIPAL NUMERICAL RESULTS OF EQUILIBRIUM AND NON-EQUILIBRIUM MEASUREMENTS

Equilibrium measurements	H_r = 31.5 kcal/mole	$\log \bar{\tau}_0 = -14.30$
Non-equilibrium measurements	$\Delta H_j = 19.7$	$\log \tau_0(0) = -10.48$
Deduced results	$\Delta H_f = 11.8$	$\Delta S_r/R = 2.3$ $c(0) = 5 \times 10^{-4}$ $T_F = 365°C$

of a vacancy, ΔH_f, is now obtained with the aid of equation (7). Its value is given in Table II. These measurements have thus enabled us to separate the composite "activation energy" for atomic mobility, H_r, into its component parts, the heat of activation for a vacancy jump and the heat of formation of a vacancy.

The same separation of the quantity ΔS_r into its component parts cannot be made from the intercepts, for while $\bar{\tau}_0^{-1}$ is proportional to exp $(\Delta S_r/R)$, the product $c(0)$ exp $(\Delta S_j/R)$ enters into the quantity $\tau_0^{-1}(0)$. We may obtain $c(0)$, however, by inserting a reasonable value for ΔS_j into equation (10). Such a value can be guessed at within narrow limits. Zener [8] has shown that both entropy terms, ΔS_f and ΔS_j, should be greater than zero, the former because of the increased vibrational freedom of neighboring atoms upon formation of a vacancy, and the latter because the saddle point configuration for a vacancy jump is associated with straining of the surrounding lattice. (The jump of a vacancy is in this respect closely analogous to the movement of an interstitial solute, which also involves a positive entropy of activation [13].) If we substitute into equation (8) the value $z\alpha\nu = 2 \times 10^{13}$ sec^{-1} ($z = 12, \alpha = 0.4$, and $\nu = 4 \times 10^{12}$) we obtain, with the value of $\bar{\tau}_0$ of Table II, $\Delta S_r/R = 2.3$. Since both ΔS_j and ΔS_f are greater than zero, reasonable values for these quantities may be obtained if each is set equal to $\frac{1}{2}\Delta S_r$. Substituting into equation (10) we obtain $c(0) = 5 \times 10^{-4}$. On the basis of the uncertainties in the quantities entering into this calculation, this value of $c(0)$ is estimated to be correct to within a factor of 4. The result is interesting, since even a value $c(0) = 10^{-4}$ seems to be surprisingly large for the concentration of vacancies frozen into this alloy.

The measurements of the temperature dependence of $\tau_i(0)$ also make possible the calculation of the freezing-in temperature, T_F, as described in the theory section (equation (11)). As indicated in that section, the high temperature values of ΔH_f and ΔS_f are required for this calculation. These are not known from the present measurements, but if low temperature values are used and a slight correction is applied to take into account the possible curvature of the plot of log $\bar{c}$ against T^{-1}, the probable error of the result is not large. The calculated value of T_F is 365°C. On the basis of the uncertainties in the quantities entering into this calculation, the reliability of this result is estimated to be $\pm$ 70°C. In view of the results of Figure 1, which show that T_F is substantially less than the quenching temperature, even for a quenching temperature below 300°C, it is quite likely that the quantity T_F in the present set of measurements is actually somewhat lower than 365°C; a value of about 300°C would be consistent both with the estimated probable error in the present calculations and with the results of Figure 1.

The Vacancy Decay Curves

The variation of τ_i with time after quenching at a constant temperature of 59°C has already been shown, both before and after cold working, in Figure 2. As demonstrated in the theory section, equation (12), the relative variations of τ^{-1} with time gives

the relative variation of the vacancy concentration with time. It was also shown that if the quantity $\tau^{-1}/\tau^{-1}(0)$ is plotted against a corrected time, t', given by equation (13), the decay curves obtained for different temperatures should fall together. A series of runs on the same well-annealed (70-30) silver-zinc wire specimen at different temperatures are shown in Figure 4, where $\tau_i^{-1}/\tau_i^{-1}(0)$ is plotted against corrected time (using 59°C as the reference temperature). These are the same runs from which

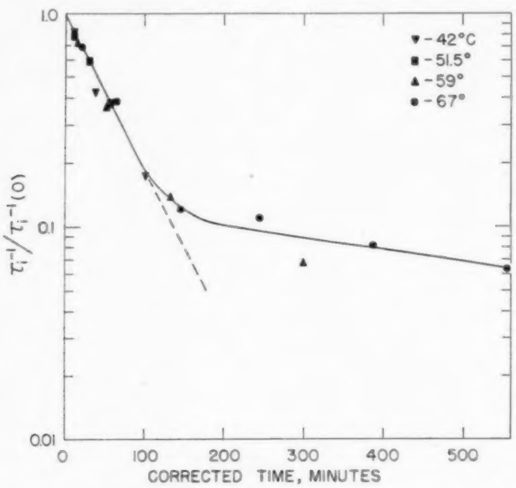

FIGURE 4. The vacancy decay curves for different measuring temperatures, plotted against corrected time (reference temperature, 59°C).

the quantities $\tau_i(0)$, discussed in the last section, are obtained. Figure 4 shows that the vacancy decay curves for various temperatures are brought into very nearly a single curve when plotted against corrected time. The small deviations that do occur may be related to the structure sensitivity of these decay curves, as previously demonstrated in Figure 2. The early part of Figure 4 shows an exponential decay, in agreement with equation (9); from this straight-line part of the curve a value of the decay time, θ, of 60 minutes is obtained at 59°C, or the ratio $\theta/\tau_i(0) = 14$, which is approximately independent of temperature.

From the numerical values of the decay time it is possible to make still another independent estimate of the freezing-in temperature, T_F. It is reasonable to assume that during the quenching operation, the time for the temperature to fall through the freezing-in temperature is of the order of magnitude of 0.01 sec., at least to within a power of ten. In order to trap vacancies, θ must therefore be equal to about 0.01 sec. at T_F. Since θ varies with temperature according to $\theta = \theta_0\, e^{\Delta H_j/RT}$ and its value at 59°C is known, we can calculate T_F in this way using the value of ΔH_j already determined (Table II). The result obtained is that $\theta = 0.01$ sec. at 300°C, in good agreement with the estimate of T_F in the last section. The agreement between these independent calculations of T_F and the reasonable values obtained indicates the self-consistency of the interpretation that has been given to these experiments.

It is possible, on the basis of the results obtained, to estimate a limiting value for the number of jumps that a vacancy can make before it is annihilated. From equation (3), the quantity τ^{-1}/α is the atomic jump frequency of the rate-controlling component of the solid solution. (As indicated in the theory section, when the jump probabilities of the two atomic species are not the same, the relaxation rate is determined by the rate of jump of the slower moving component.) If we now divide this atomic jump frequency by the vacancy concentration, c, and multiply by the mole fraction of the slower moving component, f, we obtain the quantity $\tau^{-1}f/\alpha c$ which is the number of times per second that a vacancy interchanges positions with one of the slower moving atoms. This quantity therefore represents a lower limit to the jump frequency of a vacancy. If it is multiplied by the decay time, θ, a lower limit is obtained for the number of vacancy jumps before annihilation. Since $\theta/\tau_i(0) = 14$ and $c(0)$ is estimated as 5×10^{-4}, we find that this lower limit is about 5×10^4 vacancy jumps. If dislocations are assumed to act as sinks for vacancies and the dislocation density is taken to be 10^9 lines/cm^2, then the fraction of lattice sites that may serve as sinks for vacancies is of the order 10^{-6}. A vacancy should then have a lifetime of 10^6 jumps, if we assume that it will wander at random until it comes close to a sink. This result is consistent with the lower limit of 5×10^4 quoted above.

It is noteworthy that exponential time decay occurs only in the early part of the decay curve. The sharp decrease in slope in the later part of the curve is most apparent in Figure 4 from the measurements taken at the highest temperature (67°C). These measurements could be carried farther than the others, since relaxation occurred at the greatest rates and so the largest number of successive measurements could be taken. This sharp decrease in the rate of vacancy decay at later times is under further investigation. Possible interpretations of the effect are either the exhaustion of the sinks at which vacancies are absorbed, or the existence of more than one type of imperfection that plays a role in atomic mobility.

Acknowledgement

The experimental part of this research was carried out at the University of Chicago and supported in part by the Office of Naval Research. The work at Yale University was supported in part by the Office of Ordnance Research.

References

1. Smigelskas, A. D. and Kirkendall, E. O. Trans. A.I.M.E., **171** (1947) 130.
2. Da Silva, L. C. C. and Mehl, R. F. J. Metals, **3** (1951) 155.
3. Zener, C. Acta Cryst., **3** (1950) 346.
4. Huntington, H. B. and Seitz, F. Phys. Rev., **61** (1942) 315.
5. Huntington, H. B. Phys. Rev., **61** (1942) 325.
6. Nowick, A. S. Phys. Rev., **88** (1952) 925.
7. Nowick, A. S. Phys. Rev., **82** (1951) 551.
8. Zener, C. Appl. Phys., **22** (1951) 372.
9. Kê, T. S. and Zener, C. Symposium on the Plastic Deformation of Crystalline Solids (ONR, 1950), p. 185.
10. Zener, C. Elasticity and Anelasticity of Metals (University of Chicago Press, 1948), p. 113.
11. Nabarro, F. R. N. Rep. Conf. on Strength of Solids (Physical Society, London, 1948), p. 75.
12. Seitz, F. Phys. Rev., **79** (1950) 890, 1002.
13. Wert, C. and Zener, C. Phys. Rev., **76** (1949) 1169.

Note Added in Proof*

It is actually not required that the quantity ΔH_j obtained from initial relaxation times (Figure 3) be precisely equal to the activation energy associated with the decay time, θ. A difference may be expected because the relaxation rate is determined by the slower moving component while the decay rate is determined by the faster one. A possible indication of this difference appears in Figure 4, which shows a small systematic deviation of the data for different temperatures from the mean curve. If this deviation is regarded as significant, it implies that the vacancy decay time may be associated with an activation energy of about 17 kcal/mole, in contrast to the somewhat higher value of ΔH_j. Using this rough value, we may estimate that the rate of vacancy movement at 50°C is about 50 times greater than the lower limit calculated above. The mean lifetime of a vacancy is then of the order of 10^6 jumps, in good agreement with the concept of dislocations as vacancy sinks.

*Received January 26, 1953.

EXPERIMENTAL VERIFICATION OF THE TWIN SYSTEM IN ALPHA-IRON*

H. W. PAXTON†

The crystallographic elements involved in the mechanical twinning of α-iron (i.e. the production of Neumann lamellae) have been evaluated. The technique involved the measurement on a polished surface by optical goniometry of the tilt produced by twinning a single crystal during tensile fracture at $-185°C$. It was found that the twinning plane was $\{112\}$, the twinning direction $\langle 111 \rangle$ and the angle of shear was (within experimental error) the theoretical 38°56′. Lamellae were formed in some cases on systems which would not be expected to twin in tension. It is postulated that these are accommodation systems in regions of severe local strain.

VÉRIFICATION EXPÉRIMENTALE DU SYSTÈME DE MACLAGE DANS LE FER ALPHA

Une évaluation a été faite des éléments cristallographiques qui sont impliqués dans le maclage mécanique du fer α (c.-à-d. la production des lamelles de Neumann). La technique impliquait l'emploi de la goniométrie optique pour la mesure, sur une surface polie, de la rotation produite par le maclage d'un monocristal pendant la rupture par traction à $-185°C$. Il a été trouvé, que le plan de maclage était le $\{112\}$, la direction de maclage $\langle 111 \rangle$ et l'angle de cisaillement avait (à l'erreur expérimentale près) la valeur théorique de 38°56′. Dans certains cas il y a eu formation de lamelles dans des systèmes dans lesquels on ne se serait pas attendu au maclage lors d'une extention. Il fut proposé, que ce sont des systèmes d'adaptation dans des régions de grande déformation locale.

EXPERIMENTELLE BESTÄTIGUNG DES ZWILLINGSSYSTEMS IN ALPHA-EISEN

Die kristallographischen Elemente, die an der mechanischen Zwillingsbildung d.h. der Bildung von Neumann Lamellen beteiligt sind, werden ausgewertet. Die experimentelle Technik erforderte die Messung der Neigung einer polierten Oberfläche mit Hilfe eines optischen Goniometers. Diese Neigung war durch Zwillingsbildung eines Einkristalles während des Bruches unter Zugverformung bei $-185°C$ entstanden. Als Zwillingsebene wurde $\{112\}$ gefunden, die Zwillingsachse war $\langle 111 \rangle$, und der Scherungswinkel stimmte innerhalb der experimentellen Fehlergrenzen mit dem theoretischen Wert, 38°56′, überein. In einigen Fällen wurde Lamellenbildung am System beobachtet, die unter Zug keine Zwillingsbildung zeigen sollten. Es wird angenommen, dass es sich hierbei um Angleichungsformationen im Gebiete starker örtlicher Verformungen handelt.

VOL. 1 1953

Simple considerations of lattice geometry suggest that mechanical twinning of the body centred cubic lattice can take place most easily by a homogeneous shear on a $\{112\}$ plane in the $\langle 111 \rangle$ direction lying in this plane. The crystallographic shear s required is 0.7071, and this should be equal to the macroscopic shear. Alpha-iron and its dilute alloys appear to be the only body centred cubic metals in which mechanical twinning has been definitely demonstrated.

Several workers [1; 2; 3] have shown that mechanical twins ("Neumann lamellae") in α-iron have a $\{112\}$ as composition plane. However, the shear direction and the magnitude of the shear do not appear to have been reliably determined. Orientation determinations by X-rays are difficult because of the severe local distortion of the lattice, and because of the narrowness of the twins (about 5μ). Mathewson and Edmunds [4] reported that they obtained X-ray evidence for twinning in silicon-iron being exactly as predicted theoretically, but it is difficult to assess the accuracy of the work from the published photographs. Recently, Kelly [5] has attempted an X-ray investigation using a micro-beam camera. After inferring that the twinning direction was [111] from a study of twin intersections, Smith, Dee, and Young [2] were able to show very approximately that the shear was about 0.7.

In the work to be described, it has proved possible to establish the three twinning elements (plane, direction, and shear) simultaneously by measuring the tilt, produced by mechanical twinning, of a polished surface on a fairly large single crystal.

Experimental Method

Twins were produced in electropolished Armco strip single crystals containing about 0.003 per cent C by slow tension in a bath of liquid air. The strain rate was approximately 7×10^{-4} per minute. The two crystals tested fractured on cube planes after showing so little plastic extension that no deviation from a linear stress-strain curve could be noted; their fracture stresses were as follows:

Specimen	Fracture stress	Resolved normal to (001)
1	32.7 Kg/mm²	27.3 Kg/mm²
2	32.8 Kg/mm²	29.7 Kg/mm²

Twins on four different systems were produced in each case, although the numbers on two of these were very small. It seems most likely that the twins were all produced by the shock of fracture, especially since they were only found in the vicinity of the crack.

*Received November 5, 1952.

†Department of Physical and Theoretical Metallurgy, University of Birmingham, England.

The twins could readily be detected on polished surfaces by the relief effects which they produced. The angles which their traces made with the tensile direction on two faces of known included angle (approximately 90°) were measured to the nearest 0.5° on a Vickers metallograph. The orientations of

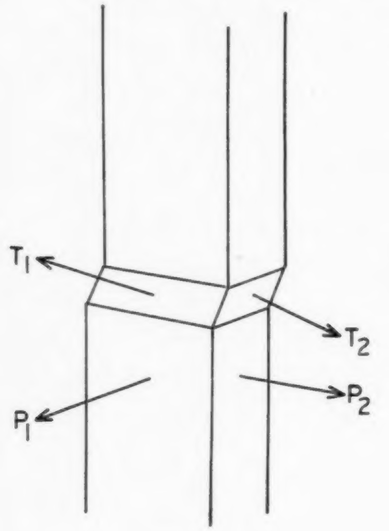

Figure 1

the crystals were determined within an accuracy of 1° by a conventional Laue back-reflection method.

It proved possible to identify the pairs of traces of each twin family on the two surfaces unambiguously by counting the number and estimating densities of traces in various regions; hence it was unnecessary to pair off all possible combinations of trace normals to find a recurring plane, as is sometimes necessary when using this method of determining planes from traces. In all 8 cases that were examined, the pole of the observed twins was within 1° of a {112} plane.

The complex nature of the deformation is shown by the fact that only 5 of the 8 twin systems which were observed should theoretically twin to relieve tensile stress. The other 3 twin systems are in all probability accommodation systems [6; 7] to relieve local strains.

When {112} had been established as the twinning plane, the shear direction and the magnitude of the shear were evaluated by the following method, due to Greninger and Troiano [8]. During the formation of twins, the surface was sheared into a position shown diagrammatically in Figure 1.

The sheared surface in the twin remained sufficiently plane to reflect incident light coherently, and measurement of the poles of the four surfaces P_1, P_2, T_1, T_2, was possible with a two circle goniometer. The accuracy was lowest on the narrow edge of the strip, where a certain amount of rounding off had been produced during the electropolishing. By taking a large number of observations the scatter could be reduced and an average taken with some degree of confidence. An internal check is of course possible with a two circle goniometer since there are two positions of the circles which can be used to obtain reflection. The value eventually chosen for any pole was the arithmetic average of the means of the observations in each setting.

These poles are plotted on a stereogram which has as its plane of projection the twin plane determined from trace measurements in two surfaces. The corresponding planes are drawn as great circles. This stage is shown in Figure 2. The direction of shear is found by noting that a, the intersection of P_1 and P_2, is sheared into b, the intersection of T_1 and T_2, by twinning. It is a stereographic property of the shear of any direction that it must move along a great circle whose intersection with the basic circle is the shear direction. The sense of the shear is obtained from the fact that a must move to b and not vice versa.

In Figure 2 the [111] direction lying in the twinning plane, as determined from the X-ray orientation, agrees well with the theoretical shear

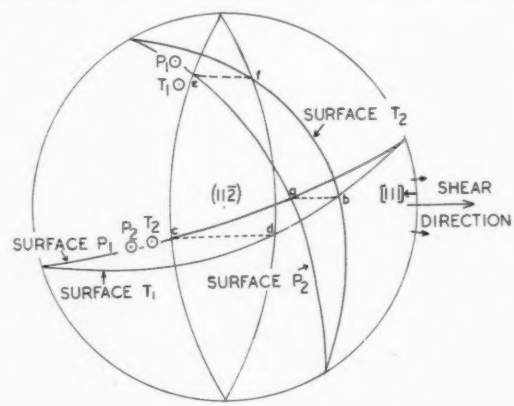

Figure 2

direction. The arrows on each side show the range of error in determination of the shear direction caused by uncertainty in T_2. The same measure of agreement was observed for the other twin systems studied.

To measure the magnitude of the shear, a stereographic projection of the unit twinning sphere [9] on the twin plane has been superimposed on Figure 2. The second undistorted plane K_2 (ec) moves to the

symmetrical position about the centre, $K_2'(fd)$. The trace normals to both planes pass through the experimentally determined shear direction. The intersections of K_2 with P_1 (c) and P_2 (e) are carried by shear to the intersections of K_2' with T_1 (d) and T_2 (f) respectively. By trial and error, symmetrical positions about the plane normal to the shear direction are found for K_2 and K_2' such that cd and ef simultaneously lie on small circles perpendicular to this plane and represent equal angles. With $s = 0.7071$, the calculated value for $cd = ef = 38° 56'$. Observations on one twin system in each of the two different crystals gave the value 37° in each case.

It was not possible to measure T_2 for all the systems in each crystal with sufficient accuracy, and thus the shear direction for these cannot be determined. An estimate of the magnitude of the shear was obtained from the tilt on one surface on the basis of $\{112\}/\langle 111\rangle$ as the twinning system. Typical values are listed in the table below.

Specimen	Twin family	$cd°$
1	α	36 ± 12
	β	36 ± 8
	γ	40 ± 12
2	α	33 ± 7
	β	40 ± 5

This method is not so accurate as the two surface measurements, but the agreement with the theoretical value is reasonable.

Acknowledgments

The author's thanks are due to Professor D. Hanson and the University of Birmingham for provision of facilities and financial support, and to Professor A. H. Cottrell and Dr. R. W. Cahn for valuable discussion.

References

1. Barrett, C. S., Ansel, G., and Mehl, R. F. Trans. A.S.M., **26** (1937) 702.
2. Smith, S. W. J., Dee, A. A., and Young, J. Proc. Roy. Soc., **A121** (1928) 477.
3. Pfeil, L. B. Carn. Schol. Mem., **15** (1926) 319.
4. Mathewson, C. H. and Edmunds, G. H. Trans. A.I.M.E., **80** (1928) 311.
5. Kelly, A. Private communication (to be published).
6. Jillson, D. C. Trans. A.I.M.E., **188** (1950) 1129.
7. Pratt, P. L. and Pugh, S. F. J. Inst. Met., **80** (1952) 653.
8. Greninger, A. B. and Troiano, A. R. Trans. A.I.M.E., **185** (1949) 590.
9. Schmid, E. and Boas, W. Plasticity of Crystals (London, F. A. Hughes, 1950), p. 72.

THERMODYNAMICS OF ORDERING ALLOYS, I. ACTIVITIES IN COBALT-PLATINUM ALLOYS AND SOME GENERAL CONSIDERATIONS ON ORDERING SYSTEMS*

R. A. ORIANI†

The activity of cobalt in solid cobalt-platinum alloys has been measured by the galvanic cell technique. The observed thermodynamic properties are not those predicted by the quasi-chemical theory for ordering alloys. The properties of this and other ordering systems are discussed from the point of view of distortional energy, thermal entropy, and electronic interactions. It is shown that in general the distortional, cr strain, energy cannot be evaluated from a comparison of the heats of solution of corresponding solid and liquid solutions.

LA THERMODYNAMIQUE DES ALLIAGES QUI SUBISSENT LA TRANSFORMATION ORDRE-DÉSORDRE, I. LES ACTIVITÉS DANS LES ALLIAGES COBALT-PLATINE ET QUELQUES CONSIDÉRATIONS GÉNÉRALES SUR LES SYSTÈMES QUI S'ORDONNENT

L'activité du cobalt dans les alliages solides cobalt-platine a été mesurée au moyen de la technique des piles galvaniques. Les propriétés thermodynamiques observées ne coincident pas avec les prédictions de la théorie quasi-chimique des alliages subissant la transformation ordre-désordre. Les propriétés de ce système ainsi que d'autres qui s'ordonnent sont discutées du point de vue de l'énergie de déformation, de l'entropie thermique et des interactions électroniques. Il est montré, qu'en général, l'énergie de déformation ne peut pas être évaluée par la comparaison des chaleurs de dissolution des solutions solides et liquides correspondantes.

THERMODYNAMIK ORDNUNGSFÄHIGER LEGIERUNGEN, I. AKTIVITÄTEN IN KOBALT-PLATIN LEGIERUNGEN UND EINIGE ALLGEMEINE ÜBERLEGUNGEN ÜBER ORDNUNGSFÄHIGE SYSTEME

Die Aktivität des Kobalts in festen Kobalt-Platin Legierungen wurde mit der galvanischen Element-Technik gemessen. Die experimentell gefundenen thermodynamischen Eigenschaften stimmen nicht mit den durch die quasi-chemische Theorie ordnungsfähiger Legierungen vorausgesagten überein. Die Eigenschaften dieses und anderer ordnungsfähiger Systeme werden vom Standpunkt der Verzerrungsenergie, der thermischen Entropie und der Wechselwirkung der Elektronen diskutiert. Es wird gezeigt, dass im allgemeinen die Verzerrungsenergie nicht durch einen Vergleich der Lösungswärme der entsprechenden festen und flüssigen Lösungen berechnet werden kann.

VOL 1 195

Introduction

The thermodynamic investigation of alloys that exhibit a superlattice may provisionally be divided into two categories: first, the study of the values and of the significance of the thermodynamic parameters that characterize the solid solutions which support superlattice reactions, and second, the problem of the nature of the ordering reaction itself. Experimental material of a thermodynamic nature is rather meager. Of the nearly fifty metallic binary systems which have been found to exhibit a superlattice reaction, thermodynamic activity measurements have been carried out on only nine; none of these is of sufficient precision or extent to furnish answers to all the pertinent questions. The phase diagrams of such systems are continually undergoing revision; new ordering reactions are being found in binaries which had presumably been thoroughly studied before, and the question of the coexistence at equilibrium of ordered and disordered phases [1; 2] has still to be settled for many systems. The sluggishness of many of the order-disorder transformations, as has been established for copper-gold alloys by Dienes [3], Borelius [4], and by the as yet incomplete work of Rhines and Newkirk [5], renders suspect any conclusions as to the thermodynamic nature of the ordering reaction drawn from the measurement of the heat capacity through the "lambda point" as done by Sykes and Jones [6] for Cu_3Au, Leech and Sykes [7] for $FeNi_3$, and Khomyakov [8] for $MgCd_3$ and MgCd.

This paper is part of a systematic investigation of the thermodynamic properties of ordering systems, endeavoring to cast some light on the factors that promote the formation of the superlattice and on the nature of the transition itself. It will be of interest to compare the experimental results with the predictions of the various statistical mechanical theories of ordering [9].

Experimental

The electromotive force developed by the cell

$$Co_{(s)} \mid Co^{++} \text{ (in electrolyte)} \mid Co(Pt)_{(s)}$$

was measured as a function of temperature and alloy composition. The electrolyte was an eutectic mixture of LiCl and KCl, melting at approximately 360°C, to which was added a very small amount of $CoCl_2$. The cell employed is shown diagramatically

*Received October 23, 1952.
†General Electric Research Laboratory, The Knolls, Schenectady, New York, U.S.A.

in Figure 1. Because of the very high temperatures involved, the portion of the cell immersed in the furnace is of quartz, graded to Pyrex at the top. An independently calibrated thermocouple of platinum-platinum, 10 per cent rhodium measures the temperature of the molten electrolyte. Each electrode is surrounded by a loosely fitting quartz tube

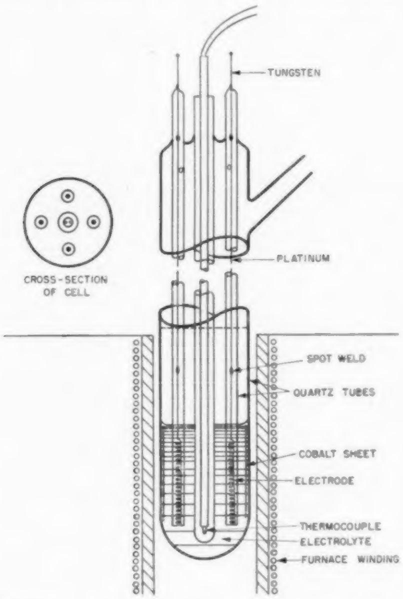

FIGURE 1. Diagram of the galvanic cell.

which projects into the electrolyte; this feature prevents accidental contact of one electrode with another, and also avoids any possibility of a current being carried from one electrode to another by electrolyte condensed in the cooler surfaces of the cell.

Each cell usually had three different alloy electrodes and one of pure cobalt. The electrodes were wound into spirals in order to lessen polarization effects by presenting as much surface as possible to the electrolyte. However, the portion of the electrodes projecting from the bath were drawn down to a few mils in diameter in order to decrease heat conduction up the suspension wires. These latter were of platinum, and were spot-welded to the electrodes to assure good electrical contact. The platinum suspension wires were silver-soldered to tungsten wires sealed through glass at the top of the cell. The thermal e.m.f. caused by all these junctions was measured at various temperatures in a separate experiment, and was found to be negligible. The voltages from the cell were measured to the nearest hundredth of a millivolt by a Leeds-Northrup K-2 potentiometer.

The KCl and LiCl salts were given a preliminary baking at 330°C for one week under vacuum in a separate apparatus. This treatment was designed to decompose the chlorates present in the salts and to remove most of the moisture. The salts were then poured as quickly as possible through the side tube into the preheated cell, and the cobaltous chloride, previously dried under a stream of hydrogen chloride, was added. The side arm of the cell was sealed to a vacuum system and the cell and contents were desiccated by heating at 330°C for two weeks under vacuum. At the end of this time, the furnace temperature was raised to melt the salts and the evacuation was continued for several hours more. Argon, purified by passage through calcium chip furnaces, the first at 550°C and the second at 200°C, was introduced at one-half atmosphere, into the cell, which was then disconnected from the accessory apparatus by sealing off the side tube. Further clean-up of the electrolyte was produced by a sheet of pure cobalt in contact with the electrolyte.

Upon opening a cell that had operated properly, the electrodes were found to be absolutely uncorroded, the electrolyte appeared a very clear, pale-blue color, and the quartz vessel was attacked only on the surface in contact with the electrolyte. Because the freezing of the salts invariably cracks and spalls the quartz, it has been found impossible to use a cell more than once. The electrodes were analyzed for platinum after the run. Because of the small weights involved, the precision of the chemical analyses was about 0.5 per cent.

The success of the electrochemical method for the measurement of thermodynamic activities of components in solid alloys depends upon reversibility of the galvanic cell, singleness of the electrode reaction, and establishment of composition equilibrium between the surface of the electrode and its interior. One can have confidence that, barring accidental impurities, the only electrode reaction is $Co \rightarrow Co^{++} + 2e$, since both the standard electrode potential and the free energy of formation at 1000°K of the chloride of cobalt are very different from the corresponding quantities for platinum. Furthermore, that platinum does not enter the reaction is confirmed by our inability to detect by emission spectroscopy platinum either in the cobalt electrode or in the electrolyte. Although there is no direct criterion for cell reversibility, strong support is given by reproducibility of e.m.f. before and after current has been drawn from the cell by allowing the measuring potentiometer to remain unbalanced. Further support for cell reversibility, as well as for diffusion equili-

brium, is obtained from the reproducibility and internal consistency of the e.m.f. values obtained upon varying the cell temperature haphazardly. The recorded values of voltage were obtained by maintaining the cell at constant temperature until all the electrode potentials had reached steady values; then the temperature was increased or decreased (the choice was usually made haphazardly), and the temperature again held constant until constancy of voltages was attained. The reproducibility thus obtained is strong basis for the belief that all the conditions for satisfactory measurement of activities were met. The times of waiting for constancy ranged from one hour to over two days, depending on the temperature level.

Experimental Results

The experimental values of electrode potential as a function of temperature and composition are presented in Table I, and are plotted in Figure 2. The scatter of the points is not excessive in view of the very high temperatures involved and in view of the non-directional way in which the cells were

TABLE I

EXPERIMENTAL DATA OF E.M.F. VS. TEMPERATURE FOR VARIOUS ALLOY COMPOSITIONS

	Electromotive Force (m.V.)							
t(°C)	$x_{Co} = 0.32_4$	0.35_1	0.47_1	0.51_6	0.56_7	0.59_0	0.69_0	0.73_1
696.4		43.9		35.8		31.7		
717.4					34.8			25.0
730.8	56.1		42.5				28.9	
735.9		49.3		39.4		34.4		
738.0		49.7		39.5		34.5		
755.2		53.2		41.3		35.7		
756.8		53.7		41.5		35.9		
763.8					38.5			25.6
765.7		55.7		42.4		36.8		
778.6	60.8		47.9				30.3	
788.3		58.6		44.4		38.5		
791.2		58.9		44.5		38.7		
797.9			48.4				30.8	
799.5		60.5		45.6		39.9		
801.5	64.2		49.0				30.5	
811.7					41.5			26.5
815.2		61.9		46.5		40.8		
816.3	64.8		49.6				31.1	
825.0		63.3		47.5		41.6		
835.4	66.5		52.6				30.6	
846.0		65.7		49.3		42.9		
851.1		66.1		49.9		42.9		
853.1					44.0			27.5
865.4		67.3		50.5		44.0		
877.3	71.7		55.6				32.0	
889.5		69.0		51.8		45.7		
897.1					47.4			29.5
907.7	74.5		58.6				32.4	

taken from one temperature to another. This independence of the electrode voltages from the manner of temperature variation contrasts with the results of Weibke and Quadt [10] for solid copper-gold alloys; they obtained different curves for the ascending-temperature and the descending-temperature portions of the runs. The consistency of the high-temperature points with those at lower temperatures and the general internal consistency of the data demonstrate the absence of spurious effects such as disturbed the higher-temperature results on solid copper-platinum alloys of Weibke and Matthes [11].

The voltage data were fitted with the best straight lines, though it appeared that the data for

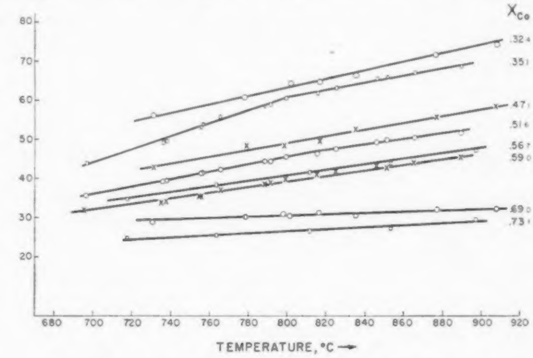

FIGURE 2. E.m.f. *vs.* temperature: Co-Pt alloys.

alloys of atom fraction cobalt of 0.35 and 0.51 are best described by two intersecting straight lines. Although the point of inflection for the 0.51 alloy appears to agree with the temperature of ordering according to the phase diagram of Newkirk *et al* [1], the facts that the data are of insufficiently high precision and that similar points of inflection are not observed for other compositions where they may be expected diminish the confidence one can place on this inflection. The knee in the curve for the 0.35 alloy, however, does seem to be beyond the range of experimental error, but it does not correspond to any transformation depicted in the established phase diagram. Nevertheless, this inflection may be connected with the ordered phase recently found by Geisler and Martin [12], which centers about the composition $CoPt_3$.

The question of the thermodynamic aspects of the transformation itself must be deferred for future study. For the present in this laboratory the problem has been transferred to the copper-gold system, for which the much lower temperatures involved lead to simpler experimental problems. Our present results for the Cu-Au system show that a thermodynamic study of the order-disorder transformations in such alloys must be carried out through much longer isothermal holding times than have hitherto been employed. This view is supported by the irreproducibility of the inflections in the curves of Weibke and Quadt [10] for the same system, and the lack of correspondence between the inflections found by Weibke and Matthes [11] for the Cu-Pt system and

TABLE II

Summary of Calculations Based on Data at 850°C

x_{Co}	dE/dT	a_{Co}	$\overline{\Delta G}_{Co}{}^{(x)}$	$\overline{\Delta G}_{Pt}{}^{(x)}$	$\Delta G^{(x)}$	a_{Pt}	$\overline{\Delta S}_{Co}{}^{(x)}$	$\overline{\Delta S}_{Pt}{}^{(x)}$	$\Delta S^{(x)}$	ΔH
0.32_4	110	0.244	− 640.5	245.9	− 41.3	0.76	2.83	− 0.36	0.67	714
$.35_1$	93.4	.256	− 705.2	278.6	− 66.7	.74	2.23	− 0.06	0.74	768
$.47_1$	86.8	.333	− 770.0	298.4	− 204	.61	2.51	− 0.27	1.04	965
$.51_6$	71.0	.359	− 805.7	320.7	− 261	.56	1.96	0.27	1.14	1020
$.56_7$	71.0	.402	− 765.5	258.5	− 322	.49	2.15	0.11	1.27	1100
$.59_0$	72.0	.410	− 814.6	320.3	− 349	.47	2.27	− 0.06	1.32	1130
$.69_0$	16.7	.521	− 631.6	− 12.9	− 440	.31	0.03	3.58	1.13	830
$.73_1$	25.0	.567	− 544.6	− 228.7	− 460	.24	0.53	3.03	1.20	890

the phase diagram of Esch and Schneider [13]. The electrical resistivity measurements of Rhines and co-workers [5] on copper-gold alloys show that holding times of weeks or months may be necessary to achieve equilibrium. The present reproducible curves below the temperatures of ordering of Co-Pt alloys may be considered as measurements upon metastable systems, the properties of which are related to the thermal history of the samples. Therefore, the results at lower temperatures will not be considered further in this paper.

Table II lists the quantities derived from the data at 850°C, a temperature well above the highest temperature of ordering. The slopes of the voltage-temperature curves are expressed as microvolts per

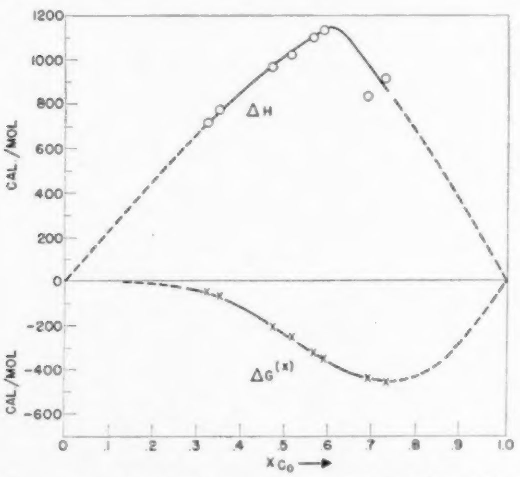

Figure 3. Cobalt-platinum system: excess free energy and heat of solution.

degree, the free energies and the enthalpy as calories per gram atom, and the entropies as calories per degree per gram atom. The activity of cobalt in the solid solution was computed by the relation

$$2FE = -RT \ln a_{Co}, \tag{1}$$

where F is the faraday, R the gas constant, T the absolute temperature, E the observed voltage, and 2 is the valence change for $Co \rightarrow Co^{++}$. In the calculation of the thermodynamic properties of Pt by the application of the Gibbs-Duhem equation, advantage was taken of the simplifications made possible by the use of excess molar quantities [14]. The excess molar free energy of solution for cobalt, $\overline{\Delta G}_{Co}$, is the excess of the actual partial molar free energy over the value it would have in an ideal solution, that is,

$$\begin{aligned} \overline{\Delta G}^{(x)}_{Co} &= \overline{\Delta G}_{Co} - \overline{\Delta G}_{Co}(\text{ideal}) \\ &= RT \ln a_{Co} - RT \ln x_{Co} = RT \ln \gamma_{Co} \end{aligned} \tag{2}$$

where γ = activity coefficient a/x. The corresponding quantity for Pt is calculated by the graphical integration of the Gibbs-Duhem equation in the form

$$\overline{\Delta G}^{(x)}_{Pt} = \int_0^{x_{Co}} \frac{\overline{\Delta G}^{(x)}_{Co}\, dx_{Co}}{(1 - x_{Co})^2} - \frac{\overline{\Delta G}^{(x)}_{Co}\, x_{Co}\, x_{Pt}}{(1 - x_{Co})^2}. \tag{3}$$

The integral excess molar free energy of solution is then:

$$\Delta G^{(x)} = x_{Co}\overline{\Delta G}^{(x)}_{Co} + x_{Pt}\overline{\Delta G}^{(x)}_{Pt} \tag{4}$$

and

$$\Delta G^{(x)} = RT[x_{Co} \ln \gamma_{Co} + x_{Pt} \ln \gamma_{Pt}]. \tag{5}$$

Similarly,

$$\begin{aligned} \overline{\Delta S}^{(x)}_{Co} &= \overline{\Delta S}_{Co} - \overline{\Delta S}_{Co}(\text{ideal}) \\ &= 2F(\partial E/\partial T)_x + R \ln x_{Co} \end{aligned} \tag{6}$$

and the $\overline{\Delta S}_{Pt}$ is calculated by equation (3) by replacing the $\overline{\Delta G}^{(x)}_i$, by $\overline{\Delta S}^{(x)}_i$. Then, the integral excess molar entropy of solution is

$$\Delta S^{(x)} = x_{Co}\, \overline{\Delta S}^{(x)}_{Co} + x_{Pt}\, \overline{\Delta S}^{(x)}_{Pt}. \tag{7}$$

The integral enthalpy of solution, since it is itself an excess quantity (the heat of solution is zero for the ideal case), is obtained by

$$\Delta H = \Delta G^{(x)} + T\Delta S^{(x)}. \tag{8}$$

The integral molar enthalpy and the excess molar

VOL. 1 1953

free energy of solution at 850°C are shown as a function of atom fraction of cobalt in Figure 3. The course of the activities of the two components with alloy composition is depicted in Figure 4; the

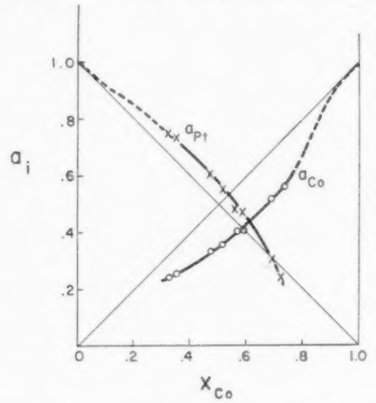

FIGURE 4. Activities at 850°C in Co-Pt alloys.

activity of platinum was obtained from the $\overline{\Delta G}_{Pt}^{(x)}$ of equation (3).

Discussion of Results

Every system exhibiting a superlattice that has been examined by X-ray diffraction at temperatures above the critical has been found to have short-range order (*vide* Walker [15] for CuPt, Cowley [16] for Cu_3Au, Roberts [17] for CuAu), so that short-range order is likewise to be expected in the cobalt-platinum system. For solid solutions the usual nearest-neighbor interaction theory [18; 19] leads to an energy of solution given by

$$\Delta H = n_{12}w = n_{12}[\epsilon_{12} - \tfrac{1}{2}(\epsilon_{11} + \epsilon_{22})] \tag{9}$$

where n_{12} is the number of nearest-neighbor pairs of atoms of dissimilar species, and the ϵ_{ij} are pairwise interaction energies between nearest neighbors of kind i, j. Calculating the entropy of mixing as the number of ways of arranging (Nx_1) atoms of species 1 and (Nx_2) atoms of species 2 to produce n_{12} pairs of the 1-2 type when long-range order is not present, setting up the free-energy expression, and finding the equilibrium number of (1.2) pairs by setting equal to zero the derivative of the free energy with respect to n_{12}, one obtains [19] as an approximation [14]

$$n_{12} = x_1 x_2 ZN(1 - 2x_1 x_2 w/RT)\,. \tag{10}$$

In this relation, x_i is the atom fraction of species i, N the Avogadro number, and Z the coordination number of the lattice. Therefore, in order to have the number of (1-2) pairs larger than the random number, w must be a negative number (i.e., $\epsilon_{12} > \frac{1}{2}(\epsilon_{11} + \epsilon_{22})$), so that the enthalpy of solution, ΔH, must be a negative quantity. Furthermore, it can be shown [20] that this treatment leads to activity coefficients smaller than unity for each of the components. Finally, because of the existence of short-range order the entropy of mixing must be smaller than that for an ideal solution.

These characteristics are possessed by copper-gold solid solutions [10] above the temperatures of long-range order. Indeed, for the composition Cu_3Au, the short-range order computed from Cowley's X-ray data [16] agrees satisfactorily [21] with that calculated from the activity data of Weibke and Quadt [10] by the nearest-neighbor theory. Similar good agreement with theory is shown by Mg-Cd, according to the recent data of Trumbore, Wallace, and Craig [22]. However, the present results on Co-Pt completely disagree with the predictions of theory in that the observed heat of solution is positive, not negative (see Table III), the entropy of solution is much larger than the ideal value, and though the deviations from Raoult's Law for the cobalt are negative throughout, the deviations for platinum are positive for much of the composition range.

As Table III shows, the Co-Pt binary is not alone in evincing disagreement with the predictions of theory for ordering alloys. Thus, although the heat

TABLE III
SUMMARY OF THERMODYNAMIC PROPERTIES OF ORDERING SYSTEMS*

Alloy 1 2	ΔG cal/gm. atom	ΔH cal/gm. atom	$\Delta S^{(x)}$ cal/gm. atom deg.	δ_1†	δ_2
Cu-Au	− 2200	− 1230	− .12	−	−
Mg-Cd	− 2460	− 1940	− .41	−	−
Co-Pt	− 1780	+ 1000	+ 1.11	−	+, −
Cu-Pt	− 3280	− 1500	+ .79	−	+, −
Pb-Tl	− 900	− 390	− .20	−	+, −

*Properties calculated at temperatures above critical temperatures for long-range order and $x = \frac{1}{2}$, except for Pb-Tl system, which is calculated at $x_{Tl} = 0.511$.

†δ_i represents the deviation of component i from Raoult's Law; if $\delta = +$, the activity coefficient is greater than unity, and if $\delta = -$, γ is less than unity.

of solution for Cu-Pt is a negative quantity as expected, the entropy of mixing is far larger than the ideal value, and the platinum has a composition range in which the deviation from Raoult's Law is positive [11]. Furthermore, as has been pointed out previously [15], the superlattice reaction at the composition CuPt cannot possibly be explained by nearest-neighbor interactions, because the segregation in the ordered structure of copper and of platinum atoms upon alternate (111) planes in a f.c.c. lattice causes the number of dissimilar nearest

neighbors to be the same below as above the ordering temperature.

The inclusion of the Pb-Tl system in Table III as an ordering alloy is done on the strength of the experimental and computational results of Tang and Pauling [23], which definitely indicate ordered structures at $PbTl_3$ and $PbTl_7$. The e.m.f. data of Olander [24] have been used by the writer to calculate the activity curve for Pb by graphical integration of the Gibbs-Duhem equation. Qualitatively, the activities of the components follow the same course as those in the Cu-Pt system; the Tl deviates negatively throughout, but the Pb deviates positively from x_{Tl} of 0 to 0.45, and then negatively. The heat and entropy of mixing for this system obey the theory.

That there are deviations from the configurational theory of nearest neighbors must be ascribed to the fact that the configurational aspect is only a part of the solution process, the other parts not being considered in the theory previously outlined. Thus, the entropy of solution must be the sum of two important terms; the first is the configurational contribution due to the number of ways of arranging the two kinds of atoms to produce n_{12} pairs of the (1-2) type. The combinatorial problem solved by Takagi considers only atoms of equal size. Hildebrand and Scott [25] and Guggenheim [26] show that the random mixing of unequal-sized atoms gives rise to a greater entropy increase than does the mixing of atoms of equal size. This is a very small correction term, amounting to 0.02 cal/mol deg. for an equimolar random solution of atoms having a 10 per cent disparity in radii, as do cobalt and platinum. This correction to the configurational entropy cannot be expected to be a significant term either for the solid solutions with which we are presently concerned, or for the many liquid metallic solutions showing entropies of mixing greater than the ideal value [27; 28].

The second contributing factor to the entropy of solution, one which is not at all considered in the configurational theory, is the entropy due to the vibrations of the atoms, sometimes called the thermal entropy [29]. It can be approximately evaluated by

$$\int_0^T (\Delta C_p/T)\, dT$$

where ΔC_p is the change in the heat capacity associated with the reaction

$$x_1 M_1 + x_2 M_2 = [(M_1)_{x_1}(M_2)_{x_2}]\,.$$

If M_1 and M_2 had the same atomic masses, and if the force constants in pure M_1, M_2 and in the solution were all the same, then Kopp's law of additivity of heat capacities would be obeyed and the thermal entropy would be zero. Data for ΔC_p for ordering alloys are generally lacking, but an idea of the possible importance of the thermal entropy can be gained by noting that if ΔC_p were to equal 0.2 cal/deg. gm. atom, and were to be constant from 100° to 1000°K, then

$$\int_{100}^{1000} 0.2\, d \ln T = 0.46 \text{ cal/deg.gm. atom.}$$

Now, the ΔC_p for the composition Cu_3Pd of copper-palladium, an ordering system, may be calculated from the equations given by Kelley [30] to be + 0.36 cal/deg. gm. atom at 900°K, so that the thermal entropy contribution for this composition should be fairly large. Incidentally, the ΔC_p for the composition CuPd may be obtained from the same source [30], and it is found to be − 0.08 cal/mol deg. at 900°K; this calculation shows the fallacy of attempting to estimate deviations from Kopp's rule by the disparity of individual atomic properties, viz. the Debye temperatures. Unfortunately, activity data for the Cu-Pd system do not exist so that the effect of the thermal entropy contributions at these two compositions cannot be checked. However, it can be seen from this example that the differences between the large observed entropies of solution for CuPt and CoPt alloys and the smaller than ideal ΔS expected by virtue of the short-range order may well be explainable by the non-additivity of the heat capacities of the components. This effect may be particularly strong in these two alloys of platinum because of the large difference in the atomic masses of the components.

The volume change upon solution may be an important factor in affecting the thermal entropy contribution, as evidenced by the measured entropies of solution of solid Mg-Cd alloys [22]. The ΔS is smaller than the ideal entropy of mixing at all compositions except those where the alloys form with an increase in volume; at such compositions, the observed ΔS is considerably larger than the ideal value. However, the relation between the thermal entropy contribution and the volume change of solution cannot in general be so direct, since, although Cu-Au [31], Cu-Pt [13], Co-Pt [32], and Tl-Pb [23] all show positive deviations from Vegard's Law (i.e., that the lattice parameter of the alloy is a linear function of the lattice parameters of the pure components) only the platinum alloys show large thermal entropies of solution.

Zener [33] has pointed out that the energetic aspect of the vibrational contribution to the entropy

of solution is the strain energy attending the solution of the solute atoms. Attempts to consider the strain-energy contribution to the heat of solution have usually artificially apportioned the latter into a "chemical," or atom-interchange energy of the sort envisioned by the theory of equation (9), and a strain energy which is necessarily positive. Lawson [34] calculates the strain energy in the solid solution as the elastic energy of distortion of an isotropic shell surrounding a solute atom, and by a simple, admittedly inappropriate assumption, extends the treatment to concentrated solutions. Heumann [35] employs the same assumptions, but instead of taking the elastic shear modulus as an intensity factor, he uses a thermal quantity, the ratio of the thermal expansion coefficient to the isothermal compressibility. Whichever way the strain energy is calculated, one obtains numbers of the order of 1 to 7 kcal/mol at a mol fraction of $\frac{1}{2}$, which are of the order of magnitude of the heats of solution observed.

However, the strain energy is only a part of the heat of solution and the interaction term, w, must add algebraically to the strain-energy term. That such an interaction energy must exist independently of strain effects is shown by the non-zero heats of solution in liquid systems, in which presumably strain energy has no role. The inclination then is to try to obtain the strain-energy contribution in solid solutions by subtracting the observed ΔH of the corresponding liquid solutions from the ΔH of the solid solutions of the same mol fraction. Lumsden [29] has done this for the Cd-Zn system, using partial molar heats of solution in very dilute solutions, the assumption being that the interaction, or chemical, term remains identical in both phases. Nevertheless, this procedure for calculating the strain energy cannot be recommended as a general rule. As the results in Table IV show, the heat of solution per mol (i.e., of $A_{x_A} B_{x_B}$ for the solid state minus that for the liquid state is usually either zero or a negative quantity. Since the distortional energy contribution must be a positive quantity, the results show that the assumptions of the separability of the strain energy from the interchange energy, and the constancy of the latter term from the liquid to the solid phase are not justified. It would indeed be remarkable if the interchange energy of the liquid solution were the same as that of the solid solution since interaction energies are strongly dependent on interatomic distances.

Though it appears difficult to obtain an experimental measure of the strain energy against which to check theoretical calculations, the energy of distortion probably plays an important part both in causing miscibility gaps in solid solutions and, as Hume-Rothery and Powell [36] have suggested, in

TABLE IV

ΔH of Solution for Solid and for Liquid Alloys at $x = \frac{1}{2}$

Alloy	ΔH. cal/gm. atom	
	Solid state	Liquid state
Cu-Au	− 1230[a]	0[b]*
Cu-Zn	− 2600[c]	− 2200[d]
Ag-Zn	− 1700[e]; − 1000[f]	− 2300[d]
Ag-Cd	− 1000[g]	− 400[d]
Ag-Au	− 947[i]	0[b]; − 523[h]
Au-Cd	− 3880[j]	− 950[d]
Cd-Mg	− 1940[k]	− 2000[b]
Bi-Tl	− 700[l]	− 1200[m]
Bi-Pb	0[n]	− 280[o]; − 330[m]
Pb-Tl($x_{Tl} = 0.8$)	− 700[p]	− 300[q]
Hg-Na	− 6600[n]; − 5000[n]	− 7500[s]; − 3200[t]
Hg-K	− 6500[r]	− 3600[u]
Fe-Si	− 9000[v]	− 9000[v]
Co-Si	− 12,000[w]	− 12,000[w]
Al-Cu	− 5000[w]	− 5000[w]

* Doubtful accuracy.

a. [10].
b. M. Kawakami, Sci. Rep. Tôhoku Univ., **19** (1930) 521.
c. Calculated by Weibke, data of A. Olander, Z. physik. Chem., **A164** (1933) 431.
d. A. Schneider and H. Schmid, Z. Elektrochem., **48** (1942) 638.
e. H. O. Samson-Himmelstjerna, Z. Metallk., **28** (1936) 197.
f. C. E. Birchenall and C. H. Cheng, Trans. A.I.M.E., **1** (1949) 428.
g. Calculated by Weibke, data of A. Olander, Z. physik. Chem., **A163** (1933) 107.
h. Calculated by Weibke, data of C. Wagner and G. Engelhardt, Z. physik. Chem. **A159** (1932) 241.
i. A. Wachter, J. Amer. Chem. Soc., **54** (1932) 4609.
j. Calculated by Weibke, data of A. Olander, J. Amer. Chem. Soc., **54** (1932) 3819.
k. [22].
l. A. Olander, Z. physik. Chem., **A169** (1934) 260.
m. C. Wagner and G. Engelhardt, Z. physik. Chem., **A159** (1932) 241.
n. O. Kubaschewski and W. Seith, Z. Metallk., **30** (1938) 7.
o. H. S. Strickler and H. Seltz, J. Amer. Chem. Soc., **58** (1936) 2084.
p. A. Olander, Z. physik. Chem., **A168** (1934) 274.
q. J. H. Hildebrand and J. N. Sharma, J. Amer. Chem. Soc., **51** (1929) 462.
r. M. Kawakami, Z. anorg. Chem., **167** (1927) 345.
s. H. E. Bent and J. H. Hildebrand, J. Amer. Chem. Soc. **49** (1927) 3011.
t. K. Hauffe, Z. Elektrochem., **46** (1940) 348.
u. J. S. Pedder and S. Barratt, J. Chem. Soc. (1933) 537.
v. F. Korber and W. Oelsen, Mitt. Kaiser-Wilhelm Inst. Eisenforsch., **18** (1936) 109.
w. W. Oelsen and W. Middel, *ibid.*, **19** (1937) 1.

producing ordering. An interesting verification of this point of view is furnished by the finding of short-range order [37] in the solid solutions of nickel-gold, despite the fact that this system has a wide miscibility gap, and is characterized by activity coefficients greater than unity, a very large positive heat of solution, and a greater than ideal entropy of solution [38].

The course of the activity-atom fraction curves for Pt in both the Cu-Pt and Co-Pt alloys may perhaps be qualitatively understood as follows. Magnetic measurements on Cu-Au alloys show that the concentration of conduction electrons is constant throughout the whole range of compositions [39], and the same situation should be true for the Mg-Cd alloys. However, this is not the case with the systems Au-Pt, Au-Pd, Cu-Pt, and Cu-Pd [39], in which the concentration of conduction electrons varies from 1 electron/atom at pure Cu or Au to $\frac{1}{2}$ electron/atom, at pure Pd or Pt. As Cu is added to Pt, the free electron from the copper serves to fill the holes in the *d*-band of the platinum atoms, lowering the magnetic susceptibility of the system. It must be supposed that the saturation of the *d*-band of the platinum causes the binding between a Pt atom and its neighbors to be less tight than it would be for Pt atoms of unsaturated electronic spins. This looser binding leads to an activity coefficient for the platinum greater than unity. When enough electrons have been added along with the copper to saturate all the *d*-band holes so that the added electrons can act as binding electrons, as shown by the susceptibility curve [40], the platinum is bound tighter to the lattice and the activity coefficient becomes less than unity. The same effect should operate in Co-Pt alloys.

Electronic effects also may account for the similar activity curves of the Tl-Pb system. Pb has two binding electrons per atom, Tl only one. As Tl is added to pure Pb, fewer binding electrons are available for the Pb atoms than would be the case were there no electronic interaction between the two species, and by the same token, there are relatively more such electrons for the Tl atoms. Consequently, the Pb manifests, by its positive deviation from Raoult's law, the weaker binding by which it is held.

Conclusions

The quasi-chemical theory of short-range order, although describing the thermodynamics very well for Cu-Au alloys, fails to do so for other ordering alloys. The observed deviations from the theory can be qualitatively explained by the probable existence of vibrational-entropy contribution to the entropy of solution and by the strain-energy contribution to the heat of solution, although the strain energy cannot yet be measured experimentally. These factors are neglected in the quasi-chemical theory, and it is difficult to understand the reasons for which the theory is so well obeyed by copper-gold alloys. The anomalous activity-composition curves may be qualitatively explained in terms of electronic interactions.

To the knowledge of the writer, no thermodynamic measurements exist which prove unambiguously the existence or non-existence of two-phase equilibrium regions about the ordered phases in ordering systems. It is intended to investigate other ordering alloys to seek an answer to this problem, as well as to look for regularities among the thermodynamic parameters of such systems. The ΔC_p of various alloy systems will be measured in order to evaluate the vibrational entropy. The measurement of the heat of solution of hydrogen in various alloys is being considered as a means of studying the electronic interactions.*

This research was supported by AEC Contract No. W-31-109-Eng.-52.

References

1. Newkirk, J. B., Smoluchowski, R., Geisler, A. H., and Martin, D. L. J. Appl. Phys., **22** (1951) 290.
2. Newkirk, J. B., Geisler, A. H., Martin, D. L., and Smoluchowski, R. Trans. A.I.M.E., **188** (1950) 1249.
3. Dienes, G. J. J. Appl. Phys., **22** (1951) 1020.
4. Borelius, G. Arkiv. Fysik, **2** (1950) 161.
5. Rhines, F. N. and Newkirk, J. B. Paper submitted to Trans. A.S.M.
6. Sykes, C. and Jones, F. W. Proc. Roy. Soc. **A157** (1936) 213.
7. Leech, P. and Sykes, C. Phil. Mag., **27** (1939) 742.
8. Khomyakov, K. G., Kholler, V. A., and Troshkina, V. A. Vestnik Moskov Univ., **5**, No. 6, Ser. Fiz. Mat. i. Estest. Nauk. No. 4 (1950) 43; Chem. Abstracts, **45**, 4544a.
9. Nix, F. C. and Shockley, W. Revs. Modern Phys., **10** (1938) 1.
10. Weibke, F. and Quadt, U. Z. Elektrochem., **45** (1939) 715.
11. Weibke, F. and Matthes, H. Z. Elektrochem., **47** (1941) 421.
12. Geisler, A. H. and Martin, D. L. J. Appl. Phys., **23** (1952) 374.
13. Esch, U. and Schneider, A. Z. Elektrochem., **50** (1944) 290.

*The possibility of this method has been briefly discussed by A. D. McQuillan [41].

14. WAGNER, C. Thermodynamics of Alloys (Addison-Wesley Press, 1952).
15. WALKER, C. B. J. Appl. Phys., **23** (1952) 118.
16. COWLEY, J. M. J. Appl. Phys., **21** (1950) 24.
17. ROBERTS, B. W. Thesis, Massachusetts Institute of Technology.
18. See, for example, FOWLER, R. and GUGGENHEIM, E. A. Statistical Thermodynamics (Cambridge University Press, 1949).
19. TAKAGI, Y. Proc. Phys. Math. Soc., Japar, **23** (1941) 44.
20. BIRCHENALL, C. E. A.I.M.E. Tech. Pub. No. 2169 (1947).
21. ORIANI, R. A. J. Appl. Phys., **21** (1950) 1068.
22. TRUMBORE, F. A., WALLACE, W. E., and CRAIG, R. S. J. Amer. Chem. Soc., **74** (1952) 132.
23. TANG, YON-CHI and PAULING, L. Acta Cryst., **5** (1952) 39.
24. OLANDER, A. Z. physik. Chem., **A168** (1934) 274.
25. HILDEBRAND, J. H. and SCOTT, R. L. The Solubility of Nonelectrolytes, 3rd ed. (Reinhold, 1950).
26. GUGGENHEIM, E. A. Thermodynamics (Interscience, 1949).
27. KLEPPA, O. J. J. Amer. Chem. Soc., **71** (1949) 3275; **72** (1950) 3346; **73** (1951) 385.
28. ELLIOTT, J. F. and CHIPMAN, J. Trans. Faraday Soc., **47** (1951) 138.
29. LUMSDEN, J. Thermodynamics of Alloys (London, The Institute of Metals, 1952).
30. KELLEY, K. K. U.S. Bureau of Mines, Bull. 476 (1949).
31. BETTERIDGE, W. J. Inst. Metals, **75** (1949) 559.
32. KOSTER, W. and GEBHARDT, E. Z. Metallk., **32** (1940) 253.
33. ZENER, C. In "Thermodynamics in Physical Metallurgy" (Cleveland, Amer. Soc. Metals, 1950).
34. LAWSON, A. W. J. Chem. Phys., **15** (1947) 831.
35. HEUMANN, T. Z. Metallk., **42** (1951) 182.
36. HUME-ROTHERY, W. and POWELL, H. M. Z. Kristallogr., **91** (1935) 23.
37. FLINN, P. A. and AVERBACK, B. L. Phys. Rev., **83** (1951) 1070.
38. SEIGLE, L., COHEN, M., and AVERBACK, B. L. Trans. A.I.M.E., **4** (1952) 1320.
39. WAGNER, C. Thermodynamics of Alloys (Addison-Wesley Press, 1952), chapter 2.
40. VOGT, W. Z. angew. Chem., **48** (1935) 734.
41. MCQUILLAN, A. D. J. Inst. Metals, **79** (1951) 73.

SOME GEOMETRICAL RELATIONS IN DISLOCATED CRYSTALS*

J. F. NYE†

When a single crystal deforms by glide which is unevenly distributed over the glide surfaces the lattice becomes curved. The constant feature of distortion by glide on a single set of planes is that the orthogonal trajectories of the deformed glide planes (the c-axes in hexagonal metals) are straight lines. This leads to the conclusion that in polygonisation experiments on single hexagonal metal crystals the polygon walls are planes, while the glide planes are deformed into cylinders whose sections are the involutes of a single curve. The analysis explains West's observation that the c-axes in bent crystals of corundum are straight lines. For double glide on two orthogonal sets of planes there is a complete analogy between the geometrical properties of the distorted glide planes and those of the "slip-lines" in the mathematical theory of plasticity. More general cases are discussed and formulae are derived connecting the density of dislocations with the lattice curvatures. For a three-dimensional network of dislocations the "state of dislocation" of a region is shown to be specified by a second-rank tensor, which has properties like those of a stress tensor except that it is not symmetrical.

QUELQUES RELATIONS GÉOMÉTRIQUES DANS DES CRISTAUX DISLOQUÉS

Quand un monocristal est déformé par glissement, qui n'est pas uniformément distribué sur les surfaces de glissement, le réseau devient courbé. La caractéristique constante de distorsion par glissement sur un seul groupe de plans est, que les trajectoires orthogonales des plans de glissement déformés (les axes-c dans les métaux hexagonaux) sont des droites. Ceci conduit à la conclusion, que dans les essais de polygonisation sur des monocristaux des métaux hexagonaux, les faces des polygones sont planes, alors que les plans de glissement sont déformés en des cylindres, dont les sections sont des développantes d'une seule courbe. L'analyse explique l'observation de West, que les axes-c dans des cristaux fléchis de corindon sont des droites. Pour le glissement double sur deux groupes orthogonaux de plans il y a une analogie complète entre les propriétés géométriques des plans de glissement déformés et celles des lignes de glissement dans la théorie mathématique de la plasticité. Des cas plus généraux sont discutés et des formules joignant la densité des dislocations aux courbures du réseau sont déduites. Il est montré que pour un réseau de dislocations à trois dimensions "l'état de dislocation" d'une région est spécifié par un tenseur de second rang, qui a des propriétés semblables à celles du tenseur de tension, à l'exception du fait, qu'il n'est pas symétrique.

EINIGE GEOMETRISCHE BEZIEHUNGEN IN VERFORMTEN KRISTALLEN

Wenn Einkristalle durch Gleitung verformt werden, und die Gleitung sich ungleichmässig über die Gleitebenen verteilt, dann wird das Kristallgitter "verbogen." Eine der immer wiederkehrenden Begleiterscheinungen der Verformung durch Gleitung im Fall einer einzigen Translationsebene ist, dass die Orthogonaltrajektorien der verformten Gleitebenen (in hexogonalen Metallen die c-Achsen) Graden sind. Daraus kann man schliessen, dass in Polygonisationsexperimenten an hexogonalen Einkristallen die Wände der Polygone Ebenen sind, während sich die Gleitebenen zu Zylindern verformt haben, deren Schnitte die Evoluten einer einzigen Kurve sind. Diese Analyse erklärt die Beobachtung von West, dass die c-Achsen von "gebogenen" Korund Kristallen Graden sind. Im Falle einer doppelten Gleitung auf zwei auf einander senkrechten Gleitebenen besteht eine völlige Analogie zwischen den geometrischen Eigenschaften der verformten Gleitebenen und den "Gleitlinien" in der mathematischen Theorie der Plastizität. Allgemeine Fälle werden diskutiert und Formeln abgeleitet, die die Dichte der Versetzungen mit der Biegung des Gitters verknüpft. Es wird gezeigt, dass in einem dreidimensionalen Netzwerk von Versetzungen der "Versetzungszustand" eines Bereiches als Tensor zweiter Ordnung dargestellt werden kann, dessen Eigenschaften denen des Spannungstensors ähnlich sind, der jedoch nicht symmetrisch ist.

1. Introduction

Suppose that a single crystal deforms by slip on a single set of parallel planes in such a way that the amount of slip is unevenly distributed over the slip planes. It may be asked: What possible geometrical forms can the slip planes take? This is a question that arises, for example, when a single crystal wire of zinc is bent plastically to study the phenomenon of polygonisation [1]. We do not deal in this paper with the curvatures on an atomic scale but only with the average curvatures over distances large compared with d, the dislocation spacing.

If the distribution of dislocations could be prescribed arbitrarily, there would be no limitation on the curvatures of the glide planes. An arbitrary distribution of dislocations, however, gives a large-scale distribution of internal stress. As an extreme example of this, if one calculates the stress at a given point due to a uniform array of positive edge dislocations one finds that the stress can increase to infinity as the array becomes infinite in extent. We show here from geometrical considerations that it is possible to have non-uniform distributions of dislocations that do not give accumulating stresses of this sort. Such arrays correspond to minimum strain energy configurations. In them the residual stresses average out over distances large compared to d. This property of the arrays may be stated

*Received November 7, 1952.
†Bell Telephone Laboratories, Murray Hill, New Jersey, U.S.A.

precisely as follows: (A) If a path is constructed through "good" crystal in the sense of Frank [2] from successive lattice translation vectors, the length l of any section of the path is equal to the undistorted length, provided $l \gg d$. The *shape* of the path will of course be changed by the distortion. The significance of assumption (A) is easier to appreciate after the analysis that follows from it has been read.

When real crystals are distorted plastically they do in fact contain large-scale distributions of residual strains, which contribute to the lattice curvature. However, the larger the amount of plastic deformation the smaller, relatively speaking, will be this contribution to the curvature; moreover, when a distorted crystal is annealed the large-scale distributions of residual strains may be expected to disappear, while the lattice curvature will still remain. In this analysis we neglect entirely the curvature attributable to the large-scale distributions of strain.

In §§2, 3, 4 we discuss single glide. This leads to the consideration of more general cases where multiple slip occurs, and then in §8 we turn to the most general problem: the curvatures of a crystal lattice produced by a three-dimensional network of dislocations.

2. Single Glide: Two-Dimensional Case

It follows from assumption (A) that in single glide the distance between any two successive glide surfaces, measured along their orthogonal trajectories, is the same at all points. Consider first a two-dimensional case (Figure 1). S_1 is the trace of a

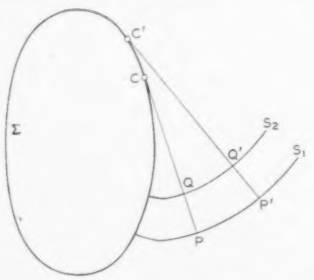

FIGURE 1. Single glide: two-dimensional case. The glide surfaces S_1 and S_2 are both involutes of Σ.

cylindrical glide surface, whose centre of curvature at P is C. As P moves along S_1 the locus of C is Σ, the evolute of S_1. S_1 can be generated by unwrapping a taut string wound round Σ and noting the locus of a given point P. Any other point Q on the string will sweep out a curve S_2, and, since PQ is fixed, S_2 evidently satisfies the condition for being another glide surface. (For the sake of rigour we should also remark that it may be shown that when PQ is a small element, S_2 is the *only* surface lying at a fixed distance PQ from S_1 measured along the orthogonal trajectories. It then follows that the same result is true for PQ finite. Huygens' construction in optics is somewhat analogous.) The glide surfaces are thus the involutes of Σ, which might be called the *generating curve* for the deformation. If the generating curve and its position in relation to the crystal are given, the deformation is completely specified. (The sense of the generating curve must also be given.)

The construction shows that the orthogonal trajectories of the glide planes, which were straight lines before the deformation, are also straight lines afterwards. They all have the same crystallographic direction, the c-axis in hexagonal crystals, although they are not parallel. Now, if a crystal is heated and made to polygonise [1] after a distortion of this type, it has been shown theoretically that the dislocation walls should form at right angles to the glide planes, for that is the position of lowest energy. Our construction shows that, apart from elastic strains, the traces of the walls will theoretically be strictly straight lines, even on a macroscopic scale. Thus, for example, when a hexagonal crystal is bent by basal glide so that the plane of bending contains its c-axis and one of the basal glide directions, the glide planes will deform into cylinders with parallel generators and the polygon walls will be planes. We shall call this case *plane bending*.

If the shape of any one glide surface, say S_1, is given, successive glide surfaces can be constructed on each side of it by drawing the normals to S_1 and connecting points at equal distances from S_1. However, when a point is at the same distance, measured along the normal to S_1, from more than one point of S_1 the construction becomes ambiguous. Such points are associated with a cusp on the generating curve. Physically, what has happened here is that flexural glide has become concentrated into a sharp kink. Figure 2 shows an instance of this. ABC is the generating curve with a cusp at B. In the area to the right of DBA the glide surfaces can be constructed by imagining a taut string to be unwrapped from the branch BA. Each point on the string sweeps out a glide surface. In the area to the left of DBC the glide surfaces can be similarly constructed by using the branch BC. There is thus an ambiguity in the area within ABC. The ambiguity is resolved in the following way. Let $EF = GH$, where EF and GH are normals to the glide surfaces.

Let the glide surface through F, constructed with branch BC, meet the glide surface through H, constructed with the branch BA, at the point J. J will then mark a sharp corner on the glide surface and the locus of J, shown by the broken line, will be a kink surface. It may be noted that the kink surface is not, in general, a plane.

The form of the glide surfaces in general represents a certain spatial distribution of edge dislocations of like sign. (Close pairs of dislocations of opposite sign produce no curvature and so are irrelevant to the present analysis.) If we look at the evolute construction in terms of dislocations we see that we have found, effectively, the distribution of least strain energy for any given base distribution along a certain part of the surface S_1.

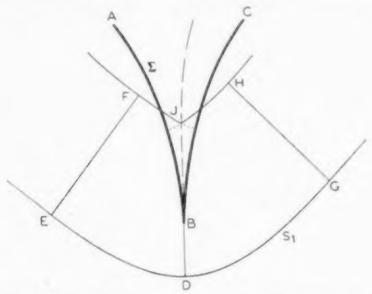

FIGURE 2. The effect of a cusp in the generating curve. Flexural glide becomes concentrated into a sharp kink.

As mentioned in §1, this approach avoids any difficulties with infinite stresses that might be caused by having an infinite array of dislocations. The method of construction automatically adjusts the stresses so that they do not accumulate, and when the density of dislocations necessary to achieve this becomes infinite (on Σ) the array naturally terminates. The evolute construction focusses attention on the avoidance of stresses *normal* to the glide planes, but it will be seen that it is the avoidance of *other* stresses that determines the curvature.

Let n be the number of excess dislocations of one sign per unit area and $\mathbf{b}$ their Burgers vector. Then if we take a square Burgers circuit [2] of unit area, as shown in Figure 3, the closure failure is $n\mathbf{b}$ and,

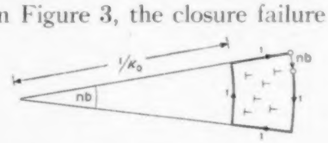

FIGURE 3. The curvature of the glide planes produced by n edge dislocations of the same sign in unit area is nb.

by hypothesis, there is no elastic stretching of the circuit. The curvature κ_0 of the glide planes in this region is therefore given by

$$\kappa_0 = nb \tag{1}$$

where $b = |\mathbf{b}|$. Thus, on PC in Figure 1, n is inversely proportional to the distance from C. We may notice that if $b \to 0$ and $n \to \infty$ in such a way that nb is constant, the strain energy $E \to 0$ but the curvature remains unchanged. Our analysis can only cover continuously varying distributions of dislocations and for this reason it cannot predict the decrease of strain energy that accompanies polygonisation. It may be noticed, however, that the above distribution ensures that when the crystal polygonises the number of dislocations per unit length is a constant in any given polygon wall.

It is a simple matter to calculate the curvature of any other lattice plane in the zone parallel to the dislocation lines. In Figure 4a, $ABCD$ is a small element bounded by glide planes, AB and DC, and their normals. Let $\phi_A, \phi_B, \ldots$ denote the orientation of the lattice at $A, B, \ldots$ measured anti-clockwise from some fixed orientation. Then the curvature of the lattice plane AC, which makes an angle θ with AB, is

$$\kappa = \frac{\phi_C - \phi_A}{AC} = \frac{\phi_B - \phi_A}{AC} = \frac{\phi_B - \phi_A}{AB}\cos\theta \tag{2}$$
$$= \kappa_0 \cos\theta$$

or

$$\kappa = nb\cos\theta\,.$$

Thus, *the curvature of any lattice plane parallel to the edge dislocation lines is equal to the component of* $n\mathbf{b}$ *parallel to the plane.* The curvature of the lattice

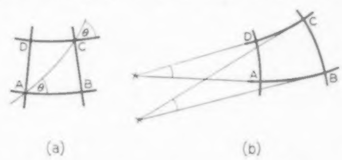

FIGURE 4. Curvatures produced by glide on (a) a single set of planes and (b) two orthogonal sets of planes, illustrating the relation $\phi_C - \phi_B = \phi_D - \phi_A$.

plane AC is to be distinguished from the curvature of a line inscribed on the crystal before deformation at the same angle θ to AB. Such a line changes its orientation relative to the crystal during the deformation, and after deformation different parts of the line will, in general, be in different crystallographic directions.

We turn now to a special case.

3. Special Case of Uniform Plane Bending

If plane bending takes place uniformly about an axis O (Figure 5a), the generating curve Σ is a circle, of radius a and centre O. The orthogonal trajectories to the glide planes (the c-axes for hexagonal metal crystals) are straight lines and the

glide planes are the involutes of the circle. Using the notation that r is the radius vector to any point P (Figure 5b), $r = r_0$ is the neutral plane, χ is the angle of intersection of the glide planes with the fibre (r = constant) through P, and χ_0 is the

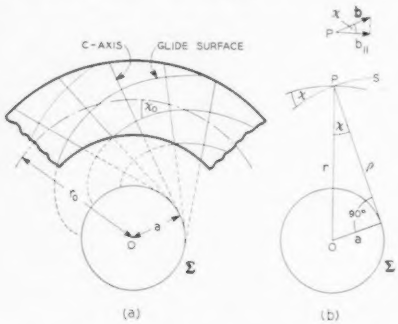

FIGURE 5. Uniform plane bending of a rod by single glide. The glide planes are the involutes of a circle, and the glide plane normals, the c-axes in hexagonal crystals, are straight lines.

angle of intersection of the glide planes with the neutral plane, we have the relations,

$$r \sin \chi = r_0 \sin \chi_0 = a; \rho = r \cos \chi = \sqrt{r^2 - a^2}.$$

The same results may be obtained by noting that, after bending, the length l of a fibre which was originally of length l_0 is given by

$$\frac{l}{l_0} = \frac{r}{r_0}.$$

On the other hand, the change in lattice orientation caused by this extension is expressed by [3]

$$\frac{l}{l_0} = \frac{\sin \chi_0}{\sin \chi}.$$

Hence $r \sin \chi = r_0 \sin \chi_0$ = constant, as before.

The radial distribution of the excess dislocation density is, from equation (1),

$$n = \frac{1}{b\sqrt{r^2 - a^2}};$$

or, more simply,

$$n = \frac{1}{b_p r},$$

where b_p is the component of b parallel to the neutral plane.

The circle $r = a$ corresponds to a compression sufficient to turn the glide planes to a position at right angles to the fibres; it also corresponds to an infinitely high density of dislocations. If the rod is bent in such a way that the neutral plane remains fixed within it, this imposes a limit to the curvature that can be applied. By using the fact that the volume is unchanged by the deformation it is easy to show that, when the innermost fibre is of radius a,

$$a^2 = r_0(r_0 - 2\delta)$$

where δ is the distance between the innermost fibre and the neutral plane *before* deformation. Using the relation $a = r_0 \sin \chi_0$ we find the minimum radii of curvature of the neutral plane and the innermost fibre respectively,

$$r_0 = \frac{2\delta}{\cos^2 \chi_0}, \quad a = \frac{2\delta \sin \chi_0}{\cos^2 \chi_0}. \tag{3}$$

In an actual experiment an attempt to bend a rod to a smaller radius than is given by these equations would result in an inward shift of the neutral plane relative to the rod. The bending would be accomplished, in fact, by a combination of bending with extension. Our formulae are independent of the history of the bending and of whether or not it is combined with extension or compression. r_0 refers always to the fibre that at the end of the deformation is found to be unchanged in length; on it, $\chi = \chi_0$. Formula (3) shows that, for a given χ_0, we can make a as small as we like by simply choosing δ small enough.

If transverse straight lines at right angles to the neutral axis were ruled on the crystal before bending, they would become curved. The calculation of their shape in polar coordinates is straightforward but tedious. The result is given in Appendix A and Figure 10.

4. Experimental Verification

We have seen that in plane bending by basal glide in a hexagonal crystal, the crystallographic planes containing the c-axis and the axis of bending remain plane in spite of the bending. We may note that this does not imply that the corresponding X-ray reflexions will be free from asterism, because successive reflecting planes are not parallel. However, with a transparent crystal the extinction directions between crossed nicols can be used to show up the effect. This has been done by West [4] with single crystals of corundum (trigonal). He found as an experimental fact, without explanation, that, in crystals bent round into a loop and a U-shape, "the c-axis through any point remains a straight line even to the boundaries of the rod." He went on to deduce that the glide planes in the uniformly bent parts were the involutes of a circle, as we saw in the last section. It may be concluded that these corundum crystals had deformed by single glide. Double glide would in general give a

different distribution of lattice rotation, as will appear in the next sections.

5. Double Orthogonal Glide: Two-Dimensional Case

We now generalise the problem of §2 by allowing further slip to take place on the set of planes at right angles to the first set. Both slip directions are taken to be in the plane of the diagram (Figures 4a, b) and, as before, we only consider edge-type dislocations running perpendicular to the plane of the diagram. Rock salt is an example of a crystal that could deform in this way.

Let Figure 4a now show a finite curvilinear quadrilateral bounded by slip-lines after slip has occurred on the first set of planes, AB, DC, but before it has occurred on the second set AD, BC. Since $\phi_A = \phi_D$ and $\phi_B = \phi_C$,

$$\phi_C - \phi_D = \phi_B - \phi_A \,. \tag{4}$$

Now let slip take place on the second set of planes (Figure 4b). This produces additional curvatures but it is easily proved that it will not affect the curvature of AB (for instance, by drawing a Burgers circuit after the manner of Figure 3). Therefore, since AB is not altered in length, $\phi_B - \phi_A$ is unaltered by the second slip. Similarly, $\phi_C - \phi_D$ is unaltered. Hence relation (4) continues to hold after the second slip. Rearranging the terms gives

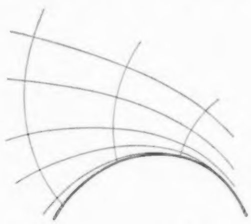

FIGURE 6. Glide on two sets of orthogonal planes.

$$\phi_C - \phi_B = \phi_D - \phi_A \,.$$

We thus find that *the lattice rotation between two given slip-lines of one family where they are cut by a slip-line of the other family is constant along their length.*

Let AB and AD in Figure 4b now be infinitesimal with lengths ds and ds' respectively. The radii of curvature ρ and ρ' respectively of the slip-lines through A are given by

$$\frac{1}{\rho} = \frac{\partial \phi}{\partial s}\,,\ \frac{1}{\rho'} = \frac{\partial \phi}{\partial s'}\,.$$

From the geometry of the small quadrilateral,

$$AB - DC = AD(\phi_B - \phi_A).$$

Therefore, if ρ_D and ρ_A are values of ρ at D and A,

$$\rho_A(\phi_B - \phi_A) - \rho_D(\phi_C - \phi_D) = AD(\phi_B - \phi_A).$$

Therefore, from equation (4),

$$\rho_A - \rho_D = AD.$$

Hence,

$$\frac{\partial \rho}{\partial s'} = -1, \quad \text{or} \quad d\rho + \rho' d\phi = 0$$

along a line of the second set. Similarly,

$$\frac{\partial \rho'}{\partial s} = 1, \quad \text{or} \quad d\rho' - \rho\, d\phi = 0$$

along a line of the first set. This means that *as one moves along the slip-lines of one set the radius of curvature of the slip-lines of the other set changes by the distance moved.* The radius decreases as one moves towards the inside of the curves. Thus, in general, the radius of curvature eventually decreases to zero and the slip-lines that are being followed run together (Figure 6). We have already had an instance of this in the special case of single glide.

The two geometrical properties of the slip-lines or glide lines expressed above are identical with Hencky's first and second theorems in the mathematical theory of plasticity [5]. On the other hand, the "slip-lines" in that theory are quite different from the slip-lines we have been discussing. They are defined as the trajectories of maximum shear stress in the stress field, or as characteristics of the fundamental hyperbolic equations of the theory. We thus have the curious situation, a sort of mathematical pun, that not only are these two dissimilar families of curves called by the same name but they also obey the same equations.

The small arc process used in the theory of plasticity to build up the slip-line field in any finite quadrilateral $ABCD$, given the form of the slip-lines AB and AD, is equally applicable here.

The answer to the question, then, as to what forms the slip planes can take after glide on orthogonal planes is that they can be any families that satisfy the Hencky relations.

6. Multiple Glide: Two-Dimensional Case

Still confining attention to the two-dimensional case of an array of parallel edge dislocations we may now consider the effect of glide on any number of different planes. If in unit area there are n_r dislocations with Burgers vector $\mathbf{b}_r$, the curvature of any lattice plane parallel to the dislocation lines is obtained (§2) by summing the components of the vectors $n_r\mathbf{b}_r$ in the direction of the plane—which is the same as taking the component of the vector

$$\sum_r n_r \mathbf{b}_r$$

in that direction. At the point considered, therefore, the dislocations are equivalent to a set on a single plane, but of course this plane will be different, in general, for every point of the crystal, according to the ratios of the n_r.

7. General Three-Dimensional Case for Single Glide

In three dimensions it may be shown by similar reasoning to that of §2 that the curves orthogonal to the glide surfaces are necessarily straight lines, even for the most general type of distortion, provided only that it takes place by glide on a single set of planes. Any number of glide *directions* may operate. However, in this case, unlike the two-dimensional case, the lattice orientation is not fixed along the normal, for the lattice can and does, in general, twist about the normal. In two dimensions the centre of curvature of S_1 at P (Figure 1) was the same as the centre of curvature of S_2 at Q and so on, namely C. Similarly in three dimensions, all the glide surfaces intersecting a given normal share the same two centres of curvature lying on their common normal. As we follow a normal, therefore, both radii of curvature change by the distance travelled. They increase or decrease respectively according to whether we are receding from or approaching the corresponding centre of curvature. Moreover, the two principal curvature directions are preserved along a given normal. The two surfaces described by the two centres of curvature as the normal moves represent the three-dimensional analogues of the evolute of two dimensions.

For a set of parallel like dislocations of general type there are simple relations (proved in Appendix B) between their direction and the curvature they produce in their glide planes. Figure 7 shows the

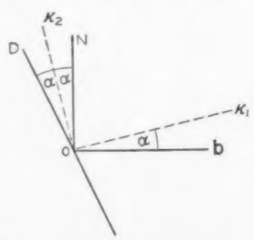

FIGURE 7. Glide on a single set of planes: three-dimensional case. The slip plane is the plane of the diagram. The principal directions of curvature bisect the angle between the dislocation lines and ON.

relations between the various directions in a glide plane. The two principal directions of curvature in the glide plane are the internal and external bisectors of the angle, of magnitude 2α, between the direction, OD, of the dislocation lines and ON, the normal to $\mathbf{b}$. Thus, if the dislocations are pure edge, $\alpha = 0$, and the directions of the principal curvatures κ_1 and κ_2 are parallel and perpendicular to $\mathbf{b}$; while if the dislocations are pure screw, $\alpha = \pi/4$, and κ_1 and κ_2 are at angles of $\pi/4$ to $\mathbf{b}$. The magnitudes of the curvatures are

$$\kappa_1 = nb \cos^2 \alpha, \qquad \kappa_2 = -nb \sin^2 \alpha,$$

where n is the number of dislocation lines per unit area normal to the lines. Hence

$$\kappa_1 - \kappa_2 = nb,$$

and is independent of α. We also have

$$\kappa_1 + \kappa_2 = nb \cos 2\alpha = n'b$$

where n' is the number of lines per unit area taken normal to ON.

8. General Three-Dimensional Case

Finally we come to the most general case that falls within the scope of this type of treatment, a three-dimensional network of dislocations. As before, we consider a region of the crystal large enough for the effects of the dislocations within it to be averaged. Alternatively, we may make the distribution of dislocations continuous by letting b approach zero and increasing the number of dislocations of each kind in proportion, so as to keep the curvatures constant (cf. §2). Our aim is to find the relation between the dislocations in the region and the curvatures of the lattice that they produce.

Consider first the dislocations. They may be specified by taking Burgers circuits in different orientations and noting the closure failures (Burgers vectors). If a Burgers circuit of unit area normal to the unit vector l_j has a Burgers vector B_i (that is to say, B_i completes the circuit when it is traversed in the sense of a right-handed screw motion along l_j) then it is shown in Appendix C that we may write

$$B_i = \alpha_{ij}\, l_j\,, \qquad (i, j = 1, 2, 3). \tag{5}$$

The summation convention is to be understood. The components B_i form an axial vector. The coefficients α_{ij} relate the two vectors B_i and l_j and therefore form a second-rank tensor; it specifies the "state of dislocation" of the region.

To calculate the α_{ij} components for a given set of dislocations the procedure would be as follows. Suppose there are dislocations with length parallel to the unit vector $\mathbf{r}$ and with Burgers vector $\mathbf{b}$. Let there be n of these dislocations crossing unit area normal to $\mathbf{r}$. The number crossing unit area normal to the unit vector $\mathbf{l}$ is $n\mathbf{r}\cdot\mathbf{l}$. The associated

Burgers vector is $\mathbf{b}(n\mathbf{r}\cdot\mathbf{l})$. Hence, in suffix notation,

$$B_i = b_i(nr_j\, l_j)$$

and, from equation (5),

$$\alpha_{ij} = nb_i\, r_j\, .$$

If there are other sets of dislocations present with different values of n, $\mathbf{b}$ and $\mathbf{r}$, the total α_{ij} is obtained by summing the values of $nb_i\, r_j$ for all the sets.

The form of α_{ij} implies that, so far as curvatures are concerned, any state of dislocation can be produced by combining nine sets of dislocations with their lengths and their Burgers vectors arranged parallel and perpendicular to the coordinate axes. The three terms of the leading diagonal represent pure screw dislocations and the six cross-terms represent the six possible types of pure edge dislocations. Alternatively, by combining the three types of dislocation lines directed along each axis the general state can be regarded as produced by three perpendicular sets of dislocations of general type. Such a representation would of course only be unique for a given set of axes.

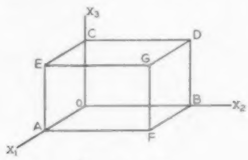

FIGURE 9

We now have to specify the curvatures of the lattice. Let $d\phi_i$ be the small lattice rotations about the three axes, in a right-handed screw sense, associated with the displacement vector dx_j. The $d\phi_i$ are the components of an axial vector. If we now write

$$d\phi_i = \kappa_{ij}\, dx_j \tag{6}$$

the coefficients κ_{ij} form a second-rank tensor which describes the curvature of the lattice.

In Appendix D we show that the dislocation tensor α_{ij} is related to the curvature tensor κ_{ij} by the equation

$$\alpha_{ij} = \kappa_{ji} - \delta_{ij}\, \kappa_{kk} \qquad (i, j, k = 1, 2, 3) \tag{7}$$

where $\delta_{ij} = 1$ for $i = j$, and $\delta_{ij} = 0$ for $i \neq j$. The reverse relation is

$$\kappa_{ij} = \alpha_{ji} - \tfrac{1}{2}\delta_{ij}\, \alpha_{kk}. \tag{8}$$

The general property of a dislocation network, that the Burgers vector is conserved along any dislocation line and at a node, is associated with a corresponding theorem in the present formulation. Consider the small rectangular parallelepiped shown in Figure 9. The faces define six Burgers circuits, and we specify that each is to be taken in the direction associated with the outward normal to the face. We now traverse all six in turn and show that the final result is that we have traversed a circuit of zero area. Thus:

$$\begin{aligned}(OCDBO + OBFAO + OAECO)& \\ + (GEAFG + GFBDG + GDCEG)& \\ = CDBFAEC + EAFBDCE = 0.&\end{aligned}$$

Therefore the total Burgers vector for the six circuits is zero. Equating the components to zero and proceeding to the limit we have

$$\frac{\partial\alpha_{11}}{\partial x_1} + \frac{\partial\alpha_{12}}{\partial x_2} + \frac{\partial\alpha_{13}}{\partial x_3} = 0$$

and two similar equations. Thus, in general,

$$\frac{\partial\alpha_{ij}}{\partial x_j} = 0. \tag{9}$$

The general analysis of the tensor α_{ij} is therefore formally the same as that for the tensor of mechanical stress with the one difference that α_{ij} is not symmetrical; equations (9) are the analogues of the equations of equilibrium.

It is interesting to notice too the formal similarity between equations (7) and the stress-strain relations in an isotropic body,

$$\sigma_{ij} = 2\mu\epsilon_{ij} + \lambda\delta_{ij}\, \epsilon_{kk}$$

with $2\mu = 1$, $\lambda = -1$; α_{ij} plays the part of the stress and κ_{ij} that of the strain, although, unlike these tensors α_{ij} and κ_{ij} are not symmetrical. These values of λ and μ give Young's Modulus $= 2$, Rigidity Modulus $= \frac{1}{2}$, Poisson's Ratio $= 1$ and Bulk Modulus $= -\frac{2}{3}$.

Since

$$\kappa_{ij} = \frac{\partial\phi_i}{\partial x_j}$$

we have

$$\frac{\partial\kappa_{ij}}{\partial x_k} = \frac{\partial^2\phi_i}{\partial x_j \partial x_k} = \frac{\partial\kappa_{ik}}{\partial x_j}.$$

By substituting α for κ from equation (8) we obtain the equations

$$\frac{\partial\alpha_{ji}}{\partial x_k} - \frac{\partial\alpha_{ki}}{\partial x_j} = \frac{1}{2}\left(\delta_{ij}\frac{\partial\alpha_{ll}}{\partial x_k} - \delta_{ik}\frac{\partial\alpha_{ll}}{\partial x_j}\right) \tag{10}$$

Of the twenty-seven possible permutations of i, j, k the equations given by those nine with $j = k$ are trivial. Of the remaining eighteen equations, owing to the symmetry in j and k, only nine are independent. Thus there are nine independent differential equations to determine the nine independent α_{ij} components.

By putting $i = j$ or $i = k$ in equations (10) a

little reduction shows that we recover the "equilibrium equations" (9).

By analogy with the strain energy function in elasticity it is useful to introduce, purely formally, the function

$$W = \tfrac{1}{2}\alpha_{ij}\,\kappa_{ij}\,.$$

Then, by differentiating and using equations (7),

$$\frac{\partial W}{\partial \kappa_{ij}} = \tfrac{1}{2}\alpha_{ij} + \tfrac{1}{2}\,\frac{\partial \alpha_{kl}}{\partial \kappa_{ij}}\,\kappa_{kl} = \tfrac{1}{2}\alpha_{ij} + \tfrac{1}{2}\kappa_{ji} - \tfrac{1}{2}\delta_{ij}\,\kappa_{kk}$$
$$= \alpha_{ij}\,.$$

W is thus a "dislocation potential." It is a function of the components of lattice curvature at any point such that its derivatives with respect to each component of curvature are each equal to the corresponding component of the state of dislocation.

9. Discussion

Eshelby [6], using a model described by Timoshenko, has discussed a state of internal stress which Nabarro [7] has called a continuous distribution of dislocations. That this state of dislocation is different from the one treated here may be seen by considering the case of single glide (§2). One way of arriving at our model of the process would be to suppose an unstrained body cut up into small cubes of side d. The structure is then bent by allowing sliding to take place parallel to one set of faces only of the cubes (flexural glide), the cubes themselves being unstrained. There will then be voids between the cubes. The strain of the cubes necessary to fill the voids is of order κd, where κ is the mean curvature of the surfaces of sliding. As $d \to 0$ with κ held constant, this strain $\to 0$. In Eshelby's model the strain does not approach zero as the cubes are made small and he is essentially concerned with a state of internal stress. The difference between our models is that we allow sliding of the cubes or other elementary pieces, as is actually produced in crystals by the movement of dislocations, while Eshelby does not.

The energy of a single dislocation at the centre of a crystal of linear dimensions R is of the general form

$$Gb^2 \ln \frac{R}{r_0}\,,$$

where G is an elastic constant and r_0 is a length of the order of atomic dimensions.* In the arrays of dislocations considered in this paper, where stresses do not accumulate, R may be taken as the mean spacing of the dislocations, say $n^{-\frac{1}{2}}$, or $(b/\kappa)^{\frac{1}{2}}$, where κ is the local curvature. The strain energy in a unit volume, therefore, which contains $n = \kappa/b$ dislocations, is of the form

$$\frac{\kappa}{b}\cdot Gb^2 \ln\left\{\left(\frac{b}{\kappa}\right)^{\frac{1}{2}}\cdot\frac{1}{r_0}\right\}.$$

This is proportional to

$$\kappa Gb \ln \frac{b}{\kappa r_0^{\,2}} = \kappa Gb \ln \frac{m}{\kappa b}\,,$$

where $m = b^2/r_0^2$, a constant that depends upon the details of the atomic arrangements on the dislocation axis. As $b \to 0$ with κ constant, the energy approaches zero, as noted in §2.

The analysis of this paper is closely related to Frank's construction [8] for grain boundaries. In fact the Frank representation is essentially a surface distribution of dislocation density, or α_{ij}, and, although we do not give this development here, the Frank formulation is deducible from the present analysis. Grain boundary arrays are a special case of these more general distributions, and have the characteristic in common that they represent a state of minimum energy and that the total energy is linear in the Burgers vector, or more precisely is of the general form noted above. The stability of polygonized arrays arises from the fact that the argument of the logarithmic term above really depends on the closest approach of the individual dislocations rather than on their average separation, given by $n^{-\frac{1}{2}}$. Polygonized arrays preserve the mean dislocation density, as pointed out in §2, but they achieve a smaller minimum separation and hence a smaller total energy than uniform distributions.

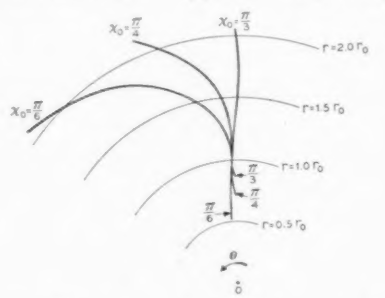

FIGURE 10. Showing the form of transverse lines after uniform plane bending of a crystal bar by single glide for three initial orientations (χ_0).

Appendix A

The equations in polar coordinates of the transverse lines on the uniformly bent crystal referred to on p. 156 are, in terms of χ as a parameter,

$$r = r_0 \sin \chi_0 \operatorname{cosec} \chi$$
$$\theta = \tfrac{1}{4}\sin 2\chi_0 \cot^2 \chi - \cot \chi - \chi + \text{const.}$$

*I am much indebted to the referee for most of the substance of the remainder of this discussion.

VOL 1 195

The curves, which in general show a reversal of curvature, all have the same shape, different members corresponding to different values of the constant in the expression for θ. The curves for $\chi_0 = \pi/6$, $\pi/4$, $\pi/3$ are drawn in Figure 10. When $0 < \chi_0 < \pi/4$, θ has a maximum on the compression side at $r = r_0 \tan \chi_0$ and a minimum at $r = r_0$. When $\chi_0 = \pi/4$, $r = r_0$ is a point of inflexion. When $\pi/4 < \chi_0 < \pi/2$, $r = r_0$ is a maximum and $r = r_0 \tan \chi_0$, on the tension side, is a minimum.

Appendix B*

In Figure 7 we regard the angle $NOD = 2\alpha$ as fixed and we calculate the curvatures of the glide plane. Take a square Burgers circuit with sides of unit length whose normal lies in the plane of the figure at an angle β to OD. The number of dislocation lines threading the circuit is $n \cos \beta$. The closure failure is thus $n\mathbf{b} \cos \beta$. The circuit makes an angle $(2\alpha - \beta)$ with $\mathbf{b}$; the component of the closure failure parallel to the circuit is $nb \cos \beta \cos (2\alpha - \beta)$ therefore. This component is a maximum or minimum when $\beta = \alpha$ and $(\alpha + \frac{1}{2}\pi)$, that is, when the normal to the circuit bisects the angle NOD internally and externally. These bisectors then are the two directions of principal curvature. Reference to Figure 3 shows that the curvatures themselves are the two corresponding values of $nb \cos \beta \cos (2\alpha - \beta)$, that is

$$\kappa_1 = nb \cos^2\alpha \text{ and } \kappa_2 = -nb \sin^2\alpha$$

Appendix C*

A proof of equations (5) is as follows. Consider the tetrahedron shown in Figure 11. Let ABC be of unit

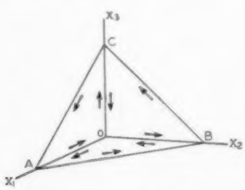

FIGURE 11

area and normal to l_j. Let a Burgers circuit of unit area normal to Ox_1 have a Burgers vector with components $(\alpha_{11}, \alpha_{21}, \alpha_{31})$. Then the circuit $OBCO$ has a Burgers vector $(\alpha_{11} l_1, \alpha_{21} l_1, \alpha_{31} l_1)$. With a similar notation $OCAO$ has a Burgers vector $(\alpha_{12} l_2, \alpha_{22} l_2, \alpha_{32} l_2)$ and $OABO$ has a Burgers vector $(\alpha_{13} l_3, \alpha_{23} l_3, \alpha_{33} l_3)$. If we now traverse these three circuits one after the other, the arms OA, OB, OC are each traversed twice, once in each direction, and therefore cancel; we are left with the circuit $ABCA$ whose closure failure must be the sum of the three for the separate circuits. Thus, for $ABCA$,

$$B_1 = \alpha_{11} l_1 + \alpha_{12} l_2 + \alpha_{13} l_3$$
$$B_2 = \alpha_{21} l_1 + \alpha_{22} l_2 + \alpha_{23} l_3$$
$$B_3 = \alpha_{31} l_1 + \alpha_{32} l_2 + \alpha_{33} l_3$$

or, briefly,

(5) $$B_i = \alpha_{ij} l_j .$$

Appendix D†

We give here a proof of equations (7). Suppose the κ_{ij} are given. Take a small square Burgers circuit of unit area normal to Ox_1 as shown in Figure 8. The

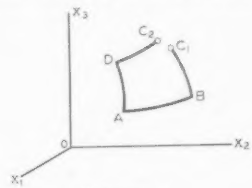

FIGURE 8

closure failure B_1 is $\overrightarrow{C_1C_2}$. This may be regarded as compounded of separate elements corresponding to the curvatures and twist as we traverse each arm of the circuit in turn; Figure 3 shows a special case of this. Taking A as fixed, as we move along $\overrightarrow{AB}$, which is parallel to Ox_2, the lattice rotations about the three axes are κ_{12}, κ_{22}, κ_{32}, from equation (6). By visualising the movements the resulting components of displacement of C_1 can be seen to be

$$\kappa_{22} - \tfrac{1}{2}\kappa_{32},\ -\kappa_{12},\ \tfrac{1}{2}\kappa_{12} .$$

The displacements of C_1 as we move along $\overrightarrow{BC_1}$ are

$$\tfrac{1}{2}\kappa_{23},\ -\tfrac{1}{2}\kappa_{13},\ 0.$$

Similarly, as we move along $\overrightarrow{AD}$ the displacements of C_2 are

$$\tfrac{1}{2}\kappa_{23} - \kappa_{33},\ -\tfrac{1}{2}\kappa_{13},\ \kappa_{13},$$

and as we move along $\overrightarrow{DC_2}$ the displacements of C_2 are

$$-\tfrac{1}{2}\kappa_{32},\ 0,\ \tfrac{1}{2}\kappa_{12}.$$

The total closure failure B_i is then given by the difference between the displacements of C_1 and C_2, thus:

$$B_1 = -(\kappa_{22} + \kappa_{33}),\quad B_2 = \kappa_{12},\quad B_3 = \kappa_{13}.$$

But, from equations (5) with $l_j = (1, 0, 0)$ we have

$$B_1 = \alpha_{11},\quad B_2 = \alpha_{21},\quad B_3 = \alpha_{31}.$$

*See page 158.

†See page 159.

Therefore,

$$\alpha_{11} = -(\kappa_{22} + \kappa_{33}),\ \alpha_{21} = \kappa_{12},\ \alpha_{31} = \kappa_{13},$$

and, in a similar way, by taking circuits normal to Ox_2 and Ox_3 we obtain

$$\alpha_{12} = \kappa_{21}\ ,\ \alpha_{22} = -(\kappa_{33} + \kappa_{11})\ ,\ \alpha_{32} = \kappa_{23}\ ,$$
$$\alpha_{13} = \kappa_{31}\ ,\ \alpha_{23} = \kappa_{32}\ ,\ \alpha_{33} = -(\kappa_{11} + \kappa_{22})\ .$$

Thus, in general, the relation between the α_{ij} describing the state of dislocation and the κ_{ij} describing the curvature is

$$(7) \qquad \alpha_{ij} = \kappa_{ji} - \delta_{ij}\,\kappa_{kk} \qquad (i, j, k = 1, 2, 3)$$

where $\delta_{ij} = 1$ for $i = j$, and $\delta_{ij} = 0$ for $i \neq j$.

Acknowledgments

Dr. C. D. West was kind enough to show me his paper on the corundum crystals before publication and I am glad to acknowledge here that it suggested to me the evolute construction of §2. I am also indebted to Dr. W. M. Lomer for his comments on the manuscript.

References

1. Cahn, R. W. J. Inst. Metals, **76** (1949) 121.
2. Frank, F. C. Phil. Mag., **42** (1951) 809.
3. Schmid, E. and Boas, W. Plasticity of Crystals (London, F. A. Hughes, 1950), p. 58.
4. West, C. D. Paper to be submitted to J. Appl. Phys.
5. Hill, R. The Mathematical Theory of Plasticity (Oxford, University Press, 1951), p. 136.
6. Eshelby, J. D. Phil. Trans., **A244** (1951) 87.
7. Nabarro, F. R. N. Adv. Phys., **1** (1952) 269.
8. Frank, F. C. Plastic Deformation of Crystalline Solids (Pittsburgh Conference, 1950), p. 150.

SECONDARY RECRYSTALLIZATION TEXTURES AND THEIR ORIGIN IN COLD-ROLLED SINGLE CRYSTALS OF SILICON IRON*

C. G. DUNN†

Single crystals in three different orientations were cold rolled 70 per cent and were annealed to produce both primary and secondary recrystallization structures. A detailed study of changes in grain size and in orientation was made using metallographic, X-ray, and magnetic torque methods. The orientations of a few early forming primaries were determined. It was concluded that relatively large primary grains in orientations deviating markedly from the primary recrystallization texture grow into secondary grains having specific preferred orientations and that the driving force for secondary recrystallization comes from grain boundary energy.

LES TEXTURES DE RECRISTALLISATION SECONDAIRE ET LEUR ORIGINE DANS DES MONOCRISTAUX DE FER-SILICIUM LAMINÉS À FROID

Des monocristaux de trois orientations différentes, ont été laminés à froid 70 pour cent et ensuite recuits pour produire les structures de recristallisation primaire et secondaire. Une étude détaillée des changements dans les dimensions des grains et l'orientation a été faite au moyen des rayons-X et des méthodes du couple magnétique et métallographique. Les orientations de quelques grains primaires formés très tôt ont été determinées. Il a été conclu que des grains primaires, relativement grands et dont les orientations différentes assez bien de la texture de la recristallisation primaire, deviennent des grains secondaires ayant des orientations préférentielles spécifiques et que la force motrice pour la recristallisation secondaire provient de l'énergie des joints intercristallins.

SEKUNDÄRE REKRISTALLISATIONSTEXTUREN UND IHR URSPRUNG IN KALTVERFORMTEN SILICON-EISEN EINKRISTALLEN

Drei Einkristalle mit verschiedener kristallographischer Orientierung wurden 70 prozent kaltverformt und dann geglüht um primäre und sekundäre Rekristallisationstexturen zu erzeugen. Eine detaillierte Untersuchung der Korngrösse und der Orientierung der Kristallite wurde mit Hilfe von metallographischen, röntgenographischen und magnetischen Messungen durchgeführt. Es wurde aus diesen Untersuchungen geschlossen, dass relativ grosse primäre Kristallite, die in ihrer kristallographischen Orientierung merkbar von der primären Rekristallisationstextur abweichen, als sekundäre Kristallite mit spezifischen, bevorzugten, Orientierungen weiterwachsen, und dass der Ursprung der Kräfte, die zur sekundären Rekristallisation treiben, in der spezifischen Energie der Korngrenzen liegt.

Introduction

When suitably oriented single crystals of silicon iron are cold rolled to a thickness of about one-fourth the original and are properly annealed, they exhibit the phenomenon called secondary recrystallization. This behavior of silicon iron is the same as that of aluminum reported many years ago by van Arkel and van Bruggen [1]. Silicon iron, like aluminum, in the early stages of annealing, undergoes primary recrystallization to a fine-grained structure with a pronounced texture. Grains at this point are "primaries." Upon further annealing, which may be at a higher temperature, only minor changes occur in the fine-grained structure during an incubation or induction period for growth of a few grains (see Fig. 1). These relatively few grains, called "secondaries," grow rapidly at the expense of the primaries and often reach tremendous sizes relative to them. The incubation and growth of secondaries as just described is called secondary recrystallization, and the pattern of the orientations obtained is called the secondary recrystallization texture.

For rolled aluminum single crystals, Burgers and Basart [2] have followed the orientation changes produced both by rolling and annealing and have shown that the secondary recrystallization texture does not consist of random orientations but rather is composed of preferred ones that fall near, but are not coincident with, the cold-rolled texture. Beck and Hu [3] recently have considered the same problem.

Secondary recrystallization has also been extensively studied in polycrystalline sheets of face-centered cubic metals and alloys, particularly copper and nickel-iron. After cold rolling reductions of about 90 per cent or more, primary recrystallization produces a fine-grained structure with a strong cube texture. Further annealing under suitable conditions produces an abrupt change from primaries to secondaries in the manner described above.

Recently Burgers [4] and also Burke and Turnbull [5] have evaluated the work in this field, which includes, of course, consideration of a number of theories on the origin of secondaries. In general, the main point of conjecture is whether secondaries depend principally (*a*) on some distribution of strains among primaries or (*b*) on the surface

*Received September 22, 1952.
†General Electric Company, Pittsfield, Massachusetts, U.S.A.

tension interactions of grain boundaries.* Since secondaries have preferred orientations, an adequate theory of the origin of secondaries also must account for this feature of their nature. In this connection there are two current points of conjecture, (1) oriented nucleation and (2) oriented growth, which have been well explained elsewhere [3; 4; 5; 6] and which will be partially discussed later in this paper.

Through application of relatively simple X-ray and metallographic techniques, recent results obtained in this laboratory indicated the possibility of determining the mechanism of secondary recrystallization in silicon iron specimens prepared from original single crystal material. The aims of the present investigation, therefore, have been to determine (1) several secondary recrystallization textures and (2) the origin of secondaries.

Experimental Procedure

Single crystal sheet specimens either 0.025 in. or 0.050 in. thick and of several inches length were prepared in a number of different orientations from fine-grained original stock (high grade commercial silicon steel of 3.25 per cent silicon) by a controlled "seed crystal" reorientation technique [7]. These single crystal specimens in a preliminary study were cold rolled different amounts and were annealed in a variety of ways to obtain both primary and secondary recrystallization. With the aid of magnetic tests on disk specimens it was found that reductions in thickness of about 70 per cent gave maximum sharpness of the primary recrystallization texture.

For the final investigation the single crystals used were limited to those 0.050 in. thick and of the orientations given in Table I. Here the abbreviations

TABLE I

ORIENTATIONS OF ORIGINAL SINGLE CRYSTAL SPECIMENS

Specimen	Deviation of $[\bar{1}10]$ From C.D.	Tilt of [001] Up From R.D.
1(a)	1½°	3°
1(b)	1°	½°
1(c)	1°	1°
2	½°	13°
3	0°	25°

C.D. and R.D. refer respectively to cross-rolling and rolling directions. All crystals have a $[\bar{1}10]$ direction essentially parallel to the direction C.D. The first three crystals, designated as specimen 1, are duplications of a (110) [001] orientation.

*The possibility that strain energy also takes the form of boundary energy in a sub-grain boundary structure is not considered here; see [4], for example.

The specimens in Table I were cold rolled unidirectionally in twenty to thirty passes on a laboratory 8-inch diameter rolling mill until a reduction in thickness of 70 per cent occurred. Specimens 1 and 2 widened 5 per cent, whereas specimen 3, which differed also in requiring more passes through the mill, widened 7 per cent.

Short and long anneals were run in the range 500°C to 1100°C in order to follow the course of recrystallization over wide ranges of time and temperature. It was observed that secondaries formed at moderate rates just below 1000°C and rapidly near 1100°C. It was found also in agreement with the phenomenon of secondary recrystallization that the induction period decreased and the number of secondaries increased with rising temperature. On the other hand, primary recrystallization occurred slowly below 600°C and fairly rapidly near 700°C.

Results

Secondary Recrystallization Textures

Secondaries were produced by annealing specimens a suitable length of time at 980°C. Transmission Laue photographs were obtained and used to determine individual orientations. These are given

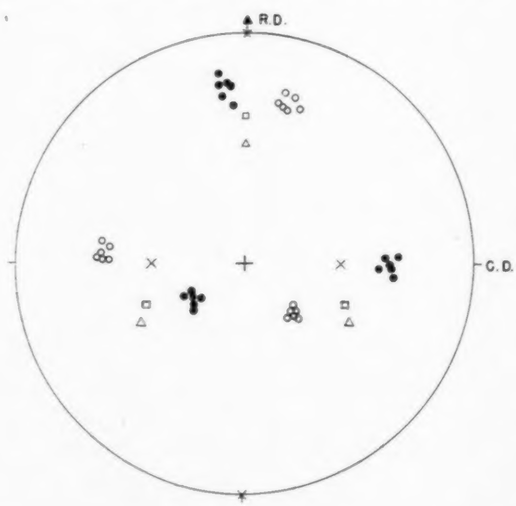

FIGURE 2. Stereographic projection giving the orientations of twelve secondaries—shown by black and white circles. Original orientation, average cold-rolled orientation, and average orientation of primaries are shown by position of squares, triangles, and crosses, respectively.

by the position of cube poles in the accompanying stereographic projections.

The orientation of secondaries and their relationship with cold rolled and primary recrystallization textures will be treated in the order of increasing

complexity. First to consider is specimen 3. Referring to Figure 2, the black and white circles give the orientations of 12 secondaries; squares give the orientation before rolling (see also Table I); triangles give the average orientation of the cold-rolled structure—a (111) ⟨112⟩ orientation—and crosses give the average orientation of the primary recrystallization structure—a (110) [001] orientation.* Considering all changes, there is a 10° rotation about C.D. due to cold rolling, a 35° rotation also about C.D. but in the opposite direction due to primary recrystallization, and still other rotations due to secondary recrystallization. Clearly the primary texture is different from the cold-rolled texture. The secondary texture is different from both the cold-rolled and the primary textures and consists of two similar preferred orientations. It is, if we call these B-orientations, a doublet B-orientation texture.

Only slightly more complicated are the results for specimen 2. Figure 3 gives the orientation of 7

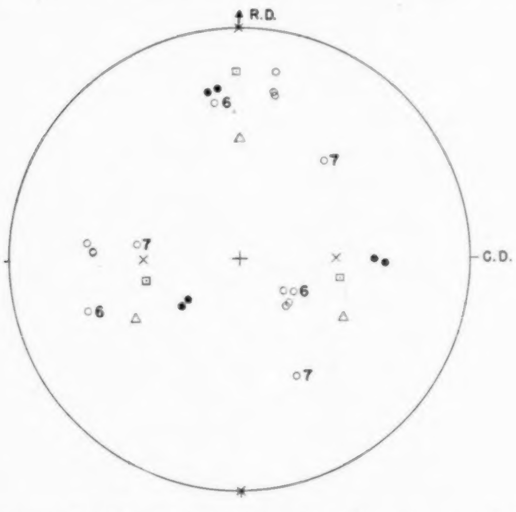

FIGURE 3. Plot giving orientations of seven secondaries of specimen 2. Original orientation, average cold-rolled orientation, and average orientation of primaries are shown by position of squares, triangles, and crosses, respectively.

secondaries and also, as in Figure 2, the other main orientations present prior to the formation of secondaries. The change in orientation due to cold rolling is 22°, but the changes due to primary and secondary recrystallization are much the same as those for specimen 3. There is a doublet B-orientation component present and two other orientations, 6 and 7, which add complexity to the texture.

*This is the preferred orientation of present commercial cold-rolled silicon steel produced by rolling and annealing polycrystalline material. Dunn has reported, however, that it occurs by secondary recrystallization [8].

The results for specimen 1, however, are complicated to say the least. The orientations of 49 secondaries comprise several preferred orientations which can be considered best in three separate plots. Figure 4 gives the orientations of 25 secondaries which, except for three scattered orientations, fall into two preferred orientations, a doublet A-orientation component of the texture. This orientation,

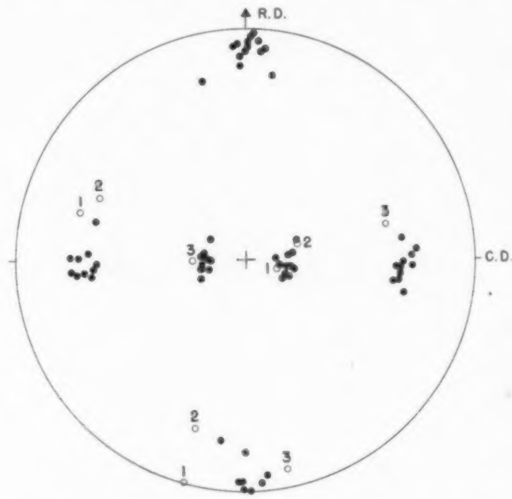

FIGURE 4. Plot giving orientations of twenty-five secondaries in specimen 1. A-orientation component.

approximately (120) [001], is the kind found by Littmann in his oriented thin gauge silicon steel strip [9]. The original cold-rolled, and primary orientations are not indicated, but the original orientation and the average primary orientation are the same, namely, (110) [001]. Therefore, except for a spread in orientation, primary recrystallization has restored the orientation of the original crystal. The cold-rolled orientation, however, is like that of specimens 2 and 3 except for greater spread about C.D. as an axis and the presence of a second (111) ⟨112⟩ component. Consequently, recrystallization here also is one of a 35° rotation about the C.D. direction and is not a case of recrystallization without change in average orientation as Decker and Harker report in their work on silicon iron [10] where the reduction in thickness was 40 per cent. The secondaries with the A-orientation described above, therefore, have orientations that are different from both the cold-rolled orientation and the average orientation of the primaries. Figure 5 shows 13 secondaries with the B-orientation described previously for specimens 2 and 3. Since all four equivalent orientations are present here, we may call this a quadruplet B-orientation component of the texture. From similarity with the results of speci-

mens 2 and 3, a quadruplet B-orientation component could be expected to arise from a doublet (111)

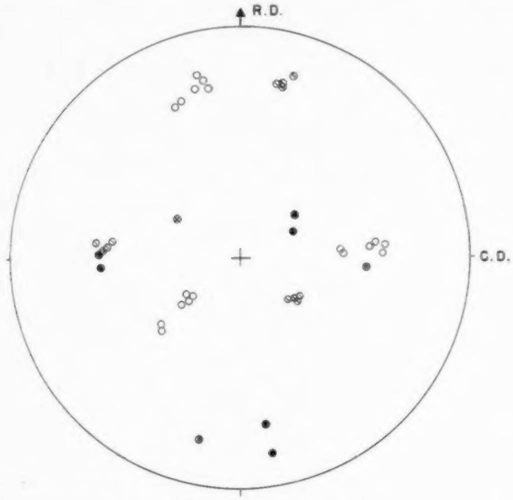

FIGURE 5. Plot giving orientation of thirteen secondaries in specimen 1. B-orientation component.

⟨112⟩ cold-rolled orientation.* Finally, Figure 6 gives the orientations of the remaining eleven secondaries. These may be called a doublet C-orientation component of the texture—a (111) ⟨110⟩ doublet, which differs from both the cold-rolled

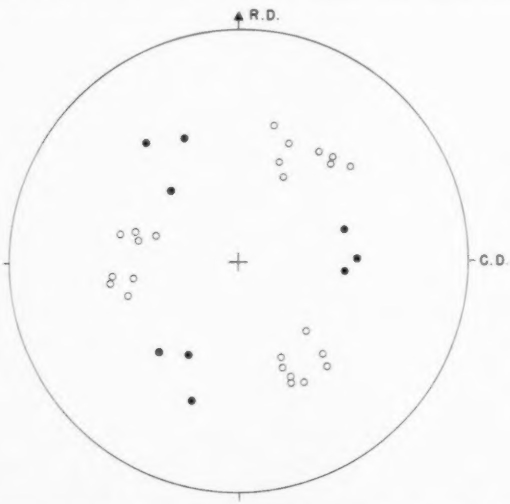

FIGURE 6. Plot giving orientation of eleven secondaries in specimen 1. C-orientation component.

orientation and the average orientation of the primaries. Except for a few unclassified orientations, the secondary recrystallization texture of specimen 1, therefore, consists of essentially three preferred orientations designated as A-, B-, and C-orientations.

Comparison of the orientation relationships in specimens 1, 2, and 3 shows one important common feature: the orientation of every secondary deviates both from the average primary orientation and the average cold-rolled orientation, a result in agreement with published data for other metals. Although all three specimens of different original orientations tend to become alike in (*a*) the cold-rolled orientation, (*b*) the primary texture, and (*c*) the secondary texture, they do display marked differences. Treatment of these differences, however, is beyond the scope of the present paper.

Origin of Secondaries

At the point when secondaries appear among primaries, it is not possible to determine precisely whether such secondaries are a select set of primaries, which have grown at the expense of other primaries, or whether they have originated in some other way that depends essentially on strained lattice regions, which are either residues of the cold-rolled structure or strained primaries. Knowledge of the structures existing prior to the appearance of secondaries, however, might permit one to decide between the possibilities. According to the above results on secondary recrystallization textures, a select set of primaries capable of growing into secondaries must have deviating orientations referred, of course, to the average orientation of the primary structure. If such primaries are found, two other conditions still must be met if they are to become secondaries: (1) they must be appreciably larger than the average primary (as will be discussed later), unless neighbouring grains have higher energy due to some form of strain; and (2) regardless of strain differences, they must have among them the orientations observed for secondaries.

In a test of the possibility that secondaries are certain primaries, which have grown at the expense of other primaries, three types of data covering early stages of both primary and secondary recrystallization were obtained. These are: (1) microstructures, (2) magnetic torque tests of disk specimens, and (3) transmission Laue photographs.

Figure 7 gives two series of micrographs of specimen 1 for various times at 980°C within the induction period for formation of secondaries; time intervals were 25 sec., 20 min., and 1 hr. One series shows the microstructure disclosed by a 4 sec. etch, the other that by a 30 sec. etch. Clearly a heavy etch is required to bring out most of the grain structure, which appears polygonized (the structure did not

*Quantitative pole figure data for the cold-rolled structures and the primary recrystallization structures of specimens 1, 2, and 3 are being obtained to supplement the present work. Results will be published later.

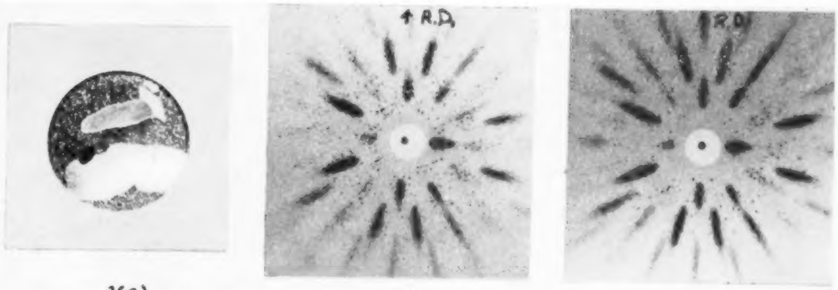

1(a) 1(b) 1(c)

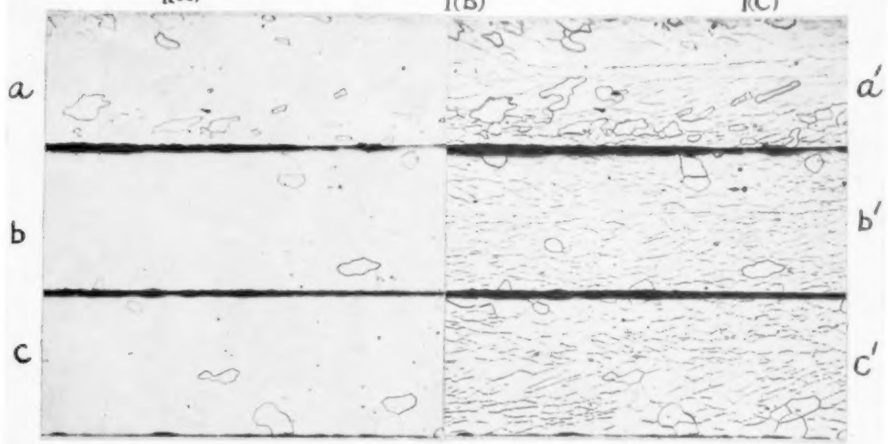

7

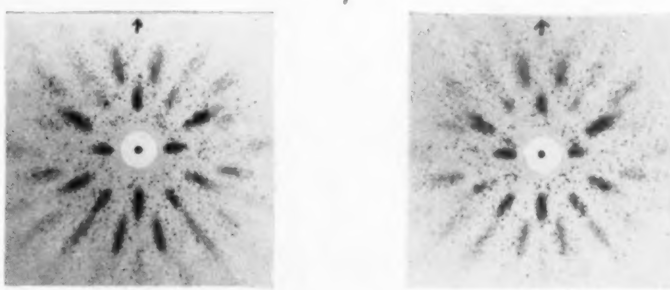

9(a) 9(b)

PLATE I

(All figures reduced to three quarters in reproduction)

FIGURE 1. Photographs showing changes in the grain structure produced by annealing: (*a*) after 36 min. at 980°C; several secondaries appear in a matrix of small primaries (natural size). (*b*) after 1 min. at 980°C (no secondaries in the disk specimen); *W*-radiation. (*c*) after 11 min. at 980°C (no secondaries in the specimen); *W*-radiation.

FIGURE 7. Micrographs of specimen 1 showing the microstructure and its dependence on annealing time at 980°C. Unprimed and primed letters refer to 4 sec. and 30 sec. Nital etch, respectively: (*a, a′*) after 25 sec. anneal. (*b, b′*) after 20 min. anneal. (*c, c′*) after 60 min. anneal. (Magnification 75 ×.)

FIGURE 9. Laue photographs of two specimens after a 1 min. anneal at 980°C: (*a*) specimen 2; (*b*) specimen 3.

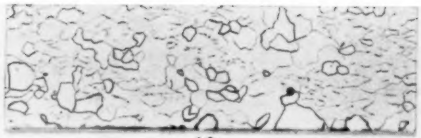

10

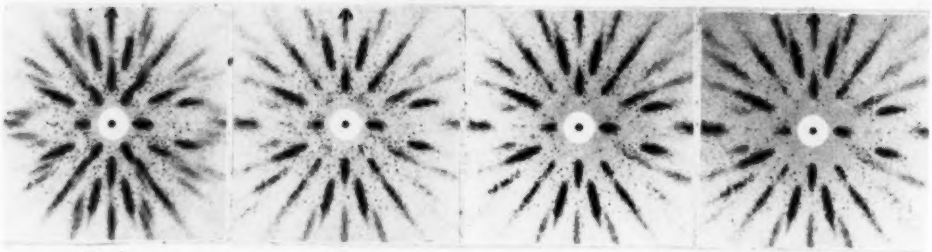

11(a) 11(b) 11(c) 11(d)

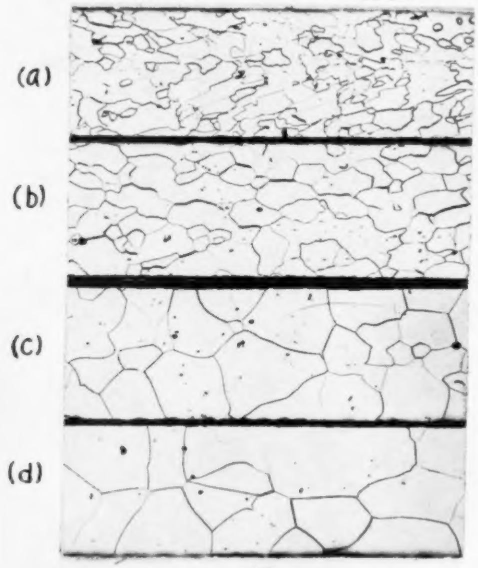

15

PLATE II

(All figures reduced to three quarters in reproduction)

FIGURE 10. Micrograph of specimen 3 after a 25 sec. anneal at 980°C; Nital etch (magnification 75 ×).

FIGURE 11. Laue photographs showing structural changes in one specific region of specimen 1 with annealing time at 980°C: (*a*) sample did not reach 980°C. (*b*) after 25 sec. at temperature. (*c*) after 20 min. (*d*) after 40 min.

FIGURE 15. Microstructure of samples of specimen 1 annealed at 550°C for 64 hr. and then for various times at 980°C; 15 sec. Nital etch: (*a*) after 64 hr. at 550°C. (*b*) after additional 1 min. at 980°C. (*c*) after additional 46 min. at 980°C. (*d*) after additional 21 hr. at 980°C. (Magnification 75 × .)

arise, however, by a polygonization process). This etching behavior is an indication in itself that most of the primaries have nearly the same orientation. (As a matter of fact, this nature of the microstructure was expected from prior information on the sharpness of the texture obtained from magnetic tests on disk specimens. These data will be given later.) The primaries that appear early in the microstructure during the etching treatment clearly have deviating orientations, hereafter called D-primaries. The others, which comprise most of the structure, will be called M-primaries.

A study of a number of samples showed that D-primaries decrease in number during the induction period of secondaries in the manner shown in

TABLE II

NUMBER OF OBSERVED PRIMARIES OF DEVIATING ORIENTATION (D-PRIMARIES) FOR SAMPLES OF SPECIMEN 1 ANNEALED FOR VARIOUS TIMES AT 980°C

25 sec.	20 min.	60 min.
275	75	Secondaries present
214	77	Secondaries present
198	47	14
352	90	25

Table II where a grain count for lightly etched samples is tabulated (see also Fig. 7).

Although these data point to the removal of D-primaries, they also show that large numbers of them persist up to the end of the induction period.

TABLE III

LINEAR SIZE OF D-PRIMARIES IN SPECIMEN 1 AFTER ANNEALING AT 980°C
(Values are in microns)

Time at temperature	Diameter of grains
25 sec.	75, 85, 95, 140, 95, 100, 140, 120, 85, 90
20 min.	100, 90, 130, 105, 110, 130, 140
60 min.	115, 120

Table III, illustrating this point further, gives some rough linear measurements on the larger ones observed in the microstructure.

The sizes of M-primaries were not measured but a simple comparison of those shown in the microstructure with the large D-primary appearing in the lower right-hand corner of Figure 7*b*′, a primary of 110μ length, indicates that the average size is appreciably smaller than the D-primaries listed in Table III. Another way to compare sizes is to count the number of M-primaries bordering one D-primary. There are 11 or 12 M-primaries adjacent to the D-primary referred to in Figure 7*b*′. Other examples with as many as 18 neighbours were seen in the microstructure.

Although it would appear from these data that there are many D-primaries large enough to grow, the data actually fail to show any increase in maximum size due to annealing. On the other hand, a reasonable distribution of sizes among D-primaries would include few of the largest and most likely to grow primaries; so the probability of observing one of these would be small.

Another method of studying structure changes, although less direct in nature, involves the measurement of magnetic properties which vary with crystal orientation. For example, the sharpness of a strong (110) [001] texture can be obtained from torque data, i.e., measurements on the torque required to hold a magnetically saturated disk specimen in various angular positions in a magnetizing field [11]. Results may be plotted as a torque curve with peak values for certain angular positions of the specimen. The important feature for the

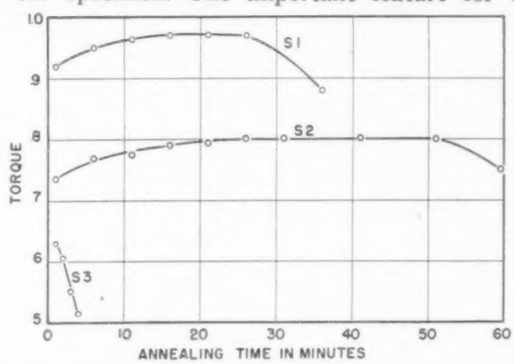

FIGURE 8. Variation of torque tests of disk samples of specimens 1, 2, and 3 with annealing time at 980°C.

present investigation is that the torque peak for single crystal disks of silicon iron is highest for a disk having the (110) plane parallel with the plane of the disk. Thus, the torque peak of any specimen, which is polycrystalline in nature, has to be lower than the torque peak of a (110) single crystal disk. Also, a simple comparison of the (110) single crystal and the polycrystalline sample is possible whenever the texture is strong and the form of the torque curve for specimen and single crystal is the same. In the present work this simple comparison is a fraction —the torque peak of the sample over the torque peak of a (110) single crystal.

Figure 8 gives torque data for samples of specimens 1, 2, and 3 annealed for various lengths of time at 980°C. Since the torque is greatest for specimen 1 and least for specimen 3, there is a

definite effect of original orientation on the sharpness of the (110) [001] texture developed by primary recrystallization. From what has been said previously about torque data of single crystals the rise in torque values early in the induction period of secondaries indicates the absorption of D-primaries (primaries deviating from (110) [001] in this case) and, as expected, the drop in torque values later heralds the visible start of secondaries. In view of this, Figure 8 also shows a marked effect of original orientation on the kinetics of growth (except specimen 2, which behaved nearly the same as specimen 1). Secondaries began forming almost immediately after recrystallization in specimen 3; whereas they did not generally appear in specimen 1 until 20 to 60 min. later. Furthermore, the number of secondaries per unit area were much greater in specimen 3 than in specimen 1. A reason for this behavior will be given later after some X-ray information on structural changes has been discussed.

The Laue photographs of Figures 1*b* and 1*c* represent the 1 min. and 11 min. points of Figure 8 for specimen 1 where the relative torque peaks are 0.90 and 0.97, respectively. They are, therefore, pictures of highly oriented crystalline aggregates. Comparison of these photographs shows that the number of isolated scattered Laue spots, which fall in the clearer areas, is considerably less in Figure 1*c* than in Figure 1*b*. This difference may be explained according to our interpretation of torque and microstructure data as the removal of D-primaries.

With decreasing amount of texture such Laue photographs show observable differences. Figure 9*a* gives a Laue photograph of a disk sample of specimen 2, which, after an anneal of 1 min. at 980°C, had a torque test of 0.73. Figure 9*b* gives the same point for specimen 3 where the torque test was 0.63. A comparison of these photographs, together with those in Figures 1*b* and 1*c*, shows that there are relatively larger individual Laue spots in Figure 9*b* than in the others, indicating larger primaries in specimen 3 than in specimens 1 and 2. Microstructure data support this view. (There are a number of relatively large D-primaries in Figure 10 which shows a micrograph of specimen 3 after a 25 sec. anneal at 980°C.) These structure differences between specimens 1 and 3, therefore, are probably sufficient to account for their behavior differences, if growth of large D-primaries results in secondaries.

Direct proof of growth of large D-primaries was sought with the aid of the above Laue technique and a template arrangement for holding the position of sample constant. With this method changes within a *specific* small volume of a sample occurring as a result of annealing could be followed. Figure 11 shows Laue photographs of this type for a series of 980°C anneals given specimen 1. The first anneal only partially recrystallized the sample. The second, representing 25 sec. at 980°C, left a small residue of cold-worked structure. The last two anneals produced a sharpening of the texture as discussed before. No appreciable enlargement of Laue spots, however, that would indicate growth of a primary were found upon superposing photographs and comparing corresponding Laue spots. Although the method was tried on a large number of areas of both specimens 1 and 3, the evidence obtained for growth was considered too weak to be cited as proof. On the other hand, this method did indicate that D-primaries were the first to form during primary recrystallization. This may not be surprising since many D-primaries are large upon completion of primary recrystallization. Rathenau and Custers in their work on nickel-iron [12] state that primaries recrystallizing last are large (no proof of this, however, was given).

Finally, an attempt was made to determine whether large primaries with the correct orientation for secondaries could be found in specimen 1. For this purpose one sample was completely recrystallized by a 2 min. anneal at 980°C while another was only partially recrystallized by a 10 min. anneal at 620°C. The largest size of primaries in the latter were 55 to 85μ. An attempt was made to X-ray individual primaries in these samples after they were reduced to a thickness of 2 mils, but suitable transmission Laue patterns for analysis were obtained only in the partially recrystallized sample.* Exposure times, using a 5-mil X-ray beam, were 20 to 24 hr.

Figure 12 gives the orientations of four primaries obtained in this way. Comparison with the orientations of secondaries of specimen 1 shows that they have the A-orientation of Figure 4. These first forming primaries, therefore, have the correct orientation to become A-oriented secondaries. The data, however, are insufficient to conclude anything about other possibilities such as: (*a*) whether first forming primaries also have the B-orientations and the C-orientations described previously for secondaries; or (*b*) whether some have the orientation of M-primaries. Obviously, more data are needed on this aspect of primary recrystallization. Nevertheless, it can be said from the data that there is a low

*In the partially recrystallized sample, the primaries were far apart and easy to X-ray singly. Simultaneous diffraction from unrecrystallized material created no problem in the analysis.

probability for random orientations among first forming primaries. (For example, a selection of three grains from a set of random orientations with their orientations within a spread of 15° would have a probability of only one in one hundred thousand.) This is of interest because one requirement of the

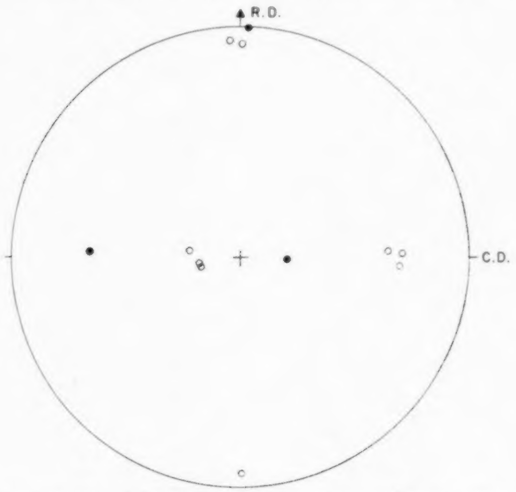

FIGURE 12. Plot of orientations of four primaries formed in the beginning stages of primary recrystallization.

oriented growth theory [3] is the presence of essentially randomly oriented primaries (which are capable of growing) in an otherwise highly oriented primary structure.

According to the foregoing results one may set forth the following conception for the formation of secondaries:*

When primary recrystallization produces a fine-grained structure with a high percentage of primaries in one preferred orientation and the remaining primaries (D-primaries) in other preferred orientations in such a way that a number of the D-primaries are appreciably larger in diameter than the average (by a factor of two or three), the large D-primaries grow into secondaries. One way for D-primaries to become relatively large is for them to incubate first in primary recrystallization and to grow fast enough to stay larger than later forming primaries. Another way for D-primaries to become large is for them to incubate early but not necessarily first and to grow more rapidly than other primaries during the removal of the cold-worked structure. Either or both of these two mechanisms could provide a distribution of grain sizes among the various kinds of primaries produced by recrystallization. The number and sizes of primaries in each preferred orientation would depend on the manner of recrystallization. (For example, suppose that specimen 3 with only B-oriented secondaries had some A-oriented primaries following primary recrystallization, but these either were too small to grow or were consumed by growth of B-oriented secondaries with shorter induction periods. The result would be no A-oriented secondaries.)

The structure and texture produced in primary recrystallization often can be changed by use of a different annealing temperature. Since annealing at 980°C produces a high percentage of M-primaries in the (110) [001] orientation in specimen 1, annealing first at lower temperature might result in less texture through relatively more growth of D-primaries (if D-primaries in general incubate first or early at 980°C, they should do the same at low temperature).

In order to test this idea, six disk samples were prepared from specimen 1, and three of them were given pre-anneals at low temperatures. (Disks D5 and D6 were from one original crystal and D1, D2, D3, and D4 from another.) Disk D6 was annealed 35 hr. at 600°C, and disks D3 and D4 were annealed 64 hr. at 550°C. According to X-ray data primary recrystallization was complete in D6 and almost complete in D3 and D4. These disks and the remaining untreated ones D1, D2, and D5 were then given a series of anneals at 980°C.

Figure 13 shows the results of torque tests on disks D5 and D6. Clearly D6, which was pre-annealed at 600°C, has considerably less texture after annealing at 980°C than the untreated disk, D5. Both

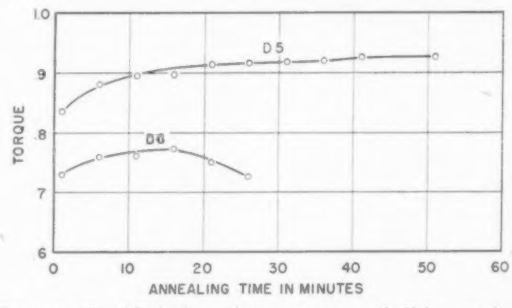

FIGURE 13. Variation of torque tests of disk samples of specimen 1 with annealing time at 980°C and the effect of a 35 hr. 600°C pre-anneal given sample D6.

disks, however, have the (110) [001] texture, which increases with annealing time until secondaries form. The number of secondaries produced in sample D6 was considerably greater than the number observed previously for disks of specimen 1 annealed only at 980°C.

Figure 14 shows the results of the other series. Again the disks that were pre-annealed at low temperature have less (110) [001] texture. Disks D1

*For theoretical discussions along these lines see [4; 5; 8].

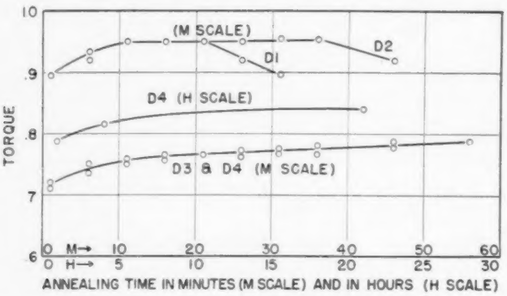

FIGURE 14. Variation of torque tests with annealing time at 980°C for disk samples of specimen 1 and the effect of pre-annealing at low temperature. Disks D3 and D4 were pre-annealed at 550°C for 64 hr.; disks D1 and D2 were not pre-annealed.

and D2 behaved in the usual way upon annealing, but disks D3 and D4, although much like D6, gave no evidence for the formation of secondaries after long anneals at 980°C. Disk D3 after 46 min. at temperature was set aside while the annealing of D4 was continued for a total time of 21 hr. As shown in the plot there was a gradual rise in torque peak.

Light etching of disks D3 and D4 indicated that normal grain growth occurred. Figure 15 illustrates the microstructures developed in samples of specimen 1 pre-annealed at 550°C and then annealed at 980°C. A comparison of the recrystallized structure here (Fig. 15*a*) with that shown formerly for 980°C (Fig. 7*a'*) discloses that 550°C pre-annealing does not produce isolated grains with a clear distinction between D-primaries and M-primaries. Figures 15*b*, 15*c* and 15*d* for increasing lengths of time at 980°C indicate a gradual coarsening of the structure which is typical of normal grain growth.

Pre-annealing at low temperature did change to a small degree the kind of texture obtained. The texture of disk D6 could be described best as (110) [001] although the shape of the torque curve indicated a small variation. On the other hand, the texture of disks D3 and D4, relative to that of D1 and D2 indicated a small lateral tilt about the rolling direction as an axis. An increase in the percent of D-primaries probably could produce this effect. The reduction in torque peaks, however, is due to more or to larger D-primaries. Annealing at low temperatures, therefore, lowered the main component orientation, (110) [001], and increased the per cent of material in deviating orientation. Further annealing probably involved growth of D-primaries at the expense of M-primaries and conversely in such a way that no single D-primary had a sufficient advantage to grow exceptionally large.

The more or less gradual transition between secondary recrystallization and normal grain growth, as illustrated by the results for disk specimens D1, D6, and D4 is, in the writer's opinion, evidence that the main driving force is that of grain boundary energy. If this is true, then the marked differences in kinetics among the samples investigated are due to differences in microstructure and texture.

Discussion of Results

If grain boundary energy per unit volume provides most of the driving force for secondary recrystallization, then, following Harker and Parker [13], one should consider grain shapes and boundary curvatures to understand why certain primaries tend to grow. Under conditions of strong single orientation texture it is also necessary to include the feature that grain boundary energy is far from constant and, in fact, depends markedly on the amount of difference in orientation. Under these conditions, equilibrium may vary appreciably from that of boundaries meeting at 120° angles.

Figures 16*a*, 16*b*, and 16*c* show idealized situations in two dimensions where a grain is surrounded by others of uniform size and where the grain boundary energy per unit area, expressed as a ratio between the grain and its neighbours, is 1, approximately 2, and approximately 3, respectively. The equilibrium

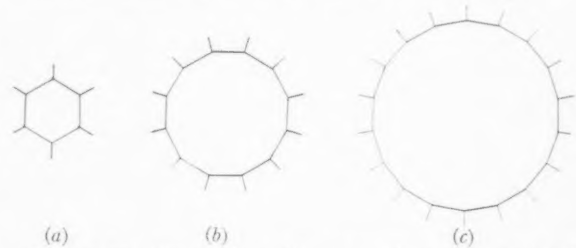

FIGURE 16. Illustrative diagrams of two-dimensional grains showing equilibrium configurations for three values of relative grain boundary energies: (*a*) polygon with 120° angles. (*b*) polygon with 150° angles. (*c*) polygon with 160° angles.

grain shape takes the form of a polygon of either 6, 12, or 18 sides with polygon angles of 120°, 150°, or 160°, respectively. If a grain has fewer sides than the equilibrium number, it will tend to become smaller under the action of grain boundary surface tension forces. On the other hand, if a grain has more sides than the equilibrium number, it will grow.

To apply the above ideas to the present work one must have some value of the relative grain boundary energy. A rough value of 2 may be assumed from the fact that large D-primaries with twelve to eighteen neighbours were observed in a near state of equilibrium (neither growing larger nor becoming smaller) in the microstructure of specimen 1. (Rathenau and

Bass [14] and also Burke and Turnbull [5] have used a figure of 2 in considerations of growth phenomena.)

For the growth process to be recognizable as one of secondary recrystallization, however, there must be a period of essentially zero rate of growth during the initial stages of annealing. The kinetics of the process can be given by analytical expressions [5] that are roughly equivalent in part to the above geometrical treatment.

To simplify the problem, we shall assume that the boundary energy of neighbouring M-primaries has one value γ_1 (this is smaller the sharper the texture) and the boundary energy between a D-primary and an M-primary has another and fixed larger value γ_m, which remains constant regardless of the sharpness of the texture. We shall also assume that only one primary grows while all surrounding primaries remain constant in size except, of course, those being absorbed.

Let d be the diameter of the growing primary, and d_1 the fixed diameter of M-primaries. Equation (1), to a good approximation, then gives the driving force or available energy per unit volume, E/V, for growth of the primary.

$$E/V = k(\gamma_1/d_1 - \gamma_m/d) \tag{1}$$

where k is a constant. Let us consider first the case of a primary in deviating orientation with $\gamma_m = 2\gamma_1$. We have

$$E/V = k\gamma_m/2d_1(1 - 2/x) \tag{2}$$

where $x = d/d_1$ is the relative size of primaries. This equation shows an increase in the driving force with increasing x. Since the driving force is positive only for values of x greater than 2, growth will not occur unless the primary has twice the diameter of its neighbours. On the other hand, if we consider growth of one of the M-primaries, γ_1 will replace γ_m in Equation (1). However, since γ_m actually is $2\gamma_1$, we get

$$E/V = k\gamma_m/2d_1(1 - 1/x) \tag{3}$$

with x having the same meaning as before. In this case, growth will occur if x is greater than 1. Since the factor $k\gamma_m/2d_1$ is the same in Equations (2) and (3), we can omit it in obtaining curves showing the dependence of driving force on values of x (see Fig. 17).

According to the curves, the driving force for growth of a D-primary is negative as it should be for values of x less than 2, which means, of course, that such a primary will be absorbed. For values of

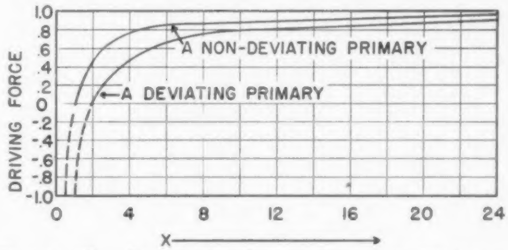

FIGURE 17. Curves showing variation of driving force with relative size of growing primary in a highly oriented matrix.

x greater than 2, the driving force is positive; when this occurs, the D-primary can grow, unless impurity particles are present.* There is, therefore, a "critical size" for growth of D-primaries and this critical size, in the present simplified treatment, corresponds to x equal to 2. Furthermore, for values of x slightly greater than 2, the driving force will be small compared to that for much larger values of x, and hence, the rate of growth will correspondingly be either small or large. Consequently, if the larger D-primaries on completion of primary recrystallization have x-values close to and slightly greater than 2, there will be a period of slow growth that can be interpreted as an induction period for growth of secondaries [5]. On the other hand, there is no corresponding growth of large M-primaries (those in non-deviating orientation) as there should be according to Figure 17 if driving force is the only factor of importance.

It is an experimental fact, however, that a grain will not grow well at the expense of others of nearly the same orientation or of the twin orientation, and the difficulty is not one of insufficient driving force. Larger activation energies for growth are involved. It appears that rate of growth can only be high when there is a fairly large difference in orientation between growing and disappearing grains. Thus, primaries of approximately the same orientation (M-primaries) will not appear to grow, while D-primaries above the critical size will proceed to grow, slowly at first, and then more rapidly as the driving force approaches its limiting value.

The dependence of growth rates on orientation differences leads to a growth selectivity concept. For example, D-primaries are more favored to grow than M-primaries in samples of specimen 1 annealed at 980°C. Growth is a competitive process, and, although some M-primaries increase in size, D-

*Since there definitely are impurity particles in the materials used in the present investigation, the above theoretical treatment requires modification [5]. Qualitatively, the modification is one of larger critical size for growth.

primaries absorb all M-primaries including those that have grown a small amount. In these samples growth selectivity, therefore, determines that the final texture will be one of preferred orientations among secondaries and not one of a single preferred orientation—a (110) [001] texture—which could have resulted from growth of M-primaries in a normal way. The above consideration of growth selectivity, however, is not an argument that growth selectivity by itself determines the secondary recrystallization texture.

In the first place, there are too many differences among the textures of specimens 1, 2, and 3 and too few of the equivalent possible preferred orientations of the A-orientation, B-orientation, and C-orientation type to indicate that the preferred orientations arose by growth of relatively large D-primaries in random orientation but with vastly different growth rates determined by orientation relationships with the average primary orientation. For example, the primary textures of specimens 1, 2, and 3 were the same except for sharpness, but only specimen 1 produced three different kinds of secondaries. Also, since a doublet A-orientation was obtained with one cube pole common with the [001] direction of the primary texture, equivalent orientations crystallographically would require the presence of two other doublets with one cube pole common with [010] or [100] and the orientations rotated approximately 20° from the primary texture. However, the last four orientations as well as equivalent ones of the B-orientation and C-orientation type were not observed.

In the second place, we cannot have oriented growth without oriented nucleation for both primary and secondary recrystallization. Let us assume that oriented growth determines the primary recrystallization texture. We require random orientations among primary nuclei; so only the fraction of material in certain orientations changes with recrystallization. This leads to a change in texture with preferred orientations of primaries. The primaries that deviate in orientations from the preferred ones will be smaller in size because of lower growth rates. None of them, therefore, will be sufficiently large to grow, and secondary recrystallization will not occur—unless, of course, strain among primaries becomes an important factor. On the other hand, if oriented nucleation is an important factor in primary recrystallization, we can readily account for the presence of large primaries in deviating orientation. This is all that is required because selective growth then suffices to determine both the secondary structure and the secondary texture.

Evidence supporting the idea of oriented nucleation in primary recrystallization of silicon iron has been published. For example, it was reported some years ago by the writer [15] that primary recrystallization of single crystals of silicon iron after cold-rolling reduction of 2 to 20 per cent produced sharp preferred crystal orientations, but not in all equivalent positions. Also, the preferred orientations were so strong that no possible selection of a random orientation set could be made from among them.

In closing the discussion, a few remarks should be made regarding the theory that secondaries have their origin in a non-uniformly strained matrix of primaries. The conceptions of Rathenau and Custers [12] and of Tiedema [16], who envisage a straining of early forming primaries through release of unbalanced stresses with only the last forming primaries free of strain, seems reasonable. Strain free primaries can grow at the expense of strained ones, like primary recrystallization in critically strained polycrystalline material. Decker and Harker [10] propose much the same theory for secondary recrystallization in commercial silicon steel, except their conception of the origin of strain differences among primaries is different—the first forming primaries are the ones most strain free and these have the (110) [001] orientation.

In the present investigation, however, early forming primaries were observed to persist without absorption over long periods of time before the appearance of secondaries. To account for the lack of absorption, it seems necessary to conclude that the strain of such primaries must have been small and, therefore, probably insufficient to produce secondary recrystallization by means of strain differences. Supporting this view is the behavior of samples pre-annealed at 550°C; these samples failed to undergo secondary recrystallization but did have a considerable increase in grain size due to normal grain growth. Although the low temperature treatment lowered the primary recrystallization texture, the texture was still strong enough for secondary recrystallization to occur. (Compare Figures 8 and 14 and note that the texture of disk D4, which developed no secondaries, is considerably higher than the texture of specimen 3, which developed secondaries.) Furthermore, it is generally agreed that grain boundary energy provides the driving force for normal grain growth. Therefore, strain differences among primaries is not required for an explanation of the behavior of samples recrystallized at low temperature and annealed further at high temperature. This is not to say that there are no strain differences, but rather that strain differences play

only a minor role. There is also disagreement with the Decker-Harker theory regarding orientation relationships because primaries in the (110) [001] orientation, in the present work, did not become secondaries; they were the primaries which disappeared through growth of secondaries. On the other hand, the Decker-Harker theory agrees better with present primary recrystallization phenomena, and this is true also for their published data. There are, however, several points of difference in the results obtained from cold-rolling and recrystallizing single crystals (these will be considered in another paper), and these results are concerned with: (1) effect of original orientation on the cold-rolled texture, (2) the active slip planes, (3) effect of original orientation on tendency to recrystallize, (4) orientation relationship between cold-rolled and primary textures, and (5) orientation of first forming primaries. Information on all these items is important to the problem of secondary recrystallization.

Summary and Conclusions

Single crystals of silicon iron of three different original orientations were given various anneals after cold-rolling reductions of 70 per cent, and different stages of completion of both primary and secondary recrystallization were investigated.

Generally, the primary recrystallization textures were sharp and of a (110) [001] type. In addition to primaries in the main orientation, there were primaries in deviating orientations. The smaller of these disappeared during the induction period for growth of secondaries, and with their removal the sharpness of the (110) [001] texture improved. The larger of them, however, remained essentially unchanged in size during the induction period of secondaries.

The secondary recrystallization textures were determined for each of the three starting orientations investigated and were found to consist of specific preferred orientations. These preferred orientations differed from both the average cold-rolled orientation and the average orientation produced by primary recrystallization.

The orientations of a few first forming primaries were determined for one specimen and were found to be precisely the orientations of a strong component of the secondary recrystallization texture.

It was also found possible by first annealing at low temperature to induce a sample to undergo normal grain growth instead of secondary recrystallization on annealing at high temperature.

From the growth behavior observed for primaries during the induction period of secondaries and the precise correlation in orientation between secondaries and first forming primaries one may advocate the following conception of the origin of secondaries in cold-rolled single crystals of silicon iron:

When primary recrystallization produces a fine-grained structure with a high percentage of primaries in one preferred orientation and the remaining primaries in other preferred orientations (deviating orientations) in such a way that a number of the latter are larger than the average size of primaries by a factor of two or three, then these large primaries in deviating orientation grow into secondaries, and the main driving force (energy per unit volume) comes from grain boundary energy.

Acknowledgment

It is a pleasure to acknowledge the valuable assistance given by Mr. H. T. Sagendorph in the preparation of specimens, in the X-ray work, and in the analysis of Laue patterns. I also wish to thank Messrs. Wei Liang Chu and A. R. Eastwood for metallographic data and Dr. David Turnbull for valuable discussions of the manuscript.

References

1. Van Arkel, A. E. and Van Bruggen, M. G. Z. Physik, **51** (1928) 520.
2. Burgers, W. G. and Basart, J. C. M. Z. Physik, **54** (1929) 74.
3. Beck, P. A. and Hu, Hsun. Trans. A.I.M.E., **185** (1949) 627.
4. Burgers, W. G. L'état solide (Brussels, Institut International de Physique, 1951), p. 73.
5. Burke, J. E. and Turnbull, D. Progress in Metal Physics, **3** (1952) 220.
6. Beck, P. A., Sperry, P. R., and Hu, Hsun. J. Appl. Phys., **21** (1950) 420.
7. Dunn, C. G. Trans. A.I.M.E., **185** (1949) 72.
8. Dunn, C. G. In "Cold Working of Metals" (Cleveland, Amer. Soc. Metals, 1949), p. 113.
9. Littmann, M. F. U.S. Patent 2,473,156 (June 14, 1949).
10. Decker, B. F. and Harker, D. J. Appl. Phys., **22** (1951) 900.
11. Bozorth, R. M. Ferromagnetism (New York, D. Van Nostrand Company, Inc. 1951), pp. 556 and 565.
12. Rathenau, G. W. and Custers, J. F. H. Philips Research Report, **4** (1949) 241.
13. Harker, D. and Parker, E. R. Trans. A.S.M., **34** (1945) 156.
14. Rathenau, G. W. and Bass, G. Physica, **17** (1951) 117.
15. Dunn, C. G. Trans. A.I.M.E., **167** (1946) 357.
16. Tiedema, T. J. Doctoral Thesis, Technische Hogeschool, Delft, (1951).

THE PREPARATION OF ALPHA-URANIUM CRYSTALS*

R. W. CAHN†

Applications of the strain-anneal and phase-change methods to the growth of alpha-uranium single crystals in uranium are described. While the strain-anneal method gave crystals which were structurally perfect, none were more than 2½ mm. in diameter, probably owing to the occurrence of twinning during deformation. By the phase-change method large, but imperfect, grains were obtained. The hypothesis is put forward that the "cells" in these imperfect grains are the consequence of kinking in the alpha phase at its interface with the beta-phase. This kinking is attributed to the change of volume accompanying the transformation.

LA PRÉPARATION DE CRISTAUX D'URANIUM ALPHA

Une description est faite des applications des méthodes de déformation-recuit et de changement de phase, à la production de monocristaux d'uranium alpha. Alors que la méthode de déformation-recuit a donné des cristaux ayant une structure parfaite, aucun ne dépassait le diamètre de 2½mm, ce qui est probablement dû à la formation de macles pendant la déformation. Par la méthode de changement de phase de grands cristaux ont été obtenus, mais ils contenaient des imperfections. Une hypothèse est avancée, que les "cellules" dans les cristaux imparfaits apparaissent comme conséquence du pliage (kinking) dans la phase alpha, à la surface de joint avec la phase bêta. Ce pliage est attribué au changement de volume qui accompagne la transformation.

DIE HERSTELLUNG VON ALPHA-URAN KRISTALLEN

Anwendung der Methode der Rekristallisation nach vorhergehender Verformung und der Phasen-Umwandlungsmethode zur Züchtung von Alpha-Uran Einkristallen werden beschrieben. Die nach der Rekristallisationsmethode gewonnenen Kristalle waren frei von Strukturfehlern, waren jedoch niemals grösser als 2½ mm. Durchmesser, wahrscheinlich wegen der während der Verformung auftretenden Zwillingsbildung. Nach der Phasen-Umwandlungsmethode konnten grosse, jedoch unvollkommene Kristalle erhalten werden. Es wird die Hypothese vorgeschlagen, dass die "Zellen" in diesen unvollkommenen Kristallen eine Folge des "kinking" der Alpha-Phase an ihrer Grenzfläche zur Beta-Phase ist. Dieses "kinking" wird auf die Volumenänderung bei der Transformation zurückgeführt.

Introduction

The work of which an account is given here was undertaken because crystals of alpha-uranium were required initially for two purposes—the study of the crystallography of the plastic deformation of uranium and the measurement of the three principal electrical conductivities. The requirements for the two applications were somewhat different. For the plasticity studies, it was essential to start with perfect crystals, i.e. crystals the orientation of which did not vary from point to point, since otherwise the identification of twinning planes and slip planes would have been impossible. A large crystal size was not essential. For the conductivity measurements, on the other hand, long single crystals were needed, but a high degree of perfection was not considered so important.

These differing requirements prompted the investigation of two distinct techniques:

1. the strain-anneal method,
2. the phase-change method.

These methods yield comparatively small but perfect crystals, and larger but imperfect crystals, respectively. Since uranium undergoes two allotropic changes in cooling from the melting point, it is obviously impossible to grow large crystals from the melt, and this approach was not investigated at all.

Since this work was completed, Holden [1] has published an account of the preparation of the *beta* phase of a uranium alloy in monocrystalline form by the phase-change method. His incidental observations on attempts to prepare alpha crystals by this method are consistent with the results of the present research.

The Strain-Anneal Method

This method is in general use for a number of metals, notably aluminium and iron. The starting material must be in a strain-free and fine-grained state, which is usually attained by fairly heavy cold work followed by an anneal. The strain-free metal is given a weak deformation, commonly by extension, and then annealed at a slowly rising temperature. If the conditions are chosen correctly, a few new crystal nuclei only are formed at the most highly strained points at some temperature which cannot be exactly predicted (hence the need for a slowly rising temperature). These nuclei invade the strained matrix and consume it entirely before the temperature has risen high enough to generate nuclei at less highly strained points. With aluminium,

*Received October 8, 1952.

†Atomic Energy Research Establishment, Harwell, England. Now at the Department of Metallurgy, University of Birmingham, England.

and sometimes with iron, a good yield of single crystals is obtained. With aluminium, they may be several tens of cubic centimeters in volume, with iron they rarely exceed 1 cm^3. With certain other metals with which the method has occasionally been tried, such as zinc and magnesium, it is very difficult to make crystals more than a few mm^3 in size. Unpublished experiments by the writer with zinc, magnesium, and zirconium, fully confirmed the existence of this difficulty. Crystals made by this method are often very perfect and give extremely sharp spots on Laue photographs, although exceptions occur in this respect.

According to Schmid and Boas [2], it is an advantage to maintain a slight temperature gradient along the specimen, since it is reasoned that only a small portion of the yet unrecrystallized part of the specimen will at any one time be at the proper temperature for recrystallization. This temperature, as it were, travels along the specimen, and the chances are that a single grain will travel along with it, consuming the unrecrystallized parts before these are able to generate fresh nuclei. If the whole of the specimen is at the same temperature, then a number of nuclei may be formed when this temperature reaches the minimum value for recrystallization to start. No data are avilable on the magnitude of the influence of a gradient. The above argument would apply *a fortiori* if a steep gradient were used, because then only a small length of the unrecrystallized part of the specimen will at any moment be at the proper temperature to recrystallize.

Material

Two different lots of uranium were used for these experiments, but the majority of the specimens were made from a batch of fairly high purity (in particular the oxide content was low), which had been cold-swaged. This material was machined into tensile specimens and subsequently annealed at 630°C *in vacuo* to recrystallize it to a fine grain size. Most of these samples were rapidly heated to temperature and furnace-cooled, special experiments showing that the rate of heating was without effect on the subsequent behaviour. A few experiments were also done with rather less pure metal containing much oxide. Unless otherwise detailed, all experiments were carried out with metal from the first batch.

Extension

All specimens were stretched on a Hounsfield tensometer with self-aligning grips. Two types of specimen were used. One was the standard type of round cross-section, with double (stepped) shoulders and a gauge diameter of $\frac{1}{8}$ in. The double shoulders were necessary to prevent premature fracture of the specimen. The second kind of specimen was flat, with a rectangular cross-section 1/8 in. $\times$ 1/16 in. and shoulders 5/16 in. to 3/8 in. wide. Flat specimens were desirable for the plasticity studies since subsequent preparation for micro-examination was facilitated. A few preliminary experiments were also done with round tapered specimens.

The extension was found in all cases by measuring, with a travelling microscope, the distances between a number of fine marks along the gauge length. With the earlier specimens the variation of elongation along the gauge length was sometimes considerable, but with the later specimens, which were fine grained and made to precision standards, the elongation was usually constant to $\pm$ 0.1 per cent.

Annealing

There was a basic limitation to the annealing temperatures it was possible to use, since the alpha-beta phase change occurs on heating at about 667°C. Since this temperature varies somewhat with purity and not all the annealing methods used were capable of really good temperature control, an upper limit of 640°C was adopted. Several methods of annealing were tried. Some specimens were simply heated at a constant temperature of 630°C. Others were heated gradually from 500°C to 630°C, and then held at 630°C, the whole process occupying several days. Some were kept at a uniform temperature along their length, others were kept in a gentle temperature gradient in a furnace based on Andrade and Roscoe's (3) design. The remaining specimens were slowly pulled through a furnace in which a very steep fixed temperature gradient was maintained.

Results

Some 35 specimens were used. Two of these were tapered cylindrical ones, with extension varying along the gauge length from a few tenths of 1 per cent to 2 per cent. The remaining specimens were given extensions ranging from 0.5–2.5 per cent. The tapered specimens were used as a rough guide in determining the optimum extension. One of them, macroetched, is shown in Figure 1. The extension at the thin end was about 1.8 per cent, and the specimen was annealed by the slow heating method.

The optimum extension with the available quality of metal was 0.8–1.4 per cent. Different specimens did not behave entirely consistently, and for this

reason it is not possible to specify an optimum extension more definitely. Since the incidence of recrystallization was capricious at 0.8–0.9 per cent extension, the majority of specimens were given extensions varying from 1.0–1.3 per cent. Figure 2 shows a typical flat specimen after recrystallization.

Varying the rate of heating or cooling in the anneal preceding the small extension did not produce any detectable difference in the final grain size. Annealing at a fixed temperature of 630°C gave appreciably smaller grains than the other annealing methods. Judging by eye, these all gave equally good results. (No statistical estimate of mean grain size was attempted.)

For uranium, at any rate, the presence of a temperature gradient, whether small or great, would seem to be of no assistance in obtaining large crystals. Perhaps if it had been possible to use a higher temperature for the final anneal, the rate of growth of the new grains would have been high enough for the presence of a temperature gradient to have had some effect. Where a gradient is beneficial, this is presumably due to only a small volume of specimen being in process of recrystallizing at any moment. This can only be the case when the linear rate of crystal growth (which of course rises with the temperature) is about the same as or greater than the rate of motion of the specimen. With uranium, the evidence suggests that this linear rate of growth was much smaller than the lowest rate of specimen movement used (0.5 mm/hr). Greater extensions (1.8–2.0 per cent) were tried to increase the rate of growth of the new grains in the steep gradient furnace method, but this did not give an increased grain size, presumably because the number of nuclei increased as well.

The largest grains found in the best specimens were 2–3 mms. across; they were accompanied by a larger number, 1 mm. or less in diameter. In no case did a grain entirely span the cross-section of a specimen, although several came close to doing so. The grains were structurally very good, the sharpness of back-reflection Laue spots showing that the orientation was usually constant across the diameter of the X-ray beam (0.2 mm) to 20 minutes of arc.

A few experiments were done with specimens made from the second (less pure) batch of uranium. The difference in behaviour of the metal containing much oxide from that of the stock normally used was striking. For example, a specimen extended 2.0 per cent had only partly recrystallized after 60 hours at 625°C. The critical extension for this material is thus considerably higher. Moreover in no case were any grains obtained that exceeded 1 mm. across.

One other approach was tried to increase the final grain size. It had been observed that when a coarse-grained aluminium was stretched 10–15 per cent and then annealed, the resultant grain size was always very large, and this without the gradual rise of temperature which is necessary if fine-grained samples are to be turned into large crystals. In the hope that uranium would behave in a similar way, some coarse-grained samples made by the strain-anneal method were re-extended by various amounts up to 3.6 per cent, and then annealed in the gradient furnaces, but the resultant grain size was no bigger than before. The experiments were too few to allow it to be definitely said that the method does not lead to any improvement, but microscopic examination of partially recrystallized specimens of this type showed that the number of nucleation sites was still large. This is very probably associated with twinning, the influence of which is discussed in the following section. It is conceivable that the large pseudo-single crystals made by the phase-change method (see below) would give larger grains after suitable straining and annealing, but this was not investigated.

Discussion

The experiments carried out were comprehensive enough to make it certain that large crystals of uranium cannot be made by the strain-anneal method, unless some entirely new approach is attempted. A suggestion for such an approach arises from the hypothesis that the difficulties experienced were due to the presence of deformation twins in the stretched uranium specimens. There is considerable evidence for this hypothesis, arising particularly from experiments with crystals of zinc [4; 5]. It is possible that if the critical deformation is imparted to the specimen at a temperature high enough to obviate twinning (about 350°C for uranium [6]) larger crystals can be made. Preliminary results have not, however, been encouraging.

The Phase-Change Method

Uranium undergoes two allotropic changes of structure as the temperature is raised. At 667°C it transforms to tetragonal beta-uranium, while this in turn transforms to body-centred cubic gamma-uranium at about 770°C. The change-points are slightly lower on cooling.

A phase-change of this kind has occasionally been used to make comparatively large metal crystals. If a rod of the metal is slowly passed through a

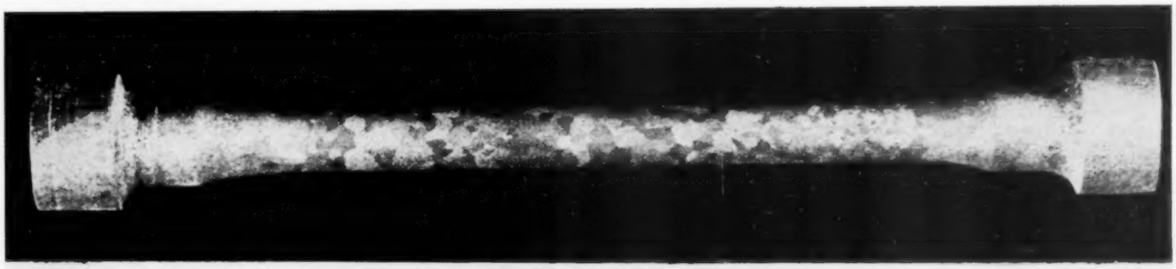

1

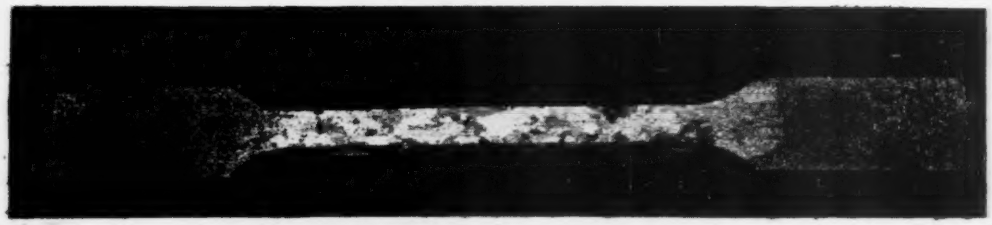

2

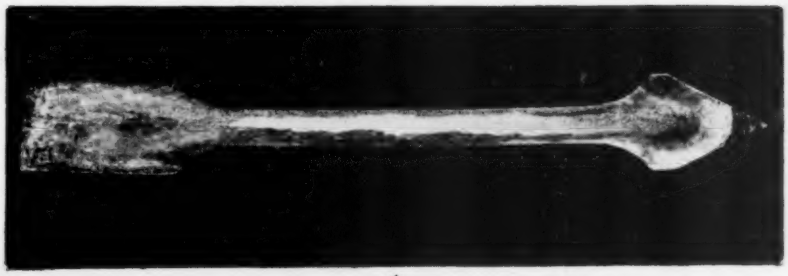

4

5

PLATE I. Figure 1—Tapered specimen, strained and annealed (3 ×). Figure 2—Flat sample made by the strain-anneal method (2 ×). Figure 4—Sample made by the phase-change method: rate of withdrawal = 0.3 cm/hr. (2 ×). Figure 5—Sample first turned into coarse grains by the strain-anneal method, *partly* converted into beta phase and then back to alpha phase. Part on right was cooled rapidly (6 ×).

6

7

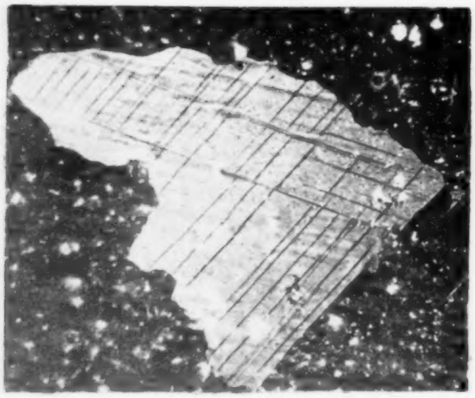

9

10

PLATE II. Figure 6—Microstructure of specimen of Fig. 5 (rapidly cooled portion) (180 ×). Figure 7—Microstructure of a sample made by the phase change, slowly transformed (0.2 cm/hr.) (140 ×). Figure 9—Island grain in a large crystal made by the phase-change method. (300 ×). Figure 10—Originally straight sample converted into columnar grains by the phase-change method (0.05 cm/hr.) ($1\frac{1}{2}$ ×).

temperature gradient in such a way that the whole rod is at a temperature in the stability range of the high-temperature phase to begin with, and the point at which transformation is taking place gradually moves along the specimen from one end, then at sufficiently slow speeds thick columnar grains or even a single crystal may be formed. This method has been successfully applied to iron by McKeehan [7] who made single crystals in wire 1 mm. in diameter, and by Wassermann [8] who made long columnar grains in rod 15 mm. in diameter. It has been used by Holden [1] to make crystals of beta-uranium in uranium-chromium alloys, starting from the gamma phase.

Experimental Method

As with the strain-anneal technique, it is an advantage to use a steep temperature gradient, since the probability of a new alpha grain being nucleated in the beta-phase ahead of an advancing alpha grain is reduced if the volume of metal which is within the narrow temperature range in which transformation can take place is kept to a minimum. A steep temperature gradient obviously has just this effect, and a furnace was designed specifically to provide such a gradient.

Figure 3 is a sketch of the furnace. It consists of two stainless steel blocks each provided with a close-fitting alumina sleeve; each sleeve has a main winding and a shorter subsidiary winding. The lower block was the cooler one, which prevented convection currents; its windings were generally not used in these experiments. (The lower windings can be used to give gentler gradients.) To get a steep gradient between the blocks, it was necessary to provide good thermal insulation between them while having them as close together as possible. This was done by placing between them a disc of silica (which is a poor conductor of heat), both surfaces of which had been polished and then coated with a thin evaporated layer of chromium to reflect heat. The disc was fitted with spacers to keep the blocks apart. As a protection against local convection currents and to help keep the blocks coaxial, a short length of silica tube passed through a close-fitting hole in the disc. Thermocouple holes were bored into the blocks as shown, and the cut-aways at the outer ends of the blocks were for minimising end-losses of heat. The whole assembly was packed in asbestos wool. The subsidiary winding on each block was in parallel with the main winding but had a rheostat in series; the currents for the windings were supplied from a voltage-stabilised source.

The furnace was calibrated by an exploring thermocouple which was moved slowly through the furnace. The temperature distribution of interest is that in the metal specimens, not that between the furnace blocks. For this reason a thick-walled stainless steel tube of roughly the same cross-section as a normal uranium sample was placed in the furnace as a dummy specimen, and the thermocouple was kept in contact with this. (Uranium was

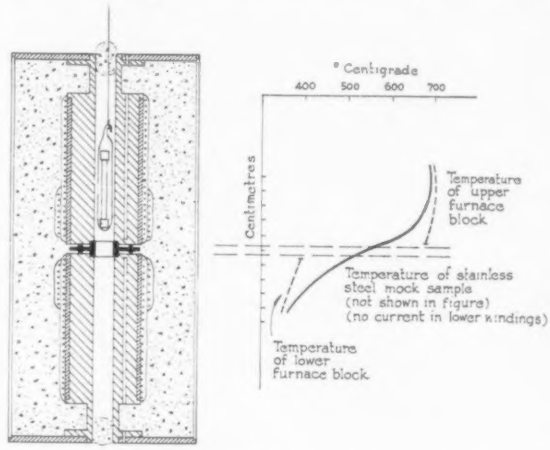

FIGURE 3. Furnace used for growing crystals. The plot shows the temperature distributions in a steel dummy specimen of 0.16 cm² sectional area, and in the furnace blocks.

not used to avoid oxidation trouble.) An open-ended silica tube surrounded the steel tube, to complete the analogy with normal uranium specimens, which were always sealed in silica. A typical plot of temperature against distance is shown by the continuous line in Figure 3. The dashed lines are the temperatures inside the two furnace blocks, obtained by sliding the block thermocouples along their holes.

A gradient of up to 80°C/cm. could be induced in a normal specimen at the temperature of the beta-alpha change. In thin sheet specimens the gradient must have been considerably greater. One factor limiting the possible gradient was the necessity for the maximum temperature in the sample not to exceed the beta-gamma change-point (770°C). In a few cases this temperature was deliberately exceeded, so that the two transformations took place in turn. However, this led to very considerable crystal imperfection and was abandoned.

The samples for the phase-change experiments were mostly machined from the stock used for the strain-anneal method. Some runs were made with shaped tensile specimens, a few of which had previously been turned into coarse grains by the strain-

anneal method. Other runs were made with rods of 1/16 in. square section, or with rolled strip 1/100 in. thick and 1/8 in. wide. In every case the end of the specimen which transformed first was tapered to a point to exclude copious nucleation at the start. For a few runs only, both ends were pointed, the specimens were first passed slowly from the cool block to the hot, left for a while, and then reversed. This was done both with fine-grained and coarse-grained initial stock, to see whether it would lead to an increase in grain-size in the beta phase, which might in turn produce a larger alpha grain size after transforming back. Normally, however, the specimens were placed direct in the hot block and passed down towards the cooler block. Various speeds were tried, ranging from 32 mm/hr. to 0.5 mm/hr. The gradient was not varied from its maximum setting.

Results

Large grains were formed consistently only with the lowest speeds, 0.5–4 mm/hr. A typical specimen, 3 × 1.5 mm. rectangular section along much of its length, passed through the furnace at 3 mm/hr., is shown in Figure 4. The narrower part of the specimen consists of three grains. The thin sheet specimens described in the preceding section were generally passed through at 2 mm/hr. and most of them consisted of a single crystal.

It was found that the size of grain obtained in the thicker specimens was not improved by starting with coarse-grained alpha stock, not even if this was first passed slowly *up* the furnace, interrupted *halfway*, and passed back again, so that the large alpha grains at the extreme position reached by the interface might have been expected to give rise to exceptionally wide columnar grains. Whatever the starting material, no appreciable advantage was gained by passing the specimen up and then reversing it, so that the technique was standardized to omit the first stage.

Figures 5 and 6 are photographs of a sample which will be described in detail because it illustrates several intersecting points. This sample was originally coarse-grained (made by the strain-anneal method), and it was passed *up* the furnace until the interface reached the place near the left edge (Figure 5) where an inked line has been drawn along the extreme boundaries of the columnar grains. The grains to the left of that are part of the original structure. The specimen was reversed at this stage and lowered at about 2 mm/hr. until the interface reached the inked line at the right. It was then removed from the furnace and allowed to cool freely. The metal to the right of the line is, as one might expect, fairly fine-grained. The irregular shape of the left-hand inked line shows that the columnar grains have indeed grown as continuations of the alpha grains which had been partly consumed when the specimen was reversed.

Figure 6 is a photomicrograph of a portion of the rapidly transformed section of the specimen. This shows, in a highly developed form, a feature which to a greater or lesser extent characterised all grains formed via the phase change. This is the presence of a cellular structure inside the grains, with an orientation divergence, usually small, between adjacent cells. This characteristic is especially marked in rapidly transformed metal, and is invariably present in cast uranium. Sometimes the cumulative orientation change is considerable, and a series of cells may form a "bridge" between what appear to be distinct grains (e.g. the "bridge" at the intersection of the arrows, Figure 6). A cellular structure is also found in the long columnar grains made by slow transformation. Here the individual cells are larger, and sometimes elongated in the direction of growth. Figure 7 shows a grain in a slowly transformed specimen, carefully set with respect to the plane of polarisation of the incident light so as to give the maximum contrast between several of the cells. All the cells within the inked boundary are parts of what macroscopically appears to be a single grain. The individual cells were commonly structurally perfect (i.e. of uniform orientation); this was known from the appearance of Laue photographs, which had reflections each split up into several very sharp spots, where the cells were small enough for the beam to straddle several of them. Laue photographs were made at 3 mm. intervals along the pseudo-single crystals in thin strip specimens used for electrical conductivity tests; a beam 0.1 mm. diameter was used, and with this the reflections were often not subdivided. Figure 8 shows the orientations at five points along one of these specimens. This stereogram is typical for all the specimens examined.

There were signs that deformation twinning sometimes played a part in the progress of the phase change. Thus Figure 9 shows an included grain in a thin sheet specimen. By rotating the stage and comparing colourations it was found that the orientation of the lattice in the twin lamellae inclined at 45° to the horizontal was close to or identical with the orientation of the large dark crystal which occupies most of the specimen. This means that the large crystal is in twin relation to the white island grain. The first-formed edge of the latter is parallel to the

twin lamellae referred to, and in addition there are two blade-shaped white islets also parallel to them. The most likely explanation of this is that several deformation twins formed in the newly-formed alpha phase just at the interface, presumably to relieve local stresses due to the change of density accompanying the phase change, and that some of these twins proceeded to grow at the expense of the

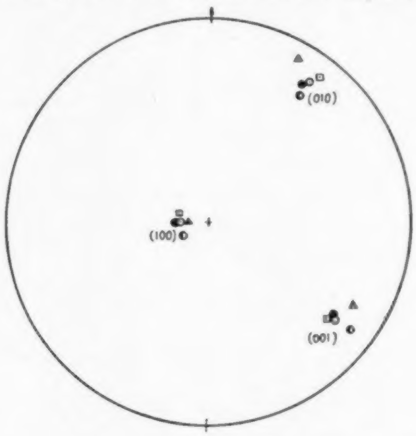

FIGURE 8. Stereogram showing orientations at five points spaced at 0.3 cm. intervals along a pseudo-single crystal made by the phase-change method.

beta phase, one of them extensively. The resultant island grain must have become riddled with twins itself because of the stresses caused by differential thermal contraction during cooling. Twins due presumably to this cause are also clearly visible in one grain in Figure 5. Specimens turned into pseudo-single crystals contained few or no twin lamellae; the orientation differences between neighbouring cells were evidently not sufficient for differential thermal contraction to cause twinning.

There is another reason for believing that the internal stresses set up by the transformation and on cooling are considerable. This is the observation that originally straight specimens often became curved after being turned into columnar grains by the phase change method. A case in point is illustrated in Figure 10. This was almost certainly due mainly to the anisotropy of thermal contraction, because the curvature was marked only where more than one grain occupied the cross-section. In specimens of the dimensions shown in Figure 10 the cross-section rarely contained more than two grains, so that the curvature was evidently caused in precisely the same way as the bending of a heated bimetallic strip. The marked density change on transformation may also play a part in distorting the structure (see below).

Discussion: The Origin of Intragranular Cells

The experiments carried out on the phase change method make it amply clear that there is no hope of obtaining perfect crystals of uranium by this method. Instead, they throw up some problems about the nature of the transformation, the answers to which can as yet only be guessed at. Why does one get columnar crystals only with very slow growth rates, and how are they nucleated? Why do the alpha grains made by phase transformations, whether rapidly or slowly, always contain cells, and why does the size of the cells depend on the rate of transformation?

It was at first thought that some sort of martensitic (shear) process was responsible for the change from beta to alpha, and that in consequence the size of alpha grains obtained depended on the size of the beta grains. At least one alloy is known in which martensitic transformation can occur without the generation of an "acicular" product [9]. It is certain that grain growth in the beta phase is rapid, for high temperature Debye-Scherrer photographs made from uranium wire have coarsely spotted lines. However, there was no sign that prolonged soaking in the beta phase increased the size of the alpha grains produced thereafter, as would be expected if the beta grain size were an important factor. Holden [1] has shown that cells were formed in the alpha phase, whether or not the beta grains from which it was formed had uniform orientations. Again, the way columnar grains could be made to grow from pre-existing alpha grains (Figure 5, left) disposes of the possibility of an oriented shear transformation, for the orientation relationship between the beta and alpha grains here was, by the nature of the experiment, arbitrary.

In the specimens cooled rapidly there were also the curious orientation "bridges" to which attention has already been drawn. It is also noteworthy that the grain boundaries in Figure 6 are very ragged, quite different from the ordinary recrystallised grain boundaries. This is undoubtedly associated with the presence of the small cells. The various observations taken together leave little doubt that each small cell is separately nucleated and that the orientation of each cell is influenced in some way by that of its neighbour, formed just previously, so that the two do not differ much. The larger cells in columnar grains are presumably to be attributed to the same cause. The nature of the influence of the growing cells on each other is obscure. It is only possible to make a guess. This is, that the fairly large volume

change accompanying the beta-alpha transformation generates large stresses in the neighbourhood of the growing grains. This stress cannot be entirely relieved by deformation of the beta phase, because this has a structure closely similar to the sigma phases in stainless steels [10] and is therefore rather hard and brittle. The alpha phase is comparatively soft at the temperature of transformation and can release the stresses by slip and kinking. It is not suggested that the beta phase does not deform at all, only that the alpha phase deforms rather more easily. (In this connection see the footnote below.) The existence of slip and kinking has been experimentally confirmed in alpha-uranium [6], and it is moreover known that a cellular structure, presumably due to kinking, is formed in alpha grains by hot deformation within the stability range of the alpha phase. If a kink band is formed in a growing alpha grain, the result is to relieve the transformation stress and to change the orientation slightly, and the reoriented part of the grain goes on growing until the same thing happens again. The discontinuous change of orientation giving rise to distinct boundaries between the cells can be understood, for kinking gives rise to just such boundaries. The creation of "bridges" between apparently distinct grains is also easily understood, for some kinks can be formed with one sense of lattice rotation (giving rise to a bridge), while adjacent parts of the crystal can kink the other way (giving rise to the apparently distinct grain).*

On the ideal mechanism of kinking [11], adjacent parts of a kinked crystal should always be rotated about an axis lying in the slip plane and normal to the slip direction. Such an axis (which should be parallel to [001]) was not found to relate the cell orientations in the pseudo-single crystals of which Laue photographs were taken. (See for instance Figure 8.) On the other hand it is known [6] that at high temperature a great deal of cross slip occurs in uranium, so that one in effect has "pencil glide" with a multiplicity of slip planes, and consequently a multiplicity of possible axes. Even so these possible axes all lie on the [100]–[010] zone, and it would be well worth while to examine the orientations of *adjacent* large cells in columnar grains (like those in Figure 7) from this point of view. The individual orientations in an experimental stereogram like Figure 8 do not correspond to adjacent cells, hence it is difficult to draw any conclusions from them regarding the mechanism of the transformation.

This hypothesis for explaining the genesis of the cell structure is speculative, and the best evidence in favour of it is that no other hypothesis has been found which can take its place.

*A strong argument for the correctness of this model is Holden's recent observation [1] that beta crystals made by progressive transformation from the alpha phase also had a cell structure. He has shown that beta-uranium is capable of slip and it is to be presumed therefore that it can kink. Holden has put forward a theory basically similar to the present one to account for this substructure in the beta phase.

Acknowledgment

This paper is published by permission of the Director, A.E.R.E.

References

1. Holden, A. N. Acta Cryst., **5** (1952) 182.
2. Schmid, E. and Boas, W. Plasticity of Crystals (London, F. A. Hughes, 1950).
3. Andrade, E. N. da C. and Roscoe, R. Proc. Phys. Soc., **49** (1937) 152.
4. Kuznetsov, V. D. and Zolotov, V. A. Zh. Eksp. Teor. Fiz. (U.S.S.R.), **5** (1935) 75 (Extensive German summary at end).
5. Kuznetsov, V. D. and Karpova, M. P. Zh. Eksp. Teor. Fiz. (U.S.S.R.), **5** (1935) 202.
6. Cahn, R. W. Acta Met., **1** (1953) 49.
7. McKeehan, L. W. Nature, **119** (1927) 705; Proc. A.I.M.E. (1928) 453.
8. Wasserman, G. Mitt. Kaiser-Wilhelm Inst. Eisenforsch., **17** (1935) 203.
9. Chang, L. C. and Read, T. A. Trans. A.I.M.E., **47** (1951) 47.
10. Tucker, C. W., Jr. Science, **112** (1950) 448; Also Acta Cryst., **4** (1951) 425.
11. Hess, J. B. and Barrett, C. S. Trans. A.I.M.E., **185** (1949) 599.

INTER-CRYSTALLINE FRACTURE AND TWINNING OF IRON AT LOW TEMPERATURES*

J. R. LOW, Jr. and R. G. FEUSTEL†

It has been found that small amounts of carbon may strongly influence the ductility and the mode of fracture of iron at low temperatures. Irons containing 0.03 to 0.05 per cent carbon normally exhibit considerable ductility and fracture by trans-crystalline cleavage when tested in tension at − 195°C. After decarburization in moist hydrogen the same materials are completely brittle at − 195°C and fracture occurs by inter-crystalline cleavage; recarburization restores the original properties and mode of fracture. Incomplete decarburization, which leaves the room temperature properties unaffected, leads to inter-crystalline fractures and brittleness at − 195°C, however, the low temperature ductility and trans-crystalline mode of fracture may be restored by homogenization. In explanation of these results it is suggested that the grain boundaries in polycrystalline iron are surfaces of low cleavage strength, and that the resistance to cleavage of these surfaces may be greatly increased by the addition of small amounts of carbon.

It has frequently been proposed that the low temperature brittleness of iron may be caused by the formation of deformation twins at low temperatures. A number of observations on twinning in decarburized and carburized irons which were made in the course of this investigation are believed to demonstrate that twinning is a secondary phenomenon and cannot be considered as a cause of low-temperature brittleness.

RUPTURE INTERCRISTALLINE ET MACLAGE DU FER AUX BASSES TEMPÉRATURES

Il a été trouvé, que de faibles quantités de carbone peuvent fortement influencer la ductilité et le mode de rupture du fer aux basses températures. Des fers contenant 0.03 à 0.05 pour cent de carbone, soumis aux essais de traction à − 195°C, montrent une ductilité considérable et cassent par clivage transcristallin. Après décarburation dans de l'hydrogène humide, les mêmes matériaux sont complètement fragiles à − 195°C et ils cassent par clivage intercristallin; la recarburation restaure les propriétés et mode de rupture originaux.

Une décarburation incomplète, qui laisse inchangées les propriétés à la température ambiante, conduit à une rupture intercristalline et à une grande fragilité à − 195°C, cependant, la ductilité observée aux basses températures et la rupture transcristalline peuvent être restaurées par homogénéisation. Ces résultats peuvent être expliqués en admettant, que les joints intergranulaires dans du fer polycristallin constituent des surfaces de basse résistance au clivage, et que la résistance de ces surfaces peut être considérablement augmentée par addition de petites quantités de carbone.

Il a été fréquemment proposé, que la fragilité du fer aux basses températures peut être causée par la formation de macles de déformation aux basses températures. Les observations concernant le maclage dans des fers décarburés et carburés faites lors de cette investigation, paraissent démontrer que le maclage n'est qu'un phénomène secondaire et ne peut pas être considéré comme cause de la fragilité aux basses températures.

INTERKRISTALLINER BRUCH UND ZWILLINGSBILDUNG IN EISEN BEI TIEFEN TEMPERATUREN

Es ergab sich, dass geringe Mengen Kohlenstoff in Eisen die Verformbarkeit und die Art des Bruches bei tiefen Temperaturen wesentlich beeinflussen können. Eisenproben, die 0,03 bis 0,05 prozent Kohlenstoff enthalten, zeigen normaler Weise erhebliche Verformbarkeit und brechen durch transkristalline Spaltung, wenn sie unter Zug bei − 195°C geprüft werden. Wenn jedoch der Kohlenstoff durch Behandlung in feuchtem Wasserstoff entfernt wird, ist das gleiche Material völlig spröde bei − 195°C und der Bruch erfolgt durch interkristalline Spaltung. Eine unvollständige Entfernung des Kohlenstoffes, die die Eigenschaften bei Zimmertemperatur nicht verändert führt bei − 195° C zu interkristallinem Bruch und Sprödigkeit. Die Verformbarkeit und der transkristalline Bruch können jedoch auch bei tiefen Temperaturen durch Homogenisierung wieder hergestellt werden. Zur Erklärung dieser Versuchsergebnisse wird angenommen, dass die Korngrenzen in polykristallinem Eisen Flächen geringer Spaltfestigkeit sind, und dass der Spaltwiderstand dieser Flächen durch kleine Mengen Kohlenstoffs stark vergrössert werden kann.

Es wird oft angenommen, dass die Sprödigkeit des Eisens bei tiefen Temperaturen durch die Zwillingsbildung bei tiefen Temperaturen bedingt sein könnte. Beobachtungen der Zwillingsbildung an kohlenstoff-freien und kohlenstoffhaltigen Eisenproben, die im Laufe dieser Untersuchungen gemacht wurden, scheinen zu zeigen, dass Zwillingsbildung ein sekundäres Phänomen ist, und nicht als Ursache der Tieftemperatursprödigkeit angesehen werden kann.

Introduction

When low carbon steels or irons fracture in a brittle manner at low temperatures and the fracture surface is examined metallographically, fracture has generally been found to have occurred by trans-crystalline cleavage of the individual ferrite grains. Recently, Fast [1] and Rees, Hopkins, and Tipler [2] have reported inter-crystalline cleavage fractures in relatively high purity irons at low temperatures. In both cases the tendency to grain boundary fracture appeared to be associated with an increase in oxygen content of the irons under study. Stanley [3] has also recently reported inter-crystalline fractures in Armco iron after annealing in hydrogen.

*Received October 30, 1952.
†Knolls Atomic Power Laboratory, General Electric Company, Schenectady, New York, U.S.A.

Fast and Rees attributed the inter-crystalline fractures which they observed to the presence of oxygen while Stanley believed that hydrogen absorbed during annealing was the cause of grain boundary fracture in his experiments. The present investigation of the influence of small amounts of carbon on the mode of fracture of iron at low temperatures leads to the conclusion that if the carbon content of iron is reduced sufficiently then grain boundary fracture will occur at low temperatures. It is suggested that the observations of the investigators cited above may perhaps be better explained on the basis of the carbon content of their materials than on the basis of either the oxygen or hydrogen content.

Since 1926, when O'Neill [4] pointed out that many of the metals which become brittle at low temperatures or high rates of loading also exhibit deformation twins under these same circumstances, there have been a number of attempts to demonstrate that deformation twinning is the cause of low-temperature brittleness [5; 6; 7; 8; 9]. It is believed that the observations concerning the formation of deformation twins which were made in the course of the present investigation, clearly demonstrate that twinning cannot be the cause of low-temperature brittleness in iron. Rather, it is concluded that the twins observed in the vicinity of a brittle fracture surface are a secondary phenomenon resulting from the high stresses associated with brittle crack propagation.

Material

The material used throughout this investigation was a low carbon, rimmed steel in the form of 0.035 to 0.040 in. thick sheet having the following initial composition (wt. per cent):

C	Mn	P	S	Si	Cu	Ni	Cr	Sn
0.05	0.37	0.010	0.015	0.004	0.012	0.010	0.024	0.0003

The composition of this material was modified by decarburizing small tensile specimens in wet hydrogen and by recarburizing following the wet hydrogen treatment. The wet hydrogen treatment consisted of heating for eight or ten hours, depending on thickness, at 700°C in flowing hydrogen which had been bubbled through water at room temperature. Carburizing was accomplished by heating for ten minutes at 690°C in a stream of hydrogen which had been bubbled through an n-heptane-cyclohexane mixture at room temperature.

The wet hydrogen decarburization treatment used is not expected to affect the composition except as regards carbon and nitrogen and possibly oxygen [10]. Typical analyses for these three elements of the variously treated specimens are shown in Table I. Except where noted otherwise, the grain size of all specimens for which mechanical properties are reported was 0.03 to 0.04 mm. diameter.

TABLE I

(wt. per cent)

Treatment	C	N	O
Sheet stock	0.03/0.05	0.003/.004	0.015/0.020
Decarburized	0.001	0.0005	0.016
Recarburized	0.014	—	—

Carbon analyses were obtained by the standard low-pressure oxygen combustion method, nitrogen analyses by the micro-Kjeldahl distillation method and oxygen analyses by the vacuum fusion method.

Experimental Methods

The small sheet tension specimens used for all mechanical tests were 0.2 in. wide and $1\frac{1}{4}$ in. between fillets. One flat face of the specimen was ground on hand-polishing papers and then electropolished before testing. This procedure permitted examination, immediately following testing, for the path of fracture and for the nature and distribution of any deformation occurring in the specimen.

All tests, unless otherwise noted, were carried out with the specimen and grips immersed in liquid nitrogen (-195°C). The testing speed was 0.05 in. per minute of cross-head travel. With the particular testing machine used it was possible to make autographic records of load *vs.* cross-head motion and all reported "load-elongation" curves are of this type. The cross-head motion can not be interpreted readily in terms of strain in the gage length of the specimen because of the unknown amount of strain which occurs in the fillets. However, such curves may be compared for identically shaped specimens and serve to illustrate differences in ductility, yielding behavior, and the general shape of the stress-strain curve.

Yield-point elongation and reduction in area to fracture were computed from measurements of dimensions after testing, the former from pointed micrometer measurements of the width and thickness within a Luder's band but away from the necked region, the latter from similar measurements at the fracture. Fracture stress values reported were obtained by dividing the load at the instant of fracture by the reduced area at fracture.

Experimental Results

Effect of Carbon on Mechanical Properties at − 195°C

Figure 1 shows typical load-elongation curves at − 195°C for the annealed low carbon sheet before treatment, as decarburized, and after recarburizing.

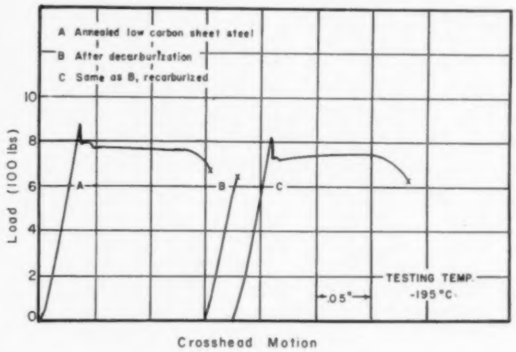

FIGURE 1

The computed mechanical properties of these various materials are listed in Table II.

The unusual shape of the load-elongation curves for the untreated material and for the recarburized specimens results from the fact that these specimens necked down and broke before the yield-point elongation was completed. At the drop in load from the upper yield point, a narrow Luder's band formed, usually near one fillet, and began to propagate down the gage length as the specimen was extended. Before the Luder's band had completely covered the gage length, necking occurred within the Luder's band and the specimen fractured. A typical broken specimen of this type is shown in Figure 2. Similar behavior has occasionally been reported [11; 12] in room-temperature tests of low carbon steel at very high testing speeds.

TABLE II
MECHANICAL PROPERTIES AT − 195°C

Material	Upper yield point (1000 psi)	Lower yield point (1000 psi)	Yield-point Elongation (%)	Fracture stress (1000 psi)	Reduction in area (%)
Annealed low carbon sheet	124	111	21	156	39.0
Decarburized	—	—	—	110 103 96	0.0 0.0 0.0
Decarburized plus vacuum anneal 24 hr., 700°C	—	—	—	105	0.0
Recarburized to 0.014 carbon	118 124 118	111 115 106	23 — 20	158 157 157	43.0 43.0 44.5

It is evident from the curves of Figure 1 and the data of Table II that the reduction of carbon by annealing in wet hydrogen completely embrittles iron at this temperature and loading rate. Further, the original ductility may be restored if carbon is re-introduced into the material. These drastic changes in ductility are accompanied by a complete change in the mode of fracture as brought out in the next section.

Tension tests at temperatures between room temperature and − 195°C have not been made, although the transition temperature of the decarburized material was determined roughly by bend tests of small strips that had been cooled to various temperatures by holding them at various distances above the surface of boiling liquid nitrogen. These bend tests showed the wet-hydrogen-treated material to be ductile above − 165°C.

Observations on the Mode of Fracture

Two methods were used to examine the fractures of tensile specimens after testing. In most cases the mode of fracture was clear from examination of the surface of the specimen which had been metallographically polished before testing. In some cases, where large amounts of plastic flow preceded fracture, this method was supplemented by nickel plating the fracture, sectioning parallel to the flat surface of the specimen to about the mid-plane, and then polishing and etching.

The low carbon sheet before decarburizing was found to fail by *trans-crystalline cleavage* of the individual grains, with the fracture surface made up almost entirely of flat cleavage facets. After decarburizing, the fracture was found to be *inter-crystalline cleavage* with the fracture surface made up almost entirely of typically curved, grain boundary surfaces. If this material was then re-carburized the fracture reverted to the original trans-crystalline cleavage type.

Figures 3 and 5 show the typical inter-crystalline cleavage fractures of the decarburized specimens while Figure 4 shows the typical trans-crystalline cleavage fracture of the original material and the recarburized specimens. The particular specimens used for Figures 3 and 4 were coarse-grained specimens broken by bending at − 195°C, however, the fracture characteristics illustrated are the same as those observed with fine-grained specimens broken in tension at this same temperature. Coarse-grained specimens are used here for purposes of illustration since with such specimens it is possible to fit the two halves of the broken specimen back together again quite precisely so that the relation

of the fracture path to the microstructure may be more clearly demonstrated.

Observations on Twinning

In all of the brittle decarburized specimens it was found that deformation twins (Neumann lamellae) were present in the one or two grains immediately adjacent to the fracture surface *but nowhere else in the specimen.* This is illustrated in Figure 4 for a coarse-grained specimen broken in bending.* Very careful examination of the entire surface of a number of tensile specimens broken at $-195°C$ failed to reveal twins anywhere except within two or three grains of the fracture surface.

As pointed out earlier, the specimens containing carbon did not deform homogeneously over the entire gage length, but necked down and broke near the center of a Luder's band covering approximately one-third of the gage length (cf. Figure 2). No twins were found in the undeformed portion of the specimen. At the edge of the Luder's band, where deformation was just beginning, typical narrow, approximately parallel-sided twins, were found such as those shown in Figure 6. As the amount of deformation increased in passing through the edge of the Luder's band the twins increased irregularly in width in one direction and became semi-lenticular in shape as shown in Figure 7. In the regions of still greater deformation within the Luder's band no further lateral growth was observed and the twinned regions became irregularly distorted, as did the individual grains. At the fracture surface, the original twins, now highly distorted, were still detectable, but no new, sharply defined twins, such as those seen near a brittle fracture, were observed.

Discussion and Conclusions

Twinning and Brittle Fracture

From time to time various investigators [4; 5; 6; 7; 8; 9] have attempted to show that the low temperature transition from ductile to brittle fracture in iron is caused by deformation twinning. The evidence generally cited in support of this hypothesis has been: the nearly simultaneous appearance of deformation twins and brittle fracture as the temperature of testing is lowered; the fact that twins are frequently observed in the neighborhood of brittle fracture; and the fact that the face-centered-cubic metals which do not twin under deformation also do not have a transition from ductile to brittle behavior at low temperatures.

The observations on the occurrence of twins in this investigation leads to the conclusion that twinning does not cause the low temperature transition in iron or contribute in any significant way to brittle fracture. As evidence in support of this conclusion, two observations may be cited:

In the case of the decarburized iron which failed in a brittle manner by inter-crystalline cleavage, twins were found only in the immediate vicinity of the fracture. Two possible explanations may be suggested for this observation. If it is assumed that the stress to cause twinning is lower than that to cause grain boundary cleavage, then the further, and unlikely, assumption must be made that the first twin formed invariably produces a sufficiently high local stress concentration to start fracture. Otherwise one would expect to see occasional twins randomly distributed over the balance of the specimen, since the whole of the specimen is under substantially the same stress at the instant the first twin forms. Rather, it seems more likely that the stress required to cause twinning in this material is significantly higher than that required to cause grain boundary fracture. Such a higher stress would exist in a highly localized region at the front end of a crack progressing across a specimen during fracture and would thus lead to the appearance of twins in a narrow band on either side of the actual fracture surface. An alternative explanation of this localization of twinning might also be that twinning must be preceded by a small amount of slip and that this deformation by slip occurs in a narrow band as the fracture proceeds across the specimens. Such an explanation is suggested by the observation that in ductile specimens twins are found only where deformation by slip has occurred.

In the case of carburized specimens, twins appeared very early in the test, in fact, simultaneously with the first plastic deformation, but did not in any case lead to fracture. In these specimens fracture occurred after considerably greater deformation and long after the formation of new twins had stopped. Here again, it is believed that the stress for twinning is higher than that required for flow and that the stress concentration required to produce twinning is provided at the ends of slip bands temporarily stopped at grain boundaries. The observation that no new twins were formed during the

*The various sets of parallel dark lines within the grains immediately adjacent to the fractures in Figures 3, 4, and 5 are deformation twins. At high magnification, those in Figures 3 and 5 are similar in appearance to the long, narrow twins of Figure 6, typical of twins in iron as they first appear. Those of Figure 4, when examined at high magnification, have an appearance similar to the twinned regions of Figure 7, where lateral growth has occurred with additional plastic deformation.

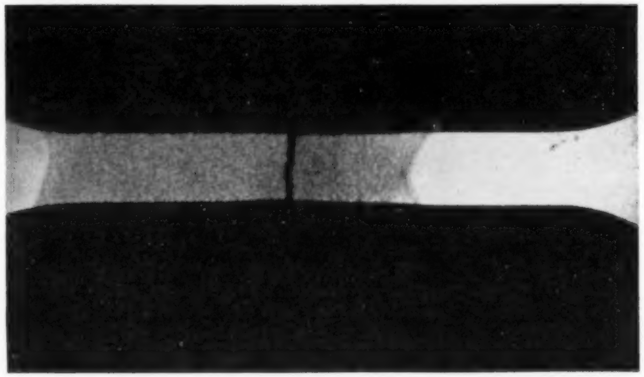

FIGURE 2. Carburized specimen, broken $-195°C$. Specimen fractured before edge of Luder's band reached the end of the gage length.

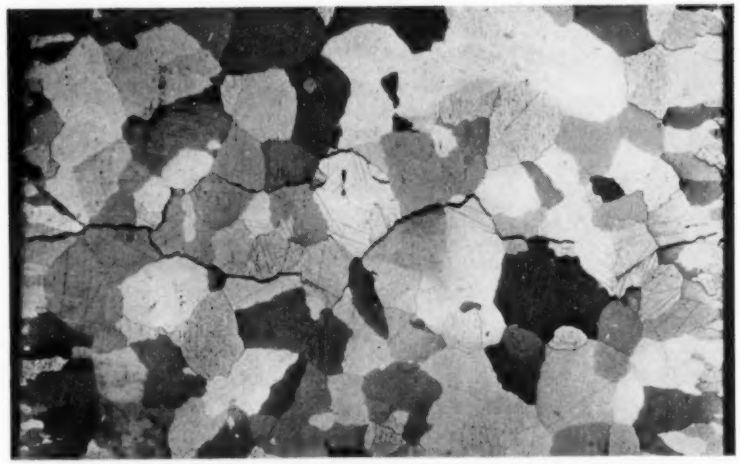

FIGURE 3. Wet hydrogen treated iron, broken $-195°C$. Intercrystalline fracture ($16\times$, reduced by one half in reproduction).

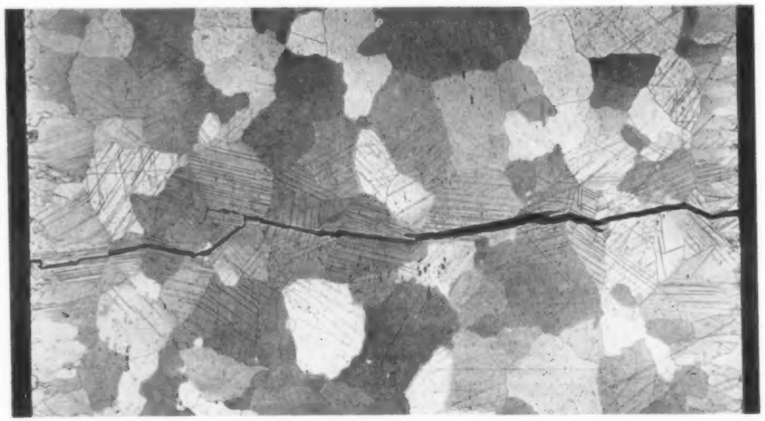

FIGURE 4. Wet hydrogen treated iron, carburized to 0.014 per cent carbon, broken $-195°C$, trans-crystalline fracture ($16\times$, reduced by one half in reproduction).

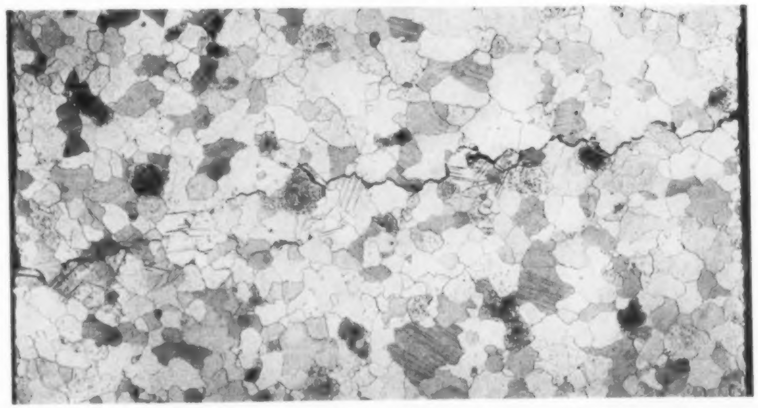

FIGURE 5. Wet hydrogen treated iron, broken $-195°C$. Twins only in first one or two grains adjacent to fracture ($17\times$, reduced by one half in reproduction).

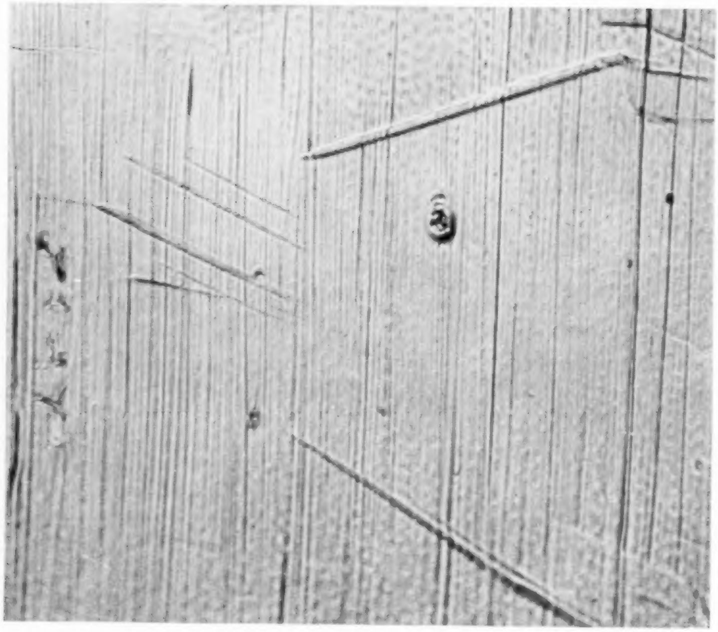

FIGURE 6. Twins at extreme edge of Luder's band in carburized specimen, broken at $-195°C$. Polished surface lightly scratched in tension direction before testing (2000 ×, reduced by one half in reproduction).

FIGURE 7. Same specimen as Figure 6. Twins in region of greater deformation showing irregular lateral growth (2000 ×, reduced by one half in reproduction).

crack propagation at fracture in these specimens is a result of the fact that the crack is propagating through highly deformed metal and it has been shown [13] that even small amounts of prior plastic deformation by slip will suppress twinning in iron.

Effect of Carbon on Mode of Fracture

With regard to the change in mode of fracture and the increase in ductility produced by the addition of carbon to the decarburized material, it should be kept in mind that all of these results apply to material containing substantial amounts of oxygen (about 0.015 wt. per cent). Fast [1] and more recently Rees, Hopkins, and Tipler [2] have found that high purity irons containing more than 0.001 to 0.003 per cent oxygen tend to fracture by inter-crystalline rather than trans-crystalline cleavage. Fast also observed that as oxygen was added to high purity iron, the impact strength at room temperature dropped sharply, but that this effect could be largely offset by the addition of as little as 0.002 per cent carbon. Fast does not comment on the effect of this carbon addition on the mode of fracture.

Rees, Hopkins, and Tipler [2] without specifying the exact mechanism, propose that the addition of oxygen to high purity iron weakens the grain boundaries, presumably as the result of a grain boundary oxide film. On the other hand, it seems highly unlikely that the short time, relatively low temperature, carburizing treatments used in the present investigation could have reduced a thin grain boundary oxide film or even have changed the oxygen content of the grain boundaries significantly. Nevertheless, these carburizing treatments did change the mode of fracture. It is therefore proposed that without carbon, the grain boundaries represent surfaces of low cleavage strength relative to either the flow or the cleavage strength of the grains themselves, and that additions of small amounts of carbon preferentially strengthen the grain boundaries so that plastic flow may occur without fracture and the material then behaves in a ductile manner. It does not appear unreasonable to assume that grain boundary surfaces should have a low cleavage strength since the atomic arrangement at such surfaces may be expected to be irregular over quite large areas with the inter-atomic distances greater, on the average, than in the crystals themselves. Such regions of greater than normal atomic separation should be more readily separated under the action of normal forces leading to crack nuclei which, as the stress is increased, ultimately attain a sufficient size to propagate rapidly over the entire cross-section.

Carbon could be expected to segregate preferentially at grain boundaries, either because of more rapid grain boundary diffusion during carburization, or after homogenization, because of the more favorable size of the interstices between the iron atoms in the irregular grain boundary region. Further, carbon atoms so segregated might well be expected to increase the cleavage strength of the grain boundary surfaces because of the added binding energy which would result from the insertion of a carbon atom between two widely separated iron atoms.

In support of the above argument the following additional experimental results may be cited. A group of specimens were decarburized for increasing periods of time at 700°C and then tested at − 195°C. For decarburization times of about 1.75 hours or longer the material was found to be brittle, with the mode of fracture predominantly inter-crystalline cleavage. Room temperature tests of specimens decarburized for these short times still showed strong yield points indicating that not all of the carbon had been removed. Vacuum annealing for two hours at 700°C following the 1.75 hour decarburization restored the original ductility at − 195°C with the mode of fracture now predominantly trans-crystalline cleavage. With much longer times of decarburization (e.g., 10 hours at 700°C) vacuum annealing treatments up to 24 hours at 700°C, failed to restore the ductility and the specimens remained brittle at − 195°C. Typical load-extension curves at − 195°C for this series of experiments are shown in Figure 8.

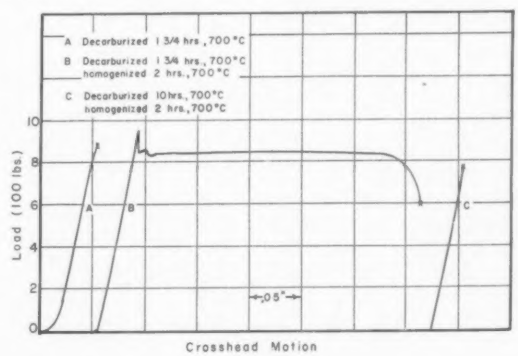

FIGURE 8

Since all of the material used in this investigation contained substantial amounts of oxygen, and in view of the conclusions of Rees and of Fast cited above that oxygen causes grain boundary fracture,

it may be that the present observations on the effects of carbon apply only to irons containing oxygen. This question can only be answered by further experiments using an iron substantially free of oxygen (e.g., less than 0.001 per cent). Such experiments are contemplated. However, the authors are of the opinion that oxygen is of secondary importance and that grain boundary fracture will be observed when the carbon content of iron is reduced to a sufficiently low level. Just how far the carbon content must be reduced cannot be stated quantitatively since present analytical methods for carbon cannot detect changes below about 0.002 per cent, but it is believed that the minimum carbon content required to prevent grain boundary fracture may be much less than this value. For example, if one makes the assumption that a large fraction of the carbon in these very low carbon irons is at the grain boundaries, then as little as 0.0005 per cent would be sufficient to provide a high concentration in these regions. From this point of view the fact that increasing the oxygen content of iron increases the tendency to grain boundary fracture would be attributed, not to any specific effect of oxygen, but to a reduction in the carbon content in a range where such a reduction would not be detected by present analytical methods.

Finally, we would like to suggest that the recently reported results of Stanley [3] and Hopkins [14], who found that high purity irons are embrittled and fracture at the grain boundaries after annealing in wet hydrogen, may be explained simply on the basis of the removal of carbon by this treatment, and not by the introduction of hydrogen, as Stanley has proposed. Some of the hydrogen annealing treatments used by Stanley are admittedly not long enough to remove all of the carbon present in his specimens, however, they may well have been long enough to remove carbon from the grain boundaries and thus cause grain boundary fracture.

References

1. Fast, J. D. Phillips Tech. Rev., **11** (1950) 303-310.
2. Rees, W. P., Hopkins, B. E., and Tipler, H. R. J. Iron and Steel Inst. (London), **169** (1951) 157.
3. Stanley, J. K. Trans. A.S.M., **44** (1952) 1097.
4. O'Neill, H. J. Iron and Steel Inst., **113** (1926) 417.
5. Davidenkow, N. N. J. Tech. Phys. (U.S.S.R.), **8** (1938) 16.
6. Shevandin, E. J. Tech. Phys. (U.S.S.R.), **10** (1940) 396.
7. Yakovlera, Y. S. and Yakutorich, M. T. J. Tech. Phys. (U.S.S.R.), **20** (1950) 420.
8. Shevandin, E. J. Tech. Phys. (U.S.S.R.), **5** (1938) 279.
9. Bruckner, W. H. Welding Journal, **29** (1950) 467-S.
10. Low, J. R., Jr. and Gensamer, M. Trans. A.I.M.E., **158** (1944) 207.
11. Winlock, J. and Leiter, R. W. E. Trans. A.S.M., **25** (1937) 181.
12. Winlock, J. and Lavergne, A. E. Trans. A.S.M., **21** (1933) 109.
13. Pfeil, L. B. Carnegie Schol. Memoirs, Iron and Steel Inst., **15** (1926) 319; **16** (1927) 153.
14. Hopkins, B. E. Trans. A.S.M., **44** (1952) 111 (discussion of [13]).

THE INTERNAL FRICTION OF TANTALUM AND COLUMBIUM FOILS AT ULTRASONIC FREQUENCIES*

J. W. MARX, G. S. BAKER, and J. M. SIVERTSEN†

The internal friction and effective elastic moduli of polycrystalline Ta and Nb foils were measured at vibrational frequencies of about 37 kilocycles and (for Nb) 111 kilocycles. Relaxation effects readily identified with O and N impurities were observed, and correlated with the low frequency data of other investigators. Activation energies for O and N diffusion in both Ta and Nb were observed to decrease with increasing temperature, while the internal friction peaks were shifted upward on the temperature scale when the impurity content was increased. Measurements extended over the temperature interval from about − 160°C to about 1000°C. Low temperature anomalies in the internal friction of Ta are believed to be caused by hydrogen. Room temperature plastic deformation of both Ta and Nb produced large but poorly defined decrement increases between 20°C and 200°C, a range which showed no anomalies for annealed specimens.

LE FROTTEMENT INTERNE DANS LE TANTALE ET LE COLUMBIUM EN FEUILLES, À DES FRÉQUENCES ULTRA-SONIQUES

Le frottement interne et les modules d'élasticité effectifs de feuilles de Ta et Nb polycristallins ont été mesurés à des fréquences de vibration d'environ 37 kilocycles et (pour le Nb) 111 kilocycles. Les effets de relaxation, facilement reconnaissables dans le cas de l'O et le N présents comme impuretés, ont été observés et reliés aux résultats obtenus par d'autres chercheurs, qui utilisaient la méthode des basses fréquences. Il a été constaté, que les énergies d'activation pour la diffusion de l'O et de N dans le Ta et le Nb diminuent quand la température monte, alors que les bosses des courbes de frottement interne sont déplacées vers le haut de l'échelle des températures, quand la quantité d'impuretés augmente. Les mesures ont été faites dans un intervalle de température allant d'environ − 160°C jusqu'à 1000°C. Il semble que les anomalies du frottement interne dans le Ta, aux basses températures, soient dues à l'hydrogène. La déformation plastique du Ta et du Nb à la température ambiante produisait des augmentations importantes, mais mal définies, du décrément entre 20°C et 200°C, alors que dans le même intervalle, les échantillons recuits n'ont montré aucune anomalie.

INNERE REIBUNG VON TANTAL-UND NIOBFOLIEN IM ULTRASCHALLFREQUENZ-BEREICH

Die innere Reibung und die effektiven Moduli der Elastizität von polykristallinen Tantal- und Niobfolien werden bei einer Schwingungsfrequenz von 37 Kilocycles und (für Niob) 111 Kilocycles gemessen. Relaxionseffekte, die von den Sauerstoff- und Stickstoff Verunreinigungen herrühren, wurden gefunden und mit den Niederfrequenzdaten anderer Autoren verglichen. Es wurde beobachtet, dass die Aktivierungsenergien für die Diffusion von Sauerstoff und Stickstoff in Niob und Tantal mit wachsender Temperatur abnehmen, während die Maxima der inneren Reibung sich nach höheren Temperaturen verschoben, wenn der Verunreinigungsgehalt vergrössert wurde. Die Messungen wurden über einem Temperaturbereich von etwa − 160°C bis etwa 1000°C durchgeführt. Es wird angenommen, dass die Temperaturanomalien durch Wasserstoff hervorgerufen werden. Plastische Verformungen von Ta und Nb bei Zimmertemperatur ruft starke aber schlecht definierte Dämpfungszunahmen im Temperaturbereich zwischen 20°C und 200°C hervor. In diesem Gebiet zeigen ausgeglühte Proben keine Anomalien.

Introduction

The use of internal friction as a means of measuring the diffusion of interstitial impurities in body centered cubic lattices is based largely upon the original work of Snoek [1]. As part of his general treatment of relaxation effects in metals, Zener [2] greatly refined the formal theory of relaxation by diffusion processes, and extended it to include reorientation of solute pairs in substitutional solution. Among the notable contributions in this field were those of Kê [3], Dijkstra [4], and Wert [5], who successfully used internal friction as a means of investigating grain boundary viscosity, solid solubilities, and diffusivities. More recent experimental work by Artman [6], Harper [7], and others [8], together with an additional theoretical study of pair reorientation by Le Claire [9], has added to the value of internal friction as a tool for the measurement of solid state processes.

In the present investigation the temperature dependence of the internal friction of polycrystalline Ta and Nb foils was determined at measuring frequencies of about 37 and, for Nb, about 111 kilocycles. The use of foil samples, instead of solid rods, facilitated the introduction of impurities from the gas phase. The high frequency data were then correlated with torsion pendulum measurements made by Ang and Wert [10], as well as with earlier data by Kê [3], to yield information on the diffusion of N and O in Ta and Nb. Ultrasonic measurements were made over the temperature interval from about − 160°C to about 1000°C.

*Received December 19, 1952.
†Department of Mining and Metallurgical Engineering, University of Illinois, Urbana, Illinois, U.S.A.

Theory

For the case of a properly mounted metallic rod vibrating longitudinally in its fundamental or harmonic modes, the most convenient measure of internal friction appears to be the logarithmic decrement, which may be defined as the energy loss per cycle divided by twice the total vibrational energy of the system. When the decrement (δ) of a body-centered cubic material which contains even traces of interstitial impurities, e.g., C, O, or N, is plotted as a function of the temperature, using a fixed vibrational frequency, well-defined decrement maxima or acoustic absorption peaks may be observed.

The specific association between absorption peak and impurity may readily be demonstrated by adding or removing the impurity in question. The work previously referred to indicates that the internal friction maxima, assuming a unique or nearly unique process, occurs when the jump frequency (ν_i) of the interstitial atom is equal to the angular frequency (ω_i) of the applied stress, i.e., $\omega_i = 2\pi f_i = \nu_i$. If T_i is the temperature at which the decrement maximum is observed for a given vibrational frequency and a specific binary system, the diffusivity D_i may be determined from the relation

$$(1) \qquad D_i = (2/3)\alpha a^2 \nu_i = (4\pi/3)\alpha a^2 f_i.$$

Here a is the lattice parameter, α is determined by lattice geometry and equals 1/24 for b.c.c. structures, and the ν_i, of course, are temperature dependent. In general, all theoretical and experimental research on interstitial diffusion may be said to reduce to a calculation or measurement of the temperature dependence of the ν_i.

Phenomenologically, the diffusion process for a given solute concentration, at least within a limited temperature range, is adequately described by the well-known expression

$$(2) \qquad D_i = D_0 \exp(-Q/RT),$$

where Q denotes an activation energy for the process and D_0 is regarded as a virtual constant. The theoretical structure of D_0 has been the object of much study, and an excellent discussion of this point has been given by Wert and Zener [11].

If the decrement of a binary interstitial solution is measured at two different vibrational frequencies, say f_2 greater than f_1, the absorption peak is displaced on the temperature scale from T_1 to T_2. Without making any assumptions about the temperature independence of D and Q, one may write, from equations (1) and (2),

$$(3) \qquad D_1/D_2 = f_1/f_2 = (D_{01}/D_{02}) \exp(-Q_1/RT_1 + Q_2/RT_2).$$

The conventional procedure is to assume that $D_{01} = D_{02}$, and that $Q_1 = Q_2 = Q$. The effective activation energy Q may then be compared from the relation

$$(4) \qquad \ln(f_1/f_2) = -(Q/R)(1/T_1 - 1/T_2).$$

Experimental Procedure

The specimens were formed from 5-mil foils of Ta and Nb, rolled into tightly wound cylinders, with the upper and lower faces ground flat, as shown in Figure 1. Supplementary investigation

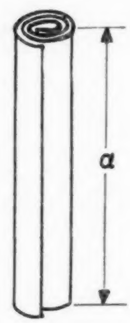

FIGURE 1. Specimen cylinder made from rolled foil.

showed that, in longitudinal vibration, such foil cylinders displayed the elastic characteristics of solid bars of the same length within the limits of the measurement. Annealing in vacuum or a suitable atmosphere was carried out after rolling and grinding the samples.

A modification of the piezoelectric driver-gauge procedure was employed to make the high frequency measurements. The resonator assembly, shown together with its essential circuit components in Figure 2, consisted of two nearly identical α-quartz crystals with adherent silver electrodes, to which a dummy bar of clear, fused silica was attached. The fused silica rod was cut so that its fifth harmonic matched the fundamental frequency of the two quartz crystals. The lengths of the specimen cylinders were also adjusted so that their fundamental frequencies matched those of the quartz bars within about 1 per cent. One of the quartz crystals acted as a driver for the system when the output of a variable frequency oscillator

was applied to its electrodes, the other crystal served as a piezoelectric gauge.

Since the lower end of the silica rod and the two quartz bars were kept within about 10° of room temperature, a mixture of beeswax and rosin

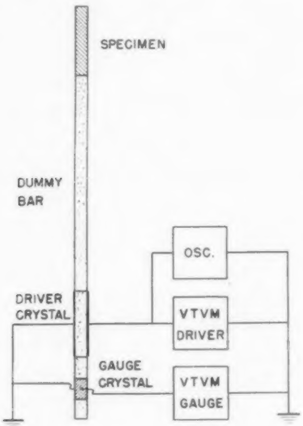

FIGURE 2. Schematic driver-gauge assembly, showing attached specimen, dummy rod, and essential circuit elements.

proved satisfactory as a cement for these interfaces. The specimen-silica interface, on the other hand, was enclosed within furnace and cryostat regions during the measurements, and a temperature resistant cement was required at this point. The use of Sauereisen Insalute cement, together with a special setting procedure, provided an adequate solution to this problem. The Insalute joint was allowed to air dry for a minimum of five days at room temperature, with a further period of about six hours under vacuum, before using. The bond formed in this fashion held at both the highest and the lowest temperatures employed, and withstood temperature cycling over about 500°C intervals.

The general development and application of piezoelectric resonators is based upon the work of many authors, among them Cady, Quimby, Balamuth, and Hunter and Siegel, and a bibliography of prior work on this subject, together with a derivation of the equations involved in making these measurements, has been given in a previous publication [12]. Details of the driver-gauge mounting have likewise been published [13], and will not be repeated here.

Briefly, the resonator assembly is suspended within its vacuum envelope by means of fine tungsten wires pressed into shallow notches in the center of the electrode faces of driver and gauge crystals. When the driver crystal is driven at its fundamental or odd harmonic frequencies, which correspond to still higher harmonics of the whole system because of the frequency matched components, the tungsten wire supports are at displacement nodes, and the glue joints at stress nodes.

The total decrement of the resonator is given by [12],

$$\delta_t = \left[\frac{K}{m_t f_t^2}\right] \frac{V_d}{V_g}, \tag{5}$$

where m_t is the total mass of the resonating unit, f_t is the resonant frequency, V_d is the output voltage of the oscillator, as applied to the driver electrodes, and V_g is the gauge signal at resonance. The resonant frequency is ascertained simply by varying the frequency of the driver signal until the gauge output is maximized. The proportionality constant K is most conveniently determined by measuring the half-width of the resonance peak for the system, either with or without an attached specimen. If a specimen is attached during the latter measurement, it is important that its decrement be amplitude independent, as is the case for quartz and silica alone.

The decrement of the specimen itself (δ_s) is obtained from the total decrement (δ_t) of the composite resonator by employing the relation [12],

$$\delta_s = \frac{m_t \delta_t - m_q \delta_q}{m_s}. \tag{6}$$

Here the subscript q refers to a property of the

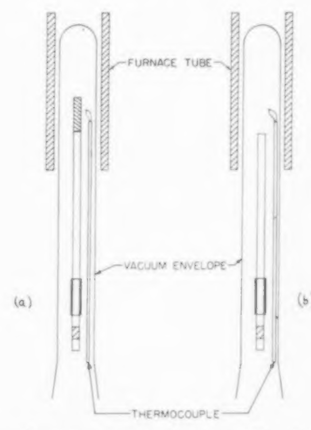

FIGURE 3. Furnace arrangement. The behavior of the driver-gauge assembly alone was first determined, as in (*b*), and then the temperature interval was traversed again with attached specimen, as in (*a*).

resonator minus the specimen. δ_q is initially determined over the whole temperature range with furnace or cryostat and thermocouples in the same

positions they are to occupy during subsequent operations with attached specimens.

The gauge signal V_g is directly proportional to the maximum vibrational strain amplitude at resonance, and the proportionality constant may be determined from a knowledge of the piezoelectric

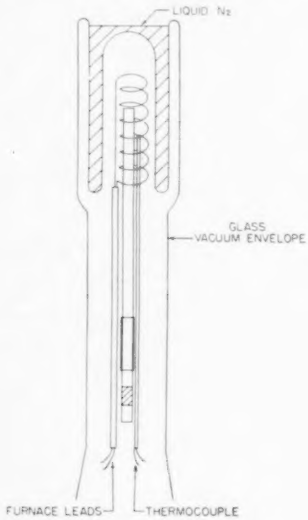

FIGURE 4. One of the cryostat arrangements employed. Other low temperature measurements were made without the heating coil shown above, using a slurry of dry ice and liquid air as the refrigerant below $-70°C$, and dry ice-acetone above. These refrigerants possessed sufficient thermal inertia, after the evaporation of the colder component, to yield warm-up rates of less than 1°C per minute.

constants and dimensions of the quartz crystals, as outlined in a preceding publication [12]. Fractional changes in the dynamic Young's modulus of the specimen segment may be observed simultaneously with the decrement measurement [13]. It can readily be shown experimentally that a properly made cement joint makes only a trivial contribution to temperature induced changes in resonance frequencies of the magnitude observed here.

Schematic furnace and cryostat arrangements are shown in Figure 3 and Figure 4. Temperature measurements above room temperature were made by means of iron-constantan thermocouples suspended in space adjacent to the center of the specimen segment, while low temperature determinations were made both with copper-constantan thermocouples attached to the specimen, and with thermocouples arranged as in the high temperature work. In general, the decrement measurements are more reliable when the thermocouple is not attached to the specimen, while temperature measurements are more precise when it is. Advantages of both procedures are secured by first determining the temperature lag between attached and suspended thermocouples for a given warm-up rate from low temperatures, and then employing this same warm-up rate with suspended thermocouples alone.

10^{-6} mm. pressures were maintained within the relatively small vacuum chamber by means of a

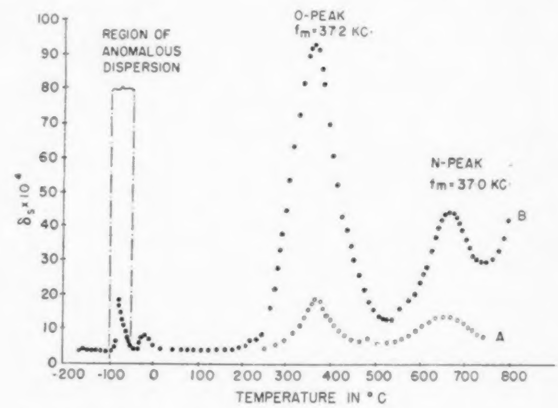

FIGURE 5. Decrement spectrum for Ta. Solid dots represent specimen intentionally loaded with O and N, open circles represent same specimen in the "as received" condition.

Welch 1405 pump backed by a Distillation Products VMF-5 oil diffusion pump. Hewlett-Packard Type 400C vacuum tube voltmeters were employed to measure V_d and V_g. Two oscillators were used. One, with a tuning sensitivity of better than 0.1 cycle at 37 kilocycles, was constructed by Michener and Handloser [14]. The other was a General Radio Type 1330-A bridge oscillator, of lesser tuning sensitivity but much wider frequency range. The latter was used for the decrement measurements on Nb at 111 kc., as reported here, and is currently being used to extend the present set of measurements to still higher frequencies.

Experimental Results

The samples of Ta and Nb, as supplied by the Fansteel Metallurgical Corporation, were specified to be better than 99.9 per cent pure on the basis of spectrographic and chemical analysis. The internal friction data indicates that small amounts of oxygen, nitrogen, and probably hydrogen are present in the material as received.

The decrement of a representative Ta foil, measured at a constant vibrational strain maximum of about 10^{-6}, is shown in Figure 5. Oxygen and nitrogen were intentionally introduced into this specimen by annealing at about 750°C in a 10^{-2} mm. air atmosphere. The pickup of impurity under these conditions emphasizes the need for high vacuum

during measurements. For comparison a portion of the high temperature curve of the same specimen in the as-received condition is also shown.

Low temperature decrement anomalies, of relatively small magnitude when compared to the identified O and N peaks, are also shown in Figure 5. The low temperature effects appear to be independent of the O and N concentration in the metal, and they are not sensibly altered by additional annealing of the original Ta at 750°C in high vacuum.

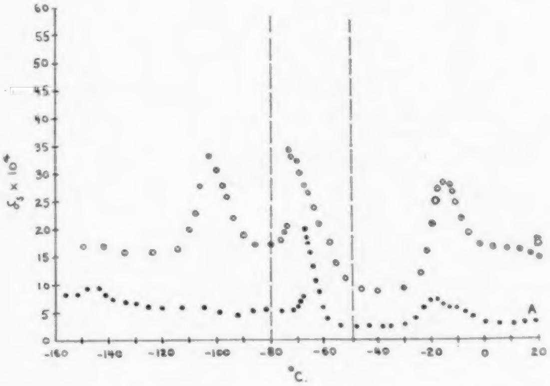

FIGURE 6. Low temperature decrement of Ta. Solid dots (A) represent foil after 850°C, 4 hour, high vacuum anneal; open circles (B) are for the same foil after 30 minutes heating at 500°C in H_2 at a pressure of one atmosphere.

Further investigation of the low temperature zone produced the results shown in Figure 6, where the decrement of the same Ta foil is shown before and after annealing in a hydrogen atmosphere for 30 minutes at 500°C. Hydrogenation raised the general background decrement, but produced no striking additional increase in the incipient peak previously noted in vacuum annealed samples at about − 18°C. A region of anomalous absorption, so titled because of the pronounced asymmetry, or virtual discontinuity, of the decrement increases noted there, was observed in all Ta samples between − 50°C and − 80°C, while the hydrogenated material showed an additional decrement maximum just below − 100°C.

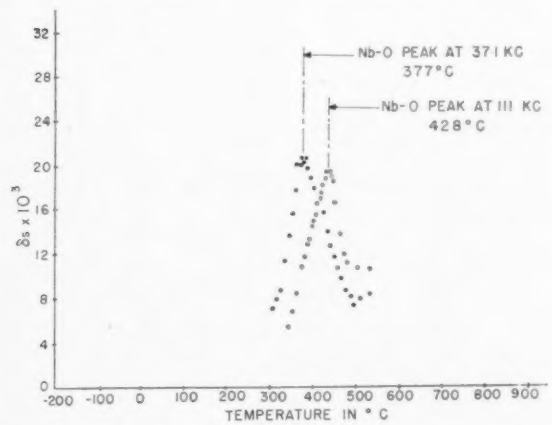

FIGURE 7. Temperature shift induced in the Nb-O peak by changing measuring frequency from about 37 kc. to 111 kc.

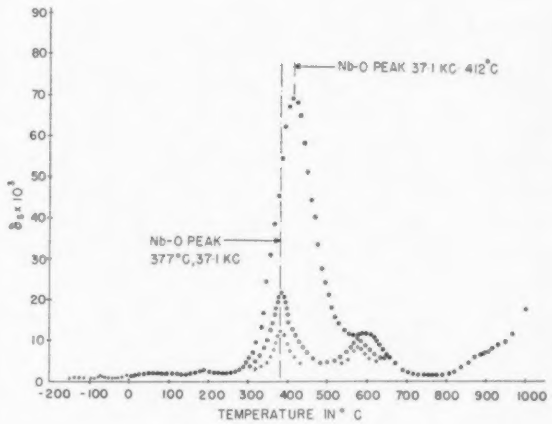

FIGURE 8. Representative displacement of Nb-O and Nb-N peaks produced by raising impurity content. Similar data was obtained for Ta.

The present data on Ta were limited to 37 kc. measuring frequencies. For the case of the Nb samples, O and N peaks were determined both at 37 kc. and 111 kc. The temperature shift in the Nb-O peak, induced by the change in measuring frequency, is illustrated in Figure 7. In general, the background decrement of high vacuum annealed Ta was less than that of similarly treated Nb, and no significant low temperature anomalies were noted for Nb. A study of the effects of hydrogenation upon the decrement of Nb has not yet been completed.

At low O and N concentrations, i.e., for decrement maxima less than 3×10^{-2}, the temperature location of the peaks appears to be independent of the impurity concentration. If *either* O or N contents were increased until the related decrements approached a 10^{-1} value, then *both* O and N peaks were displaced to higher temperatures. This behavior is shown for the case of Nb in Figure 8, where an increase in O content is observed to shift both peaks upward on the temperature scale. Similar results were produced by putting additional amounts of O or N into Ta.

Relaxation of the effective Young's modulus of an Nb foil cylinder loaded with O is shown in Figure 9. It should be noted that the relaxed modulus increases with increasing temperature, while the

temperature coefficient of the unrelaxed modulus is of opposite sign. The general effect is in excellent agreement with the theoretical prediction of Zener [2], except for the change in sign of the temperature

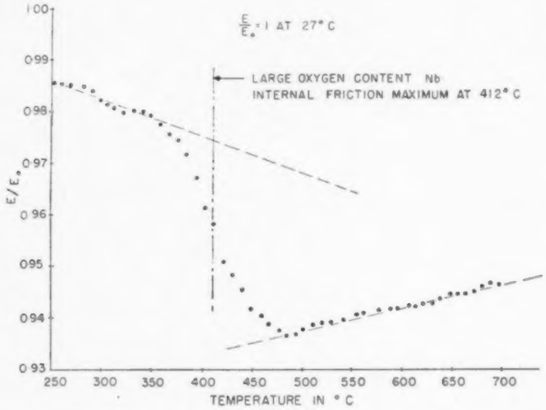

FIGURE 9. Plot of E/E_0 for Nb foil containing a large amount of O. E is the effective Young's modulus at a given temperature, and E_0 is the same quantity at a reference temperature, in this case 27°C.

coefficients, about which the theory makes no statement.

Some effects of plastic deformation are shown in Figure 10. This Ta foil, previously annealed in vacuum, was reduced 25 per cent in thickness by

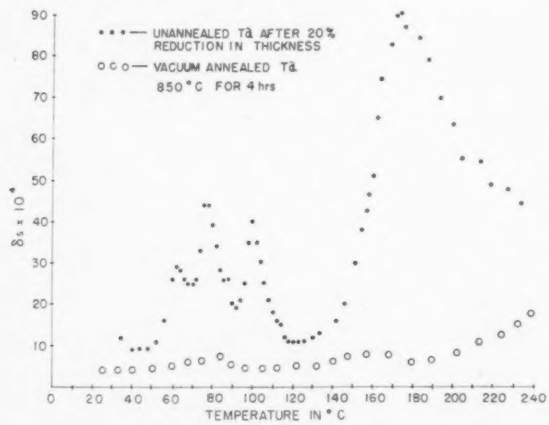

FIGURE 10. Effect of 20 per cent reduction in thickness by cold rolling on decrement of Ta. Similar effects occur in both Ta and Nb. Decrement values were changing with both time and temperature during these observations, and the shape of the curve, when plotted on a temperature scale alone, can do little more than indicate the occurrence of an unusual phenomena.

mill rolling at room temperature. A specimen cylinder was then prepared and measured without further anneal, except for such recovery as would occur in six days standing at room temperature. Large decrement increases were noted below 200°C, in regions that showed no anomalies for the original annealed material, as shown. In these regions the decrement of the deformed sample was dependent on both time and temperature. Large decrement increases would result from a small temperature rise, but these would then decay if the sample were held for a period at the higher temperature. For this reason the scatter in the data, plotted on a temperature scale, is very great, and the shape of the peak or peaks cannot be regarded as of great significance. Similar effects were observed in other Ta samples and also in Nb.

Discussion

The correlation of the present high frequency measurements with earlier low frequency internal friction studies of O and N diffusion in Ta by Kê [3], together with the more recent work of Ang and Wert [10] on both Ta and Nb, permits an examination of the diffusivities in these systems over a much wider temperature range than would be the case for the low frequency data alone. In the case of Nb the frequency change is of the order of 10^5, from about one cycle per second to 111 kilocycles, with a resulting shift of about 300°C in the O and N peaks. If one attempts to calculate activation energies in the conventional manner, i.e., by applying equation (4), with its assumptions of constant D_0 and Q, to the data, the results shown in Table I are obtained. The effective Q_i, when calculated in this fashion, appear to decrease with increasing temperature.

A similar effect has been observed in the measurement of sodium diffusion in glass by internal friction methods [13]. In considering the data on glass, the authors have pointed out that conventional diffusion measurements, such as radioactive tracer techniques, are based upon the transport of solute atoms over macroscopic distances. In the absence of any channelized regions of consistently low energy barriers, the rate of such macroscopic transport phenomena would be dominated by the frequency with which the solute atoms could surmount the highest potential barriers in their path. Internal friction methods, on the other hand, measure diffusion on an atomic scale, i.e., between adjacent lattice sites, consequently it is to be expected that the existence of a spread in the activation energies for a given solid state process would have a much greater effect on the internal friction data than upon conventional diffusion data.

The results shown in Table I simply indicate that the slopes of the ln D vs. $1/T$ curves for these

systems decrease in magnitude as the observation temperature is increased. Any identification of these slopes with a constant activation energy is obviously not justified except as a gross approximation. Recently Wells, Batz, and Mehl [19] have investigated the diffusion of carbon in austenite by a sectioning technique. In the published accounts of

TABLE I

ACTIVATION ENERGIES FOR INTERSTITIAL DIFFUSION*

System	Temperature range, °C.	Molar Q kilocalories	Observers
Ta-O	146–155	32.0	Ang
Ta-O	152–170	29.0	Kê
Ta-O	155–355	27.3	Ang, present
Ta-O	All data	27.5	All above
Ta-N	350, ± 10	44.0	Kê
Ta-N	343–360	40.5	Ang
Ta-N	360–662	39.6	Ang, present
Ta-N	All data	39.8	All above
Nb-O	148–168	27.6	Ang
Nb-O	168–377	26.0	Ang, present
Nb-O	377–423	22.0	present
Nb-O	All data	26.3	All above
Nb-N	285–310	38.6	Ang
Nb-N	310–583	35.7	Ang, present
Nb-N	583–644	28.1	present
Nb-N	All data	35.1	All above

*The calculation of Q is based upon the assumption that D_0 does not vary more than linearly with temperature for any system examined. The last entry in each group represents the effective Q as determined from the best straight line accommodation of all data on a ln D vs. $1/T$ plot.

this very excellent work, the investigators accommodated their ln D vs. $1/T$ data, for a given carbon concentration, by drawing the best possible straight line through the points, determining a constant Q from its slope. If the published results are examined critically, however, it appears that the data might be better fitted by a curve which decreased in slope at the higher temperatures. For example, their points for $1/T$ values of less than about 7×10^{-4}, which may be considered the most reliable from the experimental viewpoint, can be fitted by a straight line with a slope significantly less than that required to fit the low temperature points. This is true for all six published ln D vs. $1/T$ plots [19]. Thus it appears possible that the diffusion of carbon in austenite exhibits an effect qualitatively similar to that noted here for interstitial diffusion in Ta and Nb.

Following Wert and Zener [11], the diffusivity may in general be written

$$D = A \exp - [(Q/RT) - (\Delta S/R)], \tag{7}$$

where Q is the molar activation energy, ΔS the molar entropy change, and A the frequency factor for the diffusion process. A formally similar relation is given by the application of Eyring's reaction rate theory to the diffusion process, except that the factor A is, in this case, a linear function of the temperature. This difference makes only a trivial contribution to the results above room temperature, and the following statements may then be applied to either the rate theory development or that of Wert and Zener.

Assuming that both Q and ΔS may depend on the temperature, the relationship between the slope of the ln D vs. $1/T$ curve and the activation energy becomes

$$R\frac{d(\ln D)}{d(1/T)} = -Q - (1/T)\frac{dQ}{d(1/T)} + \frac{d(\Delta S)}{d(1/T)}. \tag{8}$$

Since the activation energy Q may readily be identified with the enthalpy change ΔH for the process, and since it follows from the definition of enthalpy that, at constant pressure,

$$(1/T)\frac{d(\Delta H)}{d(1/T)} = \frac{d(\Delta S)}{d(1/T)}, \tag{9}$$

the two derivative terms in the right-hand member of equation (8) vanish.

Thus the slope of the ln D vs. $1/T$ curve at any point is directly proportional to the activation energy, or enthalpy change, *at that temperature*, even though the activation energy itself may be a function of the temperature instead of the constant it is usually presumed to be. This fact has been emphasized by Zener [20], who points out that the use of expressions such as equation (8) has been unnecessarily restricted to systems in which Q was believed to be a rigorous constant.

It should be noted that if the diffusion process were occurring by means of two or more independent mechanisms, each with its own activation energy, the curvature of the ln D vs. $1/T$ plot would in all cases be opposite in sign to that which is observed here and indicated in the data of Wells, Batz, and Mehl. This would also be the case for a slight dispersion of the activation energies for a single process, provided that the mean value remained the same at all temperatures. The data of Ang and Wert [10] and the present authors, as used in calculating the values given in Table I, were

obtained on materials of low and approximately equal impurity content. Hence it does not appear that the observed decrease in slope is the result of either structural inhomogeneity or concentration differences, and a real temperature dependence of ΔH, or Q, is clearly indicated by the data.

A suggestion that must at least be considered is the hypothesis that the effective charge of an interstitial impurity, its degree of ionization, so to speak, may vary significantly with temperature in a transition metal. If the degree of ionization, and with it the effective ionic radius of the solute, were to change, the activation energy for diffusion should obviously be altered. Measurements of the temperature dependence of the electric resistivity should detect phenomena of this sort if they actually occur.

With a single exception the present work may be said to corroborate the general findings of previous investigators of interstitial diffusion in Ta and Nb, within the temperature range they employed. The exception is the case of carbon diffusion. The possibility that the effects previously attributed to carbon may actually be due to traces of oxygen is well within the limits of experimental error. It is the opinion of the authors that a systematic re-examination of diffusion in the Ta-C and Nb-C systems is indicated.

In view of other types of measurements on the Ta-H system, the low temperature decrement of Ta (Figure 6) is particularly interesting. Kelley [15] has observed a specific heat anomaly in the neighborhood of $-70°$C for this system, which he attributes to entropy changes resulting from the opening of additional degrees of freedom to the proton impurity in the lattice. Garstens [16] has investigated the nuclear magnetic resonance absorption line width for the same system, over a wide range of concentrations. He finds that a marked broadening of the H^+ line width occurs in the $-70°$C region, indicating that immobilization of the protons is occurring at these temperatures. On the basis of a theoretical calculation, Isenberg [17] had previously concluded that hydrogen dissolved in any known metallic lattice would be present in proton form.

In the light of these observations, the decrement discontinuities shown in Figure 6, at about $-70°$C, $\pm 10°$, might be interpreted according to the hypothetical scheme illustrated in Figure 11. The solid line shows the idealized experimental behavior of the Ta foil, while the dashed portion of the curve indicates a possible path that the system would like to have followed in the absence of any "freezing in" of the protons. The residual peak at about $-100°$C in the hydrogenated foil may be interpreted as an indication that a fraction of the proton impurity remains free, in true interstitial solution, and in equilibrium with the much larger proton fraction bound to fixed lattice positions, at this temperature. The absence of a $-100°$C maximum in the original material may simply be the result of a very low H concentration in the as-received Ta.

The gross hydrogen content of the foils after hydrogenation, as determined by the increment

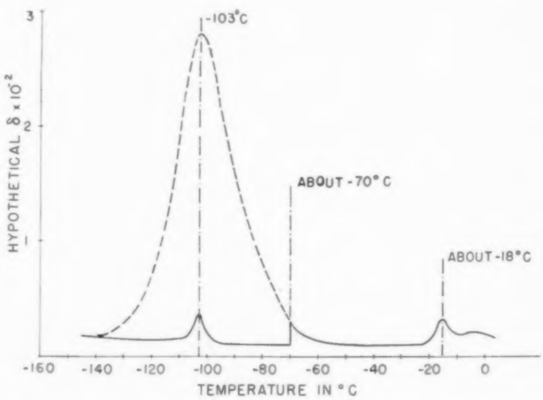

FIGURE 11. Speculative plot of low temperature Ta behavior. The solid line shows approximately what the system did, the dashed line represents a guess as to what the system might have done in the absence of the postulated "freezing in" of the hydrogen impurity.

in weight, was about 10 atomic per cent; the H content as received was probably less than 0.1 atomic per cent. The fact that such a large increase in H content increased the $-18°$C peak, in Figure 6, only slightly more than it increased the general background decrement appears to favor one of the following interpretations:

1. The $-18°$ peak is not related to the H impurity.

2. The peak is related to the H content, but is associated with the presence of H in particular lattice positions that are already almost saturated in the material originally supplied.

The pure speculation outlined in Figure 11 can be tested by measurements at still higher vibrational frequencies. Wert [18] has recently observed that a straight line relationship results when activation energies are plotted against the temperatures at which the decrement maxima are observed for a given measuring frequency. Assuming that H diffusion in Ta follows this pattern, and, further, that the assumptions involved in Figure 11 are correct, the molar Q for Ta-H diffusion can be

estimated to be about 6 kilocalories. Since the "absorption edge" at $-70°C$ may be presumed to be relatively independent of measuring frequency, decrement determinations at frequencies greater than 850 kilocycles should show the postulated H peak moved above the absorption edge on the temperature scale. Such high frequency measurements are being prepared at the present time in this laboratory.

The relatively high decrements observed below 200°C after room temperature deformation of the foils, as shown in Figure 10 for Ta, are both time and temperature dependent. The time dependence leads to very large point scatter unless a constant rate of temperature increase and a definite measurement routine are rigorously adhered to. Dislocation damping, migration of interstitials of the parent lattice, or reorientation of vacancy pairs are obvious possible mechanisms here, but the present data is too incomplete to make any further statement. This behavior is erased by vacuum anneals of less than an hour at 500°C, which is several hundred degrees less than the recrystallization temperatures, to use a rather ambiguous term, for Ta and Nb.

Acknowledgement

The writers are greatly indebted to Professor C. A. Wert, of the Department of Mining and Metallurgical Engineering, for numerous consultations and general cooperation throughout the course of the present investigation. Both Professor Wert and Mr. Choh Hi Ang, of the same department, very kindly made available much of their own torsion pendulum data on Ta and Nb for the purpose of correlation with the higher frequency measurements. Specimen materials were supplied through the courtesy of Dr. G. L. Wensch, now of the U.S.A.E.C., and the Fansteel Metallurgical Corporation. Professor J. S. Koehler, of the Physics Department, and Professor H. L. Walker, head of the Department of Mining and Metallurgical Engineering, assisted greatly in establishing the research facilities used in this work. This investigation was supported by the Office of Ordnance Research, Department of the Army.

References

1. Snoek, J. Physica, **6** (1939) 591; **8** (1941) 711; **9** (1942) 862.
2. Zener, C. Elasticity and Anelasticity of Metals (University of Chicago Press (1948).
3. Kê, T. S. Phys. Rev. **71** (1947) 533; **72** (1947) 41; **73** (1948) 267; **74** (1948) 9, 914.
4. Dijkstra, L. J. Philips Research Reports, **2** (1947) 102; J. Metals, Transactions, March (1949) 252.
5. Wert, C. A. J. Appl. Phys., **20** (1949) 943; **21** (1950) 1196.
6. Artman, R. A. J. Appl. Phys., **23** (1952) 475.
7. Harper, S. Phys. Rev., **81** (1951) 311.
8. Nowick, A. S. J. Appl. Phys., **22** (1951) 925, 1182.
9. Le Claire, A. D. Phil. Mag., **42** (1951) 673.
10. Ang, C. H. and Wert, C. A. To be published.
11. Wert, C. A. and Zener, C. Phys. Rev., **76** (1949) 1169.
12. Marx, J. Rev. Sci. Instr., **22** (1951) 503.
13. Marx, J. W. and Sivertsen, J. M. To be published in J. Appl. Phys.
14. Michener, J. W. and Handloser, J. Bulletin MDDC 1428, USAEC
15. Kelley, K. K. J. Chem. Phys., **8** (1940) 316.
16. Garstens, M. A. Phys. Rev., **81** (1951) 288.
17. Isenberg, I. Phys. Rev., **79** (1950) 736.
18. Wert, C. A. and Marx, J. W. Acta Met.
19. Wells, C., Batz, W., and Mehl, R. F. Trans. A.I.M.E., **188** (1950) 553.
20. Zener, C. In "Imperfections in Nearly Perfect Crystals" (New York, John Wiley and Sons, 1952), p. 296.

A "SUB-REGULAR" SOLUTION MODEL AND ITS APPLICATION TO SOME BINARY ALLOY SYSTEMS*

H. K. HARDY†

The thermodynamic properties have been examined for binary solutions whose excess free energy of solution is given by

$$\Delta F = A_1 x^2 y + A_2 x y^2 + RT (x \ln x + y \ln y)$$

where x and y are the atomic fractions; the model may be termed a "sub-regular" solution. The equations for the terminal solubility curves of elements with the same lattice structure can be arranged as

$$(x_1 + x_2) RT \ln x_1/x_2 + (y_1 + y_2) RT \ln y_1/y_2 = -(A_1 - A_2)(x_1 - x_2)^3$$

where the subscripts to x and y indicate the compositions in equilibrium. A straight line is obtained when the left-hand side is plotted against $(x_1 - x_2)^3$ as long as $(A_1 - A_2)$ is independent of temperature. The systems silver-copper, silver-platinum, aluminium-zinc and gold-platinum, and the high temperature part of the sodium chloride–potassium chloride solubility curve give nearly straight lines and approximate to sub-regular solutions.

The gold-iron, gold-cobalt and gold-nickel solubility curves show appreciable deviations from a straight-line plot. These systems together with potassium chloride–sodium chloride show a temperature dependence of A_1 and A_2 which introduces an entropy term of similar magnitude to the positional entropy.

UN MODÈLE D'UNE SOLUTION "SOUS-RÉGULIÈRE" ET SON APPLICATION À CERTAINS SYSTÈMES D'ALLIAGES BINAIRES

Un examen a été fait des propriétés thermodynamiques des solutions binaires, dont l'excès d'énergie libre de dissolution est donnée par

$$\Delta F = A_1 x^2 y + A_2 x y^2 + RT (x \ln x + y \ln y)$$

où x et y représentent les fractions atomiques; le modèle peut être appelé une solution "sous-régulière." Les équations des courbes extrêmes de solubilité, des éléments ayant la même structure réticulaire peuvent être écrites comme suit:

$$(x_1 + x_2) RT \ln x_1/x_2 + (y_1 + y_2) RT \ln y_1/y_2 = -(A_1 - A_2)(x_1 - x_2)^3$$

où les indices de x et y indiquent les compositions en équilibre. En traçant le diagramme de la partie de gauche de l'équation en fonction de $(x_1 - x_2)^3$ une droite est obtenue, pour autant, que $(A_1 - A_2)$ soit indépendant de la température. Les systèmes argent-cuivre, argent-platine, aluminium-zinc et or-platine, ainsi que la partie de la courbe de solubilité du système chlorure de sodium-chlorure de potassium correspondant aux températures élevées donnent approximativement des droites et se rapprochent de solutions sous-régulières.

Les courbes de solubilité des systèmes or-fer, or-cobalt et or-nickel montrent de fortes déviations du tracé droit. Dans ces systèmes, ainsi que dans le système chlorure de potassium-chlorure de sodium, A_1 et A_2 dépendent de la température, ce qui introduit un terme entropique d'une valeur semblable à l'entropie de position.

EIN MODELL EINER "SUBREGULÄREN" LÖSUNG UND SEINE ANWENDUNG AUF EINIGE BINÄRE LEGIERUNGSSYSTEME

Die thermodynamischen Eigenschaften von binären Legierungen, deren überschüssige freie Lösungsenergie durch

$$\Delta F = A_1 x^2 y + A_2 x y^2 + RT (x \ln x + y \ln y)$$

gegeben ist, wurden untersucht. Dabei sind x und y Atomprozente. Dieses Modell kann als "sub-reguläre" Lösung bezeichnet werden. Die Gleichungen für die Kurven der maximalen Löslichkeit von Elementen gleicher Gitterstruktur können wie folgt geschrieben werden:

$$(x_1 + x_2) RT \ln x_1/x_2 + (y_1 + y_2) RT \ln y_1/y_2 = -(A_1 - A_2)(x_1 - x_2)^3$$

wobei die Indices der x und y die Verbindungen im Gleichgewicht kennzeichnen. So lange $(A_1 - A_2)$ unabhängig von der Temperatur ist, erhält man eine Grade, wenn man die linke Seite der Gleichung gegen $(x_1 - x_2)^3$ aufträgt. Die Systeme Silber-Kupfer, Silber-Platin, Aluminium-Zink, Gold-Platin und, bei höheren Temperaturen, die Löslichkeitskurve von Natriumchlorid-Kaliumchlorid zeigen einen beinahe gradlinigen Zusammenhang und sind angenähert "sub-reguläre" Lösungen.

Die Löslichkeitskurven von Gold-Eisen, Gold-Kobalt und Gold-Nickel zeigen erhebliche Abweichungen von der Gradlinigkeit. Diese Systeme zeigen ebenso wie Kaliumchlorid-Natriumchlorid eine Temperaturabhängigkeit von A_1 und A_2. Dadurch wird ein Entropieterm eingeführt, der von der gleichen Grössenordnung wie die Entropie der Lage ist.

Introduction

With a few notable exceptions, the derivation and explanation of alloy phase diagrams from the basic properties of the atoms is still beset with considerable difficulties which yield only slowly to analysis. Similarly, there are often severe experimental restrictions on the thermodynamic measurements of

*Received December 7, 1952.
†Fulmer Research Institute, Stoke Poges, Bucks, England.

solid alloys. It is therefore of interest to examine the thermodynamic properties obtained by fitting the solubility data to semi-empirical expressions.

The regular solution hypothesis developed by Hildebrand [1; 2; 3] is now well established and has proved a simple means of describing the properties of many solutions. Refinements have included a new expression for the entropy of mixing in the strictly regular solution model of Fowler and Guggenheim [4]; whilst Scatchard [5; 6] and Hildebrand [3] have calculated the excess molar heat of solution in terms of the volume fractions and exchange interaction energy ($V = 2V_{XY} - (V_{XX} + V_{YY})$). In all regular solution treatments the exchange interaction energy is held independent of composition, although Guggenheim has generalised a temperature dependence [7]. Hildebrand's analysis contains the further assumption that $(V_{XY})^2 = V_{XX} \cdot V_{YY}$. Lumsden [8] has avoided a regular solution basis by using a van Laar type of equation in deriving the free energy relationships in a number of alloy systems.

Since the final equations for the free energy always contain a number of arbitrary constants, it was decided to avoid a detailed analysis but to investigate the properties of a simple regular solution model in which the exchange interaction energy was allowed to vary linearly with concentration, and in which a temperature dependence was not excluded. The results of testing this model against a number of binary solid solutions are also discussed.

Sub-Regular Solutions

The excess molar heat of solution of a binary solid solution is given by

$$(1)\quad \Delta H = \tfrac{1}{2}ZN(2V_{XY} - (V_{XX} + V_{YY}))\,xy = Axy,$$

where Z is the co-ordination number, N is Avogadro's number, V_{XY}, V_{XX}, and V_{YY} are the interaction energies, and x and y are the atomic fractions of the X and Y components.

The next most simple assumption is to make A a rectilinear function of composition so that

$$(2)\quad \Delta H = (A_1 x + A_2 y)xy = A_1 x^2y + A_2 xy^2$$

and the model may logically be termed "sub-regular." Equation (2) has been used in several instances [9; 10; 11] as a two-constant alternative to the van Laar expression for the activity/composition relation of organic solutions. Retaining the first two terms in Guggenheim's symmetrical expansion [12; 13],

$$\Delta H = xy \sum_{n=0,\ 1,\dots} B_n(x-y)^n = xy\,(B_0 + B_1(x-y))$$

produces the sub-regular solution.

The same expression results when terms are added to the regular solution equation to allow for a difference in the atomic sizes of mutually soluble metals and

$$\begin{aligned}\Delta H &= A\,xy + \sigma_X\,x^2y + \sigma_Y\,xy^2\\ &= x^2y\,(A + \sigma_X) + xy^2\,(A + \sigma_Y)\\ &= A_1\,x^2y + A_2\,xy^2.\end{aligned}$$

According to Lawson [14],

$$(3)\quad \sigma_X = \frac{4}{3}\frac{G_X}{V_X}(V_Y - V_X)^2, \sigma_Y = \frac{4}{3}\frac{G_Y}{V_Y}(V_Y - V_X)^2,$$

where G is the shear modulus and V the molar volume. Heumann [15] gives

$$(4)\quad \sigma_X = \frac{Tl_X\,V_X^0}{\psi_X\,V_X^T}(V_Y - V_X),$$

$$\sigma_Y = \frac{Tl_Y\,V_Y^0}{\psi_Y\,V_Y^T}(V_X - V_Y),$$

where l is the temperature coefficient of cubical expansion and ψ is the compressibility, V^0 and V^T are the molar volumes at absolute zero and the melting point, T is taken as the mean temperature of the melting points of the two metals. Both equations (3) and (4) give significant contributions to the heat of solution of solid alloys.

Even though equation (2) has been used previously,* many of the properties of a sub-regular solution have not been examined. The free energy per gm atom is given by

$$(5)\quad F = x\mu_X^0 + y\mu_Y^0 + A_1\,x^2y + A_2\,xy^2 + RT\,(x\ln x + y\ln y),$$

so that the chemical potentials are

$$(6)\quad \begin{aligned}\mu_X &= \mu_X^0 + RT\ln x + y^2\,(2A_1 - A_2) + y^3\,(2A_2 - 2A_1),\\ \mu_Y &= \mu_Y^0 + RT\ln y + x^2\,(2A_2 - A_1) + x^3\,(2A_1 - 2A_2).\end{aligned}$$

Differentiation gives

$$(7a)\quad \frac{\partial\mu_X}{\partial x} = \frac{RT}{x} + 2A_1\,y(1-3x) + 2A_2\,y\,(1-3y),$$

$$(7b)\quad \frac{\partial^2\mu_X}{\partial x^2} = \frac{-RT}{x^2} + 2A_1\,(6x-4) + 2A_2\,(5-6x),$$

$$(7c)\quad \frac{\partial\mu_Y}{\partial y} = \frac{RT}{y} + 2A_1\,x(1-3x) + 2A_2\,x(1-3y),$$

*See *Note Added in Proof*, p. 209.

(7d) $$\frac{\partial^2 \mu_Y}{\partial y^2} = \frac{-RT}{y^2} + 2A_1(5 - 6y) + 2A_2(6y - 4).$$

The spinodal curve is obtained by equating equations (7a) or (7c) to zero so that

(8) $$RT = 2x^2y(2A_1 - A_2) + 2xy^2(2A_2 - A_1).$$

Equations (7b) and (7d) are also zero at the critical point for phase separation, subtracting equation (7d) from (7b) and re-arranging gives

(9) $$RT\ (x - y) = 6x^2\ y^2\ (A_1 - A_2).$$

Solving between equations (8) and (9) gives A_1 and A_2 at the critical point and

(10) $$A_1 = \frac{RT_c}{6x_c^2\ y_c^2}\ (-9x_c^2 + 10x_c - 2)$$
$$A_2 = \frac{RT_c}{6x_c^2\ y_c^2}\ (-9y_c^2 + 10y_c - 2).$$

The values of A_1 and A_2 corresponding to different critical concentrations are shown in Figure 1. $A_1 = A_2 = 2RT_c$ when $x_c = 0.5$ and the equations reduce to these for a regular solution with a symmetrical solubility curve. The difference between A_1 and A_2

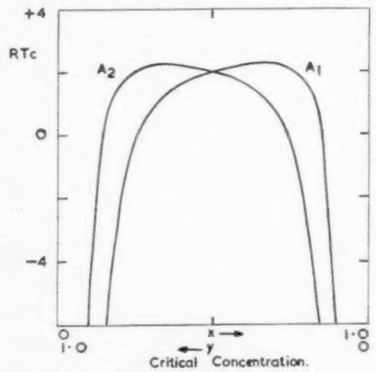

FIGURE 1. Values of A_1 and A_2 corresponding to different critical concentrations.

increases as x_c deviates from the equiatomic composition. A_1 is zero when $x_c = 0.26$ and 0.85. Solubility curves which are very strongly asymmetrical require both A_1 and A_2 to be negative.

The integral molar heats of solution are shown in Figures 2 and 3 for the values of A_1 and A_2 appropriate to different critical compositions (A_1 and A_2 independent of temperature); $x_c = 0.8$ requires that the curve shall contain both negative and positive values. It is of interest to note that Meijering [16] has proposed a curve of similar form for aluminium-copper alloys which was derived by calculation from the measured heats of formation and the solubility of copper in aluminium. A strongly negative curve is obtained when $x_c = 0.9$ and would probably be interrupted by ordering reactions. The right-hand side of Figure 3 is concave downwards. It is not clear how far the sub-regular solution model can be relied on when the critical composition

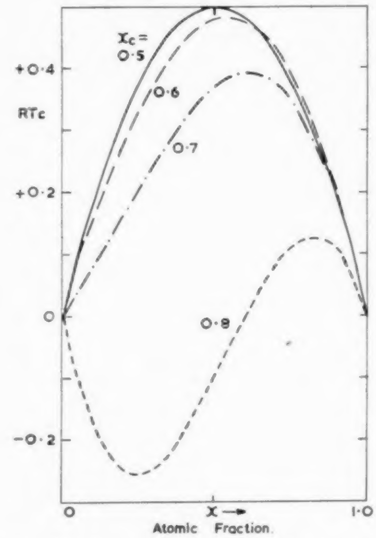

FIGURE 2. The integral molar heat of solution for A_1 and A_2 corresponding to the indicated values of x_c.

is rather distant from the equiatomic ratio as the numerical values of A_1 and A_2 become rather large.

If the same values of A_1 and A_2 apply at 0°K, the solubility will be zero at both sides of the diagram when x_c lies between 0.26 and 0.74. Some degree of

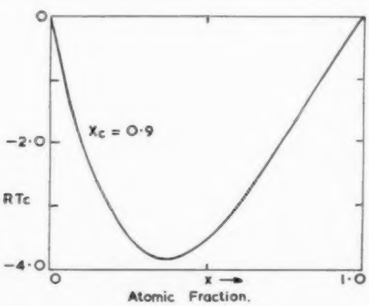

FIGURE 3. The integral molar heat of solution for A_1 and A_2 corresponding to $x_c = 0.9$.

solubility at one side of the diagram at all temperatures can be predicted when x_c lies outside this range (A_1 and A_2 held independent of temperature).

The activity/composition curves at T_c are given in Figure 4, and it will be noted that in dilute solutions the solvent always approximates to Raoult's Law whilst the solute obeys Henry's Law. When $x_c = 0.8$ the activity curves show both positive and negative deviations—a situation which is met in liquid aluminium-silver alloys [17] and in several other systems based on palladium [18].

The solid solubility boundaries are defined by the conditions

$$\mu_X(1) = \mu_X(2), \tag{11a}$$

$$\mu_Y(1) = \mu_Y(2), \tag{11b}$$

making the chemical potential of each component equal in the equilibrium co-existing phases. The values of A_1 and A_2 in equation (6) can thus be calculated from the solubility data at any temperature, since the terms in μ^0 cancel in equations (11),

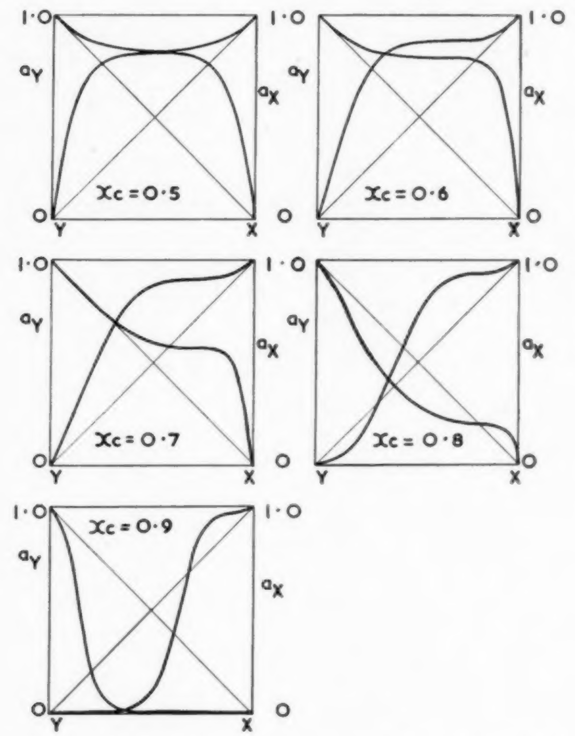

FIGURE 4. Activity/composition curves at the critical temperature for different critical compositions.

as long as the two terminal solid solutions have the same lattice structure. Only systems in which it is hypothetically possible to have unlimited solubility above a critical temperature (which may be above the melting point) are dealt with in the present work.

Subtracting equations (11a) and (11b), inserting the values from equations (6) and re-arranging leads to

$$\begin{aligned} RT \ln x_1/x_2 - RT \ln y_1/y_2 & \\ - A_1(x_1 - x_2)(3x_1 + 3x_2 - 2) & \\ + A_2(y_1 - y_2)(3y_1 + 3y_2 - 2) &= 0 \end{aligned} \tag{12}$$

where x_1, x_2, y_1, and y_2 are the atomic fractions at the solubility curves. This may be compared with the equation for the solubility curve of a regular solution which is

$$RT \ln x_1/x_2 - A(x_1 - x_2) = 0 \qquad y_1 = x_2. \tag{13}$$

Multiplying equation (11a) by $(x_1 + x_2)$ and equation (11b) by $(y_1 + y_2)$, adding and simplifying gives

$$\begin{aligned} \phi \equiv (x_1 + x_2)\, RT \ln x_1/x_2 & \\ + (y_1 + y_2)\, RT \ln y_1/y_2 & \\ = -(A_1 - A_2)\,(x_1 - x_2)^3 & \end{aligned} \tag{14}$$

in which both sides are zero for a regular solution. When the left-hand side is plotted against $(x_1 - x_2)^3$ a straight line passing through the origin at $T = T_c$ will be obtained as long as $A_1 - A_2$ is independent of temperature.

The interpretation of A_1 and A_2 is not limited to heats of solution but they can also be identified with a free energy of solution. They will then be temperature dependent, but this in no way influences the previous analysis which has, in effect, been carried out at constant temperature. The entropy and heat of solution must of course be obtained by differentiation of equation (5) and the latter is no longer given by equation (2).

Test of the Sub-Regular Solution Model

The sub-regular solution model has been tested for a number of binary metallic solutions by plotting the function ϕ against $-(x_1 - x_2)^3$. The solubility

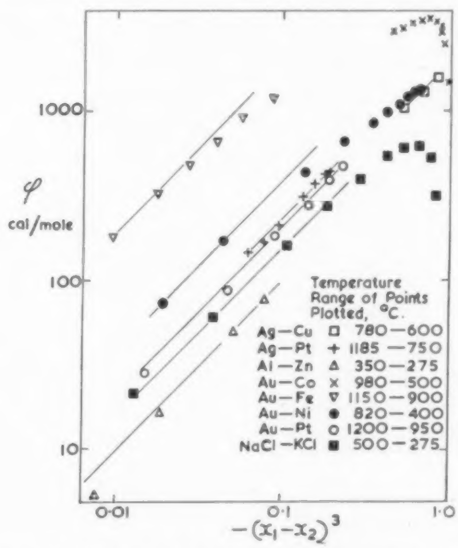

FIGURE 5. Values of the function ϕ plotted logarithmically against the logarithm of $-(x_1 - x_2)^3$.

data were read from the published curves, transformed to atomic percentages, plotted on a large scale and smooth curves drawn from which the values of x_1 and x_2 were obtained. The results are shown in Figure 5 where logarithmic plotting has been used

for both co-ordinates in order to cover a wide compositional range. Data which obey the sub-regular solution model should plot as a straight line with a 45° slope and the distance along the ordinate from the point ($\log \phi = 0$, $\log [-(x_1 - x_2)^3] = 0$) to the experimental line is the logarithm of $(A_1 - A_2)$. The numerical values of A_1 and A_2 were determined from equations (12) and (14).

Silver-Copper Alloys (*Solubility Data from Metals Handbook* [19])

It will be seen from Figure 5 that a straight line of unit slope can be drawn through the more reliable experimental points. Plotting on linear co-ordinates (Figure 6) allowed the straight line to be extrapolated through the origin. The points for the two

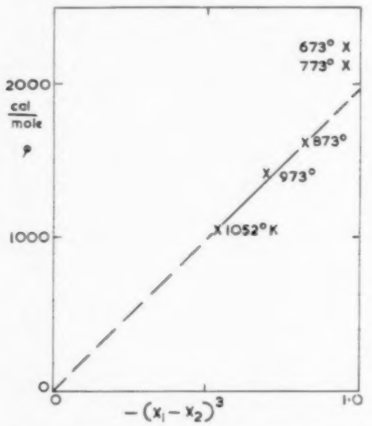

FIGURE 6. Values of the function ϕ plotted against $-(x_1 - x_2)^3$ for silver-copper solid solutions when x is the atomic fraction of copper.

lowest temperatures are rather distant from the straight line. As ϕ contains the ratio x_1/x_2 and y_1/y_2 it will vary rapidly at low solubilities and the experimental data may be slightly at fault.

The small temperature range did not allow the temperature dependence of A_1 and A_2 to be established. $A_1 = 6620$ cal/gm atom and $A_2 = 4640$ cal/gm atom, when x was the atomic fraction of copper. The critical composition would be at $x_c = 0.6$ with a maximum heat of solution of 1390 cal/gm atom. These values are in good agreement with those given by Scheil [20], using a method of graphical integration, of $x_c = 0.6$ and 1400 cal/gm atom.

Silver-Platinum Alloys (*Solubility Data from Hansen* [21])

An almost perfect straight-line fit was obtained when ϕ was plotted against $-(x_1 - x_2)^3$; see Figure 5, which could be extrapolated to pass through the origin of linear co-ordinates. The values obtained were $A_1 = 2940 + 1.35\ RT$ cal/gm atom and $A_2 = -300 + 1.7\ RT$ cal/gm atom, with x as the atomic fraction of platinum, showing only a small variation of $(A_1 - A_2)$ over the temperature range of the experimental solubility curves. The excess solution entropy of the alloys is less than in an ideal solution—for example the temperature dependence of A_1 and A_2 introduces an entropy of -0.8 cal/°C at the equiatomic composition. The heat of solution of the silver-rich alloys will be small or even negative.

Aluminium-Zinc Alloys (*Solubility Data from Raynor* [22])

Figures 5 and 7 show how the plot of ϕ against $-(x_1 - x_2)^3$ deviates only slightly from a straight line over the small temperature range investigated. The individual values of A_1 and A_2 are best given by $A_1 = 2700$ cal/gm atom and $A_2 = -240 + 1.73\ RT$ cal/gm atom, with x as the atomic fraction of

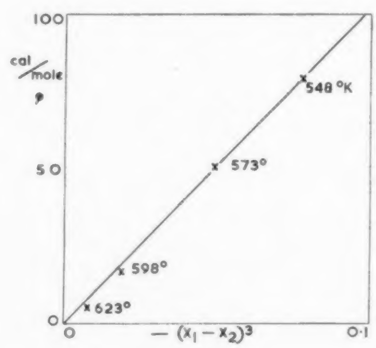

FIGURE 7. Values of the function ϕ plotted against $(x_1 - x_2)^3$ for the aluminium-zinc solid solution when x is the atomic fraction of aluminium.

aluminium. The heat of solution is small or even negative at the zinc-rich side, and there is a negative contribution to the entropy particularly in the zinc-rich alloys.

Gold-Platinum Alloys (*Solubility Data from Wictorin* [23])

Sub-regular solution behaviour is shown by the straight line in Figure 5. The solubility curve gave $A_1 = 6600$ cal/gm atom and $A_2 = 1320 + 1.17\ RT$ cal/gm atom, when x was the atomic fraction of platinum. $A_1 - A_2$ changes from 2430 to 1920 between 1200° and 950°C. There is a maximum contribution to the entropy of -0.35 cal/°C at $x = 0.33$.

TABLE I

VALUES OF THE APPARENT ENTROPY TERM IN CAL/DEGREE/GM ATOM GIVEN BY

$$\Delta S_{\text{app}} = -\frac{\partial \Delta F}{\partial T} = -x^2 y \frac{\partial A_1}{\partial T} - xy^2 \frac{\partial A_2}{\partial T}$$

System $y - x$	Temp °K	$\frac{\partial A_1}{\partial T}$	$\frac{\partial A_2}{\partial T}$	x_1	x_2	ΔS_{app} at x_1	ΔS_{app} at x_2	Positional entropy at x_1	Positional entropy at x_2
Au-Fe	1423	− 10	− 20	0.720	0.032	1.6	0.7	1.2	0.5
Au-Co	1253	− 2	− 14	0.209	0.982	1.9	0.04	1.0	0.2
Au-Ni	1113	− 11	− 18	0.717		2.6		1.2	
KCl-NaCl	773	− 4	− 6	0.66		1.0		1.3	

Gold-Iron Alloys (Solubility Data from Raub and Walter [24])

Gold-Cobalt Alloys (Solubility Data from Raub and Walter [24])

Gold-Nickel Alloys (Solubility Data from Metals Handbook [25])

The gold-iron and gold-nickel solubility data gave shallow curves when ϕ was plotted against $-(x_1 - x_2)^3$ whilst the gold-cobalt system pro-

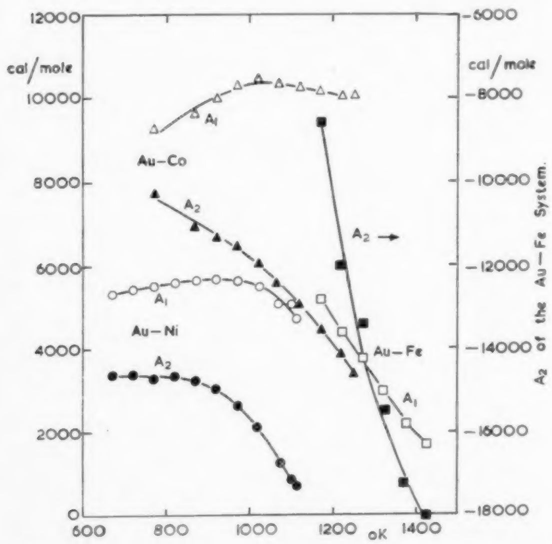

FIGURE 8. Values of A_1 and A_2 calculated from the solubility curves of gold-iron, gold-cobalt, and gold-nickel alloys when x is the atomic fraction of iron, cobalt, or nickel. The right-hand ordinate should be used for A_2 in the gold-iron system.

duced a very marked curvature (see Figure 5). The calculated values of A_1 and A_2 are shown in Figure 8 with x as the atomic fraction of the transition element. The A_1 values of the gold-cobalt and gold-nickel alloys pass through a maximum with increasing temperature, but their A_2 values decrease continuously. The strongly negative values of A_2 in the gold-iron system reflect the extremely asymmetrical nature of the solubility curve.

Assuming the sub-regular solution condition that A_1 and A_2 are independent of composition allows the apparent entropy to be calculated from the slope of the curves in Figure 8. At the highest temperatures this term is given by the values in Table I, from which it will be seen that the additional apparent entropy may be up to twice the positional entropy at the same composition. Averbach *et al.* [26] have reported that thermodynamic measurements gave the entropy of mixing of gold-nickel alloys as twice the positional entropy. They interpreted the result in terms of a specific heat change accompanying the filling of the 3d shells in nickel. The sub-regular solution model is unsuitable for such complex systems, but the results indicate that the free energy of solution and solubility curve are markedly affected by the manner in which the electronic state of the transition metal varies with temperature.

Potassium Chloride–Sodium Chloride System (Solubility Data from Scheil and Stadelmaier [27])

The solubility curve plotted as a straight line over the upper temperature range, but showed a very marked curvature at lower temperatures. The values of A_1 and A_2 are given in Figure 9, with x as the molecular fraction of sodium chloride and decrease with increasing temperature. The values are very similar at low temperatures when the solution is approximately regular. According to

Table I there is an apparent entropy at the critical temperature of approximately the same magnitude as the positional entropy.

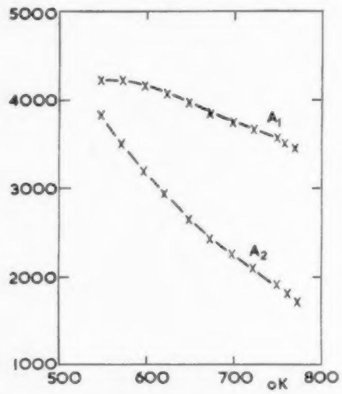

FIGURE 9. Values of A_1 and A_2 calculated from the solid solubility curve of NaCl-KCl when x is the molecular fraction of NaCl.

Cadmium-Zinc System (*Solubility Data from Hansen* [28])

The mutual solubilities at the eutectic temperature give $A_1 = 3800$ cal/gm atom and $A_2 = 4540$ cal/gm atom, when x is the atomic fraction of zinc. This is equivalent to a maximum integral molar heat of solution of 1040 cal at $x = 0.45$ compared with 960 cal calculated by Scheil [20].

Discussion of Results

The systems silver-copper, silver-platinum, aluminium-zinc, gold-platinum and the upper temperature part of the potassium chloride–sodium chloride behave approximately as sub-regular solutions because the difference between A_1 and A_2 changes only slightly over the temperature ranges investigated. The gold-iron, gold-cobalt, and gold-nickel systems show extraneous effects and cannot be held to be sub-regular solutions.

The values of A_1 and A_2 are either constant or increase with temperature in the systems silver-copper, silver-platinum, aluminium-zinc, and gold-platinum. An increase could be interpreted to mean that the difference in atomic sizes are effectively increased due to differences in the thermal coefficient of expansion so that the lattice strain energy becomes greater at higher temperatures. A_1 and A_2 tend to become more equal as the temperature is raised. This may be due simply to temperature effects, but in part probably results from the fact that the solutions in equilibrium are becoming closer in composition and consequently closer in lattice characteristics. The negative entropy term is surprising in view of the fact that terminal solid solutions, certainly of aluminium alloys, show evidence of a positive entropy term due to additional vibrational freedom [29; 30].

The values of A_1 and A_2 decrease at high temperatures in the systems gold-iron, gold-nickel, gold-cobalt, and potassium chloride–sodium chloride. This introduces a positive entropy of the same order as the positional entropy.

The phenomenological approach and the assumption in the model that the exchange interaction energy varies linearly with composition forbid a detailed discussion of the temperature dependence of A_1 and A_2. On the other hand a simple extension of the regular solution theory has enabled the asymmetrical solubility curves of several systems to be described by an equation containing only one arbitrary constant—namely $(A_1 - A_2)$.

Acknowledgements

The author's thanks are due to his colleagues at the Fulmer Research Institute for helpful conversations.

References

1. HILDEBRAND, J. H. Proc. Nat. Acad. Sci., **13** (1927) 267.
2. HILDEBRAND, J. H. J. Amer. Chem. Soc., **51** (1929) 66.
3. HILDEBRAND, J. H. and SCOTT, R. L. The Solubility of Non-Electrolytes, 3rd ed. (New York, Rheinhold, 1950).
4. FOWLER, R. and GUGGENHEIM, E. A. Statistical Mechanics (Cambridge University Press, 1949) p. 351.
5. SCATCHARD, G. Chem. Rev., **8** (1931) 321.
6. SCATCHARD, G. Trans. Faraday Soc., **33** (1937) 160.
7. GUGGENHEIM, E. A. Trans. Faraday Soc., **44** (1948) 1007.
8. LUMSDEN, J. Thermodynamics of Alloys (Inst. Metals Monograph and Report Series No. 11, 1952).
9. WOHL, K. Trans. Amer. Inst. Chem. Eng., **62** (1946) 215.
10. CARLSON, H. C. and COLBURN, A. P. Ind. Eng. Chem., **34** (1942) 581.
11. BENEDICT, M., JOHNSON, C. A., SOLOMON, E., and RUBIN, L. C. Trans. Amer. Inst. Chem. Eng., **41** (1945) 371.
12. GUGGENHEIM, E. A. Trans. Faraday Soc., **33** (1937) 151.
13. WAGNER, C. Thermodynamics of Alloys (Cambridge, Mass., Addison-Wesley, 1952), p. 48.
14. LAWSON, A. W. J. Chem. Phys., **15** (1947) 831.
15. HEUMANN, T. Z. Metallkunde, **42** (1951) 182.
16. MEIJERING, J. L. Rev. Met., **49** (1952) 906.
17. CHIPMAN, J. Discussions. Faraday Soc., **4** (1948) 23.
18. SCHMAHL, N. G. Z. anorg. allgem. Chemie, **266** (1951) 1.
19. SMITH, C. S. Metals Handbook (Cleveland, Amer. Soc. Metals, 1948), p. 1148.
20. SCHEIL, E. Z. Electrochem., **49** (1943) 242.

21. HANSEN, M. Der Aufbau der Zweistofflegierungen (Berlin, Springer, 1936), p. 49.
22. RAYNOR, G. V. Inst. Metals, Annoted Equilibrium Diagram Series, No. 1.
23. WICTORIN, C. G. Studies in Gold Platinum Alloys (Stockholm, Halggstroms, 1947).
24. RAUB, E. and WALTER, P. Z. Metallkunde, **41** (1950) 234.
25. CARAPELLA, L. A. Metals Handbook (Cleveland, Amer. Soc. Metals, 1948), p. 1172.
26. AVERBACH, B. L., COHEN, M., FLINN, P. A., UNDERWOOD, E. E., FLANAGAN, W. E., RUDMAN, P. S., HILLIARD, J. U.S. Atomic En. Comm. Publ. (1951), NYO-581.
27. SCHEIL, E. and STADELMEIER, H. Z. Metallkunde, **43** (1952) 227.
28. HANSEN, M. Z. Metallkunde, **43** (1952) 462.
29. MEIJERING, J. L. Philips Res. Rep., **3** (1948) 281.
30. ZENER, C. Thermodynamics in Physical Metallurgy (Cleveland, Amer. Soc. Metals, 1950), p. 16.
31. ZAWIDZKI, J. VON. Z. phys. Chem., **69** (1909) 630.
32. MARGULES, M. S. B. Wien Akad. (2), **104** (1895) 1243.
33. MUSIL, A. Ost. ChemZtg, **42** (1939) 371, 395; **44** (1941) 125.

Note Added in Proof*

Zawidzki [31] examined the vapour pressure (activity) curves resulting from different values of the first two terms in the Margules expansion which becomes [32]

$$\mu_X - \mu_X^0 = RT \ln x + \tfrac{1}{2}\alpha_2\, y^2 + \tfrac{1}{3}\alpha_3\, y^3\,, \qquad (15)$$
$$\mu_Y - \mu_Y^0 = RT \ln y + \tfrac{1}{2}\beta_2\, x^2 + \tfrac{1}{3}\beta_3\, x^3\,.$$

Comparison with equation (6) shows that

$$\tfrac{1}{2}\alpha_2 = 2A_1 - A_2, \quad \tfrac{1}{2}\beta_2 = 2A_2 - A_1\,, \qquad (16)$$
$$\tfrac{1}{3}\alpha_3 = -\,\tfrac{1}{3}\beta_3 = 2A_2 - 2A_1$$

so that Zawidzki's results are identical with the sub-regular solution model (see also Musil [33]).

Zawidzki also showed that equations (15) lead to

$$f_X^* = \exp\,[\tfrac{1}{2}\alpha_2 + \tfrac{1}{3}\alpha_3]/RT = \exp A_2/RT \quad \text{for } y \to 1,\ x \to 0 \qquad (17)$$
$$f_Y^* = \exp\,[\tfrac{1}{2}\beta_2 + \tfrac{1}{3}\beta_3]/RT = \exp A_1/RT \quad \text{for } x \to 1,\ y \to 0$$

for the activity coefficients at infinite dilution. Hence A_1 and A_2 can be obtained by extrapolating the tangent to the activity composition curves for the infinitely dilute solution to allow f_X^* and f_Y^* to be assessed.

*February 27, 1953.

VOL. 1 1953

THE PHASE DIAGRAM SECTION A-BC (ORDERED COMPOUND)*

H. K. HARDY†

Solutions between the A apex of the compositional triangle and a BC ordered compound have been investigated, from the statistical mechanics point of view, for comparison with the phase section from pure iron to NiAl in which a miscibility gap separates a disordered iron-rich from an ordered NiAl-rich phase. The "zeroth" approximation was used with allowance for next nearest neighbour interactions. It was predicted that the critical temperature for ordering (second order transformation) and the locus of equal equilibrium values of the long range order parameter fell linearly with additions of the A atoms. The critical temperature and composition for phase separation depend on the ratio of the BC exchange interaction energies for first and second neighbours as well as on the exchange interaction energies of the atom pairs AB and AC. Suitable values caused phase separation to occur at higher temperatures in the ordered solution than in the disordered. The theory accounts for the general properties of the iron-NiAl phase section.

LA SECTION A-BC D'UN DIAGRAMME DES PHASES (COMPOSÉ ORDONNÉ)

Il a été fait usage de la mécanique statistique dans l'étude des solutions se trouvant entre le sommet A du triangle de composition et le composé ordonné BC, en vue d'une comparaison avec la section s'étendant du fer pur jusqu'à NiAl dans laquelle une lacune de solubilité sépare la phase désordonnée, riche en fer, de la phase, ordonée, riche en NiAl. La méthode de l'approximation d'ordre zéro a été employée en tenant compte des interactions provenant des deuxièmes voisins. Il a été prédit, que la température critique de la mise en ordre (transformation de second ordre) et le lieu des valeurs des équilibres égaux du paramètre d'ordre à grande distance décroissent linéairement avec l'addition des atomes dy type A. La température et la composition critiques de la séparation des phases dépendent du rapport des énergies d'interaction d'échange des premiers et deuxièmes voisins, aussi bien que des énergies d'interaction d'échange des paires d'atomes AB et AC. Des valeurs convenables causaient la séparation des phases dans la solution ordonnée à des températures plus élevées que dans la solution désordonnée. La théorie explique les propriétés générales de la phase fer-NiAl.

DAS PHASEN-DIAGRAMM DES BEREICHES A-BC (GEORDNETE VERBINDUNG)

Es wurde die statistische Mechanik fester Lösungen zwischen dem A-Scheitel des Phasendreiecks und einer BC-geordneten Verbindung untersucht, um einen Vergleich mit dem Phasenbereich zwischen dem reinen Eisen und NiAl, wo eine Mischungslücke die ungeordnete eisenreiche Legierung von der geordneten NiAl reichen Phase trennt, zu ermöglichen. Es wurde die Methode der "nullten" Annäherung benutzt, wobei die Wechselwirkung der zweitnächsten Nachbarn in Rechnung gestellt wurde. Es wurde vorausgesagt, dass sowohl die kritische Temperatur für das Ordnen der Legierung als auch die Lage identischer Gleichgewichtswerte der Fernordnungsparameter linear mit steigendem Gehalt an A-Atomen abnehmen würde. Die kritische Temperatur und die Zusammensetzung bei der Phasentrennung hängt von dem Verhältnis der BC Austauschenergien für die nächsten und zweitnächsten Nachbarn sowie auch von den Austauschenergien der Atompaare AB und AC ab. Geeignete Werte führen in ungeordneten Legierungen Phasentrennung bei höheren Temperaturen herbei als in geordneten Lösungen. Das entwickelte Modell zeigte die allgemeinen Eigenschaften des Bereiches im Eisen-NiAl Phasendiagramm.

Introduction

The iron-nickel-aluminium phase diagram has been reported by Bradley [1] and, as shown in Figure 1, a miscibility gap separates a disordered (iron-rich) from an ordered (NiAl-rich) phase. Both phases are body centred cubic and the phase boundary is of the normal form for a miscibility gap except that, in certain sections, it extends as a funnel to higher temperatures. The tie lines run approximately parallel to the direction from the iron apex to NiAl although their directions twist slightly as the temperature is changed. The surplus iron atoms are randomly placed on the NiAl lattice which has a CsCl structure.

The object of the present work is to determine whether a simple statistical mechanical treatment will serve to account for the phase diagram section from iron to NiAl. The statistical mechanics of order-disorder reactions in binary alloys have been extensively studied and excellent reviews are given by Fowler and Guggenheim [2] and Nix and Shockley [3]. No theoretical work appears to have been carried out on the effect of ternary elements on binary order-disorder reactions or on a calculation of ternary phase diagrams in the presence of ordering. Hultgren and Tarnopol [4] limited their theoretical work to the effect of silver on the critical temperature of AuCu. Meijering [5; 6] has made a very thorough analysis of the thermodynamic properties and phase diagrams of ternary regular alloys in the absence of long range order.

The Free Energy Equation

The Bragg and Williams model [7; 8] of nearest neighbour interactions has been extended to include next nearest neighbours, but otherwise the nearest

*Received December 8, 1952.
†Fulmer Research Institute, Stoke Poges, Bucks, England.

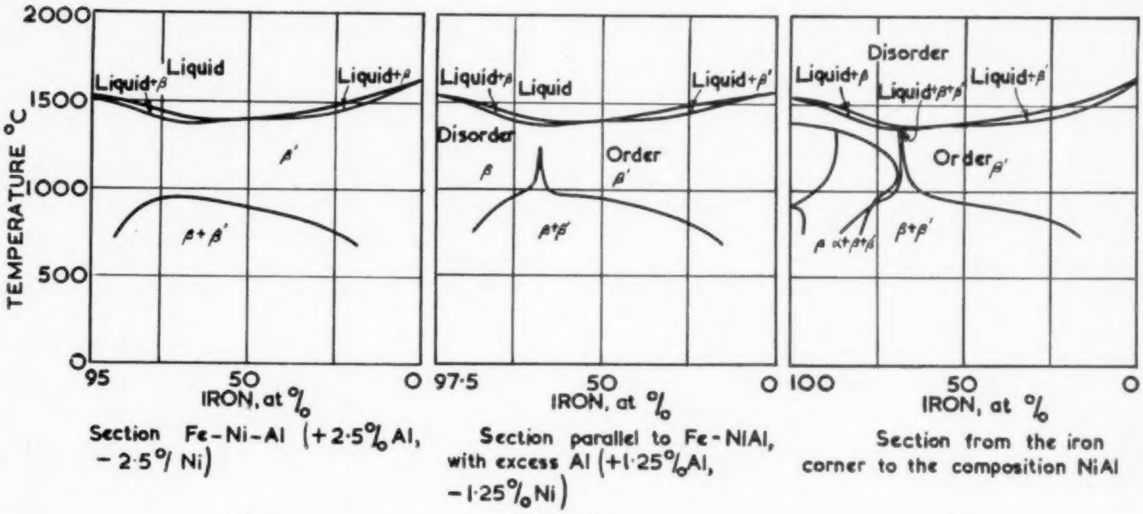

(a) (b) (c)

FIGURE 1. Sections from Fe-Ni-Al diagrams after Bradley [1] (courtesy Iron and Steel Institute).

VOL. 1 1953

neighbour assumptions of Bethe [9] have been accepted. No allowance has been made for short range order so the model is essentially the "zeroth" approximation of Fowler and Guggenheim [2] and has been adopted because of its great simplicity. The "zeroth" approximation and pair-wise counting give qualitative results for the BC order-disorder reaction at the equiatomic concentration, but is generally held to be less accurate at other compositions and is quite unsuitable for close-packed lattices. The consequent limitation to body-centred cubic lattices is not serious since comparison is to be made with iron-NiAl alloys. Qualitative agreement cannot be expected for ternary sections of all compositions, but can probably be anticipated for certain types of compositional sections such as A-BC and AB-BC.

The body-centred cubic lattice can be made up from two interpenetrating sublattices such that the nearest neighbours of a given site all belong to the other sublattice and the next nearest neighbours all belong to the same sublattice. Thus there are $\frac{1}{2}Z'N$ pairs of nearest neighbours on the two sublattices and $\frac{1}{4}Z''N$ pairs of next nearest neighbours within each sublattice where Z' and Z'' are the co-ordination numbers for the nearest and next nearest neighbours of any site. A very similar model has been used by Matsuda [10] in order to compare the relative stability of the AB and AB_3 types of super-lattice.

Consider an alloy on N lattice sites consisting of xN A atoms, yN B atoms, and zN C atoms. Let the correctly ordered B atoms occupy the I-sublattice and the correctly ordered C atoms occupy the II-sublattice. The following equations describe the distribution of the atoms over the lattice sites:

$$(1) \quad \begin{array}{lll} r_I = y + yS_B & w_I(C) = z - yS_B & w_I(A) = x \\ r_{II} = z + yS_B & w_{II}(B) = y - yS_B & w_{II}(A) = x \end{array}$$

in which r_I and r_{II} are the fractions of the I- and II-sites correctly occupied by the B and C atoms respectively; $w_I(C)$ and $w_I(A)$ are the fractions of the I-sites wrongly occupied by C and A atoms respectively; $w_{II}(B)$ and $w_{II}(A)$ are the fractions of the II-sites wrongly occupied by the B and A atoms respectively. S_B defines the degree of long range order and corresponds to the fraction of wrongly ordered B atoms transferred to correct positions.* Equation (1) holds over the (x, y, z) compositional range $(1, 0, 0)$, $(0, 0, 1)$, $(0, \frac{1}{2}, \frac{1}{2})$ for all values of S_B within $0 \leqslant S_B \leqslant 1$ so that full order corresponds to $S_B = 1$.

The configurational entropy for the "zeroth" approximation is given by

$$(2) \qquad k \ln g(N) = -\tfrac{1}{2}Nk \sum_{i=I,\,II} \theta_i \ln \theta_i$$

($\theta = r_i$ or w_i for each species of atom). The number of bonds (pairs of neighbours) is obtained directly from equations (1), and are given in Table I in which the subscript has been dropped from S_B. Let V_{AA}', V_{AA}'' etc. be the interaction energies between pairs of nearest and next nearest atoms. The total interaction energy can then be

*See Appendix.

summed over the pairs listed in Table I and simplified by introducing the exchange interaction energy terms in Table II.

TABLE I

NEAREST NEIGHBOURS

Type of pair	Number of such pairs
$B_I \ B_{II}$	$Z'N\,y^2\,(1 - S^2)/2$
$C_I \ C_{II}$	$Z'N\,(z^2 - y^2 S^2)/2$
$A_I \ A_{II}$	$Z'N\,x^2/2$
$B_I \ C_{II}$	$Z'N\,(y + yS)\,(z + yS)/2$
$C_I \ B_{II}$	$Z'N\,(z - yS)\,(y - yS)/2$
$A_I \ C_{II}$	$Z'N\,x(z + yS)/2$
$C_I \ A_{II}$	$Z'N\,x(z - yS)/2$
$B_I \ A_{II}$	$Z'N\,x(y + yS)/2$
$A_I \ B_{II}$	$Z'N\,x(y - yS)/2$

NEXT NEAREST NEIGHBOURS

Type of pair	Number of such pairs
$B_I \ B_I$	$Z''N\,y^2(1 + S)^2/4$
$C_I \ C_I$	$Z''N\,(z - yS)^2/4$
$A_I \ A_I$	$Z''N\,x^2/4$
$B_I \ C_I$	$Z''N\,2(y + yS)(z - yS)/4$
$A_I \ C_I$	$Z''N\,2x(z - yS)/4$
$A_I \ B_I$	$Z''N\,2x(y + yS)/4$
$B_{II} \ B_{II}$	$Z''N\,y^2(1 - S)^2/4$
$C_{II} \ C_{II}$	$Z''N(z + yS)^2/4$
$A_{II} \ A_{II}$	$Z''N\,x^2/4$
$B_{II} \ C_{II}$	$Z''N2(y - yS)(z + yS)/4$
$A_{II} \ C_{II}$	$Z''N2x(z + yS)/4$
$A_{II} \ B_{II}$	$Z''N2x(y - yS)/4$

TABLE II

EXCHANGE INTERACTION ENERGY TERMS

$$V_1' = 2\,V_{AB}' - (V_{AA}' + V_{BB}'),\quad Z'NV_1'/2 = W_1'$$
$$V_2' = 2\,V_{BC}' - (V_{BB}' + V_{CC}'),\quad Z'NV_2'/2 = W_2'$$
$$V_3' = 2\,V_{CA}' - (V_{CC}' + V_{AA}'),\quad Z'NV_3'/2 = W_3'$$
$$V_1'' = 2\,V_{AB}'' - (V_{AA}'' + V_{BB}''),\quad Z''NV_1''/2 = W_1''$$
$$V_2'' = 2\,V_{BC}'' - (V_{BB}'' + V_{CC}''),\quad Z''NV_2''/2 = W_2''$$
$$V_3'' = 2\,V_{CA}'' - (V_{CC}'' + V_{AA}''),\quad Z''NV_3''/2 = W_3''$$

The configurational free energy is given by

$$\begin{aligned}(3)\quad F = {} & \tfrac{1}{2}Z'N(V_{AA}'x + V_{BB}'y + V_{CC}'z) \\ & + \tfrac{1}{2}Z''N(V_{AA}''x + V_{BB}''y + C_{CC}''z) \\ & + (W_2'y(z + yS^2) + W_1'xy + W_3'xz) \\ & + (W_2''y(z - yS^2) + W_1''xy + W_3''xz) \\ & + \tfrac{1}{2}RT[y(1 + S)\ln y(1 + S) \\ & + y(1 - S)\ln y(1 - S) + (z + yS)\ln(z + yS) \\ & + (z - yS)\ln(z - yS) + 2x\ln x].\end{aligned}$$

The calculation of the thermodynamic properties from the A apex of the compositional triangle to the BC compound is based on the assumption that the tie lines accurately follow this direction at all temperatures. This can only occur if the interaction energy parameters for the AB and AC binary systems are equal, so that

$$(4)\qquad W_1 = W_1' + W_1'' = W_3' + W_3'' = W_3\,.$$

Let $W_2' + W_2'' = W_2$ and $W_2'' = \pi W_2'$, then

$$(5)\quad W_2' - W_2'' = W_2'(1 - \pi) = W_2\frac{(1 - \pi)}{1 + \pi} = W_2\rho.$$

The configurational excess free energy of solution along the section of interest is given by

$$\begin{aligned}(6)\ \Delta F = {} & W_2 y^2(1 + \rho S^2) + 2W_1xy \\ & + RT[y(1 + S)\ln y(1 + S) \\ & + y(1 - S)\ln y(1 - S) + x\ln x]\end{aligned}$$

when $y = z = (1 - x)/2$.

The Critical Temperature for Ordering

Minimizing equation (6) with respect to S leads to

$$(7)\ - W_2(1 - x)\rho\bar{S} = RT\ln\frac{1 + \bar{S}}{1 - \bar{S}},\qquad \frac{\partial\Delta F}{\partial S} = 0,$$

where $\bar{S}$ signifies an equilibrium value of S. Since $W_2\rho = -2RT_0$ where T_0 is the critical temperature

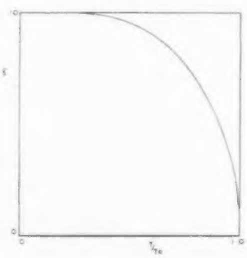

FIGURE 2. Equilibrium values of S plotted against T/T_0 from equation (8) for the binary BC compound ($x = 0$).

for ordering of the binary BC compound equation (7) can be solved as [7; 8]

$$(8)\qquad \bar{S} = \tanh\left[\frac{(1 - x)\bar{S}}{T/T_0}\right].$$

Equations (7) and (8) show that the transformation occurs by a "lambda" or second order type [11] of reaction at all concentrations. When $x = 0$ the variation of $\bar{S}$ with temperature is that found by Bragg and Williams, and is shown in Figure 2. The critical temperature for ordering and the temperature corresponding to any given value of $\bar{S}$ fall linearly with composition (see Figure 3).

The BC type of ordering is only possible as long as $(W_2' - W_2'')$ is negative, so that if W_2' be negative, π (equation (5)) must be less than $+1.0$. The

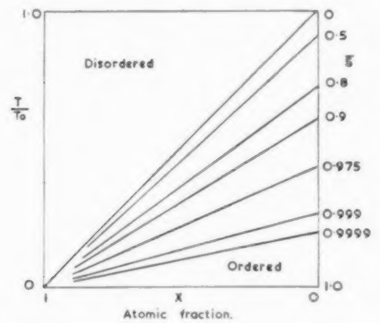

FIGURE 3. The variation of the critical temperature for ordering ($\bar{S} = 0$) with composition together with lines for equal $\bar{S}$ values.

stability of the ordered structure is increased when π is negative (W_2'' positive). The variation of the critical ordering temperature of the binary BC alloy with different ratios of W_2''/W_2' is shown in Figure 7 for the case when $W_2' = \text{const} = -2RT_0°$ and $T_0°$ is the critical temperature for ordering when $W_2'' = 0$. (See *Note Added in Proof*, p. 217.)

Temperature and Compositional Dependence of the Internal Energy, Configurational Entropy, and Activity

The values of $\bar{S}$ for different temperatures and compositions have been taken from equations (8) (Figure 3) and used to calculate the internal energy $W_2\,y^2\,(1 + \rho\bar{S}^2)$. The results are shown in Figure 4

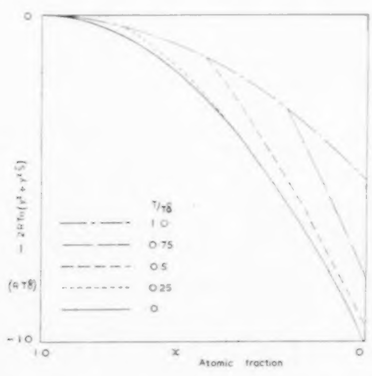

FIGURE 4. Internal energy plotted against composition using $\bar{S}$ values appropriate to different ratios of $T/T_0°$ with $W_2' = -2RT_0°$ and $W_2'' = 0$ ($\pi = 0$, $\rho = 1$), $W_1 = W_3 = 0$.

for $\rho = 1$ ($W_2'' = 0$) and $W_1 = W_3 = 0$. All the curves are concave to the compositional axis with a distinct change of slope on passing from the disordered to the partly ordered region.

The corresponding values for the configurational

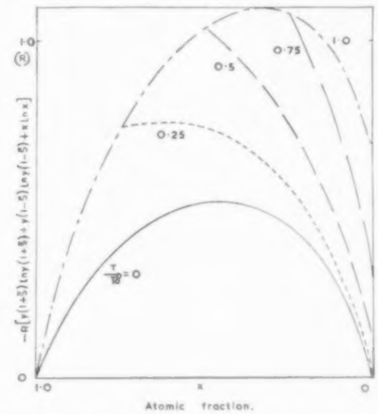

FIGURE 5. Configurational entropy, $-R[y(1+\bar{S})\ln y(1+\bar{S}) + y(1-\bar{S})\ln y(1-\bar{S}) + x\ln x]$, plotted against concentration using S values appropriate to different ratios of $T/T_0°$ with $W_2' = -2RT_0°$ and $W_2'' = 0$ ($\pi = 0$, $\rho = 1$), $W_1 = W_3 = 0$.

entropy are plotted in Figure 5 and also show a very rapid change of direction at the ordering composition.

The chemical potential has been obtained from equation (6) and

$$
\begin{aligned}
&\bar{\mu}_A = -W_2\,y^2(1+\rho\bar{S}^2) + 4W_1\,y^2 + RT\ln x,\\
(9)\qquad &\bar{\mu}_B = \bar{\mu}_C = W_2(xy + y^2(1-\rho\bar{S}^2)) + W_1\,x^2\\
&\qquad + \tfrac{1}{2}RT(\ln y(1+S) + \ln y(1-S)),\\
&\qquad S = \bar{S},\ y = z.
\end{aligned}
$$

As would be expected $\bar{\mu}_A$ is increased and $\bar{\mu}_B$ decreased by the ordering of the B and C atoms.

The Binodal and Spinodal Curves

The equation of the binodal [12] or solubility curve is obtained by equating the chemical potential of each component separately in the two phases but it proves very difficult to calculate a unique solution. In the absence of long range order this reduces to the pseudo-binary equation given by Meijering [6],

$$
(10)\qquad \frac{1}{1-2x}\ln\frac{1-x}{x} = -\frac{(W_2 - 4W_1)}{4RT}
$$

and the phase boundary is symmetrical.

The condition for the critical temperature and composition of phase separation, namely $\partial^2\bar{\mu}_A/\partial x^2 = 0$, cannot easily be solved and it is necessary to argue the behaviour of the binodal curve from the calculated spinodal curve.

The spinodal curve [12], that is the locus of points relating the temperature and composition at which $\partial\mu_A/\partial x = 0$, is given by

$$(11)\quad \frac{W_2(1-x)}{2}(1+\rho\bar{S}^2) - 2W_1(1-x) + \frac{RT}{x} - \frac{(W_2\rho)^2(1-x)^2\bar{S}^2(1-\bar{S}^2)}{2(2RT + W_2\rho(1-x)(1-\bar{S}^2))} = 0$$

in which

$$(12)\quad \frac{\partial\bar{S}}{\partial x} = \frac{W_2\rho\bar{S}(1-\bar{S}^2)}{2RT + W_2\rho(1-x)(1-\bar{S}^2)}$$

has been derived from equation (7) or (8).

Equation (12) can be simplified with aid of equation (7), and

$$(13)\quad \frac{T}{T_0} = \frac{\eta(A+4\sigma+B) - \eta^2}{A+4\sigma+B}$$

where

$$\eta = \frac{2\bar{S}}{\ln\dfrac{1+\bar{S}}{\bar{S}}},$$

so that

$$x = 1 - \frac{RT}{RT_0\eta}$$

and

$$(14)\quad A = \frac{1+\rho\bar{S}^2}{\rho}, \qquad B = \frac{\bar{S}^2(1-\bar{S}^2)}{\eta-(1-\bar{S}^2)}$$

$$W_1 = 2RT_0\sigma, \qquad W_2 = -2RT_0/\rho$$

when T_0 is the critical ordering temperature of the binary BC alloy.

Equation (13) has been solved for chosen values of $\bar{S}$, ρ and σ and the curves obtained are shown in Figure 6. The spinodal curves lie below the critical temperature for ordering (i.e., within the partially ordered region) and are markedly asymmetrical. In the absence of long range order, equation (11) can be re-arranged as

$$(15)\quad \frac{T}{T_0} = x(1-x)\left(\frac{1}{\rho} + 4\sigma\right)$$

and produces the normal symmetrical spinodal curve corresponding to the binodal curve of (10).

As shown by Figure 6, the ratio of the critical temperature for phase separation (the highest temperature of the spinodal curve) to the binary ordering temperature is lowered and the critical composition changes towards the A apex of the ternary triangle as π changes from positive to negative (W_2'' becoming more positive). Negative values of σ (W_1 and W_3) lower the critical temperature ratio and also shift the critical composition in the A-rich direction.

Figure 7 gives the critical temperature for phase separation as a function of the value of π. The results are expressed as the ratios of the critical tempera-

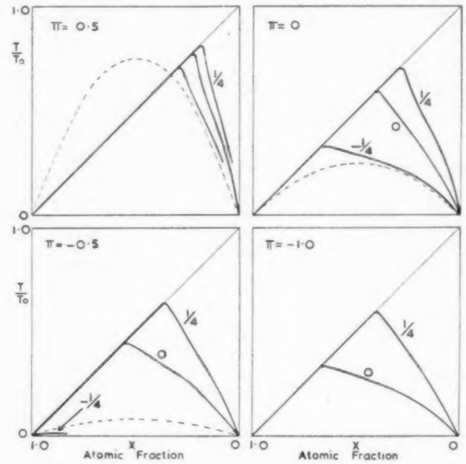

FIGURE 6. Spinodal curves for $\sigma = \frac{1}{4}$, 0, $-\frac{1}{4}$, and $\pi = 0.5$, 0, -0.5, -1.0. The symmetrical dotted curves apply for $\sigma = 0$ in the absence of long range order. T_0 is the critical temperature for ordering of the binary alloy in each case.

tures for phase separation to the ordering temperature ($T_0°$) of the binary alloy when $W_2'' = 0$, and the diagram has been drawn with a constant value of $W_2' = -2RT_0°$. The critical temperature of

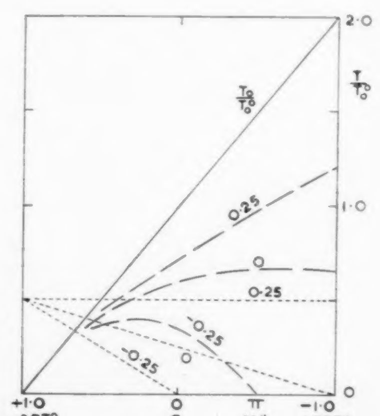

FIGURE 7. The variation with π for a constant value of W_2' of (i) the critical temperature for ordering of the binary BC alloy given by the line $T_0/T_0°$ and (ii) the critical temperature for the phase separation of the ternary ordered (dashed) and disordered (dotted) alloys for different values of σ ($W_2' = -2RT_0°$, $W_1 = 2RT_0\sigma$).

phase separation passes through a peak which is a function of the value of W_1 and W_3 (σ). When $W_2'' \to W_2'$ ($\pi \to 1.0$), phase separation occurs within the random solution at a higher temperature

than the ordering reaction. For values of π less than 0.5, the ordering reaction accentuates the tendency to form a miscibility gap as phase separation occurs at a higher temperature than in the absence of ordering. (See *Note Added in Proof*, p. 217.)

Variable Energy Parameters

The interaction energy parameters W_2 and W_1 have been held constant and independent of temperature, composition, and degree of order. W_1 will now be replaced by W_1 $(1 + cyS^2)$ to allow for the possibility of a difference in the exchange interaction energy of the AB and AC atoms in the ordered and disordered states.

Equation (8), with $W_1 = 2RT_0\,\sigma$ becomes

$$\bar{S} = \tanh\left[\frac{(1-x)\bar{S}}{T/T_0} - \frac{2\sigma c(1-x)x\bar{S}}{T/T_0}\right]. \tag{16}$$

The second term on the right-hand side does not affect the type of transformation and has been chosen so that it is zero when $\sigma = 0$, $c = 0$, $x = 1$, and $x = 0$. The critical temperature for ordering falls linearly with composition as long as $\sigma c = 0$, but Figure 8 shows how positive and negative values introduce curvilinear relations. The curves

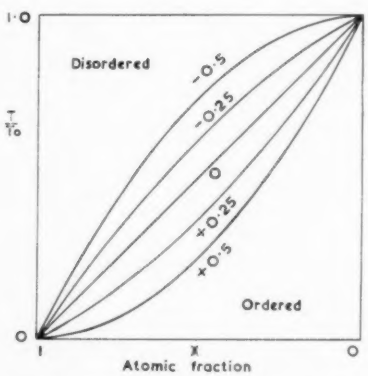

FIGURE 8. The variation of the critical temperature for ordering ($S = 0$) with composition for the values of $(c\sigma)$ indicated on the curves.

for a negative value of σc, corresponding to a less positive exchange interaction energy in the ordered than in the disordered state, have a reasonable form. The curves for a positive value of σc are not so satisfactory. There seems no reason why the critical temperature should not reach 0°K at compositions other than $x = 1$ when the exchange interaction energy is more positive in the ordered than in the disordered state.

It is to be expected that the loci of equal values of $\bar{S}$ and the shapes of the spinodal curves will reflect the form of the curves in Figure 8 when σc is not zero. The exact solutions would be complicated and, in view of the doubtful reliability of the model, they have not been worked out.

Comparison with the Iron-NiAl System

Figure 1 shows that the critical temperature for phase separation occurs at about 1000°C, and at 70–75 per cent iron. According to Figure 6, the critical composition would be matched when W_2'' is between zero and -0.5 times W_2' and W_1 between $-1/8$ and $-3/8$ of $-(W_2' - W_2'')$, so that W_2' and W_1 are negative but W_2'' positive.

A narrow two-phase region is to be expected between the ordered and disordered solutions at compositions away from $y = z$ and at temperatures above that for phase separation. Although the boundaries would have a slight curvature this two-phase region would be directed towards $T/T_0 = 1$ at $x = 0$. However, Figures 1(b) and 1(c) indicate that the two-phase funnel extends almost vertically. It is clear from Figure 8 that negative values of σc (more negative exchange interaction energies between the A-B and A-C atoms in the ordered state) would rotate the two-phase funnel towards the vertical plane.

In view of the approximations involved in the theoretical model the qualitative agreement with the experimental phase diagram is quite satisfactory. Bradley's diagram and the theoretical approach suggest that a two-phase funnel should be sought in the section of the ternary copper-nickel-aluminium from $\beta - Cu_3Al$ (disordered) to NiAl [13].

Acknowledgements

The author's thanks are due to his colleagues at the Fulmer Research Institute for helpful conversations.

APPENDIX I

The Physical Significance of the Bragg and Williams Long Range Order Parameter

Bragg and Williams [7; 8] defined their long range order parameter in terms of the probability that a given lattice position was filled by an atom of the right type. Barrett [14] has interpreted the degree of long distance order for the AB case as "the fraction of atoms that are in their right position minus the fraction that are in wrong positions." Matsuda [10] used an identical definition when studying the AB and A_3B order-disorder reactions in alloys of any composition. A number of mathe-

matical definitions have been reviewed by Klein [15] but they do not in themselves offer a clear picture of the ordering process.

The following interpretation of the Bragg and Williams parameter appears to be new and has been found to cover all cases within the "zeroth" approximation in a particularly simple manner. The long range order parameter is taken as the fraction of wrongly placed atoms on a given sublattice in the disordered state which have been transferred to their correct positions. An example will be taken to show how this definition leads easily to the equations for the fraction of correctly or incorrectly occupied sites.

Consider an alloy on N lattice sites of xN A atoms, yN B atoms, and zN C atoms. Let the lattice be made up from three interpenetrating sublattices such that the correctly ordered A, B, and C atoms will be placed on the sublattices of types I, II, and III respectively. The numbers of correctly ordered atoms are given by

$$\begin{aligned} r_I^A\, n_I N &= x n_I N + x n_{II} N S^{II\to I}_{A} + x n_{III} N S^{III\to I}_{A}, \\ r_{II}^B\, n_{II} N &= y n_{II} N + y n_{III} N S^{III\to II}_{B} + y n_I N S^{I\to II}_{B}, \\ r_{III}^C\, n_{III} N &= z n_{III} N + z n_I N S^{I\to III}_{C} + z n_{II} N S^{II\to III}_{C}, \end{aligned} \tag{A.1}$$

in which, for example, r_I^A signifies the fraction of the I lattice sites correctly occupied by the A atoms, n_I is the fraction of the N lattice sites constituting the I-sublattice, and $S^{II\to I}_{A}$ is the fraction of A atoms which were on the II-sublattice in the disordered state and which have been transferred to the I-sublattice. Since two incorrectly ordered atoms are assumed to interchange to produce two correctly ordered atoms the following identities apply

$$\begin{aligned} x\, n_{II} N S^{II\to I}_{A} &= y\, n_I N S^{I\to II}_{B}, \\ z\, n_I N S^{I\to III}_{C} &= x\, n_{III} N S^{III\to I}_{A}, \\ y\, n_{III} N S^{III\to II}_{B} &= z\, n_{II} N S^{II\to III}_{C}, \end{aligned} \tag{A.2}$$

leading to the condition

$$\frac{S^{II\to I}_{A}}{S^{III\to I}_{A}} \cdot \frac{S^{III\to II}_{B}}{S^{I\to II}_{B}} \cdot \frac{S^{II\to III}_{C}}{S^{I\to III}_{C}} = 1 . \tag{A.3}$$

We shall examine only the case in which the assumption is made that for each species (A, B, or C) the same fraction of wrongly ordered atoms is simultaneously transferred from each sublattice to the correct lattice and

$$S^{II\to I}_{A} = S^{III\to I}_{A} \equiv S_A; \quad S^{III\to II}_{B} = S^{I\to II}_{B} \equiv S_B;$$
$$S^{II\to III}_{C} = S^{I\to III}_{C} \equiv S_C . \tag{A.4}$$

Equations (A.2) and (A.4) can be used to simplify equations (A.1) leading to

$$\begin{aligned} r_I^A &= x + x\frac{(n_{II} + n_{III})}{n_I} S_A \\ &= x + y\frac{(n_{II} + n_{III})}{n_{II}} S_B \\ &= x + z\frac{(n_{II} + n_{III})}{n_{III}} S_C , \\[1em] r_{II}^B &= y + x\frac{(n_I + n_{III})}{n_I} S_A \\ &= y + y\frac{(n_I + n_{III})}{n_{II}} S_B \\ &= y + z\frac{(n_I + n_{III})}{n_{III}} S_C , \\[1em] r_{III}^C &= z + x\frac{(n_I + n_{II})}{n_I} S_A \\ &= z + y\frac{(n_I + n_{II})}{n_{II}} S_B \\ &= z + z\frac{(n_I + n_{II})}{n_{III}} S_C . \end{aligned} \tag{A.5}$$

S_A, S_B, and S_C can have any value between zero and unity but it is convenient to choose the set of equations for which $S = 1$ corresponds to full order. The equations based on S_A would then be used as long as

$$\begin{aligned} 0 \leqslant x \leqslant n_I , \; 0 \leqslant y + x\frac{(n_I + n_{III})}{n_I} \leqslant 1 , \\ 0 \leqslant z + x\frac{(n_I + n_{II})}{n_I} \leqslant 1 , \end{aligned} \tag{A.6}$$

and by letting x equal various fractions of n_I it is readily shown that S_A can have any value up to unity within the compositional triangle BOC in Figure 9. The equations based on S_B would be used in the area COA and on S_C in the area AOB.

The number of wrongly ordered B atoms on the I-sublattice is clearly the number present in the disordered state less the number transferred to the II-sublattice by ordering and

$$\begin{aligned} w_I^B &= y - \frac{n_{II}}{n_I} x S_A , & w_I^C &= z - \frac{n_{III}}{n_I} x S_A, \\ w_{II}^C &= z - \frac{n_{III}}{n_I} x S_A , & w_{II}^A &= x - x S_A , \\ w_{III}^A &= x - x S_A , & w_{III}^B &= y - \frac{n_{II}}{n_I} x S_A. \end{aligned} \tag{A.7}$$

The method can easily be extended to any number of sublattices and allowance made for one species of atom correctly occupying more than one sublattice. The generality of equation (A.3) can also be

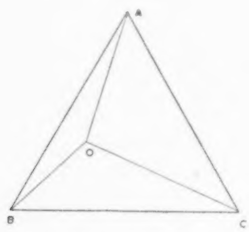

FIGURE 9. The ordered compound at O has the composition $x = n_I$, $y = n_{II}$, $z = n_{III}$ for the atomic fractions of A, B, and C, respectively.

retained and the free energy equation would then be minimised for the different species of S to give the equilibrium distribution of atoms over the sublattices.

References

1. BRADLEY, A. J. J. Iron Steel Inst., **168** (1951) 233.
2. FOWLER, R. H. and GUGGENHEIM, E. A. Statistical Mechanics (Cambridge University Press, 1949).
3. NIX, F. C. and SHOCKLEY, W. Revs. Modern Phys., **10** (1938) 1.
4. HULTGREN, R. and TARNOPOL, L. Trans. A.I.M.E., **133** (1939) 228.
5. MEIJERING, J. L. Philips Res. Reports, **5** (1950) 333.
6. MEIJERING, J. L. Philips Res. Reports, **6** (1951) 183.
7. BRAGG, W. L. and WILLIAMS, E. J. Proc. Roy. Soc., **A145** (1934) 699.
8. BRAGG, W. L. and WILLIAMS, E. J. Proc. Roy. Soc., **A151** (1935) 540.
9. BETHE, H. A. Proc. Roy. Soc., **A150** (1935) 552.
10. MATSUDA, S. J. Phys. Soc. Japan, **6** (1951) 131.
11. SLATER, J. C. Introduction to Chemical Physics (New York, McGraw-Hill, 1939), p. 291.
12. SCHREINEMAKERS, F. A. H. Z. physik. Chem., **22** (1897) 93.
13. ALEXANDER, W. O. J. Inst. Metals, **63** (1938) 163.
14. BARRETT, C. S. Structure of Metals (London, McGraw-Hill, 1943), p. 235.
15. KLEIN, M. J. Amer. J. Phys. **19** (1951) 153.
16. ADACHI, K. Sci. Rep. Tôhoku Univ., **35** (1951) 30.
17. CHANG, T. S. Proc. Roy. Soc., **A161** (1937) 546.
18. FOURNET, G. J. Physique Rad., **13** (1952) 14A.

Note Added in Proof*

A more complete analysis of ordering from a body-centred cubic lattice due to Adachi [16] has now become available. By dividing into four sublattices he finds that the ordered CsCl type of structure is replaced by the NaTl type when $\pi > 0.5$ so that the line T/T_0° in Figure 7 will be interrupted at this point. However the results for $\pi < 0.5$ are not affected when $y = z$.

It may be mentioned that Chang [17] was about the first to investigate the effect of next nearest neighbour interactions and obtained a straight line for the critical temperature as a function of π with the Bragg and Williams approximation. The recent work of Fournet [18] also supports the value of allowing for next nearest neighbour interactions.

*Received March 4, 1953.

THE MOVEMENT OF TWINS, KINKS, AND MOSAIC WALLS IN ZINC*

P. L. PRATT and S. F. PUGH†

The nucleation and controlled smooth growth of twins, seen on the cleavage face under the opaque-stop microscope, is accompanied by an increase both in width and angle of the parallel accommodation kink. The movement under stress of these kink planes, and also of curved mosaic walls, is discussed in terms of their dislocation content. The existence of non-basal plane slip in zinc is deduced from the mobility of curved walls which are stable in the fully annealed crystal.

LE MOUVEMENT DES MACLES, PLIS (KINKS) ET JOINTS DE LA STRUCTURE MOSAÏQUE DANS LE ZINC

La germination et la croissance régulière des macles, vues sur la face de clivage sous un microscope à arrêt opaque, sont accompagnées d'un accroissement de la largeur et de l'angle du pli (kink) parallèle d'adaptation. Le mouvement de ces plans de pliage, ainsi que des joints de la structure mosaïque, engendré par une tension, est discuté en termes de la quantité de dislocations qu'ils contiennent. L'existence d'un glissement qui ne s'opère pas sur le plan de base dans le zinc est déduit de la mobilité des joints courbés, qui sont stables dans un cristal complètement recuit.

DIE BEWEGUNG VON ZWILLINGEN, "KINKS" UND MOSAIKWÄNDEN IN ZINK

Die Keimbildung und das kontrollierte gleichförmige Wachstum von Zwillingskristallen, beobachtet auf der Spaltfläche mit einem Undurchsichtigsperrung Mikroskop, ist sowohl von einer Zunahme in der Dicke wie auch von einer Vergrösserung des Winkels des parallelen "Accomodationkinks" begleitet. Die Bewegung dieser "Kinkebenen" und der gekrümmten Mosaikwände unter Spannung wird als Funktion ihres Versetzungsgehalts diskutiert. Aus der Beweglichkeit der gekrümmten Wände, die in einem vollkommen ausgeglühten Kristall beständig sind, wird das Vorhandensein von Gleitung auf anderen Ebenen als der Basisebene des Zinkkristalls geschlossen.

Introduction

The appearance of twins and their accommodation kinks on the cleavage face of zinc single crystals has been described by a number of authors [1; 2; 3], and the results of their investigations agree in detail. To study the growth of these twins, and the method of formation of the kinks, a straining device has been fitted to the stage of the opaque-stop microscope.

Specimens in the form of discs, cleaved from a 0.5″ diameter single crystal rod of 99.999 per cent purity are inserted in the machine, Figure 1, behind the slot AB with a possible twin trace nearly vertical. By turning the screw E, a bending stress is applied about the vertical axis such that twins, formed in tension on the outer face of the crystal, are revealed by traces in or near the vertical direction.

Experimental Observations

Growth of Twins and Kinks

After a small amount of strain, twins were seen to nucleate and grow rapidly both in length and width on the basal plane until the stresses were relaxed. This sudden initial growth was accompanied by the familiar clicking noise. Once nucleated however, the rate of growth was determined by the rate of straining, and twins could be made to grow slowly and smoothly without further audible clicks, in agreement with the findings of Jillson [4].

*Received December 22, 1952.

†Atomic Energy Research Establishment, Harwell, England.

In Figure 2 a narrow twin trace can be seen running almost vertically, with a wide accommodation kink on the left of the twin; parallel deformation markings, with a fine structure, extend over the field of view at 30° to the twin and normal to the run of the cleavage markings. After further straining, Figure 3, the twin increased in width, and the accommodation kink became correspondingly wider. The controlled advance of the small vertical twin at the bottom of Figure 4 is shown in Figures 5–7. The parallel accommodation kink was displaced from the twin, and, instead of decreasing in width towards the tip of the twin it decreased in angle so that the end appears but faintly in the figures. As straining proceeded, the twin advanced slowly and readily penetrated the straight deformation markings running down from the top left corner. The twin grew thicker and longer until, Figure 7, it had completely crossed the field of view, and simultaneously the accommodation kink on the left of the twin advanced and increased in width and angular tilt as the twin thickened. Faint markings, parallel to the second order kink traces at 30° to the advancing twin, developed at first in the left-hand side of Figure 5 and finally covered the whole field of view in Figure 7. The mosaic boundary in the top left-hand corner moved upward steadily, in Figures 5 and 6, leaving a trace behind it, and similarly the boundary in the bottom left corner moved down to the right, Figures 6 and 7.

The steady and continuous growth of twins was frequently prevented by various types of lattice

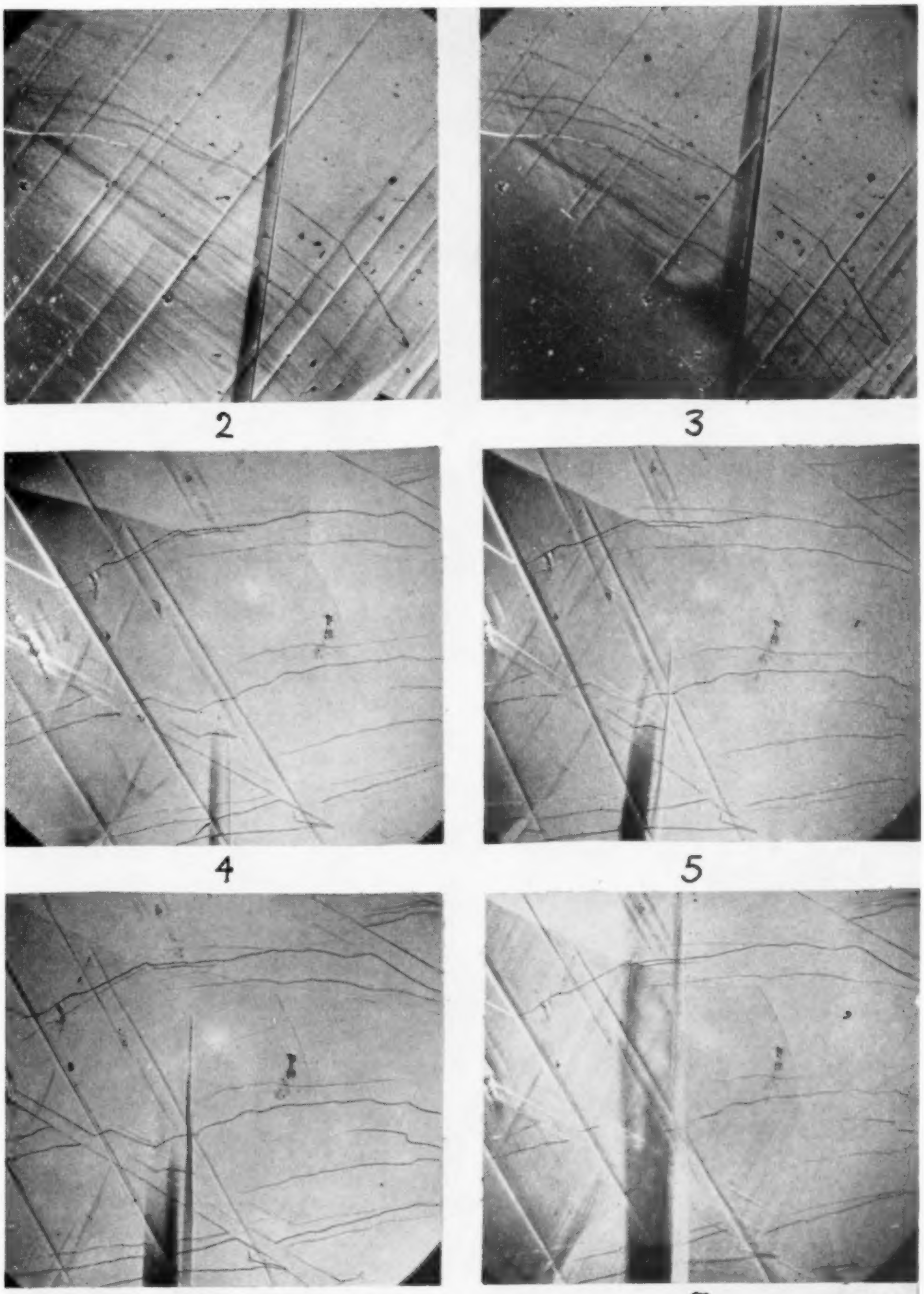

PLATE I. Figure 2—Narrow twin with accommodation kink, and markings normal to cleavage (40 ×). Figure 3—As Fig. 2 after further deformation. Figures 4-7—The advance of a twin tip with its accommodation kink under stress (40 ×).

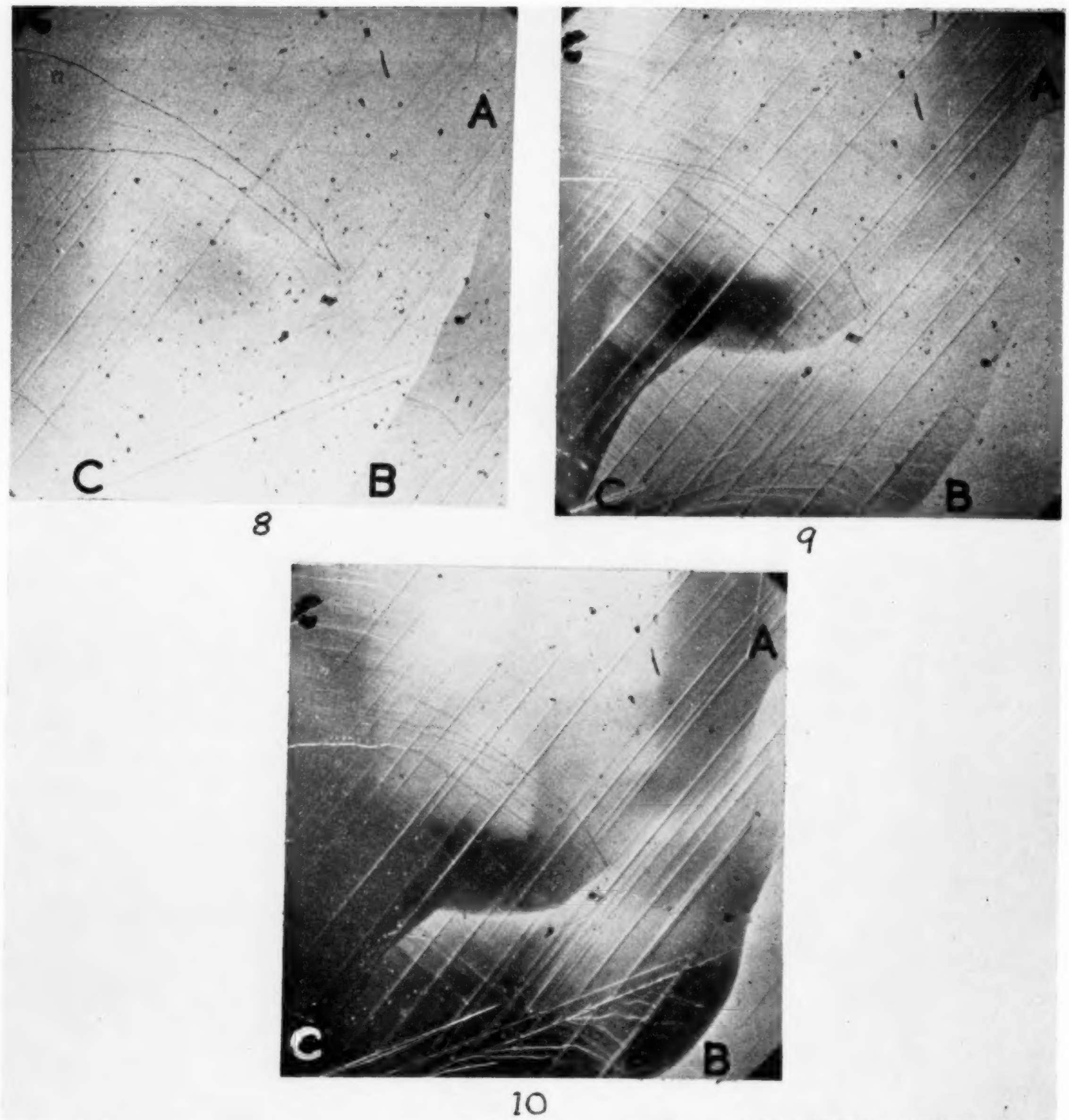

PLATE II. Figures 8–10—The increase of mosaic angle, and movement of mosaic boundaries under stress (20 ×).

imperfection. Twins advancing across a specimen were temporarily delayed at scratches on the surface until a sufficient stress had built up to force the twin through the deformed lattice near the scratch; once this region was penetrated and crossed the stress was dissipated by a rapid advance of the twin tip. Twins were held up by twins of other

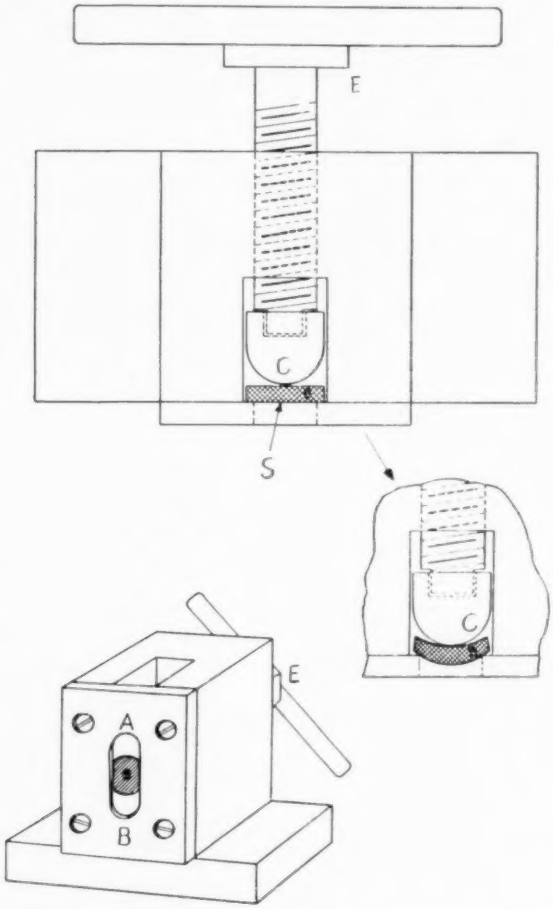

FIGURE 1. Deformation apparatus for use with opaque-stop microscope. The specimen is shown at S.

systems, and a large increase of stress was required to propagate the twin on the other side of the barrier, since the $\{10\bar{1}2\}$ twins in zinc do not form true intersections. Twin growth was also impeded by relaxation of the necessary high stresses near the twin tip, in the form of end accommodation kinks described previously. As the stress was increased, the twin eventually broke through the kink and advanced rapidly, leaving traces of the end accommodation on the surface. Detwinning of twins with parallel accommodation kinks was occasionally observed. A new kink of opposite slope was formed close to the twin, and this moved out to absorb the original kink as the detwinning proceeded.

Behaviour of Mosaics under Stress

The movement of mosaic boundaries under stress has been noted in the previous section on Figures 4–7, and this behaviour was observed in most of the crystals possessing a macro-mosaic structure. In addition, the disorientation between neighbouring units of the mosaic often increased with deformation, and this is illustrated in Figures 8–10. After each successive strain, the opaque stop was reset to the position of maximum contrast. The mosaic angle in Figure 8 is of the order of 15 minutes, and there are two main boundary lines, AB and AC. Deformation markings, perpendicular to the cleavage markings can be seen over the whole field of view. After straining, and resetting the stop, Figure 9, the low-angle boundary, AC, is more clearly visible owing presumably to increased mosaic angles; and after further straining, Figure 10, the disorientations have exceeded 1°. By noting the position of the boundary, relative to dust particles and markings on the surface, movement of the boundary AB can be clearly seen throughout the series of figures. Only those boundaries present in the crystal before deformation have been developed; no new boundaries have been created. To determine the stability of these mosaic boundaries specimens were annealed for 18 hours at temperatures just below the melting-point. No change in the position or shape of any boundaries could be detected on the cleavage face.

Discussion

It has been stated that when twins are formed at liquid air temperatures the width of the parallel accommodation kink is proportional to the width of the twin, and this was correlated with a maximum angle of kinking of 45 minutes. If this relation holds, the kink boundary should move steadily away from the twin to relieve the shear stress set up as the twin becomes thicker. The present work at room temperature shows that the kink boundaries are fully mobile, and do in fact move away as the twin thickens, but the width of the kinked part of the lattice is not truly proportional to the width of the twin. The kink angle of 45 minutes is an upper limit only, and first order kinks of lower angle are frequently observed with narrow twins. As the twins grow wider, the angle of kinking increases up to the limit; but the kink band does not always move at this stage, so that the width of the kink may decrease from perhaps ten times to about four times that of the twin. Once the kink angle has reached the upper limit, the width is more nearly dependent on that of the twin. Cahn [5] has recently associated this limited kink angle with the wedge angle at the

leading edge of the twin, which is limited by the maximum shear gradient permissible in the material.

Washburn and Parker [6] have described the mobility of a straight growth mosaic wall in a slip direction on the surface of a thin cleavage wafer. In an analogous manner, the mobility of an accommodation kink plane has been demonstrated in Figures 2 and 3 of this paper, in a direction at right angles to the slip direction. In each case the movement was produced by a shear stress parallel to the wall. Both mosaic wall and kink plane are considered to be planes of edge dislocations of like sign normal to the surface, separating areas in the first case disoriented by 2°, and in the second by about 45′. The straight mosaic wall at right angles to the slip direction is composed of dislocations all having the same Burgers' vectors lying in that slip direction; while the straight kink plane is composed of dislocations with Burgers' vectors alternately in the other two slip directions at 60° to the wall. The more general case of the movement of curved mosaic walls in a direction inclined to the slip direction has been observed in the case of bending about an arbitrary axis, as in Figures 8–10. The stress system is complex in the straining machine, but only those boundaries on the tensile surface of the specimen, at 45° to the axis of bending and therefore at 45° to the tension axis, were seen to move. From this it may be concluded that a shear stress parallel to the mosaic wall is necessary for the wall to move. Curved mosaic walls if they are to be stable in the fully annealed crystal, must consist of a complex array of dislocations. This array must involve some dislocations whose length does not lie in the basal plane, while all may be of mixed edge and screw type [7]. Therefore, when such curved walls move, slip cannot be confined to the basal plane alone. Further evidence for non-basal plane slip in zinc comes from some recent experiments of Craig and Chalmers [8] who measured the rotation due to slip in bicrystals of zinc near the grain boundary.

In addition to the movement of the mosaic walls under stress an increase in the disorientation between elements of the mosaic was observed. For specimens deformed by bending during cleavage it was found that mosaic angles increased on boundaries lying close to the axis of bending, whereas in the straining machine this correlation was not obvious. The increase of angle between elements of the mosaic can be explained by an increase in the dislocation content of the walls separating them. Dislocations already in the crystal together with others formed during straining, are swept into the walls as the angle increases, in a similar manner to the recent explanation of "cell-formation" by Greenough, Bateman, and Smith [9]. In fact this type of deformation appears to be closely related to cell-formation, but for the fact that the mosaic elements exist prior to the deformation.

The authors wish to thank Dr. H. M. Finniston for his encouragement in this work, Mr. W. M. Lomer for valuable discussion, Mr. L. Kent for preparing photographic prints, and the Director, A.E.R.E., Harwell for permission to publish these extracts from M/R 1031.

References

1. Pratt, P. L. and Pugh, S. F. J. Inst. Metals, **80** (1951-52) 653.
2. Holden, J. Phil. Mag., **43** (1952) 976.
3. Moore, A. J. W. Proc. Phys. Soc. (in press).
4. Jillson, D. C. Trans. A.I.M.E., **188** (1950) 1009.
5. Cahn, R. W. Discussion of Autumn Meeting, J. Inst. Metals, 1952-53 (in press).
6. Washburn, J. and Parker, E. R. Univ. of Calif. Inst. Eng. Research, October, 1951.
7. Lomer, W. M. A.E.R.E., Harwell, private communication.
8. Craig, G. B. and Chalmers, B. Private communication.
9. Greenough, G. B., Bateman, C. M., and Smith, E. M. J. Inst. Metals, **80** (1951-52) 545.

STRESS-INDUCED MOVEMENT OF CRYSTAL BOUNDARIES*

CHOH HSIEN LI, E. H. EDWARDS, J. WASHBURN, and E. R. PARKER†

The stress-induced movement of small angle boundaries in zinc crystals was investigated in the temperature range of 25° to 400°C. The dynamic behavior of the boundaries seemed to require that they consist of an array of edge dislocations of like sign distributed more or less uniformly over the plane of the boundary. The activation energy for the movement of the boundaries in the temperature range of 300 to 400°C was determined to be about 21,500 calories per mole. Attention was drawn to the close agreement between this value and those of the activation energies for self-diffusion, creep, and recovery in zinc crystals. A mechanism was suggested for the formation of a substructure in crystals plastically deformed at low temperatures which depended only on the stress-induced movement of small angle boundaries. This mechanism was based on observations that the rate of boundary motion decreased with increasing boundary angle. Small angle boundaries overtook and united with those of larger angle, forming slower moving, or even stationary substructure boundaries.

MOUVEMENT DE JOINTS INTERCRISTALLINS INDUIT PAR UNE TENSION

Le mouvement de joints à petit angle dans des cristaux de zinc, induit par une tension, fut investigué entre les températures de 25° et 400°C. Le comportement dynamique des joints parait nécessiter qu'il consiste en une rangée de dislocations du type Taylor-Orowan, de même signe, distribuées plus ou moins uniformément dans le plan du joint. Il a été trouvé, que l'énergie d'activation nécessaire pour le mouvement des joints entre les températures de 300° et 400°C était d'environ 21.500 calories par mole. L'attention fut attirée par le fait, que cette valeur était très proche de celles des énergies d'activation dans les phénomènes d'auto-diffusion, fluage et restauration dans les cristaux de zinc. Un mécanisme a été suggéré pour la formation d'une sous-structure dans des cristaux déformés plastiquement aux basses températures, dépendant seulement du mouvement des joints à petit angle induit par une tension. Ce mécanisme était basé sur des observations, que la vitesse du mouvement des joints diminuait quand l'angle des joints augmentait. Les joints à petit angle rattrapaient et s'unissaient à ceux à grand angle pour former des joints de sous-structure, qui se déplaçaient plus lentement ou restaient même stationnaires.

DIE BEWEGUNG VON KORNGRENZEN UNTER ZUGSPANNUNG

Die durch Zugspannungen hervorgerufene Bewegung von Kleinwinkelkorngrenzen in Zinkkristallen wurde in einem Temperaturbereich von 25° bis 400° C untersucht. Das dynamische Verhalten der Korngrenzen scheint zu erfordern, dass sie aus einer Reihe von Stufenversetzungen ("Edge Dislocations") gleichen Vorzeichens bestehen, die mehr oder weniger regelmässig über die Fläche der Korngrenze verteilt sind. Die Aktivierungsenergie der Bewegung der Korngrenzen im Temperaturbereich zwischen 300° und 400° C wurde zu etwa 21.500 Calorien pro mol bestimmt. Es wird auf die gute Übereinstimmung dieses Wertes mit der Aktivierungsenergie der Selbstdiffusion, des Kriechprozesses und der Erholung im Zink besonders hingewiesen. Ein Mechanismus der Bildung einer Feinstruktur in bei tiefen Temperaturen plastisch verformten Kristallen wird vorgeschlagen. Dieser Mechanismus erfordert nur die durch die Zugspannung hervorgerufene Bewegung der Kleinwinkelkorngrenzen und gründet sich auf Beobachtungen, dass die Bewegungsgeschwindigkeit der Korngrenzen mit zunehmendem Korngrenzenwinkel abnimmt. Kleinwinkelkorngrenzen überholten und vereinigten sich mit Korngrenzen grösseren Winkels und bildeten so langsamere oder sogar bewegungslose Feinstrukturkorngrenzen.

Introduction

Experimental observations in three fields, namely those of crystal growth, strength of small metal crystals, and grain boundary energies have helped establish the soundness of dislocation theory. Recently added to this list is the observation of stress-induced motion of small angle boundaries. The possibility that a small angle boundary might move under the action of a suitable system of shear stresses was suggested by Burgers [1] and developed more fully by Shockley [2]. The predicted motion of small angle boundaries under stress was first observed by Washburn and Parker [3]. Experimental evidence for this boundary movement was obtained through observations of a 2° boundary in a zinc crystal loaded as a cantilever beam. Subsequently, a number of additional observations of boundary motion have been made; these are reported herein.

Experimental Procedures and Observations

A. *Single Small Angle Grain Boundaries*

The crystals used in this boundary motion study were prepared from 99.99 per cent Horsehead Special zinc by a modified Bridgeman technique. The earlier observations were confined to small angle boundaries formed incidentally to solidification or cooling of the crystal. For the present investigation a technique was developed for intentionally introducing a boundary. Spherical crystals were cleaved at − 196°C to form disc-shaped specimens approximately one half inch in thickness. Each

*Received December 1, 1952.
†Department of Metallurgy, University of California, Berkeley, California, U.S.A.

specimen was supported as a simple beam and heated to 350°C. The load was applied at the mid-span through a knife edge perpendicular to the basal plane, introducing local plastic bending. After cleaving away the upper and lower surfaces, the specimen was annealed for one hour at 400°C. Although it was customary to introduce the boundaries perpendicular to a slip direction in the crystal, this method permitted arbitrary location and orientation of the boundary, and facilitated studies of their dynamic properties.

Boundary angles were measured with a long focal length reflectograph; the estimated error was ± 4 minutes. The disc-shaped specimen containing the boundary was mounted in U-shaped grips and loaded as a cantilever beam inside a small resistance furnace. Observations were made with an optical microscope looking down on the cleaved surface of the crystal in the manner schematically represented in Figure 1. Oblique illumination was used so that the location of the grain boundary was indicated by the difference in brightness across the boundary. Displacement of the boundary was measured with a Filar eyepiece which permitted the position of the boundary to be established within ± 0.001 mm. In several instances, it was deemed desirable to record the boundary movement on motion picture film for further study and analysis. When this was the case, the Filar eyepiece was removed and the

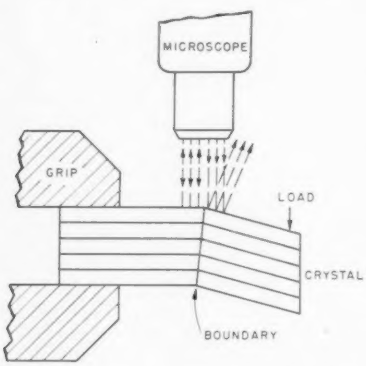

FIGURE 1. Illustration of loading method for boundary movement studies which would move boundary to left. Horizontal lines indicate slip directions; slip planes perpendicular to plane of paper.

body of the camera joined to the microscope with an extension tube. The objective lens of the microscope functioned as the camera lens.

Although the majority of observations to date have been qualitative in nature, a number of quantitative results are included in the following summary of experimental observations:

1. With the crystal loaded as a cantilever beam as indicated in Figure 1, the boundary was observed to move towards the left under the influence of the shearing stresses. The calculated critical shear stress for the boundary motion was of the order of the magnitude of the critical shear stress for slip in zinc. When the direction of the stress was reversed, the direction of the motion of the boundary was also

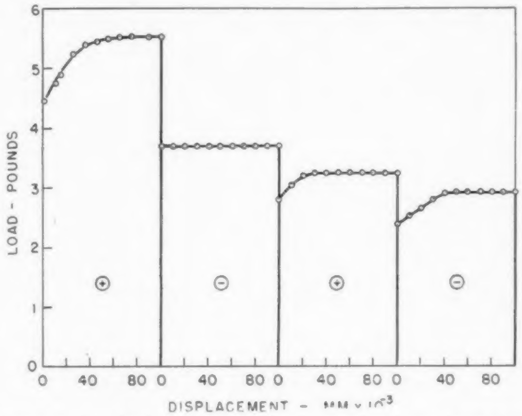

FIGURE 3. Series of curves for a moving boundary showing decrease in height of load-displacement curve when direction of movement was reversed. Rate of boundary movement held approximately constant. 25°C.

reversed and the boundary moved to the right past its original position. A series of pictures selected from the movie are shown in Figure 2. The time interval between pictures was approximately ten seconds. It should be pointed out that while there are no obvious crystallographic markings on the cleavage face of the specimen, water stains on the surface serve as convenient reference markers for the progress of the boundary movement.

With another crystal, the load required to move the boundary at a constant rate was measured at room temperature. The results are reproduced in Figure 3. A significant, but progressively decreasing reduction of the critical load was noted with each reversal of the loading direction.

2. It was the general observation that under a given load, the smaller the boundary angle, the more rapid was the displacement. The sequence of pictures in Figure 4 records the movement of two boundaries at 350°C. The boundary on the left was approximately one-half degree larger than the one on the right. Under the applied shear stresses, both boundaries moved towards the left, but at unequal rates. The more rapid movement of the smaller angle boundary resulted in a shortening of the distance between the two boundaries.

3. Whenever one moving boundary overtook another, the two united to form a single boundary. It was found that the new boundary required

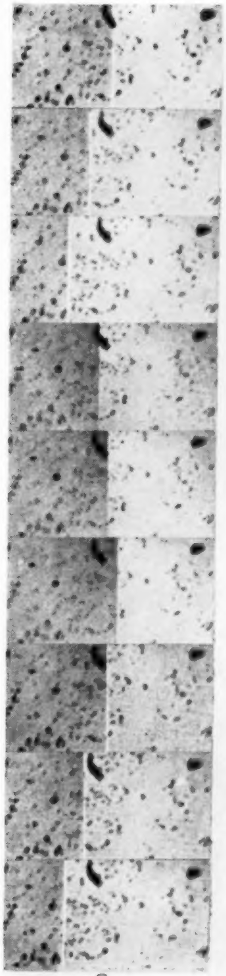

2

4

6

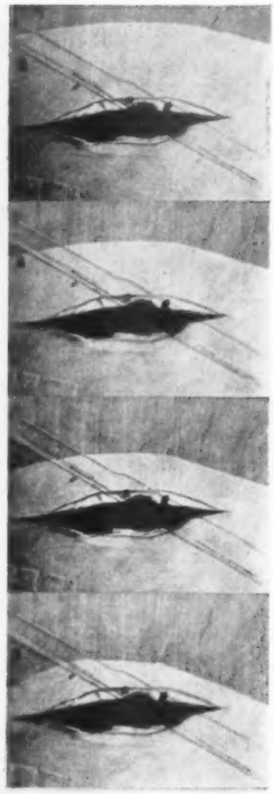

7

Plate I. (All figures reduced by one half in reproduction.) Figure 2—Series of photographs of a moving boundary showing that direction of motion reversed when shear stress was reversed; direction of motion was reversed twice; 350°C (100 ×). Figure 4—Illustration showing that rate of boundary motion decreases with increasing boundary angle; one-half degree boundary on right overtaking one degree boundary on left; 350°C (100 ×). Figure 6—Photographs showing successive stages of stress-induced union of two small angle boundaries; 350°C (100 ×). Figure 7—Retardation of boundary movement by a heavily distorted region; 350°C (100 ×).

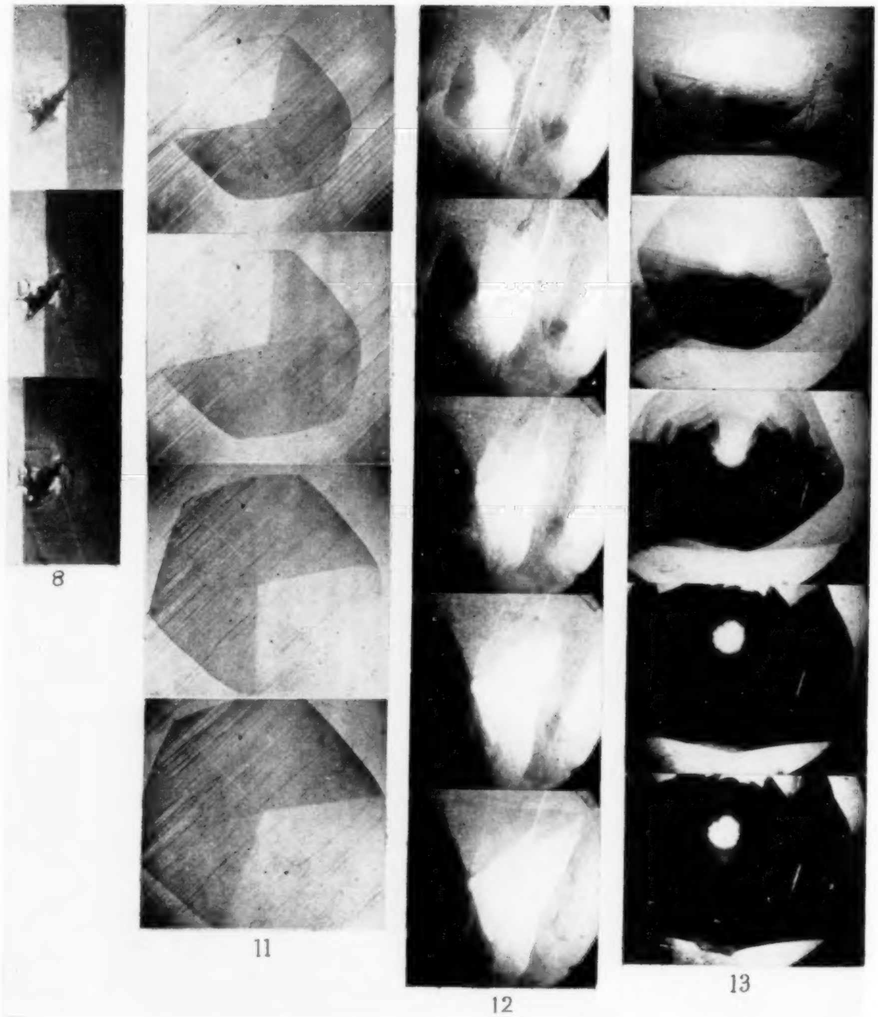

PLATE II. (All figures reduced by one half in reproduction.) Figure 8—Unhindered passage of boundary through a less severely distorted region; 350°C (100 ×). Figure 11—Stages in the growth of a hexagonal system of low angle boundaries; 350°C (10 ×). Figure 12—Retardation of a growing hexagonal system of boundaries in the vicinity of an inactive system; 350°C (10 ×). Figure 13—Deflection of a single low angle boundary in the path of a growing hexagonal system; 350°C (10 ×).

higher stresses to make it move. A typical load-displacement curve illustrating this is shown in Figure 5. The manner in which the union occurred is recorded in the series of pictures of Figure 6. Union between the boundaries involved motion of the junction along the larger of the two boundaries.

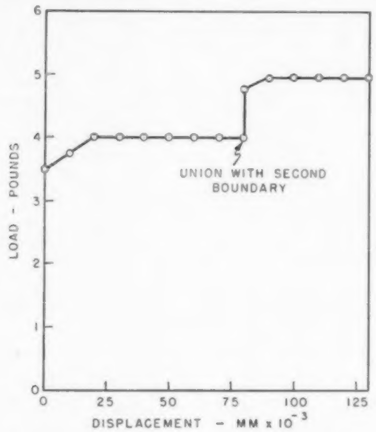

FIGURE 5. Load-displacement curves showing that when two boundaries unite the load required for continued movement is increased. Rate of motion held approximately constant. 25°C.

When the external stress was reversed during the process, the direction of motion of the junction was also reversed. The result was a gradual separation of the new boundary into the two original boundaries.

4. The motion of a boundary was retarded in the vicinity of certain imperfect regions in the crystal. The restraint imposed by the distorted material surrounding a Tukon hardness indentation is indicated in Figure 7. The photographs show that locally the radius of curvature of the boundary steadily decreased as the boundary approached the deformed area.

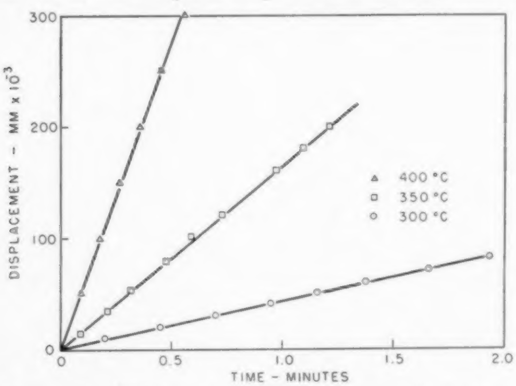

FIGURE 9. Displacement-time curves at various temperatures showing rate of movement of a typical boundary under constant load.

When the degree of cold work was much less, the movement of the boundary was not appreciably affected. This condition is illustrated in Figure 8, where the boundary can be observed to pass through the area with little or no retardation.

5. As might have been expected, the rate of movement of a boundary under a given load increased as the temperature was raised. A summary of the rates measured in the temperature range of 300 to 400°C at a stress of approximately 8 psi is presented in Figure 9.

B. *Hexagonal Systems of Small Angle Boundaries*

Another form of low angle boundary is that associated with the formation of a hexagonal-shaped substructure in zinc crystals. When a disc-shaped specimen having the basal plane parallel to the surface is heated to 350°C and a concentrated load is applied parallel to the *c*-axis by means of a conical-pointed indenter, a hexagonal system of low angle boundaries is developed. This is shown schematically in Figure 10. At this temperature,

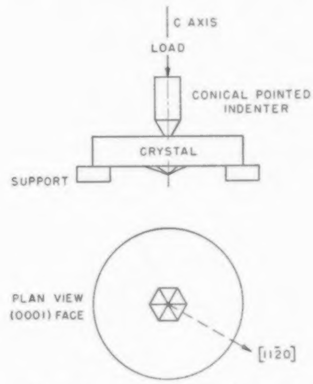

FIGURE 10. Sketch showing method of introducing a hexagonal system of low angle boundaries into a crystal.

slip occurs internally on the basal planes. Dislocations introduced initially by the local plastic bending collect in a hexagonal array to form low angle boundaries. Details of the growth of such a substructure under continued loading were best followed with a binocular microscope.

The more important experimental observations pertinent to the movement of hexagonal arrays of low angle boundaries may be summarized as follows:

1. Under conditions of constant load, growth of the substructure eventually stopped. Stages in the growth of the structure at 350°C are illustrated in the series of pictures of Figure 11. After motion of the system of boundaries had come to a halt, movement was resumed if the load was increased.

2. A second but inactive substructure of this type was a sufficient barrier in the path of an actively

enlarging system to distort the growing hexagon. To illustrate this point, the small hexagonal substructure appearing in the lower right corner of the pictures of Figure 12 was introduced. The load was then shifted to a new position on the crystal (to the left and slightly upward in the photographs) where a second substructure was formed and allowed to spread under constant load. There was a marked reluctance of the boundaries of the growing system to pass through the previously formed substructure, causing the distortion shown in the last two pictures.

3. To a somewhat lesser extent, a single small angle boundary restricted the movement of the spreading hexagonal substructure. A single straight small angle boundary was introduced into the plate-shaped crystal specimen approximately halfway from the center of the face to the edge. The crystal was then loaded to produce a hexagonal substructure that was allowed to enlarge until its boundaries impinged upon the single straight boundary. The most important feature here, aside from the distortion of the hexagonal substructure, was the repulsion between the single boundary and the hexagon. As may be seen in Figure 13, from its initial approximately straight condition, the boundary was altered to the extent of becoming noticeably curved.

Discussion

It has become apparent that plastic properties of crystals are largely determined by the presence of imperfections. The nature and distribution of these imperfections, however, and the changes accompanying plastic flow have remained obscure. Single imperfections may never be observed unless magnifications great enough to see individual atoms are achieved. However, simple small angle boundaries represent groups of imperfections whose motion through a crystal can be observed and controlled. Their behavior seems to require that they consist of an array of edge dislocations of like sign and equal Burgers vector distributed more or less uniformly over the plane of the boundary. Whether or not progress leading to a better understanding of plastic flow can be made with moving boundary investigations will depend in large measure upon the development of more satisfactory experimental techniques.

The somewhat limited observations made to date appear to be consistent with other observations of plastic behavior. Within the temperature range 300 to 400°C, the displacement rate, $\dot{\epsilon}$, of the dislocation array through the lattice under a given stress varies with temperature in accordance with the expression:

$\dot{\epsilon} = Ae^{-Q/RT}$ where A = a constant
Q = the activation energy
R = the gas constant
T = the absolute temperature

The value of the constant Q has been measured as approximately 21,500 calories per mole (Figure 14).

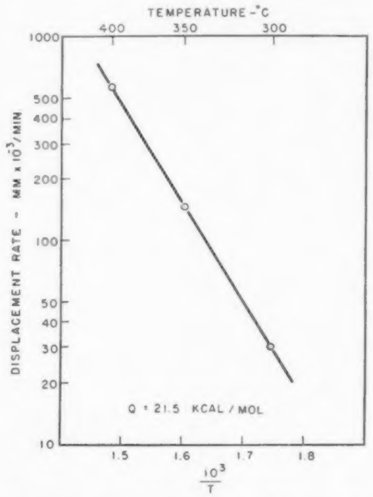

FIGURE 14. The linear relationship between log displacement rate and reciprocal of the absolute temperature yields an activation energy of approximately 21.5 kcal/mol for boundary motion at high temperatures. Stress constant at 8 psi.

It is interesting to note that the following temperature-dependent processes in zinc crystals give very similar values for the activation energy:

Self diffusion parallel to c-axis	20,400 cal/mol	[4]
Creep	20,000	[5]
Recovery after pure slip deformation	20,000	[6]

The striking agreement of the activation energies of all these processes suggests that all may involve the same basic atomic movements. This fundamental process may be interaction of vacant lattice sites with edge dislocations. The fact that motion of this dislocation array is at a rate dependent on temperature in the same way as self diffusion suggests that dislocations encounter barriers which impede their movement. The capacity of the barrier to block a section of the dislocation line appears to be removed by a diffusion process, possibly by the motion of edge dislocations at right angles to their Burgers vector through interaction with lattice vacancies. The thought that dislocations moving through a lattice encounter barriers is also suggested by the

observed lowering of the critical stress when the boundary was moved back and forth through the same volume of crystal. (Perhaps with repeated reversals of direction of motion, the boundary dislocations encountering barriers move out of their original planes into nearby ones where motion is relatively easy. An alternate interpretation of the results is that boundary dislocations become trapped and are removed from the boundary. As a consequence, the boundary angle becomes smaller and the boundary easier to move. Future experiments should clarify this point.)

At low temperatures and higher stresses, it is possible to move dislocation arrays under conditions where appreciable diffusion cannot occur. Under these conditions it is possible that experimental verification of Shockley's [7] prediction of a very low activation energy for movement of a dislocation may be obtained.

A mechanism for the formation of a substructure in plastically deformed crystals is suggested by the uniting of small angle boundaries under stress to form larger angle boundaries. With the application of external stresses, it is a reasonable assumption that small angle boundaries in crystals could form and migrate until union was effected with other moving boundaries. Stress-induced movement of the boundaries could continue until the angular magnitude of all internal boundaries attained a size characteristic of that temperature and stress level. A stable substructure could thus be created without any special activation energy being required other than that associated with the stress-induced motion of the dislocation arrays.

Acknowledgments

This investigation was sponsored by the Office of Naval Research. The authors desire to express their appreciation to the ONR staff, and in particular to O. T. Marzke and Julius Harwood, for their sustained interest and support. The authors also wish to thank D. W. Bainbridge for his many constructive suggestions and criticisms, and L. O. Seaborn and W. R. Arneson for their assistance in the construction of the apparatus.

References

1. Burgers, J. M. Proc. Phys. Soc. (London), **52** (1940) 23.
2. Shockley, W. In "Cold Working of Metals" (Amer. Soc. Metals, 1949), p. 131.
3. Washburn, J. and Parker, E. R. J. Metals, **4** (1952) 1076.
4. Miller, P. H. and Banks, R. F. Phys. Rev., **61** (1942) 648.
5. Pickus, M. R. and Parker, E. R. Trans. A.I.M.E., **191** (1951) 792.
6. Drouard, R., Washburn, J. and Parker, E. R. Office of Naval Research Project N7-onr-29516 NR-031-255, Fifth Technical Report (1952), p. 5.
7. Shockley, W. J. Metals, **4** (1952) 829.

Anisotropy of Surface Self-Diffusion of Silver*

During an investigation of self-diffusion of silver on silver surfaces, it was observed that diffusion appeared to be isotropic whenever the surface used was parallel to {100} or {111} planes. However, when the surface was parallel to {110} planes, diffusion was always faster in the ⟨110⟩ direction than in the ⟨100⟩ direction.

The diffusion was measured by the radioactive tracer technique described by Winegard and Chalmers [1]. Strain-free single crystal surfaces parallel to the required crystallographic plane were prepared [2]. In each case, a disc of silver containing the radioactive isotope Ag 110 was electroplated on the electropolished surface. An autoradiograph was taken of the spot before and after heat treatment. The density of the autoradiographs was measured with a Hilger non-recording type microphotometer. Figure 1 is typical of the curves obtained.

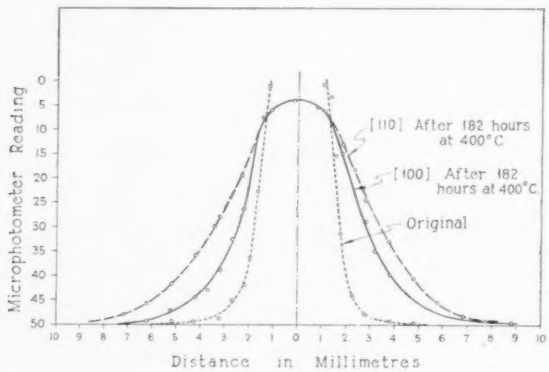

FIGURE 1. Microphotometer reading *versus* distance before and after heat treatment.

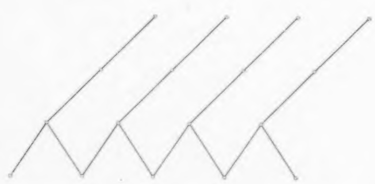

FIGURE 2. Perspective sketch of a ⟨110⟩ surface.

It is observed that diffusion is faster in the ⟨110⟩ direction than in the ⟨100⟩ direction.

The mechanism of diffusion may be similar to that described by Ahearn and Becker [3] for thorium on the surface of tungsten. The surface of a ⟨110⟩ plane for a face-centred cubic lattice consists of a series of grooves, as illustrated in Figure 2.

The direction along the "groove" is the ⟨110⟩ direction, and it seems reasonable that atoms would move faster along the grooves than across the grooves. This appears to be supported by the experimental evidence which indicates that diffusion in the ⟨110⟩ direction on the {110} plane is faster than diffusion in any other direction on any other plane.

W. C. WINEGARD

Department of Metallurgical Engineering
University of Toronto, Canada

References

1. WINEGARD, W. C. and CHALMERS, B. Can. J. Phys., **30** (1952).
2. CHALMERS, B. Metal Progress, **61** (1952) 94.
3. AHEARN, A. J. and BECKER, J. A. Phys. Rev., **54** (1938) 448.

Notes on the Theory of Annealing Textures*

The preponderance of a certain crystal orientation in the texture of an annealed metal indicates that in the matrix material numerous "nuclei" are available in this orientation and that they have the capacity to grow at the expense of the matrix during annealing. An important problem of annealing texture theory is whether the relative scarcity of grains in other orientations may be attributed to shortage of corresponding nuclei, or to their lower rate of growth. It has been shown for f.c.c. metals that the preferred orientations of the new grains are related to the matrix orientation in such a way that the interfaces between growing grains and matrix have high mobility. General agreement has not as yet been reached on the question whether the orientation dependence of grain boundary mobility alone is sufficient to account for the observed annealing textures (oriented growth theory), or whether it is necessary to assume that the availability of nuclei is also importantly orientation dependent (theory requiring oriented nucleation as well as oriented growth). The position originally taken by Burgers and Louwerse [1] that annealing textures are determined by oriented nucleation alone, now appears to have

*Received November 15, 1952.

*Received November 14, 1952.

been generally abandoned.* In the following, it will be attempted to show that the hypothesis of oriented nucleation is altogether unnecessary, even as an adjunct to the oriented growth theory.

The orientation process, which takes place on annealing of a single orientation matrix, has been studied in several face-centered cubic metals [2; 3; 4]; it usually corresponds to a 30° or 40° rotation around a [111] axis. In hexagonal close packed zirconium [5] and titanium [6], the reorientation on recrystallization was found to correspond to a rotation of 30° around the basal plane normal. In all these cases, the reorientation on annealing corresponds to a rotation around the normal of the closest packed plane, and the resulting interfaces have maximum grain boundary energy. Although this orientation is clearly unfavorable for growth from the point of view of driving energy, it corresponds to maximum grain boundary mobility and to the highest rate of growth [7]. It is probable that the observed orientation dependence of grain boundary mobility is a result of the orientation dependence of the rate of self diffusion along the boundary [7; 8].

One of the principal objections against the oriented growth theory is based on the observation that the maximum of the grain boundary energy, and presumably also of boundary mobility, as a function of disorientation, is usually quite broad. Thus, grains in orientations deviating from the maximum by 15°, or so, still grow at relatively high rates. Consequently, it has been doubted [9; 10] that the orientation dependence of grain boundary mobility would suffice to explain the sharp annealing textures which are often observed; it was suggested that a highly anisotropic distribution of nucleus orientations has to be assumed. It should be considered, however, that the maximum becomes much sharper if one considers the rate of increase of the volume of material in various orientations, rather than the linear rates of growth. On the basis of volume, the pertinent variable is the third power of the mobility. If this function is plotted against the disorientation, a much sharper maximum is, of course, obtained than for the mobility itself. There is, in addition, an effect which further exaggerates the consequences of small variations in mobility. It is clear, that the new grains are not growing independently from each other in the matrix material, but soon impinge on each other. Owing to the impingement, fast growing grains tend to "cut in front" of grains with boundaries of lower mobility (see figure), with the consequence that the latter are "pinched off." As a result of this "pinching off effect," grains with boundaries of maximum mobility are able to grow to disproportionately larger sizes than others with boundaries of only slightly lower mobility, provided that the number of nuclei per unit volume is large enough to make the competition keen. The considerations presented so far are quite generally applicable, even when the matrix has an essentially singie orientation texture. It should be noted, however, that the matrix in which the new grains are growing usually has more than one texture component. In such cases, the rate of growth of the new grains, with respect to all matrix components, should be taken into account. The highest rates of growth can be achieved only by grains which are favorably oriented for growth not only with respect to all major components of the texture, but also with respect to the minor components* and to matrix material representing the spread of orientations from these various texture components. As a result of these additional restrictions, the range of orientations favorable for growth may be considerably narrowed. This mechanism, arising from the oriented growth theory, has been proposed in particular to explain the sharpness of the cube texture [11], but it is

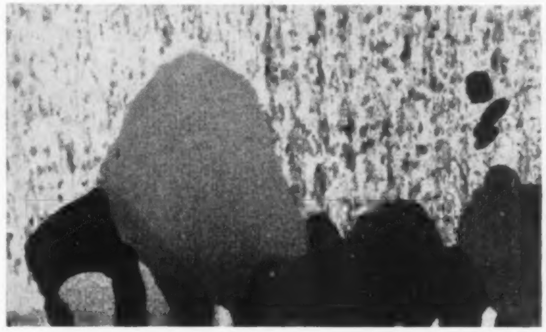

Competitive growth, in a fine grained single orientation texture aluminum matrix, of grains originated by artificial nucleation at the bottom edge of the specimen. Because of impingement, grains most favorably oriented for growth "pinch off" grains of slightly less favorable orientations. Thus, slight differences in boundary mobility have a greatly exaggerated effect on the volume of material recrystallized in various orientations. Deep etch. (Magnification 6 ×.)

*See for instance Burgers' own recent review [10].

*A minor texture component which is favorably oriented for the growth of a new grain has little effect on the rate of boundary movement, but an unfavorably oriented one may decrease the rate much more than might be expected on the basis of its volume fraction since, in this case, the individual grains of the minor texture component act as unabsorbed inclusions, or dispersed particles of a second phase.

undoubtedly effective in many other cases as well.

The second main objection raised against the oriented growth theory of annealing textures is that in the cubic crystal system there are four [111] axes, and the 30° rotation around each of these can be carried out in two directions; in a well annealed single crystal there are, therefore, eight crystallographically equivalent orientations of the type required by maximum boundary mobility. In annealing textures often only one to three of these eight possibilities are actually found to occur. This was regarded by some investigators [12; 13] as a sufficient reason for assuming oriented nucleation. It has been pointed out [8], however, that there is no reason to expect that all eight theoretically equivalent orientations are in effect crystallographically equivalent, since a deformation texture, or the texture of a recrystallized matrix in which coarsening occurs, no matter how sharply developed, will, in general not possess the symmetry of a corresponding ideal single crystal. Thus, the boundary mobilities corresponding to the eight theoretically equivalent orientations described may have quite different absolute values, some of them being much higher than others. The observed asymmetry of annealing textures can then be easily accounted for in terms of the oriented growth theory, on the basis of the asymmetry of the matrix. As a matter of fact, in most deformation textures of polycrystalline face-centered cubic metals, there are two or more major deformation texture components. It is to be expected that the lower than theoretical multiplicity of the annealing texture components is a result of the additional restrictions on the growth of new grains imposed by the complexity of the matrix texture, as discussed above. This is confirmed by an interesting recent investigation of Liu and Hibbard [14] who found that in copper with a single orientation deformation texture new crystals grow on annealing in all eight orientations discussed.

The third objection that has been cited against the oriented growth theory concerns the fact, experimentally well established by several investigators [15; 16; 17], that in slightly deformed single crystals the orientation of the grains newly formed on annealing shows considerable scatter and it is not related to the matrix orientation in any simple manner. The type of reorientation corresponding to a [111] rotation of 30° or 40° is not at all prevalent in this case. Consequently, the crystal orientations are manifestly not determined by oriented growth. It has been recognized and clearly stated [7] that the lack of a sharp, well defined annealing texture in this particular case is, in effect, due to the lack of nuclei in orientations favorable for fastest growth. It is well known that the localized lattice disorientations produced in a single crystal by slight deformation are usually quite small. Under such conditions, crystal fragments of the orientations required for fast growth may be extremely scarce. In addition, the total number of nuclei per unit volume is also very small and, therefore, competition between the new grains is relaxed. Another special situation in which the scarcity of nuclei prevents the formation of a sharp annealing texture, is found in the coarsening of copper with a very sharply developed cube orientation texture. Unpublished work by P. R. Sperry with the author showed that such material, if handled with extreme care to prevent the chance formation of nuclei by recrystallization following extraneous local deformation, is extremely reluctant to coarsen even at temperatures approaching the melting point. When coarsening does set in, the new grains have orientations not far from that of the matrix itself. Again, it is easy to interpret these findings on the basis of lack of nuclei sufficiently disoriented from the matrix for fast growth. Given enough time, eventually a grain within the scatter range of the matrix texture itself will have a chance to grow, in spite of the low mobility of its boundary. (Several investigators [3; 18; 7] found that in the two known cases of this kind, just mentioned, the artificial introduction of sufficiently random nuclei gives rise to the growth of grains in the usual orientations, characterized by high boundary mobility.) Even though in these two special cases no well defined annealing textures are formed, there is a noticeable tendency for the new grains to avoid the matrix orientation. Both this tendency and the very absence of a sharp annealing texture in these instances clearly follow from the oriented growth theory of annealing textures. There appears to be nothing here to require the oriented nucleation hypothesis, according to which sharp annealing textures result from the occurrence of nuclei only in special orientation relationships with the matrix. As a matter of fact, the lack of sharp annealing textures in slightly deformed single crystals, in contrast to heavily deformed crystals, has never been accounted for in terms of oriented nucleation.

It may be concluded that the assumption of

oriented nucleation is not necessary. However, a direct test of this assumption in its general form is very difficult, since "nuclei" are by nature small and they are detected only after growth. Usually, by the time a growing grain comes to attention, or becomes large enough for orientation determination, it has been already the subject of growth selectivity. The observed orientation distribution of such grains may not be assumed to be equivalent to that of the original nuclei, so that the latter remains unknown.

The assumption of oriented nucleation requires additional specific hypotheses regarding the nature of the nuclei, in order to "predict" annealing textures. So far, this proved to be possible only after the annealing texture itself has been experimentally determined. Thus, up to now three different specific oriented nucleation hypotheses have been proposed by various investigators in order to explain three specific annealing textures. In the original work of Burgers and Louwerse [1], the nuclei in compressed or rolled single crystals of aluminum were assumed to have formed in "local curvatures" in orientations corresponding to rotations around [112] axes lying in the slip plane and perpendicular to the slip direction. It was, however, shown later [4] that the annealing textures observed by these investigators may be derived from the matrix texture more accurately by [111] rotations. The recent, thorough investigation by Liu and Hibbard [14] with rolled single crystals of aluminum and copper confirms that the orientation relationship between annealing textures and deformation texture in fact corresponds to [111] rotations. The local curvature hypothesis for nucleus orientation is, therefore, not supported by observation. A second hypothesis for nucleus orientation has been advanced by Kronberg and Wilson [18] in connection with the coarsening of cube texture copper. According to these authors, the nucleus orientations are derived by [111] rotations, characterized by the coincidence of many atomic positions in the two crystal lattices, and by the short paths of movement necessary for the other atoms to readjust themselves from one lattice to the other. This hypothesis predicts several [111] rotations of different magnitude and some rotations around other axes. Of the predicted [111] rotations, the one nearest to the observed values of 30° and 40° is 38°. This would fit quite well the reorientation of 40° observed in aluminum, but its deviation from the 30° reorientation observed in the case of copper is distinctly larger than the experimental error. Moreover, the fact that the other predicted orientations do not actually occur is not accounted for. The inadequacy of this hypothesis is quite clear, for instance, in the case of the annealing textures investigated by Liu and Hibbard [14]. A third hypothesis was advanced by Decker and Harker [22] and by Burgers, Liu, and Tiedema [23] in order to explain the orientation of nuclei for the cube texture in cold rolled f.c.c. metals. According to this hypothesis, those grains of the deformed material which happen to have the cube orientation are the first to recover their annealed condition (without reorientation) and they are, therefore, the first available to act as nuclei. This hypothesis is apparently supported by the observation first reported by Sachs and Spretnak [19], that cold rolled Ni-Fe alloy, which develops the cube orientation on annealing, contains a cube component in its rolling texture. A minor cube texture component was also reported for cold rolled copper [20] and aluminum [21]. In an effort to produce additional support for this particular oriented nucleation mechanism, Burgers, Liu, and Tiedema have shown that, of three extended single crystals of different orientations, the one with the cube orientation polygonized first [23]. However, it remains to be shown to what extent this result, obtained with slightly extended single crystals, may be related to the behavior of grains in a severely rolled polycrystalline aggregate. At any rate, a simple consideration based on known facts indicates that the specific nucleation mechanism discussed is unlikely. Since the number of grains in cube orientation must be a small fraction of the total number of grains in rolled copper, the proposed mechanism would lead to a relatively small number of nuclei, that is, to a very large grain size in the annealed cube texture material. This is not borne out by experience; the grain size in cube texture copper is usually rather small, the same order of magnitude as that of the starting material. New, as yet unpublished results of a critical experiment by Mr. A. Merlini in this laboratory decisively prove that this mechanism of oriented nucleation leads to incorrect predictions.

In conclusion it may be stated that the reorientation on annealing, which has been so far thoroughly studied in various f.c.c. and h.c.p. metals, can be accounted for on the basis of the orientation dependence of grain boundary mobility—itself an experimental fact. Consequently, there is at

present no valid indication of any need for assuming a hypothetical effect of oriented nucleation. Because of its nature, this effect is not amenable to direct experimental verification in its general form. The three different specific oriented nucleation hypotheses advanced so far for the purpose of explaining three specific annealing textures lead to predictions in contradiction with experimental evidence.

PAUL A. BECK

Dept. of Mining and Metallurgical Engineering
University of Illinois
Urbana, Illinois, U.S.A.

References

1. BURGERS, W. G. and LOUWERSE, P. C. Z. Phys., **67** (1931) 605.
2. BOWLES, J. S. and BOAS, W. J. Inst. Metals, **24** (1948) 501.
3. RATHENAU, G. W. and CUSTERS, J. F. H. Philips Research Reports, **4** (1949) 241.
4. BECK, P. A. and HU, H. Trans. A.I.M.E., **185** (1949) 627.
5. MCGEARY, R. K. and LUSTMAN, B. Personal communication.
6. JILLSON, D. C. Personal communication; also C. J. MCHARGUE, personal communication.
7. BECK, P. A., SPERRY, P. R., and HU, HSUN. J. Appl. Phys., **21** (1950) 420.
8. BECK, P. A. Trans. A.I.M.E., **191** (1951) 475.
9. BURGERS, W. G. and TIEDEMA, T. J. Proc. Kon. Nederl. Akad. Wet., **53** (1950) 1925.
10. BURGERS, W. G. L'Etat Solide (Bruxelles, R. Stoops, 1952), p. 431.
11. BECK, P. A. Trans. A.I.M.E., **191** (1951) 474.
12. BECKER, J. J. Trans. A.I.M.E., **191** (1951) 115.
13. BURK, J. E. Trans. A.I.M.E., **194** (1952) 263.
14. LIU, Y. C. and HIBBARD, W. R. JR. Personal communication, paper to be published in Trans. A.I.M.E.
15. BURGERS, W. G. and BASART, J. C. M. Z. Phys., **51** (1928) 545.
16. LALOEUF, A. and CRUSSARD, C. Rev. Mét., **48** (1951) 461.
17. CHEN, N. K. and MATHEWSON, C. H. Trans. A.I.M.E., **194** (1952) 501.
18. KRONBERG, M. L. and WILSON, F. H. Trans. A.I.M.E., **185** (1949) 501.
19. SACHS, G. and SPRETNAK, J. Trans. A.I.M.E., **140** (1940) 359.
20. IWERONOWA, W. and SCHDANOW, G. Techn. Physics, U.S.S.R., **1** (1934) 64.
21. COHEUR, P. and LEJEUNE, J. M. Rev. Mét., **46** (1949) 439.
22. DECKER, B. F. and HARKER, D. J. Appl. Phys., **22** (1951) 900.
23. BURGERS, W. G., LIU, Y. H., and TIEDEMA, T. J. Proc. Kon. Nederl. Akad. Wet., **54** (1951) 459.

Notes on the Theory of Annealing Textures: Comments on a paper by P. A. Beck with the same title*

By courtesy of Professor Beck the manuscript of the above paper was sent to us before publication, simultaneously with the Editor's invitation to give any comment we might wish to contribute on this topic. We gladly avail ourselves of this opportunity offered to us, which we greatly appreciate.

1. In several papers [1; 2; 3; 4] we have taken the view that the occurrence of pronounced preferred orientations of the crystallites in annealled test-pieces cannot be ascribed to the sole action of what is called "growth selectivity," if we define this as a selection, by a process of orientation dependent growth, of nuclei with special orientations from a large number of available randomly oriented nuclei, all of which start to grow at the same moment in a matrix with a well-defined texture.

On the one hand we think it hardly possible that these conditions, which in our view would be required to give growth selectivity its full chance are simultaneously fulfilled in cold worked test-pieces, as beside the main deformation texture also other orientations (for example cube-oriented regions in rolled strips of cubic face-centred metals), are often represented in a somewhat greater amount. Apart herefrom, however, we think that actually the presence of such regions may be essential for the formation of the annealing texture, as they may acquire, by some process of "nucleation" to be described later on, an exceptional capacity for growth.

The purpose of Beck's paper is to show that the assumption of this last condition is unnecessary and in his paper arguments are given which refute objections raised by us and by some other investigators (Becker, Burke), against the exclusive role of oriented growth in determining recrystallization textures. We think that some of the arguments given are not sufficiently stringent to invalidate the objections raised. A few remarks concerning these points are made in the next section.

2a. Beck states that the effect of a definite orientation dependence of grain boundary mobility is more pronounced if one considers the rate of increase of the volume of the material in various orientations rather than the linear rate of growth. This is undoubtedly true. We may ask, however,

*Received January 20, 1953.

how far volume relations hold in experiments with thin plates, in which one dimension is so much smaller than the other two that continuous "3-dimensional" growth is only possible to a limited extent. But apart herefrom, the fact [5] that one can make aluminum crystals of widely varying orientations grow in the same matrix texture at approximately equal rates of growth, provided only that the orientation of the crystal is not approximately parallel or approximately in twin-position with respect to the matrix texture, makes it difficult for us to believe that even "volume-selectivity" will in itself be able to produce such a sharp recrystallization texture as for example the cube-texture in rolled material.

2b. The argument that differences in rate of growth may result in a "cutting in front" of grains with boundaries of lower mobility (see figure in Beck's paper) has to be viewed with caution, because, in determining the shape of grains, apart from the relative rates of growth, also the position of the points where and the moments at which growth starts, may have considerable influence. For example, if, close to the border of a flat strip, three crystals start *simultaneously*, and with *equal* rates, to grow from points A, B, and C in Figure 1,

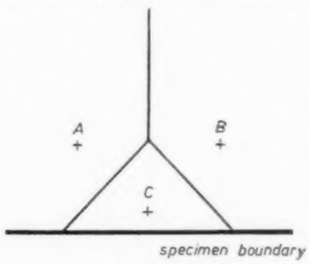

FIGURE 1

then the final boundaries (assuming "circular" growth) will be represented by the straight lines and grain C is cut off by A and B also in this case, where no difference in growth-rate was assumed.

2c. In the last section of Beck's paper an objection is raised against the supposition suggested by Burgers, Liu and Tiedema [4] (also Burgers [3]) that the cube orientation is caused by growth of lattice regions in cube-position, already present in the rolled matrix, which have obtained the capacity to grow by a specific nucleation mechanism ("polygonization"). The objection is based on the ground that due to the smallness of the fraction of the matrix occupied by such regions this mechanism would lead to a large grain size in the annealed cube-texture which is contrary to fact. Apart from the circumstance, that even in a small fraction of material the number of nuclei may very well be large, the argument brought forward would equally apply to a theory based on the assumption that the cube-texture is due to selective growth as such, as, if we see it rightly, the same cube-oriented regions in the rolled matrix must be the starting points for the final grains also in this case.

2d. Finally, we mention once again (cf. Burgers [2]) an objection raised by Becker [6] which is not discussed in Beck's paper. It concerns the fact that the recrystallization texture of a given matrix may vary with the temperature of annealing. On the basis of the selective growth theory this would imply that the anisotropy of growth rates varies considerably with temperature, which Becker finds unlikely, a conclusion with which we agree.

2e. Other points discussed in Beck's paper, such as the absence of the complete set of orientations in a recrystallized matrix which are equivalent from the point of view of orientation, and the occurrence, in slightly deformed single crystals after recrystallization, of a small number of grains with widely varying orientations, could probably be understood with both "theories" and are not conclusive for a decision in either sense.*

Considering the whole of the evidence, we agree with Beck that, at the moment at least, it is not possible to give a "direct" experimental proof that a special "oriented nucleation mechanism" may co-determine or, in special cases, even be the main cause for the recrystallization texture, since, as Beck rightly puts it, nuclei are by nature small and they are detected only after growth. For this reason, instead of bringing arguments as to the significance of definite experiments as a proof for or against the one or the other conception, we should like to set forth in a general way what, in our opinion, happens on annealing a cold-worked test-piece (or lattice region aggregate), in order to make clear to what extent, as we view it, a process of nucleation can be conceived beside a process of growth, in the hope that such an exposition will stimulate discussion on this topic.†

*In the latter case Beck assumes this to be due to lack of nuclei in orientations most favorable for fastest growth, so that the available nuclei have to grow; see in this respect our remarks in [1] and in the Solvay Report [2], page 98.

†Just after the following section was written in its general outform, we received by courtesy of Dr. C. G. Dunn of the General Electric Company at Pittsfield, Mass., a manuscript by him entitled "Secondary Recrystallization Textures and their Origin in Cold-Rolled Single Crystals of Silicon Iron," which appears in this issue, p. 163, in which some points, raised by us in a qualitative way, are brought forward more precisely and quantitatively.

3. In a piece of metal, whether cold-worked or annealed, the major part of the atoms form coherent lattice regions, as is shown by X-ray diffraction. The difference with regard to a perfect single crystal may, if we follow Seitz [7], be described in terms of lattice imperfections, among which we discern vacant lattice sites, interstitial atoms, and dislocations* As pointed out in Seitz' paper, these imperfections form individual units, clusters (vacancies) or rings (dislocations), and further groups of dislocations may combine to form boundary "planes" between lattice regions of different orientation. The "structure" of these planes depends on the orientation difference between the regions they separate and on their "position," varying from simple sets as envisaged by J. M. Burgers [8] in his well-known model of a mosaic block boundary, to complicated structures between regions of widely varying orientations ("grain" boundaries), of such complicated structure that a description in terms of specific dislocations has better be replaced by a description in terms of "regions of good and bad fit," as proposed by Mott [9].

Owing to these imperfections, the metal is, generally speaking, in a state of metastable equilibrium and tends, by means of atomic displacements, to reduce its lattice imperfections to the thermodynamic minimum. If by increase of temperature, this tendency can be followed, annealing sets in. Among the atomic displacements taking place, we may discern at least two types, with regard to the effect they produce:

(*a*) such which produce a displacement of the boundary plane between two adjoining lattice regions of different orientation;

(*b*) such which produce only a rearrangement of imperfections which is more favorable from the point of view of free energy, for example a coalescence of vacancies, a recombination of two suitably oriented dislocations of opposite sign, and in particular, an accumulation of originally dispersed dislocations in "planes" separating lattice regions of different orientation, as for example in Orowan and Cahn's [10] representation of polygonization in a bent lattice.

Of these two conceivable types, only that under (*a*), if taking place on a visible scale, shows itself as growth of one lattice region at the cost of an adjoining one, i.e. as recrystallization or (sub) grain growth. Displacements of group (*b*), on the other hand, would not make themselves known in this way, but certainly effect a "recovery" of the value of various physical properties, as electric resistance and plastic behaviour; structurally, they could bring about the formation, or increase the size, of lattice regions more or less freed from imperfections (possessing a smaller imperfection-"density").

*We consider a "pure" metal without foreign atoms.

4. Following the ideas of C. S. Smith [11] and others, the general course of the *boundary* displacements may be compared to the movement towards equilibrium positions of films in a soap-foam, the rate of displacement of individual boundaries being governed by a balance between a "driving force" given by boundary energy and degree of curvature [12; 13], and by a "mobility" [13a].

Of these factors the first and the third are dependent on the structure of the boundary, and thus on the difference in orientation between the two adjoining lattice regions and on the position of the boundary "plane" with regard to their orientations. *These two factors therefore give rise to an orientation dependence of the boundary displacement.*

So far as we know at present, both factors have relatively high values for boundaries separating regions with widely varying orientations, for example 30°–40° rotated about a 111-axis, which represents the condition for highest rate of growth in a cubic face-centred lattice in Beck's theory; but also apparently for other large orientation differences, as follows from the easy consumability of a fine-grained matrix by growing crystals with such other orientations (experiments of Tiedema [5] with aluminum and of Dunn [14] with silicon iron). On the other hand, the presence of inclusions (insular crystals) in large crystals grown in a fine-grained matrix shows that displacement is very difficult for lattice regions in approximately parallel or twin connected positions [15; 16].†

The second factor mentioned above which influences boundary displacement, namely the degree of curvature of the boundary, may be taken to be itself *not* dependent on the relative orientation between adjoining lattice regions. Here, therefore, is a factor which may compete with those factors promoting orientation dependent growth. In a matrix consisting of lattice regions (subgrains, grains) of nearly equal size, the curvature factor may be expected to play no dominant

†As brought forward by Dunn and Daniels [17], the easy movement of subgrain-boundaries makes it probable that for very small differences of orientation (1°) boundary migration again becomes easier. Although the boundary energy is low in such cases, the mobility may be high due to the *possibility* of a simple "dislocation-structure" of boundaries between nearly parallel lattice regions (such as the "J. M. Burgers-model").

part, so that the orientation dependent boundary displacement can have its way. For each boundary its direction will in general be towards the centre of curvature, as is for example most clearly shown in experiments of Beck and Sperry [18] on grain growth in high purity aluminum. The annealing treatment will finally produce a more or less general coarsening, with possibly a "sharpening" of the existing texture.

If, however, in a matrix lattice regions are present which are considerably larger than their neighbours, then, as brought forward by C. S. Smith [19] (cf. also Harker and Parker [20]), the larger regions, if sufficiently different in size of their surroundings* will have the greater chance to grow at the cost of their neighbours, because a large probability exists that their boundary with each individual neighbour is concave to the centre of this latter and has therefore the tendency to displace so as to consume the small neighbouring regions. A good example of such a "cusped" boundary can be found in a paper by Lacombe and Berghézan and is reproduced in an article by Beck [23]. Naturally, the displacement of each individual cusp is "orientation dependent," in so far it can take place at a reasonable rate only if the orientation difference between the larger region (grain) and the adjacent smaller region is sufficiently large and these two orientations are not approximately parallel or twin-related. This, however, we would not call selective growth in the sense as, we think, this expression is used by Beck, as the growth of the larger regions is not due to a selection based on their *orientation* but on their *size*, the orientation coming in only in so far it either "allows" or "does not allow" the growth to proceed at a measurable rate.†

5. Now we think it possible that in a matrix built up for the greater part of lattice regions of nearly equal size, and possibly, orientation, "bounded regions" of larger size than their immediate surroundings may be created in the course of the annealing process by atomic displacements of the type mentioned under (*b*) in paragraph 3, the "inside" of which is to a considerable degree freed from imperfections. A simple case could be the production of "polygons" in Cahn's polygonization process, but we could imagine also a "clearing up" by suitable displacements of sub-boundaries or by more complicated rearrangements. If such regions differed sufficiently in orientation from their surroundings to be bounded by *mobile* boundary planes, then they would be in a favourable condition for growth and might outdo the competing growth of already existing regions. Such a process then, for which we may perhaps use the expression "polygonization" in a somewhat wider sense, might, in our mind, be viewed as "nucleation". This is, in fact, only a somewhat more general representation of an idea, brought forward originally by Beck himself [24] and later particularly by Cahn [25], and afterwards taken over by Burgers and Tiedema [1]. We were brought hereto in particular by Tiedema's observation [26] that large aluminum crystals grown by recrystallization in a cold-worked test-piece consist of a small number of parts with slightly different orientation (order of magnitude some minutes of arc), which originate in the centre of the crystal, where, we think, "polygons" in corresponding orientations were formed.

On the basis of this conception, the possibility exists that the crystals formed on annealing originate for a considerable percentage in "nuclei" formed in the way sketched above, and possess therefore the orientations of these nuclei. As it follows from work by Dunn and Daniels [17] on silicon iron and by Burgers, Liu and Tiedema [4] on aluminum, that the capacity for "polygonization" (as shown by break-up of Laue-spots) is dependent on the state of deformation of a lattice region (for aluminum for example it is larger for a region which has been subjected to "multiple glide" than to "single glide"; cf. also Decker and Harker's work on silicon ferrite [27]), the orientation of those lattice regions which may be "polygonized" into nuclei, may vary with the foregoing cold-work process. An influence of cold-work on the texture after recrystallization is therefore directly understandable; also a dependence on annealing temperature does not seem strange, as both the temperature-dependence of "nucleation" and that of rate of growth come into play.

6. The foregoing may be summarized as follows: Essential for recrystallization is the displacement of boundaries between lattice regions of different orientation. On annealing a test-piece, this process may set in "immediately," without any necessity for "nucleation" in the sense described above, due to the displacement of *existing* boundaries. This procedure takes place in normal grain growth, or also in grain growth in a slightly deformed matrix, i.e. in what Beck and Sperry [18] call "strain induced" grain growth.

On the other hand we may envisage the possibil-

*The necessary conditions are set forth in a quantitative way by C. S. Smith [20], and by Dunn [13]; cf. also [12; 17; 21; 22].

†A similar remark occurs in Dunn's paper [13].

ity of "creating," in the course of the annealing process, by rearrangements of imperfections, lattice regions "freed" from imperfections to a relatively large degree. If such regions are, with respect to the size of their neighbours, sufficiently large, and sufficiently different from them in orientation, they may be privileged for growth and can cause the formation of individual grains, or, if present in great number, of a recrystallization texture fixed by their orientation.

It will depend on the entire "structure" of the matrix, whether this combination of necessary conditions is fulfilled. If, for example, "polygonization" occurs, but the created regions do not differ sufficiently in orientation from their surroundings, "nucleation" takes place, but appreciable growth does *not* follow. This was actually the case in the experiment by Burgers, Liu, and Tiedema [4], mentioned at the end of Beck's paper, in which it was shown that an aluminum crystal stretched for about 20 per cent parallel to a cube-axis, polygonized relatively easily. In this case, however, the polygonized regions are embedded in a surrounding of equally oriented neighbours (owing to the sharp "cube-texture" of the stretched crystal), and growth of one region at the cost of an adjacent region cannot take place, so that even on prolonged heating no recrystallization, taken as crystal growth on a "visible" scale, occurred. Perhaps this experiment presents an ideal case of what Crussard [28] calls "recrystallization *in situ*."

In conclusion we wish to say that, as we see it, the above conceptions are not conflicting with C. S. Smith's view [29] that the driving energy of "recrystallization" is finally interface energy associated with boundaries between lattice regions of different orientation, a view recently brought forward also by Beck [30] in his note "Do Metals Recrystallize."

W. G. Burgers and T. J. Tiedema

Laboratory for Physical Chemistry
Technical University
Delft, Holland

References

1. Burgers, W. G. and Tiedema, T. J. Proc. Kon. Ned. Akad. Wet., **53** (1950) 1525.
2. Burgers, W. G. In "L'Etat Solide" (Rapports et Discussions 9ième Conseil de Physique Solvay, Bruxelles, 1951).
3. Burgers, W. G. Z. Elektrochemi., **56** (1952) 318.
4. Burgers, W. G., Liu, Y. H., and Tiedema, T. J. Proc. Kon. Ned. Akad. Wet., **54** (1951) 459.
5. Tiedema, T. J. Thesis (Delft, 1951).
6. Becker, J. J. Trans. A.I.M.E., **191** (1951) 115.
7. Seitz, F. In "Imperfections in Nearly Perfect Crystals" (New York, Wiley, 1952).
8. Burgers, J. M. Proc. Phys. Soc. London, **52** (1940) 23.
9. Mott, N. F. Proc. Phys. Soc. London, **60** (1948) 391.
10. Cahn, R. W. J. Inst. Metals, **76** (1949) 121.
11. Smith, C. S. Trans. A.I.M.E., **175** (1948) 15.
12. Burke, J. E. and Turnbull, D. Progress in Metal Physics, **3** (1952) 220.
13. Dunn, C. G. Acta Met., **1** (1953) 163.
13a. Fullman, R. L. In "Metal Interfaces" (Amer. Soc. Metals Seminar, 1951).
14. Dunn, C. G. Symposium on Cold Working of Metals, A.S.T.M. (1948).
15. Tiedema, T. J., May, W., and Burgers, W. G. Acta Cryst., **2** (1949) 151.
16. Lacombe, P. and Berghézan, A. C. R. Acad. Sci., Paris, **228** (1949) 93.
17. Dunn, C. G. and Daniels, F. W. J. Metals, **191** (1951) 147.
18. Beck, P. A. and Sperry, Ph. R. J. Appl. Phys., **21** (1950) 150.
19. Smith, C. S. Trans. Amer. Soc. Metals, Preprint no. 37 (1951).
20. Harker, D. and Parker, E. R. Trans. Amer. Soc. Metals, **34** (1945) 156.
21. Rathenau, G. W. and Baas, G. Physica, **17** (1951) 117.
22. Rathenau, G. W., Smit, J., and Stuyts, A. L. Z. Phys., **133** (1952) 250.
23. Beck, P. A. In "Metal Interfaces" (Amer. Soc. Metals Seminar, 1951).
24. Beck, P. A. J. Appl. Phys., **20** (1949) 633.
25. Cahn, R. W. Proc. Phys. Soc. London, **63** (1950) 323.
26. Tiedema, T. J. Proc. Kon. Ned. Akad. Wet., **53** (1950) 1422.
27. Decker, B. F. and Harker, D. J. Appl. Phys., **22** (1951) 900.
28. Crussard, C. Rev. Mét., **41** (1944), 111, 133.
29. Smith, C. S. In "The Physics of Powder Metallurgy" (New York, 1951), p. 50.
30. Beck, P. A. J. Metals, **4** (1952) 979.

Textures in Extruded Aluminium*

One of us (K.V.G.) has obtained data on the deformation and recrystallization textures in extruded rods of superpure aluminium (Fe 0.02%, Mg $< 0.01\%$, Si 0.02%, Cu $< 0.005\%$, Al balance), which seem to us to be relevant to current theories of recrystallization. The initial $2\frac{3}{4}$ in. diameter cast billets consisted of columnar grains normal to the direction of extrusion, with $\langle 100 \rangle$ parallel to the columns. The extruded rods had a double fibre texture, with $\langle 111 \rangle$ or $\langle 100 \rangle$ parallel to the extrusion direction. The $\langle 100 \rangle$ grains, (henceforth called "X") had a faintly rumpled appearance when etched, while the $\langle 111 \rangle$ grains ("Y") contained deformation bands parallel to the extrusion direction. These bands had quite different orientations

*Received November 24, 1952.

from the body of the grains. Study was largely restricted to grains in the approximately 3/8 in. diameter core and 5/32 in. wide intermediate zone of the 1 in. diameter extruded rods, since the broken structure of the deformed grains of the peripheral zone made recognition of corresponding areas after recrystallization difficult.

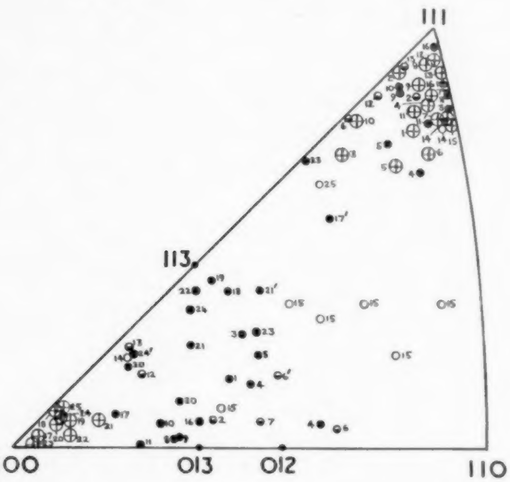

FIGURE 1. Superpure aluminium. The poles represent the extrusion direction. Crosses refer to the deformed grains, solid, half-solid, and open circles to groups of recrystallized grains in the core, intermediate and peripheral zones respectively. Poles of recrystallized grains bear numbers corresponding to their parent deformed grains.

On recrystallization, a new duplex fibre texture was formed, with a minor ⟨111⟩ component and a major component ranging from ⟨103⟩ to ⟨113⟩; Figure 1 is a specimen plot. (Note: Extruded rods of commercial aluminium showed similar deformation and recrystallization textures.) Analysis of the behaviour of individual deformed grains on annealing showed that the minor component originated in the Y grains, while both X and Y grains contributed to the major texture. The orientations of all the new grains could be rationalized in terms of rotations about ⟨111⟩ axes of the deformed grains (Figures 2 and 3). Figure 2 refers to X grains. Since all four ⟨111⟩ directions are equivalent in these grains (in the sense that all make equal angles with the ⟨100⟩ fibre axis), the orientations of all new grains have been expressed in terms of rotation about one [111] axis only. Figure 3 refers to Y grains. Here the unique [111] direction parallel to the extrusion direction must be distinguished from the other three. Rotation about this unique axis gives rise to the minor texture referred to, while rotation about any of the latter contributes to the major texture. This distinction has been expressed by choosing arbitrarily two ⟨111⟩ axes to serve as rotation axes. One of these represents *all three* non-unique axes. The other represents the unique axis and is identified by the crosses clustering near it, which stand for the extrusion directions of the deformed grains; this axis is seen to account for a disproportionate amount (about half) of the recrystallized grains.

The recrystallized structure arising from the X grains consisted of equiaxed grains. The Y grains gave rise to slightly smaller grains, often elongated normal to the extrusion direction, and generally of very uniform orientation (this is why one single trio of poles suffices to describe the orientations of the whole group). Continued annealing sometimes gave rise to secondary grains in the intermediate zones, with a ⟨103⟩-⟨113⟩ fibre texture, much scattered.

The rotations about ⟨111⟩ axes relating deformed and recrystallized grains add to the growing number of instances of this relationship, obtaining for different face-centered cubic metals and modes of deformation, which we owe largely to Beck and his co-workers [1]. Beck has argued cogently that this relationship demonstrates that the ease of growth of nuclei formed in annealed deformed grains is orientation-dependent. The mean angles of rotation in Figures 2 and 3 of the present paper are 22° for X grains and 46° for Y grains, as

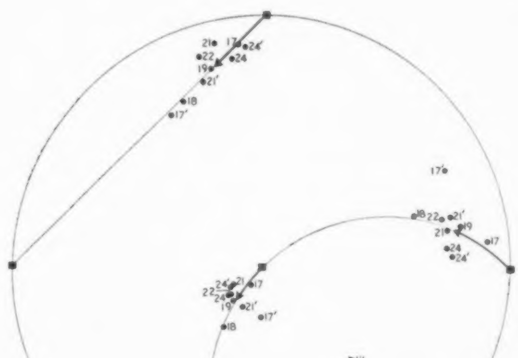

FIGURE 2. Same data as Figure 1, replotted for X grains only. Circles represent {100} poles of recrystallized grains. {100} poles of the deformed grains are in standard orientations. Crosses refer to the extrusion direction. Arrows correspond to 22° rotations about the [111] direction.

compared with the ideal angles of 22° and 38° [2]. According to Beck's theory, the mechanism of deformation should be irrelevant to the subsequent recrystallization behaviour except in as far as it affects the supply of nuclei and their range of orientation. Cahn [3] has put forward a theory in which recrystallization nuclei are regarded as minute, intensely curved lattice regions (dislocation pile-ups) that have polygonized, which renders them strain-free.

These two theories, taken together, are able to account for the above observations, and in particular for the different behaviour of the X and Y grains. The earlier idea, that preferred orientation is *entirely* due to a supply of nuclei of special

FIGURE 3. Same data as Figure 1 replotted for Y grains only. For meaning of symbols see caption to Figure 2. Arrows correspond to 46° rotations about the [$\bar{1}\bar{1}$1] and [111] directions. Poles marked "A" identify grains rotated about the unique longitudinal [$\bar{1}\bar{1}$1] axis.

orientations, has to be abandoned; instead we agree with Beck that the nuclei have only a limited degree of preferred orientation which is then enhanced by the selective growth mechanism. For an explanation of the observations on this basis, we have had to adopt the hypothesis that the structure of the X grains is less distorted than that of the Y grains. There are three pieces of evidence in support of this hypothesis:

(*a*) Because of the columnar texture in the undeformed billet; angles between the direction of extrusion and the nearest ⟨111⟩ axis in any undeformed grain were in the range 35½°–54½°, with a most probable value of 43°. The corresponding figures for ⟨100⟩ axes are 0–45° and 22½°. Consequently a smaller physical rotation of the grains, and therefore a lesser amount of distortion was needed for a grain to achieve a ⟨100⟩, or X, texture than a ⟨111⟩, or Y texture.

(*b*) The Y grains contained deformation bands, which are composed of piled-up dislocations and should therefore recrystallize particularly readily, as has in fact been observed elsewhere [4].

(*c*) Some Y grains (Nos. 10 and 16) were found to have recrystallized completely before *adjacent* X grains (22, 23, 24) had begun to do so.

In general, the less distorted a grain is, the smaller will be the *number* and *angular* range of the available nuclei, so that selective growth has less raw material to work on. This would account for the larger size of the X grains (fewer suitable nuclei being available) and for the fact that the corresponding new grains are rotated only 22° from the parent orientation. The Y grains, on our hypothesis, were more heavily deformed, and the correspondingly more copious supply of nuclei leads to the greater angle of rotation of 46° (because according to Cahn's theory these more disoriented nuclei should become active well before those rotated only 22°, and will therefore be able to consume all the deformed material). The somewhat smaller grain size can be attributed partly to the greater supply of nuclei and partly to the presence of deformation bands, which have unfavourable orientations with respect to new grains which grow easily in the material between the bands. The bands thus act as barriers, and this would explain the origin of the strings of recrystallized grains observed in regions formerly occupied by Y grains.

It is striking that the recrystallized textures formed in the Y grains had a greater homogeneity of orientations than that formed in the X grains (Figures 2 and 3). The homogeneous orientation of the aforementioned "strings" was particularly striking to direct visual examination. This difference is also to be expected because of the different degrees of deformation of the X and Y grains. A greater supply of nuclei allows the selective growth criterion to operate with greater precision. The grain size within the strings was exceptionally small—another instance of the theoretically expected correlation between homogeneity of orientation and copious nucleation.

The disproportionately frequent occurrence of the longitudinal [111] axis as rotation axis for recrystallized grains in Y grains confirms that the preferred orientation of nuclei must play an appreciable part in determining the final texture.

A similar conclusion has been drawn from analogous behaviour of the longitudinal [111] fibre axis in drawn and recrystallized aluminium wire [5].

Acknowledgements

Thanks are due to the Department of Industrial Metallurgy, University of Birmingham, for provision of facilities and financial support. One of us (K.V.G.) wishes to thank Professor C. S. Barrett and Dr. A. R. E. Singer for much helpful advice, and the National Research Council of Canada for financial support.

K. V. Gow and R. W. Cahn

Department of Metallurgy
University of Birmingham, England

References

1. Beck, P. A. and Hu, Hsun. J. Metals, **1** (1949) 627.
2. Kronberg, M. L. and Wilson, F. H. J. Metals, **1** (1949) 501.
3. Cahn, R. W. Proc. Phys. Soc. (London), **A63** (1950) 323.
4. Cahn, R. W. J. Inst. Metals, vol. **79** (1951), p. 129.
5. Beck, P. A. J. Metals, **3** (1951) 475.

Remarks on the Ferromagnetic Ground State*

We make below three observations concerning the ground state of a ferromagnet: (A) on the effect of spin-orbit coupling on conclusions drawn from the saturation magnetization with respect to the electronic structure of ferromagnetic alloys; (B) on the relative effects of dipolar and pseudo-dipolar interactions on the deviation of the magnetic moment of the ground state from absolute saturation; (C) on the failure of Van Peype's perturbation treatment of the ground state.

A. The values of the spectroscopic splitting factor g are known to vary in ferromagnetic metals from 1.95 in gadolinium to 2.2 in nickel. These values are involved directly in the magnetization, the maximum z-component of the magnetic moment associated with an electron being under these conditions $\frac{1}{2}g\mu_B$ rather than simply μ_B; the difference is the orbital contribution. Thus the effective number of *electrons* per magnetic atom is 2.0(6) in iron and 0.54 in nickel, while the effective number of *Bohr magnetons* is 2.22 in iron and 0.6×1 in nickel. Recent publications, especially those on the band and collective electron theories of ferromagnetism, have given various results to a higher apparent accuracy than is justified by the neglect of the effect of the g-value, which may amount to ten per cent. The electronic heat capacity of nickel, for example, as calculated by Fletcher [1] would be increased by perhaps 15 per cent by this effect.

*Received December 22, 1952.

B. On the atomic model of a ferromagnet with the isotropic exchange energy operator the ground state is the state of maximum multiplicity [2]—the saturation is complete. This is no longer true in the presence of magnetic dipolar or pseudo-dipolar interactions among the electrons. Holstein and Primakoff [3] find for the fractional deviation at absolute zero

$$(1) \qquad \frac{\Delta M}{M_0} = -\left(\frac{1}{\pi 2^{9/2} g S}\right)\left(\frac{4\pi\mu_B M_0}{2SJ}\right)^{3/2}$$

in the absence of an applied magnetic field. This is for a simple cubic lattice and $g = 2$. Taking $M_1 = 1500$, $S = 1$, and $J/k = 200°\mathrm{K}$, we have $\Delta M/M_0 = 1.25 \times 10^{-6}$.

The pseudo-dipolar interaction may be written as $C \sum S_d^i S_d^j$ between nearest neighbors, where d is the direction of the line joining nearest neighbors. The interaction arises through incomplete quenching of the orbital angular momentum, and it expresses the dependence of the exchange integral on the direction of magnetization. It is believed [4] to be of considerable importance in the phenomena of magnetostriction and anisotropy, and possibly in line width in ferromagnetic resonance. The constant C may be of the order of a few per cent of the isotropic exchange J, but at the same time C may be larger than the magnetic dipolar interaction between nearest neighbors by a factor of the order of 100. We might thus be led to expect that C will have a relatively large effect on the saturation deviation of the ground state. Following the method of Herring and Kittel [5] we have developed a theory of spin waves in the presence of the pseudo-dipolar interaction. (We have also checked by this method the Holstein-Primakoff calculation for the magnetic dipolar interaction.) We find, for a simple cubic lattice, the spin wave frequencies

$$(2) \quad \omega^2 = (Ak^2 - Bk_x^2 + D)(Ak^2 - Bk_y^2 + D),$$

where

$$(3) \quad A = 2Ja^2S/\hbar;\ B = Ca^2S/\hbar;\ D = g\mu_B H/\hbar.$$

The symbols have their usual meanings. The ground state magnetization reversal in the [001] direction is

$$(4) \qquad \frac{\Delta M}{M_0} \cong \frac{1}{240}\left(\frac{C}{JS}\right)^2.$$

This expression differs from equation (1) in form; the difference may be traced back through the dispersion relations to the relative ineffectiveness of the pseudo-dipolar interaction on long wavelength spin waves. The magnetic dipolar interaction involves long range forces and has a significant effect even on the long waves. With the values above and taking $C/k = 10°K$, we estimate $\Delta M/M_0 = 10 \times 10^{-6}$. This is only eight times larger than the result for the magnetic dipolar interaction, although C expressed as a field is of the order of 100 times greater than M_0, the measure of the magnetic interaction. Holstein and Primakoff [3] had remarked earlier on the relative ineffectiveness of the pseudo-dipolar interaction.

C. Van Peype [6] has given a perturbation treatment of the ferromagnetic ground state in the presence of pseudo-dipolar coupling, in connection with a calculation of ferromagnetic anisotropy at the absolute zero. This work has been described as a rigorous calculation of ferromagnetic anisotropy for a definite model. However, an inspection of his perturbed wave functions shows that his procedure is not convergent, factors of the order of the number of particles being neglected in comparison with unity. His perturbed wave functions, furthermore, have only two spins reversed and thus cannot possibly represent a system of N electrons with $\Delta M/M_0$ more than $4/N$; as $N \rightarrow \infty$, this ratio goes to zero. If we agree to ignore the lack of convergence, we calculate from his functions for spin 1/2 on a simple cubic lattice in the [001] direction.

$$\frac{\Delta M}{M_0} = -0.14\left(\frac{C}{J}\right)^2, \tag{5}$$

in disagreement with the basic property of the wave functions, as well as with our equation (4). In this circumstance the results on anisotropy must be considered as less than rigorous.

On the subject of anisotropy and spin-orbit effects on the ground state, we may note that the small value $\Delta g = g - 2 = 0.03$ estimated by Brooks [7] for nickel would be appreciably increased if instead of using the estimate 20,000 cm^{-1} for the mean width of the band one used a value in the range 250 to 500 cm^{-1} for the width of the *unfilled* part of the 3d band. The suggested range is from calculations for nickel by Fletcher [1] and Slater [8]. It is the width of the unfilled part of the band which properly enters here, and the suggested change in the numbers gives more scope for larger values of Δg, the loss on averaging presumably being larger than estimated by Brooks.

We wish to thank Dr. Elihu Abrahams for valuable discussion. This work has been supported in part by the O.N.R.

Petros Argyres and C. Kittel

Department of Physics
University of California, Berkeley

References

1. Fletcher, G. C. Proc. Phys. Soc. (London), **A65** (1952) 192.
2. An explicit proof is given by E. Teller, Z. Phys., **62** (1930) 102.
3. Holstein, T. and Primakoff, H. Phys. Rev., **58** (1940) 1098; we have uncovered a typographical error in their expressions for $M^\beta(H)$ on p. 1105; the first one should be multiplied by the factor $1/15\pi = 1/47$ and the second one by the factor $1/2^{9/2}\pi = 1/71$. This correction has kindly been verified by Professor Primakoff, and is used in our equation (1).
4. Van Vleck, J. H. Phys. Rev., **52** (1937) 1178.
5. Herring, C. and Kittel, C. Phys. Rev., **81** (1951) 869.
6. Van Peype, W. F. Physica, **5** (1938) 465.
7. Brooks, H. Phys. Rev., **58** (1940) 909.
8. Slater, J. C. Phys. Rev., **49** (1936) 537.

Thermoelectricity in Metals at Low Temperatures*

It has been suggested in the past, e.g., [1, Preface], that, since the application of quantum theory, the foundations of electron theory in metals are well established and that at best only "refinements of theory" may be looked for. However, as a result of accelerated research since the war, it now appears that this belief may well be unfounded. It is true that the electrical resistance of metals is in large measure well interpreted by the theory, although much remains to be done in quantitative study. On the other hand, definite qualitative discrepancies are found when one turns to the electronic thermal conductivity of simple metals [2; 3; 4; 5] where the theory must be carried to a closer degree of approximation; for example, the electrons responsible for conduction cannot be treated as an entirely "degenerate" gas as suffices for calculation of electrical resistance.

We are at present carrying out an experimental study of thermoelectricity on the alkali and group IB (Cu, Ag, Au) metals over a wide temperature range (down to the liquid helium region). Our experiments are already adequate to show that little detailed agreement can be found with the present theory. The basic predictions of temperature-dependence are not generally fulfilled (cf. also [6]). For even so "ideal" a metal as sodium,

*Received January 26, 1953.

the magnitude of the thermoelectric force is seriously in error, and in the case, for example, of very dilute alloys of Sn in Cu the very striking variation of thermoelectric force contrasts strongly with the theoretical predictions, e.g. [1, p. 223].

Quite apart from the general problem of the adequacy or otherwise of the basic electron theory, we believe that systematic experiments on thermoelectricity at low temperatures in conjunction with measurements of electrical conductivity will yield much information of value on the processes of electron scattering in metals.

D. K. C. MacDonald and W. B. Pearson

Physics Division
National Research Council, Ottawa

References

1. Wilson, A. H. Theory of Metals (Cambridge University Press, 1936).
2. Berman, R. and MacDonald, D. K. C. Proc. Roy. Soc. **A209** (1951) 368; **A211** (1952) 122.
3. Cornish, F. H. and MacDonald, D. K. C. Phil Mag., **43** (1952) 991.
4. Sondheimer, E. H. Proc. Phys. Soc. (London), **A65** (1952) 562.
5. White, G. K. Private communication.
6. Pullan, G. T. Private communication.

The Disordering Reaction in Ni_3Pt*

In an exploration of the nickel-platinum system, Esch and Schneider [1] failed to observe an ordering reaction at the composition Ni_3Pt. Kussmann and Nitka [2] observed superstructure lines in a Ni-Pt alloy of 25.4 atom per cent Pt which had been held at 450°C for a long time. The 31 atom per cent Pt alloy was also found to have a superstructure in later work by Kussmann and Steinwehr [3]. These last authors indicate the disordering temperature to lie somewhere between 500° and 620°C, whereas Bozorth [4] gives 600°C as an approximate figure.

As part of a broader program it seemed desirable to obtain a more precise value for the disordering temperature of Ni_3Pt. A homogeneous alloy of 25.07 atom per cent Pt was held at 500°C for 20 days, enclosed in an argon-filled Pyrex ampoule. Its resistance-temperature curve was obtained at a heating rate of 0.6°C/minute and is shown in *A* of Figure 1. The corresponding cooling curve lies almost directly upon the heating curve, and is not shown. The same sample was then held at 475°C for 26 days. Curve *B* of Figure 1 shows the resistance-temperature behavior upon heating and cooling at 1.3°C/minute.

*Received December 8, 1952.

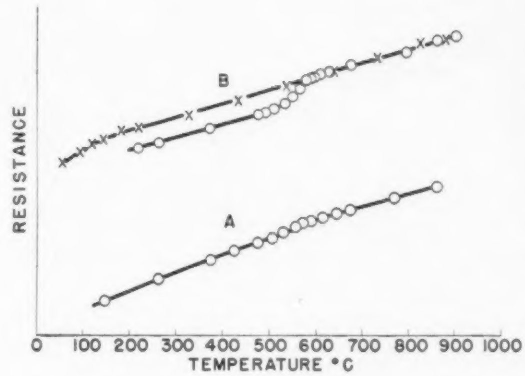

Figure 1

Both experiments agree in fixing the disordering temperature in this alloy at 580° ± 5°C. The resistance of the ordered phase increases rapidly at temperatures just below the critical, as has been observed for Cu_3Au[5]. Although the ascending and descending curves are coincident in both experiments for temperatures above the critical, at lower temperatures there is a wide disparity due to the extreme sluggishness of the ordering reaction. The low-temperature inflection in the descending branch of curve *B* marks the magnetic Curie temperature of the disordered structure. This can be fixed at about 145°C by the present work, and agrees well with the value of 140°C found by Kussmann and Nitka.

The very small inflection marking the disordering in experiment *A* shows that the amount of ordering produced by annealing at 500°C was very small. Nevertheless, X-ray diffraction work by Dr. J. B. Newkirk of this Laboratory revealed faint superlattice lines. The fact that a much larger degree of long-range order can be induced at a lower annealing temperature indicates that a mechanism of nucleation and growth is operative in this ordering reaction.

We thank Dr. D. L. Martin for furnishing the alloy, and Dr. J. B. Newkirk for the X-ray study.

R. A. Oriani and T. S. Jones

General Electric Research Laboratory
The Knolls
Schenectady, New York, U.S.A.

References

1. Esch, U. and Schneider, A. Z. Elektrochem., **50** (1944) 268.
2. Kussmann, A. and Nitka, H. Phys. Z., **39** (1938) 373.
3. Kussmann, A. and Steinwehr, H. E. von. Z. Metallk. **40** (1949) 263.
4. Bozorth, R. M. Ferromagnetism (New York, Van Nostrand Co., 1951).
5. Sykes, C. and Evans, H. J. Inst. Metals, **58** (1936) 255.

BOOK REVIEWS

Structure of Metals. By Charles S. Barrett. Second edition. New York: McGraw-Hill Book Company. 1952. Pp. xvi + 661.

"Let's look it up in BARRETT" is so close to qualifying as a cliche in any laboratory or classroom where metals are studied that it is logical to review the new edition by comparing it with the original one. The reviewer's first reaction, on looking at the new edition, was that it is not nearly as different from the old as one would expect from the progress that has been made since 1943, when the first edition appeared; the importance of crystal imperfections, in particular, has assumed prominence in the last ten years, and a large proportion of the most significant papers that have appeared during that time have been concerned with the various kinds of imperfections.

Closer scutiny, however, shows that while the chapter headings and even the sub-headings are almost unchanged, an immense amount of new material has been added. The extent of the new material is not evident until one looks at the references, very many of which are to papers that have appeared in the last ten years. There are also a substantial number of references to work which had not yet been published when the book went to press.

The emphasis on techniques is still as strong as it was in the first edition, and reference is made to several important new techniques, including the X-ray techniques usually associated with the names of Barrett and of Guinier. The potentialities of the diffraction of neutrons and of atoms are discussed.

It is, of course, impossible for every aspect of the structure of metals to be discussed fully in a single book of manageable size; but Dr. Barrett comes so close to doing so that one is led to look for omissions, although to do so is an expression of ingratitude for a splendid achievement. The most surprising gap is *diffusion*, which is not even mentioned in the index. It is also surprising that the very elegant work of C. S. Smith on the influence of interfacial tension on micro-structure received but a passing reference.

To sum up, the new edition does in 1953 what the first edition did ten years ago, and it has a place both as a textbook and a reference book on the desk of anyone who is interested in why metals behave as they do.

BRUCE CHALMERS

Thermodynamics of Alloys. By John Lumsden. London: The Institute of Metals. 1952. Pp. ix + 384.

Thermodynamics of Alloys by John Lumsden is one of a series of monographs published by The Institute of Metals (London). The book presents a detailed development of thermodynamic theory along with numerous examples showing how free energy expressions can be derived from experimental data and put to use.

To the reader brought up on cycles as the pattern for thermodynamic development, the author's approach by way of atomistics and statistical mechanics may lack some of the close correlation between experiment and equation which is maintained in the traditional approach. On the other hand, the modern physics and chemistry of metals are founded on atomic structure, so that this treatment succeeds in leaving the reader with some feeling for the modern approach. This theme of atomistics is not merely developed in the early chapters and then dropped; it is carried through the whole book, along with traditional treatment.

The first several chapters are devoted to the introduction of thermodynamic quantities and relationships. Every item is derived from first principles in considerable detail. Statistical methods and the concept of randomness are introduced in order to prepare for later development of energy and entropy calculations from models. This part of the text has been very well done. The usual thermodynamic expressions are grafted on this foundation. In discussing heat quantities the author rebukes chemists and metallurgists for continued use of the defined (thermochemical) calorie, yet quotes calories throughout the text and appears to be unaware that a strong bond of attachment lies in the identity of the present calorie (= 4.1840 abs. joules) with that used in 1930 (= 4.1833 int. j.). The author's calorie (= 4.1845 abs. j.) is obsolete.

The second portion of the text begins with the introduction of the thermodynamic quantities specifically associated with solid, liquid, and gaseous metals. This treatment is presented exhaustively and, on the whole, clearly. The introduction of the chemical potential is a bit weak; in some later developments the distinctive symbolism of the chemical potential is not fully utilized. Equilibria in one- and two-component metal systems are treated from both the theoretical

and experimental viewpoints. Here the author has used the commendable device of discussing at great length a limited number of exemplary systems (some twenty in all), so that the reader's attention is directed towards the method. Each item presented is exemplified by complete calculations based on data from the literature. In this the author makes good his promise to show how free energy equations can be used to correlate various physico-chemical measurements.

The last part of the text deals with statistical mechanical calculation of energy, entropy, and free energy. The final chapter is a collection of numerical tables designed to facilitate calculations.

The author has presented his material in a stimulating manner, in such detail that the reader without benefit of tutor should have no difficulty in following the argument. Along with the conventional treatment the author has introduced admitted speculation, but has been meticulous in distinguishing between fact and fancy. The text is recommended for the senior undergraduate level of instruction, but should not be considered as a bibliography of recent research.

F. E. W. Wetmore

Thermodynamics of Alloys. By Carl Wagner. Cambridge, Mass.: Addison-Wesley Press, Inc. 1952. Pp. viii + 161.

Thermodynamics of Alloys by Carl Wagner is a translation (by S. Mellgren and J. H. Westbrook) of the author's treatise "Thermodynamik metallischer Mehrstoffsysteme" from *Handbuch der Metallphysik*, brought up to date with respect to the literature of the past decade. The book is a concise and well-documented summary of thermodynamics of interest to metallurgists. It is clearly not intended for the novice, since the author has assumed an extensive background of general thermodynamics, phase equilibria, and physics of metals. The greater part of the material is presented as a thorough survey of the literature, woven together with an outline of theory and development which touches on only the highlights of the fundamentals. Most of the development is based on traditional thermodynamics, with but scant attention paid to models and statistical mechanics.

The first part of the text is devoted to a sketchy treatment of general thermodynamics, with some extensions relevant to the study of metal systems. Ideal and non-ideal solutions are discussed, electronic constitution is considered; and useful forms of interpolation equations are shown. Order and the basic types of disorder are presented in brief but tidy fashion. The next part introduces thermodynamic relations concerned with the commoner types of phase equilibria. Heats of formation, free energy changes, and activity coefficients are dealt with, both experimentally and theoretically. Finally, equilibria between alloys and melts are treated.

Numerous references are made to experimental results, largely by citing the original literature without comment. It is significant to point out that there are 419 literature sources listed and that reference is made to 180 binary and ternary systems, all within 133 pages of text. The book is recommended as a combined bibliography and outline for research workers and graduate students, but not for undergraduates.

F. E. W. Wetmore

SOME CURRENT PAPERS IN OTHER JOURNALS

Journal of Chemical Physics

December, 1952 (Partial Contents)

Influence of temperature and state of infrared absorption spectra: Methyl iodide. IRVING, L. MADOR and RUTH S. QUINN.

The cut-off phenomena of protein crystallography. ANDREW D. BOOTH.

Infrared studies of mixed crystals: Naphthalene-d_8 in naphthalene. WILLIS B. PERON and GEORGE C. PIMENTEL.

Thermodynamic properties of sodium vapor. A. BENTON and T. H. INATOMI.

Measurement of self-diffusion in solid polymers. F. BUECHE, W. M. CASHIN, and P. DEBYE.

Viscosity, self-diffusion, and allied effects in solid polymers. F. BUECHE.

Enhancement of X-ray induced absorption bands in alkaline earth compounds. JAMES H. SCHULMAN, ROBERT J. GINTHER, and RUSSELL D. KIRK.

The new method of studying lattice defects in solids by Debye absorption: Case semiconductors. MARIE FREYMANN and RENE FREYMANN.

On the anisotropic dissolution and the orientation of the phosphorescent dye, trypaflavin, in the crystal of citric acid. DAIJIRO YAMAMOTO.

Ionic mobility at grain boundaries. P. E. GODDARD and F. URBACH.

Internal rotation in dichlorobutine. YONEZO MORINO, ICHIRO MIYAGAWA and AKIYOSHI WADA.

The effect of hydrogen bonding on the hindered rotation of the hydroxyl group in alcohols. A. V. STUART and G. B. B. M. SUTHERLAND.

Note on the free volume equation of state for hard spheres. LOUIS H. LUND.

Born repulsion and restricted free rotation. JOHN VAN DRANEN.

January, 1953 (Partial Contents)

Study of the structure of quartz, cristobalite, and vitreous silica by reflection in infrared. I. SIMON and H. O. MCMAHON.

Molecular images with the projection microscope. The ionization potential of zinc phthalocyanine. ROBERT GOMER and DONALD A. SPEER.

Analytical method of calculating variable diffusion coefficients. LEWIS D. HALL

Investigation of crystal growth by thermal etching and oriented overgrowth. ALEXANDER SMAKULA and MYRON W. KLEIN.

Electron traps in the thallium-activated potassium chloride phosphor. PETER D. JOHNSON and FERD E. WILLIAMS.

Dielectric dispersion in the microwave region of six tetrasubstituted methanes in the solid state. J. G. POWLES, D. E. WILLIAMS, and C. P. SMYTH.

Crystal structure and lattice energy of Orthorhombic hexachloroethane. YOSHIO SASADA and MASAO ATOJI.

Electronic structure of ferrocene. H. H. JAFFE.

T^2 dependence of the low temperature specific heat of gallium. WARREN DE SORBO.

Note on frequency spectra of simple solids from specific heat data. JENN LIN HWANG.

Perturbations on exciton states in molecular crystals. HARVEY WINSTON.

On the statistical theory of crystallite length. MALCOLM DOLE.

Self-diffusion in the alkali metals. D. K. C. MACDONALD.

Non-adiabatic transitions. HENRY AROESTE.

February, 1953 (Partial Contents)

On the stability of metallo-organic compounds. H. H. JAFFE and G. O. DOAK.

Electric polarizability of polar ions. KAROL J. MYSELS.

Second-order transitions and critical phenomena. ROBERT L. SCOTT.

Investigation of the thermoluminescence of fluorite colored by X-ray irradiation. JOHN J. HILL and JACK ARON.

Neutron diffraction and atom c distribution in liquid lead and liquid bismuth at two temperatures. PAUL C. SHARRAH and G. PEDRO SMITH.

Some overlap integrals involving d orbitals. H. H. JAFFE.

Semiempirical equation for the vapor pressure of liquids as a function of temperature. ARTHUR A. FROST and DONALD R. KALKWARF.

Effect of pressure on self-diffusion in carbon disulfide. R. C. KOELLER and H. G. DRICKAMER.

Quantum-mechanical treatment of virial coefficients. JOHN E. KILPATRICK.

Nuclear magnetic resonance multiplets in liquids. H. S. GUTOWSKY, D. W. MCCALL, and C. P. SLICHTER.

Field emission from nickel surfaces. ROBERT GOMER.

Streaming potentials across glass capillaries for sinusoidal pressure. ROBERT GAY PACKARD.

Electric dipole moments of several molecules from the stark effect. S. N. GHOSH, RALPH TRAMBARULO, and WALTER GORDY.

F-bands in some mixed crystals of the alkali halides. ROBERT J. GNAEDINGER, JR.

Some thermal reactions of the higher iron carbides. ERNST M. COHN and L. J. E. HOFFER.

Photo-ionization as an important secondary process in a low frequency electrodeless discharge. A. P. SAMENA, M. G. BHATAWDEKAR, and N. A. RAMAIAH.

Neutron diffraction study of the NaCl-type modification of ND_4Br and ND_4I. HENRY LEVY and S. W. PETERSON.

Effects of neutron bombardment on a zinc sulfide phosphor. ALAN W. SMITH and JOHN TURKEVICH.

Thermodynamical study of the water-triethylamine system, near its lower critical point. A. BELLEMANS.

Application of the cell method to the statistical thermodynamics of solutions. III. Critical solutions phenomena. A. BELLEMANS.

Investigation of the heat of vaporization of carbon. WILLIAM A. CHUPKA and MARK G. INGHRAM.

Thermoluminescence of ice. EUGENE C. AVERY and LEONARD I. GROSSWEINER.

Approximate formulas for many-center integrals in the theory of molecules and crystals. OLOV LOWDIN.

Absorption band-systems of SiO and GeO in the Schumann Region. H. C. ROWLINSON and R. F. BARROW.

Nuclear quadrupole resonance in some metal chlorides and oxychlorides. H. G. DEHMELT.

Proton magnetic resonance line in liquid crystals. R. D. SPENCE, H. A. MOSES, and P. L. JAIN.
Addendum: Directed valence as a property of determinant wave functions. HOWARD K. ZIMMERMAN, JR., and PIERRE VAN RYSSELBERGHE.
Dissociation energy of fluorine. PAUL W. GILLES and JOHN L. MARGRAVE.
Partition functions for relating entropy to disorder in the melting of pure metals. JOHN F. LEE.

Journal of the Chemical Society

February, 1953 (Partial Contents)
The chemistry of bivalent germanium compounds. Part III. The polarographic behaviour of bivalent germanium. D. A. EVEREST.

Journal of the Institute of Metals, Vol. 20

February, 1953
Atmospheric corrosion and stress-corrosion of aluminium-copper-magnesium and aluminium-magnesium-silicon alloys in the fully heat-treated condition. G. J. METCALFE.
The measurement of the relative hardnesses of fine powder particles. J. B. MATTHEWS.
Crystal fragmentation in aluminium during creep. D. McLEAN.
Grain-boundary slip during creep of aluminium. D. McLEAN.
Intercrystalline corrosion in cast zinc-aluminium alloys. C. W. ROBERTS.
The constitution of chromium-manganese alloys below 1000°C. W. B. PEARSON and W. HUME-ROTHERY.

March, 1953
Symposium on the control of quality in the production of wrought non-ferrous metals and alloys. I.–The control of quality in melting and casting.
The principles of technical control in metallurgical manufacture. A. R. E. SINGER.
The control of quality in the production of brass ingots and billets. MAURICE COOK and C. L. M. COWLEY.
The control of quality in melting and casting copper and high-conductivity copper-base alloys. J. SYKES.
The control of quality in the casting of zinc and zinc alloy rolling slabs and extrusion billets. C. W. ROBERTS and B. WALTERS.
The control of quality in the melting and casting of aluminium alloys for working. R. T. STAPLES and H. J. HURST.
The control of quality in melting and casting magnesium alloys for hot working. R. G. WILKINSON and S. B. HIRST.

Journal of the Mechanics and Physics of Solids, Vol. 1

No. 2, January, 1953
Limit analysis of arches. E. T. ONAT and W. PRAGER.
The stability and strength of stocky beams. A. R. FLINT.
An analysis of the plastic bending of a thin strip in its plane. F. A. GAYDON.
An investigation of the plastic behaviour of metal rods subjected to longitudinal impact. J. D. CAMPBELL.
The autofrettage of thick tubes with free ends. D. G. B. THOMAS.
The mechanism of fatigue of metals. A. K. HEAD.
A note on the back-pull factor in strip-drawing. R. HILL.

No. 3, April, 1953
The combined bending and twisting of thin cylinders in the plastic range. M. P. L. SIEBEL.
Flange buckling in a bent *I*-section beam. J. F. DAVIDSON.
Die pressure in plane strain drawing—comparison of experiment with theory. J. G. WISTREICH.
On the plastic distortion of solid bars by combined bending and twisting. R. HILL and M. P. L. SIEBEL.
On the generality of the cubic creep function. A. J. KENNEDY.
The "elastic hysteresis" of uranium. E. R. W. JONES and W. MUNRO.

Journal of Metals, Vol. 5

No. 1, January, 1953
Evaluation of the pH and conductivity methods of slag control. P. D. S. ST. PIERRE.
Density and hydrogen occlusion of some ferrous metals. H. M. DAVIS and J. H. KEELER.
Bend plane phenomena in the deformation of zinc monocrystals. JOHN GILMAN and T. A. READ.
Preferred orientations in iodide titanium. C. J. McHARGUE and J. P. HAMMOND.
Forging of arc-melted chromium. H. L. GILBERT, H. A. JOHANSEN, and R. G. NELSON.
Flow and fracture characteristics of the aluminum alloy 24S-T4 as affected by strain thermal history. S. I. LIU and E. J. RIPLING.
Effect of alloying elements on the behavior of nitrogen in alpha iron. L. J. DIJKSTRA and R. J. SLADEK.
Systems zirconium-molybdenum and zirconium-wolfram. R. F. DOMAGALA, D. J. McPHERSON, and M. HANSEN.
Measurement of internal boundaries in three-dimensional structure by random sectioning. C. S. SMITH and LESTER GUTTMAN.
Replica method for study of the structure of lead antimony alloys. JEANNE BURBANK.
Torsion texture of 70:30 brass and armco iron. W. A. BACKOFEN and B. B. HUNDY.
Sintering of ultrafine ferromagnetic powders. N. I. ANANTHANARAYANAN and J. F. LIBSCH.
Retained austenite determinations by X-ray methods. B. L. AVERBACH.
Regarding sigma phase formation. D. S. BLOOM and N. J. GRANT.

No. 2, Section 2, February, 1953
Effect of tensile strain at low temperatures on deformation twinning in ingot iron. G. W. GEIL and N. L. CARWILE.
Slip and grain boundary sliding as affected by grain size. N. J. GRANT, I. S. SERVI, and A. CHAUDHURI.
Absolute rate theory applied to rate of growth of pearlite. J. H. FRYE, JR., E. E. STANSBURY, and D. L. McELROY.
Titanium-manganese system. D. J. MAYKUTH, H. R. OGDEN, and R. I. JAFFEE.
Titanium-tungsten and titanium-tantalum systems. D. J. MAYKUTH, H. R. OGDEN, and R. I. JAFFEE.
Microstructure and mechanical properties of iodide titanium. F. C. HOLDEN, H. R. OGDEN, and R. I. JAFFEE.
Titanium-nickel phase diagram. H. MARGOLIN, ELMRAS ENCE, and J. P. NIELSEN.
Titanium-carbon phase diagram. IRVING CADOFF and J. P. NIELSEN.
Constitution of titanium-rich Ti-Cr-Al alloys at 1800° and 1400°F. J. L. TAYLOR and POL DUWEZ.

Mechanism of plastic flow in titanium-determination of slip and twinning elements. F. D. Rosi, C. A. Dube, and B. H. Alexander.
Observation on scaling of iron. W. J. Wrazej.
Mechanical properties of high purity Ti-Al alloys. H. R. Ogden, D. J. Maykuth, W. L. Finlay and R. I. Jaffee.
System zirconium-copper. C. E. Lundin, D. J. McPherson and M. Hansen.
System zirconium-chromium. R. F. Domagala, D. J. McPherson and M. Hansen.
Kinetics of thermal reorientations in cold rolled zirconium. R. K. McGeary and B. Lustman.
Vanadium-oxygen solid solutions. A. U. Seybolt and H. T Sumsion.
Cold rolling and annealing textures of molybdenum single crystals. N. K. Chen and R. Maddin.
Allotropy in the phase $ZrCr_2$. W. Rostoker.
Grain boundary sliding and migration and intercrystalline failure under creep conditions. H. C. Chang and N. J. Grant.

The Philosophical Magazine

January, 1953 (Partial Contents)
Diffusion problems associated with the growth of crystals from dilute solution. Alfred Seeger.
A theoretical examination of the plastic deformation of crystals by glide. J. F. W. Bishop.
Second neighbour interaction in regular binary assemblies. G. M. Bell.
The interaction of dislocations and boundaries. A. K. Head.
The surface of beryl and cadmium iodide crystals. H. F. Kay and Barbara Appelbe.

February, 1953 (Partial Contents)
The properties of KH_2PO_4 below the Curie point. H. M. Barkla and D. M. Finlayson.
Instability and melting of the alkali halides. J. H. C. Thompson.
On the polarization of high energy bremsstrahlung. K. Phillips.
The L. spectra of nickel and copper. Y. Cauchois.
Note on the electronic structure of transition metals. N. F. Mott.
The multiple scattering of protons in thin foils. D. M. Skyrme.
The ionic state of LiH. J. M. Bijvoet and K. Lonsdale.
The observation of polyhedral sub-structures in crystals of silver bromide. J. M. Hedges and J. W. Mitchell.

Revue de Métallurgie, 49^e Année

Influence de l'hydrogene sur les caractéristiques de déformation et de rupture par traction du fer et de l'acier. Paul Bastien et Pierre Azou.
Le durcissement structural des aciers inoxydables austéno-ferritiques. J. Hochmann.
Désulfuration des fontes et déphosphoration des aciers Thomas par les laitiers sodiques. Francis Meunier.
Amincissement électrolytique très poussé et ses applications. I. Epelboin.
Nouveau procédé de fabrication d'acier Thomas calmé de haute qualité. Fr. Meunier et R. Soisson.
Contribution à l'étude des métaux pyrophoriques. L'oxydation du cérium et de l'uranium. Jean Loriers.
Calculs thermodynamiques concernant la nature des zones. Guinier-Preston dans les alliages aluminium-cuivre. J. L. Meijering.
Détails de fabrication de l'étoile en magnésium à l'Exposition du Festival of Britain à Londres. John L. Haughton.

Revue de Métallurgie, 50^e Année

Numéro 1, janvier, 1953
Contrôle des demi-produits par ultrasons. M. Hetzler et A. Michalski.
Sur la mise en évidence d'une relation causale entre défauts de matière et ruptures en service. H. de Leiris.
Intérêt et moyens de détermination de la limite de fatigue à chaud en atmosphère ordinaire ou contrôlée. G. Vidal.
La dureté et la résilience de quelques aciers en fonction des températures de trempe et de revenu. Frederik Herman Willeumier.
Le décapage des aciers spéciaux. G. Batta, L. Scheepers, L. Winandy et G. Dallemagne.
Perfectionnements apportés aux méthodes de préaffinage à l'oxygène pur des fontes Thomas à teneur élevée en silicium. P. Leroy.

Transactions of American Society for Metals

1952
Confidential technical meeting on refractory type materials for high temperature applications, Cleveland, November 24 and 25, 1952.
Creep and rupture of chromium-nickel austenitic stainless steels. E. J. Dulis, G. V. Smith and E. G. Houston.
The effect of composition on the temperature of spontaneous transformation of austenite to martensite in 18-8-type stainless steel. G. H. Eichelman, Jr. and F. C. Hull.
Austenite stability and creep-rupture properties of 18-8 stainless steel. Jack K. Y. Hum and N. J. Grant.
Mechanism of the carburization of some stainless steels. J. B. Giacobbe.
Creep-rupture and recrystallization of monel from 700 to 1700°F. N. J. Grant and A. G. Bucklin.
Influence of grain size on high temperature properties of monel. Paul Shahinian and J. R. Lane.
Recrystallization and grain growth in alpha brass. S. L. Channon and H. L. Walker.
Temperature dependence of the hardness of pure metals. J. H. Westbrook.
The effect of dispersions on the tensile properties of aluminum-copper alloys. R. B. Shaw, L. A. Shepard, C. D. Starr and J. E. Dorn.
Effect of alloying elements on grain boundary relaxation in alpha solid solutions of aluminum. C. D. Starr, E. C. Vicars, A. Goldberg, and J. E. Dorn.
Properties of some hydrogen-sintered, binary molybdenum alloys. W. L. Bruckhart, M. H. LaChance, C. M. Craighead, and R. I. Jaffee.
Recrystallization of wrought hydrogen-sintered molybdenum and its alloys. M. H. LaChance, W. L. Bruckart, C. M. Craighead, and R. I. Jaffee.
The effect of temperature on the rolling texture of plastically deformed low carbon steel strip. N. P. Goss.
Accelerated strain aging of commercial sheet steels. L. R. Shoenberger and E. J. Paliwoda.
Some properties of a nodular iron at elevated temperatures. M. S. Saunders and M. J. Sinnott.

Hardness of various steels at elevated temperatures. F. Garofalo, P. R. Malenock, and G. V. Smith.

Microconstituents in high temperature alloys. H. J. Beattie, Jr., and F. L. VerSnyder.

Sigma formation and its effect on the impact properties of iron-nickel-chromium alloys. A. M. Talbot and D. E. Furman.

The electrolytic separation and some properties of austenite and sigma in 18-8-3-1 chromium-nickel-molybdenum-titanium-steel. T. P. Hoar and K. W. J. Bowen.

Effect of carbon content on 18-4-1 high speed steel. Arthur H. Grobe and George A. Roberts.

The effect of silicon on the tempering of martensite. A. G. Allten and P. Payson.

Microstructure—1952 Edward deMille Campbell Memorial Lecture. Cyril Stanley Smith.

The mechanism and kinetics of the first stage of tempering. C. S. Roberts, B. L. Averbach, and Morris Cohen.

The effect of quenching and tempering on residual stresses in manganese oil hardening tool steel. Harold Jack Snyder.

A study of the mechanism of the delayed yield phenomena. T. Vreeland, Jr., D. S. Wood, and D. S. Clark.

X-ray measurement of residual stress in hardened high carbon steel. A. L. Christenson and E. S. Rowland.

The indium-arsenic system. T. S. Liu and E. A. Peretti.

Plastic stress-strain relations of alcoa 14S-T6 for variable biaxial stress ratios. Joseph Marin, L. W. Hu, and J. F. Hamburg.

The endurance limit of temper-brittle steel. R. D. Chapman and W. E. Jominy.

The effect of various heat treating cycles upon temper brittleness. L. D. Jaffee, D. C. Buffum, and F. L. Carr.

Effect of hardness on the level of the impact energy curve for temper-brittle and unembrittled steel. F. L. Carr, Manuel Goldman, L. D. Jaffe, and D. C. Buffum.

Correlation of machinability with inclusion characteristics in resulphurized bessemer steels. L. H. Van Vlack.

Determination of oxygen in metals and metal oxides by the isotopic method. A. D. Kirshenbaum and A. V. Grosse.

The influence of Boron on case hardenability in alloy car burizing steels. C. F. Jatczak and E. S. Rowland.

The role of anelasticity in creep, tension, and relaxation behavior. J. D. Lubahn.

The determination of the elastic constants of metals by the ultrasonic pulse technique. Myron B. Reynolds.

Consumable-electrode arc melting of zirconium metal. W. W. Stephens, H. L. Gilbert, and R. A. Beall.

Some properties of high purity zirconium and dilute alloys with oxygen. R. M. Treco.

The zirconium-nickel phase diagram. E. T. Hayes, A. H. Roberson, and O. G. Paasche.

The system zirconium-silicon. C. E. Lundin, D. J. McPherson, and M. Hansen.

The system zirconium-tin. D. J. McPherson and M. Hansen.

The martensite transformation temperature in titanium binary alloys. Pol Duwez.

The influence of insoluble phases on the machinability of titanium. R. M. Goldhoff, H. L. Shaw, C. M. Craighead, and R. I. Jaffee.

Mechanical properties and strain aging effects in titanium. F. D. Rosi and F. C. Perkins.

Mechanical properties, including fatigue of titanium-base alloys RC-130-B and Ti-150-A at very low temperatures. S. M. Bishop, J. W. Spretnak, and M. G. Fontana.

The titanium-oxygen system. E. S. Bumps, H. D. Kessler, and M. Hansen.

The order-disorder transformation viewed as a classical phase change. F. N. Rhines and J. B. Newkirk.

An end-quench test for determining the hardenability of carburized steels. F. X. Kayser, R. F. Thomson, and A. L. Boegehold.

Transverse mechanical properties in an SAE 1045 forging steel. A. H. Grobe, Cyril Wells, and R. F. Mehl.

ANISOTROPIC ELASTICITY WITH APPLICATIONS TO DISLOCATION THEORY*

J. D. ESHELBY,† W. T. READ,‡ and W. SHOCKLEY‡

The general solution of the elastic equations for an arbitrary homogeneous anisotropic solid is found for the case where the elastic state is independent of one (say x_3) of the three Cartesian coordinates x_1, x_2, x_3. Three complex variables $z_{(l)} = x_1 + p_{(l)} x_2$ ($l = 1, 2, 3$) are introduced, the $p_{(l)}$ being complex parameters determined by the elastic constants. The components of the displacement (u_1, u_2, u_3) can be expressed as linear combinations of three analytic functions, one of $z_{(1)}$, one of $z_{(2)}$, and one of $z_{(3)}$. The particular form of solution which gives a dislocation along the x_3-axis with arbitrary Burgers vector (a_1, a_2, a_3) is found. (The solution for a uniform distribution of body force along the x_3-axis appears as a by-product.) As is well known, for isotropy we have $u_3 = 0$ for an edge dislocation and $u_1 = 0$, $u_2 = 0$ for a screw dislocation. This is not true in the anisotropic case unless the $x_1 x_2$ plane is a plane of symmetry. Two cases are discussed in detail, a screw dislocation running perpendicular to a symmetry plane of an otherwise arbitrary crystal, and an edge dislocation running parallel to a fourfold axis of a cubic crystal.

L'ÉLASTICITÉ ANISOTROPE ET SON APPLICATION À LA THÉORIE DES DISLOCATIONS

La solution générale des équations de l'élasticité pour un solide anisotrope, homogène est trouvée dans le cas où l'état élastique est indépendant d'une (mettons x_3) des trois coordonnées cartésiennes x_1, x_2, x_3. Trois variables complexes $z_{(l)} = x_1 + p_{(l)}x_2$, ($l = 1, 2, 3$) sont introduites, les $p_{(l)}$ étant des paramètres complexes déterminés par les constantes d'élasticité. Les composantes du déplacement (u_1, u_2, u_3) peuvent être exprimées comme des combinaisons linéaires de trois fonctions analytiques, une de $z_{(1)}$, une de $z_{(2)}$, et une de $z_{(3)}$. Une forme particulière de solution est trouvée, elle donne une dislocation le long de l'axe x_3 avec un vecteur de Burgers arbitraire (a_1, a_2, a_3). (En même temps apparait, comme sous-produit, la solution dans le cas d'une distribution uniforme de la force interne le long de l'axe x_3). Dans le cas d'isotropie, $u_3 = 0$ pour une dislocation-coin et $u_1 = 0$, $u_2 = 0$ pour une dislocation-vis. Ceci n'est pas vrai dans le cas d'anisotropie, à moins que le plan $x_1 x_2$ soit un plan de symétrie. Deux cas sont discutés en détail, une dislocation-vis perpendiculaire à un plan de symétrie d'un cristal, qui est d'autre part quelconque, et une dislocation-coin parallèle à un axe quaternaire d'un cristal cubique.

ANISOTROPE ELASTIZITÄT MIT ANWENDUNGEN AUF DIE THEORIE DER VERSETZUNGEN

Die allgemeine Lösung der Elastizitätsgleichungen für einen willkürlichen anisotropen Festkörper wird für den Fall angegeben, in dem der Elastizitätszustand von einer (zB. x_3) der drei Cartesischen Koordinaten x_1, x_2, x_3 unabhängig ist. Es werden drei komplexe Veränderliche $z_{(l)} = x_1 + p_{(l)} x_2$ ($l = 1, 2, 3$) eingeführt, wobei die $p_{(l)}$ komplexe Parameter sind, die durch die Elastizitätskonstanten bestimmt sind. Die Verschiebungskomponenten (u_1, u_2, u_3) können als lineare Kombinationen von drei analytischen Funktionen, nämlich als eine von z_1, eine von z_2 und eine von z_3, ausgedrückt werden. Eine spezielle Form der Lösung wurde für eine Versetzung in der x_3-Achse mit willkürlichem Burgers-Vektor (a_1, a_2, a_3) gefunden. (Als Nebenresultat ergibt sich die Lösung für eine gleichförmige Verteilung der Kraft entlang der x_3-Achse.) Bekanntlich gilt im isotropen Fall für eine Stufenversetzung $u_3 = 0$ und für eine Schraubenversetzung $u_1 = 0$ und $u_2 = 0$. Im anisotropen Fall trifft das nicht zu, ausser wenn die $x_1 x_2$ Ebene die Symmetrieebene ist. Zwei Fälle werden eingehend diskutiert: (1) Eine Schraubenversetzung, die senkrecht zu einer Symmetrieebene eines sonst willkürlichen Kristalles verläuft, und (2) Eine Stufenversetzung, die parallel einer der vierfachen Achsen eines kubischen Kristalles verläuft.

1. Introduction

This paper develops the general theory of anisotropic elasticity for a three-dimensional state of stress in which the stress is independent of one Cartesian coordinate. The general theory is applied to the dislocation theory of metals, which has reached a state where the refinement of allowing for anisotropy is sometimes justified. However, many other practical applications of the general elasticity results are possible, particularly in engineering stress analysis where the anisotropy of the material is important. The application in the present paper, however, is restricted to dislocation theory.

The problem has already been considered for edge dislocations in a previous paper [1].§ Unfortunately the assumption there that the problem can always be treated as one of plane strain is not justified unless the dislocation line runs perpendicular to a symmetry plane. In general the solutions given in [1] represent an edge dislocation plus a concentrated force at the origin along the dislocation line.

*Received November 24, 1952.

†Department of Physics, University of Illinois, Urbana, Illinois, U.S.A.

‡Bell Telephone Laboratories, Murray Hill, New Jersey, U.S.A.

§We take the opportunity to correct some errors in [1]. On p. 904, line 5, *for* s'_{41} *read* s_{41}; p. 905, line 6 from below, *for* f_n *read* f'_n; p. 906, equation (8), *for* y^2 *read* $\lambda^2_1 y^2$, $\lambda^2_2 y^2$ respectively in the arguments of the first and second logarithms; p. 907, lines 4, 2 from below *for* (6) or (8) . . . (10) *read* (7) or (9) . . . (11); p. 910, line 8 from below, *for* case *read* ease.

In the following sections we determine successively:

(i) The most general three-dimensional state of stress in an elastically distorted region when the stress is independent of one Cartesian coordinate.

(ii) The most general analytic (continuous, continuously differentiable and single valued) distribution of stress in the region surrounding a cylinder parallel to the axis of constant stress. The excluded region may be a hole through the crystal or a line imperfection, i.e. a bad region in the sense used by Read and Shockley [2] and Frank [3].

(iii) The state of stress around a dislocation.

2. Notation and Basic Relations

Unless the coordinate axes are simply related to the axes of a crystal of high symmetry, the stress-strain relations will involve a large number of non-vanishing elastic constants. In the general case, which we shall treat, there are twenty-one elastic constants relating the six stress components and the six strain components. Clearly, unless some shorthand notation is employed, the formulas become hopelessly cumbersome and the meaning is obscured. We shall use the simple three-dimensional Cartesian tensor notation as a means of expressing lengthy relations in a concise and easily comprehended form.

Calling the rectangular coordinates x_1, x_2, and x_3 instead of x, y, z, we suppose that the elastic state is independent of x_3. Let u_i be the ith component of displacement where i can be 1, 2, or 3. *Italic subscripts* $i, j, k, \ldots$ will take the range 1, 2, 3 and *Greek subscripts* α, β, the range 1, 2. The component of stress acting in the ith direction on the plane normal to the jth axis is τ_{ij}. The strains e_{ij} are related to the partial derivatives of displacement by

$$e_{ij} = \tfrac{1}{2}\left[\frac{\partial u_i}{\partial x_j} + \frac{\partial u_j}{\partial x_i}\right]. \tag{2.1}$$

The components of the strain tensor (2.1) are to be distinguished from the usual engineering strains which are not tensor components; they are equal to e_{ij} for $i = j$, but have twice the value (2.1) for $i \neq j$.

We shall use the customary summation convention, according to which summation is understood to be carried out over repeated ("dummy") subscripts.

The most general linear relation between stress and strain involves a fourth-order tensor C_{ijkl} and is given by

$$\tau_{ij} = C_{ijkl}\, e_{kl}. \tag{2.2}$$

Considerations of symmetry and energy conservation require that

$$C_{ijkl} = C_{jikl} = C_{ijlk} = C_{klij}, \tag{2.3}$$

these relations being responsible for the fact that there are only twenty-one different elastic constants. The constants can be transformed from one set of axes x_i to another set x'_i by the relation

$$C'_{pqrs} = \cos(x_i, x'_p)\cos(x_j, x'_q)\cos(x_k, x'_r)\cos(x_l, x'_s)C_{ijkl}. \tag{2.4}$$

When the coordinate axes are along the axes of a cubic crystal all but three of the different elastic constants vanish.

3. Equilibrium Conditions

We shall first determine the most general solution for an equilibrium state of stress in a region of elastic distortion. In the present section the conditions of equilibrium will be investigated and formulas derived for the force on an internal surface. In the following section the equilibrium equations will be expressed in terms of displacement and the most general solution for both displacement and stress obtained. (By formulating the problem in terms of displacement we avoid having to deal with the compatibility conditions.) The expression for the force on an internal surface will be needed in section 5 in interpreting the general expression for an analytic distribution of stress.

We begin by considering the equilibrium of an element of material in the crystal. Since nothing varies with x_3 we take a cylindrical element with axis parallel to the x_3-axis. Let A be the cross section of the cylinder in the $x_1 x_2$ plane and let C be the closed curve bounding A. The force (per unit length) exerted across C by the material outside the cylinder is

$$F_i = \int_C \tau_{i\beta}\, n_\beta\, dc. \tag{3.1}$$

where n_1 and n_2 are components of the normal to C.

For the material inside C to be in equilibrium, it is necessary that an external force $-F_i$ should be exerted on the cylinder. We now distinguish two cases:

1. The curve C is a reducible circuit; that is, C can be shrunk to a point without passing outside the material or cutting through a singularity in the stress distribution.

2. The curve C is not a reducible circuit; instead it encloses either a hole through the material in which external forces could be applied, or a bad

region where the theory to be developed does not apply.

In case 1, clearly the resultant force F_i must vanish, since there is no physical mechanism for applying an external force in the interior of a crystal. Thus for any choice of the circuit C which does not enclose a hole or singularity, the line integral in (3.1) vanishes. This implies the existence of a vector having components ϕ_i defined throughout the good region by

$$\begin{aligned} \frac{\partial \phi_i}{\partial x_1} &= \tau_{i2}\,, \\ \frac{\partial \phi_i}{\partial x_2} &= -\,\tau_{i1}\,, \end{aligned} \tag{3.2}$$

from which the equilibrium conditions for stress

$$\frac{\partial \tau_{i\beta}}{\partial x_\beta} = 0 \tag{3.3}$$

are readily obtained.

Conversely, if we begin with the equilibrium equations (3.3), we can prove that the functions ϕ_i exist and that $F_i = 0$ for any reducible circuit.

We now consider case 2 above, where C encloses a hole or singularity. Assume that C does not pass through any singular points, so that the equilibrium equations are satisfied and the ϕ_i exist at all points on C. Then (3.1) gives

$$F_i = \int_C d\phi_i = \Delta\phi_i \tag{3.4}$$

where $\Delta\phi_i$ is the change in $\Delta\phi_i$ in going once around the curve C. When $\Delta\phi_i \neq 0$, ϕ_i is multiple valued. Alternatively we may make a mathematical cut in the $x_1 x_2$ plane; ϕ_i is then single valued and has a discontinuity $\Delta\phi_i$ across the cut.

To summarize: every equilibrium state of stress can be represented by a vector with components ϕ_i, every set of three functions ϕ_i represents an equilibrium state of stress, and the discontinuities in the functions ϕ_i correspond to a resultant force on an internal surface.

Rather than derive the differential equations for the ϕ_i (which would involve the compatibility conditions), in the next section we shall formulate the problem in terms of displacement, which has a more direct physical meaning, and use the equations of equilibrium (3.1). The ϕ_i are then obtained by integration.

However, there are some special cases in which it is convenient mathematically to represent the state of stress in the $x_1 x_2$ plane by a function ϕ called the Airy stress function, which is related to ϕ_1 and ϕ_2 by

$$\frac{\partial \phi}{\partial x_2} = -\,\phi_1, \quad \frac{\partial \phi}{\partial x_1} = \phi_2\,. \tag{3.5}$$

The relations (3.5) and the existence of ϕ follow from (3.2) and the condition $\tau_{12} = \tau_{21}$.

Only in special cases can ϕ be treated independently of ϕ_3. In such cases it is sometimes more convenient to express the state of stress in the $x_1 x_2$ plane in terms of the single function ϕ rather than in terms of the two functions u_1 and u_2.

4. General Solution

In this section we shall determine the most general solution for the displacement and thence for the stress in a region of elastic distortion. The condition of elastic distortion necessarily excludes singularities in stress, so that at all points in the elastic region the equations of equilibrium (3.1) hold. By expressing stress in terms of displacement in the three equilibrium equations, we obtain three equations for the three components of displacement.

First substituting (2.1) in (2.2) we have

$$\tau_{ij} = \tfrac{1}{2}\, C_{ijkl} \frac{\partial u_k}{\partial x_l} + \tfrac{1}{2}\, C_{ijkl} \frac{\partial u_l}{\partial x_k}\,. \tag{4.1}$$

However, by (2.3) the third and fourth subscripts of the elastic constants can be interchanged so that

$$\tau_{ij} = \tfrac{1}{2}\, C_{ijkl} \frac{\partial u_k}{\partial x_l} + \tfrac{1}{2}\, C_{ijlk} \frac{\partial u_l}{\partial x_k}\,, \tag{4.2}$$

where the two terms on the right are seen to be equal since the dummy subscripts k and l go through the same set of values. Therefore, taking account of the fact that nothing varies with x_3, we have

$$\tau_{i\beta} = C_{i\beta k\alpha} \frac{\partial u_k}{\partial x_\alpha} \tag{4.3}$$

and equation (3.3) becomes

$$C_{i\beta k\alpha} \frac{\partial^2 u_k}{\partial x_\alpha \partial x_\beta} = 0. \tag{4.4}$$

This is a set of three second-order linear partial differential equations, the solution of which is given by an arbitrary function of a linear combination of the variables x_1 and x_2. Thus,

$$u_k = A_k f[p_1 x_1 + p_2 x_2] = A_k f[p_\alpha x_\alpha] \tag{4.5}$$

where the A's and p's are determined by substituting into (3.7) which gives

$$A_k\, p_\alpha\, p_\beta\, C_{i\beta k\alpha} = 0. \tag{4.6}$$

This equation has a solution for the vector A_1, A_2, A_3 only if the determinant of the coefficients vanishes. This determinant is a sixth-order polynomial in p_1 and p_2. It is obvious that in (4.5) we

can always take $p_1 = 1$; (4.6) is then a sixth-order equation for p_2. It is shown in the appendix that since the energy density is always positive the roots are necessarily complex, and since the coefficients are real they occur in conjugate pairs. The vector $A_{(l)k}$ corresponding to a given root $p_{(l)}$ is in general complex. The condition that the displacements be real requires that the imaginary parts of corresponding pairs of solutions shall cancel. Thus we take only three roots $p_{(1)}$, $p_{(2)}$, and $p_{(3)}$, no two of which are complex conjugates, and set

$$(4.7) \qquad u_k = \sum_{l=1}^{3} A_{(l)k} f_{(l)}[z_{(l)}]$$

where

$$z_{(l)} = x_1 + p_{(l)} x_2 .$$

It will be understood throughout that where complex expressions are used only the real part is to be taken. The subscripts in parentheses distinguish the three individual solutions corresponding to the three different values $p_{(1)}$, $p_{(2)}$, $p_{(3)}$ and are not to be confused with the subscripts denoting coordinate axes.

From (4.3) and (4.7) we find that the most general equilibrium distribution of stress in the elastic region is

$$(4.8) \quad \tau_{ij} = \sum_{l=1}^{3} [C_{ijk1} + p_{(l)} C_{ijk2}] A_{(l)k} \frac{df_{(l)}}{dz_{(l)}} [z_{(l)}]$$

and the corresponding functions ϕ_i, obtained by substituting (4.8) in (3.2) and integrating, are

$$(4.9) \quad \phi_i = \sum_{l=1}^{3} [C_{i2k1} + p_{(l)} C_{i2k2}] A_{(l)k} f_{(l)}[z_{(l)}] .$$

Alternatively we may verify directly that (4.9) agrees with the first of equations (3.2); that it also satisfies the second of (3.2) follows from (4.6) which now takes the form

$$A_k[C_{i1k1} + p_{(l)} C_{i1k2} + p_{(l)} C_{i2k1} + p_{(l)}^2 C_{i2k2}] = 0.$$

We shall find below that particular solutions of (4.7) can be found which represent dislocations lying on the x_3-axis or localized forces applied to the x_3-axis. In general to express any such situation it is necessary to combine terms arising from all three values of l. Thus in the subsequent analysis, solutions will be represented as sums over the three roots.

5. Continuous Distribution of Stress Surrounding a Singularity

In the previous sections we obtained a general solution valid at all points in a region where the distortion is elastic, i.e. in a good region. No restrictions were placed on the shape of the good region, nor was it assumed that the stresses were continuous. Actually the equilibrium equations, which hold in a good region, require that the tractions be continuous across any surface but leave open the possibility of a discontinuity in the normal stress on a plane perpendicular to the surface of discontinuity.

In the present section we shall assume that the distortion is elastic everywhere in the crystal except in a cylindrical region along the x_3-axis. This excluded region may be either a hole through the crystal or a line imperfection, or bad region, of the type discussed in section 1. The good region is therefore bounded by two cylindrical surfaces, the outer one being the external surface of the crystal.

In this section we shall also introduce the requirement that the stress in the good region be continuous, single valued and have continuous derivatives. We then investigate the conditions imposed on the arbitrary functions $f_{(l)}\,[z_{(l)}]$ of the last section by the above conditions ((ii) of section 1) on the stress in the good region, and the shape of the good region. We shall reserve for the appendix the discussion of the most general solution consistent with these requirements, and use expressions for $f_{(l)}$ sufficient for the needs of physical dislocation theory.

From (4.8) we see that if τ_{ij} is to be analytic and single valued in a region of the crystal, it is sufficient (though not necessary, see the appendix) that $df_{(l)}[z_{(l)}]/dz_{(l)}$ be an analytic single-valued function in the corresponding region of the complex $z_{(l)}$ plane, which will be bounded by two closed curves corresponding to the inner and outer boundaries of the actual region in the $x_1 x_2$ plane. Therefore by Laurent's theorem $df_{(l)}[z_{(l)}]/dz_{(l)}$ can be expressed as a power series with both positive and negative powers of $z_{(l)}$. Hence

$$(5.1) \quad f_{(l)}[z_{(l)}] = \frac{D_{(l)}}{\pm\, 2\pi i} \ln z_{(l)} + \sum_{n=-\infty}^{\infty} C_{(l)n} z_{(l)}^{\,n}$$

where for convenience in connection with (5.2) below the sign of $2\pi i$ is taken to be same as the sign of the imaginary part of $p_{(l)}$.*

It is at once seen that $f_{(l)}[z_{(l)}]$ is not a single-valued function since it changes by $D_{(l)}$ per revolution about the x_3-axis, the circuit being taken in the positive direction. Thus if we make a cut joining the

*A positive circuit around the origin of the $x_1 x_2$ plane is a $\pm$ circuit in the $z_{(l)}$ plane depending on the sign of the imaginary part of $p_{(l)}$. Note that there is no summation over l. Such a summation will always be indicated explicitly.

inner and outer boundaries there will be a discontinuity

$$(5.2) \qquad \Delta u_k = \sum_{l=1}^{3} A_{(l)k}\, D_{(l)}$$

in the displacement across it.

All the other terms in (5.1) give single-valued displacements.

It is also seen, from (3.4) and (4.9), that the logarithmic term in (5.1) is the only one which contributes to the resultant force on the internal boundary

$$(5.3) \quad F_i = \Delta\phi_i = \sum_{l=1}^{3} [C_{i2k1} + p_{(l)}\, C_{i2k2}]\, A_{(l)k}\, D_{(l)}.$$

From (4.8) the stress corresponding to (5.1) is found to be

$$\tau_{ij} = \sum_{l=1}^{3} [C_{ijk1} + p_{(l)}\, C_{ijk2}]\, A_{(l)k}$$

$$(5.4) \qquad \left\{ \frac{D_{(l)}}{\pm 2\pi i}\, \frac{1}{z_{(l)}} + \sum_{n=-\infty}^{\infty} nC_{(l)n}\, z_{(l)}{}^{n-1} \right\}.$$

From (5.4) it is seen that each value of l corresponds to two linearly independent stress distributions (two because the constants are complex) each giving a discontinuity in displacement and a force. In general all three l's are required to represent any state of stress, solutions for individual l's having no simple physical meaning. We shall later consider a simple case where two l's can represent the state of stress in the $x_1\, x_2$ plane, the third l giving the stress components in the x_3 direction.

In the next section we shall discuss the terms in $D_{(l)}$ which represent dislocations and uniform distributions of force along the x_3-axis. The terms in $C_{(l)\pm n}$ enable us to satisfy arbitrary boundary conditions on the inner and outer cylindrical surfaces. The C's will not give a net force on a boundary (this is provided for by the D's) but in general the $C_{(l)-1}$ give a net couple on it.

For certain values of the elastic constants equation (4.6) may give multiple roots for p_2. Such cases are most easily dealt with by passing to the limit from a neighboring set of elastic constants for which this is not so (cf. [1]).

6. Dislocations

In this section we shall assume that the excluded cylindrical region is a line imperfection, or bad region. This requires the vanishing of the resultant force F_i exerted across the boundary between the good and bad regions since there is no mechanism whereby an external force could be applied to the bad region to maintain equilibrium.

In the previous sections we have found that for stress fields independent of x_3 the discontinuity in displacement is a constant. As is well known, in an actual crystal this constant must either vanish or be equal to a *lattice translation or slip vector* defined as *the shortest vector connecting two atoms in the crystal structure which have identical surroundings*. In a face-centered cubic metal, there are six possible slip vectors, one in each of the six [110] directions; in a body-centered cubic structure there are four possible slip vectors corresponding to the four [111] directions.

When the discontinuity in displacement vanishes, the bad region is either an extra row of atoms or a missing row. Since such a situation would be unlikely to occur unless two unlike dislocations on adjacent slip planes ran together we shall consider this as a special case of a dislocation array and proceed to investigate the stress field around a dislocation.

If the slip vector is a_k, the conditions for a dislocation are

$$(6.1) \qquad \begin{aligned} \Delta u_k &= a_k\,, \\ F_i &= 0\,. \end{aligned}$$

We should also see whether there is a net couple on the inner boundary. It may be shown to vanish however we choose the $D_{(l)}$ (cf. [1]).
From (5.2) and (5.3), conditions (6.1) become

$$(6.2) \quad a_i = \sum_{l=1}^{3} A_{(l)i}\, D_{(l)} \qquad (i = 1, 2, 3),$$

$$(6.3) \quad 0 = \sum_{l=1}^{3} A_{(l)k}\, D_{(l)}[C_{i2k1} + p_{(l)}\, C_{i2k2}] \qquad (i = 1, 2, 3).$$

Equations (6.2) and (6.3) are a system of six linear equations for the determination of the real and imaginary parts of $D_{(1)}$, $D_{(2)}$, and $D_{(3)}$. Thus in general all three l's are required to represent any simple dislocation. Similarly all three l's are required in the general case to represent a concentrated internal force at the origin.

In [1] it was assumed that a solution could always be found by taking $u_3 = 0$, that is, $A_3 = 0$. This is allowable in the sense that it will certainly represent some state of stress. For an edge dislocation it is then possible to prescribe the conditions $\Delta u_1 = a_1$, $\Delta u_2 = a_2$, $F_1 = 0$, $F_2 = 0$. F_3 is then determined and in general does not vanish unless $C_{\alpha\beta k3} = 0$. Hence, except when the $x_1\, x_2$ plane is a symmetry plane, the expressions in [1] represent the disloca-

tions they purport to, plus a force along the x_3-axis necessary to maintain a state with $u_3 = 0$. The presence of F_3 was overlooked in the original paper.

In an infinite body with the requirement that the stresses shall vanish at infinity, the $C_{(D)n}$ with $n > 0$ are excluded and so also is the more general type of dislocation considered in the appendix. Then along any straight line through the origin the stresses can be expressed as a series of inverse powers of $r = (x_1^2 + x_1^2)^{\frac{1}{2}}$. The term in r^{-1} is fixed by the $D_{(D)}$ and the higher terms by the $C_{(D)n}$, $n < 0$, that is, by conditions at the inner boundary. Thus at large distances from the origin the state of stress is determined solely by the Burgers vector.

By adjusting the $C_{(D)\pm n}$ we can make the outer surface of the cylinder stress-free. If we cut out a cylinder of finite length there will be a distribution of stress on the ends. This will have zero resultant, but not in general zero moment [4]. When these end stresses are removed the cylinder will thus be twisted and the u_i will not be independent of x_3 even if end effects are neglected.

7. Dislocations in Special Cases

In this section we consider the case where the $x_1 x_2$ plane is a plane of symmetry. Then the problem is considerably simplified in that the components of stress in the $x_1 x_2$ plane can be expressed in terms of derivatives of u_1 and u_2 only, and the stress components in the x_3 direction in terms of u_3 only; that is, $C_{\alpha\beta k3} = 0$. This means that the matrix expression for A_k splits so that A_3 does not mix with A_1 and A_2, or in other terms, $A_{(3)1} = A_{(3)2} = A_{(1)3} = A_{(2)3} = 0$.

We shall treat u_3 first for the general case where $x_1 x_2$ is a plane of crystal symmetry and then deal with u_1 and u_2 together for the more specialized case where the x_3-axis is a crystal axis in a cubic crystal. The latter results are implicit in [1], but we here carry the calculations out explicitly and reach an expression for the shear stress on any plane parallel to the slip plane of the dislocation. A knowledge of this quantity is sufficient for many problems; for example, determination of the possible stable arrangements of two-dimensional arrays of dislocations or calculation of the energies of single dislocations [1] and grain boundaries [5].

(a) *Screw Dislocation in a Simple Case*

It is convenient here to adopt a conventional notation, replacing the fourth-order tensor C_{ijkl} by the elastic constants $c_{11}, c_{12}, c_{13}, \ldots, c_{66}$, where the pair of subscripts 11 is replaced by 1, 22 by 2, 33 by 3, 23 by 4, 13 by 5, and 12 by 6. Then in the present symmetrical case where $c_{14} = c_{15} = c_{16} = c_{24} = c_{25} = c_{26} = 0$, we have

$$\tau_{23} = c_{44}\frac{\partial u_3}{\partial x_2} + c_{45}\frac{\partial u_3}{\partial x_1}, \qquad (7.1)$$

$$\tau_{13} = c_{54}\frac{\partial u_3}{\partial x_2} + c_{55}\frac{\partial u_3}{\partial x_1}.$$

Substituting these into the equilibrium equation in the x_3 direction

$$\frac{\partial \tau_{13}}{\partial x_1} + \frac{\partial \tau_{23}}{\partial x_2} = 0 \qquad (7.2)$$

gives an equation corresponding to (3.9) of the general case:

$$c_{55}\frac{\partial^2 u_3}{\partial x_1^2} + 2c_{45}\frac{\partial^2 u_3}{\partial x_1 \partial x_2} + c_{44}\frac{\partial^2 u_3}{\partial x_2^2} = 0, \qquad (7.3)$$

the solution to which is an arbitrary function of $x_1 + px_2$ where p is complex and is a root of

$$c_{44}\, p^2 + 2\, c_{45}\, p + c_{55} = 0. \qquad (7.4)$$

The two roots of (7.4) are complex conjugates and the condition that u_3 be real requires that the two solutions also be complex conjugates. We therefore take either root and set

$$u_3 = f(x_1 + px_2), \qquad (7.5)$$

where it is understood that only the real part of the complex right-hand side is to be taken. The condition that the stress be analytic requires that the arbitrary function be of the form (4.2) where only the logarithmic term need be considered here. We therefore express u_3 in terms of the complex constant D,

$$u_3 = \frac{D}{\pm 2\pi i}\ln(x_1 + px_2). \qquad (7.6)$$

If a_3 is the component of the slip vector in the x_3 direction we have: real part of $D = a_3$. From (4.9) the stress function ϕ_3 is

$$\phi_3 = [C_{3231} + p\, C_{3232}]\, f(x_1 + px_2),$$

or in the present notation

$$\phi_3 = [c_{45} + p\, c_{44}]\, f(x_1 + px_2). \qquad (7.7)$$

Therefore the vanishing of the net force $F_3 = \Delta\phi_3$ in the x_3 direction gives

$$D(c_{45} + p\, c_{44}) = 0 \qquad (7.8)$$

which is the third of equations (6.3) for the present case and determines the imaginary part of D.

The stresses are then readily determined from (7.1).

When the axis of the dislocation is parallel to a crystal axis in a cubic crystal, $c_{45} = 0$ and $c_{55} = c_{44}$, so that equation (7.3) reduces to the Laplace equation, and u_3 and the associated stresses are given by the same formulas as in the isotropic case, the constant c_{44} being used for the shear modulus [6]. This leads to $z = x_1 + ix_2$ so that $\ln z = \ln r + i\theta$ in cylindrical coordinates. The first term represents a concentrated force along the x_3-axis, the second a screw dislocation. Another simple example of practical interest is a pure screw dislocation parallel to a $\langle 110 \rangle$ direction in face centered cubic. Taking the x_1- and x_2-axes parallel to [110] and [011] respectively and using the elastic constants c_{11}, c_{12}, c_{44} referred to cube axes, we have $-p^2 = 2\, c_{44}/(c_{11} - c_{12}) = \beta^2$. It is convenient to express the two non-vanishing stress components in cylindrical coordinates:

$$
\begin{aligned}
\tau_{\theta z} &= \frac{c_{44}}{2\pi\beta}\frac{a_3}{r}, \\
\tau_{rz} &= \frac{c_{44}}{2\pi\beta}\frac{a_3}{r}\frac{(1-\beta^2)\sin\theta\cos\theta}{\cos^2\theta + \beta^2\sin^2\theta}.
\end{aligned}
\tag{7.9}
$$

(b) *Edge Dislocation in a Simple Case*

We now consider the state of stress in the $x_1 x_2$ plane when the axis of the dislocation is along the axis of a cubic crystal. As we have seen in the last section, u_3 can be treated independently and is the same as in the isotropic case. We thus have only two equations for the determination of the displacement and stress in the $x_1 x_2$ plane, and there are two independent terms in the general solution which is of the form (3.8). The constants A_1, A_2, and p are given by (3.9) which in this case becomes

$$
\begin{aligned}
(C_{1111} + p^2 C_{1212})\, A_1 + (C_{1122} + C_{1221}) p A_2 &= 0, \\
(C_{2211} + C_{2121}) p\, A_1 + (C_{2112} + p^2 C_{2222}) A_2 &= 0,
\end{aligned}
\tag{7.10a}
$$

or in terms of the small c's,

$$
\begin{aligned}
(c_{11} + p^2 c_{44})\, A_1 + (c_{12} + c_{44}) p\, A_2 &= 0, \\
(c_{12} + c_{44}) p\, A_1 + (c_{44} + p^2 c_{11})\, A_2 &= 0.
\end{aligned}
\tag{7.10b}
$$

The determinant vanishes for the four values of p given by

$$
p_{(1)} = e^{i\alpha},\quad p^*_{(1)} = e^{-i\alpha},\quad p_{(2)} = -e^{i\alpha},\quad p^*_{(2)} = -e^{-i\alpha},
\tag{7.11}
$$

where α is given by

$$
\alpha = \tfrac{1}{2}\cos^{-1}\left[\frac{2c_{12}c_{44} + c_{12}^2 - c_{11}^2}{2c_{11}c_{44}}\right],
\tag{7.12}
$$

and is real for the common cubic metals (see the appendix). The corresponding eigenvectors A_k may be chosen with $A_1 = 1$ so that the values of $A_{(l)2} \equiv A_{(l)}$ are

$$
A_{(2)} = -A_{(1)} = \frac{c_{44}e^{i\alpha} + c_{11}e^{-i\alpha}}{c_{12} + c_{44}}.
\tag{7.13}
$$

The general solution for the displacement is therefore

$$
\begin{aligned}
u_1 &= f_{(1)}[z_{(1)}] + f_{(2)}[z_{(2)}] \\
u_2 &= A_{(1)} f_{(1)}[z_{(1)}] + A_{(2)} f_{(2)}[z_{(2)}],
\end{aligned}
\tag{7.14}
$$

where $z_{(1)} = x_1 + e^{i\alpha}x_2$ and $z_{(2)} = x_1 - e^{i\alpha}x_2$. For an analytic distribution of stress the f's, as we have seen, are of the form (4.2) where only the logarithmic term need be considered. Expressing these functions in the form (6.1), we have to determine the two complex constants $D_{(1)}$ and $D_{(2)}$. These are given by (6.3) for the slip vector and (6.4) for the vanishing of the net force. For the present case (6.3) becomes

$$
\begin{aligned}
a_1 &= D_{(1)} + D_{(2)}, \\
a_2 &= A_{(1)} D_{(1)} + A_{(2)} D_{(2)} = A_{(2)}[D_{(1)} - D_{(2)}].
\end{aligned}
\tag{7.15}
$$

(6.4) becomes

$$
0 = D_{(1)}[C_{1221}\, A_{(1)} + C_{1212}\, p_{(1)}] + D_{(2)}[C_{1221}\, A_{(2)} + p_{(2)}\, C_{1212}]
$$

$$
0 = D_{(1)}[C_{2211} + p_{(1)}\, C_{2222}\, A_{(1)}] + D_{(2)}[C_{2211} + p_{(2)}\, C_{2222}\, A_{(2)}]
$$

which may be expressed in terms of c_{11}, c_{12}, c_{44} and α as

$$
\begin{aligned}
0 &= [A_{(1)} + e^{i\alpha}][D_{(1)} - D_{(2)}] \\
0 &= [c_{12} + c_{11}e^{i\alpha}A_{(1)}][D_{(1)} + D_{(2)}]
\end{aligned}
\tag{7.16}
$$

where, as throughout, only the real part of complex expressions are taken. Equations (9.7) and (9.8) are four linear equations for the real and imaginary parts of the two complex constants from which the displacements and then the stresses are obtained.

When the slip vector is in the x_1 direction so that $a_2 = 0$, we have

$$
D_{(1)} = D_{(2)} = -\frac{a_1 i}{2\sin 2\alpha}\left\{\frac{e^{2i\alpha}c_{11} - c_{12}}{c_{11}}\right\}.
\tag{7.17}
$$

The most important quantity to be determined in applications of dislocation theory is the shear stress on the slip plane. In the present case this is

$$
\begin{aligned}
\tau_{12} &= c_{44}\left\{\frac{\partial u_1}{\partial x_2} + \frac{\partial u_2}{\partial x_1}\right\} \\
&= a_1\frac{(c_{11}^2 - c_{12}^2)}{4\pi\, c_{11}\sin 2\alpha}\left[\frac{1}{x_1 + e^{i\alpha}x_2} + \frac{1}{x_1 - e^{i\alpha}x_2}\right]e^{i\alpha}
\end{aligned}
$$

$$(7.18) \qquad = a_1 \frac{(c_{11} + c_{12})}{2\pi} \sqrt{\frac{c_{44}\, c'_{44}}{c_{11}\, c'_{11}}} \cdot \left[\frac{x\,(x_1^2 - x_2^2)}{(x_1^2 + x_2^2)^2 - \frac{2(c_{11} + c_{12})}{c_{11}} \left\{ 1 - \frac{c'_{44}}{c_{44}} \right\} x_1^2\, x_2^2} \right]$$

where c'_{11}, c'_{12}, c'_{44} are the elastic constants referred to axes rotated counter-clockwise through 45° about the x_3-axis and are given by

$$(7.20) \qquad c'_{44} = \frac{c_{11} - c_{12}}{2}, \quad c'_{11} = \frac{c_{11} + c_{12} + 2c_{44}}{2}, \qquad c'_{11} + c'_{12} = c_{11} + c_{12}.$$

APPENDIX

(i) *The General Solution: Wedge Dislocations*

The most general type of multiple-valued displacement consistent with continuous and twice-differentiable strains is known from the classical work of Weingarten and Volterra (see, for example, the review article by Nabarro [7]). From their results it appears that by assuming in section 5 that $df_{(l)}/dz_{(l)}$ is analytic and single valued we have excluded Volterra's dislocation of order VI. (The first three orders are included in the analysis of the text, whilst for orders IV and V the elastic state would not be independent of x_3.) Weingarten's and Volterra's results are very general, being essentially geometrical, and depending neither on Hooke's law nor the equations of equilibrium. Nevertheless it is interesting to see how the most general dislocation state arises in our analysis. The stress is assumed to be analytic and single valued; this is equivalent to assuming that the strain is single valued and analytic. Since the strain is somewhat more convenient to work with, we use (2.1) to obtain the strain corresponding to the general equilibrium solution (4.7). This gives

$$(A.1) \qquad e_{ij} = \sum_{l=1}^{3} A_{(l)i}\, p_{(l)j} + A_{(l)j}\, p_{(l)i} \frac{df_{(l)}}{dz_{(l)}}[z_{(l)}]$$

where $p_{(l)1} = 1$, $p_{(l)2} = p_{(l)}$, $p_{(l)3} = 0$ as in the text.

Equations (A.1) are a system of only five linear equations ($i = j = 3$ being trivial) for the real and imaginary parts of the three f's. Thus (A.1) can be solved for five of these functions in terms of the sixth function and the strains. For example if we let $df_{(l)}/dz_{(l)} = U_{(l)} + iV_{(l)}$ we can solve (A.1) for $U_{(l)}$ in terms of $V_{(l)}$ and e_{ij}. Differentiating this solution with respect to the real and imaginary parts of $z_{(l)}$ gives two equations for the first derivatives of $U_{(l)}$ and $V_{(l)}$, the real and imaginary parts of $z_{(l)}$ being taken as the independent variables. These two equations added to the Cauchy-Riemann equations make four equations, which can be solved for the four first derivatives in terms of the strains, which are analytic single-valued functions. Thus $d^2f_{(l)}/d^2z_{(l)}$ is an analytic single-valued function in the good region and, by Laurent's theorem can be represented by a series of positive and negative powers of $z_{(l)}$. Therefore the most general form of $f_{(l)}$ is

$$(A.2) \qquad f_{(l)}[z_{(l)}] = \frac{B_{(l)}}{\pm 2\pi i} z_{(l)} \ln z_{(l)} + \frac{D_{(l)}}{\pm 2\pi i} \ln z_{(l)} + \sum_{n=-\infty}^{\infty} C_{(l)n}\, z_{(l)}^{n}$$

the sign of $2\pi i$ being chosen as in the text.

(A.2) differs from the expression (5.1) only in the addition of the term in $B_{(l)}$. We now consider the physical meaning of the additional term.

Unlike the other constants in (A.2) the real and imaginary parts of the $B_{(l)}$ are not independent but are related by the five equations for the vanishing of the discontinuity in strain $\Delta e_{ij} = 0$ which from (A.1) and (A.2) gives

$$(A.3) \qquad \sum_{l=1}^{3} [A_{(l)i}\, p_{(l)j} + A_{(l)j}\, p_{(l)i}]\, B_{(l)} = 0.$$

Whatever new feature is introduced by admitting the terms in $B_{(l)}$ may thus be described by a single real constant. We shall now find the physical meaning of this constant.

First consider the force $F_i = \Delta\phi_i$ corresponding to the $B_{(l)}$. From (4.9) and the first term of (A.2) we have

$$(A.4) \qquad F_i = -\sum_{l=1}^{3} C_{i2k\alpha}\, p_{(l)\alpha}\, A_{(l)k}\, B_{(l)}\, z_{(l)}.$$

Remembering that $p_{(l)1} = 1$ and $p_{(l)3} = 0$, we can write (A.4) as

$$(A.5) \qquad \begin{aligned} F_i = & -x_1\, C_{i2\beta\alpha} \sum_{l=1}^{3} p_{(l)\alpha}\, A_{(l)\beta}\, B_{(l)} \\ & -x_2\, C_{i2\beta\alpha} \sum_{l=1}^{3} p_{(l)\alpha}\, A_{(l)\beta}\, B_{(l)}\, p_{(l)\alpha}. \end{aligned}$$

The first term vanishes because $C_{i2\beta\alpha}$ is symmetrical in α and β while by (A.3) the sum over l is unsymmetrical. This fact enables us to write the second term as

$$(A.6) \qquad F_i = -x_2\, C_{i\beta k\alpha} \sum_{l=1}^{3} p_{(l)\alpha}\, p_{(l)\beta}\, A_{(l)k}\, B_{(l)},$$

which vanishes by the equilibrium conditions in the form (4.6). Thus the $B_{(l)}$ give no contribution to the

force and equation (5.3) for F_i in terms of the $D_{(l)}$ is still valid.

Let us now consider the discontinuity in displacement corresponding to the $B_{(l)}$ term in (A.2). This is

$$\Delta u_k = \sum_{l=1}^{3} A_{(l)k} B_{(l)} p_{(l)\alpha} x_\alpha . \tag{A.7}$$

If we define

$$\omega = \sum_{l=1}^{3} A_{(l)1} B_{(l)} p_{(l)2} \tag{A.8}$$

and make use of (A.3), (A.7) can be written in the vector form

$$\Delta \bar{u} = \bar{\omega} \times \bar{X} \tag{A.9}$$

where $\bar{X}$ has components x_1 and x_2 and $\bar{\omega}$ is parallel to the x_3-axis and of magnitude ω (A.8). Thus the discontinuity in displacement corresponding to the $B_{(l)}$ term in the general expression (A.2) represents a rigid body rotation of the adjoining surfaces about the x_3-axis. This would occur if a cylinder were cut and sprung open or a wedge-shaped piece were cut out and the adjoining surfaces cemented together. In a crystal there would clearly be a relative rotation ω of the lattices on opposite sides of the cut, so that the wedge solution is inadmissible in applications to a crystal lattice.

(ii) *Proof that the $p_{(l)}$ are Complex*

The condition that the energy density be positive for any state of strain is

$$C_{ijkm}\, e_{ij}\, e_{km} = C_{ijkm} \frac{\partial u_i}{\partial x_j} \frac{\partial u_k}{\partial x_m} > 0 \tag{A.10}$$

for any real set of e_{ij} or $\partial u_i / \partial x_j$ not all of which vanish.

Suppose that in (4.6), $p_1 = 1$ and p_2 is real. Then the ratios of the A_k found by solving the three equations (4.6) will be real. Hence the A_k may be chosen real and not all zero. Multiplying (4.6) by A_i and summing over i we have

$$A_i A_k p_\alpha p_\beta C_{i\beta k\alpha} = 0.$$

Accordingly the choice

$$\frac{\partial u_k}{\partial x_\alpha} = A_k p_\alpha \ (\alpha = 1, 2), \ \frac{\partial u_k}{\partial x_3} = 0$$

will lead to a zero energy density for a non-zero strain. Hence the assumption that p_2 is real is inadmissible.

We can also give a direct proof from the determinantal equation itself in the special cases considered. It is convenient to write (A.10) in the form

$$\sum_{i=1}^{6} \sum_{j=1}^{6} c_{ij}\, e_i\, e_j > 0 \tag{A.11}$$

with $e_{11} = e_1, \ldots, 2e_{23} = e_4, \ldots$. Putting $e_4 = p$, $e_5 = 1$, and the other e_i zero we have $c_{44}\, p^2 + 2c_{45}\, p + c_{55} > 0$, showing that the p of equation (7.4) cannot be real.

The quantity α (equation 7.12) can be written in the more expressive form

$$\alpha = \cos^{-1} \sqrt{\left\{ \tfrac{1}{2} \frac{1}{1-\sigma} \left(1 - \frac{1}{A}\right) \right\}}$$

where $\sigma = c_{12}/(c_{11} + c_{12})$ is Poisson's ratio for extension in the $\langle 100 \rangle$ direction and $A = 2\ c_{44}/(c_{11} - c_{12})$ is the "anisotropy factor" for a cubic crystal [8]. (We are indebted to Dr. H. Brooks for pointing this out.) We have to show that α is never purely imaginary. In (A.11) put successively $e_1 = 1$; $e_4 = 1$; $e_1 = \pm e_2$; $e_1 = e_2 = e_3$, with the unspecified e_j zero in each case. We find that c_{11}, c_{44}, $c_{11} \pm c_{12}$, $c_{11} + 2c_{12}$ are all positive. (Note that $c_{11} = c_{22} = c_{33}$ and $c_{12} = c_{23} = c_{31}$ in a cubic crystal.) From these relations we easily show that

$$-1 < \sigma < \tfrac{1}{2} \text{ and } A > 0.$$

It follows that $\cos \alpha$ is purely imaginary if $0 < A < 1$ or purely real and less than unity if $1 < A < \infty$, and so α is complex or purely real. From Table 3 of [8] it is seen that the common cubic metals fall into the class with real α.

The quantity β^2 introduced at the end of section 7a is equal to A and so the associated p is purely imaginary.

References

1. ESHELBY, J. D. Phil. Mag., 7, **40** (1949) 903.
2. READ, W. T. and SHOCKLEY, W. In "Imperfections in Nearly Perfect Crystals" (New York, John Wiley and Sons, 1952), p. 77.
3. FRANK, F. C. Phil. Mag., 7, **42** (1951) 209.
4. ESHELBY, J. D. J. Appl. Phys., **24** (1953) 176.
5. READ, W. T. and SHOCKLEY, W. In "Imperfections in Nearly Perfect Crystals" (New York, John Wiley and Sons, 1952), p. 352.
6. BURGERS, J. M. Proc. Acad. Sci. Amst., **42** (1939) 378.
7. NABARRO, F. R. N. Advances in Physics, **1** (1952) 269.
8. ZENER, C. Elasticity and Anelasticity of Metals (Chicago University Press, 1948), p. 16.

CRYSTALLOGRAPHY OF PHASE TRANSFORMATIONS*

ALFRED H. GEISLER†

Microstructural and crystallographic features which are associated with transformation products are generalized on the basis of factors such as interfacial surface energy, strain energy and diffusion. In the case of diffusion-controlled Widmanstätten structures, surface energy factors such as a discrete orientation relationship, a low index habit plane and a tendency for a pseudomorphic or coherent crystal structure are dominant. Factors associated with tolerable strain energy, such as stress relief by recrystallization or concurrent plastic deformation, play only minor roles in diffusion-controlled transformations. On the other hand, it is proposed that in the case of diffusionless martensitic structures the strain energy factors, such as spontaneous deformation by slip and twinning, dominate to modify the factors established by interfacial surface energy. The strain energy factors lead to modified or pseudo-habits and pseudo-orientation relationships in much the same way as surface energy may lead to a pseudomorphic crystal structure. The consequence of spontaneous deformation by slip is illustrated for martensitic structures in iron-base alloys. It is proposed that the (111)A habit and Kurdjumow-Sachs orientation relationship are primitive characteristics of the γ to α transformation in iron-base alloys and that spontaneous slip modifies these characteristics to those observed for bainitic and martensitic structures. The suggestion is advanced that the (225)A habit arises because of rotation of the interface away from (111)A by slip in the austenite whereas the (259)A habit is associated with the dominance of slip in the martensite. Slip in each phase can account for lattice rotations that explain variables of the observed orientation relationships. A generalization that the habit plane tends to be one with indices of the type $\{hhl\}$ in a variety of martensitic structures involving cubic phases is explained by spontaneous deformation. On the basis of this viewpoint, shear transformations and martensitic structures are to be regarded as being *accompanied* by shear rather than *generated* by shear.

LA CRISTALLOGRAPHIE DES TRANSFORMATIONS DE PHASES

Les caractéristiques cristallographiques et de microstructure associées aux produits de transformation sont généralisées, en se basant sur des facteurs tels que l'énergie interfaciale, l'énergie de déformation et la diffusion. Dans le cas des structures Widmanstätten contrôlées par la diffusion, les facteurs prédominants sont ceux, qui relèvent de l'énergie de surface, tels qu'une relation discrète d'orientation, un plan limite (habit plane) à bas indices et la tendance à une structure cristalline pseudomorphe ou cohérente. Les facteurs associés à une énergie de déformation tolérable, tels que le relâchement de tension par recristallisation ou par déformation plastique concourante, ne jouent que des rôles peu importants dans les transformations contrôlées par la diffusion. D'autre part, il est proposé, que dans le cas des structures martensitiques, à l'absence de diffusion, les facteurs qui relèvent de l'énergie de déformation, tels que la déformation spontanée par glissement et maclage, prédominent et modifient les facteurs établis par l'énergie interfaciale. Les facteurs relevant de l'énergie de surface mènent à des modifications des plans limites et des relations d'orientation, ou à des pseudo-plans limites et des pseudo-relations d'orientation, tout comme l'énergie de surface peut mener à une structure cristalline pseudomorphe. La conséquence d'une déformation spontanée par glissement est exposée pour le cas des structures martensitiques dans des alliages à base de fer. Il est proposé, que le plan limite (111)A et les relations d'orientation de Kurdjumow-Sachs sont des caractéristiques primitives de la transformation de γ en α dans les alliages à base de fer, et que le glissement spontané modifie ces caractéristiques pour les rendre semblables à celles observées dans les structures bainitiques et martensitiques. Il est aussi suggéré, que le plan limite (225)A apparaît à cause d'une rotation de la surface de séparation, qui l'éloigne de (111)A par glissement dans l'austenite, alors que le plan limite (259)A est associé à la prédominance du glissement dans la martensite. Le glissement dans chaque phase peut expliquer les rotations des réseaux, qui à leur tour expliquent les variations observées dans les relations d'orientation.

La généralisation de l'idée, que la tendance du plan limite est, d'en être un, ayant des indices du type $\{hhl\}$ dans de nombreuses structures martensitiques impliquant des phases cubiques, est expliquée par une déformation spontanée. En adoptant ce point de vue, il faut considérer les transformations par cisaillement et les structures martensitiques, comme accompagnées d'un cisaillément, plutôt qu'engendrées par ce dernier.

KRISTALLOGRAPHIE DER PHASENUMWANDLUNG

Mikrostrukturelle und kristallographische Eigenschaften von Transformationsprodukten wurden auf einer allgemeinen Basis als Funktion von Faktoren wie Grenzflächenenergie, Verzerrungsenergie und Diffusion diskutiert. Im Falle der diffusionsbestimmten Widmannstättenschen Strukturen dominieren die Oberflächenenergiefaktoren, wie z.B. eine bestimmte kristallographische Orientierungsbeziehung, eine hochsymmetrische Habitus-Ebene oder eine Tendenz zur Bildung pseudomorpher oder coherenter Kristallstrukturen. Faktoren, die sich auf die höchstzulässige Verzerrungsenergie beziehen, wie Spannungserholung durch Rekristallisation oder gleichzeitige plastische Verformung spielen bei diffusionsbestimmten Umwandlungen nur eine geringe Rolle. Andrerseits wird vorgeschlagen, dass im Falle der diffusionslosen martensitischen Strukturen die Faktoren der Verzerrungsenergie, wie spontane Deformation durch Gleitung oder Zwillingsbildung, dominieren und den Einfluss der Grenzflächenenergiefaktoren modifizieren. Die Verzerrungsenergiefaktoren führen modifizierte oder Pseudo-Habitusformen und Pseudoorientierungen in der gleichen Weise herbei wie die Grenzflächenfaktoren zu pseudomorphen Kristallstrukturen führen können. Die Folgen der spontanen Deformation durch Gleitung werden für den Fall der Martensitischen Strukturen in Legierungen mit Eisenbasis dargestellt. Es wird vorgeschlagen, dass der (111)A Habitus

*Received November 28, 1952.

†General Electric Research Laboratory, The Knolls, Schenectady, New York, U.S.A.

und die Kurdjumow-Sachs Orientierungen die ursprünglichen Charakteristika der γ zu α Transformation von Legierungen mit Eisenbasis sind, und dass spontane Gleitung diese zu den beobachteten bainitischen und martensitischen Strukturen modifiziert. Weiterhin wird die Hypothese aufgestellt, dass der (225)A Habitus als Folge der Drehung der Grenzfläche fort von (111)A bei Gleitung im Austenit entsteht, wahrend der (259)A Habitus mit der überwiegenden Gleitung im Martensit verbunden ist. Gleitung in jeder der Phasen kann für die Kristallgitterdrehungen verantwortlich gemacht werden, die ihrerseits Veränderungen in dem beobachteten Verhältnis der graphischen Orientierungen erklären. Die Verallgemeinerung, dass die Habitus-Ebene in einer Anzahl verschiedener martensitischer Umwandlungen, an denen kubische Phasen teilnehmen, die Neigung hat als Ebene vom Typ $\{hhl\}$ zu erscheinen, wird durch spontane Deformation erklärt. Von diesem Gesichtspunkt aus erscheinen Scherungsumwandlungen und martensitische Strukturen von Scherung *begleitet* und nicht durch Scherung *hervorgerufen*.

Introduction

Undoubtedly the decomposition of austenite in iron-base alloys has been the most extensively investigated transformation in the alloys of a single base metal. Consequently the knowledge for these alloys should form an important part of any generalization regarding transformations. The investigations have been about equally concerned with the crystallographic mechanism, with the kinetics, and with the property changes produced by heat treatment. On the basis of these studies three primary reaction products, namely, pearlite, bainite, and martensite have been identified and their formation has come to be regarded as three distinct processes. Of these three processes, the nature of the formation of martensite has been perhaps the most evasive. Consequently any discussion of the crystallography of transformations should devote a substantial proportion to the features of martensitic structures found in iron-base alloys. Martensitic transformations have also been found in a number of other metals and alloys, and their characteristics have been enumerated in detail in a recent review [1]. Perhaps the unique feature of the transformation is that a new structure is formed in a "diffusionless" manner; the reaction occurs under conditions in which chemical segregation by long range diffusion in solid solutions does not occur or in pure metals diffusion need not occur. The kinetics of the process have been clarified by the recent theory of nucleation [2]. Various proposals during the last few years regarding the mechanism of formation of martensite which were based on crystallographic aspects have necessitated the present critical review from which will evolve a new and more general viewpoint on the mode of formation, one consistent with nucleation theory.

Observations for Iron-base Alloys

In addition to a knowledge of the initial and final crystal structures, crystallographic data from which mechanisms may be proposed are of two types: (1) orientation relationship of the product lattice relative to the matrix lattice, and (2) habit plane which defines the interface between the matrix and plate-like particles of the product and which is usually referred to the matrix lattice. The orientation relationship is usually expressed as a pair of mutually parallel planes in the two lattices—the conjugate planes— and a pair of parallel directions. On the other hand, the most general description of the orientation relationship from X-ray diffraction data is in terms of two or more sets of parallel directions such as:

$$[101]\mathrm{M} \,/\!/\, [111]\mathrm{A}$$
$$[1\bar{1}\bar{1}]\mathrm{M} \,/\!/\, [1\bar{1}0]\mathrm{A}$$
$$[12\bar{1}]\mathrm{M} \,/\!/\, [11\bar{2}]\mathrm{A}$$

The above relationship was found by Kurdjumow and Sachs [3] and later confirmed by Wassermann [4] for the orientation of martensite (M) relative to austenite (A) in a 1.4 per cent carbon steel. In order to specify parallel conjugate planes such as (101)M // (111)A, further information such as a knowledge of habit plane or favorable matching of atomic arrays on the two planes is required. Kurdjumow and Sachs proposed that the atomic movements to form martensite from austenite could be represented by the shearing of $\{111\}$A planes in a $[\bar{2}11]$ direction followed by suitable expansions and contractions to complete the transformation.

The orientation of martensite in an Fe–30 per cent Ni alloy transformed at $-$ 195°C was found by Nishiyama [5] to be somewhat different from the above: rotated 5°16′ about an axis normal to the conjugate planes to give a different pair of parallel directions. This orientation was confirmed by Wassermann [4] whereas Mehl and Derge [6] found that the Kurdjumow and Sachs relation obtained at 20°C to 240°C and the Nishiyama at $-$ 195°C in Fe-Ni alloys. Nishiyama also proposed a mechanism for the formation of martensite in which the atom movements could be represented by the shearing of $\{111\}$A planes followed by adjustments in atomic spacings. Several other orientation relationships

TABLE I

CRYSTALLOGRAPHIC RELATIONSHIPS FOR TRANSFORMATION IN IRON-BASE ALLOYS

Observer	Material	Angular separations $[101]M:[111]A$	$[1\bar{1}\bar{1}]M:[1\bar{1}0]A$	$[12\bar{1}]M:[11\bar{2}]A$	Others
Kurdjumow and Sachs [3]	Fe–1.4 per cent C	0°	0°	0°	
Greninger and Troiano [7]	Fe–22 per cent Ni–0.8 per cent C	1°	2½°	—	$[10\bar{1}]M:[11\bar{2}]A = 2°$
Neerfeld and Mathieu [8]	Fe–30 per cent Ni Fe–18 per cent Ni–8 per cent Cr	1°2′	5°16′	5°16′	$[102]M$ // $[112]A$ $[010]M$ // $[1\bar{1}0]A$ $[201]M$ // $[11\bar{1}]A$
Young [9]	Meteoric Iron (Fe–Ni)	0.6 to 2.1°	0.8 to 3.1°	—	
Nishiyama [5]	Fe–30 per cent Ni	0°	5°16′	5°16′	$[101]M$ // $[11\bar{2}]A$ $[010]M$ // $[1\bar{1}0]A$

which are intermediate between that of Kurdjumow and Sachs and that of Nishiyama have been identified and the angular differences are shown in Table I.

The habit of the martensite plate which was once believed to be {111}A as for ferrite in slowly cooled Fe-C and Fe-Ni alloys was found by Greninger and Troiano [10] to be irrational and dependent upon alloy composition. For iron-carbon alloys they found that the habit plane was approximately {225}A in alloys with 0.55 to 1.4 per cent carbon and {259}A in an alloy with 1.78 per cent carbon. The {259}A habit was also observed for a Fe–1.23 per cent C–11.5 per cent Ni alloy cooled to − 77°C

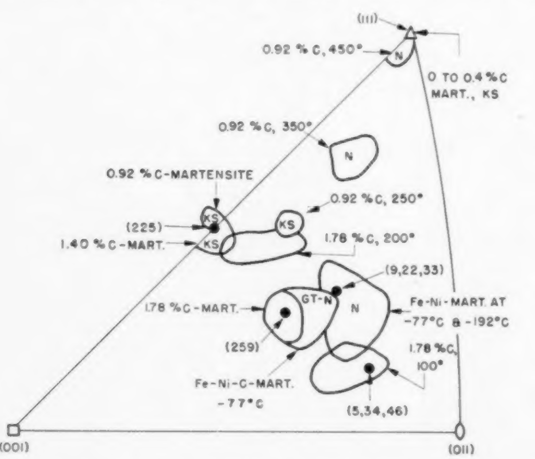

FIGURE 1. Orientation relations and stereographic projection of areas containing observed poles of habit planes for products of austenite decomposition.

while the habit was only slightly different from {259}A for a Fe–32.5 per cent Ni alloy when cooled to either − 77°C or − 195°C. The observed habit planes spread over the areas outlined in Figure 1. In low carbon alloys they report a plate-like array of martensite "striations" parallel to {111}A much the same as Mehl and Smith [11] observed for pure iron. The habits of isothermally formed bainitic products were also determined by Greninger and Troiano; they are included in Figure 1 since they too tend to be irrational and increasingly depart from {111}A as the temperature of formation is lowered. Similar results for the habits of martensite and bainite were observed by Smith and Mehl [12] in a 0.78 per cent C alloy and their results of orientation relationships are indicated in the habit areas for the 0.92 per cent C steel in Figure 1 along with those of Kurdjumow and Sachs (KS) and Nishiyama (N) for Fe–1.4 per cent C and Fe-Ni alloys, respectively. The Kurdjumow and Sachs relation has been found to obtain for ferrite in slowly cooled 0.4 per cent C hypoeutectoid steels by Mehl, Barrett and Smith [13] and in slowly cooled Fe–27 per cent Ni alloy by Mehl and Derge [6]. Mehl and Smith [11] concluded that the Kurdjumow and Sachs relation probably obtained for quenched pure iron but their pole figure analysis exhibited considerable spread toward the Nishiyama relation.

As the result of finding habit planes of high index rather than {111}A, Greninger and Troiano [10] concluded that "the whole picture of shearing processes appears untenable." This conclusion was based on the assumption that the (111)A plane proposed for shear should be parallel to the habit plane and has led to the abandonment of the simple pictures of Kurdjumow-Sachs and Nishiyama for describing the atom movements during the transformation [14]. In a subsequent paper Greninger and Troiano [7] made an analysis of the relief effects formed on the surface when an Fe–22 per cent Ni–.8 per cent C alloy was transformed at − 195°C and proposed that the martensite was

formed by the operation of two successive shearing processes. To explain the relief effects it was assumed that the first shear occurred parallel to the habit plane in the experimentally determined direction. A second shear using the normal glide elements (112)M[11$\bar{1}$]M was then required to complete the transformation. Greninger and Troiano observed the intermediate orientation relation listed in Table I for the untempered alloy, and found that on tempering at 500° to 900°C the relation changed so that (111)A and (101)M became parallel with a departure of only about 1° from the Nishiyama relation. These observations are indicated in Figure 1 by the symbol GT-N near the (9, 22, 33) index which was approximately the habit observed by Greninger and Troiano for a single martensite crystal that had been polished parallel to the habit plane. The results on the latter sample represent the only observations yet published which relate the orientation of the martensite lattice directly to the habit plane of the martensite plate.

The approach of Jaswon and Wheeler [15] is a mathematical one based solely on the initial and final structures and their relative orientations with no consideration given to atomic paths. They criticize previously proposed mechanisms for the formation of martensite since the prescribed paths appeared to be arbitrary. They assumed that of all the possible distortions of a unit cell of austenite which could generate a unit cell of martensite of a chosen variant of the Kurdjumow and Sachs orientation relationship the one which actually occurred was the one which produced the minimum displacements of the atoms. In this way a unique correspondence was set up between the positions of atoms in the austenite structure and their subsequent positions in the martensite structure which confirmed that proposed by Kurdjumow and Sachs. When this correspondence is known a strain tensor can be set up to represent the distortion of the austenite structure which is required to form martensite. Solution of the strain tensor for the three proper planes which do not rotate gave the interesting result that one of these unrotated planes was the (111)A, the second deviated up to 1° from (111)A with increasing carbon content, and the third was within $1\frac{1}{2}$° of (225)A. These three solutions for planes which do not rotate were assumed to represent the habit planes: (111)A for low carbon alloys and (225)A for higher carbon contents up to 1.4 per cent. A further conclusion of the Jaswon-Wheeler analysis was that the tetragonality of martensite developed as a necessary consequence of the assumption that the displacements of the iron and carbon atoms in austenite constitute a common homogeneous deformation when martensite is formed.

Bowles [16] has confirmed the minimum displacement hypothesis of Jaswon and Wheeler by demonstrating that these displacements produce the lattice plane transformations observed by Greninger and Troiano. Bowles concluded that paths must be ascribed to the atoms in order to explain the observed relief effects since the simple homogeneous distortion from the initial to the final structures analyzed by Jaswon and Wheeler made no provision for explaining the relief effects. Bowles proposed that Greninger and Troiano imposed an unjustified restriction when they analyzed the martensite relief as a shear. Instead Bowles proposed to resolve the total transformation strain into two homogeneous distortions, each of which was characterized by a single direction of motion of atoms and an undistorted or invariant plane. The mode of operation of a single Bowles-type strain is illustrated by Figure 2 for a simple, arbitrary case. By a method of stereographic analysis of a variant of the Kurd-

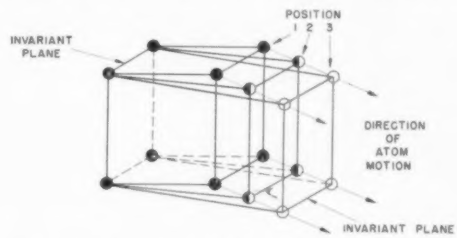

FIGURE 2. An example of the distortion of a simple cubic cell by a Bowles-type strain.

jumow-Sachs orientation relationship, Bowles used the Jaswon and Wheeler result that the (225)A and the (111)A planes are not rotated and proposed that the first distortion was [$\bar{1}\bar{1}$2]A (225)A and the second distortion was [11$\bar{1}$]M (112)M where the direction refers to the direction of atom movement and the plane is the undistorted plane for each direction of atom movement. The first distortion which utilized the habit plane as the undistorted plane produced the surface relief effect which consisted of a simple tilting of the surface about its intersection with the habit plane. The observed relief effects for a 1.35 per cent C steel were confirmed in this way. The second distortion was the same simple shear proposed by Greninger and Troiano and had to be assumed to occur heterogeneously between opposing blocks of unit cells in order to cause no observable change in the shape of the plate.

Machlin and Cohen [17] studied the relief effects for an iron–30 per cent nickel alloy as an example of a {259}A habit system with the idea of correlating this habit with either the Greninger-Troiano or Nishiyama orientation relationship much the same as Bowles had done for the (225)A habit and Kurdjumow-Sachs relationship. The displacement of scratches on three mutually perpendicular surfaces of a single crystal were measured and used to express a strain matrix. It was shown that the measured strain was not sufficient to generate the martensite lattice from the austenite as a single homogeneous strain in agreement with previous observations of Greninger and Troiano and Bowles. Machlin and Cohen showed that the invariant plane of the strain agreed fairly well with the habit plane and it was assumed that the measured strain was the first of the two Bowles-type strains.* The second strain was then calculated on the basis of the Greninger-Troiano orientation relationship. Their results gave the following descriptions of the two strain elements:

	First Strain	Second Strain
Invariant Plane	(259)A within 2°	(235)M
Direction of atom motion	$[\bar{1}\bar{5}6]$A within 2°	$[11\bar{1}]$M

Machlin and Cohen found on checking by the stereographic analysis proposed by Bowles that the first invariant plane was somewhat closer to (9, 22, 33)A than to (259)A. Their results suggested that different orientation relations will be associated with different habit planes: Kurdjumow-Sachs relation with {225}A habit, Greninger-Troiano relation with {259}A habit and Nishiyama relation with {5, 34, 46}A habit. They explain the correlation by implying that the first strain corresponding to the minimum activation energy path will determine the habit plane as the invariant plane and this in turn will uniquely determine the final orientation relationship. A cooperative phenomenon whereby a plate in one orientation stimulated others of specific orientations was discussed for both habit systems. They showed metallographic evidence for the existence of a macroscopically heterogeneous strain corresponding to the predicted second strain. Subbands within the martensite were revealed by tempering an Fe-Ni-C alloy presumably by the precipitation of carbides along the twin-like boundaries.

*The habit plane defined by the austenite-martensite interface in the microstructure, the invariant plane of the Bowles-type strain or that plane which is not distorted in the Machlin-Cohen analysis of surface relief effects, and one of the proper planes of the strain tensor in the Jaswon-Wheeler analysis based on coordinates of atom sites consequently are regarded as coinciding and are presumably synonymous.

Barrett and Bowles [1] have extended the double strain analysis to intermediate orientation relationships between the Kurdjumow-Sachs and Nishiyama to show the manner in which the predicted habit plane varies from {225}A for the former. The prediction for the Nishiyama was {110}A which is in some disagreement with that predicted by Machlin and Cohen.

Frank [18] has proposed a dislocation mechanism for transforming the austenite lattice to the martensite lattice using the {225}A habit and Kurdjumow-Sachs orientation relationship. The model is confronted with the same difficulty as the previously described ones in that small adjustments in interatomic spacing must occur sometime during the transformation to give the correct lattice parameters. Frank proposed that this strain is taken elastically, and subsequently adjusted by plastic deformation in conformance with all the observations of minor slip and twinning accompanying the transformation. He proposed that the Bowles first distortion was analogous to a shear on the (101)M plane, accompanied by change in lateral spacing and the second to a heterogeneous shear generated by the motion of $[11\bar{1}]$M screw dislocations on the (112)M plane. A notable difference is that the latter motion does not need to be specified as occurring *second*, and in the martensite lattice; instead he visualizes the dislocations moving in the transformation front, and the deformations occurring simultaneously. Frank noted that probably the Greninger-Troiano relationship could be given an essentially similar interpretation but that no interpretation of the Nishiyama relationship had yet been found. He suggested that since the martensitic transformation in steels could go in alternative ways, the choice is presumably determined at the nucleation of a martensite plate. He discussed various factors which could influence the volume and surface free energies which govern nucleation and emphasized the production of a minimum in the surface free energy to favor the chosen orientation for the nucleation of martensite plates.

Limitations of Double Strain Mechanisms and Some General Aspects of Transformation Structures

Although much thought and excellent analytical work have been directed to an understanding of martensitic structures, the current status is not very satisfying. It is not at all certain that the double strain paths which have been ascribed to the atom motions for forming the new structure exclude simple

mechanisms that are equally consistent with the facts. Nor is it certain that the macroscopic distortions and surface relief effects upon which are based double strain proposals are in any direct way involved in the formation of the martensite lattice from the austenite. In other words while it is obviously true that the visible distortions accompany the formation of martensite, they may have no role in the primitive process of forming a body-centered lattice from the face-centered cubic austenite. More specifically, past treatments are not satisfying because successful analysis of the {259}A habit has not been made in any of the previous reports; the attempt of Machlin and Cohen suggests {9, 22, 33}A which is 4°53′ from {259}A (see Figure 1). This result agrees well with the habit observed by Greninger and Troiano from which one can conclude that the {9, 22, 33}A habit rather than {259}A corresponds to the Greninger-Troiano orientation relationship.* The {259}A habit thus remains unexplained. The whole assumption that a particular habit plane must be associated with a particular orientation relationship is of questionable validity particularly when results for bainitic structures are considered along with martensite as in Figure 1.

Why the habit and orientation relationships vary from pure iron to different alloys and with temperature still remains as the most prominent question concerning martensite. Perhaps some insight might be gained by rationalizing the structural features associated with transformations.

In diffusion-controlled transformations the structural features can be fairly well rationalized on the basis of the energetic aspects of nucleation. For example, discrete and simple orientation relationships obtain between the parent lattice and the product with parallelism of low index planes of good matching in order to minimize interface energy. If additional elastic strain energy can be tolerated then the product forms coherently with precise matching at the interface and with still further reduction in the surface energy. A spherical shape is consistent with minimum surface energy but when surface energy can be minimized by the existence of orientation relations and coherency other factors tend to control shape. The particles are frequently platelike with well-defined, rational orientations. The occurrence of plates has been attributed to (1) more favorable diffusion conditions, (2) minimum strain energy for a given volume of material, and (3) minimum surface energy when the largest surface is that of good lattice match. The orientation of the plates, that is, the habit plane, depends either upon the attainment of minimum strain energy as controlled by the anistropy of the elastic constants of the product† or again upon the minimum surface energy provided by the orientation relationship with the low index conjugate planes being parallel to the habit plane. Martensite when tetragonal is a transition structure but it is not coherent on the conjugate planes like the usual coherent precipitate. The tetragonality arises by virtue of the carbon atoms in austenite being moved along with the iron rather than by virtue of coherency at the interface. The habit plane for martensite is neither well defined nor rational thus it is difficult to account for on the basis of minimum surface energy. Presumably such a criterion based on irrationality of habit forms the basis for discarding the simple atomic movements described by Kurdjumow and Sachs and Nishiyama when irrational habit planes were discovered. The habit plane of martensite is usually defined by considering a line symmetrically placed down the center of the acicular cross-section. Because of the spread in the observations for a single observed habit plane (Figure 1) and because the interface is seldom straight (the particles are frequently lenticular with many minor irregularities), alloting rigorous crystallographic significance to it with its irrational indices is probably the most dissatisfying part of recent treatments of the martensitic structure. It is proposed that the habit plane of martensite originates neither from a requirement of minimum surface energy at the interface nor from a direct role in the crystallographic process; instead some other factor must be dominating the development of the irrational habit plane. Some factors associated with strain energy should be considered.

While the characteristics of the Widmanstätten figure have been the main concern in studies of diffusion-controlled transformation structures, a number of other features of relatively minor importance have now been rationalized. In contrast to the dominant role which *surface* energy plays in dictating the Widmanstätten pattern, these miscellaneous features are attributed to processes which tend to minimize *strain* energy during the transformation.

*The habit which is marked "H" in Figure 9 was determined from a gnomonic projection of a martensite plate published by Greninger and Troiano. Frank [18] referred to this habit as {3, 10, 15}A which is 4°50′ from {259}A and 3°20′ from {9, 22, 33}A.

†This condition is probably most effective when the precipitate and the matrix have the same crystal structure with the same orientation so that several choices for good matching of low index planes are possible in order to have an interface of low energy.

The processes include matrix recrystallization and plastic deformation which may occur concurrently with transformations in order to relieve the transformation stresses [19]. Recrystallization which is manifested by nodular growth starting from grain boundaries has been identified for all three types of transformations in solid solutions: eutectoid decomposition (pearlite), precipitation (discontinuous precipitation), and ordering [20]. This nodular process is strongly diffusion-controlled and thus need not be considered further here. On the other hand, evidence for concurrent plastic deformation should be examined in detail.

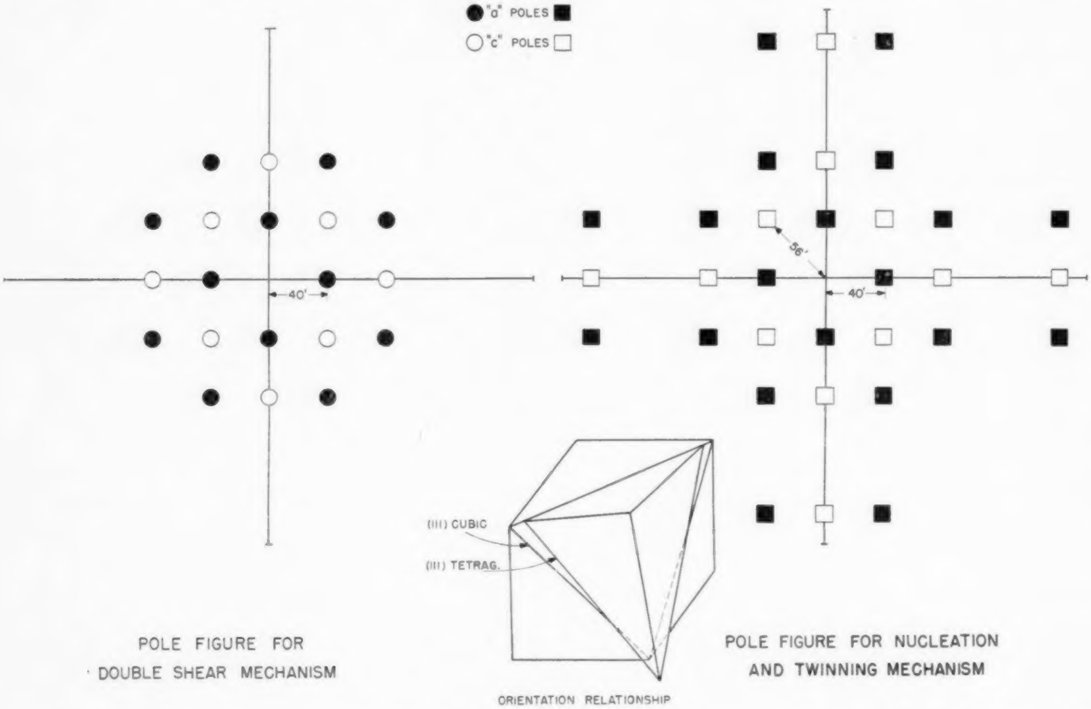

FIGURE 3. Distribution of {100} poles for tetragonal product of transformation in a In–20.75 per cent Tl alloy. The "a" poles refer to (100) and (010) while "c" refers to (001).

The dominating factor in transformations which has not previously been considered in explaining the martensitic structure possibly resides in the plastic deformation which may accompany the various diffusion-controlled transformations. Much evidence has now been rationalized. Of the precipitation alloys, the case of copper-beryllium is outstanding [21]. Prominent striations which have been referred to as a martensitic structure [22] have been attributed by Guinier [23] to slip on {110} matrix planes as the result of transformation stresses. A spread of $\pm 2°$ in the orientation relationship has been attributed to lattice rotation accompanying the slip [21]. Surface relief effects similar to those observed for martensite have been detected for both Cu-Be and Al-Cu precipitation alloys during isothermal aging [24; 25]. The relief effects and striations which are revealed by etching of Cu-Be alloys are synonymous. Similar striations which have been observed for Cu-Au and Co-Pt ordering alloys have likewise been attributed to plastic deformation resulting from transformation stresses by Newkirk and co-workers [19] who referred to the process as "self-deformation," but "spontaneous deformation" is perhaps a more descriptive term and will be used here. Young [9] found that the various misalignments listed in Table I for a number of samples of ferrite in meteoric iron were not random but the $(110)\alpha$ pole followed a great circle through the $(111)\gamma$ pole. He attributed the rotation to simple shear on $\{111\}\gamma$ planes that presumably occurred while the meteor was still hot but after or during the transformation.

Spontaneous deformation by twinning during transformations has been the suspected source of another type of striation which has been observed in micro structures. Lipson *et al.* [26] attributed the banded structure of ordered Fe-Pt alloys to twinning on {110} planes of the ordered tetragonal phase as it

formed in the disordered cubic matrix. A similar microstructure in In-Tl alloys can likewise be attributed to twinning [27]. Instead of assuming that the conjugate planes of the face-centered cubic matrix and tetragonal product are the {100} type as required for no change in orientation as has previously been done [28], a better model for explaining the X-ray diffraction data is to allow the slight change in orientation required for {111} conjugate planes as in the lower central drawing of Figure 3. The orientation relationship is precisely

$$(111)\mathrm{C} \mathbin{/\!/} (111)\mathrm{T}$$
$$[1\bar{1}0]\mathrm{C} \mathbin{/\!/} [1\bar{1}0]\mathrm{T}$$

where C refers to the cubic matrix and T to the tetragonal product. Such an orientation relationship will produce four "*a*" type poles at 40′ to the parent cube axis and four "*c*" type poles at 56′ to the cube axis precisely the same as for the double shear mechanism proposed by Bowles and co-workers [28] as shown in Figure 3. If the four *first* order twins are formed for each orientation of the parent product then the additional poles in Figure 3 (right) are predicted. It will be noted that the pole figure for Bowles' double shear mechanism which agreed with the data is exactly duplicated by the central part of the pole figure for the nucleation and twinning mechanism. The additional poles more remote from the center where the parent cube pole is located probably represent the two twins which do not relieve transformation stresses and thus are not formed. Of the four possible twins for a tetragonal lattice there are states of stress for which only two twins would be effective and in the present case the two effective ones evidently are those which produce "*a*" or "*c*" poles as close to the cube pole as possible.

The alternative mechanism for explaining the data for In-Tl alloys evidently needs further clarification since the response to the twinning proposal [29] indicated misunderstanding regarding the number of possible orientations and type of twinning. While details may be incomplete, the twin mechanism is outlined in Figure 4 making use of all known experimental data. On this view the boundaries of the main bands are regarded as merely the termination of lamellae of untwinned product (P) and first order twins (T) and have little significance when regarded as a habit plane. Parallel main bands are distinguishable from each other not by being twins but by being made up of differently oriented parent products and their twins. ***Second order twins are in no way involved*** contrary to the twinning mechanism that was tested by Bowles and co-workers. While there are 12 possible parent orientations of the product according to the orientation relationship previously mentioned and 24 twin orientations, only 4 parent and 8 twins are involved in a single set of main bands as shown on the right of Figure 4. Superposition of some of the poles occurs to give the 8 apparent orientations discussed by Bowles [28]. The twins which explain the pole figure are also those which make an angle of 60° to the main bands and 90° to each other when they coexist in a single main band as observed by Bowles. A possible mechanism of nucleation and growth is illustrated at the left in Figure 4. A coherent nucleus forms and

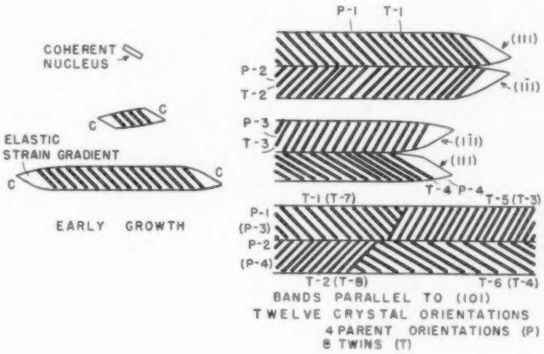

FIGURE 4. An interpretation of the microstructure when twinning occurs during transformation. The thick lines represent twins of the product. The various orientations of a tetragonal parent product and first order twins constituting a single series of parallel main bands are indicated at the right.

grows along the (111) plane in conformance with the observed orientation relationship where the (111) planes are the conjugate planes in the two phases. When the size reaches that at which the strain energy becomes intolerable, a twin forms. Further edgewise growth is accompanied by the spontaneous production of twins behind the moving coherent tips that are marked "*C*". Side-wise growth may consist of the edgewise advance of the lamellae of product and twin into the cubic matrix. The main bands are not smooth but reflect a slight uneveness in the termination of the twins (see [28, Figure 1]) and at very high magnification discontinuities in the main band interface suggest that the edges of the untwinned product may tend to retain a coherence with the cubic matrix [30, Figure 7]. The latter micrograph shows that the spacing of the twins is not as regular as illustrated in Figure 4. Nevertheless, the facts can be adequately interpreted on the basis of spontaneous twinning during the transformation in In-Tl alloys.

The martensitic structure in a Cu–13.6 per cent Al alloy has several features which suggest that the transformation here is likewise accompanied by twinning in the product [31]. Two orientation relationships are observed for the product, γ', in a single matrix crystal: one is the parent product and the second is the twin formed on the $(10{\cdot}1)$ plane. The microstructure shows that the γ' plates contain fine parallel striations which Greninger has pointed out are suggestive of twinning [31]. The twinning interpretation does not require that the so-called main bands remain either planar or parallel with each other as observed in In-Tl. Indeed, slightly inclined but planar main bands have been observed for a martensite plate in Cu-Al [31, Figures 5 and 6; 14, Figure 1*d*]. On this viewpoint the twins may terminate on quite irregular boundaries and probably do so in some alloy systems.

The existence of orientation relationships both in transformations and in overgrowths provides an analogy which one should explore in detail in interpreting structural features. Of interest here is the fact that the role of plastic deformation in relieving stresses during the formation of oriented overgrowths has been recognized [32]. The most important effect of the strain transition process is the possibility of a loss or change in the initial orientation in this case. Van der Merwe [32] has summarized the evidence which include disorientation by slip as the deposited film increased in thickness observed for a variety of substances and twinning in films of silver or nickel or rocksalt. Cochrane [33] has attributed the observed twinning in deposits of cobalt or nickel on copper to strains when the overgrowth tends to form coherently with the substrate. In a study of metal films on various inorganic substrates Thirsk [34] likewise suggested that any strains induced by a coherent underlayer were relieved by slip processes while submicroscopical twinning specifically was provided a role in the process of film formation. Van der Merwe [32] has outlined the stress relief process based on dislocation theory for the formation of coherent monolayers and growth with a spontaneous generation of dislocations at free boundaries when the misfit exceeds a critical value, somewhat greater than 9 per cent for a monolayer and less when coherent films thickens.* The energy required to strain a thick film to make it coherent with the substrate will be much greater than that necessary to cause the spontaneous generation of dislocations which eventually make up the incoherent interface. Such spontaneous flow is identical in purpose to that which has been proposed for heterogeneous transformations.

The double strain interpretation also is not satisfying because the microstructures of transformation products which have been referred to as martensitic vary appreciably in character from one material to another. This condition is in marked contrast to the microstructures observed for diffusion-controlled transformations: when the Widmanstätten pattern is resolvable the microstructures of aged alloys of widely diverse compositions such as Al-Cu, Cu-Ni-Co or Alnico 5 (Fe-Ni-Al-Co-Cu) are practically indistinguishable. On the other hand, martensitic structures in In-Tl and Fe-base alloys for both of which double strain mechanisms have been proposed have markedly different microstructures. The microstructure of In-Tl alloys exhibits large colonies of parallel main bands whereas Fe alloys exhibit single plates of varying orientation. The substructure of In-Tl is prominent and well developed but that in Fe-C is revealed with difficulty since carbide precipitation is required. Finally, the geometric features and orientation relationship for martensite in In-Tl are rational and discrete whereas those for Fe-base martensite are rather variable. It would seem that the two alloys could hardly have in common a double strain mechanism of martensite formation. Perhaps some insight might be gained by considering analogous structures that form in a diffusion-controlled transformation. One such transformation is the ordering of Co-Pt alloys in which the disordered face-centered cubic phase can be retained by quenching from 900-1000°C and the ordered face-centered tetragonal phase can be formed by aging in the range of 400-700°C. A variety of microstructures formed during ordering have been observed and some prominent features have been attributed to spontaneous deformation [19]. Some of the microstructures shown in Figure 5 have analogues among the martensitic structures. The structure in Figure 5*a* with main bands and sub-bands is very similar to that for In-Tl alloys [28]. Both bands are parallel to $\{110\}$ planes while the sub-bands make angles of 60° with the main band and 90° with each other analogous to In-Tl. The only difference between the two alloy systems is in conjugate planes of the product; $\{111\}$ type in In-Tl and $\{110\}$ type in Co-Pt. The irregular nature of the main band interface caused by the varied termination of the twins is clearly shown for the thickest main band near the top of Figure 5*a*. Other areas of the same

*See [50] for the detailed treatment.

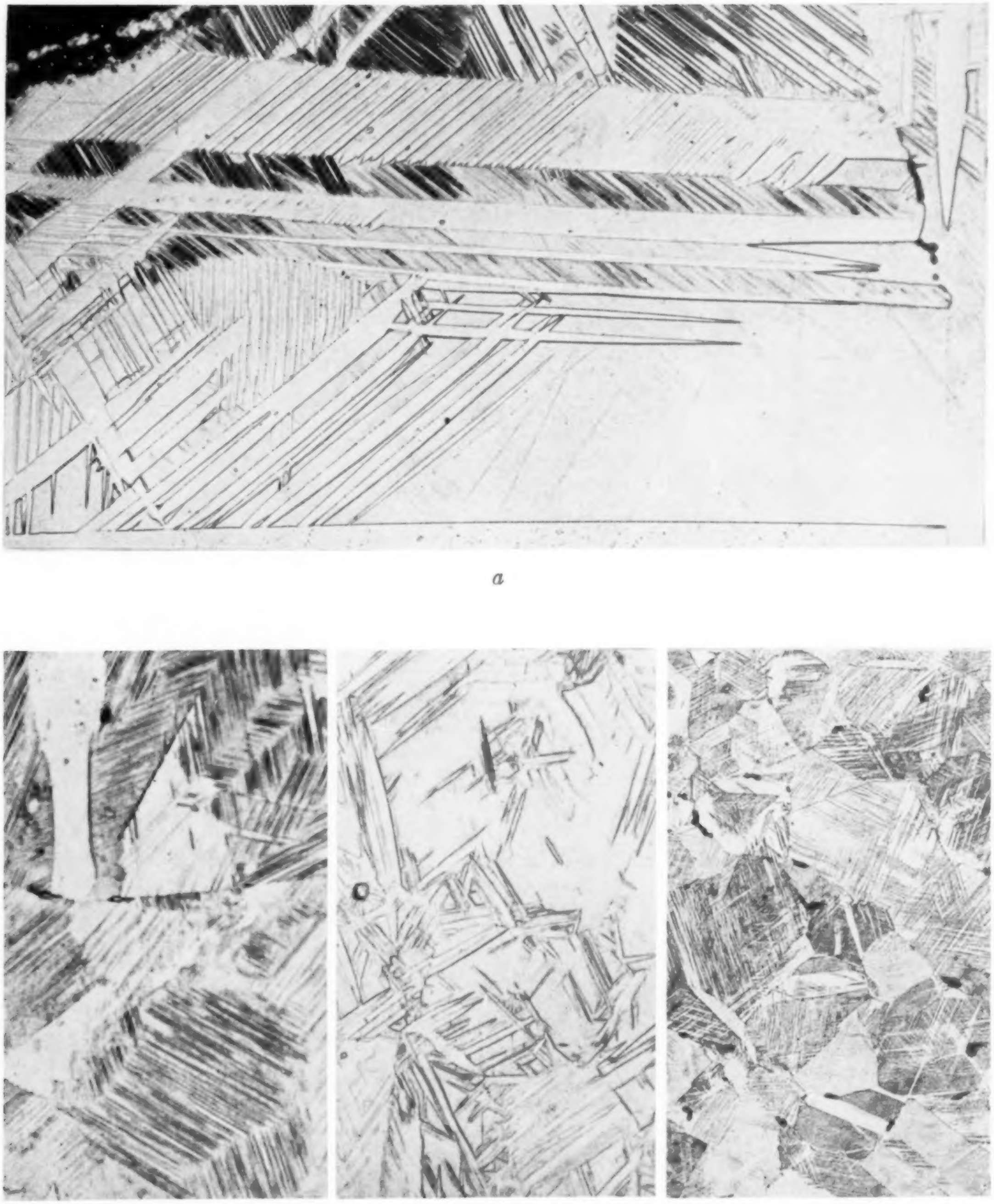

a

b *c* *d*

FIGURE 5. Martensite-like microstructures of an ordering Co-Pt alloy: (*a*) Twinned structure consisting of main bands and sub-bands similar to that observed for In-Tl alloys (500 ×). (*b*) Twinned areas of irregular outline with less prominent or no main bands (500 ×). (*c*) Acicular structure somewhat like martensite in iron-base alloys (500 ×). (*d*) Striated structure of fully ordered alloy (100 ×).

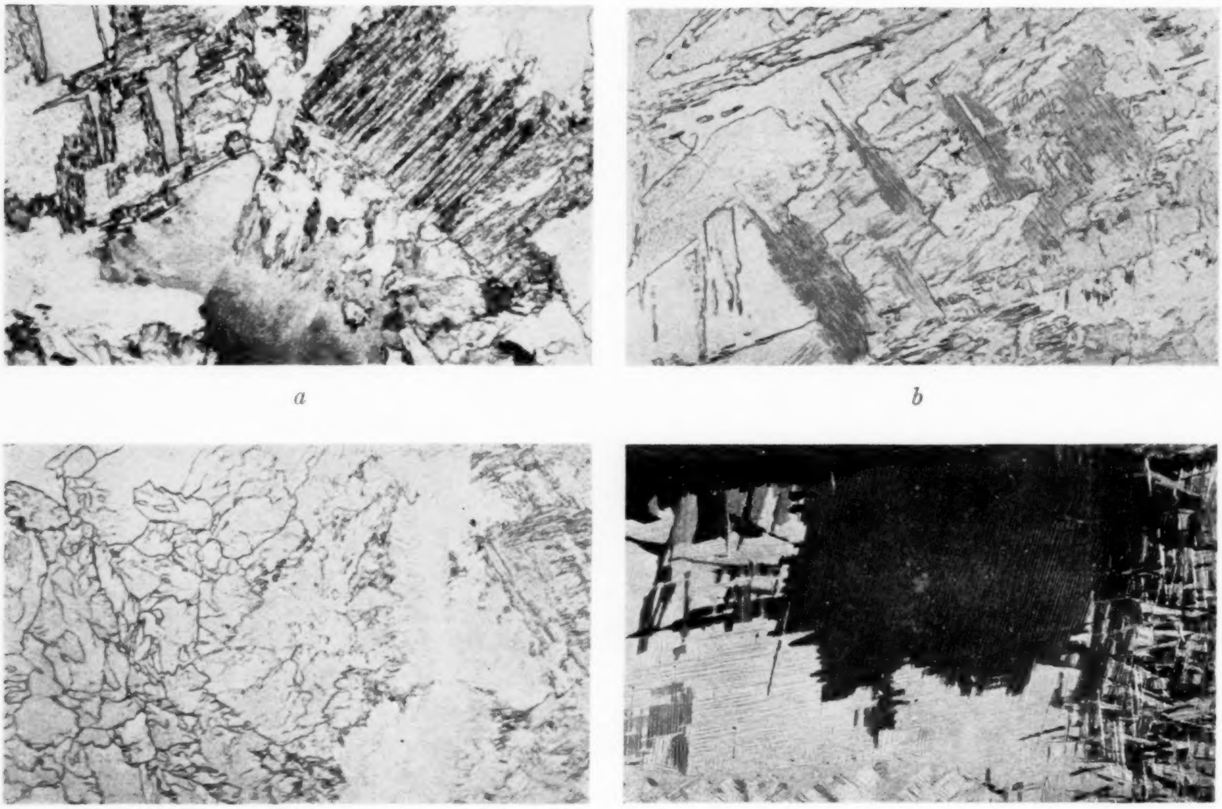

a b

c d

FIGURE 14. Micrograph showing striated and polygonal martensitic structures of transformation products (a–c: Iron–4 per cent copper alloy quenched from 1300°C. d: Arc melted sponge titanium cooled in mold and without further heat treatment). (a) Striated structure near surface (above) of 0.050″ sheet that had been quenched in cold water (150 ×). (b) Striated tending towards acicular structure in 0.025″ sheet that had been quenched in ice brine (150 ×). (c) Polygonal structure near center of above sample (a) showing gradation from striated structure near surface at right (150 ×). (d) Irregularly outlined striated crystals with tendency for acicular product at edges of the field of inspection (4 ×).

sample exhibited striated zones of irregular outline as in Figure 5*b* rather than the planar boundaries of main bands thus illustrating that consistent macroscopic geometry of the matrix-product interface is not required. Likewise the nature of the growing main band edge which has not been described previously for In-Tl alloys is very evident in Figure 5*a*. The sides which gradually taper to a point extending into the disordered phase somewhat resemble a stress catenary and could hardly have any rigorous crystallographic significance. The taper envisioned for the advancing edge in the sketches in Figure 4 probably should not be so pronounced. The structure for a Co-Pt alloy in Figure 5*c* is rather similar to that for martensite in Fe alloys. The plates are lenticular with a variety of orientations and frequent impingement; presumably they are the same as the main bands in Figure 5*a* but the twinned substructure is too fine to be resolved. The structure in Figure 5*d* which is also typical of the striations in aged Cu-Be [35] and ordered Cu-Au [36] alloys is very similar to the martensitic structure of cobalt. Again the geometry is rather hazy but the structure looks somewhat like the strain markings which can be developed on etching alpha brass [37]. The structures in Figures 5*a* to 5*c* are developed on ordering at temperatures near the equilibrium transformation range and that in Figure 5*d* at intermediate temperatures. After ordering at the lower temperatures the spontaneous recrystallization process manifests itself while self deformation is little evident or absent [19].

In view of the foregoing evidence, there is sufficient doubt in the validity of the proposed double strain mechanisms and sufficient reason to warrant the exploring of a new viewpoint based on spontaneous deformation for explaining martensitic structures in iron-base alloys. Slip in the matrix or product, and twinning in the product represent three modes of spontaneous deformation which have been illustrated in the preceding discussion.

An Alternate Interpretation of Martensite Structures in Iron Alloys

A new interpretation must satisfactorily explain irrational orientation relationships, irrational habit planes, and the existence of surface relief effects, substructure including a midrib and a cooperative phenomenon whereby a plate in one orientation tends to stimulate the formation of plates in other related orientations. It appears that the feature needing immediate explanation is the departure of the habit plane from {111} austenite planes.

Since there is no evidence yet that twinning accompanies the martensite reaction in iron alloys, the more attractive type of spontaneous deformation to explore is that simulated by crystallographic slip. In order to visualize the possible role of slip, consider the modification that can be induced in a single crystal by slip on a single system [38]. When a single crystal is subjected to compression and the compression surfaces are rigid, then the slip planes rotate towards the compression surfaces. If the compression surfaces are not rigid, the outward form of the crystal can rotate to keep the slip planes parallel with their original orientation. Similar rotations either of the lattice or of the stress surface occur when the stress is in tension and the slip is restrained or unrestrained, respectively. Rotation of the stress surface during unrestrained slip at once appears as an attractive possibility for explaining the rotation of the observed habit away from {111} austenite planes; rotation of the lattice under the action of restrained slip may explain the variable orientation relationships. Application of this idea to the formation of a martensite plate is illustrated in Figure 6. A coherent plate of martensite forms

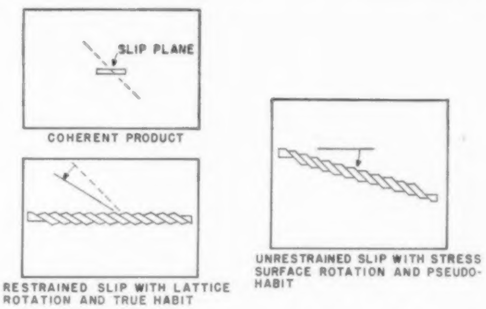

FIGURE 6. Modes of stress relieval by slip concurrent with growth of a transformation product (space between slip bands exaggerated for clarity).

parallel to the conjugate planes (111)A: (101)M with lattice parameters modified to afford a precise fit on the (111)A plane. The plate grows coherently along the (111)A plane with minimum surface energy as in a diffusion-controlled transformation. When it reaches a size at which the coherency stress energy becomes intolerable, slip occurs to minimize strain energy before further growth can proceed. If the (111)A habit is unmodified, i.e. stress surfaces are rigid, continued slip during growth causes lattice rotation as in the lower left drawing of Figure 6. On the other hand, when slip first starts subsequent growth could be along a path displaced from the initial (111)A plane so that in effect the stress surface, i.e. habit, rotates as in the

drawing at the right of Figure 6. Such rotation during growth is permissible from the standpoint that the establishment of an edgewise diffusion gradient is not required in martensite transformations. It should be emphasized that rotation through the austenite of a well-grown martensite plate is *not* proposed for such a rotation is to be regarded as energetically unfavorable [15]. The extent of habit rotation will depend upon the magnitude and frequency of the unit slip. The shape of the particle will depend upon the variation in frequency of the slips along the length of the cross section during lateral growth. Curved interfaces and lenticular shapes can arise from a gradient in frequency of slips.* There will be an equilibrium frequency of slips subsequently established at the center of the particle during growth and this frequency will define the stable degree of rotation of the habit. Edgewise growth will be accompanied by the continuous outward movement of the gradients at the edges with an accompanying change in orientation of the interface from the initial to the stable habit. Interface rotation even during the early growth will be such that fresh austenite is always being consumed and any "untransforming" of the austenite will be unnecessary. The rotated position of the interface will be referred to as the pseudo-habit in order to distinguish its irrational form from the low index habit parallel to conjugate planes given by the orientation relationship, (111)A in case of iron-base alloys.

Now that a possible alternate method of interpreting the martensitic structure in iron alloys has been presented, some of the possible ramifications may be pointed out. In describing Figure 6 the plates were regarded as martensite and the slip was considered as being concentrated in this product. The slip likewise could be concentrated in the austenite in which case the plates in Figure 6 may be regarded as volumes of austenite surrounding plates of martensite which are not shown. That the two possibilities are attractive in distinguishing between the {259}A pseudo-habit and the {225}A pseudo-habit became apparent on reviewing observations of Greninger and Troiano [10]. They found that the austenite grains in quenched 1.78 per cent C steel were free from any distortion in so far as one could judge from the sharpness of back-reflection Laue spots. The austenite Laue spots from quenched 1.4 per cent C steel were about twice the size of those from 1.78 per cent C steel suggesting appreciable distortion in the austenite.† These observations suggested the desirability of attempting to correlate the {225}A pseudo-habit with slip in the austenite (1.4 per cent C) and the {259}A pseudo-habit with slip concentrated in the martensite (1.78 per cent C).

The interpretation of the {225}A pseudo-habit should be considered first since it represents the case where the greater advance has been made by the Bowles and Jaswon-Wheeler analyses. For this purpose one may ignore the martensite phase for the moment to consider ways in which the austenite can be deformed to satisfy the observed effects. By way of illustration there are at least two sets of slip elements for plastic flow in the austenite which can provide the rotation of the stress surface from (111)A to (225)A as shown in Figure 7.‡ If the

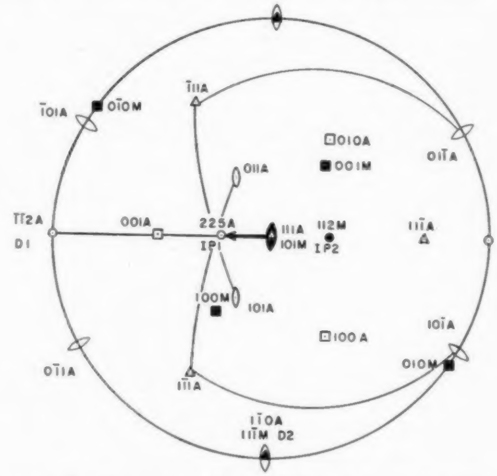

FIGURE 7. Stereographic projection of some slip elements which might operate to rotate the habit from (111)A to (225)A and elements of the Bowles double strain analysis of the {225}A habit.

Double Strain Elements		
Strain	Invar. Plane	Dir. Motion
First	(225)A	$[\bar{1}\bar{1}2]$A
Second	(112)M	$[11\bar{1}]$M
For K-S Relation		

Plastic Flow in Austenite	
Simple Slip	
(111)A	$[\bar{1}\bar{1}2]$A
Duplex Slip	
$(1\bar{1}1)$A	[011]A
$(\bar{1}11)$A	[101]A

*This concept is expressed in Figure 12.

†For carbon contents below about 1.4 per cent (corresponding to increasing amounts of martensite present in a quenched specimen) the back-reflection Laue spots (if any) were so ill defined as to render the method unsuitable for orientation determination.

‡The case for simple slip indicated in Figure 7 is a special one where the slip plane (normally {111} planes in face-centered cubic metals) and true habit plane (also {111} planes by coincidence) are parallel. The more general case is probable one in which slip and habit planes are not parallel as indicated by duplex slip in Figure 7 and by the diagram in Figure 6, an assumption which must be confirmed by experiment.

principal transformation stress is one of tension in a direction between $[\bar{1}\bar{1}2]$A and [225]A (slightly removed but not on these poles), then the operation of simple slip on a (111)A plane in the $[\bar{1}\bar{1}2]$A direction would produce a rotation of the pole of the slip plane toward the stress axis so that the interface rotates from (111)A towards (225)A, the pseudo-habit plane. The slip direction $[\bar{1}\bar{1}2]$A was chosen to be the same as the direction of atom motion for the first strain of the double strain mechanism proposed by Bowles. The same movement can be simulated by slip in conventional directions on the (111)A plane if $[\bar{1}01]$A and $[0\bar{1}1]$A are used cooperatively. Since relief effects have been associated only with the first strain which has been described in elements of the austenite lattice, then plastic flow of the austenite by simple slip on an appropriate system can equally explain the observed surface tilting as in Figure 8. The Bowles-type strain is an unequalled type of distortion when applied to describe changes in atomic positions as in Figure 2. However, when used to describe the change in outward form of a crystal as in the case of relief effects, it is no longer unique. The proposal of Greninger and Troiano for shear on the pseudo-habit plane as well as that of spontaneous deformation serve equally well. The assumed relationship between simple slip and a Bowles-type strain is that the slip direction and direction of atom motion are

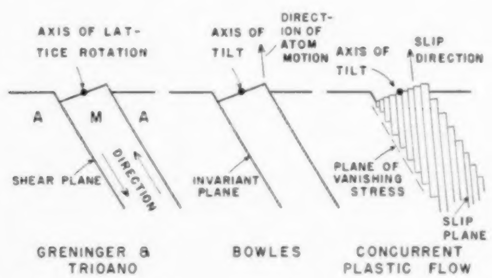

FIGURE 8. Various interpretations of surface relief effects that accompany martensite formation.

synonymous and that the slip plane is the plane that is defined by the slip direction and the normal to the slip direction in the invariant plane. The slip plane and invariant plane belong to the same zone with the zone axis normal to the slip direction. Since the zone axis is also the axis of habit rotation, the relation may be illustrated by considering Figure 2 where rotation of the top surface of the cell in Figure 2 is similar to rotation of the interface by unrestrained slip in Figure 6 (right).

The same relief effects and habit rotation can also be achieved by two symmetrically deployed slip systems of duplex slip noted in Figure 7. These systems would operate if the principal stress is a compressive stress along a direction between [111]A and [225]A. A second pair of systems employing the same planes indicated in Figure 7 for duplex slip but with $[10\bar{1}]$A and $[01\bar{1}]$A directions would conform with the direction of atom movements along $[\bar{1}\bar{1}2]$A postulated by Bowles although a simple relationship between the Bowles strain and duplex slip need not apply. The one advantage of considering duplex slip in the austenite is that it offers a possible explanation for the cooperative phenomenon whereby the three $\{225\}$A type habits around the (111)A pole share the three slip systems in pairs. Further reference to this phenomenon will be made later. It should be emphasized that the slip elements mentioned above merely serve to illustrate the mode of habit rotation by slip. Several other possibilities exist* and the operative ones will have to be determined by experiment.

Stereographic analyses provide solutions of the slip elements which will account for the interface rotation from the true habit plane towards the pseudo-habit plane; however, they do not predict quantitatively the extent of the rotation, i.e., the stopping point of the pole of the interface which will depend upon the transformation stresses and the strains which must be relieved. The necessary strain relieval and the quantitative extent of plastic flow in the austenite to form the $\{225\}$A pseudo-habit may be regarded as that calculated by the Jaswon-Wheeler analysis [15]. They calculated the strain to form martensite from austenite and the same calculations should apply from the reverse viewpoint of specifying the strain in the austenite when martensite is formed. Applicable interpretations of *all* three proper planes of the strain tensor can likewise be suggested. The $\{111\}$A proper plane is that for the normal habit as pointed out by Jaswon and Wheeler. The $\{225\}$A proper plane is the pseudo-habit plane: the plane to which the interface rotates from $\{111\}$A as the slip in the austenite relieves the transformation stress. The third proper plane which is about 1° from (111)A for a 1.7 per cent C steel was not interpreted by Jaswon and Wheeler; the suggestion is now advanced that it represents the lattice rotation which may accom-

*Other possible slip elements become apparent on consulting Figure 15.

pany the slip in the austenite. Such rotation is observed in the Greninger-Troiano orientation relationship where the (101)M plane is rotated to 1° from (111)A (Table I).*

Other pseudo-habits for iron-base alloys are best analyzed by considering crystallographic elements in the martensite. Analyses of the Greninger-Troiano habit and orientation are summarized in Figure 9. The four elements for duplex slip in the

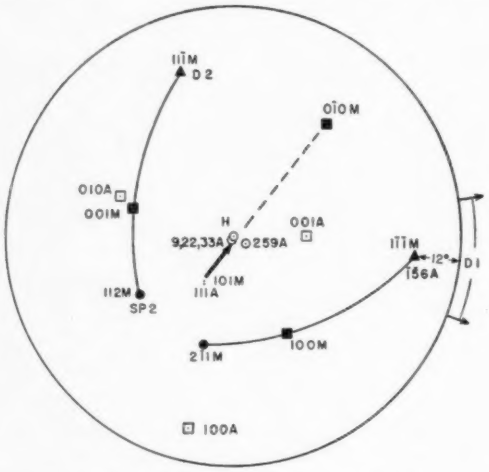

FIGURE 9. Stereographic projection of elements for various analyses of the Greninger-Troiano habit and orientation relationship.

Double Shear (G-T)			Double Strain (M-C)		
Shear	Plane	Dir.	Strain	Invar. Plane	Dir. Motion
First	H	D1 ± 15°	First	9,22,33A	$\bar{1}$56A
Second	112M	1$\bar{1}$1M	Second	235M	11$\bar{1}$M

Duplex Slip in Martensite
(2$\bar{1}\bar{1}$)M [1$\bar{1}\bar{1}$]M
(112)M [11$\bar{1}$]M
Pseudo-habit = (3$\bar{2}$3)M

martensite which can be chosen to explain rotation of the interface from (111)A to the pseudo-habit, H, include three elements which have appeared in previous proposals. The three consist of the plane and direction for the second shear of the Greninger-Troiano proposal (G-T) and the directions of motion for the first and second strains of the Machlin-Cohen (M-C). The direction [$\bar{1}$56]A coincides with the [1$\bar{1}\bar{1}$]M. When referred to the martensite structure the pseudo-habit is approximately (3$\bar{2}$3)M which will become of notable significance in a later section of the paper.

A possible solution of the (259)A pseudo-habit when associated with the Kurdjumow-Sachs orientation relationship is given in Figure 10. Duplex slip in the martensite on the normal {112}M type planes in the normal ⟨111⟩M type directions provides an explanation of the (259)A pseudo-habit. Two martensite crystals, M-1 and M-2 are considered in order to illustrate the manner in which the two crystals can share a common slip system. The duplex operation of the slip systems (12$\bar{1}$)M-1 [$\bar{1}$11]M-1 and ($\bar{1}$21)M-1 [11$\bar{1}$]M-1 will rotate the interface from (111)A to (952)A for the crystal in the orientation M-1 whereas operation of the systems ($\bar{1}\bar{2}$1)M-2 [1$\bar{1}\bar{1}$]M-2 and (1$\bar{2}\bar{1}$)M-2 [11$\bar{1}$]M-2 (parallel to the second combination above) will rotate the interface from (111)A to (592)A for the crystal, M-2, with a second variant of the Kurdjumow-Sachs orientation relationship. The pseudo-habit plane expressed relative to the martensite lattice is approximately (455)M. As mentioned in explaining the

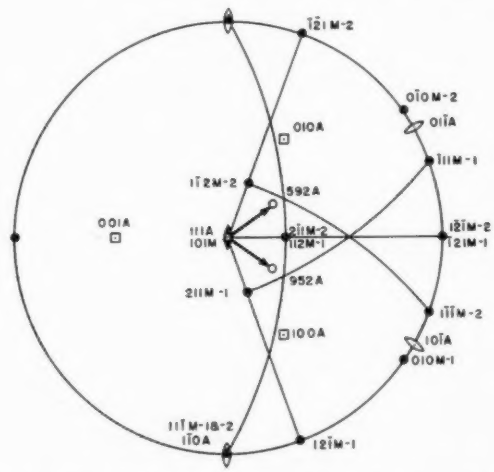

FIGURE 10. Stereographic projection of some slip elements which might operate to rotate the habit from (111)A to the {259}A habit by slip in the martensite (K-S relation):

Duplex Slip in Martensite
For crystal M-1 on 952A
(12$\bar{1}$)M [$\bar{1}$11]M
($\bar{1}$21)M [11$\bar{1}$]M
Latter in common with one for M-2 on 592A. Pseudo-habit = (455)M.

{225}A habit, it is likely that other possible slip elements rather than those illustrated in Figures 9 and 10 will be more favorable, depending on the actual stress configuration, but the operative slip systems must be determined experimentally.

Calculation of the strain in the martensite imposed by the austenite is also possible using a Jaswon-Wheeler type analysis in the reverse sense. The approach is developed by considering the atomic displacements required to form austenite

*Young [9] also attributed the rotation of the intermediate orientations of (110)M from the Nishiyama relation in Table I to slip as mentioned previously.

from martensite; the strain is considered equivalent to that imposed upon the martensite by the austenite. The strain tensor obtained by inverting some of the included matrices expresses the strain in the martensite when it is formed. Solution of the strain tensor for the three proper planes provides some interesting results analogous to those mentioned previously for spontaneous deformation in the austenite. The detailed analysis will not be presented, but it was found that for the martensite to austenite transformation the strain tensors, $\sigma_{0\%\,C}$ and $\sigma_{1.7\%\,C}$ can be obtained simply by interchanging the rows and columns of the tensors given by Jaswon and Wheeler [15] for the austenite to martensite transformation. The proper planes can be identified by the procedure which they outlined. The proper planes are first $(11\bar{1})$M for all carbon contents, second within 1° of $(25\bar{2})$M for all carbon contents, and third $(11\bar{1})$M for 0 per cent C to 6° from $(11\bar{1})$M for 1.7 per cent C. These planes are all normal to the (101)M // (111)A conjugate planes. The $(11\bar{1})$M plane is parallel with the $(1\bar{1}0)$A plane as specified in the orientation relationship whereas $(25\bar{2})$M is parallel with the $(\bar{7}43)$A plane. Interpretations of these planes can be suggested as has been done previously for strains in the austenite. The $(11\bar{1})$M plane is unrotated because it is one of the elements of the Kurdjumow-Sachs orientation relationship. The $(\bar{7}43)$A plane is that to which the interface tends to rotate with the (259)A an intermediate position in the rotation. In reference to Figure 1, the $(\bar{7}43)$A pole is located in the second stereographic triangle below that shown, 90° from (111)A and towards the great circle from the (111)A to the (011)A pole. If the interface rotated towards the $(\bar{7}43)$A pole, it would pass near (5, 34, 46) and (011). If at the same time plastic flow occurred in the austenite tending to rotate the interface from (111)A towards (225)A, then the interface may compromise on the (259)A position when sufficient flow has occurred to relax the transformation stresses. The (259)A pseudo-habit might be explained in this manner. It is not certain whether either this possibility or that suggested in Figure 10 for exclusive flow in the martensite is the unique one. Actually there are still other possibilities. First, the correct variant of the habit plane for the standard variant of the Kurdjumow-Sachs orientation relationship is not known;* it may be different from that assumed in which case other slip elements would be operative. Second, the second elements of the orientation relationship, i.e. $(11\bar{1})$M // $(1\bar{1}0)$A may be operative as conjugate planes in which case the initial interface could rotate from $(1\bar{1}0)$A towards $(7\bar{4}\bar{3})$A by operation of appropriate slip systems in the martensite.

An interpretation of the third proper plane of the strain tensor for plastic distortion in the martensite likewise may be advanced. The proper plane which varies for 0 to 6° from $(11\bar{1})$M with increasing carbon content may be the factor that rationalizes the Nishiyama orientation relationship and those intermediate ones in Table I in which the $[1\bar{1}\bar{1}]$M direction is misaligned with the $[1\bar{1}0)$A direction. Lattice rotation resulting from the transformation stresses is thus suggested. The $[1\bar{1}\bar{1}]$M rotates up to 6° in order to relieve the strains in the martensite. Operation of one of the slip systems indicated in Figure 10 will produce the 5°16′ rotation about (101)M necessary to change the orientation relationship from that of Kurdjumow and Sachs to that of Nishiyama as illustrated in Figure 11. Such an

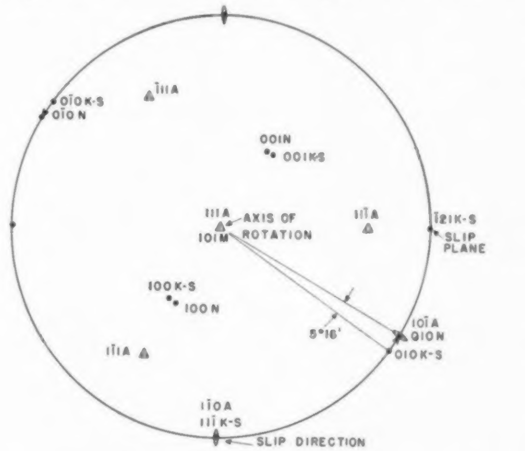

FIGURE 11. Slip elements for lattice rotation from the Kurdjumow-Sachs to the Nishiyama orientation relation by slip in the martensite.

operation of the single slip system would rotate the interface in a different manner from that accomplished by duplex slip and a modified pseudo-habit plane would arise.

A possible role of duplex slip in the martensite in causing rotation of the austenite-martensite interface is suggested in Figure 12. It is assumed that one slip system operates in one half of the martensite plate and the second operates in the other half with their plane of impingement offering an explanation of the midrib. Probably the situation is more complex

*Bowles has pointed out that this limitation is present in his analysis; he assumed that the standard variant is (111)A //(101)M, $[1\bar{1}0]$A//$[1\bar{1}\bar{1}]$M so that of the 24 possible orientations only the martensite crystal with the above was associated specifically with the (225) plane of the habit family.

but a low angle imperfection rather than a composition gradient is a logical explanation of the midrib. The particle is first parallel to the conjugate planes and grows until the stresses become intolerable. Plastic flow then commences and continues concurrent with further growth at the same time causing a rotation of the interface to the stable orientation which is detected as the pseudo-habit plane. The area bounded by the outline and the top interface of the particle in Figure 12 represents the strain energy—a product of stress, the vertical height, and strain which is proportional to a lateral dimension. The strain energy would become intolerable if the coherent particle continued to grow edgewise and the area continuously increased. Plastic flow causes a reduction in the stress to keep the outlined area representing strain energy at a tolerable value. An analogy of the curved interface for a lenticular particle with a stress catenary is probably reasonable. Actually the interface is probably made up of submicroscopic steps much the same as the larger ones when twinning occurs as in Figure 5*a*. The stable nucleus for the transformation might be the particle at any of the stages shown in Figure 12,

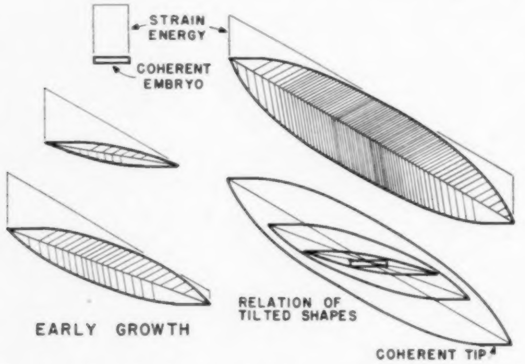

FIGURE 12. Habit rotation accompanying martensite formation by coherent nucleation and duplex slip. Operative slip planes are indicated by shading. Particle with stable midrib orientation shown in upper right is ready for extensive edgewise growth with minimum surface energy at advancing tips and minimum strain energy on balance of surface.

but presumably the embryo would be coherent on the {111}A plane since the misfit does not exceed 9 per cent if this value from the work of Van der Merwe may be considered applicable.

If the spontaneous deformation may be interpreted in terms of duplex slip, then the cooperative phenomenon discussed by Machlin and Cohen [17] may be interpreted as in Figure 13. Sharing of slip elements to relieve stresses in martensite plates with different variants within the family of habit planes was mentioned earlier when stereographic analyses were presented for flow in the austenite and flow in the martensite (Figures 7 and 10). Traces of slip planes are sketched in Figure 13 to show how three orientations of the (225) habit at the left might share three slip systems in pairs to form clusters of martensite plates in 3 of the possible 12 orientations; at the right two orientations of the (259) habit

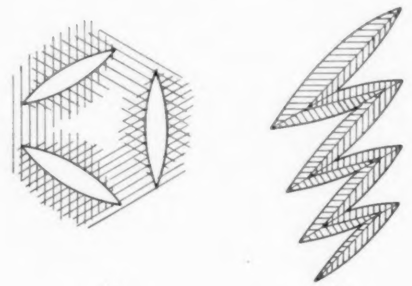

(*a*) (*b*)

FIGURE 13. An interpretation of the cooperative formation of martensite plates of related orientation by sharing of a common, parallel slip system of a pair for duplex slip: (*a*) by slip in austenite, (225) habit; (*b*) by slip in martensite (259) habit.

could share one of three slip systems to give the characteristic zig-zag traces with acute angles [10].

Discussion and Application to Other Martensitic Structures

On the basis of the new viewpoint the irrational features of martensitic structures are to be regarded as the result of spontaneous plastic flow accompanying the transformation. The dominant role of the shear is to minimize the strain energy and not necessarily to generate the new crystal structure. On this basis it is not necessary to draw a marked distinction between martensitic structures and those referred to as bainitic in iron-base alloys. There is no requirement that the crystallographic mechanism of forming the ferritic phase or the resulting microstructure in general will be different. A primitive mechanism should obtain for iron and the same should apply to its alloys as was once pointed out [11]. Any subsequent modification of the structure will occur by virtue of the particular mode by which the transformation stresses are relieved. Slow processes of stress relief such as recrystallization and recovery will occur when time and temperature are sufficient for bulk diffusion while the faster process of spontaneous deformation will occur when time is short. The habit plane and orientation data for iron-base alloys which are summarized in Figure 1 can be rationalized when the

modes of minimizing strain energy are provided a role in interpreting the structures. The five pertinent modes include recovery and the four effects of spontaneous deformation, (1) interface rotation from (111)A in the direction towards (001)A by slip in the austenite, (2) lattice rotation from the Kurdjumow-Sachs relation towards the Greninger-Troiano relation by slip in the austenite, (3) interface rotation from (111)A in the general direction of (011)A by slip in the martensite, and (4) lattice rotation from the Kurdjumow-Sachs relation towards the Nishiyama by slip in the martensite. A sixth mode, twinning in the ferritic phase with interface rotation from (111)A towards (011)A as in In-Tl alloys, may play a role in some ferrous alloys that transform at low temperatures where Neumann bands may form. Combinations of these modes can explain the data for martensite in Figure 1. A specific habit plane need not be associated with a specific orientation relationship as proposed by Machlin and Cohen when more than one mode of stress relief is operative. Likewise, it is unnecessary to assume that solute atoms affect the orientation of the nucleus to explain the various habits and orientation relations as Bowles has suggested.

In regard to the bainitic structures the time and temperature are sufficient to permit diffusing of carbon to cause carbide precipitation and to achieve part of the stress relief by recovery; the higher the temperature, the greater the contribution from recovery and lattice rotation and the less the contribution required from interface rotation so that the pseudo-habit is nearer to (111) as shown in Figure 1. The feature common to martensite and bainite presumably is that spontaneous deformation is a dominant factor in modifying the primitive product since the habit of bainite is irrational or the lattice is rotated as in martensite. A striated substructure parallel to (111)A which has been reported for lower bainite [39] can be interpreted as evidence for plastic flow during the formation of this structure also in common with martensite.* The observation of Greninger and Troiano [7] that the orientation relationship for their Fe-Ni-C alloy changed during tempering to the Nishiyama relation suggests that stresses are further relieved in martensite by lattice rotation during tempering as in bainite during the initial formation. Van der Merwe [26] has pointed out in regard to overgrowths that in all cases whatever the mechanism of the slip process, some residual stresses are likely to remain. Presumably the reheating of martensite for tempering provides sufficient atomic mobility to promote the lattice rotation. The lattice rotation during tempering might also accompany the formation of a polygonal subgrain structure from the spontaneous flow structure, for a polygonal subgrain structure in tempered martensite has been observed. The substructure in higher bainite has been known for a long time; ill-defined striations† similar to those for pure iron, for low carbon alloys and for the alloy shown by Figure 14*a* and Figure 14*b* are readily apparent. These striations are to be regarded as evidence of spontaneous deformation also. Microstructurally the product differs from martensite merely in that it is not confined by a lenticular interface but extends into a volume of rather irregular outline probably characteristic of a slower rate of formation. When faster rates of formation are required, there is some tendency for the formation of an acicular product as in Figure 14*b*. A similar structure consisting of striated product of irregular outline mixed with acicular product is observed for titanium, Figure 14*d*. Bowles and Mackenzie [41] have referred to a similar structure in an Fe-Ni-C alloy as "laminated" martensite; when regarded from the viewpoint of spontaneous deformation the structure is completely rational. Finally the irregular structure of clear grains on the left side of Figure 14*c* is occasionally observed after transformations; its close association with the striated structure suggests that it may be a mode of coalescence of dislocations though polygonalization of the slipped regions.

In the preceding discussions the assumption was made that the primitive mode of forming ferrite involved the Kurdjumow-Sachs orientation relationship and the {111}A true habit planes. Factors which seem to justify this choice can now be summarized. First these conditions are observed for slowly cooled alloys such as Fe-Ni and hypoeutectoid Fe-C when recovery can accomplish stress relief without gross structure modification through spontaneous deformation. Second, all the various orientation relationships specify a conjugate plane within 1° of {111}A which supports the choice of this family of planes for the primitive habit. Third, the orientation relaxes to the Nishiyama relation to

Note added in Proof.* (Received February 23, 1953.) Likewise, surface relief effects can no longer be regarded as characteristic of only diffusionless transformations with the strain representing part of the atom movements by shear, for bainite formed by nucleation and slow growth also produces distortions [Ko, T. and Cottrel, S. A. J. Iron Steel Inst., **172 (1952) 307–313].

†See, for example [40, Figure 24].

TABLE II

HABIT PLANES FOR MARTENSITIC STRUCTURES

Material	Lattice Change	Pseudo-Habit	Reference
Fe–0 to 0.40%C	F.C.C. → B.C.C. or B.C. Tet.	111 A	10, 11
Fe–0.55 to 1.4%C	F.C.C. → B.C. Tet.	225 A	10
Fe–1.5 to 1.8%C	F.C.C. → B.C. Tet.	554 M*	
		259 A = 332 M†	10
Fe–1.2%C – 11.5%Ni	F.C.C. → B.C. Tet.	259 = as above	10
Fe–0.8% – 22% Ni	F.C.C. → B.C. Tet.	332 M*	7
		9, 22, 33 A = 774 M†	17
		3, 10, 15 A = 332 M†	18
Fe–27 to 34% Ni	F.C.C. → B.C.C.	as above	10
Cu–11 to 13.1%Al	B.C.C. → Dist. H.C.P.β'	331	31
Cu–12.9 to 14.7%Al	B.C.C. → H.C.P.γ'	221	31
Cu–25%Sn	B.C.C. → ?β'	331	42
Cu–40%Zn	B.C.C. → ?β'	551 or 661	42
Au–34%Cd	B.C.C. → Ortho.	331	43
Li	B.C.C. → H.C.P.	441	44
Ti	B.C.C. → H.C.P.	88, 11	45
Ti–5%Mn	B.C.C. → H.C.P.	334 and 443	46
Zr	B.C.C. → H.C.P.	?‡	47
Co	F.C.C. → H.C.P.	111	1
In–28 to 37%Tl	F.C.C. → F.C. Tet.	110	31

*From stereographic analyses.
†By conversion using Bowles' transform for Kurdjumow-Sachs relation.
‡The results which have been reported for Zr are ambiguous [47]. Either {569} or {451} obtains with sufficient spread so that the pseudo-habit for Zr probably also conforms to the {*hhl*} generalization.

relieve additional stress during tempering thus suggesting that the orientation may have started from that specified by Kurdjumow-Sachs. Finally, the mismatch for martensite on austenite is somewhat less when the Kurdjumow-Sachs relation obtains.*

Although the preceding discussion has been devoted mainly to iron-base alloys, the principles should equally apply to other martensitic structures. Space does not permit a detailed analysis of each system, but a simple generalization suggests that spontaneous deformation plays a prominent role in controlling the pseudo-habit plane. Observed values are listed in Table II. Those habit planes which have been identified with deformation in the martensite have been converted to the corresponding planes in the martensite as mentioned in earlier discussion (Figures 9 and 10). The obvious generalization is that the pseudo-habit for cubic crystals tends to be a plane of the type (*hhl*) where two indices are the same. The significance of this type plane is that it is contained in the zone that has the axis [1$\bar{1}$0] which also contains simple planes such as (001), (110), (111), and (112) as in Figure 15. These low index planes may be prevalent true habit planes from which the interface can rotate to {*hhl*} using [1$\bar{1}$0] as the axis of rotation. Such an axis of rotation will be used during the spontaneous deformation when simple slip occurs on (111) or (112) planes with appropriate ⟨110⟩, ⟨112⟩, or ⟨111⟩ directions or when duplex slip occurs on a pair of systems that are symmetrically deployed relative to the [1$\bar{1}$0] zone axis. Many such systems are evident in Figure 15, especially if non-conventional elements such as {110} planes and [112] directions in face-centered cubic metals may be considered. The state of stress may well be such as to cause the operation of these less conventional elements, such as a (110) slip plane observed by Guinier for the copper solid solution containing beryllium, rather than the usual ones which operate under externally applied stress. The stress configuration is probably complex; it would more likely lead to duplex slip than simple slip, but because of the crystal symmetry it might always be resolvable into a principal uniaxial component in a {110}

*Young [9] regarded the Nishiyama relation as the primitive one since it involves simple symmetrical movements of the atoms and it obtains at low transformation temperatures where the thermal agitation presumed necessary for lattice rotation by shearing in the nucleus is unavailable. In so far as demonstrating the principles of spontaneous deformation, the choice is arbitrary.

plane* which becomes the rotation plane—*RP* in Figure 15— using the plane normal for the rotation axis simulated by the symmetrically deployed slip systems. The observed pseudo-habit planes plotted in Figure 15 tend to cluster on either side of (110) and (111) poles which is probably significant since these are the two types of planes which are used to specify the orientation relationships among the alloys listed in Table II; they represent one of the conjugate planes which thus may be regarded as the true habit plane. The rotation from the (110) or

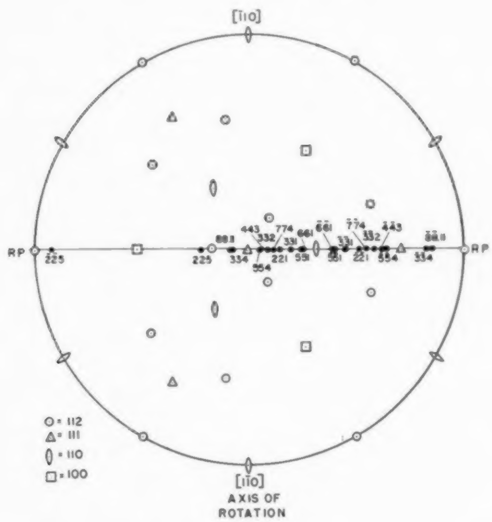

FIGURE 15. Stereographic projection of poles of observed habit planes for a variety of cubic (matrix) alloys and low index true habit planes that are located in the plane of rotation, *RP*, with a symmetrical distribution of poles which may act as slip elements.

(111) plane to any of the pseudo-habit planes is less than that from the (100) plane which is one of less atomic packing and does not serve as the true habit for any of the alloys considered here. The {*hhl*} generalization for habit planes could hardly be a coincidence for the many alloy systems in Table II; it probably was not recognized earlier because the {259}A indices fit only when the martensite plane on the interface rather than the austenite plane is considered. Regardless of the complexity of the pseudo-habit plane only the flow elements with simple indices such as (111), (110), and (112) are needed to explain martensitic structures in cubic metals.

*Evidently in some cases there is a residual component in a plane normal to *RP* to cause the martensite lattice rotation from the Kurdjumow-Sachs to the Nishiyama orientation relationship (Figure 11).

Conclusion

A general classification of the structural aspects of both diffusion-controlled and diffusionless transformations appears to be possible. The classification is based upon energetic factors such as interfacial surface energy, strain energy, and diffusion rather than upon any proposed differences in mechanism or kinetics of forming the primitive product. All the factors participate to varying degree in all transformations but the dominance of one or another exerts a controlling influence. In diffusion-controlled Widmanstätten structures surface energy factors such as a discrete orientation relationship, a low index habit plane and a tendency for a pseudomorphic or coherent crystal structure dominate. These factors have been long recognized; factors that modify strain energy should now be recognized rather than attempting to rationalize all structures on the basis of interfacial energy. In martensitic structures strain energy factors such as spontaneous deformation by slip and twinning dominate to modify the factors established by interfacial energy. The strain energy factors lead to modified or pseudohabits and pseudo-orientation relationships much the same as surface energy may lead to a pseudomorphic crystal structure. Thus, spontaneous deformation has attractive possibilities of qualitatively explaining a variety of microstructural and crystallographic features associated with martensitic structures. Microstructurally the transformed zone may be either lenticular or irregular in outline both with substructure or it may be polygonal free of substructure; it may form either slowly or rapidly, isothermally or athermally according to kinetics, but the conventional distinction of *generation* by shear in contrast with nucleation and growth is not necessary to explain the observations regarding structure. On the viewpoint that spontaneous deformation induces irrational habit and irrational orientation, the limiting case of a martensitic structure would be a spherulite such as nodular graphite [48; 49]; the habit plane which might have existed for an initial orientation relationship is completely warped into a sphere while any orientation relationship has degenerated by systematic lattice rotations to give the unique orientation of the segments within the particle whereby the basal planes tend to be normal to radii. Tendencies for a martensitic structure in diffusion-controlled transformations and overgrowths are manifested by slip and twinning which may be evident by striated microstructures and by faulted or slightly rotated crystal structures. On the basis of this generalization

it is not necessary to assume any mechanism other than a simple atom by atom movement to form the new structure followed by shear to relieve transformation stresses. When the transformation is diffusionless the movement is visualized as being well organized with one atom pulling the others and obeying the principle of minimum displacement, but the path may be either more direct or more complex than those which have been resolved by two components.

No claim is made that the slip elements listed in Figures 7, 9, 10, 11 are the unique ones that operate in the martensite reaction in iron-base alloys. Instead they were used mainly to demonstrate the principles of spontaneous deformation. A thorough study of substructure and correlation of martensite orientation with the specific variant of the habit plane are needed for both {225} and {259} pseudo-habits before the details of any of the proposed mechanisms (including "double strain") can be regarded with confidence. While the deformation can be described stereographically in terms of slip and twinning, the more fundamental description probably resides in a treatment by the flow of dislocations. An expansion of the application of dislocation theory to stress relief in over-growth [50] and the dislocation treatment of martensite [18] applied from the viewpoint of relieving stress in either the austenite or the martensite rather than generating the new structure appear to be attractive. The interface during growth might be achieved by a mobile array of dislocations which responds to stress, spontaneous or applied. Dislocation theory should offer possibilities for both interpretation and quantitative treatment of factors such as reversibility, applied stress, and nature of demobilization (whether as twins, slips, or polygons) as they are related to spontaneous flow during particle growth after nucleation.

Acknowledgement

The author is most grateful for the helpful comments of W. R. Hibbard, Jr. and D. Turnbull on the manuscript. The assistance of previous collaborators listed among the references has contributed appreciably to the culmination of the viewpoint expressed here.

References

1. Bowles, J. S. and Barrett, C. S. Progress in Metal Physics, **3** (1952) 1–41.
2. Fisher, J. C., Hollomon, J. H., and Turnbull, D. Trans. A.I.M.E., **185** (1949) 691–700.
3. Kurdjumow, G. and Sachs, G. Z. Physik., **64** (1930) 325; Naturwiss., **18** (1930) 534.
4. Wassermann, G. Mitt. Kaiser-Wilhelm Inst. Eisenf., **17** (1935) 149–155.
5. Nishiyama, Z. Sci. Rept. Tôhoku Imp. U., **23** (1934) 637-664; Kinsoku no Kenkyu **11** (1934) 561–589.
6. Mehl, R. F. and Derge, G. Trans. A.I.M.E., **125** (1937) 482–496.
7. Greninger, A. B. and Troiano, A. R. Trans. A.I.M.E., **185** (1949) 590–598.
8. Neerfeld, H. and Mathieu, K. Arch. Eisenh., **20** (1949), 69–73.
9. Young, J. Phil. Trans. Roy. Soc., **238A** (1939) 393–421.
10. Greninger, A. B. and Troiano, A. R. Trans. A.I.M.E., **140** (1940) 307–332.
11. Mehl, R. F. and Smith, D. W. Trans. A.I.M.E., **113** (1934) 203–209.
12. Smith, G. V. and Mehl, R. F. Trans. A.I.M.E., **150** (1942) 211–226.
13. Mehl, R. F., Barrett, C. S., and Smith, D. W. Trans. A.I.M.E., **105** (1933) 215–249.
14. Cohen, M. In "Phase Transformations in Solids" (New York, John Wiley and Sons, 1951), pp. 588–659.
15. Jaswon, M. A. and Wheeler, J. A. Acta Cryst., **1** (1948) 216–224.
16. Bowles, J. S. Acta Cryst., **4** (1951) 162–171.
17. Machlin, E. S. and Cohen, M. Trans. A.I.M.E., **191** (1951) 1019–1029.
18. Frank, F. C. Acta Met., **1** (1953) 15–21.
19. Newkirk, J. B., Geisler, A. H., Martin, D. L., and Smoluchowski, R. Trans. A.I.M.E., **188** (1950) 1249–1260.
20. Geisler, A. H. Metal Interfaces (Cleveland, Amer. Soc. Metals, 1952), pp. 269–295.
21. Geisler, A. H., Mallery, J. H. and Steigert, F. E. Trans. A.I.M.E., **194** (1952) 307–316.
22. Northcott, L. J. Inst. Met., **59** (1936) 225–252.
23. Gunier, A. and Jacquet, P. Rev. Met., **41** (1944) 1–16.
24. Guinier, A. and Jacquet, P. Nature, **155** (1945) 695.
25. Gayler, M. L. V. Nature, **156** (1945) 333.
26. Lipson, H., Shoenberg, D., and Stupart, G. V. J. Inst. Met., **67** (1941) 333–340.
27. Geisler, A. H. and Martin, D. L. Discussion to [28], Trans. A.I.M.E., **191** (1951) 1057–1060.
28. Bowles, J. S., Barrett, C. S., and Guttman, L. Trans. A.I.M.E., **188** (1950) 1478–1485.
29. Guttman, L. Reply to [27], Trans. A.I.M.E., **191** (1951) 1060.
30. Guttman, L. Trans. A.I.M.E., **188** (1950) 1472–1477.
31. Greninger, A. B. Trans. A.I.M.E., **133** (1939) 204–221.
32. Van der Merwe, J. H. Crystal Growth (London, Faraday Soc., 1949), pp. 201–214.
33. Cochrane, W. Proc. Phys. Soc., **48** (1936) 723–735.
34. Thirsk, H. R. Proc. Phys. Soc., **63B** (1950) 833–839.
35. Harker, D. and Murphy, M. J. Trans. A.I.M.E., **161** (1945) 75–89.
36. Harker, D. Trans. A.S.M., **32** (1944) 210–234.
37. Burke, J. E. and Barrett, C. S. Trans. A.I.M.E., **175** (1948) 106–117.
38. Barrett, C. S. Structure of Metals, 2nd ed. (New York, McGraw-Hill, 1952), Chap. XV.

39. COHEUR, P. and HABRAKEN, L. Rev. Univ. Mines, Met. Trab. Pub. **94** (1951) 107–111.
40. MEHL, R. F. and DUBE, A. In "Phase Transformations in Solids" (New York, John Wiley and Sons, 1951), pp. 545–582.
41. BOWLES, J. S. and MACKENZIE, J. K. Discussion to [17], Trans. A.I.M.E., **194**, (1952) 1201–1204.
42. GRENINGER, A. B. and MOORADIAN, V. G. Trans. A.I.M.E., **128** (1938) 337–355.
43. CHANG, L. C. and READ, T. A. Trans. A.I.M.E., **191** (1951) 47–52.
44. BOWLES, J. S. Trans. A.I.M.E., **191** (1951) 44–46.
45. NEWKIRK, J. B. and GEISLER, A. H. Acta Met., **1** (1953).
46. LIU, J. C. and MARGOLIN, H. Conf. on Crystallography of Ti and its Alloys, New York Univ., 1952.
47. VAN GINNEKEN, A. J. J. and BURGERS, W. G. Acta Cryst., **5** (1952) 548–549.
48. STAUSS, H. E., VAN BATCHELDER, F. W., and SALKOVITZ, E. I. Trans. A.I.M.E., **191** (1951) 249.
49. WELD, H. M., CUNNINGHAM, R. L., and BOSWELL, F. W. C. Trans. A.I.M.E., **194** (1952) 738–742.
50. FRANK, F. C. and VAN DER MERWE, J. H. Proc. Roy. Soc., **198A** (1949) 205–225.

THE KINETICS OF FORMATION AND STRUCTURE OF ANODIC OXIDE FILMS ON TANTALUM*

D. A. VERMILYEA†

The rate of formation of anodic oxide films on tantalum was studied using aqueous electrolytes. The thicknesses of the oxide films were measured by comparing the interference colors with a calibrated step gage. The equation which describes the kinetics of formation of the films is

$$\frac{dx}{dt} = A \exp\left(BF - \frac{Q}{kT}\right)$$

where $B \neq f(T)$. This equation is not in agreement with the predictions of a recent theory by Mott and Cabrera which should apply to this process. The rate of formation of a film is not affected by its past history, the state of cold work of the metal, or by changes in the nature and concentration of the aqueous electrolyte. The efficiency of the process is 98 per cent at all temperatures and rates of formation. The films consist of amorphous Ta_2O_5, and recrystallize between 500 and 800°C.

LA CINÉTIQUE DE FORMATION ET LA STRUCTURE DE FILMS ANODIQUES SUR LE TANTALE

La vitesse de formation de films anodiques d'oxyde sur le tantale a été étudiée dans des électrolytes aqueux. Les épaisseurs des films d'oxyde ont été mesurées en comparant les couleurs d'interférence avec un calibre à gradins. L'équation qui décrit la cinétique de formation des films est:

$$\frac{dx}{dt} = A \exp\left(BF - \frac{Q}{kT}\right)$$

où $B \neq f(T)$. Cette équation n'est pas en accord avec les prédictions d'une récente théorie de Mott et Cabrera, qui devrait s'appliquer à ce procédé. La vitesse de formation d'un film n'est pas influencée par son histoire, le degré d'écrouissage du métal, ou par des changements dans le genre et la concentration de l'électrolyte aqueux. Le rendement du procédé est de 98 pour cent à toutes les températures et toutes les vitesses de formation. Les films consistent en du Ta_2O_5 amorphe et cristallisent entre 500 et 800°C.

DIE KINETIK DER BILDUNG UND DIE STRUKTUR ANODISCHER OXYDFILME AUF TANTAL

Die Geschwindigkeit der Bildung von anodischen Oxydfilmen auf Tantal in wässrigen Elektrolyten wurde untersucht. Die Filmdicken wurden durch Vergleich der Interferenzfarben mit denen geeichter Interferenzstufen gemessen. Die Gleichung, die Kinetik der Filmbildung beschreibt ist

$$\frac{dx}{dt} = A \exp\left(BF - \frac{Q}{kT}\right)$$

wobei $B \neq f(T)$ ist. Diese Gleichung steht im Widerspruch zu den Voraussagen der neuen Theorie von Mott und Cabrera, die für diesen Prozess gelten sollte. Die Geschwindigkeit der Bildung eines Films wird weder durch dessen Vorgeschichte, noch durch den Kaltbearbeitungszustand des Metalles oder durch Änderungen in der Art oder Konzentration des wässrigen Elektrolyten beeinflusst. Die Ausbeute des Vorgangs ist bei allen Temperaturen und Bildungsgeschwindigkeiten 98 prozent. Der Film besteht aus amorphem Ta_2O_5 und rekristallisiert zwischen 500 und 800°C.

Introduction

It has been known for many years that the growth of oxide films on metals follows entirely different rate laws at different temperatures. The parabolic law, characteristic of thick films formed at high temperatures, is adequately explained by the Wagner theory [1] which assumes that the rate-controlling step of the process is the diffusion of ions through the film to the reaction interface. The logarithmic rate law observed for the formation of thin films at low temperatures, on the other hand, is not yet well understood.

The most promising theory to explain the logarithmic law was proposed recently by Mott and Cabrera [2]. The basic postulate of this theory is that the rate determining step is the transfer of an ion across an interface. A strong electric field, produced by a layer of adsorbed oxygen ions at the oxide-atmosphere interface, lowers the energy barrier for ionic diffusion. Under the influence of this field, which is of the order of 10^7 volts per centimeter, the motion of ions is shown to be overwhelmingly in the direction of the field, the number of jumps in the reverse direction being negligible. The rate of growth of the oxide is determined by the rate at which ions jump from the metal or from the adsorbed oxygen layer into the oxide under the influence of the electric field.

The rate equation derived by Mott and Cabrera for this process is:

$$\frac{dx}{dt} = \nu N V \exp - \left(\frac{Q - q\lambda F}{kT}\right) \qquad (1)$$

*Received December 19, 1952.
†General Electric Research Laboratory, The Knolls, Schenectady, New York, U.S.A.

where ν is the vibration frequency, N the number of atoms in position to jump into the film, V the volume of oxide per metal ion, Q the activation energy, q the charge of the ion, λ the distance from the equilibrium position of an ion in the metal to the top of the energy barrier, and F the electric field. An approximate integration of equation (1), valid only for $q\lambda F/kT \gg 1$, gives the following logarithmic relation between thickness and time:

$$\frac{I}{x} = a - b \ln t \tag{2}$$

where a and b are constants for a given temperature.

One consequence of the logarithmic law is that the rate of growth is initially very great, but decreases rapidly so that the oxide approaches a limiting thickness. A limiting thickness may be calculated from equation (1), assuming an arbitrary very small rate, and has the form:

$$X_L = \frac{C}{T_c - T} \tag{3}$$

where X_L is the limiting thickness, C is a constant, and T_c is a critical temperature. At a rate growth of one atom layer per day the critical temperature is $Q/39k$. For air oxidation of aluminum and copper, Mott and Cabrera have found fair agreement between the temperature dependence of experimentally determined values of limiting thickness and the theory when reasonable values for the various parameters were assumed. For aluminum, the predicted critical temperature above which the logarithmic law no longer holds is in good agreement with the theory. The theory was also applied to data obtained by Guntherschulze [3] for the anodic oxidation of aluminum, and again reasonable values were obtained for the various parameters in the equation. Unfortunately data for anodic oxidation were not available over a range of temperatures, and the theory was applied to results obtained at only one temperature.

It was believed that a more critical evaluation of the theory could be made by studying the actual rates of growth of the films rather than the limiting film thickness. Anodic oxidation has the advantage, for such an evaluation, that the applied voltage can be measured accurately and varied over a wide range, while in air oxidation it is a fixed value equal to the difference in potential between the metal and the adsorbed ions. It is thus possible to study the rate of growth of anodic films over a wide thickness range and to vary the field in the oxide at will. It should therefore be possible to measure all of the parameters accurately and to test the functional relationship given by equation (1). After an examination of the literature on anodic oxidation it was decided to study the formation of anodic films on tantalum because they were reported to be very stable and also because they exhibit brilliant interference colors which may be used as a measure of thickness. Since there have been conflicting reports on the structure of these films the present investigation also includes a crystal structure study.

Many studies of the growth of anodic oxide films on tantalum were made by Guntherschulze and co-workers, and a summary of the work may be found in a book by Guntherschulze and Betz [3]. The types of curves found for anodic oxidation at constant current are shown in Figure 1. The ideal

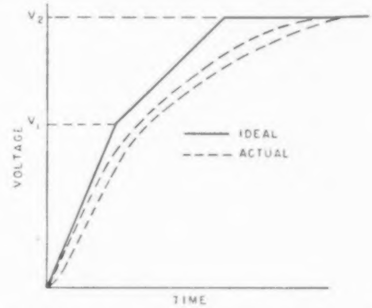

FIGURE 1. Voltage-time curve obtained during the formation of anodic films on tantalum at constant current, according to Guntherschulze [3].

behavior is represented by the solid curve which shows a linear rise of voltage with time up to V_1, called the "spark voltage." Above V_1 the voltage still rises linearly at a slower rate to V_2, the "maximum voltage," after which it remains constant. The actual curves shown by Guntherschultze often exhibited curvature like the dotted lines in the figure.

The present investigation was concerned only with the formation of films below the "spark voltage." Guntherschulze reported that the slope of the voltage-time curve in this voltage range was independent of the nature and concentration of the electrolyte for all dilute aqueous electrolytes. Capacity measurements showed that the thickness was proportional to the applied voltage below the spark voltage, which means that the electric field in the oxide is constant under the condition of constant current. Also, since the thickness is proportional to the voltage it must also be proportional to the time, which means that the efficiency is constant. The value of the efficiency calculated from capacity measurements was about 40 per cent.

Guntherschulze also investigated the relationship between current density and electric field at constant temperature. He obtained an equation of the type:

$$(4) \qquad i = A \exp (BF)$$

where i is the current density, F the field, and A and B are constants. The data show considerable scatter and could be represented equally well by expressions involving $\exp(-B/F)$. Since the reported efficiency was only 40 per cent it would be difficult to relate equation (1) to the growth of the oxide film.

Van Geel and Emmens (4) reported that the current was proportional to the reciprocal of the time during the formation of anodic oxide films on tantalum. If the efficiency is constant, as Guntherschulze's results imply,

$$(5) \qquad dx = k\, i\, dt\ ;$$

and if

$$(6) \qquad i = \frac{c}{t},$$

the expression for the thickness as a function of time is

$$(7) \qquad x = a + b \ln t$$

where a and b are constants. This rate law is probably almost indistinguishable experimentally from the equation derived by Mott and Cabrera.

The crystal structure of thin anodic films on several metals was determined by Burgers, Classen, and Zernicke [5], who reported that the tantalum film consisted of normal orthorhombic Ta_2O_5. They did not state the conditions of formation of the film and no X-ray data were given. Spauschus [6] has used reflection electron diffraction to study the structure of anodic films on tantalum and reported that only the diffuse rings characteristic of amorphous substances appeared in the patterns. Spauschus also reported values of interplanar spacing for crystals of Ta_2O_5 that do not agree with those published in the A.S.T.M. card index.

Experimental

Specimen Preparation

The tantalum was obtained from Fansteel Metallurgical Company, and their chemical analysis shows Ta 99.9+ %, C .03% max, Fe .03% max. Rolled sheet was used for all the experimental work, and was annealed prior to all experiments except those designed to determine the effect of cold work on the rate. Specimens were chemically polished by dipping for a few seconds in a mixture consisting of 5 parts 95% H_2SO_4, 2 parts 70% HNO_3, and 2 parts 48% HF. This treatment removed all scratches and any grease or other foreign materials, and left a surface comparable to that obtainable by electropolishing.

The type of specimen used for the rate studies is shown in Figure 2. Before a specimen was used the tab was anodized to 400 volts and the end scraped bare so that electrical contact could be made. This

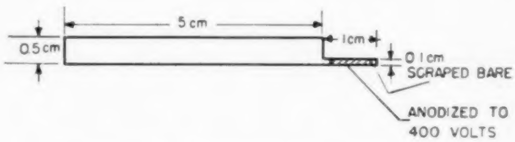

FIGURE 2. Specimen used for rate studies.

procedure was necessary so that an accurate measurement of the area could be made. If the tab was not previously anodized the oxide would creep up along the tab during a run so that the total surface exposed was continually changing.

Apparatus and Procedures for Rate Studies

Dilute aqueous electrolytes were used for all of the rate studies. Two different methods were employed to determine the relationship between rate of growth, temperature, and field. The first method was to anodize at constant current and measure the voltage and thickness periodically. The regulation of the constant current supply used was only $\pm$ 5 per cent at low currents, but by manually adjusting the current a few times during the course of a run it was easily possible to maintain the current within one per cent. The second method was to keep the voltage constant and measure the thickness and current at various times. The constant voltage power supply would maintain the voltage within one per cent from 0 to 500 volts and from 0 to 300 milliamperes for long periods of time.

A block wiring diagram of the apparatus is shown in Figure 3. Switch S_1 selects the power supply to be used. When the constant current supply is used switches S_2 and S_3 are closed, shorting the output of the supply through contacts 1R1 of relay 1. The current output is read on the ammeter and adjusted to the desired value. When switch S_4 is closed, the electronic timer energizes relay 1 for an amount of time which may be varied from 0.1 to 7 seconds. When relay 1 is energized the contacts 1R1 open permitting the current to flow through the cell, while contacts 1R3 close starting the timing clock. The time can be read to .001 seconds. Relay 1 may also be energized manually for longer times

with a separate switch (not shown). When the constant voltage supply is to be used, switches S_2 and S_3 are opened and the voltage is adjusted to the desired value. When relay 1 is energized contacts 1R2 close applying the voltage to the cell.

The temperature of the electrolyte was kept constant within $\pm$ 0.05°C by means of a water bath.

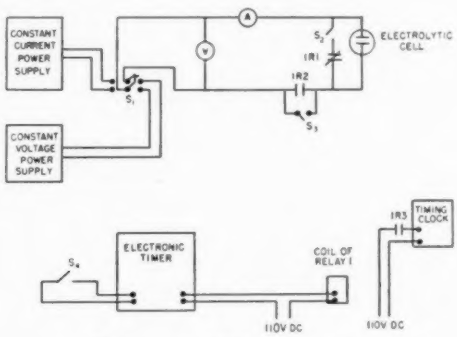

FIGURE 3. Wiring diagram.

Thickness Measurement

The method used to measure thickness makes use of the striking interference colors exhibited by the anodic film. Unknown thicknesses were measured by visual comparison with a color step gage which was calibrated by measurements of weight changes.

For the master calibration gage, specimens 6 cm. by 4 cm. were anodized at 2 ma/cm² to voltages up to 390 volts using 0.1 per cent Na_2SO_4 at 48°C, and the weight of each specimen was measured before anodization and after the desired voltage was reached. The specimen was then held at constant voltage until the current density of 0.1 ma/cm² was reached, and the weight was again measured. Measurements of reflected intensity versus wavelength of incident light were made using a recording spectrophotometer.* Smaller specimens like the one shown in Figure 2 were anodized at closer voltage intervals under the same conditons and used for the working step gage.

The thickness of each specimen of the master gage was calculated from the weight changes, optical measurements, and Faraday's law. It will be shown later that the composition of the film is Ta_2O_5, and thickness calculations were made with the assumption that the density of the film was the same as the bulk density of Ta_2O_5 (8.74 gm/cc). At a current density of 2 ma/cm² the least square slope of the thickness-voltage plot was 14.95°Å/volt from weight measurements and 15.27°Å/volt from Faraday's law. The efficiency is therefore 98 per cent, in comparison with 40 per cent measured by Guntherschulze. If the efficiency were actually 40 per cent gas evolution should be observed at the anode, but no such gas evolution is observed. Since Guntherschulze calculated the thickness from capacity measurements, the lack of agreement may be the result of an incorrect value for the dielectric constant.

At a current density of 0.1 ma/cm² the least square equation for the thickness-voltage plot was

$$x = 19 + 16.32\ V \tag{8}$$

where X is in Å. The probable errors are .06Å/volt in the slope and 11 in the intercept. Equation (8) was used to calculate the thickness of each specimen of the final working gage.

The optical measurements provided an independent check of the thickness-voltage relationship. The thickness of a film may be calculated from the wavelength at which the reflected intensity is a minimum if the refractive index of the film is known. Analysis of the spectrophotometer traces obtained from films which were thick enough to give minima corresponding to several orders of interference indicated that the refractive index should depend on the wavelength according to the empirical equation:

$$n = n_0 + \frac{5.5 \times 10^{-28}}{8}. \tag{9}$$

The value of n_0 required to give agreement between weight and optical measurements is 2.449, and the values of refractive index at 7000 and 4000Å are then 2.45 and 2.53 respectively.

According to Waber [7] the refractive index of crystals of Ta_2O_5 is:

$$n = 2.033 + \frac{8.74 \times 10^{6}}{2}. \tag{10}$$

This equation gives values at 7000 and 4000Å of 2.21 and 2.58 respectively. Although the variation of refractive index with wavelength obtained in the present investigation is much less than that found by Waber, the values are in the same range. The optical measurements therefore give further confirmation that the film is actually Ta_2O_5 and the agreement between the thickness calculated from weight changes and optical measurements is satisfactory. The high precision of the optical method

---

*The author is indebted to Mr. C. E. Dorland of the Campbell Avenue Plant, General Electric Company, for the spectrophotometer traces.

is shown by the thickness-voltage plot in Figure 4. The reason that the line does not go through the origin is that the phase change on reflection from the metal-oxide interface is not exactly 180°, and the constant phase difference is equivalent to a difference in thickness.

An estimate of the errors in thickness which would be caused by the observed variations in current density, temperature, and voltage indicated that the maximum errors in the thickness of individual specimens of the final step gage would be as follows:

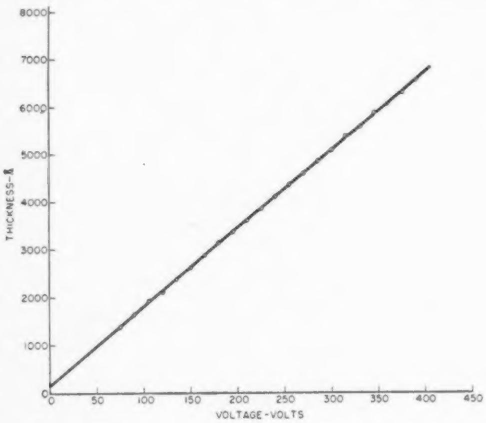

FIGURE 4. Thickness versus voltage from optical measurements.

Thickness range	Maximum error
200– 500Å	1Å
500–2500Å	4Å
2500–5000Å	8Å

The absolute accuracy could be in error by several per cent if the density of the thin film is not the normal bulk density. The error in actually using the step gage to estimate the thickness of an unknown film may be much greater than the maximum errors given above because of the inability of the observer to distinguish color differences between specimens. From 500 to 900Å the color change is so gradual that specimens with less than 30Å thickness difference cannot be distinguished with certainty. In most ranges of thickness differences of 8Å may be detected, while in the range from 350 to 450Å differences as small as 2Å may be detected.

Determination of Film Structure and Composition

The structure of the oxide films was determined by means of reflection electron diffraction from films in place on the substrate and by X-ray diffraction from films both in place and stripped from the substrate. The films were stripped by cutting the tantalum sheet and removing small sections of the cracked oxide next to the cut.

The composition of the oxide films was determined indirectly by comparing thicknesses calculated from weight changes with those predicted from Faraday's law, from observations of weight changes on heating the films in a vacuum, and from the structure of recrystallized films.

Results

Kinetic Studies at Constant Current

The purpose of the studies at constant current was to obtain the relationship between rate of growth, field, and temperature. The field and rate of growth were obtained from the slopes of thickness-voltage and thickness-time plots for different temperatures and rates. Figure 5 shows typical curves obtained for a run at 8 ma/cm^2 and 19°C. Least square plots were made to determine the field since the total variation of field at any temperature was only about 40 per cent and it was therefore necessary to know the individual values very accurately.

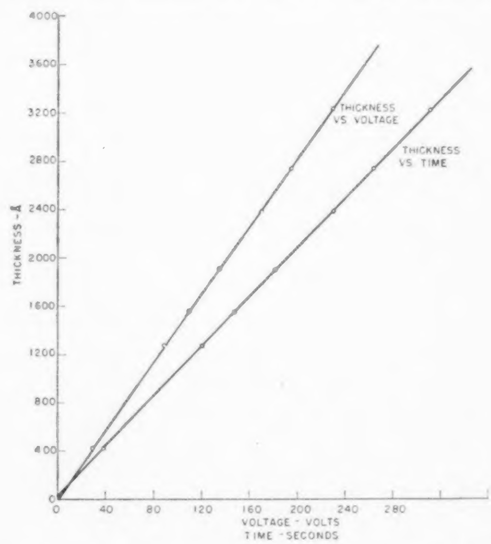

FIGURE 5. Thickness as a function of voltage and time at 8 ma/cm^2 in 1 per cent Na_2SO_4 at 19°C.

The probable error was $\pm$ 0.00015 volts/Å in the field, or about 0.2 per cent at a field of .075 volts/Å.

Figure 6 shows a plot of the logarithm of the rate versus field for five temperatures. In the figure the field scale has been shifted so that the curves coincide at ln $(dx/dt) = 0$. It may be seen that the plots are identical within experimental error for all temperatures, and consist of a linear region at low fields followed by a more rapid increase of rate

with field at high fields. The slopes of the linear portions averaged 505 with a range of $\pm$ 10. The equation for the linear regions of the curves could therefore be written:

$$\ln \frac{dx}{dt} = \ln C + BF \tag{11}$$

where $B = 505$ and C is a function of temperature.

TABLE I

RATE AS A FUNCTION OF FIELD AT CONSTANT TEMPERATURE

$\ln (dx/dt) = \ln C + BF$

Temperature °C	$\ln C$	B
0.5	−35.65	506
19	−33.77	510
40.5	−31.70	500
60.5	−30.25	512
79	−28.90	497

The data are given in Table I. A plot of ln C versus the reciprocal of the absolute temperature gave the

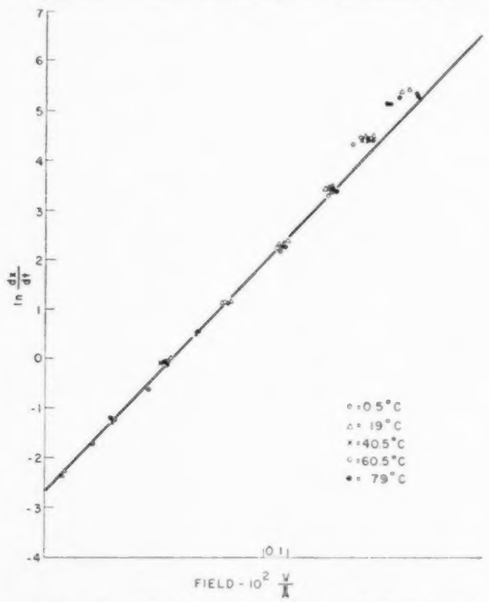

FIGURE 6. Ln (dx/dt) as a function of field at various temperatures. The field scale has been shifted for each curve so that all coincide at ln $(dx/dt) = 0$.

straight line shown in Figure 7. The activation energy calculated from the slope of the line is 0.71 eV(16.4 kcal per mol), and extrapolation to $1/T = 0$ gave a value of -5.5 for the intercept. The data obtained from the linear portion of the ln (dx/dt) versus field curves are therefore described by the equation:

$$\frac{dx}{dt} = A \exp - \left(\frac{Q}{kT} - BF\right) \tag{12}$$

where $A = e^{-5.5}$, $B = 505$, $Q = 0.71$ eV(16.4 kcal/mol) and where the rate is in Å/second and the field in volts/Å.

It is believed that the explanation for the deviation of the ln (dx/dt) versus field plot from linearity at high rates of formation is that the heat generated by the passage of current through the oxide cannot be conducted away rapidly enough, so that the

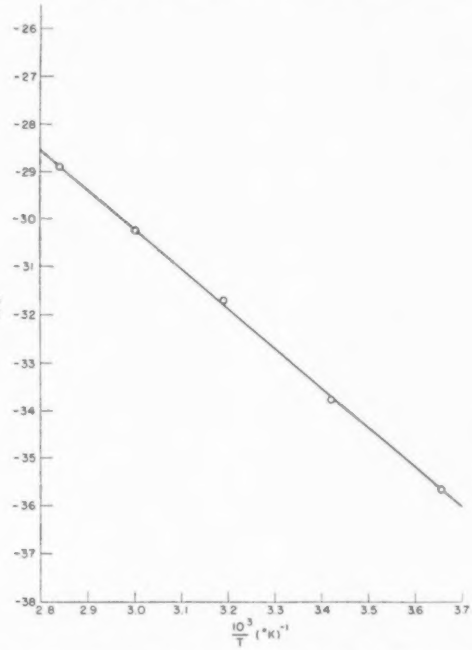

FIGURE 7. Temperature dependence of the intercepts of the ln (dx/dt) versus field curves at zero field.

film is heated above the temperature of the electrolyte.* A rough calculation of the magnitude of this temperature rise, assuming that heat was supplied at a constant rate at the surface of an infinite block of tantalum, gave 2°C per $(\text{second})^{\frac{1}{2}}$ at a rate of formation of 90Å per second (ln $(dx/dt) = 4.5$). At this rate the interval between measurements was about 4 seconds, so the maximum temperature rise would be 4°C and the average temperature would be at least 2°C higher than the bath temperature. From the measured activation energy a temperature rise of 2°C would increase the logarithm of the rate by about 0.2, while the observed increase was 0.3. The boundary conditions assumed for the calculation are not exactly fulfilled, however, since in these experiments heat is being added at both sides of a thin sheet. The temperature rise would therefore be somewhat greater than 2°C, and might easily be great enough to account for the observed

*The author is indebted to Dr. J. C. Fisher of the Research Laboratory for this explanation.

increase in rate. It may be concluded that equation (12) is probably valid over the complete range of temperatures, fields, and rates of formation.

Several other important observations were made from the data obtained from constant current runs. First, the efficiency obtained by comparing the observed rate with Faraday's law was constant with an average value of 98.4 per cent over the entire range of temperatures and rates. Since the original calibration of the step gage gave an efficiency of 98 per cent, these results mean that the efficiency is the same under all conditions. Second, the intercept of the thickness-time plot at zero time was constant with an average value of 33Å, which probably means that a thin air-formed oxide film was present initially. Third, the intercept of the thickness-voltage plot at zero thickness varied with the rate of formation, as shown in Figure 8. The increase in intercept with increasing rate means that less voltage drop actually occurs across the oxide film at the higher rates, the rest occurring as voltage drop in the electrolyte and polarization.

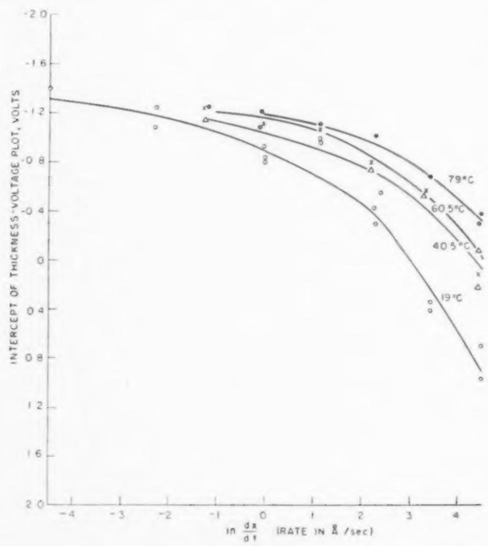

FIGURE 8. Polarization and voltage drop in the electrolyte as a function of log rate.

The curves shown in Figure 8 appear to be asymptotic to about − 1.4 volts at very small rates. This negative voltage intercept is the potential of the electrochemical reaction occurring in the cell during the formation of the oxide film and this potential is present across the oxide in addition to the applied voltage. This potential must be added to the applied potential when the field in the oxide is calculated.

Kinetic Studies at Constant Voltage

Rate studies were made at constant voltage in order to test equation (2) derived by Mott and Cabrera, and also to check the results from the constant current runs. Two corrections were necessary in making a run at constant voltage. The first was a compensation for the polarization and voltage drop in the electrolyte, and made use of the results reported above for runs at constant current. At the

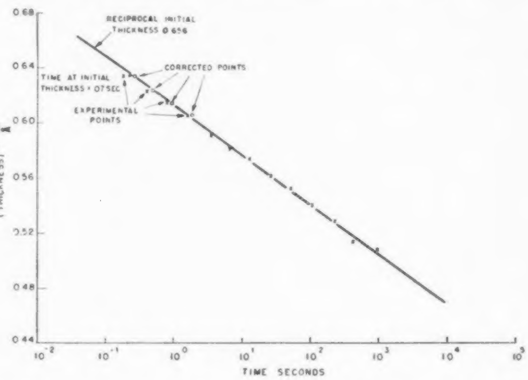

FIGURE 9. Method of correcting the initial points of the constant voltage runs.

start of each portion of a run the field which would be present in the oxide was estimated from the observed thickness. The rate corresponding to this field was obtained from the ln (dx/dt) versus field curves shown in Figure 7, and the sum of polarization and voltage drop for that rate were read from Figure 8. This latter sum was added to the desired voltage and applied across the cell for the desired time interval. The maximum correction was about 2.5 volts, and no correction was necessary for times greater than one or two minutes.

The second correction was made to the data after the run was completed. The procedure used in making these runs was to form an initial oxide film at a voltage about 10 volts below the final voltage in order to prevent excessive initial currents. If the full voltage had been applied at once this initial film would have formed in time t'. The true initial time was therefore t' instead of zero and results should be plotted against $t + t'$ where t is the recorded time. To find t' the reciprocal of the thickness was plotted against the logarithm of the time, the straight portion at longer times extrapolated to the reciprocal of the initial thickness, and the time read from the graph (see Figure 9). This time was then added to all the recorded times and the results were replotted using $t + t'$. The values for t' were usually between 0.2 and 0.5 seconds.

Plots of $1/x$ and x versus log time for a run at 19°C are shown in Figure 10. It may be seen that $1/x$ versus log time is linear to about 1000 seconds, after which the rate of growth decreases. The thickness–log time plot, on the other hand, is straight after about 50 seconds. It appears that two mechanisms are involved in the process, the first predominating at short times and the other at long times.

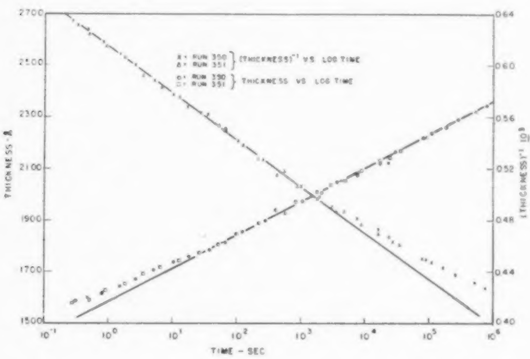

FIGURE 10. Duplicate reciprocal thickness and thickness versus log time plots for anodization at 120 volts in 1 per cent Na_2SO_4 at 19°C.

At short times the constant voltage results give a growth law which has the same form as that predicted by the theory of Mott and Cabrera. However, according to the theory the slope of the $1/x$ versus ln time curve should be $kT/q\lambda V$, and should therefore vary linearly with temperature. The actual slopes, given in Table II, were independent of temperature with an average value of 0.371×10^{-4} and a scatter of $\pm 0.003 \times 10^{-4}$. From this average slope the value of the constant B in equation (12) may be calculated. Comparison of equations (1) and (12) shows that the quantity q/kT in the former equation has been replaced by B in equation (12). Since the theory predicts that the slope of the $1/x$ versus log time plot should be $2.3kT/q\lambda V$, the constant B in equation (12) should be $2.3/V$(slope of $1/x$ vs log t plot). These runs were made at 120 volts and to this voltage must be added the 1.4 volts due to the chemical reaction. The constant B is then 512, in excellent agreement with the value 506 determined from constant current runs.

TABLE II

THICKNESS AS A FUNCTION OF TIME AT CONSTANT VOLTAGE

$10^4/x = a - b \ln T$

Temperature °C	a	b
0.5	6.43	.370
19	6.165	.372
40.5	5.85	.373
60.5	5.6	.373
79	5.395	.373

From equation (2) the rate of growth obtained by differentiation is:

$$\frac{dx}{dt} = \frac{x^2 b}{t}. \tag{13}$$

Rates of growth were calculated for various temperatures and fields and the activation energies determined by plotting ln (dx/dt) versus $1/T$. A value of 0.695 eV(16 kcal/mol) was obtained for the activation energy at fields from 0.050 to 0.075 Å/volt in good agreement with the value of 0.71 eV obtained from constant current runs.

From equation (13) and the fact that the process is nearly 100 per cent efficient, it would be expected that a plot of current density against x^2/t would be linear. A plot of log i versus log (x^2/t) is shown in Figure 11. It may be seen that the curve is linear with a slope of 1 to $(x^2/t)\ 10^{-3} = 1$. The time at which the log i versus log (x^2/t) curve departs from linearity is the same as the time at which the $1/x$ versus log time curve departs from linearity. Since both of these curves deviate from linearity at about the same time, it appears reasonable that

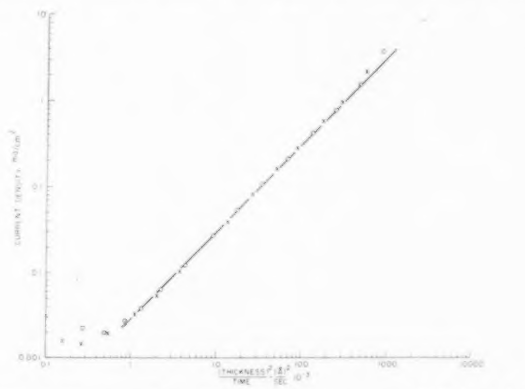

FIGURE 11. Log-log plot of current versus x^2/T for the same runs shown in Figure 12.

some change in the film is taking place, causing the rate of growth to decrease while the current remains approximately constant. The mechanism of this deviation will be the subject of another investigation.

Effect of Cold Work and Nature and Concentration of the Electrolyte

The effects of nature and concentration of the electrolyte and of cold work on the kinetics were

determined in a separate investigation (8). The rate of formation was found to be the same for all specimens regardless of the amount of cold work. It was also found that the same rate of growth was obtained under a given set of conditions regardless of the nature and concentration of the electrolyte for all dilute aqueous electrolytes.

History Studies

It might be expected that the rate of growth of a film under a given set of conditions would be structure sensitive, and that the film structure might be changed by different rates and temperatures of formation. Several tests were performed to determine whether there is any detectable effect of the past history of a film on its subsequent growth.

Several experiments were performed to determine whether there was any rate history dependence. In one such experiment two films were formed to 100 volts in 0.1 per cent Na_2SO_4 at 0°C, one at a current density of 10 ma/cm² and the other at 0.1 ma/cm², corresponding to growth rates of 52.4 and .524 Å/second respectively. The two specimens were then held at 100 volts and the thickness and current density were measured periodically. The plots of thickness versus current density, Figure 12,

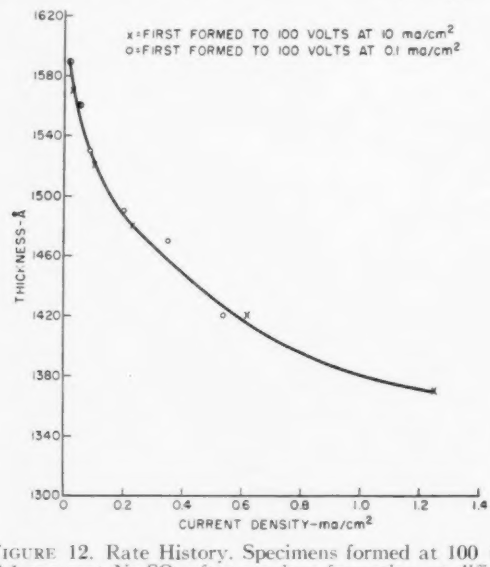

FIGURE 12. Rate History. Specimens formed at 100 volts in 0.1 per cent Na_2SO_4 after previous formation at different rates.

are the same within experimental error. In another test specimens were formed to 100 volts at 20 ma/cm² and 1 ma/cm² in 0.1 per cent Na_2SO_4 at 27°C, and then both held at 100 volts until the current density was 0.1 ma/cm². The thickness of both films was 1585 ± 8 Å, or the same within 0.5 per cent. Since the efficiency is constant the current density is proportional to the rate of formation, while the thickness at constant voltage is a measure of the field. The above results, means, therefore, that the rate of formation at a given field is independent of the previous rate of formation of the film.

Many experiments were performed to determine whether there is any thermal history dependence.

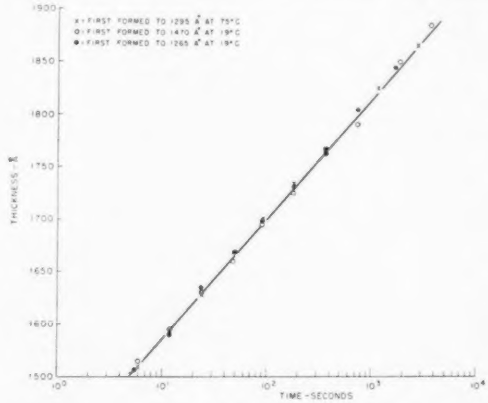

FIGURE 13. Thermal History. Specimens anodized at 110 volts in 0.1 per cent Na_2SO_4 at 19°C after previous formation at different temperatures.

In constant current experiments specimens were formed to 150 volts at one temperature and then further at a second temperature. All runs were made at 2 ma/cm² in 0.1 per cent Na_2SO_4. The slopes of the voltage-time curves for specimens formed at 88°C averaged 0.585 volts/second, while those formed at 0°C to 150 volts gave slopes averaging 0.588 volts/second on subsequent formation at 88°C. The slopes for specimens formed at 0°C averaged 0.732 volts/second while those formed first at 88°C gave slopes averaging 0.730 at 0°C. The slopes of the curves at a particular temperature agree to well within the experimental error of ± 0.01 volts/second whether the specimens were formed entirely at that temperature or first at some other temperature.

The constant voltage experiment to determine whether there was a thermal history effect consisted of forming films of approximately the same thickness at 19°C and 75°C and then forming both specimens further at 19°C. For simplicity, polarization and electrolyte voltage drop were neglected. The data are shown in Figure 13, and it may be seen that there is no thermal history dependence.

From all of these experiments it may be concluded that the rate of formation of anodic oxide films on tantalum depends only on the instantaneous

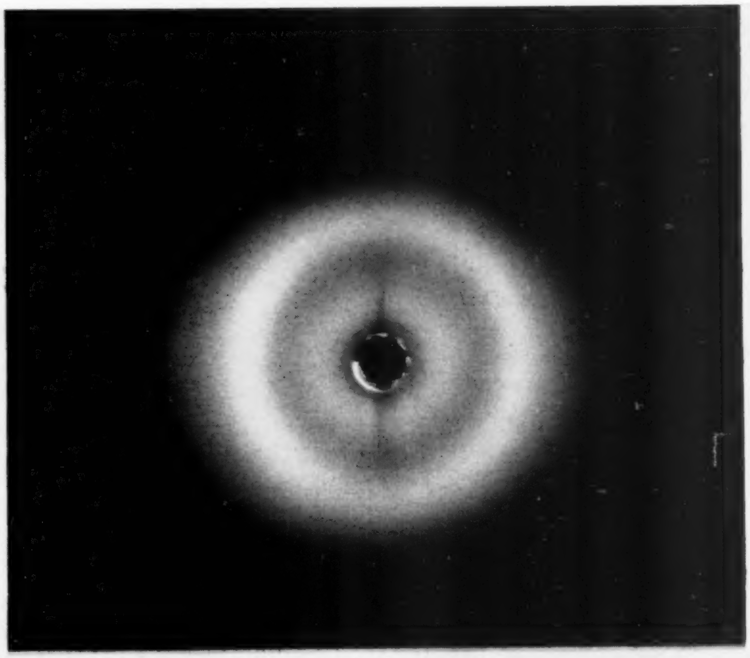

14

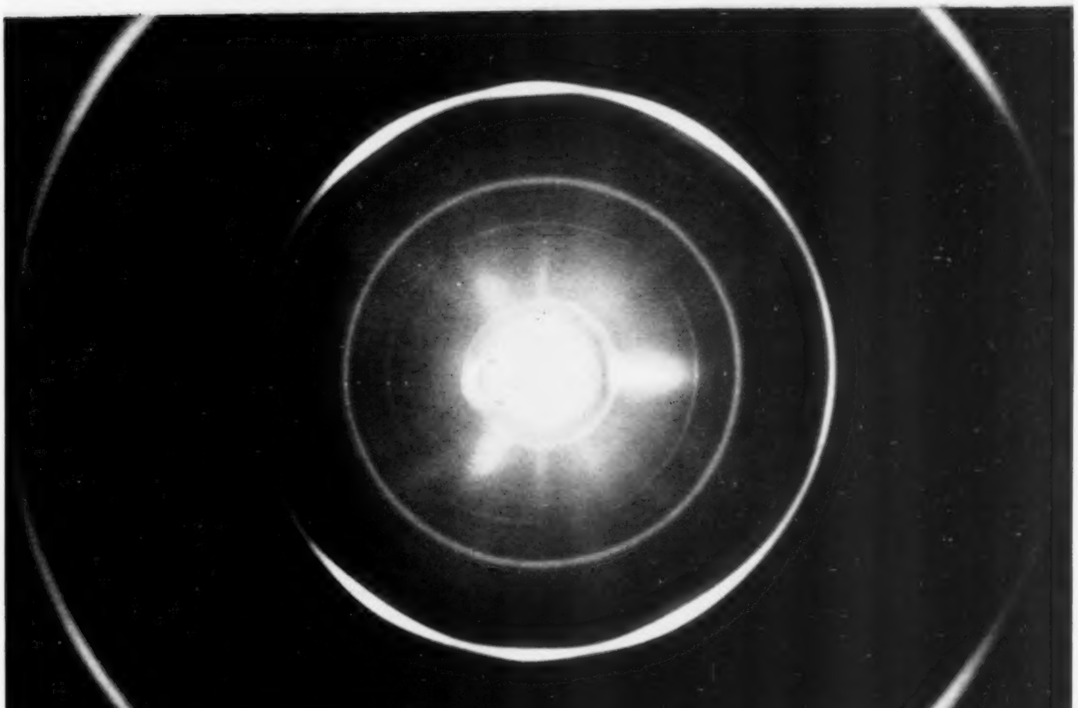

15

FIGURE 14. X-ray transmission pattern of a stripped oxide film 5000Å thick.

FIGURE 15. X-ray pattern obtained by transmission through thin tantalum sheet with a recrystallized oxide film 4500Å thick.

electric field and temperature, and is the same for all aqueous electrolytes.

*Structure and Composition of the Oxide Film**

X-ray and electron diffraction studies of oxide films as formed gave only diffuse patterns of the type shown in Figure 14. Apparently the oxide film is amorphous or very finely crystalline in agreement with Spauschus [6].

TABLE III

COMPARISON OF Ta_2O_5 PATTERNS

Pure Ta_2O_5* Interplanar Spacing d(Å)	Intensity †	ASTM Index		Recrystallized Anodic Film on Tantalum		
		d	I	d	Appearance of line	Source of line
3.882	s	5.7	17	3.87	smooth, weak	Ta_2O_5
3.149	s	3.96	100	3.16	smooth, weak	Ta_2O_5
3.092	m	3.49	27			
2.449	s	3.23	23	2.47	smooth, weak	Ta_2O_5
2.420	m	3.05	33			
1.939	m	2.95	13	2.37	strong, arced	Ta110
1.829	m	2.81	58			
1.793	m	2.61	23			
1.654	s	1.98	42	1.65	strong, arced	Ta200 plus Ta_2O_5
1.644	w	1.87	17			
1.628	m	1.77	50			
1.573	m	1.66	10			
1.544	w	1.62	27			
1.474	vw	1.32	13			
1.459	m					
1.438	vw					
1.379	vw					
1.332	m					
1.319	m					
1.295	vw					
1.224	s					
1.210	w					
1.200	s					
1.196	s					
1.183	vw					
1.175	vw					

*This oxide sample was obtained from R. N. Brissey of the Thompson Laboratory, Lynn River Works, General Electric Company.

†s = strong; m = medium; w = weak; vw = very weak.

In order to determine the approximate recrystallization temperature, specimens with oxide films approximately 4,500Å thick were heated to various temperatures in a vacuum of 0.01 micron. These oxide films were prepared on very thin metal sheet so that X-ray diffraction could be obtained by transmission. No recrystallization occurred after heating for 4 hours at 500°C. The pattern from a specimen heated for one hour at 800°C, however, showed new smooth lines in addition to the arced lines from the cold-rolled tantalum, as shown in Figure 15. The interplanar spacing values calculated from these lines are given in Table III which also includes the data given in the ASTM index for Ta_2O_5 and results obtained from pure Ta_2O_5 powder. The lines for pure Ta_2O_5 do not agree with those from the index, in agreement with the results of Spauschus [6]. The new lines in Figure 4 agree with those obtained for the pure Ta_2O_5 powder. The film is therefore amorphous as formed and recrystallizes to Ta_2O_5 between 500 and 800°C.

In order to determine whether any water of hydration was present in the oxide film a specimen with a 3000Å film was heated to 500°C for one hour in a vacuum of .01 micron. The weight increase on anodization was .0051 grams, which corresponds to .0282 grams of Ta_2O_5. There was no detectable weight change after heating at 500°C. A change of .0001 gram, or 0.35 per cent, would have been detected in the weighing, and if the composition of the film had been $Ta_2O_5 \cdot H_2O$ the amount of water present would have been 4 per cent. Since it seems likely that heating the film at 500°C would have driven off any water of hydration, it seems certain that little if any was present.

Discussion of Results

Equation (12), which describes the rate data obtained for anodic oxidation, may be compared with equation (1) derived by Mott and Cabrera. While they have the same form there are three major points of disagreement. First, the constant B in equation (12) is independent of temperature. In order for equation (1) to fit the data, therefore, it would be necessary for $q\lambda$ to vary linearly with temperature, and have a value of zero at absolute 0. It appears unlikely that either the ionic charge or the jump distance or their product would show such a variation with temperature. Second, the value of BF in equation (12) is greater than Q/kT for nearly all rates, which means that if the effect of the field were to lower the energy barrier for diffusion the barrier would be entirely obliterated. Third, the value of the constant A should have a value of about 10^{12} according to the theory, while a value of about 10^{-2} was found experimentally.

It is therefore apparent that the mechanism proposed by Mott and Cabrera must be modified in order to explain the kinetics of anodic oxidation.

*The author is indebted to Miss E. I. Alessandrini, Mrs. B. F. Decker, and Mrs. A. S. Cooper of the General Electric Research Laboratory for obtaining the diffraction patterns.

It should be pointed out that the application of equation (1) to data from one temperature only would give entirely reasonable values for all of the various parameters. It is only when different temperatures are considered that it becomes apparent that the theory does not hold.

Although according to equation (12) the activation energy is independent of the field, a small field dependence might not have been detected. For example, the lowering of the energy barrier for a singly charged ion would be λF, where λ is half the jump distance. If λ is 1Å the barrier would be lowered 0.075 and 0.05 eV at fields of 0.075 and 0.05 volts/Å, respectively. The change in the barrier from the maximum to the minimum field would thus be only 0.025 V, which might not be detected. Thus an equation of the type:

$$\frac{dx}{dt} = A \exp BF \exp - \left(\frac{Q - bF}{kT}\right) \tag{14}$$

might be used to describe the data if the value of b is less than 2.

At the present time the mechanism which gives rise to equation (12) is not known. The form of the equation makes it appear possible that the field determines the number of atoms or ions which may diffuse and that these then diffuse thermally, but the details of the process are not clear.

Conclusions

1. The expression

$$\frac{dx}{dt} = A \exp\left(BF - \frac{Q}{RT}\right)$$

where $B \neq f(T)$ describes the rate of growth of anodic oxide films on tantalum. The mechanism which gives rise to this law is not known.

2. The theory proposed by Mott and Cabrera cannot explain the observed kinetics.

3. The rate of formation of a film is not effected by its past history, the state of cold work of the metal, or by changes in the nature and concentration of the electrolyte.

4. The anodic film on tantalum consists of amorphous Ta_2O_5 with a recrystallization temperature between 500 and 800°C.

Acknowledgment

This work, performed at the General Electric Research Laboratory, is part of a thesis submitted to Rensselaer Polytechnic Institute as part of the requirements for the doctor's degree in metallurgy.

The author wishes to acknowledge many valuable discussions with D. Turnbull, L. Apker, M. H. Hebb, J. K. Bragg and others of the General Electric Research Laboratory, and A. F. Torrisi and R. A. Ruscetta of the Capacitor Laboratory.

References

1. Wagner, C. Z. phys. Chem., **B21** (1933) 25.
2. Mott, N. F. and Cabrera, N. Rep. Progr. Phys., **12** (1948-49) 163.
3. Guntherschulze, A. and Betz, H. Elektrolyt-Kondensatoren (Berlin, M. Krayn, 1937).
4. Van Geel, W. Ch. and Emmens, H. Z. Phys., **69** (1931) 765.
5. Burgers, W. G., Classen, A., and Zernicke, J. Z. Phys., **74** (1932) 593.
6. Spauschus, O. Private communication.
7. Waber, J. T., Sturdy, G. E., Wise, E. M., and Tipon, C. R. Jr. J. Electrochem. Soc., **99** (1952) 121.
8. Vermilyea, D. A. To be published.

FURTHER NOTES ON THE SHAPE OF METAL GRAINS: SPACE-FILLING POLYHEDRA WITH UNLIMITED SHARING OF CORNERS AND FACES*

C. S. SMITH†

A statement in an earlier paper that there is a topological limit to the sharing of corners in a network of three-dimensional cells analogous to metal grains is shown to be wrong. New space-filling irregular polyhedra sharing faces with as many as 20 neighbors are sketched. No plane-faced space-filling polyhedron can exist that meets the requirements of surface-tension equilibrium at interfaces and junctions. A relation is derived for the sum of angles at each vertex in a three-dimensional space-filling array of plane-faced polyhedra.

NOTES ADDITIONNELLES SUR LA FORME DES GRAINS DES MÉTAUX; POLYÈDRES REMPLISSANT L'ESPACE, AVEC UN PARTAGE ILLIMITÉ DES COINS ET FACES

Il est montré, qu'une déclaration faite dans un article antérieur, qu'il existe une limite topologique au partage des coins dans un réseau de cellules à trois dimensions, analogues aux grains des métaux, est incorrecte.

De nouveaux polyèdres non réguliers avec les faces partagées par jusqu'à vingt voisins sont schématisées.

Il est impossible de construire une figure à faces planes, remplissant l'espace, qui soit conforme aux conditions de tension de surface aux surfaces de joint.

WEITERE BEMERKUMGEN ZUR FORM VON METALLKRISTALLITEN, DREIDIMENSIONALE POLYEDER MIT UNBEGRENZTER ANZAHL GEMEINSAMER ECKEN UND FLAECHEN

Es wird gezeigt, dass die in einer frueheren Arbeit gemachte Aussage, dass eine topologische Begrenzung der Anzahl der gemeinsamen Ecken in einem dreidimensionalen den Metallkristalliten analogen Zellwerk existiert, falsch ist. Neue, nicht-regulaere Polyeder mit Flaechen, die bis zu 20 Nachbarn gemeinsam sind, werden beschrieben. Es ist nicht moeglich, einen dreidimensionalen von ebnen Flaechen begrenzten Koerper zu konstruieren, der an den Grenzflaechen den Oberflaechenspannungsbedingungen genuegt.

VOL. 1 1953

In a paper [1] on the shape of aggregates such as bubbles, metal grains, or cells in undifferentiated biological tissue (all of which tend toward a structure possessing minimum interface area), it is suggested that the maximum achievable number of corners in a corner-sharing space-filling array of polyhedral cells is six per polyhedron, and it is implied that the minimum interface area occurs when there is maximum sharing of corners and faces for a given number of three-dimensional cells. *These statements are wrong.* Professor Edward Teller [2] has called attention to a simple operation that permits an increased sharing of interfaces, which can be continued apparently without limit, and without detriment to the space-filling properties of the structure.

Consider an array of truncated octahedra (Figure 2), each with eight hexagonal faces, six four-sided faces.‡ In a space-filling stack each face is shared by two polyhedra, and each corner (shared by polyhedra) represents the point where two quadrilateral and four hexagonal faces meet. The unit junction of edges will be as shown in Figure 1a, which represents the junction of three polyhedra sharing the vertical edge and two additional polyhedra meeting the initial three at the top and bottom vertices, respectively. Now extend the apices of the top and bottom polyhedra, which initially have no contact with each other, until they meet in the middle of the array, as in Figure 1b, forming a triangular face which they have in common. By this means, two corners have been replaced with three, one edge with three, and a new face has been introduced, without changing the number of polyhedra or the manner in which 2-, 1-, or 0-dimensional cells meet.§

If we wish to construct a polyhedron that by mere duplication and translation will fill space, it is obvious that for every projection of this kind, sharing a triangular face with a "next to nearest" neighbor, there must be three matching cutaway

*Received September 8, 1952; in revised form, January 20, 1953.

†Institute for the Study of Metals, University of Chicago, Illinois.

‡Following the example of Lord Kelvin, biologists and metallurgists (including the writer, heretofore) have generally called the polyhedron in question the "tetrakaidecahedron." Mathematicians, however, prefer the term "truncated octahedron" for the plane-faced solid, in order to distinguish it from other 14-faced polyhedra, although the name "minimum-area tetrakaidecahedron" is acceptable for Kelvin's minimum-area cell with eight doubly curved faces. The truncated octahedron was, of course, known to Archimedes. It was rediscovered in the late fifteenth century by Francesca, but its unique features were first pointed out by Kelvin.

§No consideration is here made of arrays with other than four polyhedra meeting a a point, since the maximum sharing of corners has been taken as a prime desideratum.

portions on each polyhedron, in such positions as to meet the projection when the bodies are stacked. Starting with a truncated octahedron with 24 corners, there can be at most 6 male and 18 fractional female corners. The simplest operation to make a stackable body is to add a single pair of projections, as in Figure 3. This brings the cell in contact with two more neighbors than it had as a simple truncated octahedron, making a total of 16. If two pairs of projections are used with appropriate nesting sections, these may be disposed either at angles to each other, as in Figure 4, or in the same plane, as in Figure 5. Though the symmetry is higher in the latter case, the additional projections have not increased the number of neighbors over those of Figure 3. Figure 6 shows the result of adding three pairs of projections, utilizing all 24 original corners. Table I lists some topological characteristics of the various polyhedra, both as separate bodies and when in a space-filling array with shared faces, edges, and corners. These can be compared with the values given in Table III of [1].

The number of corners can be still further increased in uniform space-filling bodies by reaching out to a further shell of neighbors by extending one corner of the triangular face on the end of each projection in Figures 3 to 6, thus making a triangular face shared with a similarly distorted apex of another polyhedron in the next shell of neighbors. This kind of operation can be continued indefinitely without affecting the space-filling properties of the body but with continued increase of the number of corners, edges, polygons, and faces that it possesses.

If the requirement of space-filling by repetition alone be removed, then obviously practically limitless arrays of polyhedra can be constructed. Any one cell, as in a soap froth, regardless of the number of apices that it may have, can have every apex converted to a triangle and extended to meet a cell that it would not otherwise touch. There are, however, limitations on similar extensions of its neighbors: If only a single-stage extension of this type is permitted, the total number of corners per polyhedron on the average for the whole array

TABLE I

	Polyhedra with				
	Truncated octahedron (Fig. 2) 14 neighbors	2 added projections (Fig. 3) 16 neighbors	4 added projections (Fig. 4) 18 neighbors	4 added projections (Fig. 5) 16 neighbors	6 added projections (Fig. 6) 20 neighbors
No. of edges per face, n	F_n	F_n	F_n	F_n	F_n
10	—	—	2	4	—
9	—	—	—	—	6
8	—	4	—	—	—
7	—	—	4	—	—
6	8	—	2	4	—
5	—	8	—	—	6
4	6	—	6	4	—
3	—	4	4	4	8
2	—	—	—	2	—
Properties of separate polyhedra					
No. of corners, C	24	28	32	32	36
No. of edges, E	36	42	48	48	54
No. of faces, F	14	16	18	18	20
Edges per average face ($\bar{n}$)	$5\frac{1}{7}$	$5\frac{1}{4}$	$5\frac{1}{3}$	$5\frac{1}{3}$	$5\frac{2}{5}$
Properties of extended space-filling face-sharing arrays of polyhedra					
No. of corners per cell, C/B	6	7	8	8	9
No. of edges per cell, E/B	12	14	16	16	18
No. of faces per cell, P/B	7	8	9	9	10

In addition to the Euler relations which apply to every polyhedron, the above all conform to the requirements that $\sum(6 - n)F_n = 12$ and that $E = 3(F - 2)$ and $C = 2(F - 2)$ when the polyhedra are considered as separate bodies, or that $E/B = 2(P/B - 1)$ and $C/B = P/B - 1$ when the sharing of features on stacking is allowed. Conformity to these criteria is a necessary though not sufficient requirement for stacking with four-ray corners.

FIG. 1a

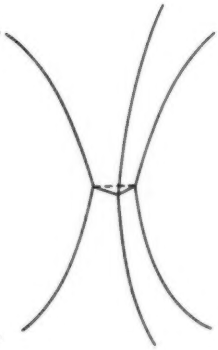

FIG. 1b

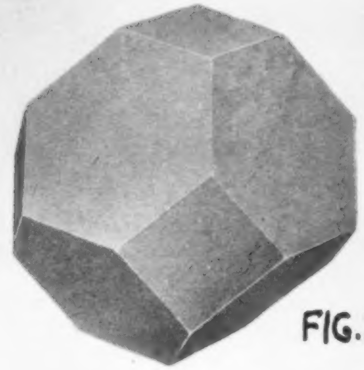

FIG. 2

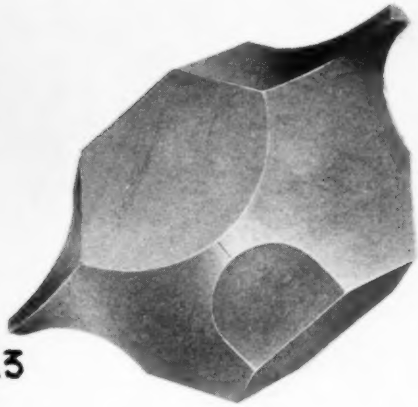

FIG. 3

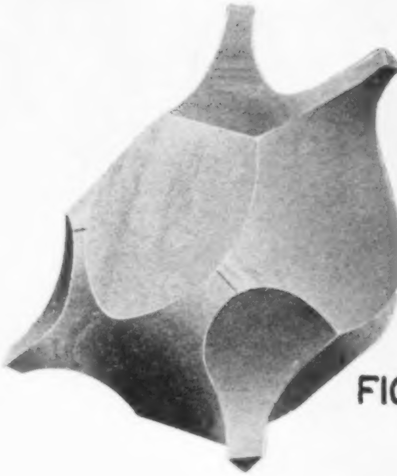

FIG. 4

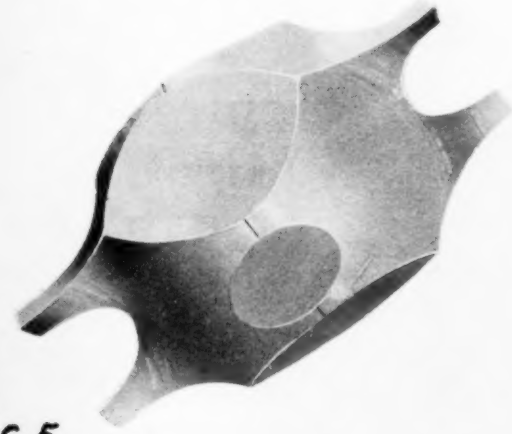

FIG. 5

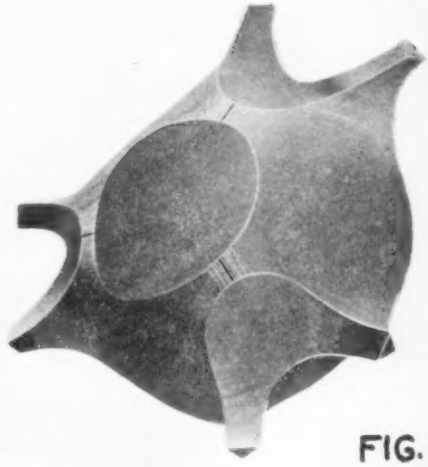

FIG. 6

cannot exceed eight (since, of the initial optimum six, only one is extendable if the necessary three female distortions are allowed for).

It is interesting to notice that, in the bodies represented in Figures 3 to 5, the connection between next-to-nearest neighbors is of a one-dimensional character. It does not seem to be possible to make closed loops of second-nearest neighbors, i.e. of polyhedra touching only at the ends of their projections.

Most physical or biological assemblages of cells tend to approach a minimum interface area. Spatial connection with a maximum number of neighbors is not usually a matter of great importance, particularly in the asymmetrical manner possible with the new polyhedra. If the requirement is merely that of connection and the requirement of exact repetition is removed, then there are clearly innumerable possibilities as in a multiply-branched nerve network. It may, however, turn out that there are certain physical or biological structures in which both repetition and multiple neighbors are desired, and in these an approximation to the new polyhedra might be found.

In two dimensions there is coincidence between the topological maximum ($C/P = 2$) and the minimum length of interface that will give extended subdivision of space. A uniform straight-sided hexagonal network corresponds both to the shortest boundary length and to the maximum possible number of corners per polygon. (Other configurations possessing the same C/P ratio can have larger boundary length for the same number of cells, but the physical and topological conditions become identical at the limit.) In three dimensions there is no such coincidence; indeed, there is no topological limit whatever to the number of corners or faces that can be shared. The special value $C/B = 6$ that corresponds to the truncated octahedron and distorted forms thereof is a maximum value only under additional non-topological restrictions of convexity, symmetry, or area of interface. The "proof" in [1] that $\bar{n} = 5\frac{1}{7}$ for minimum interface area is erroneous, although the fact itself remains probably true.

The Impossibility of Combining Plane Faces with Angles of $109\frac{1}{2}°$

There is another approach to the problem of the minimum area cell, based on the fact [3]—discovered by Descartes—that the sum of all face angles of any plane-convex polyhedron is exactly 4π less than the sum of corner angles in a sphere covered with spherical polygons equivalent to the polyhedron under consideration; i.e.,

$$2\pi C - \sum \phi = 4\pi \tag{1}$$

where C is the number of vertices, and $\sum\phi$ is the sum of all of the face angles in the polyhedron. If $2\pi - \sum_V \phi$ is the average angular deficiency at one vertex, then

$$C(2\pi - \textstyle\sum_V \phi) = 4\pi \tag{2}$$

or

$$C = \frac{4\pi}{2\pi - \sum_V \phi}. \tag{3}$$

Thus, a cube with eight corners has an angular deficiency at each vertex of $\pi/2$ and a tetrahedron, with four corners, of π. A pentagonal dodecahedron has 20 corners, each deficient by $\pi/5$, and the truncated octahedron (Figure 2) has a deficiency of $\pi/6$ at each of its 24 corners. A rhombic dodecahedron achieves the required average corner deficiency of $\frac{2}{7}\pi$ by combining eight corners with a deficiency of $(2\pi - 3 \times 109\frac{1}{2}°)$ with six corners each deficient by $(4 \times 109\frac{1}{2}° - 2\pi)$.

Returning to space-filling, it seems probable that the ideal cell with minimum interface area must have faces as nearly plane as possible, intersecting in the manner so beautifully illustrated by soap films in the center of a tetrahedral wire frame (Cf. Figure 18, reference 1), namely, six plane films meeting in groups of three at 120° to each other, forming four edges, which edges all meet at a point at an angle of 109.472 degrees (i.e., $\cos^{-1} -\frac{1}{3}$). Now it is obvious that no single plane polygon can have all its corner angles of this value, for $\bar{n} = 2\pi/(\pi - \bar{\theta})$ and it would need to have 5.11 sides, an irrational number. It is not immediately apparent that this could not be achieved as an average of different kinds of polygons; indeed it is tantalizingly close to the $5\frac{1}{7}$ number characterizing the truncated octahedron. However, one can exclude *any* plane solution by utilizing Equation (3) to determine the number of vertices that our supposedly ideal plane-faced polyhedron would have if all corners were composed of three $109\frac{1}{2}°$ angles. It is the following:

$$C = \frac{720}{360 - 3 \times 109.472} = 22.794.$$

Since this is not a whole number, no plane-faced polyhedron can possibly have the desired corner angle. Some curvature of the faces is, therefore, necessary. Since for stacking the corners must be an exact multiple of four, a 24-corner body seems to be the nearest possibility—the Kelvin tetrakaideca-

hedron. The pentagonal dodecahedron with 20 corners does not deviate far from the required number of corners or angles, though it lacks the symmetry necessary to form a lattice. Empirical studies [4] show this to be the only regular polyhedron to be approximated in a froth of soap bubbles. It is indeed a relatively common form—in contrast to the virtual non-existence of the tetrakaidecahedron.

Vertex Angle Sums in Polyhedral Networks

There is an additional interesting characteristic of space-filling polyhedra, provided that they are plane-faced (hence of no interest in foams), but without any other limitation. If there are V polyhedra meeting at each point in space, and if each polyhedron when considered as a separate body has C vertices, then the sum of all angles at one vertex must be

$$\sum_V \phi = \pi V\left(1 - \frac{2}{C}\right). \tag{4}$$

This results directly from the fact that the three-dimensional vertex has meeting at it exactly $Vr/2$ faces, where r is the number of faces meeting at a vertex of the separate polyhedra, and consequently $\sum_V \phi$ is exactly $V/2$ times the sum of the angles given for one vertex by Equations (1–3).

It should be noted that the vertex angle sum is not affected by any distortion as long as the faces remain plane and the numbers of faces and polyhedra meeting at a vertex remain unchanged. If all vertices are not identical, then $\sum_V \phi$, V, and C are the appropriate average numbers; the relations then apply to any connected space-filling array of plane-faced cells, regardless of how many different types of polyhedra may actually be involved. It follows immediately from Equation (4) that the sum of plane angles at each vertex in an array of cubical cells (for which $N = 8$, $C = 8$) is 6π; that of an array of truncated octahedra ($N = 4$, $C = 24$) is $11\pi/3$ and that of an array of rhombic dodecahedra ($N = 14/3$, $C = 14$) is 4π.

Note Added January 13, 1953

A reader of the manuscript has called attention to the important paper by E. von Federow [5], in which it is shown that space-filling polyhedra cannot be convex if they have more than 14 faces.

Acknowledgment

Professor Edward Teller's wisdom in pointing out the simple fact that precipitated this reconsideration is deeply appreciated; he is not responsible for any errors that may have crept into the extension of his idea.

References

1. Smith, C. S. In "Metal Interfaces" (American Society for Metals, Cleveland, 1952), pp. 65–113.
2. Teller, E. University of Chicago, private communication.
3. See, for example, H. S. M. Coxeter, Regular Polytopes (London, 1948), p. 23.
4. Matzke, E. B. Amer. J. Botany, **33** (1946) 58–80.
5. von Fedorow, E. Zeitschrift für Krystallographie und Mineralogie, **21** (1893), 689–92.

THE FORMATION OF η CARBIDES*

KEHSIN KUO†

η carbides exist in two forms, η_1 with the ideal general formula A_3B_3C, and η_2 with the ideal general formula A_2B_4C. Here A represents a transition metal of period IV and B a metal of period V or VI in the periodic system. It has been proved that metals A and B have diagonal positions in the periodic table, the connecting line from A to B running downwards to the left, as shown by the η carbides found in this investigation: V_3Zr_3C, Cr_3Nb_3C, Mn_3Mo_3C, Mn_3W_3C, Fe_2Mo_4C, Co_2Mo_4C, Ni_3Mo_3C, and Ni_2Mo_4C.

Ta does not form a double η carbide with any transition metal of period IV, but many triple carbides containing Ta as B atom are found to exist; e.g., $(V,Fe)_3Ta_3C$, $(V,Co)_3Ta_3C$, $(V,Ni)_3Ta_3C$, $(Cr,Fe)_3Ta_3C$, $(Cr,Co)_3Ta_3C$, $(Cr,Ni)_3Ta_3C$, and $(Cr,Cu)_3Ta_3C$. Nb also forms a triple carbide $(V,Ni)_3Nb_3C$.

The formation of this family of carbides is discussed from the point of view of the relative strength of the transition metal-carbon bond, of the atomic size factor, and of the possibility of their being electron compounds.

LA FORMATION DES CARBURES η

Les carbures η existent en deux formes, η_1 dont la formule générale, idéale est A_3B_3C, et η_2 dont la formule générale, idéale est A_4B_4C. Ici A représente un métal de transition de la quatrième période et B un métal de la cinquième ou sixième période de la classification périodique. Il a été prouvé que les métaux A et B occupent des positions aux extrémités de diagonales dans le tableau périodique, la ligne qui joint A et B se dirigeant vers le bas et à gauche. Ceci est bien montré dans les carbures η qui ont été trouvés lors de cette investigation: V_3Zr_3C, Cr_3Nb_3C, Mn_3Mo_3C, Mn_3W_3C, Fe_2Mo_4C, Co_2Mo_4C, Ni_3Mo_3C, Ni_2Mo_4C.

Ta ne forme de carbure double η avec aucun des métaux de transition de la quatrième période, mais il a été montré, qu'il existe plusieurs carbures triples contenant du Ta comme atome du genre B; par exemple: $(V,Fe)_3Ta_3C$, $(V,Co)_3Ta_3C$, $(Cr,Fe)_3Ta_3C$, $(Cr,Co)_3Ta_3C$, $(Cr,Ni)_3Ta_3C$, $(Cr,Cu)_3Ta_3C$. Nb forme aussi un carbure triple $(V,Ni)_3Nb_3C$.

La formation de cette famille de carbures est discutée du point de vue de l'intensité relative du lien entre le métal de transition et le carbone, des dimensions des atomes et de la possibilité d'existence de composés électroniques.

DIE BILDUNG VON η CARBIDEN

Carbide kommen in zwei Formen vor, η_1 mit einer idealen Summenformel A_3B_3C, und η_2 mit einer idealen Summenformel A_2B_4C. A bedeutet hier ein Übergangsmetall der vierten Gruppe und B ein Metall der fünften oder sechsten Gruppe des periodischen Systems. Es wird gezeigt, dass die Metalle A und B diagonale Stellungen im periodischen System haben, die Trennungslinie zwischen A und B läuft von der linken Seite des periodischen Systems nach unten, wie es die η Carbide dieser Untersuchung zeigen: V_3Zr_3C, Cr_3Nb_3C, Mn_3Mo_3C, Mn_3W_3C, Fe_2Mo_4C, Co_2Mo_4C, Ni_3Mo_3C, and Ni_2Mo_4C.

Ta bildet mit keinem der Übergangsmetalle der vierten Gruppe Doppel η Carbide, aber es wurde gefunden, dass Trippelcarbide, die Ta als B-Atome enthalten, existieren: Z. B. $(V,Fe)_3Ta_3C$, (V,Co) $(V,Ni)_3Ta_3C$, $(Cr,Fe)_3Ta_3C$, $(Cr,Co)_3Ta_3C$, $(Cr,Ni)_3Ta_3C$, and $(Cr,Cu)_3TaC$. Auch Nb bildet ein Trippelcarbid $(V,Ni)_3Nb_3C$.

Die Bildung diser Carbidfamilie wird vom Standpunkt der relativen Festigkeit der Übergangsmetall-Kohlenstoff Bindung, der Atomdimensionen und der Möglichkeit, dass diese Carbide Elektronenverbindungen darstellen, diskutiert.

Introduction

Westgren and Phragmén [1] identified the Fe_3W_3C carbide in a high speed steel, and this carbide and its isomorphous carbides were thereupon commonly called high speed steel carbide. However, it has been pointed out recently [2] that it is the W_2C carbide, not Fe_3W_3C, which is responsible for the characteristic properties of high speed steel. Hence the term high speed steel carbide is somewhat misleading, and the designation η carbide, used by Takeda [3] for the carbide Co_3W_3C, is therefore used here for the family of carbides with the general composition M_6C.

η carbide is known to exist in two forms: η_1 has the ideal general formula A_3B_3C, and η_2, A_2B_4C, where A represents Fe, Co, or Ni, and B represents W [1; 4–8]. Mo also forms the η_1 carbide with Fe and Co [1; 9]. These two forms belong to the same space group $Fd3m$, having 96 metal and 16 carbon atoms on a f.c.c. lattice, but the distribution of the metal atoms differs slightly.

According to Westgren [4], the atoms of the η_1 carbide occupy the following positions (notation according to the International Tables for X-Ray Crystallography):

16 A in (d)
32 A in (e) } forming a network of tetrahedra

48 B in (f) forming a network of octahedra of which every second one is regular and the intermediate ones slightly distorted.

16 C probably in (c), occupying the centres of the slightly distorted B octahedra. The carbon positions could not be determined directly from X-ray intensities because of the weak scattering power of the carbon atom as compared with the metal atoms.

*Received January 13, 1953.

†Institute of Chemistry, University of Uppsala, Sweden.

The η_1 carbide has a large range of homogeneity, the limits of which closely correspond to the formulae A_3B_3C and A_4B_2C. The extension of the range towards the latter formula implies that A atoms are substituted for B atoms in (*f*), so that with the composition of A_4B_2C this position is occupied by 16 A +32 B in a random distribution.

According to Kislyakova [6], confirmed recently by Kiessling [7], the atoms of the η_2 carbide are distributed as follows, in the same positions as mentioned above:

16 B in (*d*)
32 A in (*e*)
48 B in (*f*)
16 C probably in (*c*)

This gives the formula A_2B_4C. As the B atoms are larger than the A atoms, the larger amount of B in η_2 as compared with η_1 causes the cube edge of η_2 to be slightly larger than that of η_1 containing the same metals.

As both η_1 and η_2 always contain six metal atoms per carbon atom they are both often designate M_6C carbides.

Recently, Karlsson [10] found a series of metallic oxides isomorphous with the η_1 carbide, with the composition A_3B_3O—where A represents Mn, Fe, Co, Ni, or Cu, and B represents Ti. In another series of oxides of this type, A was represented by V, Cr, or Mn and B by Zr [11]. The oxygen positions could here be determined from the X-ray intensities, and the findings confirm the suggestion made by Westgren concerning the carbon position of the η carbides.

The present investigation was undertaken to discover whether η carbides exist among the transition metals, and whether there are any general conditions for their appearance.

Experimental Methods

The carbides were prepared from high purity metals and "Tierkohl." The metals used were of the following qualities: Titanium and Zirconium (degassed *in vacuo* from the respective hydrides, Metal Hydride Corp., Grade R.), Vanadium (99.75%, Vanadium Corporation of America), Niobium and Tantalum (Fansteel Metallurigcal Corporation, 99%), Chromium and Manganese (Ferrolegeringar, 99.9%), Molybdenum, Wolfram, Iron, and Copper (Schering-Kahlbaum, puriss.), Cobalt (J. D. Riedel, puriss. nickel-free), and Nickel (E. Merck, puriss. cobalt-free).

The finely powdered mixtures, about 1 g., were pressed into pellets under a pressure of 20 ton/cm². The pellets were then sintered in a vacuum graphite furnace at 1500–1800°C. The crucibles used were of magnesia or zirconia. However, it was found convenient to prepare the carbides containing manganese in evacuated silica tubes, heated to 1000°C for 50 hours, on account of the high volatility of this metal.

The phase analyses were made from powder photographs taken with CuKα radiation, using a Guinier type camera with a bent quartz monochromator.

No chemical analyses have been made, because the sintered products were usually found to contain several carbide phases. The formulae assigned to the η carbides in the following are the ideal formulae.

Double Carbides

The term "double carbide" is used here for carbides the formation of which needs the presence of two and only two metals. After finding the double carbides Fe_3W_3C and Fe_3Mo_3C, Westgren *et al.* [5] tried to replace Fe with Cr, Mn, Co, or Ni, but only Co_3W_3C and Ni_3W_3C were obtained. Later, the carbide Co_3Mo_3C was also reported [9]. The η_2 carbides reported earlier are Fe_2W_4C, Co_2W_4C, and Ni_2W_4C [6; 7; 8].

The following double carbides with η carbide structure were found in the present investigation:

η_1		η_2	
V_3Zr_3C,	$a = 12.12$Å	Fe_2Mo_4C,	$a = 11.26$Å
Cr_3Nb_3C,	$a = 11.49$Å	Co_2Mo_4C,	$a = 11.25$Å
Mn_3Mo_3C,	$a = 11.13$Å	Ni_2Mo_4C,	$a = 11.25$Å
Mn_3W_3C,	$a = 11.13$Å		
Ni_3Mo_3C,	$a = 11.05$Å		

However, if η_1 exists together with η_2, as in the case of Ni_3Mo_3C and Ni_2Mo_4C, the cube edge of the former carbide is less than the above values (e.g., for Ni_3Mo_3C, only 10.90Å). This is probably not a new carbide phase, since no change in line intensity from the η_1 carbide with a normal cube edge can be detected. It perhaps corresponds to the A-rich end of the homogeneity range of the η_1 carbide. The η_2 carbides found before, A_2W_4C, also have the above-mentioned cube edge, 11.25Å [7; 8]. Table I shows part of the periodic table with connecting lines between metals which have been found to form η phases containing not more than two metals.

Ta does not form η carbides with any metal of period IV, nor does it with Mo (see Table I). Hf has not been studied. The η_2 carbide may also exist in other metal systems (e.g. V-Zr-C), in which the η_1 carbide has been found, although the η_2 form has

TABLE I

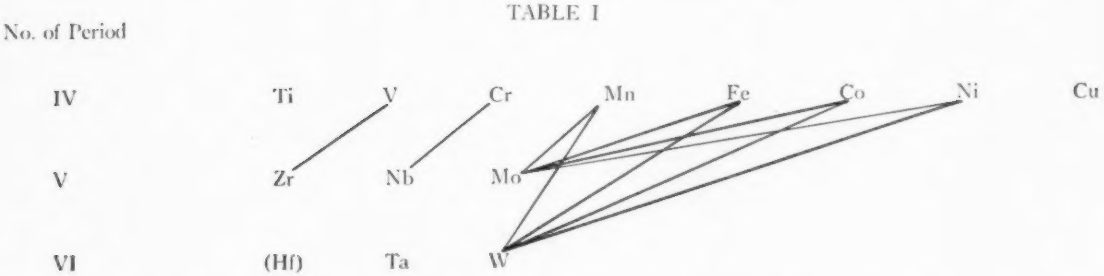

not yet been detected. In the following, only the conditions for the formation of the η_1 carbides will be discussed.

By examining the positions in the periodic table of the metal pairs which form the η_1 carbide, the following observations can be made:

1. A belongs to period IV, while B belongs to period V or VI. A and B are always situated in diagonal positions, the connecting line from A to B running downwards to the left.

2. The affinity of the transition metals for carbon increases within each period from right to left, i.e., from Ni to Ti, from Mo to Zr, and from W to Ta. The variation within a group, i.e., when moving vertically in Table I, has not yet been definitely established, but it seems as though the affinity for carbon increases slightly when moving upwards.* For the formation of the η_1 double carbides it is necessary for both A and B to possess similar affinities for carbon. For instance, Zr and Fe will not form a double carbide because the zirconium, with its greater affinity will seize all the carbon to form ZrC.

3. The ratio of the atomic radii of B to A lies within the narrow range 1.10–1.18. However, the attainment of this ratio of atomic radii is not in itself a sufficient condition for the formation of η_1 carbides, since there are metal pairs with this ratio which fail to form the η_1 carbide, e.g., Ta and Cr.

The formation of Fe_3Mo_3C in the system Fe-Mo-C has been studied in detail [12]. At 700°C. the equilibrium carbides in the iron-rich corner of this system are:

Atomic Ratio of Mo:C in the Alloy	Carbides in Equilibrium
A.R. < 1	MoC + Fe_3C
A.R. = 1	MoC
2-3 < A.R. < 1	MoC + η_1
4-5 < A.R. < 2-3	η_1
A.R. < 4-5	η_1 (+ Fe_7Mo_6)

*An experiment carried out by the author agrees with this supposition. Wolfram carbide WC was mixed with chromium and the mixture heated in vacuum in a graphite tube furnace. A violent reaction occurred at 1200°C. and powder photographs showed the products of the reaction to be wolfram and chromium carbide $Cr_{23}C_6$. We therefore have

$$6\ WC + 23\ Cr = 6\ W + Cr_{23}C_6.$$

The η_2 carbide was not found when there was iron in excess. The formation of η_1 carbides in other A-B-C systems may follow the same relationship with respect to the composition of the alloys as that stated above.

Triple Carbides

The results reproduced in Table I gives the impression that the inability of Ta to form the η_1 phase with the metals of period IV is due to the fact that the only metal in this period suitable for such a formation must have properties intermediate between those of Cr and Mn. The reason may be that Ta has a lower affinity for carbon than Nb has, and that Cr (and the metals before Cr) is too strong and Mn (and the metals after Mn) too weak a carbider-former to form the η_1 carbide with Ta.

Whatever the reason, it seems probable that a suitable mixture of period IV metals should have mean properties enabling it to serve as metal A together with Ta as metal B in forming a η_1 carbide. Experiments carried out in order to test this idea led to the preparation of several triple η_1 carbides containing Ta. A triple carbide containing a mixture of V and Ni as metal A and Nb as metal B was also prepared. Here the mixture of V and Ni evidently had mean properties close to those of Cr. The new carbides found were:

$(Cr,Fe)_3Ta_3C$, a = 11.40Å
$(Cr,Co)_3Ta_3C$, a = 11.40Å
$(Cr,Ni)_3Ta_3C$, a = 11.35–11.44Å
$(Cr,Cu)_3Ta_3C$, a = 11.52Å
$(V,Fe)_3Ta_3C$, a = 11.54Å
$(V,Co)_3Ta_3C$, a = 11.56Å
$(V,Ni)_3Ta_3C$, a = 11.56Å
$(V,Ni)_3Nb_3C$, a = 11.50Å

Experiments were also performed using Zr, Mo, or W as the B metal, but no triple carbide was formed. Nb was found to form only one triple carbide, as mentioned above, with various combinations of A metals. Hafnium carbides have not been investigated. From the position of Hf in the periodic

table, it is to be expected that Hf, like Ta, can at least form triple η_1 carbides.

It would be interesting to determine the proportions of the two metals functioning as A in these triple carbides. It could be expected, for example, that a carbide with A = Cr, Fe would contain less Cr than a carbide with A = Cr, Ni. Unfortunately, it has not been possible to obtain composition data by chemical analysis because of the presence of other phases. Conclusions drawn from unit dimensions only are also of little value, because the amount of each of the three metals may vary. For the same reason, the figures given above cannot be taken to characterise the carbide phase in question.

It should be noted, however, that the variation of the cube edge of $(Cr,Ni)_3Ta_3C$ from 11.35 to 11.44Å is caused by a variation of the ratio Cr:Ni. For $(Cr,Cu)_3Ta_3C$ a still larger cube edge, 11.52Å, was found. This may be due to the radius of the Cu atom (1.28Å for coordination number 12) being larger than the radius of the Ni atom (1.25Å), but also to the fact that less Cu than Ni ought to be required for the formation of the carbide, so that more Cr (radius 1.30Å) is present.

Instead of varying the mean properties of the metal mixture serving as A, a suitable variation in B by partial substitution might be expected to produce a similar effect. An attempt was made to prepare the carbide $Cr_3(Ta,Zr)_3C$ in this way but without success. The double carbides Cr_3Zr_3C and Cr_3Mo_3C could not be found, but as Cr_3Nb_3C could be prepared, it was thought that a mixture of Zr and Mo could be substituted for Nb, thus forming the carbide $Cr_3(Zr,Mo)_3C$. Efforts to prepare this triple carbide were also unsuccessful.

The η Carbides as Electron Compounds

The above conditions for the formation of η carbides are in certain respects analogous to some conditions found for the formation of Laves and sigma phases. It is known, for example, that Nb and Ta form Laves phases (BA_2) with Cr ($MgCu_2$ type), Mn ($MgZn_2$ type), Fe ($MgZn_2$ type), and Co ($MgCu_2$ type), but not with V or Ni [13; 14]. However, Laves phases $Nb(V,Ni)_2$ and $Ta(V,Ni)_2$, both of $MgZn_2$ type, can be prepared [15].

Similarly, W and Mo are known to form sigma phases with Fe and Co but not with Cr and Ni [16]. Nor does Cr form a sigma phase with Ni. But ternary sigma phases were found to exist in both the systems W-Cr-Ni [15] and Mo-Cr-Ni [17].

As the electron/atom ratio is considered to be an important factor for the stability of both Laves and sigma phases [18; 19], it seems rather likely that this factor also plays a role in the formation of the η carbides. As a matter of fact, Karlsson [11] has already made the suggestion that the oxides of the η_1 carbide structure are electron compounds. Beattie and VerSnyder [20] recently gave the electron/atom ratio of the Fe_3W_3C carbide to be 7:1; however, the present author considers their treatment not rigorous enough to give this figure any physical meaning.

Until we obtain more insight into the electronic structures of the transition metals, especially those belonging to periods V and VI, any further speculation is probably fruitless, the more so since the atomic size factor, the relative strength of the transition-metal to carbon bond, and the electron/atom ratio may all be of importance for the stability of the η carbides.

Acknowledgement

The author wishes to thank Prof. G. Hägg, Mr. N. Karlsson, and Dr. R. Kiessling for encouraging discussions. He also wishes to acknowledge the assistance of Mr. L. E. Persson and the financial aid from the Swedish State Council for Technical Research.

References

1. Westgren, A. and Phragmén, G. Trans. Amer. Soc. Steel Treating, **13** (1928) 539.
2. Kuo, K. Research, **5** (1952) 339.
3. Takeda, S. Sci. Rep. Tôhoku Univ., Honda Anniversary Volume (1936) 864.
4. Westgren, A. Jernkontorets Annaler, **117** (1933) 1.
5. Adelsköld, V., Sandelin, A., and Westgren, A. Z. anorg. Chem., **212** (1933) 401.
6. Kislyakova, E. N. J. Phys. Chem. (U.S.S.R.), **17** (1943) 108.
7. Kiessling, R. Symposium on the Reactivity of Solids, Gothenburg, Sweden, June 9–13 (in press).
8. Rautala, P. and Norton, J. T. Trans. A.I.M.E., **194** (1952) 1045.
9. Badger, F. S. and Sweeny, W. O. Amer. Soc. Testing Material, Symposium on Materials for Gas Turbines (Philadelphia, 1946), p. 99.
10. Karlsson, N. Nature, **168** (1951) 558.
11. Karlsson, N. Private communication.
12. Kuo, K. J. Iron Steel Inst., **173** (1953) April.
13. Wallbaum, H. J. Z. Kristallogr. Mineral., petrogr. Abt., **A103** (1941) 391.
14. Duwez, P. and Martens, H. Trans. A.I.M.E., **194** (1952) 72.
15. Kuo, K. Unpublished work.
16. Goldschmidt, H. J. Research, **2** (1949) 343; **4** (1951) 343.
17. Rideout, S., Manly, W. D., Kamen, E. L., Lement, B. S., and Beck, P. A. Trans. A.I.M.E., **191** (1951) 872.
18. Laves, F. and Witte, H. Metallwirtschaft, **15** (1936) 15, 840.
19. Sully, A. H. J. Inst. Metals, **80** (1951-52) 173.
20. Beattie, H. J., Jr. and VerSnyder, F. L. Amer. Soc. Metals (1952), preprint no. 1.

THE EFFECT OF DEFORMATION ON THE ELECTRICAL RESISTIVITY OF SOME COBALT-NICKEL ALLOYS*

T. BROOM† and C. S. BARRETT‡

Resistivity determinations on annealed and deformed wires of some cobalt-nickel alloys have confirmed that stacking faults can make a large direct or indirect contribution to the increase in resistivity due to cold-work. Although the relative densities of stacking faults in the various alloys had generally to be deduced from the known transformation characteristics, X-ray evidence was obtained for the presence of stacking faults in the deformed alloy which had the largest increase in resistivity.

LES EFFETS DE LA DÉFORMATION SUR LA RÉSISTIVITÉ DE CERTAINS ALLIAGES DE COBALT-NICKEL

Les déterminations de la résistivité, effectuées sur des fils recuits et déformés, de certains alliages de cobalt-nickel, ont confirmé l'hypothèse, que les défauts d'empilage (stacking faults) peuvent jouer un rôle important, direct ou indirect, dans l'accroissement de la résistivité due à l'écrouissage. Quoique les densités relatives des défaults d'empilage dans les divers alliages aient été, en général, déduites des caractéristiques de transformation connues, une preuve de la présence des défauts d'empilage dans l'alliage déformé, dont l'accroissement de la résistivité était le plus grand, a été obtenue au moyen des rayons X.

DER EFFEKT DER VERFORMUNG AUF DEN ELEKTRISCHEN WIDERSTAND EINIGER KOBALT-NICKEL LEGIERUNGEN

Widerstandsmessungen an geglühten und verformten Drähten einiger Kobalt-Nickel Legierungen bestätigten, dass "stacking faults" einen grossen direkten oder indirekten Anteil an der Zunahme des Widerstandes, die man nach Kaltbearbeitung der Drähte beachtet, ausmachen können. Obwohl im allgemeinen aus dem bekannten Verhalten bei der Transformation auf die relative Dichte der "stacking faults" geschlossen wurde, konnte der direkte röntgenographische Nachweis für das Vorhandensein der "stacking faults" in den verformten Legierungen, die die grösste Widerstandszunahme zeigten, gebracht werden.

1. Introduction

In order to account for the large increases in resistivity due to deformation in some alloys it has been suggested [1] that stacking faults associated with dislocations make an important contribution to the scattering of conduction electrons. These faults arise from the dissociation of certain dislocations into two partial dislocations separated by a region of faulty stacking, as first shown by Heidenreich and Shockley for edge dislocations in a close-packed lattice [2]. The separation of the two partials is governed by an equilibrium between their mutual repulsions and the attractive force resulting from the surface energy of the stacking fault. In cubic close-packed metals the lamella of stacking fault associated with an edge dislocation has the hexagonal stacking sequence, and so large stacking faults are to be expected when the difference in energy between the cubic and hexagonal forms of packing is small. Unfortunately it is not easily possible to evaluate this difference for any particular metal or alloy with any certainty, but in some alloy systems where a cubic phase transforms directly to a hexagonal one, it is possible to infer that the size of stacking faults is a maximum, for a given composition, near the transformation temperature, or, for a given temperature, near the transformation composition. An example of this is provided by the cobalt-nickel system which has been investigated by Hess and Barrett [3]. They showed that the temperature of the strain-induced transformation between the close-packed cubic (high-temperature) phase and the hexagonal (low-temperature) phase was reduced from $\sim 420°C$ in pure cobalt to $\sim 20°C$ by the addition of 30 per cent nickel. Further, they deduced that their results locate, on a temperature-composition diagram, the line of equal free energy of the two close-packed structures.

Some exploratory experiments [1] showed that, for a specified deformation at room temperature, the increase in resistivity in an alloy containing 30 per cent nickel was markedly greater than in an alloy containing 40 per cent nickel, or in pure cobalt. The present work had as its object a more thorough investigation of the effect of deformation on the resistivity of some cobalt-nickel alloys.

2. Experimental

(i) *Materials*

The alloys used were kindly donated by the Mond Nickel Co. Ltd.: their full analyses have been given in a paper concerned with the lattice parameters

*Received January 20, 1953.
†Department of Metallurgy, University of Birmingham.
‡Institute for the Study of Metals, University of Chicago.

of binary cobalt-nickel alloys [4]. Table I gives the designation of the alloys, their nickel contents, and approximate transformation temperatures according to Hess and Barrett [3].

TABLE I

Alloy	Nickel (wt%)	Transformation temp. (°C)
KSE	25.9	~235°
KOO	31.1	~ 20°
KON	41.1	Does not transform

The alloys were hot-rolled to $\frac{1}{4}$-in. dia. rod from $\frac{5}{8}$-in. dia. round bar and thereafter cold-drawn with intermediate anneals to $\frac{1}{8}$-in. dia. wire, at which size resistivity studies were commenced.

(ii) *The Resistivity of Annealed Alloys*

The resistivities of the alloys used in this investigation were: KSE, 10.9; KOO, 10.4; and KON, 10.8 micro-ohm centimetres at 25°C, determined after prolonged annealing at 1,000°C followed by rapid cooling. These correspond fairly well with the results given by Bozorth [5] for commercial alloys. However, as Bozorth has drawn attention to the large discrepancies between published values of the resistivities of cobalt-nickel alloys, the possibility of the existence of long-range order in the 75/25-composition region was recognized and to investigate this, resistance measurements were made on the alloys in the temperature range 0 to 1,000°C. Heating and cooling were carried out in an argon atmosphere, generally at a rate of 200°C/hour. In spite of variations in this rate and prolonged heat treatments at high temperature, there appeared no unusual features in the resistance-temperature curves other than the changes of slope associated with the Curie temperature of each alloy. Up to these temperatures, the resistance-temperature curves of the alloys were parallel, and it was thus established that the room-temperature minimum in resistivity around 30 per cent nickel was not simply a low-temperature anomaly. Further, the results showed that any ordering must be extremely sluggish in annealed alloys and could almost certainly be eliminated by rapid cooling from a high temperature. However, it was later found that when the alloys were annealed at 600°C after heavy deformation, their resistivities were significantly lower than when they were annealed at 1,000°C. The differences were about 4 per cent for KON and KOO and about 7 per cent for KSE. These results suggest that ordering may occur at the composition corresponding to Co_3Ni; the establishment of order may be assisted if recrystallization is carried out at a temperature a little below the critical temperature for ordering.

(iii) *Deformation by Wire-drawing*

In order to avoid the possible complication of a resistivity change during deformation due to the destruction of any order which might result from a low-temperature anneal, the standard annealing treatment adopted for all wires was that of heating in argon for two hours at 1,000°C followed by rapid cooling (~50°C/sec) to room temperature. In determining fractional changes in resistivity due to wire-drawing, a major source of error is in the measurement of wire diameters. This difficulty was avoided by re-annealing the wires after deformation and assuming that the fractional change in resistivity on drawing, $\Delta\rho/\rho$, was equal to the change in resistance on re-annealing relative to the resistance of the re-annealed wire.

A series of experiments was carried out in which wires of each alloy were drawn at 0° and 100°C, using tungsten carbide dies. The rate of drawing was never greater than 10 cm./min., and during drawing the die in use was immersed in a well-stirred water bath maintained at the required temperature. The results obtained for the reduction from 0.072-in. to 0.063-in. dia. are shown in Figure 1.

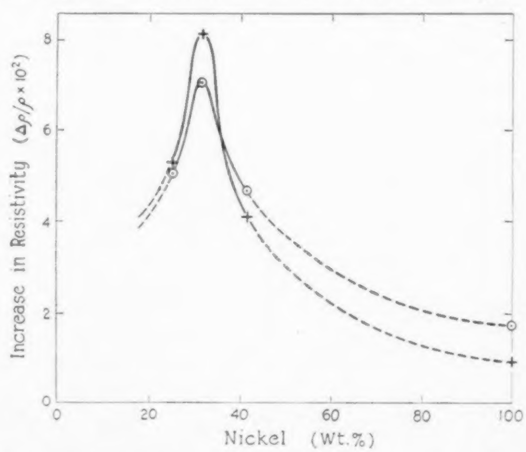

FIGURE 1. The effect of deformation on the electrical resistivity of cobalt-nickel alloys. (Data for nickel from reference 1.) 35% reduction of area (by wire drawing). +, 100°C; O, 0°C.

In this case the wires were all coated with "Aquadag" before drawing to ensure comparable lubrication in the die. The results for three other reductions were all similar in that a very pronounced maximum of increase in resistivity was found at the composition of the alloy KOO which has a transformation temperature of 20°C. Wires of this alloy were also

drawn at 28° and 50°C with the results shown in Figure 2.

(iv) *Deformation by Extension*

In order to investigate the increase of resistivity for small deformations, the re-annealed wires from

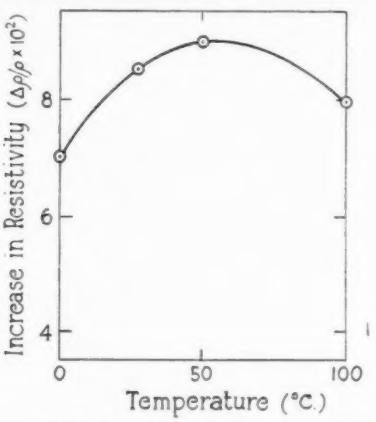

FIGURE 2. The effect of temperature of deformation on the resistivity of the alloy KOO (31% Ni; transformation temperature $\sim$ 20°C). 35% reduction of area (by wire drawing).

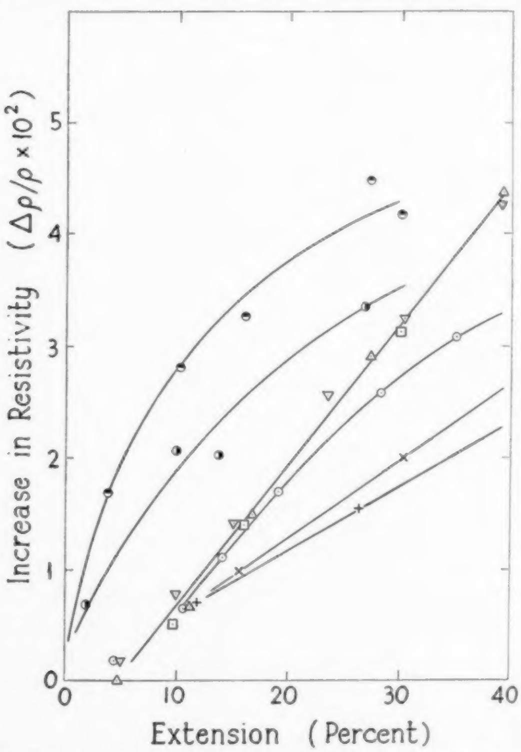

FIGURE 3. The effect of temperature of extension on the resistivity of KSE (26% Ni; transformation temp. $\sim$ 235°C); KOO (31% Ni, transformation temp. $\sim$ 20°C); and KON (41% Ni, no transformation).

◓ KSE	16°C	○ KOO	0°C	× KON	19°C
◑	90	▽	16	+	90
		△	50		
		□	90		

the wire-drawing experiments were extended at various temperatures. All resistance measurements were made at 25°C, the wires being removed from the straining device for this purpose. Relative resistivity changes were calculated from the measurements of resistance and extension. These results are shown in Figure 3. During the room-temperature extensions, data were collected which enabled the stress-strain curves of the materials to be drawn (Figure 4).

(v) *X-ray Diffraction Data*

Debye-Scherrer patterns of drawn and etched wires of the alloy KOO showed a few faint lines due to the hexagonal structure when the deformation was carried out at 20°C or lower, and none when wires were drawn at 28°C or higher. This is in full accord

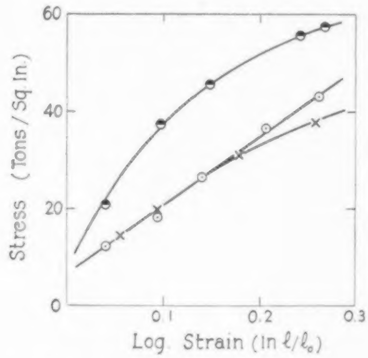

FIGURE 4. Stress-strain curves (room temperature) for three cobalt-nickel alloys. ◓, KSE; ○, KON; ×, KOO.

with the results of Hess and Barrett [3]. With the object of attempting to use Paterson's analysis [6] of the effect of stacking faults on diffraction patterns, some measurements were made on films obtained using etched-wire specimens, Co K_α radiation, and a Phillips 11.46-cm. camera. The analysis predicts, in addition to "fault broadening," shifts of the diffraction lines in a powder pattern. Thus, the observed Bragg angles of lines from (200) and (222) planes should decrease, and those from (111) and (220) planes should increase when the density of deformation faults increases. In the present experiments, the positions of the peaks of high-angle lines could not be measured accurately owing to their great widths, and in any case results for them are difficult to interpret owing to the necessity for allowing for the separation of the lines due to K_{α_1} and K_{α_2}. Attention was therefore concentrated on the separation of the lines from the (111) and (200) planes. The data are presented in Table II.

TABLE II

X-RAY DIFFRACTION PATTERNS: SEPARATION OF LINES FROM (111) AND (200) PLANES

Alloy	Condition	Film No.	Measurement	$\theta_{(200)} - \theta_{(111)}$
KOO (31% Ni)	Annealed	By calculation	[4]	4.410°
	"	1	Visual	4.427, 4.407
	"	2	Visual	4.419
	Drawn 30%, 50°C	3	Visual	4.385, 4.357, 4.374
	Extended 45%, 50°C	4	Photometer	4.364
KON (41% Ni)	Annealed	By calculation	[4]	4.400
	"	5	Visual	4.430, 4.394, 4.405
	Drawn 30%, 18°C	6	Visual	4.410, 4.405

3. Discussion

The results confirm previous evidence [1] of the importance of stacking faults in affecting the increase of resistivity due to deformation in some alloys. This is strikingly shown in Figure 1, where the maximum increase in resistivity is given at a composition where the density of stacking faults would be expected to be great for deformations at around room temperature. The comparison of the behaviour of the alloy KON (no transformation) with that of the alloy KOO deformed at 50°C or higher (above its transformation temperature) can be made with confidence, as under these conditions the alloys remain cubic. However, caution must be exercised in interpreting the increases given by the alloy KSE, which transforms to give an appreciable proportion of hexagonal phase, as the resistivity of the cubic structure relative to that of the hexagonal, and the effect of anisotropy of resistivity in the hexagonal phase are both unknown. The inference of greater fault density in KOO than in KON is confirmed by the X-ray data given in Table II, which show that the relative positions of lines from (111) and (200) planes were certainly affected by deformation in the alloy KOO and not in KON. The quantitative evaluation of fault density by the analysis of Paterson [6] is complicated, owing to the super-position of effects due to particle size and strain broadening, and has not been attempted. The X-ray observation that faults are present in a cubic alloy deformed above its transformation temperature has not previously been made although Hess and Barrett [3] searched for such faults by means of an oscillating-crystal technique. On theoretical grounds, deformation faults of appreciable size can be expected at temperatures slightly above the transformation temperature. The repulsion between the two partial dislocations in an extended dislocation varies inversely as the distance between them, and if the energy of the stacking fault relative to that of the lattice decreases steadily as the temperature is lowered (as is presumably the case for the cubic phase), there comes a point when the separation of the partials is so large that they are effectively independent, and the size of the fault will no longer depend on an equilibrium between the repulsion of the partials and the attractive force due to energy difference.

It is possibly for this reason that in Figure 2 there is only a very broad maximum of increase in resistivity for a given deformation carried out at various temperatures in a range which included the transformation temperature. Indeed, the results in Figure 3 show no significant differences in increase in resistivity for wires of KOO deformed up to 40 per cent extension in the range 16° to 90°C.

The effects of pure extension and of wire-drawing are obviously comparable in the case of the alloys KOO and KON. However, Figure 3 shows that KSE gives a very rapid initial increase in resistivity. This alloy transforms to hexagonal + cubic when deformed at temperatures below 235°C. The rapid increase is interpreted as due to the creation of large numbers of stacking faults which are necessary for the accomplishment of transformation. At greater deformations the proportion of hexagonal to cubic may become constant (as discussed below), and then the feature controlling the increase in resistivity may, as before, be the size of stacking faults, which would be expected to be smaller than in KOO. Thus the rate of increase of resistivity with deformation decreases, and for large deformations (Figure 1) the increase for KSE is less than that for KOO.

The stress-strain curves (Figure 4) are of interest in this connection. That of KSE is much higher than that of KOO (or KON), and this suggests considerable work-hardening and pile-up of dislocations in the two-phase alloy. It is probable that pile-up of dislocations due to crossing slip and to boundaries of phases is much more rare in the hexagonal phase than in the cubic. The accumulation of dislocations in the cubic phase will interfere with the particular dislocation movements necessary for transformation and so will prevent complete conversion to hexagonal. Hess and Barrett, writing of their experiments [3], have commented on the difficulty of conversion from cubic to hexagonal and on the ease of reversion. From the present viewpoint, the ease of reversion is accounted for by the reasonable assumption that no great accumulation of dislocations occurs in the hexagonal phase, so that there is little hindrance to the dislocation movements which accomplish the reversion.

Finally it should be pointed out that, although it has been suggested that stacking faults are the direct cause of a high increase in resistivity by reason of their effect on the conduction electrons, it is possible that they influence the resistivity simply because they can act, during deformation, as generators of other lattice defects such as vacancies, interstitials, and sessile dislocations.

Acknowledgements

The authors are grateful to Professor D. Hanson for many facilities accorded them during the course of the investigation which was carried out in the Department of Metallurgy, University of Birmingham.

References

1. BROOM, T. Proc. Phys. Soc., **65** B (1952) 871.
2. HEIDENREICH, R. D. and SHOCKLEY, W. Rep. Conf. Strength Solids (London, Physical Soc., 1948), p. 57.
3. HESS, J. B. and BARRETT, C. S. J. Metals, **4** (1952) 645.
4. TAYLOR, A. J. Inst. Metals, **77** (1950) 585.
5. BOZORTH, R. M. Ferromagnetism (New York, Van Nostrand, 1951), p. 278.
6. PATERSON, M. S. J. App. Physics, **23** (1952) 805.

INFLUENCE OF STRESS ON MARTENSITE NUCLEATION*

J. C. FISHER and D. TURNBULL†

The stresses produced by plastic deformation and by prior transformation are known to stimulate the transformation of austenite to martensite. Recent experiments have also revealed the quantitative effect of homogeneous tensile and compressive stresses. In this report the previously developed theory of martensite nucleation is extended to include the influence of external stresses. It is found that there is an effect both due to the volume change in the transformation and due to the shear associated therewith. Both effects combine additively to alter the change in volume free energy associated with the transformation. Quantitative predictions of the influence of simple tensile and compressive stresses upon the temperature at which the martensite transformation begins in carbon steels are in reasonable agreement with the experiments of Kulin, Cohen, and Averbach. The importance of stresses produced by plastic deformation, by prior transformation, and by the presence of a few dislocations in annealed austenite is discussed qualitatively.

L'INFLUENCE DE TENSIONS SUR LA GERMINATION DE LA MARTENSITE

Le rôle de stimulant joué par les tensions produites par la déformation plastique et par les transformations antérieures, sur la transformation de l'austenite en martensite, est bien connu. De récentes expériences ont aussi révélé l'effet quantitatif des tensions homogènes d'extension et de compression. Dans ce rapport, la théorie de germination de la martensite, développée antérieurement, est étendue pour englober le problème de l'influence des tensions externes. Il a été constaté, qu'il y avait des effets dus aussi bien au changement de volume, qu'au cisaillement associé à ce dernier. Les deux effets s'ajoutent pour modifier le changement d'énergie libre volumique associé à cette transformation. Les prévisions quantitatives concernant l'influence des tensions simples d'extension et de compression sur la température à laquelle commence la transformation martensitique dans des aciers au carbone s'accordent assez bien avec les résultats des expériences de Kulin, Cohen et Averbach. L'importance des tensions produites par la déformation plastique, par des transformations antérieures et par la présence de quelques dislocations dans l'austenite recuite, est discutée qualitativement.

DER EINFLUSS VON SPANNUNGEN AUF DIE MARTENSITBILDUNG

Es ist bekannt dass Spannungen, die von vorhergehender Verformung oder von früheren Transformationen herrühren, die Transformation von Austenit zu Martensit erleichtern. Neue Versuche haben ausserdem den quantitativen Effekt von homogenen Zug- und Druckspannungen gezeigt. In der vorliegenden Arbeit wird die früher veröffentlichte Theorie der Martensitbildung weiter ausgearbeitet, um den Einfluss von äusseren Spannungen einzubeziehen. Es wurde gefunden, dass sowohl ein Effekt der Volumenänderung bei der Umwandlung als auch der damit verbundenen Scherung vorhanden ist. Beide Effekte tragen additive zur Modifizierung der mit der Umwandlung verbundenen Änderung der freien Energie bei. Quantitative Voraussagen des Einflusses einfacher Zug- und Druckspannungen auf die Temperatur, bei der in kohlenstoffhaltigen Stählen die Umwandlung zu Martensit beginnt, stehen in zufriedenstellender Übereinstimmung mit Versuchen von Kulin, Cohen und Averbach. Die Wichtigkeit von Spannungen die durch plastische Verformung, durch vorhergehende Umwandlungen oder durch das Vorhandensein einiger Versetzungen in geglühtem Austenit erzeugt werden können, wird qualitativ diskutiert.

Stresses will influence martensite nucleation in two ways. First, because there is a volume expansion associated with the transformation, the difference in volume free energy between austenite and martensite will be altered by tensile and compressive stresses. Second, because there is a shear associated with the transformation, the strain energy of nucleus formation will be altered by shear stresses.

Theory

Let Δf_v be the volume free energy difference between martensite and austenite. Consider first the change in Δf_v associated with the presence of a stress σ_n normal to the habit plane of the nucleus. Martensite nuclei are lenticular in shape [1], and for this reason most of the volume expansion occurs in a direction normal to the habit plane, or plane of the lens. The work expended in pushing against the stress σ_n is $-\sigma_n \Delta v$ per unit volume of martensite, where σ_n is negative for compression and where Δv is the volume change associated with the transformation of a unit volume of austenite to martensite. σ_n is the only tensile or compressive stress that has an influence upon Δf_v, for the entire volume expansion takes place in the direction of σ_n.

Consider next the change in strain energy associated with a shear stress. The only shear stress component of interest is the one that aids the martensite shear. It will be designated by τ_m.

Assume for simplicity that the austenite surrounding a martensite plate of radius r and thickness t is strained uniformly by the formation of the martensite plate throughout a spherical volume of radius r. The mean strain associated with the formation of the plate will be

*Received January 23, 1953.
†General Electric Research Laboratory, The Knolls, Schenectady, New York, U.S.A.

$$\epsilon_1 = \theta \cdot \tfrac{1}{2}t \cdot 1/r$$

where θ is the martensite shear angle, $\theta \cdot \frac{1}{2}t$ is the tangential displacement of the austenite at the surface of the martensite plate, and the ratio of $\theta t/2$ to r is the mean shear strain.

In the presence of a stress τ_m, there will have been a strain

$$\epsilon_0 = -\tau_m/G$$

already present in the austenite. The negative sign is required for those habit planes for which the formation of martensite is aided. The net strain, being the sum of that already present and that introduced by transformation, is

$$\epsilon = \epsilon_1 + \epsilon_0 = \theta t/2r - \tau_m/G.$$

The energy per unit volume is

$$E_v = \tfrac{1}{2}G\epsilon^2 = \tfrac{1}{2}G(\theta t/2r - \tau_m/G)^2$$

and the total strain energy is

$$E = 4\pi r^3 E_v/3.$$

Actually, we are concerned with the energy *change* on forming a martensite plate. The energy in a volume of austenite of radius r before transformation is

$$E_0 = (4\pi r^3/3)(\tfrac{1}{2}G\epsilon_0^2),$$

and the change of energy on forming a martensite plate is

$$\begin{aligned}\Delta E &= E - E_0\\ &= (2\pi r^3 G/3)\{(\theta t/2r - \tau_m/G)^2 - (\tau_m/G)^2\}\\ &= (G\theta^2/6)\pi r t^2 - (4\tau_m\theta/3)\pi r^2 t/2.\end{aligned}$$

The strain energy associated with the formation of a martensite plate is seen to be made up of two terms. The first, $(G\theta^2/6)\pi r t^2$, is that previously deduced for martensite forming in unstressed austenite [1]. The second, $-(4\tau_m\theta/3)\pi r^2 t/2$, is zero when the stress τ_m is zero, is zero when the martensite shear angle θ is zero, and is proportional to the volume of the martensite plate $\pi r^2 t/2$. The second term therefore affects the energy of formation of a martensite plate as though it were a modification of the volume free energy.

The free energy of formation of a martensite plate in stressed austenite now can be written

$$(1)\quad W = 2\pi r^2\gamma + (\pi r^2 t/2)(\Delta f_{vo} - \sigma_n\Delta v - 4\tau_m\theta/3) + (G\theta^2/6)\pi r t^2,$$

where Δf_{vo} is the volume free energy change accompanying transformation in the absence of stress. The energy of formation of a critical size nucleus is

$$(2)\quad W^* = 8192\pi(G\theta^2/6)^2\gamma^3/27(\Delta f_{vo} - \sigma_n\Delta v - 4\tau_m\,\theta/3)^4,$$

and the volume of a critical size nucleus is

$$(3)\quad V^* = -32{,}768\pi(G\theta^2/6)^2\gamma^3/27(\Delta f_{vo} - \sigma_n\Delta v - 4\tau_m\theta/3)^5.$$

Estimate of the Influence of Stress upon M_s

In iron-carbon alloys, as one limit, martensite nucleation occurs at the sites of local composition fluctuations; the nucleation condition for a given site being that V^* equal the volume of the depleted region [1]. In iron-nickel alloys, as the other limit, martensite nucleation occurs more or less homogeneously, at a steady rate that is proportional to $\exp(-W^*/kT)$ [2]. In either event, the M_s criteria are that V^* or W^*/T be constant, for the M_s temperature in an alloy is that temperature at which an appreciable number of athermal martensite nuclei have formed during cooling, or at which the rate of isothermal martensite nucleation becomes significant. Taking account of the forms W^* and V^* as given above, the M_s criteria reduce to

$$(4)\left\{\begin{aligned}\Delta f_v &= \text{const}\ \ \text{(for athermal martensite)}\\ \Delta f_v T^{1/4} &= \text{const}\ \ \text{(for isothermal martensite)}\\ \Delta f_v &= \Delta f_{vo} - \sigma_n\Delta v - 4\tau_m\theta/3\end{aligned}\right.$$

In the subsequent discussion, only athermal martensite will be considered. If the temperature is changed by ΔT, Δf_v also is changed by an amount

$$\Delta(\Delta f_v)_1 = (\partial\Delta f_v/\partial T)\Delta T = (\partial\Delta f_{vo}/\partial T)\Delta T.$$

On the other hand, introduction of the stresses σ_n and τ_m also changes Δf_v relative to its value in the absence of stress by an amount $\Delta(\Delta f_v)_2 = -\sigma_n\Delta v - 4\tau_m\theta/3$. The total change in Δf_v is the sum of $\Delta(\Delta f_v)_1$ and $\Delta(\Delta f_v)_2$,

$$\Delta(\Delta f_v) = (\partial\Delta f_{vo}/\partial T)\Delta T - \sigma_n\Delta v - 4\tau_m\theta/3.$$

Since the M_s criterion for athermal martensite is $\Delta(\Delta f_v) = 0$, the above equation can be solved for the change in M_s, $\Delta M_s = \Delta T$, associated with the stresses σ_n and τ_m:

$$(5)\quad \Delta M_s = \Delta T = (\sigma_n\Delta v + 4\tau_m\theta/3)/(\partial\Delta f_{vo}/\partial T).$$

Comparison with Experiment

From the above equation, it is possible to estimate the changes in M_s temperature corresponding to

various stress states. Consider first a hydrostatic pressure p. The normal stress then is $\sigma_n = -p$ and the shear stress is $\tau_m = 0$. The change in M_s is

$$\Delta M_s = -p\Delta v/(\partial \Delta f_{vo}/\partial T).$$

For the steel investigated by Kulin, Cohen, and Averbach [3], $\partial \Delta f_{vo}/\partial T$ in the neighborhood of M_s at $-37°C$ can be calculated [4] to be

$$\partial \Delta f_{vo}/\partial T \approx 0.90 \text{ cal/mole °C}$$

$$\approx 5.3(10)^6 \text{ ergs/cm}^3 \text{ °C}.$$

The relative volume change is

$$\Delta v \approx 0.04.$$

For a pressure of 1000 atmospheres (10^9 dynes/cm^2) the change in M_s then is

$$\Delta M_s = -10^9 (.04)/5.3\,(10)^6 = -7.5°\text{C}.$$

Consider next simple tension or compression. Here the value of ΔM_s varies from plane to plane as the values of σ_n and τ_m vary. The planes of interest in such cases are those for which M_s is raised the most (or depressed the least), for it is on such planes that martensite first begins to form at an appreciable rate. The problem, then, is to find the plane for which $\sigma_n \Delta v + 4\tau_m\theta/3$ is a maximum.

Let the normal to the plane in question make an angle ϕ with the axis of tension. The normal stress on this plane then is

$$\sigma_n = \sigma_0 \cos^2 \phi$$

where σ_0 is the tensile or compressive stress. The corresponding shearing stress is

$$\tau_m = |\sigma_0| \sin \phi \cos \phi,$$

the absolute value of σ_0 being taken because martensite always will shear in such a way that the shear stress aids the transformation. The quantity to be maximized is

$$\sigma_n\Delta v + 4\tau_m\theta/3 = f(\phi) = \sigma_0\Delta v \cos^2 \phi + (4|\sigma_0|\theta/3) \sin \phi \cos \phi.$$

Maximizing,

$$\text{(6)} \quad \tan 2\phi = (4\theta/3\Delta v)|\sigma_0|/\sigma_0 = (4\theta/3\Delta v) \text{ sig } \sigma_0$$

where sig $\sigma_0 = +1$ for tension and -1 for compression (sig x is, in effect, the algebraic sign of x).

For the alloy of Kulin, Cohen, and Averbach, $\theta \approx 1/6$, so that

$$\phi = \tfrac{1}{2} \text{ arc tan } 5.6 = 40° \text{ for tension,}$$

$$\phi = \tfrac{1}{2} \text{ arc tan } (-5.6) = 50° \text{ for compression.}$$

The corresponding changes in M_s for stresses of 15,000 psi are

$$\Delta M_s = 25°\text{C for tension,}$$

$$\Delta M_s = 17.5°\text{C for compression.}$$

These values are compared with experiment in the table.

TABLE I

COMPARISON OF CALCULATED AND EXPERIMENTAL VARIATIONS OF M_s WITH STRESS

Stress state	Calculated	Measured [3]
Tension	25°C	17°C
Compression	17.5°C	10°C
Hydrostatic compression	− 7.5°C	—

For both tension and compression, the calculated ΔM_s exceeds the experimental by about 8°C. Part of this difference may be due to the fact that in tension or compression only a fraction of the possible martensite habit planes and shear directions lie in the most favorable orientation, so that the density of effective nuclei has been decreased; a factor that was neglected in the calculation.*

Influence of Plastic Deformation and Prior Transformation

It has been pointed out that elastic distortion resulting from dislocations, plastic deformation, and prior transformation will tend to favor further transformation in the distorted regions [1; 5]. This idea can be put in quantitative form by means of the theory developed above.

The stresses in a plastically deformed material vary from place to place in a manner that is not easy to compute. On the other hand, the *mean* stress in a plastically deformed metal can be estimated. Calculations based upon Taylor and Quinney's measurements [6] of stored energy suggest that there are about 10^{12} dislocation lines passing through each square centimeter of area in a heavily cold-worked metal. The mean spacing of these dislocations, assuming them to be spaced at random, is about 10^{-6} cm. Since the shear stress at a distance r from a screw dislocation with Burgers vector **b** is $Gb/2\pi r$, the mean shear stress due to the presence of the random array under consideration is about $Gb/$

*We are indebted to the referee for pointing out that if the habit planes of potential martensite nuclei are oriented at random, the *average* value of ΔM_s for all habit planes is in close agreement with experiment. For 15,000 psi tension, the average ΔM_s is 16.5°C, and for 15,000 psi compression the average ΔM_s is 11.5°C.

$2\pi r \approx 3(10)^9$ dynes/cm² or about 45,000 psi. The corresponding change in M_s, according to equation (5), is $\Delta M_s \approx 120°C$, which is beyond the range of accuracy of the equation. The greatest error in this estimate probably results from the assumption that the 10^{12} dislocations are spaced at random. More probably, they are spaced in such a way that the mean shear stress is considerably reduced, and a better estimate probably would find ΔM_s considerably less than 120°C.

In an annealed metal there are far fewer dislocations, perhaps as few as 10^8/cm². They are arranged in small-angle grain boundaries, minimizing the associated strain energy. Even if they were distributed at random, the mean stress would produce a ΔM_s of only about one degree. Near each individual dislocation, however, in a very small fraction of the total volume of the metal, the stress rises to an appreciable level, being approximately $Gb/2\pi r$ at a distance r from a screw dislocation with Burgers vector $\mathbf{b}$ as described above. The value of r appropriate to the maximum ΔM_s is essentially the radius of a critical size nucleus, $r \approx 10^{-6}$ cm. The corresponding ΔM_s is about 120°C, the same as was estimated for the entire volume of a heavily cold-worked metal.

VOL. 1 1953

The stresses in the neighborhood of a full-grown martensite plate probably are equal to the yield strength of the austenite, say 30,000 psi, giving $\Delta M_s \approx 80°C$.

The stresses in a cold-worked metal, near an isolated dislocation, and near a martensite plate, all have been shown to raise the M_s by several tens of degrees; perhaps, in extreme cases by as much as 100°C. This change in M_s results directly from an effective change in the volume free energy difference between martensite and austenite. Martensite nucleation is favored in the neighborhood of a dislocation, for example, because the energy of formation of a critical size nucleus is modified by stress; not because the dislocation is in any sense a subcritical martensite nucleus.

If ΔM_s were computed more precisely, it should be possible to account quantitatively for the effects of cold work and for the autocatalytic features of the martensite transformation, which are present to a most pronounced degree in the burst phenomenon described by Machlin and Cohen [5].

The Role of Stress in Heterogeneous Nucleation

It is well known that nuclei for condensation or for crystallization from the liquid usually form preferentially on the surfaces of various foreign particles (composition heterogeneities) present in the system. Heterogeneity-catalyzed nucleation of this sort is termed heteregeneous nucleation. Based on the theory just outlined, we may draw some conclusions relating to heterogeneous nucleation of the martensite transformation.

Preferential nucleation on the surface of foreign particles is much less likely for martensite than for condensation or for crystallization from liquids, because (1) the number of martensite nuclei required to effect appreciable transformation is likely to be quite large relative to the number of foreign particles, particularly where the austenite grain size is small, and because (2) preferential nucleation of martensite can take place only on the surfaces of those composition heterogeneities that are more effective than the parent austenite itself in promoting martensite nucleation.

On the other hand, the theory outlined above predicts that martensite nuclei should form preferentially in regions of the lattice subjected to shear or tensile stresses, as in the neighborhood of a dislocation. A cold-worked metal must contain a high dislocation density and many other regions of residual stress. These regions of residual stress, in the vicinity of dislocations and elsewhere, are structural heterogeneities; hence the nucleation of martensite in a cold-worked metal should be structurally heterogeneous.

A thoroughly annealed metal that is not already partially transformed to austenite should be relatively free of regions of residual long-range stress. Nevertheless, an annealed piece of metal of macroscopic dimensions almost invariably contains a small concentration of dislocations that may promote nucleation of martensite. For this reason, it is possible that the nucleation of martensite has been structurally heterogeneous to an important degree for all martensite transformation studies heretofore reported.

A question arises as to the possibility of observing truly homogeneous martensite nucleation. It seems likely that the density of trapped dislocations in annealed single crystals will be less for smaller crystals. Therefore it is possible that the nucleation of martensite in very small crystals, say less than ten microns in diameter, would be structurally homogeneous. From this point of view an investigation of the frequency of martensite nucleation in small crystals would be very interesting.

In some instances stabilization may be caused by the relaxation of residual stresses in the austenite,

for stress relaxation, according to our theory, reduces the probability of martensite nucleation. It is interesting that a relaxation of stress amounting only to 15,000 psi (e.g. $\backsim$ 0.01 cal/cc, or less than 0.1 per cent of Δf_{vo}) may lower the M_s temperature in the stressed region by 20°C or more. On this basis it is expected that stabilization will be more marked in previously cold-worked or partially transformed austenite than in fully annealed untransformed austenite.

Conclusion

The influence of stress upon the transformation from austenite to martensite is explained satisfactorily by the theory of martensite nucleation. Compressive stress normal to a martensite plate lowers the M_s temperature, whereas tensile stress normal to the plate and shear stress in the plane of the plate both raise M_s. The residual stresses produced by plastic deformation are sufficient to account for the influence of plastic deformation in causing transformation above the normal M_s, and stresses produced by prior martensite transformation appear to be sufficient to account for the autocatalytic burst phenomenon observed in some alloys. A question is raised as to the possible role of dislocations in causing some heterogeneous martensite nucleation even in well-annealed austenite.

Acknowledgement

We wish to acknowledge some stimulating conversations on this subject with Professor Morris Cohen of the Massachusetts Institute of Technology.

References

1. Fisher, J. C., Hollomon, J. H., and Turnbull, D. Trans. A.I.M.E., **185** (1949) 691.
2. Fisher, J. C. Acta Met., **1** (1953) 32.
3. Kulin, S. A., Cohen, M., and Averbach, B. L. J. Metals, **4** (1952) 661.
4. Fisher, J. C. Trans. A.I.M.E., **185** (1949) 688.
5. Machlin, E. S. and Cohen, M. J. Metals, **3** (1951) 746.
6. Taylor, G. I. and Quinney, H. Proc. Roy. Soc., **143** (1934) 307; **163** (1937) 157.

THE ESTIMATION OF DISLOCATION DENSITIES IN METALS FROM X-RAY DATA*

P. GAY, P. B. HIRSCH, and A. KELLY†

Recent work has shown that substructures are formed within the grains of a cold-worked polycrystalline metal. In this paper, methods are described by which the density of the excess dislocations of one sign in the boundaries between the particles can be found from data obtained from X-ray diffraction photographs. The methods may be extended to give estimates of the excess and total dislocation densities within the particles and the densities in annealed metals.

The results for both cold-worked and annealed metals show that the present estimates are less than the usually accepted values. The discrepancy in the case of the cold-worked metals could be due to a different distribution of dislocations in the boundaries which may not be detected by the existing X-ray methods; however a strict comparison cannot be made until more reliable data are available from other physical measurements. It is shown that the usually accepted figure for the dislocation density in annealed metals has no theoretical or experimental support and that the dislocation density in some metal crystals may be very much less.

UNE ESTIMATION DES DENSITÉS DES DISLOCATIONS DANS LES MÉTAUX D'APRÈS LES DONNÉES OBTENUES AU MOYEN DE RAYONS X

Des travaux récents ont montrés, que lors de l'écrouissage des métaux polycristallins, il y a formation d'une sous-structure.

Dans cet article, certaines méthodes sont décrites, au moyen desquelles il est possible d'évaluer l'excès des dislocations d'un signe donné dans les joints de la sous-structure, en partant des données obtenues des photographies de diffraction des rayons X.

Ces méthodes peuvent être étendues pour permettre l'évaluation de l'excès et de la densité totale des dislocations au sein de la sous-structure, ainsi que les densités dans les métaux recuits.

Les résultats obtenus pour les métaux écrouis et recuits montrent, que les présentes estimations donnent des valeurs inférieures à celles, qui sont généralement acceptées. Dans le cas des métaux écrouis, la différence peut être due à une distribution différente des dislocations dans les joints, qui ne peut pas être décelée au moyen des méthodes existantes à l'heure actuelle dans le domaine des rayons-X; il est, cependant, impossible de faire des comparaisons correctes avant d'avoir des données plus sûres, provenant d'autres mesures physiques. Il est montré, que les chiffres généralement acceptés pour la densité des dislocations dans des métaux recuits ne sont confirmés ni par la théorie ni par l'expérience, et que la densité des dislocations peut, dans certains cristaux métalliques, être de beaucoup inférieure à ces valeurs.

DIE ABSCHÄTZUNG DER VERSETZUNGSDICHTE IN METALLEN AUS RÖNTGENOGRAPHISCHEN DATEN

Neuere Untersuchungen haben gezeigt, dass innerhalb der Kristallite eines kaltbearbeiteten Metals "Mosaikblöcke" entstehen; in der vorliegenden Arbeit werden Methoden beschrieben, mit Hilfe derer die Dichte der überzähligen Versetzungen eines Vorzeichens in den Grenzen zwischen den Mosaikblöcken auf Grund von Röntgenfeinstrukturdaten gefunden werden kann. Diese Methoden können auf die Abschätzungen der Dichte der überzähligen und der gesamten Versetzungen innerhalb der Mosaikblöcke und der Versetzungsdichte in geglühten Metallen ausgedehnt werden.

Die Ergebnisse sowohl für kaltbearbeitete als auch geglühte Metalle zeigen, dass die angegebenen Schätzungen geringer als die üblicherweise angenommenen Werte sind. Der Unterschied im Falle der kaltbearbeiteten Metalle könnte auf eine andere Verteilung der Versetzungen an den Blockgrenzen zurückzuführen sein, die mit den heutigen Röntgenmethoden nicht nachweisbar ist. Ein strenger Vergleich kann jedoch solange nicht angestellt werden, als nicht zuverlässigere Daten aus anderen physikalischen Messungen zur Verfügung stehen. Es wird gezeigt, dass die allgemein zitierten Werte der Versetzungsdichte von geglühten Metallen weder theoretisch noch experimentell fundiert ist, und dass die Versetzungsdichte einiger geglühter Metalle sehr wohl viel geringer sein kann.

1. Introduction

Estimates of the dislocation densities in annealed and cold-worked metals are based on the theoretical interpretation of experimental measurements of the yield stress in metals [1], on the energy stored within metals after cold-work [2], and on magnetic measurements [3]. The values derived are of the order of 10^8 dislocation lines per sq. cm. and 10^{12} dislocation lines per sq. cm., for the annealed and severely cold-worked metals, respectively. The significance of these values is dependent on the validity of the theoretical interpretations by which they have been derived; nevertheless, in the absence of any reliable experimental method of determination, they have become generally accepted. This paper describes a method by which it is possible to derive approximate values from X-ray data; the results obtained using this method are significantly different from the accepted values. The discrepancy may be accounted for by assuming the existence of particular distributions of dislocations which cannot be detected by X-ray methods, but it is clear that a re-examination

*Received December 22, 1952.

†Crystallographic Laboratory, Cavendish Laboratory, Cambridge, England.

of the data on which the original estimates are based is necessary before final conclusions may be drawn.

It is found experimentally that on cold-working a metal the sharp diffraction spots obtained on X-ray photographs of annealed polycrystalline material spread into arcs around the Debye Scherrer rings [4; 5; 6; 7]; thus the material within the original grains covers a range of orientations after cold-work. Usually these misorientations are far greater than those which could reasonably be expected if the original grains were thought to be purely elastically bent (the maximum possible value of the elastic curvature can be obtained from the broadening of the arcs [8]). It has been concluded therefore that the grains are plastically bent after the deformation, i.e. they may be regarded as containing an excess of dislocations of one sign. The amount of curvature is related to the number of excess dislocations within the grains, and may thus be used to estimate the dislocation density. It is on this principle that the methods described in this paper are based.

2. The Methods of Estimation

The quantitative estimates of dislocation densities, although they may be derived in different ways under different experimental conditions, are all based on the considerations set out in this paragraph. Let us suppose that the material consists of blocks of size t, which are separated from each other by single walls of edge (or screw) dislocations. If h is the spacing of dislocations in the walls, the number of dislocations per boundary wall is t/h; thus the density of dislocations in the boundaries (D_B) is $t/h \times 1/t^2 = 1/ht$, since, on the average, there is one boundary wall per side of particle. However the angle (α) between the two particles defined by the boundaries is s/h (provided α is small) [9], where s is the Burgers vector, and so

$$D_B = \alpha/st.$$

In order to determine the density therefore, values of α and t must be deduced from the X-ray photographs.

The relationship may be most conveniently applied to photographs in which the arcs around the Debye-Scherrer rings are resolved into spots; from such photographs estimates of both α and t can be obtained. Even where the arcs are not resolved, some limiting values of the densities may be derived. It is convenient to treat two types of case:

(a) *Application to Spotty Diffraction Arcs*

From such photographs, the particle size, t, may be found by the method of counting spots [5]; the smallest values of t which can be detected are $\sim 10^{-4}$ cm. using fine-beam back-reflexion methods, and considerably smaller (down to $\sim 10^{-5}$ cm. in favourable circumstances) using microbeam-transmission methods [6].

The magnitude of α cannot be determined directly. From the lengths of the arcs into which the spots are clustered on the X-ray photographs it is possible to determine the total angle β over which the material within an original grain is misorientated. The angular misorientation α between adjacent particles in the original grain is dependent on the manner in which the particles are arranged within the grain. Two limiting conditions may be distinguished:

(i) It can be assumed that the grain is uniformly bent. In this case $\alpha = (t/T)\beta$, where T is the original grain size, and thus

$$D_B = \beta/sT$$

and is independent of the particle size.* This must be considered as a lower limit of the dislocation density in the boundaries, for the value of α derived in this way must be a minimum. The relationship may also be regarded as giving the actual density of excess dislocations of one sign within the grain.

(ii) It can be assumed that the particles are misorientated about a mean position. In this second limiting assumption, an upper limit of α is found. The relation connecting the mean angle between the particles and the total angular misorientations may be derived in the following way. Let it be assumed that the particles are distributed about the mean position in the form of a Gaussian distribution. Then the probability of the occurrence of a particle at an angle θ from the mean position is proportional to $e^{-h^2\theta^2}d\theta$; similarly for a neighbouring particle to occur at an angle ϕ from the mean position, the probability is proportional to $e^{-h^2\phi^2}d\phi$. The probability for both particles to be simultaneously at angles θ and ϕ from the mean position is therefore $e^{-h^2(\theta^2+\phi^2)}d\theta \,.\, d\phi$; this represents the probability of the occurrence of an angle $|\theta - \phi|$ between the adjacent particles. Hence the mean value of the angle between particles for such a distribution may be written

$$\frac{\int_{-\infty}^{\infty}\int_{-\infty}^{\infty} |\theta - \phi| e^{-h^2(\theta^2+\phi^2)} d\theta \,.\, d\phi}{\int_{-\infty}^{\infty}\int_{-\infty}^{\infty} e^{-h^2(\theta^2+\phi^2)} d\theta \,.\, d\phi}$$

*It should be noted that if the incident X-ray beam does not overlap completely an original grain (e.g., when using a microbeam to examine specimens of coarse original grain size), T should be replaced by the dimensions of the beam diameter, since in these circumstances not all of the original grain is contributing to the diffraction pattern.

After reduction of this expression with the aid of standard forms, the remaining integral can be evaluated graphically. It is found that the mean angle between particles is

$$\alpha = 0.36\beta \doteqdot \beta/3$$

(In this treatment, the measured angular spread β of the particles in the original grain is identified with the half-width of the Gaussian distribution curve.) Thus

$$D_B = \beta/3st$$

In general α, and hence D_B, will lie between the two limits discussed above. By careful examination of the X-ray photographs it is possible in some cases to determine which of the two limiting assumptions about the distribution of the particles within the grains is more nearly correct. For example, in aluminium it is frequently observed that neighbouring diffraction spots are linked by a wavy continuous background [5]; thus neighbouring diffraction spots arise from reflexions from neighbouring regions of the grain, and so locally the metal has a structure approximating to that of the first assumption. In Table I, values of D_B are given for a number of different metals calculated from the same experimental data for both models; it is seen that the difference between the two values is not usually prohibitively large. Also included in this table are values of α and D_B which are derived as the geometric mean of the limiting values; this mean value may be considered to be accurate to within a factor of about two or three in most cases. The method yields the most consistent results when the original grain size (or the beam diameter) is small, since then the limiting values are close together.

The values of D_B obtained in this way are actually estimates of excess dislocations of one sign in the boundaries between the particles. After cold-work, the boundaries are found to be distorted, and cannot therefore be considered as single walls of dislocations; hence it is possible that, in addition, equal numbers of dislocations of the same type and of opposite sign together with other types of dislocations can coexist in the boundaries. The presence of such dislocations cannot be estimated by X-ray methods. From an examination of X-ray photographs taken some time after deformation, it is found, for aluminium and the softer metals, that the diffraction effects due to the distorted boundary regions gradually disappear: thus during recovery the dislocations rearrange themselves (to lower the strain energy), and dislocations of both signs (if any) annihilate each other leaving only the excess dislocations of one sign. After recovery of the metal, therefore, the boundaries are no longer distorted,

OL.
1
953

TABLE I

CALCULATION OF DISLOCATION DENSITIES FROM SPOTTY DIFFRACTION ARCS

Metal	Deformation (% of original thickness)	Particle size ($\times 10^{-4}$cm)	Original grain size ($\times 10^{-4}$cm)	Misorientation within original grain (β)	Values of α		Geometric mean of α	Density of excess dislocations of one sign in boundaries (lines/sq. cm.)		Mean value of excess dislocation density (lines/sq.cm.)	Maximum value of the total density of dislocations within particles (lines/sq. cm
					Model (i)	Model (ii)		Model (i)	Model (ii)		
Aluminium	57	2	20	15°	1.5°	5°	3°	4.5×10^9	2×10^{10}	9×10^9	6×10^9
Copper	7.3	2.8	24.6	2°	0.25°	0.66°	0.35°	6×10^8	1.5×10^9	8×10^8	8×10^8
Copper (foil)	heavily rolled (∼50%)	0.6	20	15°	0.5°	5°	1.5°	5.5×10^9	5.5×10^{10}	2×10^{10}	—
Gold (foil)	heavily beaten	0.2 (by electron diffraction)	10	24°	0.5°	8°	2°	1.5×10^{10}	2.5×10^{11}	6×10^{10}	—
Gold (foil)	heavily rolled (∼60%)	0.6 (by X-ray methods)	15 (beam diameter)	20°	0.8°	7°	2°	8×10^9	7×10^{10}	2×10^{10}	—
Iron	57	2	25.3	14°	1°	4.66°	2°	4×10^9	1.5×10^{10}	7×10^9	—
Lead	12	6	200 (beam diameter)	4.5°	0.14°	1.5°	0.5°	10^8	1.25×10^9	4×10^8	—
Nickel	6.6	2.8	21	3.5°	0.5°	1.2°	0.75°	10^9	3×10^9	1.5×10^9	8×10^8
Tin (tetragonal)	35	20	1000	31°	0.6°	10.33°	2.5°	3.5×10^8	6×10^9	1.5×10^9	—
Zinc	15	8	200 (beam diameter)	7°	0.3°	2.3°	1°	2.5×10^8	2×10^9	8×10^8	—

and it is likely that they are formed by single walls of edge or screw dislocations. During recovery the angles between the particles do not change appreciably [10], so that the estimates given in Table I are of the total density of dislocations in the boundaries after recovery has taken place.

In addition to the dislocations in the boundaries, it is possible that there are dislocations within the particles. The distinction between a particle and a boundary region lies in the fact that the curvature across a particle is less than that across a boundary; thus the density of excess dislocations of one sign must be lower in the particles than in the boundaries. If the curvature of the particle may be estimated, an upper limit of the excess density may be calculated [11]. Further, it is possible to estimate the maximum total density of dislocations inside the particles; the method employed is described in the next section.

(b) *Application to Continuous Diffraction Arcs*

When the diffraction arcs are unresolved, t cannot be determined unambiguously; usually limits may be assigned within which the particle size must lie [6]. As before it is convenient to discuss the two limiting models.

(i) When the grain is uniformly bent, the density of excess dislocations of one sign is again given by β/sT. Thus the excess density of dislocations may be determined without knowledge of t.

(ii) In the second case, α may be put equal to $\beta/3$ as before; now, however, two limits for the density are obtained, corresponding to the upper and lower limits of particle size. If the lower limit of t is obtained by ascribing the whole of the observed line broadening to a small-particle-size effect [4], the calculated values of dislocation densities from the two models are often widely different, and hence the actual density is uncertain. Results obtained by applying this treatment to back-reflexion photographs of copper and nickel are given in Table II. More recent results, using microbeam-transmission methods which enable a value of t to be found, have shown that the true excess density in copper is near to the lower limit (cf. Table I).

A special application of this method can be used to determine the total density of dislocations in particles. The upper limit of the total dislocation density may be found if it is assumed that there is a random distribution of dislocations within the particles; these dislocations are arranged to form subsidiary mosaics, each one of which is defined by a single dislocation. The dislocations are spaced at distance h apart. In the limiting case $\alpha = \beta/3$ as before, where β now corresponds to the angular spread of the reflexion from the particle due to the mosaic structure; estimates of β can therefore be obtained from the observed widths of the diffraction spots by methods described elsewhere [8]. As before $\alpha = s/h$, so that the upper limit of the total dislocation density is given by $1/h^2 = \beta^2/9s^2$. Some values of the maximum total density in the particles derived in this way are given in Table I. It is seen that the total density in the particles is, at the most, of the same order of magnitude as the density in the boundaries. It must be noted that values of β derived from spot-shape measurement are generally too large; it is possible that an appreciable contribution to the measured spot width is made by elastic distortion of the particles or their small size, in addition to the contribution due to plastic curvature.

TABLE II

CALCULATION OF DISLOCATION DENSITIES FROM CONTINUOUS DIFFRACTION ARCS FOR THE METALS COPPER AND NICKEL

	Copper	Nickel
Deformation (% of original thickness)	49	33
Misorientation within original grain (β)	15°	7.5°
Density of excess dislocations of one sign in boundaries (lines/sq. cm.)		
Model (i)	4×10^9	3×10^9
Model (ii)	10^{12}	5×10^{11}

A simple extension of these arguments may be applied to reflexions from annealed metals; some values of the dislocation densities obtained are given in Table III. Estimates of β were made by the measurement of the shapes of diffraction spots on microbeam back-reflexion photographs of annealed metals. A value obtained by using the data of Guinier and Tennevin [12] is also included in this table.

TABLE III

CALCULATIONS OF THE MAXIMUM VALUE OF DISLOCATION DENSITIES IN ANNEALED METALS

Metal	Range of misorientation within grain	Upper limit of dislocation density (lines/sq. cm.)
Aluminium	3′	3×10^8
Aluminium (Guinier & Tennevin)	30″	5×10^6
Copper	1′	2×10^7

3. Discussion

The results which have been obtained using these methods indicate that there are more dislocations in the boundaries than in the particles. In this work it has been assumed that the dislocations in the particles are randomly arranged; if a regular array of dislocations of the type described by Taylor [1] existed within the particles, these might not be detected by the X-ray methods employed. At present, the existence of such an array is thought to be physically unlikely, and it seems probable that the results of the present work are valid.

Further, it has been shown that the density of dislocations within a heavily worked metal is generally less than the usually accepted value of 10^{12} dislocation lines/sq.cm. It is possible that the discrepancy is due to the presence in the boundaries both of equal numbers of dislocations of the same type and of opposite signs, and of other types of dislocations. For example, according to the model of the cold-worked state proposed elsewhere [10], the boundaries between the particles are the slip bands. Each slip band contains a large number of screw and edge dislocations piled up against a barrier. The rotation of one particle relative to another is then due to the excess of screw dislocations, so that the density of dislocations calculated is that of the excess screw dislocations on the slip bands. In addition to these screw dislocations, there will be edge dislocations and possibly equal numbers of screw dislocations of either sign, which will cause distortion of the boundary and particles, but will not cause a rotation. At present no method of estimation of such a distribution has been found.

The validity of the theoretical evidence for the figure of 10^{12} lines/sq.cm. is somewhat uncertain. The most acceptable estimate is derived from measurements of the energy stored in the metal after cold-work, for which few results are available [13; 14]. More experimental measurements of the stored energy in pure metals are needed before a proper comparison of the results of the two methods may be made. An important point to be considered is that the dislocations are not uniformly distributed throughout the cold-worked metal. This result is not in agreement with an interpretation by Read and Shockley [15] of the results obtained by Warren and Averbach [16] on cold-worked α-brass. However, no exact comparison is possible because α-brass has not yet been examined by the microbeam method.

The present estimates of dislocation densities in annealed metals are also found to be less than the usually accepted value of 10^8 dislocation lines/sq.cm. In this case, however, there is no experimental evidence in support of this latter value, and the figure of 10^8 lines/sq.cm. seems to have arisen from the values of the size of the "mosaic" blocks introduced by Darwin to explain the intensity of X-ray reflexions from imperfect crystals. It must be made quite clear that the mosaic block model, employed by Darwin, was used only because it was the model which was most amenable to calculation. A decrease of extinction is, in fact, brought about by any distribution of imperfections. The imperfections in natural crystals may vary over a wide range; some crystals (e.g., calcite) behave almost as perfect crystals, and thus may not contain any dislocations. Relatively perfect metal crystals have also been found; the width of reflexion determined by Guinier and Tennevin [12] for an aluminium crystal leads to the conclusion that the density in annealed metals can, in fact, be very much less than 10^8 lines/sq.cm. (see Table III).

4. Acknowledgements

It is a pleasure to thank Sir Lawrence Bragg and Dr. W. H. Taylor, in whose laboratory this work was carried out, for their constant help and encouragement. The authors would like to record their gratitude to Professor A. H. Cottrell (Department of Metallurgy, University of Birmingham) for many helpful discussions. The work was carried out while two of the authors (P. G., A. K.) were in receipt of maintenance grants from the Department of Scientific and Industrial Research.

References

1. Taylor, G. I. Proc. Roy. Soc., **145** (1934) 362, 388.
2. Seitz, F. and Read, T. A. J. Appl. Phys., **12** (1941) 170.
3. Brown, W. F., Jr. Phys. Rev., **60** (1941) 139.
4. Wood, W. A. Proc. Roy. Soc., A **172** (1939) 231.
5. Hirsch, P. B. and Kellar, J. N. Acta Cryst., **5** (1952) 162.
6. Gay, P. and Kelly, A. Acta Cryst., **6** (1953) 165.
7. Gay, P. and Kelly, A. Acta Cryst., **6** (1953) 172.
8. Hirsch, P. B. Acta Cryst., **5** (1952) 168.
9. Burgers, J. M. Proc. Phys. Soc. Lond., **52** (1940) 23.
10. Gay, P., Hirsch, P. B., and Kelly, A. Submitted for publication in Acta Cryst.
11. Hirsch, P. B. Acta Cryst., **5** (1952) 172.
12. Guinier, A. and Tennevin, J. Comptes Rendus, **226** (1948) 1530.
13. Quinney, H. and Taylor, G. I. Proc. Roy. Soc., A **163** (1937) 157.
14. Welber, B. J. Appl. Phys., **23** (1952) 876.
15. Read, W. T. and Shockley, W. Imperfections in Nearly Perfect Crystals (New York, Wiley, 1952). Discussion of paper by Warren and Averbach.
16. Warren, B. E. and Averbach, B. L. Imperfections in Nearly Perfect Crystals (New York, Wiley, 1952).

NOTE ON THE FORMATION AND DEVELOPMENT OF CELLS IN POLYCRYSTALLINE ZINC*

R. C. GIFKINS and J. W. KELLY†

When zinc is deformed at elevated temperature, it has been found, using multiple-beam interferometry, that the cell sub-structure develops from surface curvatures. Simple undulations become saw-tooth facets and more complex curvatures become many-sided pyramids. Further deformation increases the tilt between the facets and often new curvatures and cells appear within those already present. There are also some special features associated with the grain boundaries. These results are discussed briefly in relation to current theories of the formation of sub-structures.

NOTE SUR LA FORMATION ET LE DÉVELOPPEMENT DE CELLULES DANS DU ZINC POLYCRISTALLIN

Quand on déforme du zinc à une température élevée, on constate, en employant un interféromètre à rayons multiples, que la sous-structure cellulaire se développe en partant des courbures de surface. Les ondulations simples deviennent des facettes à dents de scie et les courbures plus complexes deviennent des pyramides à faces multiples. Quand on continue la déformation, la rotation entre les facettes augmente et souvent de nouvelles courbures et cellules apparaissent au sein de celles, qui étaient déjà présentes. L'existence de certaines caractéristiques spéciales, liées aux joints intergranulaires, a aussi été constatée. Ces résultats sont discutés brièvement en relation avec les théories courantes sur la formation des sous-structures.

MITTEILUNG ÜBER DIE ENTSTEHUNG UND AUSBILDUNG VON ZELLEN IN POLYKRISTALLINEM ZINK

Es wurde mit Hilfe von Interferenz-Messungen mit einem "multiple-beam" Interferometer gefunden, dass sich eine Zell-Feinstruktur aus den Oberflächenkrümmungen am Zink bildet, wenn dieses bei höheren Temperaturen verformt wird. Einfache Wellen werden zu zackenartigen Fazetten, und kompliziertere Krümmungen werden zu vielflächigen Pyramiden. Weitere Verformung vergrössert die Neigung der Fazetten zueinander, und häufig erscheinen neue Krümmungen und Zellen in den bereits vorhandenen. Ausserdem findet man einige spezielle Erscheinungen, die auf Korngrenzen zurückgehen. Diese Ergebnisse werden kurz in ihrer Beziehung zu den gegenwärtigen Theorien über die Bildung von Feinstrukturen diskutiert.

The technique of multiple-beam interferometry has been used to study the formation and development of the cell sub-structure in polycrystalline zinc of high purity. Specimens were prepared and polished in the manner described by Ramsey [1] and deformed rapidly in tension at 240°C and at 0.25 per cent per hour at 200°C. The general observations of Ramsey [1] on the formation of angularly shaped cells were confirmed and extended by the interferometric observations, which are illustrated in Figures 1–13, taken on specimens deformed at 240°C. Except for Figure 7, the illustrations are in pairs taken at various strains; the first of each pair is a photomicrograph obtained using very oblique illumination and the second is the corresponding interferogram from the unsilvered zinc surface.

Formation of Pyramids of Cells

Figures 1–6 show an area at 1, 3, and 5 per cent extension and illustrate, in grain *A*, a typical manner of cell development to form a many-sided pyramid. There is also a tendency to form a pyramid in grain *B*. The evenly spaced, parallel and straight fringes from cells in Figure 6 denote a remarkable flatness of the facets formed. The amount of slip present in grains showing the pyramid formation was generally small.

Formation of Banded Cells

A simpler cell configuration was noted, either before straining or at low strains, in many grains in which slip was usually more marked. The presence of slip before deformation was presumably the result of thermal changes during polishing of the anisotropic material. Figure 7 is the interferogram of an area before straining, and Figures 8–13 are micrographs taken at extensions of 1, 5, and 10 per cent. In grain *C*, Figure 8, it can be seen that there is slight shadowing where cusps on the fringes in Figure 9 indicate a cell boundary *CD*. The major part of the rest of the grain has developed undulations transverse to the original slope shown in Figure 7; the curvature of these undulations is greatest along lines approximately parallel to *CD*. On further deformation the undulations straightened out into the saw-tooth alternations of slope seen in Figure 11 and the cells, clearly shadowed in Figure 10, have boundaries approximately at right angles to the slip traces. These results are very similar to those found by Ramsey [2] in studying sub-grain formation in closely packed deformation bands in

*Received January 14, 1953.
†Baillieu Laboratory, University of Melbourne, Australia.

A

1 B

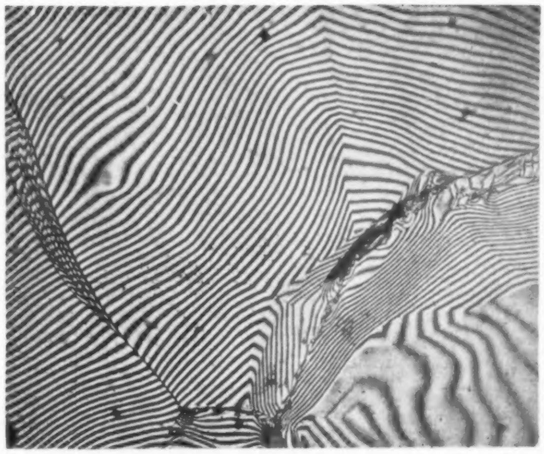

2

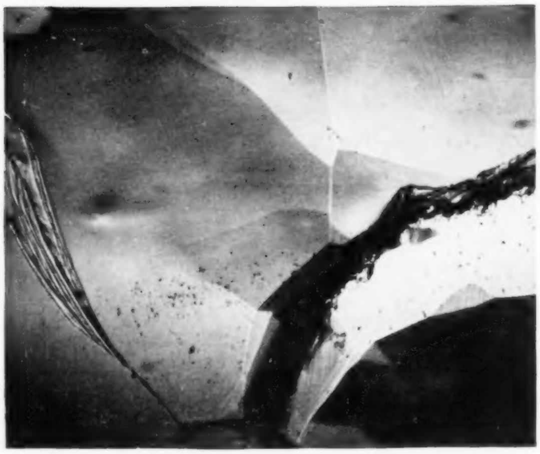

3

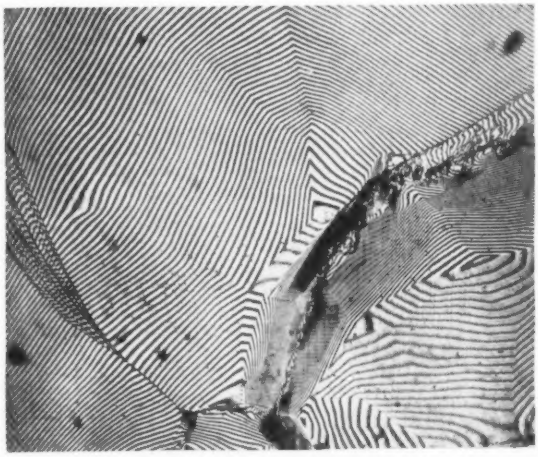

4

5

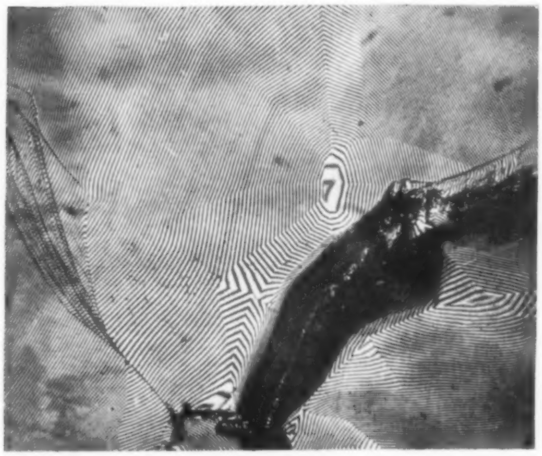

6

PLATE 1. Figures 1, 3, and 5—Cell structure at 1, 3, and 5 per cent respectively; very oblique illumination (80 ×). Figures 2, 4, and 6—Multiple-beam interferograms corresponding to Figs. 1, 3, and 5 (80 ×).

7

F

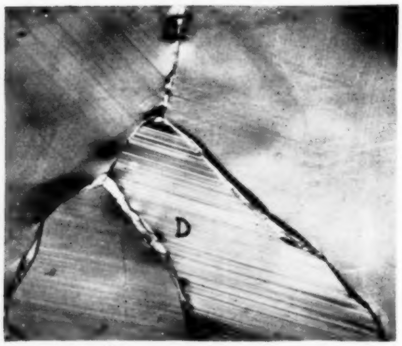

C 8 E

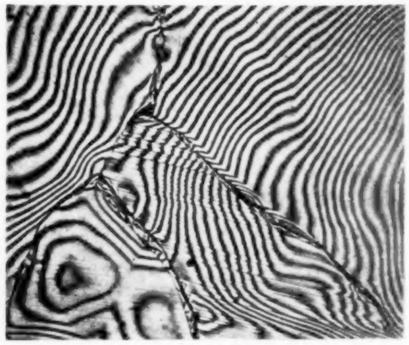

9

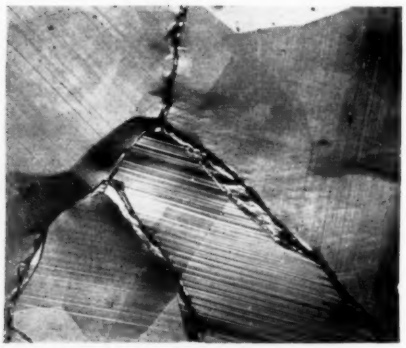

10

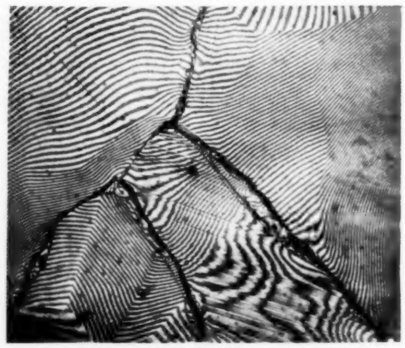

11

12

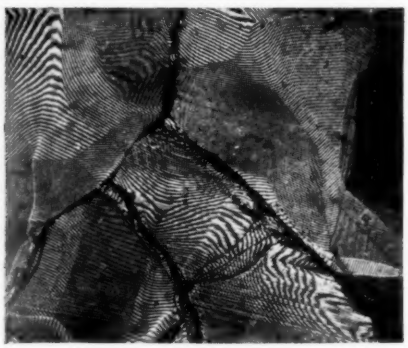

13

PLATE II. Figure 7—Interferogram from another area before tensile deformation (60 ×). Figures 8, 10, and 12—Area shown in Fig. 7; cell structure at 1, 5, and 10 per cent; very oblique illumination (60 ×). Figures 9, 11, and 13—Multiple beam interferograms corresponding to Figs. 8, 10, and 12 (60 ×).

aluminium. At a later stage, in Figures 12 and 13, the cells in the zinc tilted further and lost the symmetrical alternation of slope with the development of further facets; the curvatures from which the latter developed can just be discerned in Figure 11.

Cells having similar banded form and changes of slope to those in grain *C* were present in grain *E*, but here the curvature and facets are less obvious, because the fringes are approximately parallel to the cell boundaries; however, the process can be detected in the changes of fringe spacing.

It should be noted that cells can often be seen at an earlier stage with oblique illumination than with fringes. The present authors believe this to be due to a combination of shadowing of undulations and the optical paradox first discussed by Burch and Stock [3], whereby broad undulations give sharp diffraction lines and similar narrow features give broad diffraction lines, when focus is not quite sharp. On the other hand, fringe patterns accurately record changes in height and must be regarded as an unambiguous and sensitive method of detecting the formation of a boundary.

The Influence of Grain Boundaries on Cell Formation

It has been noted previously [1] that cells often form near grain boundaries at an early stage of deformation and that such cells are frequently long and narrow with their boundaries parallel to the grain boundary. Examples are shown in Figures 1–6 near the boundary between grains *A* and *B* and in grain *F*, Figures 8–13. The fringe patterns suggest that a curvature is introduced into the surface by "drag" during relative movement of grains, for the slope is greatest near to the boundary.

Figures 8–11 also show, in grains *C* and *E*, that cells in neighbouring grains may form in a related manner. Apparently, curved regions may comprise parts of more than one grain and only be modified slightly by the presence of a grain boundary.

It can also be seen that small areas of marked curvature or small cells are formed in the complex boundaries, such as that between grains *A* and *B* in Figures 3 and 4; the fringes show that migration traces, forming small steps, are also present. Other grain boundaries, such as that at the top of grain *A*, migrate to form a series of regular ridges and troughs.

Discussion

The results may be summarised as follows. At an early stage of deformation (< 1 per cent extension) the surface becomes curved, the curvature being greater in a few well-defined places. These regions are often close to grain boundaries. In some grains, usually those showing marked slip, regular undulations form.

As to whether the curvature is due to polygonisation followed later by recrystallisation *in situ* using these terms in the way first proposed by Lacombe [4], or by fragmentation followed by stress-recovery as suggested by Wood [5], the present results give no clear indication. The present authors suggest, however, that at the stage shown in grain *C*, Figures 8 and 9, the lattice may be in a state analogous to a brick arch, made of very small, irregularly sized bricks, with dislocations taking the place (though not the function) of the mortar. The curvature is greatest at the top of the arch; these suggestions are illustrated by a sketch in Figure 14 in which the

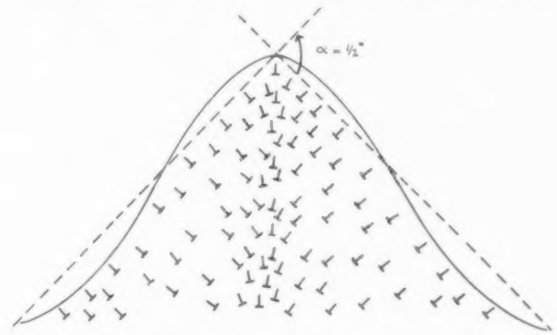

FIGURE 14. Schematic representation of undulation in zinc at stage shown in grain *C*, Figs. 8 and 9.

variation in dislocation density is indicated. It should be noted that the angle α, calculated from the fringes in Figure 8, is very small, being about $30'$.

On further deformation at elevated temperature the dislocations move to the apex of the arch to form cells by what has been termed "polygonisation under stress" [6]; the position of the cell boundary is therefore set by the curvature in the manner suggested by Ramsey [2] rather than by the mechanism originally postulated by Cahn [7]. Once the facets have formed, the increased tilt without major curvature can be attained by further movement of dislocations to the cell boundaries.

The formation of the pyramidal features appears to be the result of more complex curvatures which tend to produce shallow domes rather than ridges or troughs.

In aluminium it has been found that the process of cell formation and development is less easy to follow metallographically, especially at strains below

7–10 per cent. The present authors have found evidence of the formation of cells in bands of similar orientation at 300°C, thus extending the observations discussed by Rachinger [8]; it is hoped to publish this work shortly. It seems likely that the formation of cells from undulations in zinc represents a very simple case, because of both the simple curvatures and the simpler glide system.

Acknowledgements

The work reported in this note formed part of the joint programme of research of the Physical Metallurgy Section of the Commonwealth Scientific and Industrial Research Organization and the Metallurgy Research Department of the University of Melbourne, and was carried out at the Baillieu Laboratory under the general direction of Professor J. Neill Greenwood, whose advice and encouragement are gratefully acknowledged. The authors also wish to thank their colleagues for helpful discussions.

References

1. Ramsey, J. A. J. Inst. Metals, **80** (1951-52) 167.
2. Ramsey, J. A. J. Inst. Metals, **81** (1952-53) 61.
3. Burch, C. P. and Stock, J. P. P. J. Sc. Inst., **19** (1942) 71.
4. Lacombe, P. Private communication to R. W. Cahn; Progress in Metal Physics, **2** (1950) 156.
5. Wood, W. A. and Suiter, J. W. J. Inst. Metals, **80** (1951-52) 501.
6. Rachinger, W. A. J. Inst. Metals, **80** (1951-52) 415.
7. Cahn, R. W. J. Inst. Metals, **76** (1949) 121.
8. Rachinger, W. A. Bull. Inst. Metals, **1** (1952) 125.

KINEMATOGRAPHIE VON GLEITLINIEN AUF AL-EINKRISTALLEN*

R. BECKER und P. HAASEN†

Es werden kinematographische Beobachtungen des Wachsens von Gleitlinien auf Al-Einkristallen unter konstanter Last beschrieben. Bei einer Film-Aufnahmefrequenz von 50 Bildern pro sek gelingt es, das Entstehen lichtmikroskopisch sichtbarer Gleitlinien zeitlich aufzulösen.

Es wird beobachtet, wie die Gleitlinien im Laufe der Zeit sowohl in der Kristalloberfläche länger werden als auch stärker hervortreten: die Gleitstufen werden tiefer. Die maximale Geschwindigkeit des Längenwachstums in der Scheitelfläche wird zu etwa 10^{-2} mm/sek gemessen. Das Tiefenwachstum der Gleitlinien auf der Scheitelfläche wird photometrisch verfolgt. Dabei ergibt sich, dass es höchstens mit einer Geschwindigkeit derselben Grössenordnung verläuft. Die Helligkeit-Zeit-Kurve einer Linie hat stufenartigen Charakter. Benachbarte Gleitlinien entwickeln sich synchron.

Diese Ergebnisse werden im Versetzungsbild diskutiert. An Hand eines speziellen Modells lassen sich daraus die maximalen Versetzungsgeschwindigkeiten abschätzen. Diese erweisen sich als klein gegen die Schallgeschwindigkeit. Ausserdem laufen die Schraubenversetzungen danach wesentlich langsamer als die Stufenversetzungen.

Aus dem Modell und diesen Versetzungsgeschwindigkeiten werden die auf der Seitenfläche des Kristalls zu erwartenden Wachstumsgeschwindigkeiten angegeben und an Beobachtungen von Chen und Pond diskutiert.

CINEMATOGRAPHIC INVESTIGATIONS OF SLIP-LINES ON ALUMINIUM SINGLE CRYSTALS

Cinematographic observations of the growth of slip-lines on Al single crystals under constant load are reported. The film speed of 50 frames per second allows the resolution in time of the formation of visible (i.e. by means of a light-microscope) slip-lines.

The observations showed how with increasing time the length of the slip-lines in the crystal surface increases and how they also become more marked: the glide-steps become deeper. The maximum speed of the longitudinal growth in the top-surface was measured to approximately 10^{-2} mm/sec. The increase in depth of the slip-lines in the top-surface was measured photometrically and it was found that this phenomenon has a maximum speed equal to that of the longitudinal growth. The light-intensity vs. time curve of a slip-line has a step-like shape. Neighboring sliplines develop synchronously.

These results are discussed in terms of the dislocation theory. By means of a special model the maximum speeds of the dislocations can be estimated. They are small compared with the velocity of sound. Furthermore, this picture yields a much slower speed for the screw dislocations than for the edge dislocations. From this model and from the above-mentioned speeds of the dislocations the speed of propagation of slip-lines to be expected on the side faces of the crystal are deduced and discussed in connection with observations by Chen and Pond.

UNE ÉTUDE CINÉMATOGRAPHIQUE DES LIGNES DE GLISSEMENT SUR DES MONOCRISTAUX D'ALUMINIUM

Des observations cinématographiques de la croissance des lignes de glissement sur des monocristaux d'aluminium sous charge constante sont rapportées.

Avec une vitesse du film de 50 images par seconde, il est possible d'obtenir une résolution dans le temps de la croissance des lignes de glissement visibles au microscope optique. Il a été remarqué, qu'avec le temps, la longueur des lignes de glissement sur la surface du cristal augmentait et qu'elles devenaient plus prononcées: les gradins de glissement devenaient plus profonds. La vitesse maximum de la croissance longitudinale sur la surface supérieure était d'environ 10^{-2} mm/sec.

La croissance en profondeur des lignes de glissement sur la surface supérieure a été mesurée photométriquement, il fut ainsi trouvé, que ce phénomène se passe avec une vitesse, tout au plus, du même ordre de grandeur, que la vitesse de croissance longitudinale. En traçant l'intensité de la lumière en fonction du temps, pour une ligne de glissement, on obtient une courbe en gradins. Les lignes de glissement voisines se développent d'une façon synchrone.

Ces résultats sont discutés en termes de la théorie des dislocations.

Au moyen d'un modèle spécial, il est possible d'évaluer les vitesses maxima des dislocations. Elles sont faibles en comparaison avec la vitesse du son. En plus de cela, il apparaît, que les dislocations-vis se déplacent beaucoup plus lentement, que les dislocations-coins.

En partant de ce modèle et des vitesses des dislocations mentionnées ci-dessus, il est possible de déduire les vitesses probables de propagation des lignes de glissement sur les surfaces latérales des cristaux, ces résultats sont discutés en relation avec les observations de Chen et Pond.

Einleitung

Die Oberfläche eines Einkristalls ist nach hinreichender plastischer Verformung mit Gleitlinien bedeckt, die man lichtmikroskopisch oder gar mit blossem Auge feststellen kann. Man deutet diese Gleitlinien als Spuren betätigter kristallographischer Gleitebenen auf der Kristalloberfläche [1].

Einige Autoren stellen fest [2, 3], dass die Gleitlinien beim Anbringen einer (normalen) Last am Kristall im Rahmen der Messgenauigkeit "sofort" erscheinen. Mott [5] nimmt in seiner Theorie der Verfestigung an, dass die Ausbildung einer elemen-

*Eingegangen 5. Januar 1953.

†Institut für theoretische Physik der Universität, Göttingen, Germany.

taren Gleitstufe einige Mikrosekunden dauert. Crussard [6] hat in Versuchen bei kontinuierlicher, langsamer Steigerung der Last (konstante Dehngeschwindigkeit) ein Wachsen von Gleitlinien beobachtet (vgl. auch [7]). Auch unter *konstanter* Last stellt er qualitativ fest, dass Gleitlinien weiterwachsen. Das ist auch zu erwarten, da man aus genauen Messungen des Fliessens von Einkristallen (Dehnungs-Zeit-Kurven) [8] weiss, dass die plastische Dehnung nach Aufbringen einer Last noch über Stunden und Tage merklich fortschreitet.

Auch die Tatsache, dass die im gewöhnlichen Zugversuch gemessene Verfestigung für Verformungsgeschwindigkeiten $\dot{\epsilon} \approx 10^{-2} - 10^{-4}$ sek^{-1} erheblich von $\dot{\epsilon}$ abhängt, weist darauf hin, dass die Gleitgeschwindigkeit relativ klein ist.

Um die Geschwindigkeit des Gleitvorgangs zu ermitteln, ist in der im folgenden beschriebenen Untersuchung der zeitliche Ablauf der Entstehung einzelner Gleitlinien unter konstanter Last kinematographisch beobachtet worden (bei Raumtemperatur).

Chen und Pond [9] haben in neuester Zeit ähnliche Versuche bei kontinuierlicher Belastung gemacht. Wir werden auf diese Arbeit, die uns erst nach Abschluss unserer Versuche zugegangen ist, weiter unten näher eingehen.*

Mit dem Wort "Gleitlinie" ist im folgenden stets ein lichtmikroskopisch sichtbares Gleitband gemeint. Seit einigen Jahren weiss man aus elektronenmikroskopischen Untersuchungen [10; 11; 12], dass ein Gleitband in einzelne Gleitlamellen von etwa 200 ÅE Dicke unterteilt ist. Diese Lamellen sind um grössenordnungsmässig 1000 ÅE bei Al und Raumtemperatur† über ihre Nachbarn abgeglitten (Tiefe der elementaren Gleitstufe). Holden [3] hat mit dem Tolansky-Verfahren die Entstehung solcher Gleitstufen auf Al-Einkristallen beobachtet und bei "normaler Belastungsgeschwindigkeit" festgestellt, dass die ganze Gleitstufe "momentan" erscheint (vgl. oben). Bei "langsamer Verformung" beobachtet er ein Wachsen der Gleitstufen unter konstanter Last über eine Stunde, nachdem die erste Hälfte jeder Stufe "momentan", d.h. in den ersten Sekunden nach der Belastung entstanden ist.

Mit dem Lichtmikroskop wird man nur Gleitbänder wachsen sehen können, die schon aus mehreren Lamellen bestehen, d.h. man wird beobachten, wie die weiteren Gleitlamellen des Bandes hinzukommen. Mit Hilfe des Films ist dieser Vorgang zeitlich aufgelöst und zur weiteren Auswertung registriert worden.

*Dr. Chen und Dr. Pond haben uns freundlicherweise ihren 3.-5. Arbeitsbericht für das Office of Air Research vor der Veröffentlichung zur Verfügung gestellt.

†2000ÅE nach [10; 11], 400 ÅE nach [12].

Versuchsanordnung

Die technischen Vorbereitungen der Versuche umfassten: (A) die Herstellung von Einkristallen mit brauchbaren Oberflächen; (B) die Entwicklung eines geeigneten Zugapparates; (C) die Ermittlung der günstigsten optischen Anordnung und Film-Aufnahmefrequenzen.

A. Es wurden Einkristalldrähte aus 99,99 . . . Al durch Rekristallisation nach kritischer Dehnung hergestellt. Anfangs wurden 1, 5 mm dicke Kristalle mit geätzten Oberflächen verwendet, später solche von 4 mm Durchmesser, die nach dem Ätzen rein elektrolytisch poliert wurden (Bad: 2 Teile Methylalkohol auf 1 Teil conc. Salpetersäure). Die Kristalle wurden vorsichtig in 2-4 Stücke von je 5-7 cm Länge zerschnitten. Wir überzeugten uns durch Laue-Aufnahmen davon, dass der Asterismus bereits 5-10 mm von der Schnittstelle entfernt vollständig verschwunden war. Die Orientierung der Drahtachsen im Kristallgitter wurde durch Drehaufnahmen ermittelt und ist in Abb. 1 für die untersuchten Kristalle in der üblichen stereographischen Projektion angegeben. Wir hatten also von jeder Orientierung mehrere Proben zu Vergleichs-Versuchen zur Verfügung. Eine Probe wurde dazu benutzt, um in einem Vorversuch die gewünschte Beobachtungsrichtung relativ zur Gleitrichtung festzulegen.

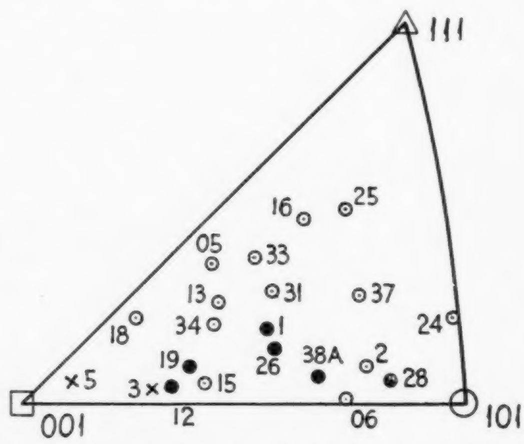

Abb. 1. Orientierung der Drahtachsen der Kristalle: ∘ 4 mmϕ; • 4 mmϕ, ausgewertet; × 2 mmϕ.

B. Den Zugapparat zeigt Abb. 2. Der Kristall wurde beidseitig belastet, damit im Verlauf der Dehnung die beobachtete Stelle in der Mitte des Kristalls nicht aus dem Bildfeld wanderte. Zur

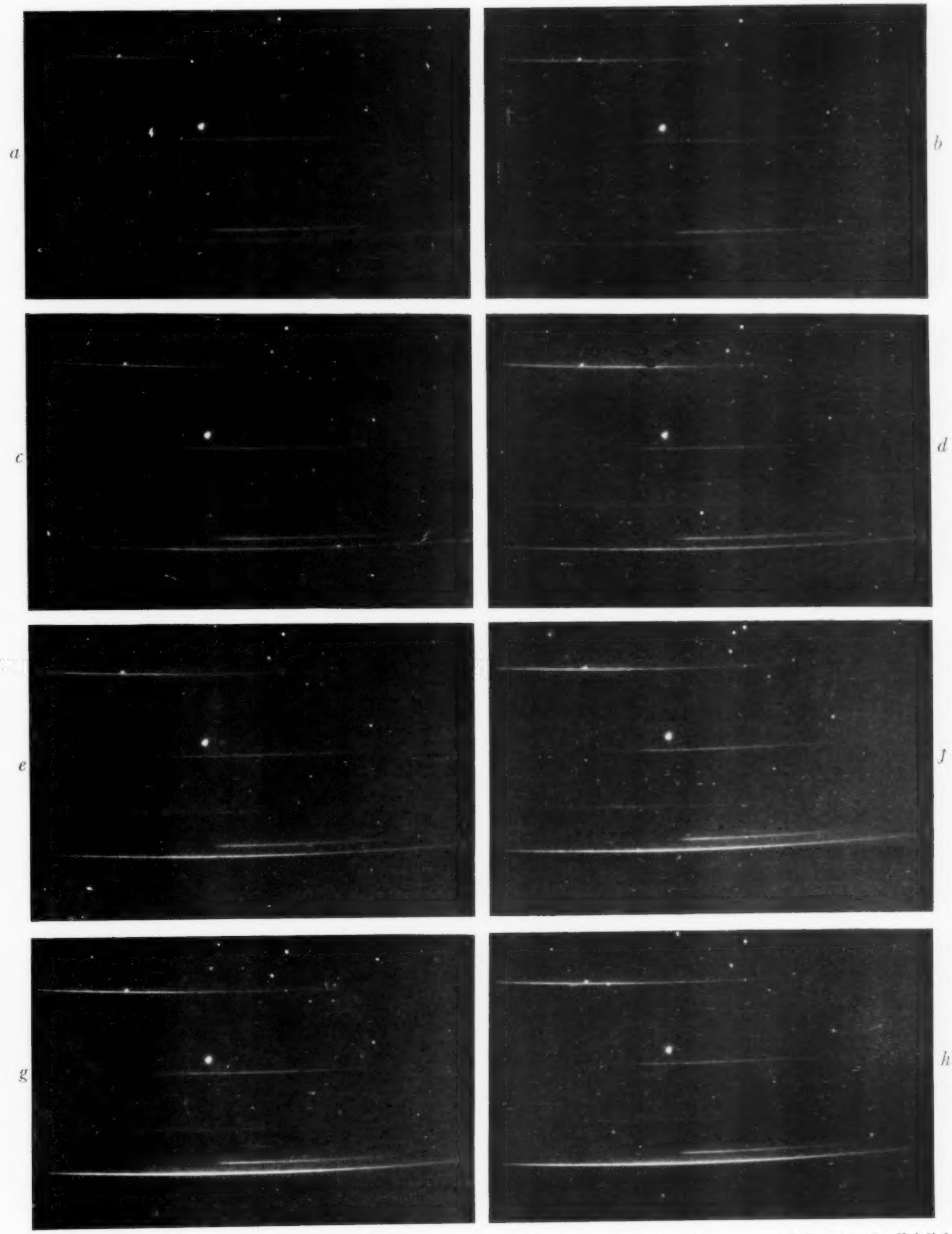

ABB. 3. Bildfolge aus einem Zeitdehnerfilm; Kristall Nr. 19a. Konstante Schubspannung 360 g/mm². Zeitlicher Abstand der Bilder 1/10 sek. Vergrösserung 440 × (Bildhöhe ≈ 0, 2 mm). Ausschnitt $\frac{1}{4}$ des Filmbildes.

Belastung wurden Gewichte von Hand (an Fäden) auf eine Waagschale gesetzt, die durch ein Ölbad gedämpft war. Ein Stahldraht (ϕ 0, 5 mm), der über Kugellager lief, übertrug die Spannung auf die Kristallfassungen (aus Al). In diese war der Kristall mit Schellack eingekittet.

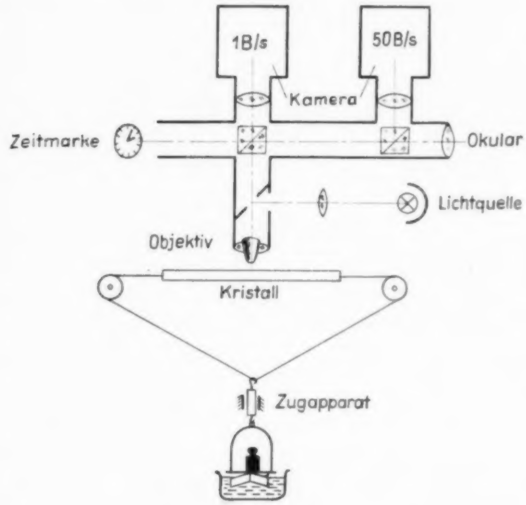

ABB. 2. Versuchsanordnung.

Die Dehnung wurde mit Hilfe eines besonderen Messmikroskops ermittelt, das mit einem Mikrometertrieb am Kristall entlang bewegt werden konnte. Dazu waren auf dem Mittelteil des Kristalls zwei Marken in etwa 1, 5 cm Entfernung angebracht.

C. Die optische Anordung und die Film-Aufnahmeapparatur sind ebenfalls in Abb. 2 skizziert. Das Beobachtungs-Mikroskop (22fache oder 44fache Vergrösserung auf dem Film) befand sich über der Mitte des Kristalls. Eine Hg-Höchstdrucklampe erzeugte mittels Ringspiegel im Tubus und Leitz-Ultropak-Objektiv eine allseitige Dunkelfeldbeleuchtung (helle Gleitlinien auf dunkler Kristalloberfläche). Die von allen Seiten streifend einfallende Beleuchtung hatte sich in Vorversuchen als besser geeignet erwiesen als die übliche einseitige Dunkelfeldbeleuchtung, bei der die Sichtbarkeit der Linien von ihrer Lage zur einfallenden Strahlung abhängt.

Bereits nach den ersten Versuchen erwies es sich als zweckmässig, mit zwei Film-Aufnahmefrequenzen zu arbeiten, um sowohl das schnelle erste Entstehen der Gleitlinien unmittelbar nach der Belastung (50 Bilder/sek) wie auch ihr langsames Nachwachsen (1 Bild/sek) zu erfassen. Ein Prisma verteilte das vom Objektiv kommende Licht im Verhältnis 1: 50 auf die beiden Kameras. Es wurde 16 mm-Gevaert-Positiv-Schmalfilm verwendet.

Versuchsdurchführung und unmittelbare Ergebnisse

Es wurden etwa 30 Kristalle gedehnt und gefilmt. Bei den meisten wurde die Schubspannung in 15-20 Stufen um jeweils etwa 45 g/mm² (kritische Schubspannung ≈ 100 g/mm²) in Abständen von ca. 1 min erhöht. Die Enddehnung betrug 5-10 Prozent je nach der Orientierung des Kristalls.

Nach dem Erscheinen der ersten Gleitlinien wurde die Zeitrafferkamera (1 B/sek) eingeschaltet und lief während des ganzen Versuchs. Die Zeitdehnerkamera (50 B/sek) wurde unmittelbar vor jedem Belastungsschritt für die Dauer von jeweils 5 sek in Betrieb genommen.

Die zeitliche Auflösung reichte gerade aus, um die Entwickling der Gleitlinien verfolgen zu können. Ein Beispiel aus einem Zeitdehnerfilm zeigt Abb. 3.

Bei unseren Beobachtungen liegt die Bildebene etwa tangential zu den Schéiteln der Gleitellipsen ("Scheitelfläche"), d.h. den Stellen auf dem Umfang des Kristalldrahtes, die nach der einfachen Vorstellung [1] eine maximale Tiefe der Gleitstufen zeigen sollen.

Man erkennt, dass die Helligkeit der entstehenden Linie nicht gleichmässig mit der Zeit zunimmt. Um den zeitlichen Verlauf der Linienentwicklung genauer zu bestimmen, wurde deshalb die Helligkeit einer Linie von Bild zu Bild photometrisch verfolgt. Ergebnisse solcher Messungen werden im folgenden diskutiert.

Auch im Zeitrafferfilm sind Gleitlinien-Entwicklungen sichtbar (Photometerkurve Abb. 7). Ausserdem ermöglicht dieser Film dank der eingeblendeten Zeitmarke die eindeutige Zuordnung der Belastung zu einzelnen Abschnitten des Zeitdehnerfilms.

Neben dem photometrisch vermessenen Tiefenwachstum der Gleitstufen wurde auch ein Längenwachstum von Gleitlinien beobachtet und ausgemessen.

Auswertung der Filme

1. *Tiefenwachstum*

Zur photometrischen Ausmessung der Helligkeit einer Linie wird das entsprechende Filmbild vergrössert auf einen Schirm projiziert. Dieser Schirm besitzt einen drehbaren und verschiebbaren Spalt, der etwas breiter als das Bild der voll entwickelten Linie ist und fünf mal so lang wie breit. Ein Ausschnitt des Linienbildes wird auf den Spalt gelegt und beleuchtet die dahinter befestigte Selen-Photozelle. Deren Strom wird mit einem Spiegel-Galvanometer gemessen. Um Beleuchtungsschwankungen bei der

Aufnahme des Films auszugleichen, ist die Linienhelligkeit Bild für Bild auf die Helligkeit einer bestimmten Oberflächenrauhigkeit (Staubkorn) bezogen worden.

Damit erhält man für die auf Abb. 3 entstehende Linie die in Abb. 4 gezeigte Helligkeit-Zeit-Kurve. Man erkennt, dass sich die Linie stufenartig entwickelt.

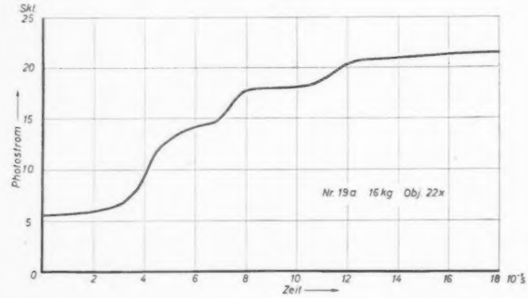

Abb. 4. Helligkeit-Zeit-Kurve einer Gleitlinie; Kristall Nr. 19a, Schubspannung 360 g/mm², Vergrösserung auf dem Film V = 44 ×; vgl. Abb. 3.

Dass die Linienentwicklung wirklich in zum Teil ganz groben Stufen erfolgt, zeigen Abb. 5 und Abb. 6, die auch die Streuung der Messpunkte erkennen lassen.

Abb. 7 zeigt das langsame Entstehen einer Gleitlinie bei Zeitraffung.

Die Linie beginnt erst ungefähr 20 sek nach der letzten Belastung zu wachsen. Auf diesen Zeitpunkt ist der Anfang der Zeitachse gelegt worden. Am Ende der Kurve wird weiter belastet.

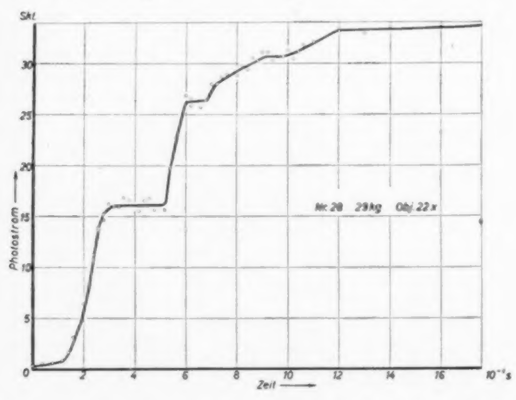

Abb. 5. Helligkeit-Zeit-Kurve einer Gleitlinie; Kristall Nr. 28, Schubspannung 650 g/mm², V = 44 ×.

Bei manchen Belastungsschritten entstehen mehrere Linien im Bildfeld. Abb. 8 und Abb. 9 demonstrieren, dass die zeitliche Entwicklung weitgehend synchron verläuft. Die obersten Photometerkurven (Nr. 1) beider Diagramme, die relativ steile und hohe Stufen haben, gehören zu Gleitlinien, die dicht neben bereits früher entstandenen Gleitlinien liegen: Abstand ≈ 5μ. ("Doppellinien"). Diese selbst wachsen bei diesem Belastungsschritt nicht weiter.

Bei Kristall Nr. 38 Aa (Abb. 10) ist eine Linie, die vom Rande in das Bild hineinwächst, an zwei Stellen im Abstand von ≈ 10μ photometriert worden. Man erkennt, dass ähnliche Stufen bei beiden

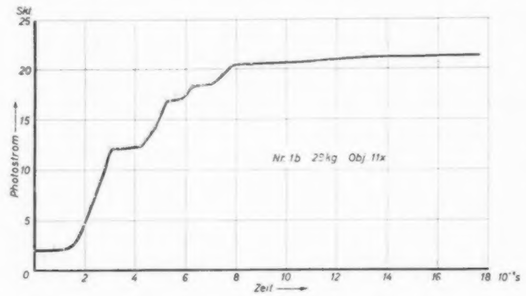

Abb. 6. Helligkeit-Zeit-Kurve einer Gleitlinie; Kristall Nr. 1b, Schubspannung 650 g/mm², V = 22 ×.

Messstellen mit einer bestimmten zeitlichen Verzögerung gegeneinander auftreten. Diese entspricht einer Längenwachstumsgeschwindigkeit der Gleitlinien auf der Kristalloberfläche von etwa 10^{-1} mm/sek. An anderen Stellen ist diese Geschwindigkeit auch direkt gemessen worden (s. folgender Abschnitt).

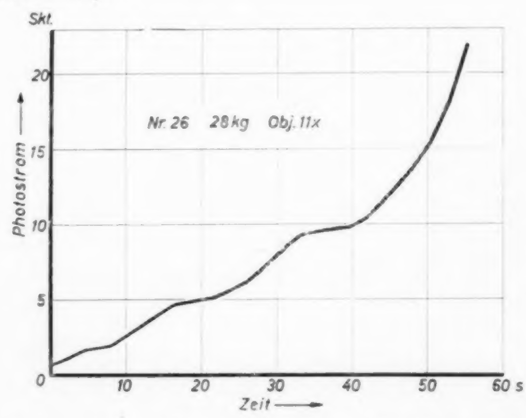

Abb. 7. Helligkeit-Zeit-Kurve einer Gleitlinie; Kristall Nr. 26, Schubspannung 630 g/mm², V = 22 ×. Beobachtungszeit etwa eine Minute.

Mit wachsender Verfestigung (Vorlast) scheint die Geschwindigkeit des Tiefenwachstums abzunehmen: vgl. dazu Abb. 8 mit Abb. 9. Der Kurventyp Nr. 3 auf Abb. 9 wird vorherrschend.

Chen und Pond [9] stellen ebenfalls fest, dass zunehmende Verfestigung die Linienentwicklung verlangsamt.

Versuche mit verschieden grossen Belastungsschritten (90 g/mm² in Abb. 11 gegenüber 25 g/mm² in Abb. 6) in gleichem zeitlichen Abstand (1 min) ergeben steilere Stufen bei der höheren Belastung. Wird hingegen die normale Belastung von 45 g/mm² alle 10 sek statt alle 60 sek aufgebracht, dann

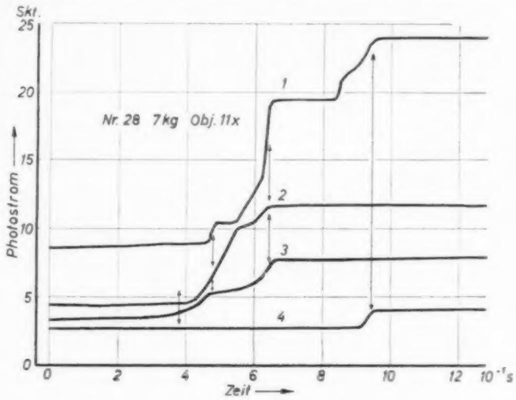

Abb. 8a

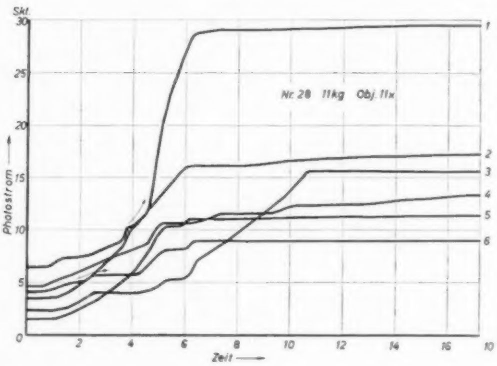

Abb. 9a

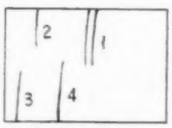

Abb. 8b

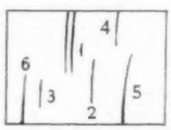

Abb. 9b

Abb. 8 u. 9. Helligkeit-Zeit-Kurven benachbarter Gleitlinien (dazu Lageskizzen). Kristall Nr. 28, Schubspannung 160 u. 250 g/mm², V = 22 ×.

wachsen die Gleitlinien sehr langsam in kleinen Stufen (Abb. 12 zu vergleichen mit Abb. 10).

Es muss jedoch betont werden, dass die drei letztgenannten Aussagen wegen der geringen Zahl von Messungen nicht sehr zuverlässig sind.

2. *Längenwachstum*

Auf manchen Filmen beobachtet man, dass sich Gleitlinien, die bei geringer Dehnung meist nur als kurze Stücke zu sehen sind, in ihrer eigenen Richtung verlängern. Indem man die Verschiebung einer Stelle von geringer Helligkeit der Linie von Bild zu Bild ausmisst, kann man dieses Längenwachstum unmittelbar verfolgen.

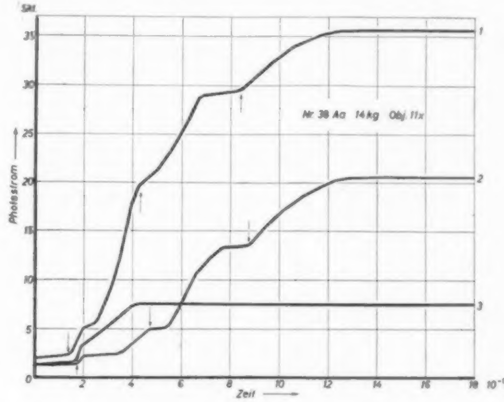

Abb. 10a

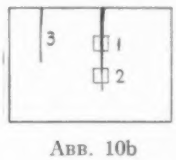

Abb. 10b

Abb. 10. Helligkeit-Zeit-Kurven benachbarter Gleitlinien. Eine Linie ist an zwei Stellen photometriert worden (vgl. dazu Lageskizze). Kristall Nr. 38 Aa, Schubspannung 315 g/mm², V = 22 ×.

Abb. 13 zeigt im Diagramm die Verlängerung von Gleitlinien über der Zeit und Tabelle I die daraus berechnete maximale Längenwachstumsgeschwindigkeit für verschiedene Linien.

TABELLE I

Kristall Nr.	Schubspanng. g/mm²	maximale Geschwindigkeit in 10^{-2} mm/sek
26	450	0, 19
19a	590	7, 3 und 9, 3
19b	610	2, 5
38Aa	315	7, 0
38Aa	540	2, 3 und 4, 5
38Aa	770	2, 9
12	700	0, 49
12	650	14
5	1100	11

Die maximale Geschwindigkeit des Längenwachstums v_L beträgt also $10^{-1} - 10^{-2}$ mm/sek. Diese Messungen sind allerdings weniger genau als die oben beschriebenen des Tiefenwachstums und gestatten kaum Einzelheiten im zeitlichen Verlauf des Längenwachstums zu erkennen ausser der, dass die Geschwindigkeit im Laufe dieser Linienentwicklung abnimmt.

Chen und Pond beschreiben in der genannten Arbeit [9] im wesentlichen ebenfalls kinemato-

graphische Beobachtungen des Längenwachstums von Gleitlinien. Sie belasten Al-Einkristalle kontinuierlich mit konstanter Geschwindigkeit. Diese Autoren finden auf der Scheitelfläche Geschwindigkeiten v_L zwischen $7,6$ mm/sek und Null. Der Unterschied zu unseren Messungen kann durch die Art der Belastung und Oberflächenbehandlung bedingt sein*.

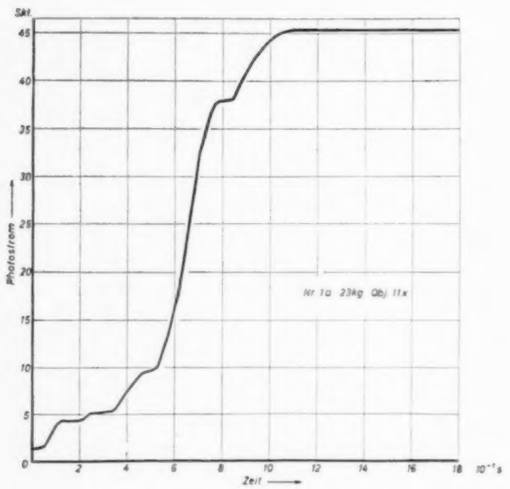

Abb. 11. Helligkeit-Zeit-Kurve einer Gleitlinie; Kristall Nr. 1a, Schubspannung 520 g/mm², V = 22 ×.

Diskussion

Für quantitative Aussagen über das Tiefenwachstum der Gleitlinien benötigen wir die Beziehung zwischen Photometerstrom und Tiefe einer Gleitstufe. Diese ist experimentell schwer zu erfassen. Wir erwarten in grober Näherung Proportionalität zwischen der Intensität einer Linie und ihrer Tiefe, d.h. zwischen Photostrom und Stufentiefe. Ausserdem schätzen wir die mittlere Tiefe der vollentwickelten Gleitstufen folgendermassen ab: Bei der in unseren Versuchen erreichten Enddehnung von $\epsilon = 10$ Prozent haben die Gleitlinien einen mittleren Abstand von $d = 10\mu$, d.h. die Gleitstufen haben eine mittlere Tiefe von etwa $s = \epsilon \,.\, d = 1\mu$. Dieses Ergebnis erscheint vernünftig, denn kleiner als

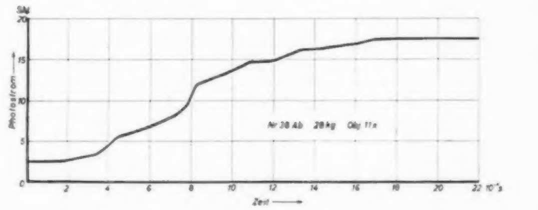

Abb. 12. Helligkeit-Zeit-Kurve einer Gleitlinie; Kristall Nr. 38 Ab, Schubspannung 630 g/mm², V = 22 ×.

$0,1\mu$ kann s bei lichtmikroskopisch sichtbaren Stufen nicht sein, während Crussard [6] als oberen Grenzwert bei Al-Einkristallen mit ähnlicher Dehnung $s \approx 3\mu$ angibt.

Aus unseren Photometerkurven ersehen wir, dass sich derartige Gleitstufen in Zeiten entwickeln, die grösser als 2/50 sek sind (der Belastungsvorgang dauert sicher weniger lange. Ausserdem beginnen manche Linien erst beträchtliche Zeit nach der Belastung zu wachsen.)

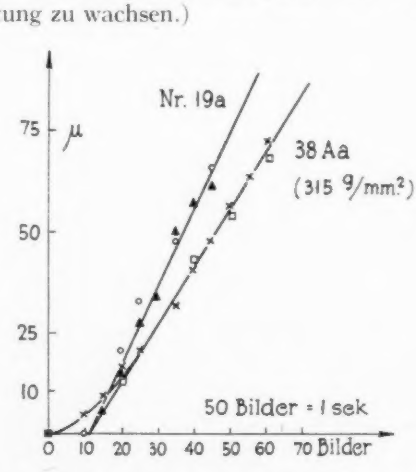

Abb. 13. Verlängerung von Gleitlinien als Funktion der Zeit.

Aus maximaler Gleitstufentiefe und minimaler Entwicklungszeit folgt als maximale Geschwindigkeit des Tiefenwachstums $v_T = 2,5 \,.\, 10^{-2}$ mm/sek. Eine untere Grenze für diese Geschwindigkeit existiert offensichtlich nicht.

Die grössten Tiefenwachstumsgeschwindigkeiten v_T ergeben sich somit als von derselben Grössenord-

*Chen und Pond untersuchen aus der Schmelze hergestellte 99,997-Al-Einkristalle, die einen um den Faktor 7 grösseren Querschnitt als unsere Rekristallisationseinkristalle haben. Sie polieren ihre Kristalle zuerst mechanisch, dann (nach einer Ätzung) elektrolytisch nach derselben Methode wie wir. Brown und Honeycombe [13] haben auf die Unterschiede im Gleitlinienbild aufmerksam gemacht, die bei kleinen Dehnungen zwischen rein elektrolytisch polierten Kristallen einerseits und mechanisch vorpolierten und elektrolytisch nachpolierten Kristallen andererseits bestehen. Im wesentlichen bewirkt die mechanische Vorpolitur die Bildung von gröberen Gleitlinien im Anfangsstadium, die natürlich leichter sichtbar sind. Brown [4] nimmt ausserdem an, dass das Verhältnis von in der Tiefe wachsenden Gleitlinien zu in der Länge wachsenden bei den rein electrolytisch polierten Kristallen grösser ist als bei den mechanisch vorpolierten. Wir haben allerdings aus weiter unten erwähnten Gründen nur Linien mit relativ grosser Verlängerung ausgemessen.

Die Bildfrequenz bei Chen und Pond beträgt 32/sek statt 50/sek bei uns. Wenn man unsere stufenweise Belastung überhaupt mit der kontinuierlichen von Chen und Pond vergleichen darf, ist die mittlere Belastungsgeschwindigkeit (und Dehnungsgeschwindigkeit) dort um einen Faktor 30 grösser als bei uns.

nung wie die maximal gemessene Längenwachstumsgeschwindigkeit v_L, nämlich zu 10^{-2} mm/sek.

Was bedeuten diese gemessenen Geschwindigkeiten im Versetzungsbild? Bei näherer Betrachtung wird sich herausstellen, dass sie nicht ohne weiteres mit Versetzungsgeschwindigkeiten identifiziert werden dürfen [14]. Wir diskutieren im folgenden einige mögliche Verknüpfungen:

1. *Auf der Scheitelfläche*

(*a*) Das *Tiefenwachstum* der Gleitlinien wird dort durch Stufenversetzungen verursacht, die aus der Oberfläche treten. Diese Versetzungen kommen von den der Oberfläche nächstgelegenen Frank-Read-Quellen. Wir nehmen an, dass die Versetzungen in dem zeitlichen Abstand durch die Oberfläche gehen können, in dem sie dort ankommen (das ist keine selbstverständliche Voraussetzung, aber die einzige, die Rückschlüsse auf die Vorgänge im Kristallinneren gestattet). Dann gibt es zwei Möglichkeiten zur Deutung des Tiefenwachstums, je nachdem, ob die Erzeugung oder die Abwanderung der Versetzungen von der Quelle die Gleitgeschwindigkeit bestimmt. Nimmt man zunächst letzteres an, dann bietet sich an der Oberfläche des Kristalls das in Abb. 14 gezeigte Bild.

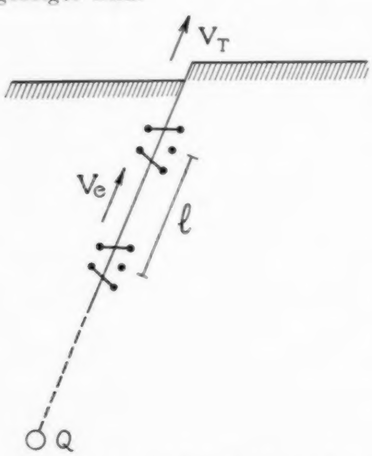

ABB. 14. Versetzungsmodell des Tiefenwachstums auf der Scheitelfläche.

Es laufen Stufenversetzungen im Abstand l mit der Geschwindigkeit v_e von der Quelle Q auf die Oberfläche zu. Jede austretende Versetzung vergrössert die Gleitstufe um b (Betrag des Burgersvektors). Dann ist die Geschwindigkeit des Tiefenwachstums

$$v_T = b \cdot \frac{v_e}{l}.$$

Man erhält somit den grösstmöglichen Wert für v_e, wenn man die maximal gemessene Tiefenwachstumsgeschwindigkeit $v_T = 100^{-1}$ mm/sek mit der grössten freien Weglänge im Kristall $l = 10^4\ b$ (Mosaikblockdurchmesser) multipliziert, zu $v_e =$ 100 mm/sek., d.h. $10^{-4}\cdot$ Schallgeschwindigkeit in Al.

Zum anderen möglichen Fall, bei dem die Abwanderung der Versetzungen von der Quelle schneller als ihre Erzeugung vor sich geht, gelangt man, wenn man sich die in Abb. 14 skizzierte Gleitebene auf der von der Oberfläche abgewandten Seite der Quelle bis zum nächsten Hindernis ergänzt. Dann werden die vor diesem Hindernis sich aufstauenden Versetzungen aus Q schliesslich die an der Quelle wirkende Schubspannung soweit erniedrigen, dass weitere Versetzungen die Quelle nur noch unter Mithilfe thermischer Schubspannungen verlassen können. Erzeugt die Quelle auf diese Weise ν Versetzungen pro sek, dann ist $v_T = \nu_{max} \cdot b$ unter der Voraussetzung, dass $v_e \gg \nu \cdot b$ ist. Man erhält $\nu_{max} = 10^5$ pro sek, aber keine weitere Aussage über die Versetzungsgeschwindigkeit.

(*b*) Das *Längenwachstum* von Gleitlinien auf der Scheitelfläche sollte nach der einfachsten Vorstellung durch Bewegung von Schraubenversetzungen entlang der Oberfläche zustandekommen. Doch kann auch ein successives Austreten von nebeneinander liegenden Stufenversetzungsteilen in die Oberfläche eine Verlängerung der Gleitlinien bewirken. Wir diskutieren beide Fälle wieder in dem Modell (Abb. 15) der durch Quellen und Hindernisse unterteilten Gleitebene:

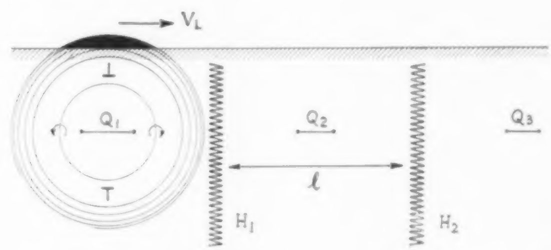

ABB. 15. Versetzungsmodell des Längenwachstums auf der Scheitelfläche.

Zunächst erzeuge eine Quelle Q_1 Versetzungsringe, die bis zur Oberfläche und zum Hindernis H_1 laufen. Man erkennt, dass dabei nicht nur die Tiefe, sondern auch die Länge der entstehenden Gleitstufe wächst. Diese Art von "Längenwachstum" kann sicher nicht die beobachteten Linienverlängerungen von einigen 10^{-1} mm ($l \approx 10^{-3}$ mm vgl. oben) erklären. Dazu braucht man mehrere Quellen $Q_1, Q_2, Q_3 \ldots$ Die vor dem Hindernis H_1 sich aufstauenden Schraubenversetzungen von Q_1

erhöhen die wirksame Schubspannung am Ort von Q_2 so, dass diese Quelle ihrerseits Versetzungen erzeugt, die nach H_2 laufen usw. Die Geschwindigkeit der Verlängerung der so entstehenden Gleitlinie v_L wäre dabei durch die Geschwindigkeit v_s von Schraubenversetzungen im Kristallinneren bestimmt.

Wir erhalten somit aus unseren Messungen grössenordnungsmässig $v_s \approx 10^{-2}$ mm/sek, also eine Schraubenversetzungsgeschwindigkeit, die etwa $l/b \leqslant 10^4$ mal kleiner ist als die Geschwindigkeit der Stufenversetzungen v_e. Diese Folgerung aus unseren Experimenten, dass die Schraubenversetzungen nur sehr viel langsamer als die Stufenversetzungen laufen können, entspricht durchaus den theoretischen Vorstellungen [5], nach denen die Bewegung von Schraubenversetzungen durch Erzeugung von Löchern wesentlich behindert wird.

2. *Auf der "Seitenfläche"*

Auf der "Seitenfläche", d.h. auf einer zur Scheitelfläche nahezu senkrechten Kristalloberfläche (die also die Gleitrichtung fast enthält), erwarten wir ähnliche Verhältnisse, nur sind dort die Rollen von Stufen- und Schraubenversetzungen vertauscht. Die Gleitrichtung muss noch eine Komponente senkrecht zur Beobachtungsfläche haben, damit man überhaupt Gleitlinien sehen kann. Wir stellen in der folgenden Tabelle II die nach dem obigen Modell dort zu erwartenden maximalen Geschwindigkeiten des Längen- und Tiefenwachstums denen auf der Scheitelfläche gegenüber, aus denen wir oben die maximale Geschwindigkeit der Stufenversetzungen zu $v_e = l/b \cdot 10^{-2}$ mm/sek und die der Schraubenversetzungen zu $v_s = 10^{-2}$ mm/sek bestimmt haben.

TABELLE II

Maximale Geschwindigkeit	*Auf der Scheitelfläche*	*Auf der Seitenfläche*
des Tiefenwachstums	$(b/l)v_e$	$(b/l)\ v_s$
des Längenwachstums	v_s	v_e

Wir erwarten also, dass das Tiefenwachstum auf der Scheitelfläche wesentlich schneller als auf der Seitenfläche vor sich geht, während es beim Längenwachstum umgekehrt sein sollte.

Chen und Pond [9] beobachten, dass die Gleitlinien auf der Seitenfläche des Kristalls stets in ganzer Länge erscheinen. Sie interpretieren dieses Ergebnis im Versetzungsbild dadurch, dass sie als Geschwindigkeit der Stufenversetzungen Schallgeschwindigkeit annehmen. Nach der obigen Diskussion erscheint uns das nicht möglich, zumal die Autoren selbst qualitativ ein Tiefenwachstum von Gleitlinien auf der Scheitelfläche bemerken. Wir möchten in ihrem Resultat eine Bestätigung des obigen Schlusses sehen, dass die Stufenversetzungen schneller als die Schraubenversetzungen laufen. Die Geschwindigkeit v_e ist zwar klein gegen die Schallgeschwindigkeit, aber zu gross, als dass das Längenwachstum auf der Seitenfläche bei dieser Filmfrequenz zeitlich aufgelöst werden könnte.

Aus der Fig. 11 der genannten Arbeit [9] scheint hervorzugehen, dass das Tiefenwachstum auf der Seitenfläche vergleichsweise langsam verläuft*.

Zur Deutung der *Stufenstruktur* der "Abgleitung"-Zeit-Kurve einer Linie ist man versucht, das elektronenmikroskopische Resultat heranzuziehen, dass ein Gleitband durch Addition von Elementarstufen von jeweils 1000-2000 ÅE Tiefe wächst. Bei den von uns erreichten Dehnungen werden etwa 5-10 Gleitlamellen pro Band bei Al beobachtet. Danach möchte man eine Stufe in unserer Photometerkurve der Entstehung einer weiteren Lamelle des Gleitbandes zuordnen. Auch bei genauen Messungen des Fliessens von Einkristallen werden zuweilen derartige Stufen oder Wellen beobachtet [8]. In den Fliesskurven überlagert sich sonst das Wachsen vieler Gleitbänder auf der ganzen Messlänge des Kristalls.

Aus diesen Fliesskurven ist auch geläufig, dass die Abgleitung manchmal nicht sofort nach der Belastung einsetzt, sondern erst mit u.U. beträchtlicher zeitlicher *Verzögerung* ("Anfangsknick"). Dies ist z.B. auch auf Abb. 7 und beim Vergleich der Kurven auf Abb. 8 zu erkennen. Diese Verzögerung könnte durch die Wechselwirkung der Gleitbänder bedingt sein, indem Versetzungen, die auf einer Gleitebene in Bewegung geraten sind, die Nachbarebenen durch ihr Schubspannungsfeld erst zum Gleiten anstossen. Diese Vorstellung erklärt auch die im ganzen betrachtet synchrone zeitliche Entwicklung benachbarter Gleitlinien (Abb. 8 und 9). Aus einer Berechnung [15] des Spannungsfeldes einer Versetzungsverteilung, die einer verfestigten Gleitebene nach dem Quellenmodell entspricht, folgt, dass die Wechselwirkung von Gleitebenen auch über Entfernungen von der Grössenordnung der Gleitbandabstände beträchtlich ist, ein Befund, den man schon aus der bei grossen Dehnungen fast regelmässigen Verteilung der Gleitbänder über die Kristallänge

*Die beiden Bilder dieser Figur haben den relativ grossen zeitlichen Abstand von 13 sek = 416 Bildern, was jedenfalls nicht ein "plötzliches" Erscheinen der gezeigten Linien beweist.

ablesen kann. Insbesondere stellt sich heraus, dass eine betätigte Gleitebene die äussere Schubspannung in einer Nachbarebene im Abstand l stellenweise verstärkt (bis zu 20 Prozent), wobei l die Lineardimensionen in der Gleitebene: Intervallänge $\approx$ Mosaikblockdurchmesser kennzeichnet. Nimmt man l üblicherweise zu einigen μ an, dann sollte eine Gleitlinie in solchem Abstand von einer schon betätigten Gleitebene sich besonders leicht ausbilden. Diese Vorstellung wird durch die obigen Beobachtungen an *Doppellinien* (Abb. 8 und 9, Kurven 1) gestützt.

Solche Beobachtungen über oft bevorzugte Bildung von Doppellinien bzw. Gleitbandbündeln bei kleinen Deformationen passen schlecht zu der statistischen Aussage von Chen und Pond über die Lage einer neuentstehenden Gleitlinie in Bezug auf ihre beiden Nachbarn.

Den Einfluss zunehmender Verfestigung auf die Gleitlinienentwicklung möchten wir in diesem Bilde als Wirkung der Störung der regulären Gleitung verstehen: Die Versetzungen müssen die während der Verformung in der Gleitebene entstehenden Hindernisse (sessile dislocations, Löcher) überwinden. Dementsprechend wird die Gleitlinienentwicklung verlangsamt (Abb. 8 und 9). Zunehmende Belastungsgeschwindigkeit bedeutet stärkere Störung und damit stärkere Verfestigung, also Verlangsamung des Linienwachstums (Abb. 12).

Die Filmaufnahmen wurden in Zusammenarbeit mit dem Institut für Film und Bild in Göttingen vorbereitet und durchgeführt. Wir sind dessen Leiter, Herrn Dr. G. Wolf, und seinen Mitarbeitern, besonders dem Kameramann, Herrn E. Heyse, sehr zu Dank verpflichtet.

Herrn Dr. G. Leibfried verdanken wir zahlreiche Anregungen und ermutigende Diskussionen.

Herr Prof. Dr. G. Masing, Göttingen, stellte uns freundlicherweise die Einrichtungen seines Instituts zur Herstellung der Einkristalle zur Verfügung.

Die Durchführung dieser Untersuchung wurde durch dankenswerte Unterstützung der Deutschen Forschungsgemeinschaft sowie der Göttinger Akademie der Wissenschaften ermöglicht.

Literatur

1. Schmid, E. und Boas, W. Kristallplastizität (Berlin, Springer, 1935).
2. Maddin, R., Mathewson, C. H. und Hibbard, E. R. Trans. Amer. Inst. Min. Met. Eng., **175** (1948) 86.
3. Holden, J. M.Sc. thesis Manchester (nach [4]).
4. Brown, A. F. Advances in Physics, **1** (1952) 427.
5. Mott, N. F. Phil. Mag., **43** (1952) 1151.
6. Crussard, M. C. Rev. Métallurgie, **42** (1945) 286.
7. Yamaguchi, K. Sci. Pap. Inst. Phys. Chem. Res., Tokyo, **11** (1929) 223.
8. Haasen, P. und Leibfried, G. Z. Metallkunde, **43** (1952) 317.
9. Chen, N. K. und Pond, R. B. J. Metals, **4** (1952) 1085.
10. Heidenreich, R. D. und Shockley, W. Rep. Bristol Conference (1948) 57.
11. Brown, A. F. Nature, **163** (1949) 961.
12. Wilsdorf, H. und Kuhlmann-Wilsdorf, D. Z. angew. Physik, **4** (1952) 361, 409, 418.
13. Brown, A. F. und Honeycombe, R. W. K. Phil. Mag., **42** (1951) 1146.
14. Haasen, P. und Leibfried, G. Disc. zu [9], J. Metals (1953) im Druck.
15. Haasen, P. Dissertation Göttingen, 1953.

THE HARDENING OF METAL CRYSTALS BY PRECIPITATE PARTICLES*

J. C. FISHER, E. W. HART, and R. H. PRY†

The dependence of the hardening effect of precipitate particles is computed in terms of a model in which the precipitate particles cause the dislocations from activated Frank-Read sources to form closed loops about the particles. The back stress resulting from the closed loops increases the effective critical stresses of the Frank-Read sources. The results of the analysis are shown to be in fair agreement with the relevant experimental data.

LE DURCISSEMENT DE MÉTAUX PAR DES PARTICULES DE PRÉCIPITÉ

L'effet durcissant des particules de précipité est calculé au moyen d'un modèle, dans lequel les particules de précipité forcent les dislocations provenant des sources de Frank-Read activées, à former des boucles fermées autour de ces particules. La réaction, produite par les boucles fermées, augmente les tensions effectives, critiques des sources de Frank-Read. Les résultats de l'analyse concordent assez bien avec les données experimentales.

DIE AUSHÄRTUNG VON METALLKRISTALLEN DURCH AUSGESCHIEDENE FREMDANTEILE

Die Abhängigkeit der Aushärtungswirkung von ausgeschiedenen Fremdanteilen wird im Rahmen eines neuen Modelles berechnet. In diesem Modell führen die ausgeschiedenen Teilchen dazu, dass die Versetzungen, die aus einer Frank Read Quelle stammen, um die Fremdteilchen Ringe ("loops") bilden. Die Gegenspannung, die diese Ringe erzeugen, erhöht die effektive kritische Zugspannung der Frank Read Quellen. Es zeigt sich, dass die Ergebnisse dieser Analyse in zufriedenstellender Übereinstimmung mit den entsprechenden experimentellen Daten stehen.

Introduction

The hardening effect produced by precipitate particles in metal crystals seems to be dependent on both the size and the spacing of the particles. The size effect was inferred by Merica and his collaborators [1] from studies of the age hardening of duralumin, and it was proposed that the hardening reached a maximum for precipitate particles just under the limit of microscopic observability. A qualitative explanation of this type of hardening was offered by Jeffries and Archer [2] whereby the precipitate particles acted to block crystallographic slip. Mott and Nabarro [3] estimated the yield strength in terms of the strains produced by precipitation and the increased stress required to force dislocations through adversely strained material. The dependence of the hardening on particle spacing has been investigated in steel [4] and more recently in aluminum-copper alloys [5]. A theory of the dependence on spacing was proposed by Orowan [6], who showed that the stress required to force a dislocation between two precipitate particles was inversely proportional to their spacing.

The treatment of the present paper attempts to account for the influence of the size and spacing of precipitate particles on the strength of metal crystals in terms of a simple mechanical model. The underlying slip process is assumed to depend on the activation of slip sources, such as those proposed by Frank and Read [7], with consequent large amounts of slip resulting on each plane so activated. The nature of the strengthening effect here will be seen to be essentially different from that envisaged in either of the two foregoing theories.

The model adopted to compute the hardening increment due to included precipitate particles is that previously reported by us in abstract [8]. Dislocation loops radiating from a Frank-Read source in an active slip plane bend about partially impenetrable particles that intersect the plane, leaving trapped closed loops about them as shown in Figures 1 and 2. The trapped loops exert a back-stress throughout the plane, thereby raising the effective critical stresses of all Frank-Read sources in the plane. This back stress is identified with the hardening increment due to the precipitate. It depends on the steady state number of loops that each particle can support, the radial distribution of loops about each particle, and the size and spacing

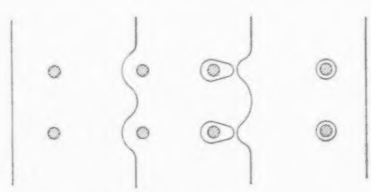

FIGURE 1. Four views, in sequence from left to right, of the propagation of a segment of a dislocation line past a row of impenetrable particles leaving residual loops about the particles.

*Received October 28, 1952.
†General Electric Research Laboratory, The Knolls, Schenectady, New York, U.S.A.

of the particles. These effects are computed in the following sections.

Calculation

A. Loop Distribution

For simplicity in calculation consider that in any slip plane the sections of the precipitate particles are circles of radius r of mean spacing $2R$. Let each particle support N loops and designate the radius of the nth loop about each particle by r_n. In the following all stresses are measured in units of G, the rigidity; lengths in units of b, the Burger's vector of the elementary dislocations for slip in the plane; and energy in units of Gb^3.

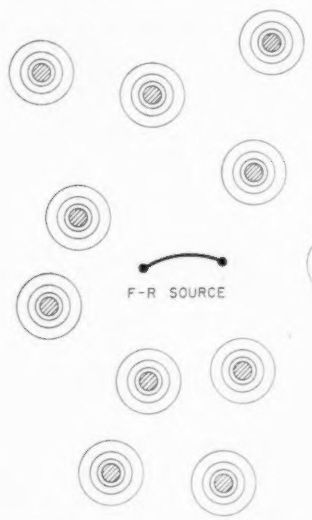

FIGURE 2. The model of a hardened plane containing a Frank-Read source after steady state has been reached. Each circle about a precipitate particle represents a few hundred dislocation loops. The components of the figure are not necessarily in proper relative scale.

It has been shown that the stresses [9] and forces of interaction [10] associated with dislocations can be computed by means of a magnetic analog, in which the dislocation line is thought of as a current-carrying wire. Making use of this analog, the stress component* in the plane containing a dislocation loop and resolved in the direction of the Burger's vector is

$$(1) \qquad \tau = [1 - \tfrac{1}{2}\nu/(1-\nu)]h.$$

Here ν is Poisson's ratio, and h is the magnitude of the component of magnetic field normal to the plane which would be produced in a medium of unit permeability by a circular loop, congruent to the dislocation loop, carrying unit current (all in rationalized units). Then, in view of the magnetic analog force law it is clear that we may consider the interaction energy of the concentric loops about any one particle as given by an analogous magnetic interaction energy of similarly disposed current loops. The energy of the N loops about one circular particle of radius r and in an external stress field, τ, (which may include the stresses due to the other loop concentrations) is

$$(2) \qquad E = \tfrac{1}{2}\sum_{m=0}^{N}\sum_{n=m}^{N}\epsilon_{mn} + \tau\sum_{n=0}^{N}\pi r_n^2,$$

where

$$\epsilon_{mn} = \tfrac{1}{2}(r_m + r_n)\,k_{mn}^4 C(k_{mn}),$$
$$k_{mn}^2 = 4\,r_m r_n/(r_m + r_n)^2,$$
$$k^4 C(k) = (2 - k^2)\,K(k) - 2E(k),$$

and K and E are complete elliptic integrals [11]. The interaction term, ϵ_{mn}, will be recognized as the mutual inductance of concentric circular loops of radii r_m and r_n. Terms for which $n = m$ represent the self-energies of the dislocation loops. Although the self-energies are infinite in equation (2), they become finite and of approximately the correct magnitude when the sum is replaced by an integral as in equation (3). For simplicity we assume $\nu = 0$. When $\nu \neq 0$, the only difference will be seen to be a slight change in the magnitude of the hardening stress.

The distribution of radii has been approximated by a variational method. The trial function used for the radii is

$$r_n = r\,e^{n\alpha},$$

a form that was suggested by the behavior of other trial functions that were considered. It is then convenient to make the substitutions

$$x = n/N, \quad y = (m-n)/N, \quad \gamma = N\alpha,$$

and to replace the sums by integrals. Then equation (2) becomes

$$(3) \quad E = \tfrac{1}{2}N^2\int_0^1 dy\int_0^{1-y} dx\,\epsilon_{xy} + N\pi r^2\tau(e^{2\gamma} - 1)/2\gamma$$

where

$$\epsilon_{xy} = \tfrac{1}{2}re^{x\gamma}(1 + e^{y\gamma})\,k^4\,C(k)$$
$$k^2 = 4e^{y\gamma}/(1 + e^{y\gamma})^2.$$

*At any radius from the center of the dislocation loop, the resolved shear stress depends upon the angle between the radius vector and the Burger's vector. The angular dependence of τ is small, and it is the mean value of τ, averaged over angle, that appears in equation (1).

The integration over x may be carried out immediately with the result

$$(4) \qquad E = \tfrac{1}{4}N^2\tau[F(\gamma) + 2\pi(r/N)\tau(e^{2\gamma} - 1)/\gamma],$$

$$(5) \quad F(\gamma) = \gamma^{-1}\int_0^1 dy[e^{(1-y)\gamma} - 1](1 + e^{y\gamma})k^4C(k).$$

$F(\gamma)$ was computed numerically and is shown graphically in Figure 3. It may be noted that the second term in the bracket of (4) is negligible

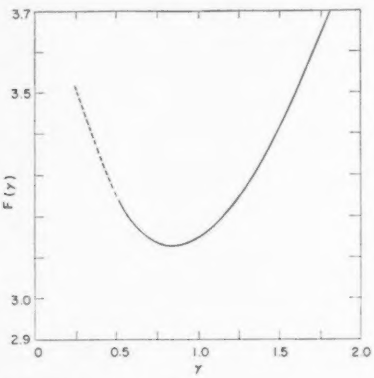

FIGURE 3. $F(\gamma)$ vs. γ. The minimum occurs at about $\gamma = 0.84$.

compared to $F(\gamma)$ and so the distribution of loops is well determined by minimizing $F(\gamma)$. This is so because, as will be shown, N/r is of the order of the ideal strength of the crystal and is therefore of the order of 10^{-1} while τ is about 10^{-3}.

It will be noted from Figure 3 that the minimum of E occurs at about $\gamma = 0.84$. This value is relatively independent of τ in view of the foregoing argument and so

$$r_N = re^{\gamma} \sim 2.3r.$$

This shows that, whatever the value of N, the loops occupy an annular space of radial width about $1.3r$ about the particle. Note also that because of the neglect of the term proportional to τ the calculation is independent of the value of ν.

B. *The Hardening Stress*

The hardening stress, τ_h, may be approximated from equation (1), assuming that the sources affected are far from the loops compared to the loop dimensions, and assuming a uniform distribution of precipitate particles in the plane. Since the concentration of particles is $(\pi R^2)^{-1}$, and the "magnetic dipole strength" of the loops about each structure is given by the sum of the areas of the loops about it, the hardening stress is

$$
\begin{aligned}
\tau_h &= (\pi R^2)^{-1}\sum_{n=0}^{N} \pi r_n^2 \cdot (4\pi)^{-1}\int dS\cdot r^{-3} \\
(6) \qquad &= N(r/R)^2[(e^{2\gamma} - 1)/2\gamma]\cdot \tfrac{1}{2}\int_{R_m}^{\infty} dr\cdot r^{-2} \\
&= \tfrac{1}{2}(r/R)^2 N R_m^{-1}\cdot(e^{2\gamma} - 1)/2\gamma.
\end{aligned}
$$

R_m is the distance of closest approach of a source to a precipitate particle, averaged over the extent of the source. This number is some fraction of R and will be written R/c where c is probably of the order of 3. Equation (6) may now be simplified by using the above value of γ and noting that $(r/R)^2$ is the volume fraction, f, of precipitate in matrix plus precipitate. Then, reintroducing the dependence on ν,

$$(7) \qquad \tau_h = 1.3\, c\,[1 - \tfrac{1}{2}\,\nu/(1-\nu)](N/r)\,f^{3/2}.$$

If ν is taken to be $\frac{1}{3}$ and c is taken to be 3,

$$(8) \qquad \tau_h = 3(N/r)\,f^{3/2}.$$

Discussion

The hardening stress computed in the above sections is the increased stress required to activate the slip sources in a slip plane. It is a stress increment, to be added to the corresponding stress for the metal matrix without precipitate particles. As computed above, the hardening stress is expected to increase with strain for the first few per cent, until N has reached a steady state value. Subsequently, the hardening stress should be independent of strain. The steady state value of N cannot be computed precisely, but its magnitude can be estimated, and its dependence on r can be in part anticipated.

The stresses sustained in the precipitate particle and in the region immediately surrounding it are of the order of N/r. It is expected that this number cannot exceed the ideal limiting strength of either the precipitate or the matrix. N/r then has an expected upper limit of about 0.1. In terms of the surrounding dislocation loops, this further means that no two dislocation loops are closer than 10 Burger's units. It should be further expected that as the particle radius exceeds some minimal radius, r_m, the stress that can be sustained by the particle decreases. We shall, therefore, write τ_c in place of N/r, with the expected properties mentioned above. Then (8) becomes

$$(9) \qquad \tau_h = 3\,\tau_c f^{3/2}.$$

Equation (9) can be used to make an absolute

estimate of the hardening strength. For $f = 0.04$ and $\tau_e = 0.1$,

$$\tau_h = 2.4 \times 10^{-3},$$

remembering that the unit of stress here is the rigidity modulus, G. For Al with $CuAl_2$ precipitate this would be

$$\tau_h = 7 \times 10^3 \text{ psi}.$$

Dorn and co-workers [5] obtain a range of 5 to 10×10^3 psi for this concentration of $CuAl_2$ and for a range of particle sizes.

The data which these authors report are susceptible to further analysis in terms of the parameters of this theory. Figure 4 is a plot of $f^{3/2}/\tau_h$ versus

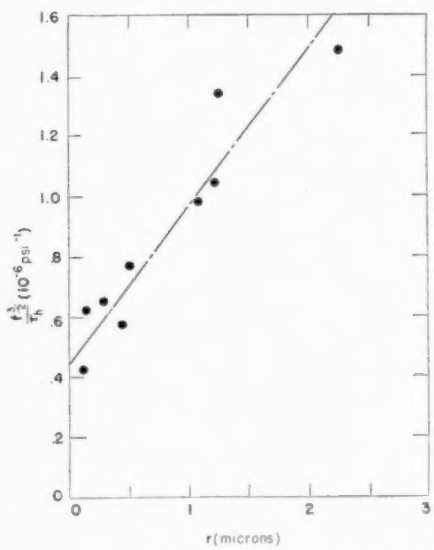

FIGURE 4. According to equation (9), the ratio $f^{3/2}/\tau_h$ should be proportional to $1/\tau_c$, the reciprocal of the limiting strength of a precipitate particle. This ratio is plotted versus particle radius for $CuAl_2$ precipitated in aluminum. Data of Shaw, Shepard, Starr, and Dorn [5] for tension tests at 78°K in alloys of 3 to 5 per cent nominal concentration of Cu in Al.

r at 15 per cent strain for their data at 78°K. The range in concentration is only about 3 to 5 per cent and the particle radii are as shown in the figure. The scatter from monotonic behavior as a function of r is within the probable uncertainty of the determination of the parameters and shows fair confirmation of the expected dependence on r, in that τ_c, the critical stress for yielding of the particles or surrounding material, decreases with increasing particle size.

Conclusions

It has been shown that the model proposed for the explanation of precipitate hardening is in fair agreement with the available experimental data in a number of features. The hardening is independent of strain after the first few per cent of strain are accomplished. The magnitude of the hardening effect, as given by equation (9), can be simply approximated on an absolute basis. The predicted dependence on precipitate concentration and on particle radius is not inconsistent with observation.

In order that the quantitative predictions be fully tested experimental measurements are needed for a wider range of particle radii and concentrations. It would be preferable that such measurements were carried out on single crystals since the problem of grain size control and grain boundary precipitation would then be eliminated.

Acknowledgement

This work received support from the Flight Research Laboratory, Wright Air Development Center.

References

1. MERICA, P. D., WALTENBERG, R. G., SCOTT, H. Trans. A.I.M.E., **64** (1921) 41.
2. JEFFRIES, Z. and ARCHER, R. S. Chem. and Met. Eng., **24** (1921) 1057.
3. MOTT, N. F. and NABARRO, F. R. N. Proc. Phys. Soc. (London), **52** (1940) 86.
4. GENSAMER, M., PEARSALL, E. B., PELLINI, W. S., LOW, J. R., JR. Trans. Amer. Soc. Metals, **30** (1942) 983.
5. SHAW, R. B., SHEPARD, L. A., STARR, C. D., DORN, J. E. 18th Tech. Rep., Univ. of Calif., Inst. of Eng. Res. (1952).
6. OROWAN, E. Discussion, "Symposium on Internal Stresses," Institute of Metals (London, 1947), p. 451.
7. FRANK, F. C. and READ, W. T. Phys. Rev., **79** (1950) 722.
8. HART, E. W., FISHER, J. C., and PRY, R. H. Phys. Rev., **87** (1952) 211.
9. HART, E. W. Unpublished work.
10. PEACH, M. and KOEHLER, J. S. Phys. Rev., **80** (1950) 436.
11. JAHNKE, E. and EMDE, F. Tables of Functions (New York, Dover Publications, 1943), p. 73.

IONIC CURRENTS IN THIN FILMS OF ZIRCONIUM OXIDE*

A. CHARLESBY†

The electrical properties of thin oxide films on zirconium, formed by anodising in suitable electrolytes, have been studied. This paper deals with the ionic currents and laws of growth. Optical methods show the film to be uniform in structure, and both optical and capacity measurements have been used to measure its thickness. At room temperature this is found to be proportional to the formation voltage, and depends to a much lesser extent on the formation current. From optical data a film thickness of 21Å per volt is deduced. Capacity measurements lead to a figure of 20Å per volt assuming a value of 20 for the dielectric constant of the oxide.

The results obtained are consistent with the following relationship between ion current i_+ and electrostatic field across the film:

$$i_+ = A_+ \exp B_+F$$

where A_+ and B_+ are constant at room temperature. From the approximate value of B_+, it is deduced that the barrier opposing ionic flow from the metal has a width of 2.8Å.

The effect of varying the type of electrolyte has been studied. Certain electrolytes, e.g. dilute sulphuric acid, which gives a porous conducting oxide film on aluminium, produce insulating films on zirconium. Electrolytes which produce insulating oxide films on aluminium also do so on zirconium.

LES COURANTS IONIQUES DANS DE MINCES COUCHES D'OXYDE DE ZIRCONIUM

Une étude a été faite des propriétés électriques de minces couches d'oxyde de zirconium, formées par oxydation anodique dans des électrolytes convenables. Cet article a trait à des courants ioniques et les lois de croissance. Il a été montré par l'emploi de méthodes optiques, que la structure de la couche est uniforme, son épaisseur a été établie en employant des mesures de capacité, ainsi que des mesures optiques. Il fut constaté, qu'à la température ambiante, l'épaisseur de la couche est proportionnelle au voltage de formation, et ne dépend que peu du courant de formation. Une épaisseur de 21Å par volt est déduite des données optiques. Les mesures de capacité conduisent à une valeur de 20Å par volt, ceci en admettent, que la valeur de la constante diélectrique de l'oxyde est de 20.

Les résultats obtenus sont en accord avec la relation suivante entre le courant ionique i_+ et le champ électrostatique à travers la couche:

$$i_+ = A_+ \exp B_+F$$

où A_+ et B_+ sont constants à la température ambiante. Il est déduit de la valeur approximative de B_+, que la barrière qui s'oppose à l'écoulement des ions du métal, a une largeur de 2, 8Å.

L'effet de l'emploi de différents types d' électrolyte fut aussi étudié. Certains électrolytes, par exemple l'acide sulphurique dilué, qui donne une couche d'oxyde poreux et conducteur sur l'aluminium, produit des couches isolantes sur le zirconium. Les électrolytes, qui produisent des couches d'oxyde isolant sur l'aluminium, en font autant sur le zirconium.

IONENSTRÖME IN DÜNNEN ZIRKONOXYDFILMEN

Die elektrischen Eigenschaften dünner Oxydfilme auf Zirkon, die durch Anodisieren in geeigneten Elektrolyten gebildet wurden, wurden untersucht. Die vorliegende Arbeit beschäftigt sich mit den Ionenströmen und den Gesetzen des Wachstums. Die gleichmässige Struktur des Filmes wurde durch optische Messungen gezeigt, und seine Dicke wurde sowohl durch optische als auch durch Kapazitätsmessungen bestimmt. Bei Zimmertemperatur wurde diese proportional der Bildungsspannung gefunden; sie hängt sehr viel weniger vom Strom bei der Filmbildung ab. Aus optischen Daten wurde eine Filmdicke von 21Å per Volt ermittelt. Kapazitätsmessungen ergaben einen Wert von 20Å per Volt, wobei der Wert der Dielektrizitätskonstanten des Oxyds zu 20 angenommen wurde.

Die Resultate der Versuche sind im Einklang mit folgender Beziehung zwischen dem Ionenstrom i_+ und dem elektrostatischen Feld in dem Film

$$i_+ = A_+ \exp B_+F$$

wobei A_+ und B_+ bei Zimmertemperatur Konstanten sind. Aus dem ungefähren Wert von B_+ wird geschlossen, dass der Wall, der dem Ionenfluss aus dem Metall entgegensteht, eine Dicke von 2.8Å hat.

Der Effekt der Änderung des Elektrolyt-typs wurde untersucht. Gewisse Elektrolyte, wie z. B. verdünnte Schwefelsäure, die auf Aluminium porige, leitende Oxydfilme erzeugen, formen auf Zirkon isolierende Filme. Elektrolyte, die auf Aluminium isolierende Filme erzeugen, wirken in gleicher Weise auf Zirkon.

Introduction

By anodising aluminium in suitable electrolytes, thin insulating oxide films can be formed. Some electrical properties of these films have been investigated, and it was shown that the total current passing through the electrolyte is partly ionic and partly electronic. Only the former is responsible for film growth. A similar investigation has been carried out for the thin insulating oxide films formed on zirconium. Among the main differences between these two metal oxides may be mentioned the interference colours shown by zirconium oxide, and the higher electron currents which flow during formation. In this paper the ion currents associated

*Received December 22, 1952.
†Atomic Energy Research Establishment, Harwell, England.

with the formation of thin oxide layers on zirconium will be considered.

Determination of Oxide Thickness

Two independent methods have been used to measure the thickness of the oxide layer which has been produced anodically. One is based on the optical thickness of the oxide, its colour being compared with that of an air film of known thickness. This leads to a value for $\delta\mu$, where δ is the film thickness, and μ the refractive index, assumed uniform. The other method is based on a measurement of the electrostatic capacity between the zirconium metal and the electrolyte. The capacity per unit area C_0 in e.s.u. equals $\epsilon/4\pi\delta$ where ϵ is the dielectric constant of the oxide.

Guntherschulze and Betz [1] have measured $\delta\mu$ and C_0 for a number of metallic oxides, including zirconium oxide. To evaluate δ they assumed that $\mu^2 = \epsilon$. At the low frequencies at which C_0 was measured this assumption is not true, so that their conclusions (leading to a value for ϵ of 12.5) are not valid. A value for ϵ of about 20 is reported by the Titanium Alloy Manufacturing Company of New York, but this applies to the bulk material (baddleyite). An electron diffraction study by Hart [2] of the thin oxide films formed by our technique shows that these films are largely amorphous in character, so that this value for ϵ is not necessarily correct. A set of measurements of the weight increase, and the oxygen liberated during formation, carried out by Polling and Charlesby leads to a higher value for ϵ of about 28. A direct determination of the refractive index μ for these thin films is described below.

Preparation of Specimens

Zirconium sheet metal (obtained from Murex Ltd.) contained as main impurities hafnium (0.5–3%), carbon (0.15%), oxygen (0.08%), nitrogen (0.04%), and iron (0.06%). Various means of cleaning the surface were attempted, including electropolishing. The most satisfactory results were obtained by polishing with emery paper down to 0000 under a layer of white spirit. Finally the specimen was cleaned in acetone and distilled water and then dried.

Thin films of oxide were deposited on the metal by anodising in suitable electrolytes, using a platinum cathode. In the case of aluminium the nature of the oxide layer is largely determined by the electrolyte used, and is very dependent on impurities in the metal and the electrolyte. A solution of oxalic acid, for example, produced a thick porous layer of aluminium oxide even at relatively low voltages, and this film can be increased in thickness without any great increase in the formation voltage. A solution of ammonium borate on the other hand produces a thin film, which is insulating, and whose thickness is proportional to the applied voltage over a wide range. Similar insulating oxide films can be produced in zirconium, even in electrolytes such as dilute sulphuric which produce non-insulating oxide films on aluminium.

Most of the experiments described in this paper were carried out in aqueous ammonium borate solution. Several experiments using other electrolytes were also carried out.

Electrical Method

If during film formation the current is kept constant, the voltage V_f across the electrolytic cell increases uniformly with time. At the same time the reciprocal capacity $(1/C_0)$ rises uniformly, so that for any given formation current and temperature, the product $C_0 V_f$ is approximately constant. This is shown in Table I.

TABLE I

$C_0 V_f$ AS A FUNCTION OF V_f AT CONSTANT i_f
(Specimen Z6; nominal area 10.3 cm², 18°C)

	V_f (volts) 12	30.9	41	72.4	85	180	245	i_f (μa/cm²)
$C_0 V_f$ (μF volt/cm²)	10.9	10.3		10.6			9.4	960
	—	9.4	9.3	9.1	9.0	7.6	8.0	96

The slight change in $C_0 V_f$ may be due in part to the difference between the true formation voltage, which is applied across the oxide layer itself, and the quantity V_f which also includes the potential drop across the electrolyte.

It was observed that a minimum voltage V_i is required to initiate film growth. To eliminate this source of error it is convenient to consider the ratio $dV_f/d(1/C_0)$ instead of $C_0 V_f$.

At a given formation current density i_f and temperature, $dV_f/d(1/C_0)$ is constant, independent of film thickness δ. Measured in e.s.u.,

$$\frac{dV_f}{d(1/C_0)} = \frac{\epsilon}{4\pi}\frac{dV_f}{d\delta} = \frac{\epsilon}{4\pi}F_f,$$

where F_f is the field across the oxide film and is thus independent of δ.

TABLE II

$dV_f/d(1/C_0)$ AT VARIOUS FORMATION CURRENTS i_f AND AT 18°C

Specimen	i_f (μa/cm^2)	$dV_f/d(1/C_0)$ (μF volt/cm^2)	F_f (10^6 volt/cm)
Z6	24	7.2	4.1
	96	7.55	4.3
	960	9.3	5.3
Z14	20–40	7.25	4.1
	100	7.4	4.2
	200	7.7	4.3
Z21	100	8.2	4.6
	200	8.7	4.9
	500	9.1	5.2
	1000	9.5	5.4
	2000	9.3–9.9	5.3–5.6
Z21G	100	8.3–8.6	4.7–4.9
	200	9.2	5.2
	500	9.7	5.5

TABLE III

VALUES OF $C_0\ V_f$ FOR SPECIMEN WITH (1) HEAVILY SCRATCHED SURFACE AND (2) HIGHLY POLISHED SURFACE
(Nominal area assumed = 20 cm^2; i_f = 5 ma/cm^2)

1	V_f	(volts)	49.8	99	169	249
	$C_0\ V_f$	(μF volts/cm^2)	11.7	10.8	10.3	10.4
2	V_f	(volts)	67	110	188	246
	$C_0\ V_f$	(μF volts/cm^2)	11.4	10.51	9.87	9.65

Table II gives some observed values of $dV_f/d(1/C_0)$ for various specimens and current densities, and the corresponding values of F_f, assuming a value for ϵ of 20. If the correct value for ϵ is 28, these values of F_f must be multiplied by 0.7. Table II shows that the formation field F_f varies but slightly with the formation current i_f. A tenfold increase in the latter only increases F_f by some ten per cent. Since the formation current i_f comprises both an ion current and electron current, each of which varies with the applied field, little fundamental information is to be gained by studying more closely the variation of F_f with i_f.

One possible source of error arises in the measurement of C_0, the capacity per unit surface area. The true surface area is unknown, and is larger than the nominal (geometrical) area assumed in Tables I and II. The magnitude of the factors required to allow for this difference is not likely to be large, since specimens polished in a number of ways gave very similar values for $C_0\ V_f$, when C_0 was computed from the nominal surface area. In Table III for example, data are given for a heavily scratched specimen, of nominal surface area 20 cm^2. The specimen was then cleaned and very carefully repolished, and reanodised. The values of $C_0\ V_f$ for these two different surface treatments differ by only a few per cent. The relatively high value of $C_0\ V_f$ is due to the high formation current.

It is concluded that at room temperature, assuming ϵ equals 20, the field F_f across the oxide film required to produce appreciable ion flow and film growth is about 5×10^6 volts/cm. F_f is independent of film thickness, but increases very slightly with rise in the ion current.

Optical Method

Preparation of standards. Thin films of ZrO_2 show strong interference colours, the colour depending on the voltage of formation at room temperature, and to a much lesser extent on the formation current. Standards were prepared on four zirconium strips, successive intervals of 5 mm. of these being formed at increasing voltages at intervals of 4 volts. In most regions these voltage differences produced appreciable changes in colour. The total range covered extended from 2 volts to 200 volts, each voltage being covered twice on different strips. The time of formation at each voltage was two minutes.

Other standards were also prepared in which the time of formation of each voltage was proportional to the voltage of formation. There did not appear to be any great difference between these two sets of standards.

The value of these standards is that by comparing specimens with them an approximate estimate of film thickness can be obtained visually. Moreover, any changes in film structure or thickness resulting from various forms of treatment are readily revealed.

Determination of refractive index. An estimate of the refractive index of the oxide layer on zirconium was made by means of the change in interference colours observed when the film is viewed at oblique incidence. It is assumed that the difference in the phase angles introduced on reflection at the air-oxide or metal-oxide face is independent of the angle of incidence. To verify this assumption the colour of a thin (10 volt) film was examined at various angles of incidence in a medium of high refractive index (carbon bisulphide). The colours observed changed little, if at all. Thus the colour changes

observed for thicker films when the angle of incidence is altered must be due to the different path lengths.

It can be shown that, neglecting any changes in phase angle with angle of incidence, the optical path difference as between rays reflected from the oxide-air face and the oxide-metal face is given by $2\delta\mu \cos \beta$, where μ is the refractive index of the oxide, and β is the angle between the ray in the oxide and the normal to its surface. Thus if $\beta = 0$ the path difference is $2\delta\mu$. At any other angle the path difference, and hence the apparent thickness of the film as determined from its colour, is reduced by the factor $\cos \beta$.

In the experiment, the standard oxide specimens were used. They were immersed in carbon bisulphide (of refractive index $\mu_1 = 1.632$) and a series of pairs of voltages found V_p, V_g such that the colour of the film formed at V_p when viewed at right angles to the surface was equal to that of the film formed at V_g, viewed at glancing incidence. The observations were made in daylight by two independent observers.

Since the film thickness δ is proportional to the formation voltage V_f the ratio V_g/V_p gives $\cos \beta$ directly. Some values are given in Table IV.

TABLE IV

APPARENT FILM THICKNESS AT NORMAL AND GLANCING INCIDENCE

V_p	39	49	60	64	66	70	79	79	87	91
V_g	60	72	96	97	95	107	111	116	132	132
$\cos \beta$	0.65	0.68	0.625	0.66	0.695	0.654	0.71	0.68	0.66	0.69

Since there is no appreciable change in the value of $\cos \beta$ throughout the range of thickness studied, the neglect of phase angle is justifiable. From the mean value of $\cos \beta$ (0.67) and the refractive index of carbon bisulphide, a value of 2.20 is obtained for the refractive index of thin films of ZrO_2. This value is probably correct to within several per cent. Since the refractive indices for the monoclinic bulk oxide are 2.12, 2.19, 2.20 it appears that these thin oxide layers have a refractive index similar to that of the bulk material. In the following calculations a value of 2.2 is used.

The corresponding value used by Gunterschulze and Betz [1] is 3.45. Hence their estimated film thicknesses are too low by a factor of 3.45/2.2 or 1.57, and the field across the film too high by the same factor.

Measurement of optical thickness. The range of colours obtained by anodising zirconium at various voltages can be compared with the colours of air films of various thickness; knowing μ, the refractive

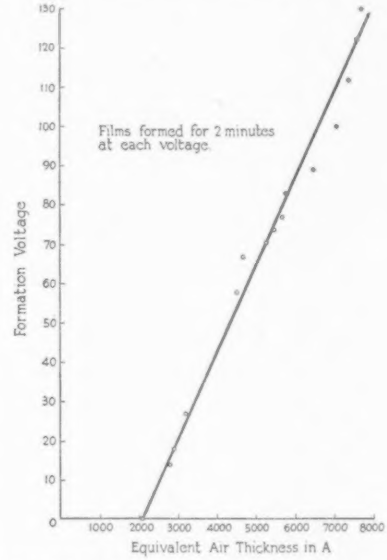

FIGURE 1. Zirconium oxide film thickness as a function of formation voltage. $\mu\delta = 2050 + 46 V_f$.

index of the oxide, the film thickness can be immediately deduced.

Figures 1 and 2 show the relation between formation voltage and equivalent air thickness (as judged from the colour) for a range of formation voltages, and for a standard formation time of two minutes at 20°C. The air thicknesses equivalent to any given colour are taken from the tables of Rollet [3] and of Quincke which differ in origin owing to a phase change. The plots are linear with the possible exception of those for very thin films (Figure 2).

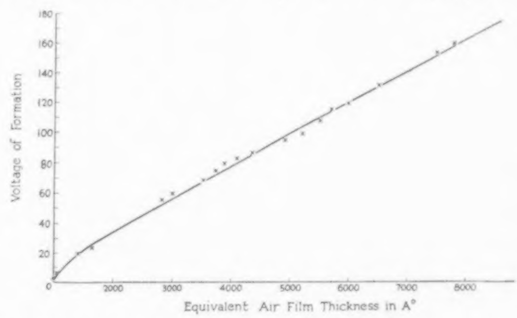

FIGURE 2. Zirconium oxide: optical thickness *vs* voltage of formation (2 minutes at each voltage). $\mu\delta = 46$ Å/volt.

If the refractive index throughout the film is uniform (as appears to be demonstrated by Table IV), then this linearity shows that the film thickness is proportional to formation voltage to within experi-

mental error. The slope of the curve gives an optical film thickness $\delta\mu$ of 46 Å per volt. Similar experiments by Guntherschulze and Betz gave a value of 43 Å per volt.

With a refractive index μ of 2.2, as deduced above, the film thickness δ amounts to 21 Å per volt. This compares with the value of 20 Å per volt, deduced from capacity measurements on the assumption that $\epsilon = 20$. The formation field F_f corresponding to the optical measurements is 4.8×10^6 volt/cm.

Ion Current as a Function of Field Strength

At formation fields in the neighbourhood of 5×10^6 volt/cm, the formation current increases very rapidly with field strength. Measurements of the weight increase of the zirconium specimen, as compared with the total charge passed, show that not all the current contributes to film growth. It is assumed that the formation current comprises both ion and electron currents, each of which varies with the field strength. In the case of aluminium anodised in ammonium borate solution, at current densities of the order of 1 ma/cm², the formation current is almost entirely ionic. It was therefore possible to use several methods to relate ion current (i_+) to field F. The formula deduced can be written:

$$i_+ = A_+ \exp B_+F, \tag{1}$$

where A_+, B_+ are constants at a given temperature. At 20°C, B_+F is about 30 for aluminium oxide.

On the basis of this formula, it was shown theoretically [4] that at constant formation voltage V_f, the ion current decays with time at a rate which depends on B_+F. Thus if B_+F is about 12, $d(\log i_+)/d(\log t) = -0.87$, while if $B_+F \sim 32$, $d(\log i_+)/d(\log t) = -0.94$. Moreover, the product $i_+t \sim q/B_+F$ where t is the formation time at constant voltage, and q the ion charge/cm² passed in time t. After the first few seconds q increases very slowly, so that i_+t is nearly constant. These conclusions were verified in the case of oxide films formed on aluminium. For oxide films formed on zirconium they can no longer be applied owing to the intrusion of an unknown large electron current. The slope $d(\log i_f)/d(\log t)$ was much lower than that deduced from the formula (1), giving values of about -0.6 to -0.7 for various specimens while the product $i_f\,t$ varied from 0.066 coul/cm² after 10 minutes to 0.3 coul/cm² after 1000 minutes. These results indicate that the electron current is not negligible and that it decreases with time less rapidly than the ion current.

There remains a method of relating i_+ and F_f which does not involve the electron current, and which has been found to give satisfactory results in the case of aluminium oxide films. This is based on the measurement of film growth with time, at constant formation voltage. It has been shown [4] that if formula (1) is valid, the relationship between film thickness δ and time t at formation voltage V_f is given by the following relation:

$$\log t = -(mB_+\,V_f/\delta) + c - \log(A_+\,r/B_+\,V_f) \tag{2}$$

where $r = \delta/q$ and m and c are quantities which vary slowly with time. Their values are given in Table V.

TABLE V

CALCULATED VARIATION OF PARAMETER m AND c WITH B_+V/δ

B_+V/δ	10–15	15–20	20–25	25–30	30–35	35–40	40–45	45–50
m =	.50	.48	.47	.465	.46	.457	.454	.452
c =	$\bar{2}.58$	$\bar{2}.31$	$\bar{2}.10$	$\bar{3}.94$	$\bar{3}.80$	$\bar{3}.67$	$\bar{3}.58$	$\bar{3}.48$

Replacing the film thickness δ in terms of the capacity C_0 per unit area,

$$\Delta(\log t) = -\,mB_+V_f\,\Delta C_0/\delta C_0 = -\,mB_+F_f\,\Delta C/C,$$

where C is the capacity of the total area of the specimen and ΔC is the charge in this capacity in time corresponding to $\Delta \log t$. No measurements of ion or electron current are necessary nor need the surface area be known.

Plots of ΔC against $\log t$ for specimens formed at various voltages gave linear relationships over ranges in time of over 100 to 1. Some values of mB_+F_f obtained from these plots are shown in Table VI. From the mean value of 8.3 for mB_+F_f

TABLE VI

DECAY OF CAPACITY WITH TIME AT 18°C
AMMONIUM BORATE SOLUTION

Specimen	V_f (volts)	Range (minutes)	$\dfrac{C\Delta(\log t)}{\Delta C} = mB_+F$
Z5	70	2–1040	8.6–8.4
Z11	16.25	7.5–28	8.6
Z14	24.5	23–90	8.2
	50.9	3–1100	8
	100	8–160	8.4

a value of 17 for B_+F_f and 0.48 for m are deduced. Then if $F_f \sim 5 \times 10^6$ volt/cm, B_+ equals 3.4×10^{-6} cm/volt.

From the mean value of 8.3 for $C\,\Delta(\log t)/\Delta C$, a mean value of 17 for B_+F, and 0.48 for m are deduced.

Change of Colour with Time

The increased film thickness is also demonstrated by the change in colour with time. Two specimens were formed at 70.4 volts, different parts of the specimen being kept at this voltage for times from one to 1000 seconds. Small changes in colour were observed; these could be matched visually against the standard zirconium oxide films, formed at various voltages for two minutes. Over a small range of colours it is justifiable to take the film thickness as proportional to the formation voltage at a constant formation time.

Plots of $1/V_s$ (V_s being the voltage of the standard matching the colour of the specimen, and therefore proportional to its thickness) against log t gave approximately linear relationships, confirming formula (2). The values for mB_+F in dilute sulphuric or in ammonium borate electrolyte were 10 ± 1, in approximate agreement with the electrical capacity measurements. No great accuracy can be claimed for these optical measurements, since the range of colour variation observed is small.

Formation Rate

The formation rate $dV_f/i_f\,dt$ is the rate of increase of formation voltage per unit current density, and is usually expressed in volts/min per ma/cm^2. From it the current efficiency η, i.e., the proportion of the total current which goes to build up the film, can be estimated. If the total formation current i_f consists of an ion current i_+ and an electron current i_-, $\eta = i_+/(i_+ + i_-)$, then

$$(3) \qquad \frac{dV_f}{i_f\,dt} = \eta\frac{dV_f}{i_+\,dt} = \eta\frac{dV_f}{dq} = \eta r F_f,$$

where dq is the ion charge per unit area needed to increase the film thickness by $d\delta$, and r is the constant ratio $dq/\delta r$. For ZrO_2, r equals $319 \times 10^{-6}/\rho$, where ρ is the density. If ρ equals 5.7, as for the bulk monoclinic oxide, r equals 56×10^{-6}. The maximum formation rate occurs when η equals unity and the formation current consists entirely of ions. It then amounts to $56 \times 10^{-6} F_f$ or 17 volts/min per ma/cm^2 if $F_f \sim 5 \times 10^6$ volts/cm ($\epsilon = 20$). This maximum formation rate will vary slightly with formation current, since a small change in F_f produces a large change in i_f.

To measure η, a specimen was formed at a single current density over the entire voltage range (0–250 volts) but with interruptions for the measurement of capacity. It was then repolished and reformed at a different current density over the same voltage range. Figure 3 shows that for a given formation current density i_f the formation rate, represented by the slope of each curve, is constant; moreover, it increases with i_f. This is to be expected since both η and F_f in (3) increase with i_f.

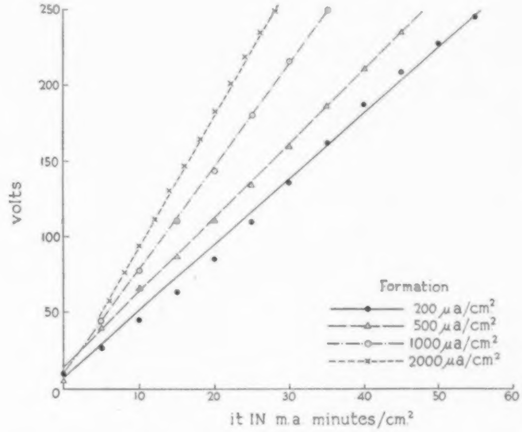

FIGURE 3. Variation of applied potential with charge passed at various formation currents.

In Figure 4 are shown plots of V_f against the reciprocal capacity $1/C_0$. The slopes are proportional to F_f; it is seen that these vary but slightly with current density i_f. Thus most of the variation in the formation rate with current density arises from the change in η. As the current density rises there is a rapid increase in the proportion of the total formation current consisting of ions. These results are shown in Table VII. The formation current cannot greatly exceed 2 ma/cm^2 without heating the electrolyte, and hence affecting the formation rate.

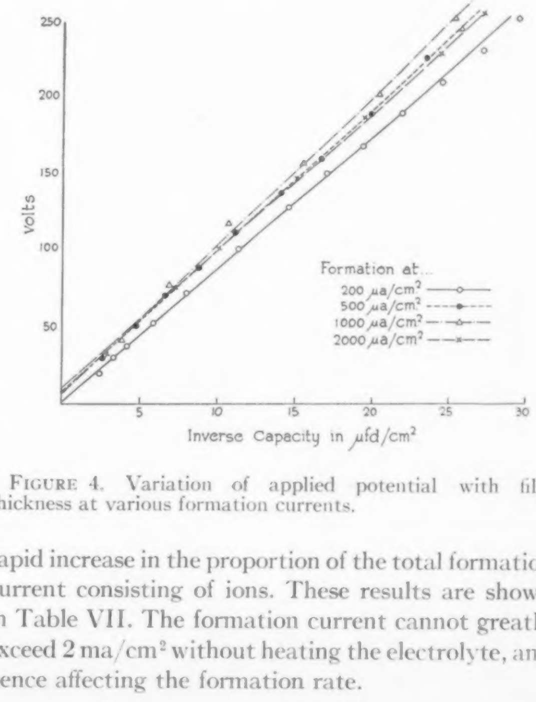

FIGURE 4. Variation of applied potential with film thickness at various formation currents.

At very low formation current densities the current efficiency should become very small indeed. An experiment was carried out to verify this conclusion. A specimen Z24 was polished and cleaned in white spirit, and formed for 5 minutes at 48 volts. The capacity and colour were measured, and it was

TABLE VII

FORMATION RATE, FIELD STRENGTH AND CURRENT EFFICIENCY AS A FUNCTION OF FORMATION CURRENT (Specimen Z21, nominal surface area 20 cm², temperature 18°C)

i_f (μa/cm²)	$\frac{dV_f}{i_f dt}$ $\left(\frac{\text{Volts}}{\text{min}} \text{ per } \frac{\text{ma}}{\text{cm}^2}\right)$	$\eta\, rF_f$ $\left(\frac{\text{volt}}{\text{coul/cm}^2}\right)$	$\frac{dV}{d(1/C_0)}$ $\left(\frac{\mu\text{F volt}}{\text{cm}^2}\right)$	F_f ($\epsilon = 20$) (10^6 volt/cm)	$\eta = i_+/(i_+ + i_-)$
100	1.8	30	—	—	(0.11)
200	4.4	73	8.8	5	0.26
500	4.95	82.5	9.0	5.1	0.29
1000	6.9	115	9.4	5.3	0.39
2000	8.75	146	9.2	5.2	0.50
5000	—	—	9.8	5.5	—

then connected to a voltage supply which passed 5 μa/cm² for a period of 6 days. The total charge passed was about 2.5 coul/cm². If all the charge consisted of ions the increased film thickness δ should be 14000 Å. In fact there was no appreciable change in thickness as measured by capacity or colour changes, although a variation of 100 Å would be readily detected. It is concluded that the current efficiency must be less than 0.7 per cent at a current density of 5 μa/cm².

The data in Table VII could in theory be used to give a relationship between i_+ and F_f, but the range of values of the latter is too small to provide reliable results. However an approximate value for A_+ in formula (1) can be deduced assuming that $B_+F_f \sim 17$ as deduced above. Thus if $i = 1$ ma/cm², $\eta \sim 0.39$ and A_+ is of the order of 10^{-11} amps/cm² at about 18°C. This is an approximate value only, which further experiments have shown to vary rapidly with temperature.

Effect of Electrolyte

Insulating oxide layers can be produced on zirconium with a wider variety of electrolytes than is possible in aluminium. Thus it is possible to anodise a zirconium specimen in an electrolyte consisting of dilute sulphuric acid, and obtain an insulating layer; in the case of aluminium the film produced is porous, and thick films of the oxide can be produced at low voltages. On the other hand, no insulating films on either metal can be produced in an electrolyte containing chlorine ions.

Some preliminary experiments have been carried out on the effect of different electrolytes. Different strips of zirconium cut from the same polished specimen were anodised in dilute boric acid or salt, citric acid, sulphuric acid, phosphoric acid, nitric acid, sodium chloride, potassium carbonate, and chromate. Measurements of the formation rate (dV/idt), the capacity per unit area C_0, and the colour were used to indicate changes in the oxide structure.

Oxide layers prepared in citric acid, ammonium borate or boric acid were found to be similar in colour and capacity at a given voltage (i.e. thickness) and formation rate. Dilute sulphuric acid used as an electrolyte produced apparently somewhat thinner films (as measured by colour or capacity) than were produced on boric acid under identical conditions of formation. The difference in film thickness of about 10 per cent is however not necessarily significant. Insulating layers could be formed in dilute nitric acid, but here the character and structure of the film were different. This conclusion is confirmed by an electron diffraction study of the surface [2], which shows that the oxide consists of a cubic modification of ZrO_2 ($a_0 = 5.103$ Å) when zirconium is anodised in nitric acid (0.1 normal), whereas dilute sulphuric, borate etc., give patterns which are mainly amorphous but contain some crystallites of cubic ZrO_2 ($a_0 = 5.103$ Å). Potassium carbonate electrolyte produces an insulating layer, somewhat different from that obtained in dilute sulphuric acid. No film could be formed in a sodium chloride electrolyte, while in an electrolyte containing potassium chromate thick films were produced which flaked off very readily.

These results indicate that the character of the film produced in different electrolytes varies not only with the electrolyte, but with the metal as well. An electrolyte containing dilute sulphuric acid produces an insulating film on zirconium, and a porous film on aluminium, whereas boric acid produces an insulating film in both cases. Moreover, different types of insulating films can be formed. This difference cannot be due to differences in the electron currents, since these affect the apparent formation rate, but not the final film thickness obtained after prolonged formation. These results are consistent with the assumption that the different electrical behavior of thin films, for example of aluminium oxide, anodised in various electrolytes,

arises from the difference in solubility of the oxide formed.

Discussion

Two different methods—one electrical, the other optical—lead to the conclusion that the thickness of the oxide layers formed by anodising zirconium in suitable electrolytes is proportional to the formation voltage. At 20°C the thickness of the oxide amounts to about 20 Å per volt, corresponding to a field intensity of 5×10^6 volt/cm. Owing to the uncertainty in the value of the dielectric constant ϵ, the true value may indeed be different; between 30 Å and 12.5 Å. The value deduced by optical means gives 21 Å per volt, which agrees with the value deduced if $\epsilon \sim 20$. If the formation current is reduced by a factor of ten the film thickness at a given formation voltage is increased very slightly, by only about 10 per cent.

The relation between ion current i_+ and field F can be expressed in the same form as for aluminium oxide:

$$i_+ = A_+ \exp B_+ F,$$

but in the case of zirconium oxide $A_+ \sim 10^{-11}$ amp/cm^2 and $B_+ \sim 3.4 \times 10^{-6}$ cm/volt. According to Mott's theory of oxidation, $B_+ = 3ae/kT$, where a is the barrier width (trough to peak) opposing ion flow, $3e$ is the charge per ion, T is the absolute temperature, and k is Boltzmann's constant. With the value for B_+ of 3.4×10^{-6}, $a = 2.8$ Å.

The current efficiency is lower than for aluminium oxide, owing to the high electron currents flowing during formation. To produce current efficiencies approaching 100 per cent would require very high current densities, in which case the heating of the electrolyte would be considerable.

The range of electrolytes in which insulating films are formed on zirconium is greater than for aluminium. This is presumably associated with the smaller solubility of the zirconium oxide resulting in a less porous structure.

Acknowledgements

The author wishes to thank the Director A.E.R.E., for permission to publish this report, and to record his appreciation of the interest shown by Dr. H. M. Finniston in this work. Messrs. Polling, Tilsley, and Neale were responsible for much of the experimental work, and their assistance is gratefully appreciated.

References

1. Gunterschulze, A. and Betz, H. Z. Elektrochem., **37** (1931) 726.
2. Hart Private communication.
3. Rollet, Handbuch der Physik, vol. 20, p. 20.
4. Charlesby, A. Proc. Phys. Soc. London, **B66** (1953) 317.

ELECTRON AND PHOTOCURRENTS IN THIN FILMS OF ZIRCONIUM OXIDE*

A. CHARLESBY†

In the previous paper the formation of thin oxide layers of zirconium by electrolytic means has been discussed. This paper deals with the flow of electron and photoelectric currents when electrostatic fields are applied across thin oxide films formed on zirconium by electrolytic means.

At electric fields insufficient to produce appreciable ionic flow, an electron current i_- is observed which depends on the field strength F:

$$i_- = 2A_- \sinh B_-F,$$

where A_- and B_- vary with temperature,

$$A_- = A_0 \exp\left(-U/kT\right), \quad B_- = ae/kT.$$

A physical interpretation of this phenomenon is that the applied field helps the electrons to surmount an energy barrier of height U, and half width a. The values deduced for U and a are 0.375 e.v. and 3.6Å. A phenomenon of ageing is observed. An oxide film kept at voltage for long periods shows a marked reduction in the value of A_0. Possible reasons for this ageing phenomenon are discussed. Photocurrents through the film are observed when ultra-violet light falls on it. The relationship between the photocurrent i_p and the field F is similar to that observed for the (dark) electron current but with different values of the constants: $U = 0.15$ e.v., and $a = 2$Å. No ageing effect is observed in the photocurrent.

LES COURANTS ÉLECTRONIQUES ET PHOTO-ÉLECTRIQUES DANS DE MINCES COUCHES D'OXYDE DE ZIRCONIUM

L'article précédent traitait de la formation de minces couches d'oxyde de zirconium par voie électrolytique. Cet article-ci traite de l'écoulement d'électrons et de courants photo-électriques produits par l'application de champs électrostatiques à travers ces couches.

Quand les champs sont insuffisants pour produire un échappement ionique appréciable, un courant électronique i_- est observé, il dépend de l'intensité du champ F:

$$i_- = 2A_- \sinh B_-F,$$

où A_- et B_- varient avec la température suivant les expressions,

$$A_- = A_0 \exp\left(-U/kT\right), \quad B_- = ae/kT.$$

L'interprétation physique de ce phénomène est, que le champ appliqué aide les électrons à surmonter une barrière énergétique de hauteur U et de demi-largeur a. Les valeurs déduites pour U et a sont 0,375 e.v. et 3,6Å respectivement. Un phénomène de vieillissement a aussi été constaté; une couche d'oxyde maintenue sous une différence de potentiel pour de longues périodes, montre une nette réduction dans la valeur de A_0. Les causes possibles de ce vieillissement sont discutées. Des courants photo-électriques sont observés à travers la couche, quand de la lumière ultra-violette tombe dessus. La relation entre le courant photo-électrique i_p et le champ F est semblable à celle qu'on observe pour le courant électronique, mais avec des valeurs différentes des constantes: $U = 0,15$ e.v., et $a = 2$Å. Dans le cas des courants photo-électriques, le vieillissement n'a pas été constaté.

ELEKTRONEN UND PHOTOSTRÖME IN DÜNNEN ZIRKONOXYDFILMEN

In der vorhergehenden Arbeit wurde die Bildung von Oxydschichten auf Zirkon durch elektrolytische Prozesse diskutiert. Die vorliegende Arbeit behandelt Elektronen- und photoelektrische Ströme die auftreten, wenn elektrostatische Felder an den auf Zirkon elektrolytisch gebildeten Oxydfilm angelegt wird.

Bei Feldstärken, die nicht gross genug sind um einen messbaren Ionenstrom hervorzurufen, wird ein Elektronenstrom i_- beobachtet, der von der Feldstärke F abhängt:

$$i_- = 2A_- \sinh B_-F,$$

wobei A_- und B_- von der Temperatur abhängen,

$$A_- = A_0 \exp\left(-U/kT\right), \quad B_- = ae/kT.$$

Die physikalische Deutung dieser Erscheinung ist, dass das äussere Feld den Elektronen hilft, eine Energieschwelle der Höhe U und der Halbwertsbreite a zu überwinden. Die für U und a entnommenen Werte sind $U = -0,375$ e.V. und $a = -3.6$Å. Ein Alterungsphänomen wird beobachtet, wobei ein Oxydfilm, der über lange Zeiten unter Spannung gehalten wird, eine deutliche Verringerung des Wertes von A_0 zeigt. Mögliche Gründe für das Auftreten dieser Alterungserscheinung werden diskutiert. Photoströme werden beobachtet, wenn ultraviolettes Licht auf diese Filme fällt. Die Beziehung zwischen dem Photostrom i_p und dem Feld F sind der des Elektronen (dunkel)stroms ähnlich, haben jedoch andere Werte der Konstanten: $U = 0,15$ e.V., $a = 2$Å. Im Fall der Photoströme wurde keine Alterung beobachtet.

Introduction

In a previous report [1] it was shown that when aluminium is anodised in suitable electrolytes (e.g., ammonium borate) thin insulating layers are formed. At voltages close to the formation voltage the current flowing through these films consists largely of ions, which cause the film to grow. At lower voltages V across the film the current is mainly electronic in character, and no film growth occurs. The relationship between electron current i_- and field F across the film obeys the relationship

$$i_- = 2A_- \sinh B_-F = 2A_- \sinh B_-V/\delta = 2A_- \sinh V/V_0,$$

where A_- and B_- are parameters depending on the

*Received December 22, 1952.

†Atomic Energy Research Establishment, Harwell, England.

temperature, δ is the film thickness, and V_0 equals δ/B_-. The formula may be derived from a physical model in which the field F is necessary to enable electrons to surmount a barrier (of height U and half width a) opposing the motion of electrons through the film. Then it can be shown that

$$A_- = A_0 \exp(-U/kT),$$
$$B_- = ae/kT,$$

A_0 being a constant independent of temperature.

This relationship has been studied in greater detail in the case of oxide layers on zirconium. The phenomena associated with the ageing of the specimen are also investigated. The technique of film formation and the study of oxide growth are discussed elsewhere.

When ultra-violet light is incident on the oxide, increased electron currents flow. These photoelectric currents are also studied in this paper.

Electron Current at Room Temperature

For a number of specimens the current flowing through the films at room temperature has been measured as a function of applied voltage across the electrolytic cell. Since the resistance of the ammonium borate electrolyte is small compared with that of the oxide film, the same voltage is also applied across the film, apart from any potential drops at the various surfaces. For the higher voltages and thicker films these may be neglected.

Provided the applied voltage V is less than about 90 per cent of the formation voltage, the current i consists almost entirely of electrons. This can be shown to be true if the constants in the formulae relating ionic and electronic currents to field strength are known, but can in any case be verified directly since measurements of capacity before and after a series of electron current measurements indicate that the film has not grown in thickness.

The values of A_-, B_- are determined by plotting i against V on log-log paper and comparing the curve obtained with a plot of y against x (where $y = \sinh x$) on the same scale. This latter curve is characterized by a linear portion of unit slope for $x < 0.8$ and a rapidly increasing slope for higher values. Thus a direct and fairly accurate determination of the constants A_-, V_0 is possible, V_0 being equal to δ/B_-.

The film thickness δ itself is determined from measurements of the capacity of the oxide film. In the following tables it is assumed that the dielectric constant ϵ of the oxide layer is 20.

Table I shows typical sets of results for two specimens. The value of B_- is unaffected by errors in the area of the specimen; A_- is directly affected by such errors, but this error is quite negligible when compared with the other factor involved, namely the age of the specimen. If measurements are taken immediately after formation of a specimen, high values of A_- are obtained. If the specimen is allowed to age, i.e. to stand for some time at formation voltage, A_- decreases rapidly. This effect is not due to the increased film thickness which occurs during ageing since this increase is small (of the order of 10 per cent) and is taken into account in the measurement of the capacity. In any case, errors in film thickness do not affect A_-, but alter the value of B_-.

TABLE I

ELECTRON CURRENT AS A FUNCTION OF FIELD
($i_- = 2A_- \sinh B_-F$; temperature 18°C)

Specimen	V_f (volts)	i_f (μa/cm)	Age from formation minutes	$2A_-$ (μa/cm²)	$1/B_-$ 10^6 volts/cm
Z14	10.25	3	3000	0.08	0.75
(surface	24.5	17	110	0.1	0.8
area 50 cm² nominal)	{50.5	96	9	1.4	1.05
	50.5	2	1093	0.1	0.8
	100	18	167	0.46	1.0
	250	26	1000	2.6	1.0
Z5	70	5	well aged	0.03	0.8
(Surface	170	200?	new	0.13	0.75
area 9.1 cm² nominal)		100	during formation	0.1	0.8

V_f = formation voltage i_f = current at formation voltage

The age of the specimen can also be represented by the value of the current i_f measured at the formation voltage. When a specimen is allowed to age the formation current decreases with time. This is in part due to the decrease in ion current i_+ which is included in the total current i_f, and which varies rapidly with the applied field. At constant formation voltage V_f the film thickness increases slightly with age, and the small resultant decrease in field F_f has a considerable effect on i_+ and hence on i_f $(= i_+ + i_-)$. The electron current i_- is less affected by the small change in F_f, so that for an aged specimen the total current is mainly electronic, even at formation voltage. This decrease in i_f with time is shown in Table I (50.5 volts).

The cause of the ageing of oxide films has not yet been determined. It cannot be due to space charges building up in the film, since an aged specimen retains this characteristic even when allowed to stand for days without any applied voltage. It

would appear to arise from changes in the structure of the film, imperfections occurring during the initial growth of the film being annealed out.

The differences between the B_- values for Z14 and Z5 may arise in part from the difference between the true and nominal surface areas for these two specimens. No attempt has been made to correct the results for this difference, which is unknown. There is a slight change in B_- with V_f, but this is not significant, since it is possible to obtain values of B_- more nearly equal without greatly altering the goodness of fit with the sinh curve.

Figure 1 shows the effect of formation voltage V_f and specimen age on the relationship between electron current and voltage. The curves are computed sinh curves, while the digits represent observed values. The values of A_- and B_- corresponding to these curves are given in Table II.

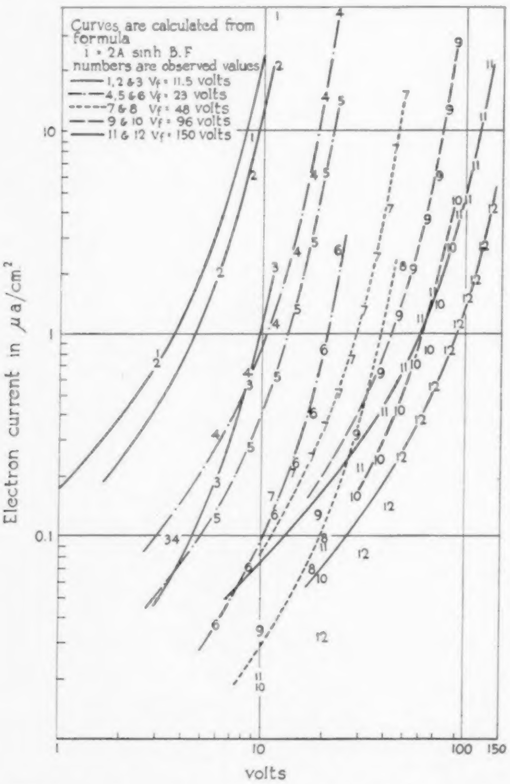

FIGURE 1. Electron current as a function of applied voltage and film age (see Table II).

Except for very thin films, corresponding to a formation voltage V_f of about 10 volts, A_- and B_- are independent of V_f. For very thin films the potential drop elsewhere than across the oxide layer may form an appreciable part of the total. It is of interest that similar deviations for the thinnest films are observed in the product $C_0\ V_f$, and in the work on photocurrents described below. This potential drop may arise at any of the interfaces present in the electrolyte cell. Another possibility is that minute surface irregularities or corrugations are present on the surface of the metal. If these are of the order of 10–100 Å in height, the true surface area will be greater for thin films than for thick ones. The measured value of the capacity will then be higher for such thin films, leading to a high value of $C_0\ V_f$, a low value for δ, a high value for the field F and for $1/B_-$ as well as a low value for the initial formation rate. All these are in fact observed.

TABLE II

ELECTRON CURRENT AS A FUNCTION OF FILM AGE AND FIELD ($i_- = 2A_- \sinh B_-F$; specimen Z22; nominal area 10 cm²; 18°C)

V_f (volts)	i_f (μa/cm²)	C_0 (μF/cm²)	Age since formation (approx.)	$2A_-$ (μa/cm²)	$1/B_-$ (10^6 volts/cm)
11.5	40	0.868	10 min.	0.34	1.0
	20	0.81	30 min.	0.22	0.94
	1.8	0.656	16.5 hrs.	0.028	0.85
23	50	0.417	12 min.	.11	0.9
	15	0.36	80 min.	.06	0.8
	2.4	0.29	70 hrs.	.02	0.75
48	20	0.166	90 min.	.052	0.75
	2.9	0.140	15 hrs.	.018	0.7
96	30	.0835	20 min.	.12	0.7
	6	.0725	15.5 hrs.	.06	0.7
150	60	.0535	45 min.	.19	0.75
	9.3	.046	18 hrs?	.1	0.75

At very low currents ($\ll 1\mu$a/cm²) hysteresis effects appear; the electron current depends not only on the applied field, but to some extent on the previous history of the specimen. The electron current will be different depending on whether the field was lower or higher previously. This effect is ascribed to the formation of space charges within the oxide layer, or at its surface.

Effect of Temperature on the Electron Current

At constant field strength the electron current rises rapidly with temperature. Figure 2 shows this rise for a specimen of thickness 2700 Å (from capacity measurements, assuming ϵ equal to 20) and under a constant potential difference of 54.5 volts. The mean field throughout the film is 2.0×10^6 volts/cm, which is well below the field required to produce appreciable ionic flow. The current through the film can be represented by the empirical formula

$$i_- = i_0 \exp\ (-W/kT),$$

where $i_0 = 5$ amps/cm², $W = 0.46$ e.v.

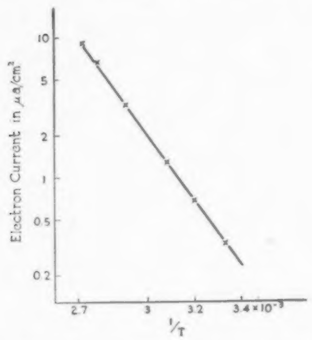

FIGURE 2. Electron current as a function of temperature, measured at a field strength of 2.0×10^6 volts/cm.

Figure 3 shows that the variation of electron current with applied fields obeys the sinh function closely over a range of temperature. The equation for electron current can be written

$$i_- = 2A_- \sinh B_- F = 2A_- \sinh V/V_0$$

$$2A_- = 2A_0 \exp(-U/kT), \quad V_0 = \delta/B_- = \delta kT/ae$$

where U represents the barrier height, and a the barrier half-width opposing the flow of electrons through the film.

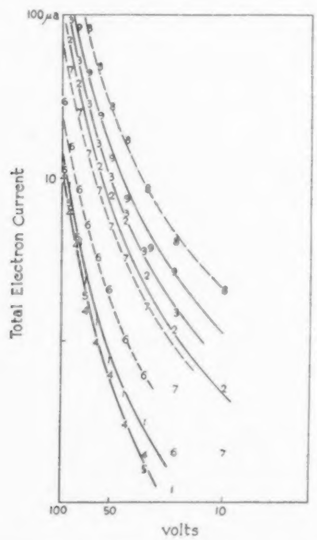

FIGURE 3. Electron current as a function of applied voltage at various temperatures (see Table II). Curves are computed from sinh formula; digits are observed values.

Run	Temp.	Run	Temp.	Run	Temp.
4, 5	4°C	2, 7	60°C	8	100°C
1	19.5°C	3	80°C		
6	40°C	9	90°C		

The values of A_-, V_0, $1/B_-$ and of k/ae for best fit of each curve are given in Table III. The variation of A_- with temperature, shown in Figure 4 obeys the required equation, with $2A_0$ equal to 0.033 amps/cm², and U equal to 0.375 e.v. No account has been taken of ageing since all readings were taken shortly after formation, and the variation of A_- with age is small compared with the change due to temperature.

The quantity $V_0/\delta T$ shown in the last columns should not vary with temperature if a is constant. In fact a small variation is observed, of the order of 10 or 20 per cent. In view of the wide variation in A_- (a range of over 70 to 1) it is doubtful whether this is significant. Differences in the value of V_0/δ ($= 1/B$) for different specimens are most probably due to errors caused by taking the true surface area as equal to the nominal or geometrical surface

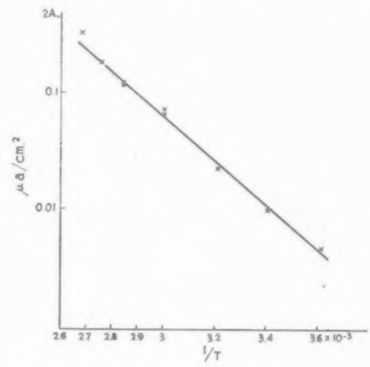

FIGURE 4. Electron current; variation of parameter A_- with temperature. $A_- = A_0 \exp(-U/kT)$, $U = 0.375$ e.v., $2A_0 = 3.3 \times 10^4$ μa/cm.²

area. These errors are directly reflected in a corresponding change in B_-.

If $V_0/\delta = 0.7 \times 10^6$ at 20°C, $a = 3.6$ Å; a represents the half-width of the potential barrier opposing the flow of electrons so that these values, which are of the order of inter-atomic distances, are very reasonable. This conclusion is rendered more convincing when it is remembered that at no stage have molecular distances been introduced, all measurements of capacity, current, and voltage being of a macroscopic character. The barrier height (0.375 e.v.) also appears reasonable.

TABLE III

EFFECT OF TEMPERATURE ON ELECTRON CURRENT
($i_- = 2A_- \sinh V/V_0$; specimen Z23; nominal surface area 11 cm²)

Run	T °C	$2A_-$ (μa/cm²)	V_0 (volts)	δ(Å)	$V_0/\delta = 1/B_-$ (10^6 volts/cm)	$V_0/\delta T = k/ae$ (10^3volts/cm°C)
4,5	4	0.0045	16	2700	0.59	2.1
1	19.5	0.01	18	2550	0.71	2.4
6	40	0.023	19	2800	0.68	2.2
2	60	0.073	18	2600	0.69	2.1
7	60	0.068	19	2800	0.68	2.0
3	80	0.12	19	2650	0.71	2.0
9	90	0.18	19	2800	0.68	1.9
8	100	0.33	19	2800	0.68	1.8

Effect of Surface Impurities on the Electron Current

Attempts were made to discover whether the electron currents are related in any way to the presence of impurities on the surface of either the metal or the oxide. The major impurities in the zirconium used were hafnium, carbon, and iron. The effect on the formation rate, the capacity, and on the electron current was observed of increasing the amount of carbon by a large factor. To avoid introducing differences in surface structure or polishing technique adjacent parts of the same specimen were used.

A specimen was polished with emery down to 0000, metal polish, washed in ether, acetone, and three times in distilled water. An area of 0.5 cm^2 in the middle of the specimen was marked with a graphite pencil. The area (5.4 cm^2) of the lower third of the specimen (α) was uncoated, that of the middle third (β) (5.4 cm^2) contained the graphited surface. The top third was not used. Table IV shows that the presence of graphite on the surface has no noticeable effect on the electron current.

TABLE IV

EFFECT OF SURFACE CONTAMINATION ON ELECTRON CURRENT (Specimen Z27)

	α	$\alpha + \beta$	β	Units
Formation rate (at 2ma/cm^2)	9	—	9	$\frac{\text{volt}}{\text{min}}$ per $\frac{\text{ma}}{\text{cm}^2}$
Electron current at voltage of				
60	1000	2000	1000	μa/cm^2
50.5	240	400	160	
40.2	98	160	62	
30.1	47	90	43	
20	20	46	26	
10	6	20	14	

An area of 1 cm^2 of the oxide film was coated with graphite after formation. This produced no effect on the electron current.

In a second experiment three strips of the same specimens were used. One was uncoated, the other graphited with a pencil, and the third painted with aquadag. The formation rate and capacity were measured, the latter at two formation currents. A complete set of electron current/voltage curves for newly formed ($i_f = 0.45$ ma/cm^2) and older ($i_f \sim 0.18$ ma/cm^2) films were also obtained. These fitted the sinh curve formula in all cases, with similar values of B_-.

TABLE V

EFFECT OF GRAPHITE ON FORMATION RATE AND ON ELECTRON CURRENT (Specimen Z31)

	Ungraphited	Graphited 1 cm^2	Aquadag 1 cm^2	Units
Surface area	5.5	5	5.5	cm^2
Formation rate	7	6.5	7.1	$\frac{\text{volt}}{\text{min}} / \frac{\text{ma}}{\text{cm}^2}$
at i_f	900	1000	900	μa/cm^2
$C_0 V_f$	10.4	10.4	10.4	μF volt/cm^2
at i_f	450	400	400	μa/cm^2
δ =	1760	1760	1800	Å
Electron current parameters				
A_- =	0.4	0.4–0.35	0.25–0.35	μa/cm^2
V_0 =	15	15	15	volts
$V_0/\delta = 1/B_-$	0.88×10^6	0.88×10^6	0.88×10^6	volts/cm
$C_0 V_f$	8.55	8.8	8.7	μF volt/cm^2
at i_f	180	150	180	μa/cm^2
δ =	2160	2100	2130	Å
Electron current				
A_- =	0.24	0.2	0.2	μa/cm^2
V_0 =	17	17	17	volts
$V_0/\delta = 1/B_-$	0.81×10^6	0.81×10^6	0.81×10^6	volts/cm

Table V shows that there was no significant difference between any of these specimens in spite of the enormous range in surface impurities.

After formation, the graphite layer was found on the surface of the oxide-layer, from which it could be rubbed off quite readily. The oxide layer growth therefore took place below each granule. It is inferred that surface impurities are not primarily responsible for the electron current. This view is supported by the ageing phenomenon: aged films give a considerably decreased electron current, due to a reduction in A_-, while B_- is unchanged. This would seem to indicate that the electron current is related to imperfections in the oxide layer structure, which gradually anneal out. However the possibility that space charges form, and inhibit electron flow, cannot be ruled out.

Photocurrents Produced by Ultra-Violet Radiation

In the presence of ultra-violet radiation, the electron current through the zirconium oxide film is increased. No changes in colour or capacity take place, so that any ion current arising from this radiation must be negligible.

When ultra-violet radiation is first allowed to fall on a thin film of the oxide, the electron current increases immediately (< 1 sec.) to a higher value,

then rises more gradually. If the radiation is removed, the current drops rapidly to a value which is higher than the original "dark" current, then sinks very slowly to its previous value.

The explanation appears to be that ultra-violet radiation produces a photoelectric current i_p, and in addition increases the dark electron current, presumably by reducing the space charges present in the film. In the case of aluminium these space charges produce an electric field opposite to that applied externally, and hence reduce the electron current flowing. The partial destruction of these space charges by ultra-violet radiation therefore results in an increased dark current after the end of exposure until sufficient time has elapsed for the charges to be reconstituted.

Photoelectric Current and Applied Field

Specimen Z22 was formed at a number of voltages, and aged for different periods. The light source consisted of a Mazda stabilised ultra-violet lamp placed at a distance of 17.5 cm. from the specimen. The photoelectric current was taken as the difference between the total current after 10 seconds exposure, and the mean dark current immediately before and after completion of exposure. Figure 5 shows i_p,

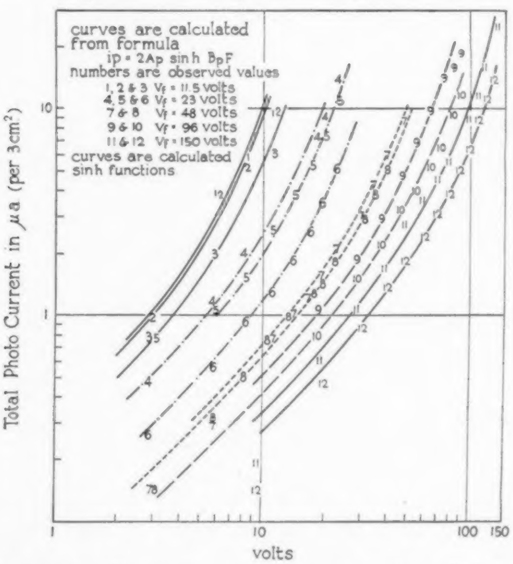

FIGURE 5. Photocurrent as a function of applied field, film thickness, and age (see Table VI).

the photoelectric current, plotted as a function of the applied voltage, compared with the sinh function adjusted for best fit:

$$i_p = 2A_p \sinh B_p F = 2A_p \sinh V/V_p, \; V_p = \delta/B_p.$$

Values of A_p, V_p, and B_p are given in Table VI for films of various thickness and ages. The film thickness δ was deduced from capacity measurements, assuming as before the nominal surface area, and ϵ equal to 20.

TABLE VI

PHOTOCURRENT AS A FUNCTION OF FILM AGE, THICKNESS, AND APPLIED FIELD

Nominal surface of specimen (Z22) = 10 cm²

Surface exposed to ultra-violet radiation = 3 cm²

$$i_p = i_{\text{total}} - i_{\text{dark}}$$

$$i_p = 2A_p \sinh V/V_p = 2A_p \sinh B_p F$$

V_f (volts)	Run number	i_f (μa/cm²)	Age	δ (Å)	V_p (volts)	$2A_p$ (μa/3 cm²)	$1/B_p = V_p/\delta$ (10^6 volt/cm)
11.5	1	40	10 min.	205	3.4	1.1	1.66
	2	20	30 min.	219	3.6	1.1	1.64
	3	1.8	16½ hrs.	270	4.2	1.0	1.56
23	4	50	12 min.	425	6.6	1.1	1.55
	5	15	1.3 hrs.	495	7.3	1.1	1.47
	6	2.4	70.5 hrs.	585	10	1.0	1.71
48	7	20	90 min.	1070	16	1.05	1.71
	8	2.9	14 hrs.	1270	17.5	1.05	1.37
96	9	30	20 min.	2140	22	1.1	1.02
	10	6	15.6 hrs.	2420	26.5	1.1	1.10
150	11	60	45 min.	3350	33	1.1	1.07
	12	9.3	18 hrs.	3880	40	1.1	1.03

Except for the thinnest films, newly formed films (e.g. run 1) and the lowest currents (< 0.1 μa/cm²) the agreement with the sinh function is good. The discrepancy in the case of the thinnest films agrees with similar discrepancies observed for ion and electron currents, when the formation voltage is of the order of 10 volts or less, and is probably in part due to erroneous values of δ deduced from the capacity measurements. The departure from the sinh curve at low photoelectric currents, while not certain, could readily arise from the slow destruction of the space charges in the film by the ultra-violet light. These space charges are sufficiently great to give currents comparable with those measured; moreover, the time to reach equilibrium at low fields and currents is quite considerable (of the order of minutes), so that equilibrium may not have been reached.

The coefficient $2A_p$ is seen to be independent of formation voltage or film thickness, as for the electron current. Unlike the latter it is also independent of film age.

The coefficient B_p is also independent of film age but shows an appreciable increase with film thickness, the increase being about 60 per cent for a range in film thickness of about 20 times. The reason for this increase is not clear. It cannot be due to absorption of the ultra-violet, since this would affect

A_p rather than B_p. The value of B_p is obviously different from B_-, which is obtained from measurements of the dark electron current.

Effect of Temperature on the Photocurrent

Figure 6 shows that the photocurrent at a given field is affected by temperature, though to a much lesser extent than is the electron current. Table VII gives the values of A_p, V_p, and B_p for the sinh curves shown in this figure.

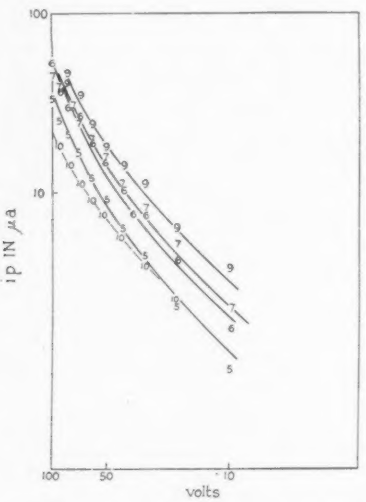

FIGURE 6. Effect of temperature on photocurrent i_p. Curves are computed from sinh formula; digits are observed values: 10 at 0°C, 5 at 4°C, 6 at 40°C, 7 at 60°C, 9 at 90°C.

TABLE VII

EFFECT OF TEMPERATURE ON PHOTOCURRENT

$i_p = 2A_p \sinh B_p F = 2A_p \sinh V/V_p$

Specimen Z23 formed at 100 volts, 3 days

Nominal area 11.8 cm²: distance from ultra-violet lamp 10 cm.

T (°C)	V_p (volts)	$2A_p$ μa/3 cm²	δ (Å)	V_p/δ (10^6 volts/cm)	$V_p/\delta T$ (10^3 volts/cm °C)
4	33	3.8	2700	1.23	4.4
40	37	7.3	2800	1.32	4.2
60	40	9.0	2800	1.43	4.3
90	43	13.0	2800	1.53	4.2

The quantity $V_p/\delta T$ is independent of temperature. By analogy with the electron current it can be put equal to k/ae. If $V_p/\delta T = 4.3 \times 10^3$, $a = 2$Å. This distance is different from that for the dark electronic current, but is again of atomic or electron orbital size.

The coefficient A_p is found to vary with temperature, but to a much less marked extent than for the dark current. It can be represented by the equation

$$2A_p = 2A_{p0} \exp\left(-U_p/kT\right),$$

$$A_{p0} \sim 700\ \mu\text{a/cm}^2, \quad U_p \sim 0.15\ \text{e.v.}$$

Conclusions

The electron current i_- observed in thin oxide layers on zirconium depends on the average field F through the film

$$i_- = 2A_- \sinh B_- F.$$

The results obtained are consistent with a theory that the effect of the field is to assist electrons to move over a barrier which opposes their motion. If U_- and a_- represent the dimensions of this barrier, the theoretical formula for electron flow is as follows:

$$i_- = 2A_0\,(-U/kT)\sinh\,(aeF/kT).$$

The observed results give values for U and a of 0.375 e.v. and 3.6 Å. The quantity A_0 varies markedly with film age, and this tends to show that the electron current is associated with film imperfections which heal with time. Experiments with graphite on the oxide surface indicate that the electron current is not primarily due to impurities in the film.

Photocurrents are observed when the oxide layer is exposed to ultra-violet light. These may be due in part to the destruction of some space charges in the film. These currents were not found to promote film growth and must therefore be electronic in character. Their variation with field strength is similar to that for the (dark) electron current. The constants U and a are different however: 0.15 e.v. and 2.0 Å. Film age has no effect on the photocurrent, which cannot therefore be due to the healing of lattice imperfections, but must be intrinsic to the oxide structure.

Acknowledgements

Acknowledgements are due to the Director A.E.R.E., for permission to publish the results of this investigation. The author wishes to record his appreciation of the interest shown by Dr. H. M. Finniston, Head of the Metallurgy Division, A.E.R.E. Thanks are also due to Mr. A. H. Tilsley, B.Sc., and Mr. Neale for assistance in much of the experimental work.

References

1. CHARLESBY, A. Proc. Phys. Soc. London, **B66** (1953) 317.
2. CHARLESBY, A. Acta Met., **1** (1953)340.

ON THE POROSITY OBSERVED IN THE KIRKENDALL EFFECT*

F. SEITZ†

An attempt is made to interpret the formation of voids in the Kirkendall experiment in terms of preceding analyses of vacancy diffusion. In particular, use is made of the viewpoint that the presence of voids is related to a super-concentration of vacancies in some region of the diffusion zone. It is pointed out that the expressions obtained for the vacancy current in preceding papers permit the derivation of relations governing the superconcentration, when amplified with the introduction of appropriate concepts and parameters. It is concluded that the maximum excess concentration of vacancies is achieved in one edge of the diffusion zone when the time required for a vacancy to drift through this zone is equal to the lifetime of the vacancy and that the superconcentration of vacancies could achieve values of about 2 in the cases in which void formation has been observed, if earlier formation of voids actually does not limit the attainable supersaturation. Studies of the formation of voids in a number of couples, such as Cu-Ni, Cu-Zn, Cu-Al and Ag-Au make it possible, with suitable assumptions, to estimate the lifetime of a vacancy in this system. A value of about 10^{11} jumps is obtained if it is assumed that the observed voids are able to grow only when the superconcentration is near the maximum

SUR LA POROSITÉ OBSERVÉE DANS L'EFFET KIRKENDALL

Une tentative est faite, d'interpréter la formation des vides dans l'expérience de Kirkendall, en termes des analyses précédentes de la diffusion des lacunes réticulaires. Il est fait usage, plus particulièrement, du point de vue, que la présence des vides est en rapport avec la surconcentration des lacunes dans une certaine région de la zone de diffusion. Il est signalé, que les expressions obtenues pour un courant de lacunes, dans les articles précédents, permettent, quand on y introduit les concepts et paramètres appropriés, de dériver les relations qui régissent la surconcentration. Il est conclu, que l'excès maximum de la concentration est atteint dans une lisière de la zone de diffusion, quand le temps nécessaire à une lacune pour traverser cette zone est égal à la durée de vie de la lacune, et que la surconcentration de lacunes pouvait atteindre des valeurs d'environ 2 dans les cas où la formation des vides a été observée, pour autant que les vides formés antérieurement ne limitent pas la sursaturation qu'il est possible d'atteindre. Des études faites sur la formation des vides dans de nombreux couples, tels que Cu-Ni, Cu-Zn, Cu-Al et Ag-Au, permettent, en admettant certaines hypothèses, d'évaluer la durée de vie d'une lacune dans ce système. Une valeur d'environ 10^{11} sauts est obtenue, si on admet, que les vides observés peuvent augmenter seulement quand la surconcentration se rapproche de sa valeur maximum.

ÜBER DIE IM KIRKENDALL-EFFEKT BEOBACHTETE POROSITÄT

Es wird versucht, die Bildung von Löchern in Kirkendall-Versuchen mit Hilfe einer früher veröffentlichten Analyse der Diffusion von Leerstellen zu erklären. Dabei wird im einzelnen der Gesichtspunkt zu Grunde gelegt, dass das Vorhandensein von Löchern mit einer übergrossen Konzentration (Superkonzentration) von Leerstellen in gewissen Gebieten der Diffusionszone verknüpft ist. Es wird darauf hingewiesen, dass die Gleichungen, die in früheren Arbeiten für den Leerstellenstrom abgeleitet wurden, die Ableitung von Beziehungen, die der Superkonzentration zu Grunde liegen, gestatten, wenn die geeigneten Variablen und die notwendigen Definitionen eingeführt werden. Es ergibt sich, dass die maximale Überschusskonzentration der Leerstellen an einer Kante der Diffusionszone auftreten kann, wenn die Zeit, die eine Leerstelle braucht um durch diese Zone zu diffundieren, gleich der Lebensdauer der Leerstelle ist. Ausserdem zeigt sich, dass die Superkonzentration von Leerstellen in Fällen, in denen die Bildung von Löchern experimentell beobachtet wurde, Werte von etwa zwei erreichen könnte, falls die vorhergehende Bildung von Löchern die tatsächlich erreichbare Superkonzentration nicht begrenzt. Untersuchung der Lochbildung an einer Anzahl von Metallpaaren wie Cu-Ni, Cu-Zss, Cu-Al, und Aq-Au ermöglichen es, unter geeigneten Annahmen die Lebensdauer einer Leerstelle in diesem System abzuschätzen. Man erhält einen Wert von 10^{11} Platzwechseln, wenn man annimmt, dass die beobachteten Löcher nur wenn die Superkonzentration in der Nähe ihres Maximalwertes ist, wachsen können.

VOL. 1 1953

1. Introduction

The Kirkendall experiment has focussed new attention on the mechanism of diffusion in metallic systems. Since 1947, when Smigelskas and Kirkendall [1] first presented their results for diffusion in the copper-zinc system, a number of investigators, most notably Correa da Silva and Mehl [2], Alexander, Balluffi, Kuczynski and their associates at the Sylvania Electric Laboratory [3], Barnes [4], Bückle and Blin [5], and Seith and Kottman [6], have confirmed and amplified the original measurements. There is now no longer doubt that a marker shift occurs in many diffusion couples involving the face-centered cubic metals and that the factors producing this marker shift are a general feature of the mechanism of diffusion. It also seems to be generally established [3, 4] by all of the investigators that in certain couples, such as Cu-Zn, Cu-Ni, Ag-Au, porosity always develops on one side of the original interface when the Kirkendall shift occurs. Correa da Silva and Mehl suggested that the porosity might be a feature of individual couples or

*Received January 30, 1953.
†Department of Physics, University of Illinois, Urbana, U.S.A.

specimens. However, the work of the other investigators in the intervening period has indicated fairly conclusively that the porosity observed by Smigelskas and Kirkendall probably is a general phenomenon which must be regarded as an essential part of the diffusion process. Indeed, Barnes, who studied diffusion in the copper-nickel system, found that the volume of the pores is a substantial fraction of the volume in the Kirkendall shift. This shift would be approximately doubled in his specimens if the pores were to collapse. The present paper will be devoted to the factors which influence this porosity.

The essential historical facts concerning the theory of the Kirkendall effect are as follows:

1. Darken [7] first proposed a purely macroscopic formalism to explain the results. He suggested that each constituent atom, say A and B, in the couple must be given its own characteristic diffusion coefficient, D_a and D_b, with the auxiliary restriction that if an excess of atoms diffuse into or out of a given volume of the lattice, the volume would expand or contract in order to preserve the equilibrium atomic density of the alloy having composition corresponding to the constituents of the volume. This formalism leads to the Kirkendall shift whenever D_a and D_b differ. Still further, Darken showed that under his assumptions the chemical diffusion coefficient D_c is given by the relation

$$D_c = f_b D_a + f_a D_b \tag{1}$$

where f_a and f_b are the atomic fractions of A and B atoms in the volume. Porosity plays no role in Darken's formalism, since it is assumed that the lattice will swell or shrink in such a way as to maintain the equilibrium density.

2. The writer [8] made a first attempt at an atomic interpretation of the Kirkendall effect using vacancy theory and the assumption that a given vacancy would have different probabilities of interchanging places with an A atom and with a B atom. This theoretical treatment, which contained very general assumptions and which was initiated in order to shed light on Johnson's experiments [9] concerning the chemical and radioactive diffusion coefficients in the silver-gold system, treated the variable which describes vacancy density in the system as a disposable function to be determined by separate reasoning. The writer focussed attention on the special case in which the vacancy current I_v is constant in space throughout the diffusion zone and varies with time as $1/\sqrt{t}$, as if this current arose from the diffusion of vacancies between two reservoirs whose dimensions are large compared to the dimensions of the diffusion zone. This assumption concerning the vacancy current does not lead to Darken's equations, although it did give a qualitative interpretation of the knowledge concerning the Kirkendall effect which existed at the time.

3. Bardeen [10] then demonstrated that Darken's equations can be derived with the use of vacancy theory if one assumes that there is a sufficient density of sources and sinks of vacancies throughout the diffusion zone to maintain the equilibrium concentration of vacancies over regions small compared with the dimensions of the diffusion zone. This analysis was based on the use of a very simple model of the diffusing system.

4. The writer [11] subsequently showed, first, that his general equations contain Bardeen's solution as a special case of a family of solutions obtained when the density of vacancies has the equilibrium value at each position, and, second, that Darken's equations also follow if diffusion occurs by the interstitial mechanism. In fact, there is a very close parallel between the equations derived from vacancy and interstitial diffusion. Thus, as intuition indicates, the validity of Darken's equations does not allow one to distinguish between interstitial and vacancy diffusion.

5. Bardeen and Herring [12] summarized the existing situation in a review article prepared in the fall of 1950. They placed emphasis upon the hope, gained from available experiments, that one might expect to have the vacancy distribution at equilibrium in most typical systems, so that the behavior of a diffusion couple would generally be amenable to the regularities implied in Darken's equations. They stressed the fact that this would require that the lifetime of vacancies be limited, and placed an upper limit of 10^9 jumps as the desired maximum for practical obedience to Darken's relation. They felt, in turn, that this was a feasible upper limit in view of the fact that of the order of one atom in 10^7 is believed to be near the center of a dislocation line in typical materials. The apparently universal appearance of porosity whenever the Kirkendall effect is strong compels us to re-examine the basis of this viewpoint.

It is natural to suppose that the pitting observed during diffusion arises as the result of a large deviation from the equilibrium density of imperfections—a superconcentration of vacancies or a subnormal concentration of interstitial atoms. Presumably the ideal sources for vacant lattice sites or interstitial atoms within single crystals are jogs on long dislocations with edge components. These can act as

sources or sinks with the equilibrium energy. Such sites, along with grain boundaries in polycrystalline specimens, will act as sinks for vacancies or sources for interstitial atoms even when there are small deviations from the equilibrium concentrations. Naturally they may also act when the deviations from equilibrium are large. There is no good reason why voids should form when long edge dislocations act as sinks for vacancies or sources for interstitial atoms if the density is very close to equilibrium since the consequent "climbing" of dislocations should be compensated by continuous contraction of the specimen.

Small voids, cracks, or inclusions may act as sinks for vacancies or sources for interstitial atoms, and produce large voids when an appropriate supersaturation of the former or subnormal concentration of the latter is present. In the simple case in which the initial voids are spheres of radius r, the excess concentration of vacancies, N_v, needed to make them grow is given by the Thomson-Gibbs relation [13]

$$\ln \frac{N_v}{N_{vo}} = \frac{2s}{kTNr}$$

where N_{vo} is the equilibrium value of the vacancy density, s is the surface energy per unit area, k is Boltzmann's constant, T is the absolute temperature, and N is the atomic density. The nuclei of these voids may be occupied with foreign material and hence preserved under equilibrium conditions. In typical cases, vacancies will condense at spherical voids containing the volume equivalent to about 1,000 vacant lattice sites if N_v/N_{vo} is in the vicinity of 2, or greater.

Vacancies may condense to form voids in the perfect crystal if N_v/N_{vo} is of the order of 100, or greater. In the case of the interstitial mechanism, voids may be produced in the perfect lattice by the generation of interstitial atoms if the density of interstitials is at least 100 times below normal.

When N_v/N_{vo} is very near to unity, the Thompson-Gibbs relation may be written

$$R \cong \frac{2s}{kTNr} \qquad (R \ll 1)$$

where $R = (N_v/N_{vo}) - 1$ is the *relative excess concentration*.

At the present time we do not know enough about the nuclei on which the voids form to give effective values of r that may be associated with them. Or, expressed in another way, we do not know the critical value R_c of the relative excess concentration R needed to cause these nuclei to accumulate vacancies and grow into pores. Evidence bearing on this point will be discussed in Section IV. In general it appears that the effective value of r may vary from one specimen to another, depending upon the history of the specimen, as well as from one nucleus to another in the same specimen. That is, there appears to be considerable heterogeneity in the nuclei responsible for pores in the various substances in which porosity has been observed to date. It will be demonstrated, in the next section, that values of the excess relative concentration R in the neighborhood of unity are possible in typical materials showing the Kirkendall shift, at an appropriate phase in the diffusion cycle. Since this possibility exists, particular attention will be devoted to the case in which values of R of the order of unity are necessary to form pores. This would be the case if the nuclei were homogeneous and if the largest radius of curvature of the nuclei was of the order of 10 atomic diameters. Thus if they were spheres they would be small even on the scale of the electron microscope. The specimens of Cu-Ni investigated by Barnes may actually correspond to this limiting state of affairs. Herring [private communication] has stressed the point of view that the nuclei responsible for the porosity observed in connection with the Kirkendall effect in many materials may operate for values of R much smaller than unity, of the order of 1 per cent or even less. This is equivalent to assuming that the corresponding effective values of r are of the order of 1,000 atomic distances, or possibly larger. There is evidence, discussed at least partly in Section IV, to support this point of view. What is most likely is that there is a distribution in range of the effective values of r and that at least a portion of the pores observed form on nuclei for which r is in the vicinity of 1,000 atomic distances. On the other hand it is by no means certain that such nuclei are dominant in all materials. The issue must apparently be settled by further experiment. Unfortunately it is not a trivial one, for, as we shall see, the following analysis makes it possible to obtain estimates of the mean number of jumps vacancies make between source and sink, provided one assumes values of the excess concentration needed to condense vacancies. The results are sensitive to the value of R_c that is assumed necessary in order to generate pores.

II. Formal Concepts

For simplicity, we shall assume that diffusion occurs primarily by the vacancy process. The known

experimental facts do not seem to permit a distinction between the vacancy and interstitial mechanisms at the present time; however, the theoretical analyses make the former seem much more likely. In addition, the qualitative consequences apparently would be identical in the two cases as far as matters of interest in the present discussion are concerned.

The writer [9, 11] has shown that a formal approach to the discussion of vacancy diffusion can be made by introduction of the quantities $\pi_a(n_1, n_2)$ and $\pi_b(n_1, n_2)$ which represent the probabilities per unit time that a vacancy in one plane normal to the concentration gradient, in which the planar density of A atoms is n_1, will jump to the next parallel plane, in which the planar density of A atoms is n_2, in such a way as to interchange places with the A and B atom, respectively. $\pi(n_1, n_2) = \pi_a(n_1, n_2) + \pi_b(n_1, n_2)$ is the total probability for the jump between planes 1 and 2. In terms of these quantities the vacancy current is I_v

$$(2)\quad I_v = -\pi(n_a)\lambda\frac{dn_v}{dx} + n_v\left(-\frac{\partial\pi}{\partial\xi} + \frac{\partial\pi}{\partial\eta}\right)\lambda\frac{dn_a}{dx}$$

in which λ is the interplanar spacing, n_a and n_v are the average planar densities of A atoms and vacancies in a given vicinity, $\pi(n_a)$ is the value of $\pi(n_1, n_2)$ when $n_1 = n_2 = n_a$, and $\partial\pi/\partial\xi$ and $\partial\pi/\partial\eta$ are the derivatives of $\pi(n_1, n_2)$ with respect to n_1 and n_2 evaluated for $n_1 = n_2 = n_a$. It is assumed the concentration gradient is in the x direction. In the following it will be convenient to replace the mean planar densities n_i by the mean volume densities N_i in accordance with the relation

$$(3)\qquad N_i = n_i/\lambda.$$

Similarly, as a convenient shorthand, we shall write

$$(4)\qquad \left(\frac{\partial\pi}{\partial N}\right) \equiv \lambda\left(-\frac{\partial\pi}{\partial\xi} + \frac{\partial\pi}{\partial\eta}\right).$$

Equation (2) then becomes

$$(5)\qquad I_v = -\pi\lambda^2\frac{dN_v}{dx} + N_v\left(\frac{\partial\pi}{\partial N}\right)\lambda^2\frac{dN_a}{dx}.$$

The first term in (5) evidently represents the normal Fick term for the vacancy current associated with the vacancy gradient dN_v/dx, the diffusion coefficient being

$$(6)\qquad D_v = \pi\lambda^2.$$

The second term is the Kirkendall term, for it vanishes when the chemical gradient is absent and evidently describes the ability of the chemical gradient to "pump" vacancies from one portion of the lattice to another. The critical parameter in the Kirkendall term clearly is the quantity (4) for it provides a measure of the anisotropy of the lattice, as far as vacancies are concerned, in a region where a chemical gradient exists. The coefficient of N_v in the second term of (5) namely

$$(7)\qquad v = \left(\frac{\partial\pi}{\partial N}\right)\lambda^2\frac{dN_a}{dx}$$

is the average velocity with which the vacancy is pumped through the gradient.

It is interesting, for the purposes of the following discussion, to consider the case in which $\pi(n_1, n_2)$ has the simple form

$$(8)\qquad \pi(n_1, n_2) = \alpha n_2^{\rho}$$

in which α and ρ are constants. This expression leads to the simple relation

$$(9)\qquad N_a\left(\frac{\partial\pi}{\partial N}\right) = \rho\pi(N_a)$$

so that the parameter ρ provides a somewhat primitive measure of what might be termed the "order" of the Kirkendall effect. The form (8) has more merit than mere mathematical convenience. For example, the case $\rho = 0$ corresponds to the situation in which A and B atoms are identical as far as vacancy migration is concerned. It describes the circumstance in which the jump frequency π is independent of the relative density of A and B atoms in the neighboring planes. Similarly the case $\rho = 1$ represents a situation in which the vacancies strongly prefer to exchange places with A atoms and in which the B atoms merely dilute the A atoms. Finally, the case in which $\rho > 1$ corresponds to a simplified form of the situation in which the vacancies prefer to interchange with A atoms and in which the presence of B atoms has an inhibiting influence upon the rate of interchange of a given vacancy with an A atom in the neighboring plane. Clearly the cases in which $\rho \neq 0$ correspond only schematically to real ones; however they will provide valuable insight in the following. The use of (8) without an added constant term implies that when $\rho \neq 0$ the jump frequency is negligible in the specimen of pure B atoms. This is probably not invariably the case in actual specimens, but is frequently true. For example, it is probably true in CuNi at 1080°C.

It is clear that if N_v maintains the equilibrium value corresponding to the local concentration in each region of the specimen, I_v in (5) will be purely a function of composition. This is one of the condi-

tions on the vacancy diffusion mechanism which is requisite if Darken's equations are to be valid.

In addition to the previous, essentially exact formal relations (2) to (7), it is convenient to introduce the following more approximate, or average relationships:

1. For simplicity, we shall assume that the chemical gradient extends uniformly over the region

$$d = 2\sqrt{(D_c t)} \tag{10}$$

in which D_c is the average chemical diffusion coefficient (see Equation (1)) and t is the time since initiation of the diffusion experiment with plane parallel slabs. Actually, the chemical gradient will be more nearly like a Gaussian function; however, the introduction of the parameter d provides a useful simplification.

In the approximation in which the concentration gradient is treated as uniform over the distance d, the gradient is

$$\frac{dN_a}{dx} = \frac{\Delta N_a}{d} \tag{11}$$

where ΔN_a is the difference in concentration across the entire couple.

2. We shall assume that the sources and sinks for vacancies are distributed throughout the single crystals of which the specimens are composed. Experimental evidence shows that grain boundaries frequently are excellent sources and sinks; however, attention will be focussed on the sources and sinks within the grains which persumably are closely associated with dislocations when the density of vacancies is near to the equilibrium value. If N_t is the density of sinks which may presumably also act as sources and σ_t is the cross section for capture of a wandering vacancy by a sink, the number of jumps a free vacancy makes on the average before being captured is

$$\omega = \frac{1}{N_t\sigma_t\lambda} \tag{12}$$

and the mean time the vacancy is free is

$$T = \frac{1}{\nu N_t\sigma_t\lambda} \tag{13}$$

where ν is the jump frequency, which differs from $\pi(n_a)$ by a constant near unity and may be set equal to this quantity in a semi-quantitative treatment. Among other things, T is the critical relaxation time for establishing the equilibrium density of vacancies in the normal crystal.

3. The average distance Δ which a vacancy may drift in the concentration gradient dN_a/dx under the pumping action of the gradient before being captured at a sink is given by the relation

$$\Delta = vT = \left(\frac{\partial\pi}{\partial N}\right)\lambda^2 \frac{dN_a}{dx}\frac{1}{\nu N_t\sigma_t\lambda}\ . \tag{14}$$

In the approximation in which dN_a/dx is replaced by (11), ν is replaced by $\pi(n_a)$, and the latter is assumed to satisfy the relation (9), (14) becomes

$$\Delta = \rho\frac{\Delta N_a}{N_a}\frac{\lambda}{N_t\sigma_t d} = \rho\frac{\Delta N_a}{N_a}\frac{\lambda^2}{d}\omega\,. \tag{15}$$

As a distance, Δ has direct physical meaning only when it is smaller than or comparable to d. In other cases the calculated value is an important physical parameter of the theory.

4. Consider a group of vacancies which initially are closely spaced and are allowed to migrate in the concentration gradient. Although they migrate with the average velocity (7), they will tend to become dispersed as a result of Brownian motion. We shall have use for the amount of dispersion in travelling distance d and in travelling for a time T.

The mean time for a vacancy to drift a distance d is

$$t_d = \frac{d}{v}\,. \tag{16}$$

The dispersion distance during this time may be expressed by the quantity

$$\begin{aligned} \delta d &= 2\sqrt{D_v t_d} = 2\left[\frac{\pi(n_a)d}{\left(\frac{\partial\pi}{\partial N}\right)\frac{dN_a}{dx}}\right]^{\frac{1}{2}} \\ &\cong 2d\left(\frac{N_a}{\rho\Delta N_a}\right)^{\frac{1}{2}}. \end{aligned} \tag{17}$$

The right-hand expression is valid when the approximations (9) and (11) are used. In this simplified limit, the fractional dispersion $\delta d/d$ has the value $2\sqrt{(N_a/\rho\Delta N_a)}$, which is independent of d and hence of time.

The corresponding dispresion distance $\delta\Delta$ for time T is $2\sqrt{(D_v T)}$ which, using (15), can be expressed in the form

$$\delta\Delta = \delta d\left(\frac{\Delta}{d}\right)^{\frac{1}{2}} = 2\lambda\omega^{\frac{1}{2}}. \tag{18}$$

The quantity $\delta d/d$ will be of considerable interest in the next section. It evidently can be small compared with unity only if ρ is larger than unity and if $N_a/\Delta N_a$ is not too great compared with unity.

It is interesting and useful to estimate the value

of ρ which obtains in the cases in which the Kirkendall effect has been measured and is known to be large (for example, the case of 73Cu27Zn for which $D_{zn}/D_{cu} \backsim 5.8$). According to Equation (23) of reference [11] the velocity V of displacement of a given segment of the diffusion zone at which the concentration gradient is dN_a/dx is

$$V = \frac{1}{N} I_v$$

in which N is the total density of atoms (designated by c in reference [11]), provided the vacancies condense, as is assumed to be the case in the ideal Kirkendall experiment. The experiments carried out thus far correspond to cases in which the vacancies usually migrate to the member of the couple having the constituent with highest vapor pressure (for example Zn in Cu-CuZn and Cu in Cu-Ni). This is also the member in which one should expect the higher density of vacancies at any given temperature. Thus the main vacancy flow in these specimens is opposite to that given by the first term in (5), and we may conclude that the second term gives a greater contribution.

If we assume we are dealing with the limit in which N_v is determined by the concentration of A atoms, so that near the interface

$$\frac{dN_v}{dx} = \frac{dN_v}{dN_a}\frac{dN_a}{dx} \sim \frac{N_v}{\Delta N_a}\frac{dN_a}{dx},$$

the ratio of the absolute value of the second term in (5) to the first is, in order of magnitude,

$$\rho\,\frac{\Delta N_a}{N_a}.$$

Thus ρ should not be small compared with unity.

Further evidence in the same direction is obtained by comparing Vt, the Kirkendall shift in time t, with d, the diffusion range, given by (10). We readily find, using the relation (11),

$$\frac{Vt}{d} \sim \rho\,\frac{\Delta N_a}{N_a}\frac{N_v}{N}\frac{D_v}{D_c}.$$

Since D_v/D_c should be of the order of N/N_v whenever the Johnson-Wagner effect is not prominent, it follows that $\rho\,\Delta N_a/N_a$ should not be small compared with unity if the Kirkendall effect is appreciable.

III. The Migration of Vacancies in the Diffusion Zone

In the standard diffusion couple, d is initially zero and increases linearly with the square root of the time (Equation (10)). On the other hand, Δ is initially very large, as a parameter at least, and decreases inversely as the square root of the time in the approximation (15). If diffusion continues sufficiently, d and Δ will cross and their relative values will be reversed. The limit in which Δ is small compared with d, that is, the limit of long time, evidently corresponds to the case in which the local density of vacancies is maintained very close to the equilibrium value, for a given vacancy travels only a relatively short distance along the chemical gradient in passing from the source to the sink. In brief, the situation in which Δ is small compared with d corresponds closely to the approximation described by Bardeen [10] and emphasized by Bardeen and Herring [12], which leads to Darken's equations; the drift current does not upset radically the local equilibrium of vacancies.

The opposite approximation, in which Δ is larger than or comparable to d, is the one in which we may expect to find the conditions which lead to vacancy concentrations appreciably different from the equilibrium concentration. For then the vacancies produced in the diffusion zone may drift to one end of this zone and accumulate there so as to give an abnormally high concentration.

Assume for the moment that the rate of vacancy production per unit volume per unit time in the diffusion zone is q. Since the relaxation time for the attainment of equilibrium is T (Equation (13)), the equilibrium density of vacancies is assumed to be qT. The number of vacancies generated in time t in a volume of the gradient domain possessing a thickness d parallel to the gradient and unit cross section in the normal direction is dqt. These vacancies will be swept to the edge of the diffusion zone by the gradient and will be compressed to a thickness $2\sqrt{(D_v t)}$ if, as we shall assume to be the case, the principal factor limiting compression is Brownian motion. Thus the concentration of the displaced vacancies in this compressed zone which are collected in time t, assumed small compared with T, is

$$\frac{dqt}{2\sqrt{(D_v t)}} \qquad (t < T) \tag{19}$$

or the density R_t relative to the equilibrium value qT is

$$R_t = \frac{dqt}{2\sqrt{(D_v t)}}\frac{1}{qT} = \frac{d}{\delta\Delta}\left(\frac{t}{T}\right)^{\frac{1}{2}} \qquad (t < T,\ \Delta > d) \tag{20}$$

Before employing (20), we must decide whether the displaced vacancies which reach the edge of the diffusion zone constitute the entire concentration there or whether they add to an appreciable density

of vacancies already present which have not been swept away because the gradient in concentration is not sufficiently high. In the first case, R_t would give the relative concentration in the end zone, whereas in the extreme instance of the second case, the relative density in this zone would be $1 + R_t$. This issue could be determined precisely on theoretical grounds only by solving the basic equations governing vacancy migration, generation, and disappearance for a number of typical cases and examining the results. A somewhat simplified form of this procedure, which is analogous to that employed in solving the equations governing the distribution of neutrons in nuclear reactors [14], is developed in the appendix to this paper and is solved for a typical case. The results bear out the conclusions drawn on qualitative grounds in the next paragraphs. It is evident, however, that the more mathematical approach could be expanded with profit.

If R_t is large compared with unity for a substantial part of the range of time of interest, namely when $t \leqslant T$, the isssue is not critical since an appreciable supersaturation of vacancies is guaranteed. On the other hand, when R_t is near to or smaller than unity throughout the range of time, we must conclude that the random notion of the vacancies is sufficiently great that the bunching which results from the gradient is comparatively weak even in the region where the gradient is strongest. It follows that the influence of the gradient should be even less in the end zone where the vacancies tend to accumulate; hence the vacancies generated in that region should be added to those which arrive there by displacement. In brief, it seems appropriate to assume that the effective concentration of vacancies in the end zone is $1 + R_t$, so that R_t measures the relative concentration *above* saturation. Since R_t is always positive, we may expect a slight degree of supersaturation under all conditions, even though this may be insufficient to produce pores.

In the opposite limit in which Δ is small compared with d, only a fraction of the vacancies produced in the diffusion zone accumulate at the boundary of this zone since most die while migrating in the direction of the boundary. The value R of the excess relative concentration may be determined easily by the condition that the vacancy current in the diffusion zone arising from the drift velocity (7), namely $\rho N_{v0} D_v \Delta N_a / N_a d$, where N_{v0} is the equilibrium density of vacancies, be equal to the diffusion current in the region beyond the boundary where there is no concentration gradient. Since the relaxation distance in the latter region is $\delta\Delta$, the second current is $D_v \delta N_v / \delta\Delta$, where δN_v is the excess concentration of vacancies at the boundary. We obtain from this relation

$$R \sim \rho \frac{\Delta N_a}{N_a} \frac{\delta\Delta}{d} = 2\rho \frac{\Delta N_a}{N_a} \frac{\lambda}{d} \omega^{\frac{1}{2}}. \tag{21}$$

This corresponds to case (b) in the Appendix.

The condition necessary for strong supersaturation during the diffusion process is that R_t (Equation (20)) be comparable to or greater than unity when (20) takes its maximum value for $t = T$, that is

$$R_T = \frac{d}{\delta\Delta} \geqslant 1$$

or

$$R_T = \frac{d}{\delta d} \left(\frac{d}{\Delta}\right)^{\frac{1}{2}} > 1 \qquad (\Delta > d) \tag{22}$$

(see Equation (18)).

In the approximation corresponding to the right-hand side of (17), the ratio $d/\delta d$ is independent of d or t, that is, is a constant of the diffusing system. Hence (22) will be satisfied at some time during the diffusion process if

$$\frac{d}{\delta d} > 1.$$

The left-hand side of the relation (22) shows that under all conditions the time at which the greatest supersaturation of vacancies occurs is that for which Δ and d are about equal.

Conversely, we saw at the end of the last section that we have good reason to expect $\rho \Delta N_a / N_a$, and hence $d/\delta d$, to be near unity for couples having a strong Kirkendall effect. It follows that in such systems R_T should be near unity when Δ and d become equal. Since Δ involves the unknown $N_t \sigma_t$, or T, we cannot determine directly, at least at present, the value of d at which this occurs. Instead we must attempt to infer the result from experiments with use of what at present are somewhat arbitrary hypotheses.

It is natural, as remarked in Section I, to assume that the ease with which pores are formed is directly related to the degree of supersaturation. We shall assume at start that they will first occur at irregular sites, such as voids and small inclusions, when the concentration of vacancies is of the order of twice the equilibrium concentration in moderately perfect single crystals. This will not happen during the initial phase of diffusion, in what we have termed the ideal case, for R_t should approach zero at values of t small compared with T, according to Equation (20).

In actual systems, it is possible that T is relatively small near the junction of the couple because of a relatively high degree of imperfection at the interface. Thus pores might form there even though they would not if T had the average value for the remainder of the specimen. Similarly, once pores are formed in a given region of the specimen, because of a suitable excess concentration of vacancies, the pores may act as new sources and sinks for vacancies and decrease T locally. The jogs on incompleted rows of atoms on incomplete surfaces should act as effectively as jogs on dislocation lines in producing and absorbing vacancies.

Thus T may actually be variable during the course of the diffusion cycle, being large until porosity develops in such a way that the spacing between pores is smaller than the value of $\delta\Delta$ which obtained prior to the formation of pores. It is even possible in particular cases that the lifetime of vacancies is determined by the geometry of the specimens. This will occur if the linear dimensions of the specimen are not large compared with $\delta\Delta$ determined from the volume density of trapping centers, so that the vacancies have an appreciable chance of dying at the surface.

As d increases, the pores formed during the early portion of diffusion may find themselves in a region of sub-equilibrium concentration of vacancies because the boundaries of the diffusion zone have continued to move and all vacancies are swept on to the new boundary. Under these conditions the old pores may act primarily as sources of vacancies and decrease in size, the vacancies being reabsorbed at the diffusion boundary.

In any event, new pores should cease being formed when d exceeds Δ sufficiently. The critical value of d for which this occurs depends upon R_c, the critical value of the excess relative concentration needed to form pores about the available nuclei. If R_c is near unity, pore formation should cease when d exceeds Δ appreciably, or, using (15), when

$$d \sim \left(\rho \frac{\Delta N_a}{N_a} \omega\right)^{\frac{1}{3}} \lambda \sim \omega^{\frac{1}{3}}\lambda, \tag{23a}$$

the right-hand approximation being valid when $\rho\Delta N_a/N_a \backsim 1$. On the other hand, if R_c is much smaller than unity, pore formation will cease when d increases to the point where R given by (21) decreases to the value R_c. This is equivalent to the conditions, analogous to (23a),

$$d \sim 2\rho \frac{\Delta N_a}{N_a} \omega^{\frac{1}{3}} \frac{\lambda}{R_c} \sim \omega^{\frac{1}{3}} \frac{\lambda}{R_c}. \tag{23b}$$

As was remarked at the end of the previous section, we do not have at present exact values of R_c. Indeed there is evidence (Section IV) to show that R_c may vary from specimen to specimen and from one region to another within a given specimen. It is convenient for present purposes to focus some attention on the case in which the nuclei are fairly homogeneous and in which R_c is of the order of unity, examining the consequences of these assumptions. Under such conditions the relations (23a) should be used. We shall postulate that the width of the porous zone is equal to the value of d for which (23a) is valid. This postulate will allow us to determine values of $N_t\sigma_t$, or of ω, typical of the zone *when pores are present.* These values of N_t presumably are larger than those which obtain for a non-porous specimen since the surfaces of the relatively large pores provide traps which can act even if the excess concentration is small.

If R_c actually is much smaller than unity, of the order of 10^{-2} or less, the relations (23b) would be more appropriate to use instead. It is evident that the values of ω that would be computed in the two cases from the same values of d would differ in the ratio R_c^2 and hence could be radically different.

The specimens of Cu-Ni studied by Barnes seem to provide ideal examples for this type of analysis. He has found that when measurements are carried out at sufficiently high temperature (1010°C to 1080°C), the pores which form in a late stage of the diffusion cycle tend to be large and to cluster in a plane normal to the diffusion gradient, that is, parallel to the original interface, as if any pores which might have formed initially near the interface were dissolved. In this connection Barnes has noted that the volume density of pores in his specimens is approximately constant, independent of time and temperature for which diffusion occurred. This, in turn, suggests that in his specimens at least the nuclei responsible for pore formation may be very homogeneous. In a typical case, illustrated by Figures 5 and 6 of his manuscript, the pores are about 5 mm from the original boundary on a scale of magnification of 150, corresponding to $\Delta = 7 \times 10^{-3}$ cm if the condition (23a) is valid. The corresponding value of $N_t\sigma_t$ derived from Equation (23a) by setting $\Delta N_a/N_a = 1$ and $\lambda = 2 \times 10^{-8}$ cm is $4 \times 10^{-4}\rho$ cm^{-1}. If we assume that at these temperatures the vacancy must be captured directly by a jog at a dislocation or on a surface of a pore to be retained and that, as a result, $\sigma_t \backsim 10^{-15}$ cm^2, we obtain

$$N_t \backsim 4 \times 10^{11}\, \rho \text{ cm}^{-3}.$$

VOL 1 195

Apparently it is necessary to assume that ρ is at least of the order of unity in order to obtain consistent results in the cases in which pronounced Kirkendall effect is observed. In any case, we conclude that N_t is of the order of 10^{12} cm^{-3} if $R_c \backsim 1$. Since the density of atomic sites which are immediately adjacent to edge dislocation lines should be nearer to 10^{15} cm^{-3} in typical materials, if the customary estimate that there are about 10^8 dislocation lines per cm^2 is correct, this value of N_t is in accordance with the notion that only a small fraction ($\backsim 10^{-3}$) of the places along dislocation lines can act as sources or sinks for vacancies at the temperature at which the measurements are made.

Balluffi and Alexander [3] have made somewhat similar observations on the copper-nickel system in specimens held at 1055°C for 239 hours, and have found porosity extending over a distance about three times larger than that observed in Barnes's specimens (see Fig. 7 in the second paper of reference [3]). If we make the somewhat dubious assumption that R_c is the same in the two cases, we apparently must conclude that $N_t\sigma_t/\rho$ is about ten times smaller in the specimens studied by Balluffi and Alexander than in those examined by Barnes, for $N_t\sigma_t/\rho$ varies inversely as the square of the thickness of this zone (see Equation (23a) or Equation (15) for the case in which $\Delta = d$). Since there is no reason to expect ρ to be different in the two cases, we may then conclude that $N_t\sigma_t$ is ten times smaller in the first case.

Smigelskas and Kirkendall seem to have observed pitting in 70-30 brass specimens, studied at 785°C, at distances at least ten times larger than those observed in Cu-Ni by Barnes. Similar results are found by Balluffi and Alexander [3] at 880°C. If the condition $R_c \backsim 1$ is valid, we apparently must conclude that $N_t\sigma_t/\rho$ is at least thirty times smaller in typical specimens of this material than in the specimens of Cu-Ni, at the temperature of measurement, for $N_t\sigma_t/\rho$ varies inversely as the square of the thickness of this zone and only directly as the first power of $\Delta N_a/N_a$. It is difficult to indicate the source of this difference, inasmuch as at least three variables are involved. At the present time, it seems reasonable to assume tentatively that a value of ρ larger than 5 is excessive and conclude that $N_t\sigma_t$ is at least ten times smaller in brass than in CuNi.

The ratio $d/\delta d$ has a value of about 0.6 for the brass specimens if ρ is assumed to be about 5. This is sufficiently near unity to suggest no conflict with the view that the degree of supersaturation required to produce voids corresponds to $R_T \backsim 1$ or greater.

Bückle and Blin [5] have observed voids at a distance of 3×10^{-2} cm from the interface in specimens of copper interdiffusing with 7 per cent Cu-Al alloy for 25 days at 800°C. Thus $N_t\sigma_t/\rho$ seems to be of the order of one hundred times smaller in this case than in that of Cu-Ni if R_c is the same. Again it would appear reasonable to suppose that $N_t\sigma_t$ is substantially smaller in this couple than in Cu-Ni.

Finally, Balluffi and Alexander [3] have observed porosity over a distance of about 1.2×10^{-2} cm in couples of silver and gold held at 920°C for 44 hours. In this example $N_t\sigma_t/\rho$ appears to be about one-fourth as large as in Barnes's specimens of Cu-Ni, if R_c is the same in the two cases.

IV. Concluding Comments

Although the preceding discussion seems to tie pore formation into the general picture of events surrounding the Kirkendall effect, it leaves many basic questions either unanswered or in little more than a qualitative state. For example, several key issues are as follows:

1. What are the nuclei of the voids? Several investigators have speculated on this point. They could be a configuration of dislocations, such as the spiral prismatic dislocation [15], which is unable to achieve equilibrium when in a highly supersaturated atmosphere of vacancies and forms a void as a result of the rapid accumulation. They could also be small voids or inclusions (motes) about which a superconcentration of vacancies condense. Or, the voids could form in the perfect lattice when the superconcentration is high. The first and second processes are not radically different; however, it would be interesting to know if the third process actually occurs. The writer is inclined to discount it since it requires values of $R_T \backsim 100$ and hence values of ρ of the order of 10^4, which seem exceedingly high. Granting this, we are left with the outstanding problem of determining the excess relative concentration R_c needed to cause the effective nuclei to form voids.

2. It is not entirely clear why porosity varies so much from one specimen of a given material to another or why it is so much more broadly distributed throughout the diffusion zone in the brass specimens that have been studied than in Cu-Ni or Ag-Au. Barnes has suggested that the pores tend to become large and localized at high temperatures. There is little doubt that this is true of the Cu-Ni specimens he studied in the range between 1010°C and 1080°C, just below the melting point of Cu. On the other hand Balluffi and Alexander seem to

have observed broadly distributed porosity both in couples of copper and nickel, in the same temperature range, and in couples of copper and brass which were treated at 880°C, which is close to the melting point of the 70-30 brass used, namely 902°C. From the published figures, the writer cannot detect a significant difference between the distribution of pores in these specimens of brass and those observed by Smigelskas and Kirkendall at 785°C; however the pores may be larger in the first case.

The most reasonable explanation of the variation in porosity between specimens is that there may be a distinct difference in the size of the nuclei for pores in different specimens, both of like and unlike materials. It has been assumed implicitly in the previous sections that the nuclei for pores are more or less the same in various cases, having a fairly well defined equilibrium vapor pressure for vacancies. Actually the nuclei may vary over a wide range from one material to another. In fact it is not unreasonable to suppose that there may be a range of nuclei within a given specimen. In the couples studied at the Sylvania Laboratories, one frequently observes a few pores relatively far from the principal group adjacent to the fiducial markers, as if the distribution of nuclei were so wide that a relatively few nuclei could act to form pores for excess concentration of an order of magnitude less than the average.

This aspect of the present topic might be greatly clarified by observations on couples in which one or both specimens contain, as a result of intentional addition, specified amounts of fine sols of materials of known size which are not soluble in the metals. For example silica sols or fine carbon blacks in the range of 50Å or less might be ideal for this purpose.

It seems difficult to draw further reliable conclusions concerning the pores from the available experimental information, although a few tentative suggestions can be gleaned, particularly from Barnes's measurements. He has found in the case of the Cu-Ni specimens that the typical couple swells in such a way that the expansion varies as $\sqrt{t}$, at least during the initial period of about 25 hours when the diffusion takes place at 1065°C. This behavior was studied over a range of time extending from about 15 minutes to somewhat more than 25 hours in two specimens. The diffusion distance d is of the order of 10^{-4} cm at the time of the first observations. This result suggests that pores form very early in the diffusion process and behave in a "uniform" manner during the subsequent history of the specimen, if we assume that the swelling is a result of the growth of pores. Were it certain that ω is as small as 10^8 or 10^9, so that the Darken-Bardeen approximation would be valid for values of d of the order of 10^{-4} cm and larger, we might conclude that a fixed fraction of the vacancy current, which would vary as $1/\sqrt{t}$ under these conditions, goes into the formation of pores. It is difficult to believe that any such simple conclusion can be drawn in a direct manner, however, for the principal porosity appears at a distance of the order of 10^{-2} cm in cases in which diffusion has taken place for sufficiently long. It seems more likely that the pores formed initially redissolve and that the $\sqrt{t}$ law is the result of a combination of several effects.

In this connection, Barnes has found that the swelling in the direction of the diffusion gradient is between a third and a half of the Kirkendall shift in a typical specimen. A similar conclusion can be drawn for the couples of copper and alpha brass from the measurements of Bückle and Blin [5]. It would follow that between a third and a half of the vacancy current in the diffusion zone is transferred to the pores if a direct diversion of a vacancy current varying as $1/\sqrt{t}$ actually occurred.

Cyril S. Smith has pointed out to the writer that when brass is dezincified by evaporation, the channels through which the zinc emerges, and which presumably have their origin in pores, are sufficiently small that they can act selectively as semi-permeable barriers for gases, permitting small molecules to pass and holding back large ones. This observation supports the view that the pores can be very small at one stage in the diffusion process.

3. Although the preceding analysis of the Kirkendall effect indicates that in the Cu-Ni system studied by Barnes the quantity $\rho/N_t\sigma_t$ may have a value of the order of 2.5×10^3 cm, the individual estimates of ρ, N_t and σ_t obtained by resolving this are highly conjectural even if the important uncertainty in R_c is disregarded. It would be good to have a better understanding of the individual parameters and the way in which they vary with temperature. If we assume that a value of ρ of the order of 1 is not radically in error in cases in which the voids are observed, we may conclude with modest assurance that the quantity $\omega = 1/N_t\sigma_t\lambda$ is approximately 10^{11} provided R_c is near 1. This composite quantity represents the number of jumps a free vacancy makes before becoming trapped. If the assumptions that $R_c \backsim 1$ is correct, ω apparently is not always less than 10^9 as Bardeen and Herring hoped might generally be the case.

The evidence concerning the width of the porous zone in brass, Cu-CuAl, and Ag-Au indicates that $\rho/N_t\sigma_t$ may be larger in these cases than in CuNi. However, it does not seem safe to conclude that the values of ω are larger since the relative values of ρ are not known and it is not certain that R_c is the same in all materials.

Herring [private communication] has called the writer's attention to the possibilities inherent in the experiments of Kuczynski and Alexander [3]. These investigators have studied diffusion in the vicinity of the junction between a metal wire of small diameter (5 to 10 mils) and essentially flat metallic surfaces. The results are somewhat complicated since they are probably accompanied by the Kirkendall shift, at least when the two metals are different, by redeposition through vaporization and condensation and through surface migration, and possibly by plastic flow under surface tensional forces. In all cases the two sharp, cusped voids formed by tangency of circular cylinder and plane are transformed relatively rapidly to two grooves with continuous curvature, forming thereby a bonded neck between the plane and cylinder. These grooves are usually displaced in the course of diffusion in the direction that might be expected from the Kirkendall shift, although it is not evident that the Kirkendall effect is the only factor operating. In any event, the radius of curvature at the base of the grooves is of the order of 10μ in many of the photographs shown in the paper. The width of the necks and of the diffusion zone is of the order of 100μ in typical cases. If ω is as large as 10^{11}, $\delta\Delta$ should be of the order of 100μ, whereas it is only of the order of 10μ if ω is as small as 10^9.

If ω is as large as 10^{11}, we should expect the surface of the specimens to play an important role in determining the flow of vacancies. In particular, if $R \backsim 1$ inside the specimen we might expect the shape of the groove to show asymmetrical form since it would receive vacancies preferentially from one side, the radius of curvature not being great enough for the base of the groove to act as a source rather than a sink for values of $R \backsim 1$. On the other hand, if ω is nearer 10^9 and if R is much smaller than unity, in the stages of diffusion shown in the pictures, the base of the groove might be expected to be more symmetrical, as is observed.

Unfortunately a study of the work of Kuczynski and Alexander seems to raise at least as many problems as it solves. On the whole the grooves remain deep throughout the course of the experiment (see Fig. 3 for the case of a copper wire on nickel, for example), indicating that the grooves actually receive vacancies from the interior. Thus it is possible that vacancies are flowing to the surface in considerable number and that factors other than vacancy flow determine the shape of the groove. Moreover it is not known whether or not internal porosity exists and is the same in these specimens as in the case of planar specimens. It would be exceedingly interesting to have information on this point.

4. It is quite possible that σ_t varies substantially with the temperature. For example it is possible that at relatively low temperatures a vacancy is trapped whenever it finds itself near a dislocation line. Thereafter it may only move along the dislocation until it finds a jog where it can disappear. On the other hand, at high temperatures, such as those used by Barnes, it is possible that the vacancy will re-evaporate from an average position on a dislocation line and is truly trapped only if captured directly at a jog. Thus it is conceivable that σ_t could vary by a factor of the order of 1,000 from low temperatures to high. Any variations of this type in σ_t would presumably be reflected in variation of $\rho/N_t\sigma_t$ or ω.

5. At the time this is written, essentially all the couples on which extensive measurements have been reported are composed of face-centered cubic metals. It is conceivable that an exceedingly low density of sources and sinks of vacancies is one of the characteristics of well-annealed face-centered cubic metals. The density of sources and sinks for vacancies in well-annealed specimens of single crystals may vary substantially from one crystal type to another so that the ease with which pores are formed is different for different types.

Balluffi has called the writer's attention to as yet unpublished observations on specimens of beta brass containing 52 atomic per cent of zinc which have been dezincified by evaporation at 835°C in an evacuated capsule containing chips of 40 atomic per cent beta brass. Appreciable porosity was observed. Other measurements show that $D_{\mathrm{Zn}}/D_{\mathrm{Cu}} = 3.4$ in this case, so the Kirkendall effect is strong. Since beta brass is body-centered cubic, these results indicate that the body-centered cubic lattices probably do not behave radically differently from face-centered cubic ones.

It would be exceedingly interesting to have comparable observations on the alkali halides or on silicon-germanium specimens since these materials probably do not form partial dislocations, at least of the kind normally responsible for slip.

Evidence presented in paragraph (9) below,

dealing with observations very different from those on porosity, indicates that the density of sinks for vacancies is low in alpha iron.

6. If the preceding analysis is essentially right, one might expect to observe the Kirkendall effect without observing porosity. To speak in terms of the approximate parameters employed, the Kirkendall effect will be observed whenever ρ is greater than zero, whereas a value near to, or larger than, unity is presumably needed for voids if the condition that $R_T \backsim 1$ is correct. Correa da Silva and Mehl [2] did not find voids in all specimens they studied; however, their excellent observations probably are not adequate in this respect since they did not carry out an exhaustive search for pores. It would be interesting to know if voids can be found in specimens having a relatively small Kirkendall effect. Balluffi and Alexander have found porosity in the silver-gold system which shows one of the relatively small, although by no means negligible, displacement effects.

7. Greenough [16] has recently demonstrated that diffusional viscous flow in solids, of the type postulated by Nabarro [17] for low stresses, is essentially negligible in single crystals of silver, although it is observed in polycrystals. This flow is presumed to arise from vacancy currents between grain boundaries and the surface of the specimen under the action of the applied stress. Herring [18] first predicted that the diffusional viscous flow would be negligible in single crystals on the basis of the argument that dislocations would not act indefinitely as regions where the vacancy current has non-vanishing divergence because the forces between dislocation lines would bring them to equilibrium after a relatively small amount of displacement, insufficient to produce as much plastic flow as is observed in polycrystals for similar stresses. The preceding analysis suggests an alterative or concurrent explanation: The number of independent atomic sources or sinks within the grains may be very small compared with the number at crystal boundaries, so that the sustained vacancy currents from and to the former are negligible compared with those from and to the latter, as long as the vacancy density departs only slightly from the equilibrium values, which is presumed to be the case during diffusional viscous flow.

8. Ellwood and Bagley [19] have observed changes in the density of certain binary alloy systems for appropriate compositions and have interpreted this effect as the result of the incorporation of vacant lattice sites in such a way as to fill out Brillouin zones. For example a specimen of 80Cu20Ni decreased in density by about 4.5 per cent after being annealed at 900°C for 4,175 hours. Similar effects have been observed in aluminum-zinc and gold-nickel alloys. One cannot help but wonder if this effect is attributable to porosity, similar to that accompanying the Kirkendall effect, developed as a result of diffusion which occurs during the annealing procedure and which is a consequence of gradients in composition inherent in preparation of the alloy. In fact the investigators have observed "considerable micro-porosity" near some of the grain boundaries during the heat treatment. The diffusion distance d employed in the present paper would be of the order of 0.1 cm for times of the order of magnitude of those employed for heat treatment of the copper-nickel system at 900°C. It is possible that only a small fraction of the nuclei for pores, which may operate at relatively small excess concentrations of vacancies, are effective in these experiments. It is also possible that R_c is generally much less than unity and that the typical nuclei responsible for the pores in the Kirkendall effect are active in Ellwood's specimens.

9. Buffington and Cohen [20] have observed that self-diffusion in α-iron may be accelerated, at a given temperature, by applying stresses which induce creep during diffusion. The enhancement in the diffusion rate appears to be related primarily to the rate of plastic flow, the ratio D_s/D_u of the diffusion coefficient D_s, when stresses are applied, to the coefficient D_u in the unstressed specimen being $1 + c\dot{\epsilon}$ at 890°C. Here $\dot{\epsilon}$ is the strain rate and c is a constant which has the value 50 when $\dot{\epsilon}$ is expressed in units of hours^{-1}. A total strain of 0.27 was induced by creep in the typical specimen. The shortest period for attainment of this strain was approximately one hour. The diffusion coefficient in the absence of strain is approximately 4×10^{-11} cm^2/sec at 890°C, the activation energy being approximately 59,800 cal per mol.

The most straightforward interpretation to give to these measurements is to assume that the lattice defects produced [15] as a result of plastic flow, at a rate proportional to the strain rate, enhance the diffusional effects caused by the thermally induced lattice defects. If we assume that the latter are predominantly vacancies, this assumption leads to most nearly consistent results if we also assume the lattice defects induced by plastic flow are predominantly vacancies, since we might expect the diffusion rate to be suppressed for small rates of strain if the thermal diffusion were the result of vacancies

whereas plastic flow induced primarily interstitial atoms.

With this assumption, we may proceed to estimate the lifetime of vacancies. If η is the number of vacancies produced per unit strain, ϵ is the strain, t is the time over which the strain is produced, π is the jump frequency for vacancies, N_{vt} is the density of thermally induced vacancies, and ω is the number of jumps a vacancy makes on the average in the course of finding a sink, we may obtain the following expression for the ratio of the equilibrium density of vacancies produced by plastic flow to the density produced thermally

$$\epsilon\eta\omega/\pi t N_{vt}.$$

We shall set this equal to the measured quantity $c\dot{\epsilon}$ giving the enhanced component of diffusivity. We may also make use of the relation $D_u \cong N_{vt}\pi\lambda^2/N$, where N is the density of atoms and λ is the atomic spacing, and give this combination of parameters its experimental value for 890°C, cited above. Since ϵ/t is the average strain rate, we readily find

$$\omega = cND_u/\eta\lambda^2.$$

Taking $\lambda^2 = 10^{15}$ cm², $N = 9 \times 10^{22}$, and $\eta = 2 \times 10^{19}$ per cc, the latter being a conservatively small value, we find

$$\omega \backsim 10^{13}.$$

This value of ω is large compared with values of the order of 10^{11} and 10^{12} obtained for other materials by the means described in preceding paragraphs. There is, however, enough uncertainty both in the arguments employed and in the values of the parameters used in deriving ω that the value cannot be accepted as reliable or final, but merely as suggestive.

If we assume that the activation energy of approximately 60,000 cal/mol found for α-iron may be divided into a value of 40,000 cal/mol for the generation of vacancies and a value of 20,000 cal/mol for the migration of vacancies, the equilibrium density of vacancies at 890°C is found to be about 10^{17} per cc, whereas the jump frequency is about 10^{10}/sec. If the second of these quantities is approximately correct, the value $\omega \backsim 10^{13}$ implies that the lifetime of vacancies is of the same order as the time of creep in the more rapid experiments.

The maximum relative increase in diffusion rate observed by the investigators is about 15. One must conclude that the density of vacancies achieves values of the order of 15 above the thermal equilibrium density during the most rapid deformations, if the interpretation of this enhancement in terms of the production of vacancies by plastic flow is correct. Presumably an appreciable fraction of these vacancies should precipitate in such a way as to form voids, if the principles used in the explanation of the voids observed in connection with the Kirkendall effect are also applicable in the present case. Since the total strain was 27 per cent, of the order of 5×10^{18} vacancies per cc should be produced, provided the conclusions drawn [15] for the case of copper are valid for iron. It would be interesting to know if porosity is observable.

We would face difficulty in understanding a value of ω as large as that calculated above in the deformed diffusion specimens if interstitial atoms are produced by plastic flow in numbers comparable to vacancies, for one might expect ω to drop to values near 10^6 if 10^{17} interstitial atoms are present. On the whole, a consistent interpretation of the Buffington-Cohen experiment along the lines discussed here appears to require that creep produce predominantly the defect responsible for normal thermal diffusion. This conclusion is very remarkable in itself, if further research sustains it, for it suggests that the vacancies which enhance the diffusion coefficient in the Buffington-Cohen experiment may be generated thermally rather than geometrically, that is, under circumstances which markedly favor the imperfection which has the lowest energy of formation. This, in turn, suggests that the mechanism by which vacancies are produced during plastic flow at elevated temperatures may not be the same as that which operates at lower temperatures.

The writer is indebted to several friends and colleagues for critical comments concerning this work. Particular mention should be given to Drs. Conyers Herring, R. S. Barnes, R. Balluffi, and L. Slifkin.

Appendix

We shall consider, in a somewhat idealized manner, the equations governing the accumulation of vacancies at the edge of the diffusion zone and their solutions.

The rate at which vacancies accumulate in a unit volume of the crystal may be expressed in the form

$$\frac{\partial N_v}{\partial t} = -\operatorname{div} I_v + \frac{1}{T}(N_{vo} - N_v) \tag{24}$$

in which $-\operatorname{div} I_v$ is the increase in density as a result of flow of vacancies, N_{vo}/T is the rate of spontaneous generation of vacancies, with N_{vo} the equilibrium density of vacancies and T the lifetime, and N_v/T is the rate of decay of vacancies at traps.

For simplification, we shall assume that T and N_{vo} are constant throughout the specimen. Actually T may be dependent upon the history of the material and may vary both from position to position, and as a function of N_v, increasing with increasing values of the latter. Moreover, N_{vo} will usually be a function of chemical composition.

I_v may be taken in the form

$$(25)\quad I_v = -D_v \operatorname{grad} N_v + N_v\left(\frac{\partial \pi}{\partial N}\right)\lambda^2 \operatorname{grad} N_a$$

(see Equation (5)) in which D_v is the diffusion coefficient for vacancies. We shall simplify the problem further by the following assumptions: (1) the diffusion gradient is in the x direction; (2) the system is in a steady state so that $\partial N_v/\partial t = 0$; $(\partial\pi/\partial N)$ may be replaced by the approximate form $\rho\pi/N_a$ (see Equation (9)). The equation for N_v then becomes

$$(26)\quad D_v \frac{d}{dx}\left(\frac{dN_v}{dx} - \frac{\rho\, dN_a}{N dx} N_v\right) + \frac{1}{T}(N_{vo} - N_v) = 0.$$

The procedure of treating the chemical gradient as if it were instantaneously fixed and seeking a stationary-state solution for the vacancy density is justifiable as long as D_v is far larger than the chemical diffusion coefficient D_c, which is normally the case. Under these circumstances, the chemical gradient will not change appreciably during the time T in which the vacancies come to equilibrium.

The quantity dN_a/dx is normally a continuous function of x. For example, if the chemical diffusion coefficient is a constant, D_c, and if diffusion is not appreciably affected by the presence of voids, dN_a/dx is

$$(27)\quad \frac{dN_a}{dx} = \frac{\Delta N_a}{\sqrt{(\pi d)}} \exp\left(-x^2/4D_c t\right)$$

in which ΔN_a is the total difference in composition on both sides of the couple and $d = 2\sqrt{(D_c t)}$.

Whenever dN_a/dx is a function of x/d, (26) may be expressed in the form

$$(28)\quad \frac{d}{dy}\left(\frac{d\phi}{dy} - f(y)\phi\right) + \frac{d^2}{D_v T}(1-\phi) = 0$$

where $y = x/d$, $\phi(y) = N_v(x)/N_{vo}$ and $f(y) = (\rho/N_a)(\partial N_a/\partial y)$. The coefficient of $(1-\phi)$ in the last term evidently is $(2d/\delta\Delta)^2$, where $\delta\Delta$ (Equation (18)) measures the dispersion of the vacancies as a result of Brownian motion after time T.

The boundary conditions to be placed upon ϕ are continuity of this function and its first derivative if the function $f(y)$ is continuous. Othedrwise ϕ an the vacancy current (25) should be continuous at points of discontinuity in $f(y)$.

It is possible to obtain a simple analytical solution of Equation (28) in the case in which the gradient of N_a is assumed to be constant in a region of width d and is taken to be zero everywhere else. In the regions where $f(y)$ is zero, (28) takes the form

$$(29)\quad \frac{d^2\phi}{dy^2} + \gamma^2(1-\phi) = 0$$

whereas in the region where $f(y)$ is constant

$$(30)\quad \frac{d}{dy}\left(\frac{d\phi}{dy} - 2a\phi\right) + \gamma^2(1-\phi) = 0$$

where $\gamma^2 = d^2/D_v T$ and $2a = \rho\Delta N_a/N_a$.

If we assume that the discontinuities occur at $y = \pm\frac{1}{2}$, the form of ϕ in the various ranges is as follows

(a) $y < -\frac{1}{2}$

$$(31)\quad \phi = 1 + A\exp(\gamma y)$$

(b) $-\frac{1}{2} < y < \frac{1}{2}$

$$(32)\quad \phi = 1 + C\exp(\omega_1 y) + D\exp(\omega_2 y)$$

(c) $y > \frac{1}{2}$

$$(33)\quad \phi = 1 + B\exp(-\gamma y)$$

where γ is the positive root of γ^2 and

$$(34)\quad \begin{aligned}\omega_1 &= a + \sqrt{(a^2+\gamma^2)},\\ \omega_2 &= a - \sqrt{(a^2+\gamma^2)}.\end{aligned}$$

It may be noted that γ measures the relaxation distance outside the diffusion zone, whereas $2a/\gamma^2$ is the distance, in units of d, which a vacancy migrates in the diffusion zone before being captured. When $2a/\gamma^2$ is one or greater, the vacancies go the entire distance.

Applications of the appropriate boundary conditions lead to the relations

$$(35)\quad \begin{aligned} C &= 2a \times \frac{\gamma\cosh(\omega_2/2) - \omega_1\sinh(\omega_2/2)}{2\gamma^2\sinh[(\omega_1-\omega_2)/2] + \gamma(\omega_1-\omega_2)\cosh[(\omega_1-\omega_2)/2]},\\ D &= -2a \times \frac{\gamma\cosh(\omega_1/2) - \omega_2\sinh(\omega_1/2)}{2\gamma^2\sinh[(\omega_1-\omega_2)/2] + \gamma(\omega_1-\omega_2)\cosh[(\omega_1-\omega_2)/2]}\end{aligned}$$

A and B may be evaluated from the relations

$$(36)\quad \begin{aligned} A &= C\exp((\gamma+\omega_1)/2) + D\exp((\gamma+\omega_2)/2),\\ B &= C\exp((\gamma-\omega_1/2) + D\exp((\gamma-\omega_2)/2).\end{aligned}$$

A number of interesting cases may be considered:

(a) $a = 1, \quad \gamma = 1.$

Since the ratio $2a/\gamma^2$ measures the distance the vacancies migrate in the diffusion zone, this case

represents an example in which the vacancies drift through the zone on the average and in which a and γ have what might be termed intermediate values.

We readily find $\omega_1 = 2.41$, $\omega_2 = -0.41$, $C = 0.304$, $D = -0.487$. The values of ϕ at the boundary points are

$$(37) \qquad \begin{aligned} \phi &= 1.62 \text{ at } y = \tfrac{1}{2}, \\ \phi &= 0.49 \text{ at } y = -\tfrac{1}{2}. \end{aligned}$$

Thus there is a 62 per cent excess of vacancies at the positive boundary point, to which vacancies are pumped, and a 51 per cent deficit at the negative boundary point. It is evident that the maxima and minima of ϕ occur at these points.

(b) γ very large compared with unity and with a.

This corresponds to a case in which $d/\delta\Delta$ is large and in which the vacancies do not migrate throughout the diffusion zone in one lifetime so that we might expect the Darken-Bardeen situation to be most nearly realized. We find

$$(38) \qquad \begin{aligned} &\omega_1 \rightarrow \gamma + a \rightarrow \gamma, \quad \omega_2 \rightarrow -\gamma + a \rightarrow -\gamma, \\ &C \rightarrow \frac{a}{\gamma} \exp(-\gamma/2), \quad D \rightarrow -C. \end{aligned}$$

Thus $\phi \rightarrow 1 \pm a/\gamma$ at $y = \pm \frac{1}{2}$, respectively, and the deviations from unity are small.

(c) a large compared with unity and γ.

$$\omega_1 \rightarrow 2a, \quad \omega_2 \rightarrow -\gamma^2/2a,$$

$$C \rightarrow a \frac{1 + \gamma/2}{\gamma \sinh a + a \cosh a} \rightarrow \frac{1 + \gamma/2}{\cosh a},$$

$$D \rightarrow -a \frac{\cosh a + (\gamma/2a) \sinh a}{\gamma \sinh a + a \cosh a} \rightarrow -1.$$

The values of ϕ at the two boundaries are

$$(39) \qquad \begin{aligned} &\phi \rightarrow 2 + \gamma \text{ at } y = \tfrac{1}{2}, \\ &\phi \rightarrow 2 \exp(-2a) \text{ at } y = -\tfrac{1}{2}. \end{aligned}$$

Thus the specimen is essentially depleted of vacancies at the negative boundary, whereas the excess concentration is $1 + \gamma$ at the positive junction. This evidently corresponds to a case in which the Kirkendall effect is very strong and in which a relatively large excess of vacancies accumulates at the positive boundary.

It is interesting to note that in case (c) the value of ϕ at $y = \frac{1}{2}$ increases linearly with γ, which is proportional to d. Thus when a is large, the concentration of vacancies increases during the diffusion process until γ^2 becomes comparable to a, or until $2a/\gamma^2$ becomes comparable to unity. Thereafter, we may expect the maximum of ϕ to decrease with increasing d, in accordance with case (b). Thus, in this repect, the foregoing solution bears out the conclusions drawn on more qualitative grounds in the text. We may note, however, that for small values of γ, $\phi \rightarrow 2$ at $y = \frac{1}{2}$ according to (39). Thus the density of vacancies at this point is twice the equilibrium value even when d is small, in contrast with the value $\phi = 1 + R_t \rightarrow 1$ for small d anticipated in Section III. The difference evidently arises from the assumption, contained in Equation (28), that the equilibrium density of vacancies is the same on both sides of the couple. As a result, an appreciable numper of vacancies found at $y = \frac{1}{2}$ originate at regions where $y < -\frac{1}{2}$ when a is large. In computing R_t in Section III, in contrast, it was assumed that the extra vacancies found at $y = \frac{1}{2}$ originate entirely in the diffusion zone. The latter assumption is probably much more realistic for the couples studied experimentally thus far.

References

1. Smigelskas, A. D. and Kirkendall, E. O. Trans. Amer. Inst. Min. Met. Eng., **171** (1947) 130.
2. Correa da Silva, L. C. and Mehl, R. F. Trans. Amer. Inst. Min. Met. Eng., **191** (1951) 155.
3. Balluffi, R. and Alexander, B. H. J. App. Phys., **23** (1952) 953, 1237; J. Metals, **4** (1952) 1315; Kuczynski, G. C. and Alexander, B. H. J. App. Phys., **22** (1951) 1344; Kuczynski, G. C. J. App. Phys., **21** (1950) 632,
4. Barnes, R. S. Proc. Phys. Soc., **65B** (1952) 512. See also LeClaire, A. D. and Barnes, R. S. J. Metals, **3** (1951) 1060.
5. Bückle, H. and Blin, J. J. Inst. Metals, **78** (1952) 385.
6. Seith, W. and Kottmann, A. Naturwissenschaften, **39** (1952) 40, 41.
7. Darken, L. S. Trans. Amer. Inst. Min. Met. Eng., **175** (1948) 184.
8. Seitz, F. Phys. Rev. **74** (1948) 1513.
9. Johnson, W. A. Trans. Amer. Inst. Min. Met. Eng., **147** (1942) 331.
10. Bardeen, J. Phys. Rev., **76** (1949) 1403.
11. Seitz, F. Acta Cryst., **3** (1950) 355.
12. Bardeen, J. and Herring, C. Imperfections in Nearly Perfect Crystals (New York, Wiley, 1952), p. 261.
13. See, for example, Volmer, M., Kinetik der Phasenbildung (Dresden-Leipzig, Steinkopf, 1939); Crystal Growth (Disc. Faraday Soc., no. 5, 1949).
14. See, for example, Soodak, H. and Campbell, E. C., Elementary Pile Theory (New York, Wiley, 1950).
15. Seitz, F. Advances in Phys., **1** (1952) 43.
16. Greenough, A. P. Phil. Mag. 43 (1952) 1075. This paper contains a review of other literature.
17. Nabarro, F. R. N. Report of a Conference on the Strength of Solids (London, Physical Society, 1948), p. 75.
18. Herring, C. J. App. Phys., **21** (1950) 459.
19. Ellwood, E. C. Nature, **163** (1949) 722; **170** (1952) 580; J. Inst. Metals, **80** (1951) 217. Ellwood, E. C. and Bagley, K. Q. J. Inst. Metals, **80** (1952) 617.
20. Buffington, F. S. and Cohen, M. J. Metals, **4** (1952) 859.

LETTERS TO THE EDITOR

Crystallographic Aspects of the Beta to Alpha Transformation in Titanium*

Although numerous studies have been made of various aspects of the beta to alpha transformation which occurs on cooling titanium, studies of the crystallography of the transformation have been relatively neglected. The alpha phase of titanium has a hexagonal close-packed lattice with a c/a ratio of 1.587. Above 883°C this phase transforms to the body-centered cubic beta phase. No significant hysteresis is associated with the transformation in the pure metal on heating or cooling. The effect of most alloying elements is to depress the transformation temperature though a few, notably aluminum, nitrogen, oxygen, and carbon, have the effect of stabilizing the alpha phase and therefore raise the transformation temperature.

In this note three aspects of the beta to alpha transformation in commercially pure titanium are reported; namely,

I. The orientation of the alpha lattice with respect to its parent beta lattice.

II. The nature of striations found in the macrostructure and their relation to the habit plane of an acicular product.

III. The phenomenon of reversion to the original lattice orientation, of an isolated alpha crystal, after it had been heated into the beta range and then cooled.

About seven pounds of commercially pure sponge titanium were arc melted in a water-cooled copper crucible. The ingot was cooled in the crucible and, except where specifically stated, no further heat treatment was given.

The grain size of the ingot was very large which was convenient for single crystal techniques. The etched surface of a slab which was cut from the middle of the ingot is shown by Figure 1. The outlines of the former beta grains are evident. It was established by Laue studies that the striated patches within the previous beta grains are single alpha grains. The Laue spots from such grains are normally sharp and frequently crystals were found which gave transmission patterns containing Kikuchi-type lines [1].

I. *Orientation of the Alpha Lattice with respect to its Parent Beta Lattice*

In 1933 Burgers [2] reported the orientation relation between hexagonal alpha zirconium and the cubic beta phase from which the alpha formed. Owing to the similarity of zirconium and titanium, the same relationship hss been assumed to hold for titanium though it has never been experimentally demonstrated.

Burgers' method was to observe directly the orientation of the alpha lattice by an X-ray method, and to derive the orientation of the parent beta lattice from the external symmetry of the crystal. The external symmetry was related to the cubic lattice because, at the temperature where the crystal was originally formed, the stable structure was body-centered cubic.

The present method for determining the alpha-beta orientation relationship also involves direct X-ray observation of the alpha lattice orientation. The parent beta orientation, however, was deduced from the relative orientations of several alpha grains, which were descended from the same parent beta. Figure 2 shows an enlarged view of part of the surface of Figure 1. A typical transformed beta grain is shown here extending diagonally across the macrograph and is clearly outlined by a continuous grain boundary, whereas the alpha grains, which formed from the parent beta grain, are bounded by jagged interpenetrating projections. The orientation of the alpha grains could be easily determined by back reflection Laue photographs. When the orientations of several alpha grains within the same parent beta grain are plotted on the same stereographic projection, the relationship existing among them may be quickly seen. Such a plot for the large transformed beta grain in Figure 2 is shown in Figure 3. Here the (00.1) pole and a $\langle 11.0 \rangle$ direction are used to define the orientations of the lattices of four alpha grains. Notice that by rotating all the alpha crystals as a unit, each of the $(00.1)_\alpha$ poles may be made to coincide with a $\{110\}_c$ pole of a cubic lattice. This cubic lattice must be the body-centered cubic structure of the parent beta phase. Also, by the same rotation, one of the $\langle 11.0 \rangle$ directions of each of the hexagonal lattices comes into coincidence with a $\langle 111 \rangle$ direction of the cubic lattice.† This orientation relationship is identical to that given by Burgers for Zr; namely,

$$(00.1)_\alpha \,//\, \{110\}_\beta$$
$$\langle 11.0 \rangle_\alpha \,//\, \langle 111 \rangle_\beta$$

*Received November 28, 1952.

†Other $\langle 11.0 \rangle_\alpha$ directions fall about 10° or 50° from $\langle 111 \rangle_\beta$ as required by the orientation relationship.

FIGURE 1. Etched surface of arc melted sponge titanium (actual size).

FIGURE 2. Typical former beta grain made up of alpha crystals. Arrows refer to directions used in Figures 3 and 4. (4×)

It should be noted that the orientations of only two alpha grains within one transformed beta grain are necessary to fix the orientation of the parent beta lattice. Yet the lattice orientations of as many as four alpha grains within the same

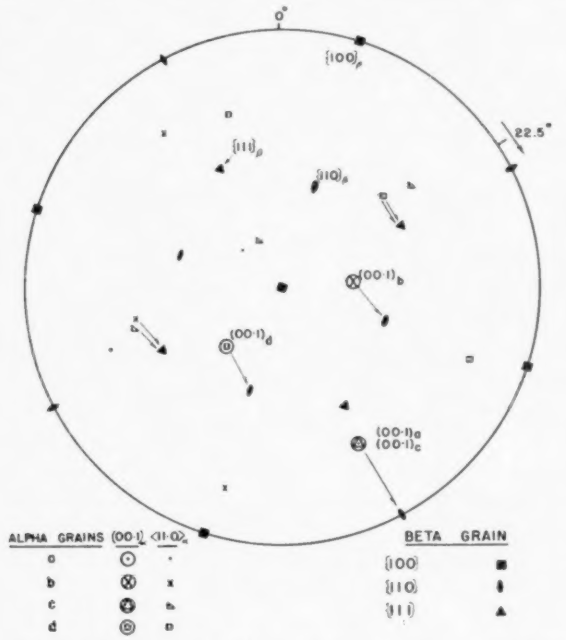

FIGURE 3. Stereographic projection showing orientations of several alpha crystals which formed from the large parent beta crystal in Figure 2. Arrows indicate 22.5° rotation necessary to bring conjugate poles into coincidence with matrix poles for standard orientation represented by filled symbols.

former beta grain have been found to hold the Burgers relationship with respect to the lattice of the parent beta grain. It is quite improbable that this would happen accidentally. The example cited above is only one of several studies that have been made of former beta grains, all of which gave the same results. Thus it appears that the orientation relationship proposed by Burgers for the two forms of zirconium can also be shown experimentally to hold for titanium.

II. *Striations in the Microstructure and Habit Plane*

The crystallographic aspects of two distinct macrostructural features were studied. The features consisted of the parallel striations in the irregularly outlined alpha crystals a, b, c, and d in Figure 2 and the intersecting acicular product in the major portion of Figure 2. The latter was suggestive of a Widmanstätten pattern but the habit plane did not correspond with $\{110\}_\beta$ planes of the parent lattice which have occasionally been reported to be the habit planes on which the alpha phase forms. On the other hand, previous analyses of the habit plane based merely on a count of trace directions and angles between traces on one surface have not been found reliable and in this case could not be confirmed by stereographic analysis. Instead, the more reliable technique of studying traces of the same structure on two inclined surfaces was used. One such analysis applied to the parallel striations is illustrated by Figure 4. The directions of the striations in alpha grains a, b, c, and d of Figure 2 were found to bear no simple relationship to the orientation of the former beta lattice. Instead, numerous analyses showed that the striations were caused by planes lying parallel ($\pm 2°$) to $\{14.0\}_\alpha$ planes of the hexagonal lattice. These planes lie close to $\{8,8,11\}_\beta$ in the parent cubic lattice. The striations were parallel to some of the acicular product and thus it was concluded that the habit plane for the acicular product was the same family as that of the striations. These results are in accord with those for zirconium in which the habit plane was also observed to be irrational [3]. Likewise, the $\{8,8,11\}_\beta$ habit is in good agreement with the $\{334\}_\beta$

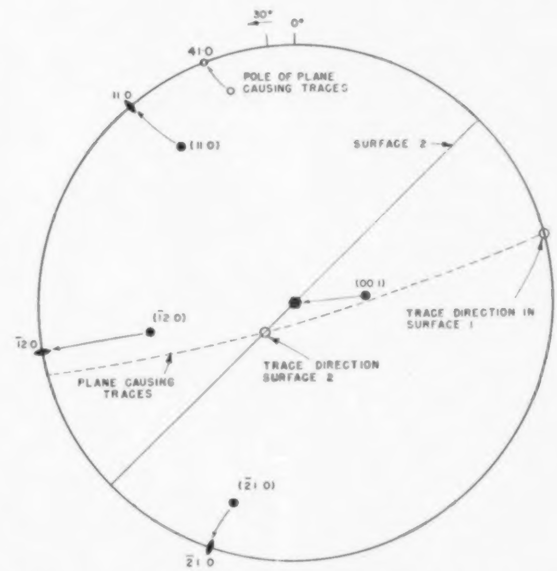

FIGURE 4. Two-surface stereographic analysis of striations in grain of Figure 2. Filled symbols indicate the orientation of the alpha lattice.

family reported for martensite in a quenched Ti-Mn alloy [4]. Since none of these indices are simple, they presumably do not represent the true habit plane of the alpha lattice forming in the beta matrix but rather a pseudo-habit caused by some

sort of deformation process resulting from transformation stresses. This phenomenon is discussed in relation to phase transformations in general in another paper [5].

Work on this subject is being continued.

III. *Reversion of Alpha Grains to their Original Orientation*

Repeated experiments have shown that isolated alpha crystals which were cycled through the critical temperature or held for many hours at temperatures around 1000°C usually failed to become polycrystalline or even show a change in the orientation of the original alpha grain on cooling. This effect probably explains the known difficulty of refining the grain size of titanium-base alloys by heat treatment. If it is true that a single crystal of alpha titanium transforms to a single crystal of the cubic beta phase on heating above the critical temperature, then reversion to the alpha phase on cooling must be nucleated in such a way as to produce the same alpha orientation as in the original crystal. The Burgers orientation relationship permits twelve possible orientations which an alpha grain could assume with respect to its parent beta grain. Therefore, it is improbable that an alpha grain would favor any one of these twelve orientations without the influence of some nucleating agent. Such an agent may be a crystalline inclusion, an oriented overgrowth or a special condition of stress. Similar reversion to the original orientation of the low temperature phase was reported for Zr by Burgers [2], for Tl by Dehlinger [6], and for Co by Dehlinger *et al.* [7].

J. B. Newkirk and A. H. Geisler

General Electric Research Laboratory
The Knolls
Schenectady, New York, U.S.A.

References

1. Geisler, A. H., Hill, J. K., and Newkirk, J. B. J. App. Phys., **19** (1948) 1041–9.
2. Burgers, W. G. Physica, **1** (1933–4) 561.
3. Van Ginneken, A. J. J. and Burgers, W. G. Acta Cryst., **5** (1952) 548.
4. Liu, Y. C. and Margolin, H. The Quench Hardening of Titanium-Manganese Alloys (Interim Technical Report No. 2 on Contract DA-30-069-ORD-207 to Watertown Arsenal Laboratory, Watertown, Mass.).
5. Geisler, A. H. Acta Met., **1** (1952).
6. Dehlinger, U. Metallwirt., **11** (1932) 223–5.
7. Dehlinger, U., Osswald, E., and Bumm, H. Z. Metallk., **25** (1933) 62–3.

Specific Heat and Energy of Transformation of Mg_3Cd*

The binary alloy system composed of magnesium and cadmium presents many unusual features and consequently has been the subject of numerous investigations [1; 2; 3]. Nevertheless, complete agreement has not yet been reached regarding the nature of the transformations which this alloy system undergoes as its temperature and composition are varied. In order to specify the character of the transition between different states of an alloy, it is essential to know the behavior of the specific heat over the relevant range of temperature. Thus Homiakov, Holler, and Troshkina [4] have obtained such curves for the two alloys MgCd and $MgCd_3$, and have concluded that at a temperature of 251°C the former undergoes a first order transformation, whereas the latter undergoes only a second order transformation in the region of 80°C. However the alloy system Mg_3Cd has not been hitherto investigated in this fashion, although its heat of formation has been obtained at a temperature of 25°C [5], and, together with other thermodynamic properties, at 270°C [6]. Therefore, we undertook to carry out a determination of the specific heat of this alloy between 50°C and 200°C.

The specific heat measurements were carried out in an adiabatic calorimeter described in detail elsewhere [7]. Heat was supplied to the sample, which was made in the form of a highly polished cylinder approximately $\frac{3}{4}''$ in diameter and $3''$ long, by means of a small internal nichrome heating element. To minimize losses due to conduction and convection, the sample was suspended within an evacuated chamber by means of a pair of $0.006''$ nichrome wires which served also as the heater leads. Furthermore, to reduce heat losses due to radiation, the calorimeter chamber was also provided with a highly polished copper guard ring shield, the temperature of which was kept nearly at the temperature of the sample by means of a manually controlled electric heating element. Power was supplied to the internal heater by an electronically regulated d.c. power supply, which kept the output voltage constant to one part in 150,000, in series with a large oil-cooled manganin resistor. The value of this resistor was nearly that of the heater (about 600 ohms). With this arrangement, the power input was constant to $\pm$ 1/15 per cent despite a variation of about 5 per cent in the resistance of the nichrome heating element.

*Received January 16, 1953.

Specific heat values were obtained at different rates of heating by measuring at frequent intervals the temperature of the sample as a function of time. All temperature measurements were made with a chromel-alumel thermocouple imbedded in the sample, in conjunction witha Rubicon thermofree

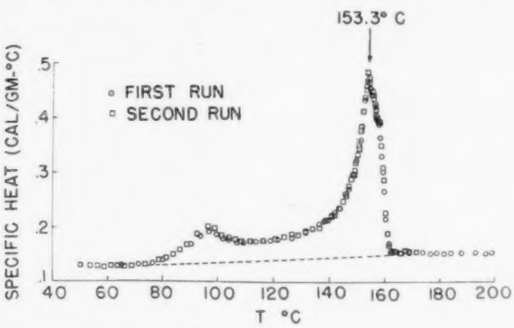

FIGURE 1. Specific heat of the alloy Mg_3Cd as a function of temperature. The rate of heating used was about 0.01 cal/gm sec.

potentiometer. The thermocouple had been previously compared wth a similar couple calibrated by the National Bureau of Standards.

The sample was prepared in the following manner. An oversize casting of the alloy was prepared by the method described by Satterthwaite [8]*. The cadmium and magnesium were respectively 99.95 and 99.99 per cent pure. After preparation, the casting was lightly machined, sealed in a glass container filled with helium and maintained at a temperature of 300°C for two months to homogenize the alloy. The sample used in the measurements was machined from the center of this piece and then annealed at 300°C for several hours. Prior to each measurement the alloy was ordered for at least four hours at a temperature of 110°C and then cooled slowly to room temperature. As a check upon the uniformity of the resultant alloy, material taken from the upper and lower ends of the sample thus prepared was analyzed for its cadmium content by the sulfide method [9].† Four determinations yielded an average composition of 24.7 atomic per cent cadmium with a deviation from this value of less than $\pm$ 0.05 atomic per cent in the individual values.

Figure 1 shows the results of two measurements of the specific heat of this sample, both obtained at the rate of heating of about 0.01 cal/gm sec. which allowed initially a rate of temperature rise of about 4°C/min. The specific heat values have been corrected for the small but not negligible effect of heater capacity, which never exceeded 4 per cent of that of the whole system over the entire temperature range.

As can be seen from the figure, the specific heat of the alloy Mg_3Cd up to 75°C is very close to 0.130 cal/gm °C while beyond 165°C its value remains nearly constant at 0.155 cal/gm °C. These values are to be compared with 0.141 cal/gm °C and 0.146 cal/gm °C which are obtained in the lower and higher temperature regions, respectively, by applying Kopp's law and making use of the accepted values of the specific heats of the components [10]. The value in both cases agrees with the calculated one to within 10 per cent.

In the region between 80°C and 165°C however, the specific heat displays two peaks, a large one at 153.3°C and a smaller one at 97°C. Unlike that of MgCd the specific heat of the present alloy remains finite throughout the range of temperatures involved here. The resolving power of the apparatus is such that an infinite specific heat resulting from a latent energy absorption of as little as 0.3 cal/gm could be readily detected. The transformation must therefore be classed as of the second order.

In view of the fact that the processes leading to the peaks are second order ones, it is to be expected that the shape of the corresponding part of the specific heat versus temperature curve might be dependent upon the rate of heating. In order to investigate the possible existence of such an effect a second pair of experiments was carried out at a rate of heating of some 0.03 cal/gm sec. which is three times that used previously. The resulting curves are shown in Figure 2. It may be noted that the

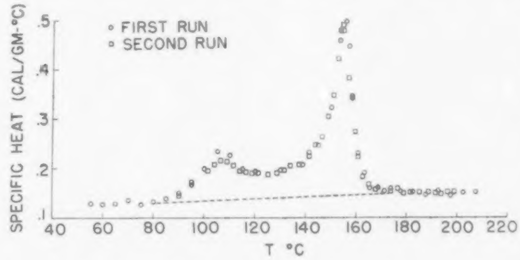

FIGURE 2. Specific heat of Mg_3Cd using a higher rate of heating (approximately 0.03 cal/gm sec.).

second and higher peak is located at nearly the same point as before and is little changed in slope while the smaller peak is shifted to 108°C and seems slightly broader. It follows that the temperature of 153.3°C at which the second peak is located is a curie point for the alloy in equilibrium. The

*We wish to acknowledge our indebtedness to Professor W. E. Wallace and the University of Pittsburgh for the use of their facilities in preparing the alloy.
†We are indebted to D. Otterson for the analysis.

location of the smaller peak on the other hand varies with rate in very much the fashion one would expect if it were determined by a rate process.

The total heat of transformation, represented by the area between the experimental curve and the curve to be expected in the absence of a transformation (indicated by the dashed line), is obtained as 6.5 cal/gm or 0.30 Kcal/gm atom, which is the average obtained from the separate determinations shown in Figures 1 and 2. This is to be compared with the value of 0.24 Kcal/gm atom for $MgCd_3$ obtained by Homiakov, Holler, and Troshkina for the case of $MgCd_3$ which undergoes second order transformation at 78°C.

We are indebted to Dr. G. Groetzinger and Dr. P. Schwed for helpful discussions.

B. Welber, R. Webeler, and F. Trumbore

Lewis Flight Propulsion Laboratory
National Advisory Committee for Aeronautics
Cleveland, Ohio

References

1. Boudouard, O. Comptes Rendus, **134** (1902) 1431.
2. Hume-Rothery, W. and Rowell, S. W. J. Inst. Metals, **38** (1927) 137.
3. Grube, G. and Schiedt, E. Z. anorg. Chem., **194** (1934) 190.
4. Homiakov, K. G., Holler, V. A., and Troshkina, V. A. Moscow University, Reports, **6** (1950) 55.
5. Buck, T. M., Jr., Wallace, W. E., and Rulon, R. M. J. Amer. Chem. Soc., **74** (1952) 136.
6. Trumbore, F. A., Wallace, W. E., and Craig, R. S. J. Amer. Chem. Soc., **74** (1952) 132.
7. Welber, B. J. Appl. Phys., **23** (1952) 876.
8. Satterthwaite, C. B. Ph.D. Thesis, University of Pittsburg (1950).
9. See for example Hillebrand and Lundell, Applied Inorganic Analysis (John Wiley and Sons, 1929), p. 204.
10. Specific heats of Mg and Cd taken from U.S. Bur. Mines Bulletin II 476 (U.S. Government Printing Office, 1949).

Thermal Stabilization of Austenite Iron-Carbon-Nickel Alloys*

We have read, with considerable interest, the paper on thermal stabilization of austenite in iron-carbon-nickel alloys by E. R. Morgan and T. Ko that appeared in the January issue of *Acta Metallurgica*. It is interesting to compare some of their conclusions with data obtained at the National Bureau of Standards in a study of the factors affecting the M_s in two SAE 1050 steels.

Messrs. Morgan and Ko note that, except for two steels (1.0% C, 10% Ni, and 1.3% C, 5% Ni), the M_s was dependent upon the quenching medium used, an indication that the rate of cooling through the austenitic range must have an effect upon the martensitic transformation. They ascribe this depression in M_s with slower rates of cooling to a stabilization effect that occurred during cooling within a certain temperature range above the M_s. Thus, in a steel containing 1.0 per cent C and 5 per cent Ni, this temperature range was found to be between 310° and 405°C (590° and 760°F). They do not, however, explain the two exceptions where no such effect occurred.

We found that varying the cooling rate from 1400° to 2200° to 5000°F per second in the temperature range 1300° to 900°F had no significant effect on the temperature of M_s in the two steels studied. Although not calculated, the three quenching media used had widely different cooling rates at lower temperatures. If the M_s of all steels were indeed sensitive to a stabilization effect at some temperature above the M_s it would seem that widely different cooling rates would have an effect upon the M_s. That the M_s of some steels are not so affected is shown by the data of Messrs. Morgan and Ko as well as our own.

The authors also comment on the fact that their data show that the grain size had no effect upon the progress of the martensite transformation. This finding is contrary to ours as we find that not only do coarser austenite grains result in a decrease in the rate of the austenite → martensite reaction in an appreciable temperature range below the M_s, but that it also raises the M_s itself. As an indication of the magnitude of these changes, the rate of formation of martensite in one of the steels was approximately 0.7 per cent per degree F drop in temperature below the M_s when the austenite grain size was ASTM No. 5 and 0.2 per cent per degree F drop in temperature when the austenite grain size was ASTM No. 2. The M_s corresponding to these two grain sizes was 590° and 613°F, respectively. It was established that these differences were actually associated with the austenite grain size and the temperatures from which the various samples were quenched.

It must be emphasized that our findings are concerned only with the steels noted. A formal paper embodying the results of our studies is now in the process of preparation. In view of the many disagreements among various investigators as to the effects of certain variables on the martensite reaction, it must be concluded that our understanding of the natural laws governing this phenomenon is far from complete.

Samuel J. Rosenberg

National Bureau of Standards
U.S. Department of Commerce
Washington, D.C.

*Received February 23, 1953.

Theory of Initial Stress-Strain Curves in Face-Centered Metals*

In an earlier paper [1] work-hardening by two mechanisms was considered: first, at small strains source hardening occurs, i.e., the longest free lengths of a dislocation generate and produce glide until they are locked by some process not yet understood. The hardening occurs because as the long dislocations are used more stress is required to make the short dislocations generate. At large strains the many dislocations present prevent additional dislocation motion; this is called *interaction hardening*.

The temperature dependence of the source hardening in aluminum can be understood if it is assumed that all of the closely spaced glide lamellae found by electron microscopy in one slip band result from one source. The number of lamellae per band increases with increasing temperature.

Blewitt [2] and co-workers have found that initial hardening in copper is the same at room temperature as it is at liquid nitrogen temperatures. This is consistent with the present electron microscope observations on copper. Barrett [3] did not find multiple lamellae in copper at room temperature. Brown [4] could not resolve lamellae but found glide of 1500 Å at one slip band and 3000 Å at another in copper at room temperature. This suggests that copper behaves at room temperature in a manner similar to aluminum at liquid nitrogen temperature (i.e., in copper at room temperature there may be one or two as yet unresolved lamellae per band). A search should be made for multiple lamellae and initial stress-strain curves dependent on temperature in copper crystals at elevated temperatures.

In the earlier paper [1] it was suggested that the internal stresses resulting from thermal fluctuations produce lamellae by enabling a screw dislocation in a locked slip lamella to undergo cross slip and subsequent Frank-Read generation on a slip plane parallel to the initial locked lamella. It was stated that the number of lamellae per slip band would depend on the stress, the temperature, and the speed of deformation. The temperature dependence was explicitly considered and was found to agree reasonably well with experiments.

Recent data by Brown [5] on the number of lamellae per band in aluminum strained at different rates is, qualitatively at least, in agreement with the above theory. On rapid straining at 450°C, Brown obtained about 11 lamellae per band. On straining at a rate of 1% per day at 450°C he obtained 50 lamellae per band. In both cases the examination was made after a strain of about 10%; the average glide per lamellae was about 2000 Å in both tests. Thus, in the slow test more thermal fluctuations of the necessary linear size and strength were observed because it was possible to wait longer for them.

If the suggestions made connecting the lamella structure and the slope of the initial portion of the stress-strain curve are correct then the fact that the lamella structure is rate dependent implies that the the slope of the initial part of the stress-strain curve is also rate-dependent. In fact, Brown's data indicates that a change of a factor of four can be obtained in the initial slope at 450°C by varying the strain rate. This should be verified experimentally.

This work is supported by the O.N.R.

J. S. Koehler

Department of Physics
University of Illinois
Urbana, Illinois, U.S.A.

References

1. Koehler, J. S. Phys. Rev., **86** (1952) 52.
2. Blewitt, T. H. Durham Meeting, Amer. Phys. Soc., March, 1953.
3. Barrett, C. S. Trans. A.I.M.E., **156** (1944) 62.
4. Brown, A. F. Advances in Physics, Phil. Mag. Supplement, **1**, no. 4 (1952).
5. Brown, A. F. J. Inst. Metals, **80** (1951) 115.

*Received March 11, 1553.

The Structure of Gamma Manganese*

The crystal structure of gamma manganese cannot be determined easily by X-ray methods owing to its temperature range of stability, 1100 to 1138°C, its high vapor pressure and its reactivity. Recently experimental workers [1; 2] have suggested that gamma manganese is face-centered-cubic in structure. Their suggestions are based upon X-ray determinations of the crystal structures of manganese rich binary alloys. They found that in certain single phase binary alloys the gamma phase was face-centered-cubic at elevated temperatures but became face-centered-tetragonal on quenching to room temperature. Basinski and Christian [2] have demonstrated that, in the case of Mn-Cu alloys containing less than 95 per cent manganese, the tetragonal phase forms during cooling by means of a martensitic transformation and that the M_s temperature decreases sharply with increasing copper content.

*Received March 6, 1953.

The gamma phase of pure manganese cannot be retained at lower temperatures even by drastic quenching, although a face-centered-tetragonal form of manganese with an axial ratio of approximately $c/a = 0.94$ may be prepared by electrolysis. Zener [3] has suggested that the tetragonality of this form of manganese is due to antiferromagnetism. Antiferromagnetism is a type of paramagnetism in which the lattice arrangement is such that the magnetic moments of neighboring atoms are aligned antiparallel, producing a zero resultant moment. By analogy with forces between magnets, neighboring atomic moments of parallel orientation should result in a mutual repulsion between the atoms, compared with atomic moments of antiparallel orientation. Consequently, a distorted face-centered-cubic structure having an axial ratio of less than 1.0 will be produced if each (002) plane is composed of atoms with parallel moments and alternate (002) planes have antiparallel orientations. The resultant magnetic moment of such a lattice would be zero if all atomic moments were of equal magnitude.

It has been shown by Isobe [4] that the magnetic susceptibility of high-purity gamma manganese increases with increasing temperature. An increase of susceptibility with temperature is characteristic of antiferromagnetic materials. Paramagnetic materials which are not antiferromagnetic exhibit a magnetic susceptibility which either is independent of, or decreases with, increasing temperature.

It is to be expected that an antiferromagnetic Curie temperature will be a function of the energy of interaction between the electrons in the partially filled 3d shells. On the basis of Isobe's determinations of the magnetic susceptibility of manganese as a function of temperature, it may be concluded that the Curie temperature for gamma manganese lies above the melting point, 1245°C. Néel [5] has estimated a Curie point of 1720°K for manganese and has deduced that the effective magnetic moment of a manganese atom is of the order of 4.0 Bohr magnetons. This value for the magnetic moment is consistent with that calculated [6] for manganese in the ferromagnetic Heusler alloys.

In comparison with the ferromagnetic Curie temperatures of iron, cobalt, and nickel, an antiferromagnetic Curie point of the order of 1450°C is reasonable for interacting moments of 4.0 Bohr magnetons situated on a manganese lattice. However, the addition to manganese of solute elements of the B sub-groups, such as copper or germanium, will almost certainly result in an increase in the number of 3d electrons associated with each of the manganese atoms. This will reduce the magnetic moment of each manganese atom and therefore the Curie temperature of the lattice.

Above the Curie temperature, the alloy will be paramagnetic and face-centered-cubic with random orientation of magnetic moments. Below the Curie temperature, the alloy will become antiferromagnetic and lattice distortion will appear. The degree of lattice distortion would be expected to increase with decreasing temperature below the Curie point. It is significant that Basinski and Christian [2] have observed that the axial ratio for a quenched 88.9 per cent Mn–11.1 per cent Cu alloy, diverged further from 1.0 as the temperature was decreased, and reached a value of $c/a = 0.95$ at -183°C.

It is possible, therefore, that a manganese-based binary alloy may become face-centered-cubic in structure at high temperature by virtue of the fact that the gamma solid solution is then above its Curie temperature. It is, however, by no means certain that pure gamma manganese is also face-centered-cubic. In fact the only experimental observations of the properties of pure gamma manganese, namely those of Isobe [4], indicate that it is both paramagnetic and antiferromagnetic. The latter condition can be satisfied by a face-centered-tetragonal lattice, but not by a face-centered-cubic lattice.

Eric R. Morgan

Metallurgical Department
Scientific Laboratory
Ford Motor Company
Dearborn, Michigan, U. S. A.

References

1. Zwicker, U. Z. Metallk., **42** (1951) 246.
2. Basinski, Z. S. and Christian, J. W. J. Inst. Metals, **80** (1952) 659.
3. Zener, C. Phys. Rev., **81** (1951) 440.
4. Isobe, M. Tôhoku Imp. Univ. Res. Inst., Sci. Rep., **A3** (1951) 78.
5. Neel, L. Proc. Phys. Soc. London, **65** (1952) 869.
6. Coles, B. R., Hume-Rothery, W., and Myers, H. P. Proc. Roy. Soc., **A196** (1949) 125.

BOOK REVIEW

Metal Data. By S. L. Hoyt. Second edition. New York: Reinhold Publishing Corporation. 1952. Pp. xiv + 526.

This is a new edition of *Metals and Alloys Data Book*, which was published in 1943. It is extensively modified by the substitution of new material for old and by the addition of substantial new sections; some of these reflect the growing importance of metals such as molybdenum, titanium, and zirconium, which have emerged or are emerging from the academic atmosphere of the chemistry book into the hard world of practical applications. Another important metallurgical development that is reflected in the new edition is the section on the so-called "Super-Alloys"; that is, alloys developed for use under the conditions that are encountered in gas turbine engineering. *Metal Data* contains a wealth of empirical information; the author does not attempt to interpret or explain, and the book does not therefore make any contribution to the understanding of metals. It will undoubtedly be of the greatest value to very many practising metallurgists, and it will be the source of much useful and interesting information for many whose thirst for knowledge about metals is less practical.

The reviewer, according to custom, looks diligently for something to criticize; he is not in a position to question the validity of the data, which he is happy to accept; he is filled with admiration at the skill with which such a vast amount of information is presented in such accessible form, and in relatively small space: he cannot think of anything which has been left out; the only fault he can find is so trivial that it emphasizes the quality of the rest—it is in the iron-carbon diagram, on page 18, and on the dust cover, in which austenite and ferrite are described as solid solutions of carbide in gamma-iron and alpha-iron respectively: why not carbon? But this is a matter of interpretation and the purpose of this particular diagram, and of the whole book, is to present data.

B. Chalmers

SOME CURRENT PAPERS IN OTHER JOURNALS

Journal of Chemical Physics

March, 1953 (Partial contents)

High temperature susceptibility of permanent dipole lattices. Robert Rosenberg and Melvin Lax.

Electric resistivity of interstitial compounds of graphite. S. Mrozowski.

Presence of free sodium in sodium chloride crystals containing color centers and color center precursors. Michael Hacskaylo and Dumas Otterson.

April, 1953 (Partial Contents)

Decomposition of nitrate crystals by ionizing radiations. Gerhart Hennig, Robert Lees, and Max S. Matheson.

On the kinetics of the disorder-order transformation in Cu_3Au. Norman W. Lord.

Diffusion with a sharp moving boundary. Hiroshi Fujita.

Concerning the low temperature specific heat of tellurium. Warren DeSorbo.

Journal of the Chemical Society

April, 1953 (Partial Contents)

Passivity of metals. Part XII. Intense attack at the water-line of otherwise passive metal. A. M. Peers and U. R. Evans.

The properties of freshly formed surfaces. Part XIX. Dynamic surface potentials and the desorption process: the spreading of decyl alcohol films. C. C. Addison and D. Litherland.

The properties of freshly formed surfaces. Part XX. An examination of the use of dynamic surface potentials in the study of adsorption rates. C. C. Addison and D. Litherland.

The properties of freshly formed surfaces. Part XXI. The influence of chain length and structure on the surface potentials of aqueous solutions of alcohols. C. C. Addison and D. Litherland.

Journal of the Institute of Metals, Vol. 81

Part 8, April, 1953

Presidential address. F. C. Thompson.

The kinetics of the eutectoid transformation in zinc-aluminium alloys. R. D. Garwood and A. D. Hopkins.

The liquid immiscibility region in the aluminium-lead-tin system at 650°, 750°, and 800°C. Morgan H. Davies.

The influence of thallium on the creep of lead. R. C. Gifkins.

Some metallographic observations on aged aluminium-copper alloys. I. J. Polmear and H. K. Hardy.

The log-log plot of solubility data in ternary metallic systems. H. K. Hardy.

Part 9, May, 1953

Mechanical anisotropy in some ductile metals. W. A. Backofen and B. B. Hundy.

The formation of intercrystalline voids in solution-treated magnesium-aluminium alloys. E. Lardner.

A note on the mathematical analysis of creep curves. L. M. T. Hopkins.

Equilibrium relations at 460°C in aluminium-rich alloys containing 0–7% copper, 0–7% magnesium, and 0.6% silicon. H. J. Axon.

The constitution of nickel-rich alloys of the nickel-chromium-aluminium system. A. Taylor and R. W. Floyd.

Journal of Metals, Vol. 5

No. 3, March, 1953

Residual stresses introduced during metal fabrication. K. R. van Horn.

Tristage crystallization process for utilizing western ferrophosphorus. L. H. Banning, W. E. Anable, and R. T. C. Rasmussen.

Directional properties of 2S aluminium. K. T. Aust and F. R. Morral.

Some applications of the thermodynamic theory of irreversible processes to physical metallurgy. E. S. Machlin.

Measurement of particle sizes in opaque bodies. R. L. Fullman.

Preferential etch for use in optical determination of germanium crystal orientation. R. H. Wynne and Colman Goldberg.

Grain boundary films in boron steels. J. W. Spretnak and R. Speiser.

No. 4, April, 1953

Effect of various elements on hot-working characteristics and physical properties of Fe-C alloys. C. T. Anderson, R. W. Kimball, and F. R. Cattoir.

Stabilization of the austenite-martensite reaction in a high chromium steel. S. C. Das Gupta and B. S. Lement.

Effects of macrostructure on the performance of alnico permanent magnets. D. G. Ebeling and A. A. Burr.

Vanadium-uranium constitutional diagram. H. A. Saller and F. A. Rough.

Silver-cadmium eutectoid. G. R. Speich and D. J. Mack.

Kinetics of the oxidation of galena in sodium hydroxide solutions under oxygen pressure. J. E. Andersen, J. Halpern, and C. S. Samis.

Formation of deformation bands in Al-3 Pct Mg monocrystals during cold rolling. J. Herenguel, P. Lacombe, and P. Lelong.

Statistical grain structure studies: Plane distribution curves of regular polyhedrons. F. C. Hull and W. J. Houk.

The Philosophical Magazine

March, 1953 (Partial Contents)

The exchange energy of nearly free electrons in metals. E. P. Wohlfarth.

The electrical resistivity of gold at very low temperatures. A. J. Croft, E. A. Faulkner, J. Hatton, and E. F. W. Seymour.

A dislocation mechanism for the growth of hopper crystal faces and the growth of salol crystals from solution and from the melt. S. Amelinckx.

April, 1953

Some experiments on photographic sensitivity. J. M. Hedges and J. W. Mitchell.

The laminar boundary layer of a rotating body of revolution. C. R. Illingworth.

The reaction ^{181}Ta (γ, 2n) ^{179}Ta at 17.6 MeV and some remarks on nuclear photodisintegration. J. H. Carver, R. D. Edge, and D. H. Wilkinson.

Neutrons produced by high energy protons. T. C. Randle, J. M. Cassels, T. G. Pickavance, and A. E. Taylor.

The role of preferred orientation in elasticity investigations. G. Bradfield and H. Pursey.

Anomaly in the rigidity modulus of copper alloys for small concentrations. J. FRIEDEL.

Bombardment of ordered Cu_3Au by 1 MeV electrons. C. E. DIXON, C. J. MEECHAN, and J. A. BRINKMAN.

Radiative widths of dipole transitions in light elements. D. H. WILKINSON.

Revue de Métallurgie, 50e Année

Numéro 2, février, 1953

Le remplacement des éléments d'alliage par le bore dans les aciers de cémentation et de traitement. ROBERT SCHERER et KARL BUNGARDT.

Recherches sur l'existence de précipitations de carbures lors du vieillissement des alliages fer-carbone, à l'aide de micrographies optiques et électroniques. H. J. SEEMANN, D. HARTNAGEL et V. HINTZPETER.

Détermination métallographique des températures subies en service. Cas des alliages réfractaires nickel-chrome tenaces à chaud du type 80-20. CH. BÜCKLE, P. A. JACQUET et J. POULIGNIER.

Essais de résistance de longue durée à température ambiante sur des éprouvettes entaillées en alliages d'étain. W. SIEGFRIED.

Analyse non destructive d'objets métalliques anciens. GEORGE AMBROSINO et PIERRE PINDRUS.

Etude de l'homogénéisation des ségrégations dendritiques de phosphore et d'arsenic dans les aciers, par la méthode autoradiographique. A. KOHN.

Numéro 3, mars, 1953

Analyse quantitative des laitiers par la méthode combinée des solutions et des pastilles comprimées. E. V. ROUIR et A. M. VANBOKESTAL.

Comparaison expérimentale de diverses techniques de détection des fissures par ressuage. H. DE LEIRIS.

Désorientations internes observées sur monocristaux de solution solide Al-Mg à 3% déformés par laminage à froid. J. HERENGUEL, P. LELONG et P. LACOMBE.

Notes sur la production de petits lingots du type « billett » en acier semi-calmé élaboré sous un seul laitier au four à arc basique. MAX PETITDIDIER.

Connaissances récentes sur la formation des cornes à l'emboutissage de l'aluminium et les possibilités de les supprimer. H. A. J. STELLJES.

Contribution à l'étude des fontes à graphite sphéroïdal et à leurs applications. CORNELIO GIANOLA.

Microscope électronique à émission, ses applications en métallurgie. ALBERT SEPTIER.

Le volume-débitgraphe adapté à l'emploi au convertisseur Thomas de vent enrichi en oxygène. R. MICHAUX et P. LEROY.

ORDRE À PETITE DISTANCE DANS LES SOLUTIONS SOLIDES MÉTALLIQUES DE SUBSTITUTION*

GERARD FOURNET†

On montre qu'il existe toujours un ordre à petite distance dans les solutions solides de substitution. Dans le cas d'un modèle très simple nous donnons les expressions des différents paramètres d'ordre à petite distance.

SHORT RANGE ORDER IN SUBSTITUTIONAL SOLID SOLUTIONS IN METALS

It is shown that short range order always exists in substitutional solid solutions. Expressions are given for the different parameters of short range order for a very simple model.

NÄHEORDNUNG IN SUBSTITUTIONSMISCHKRISTALLEN VON FESTEN METALL-LÖSUNGEN

Es wird gezeigt, dass in allen Substitutionsmischkristallen fester Lösungen immer eine Näheordnung existiert. Für ein sehr einfaches Modell werden die Ausdrücke für die verschiedenen Parameter der Näheordnung angegeben.

I. Introduction

Les solutions solides métalliques de substitution ont d'abord été regardées comme des ensembles de plusieurs espèces d'atomes qui sont répartis *au hasard* aux noeuds d'un réseau plus ou moins déformé.

On sait cependant que pour les alliages subissant les modifications ordre-désordre les expériences et les théories montrent la persistance d'un ordre à petite distance quand tout effet d'ordre à grand distance a disparu; cette notion d'ordre à petite distance semble avoir été d'abord uniquement réservée à de tels alliages : les premières expériences prouvant l'existence d'un tel ordre dans les alliages ne subissant aucunes modifications ordre-désordre (Au-Ag, Guinier [1]) étaient citées comme des curiosités ou des anomalies.

Par analogie avec les résultats des études expérimentales et théoriques relatées ci-dessus et qui prouvent que l'existence d'un ordre à petite distance dans une substance cristallisée n'est pas liée à l'existence d'un ordre à grande distance, nous pensons que *les phénomènes d'ordre à petite distance sont toujours présents dans les solutions solides métalliques* bien que par définition les phénomènes d'ordre à longue distance en soient absents.

Ce n'est pas là une proposition complètement nouvelle; elle se trouve plus ou moins implicitement admises dans plusieurs mémoires. Hume-Rothery [2] déclare « It is almost certain that in most primary solid solutions there is a short range order » ; Barrett [3] énonce: « Ideally, solute and solvent atoms are distributed at random on the atoms sites but this completely disordered distribution is probably rarely attained » . Nous voulons simplement insister sur la généralité du phénomène.

Quelle que soit le modèle de solutions solides adopté les différents atomes constituants possèdent des propriétés différentes; pour deux espèces d'atomes données chaque atome « préfère »—suivant les lois de l'équilibre thermodynamique—être entouré d'atomes semblables ou dissemblables; nous voyons ainsi apparaître très simplement le processus d'ordre à petite distance.

Signalons enfin qu'en liaison avec notre travail théorique, et à l'occasion d'une étude des alliages Al-Ag, une preuve expérimentale (Walker, Blin et Guinier [4]) de l'existence d'un ordre à petite distance dans les solutions solides Al-Ag vient d'être apportée.

2. Définition de l'Ordre à Petite Distance

Les différentes probabilités que nous aurons à considérer sont:

—$n_{1,A}(\mathbf{x}_k)$ probabilité de trouver un atome A au noeud k défini par l'extrémité du vecteur $\mathbf{x}_k$;

— $n_{2,AB}(\mathbf{x}_k, \mathbf{x}_j)$ probabilité de trouver *à la fois* un atome d'espèce A au noeud k et un atome d'espèce B au noeud j.

Dans le cas des substances sans ordre à grande distance (cas des solutions solides), $n_{1,A}(\mathbf{x}_k)$ est identique à p_A quand $p_A N$ désigne le nombre d'atomes d'espèce A, sur les N noeuds du réseau considéré; la probabilité $n_{2,AB}(\mathbf{x}_k, \mathbf{x}_j)$ ne dépend alors que du module du vecteur $\mathbf{x}_k - \mathbf{x}_j$ aussi la noterons nous par $n_{2,AB}(r_q)$ quand les noeuds k et j sont en position de $q^{ièmes}$ voisins.

Nous dirons qu'il existe un ordre à petite distance entre $q^{ièmes}$ voisins quand le fait de savoir qu'il

*Received March 24, 1953.

†ONERA, Paris, France. Maintenant aux Laboratoires de la Société Alsacienne de Constructions Mécaniques (Télécommunications), 51 rue de l'Amiral Mouchez, Paris 13, France.

existe un atome d'espèce A au noeud k modifie la probabilité de trouver un atome d'espèce B au noeud j ($q^{ième}$ voisin du noeud k), c'est-à-dire quand $n_{2.AB}(r_q)$ est différent de $p_A\, p_B$.

Les fonctions $n_{2.CD}$ (où C et D peuvent désigner indifféremment toutes les espèces d'atomes) ne peuvent être choisies indifféremment; ces fonctions doivent satisfaire les relations:

$$(1) \qquad \sum_D n_{2.CD}(r) \equiv p_c.$$

Pour un alliage binaire AB nous obtenons:

$$(2) \qquad n_{2.AA}(r_q) + n_{2.AB}(r_q) \equiv p_A,$$

$$(3) \qquad n_{2.BA}(r_q) + n_{2.BB}(r_q) \equiv p_B;$$

il existe deux relations entre les trois fonctions n_2 ($n_{2.AB} \equiv n_{2.BA}$) de sorte que nous pouvons toutes les exprimer en fonction d'une seule d'entre elles. En choisissant $n_{2.AA}$ comme variable principale nous trouvons ainsi:

$$(4) \qquad n_{2.AB}(r) \equiv n_{2.BA}(r) = p_A - n_{2.AA}(r),$$

$$(5) \qquad n_{2.BB}(r) = p_B - p_A + n_{2.AA}(r).$$

Dans le cas général où m espèces d'atomes sont présents il existe $m(m+1)/2$ fonctions n_2 différentes liées par m relations; il y a donc $m(m-1)/2$ fonctions n_2 principales. Nous voyons ainsi que les solutions solides binaires se présentent de façon très spéciale (une seule fonction n_2 suffit à tout déterminer); c'est pour cela qu'il est relativement facile d'obtenir des renseignements précis (thermodynamique, diffusion des rayons X etc.) pour ces solutions.

3. Ordre à Petite Distance et « Théorie Statistique des Propriétés des Solutions Solides »

Smoluchowski [5] envisage les influences des fluctuations locales dans la solution solide; il suppose au préalable un désordre idéal c'est-à-dire que $n_{2.CD} = p_C\, p_D$. La probabilité pour que les z atomes voisins d'un noeud A comprennent r atomes A est alors $P(r) = C_z^r\, p_A^r\, p_B^{z-r}$; la contribution moyenne qu'apporte un atome A de la solution solide à un phénomène physique quelconque M dépendant de r est alors proportionnelle à

$$(6) \qquad \sum_r P(r) M(r)$$

alors que la contribution similaire due à l'entourage moyen

$$\bar{r} = \frac{\sum rP(r)}{\sum P(r)} = zp_A$$

serait:

$$(7) \qquad M(zp_A).$$

Smoluchowski a montré que dans certaines conditions les expressions du type (6) étaient en meilleur accord avec les faits que les expressions simples du type (7).

L'existence d'un ordre à petite distance conduit à remplacer la probabilité $P(r)$ détaillée ci-dessus par:

$$(8) \qquad C_z^r \left(\frac{n_{2.AA}}{p_A}\right)^r \cdot \left(\frac{n_{2.AB}}{p_A}\right)^{z-r}.$$

Nous voyons ainsi que les considérations statistiques de Smoluchowski et la notion d'ordre à petite distance sont indépendantes.

4. Définition du Modèle de Solution Solide Adopté

Nous choisissons un modèle tout à fait analogue à celui adopté pour la plupart des théories des modifications ordre-désordre:

1° Le réseau est parfait, sans distorsion, tous les noeuds sont occupés; on néglige tout effet d'agitation thermique.

2° On admet que l'énergie potentielle totale est la somme des énergies mutuelles des atomes pris deux à deux.

Ce modèle, outre les bonnes prévisions qu'il permet de faire au sujet des modifications ordre-désordre, nous a permis récemment d'expliquer les déviations expérimentales relatives à la loi de Vegard [6].

5. Expression de l'Intensité du Rayonnement X Diffusé par une Solution Solide

La diffusion des rayons X constitue un moyen d'études important—et le seul direct—de l'ordre à petite distance. Les expressions de l'intensité du rayonnement diffusé ont déjà été données par Wilchinsky [7; 8] et de façon plus complète par Smoluchowski [9]. Nous avons retrouvé ces expressions à partir d'une formule plus générale que nous avons établie par ailleurs [10] :

$$(9) \quad I(\mathbf{h}) = I_e(h)\bar{N}\{p_A p_B[F_A(h) - F_B(h)]^2 - \sum_{\mathbf{r}\neq 0} \cos(\mathbf{h}\cdot\mathbf{r})b(r,h)\} + I_e(h)[p_A F_A(h) + p_B F_B(h)]^2 \sum_k \sum_j \cos[\mathbf{h}\cdot(\mathbf{x}_k - \mathbf{x}_j)]$$

où $\mathbf{h}$ désigne le vecteur $2\pi(\mathbf{s} - \mathbf{s}_0)/\lambda$; $\mathbf{s}$ et $\mathbf{s}_0$ étant les vecteurs unitaires dirigés suivant les rayons diffusés et incident (le module h de $\mathbf{h}$ possède la valeur $4\pi \sin\theta/\lambda$ si 2θ désigne l'angle de diffusion); $I_e(h)$, l'intensité diffusée par un électron placé dans les conditions considérées; et $F_A(h)$, le facteur de structure de l'atome d'espèce A. La fonction $b(r, h)$ est égale à :

$$(10)\quad b(r, h) = \sum_C \sum_D F_C(h) p_C \left[p_D - \frac{n_{2.CD}(r)}{p_C} \right] F_D(h)$$

où les indices C et D peuvent désigner toutes les espèces présentes d'atomes (ici A et B).

Le deuxième terme de (9) contenant la double somme, représente des termes analogues en tous points à ceux qui correspondent à un cristal parfait; ce terme sera responsable des taches ou des raies de diffraction. Nous nous occupons maintenant uniquement du premier terme qui conduit à des variations lentes de l'intensité en fonction de l'angle; dans tout ce qui suit « intensité diffusée » nous servira à désigner ce premier terme uniquement.

Les relations (1) permettent de mettre $b(r, h)$ sous la forme :

$$(11)\quad b(r, h) = [F_A(h) - F_B(h)]^2 \cdot [p_A^2 - n_{2.AA}(r)].$$

L'« intensité diffusée » peut donc s'exprimer par :

$$(12)\quad I(\mathbf{h}) = I_e(h)\bar{N}[F_A(h) - F_B(h)]^2 \cdot \left\{ p_A p_B - \sum_{\mathbf{r}\neq 0} \cos(\mathbf{h}\cdot\mathbf{r}) \cdot [p_A^2 - n_{2.AA}(r)] \right\} ;$$

afin de pouvoir mettre le produit $p_A\ p_B$ en facteur nous écrirons :

$$(13)\quad I(\mathbf{h}) = I_e(h)\bar{N} p_A p_B [F_A(h) - F_B(h)]^2 \cdot \left\{ 1 + \sum_{\mathbf{r}\neq 0} \cos(\mathbf{h}\cdot\mathbf{r}) \frac{p_A}{p_B} \left[\frac{n_{2.AA}(r)}{p_A^2} - 1 \right] \right\} .$$

Nous avons fait apparaître les quantités $n_{2.AA}$ dans cette formule parce que ce sont des expressions que nous calculerons dans la suite de cet article. On peut obtenir une expression plus symétrique de l'intensité en faisant intervenir les quantités $n_{2.AB}$ puisque :

$$(14)\quad \frac{p_A}{p_B}\left[\frac{n_{2.AA}(r_q)}{p_A^2} - 1 \right] = 1 - \frac{n_{2.AB}(r_q)}{p_A p_B} = \alpha_q ;$$

on reconnaît dans l'expression (14), la valeur des coefficients α_q utilisés par Warren et ses élèves.

L'intensité diffusée peut alors s'exprimer par :

$$(15)\quad I(\mathbf{h}) = I_e(h)\bar{N} p_A p_B [F_A(h) - F_B(h)]^2 \cdot \left\{ 1 + \sum_{\mathbf{r}\neq 0} \alpha_q \cos(\mathbf{h}\cdot\mathbf{r}) \right\} .$$

Pour détailler la notation $\sum$ par rapport à $\mathbf{r}$, considérons par exemple le système cubique à faces centrées; il existe 12 premiers voisins d'un atome quelconque et par conséquent nous aurons dans la somme en question 12 termes facteurs de α_1; chacun de ces termes sera de la forme : $\cos\,(h\ r_1 \cos\phi)$ où ϕ désigne l'angle formé par $\mathbf{h}$ et un des douze vecteurs $\mathbf{r}_1$.

Quand il n'y a pas d'ordre à petite distance les coefficients α_q sont nuls et l'intensité devient égale à :

$$(16)\quad I(h) = I_e(h)\bar{N} p_A p_B [F_A(h) - F_B(h)]^2,$$

formule fournie par Laue [11]. *L'ensemble des considérations et hypothèses faites par Smoluchowski* [5] *conduit à prévoir cette dernière expression* (16) *pour l'intensité diffusée.*

L'intérêt des formules (13) et (15) est qu'elles ne font intervenir *qu'une seule* des fonctions n_2 et que par conséquent on peut donner une interprétation simple de ces formules.

6. Calcul des Termes $n_{2.AA}(r_q)$

Nous désignons maintenant p_A par p et $n_{2.AA}$ par n_2.

Pour le calcul des n_2 nous utiliserons les données de l'article d'Yvon [12] sur les transformations ordre-désordre et nous renvoyons le lecteur pour les définitions et les autres développements à un autre article [13]. Nous employons toujours l'approximation :

$$(17)\quad \log n_{2,ij} = \log B_{2,ij} + \sum_k \log B_{3,ijk}.$$

La plupart des solutions solides appartiennent au système cubique faces centrées aussi nous n'examinerons que ce cas. Nous avons déjà donné pour ce type de réseau [14] les expressions permettant le calcul des n_2 quand on suppose que seules les énergies entre premiers et seconds voisins sont non nulles et que l'on ne fait intervenir que les termes B_2 et B_3. Ces expression sont les suivantes :

$$(18)\quad \log\frac{n_2(r_1)}{p^2} = \log\frac{B_2(w_1)}{p^2} + 4\log B_3(w_1; w_1, w_1) + 4\log B_3(w_1; w_1, w_2),$$

$$\log\frac{n_2(r_2)}{p^2} = \log\frac{B_2(w_2)}{p^2} + 4\log B_3(w_2; w_1, w_1),$$

$$\log\frac{n_2(r_3)}{p^2} = 2\log B_3(1; w_1, w_1) + 2\log B_3\,(1; w_1, w_2),$$

$$\log \frac{n_2(r_4)}{p^2} = \log B_3(1; w_1, w_1) + 2 \log B_3(1; w_2, w_2),$$

$$\log \frac{n_2(r_5)}{p^2} = \log B_3(1; w_1, w_2),$$

$$\log \frac{n_2(r_8)}{p^2} = \log B_3(1; w_2, w_2),$$

$$\log \frac{n_2(r_6)}{p^2} = \log \frac{w_2(r_7)}{p^2} = \log \frac{n_2(r_9)}{p^2} = \ldots = 0\cdot$$

La quantité w_q représente

$$w_q = e^{-W_q/kt}$$

où l'énergie W_q est définie par

$$W_q = W_{AA.q} + W_{BB.q} - 2W_{AB.q} \equiv W(r_q) \tag{19}$$

quand $W_{AB.q}$, par exemple, désigne l'énergie potentielle de deux atomes A et B situés sur deux noeuds en position de $q^{\text{ièmes}}$ voisins; nous n'aurons à considérer que deux valeurs de w_q: w_1 (premiers voisins) et w_2 (seconds voisins).

Nous devons maintenant évaluer les valeurs des termes des types suivants :

$$B_2(a),\ B_3(1; a, b),\ B_3\ (1; a, a),\ B_3\ (a; a, b,),\ B_3\ (b; a, a),\ B_3(a; a, a)$$

où a et b désignent indifféremment les valeurs w_1 et w_2 que peut prendre w_q.

L'expression de $B_2(a)$ est [12]

$$B_2(a) = \frac{1 + (a-1)2p - \sqrt{(2p-1)^2 + 4ap(1-p)}}{2(a-1)}. \tag{20}$$

Calcul de $B_3(1; a, b)$

En écrivant que les probabilités n_i, n_j et n_k (figure 1) possèdent une valeur commune égale à p nous obtenons (voir [14])

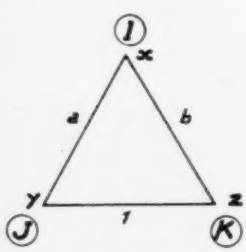

FIGURE 1

$$n_i = n_j \quad \text{soit } x(1 + zb) = y(1 + z) \tag{21}$$

$$n_i = n_k \quad \text{soit } x(1 + ya) = z(1 + y) \tag{22}$$

$$n_i = p \quad \text{soit}$$

$$p = \frac{x + xya + xzb + xyzab}{1 + x + y + z + xya + yz + xzb + xyzab} = \frac{x(1 + ya)(1 + zb)}{(1 + y)(1 + z) + x(1 + ya)(1 + zb)} \tag{23}$$

En considérant la relation (23) comme une équation en x, nous obtenons :

$$x(1-p) = p\,\frac{(1+y)(1+z)}{(1+ya)(1+zb)} = \frac{p}{yz}\cdot\frac{z(1+y)}{(1+ya)}\cdot\frac{y(1+z)}{(1+zb)} = \frac{p}{yz}\,x^2$$

d'où

$$x = yz\,\frac{1-p}{p}. \tag{24}$$

Pour obtenir l'équation en y nous effectuons les transformations suivantes :

$$p = \frac{(1+ya)(1+zb)x}{(1+y)(1+z) + x\cdot\dfrac{z(1+y)}{x}\cdot\dfrac{y(1+z)}{x}} = \frac{(1+ya)(1+z)y}{(1+y)(1+z)\left(1 + \dfrac{p}{1-p}\right)}$$

d'où

$$(1-p)ay^2 + (1-2p)y - p = 0; \tag{25}$$

en remarquant que d'après sa définition y est obligatoirement positif nous obtenons :

$$ya = \frac{-(1-2p) + \sqrt{(1-2p)^2 + 4ap(1-p)}}{2(1-p)}. \tag{26}$$

De même façon on peut établir que

$$zb = \frac{-(1-2p) + \sqrt{(1-2p)^2 + 4bp(1-p)}}{2(1-p)}.$$

Le calcul du terme $B_3(1; a,b)$ s'effectue en identifiant les deux expressions de n_{jk} :

$$n_{jk} = \frac{yz + xyzab}{(1+y)(1+z) + x(1+ya)(1+zb)} \equiv B_2(1)B_3(1; a, b)$$

puis en transformant la première expression en :

$$n_{jk} = \frac{x^{-1}yz + yazb}{(1+ya)(1+zb)(1+xy^{-1}z^{-1})} = \frac{p(1-p)^{-1} + yazb}{(1+ya)(1+zb)(p^{-1})},$$

nous pouvons obtenir

$$B_3(1; a, b) = \frac{(1-p)^{-1} + p^{-1}yazb}{(1+ya)(1+zb)}. \tag{27}$$

Nous avons trouvé que la méthode la plus rapide d'effectuer les calculs numériques était de passer par l'intermédiaire de la détermination des valeurs de ya et zb.

Calcul de B_3 (1; a, a)

Nos calculs précédents sont valables à condition de supposer que $a = b$ et par conséquent que $y = z$; le résultat est donc :

$$B_3(1; a, a) = \frac{(1-p)^{-1} + p^{-1}(ya)^2}{(1+ya)^2}. \tag{28}$$

Nous avons obtenu une autre expression du terme $B_3(1;\, a, a)$ où le radical ne figure qu'au dénominateur mais l'expression que nous donnons permet les calculs numériques les plus rapides.

Calculs des $B_3(a;\, a, b)$ et $B_3(b;\, a, a)$

En écrivant que d'une part, $n_i = n_j$ (fig. 2) soit :

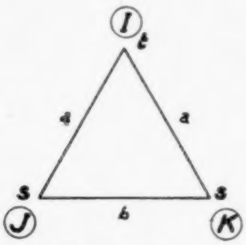

FIGURE 2

$$t(1 + sa) = s\,(1 + sb) \tag{29}$$

et que d'autre part $n_i = p$ soit :

$$p = \frac{t + 2tsa + s^2a^2bt}{1 + t + 2s + 2tsa + s^2b + ts^2a^2b}$$

$$= \frac{t(1 + 2sa + s^2a^2b)}{(1 + 2s + s^2b) + t(1 + 2sa + s^2a^2b)}$$

nous obtenons pour l'expression de t

$$t = \frac{p}{1-p} \cdot \frac{1 + 2s + s^2b}{1 + 2sa + s^2a^2b}$$

ce qui permet de déterminer s au moyen de l'équation :

$$\frac{p}{1-p} \cdot \frac{1 + 2s + s^2b}{1 + 2sa + s^2a^2b} = \frac{s(1 + sb)}{1 + sa} \tag{30}$$

ou encore

$$\begin{aligned} (31)\quad & s^4(1-p)a^2b^2 + s^3[(1-p)a^2b + (2-3p)ab] \\ & + s^2(1-2p)(2a+b) + s(1 - 3p - ab) - p = 0. \end{aligned}$$

Le calcul de $B_3(a;\, a, b)$ s'effectue en identifiant les deux expressions de n_{ij}

$$n_{ij} = \frac{tsa + ts^2a^2b}{(1 + 2s + s^2b) + t(1 + 2sa + s^2a^2b)}$$

$$\equiv B_2(a)\, B_3(a; a, b)\ ;$$

après transformation

$$n_{ij} = \frac{sa(1 + sab)}{(1 + 2s + s^2b)t^{-1} + (1 + 2sa + s^2a^2b)}$$

$$= \frac{sa(1 + sab)}{(1 + 2sa + s^2a^2b)[1 + (1-p)p^{-1}]}$$

d'où

$$B_3(a; a, b) = \frac{sa + s^2a^2b}{1 + 2sa + s^2a^2b} \cdot \frac{p}{B_2(a)}. \tag{32}$$

De même, pour atteindre la valeur de $B_3(b;\, a, a)$, nous considérons en premier lieu :

$$n_{jk} = \frac{s^2b + ts^2a^2b}{(1 + 2s + s^2b) + t(1 + 2sa + s^2a^2b)}$$

$$\equiv B_2(b)\, B_3(b; a, a)$$

pour obtenir :

$$B_3(b; a, a) = \frac{sb\,\dfrac{1 + sa}{1 + sb} + s^2a^2b}{1 + 2sa + s^2a^2b} \cdot \frac{p}{B_2(b)}. \tag{33}$$

Calcul de $B_3(a;\, a, a)$

Nos calculs précédents concernant $B_3(a;\, a, b)$ ou $B_3(b;\, a, a)$ sont valables à condition de poser $b = a$ et par conséquent $s = t$; nous désignerons maintenant la valeur commune de s et t par r.

L'équation en r s'obtient directement à partir de l'équation en s (30)

$$\frac{p}{1-p} \cdot \frac{1 + 2r + r^2b}{1 + 2ra + r^2a^3} = r, \tag{34}$$

soit encore :

$$r^3a^3(1-p) + r^2a(2-3p) + r(1-3p) - p = 0\ ; \tag{35}$$

l'expression de $B_3(a;\, a, a)$ est alors :

$$B_3(a; a, a) = \frac{ra + r^2a^3}{1 + 2ra + r^2a^3} \cdot \frac{p}{B_2(a)}. \tag{36}$$

Nous sommes donc maintenant en mesure de prévoir le réseau réciproque de la solution solide considérée (nous avons déjà effectué ce travail dans le cas des alliages Au-Cu_3 au-dessus de leur température critique). Dans l'intensité diffusée :

$$I(\mathbf{h}) = I_e(h)[F_A(h) - F_B(h)]^2 \cdot \Big\{1 + \sum_{\mathbf{r}\neq 0} \alpha_q \cos(\mathbf{h}\,.\,\mathbf{r})\Big\} \tag{15}$$

nous pouvons considérer à l'intérieur de l'accolade le coefficient $i_q(\mathbf{h})$ d'un α_q déterminé; ce coefficient

est la somme de c_q cosinus, c_q étant le nombre de $q^{ièmes}$ voisins d'un atome quelconque. A titre d'exemple les figures 3 et 4 représentent les courbes de niveau de $i_1(\mathbf{h})$ et $i_2(\mathbf{h})$ relative au plan (1.0.0.) du réseau réciproque (chaque figure représente une maille).

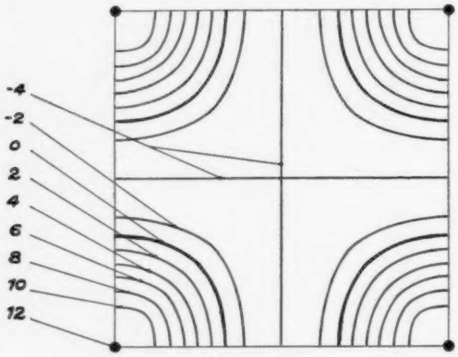

FIGURE 3

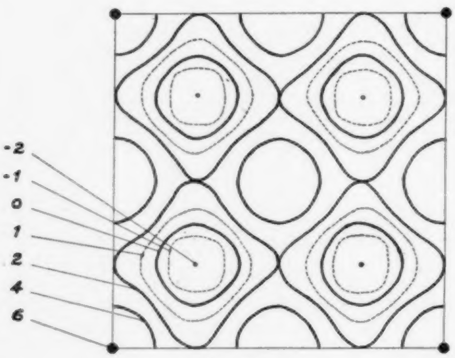

FIGURE 4

La valeur de la limite de l'intensité diffusée aux très faibles angles s'obtient à partir de la formule générale :

$$(15\text{ bis})\quad I(0) = I_e(0)(z_A - z_B)^2\left\{1 + \sum_{q=1}^{\infty} c_q\alpha_q\right\}.$$

7. Cas des Solutions Solides Peu Concentrées en un des Eléments

Nous choisissons pour atomes dont nous effectuons la statistique ceux qui sont en faible proportion; p est donc petit (inférieur à 0, 1 par exemple). Nous avons calculé les développements limités des termes B_2 et B_3.

Le calcul relatif à $B_2(a)$ est simple :

$$B_2(a) = ap^2[1 - 2(a-1)p + p^2(a-1)(5a-4) + \dots].$$

Pour déterminer la valeur du terme $B_3(1;\, a,\, b)$ il convient d'établir les développements :

$$y = p[1 + p(2-a) + \dots],$$

$$z = p[1 + p(2-b) + \dots]$$

ce qui fournit en définitive :

$$B_3(1;a,b) = 1 + p(a-1)(b-1) - p^2(a-1)(b-1)(2a+2b-1) + \dots.$$

La valeur de $B_3(1;a,a)$ s'obtient immédiatement

$$B_3(1;a,a) = 1 + p(a-1)^2 - p^2(a-1)^2(4a-1) + \dots.$$

La détermination du développement du paramètre

$$s = p[1 + (3-a-b)p + (9 - 8a - 7b + 3a^2 + 3ab + 2b^2 - a^2b)p^2 + \dots]$$

permet de calculer

$$B_3(a;a,b) = 1 + p(a-1)(b-1) - p^2(a-1)(b-1)(4a+2b-3) + \dots$$

$$B_3b;a,a) = 1 + p(a-1)^2 - p^2(a-1)^2(4a+2b-3) + \dots$$

$$B_3(a;a,a) = 1 + p(a-1)^2 - p^2(a-1)^2(6a-3) + \dots.$$

Il est difficile de donner une limite de validité de ces développements; tous font intervenir les quantités $(a-1)$ ou $(b-1)$ ce qui indique que le domaine de validité de nos développements par rapport à la variable p est d'autant plus grand que les valeurs de a et de b sont plus voisines de l'unité (ce qui correspond à de faibles valeurs de W/kT); nous obtenons ainsi les valeurs de $n_2(r_q)$ puis des coefficients α_q,

$$\alpha_1 = p\{(w_1 - 1) + p[2w_1(2w_1 + 2w_2 - 5) + 1](w_1 - 1) + \dots\}$$

$$\alpha_2 = p\{(w_2 - 1) + p[4w_2(w_1-1)^2 - 2w_2(w_2-1) + (w_2-1)] + \dots\}$$

$$\alpha_3 = p^2\{2(w_1-1)^2 + 2(w_1-1)(w_2-1) + \dots\}$$

$$\alpha_4 = p^2\{(w_1-1)^2 + 2(w_2-1)^2 + \dots\}$$

$$\alpha_5 = p^2\{(w_1-1)^2 + \dots\}$$

$$\alpha_8 = p^2\{(w_2-1)^2 + \dots\}$$

$$\alpha_6 = \alpha_7 = \alpha_g = \dots = 0$$

Examen de la limite de l'intensité diffusée aux très faibles angles

L'évaluation de la somme $\sum_q c_q \alpha_q$ (expression 15 bis) fournit :

$$p[c_1(w_1 - 1) + c_2(w_2 - 1)] + p^2[\ldots] ;$$

de façon absolument générale le coefficient du terme en p serait $\sum_q c_q(w_q - 1)$. Nous voyons ainsi que *dans le cas où la concentration d'un des deux métaux est faible* l'intensité diffusée est inférieure à l'intensité prévue par Laue (qui correspond au terme 1 dans l'accolade de l'expression 15 bis) si les énergies W_q sont positives, c'est-à-dire si les atomes A et B ont tendance à former deux couples AB au lieu et place d'un couple AA et d'un couple BB; nous prévoyons ainsi que *la valeur de $I(0)$ relative à des alliages subissant les modifications ordre-désordre doit être inférieure à la valeur prévue par Laue;* dans le cas contraire c'est la conclusion inverse qui serait valable. Les expériences (Au-Cu_3 et Al-Ag) ont confirmé ce fait.

Nous avons fait remarquer que le développement par rapport à p est également un développement en $w - 1$; nous voyons ainsi que pour les températures élevées les coefficients α tendent vers zéro. L'expression de Laue apparaît ainsi comme l'expression limite valable aux hautes températures (en supposant que les conditions physiques soient telles que la solution solide existe encore).

8. Conclusion

Nous venons ainsi de montrer que pour modèle simple de solutions solides on peut prévoir l'existence d'un ordre à petite distance dans la répartition des atomes; nous donnons une méthode de calcul pour déterminer les différents paramètres d'ordre à petite distance. L'expérience a confirmé pour des solutions solides Al-Ag l'existence d'une telle répartition d'atomes. Nous avons déjà donné brièvement nos prévisions théoriques relatives à cet alliage; elles sont en bon accord avec les faits [15]. Notons que les phénomènes de diffusion des rayons X produits par l'ordre à petite distance étant toujours faibles, il conviendra d'employer une très bonne technique expérimentale si on veut les mettre en évidence.

Dans le cadre du modèle de solution solide que nous avons adopté la diffusion des rayons X est liée aux valeurs de la fonction $W(r)$ alors que nous avons montré par ailleurs que l'étude des écarts à la loi de Végard permettait d'atteindre les *dérivées* de la fonction $W(r)$; nous voyons ainsi apparaître une relation entre ces deux types de phénomènes, relation qui nous a permis de confirmer certains résultats théoriques sur la loi de variation du paramètre des solutions solides Ag-Au.

Ce travail peut se poursuivre en examinant, d'une part, l'influence de l'ordre à petite distance sur différentes propriétés mégnétiques, et d'autre part, et étendant les mêmes considérations à des solutions ternaires.

Bibliographie

1. Guinier, A. Proc. Phys. Soc. London, **57** (1945) 310.
2. Hume-Rothery, W. Atomic Theory for Students of Metallurgy (London, The Institute of Metals, 1946), p. 110.
3. Barrett, C. S. Structure of Metals, 2ème édition (New York, McGraw-Hill, 1952), p. 221.
4. Walker, C., Elin, J., et Guinier, A. C. R. Acad. Sci., Paris, **235** (1952) 254.
5. Smoluchowski, R. J. Phys., **12** (1951) 389; Phys. Rev. **84** (1951) 511.
6. Fournet, G. À paraître dans J. Phys. (1953).
7. Wilchinsky, Z. Phys. Rev., **63** (1943) 223.
8. Wilchinsky, Z. J. Appl. Phys., **15** (1944) 806.
9. Smoluchowski, R. Phys. Rev., **64** (1943) 257.
10. Fournet, G. Bull. Soc. Franç. Min. Crist., **74** (1951) 37.
11. Laue, M. von. Röntgenstrahlinterferenzen (Leipzig, 1941).
12. Yvon, J. Cahiers de Phys., **28** (1945) 1.
13. Fournet, G. J. Phys. (Phys. Appl.), **13** (1952) 14A.
14. Fournet, G. J. Phys., **14** (1953) 226.
15. Fournet, G. À paraître dans C. R. Acad. Sci., Paris (1953).

THE LOCATION OF OXYGEN ATOMS IN VANADIUM-OXYGEN ALLOYS BY MEANS OF NEUTRON DIFFRACTION*

C. W. TUCKER, Jr.,† A.U. SEYBOLT,‡ and H. T. SUMSION†

A comparison of X-ray and neutron diffraction is made for the purpose of locating oxygen atoms in vanadium-oxygen alloys. In the region of low oxygen content, neutron diffraction possesses a large advantage because of the large scattering factor for oxygen and the low value for vanadium with neutrons. In an alloy containing 21.0 atomic per cent oxygen, the oxygen atoms are found in the octahedral positions of a body-centered tetragonal lattice, as inferred by earlier workers using X-ray diffraction.

LA DÉTERMINATION DE L'EMPLACEMENT DES ATOMES D'OXYGÈNE DANS LES ALLIAGES VANADIUM-OXYGÈNE, AU MOYEN DE LA DIFFRACTION DES NEUTRONS

Une comparaison est faite entre la diffraction des rayons X et la diffraction des neutrons dans le but de la localisation des atomes d'oxygène dans les alliages vanadium-oxygène. Dans le cas de la diffraction des neutrons, le facteur de dispersion est grand pour l'oxygène et faible pour le vanadium, cette méthode est, par conséquent, beaucoup plus avantageuse dans la région de faibles teneurs en oxygène. Dans un alliage contenant 21,0 pour cent en atomes d'oxygène, les atomes d'oxygène ont été trouvés dans les positions octaèdriques d'un réseau tétragonal centré, ce qui coïncide avec les résultats des travaux antérieurs faits par des chercheurs utilisant la diffraction des rayons X.

DIE BESTIMMUNG DER LAGE DER SAUERSTOFFATOME IN VANADIUM-SAUERSTOFF LEGIERUNGEN MITTELS NEUTRONENBEUGUNG

Ein Vergleich zwischen Röntgen- und Neutronenbeugung wird angestellt, um die Lage der Sauerstoffatome in Vanadium-Sauerstofflegierungen festzustellen. Im Gebiet der niedrigen Sauerstoffkonzentrationen hat die Neutronenbeugung wegen des grossen Streufaktors des Sauerstoffs und des kleinen Streufaktors des Vanadiums für Neutronen grosse Vorteile. In einer 21 prozent Sauerstoff enthaltenden Legierung befanden sich die Sauerstoffatome in den Oktaederplätzen eines tetragonal raumzentrierten Gitters, wie es bereits Autoren früherer Arbeiten auf Grund von Röntgenbeugungsdiagrammen annahmen.

Introduction

The value of the neutron diffraction technique in the study of certain types of crystal structure problems has now been amply demonstrated. Such problems usually involve those cases for which the relative X-ray scattering powers of the various atoms in the crystal are not favorable for distinguishing the X-ray scattering by the different atoms involved.

We have recently had occasion to study the positions of oxygen atoms in vanadium-oxygen alloys. This problem constitutes an interesting application of the neutron technique since, for neutrons, vanadium has a very much smaller scattering amplitude than oxygen, while with X-rays the opposite is true.

The problem arose from some metallurgical studies of vanadium-oxygen solid solutions made by Seybolt and Sumsion [1]. Their work shows that as oxygen is added to pure vanadium, with its body-centered cubic structure ($a_0 = 3.026$ Å), faint lines of a body-centered tetragonal structure first appear at 3.2 atomic per cent oxygen. They designated this phase as the β-phase and found its lattice parameters to be $a_0 = 2.99$ Å, $c_0 = 3.26$ Å, giving an axial ratio of 1.090. These parameters remain constant up to 15 atomic per cent oxygen which marks the phase boundary for the pure β-phase. Beyond this and up to 22 atomic per cent oxygen, the structure becomes more tetragonal, reaching limiting values of $a_0 = 2.94$ Å, $c_0 = 3.50$ Å with an axial ratio of 1.19. Above the 22 per cent region, there is a two-phase region involving the β-phase and VO. The compound VO has the rock salt structure with $a_0 = 4.081$ Å. The problem which naturally arose was the location of the oxygen atoms in the tetragonal β-phase.

For the simple crystal structure of the β-phase, the structure factor for every reflection involves either the sum or the difference of the vanadium and oxygen atomic scattering factors. Thus, for maximum sensitivity in locating oxygen atoms, one compares reflections for which the scattering by the oxygen and vanadium atoms oppose and reinforce one another. In the alloy containing the maximum amount of oxygen in the β-phase, namely 22 atomic per cent oxygen, one compares reflections for which the factors $(f_V + 0.28\, f_O)$ and $(f_V - 0.28\, f_O)$, where f_V is the vanadium atomic scattering factor and f_O that for oxygen, are involved. The atomic scattering factors for X-rays vary with $(\sin\theta)/\lambda$, and for a typical value, the above functions would be 18 for "in phase" and 15 for "out of phase" scattering by the

*Received March 20, 1953.

†Knolls Atomic Power Laboratory, General Electric Co., Schenectady, New York, U.S.A.

‡Present address: General Electric Research Laboratory, The Knolls, Schenectady, New York.

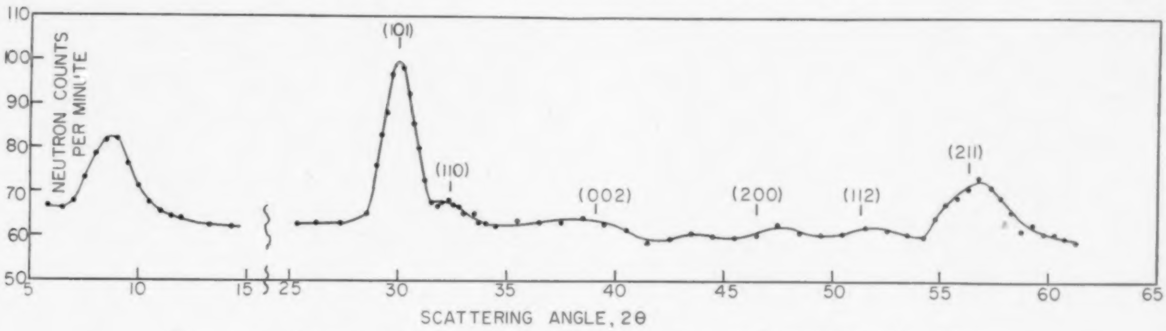

FIGURE 1. Neutron diffraction pattern of 21.0 atomic per cent oxygen-vanadium alloy.

vanadium and oxygen atoms. For neutrons, due to the relatively high scattering cross section of oxygen and the low value for vanadium, the functions become (aside from a scale factor) + 11 for "in phase" and − 21 for "out of phase" scattering. Thus, while the oxygens make only 18 per cent difference in the X-ray case, they change the structure factor by a factor of 2 in the case of neutrons. From the above discussion, it is clear that in the case of the 22 atomic per cent oxygen β-phase alloy the neutrons could be expected to give a decisive answer regarding the oxygen atom positions, whereas the X-rays would require very accurate intensity measurements.

A neutron diffraction pattern of the β-phase was obtained for us by E. O. Wollan and W. C. Koehler of the Oak Ridge National Laboratory by the techniques which have previously been described by Wollan and Shull [2]. The integrated power in the diffraction peaks has been placed on an absolute basis by comparison with the powder pattern for nickel for which the coherent scattering cross section has been accurately determined, $\mathrm{Ni_{coh}} = 13.4 \pm 0.2$ barns. The powder formulas are the same as for X-rays except that with neutrons there is no polarization factor. For cylindrical samples as used here,

$$P_{hkl} = \frac{\gamma^2 BN}{n^2}\,\frac{\rho'}{\rho}\,\frac{j_{hkl}\,F^2_{hkl}}{\sin\theta\,\sin 2\theta} \tag{1}$$

where

P = observed intensity in counts per minute;
γ^2 = apparatus and calibration constant;
B = absorption correction;
N = number of molecules per cm^3;
n = number of molecules per unit cell;
ρ', ρ = powder and solid densities, respectively;
F = structure amplitude per unit cell in $\mathrm{cm} \times 10^{12}$;
j = multiplicity factor;
θ = Bragg angle.

The oxygen amplitude has been taken as 0.58×10^{-12} cm from the work of Shull and Wollan [3] and the vanadium amplitude, as -0.48×10^{-12} cm from the work of Peterson and Levy [4].

The sample of the β-phase was prepared by arc melting a mixture of V and V_2O_3 in an argon atmosphere. Chemical analysis gave a composition of 21.0 atomic per cent oxygen. X-ray diffraction measurements showed a body-centered tetragonal structure with $a_0 = 2.948$ Å, $c_0 = 3.478$ Å and an axial ratio of 1.180. Because of the relatively low scattering by the oxygen atoms, it was not possible to locate the oxygen atoms definitely. The tetragonal structure given by Klemm and Grimm [5] for this phase is one in which the oxygen atoms take the octahedral positions in the body-centered cubic structure of vanadium metal. The structure is entirely reasonable, but it was not felt that their intensity estimates established the tetragonal structure beyond question, although the structure has the further plausibility that it is identical with the structure later found by Jack [6] for nitrogen martensite.

To settle the question of the oxygen atom positions, a neutron diffraction pattern of the 21.0 atomic per cent oxygen alloy was made covering the range of Bragg angle, θ, from 2° to 31° with neutrons of wave length of 1.163 Å. The pattern is shown in Figure 1. The region between $\theta = 7°$ to 12.5° is not shown in the figure since the measurements showed no structure in this region. The short vertical lines above the neutron peaks show the position of the corresponding X-ray reflections. A comparison of the observed and calculated structure factors is shown in Table I. The observed structure factors were calculated from equation (1) which reduces to

$$P_{hkl} = 9.90\,\frac{j_{hkl}\,F^2_{hkl}}{\sin\theta\,\sin 2\theta}. \tag{2}$$

The calculated structure factors are based on a tetragonal unit cell in space group D_{4h}^{17} (Internationale Tabellen [7]) with two vanadium atoms at 000 and $\frac{1}{2}\frac{1}{2}\frac{1}{2}$ and 0.532 oxygen distributed randomly at $0\,0\,\frac{1}{2}$ and $\frac{1}{2}\,\frac{1}{2}\,0$. This produces a factor $(0.266 f_o +$

f_v) in the structure factor for reflections with l even and the factor $(0.266 f_o - f_v)$ for reflections with l odd.

TABLE I

OBSERVED AND CALCULATED VALUES FOR P_{hkl} AND F_{hkl} IN A 21.0 ATOMIC PER CENT OXYGEN ALLOY OF THE β-PHASE

hkl	P (observed)	P (calculated)	F (observed)	F (calculated)
	100		0.23	
(101)	133	99.7	0.47	0.41
(110)	21	12	0.28	0.21
(002)	10	4	0.32	0.21
(200)	10	6	0.27	0.21
(112)	17	10	0.27	0.21
(211)	85	66	0.46	0.41

The agreement between the observed and calculated structure factors in Table I is seen to be only fair on an absolute basis. However, on a relative basis the agreement is quite satisfactory. Since the reflections with l odd have structure factors of 1.7 times those with l even (compared to a value of 2.0 for the assumed structure), the data serve very well to establish the fact that the positions of the oxygen and vanadium atoms are as given by the Klemm and Grimm structure [5]. The fact that the agreement is only fair between the 1.7 value for the ratio of the observed structure factors for "out of phase" and "in phase" reflections and the 2.0 value for the calculated value, is probably due to the "in phase" reflections being just barely observable and their intensity values, therefore, considerably less accurate.

There are two points regarding the data in Table I which need discussion. First, there is an extra reflection which occurs at a Bragg angle of 4° 24′, the first in the table, which is apparently not a part of the structure. This extra reflection may be due to an impurity of some type, possibly from a trace of a higher oxide of vanadium. However, assuming that it is a reflection of low index with $j = 2$, it actually has a structure factor somewhat less than the weak reflections which are just observable. The fact that it appears so important in Figure 1 is due to the factor $1/(\sin \theta \sin 2\theta)$ in equation (1). This factor greatly enhances the apparent importance of the reflections with very low Bragg angles. An alternative explanation for this peak is that it is associated with short range order of the oxygen atoms. However, the large interplanar spacing for the peak, 7.6 Å, probably eliminates this possibility. The further possibility that the oxygen atoms are ordered on planes perpendicular to the c-axis in alternate unit cells (thus producing a spacing of $d = 7.0$ Å) can also be ruled out, as it would produce other reflections which are not observed. The possibility that the peak may be of magnetic origin has not yet been fully investigated.

The fact that the observed structure factors in Table I are about 20 per cent higher than the calculated values is more difficult to reconcile. By assuming that the true composition of the alloy is 25 rather than 21 atomic per cent oxygen the agreement is much better. However, examination of the X-ray data of Seybolt and Sumsion [1] definitely indicates that the β-phase cannot retain more than 22 per cent oxygen, unless there is some (and the same) systematic error in the two methods of chemical analysis used on their alloys. But, since the relative values of the structure factors for the β-phase are in good agreement, and the calculated intensities are highly sensitive to small variations in oxygen content, it does not seem necessary to question the validity of the structure of Klemm and Grimm [5] for the β-phase.

This work is another example of the usefulness of neutron diffraction in determining atomic positions in special cases with relatively simple structures and favorable values of the coherent scattering amplitudes. Vanadium compounds constitute a rather special case because of the anomolously small coherent scattering amplitude of vanadium. The neutron method is applicable when a majority of the atoms are vanadium, whereas X-ray diffraction would have been employed for determining the position of a small fraction of vanadium atoms in the presence of a large fraction of oxygen atoms. The work confirms the structure suggested by Klemm and Grimm [5] for the β-phase. In this structure the oxygen atoms take the octahedral positions in the body-centered cubic vanadium structure and thereby deform it into the observed tetragonal structure.

Acknowledgement

It is a pleasure to acknowledge the assistance of Dr. E. O. Wollan and W. C. Koehler of the Oak Ridge National Laboratory, who arranged for and obtained the neutron diffraction pattern of the β-phase.

References

1. SEYBOLT, A. U. and SUMSION, H. T. Trans. A.I.M.E., submitted for publication, 1952.
2. WOLLAN, E. O. and SHULL, C. G. Phys. Rev., **73** (1948) 830.
3. SHULL, C. G. and WOLLAN, E. O. Phys. Rev., **81** (1951) 527.
4. PETERSON, S. W. and LEVY, H. A. Phys. Rev., **87** (1952) 462.
5. KLEMM, W. and GRIMM, L. Z. anorg. Chem. **250** (1942-43) 42.
6. JACK, K. H. Proc. Roy. Soc., **A208** (1951) 200.
7. Internationale Tabellen Zur Bestimmung von Kristallstructuren (Berlin, Borntraeger, 1935).

THE SURFACE STRUCTURES OF DEFORMED ALUMINIUM, COPPER, SILVER, AND ALPHA-BRASS, AND THEIR THEORETICAL INTERPRETATION*

DORIS KUHLMANN-WILSDORF† and HEINZ WILSDORF‡

The surfaces of deformed aluminium, copper, silver, and α-brass are investigated with an electron microscope using the same preparation technique throughout. The three pure metals examined show similar surface structures after deformation, namely an elementary structure and slip bands. On deformed α-brass neither an elementary structure nor slip bands are visible, but instead single slip lines, apparently arranged at random.

This evidence is discussed theoretically and the following conclusions are drawn:

1. The simultaneous occurrence of slip bands and elementary structure on the three pure metals and the absence of both on α-brass strongly supports the idea, put forward in a previous paper, that slip bands develop out of an elementary structure.

2. The two types of surface structure indicate two different mechanisms of plastic deformation. These two mechanisms of plastic deformation are discussed, and the conclusions drawn are compared with experimental evidence.

LES STRUCTURES DES SURFACES DE L'ALUMINIUM, CUIVRE, ARGENT ET LAITON α DÉFORMÉS, ET LEUR INTERPRÉTATION THÉORIQUE

Les surfaces d'aluminium, cuivre, argent et laiton α ont été examinées au moyen du microscope électronique en employant toujours la même technique de préparation. Les trois métaux purs qui ont été examinés, montrent après déformation, des structures de surface similaires, à savoir, une structure élémentaire et des bandes de glissement. Sur le laiton α ni la structure élémentaire ni les bandes de glissement ne sont visibles, mais par contre on voit des lignes de glissement individuelles, arrangées apparemment d'une façon quelconque.

Ces résultats sont discutés du point de vue théorique et les conclusions suivantes en sont tirées:

1. L'appariton simultanée des bandes de glissement et de la structure élémentaire sur les trois métaux purs et l'absence de toutes les deux sur le laiton α, supportent fortement l'idée, présentée dans un article précédent, que les bandes de glissement se développent en partant d'une structure élémentaire.

2. Deux genres de structures de surface indiquent deux mécanismes différents de déformation plastique.

Ces deux mécanismes de déformation plastique sont discutés et les conclusions qu'on en tire sont comparées avec les résultats expérimentaux.

DIE OBERFLÄCHEN VON VERFORMTEM ALUMINIUM, KUPFER, SILBER, UND α-MESSING UND IHRE THEORETISCHE DEUTUNG

Die Oberflächen von verformtem Aluminium, Kupfer, Silber und α-Messing wurden elektromikroskopisch untersucht; in allen Fällen wurde die gleiche Präparationstechnik angewandt. Die drei reinen Metalle zeigen nach ihrer Verformung ähnliche Oberflächenstrukturen, nämlich eine Elementarstruktur und Gleitbänder. Am verformten α-Messing sind weder die Elementarstruktur noch Gleitbänder zu erkennen, statt dessen sieht man einzelne anscheinend ungeordnete Gleitlinien.

Diese Befunde wurden theoretisch diskutiert, und die folgenden Schlussfolgerungen werden daraus gezogen:

1. Das gleichzeitige Auftreten von Gleitbändern und Elementarstruktur in den drei reinen Metallen und das Fehlen beider Erscheinungen im α-Messing ist eine starke Stütze für die in einer früheren Arbeit veröffentlichte Hypothese, dass sich Gleitbänder aus einer Elementarstruktur entwickeln.

2. Die beiden Typen der Oberflächenstruktur deuten auf zwei verschiedene Mechanismen in der plastischen Verformung hin.

Diese beiden Verformungsmechanismen werden diskutiert, und die daraus gezogenen Schlüsse werden mit den experimentellen Resultaten verglichen.

I. Introduction

During recent years, and especially since the discovery of slip lamellae in the slip bands of aluminium by Heidenreich and Shockley [1; 2] and their closer examination by Brown [3; 4; 5], interest in the surface structures of deformed metals has increased greatly. The results obtained by the examination of surfaces of deformed metals have already partly been incorporated in, or even been chosen as the basis of, a number of new theories in the field of plastic deformation. In particular, the results obtained by Brown that on aluminium slip lines or slip lamellae are formed suddenly, and are all of about the same strength (approximately 2000 Å), have given rise to much speculation. In a recent investigation [6; 7; 8], however, the authors failed to confirm Brown's result of a nearly constant slip on each slip line in aluminium, while the speed with which slip lines form could not be investigated conclusively. Instead the

*Received March 24, 1953.

†Department of Physics, University of the Witwatersrand, Johannesburg, South Africa.

‡National Physical Laboratory, South African Council for Scientific and Industrial Research, Pretoria, South Africa.

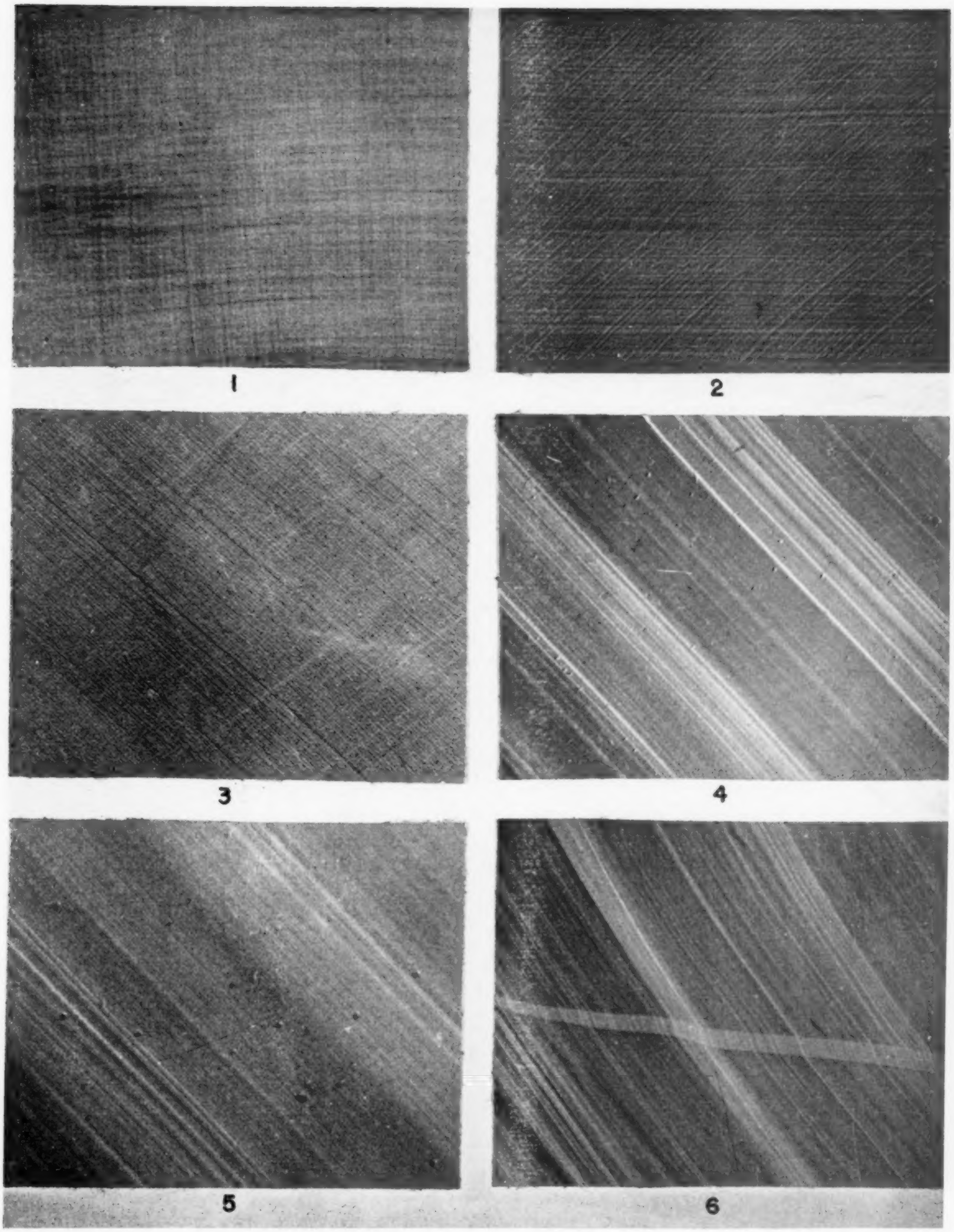

PLATE I. Figure 1—Elementary structure on polycrystalline super-purity aluminium; elongation 41 per cent; 20,000× Figure 2—Elementary structure on polycrystalline super-purity copper; elongation 23 per cent; 20,000×. Figure 3—Elementary structure on polycrystalline super-purity silver; elongation 27 per cent; 20,000×. Figure 4—Slip bands and elementary structure on super-purity aluminium single crystal; elongation 18 per cent; 10,000×. Figure 5—Slip bands and elementary structure on super-purity copper polycrystal; elongation 17 per cent; 20,000×. Figure 6—Slip bands and elementary structure on super-purity silver polycrystal; elongation 27 per cent; 20,000×.

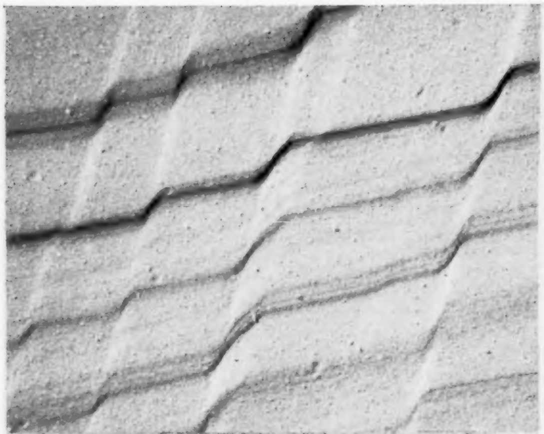

7

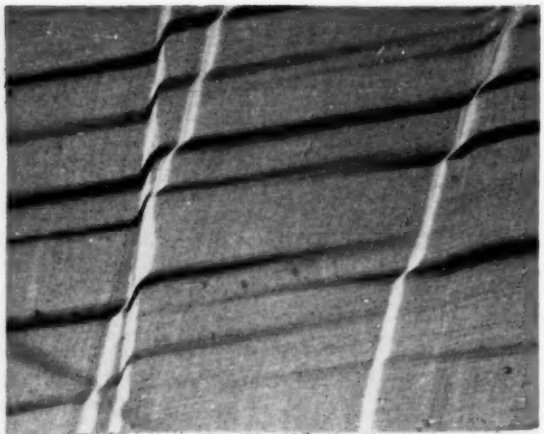

8

9

10

12

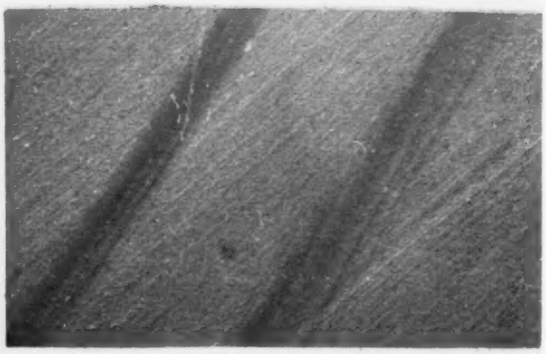

13

PLATE II. Figure 7—Two systems of slip bands on super-purity aluminium crystal; elongation 20 per cent; 7,500×. Figure 8—Two systems of slip bands on super-purity copper polycrystal; elongation 23 per cent; 10,000×. Figure 9—Two systems of slip bands on super-purity aluminium single crystal; elongation 28 per cent; 6,000×. Figure 10—Two systems of slip bands on electrolyte copper polycrystal; elongation 25 per cent; 6,000×. Figure 12—"Uncrystallographic" slip band on polycrystalline super-purity aluminium; elongation 21 per cent; 15,000×. Figure 13—"Uncrystallographic" slip band on polycrystalline super-purity copper; elongation 23 per cent; 22,500 ×.

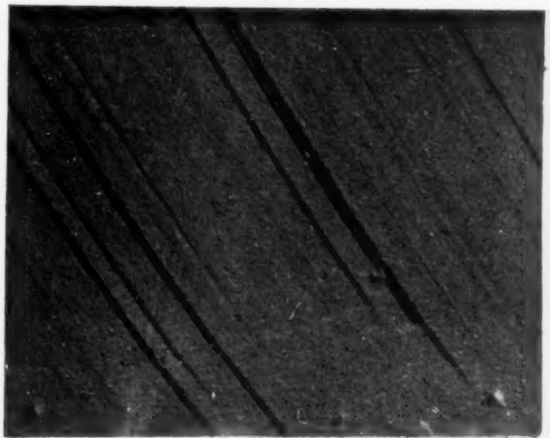

14

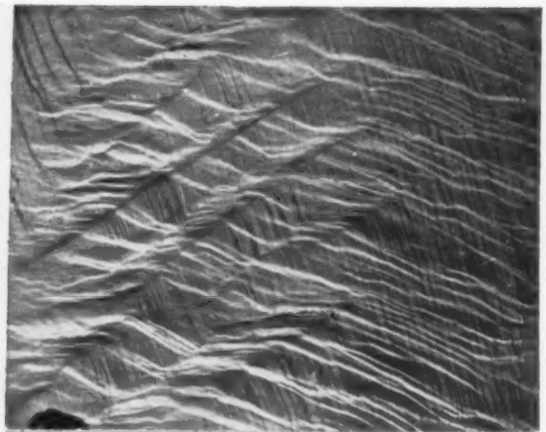

17

15

16

18

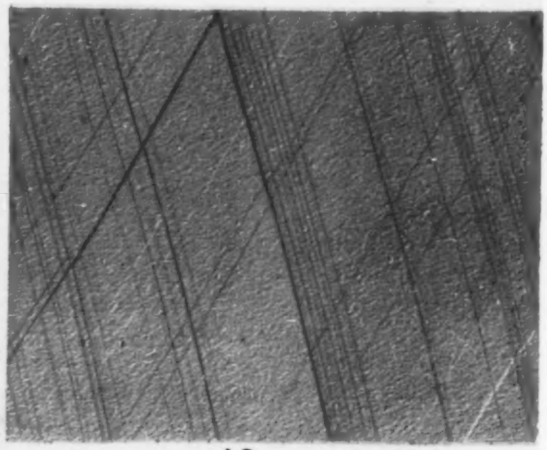

19

Plate III. Figure 14—Cross slip on electrolyte copper; elongation 11 per cent; 30,000×. Figure 15—Fan-shaped array of slip lines on commercial polycrystalline silver; elongation 16 per cent; 15,000×. Figure 16—Fan-shaped array of slip lines on polycrystalline electrolyte copper; elongation 11 per cent; 20,000×. Figure 17—Curious structures on polycrystalline super-purity copper near fracture, thought to be deformation twins; 1600×. Figure 18—As in Figure 17 but 4000×. Figure 19—A slip-band-like array of slip lines in one system crossed by a "mixed system" on polycrystalline α-brass; elongation 5 per cent; 20,000×.

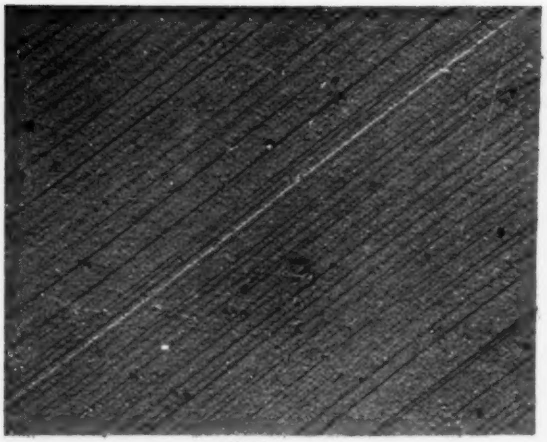

20

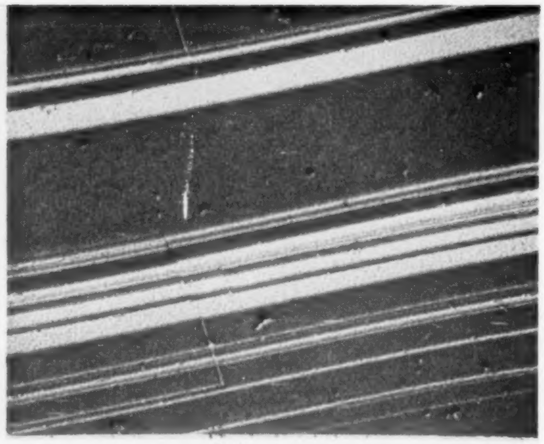

21

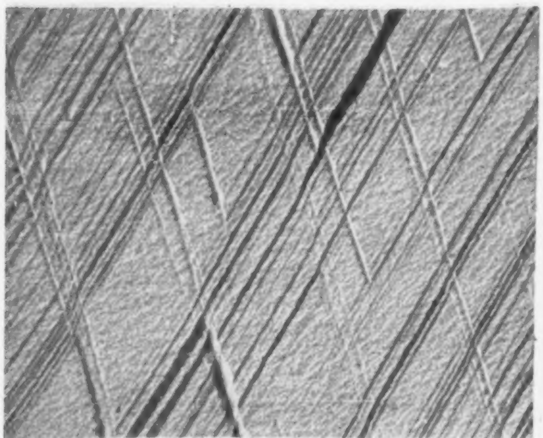

22

23

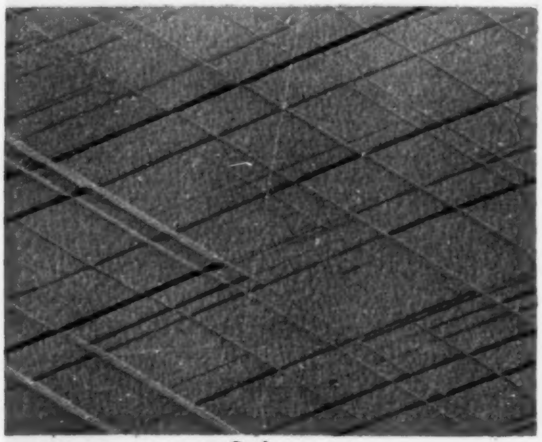

24

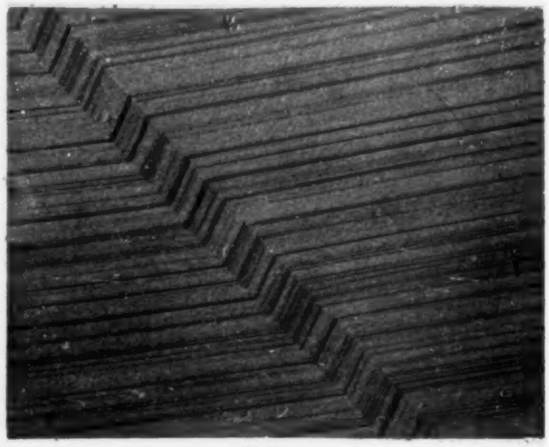

25

PLATE IV. Figure 20—A field of closely spaced regular slip lines of polycrystalline α-brass; elongation 5 per cent; 20,000×. Figure 21—A slip-free region between slip lines of greatly varying depth on polycrystalline α-brass: note the exceedingly closely spaced lines at the centre of the photograph; elongation 5 per cent; 20,000×. Figure 22—Cross slip on polycrystalline α-brass; elongation 15 per cent; 20,000×. Figure 23—Apparently uncrystallographic slip lines caused by double slip: polycrystalline α-brass; elongation 24 per cent; 15,000×. Figure 24—Cross slip on polycrystalline α-brass; elongation 5 per cent; 20,000×. Figure 25—A system of slip lines crossing a narrow twin: polycrystalline α-brass; elongation 15 per cent; 5000×.

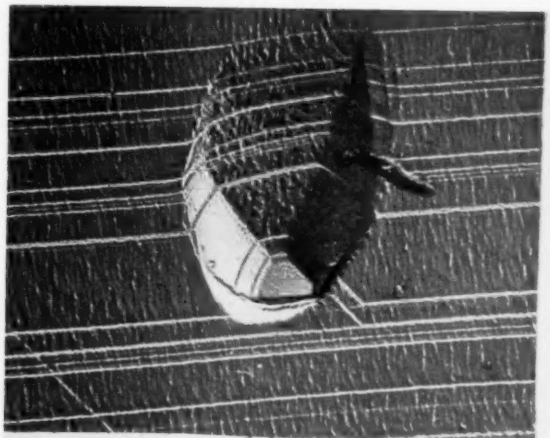

26

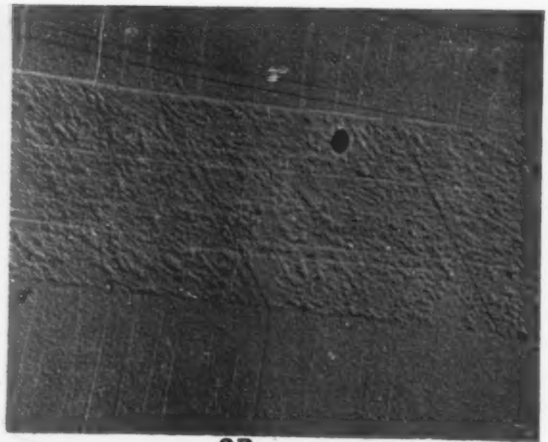

27

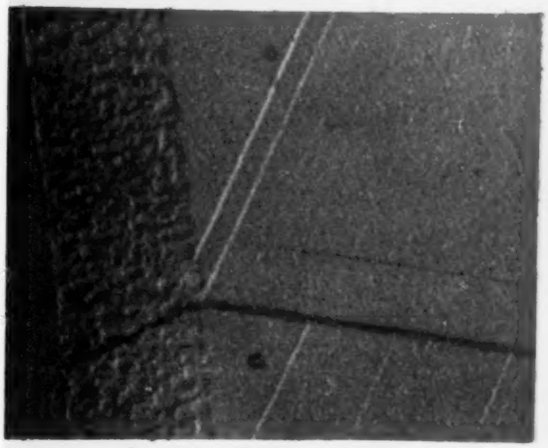

28

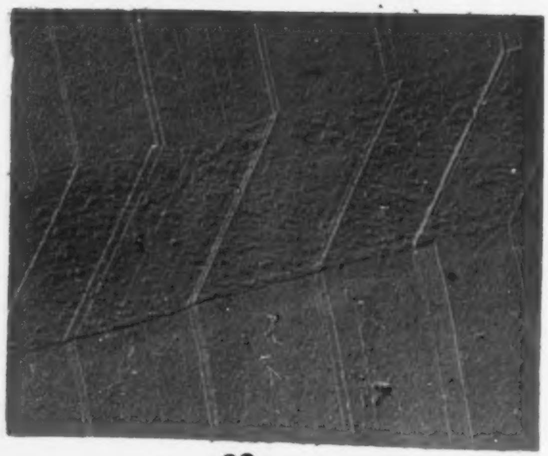

29

PLATE V. Figure 26—Peculiar cross slip near an etch pit in α-brass; elongation 5 per cent; 15,000×. Figure 27—A twin constituting a strong obstacle against the light slip lines approaching it from the lower part of the photograph: polycrystalline α-brass; elongation 3 per cent; 20,000×. Figure 28—Slip line turning away from a narrow twin in α-brass; elongation 5 per cent; 40,000×. Figure 29—Irregularities in a series of slip lines crossing a narrow twin: polycrystalline α-brass; elongation 3 per cent; 20,000×.

slip distances on very pure aluminium, deformed with normal strain rates at room temperatures, were found to vary continuously from a few Ångstroms to 1200 Å or possibly even more. Lines as deep as 2000 Å, however, have never been observed at all. The average slip on the slip lines was between about 300 and 400 Å. Moreover, a new surface structure, called the *elementary structure*, covering the whole surface between the slip bands was discovered.

To explain this discrepancy two ways are open: either by some unfortunate circumstance the preparation techniques used by Heidenreich and Shockley [1; 2] and by Brown [3; 4] do not give a true picture of the surfaces, or otherwise the surface structures on aluminium vary greatly with the conditions of straining or the purity of the aluminium or both. As Brown arrives at the slip distance of 2000 Å for quite different straining conditions the latter explanation is unlikely, and therefore we are inclined to believe in the former. But whatever the reason for the discrepancy, serious doubt is cast on theories based on the existence of a definite, almost invariable slip distance.

So far the surface structures of only aluminium have been investigated in detail. Therefore it seemed of paramount importance to examine some other metals in order to obtain information as to the extent to which the surface structures on deformed aluminium are characteristic of this metal only, and to what degree they are of general significance.

The metals investigated in the present paper are electrolytic copper; oxygen-free super-purity copper and super-purity silver, both from Johnson, Matthey and Co. Ltd., London; commercially pure silver (about 99.8–99.9); and commercial 70 : 30 α-brass. The specimens were rolled and, after heat treatment, polished electrolytically without any previous mechanical polishing.* The specimens were subsequently elongated at room temperature at a strain rate of about 1 per cent per second. The electron microscopic replicas were prepared by methods similar to that described elsewhere [6]. Without exception, silicon monoxide was directly evaporated on to the polished, deformed metal surfaces. Thus the obvious differences in the surface structures of the various metals examined are real, and cannot be attributed to varying experimental techniques.

Following the nomenclature of earlier papers, the surface steps visible with the light microscope, but consisting of a number of finer steps only resolvable in the electron microscope, are called slip *bands*. The individual steps in them, or in general any atomic planes on which slip has taken place, are called slip *lines*. The *height* of a slip line or of a slip band means the amount of slip which has taken place on it, and slip *lamella* means the material between two neighbouring slip lines in a slip band.

*A detailed account of all experimental methods employed will be published shortly.

II. The Surface Structures on Deformed Polycrystalline Copper and Silver

1. *Investigation with Electron Microscope*

The surface structures investigated on the deformed copper and silver, irrespective of purity, are similar to those on aluminium described elsewhere [6; 7; 8]. On copper and silver, as on aluminium, an elementary structure forms at low strains, becoming somewhat more marked as the strain increases, and only then do slip bands appear. Figures 1, 2, and 3 show examples of the elementary structure and Figures 4, 5, and 6 give examples of slip bands on aluminium, copper, and silver. As copper has been examined more closely than silver and consequently more photographs are available from copper, the close resemblance of the structures on aluminium to those on the other metals is demonstrated only for the case of copper, in Figures 7 and 8, 9 and 10, but the structures are much the same for silver. Indeed, it is often difficult to distinguish between replicas taken from aluminium, copper, and silver, as may be seen from Figures 4 to 10.

The only important difference which has so far been discovered between the three metals is visible in Figure 1, 2, and 3: The lines of the elementary structure are much clearer, deeper, and more closely spaced on copper and silver than on aluminium. While on aluminium at medium strains the average spacing of the elementary lines is about 400 Å (see Table I of [9]), it is only about 250 Å for silver and 300 Å for copper. Also, the slip lines in the bands are more closely spaced in copper and silver than they are in aluminium. Again, in copper and silver, as already found in aluminium [8], the spacing of the elementary lines is similar to that of the lines in the slip bands. Thus, it is much more difficult to find fully resolved slip bands on copper and silver than it is on aluminium.

In Figure 11, stress-strain curves for the super-purity aluminium, copper, and silver are given. From these it can be seen that between about 8 per cent and 20 per cent elongation the stress is from 1.5 to 2 times greater in silver than in aluminium, and from 4 to 4.5 times greater in copper than in aluminium. Elsewhere [9] it was deduced theoretic-

ally that the average spacing of the elementary structure should be given by $\bar{d} = 1.5 \times Gb/[8\pi(1 - \mu)\tau]$ where G is the modulus of rigidity, b the Burgers vector of the dislocations, μ Poisson's ratio, and τ the resolved shear stress. If we now take into consideration the values for μ, b, and G in the three different metals as well as the above ratios for the stresses involved in producing the elementary structures, we expect the average spacing of the elementary lines in aluminium, silver, and copper to be in the ratio of 1 : 0.63 : 0.36, or if we accept the value of 400 Å as representative of aluminium, we find 250 Å for silver and 150 Å for copper. Thus for silver the agreement between the expected and the experimental value is excellent, but the agreement

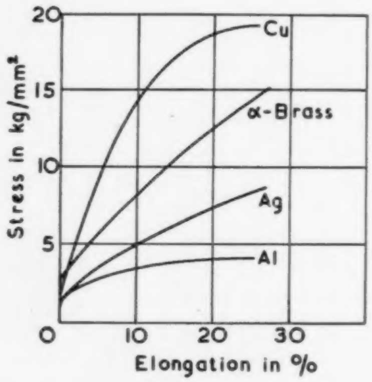

FIGURE 11. Average stress-strain curves of the super-purity aluminium, copper, silver, and the commercial α-brass examined.

is not very good for copper. The value of 400 Å for aluminium, on the other hand, was previously [9] found to be somewhat smaller than the result from the above equation, so that the value of 300 Å for copper again is not very far from the theoretical result. Since necessarily all those measurements are not very reliable it does not seem worthwhile to go deeper into the matter than to state:

1. The average spacings of the lines in the elementary structure found on copper and on silver differ from the corresponding theoretical values by approximately the same amount as previously found for aluminium [9].

2. The thickness of the lamellae in the slip bands of each of the three metals is comparable with the spacing of the elementary lines in its own elementary structure.

2. *Investigation with Light Microscope*

The presence of deeper and more closely spaced elementary lines in copper and silver has an important consequence: while on aluminium the strain produced by the elementary structure alone was found to be in the range of a few per cent only [6; 9], it must obviously be much greater for copper and silver. This was tested by an investigation with a light microscope, comparing surface structures on deformed aluminium with those on copper and, as will be briefly discussed later, on α-brass. It had been found very early in the authors' study of slip bands, even before the actual discovery of the elementary structure, that before the first slip bands appear, very faint striations, just visible in the light microscope, form on the surface of deformed aluminium. As the deformation increases and slip bands become visible the striations apparently vanish, probably because, with the then existing constrast between dark bands and bright background, the eye can no longer perceive them. These striations seem to have been observed also by Hanson and Wheeler [10].

After discovery of the elementary structure, it seemed obvious to correlate the striations with it, and with this knowledge it was attempted either to confirm or disprove the idea that in copper and silver the elementary structure is responsible for a substantial part of the plastic deformation. The result is given in Table I. From this table it is clear that in super-purity aluminium strained at room temperature the first slip bands appear at an elongation of

TABLE I

Substance	Grain size	Elongation %	Proportion of grains with no discernible surface structure	Proportion of grains with striations only	Proportion of grains with slip bands
Al	~3 mm.	0.5	Some	Most	Few
		1.5	Some	~60%	~30%
		3.5	None	Few	Most
Al	~0.25 mm.	0.1	Most	Very few	None
		0.25	Most	~10%	None
		1.1	Some	Many	Many
		3.1	Very few	Some	Most
Al	~0.2 mm.	0.4	~40%	~50%	Few
		1.2	Few	~90%	~10%
		2.2	None	~60%	~40%
		4.3	None	~10%	~90%
		8.3	None	Very few	Nearly all
Cu	~0.2 mm.	0.4	~50%	~50%	None
		1.3	Few	Nearly all	None
		10	None	Most	Some
		18	None	Some	Most
		27	None	Few	Nearly all
Cu	~0.02 mm.	0.2	All	None	None
		0.9	Nearly all	Few	None
		2.0	~50%	~50%	None
		3.8	Few	Most	Few
		7.6	Few	Most	Few
		11.6	None	~80%	~20%
		22.0	None	~60%	~40%

about 0.3 per cent, and that at 2 to 3 per cent half the grains show slip bands. This latter strain may be taken as roughly the strain due to an elementary structure in aluminium. On copper, on the other hand, no slip bands were formed below about 2 per cent elongation and only at a strain of more than 15 per cent are slip bands visible in 50 per cent of the grains, i.e., in copper the elementary structure is responsible for 15 per cent elongation or more. In agreement with these results, no slip bands have ever been detected on copper and silver at strains up to several per cent during the present electron-microscope observations, whereas on aluminium, for the same strains, they were plentiful. An increase in grain size seems to have the effect of increasing the number of slip bands at a given strain, in agreement with the observations by Hanson and Wheeler [10] for slow strain rates.

3. *Some Special Observations*

Usually it is difficult to interpret and summarize observations concerning slip bands because, as well as the familiar straight, parallel bands, there are slip band clusters, deformation bands, early multiple slip and wavy slip bands, all of which tend to confuse the observer. Even the first very faint striations preceding the slip bands did not always seem straight, but in some grains seemed wavy from the very beginning when observed with the light microscope. In a few cases it was definitely observed that in grains with wavy striations the slip bands formed were also wavy. This is highly interesting, for should this be a general rule, it would mean that the special form of the slip bands is determined *very* early in the deformation process. On the other hand, this observation gives additional strong support to the theory [9] explaining the formation of slip bands from the elementary structure.

As was just mentioned, the slip bands of aluminium, as well as those of copper, occasionally do not run parallel to the slip lamellae, leading to wavy slip bands or slip bands which are reasonably straight, but are inclined across the direction of the slip lamellae. For aluminium this has been discussed briefly elsewhere [7]. Figures 12 and 13 give examples. In no case was intimate cross slip found to be responsible for slip bands having an irregular direction over appreciable distances, but in all cases these wavy bands consisted of short pieces of slip lines on one or two different systems. This result might be of interest in connection with a recent paper by Trotter [11] who observed irregular slip traces on aluminium, slowly strained at an elevated temperature, and believed them to be formed by intimate cross slip. However, as no experimental evidence has as yet been obtained for aluminium or any other metal strained slowly at elevated temperatures, it is not yet possible to decide which is the correct interpretation of the photographs obtained by Trotter.

A few isolated instances of cross slip were found on electrolytic copper (Figure 14) but no cross slip at all could be found on super-purity copper and silver. Moreover, the cross slip shown in Figure 14 is of a type not so far observed on aluminium.

Another phenomenon, not found on aluminium, is shown in Figure 15 for silver and Figure 16 for copper. In both metals this fan-shaped array of short slip lines was fairly common, although apparently it forms only at twin boundaries. This may explain why the phenomenon is absent in aluminium; it may be some form of forced uncrystallographic slip.

Figures 17 and 18 show a strange structure which the authors are inclined to regard as deformation twins. Similar structures were also observed during the examination of copper surfaces with a light microscope. They apparently only form at very high strains.

III. The Surface Structures on Deformed Polycrystalline α-Brass

1. *General Observations*

The surface structures on deformed α-brass are very varied and distinctly different from those on aluminium, copper, and silver. In particular, the slip lines on brass do not assemble to form slip bands as they do in the other metals investigated, but they are apparently arranged at random and are of greatly varying depths. While the finest slip lines on brass compare with the elementary lines of aluminium, the slip on the strongest may exceed 6000 Å. Lines caused by a slip of several thousand Å are not rare, and are found side by side with the very finest lines. Occasionally groups of closely spaced slip lines of more or less uniform depth are found which resemble slip bands (Figure 19). Such structures are rare and are never, even remotely, as regular as slip bands in aluminium. Therefore the authors are inclined to regard them as accidental, or possibly caused by some geometrical softening [12]. Nevertheless, the same specimens which in the electron microscope show only an array of slip lines of varying strength, give the usual impression of being covered with slip bands when observed in the light microscope.

Sometimes surface regions are found on which the slip lines are spaced rather uniformly and are of comparatively even strength so that the impression of an elementary structure is created (Figure 20). Nevertheless it is obvious that no real elementary structure forms on brass. Thus at elongations of up to several per cent, where slip lines of all depths may be observed, regions as wide as 1 or 2μ exist on which not a trace of slip can be detected (Figure 21). With increasing deformation those regions are gradually filled up with slip lines. That no elementary structure forms on α-brass is also clear from some light-microscope observations. A specimen with an average grain size of 0.4 mm. exhibited sharp slip lines and some cross slip in about two-thirds of the grains already at 0.1 per cent elongation—a statement which should be compared with the results for aluminium and copper given in Table I.

In brass, as in aluminium, copper, and silver, there seems to be a smallest possible distance between two neighbouring slip lines. This, however, is very difficult to prove conclusively, expecially as no single crystals have been examined. The smallest distances found between neighbouring lines were in the order of 120 Å (see for example Figures 21 and 28). This figure is by no means accurate and is meant to serve as a rough guide only. It may be inaccurate by as much as a factor of 2, mainly because the orientation of the crystals is not known. If we calculate the theoretical smallest distance of separation according to the equation [9] $d_0 = Gb/[8\pi(1 - \mu)\tau]$, where G, b, and μ have the same meaning as before, we obtain $d_0 = 140$ Å for $\tau = 4$ kg/mm^2, which is a medium stress.

A distinct influence of either grain size or heat treatment on the depth of the slip lines was found. On polycrystals with grain diameters from 0.05 to 0.3 mm., produced by annealing at 560°C. for 40 minutes, the slip on individual lines only rarely exceeded 1000 Å, the average being about 200 to 500 Å. Polycrystals annealed for a few hours at 920°C. with grains of about 1 mm. diameter, however, exhibited numerous slip lines with slip of several thousand Å, and the slip on the majority of the lines was about 500 to 1000 Å. These figures are not the result of accurate measurements, but even with painstaking measurements it would be extremely difficult to give reliable figures, because the slip lines on each specimen vary very greatly in strength—fine, medium and broad steps being distributed over the surface irregularly.

It is likely that the important factor influencing the depth of the slip lines is grain size rather than heat treatment because in all cases, starting from rolled material, complete recrystallization had taken place. Such an influence may be understood theoretically. The greatest amount of slip which can take place on a single slip plane in a polycrystal, disregarding possible recovery processes, is that caused by a row of piled-up dislocations or dislocation loops extending right through a crystal from grain boundary to grain boundary. This slip can be calculated using a formula derived by Leibfried [13] as $s \cong \tau l/G$ where s is the slip in the neighbourhood of the source of dislocations, l the length of the active slip plane, and G the modulus of shear which for α-brass is about 4000 kg/mm^2. For a shear stress of $\tau = 4$ kg/mm^2, we thus find that the maximum shear which can take place in a single slip line is 1000 Å for a crystal diameter of 0.1 mm., and 10,000 Å for a diameter of 1 mm. This upper limit for the slip on individual slip lines is in good agreement with the greatest depths observed in slip lines as discussed above.

Observations made during the examination of the surface of deformed brass with a light microscope also support this view as the very first slip lines were already found mostly to extend from grain or twin boundaries to grain or twin boundaries. Furthermore, not only were the slip lines very much stronger in a specimen of 0.4 mm. average grain diameter than they were in a specimen with about a tenth that grain size, but also within each specimen the small crystals generally exhibited finer slip lines than the bigger crystals. Thus it seems safe to conclude that grain size (together with the resolved shear stress) rather than heat treatment, determines the average depth of the slip lines in brass.

In polycrystalline α-brass it was found more often than it had been observed in aluminium [7] that slip lines appearing light were interspersed in a set of lines which were dark and vice versa. It could be confirmed that such colour differences indicate that the lines belong to different slip systems acting on the same slip plane [7], for, where slip lines are crossed by a "mixed system," they sometimes are clearly shifted in one direction by the dark lines and in the opposite direction by the white lines. As only the minority of probable slip system combinations will give rise to dark and light lines within one set of parallel lines, the greater number of such "mixed systems" will remain undiscovered. Taking this fact into consideration, it appears that "mixed systems" are not at all rare in brass (see for example Figures 19 and 20).

A special effect, not yet completely understood, is visible on a number of specimens, namely that a slip

line appearing dark throws a white shadow (see for example Figure 22). Probably those lines are either slip lines in compression, or else normal slip lines which without shadowing would have appeared dark and which are oriented so as to throw a white shadow.

In some slip line patterns arising through multiple slip it may appear as if uncrystallographic slip (i.e. slip other than on (111)-planes) had taken place (Figure 23). The explanation always is that slip lines which are formed early in the deformation are cut more often by lines of the crossing system, and therefore suffer stronger displacements, than lines which are formed later. But even the lines which are formed very late in the course of the deformation often are curved because they meet a surface much stepped by the preceding deformation [7]. In Figure 23 the displacements produced by the two causes are in opposite directions. No truly uncrystallographic slip has ever been observed on brass.

2. *Cross Slip*

Cross slip in α-brass is abundant and often leads to delightful but very intricate patterns. It may interconnect the slip lines until sometimes, especially at high deformations, more or less all lines of one system are linked with each other (Figure 24). It may also be absent or may be nearly absent as can be seen from Figures 23 and 25. Often the slip lines as a whole turn into the cross slip system and back abruptly, but even more frequently cross slip lines just branch off slip lines. Where that happens there is a sudden change in the depth of the slip lines, as should be expected (Figure 22). This observation proves that slip lines, or parts of them, may grow in depth as the deformation proceeds, unless one is willing to believe that whole networks of interconnected lines are formed suddenly.

Because cross slip lines are of the same character as the main slip lines, i.e. are as straight and have about the same depth, patterns may arise in which it is no longer possible to decide which are cross slip lines and which are lines of the most highly stressed system. Indeed one often gets the impression that the two systems have the same right, and act in the same manner as normally two systems act in double glide, although by the geometry of translation the two systems involved never can be the two most highly stressed systems (Figure 24).

A special type of cross slip already observed in aluminium [7] was also found in brass. It exists in the immediate neighbourhood of etch pits and was first described by Cahn [14]. Elsewhere [7] it was said that probably this type of cross slip did not extend into the interior of the metal but ended on the etch pit. This idea, however, could not be proved using aluminium specimens, but with a lucky photograph of brass it now can be verified (Figure 26). On this photograph all the slip lines traversing the pit are to be seen clearly and can be followed from one side right across the etch pit to the other side. Within the etch pit all slip traces, including those which are linked to the cross slip lines, obviously belong to the same system, i.e., the active slip system. This shows that the cross slip does not extend beyond the pit.

3. *The Interaction of Slip Lines with Twin Boundaries*

Annealing twins are a common feature in α-brass. Some are in the form of narrow bands the width of which remains constant over a length of many microns, others are wide and of irregular shape, but all are bounded by (111)-planes. This allows one to distinguish between twin boundaries and grain boundaries.

Sometimes a twin boundary seems to constitute a strong obstacle to crossing slip lines, as for instance in Figure 27. All the white slip lines approaching the boundary from below gradually fade out before reaching the twin. (The light traces on the top of the photograph most probably do not belong to the same system.)

Occasionally a slip line changes into a cross slip line either directly at the twin boundary or in its immediate neighbourhood (Figure 28).

Often whole series of slip lines, meeting a twin boundary, cross it with change of direction (Figure 25). Usually, however, even in such cases there is evidence that the twin boundary is not crossed without disturbances. In Figure 25 for instance, the slip line pattern is not quite the same on both sides of the twinned region. The changes always occur abruptly at the twin boundaries. What usually happens at those places can be seen on Figure 29: a short piece of cross slip in the twin boundary itself is fitted into the lines.* Although the twin boundaries are (111)-planes, i.e., possible slip planes, this of course can happen only when the twin boundary contains the slip direction. Quite often narrow twins show slip lines parallel to their boundaries (see for example Figure 27), but the other traces found in a narrow twin nearly always cross its boundaries.

From the above observations it can be concluded that twin boundaries are a powerful obstacle to crossing slip lines when they do not contain the slip

*In a recent paper H. Czyzewski [J. Appl. Phys., **22** 1951, p. 846] has also described this effect.

direction, and that they are a weak obstacle when the slip direction is contained in them. Barrett [15] and Nabarro [16] have already come to this conclusion.

IV. Theoretical Interpretation of the Results

1. *Elementary Structure, Slip Lines, and Slip Bands*

In this section we shall discuss and compare the surface structures of the pure face-centered cubic metals, aluminium, copper, and silver, on the one hand, and the face-centred cubic alloy α-brass on the other. It is assumed that the surface structures are representative of the process of plastic deformation, not only at the surfaces but also in the bulk of the metal. At present it is not possible to decide definitely whether this assumption is justified. The greatest argument against it seems to be the dependence of slip lamellae thickness on surface orientation discovered recently [8]. Following an idea by Hollomon [17], Frank-Read sources situated near a surface have a lower threshold stress than those situated in the interior. With this idea an explanation of the orientation effect might be found in which it is not necessary to assume a fundamental difference between the plastic properties in the surface regions of metal crystals and the bulk of the metal.* Thus we may dispose of what is probably the strongest argument against the above assumption.

When discussing the pure metals investigated we shall mainly refer to aluminium because its surface structures are particularly well known, and it appears as if there are no significant qualitative differences between the structures on aluminium, silver, and copper.

The most important question which has to be answered is: Why do the pure metals show an elementary structure and slip bands and why is neither found on α-brass? According to a theory of slip band formation in an earlier paper [9], an elementary structure is formed when a metal contains many more possible sources than can become active because the dislocations of the different sources interfere strongly with each other's motion. Out of the elementary structure the slip bands are formed, a process involving the annihilation of dislocations in the immediate neighbourhood of a growing slip line. Hence to put it very briefly, an elementary structure will be formed when there are so many possible sources of dislocations that they seriously hinder each other, and slip bands will form only when an elementary structure is present. The logical conclusion then is that in α-brass the number of sources of dislocations which may become active at comparatively low stresses is small. The fact that in brass there are neither slip bands nor an elementary structure is a very powerful argument for this theory.

*See also Section V, part 2.

The presence of an elementary structure in the pure metals and its absence in brass provide a simple explanation for the behaviour of strain markings. On α-brass it is comparatively easy to produce strain markings, i.e. to etch the repolished surface of a deformed specimen so that the slip traces reappear [19; 20]. This is not possible in aluminium or copper using ordinary etching reagents, and becomes increasingly difficult with homogeneous copper-zinc alloys as their zinc content is reduced. The reason for this behaviour probably is that on copper and aluminium an elementary structure exists in which the density of the dislocations is about the same as in the slip bands, for the spacing of the lines is much the same in both, and the average density of dislocations on each line is solely determined by the stress. Consequently there is no reason why in copper or aluminium an etchant should attack the slip bands more strongly than the regions between them. In brass, on the other hand, the regions between the slip lines contain no or only few dislocations, and therefore are attacked less than the immediate neighbourhood of the slip lines, made thermodynamically unstable by the presence of the dislocations piled-up in them. Moreover, McLean [21] and Jacquet [22] find that slip lines which cross whole grains nevertheless often etch up solely, or particularly strongly, near the grain boundaries, where according to our theory the dislocations are most densely packed.

2. *The Deformation During Single Glide*

From the stress-strain curve of brass we know that its yield point is much higher than the yield point of aluminium, copper, and silver (Figure 11). Thus the first sources to start acting in brass not only are very much fewer, but they also require a higher stress to be activated.† Because of the great average distance between active slip planes the interaction between dislocations of different sources, which as

†Possibly the high yield stress in α-brass is due to the locking of dislocation sources by impurity atmospheres (Cottrell [38]). This idea easily explains why, as discussed in the following paragraph, a source of dislocations once activated goes on to release dislocations until equilibrium is reached. Later, Section V, part 2, we shall return to this point.

we saw plays a great role in the pure metals considered, is practically absent during single glide in α-brass. Moreover, as the yield stress is high in brass, there can be few other obstacles, besides crystal or twin boundaries, powerful enough to interfere effectively with the motion of the dislocations. Therefore the series of dislocations emitted by the sources will often, or perhaps mostly, expand unhindered until they meet a grain boundary or an unfavourably oriented twin boundary. Consequently, even at small deformations, we observe slip lines of great depth depending on the average grain size.

In agreement with this view is the following experimental result: If α-brass single crystals are stressed slightly beyond the yield stress, then unloaded and stressed again, new slip lines sometimes appear before the highest previous stress is reached [23]. Again, when brass single crystals are kept loaded just below the yield point, they may show no creep for hours and then suddenly start to creep with an increasing velocity which then dies down again. At the same time slip lines appear. There seems to be a direct proportionality between the creep strain and the number of slip lines [24]. These observations indicate that once a slip line is started in brass, most probably by thermal activation aided by stress, it grows without work-hardening until it approaches its final depth, determined by the length of the active slip plane and the resolved shear stress.

The fact that in single crystals of brass the slip lines tend to form clusters [19] is probably due to geometrical softening [12]. The authors do not believe that slip line clusters in brass are analogous to slip bands in aluminium.

Thus it seems very likely that the work-hardening in brass, at least at small and medium strains, is mainly due to the exhaustion of sources with low threshold stresses rather than to serious lattice disturbances. In aluminium, copper, and silver, by contrast, work-hardening is due to the interaction of the dislocations emitted by different sources belonging to the same, and apparently often also to different slip systems [25], leading to deformation bands and possibly still other strong lattice defects like aggregates of vacant lattice sites and sessile dislocations. As without the creation or strengthening of lattice defects the slip on each slip line increases proportionally with the stress, we understand why work-hardening in α-brass usually is small compared with that in copper. This view also is in accordance with X-ray evidence: Aluminium single crystals show strong asterism at small strains, but brass crystals have no asterism even after large strains, until the onset of double glide [23; 26; 27].

It is thought that asterism is a consequence of deformation bands [14; 28; 29] and in fact apparently no deformation bands have ever been observed on brass crystals. If we follow an earlier paper [30] and consider deformation bands as a disturbance forming through interacting dislocations at the boundaries of regions containing a strong surplus of dislocations of different types belonging to the same or to two different systems [7],* then it becomes obvious that no deformation bands can form on brass: in brass the slip lines are on the average much too widely spaced to permit a general interaction of the dislocations in parallel slip lines. Rows of dislocations moving in different directions will normally just bypass each other. Thus in brass we not only expect no deformation bands, but at the same time the mentioned regions cannot form. In metals with an elementary structure, however, the acting slip planes are so closely spaced that rows of dislocations moving in different directions must interact whenever they meet.

From the assumption of a limited number of dislocation sources which, as soon as they are activated, release dislocations without work-hardening until equilibrium is reached, (often or even mostly when the foremost dislocations meet crystal boundaries), it follows that we would expect a strong influence of grain size on the stress-strain curve in the case of α-brass. This follows because in equilibrium the slip due to a row of dislocations is practically proportional to the resolved shear stress and to the space occupied by them [13; 31] and because it seems likely that the grain size will not have a very pronounced effect on the number of sources. If the distribution of the sources as well as their threshold stresses were completely independent of grain size, and all slip lines extended to the grain boundaries, we actually should expect the strain for any given stress to be proportional to the grain size as long as no multiple slip takes place. In aluminium and copper, however, the effect of grain size on the stress-strain curve should be much smaller. In these metals hardening goes on by the interaction of dislocations everywhere in the material.

The authors failed to find in the literature reliable experiments on the influence of grain size on the

*It seems likely that the subgrains discovered by Wood and subsequently investigated by a number of scientists are those regions envisaged in the earlier theoretical paper [30]. Most of the numerical values given in the literature of size, average disorientation, and stress at which the regions have formed, are roughly consistent with this view.

stress-strain curve. Therefore, a rough experiment was carried out with brass and copper, plotting the stress-strain curves of these metals for different grain sizes. The curves obtained (Figure 30) indicate a strong influence of grain size in the case of brass and none in the case of copper. It must be admitted, however, that different heat treatments, as stated in the legend to Figure 30, have been used to obtain the various grain sizes so that not too much significance must be attached to those curves, although they are in full agreement with the above prediction. Further experiments in this direction are highly desirable.

3. *Multiple Slip and Cross Slip*

As was shown previously [7], the cutting of a slip band by a slip band of a different system is a difficult process in aluminium, i.e., a slip band constitutes a powerful obstacle against crossing slip bands. Never-

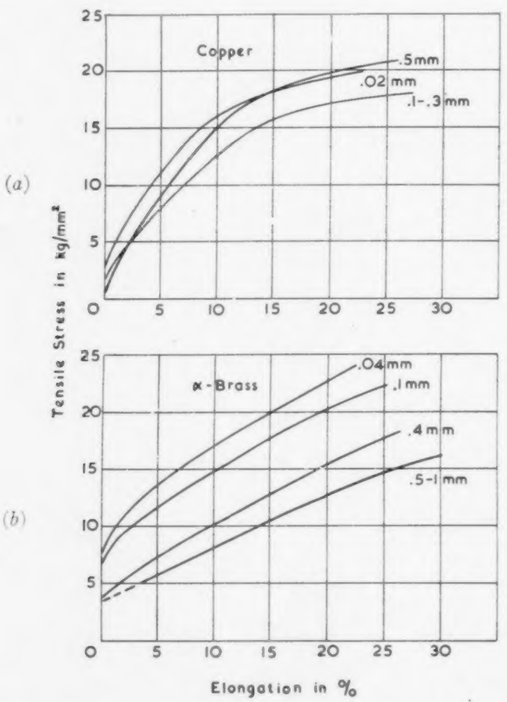

FIGURE 30. Stress-strain curves showing the influence of grain size in the case of (*a*) copper and (*b*) α-brass. Heat treatment as follows:

Copper: grain size 0.5 mm., 1 h. 900°C., elongated 2% and 5 h. 900°C.
0.02 mm., 2 h. 550°C.
0.1–0.3 mm., 5 h. 900°C.
All in vacuo

α-Brass: grain size 0.04 mm., 2 h. 500°C.
0.1 mm., 5 h. 650°C.
0.4 mm., 3 h. 860°C.
0.5–1 mm., 5 h. 900°C.
All in air

theless the onset of double glide in aluminium is not marked by a sudden increase or decrease in work-hardening (see for example [32, Figure 90a]). This is not surprising because, as argued above, the source of work-hardening in aluminium, starting from the smallest deformations, is the interaction between dislocations, i.e., processes akin to the mutual cutting and blocking of dislocations which must take place during multiple slip. In α-brass, although we have no visible evidence for it, the cutting of slip lines through each other is undoubtedly a difficult process just as it is in aluminium. The fundamental difference between brass and aluminium is that with the beginning of double glide in the former (due to the unavoidable mutual cutting of slip lines) a new source of work-hardening is introduced which is not present during single glide. In brass, dislocations of different sources start to interact only with the onset of double glide. The observations by von Göler and Sachs [33] on the behaviour of single crystals of brass in tension bear this out.

In single crystals of aluminium and copper double slip starts as soon as the symmetrical position for the two most highly stressed systems is reached. In contrast brass continues to slip on the first system until the resolved shear stress on the second system is substantially higher than that on the first. Once the second system starts to act, and its slip traces appear, the load may actually drop. At that point the slip on the first system stops completely and the second system acts alone. The orientation then changes according to the action of the second system, but this in turn continues to act alone even after the symmetrical position is crossed again so that now the second system is under a smaller shear stress than the first. Furthermore, as soon as the second system becomes active, the slope of the stress-strain curve decreases discontinuously i.e., the work-hardening drops sharply. In other words, interpreting these results according to our new knowledge, after the slip lines of the second system succeeded in cutting those of the first system, thereby removing the major obstacles to slip on the second system, it again shows the same slight initial work-hardening which is typical for brass and which, as previously explained, is due to the spread of rows or sequences of dislocations without work-hardening until their equilibrium position is reached.

Finally, we may mention the behaviour of critically oriented brass crystals as described by Burghoff [34]: of three brass crystals critically oriented, so that they should have extended by multiple slip from the start, two slipped on one system only up

to several per cent elongation. In the third crystal two slip systems acted, but in segments such that in each segment only single glide took place. Obviously all these observations are in perfect agreement with the interpretation of the behaviour of slip lines in brass as given above.

A last question still to be answered is: Why is cross slip prominent in brass but rare in aluminium, silver, and copper? It was explained in the preceding paragraph that, in the pure metals exhibiting an elementary structure, double slip is not a significantly more difficult process than single slip, but that it is so in α-brass. Consequently, any complex deformation in the pure metals considered can easily be accommodated through multiple slip (unpredicted slip in single crystals). In brass, on the other hand, the cutting of slip lines (or rather the mutual cutting of individual dislocations) is comparatively such a difficult process that it is avoided if possible. If we now consider the motion of dislocations leading to cross slip then we realize that in cross slip it is not necessary for dislocations to cut mutually while it is unavoidable for any other multiple slip on non-parallel planes. Therefore in brass cross slip will be substituted for double slip wherever possible. The much more frequent occurrence of "mixed systems" in brass, as compared with aluminium, points in the same direction. Here complex slip is accommodated by slip on different slip systems having the same slip plane—in the second possible mechanism of multiple slip in which no dislocations cut mutually. This is energetically more favourable than normal double slip only as long as the active slip planes (the slip lines) are far enough apart from each other not to interact strongly, which usually is the case in brass but not in the metals with an elementary structure.

VOL. 1 1953

V. Some Theoretical Considerations

1. *The Elementary Structure*

Although the ideas put forward in the preceding section are in agreement with experimental evidence it cannot be claimed that all problems have been solved. Very much remains to be done. In the following some of the problems will be discussed.

With regard to the question of how in detail an elementary structure is formed, it seems certain that the presence of very many easily activated sources cannot be the only necessary condition for its formation. In addition, the emission of the dislocations from the sources or their motion through the metal (probably hindered by obstacles in their path) must be a slow process. If the creation of the dislocations was rapid *and* they moved with about 50 per cent of the velocity of sound or more, as maintained by Mott [35] and Fisher, Hart, and Pry [36], then the first sources which start to act should immediately give rise to long deep steps. In the pure metals containing an elementary structure, however, deep steps are only formed after the elementary structure. Therefore the experimental evidence of an elementary structure discredits the idea of a generally dynamic formation of dislocations, but points to a slow and steady creation of dislocations.

It is not thought that a metal exhibiting an elementary structure under certain conditions of straining will do so under all conditions. On the contrary, speed and temperature of deformation, and even grain size will probably have an influence so that it is quite possible that, under certain conditions of straining, a metal may show an elementary structure but not under others.

In aluminium, slip bands are formed at small strains; this might indicate that at normal strain rates and room temperature this metal is just in a boundary condition between deforming with and without an elementary structure. In copper and silver, on the other hand, we then would have conditions in which the elementary structure is more stable. "Easy glide" in aluminium therefore might indicate a plastic deformation without the formation of an elementary structure. These latter considerations, however, are purely speculative, and are given as a possibility rather than as the authors' opinion.

2. *Dislocation Sources*

The nature of the sources of dislocations is still open to speculation, but the type of sources described by Frank and Read [18] seems to fit all experimental observations. Therefore we shall base our discussion on them. We shall also follow the suggestion by Mott [35; 37] that the dislocation sources of Frank-Read type are the short parts of dislocations forming a three-dimensional network which is thought to be present in every metal. This idea is consistent with the density of slip lines in the elementary structure of aluminium. The minimum resolved shear stress τ required to activate a source of dislocations is given by $\tau_y \cong G \times b/l$ where l is the length of the dislocation-pieces from junction to junction forming the network. For sources ending at a free surface this critical stress must be halved according to Hollomon [17]. As was pointed out previously [9], about 10^9 dislocation sources per cm^2 are sufficient to produce

the elementary structure on aluminium up to the highest stresses, and, according to our new knowledge of the elementary structure on copper and silver, somewhat fewer are required in those metals. What then must be the minimum thickness of the surface layer providing the necessary sources of dislocations for the elementary structure? From $\tau_{ys} = Gb/2l$ we find for a stress of, say $\tau_{ys} = 2$ kg/mm², $l \cong 2 \times 10^{-5}$ cm. or a density of dislocation sources of about 10^{14} per cc. With this density of sources the minimum thickness of the surface layer containing all the sources responsible for the elementary structure becomes 10^{-5} cm, in good agreement with the value for $l = 2 \times 10^{-5}$ just deduced.

At a stress of about 0.8 kg/mm², which is about the lowest stress yielding a complete elementary structure in aluminium, the corresponding values are: dislocation density necessary to form the elementary structure $\cong 10^8$/cm² (see Table I in [9]); l calculated from formula $\cong 6 \times 10^{-5}$ cm. giving a density of sources of about 5×10^{12} per unit volume; and the minimum thickness of the surface layer containing sufficient sources to form the elementary structure becomes 2×10^{-5} cm.

We next turn to the question of why α-brass contains so few sources and why these are so much more difficult to activate than those in the pure metals examined. The answer to this problem cannot simply be that in brass the dislocation network, providing the sources, has a greater average distance between the junctions, because this would lead to a lower instead of a higher yield stress in brass compared with the pure metals.

One way in which to account for the high yield stress of brass presents itself immediately, namely that it is caused by the blocking of dislocation sources through impurity atoms in the manner proposed by Cottrell [38]. This possibility has recently been discussed by Mott [35], and in fact is very attractive, partly because it at once explains the rather sharp yield point usually found in brass single crystals.* However, it presents the difficulty that we have to explain why dislocation sources are locked by Cottrell-atmospheres in α-brass and not in the other metals investigated, although their impurity contents should be amply sufficient to block all sources in them. The answer to this problem may be found in the different rates of diffusion in the four metals concerned. Also it is quite possible that the dislocation sources in brass are locked through concentration variations within the mixed lattice; or in other words that the zinc atoms play the role normally played by impurity atoms. Thus, until more information is available, a possible explanation for the few sources and their high threshold stress in brass is the presence of a widely spaced dislocation network in which "atmospheres" locking the dislocation sources are easily formed.

A great advantage of this idea is that with it the typical form of the stress-strain curve of brass single crystals is easily explained. According to the theory of anchored dislocations by Cottrell [38], and also recent considerations by Mott [35], the threshold stress for all anchored sources, irrespective of their normal value, should be the same unless their normal threshold stress is higher than the stress at which dislocations break free from their atmospheres. In single crystals of brass with a rather uniform resolved shear stress throughout, practically all sources belonging to one slip system should therefore have started to act at a stress of, say, 10 or 20 per cent above the yield point, and from then on only a few new sources can be activated until the beginning of double glide. Further, following the conclusions drawn in the preceding chapter, the majority of the sequences of dislocations spread out to their final extension as soon as they are formed. Now, the plastic strain is proportional to the number of active sources, proportional to the average length of the slip lines, and proportional to the stress. Consequently we expect a stress-strain curve with a sharp yield point followed by a horizontal part which then turns into a straight line, the elongation of which should go through the origin of the co-ordinate system, because neither the number of sources nor the length of the slip lines should change according to the above. In Figure 31 this type of curve predicted is compared with experimental stress-strain curves of brass, and of $AuCu_3$ crystals, which apparently behave in much the same manner as brass crystals. The similarity between the experimental curves and the type of curve predicted is striking. However, the idea that all sources in brass single crystals have started to act at a stress near the yield point, and the idea that in them slip lines do not normally grow longer when the stress is increased, ought to be tested experimentally.

3. *Slip Bands*

We do not know whether slip bands are started just through thermal fluctuations of particular

*While writing the present paper the authors were not aware of recent investigations by Cottrell and Ardley (to be published) who found a true yield point in α-brass crystals and explain it by the anchoring of dislocation sources through "atmospheres." The authors are indebted to Professor Cottrell for directing their attention to this work.

strength or through a special process not yet understood. At present it seems improbable that the formation of slip bands is due to a dynamical process. This not only follows because the presence of an elementary structure indicates a non-dynamic creation of dislocations, but because there is no experimental evidence in its favour.

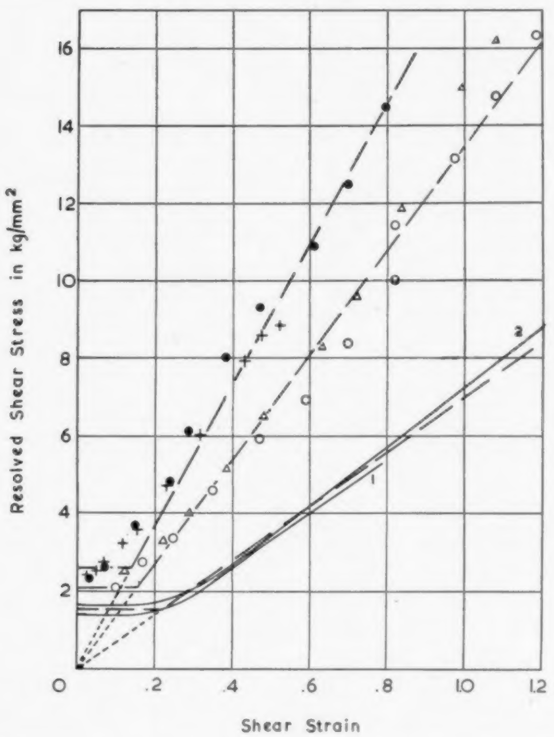

FIGURE 31. Comparison between the theoretical stress-strain curve predicted and experimental results.

α-brass crystals: (1) von Göler and Sachs [33]; (2) Masima and Sachs [39].

Cu_3Au crystals: Blewitt and Koehler [40] (△,○); Sachs and Weerts [41] (+,●).

The starting point for the theories of dynamical slip band formation was the view expressed by Heidenreich and Shockley [1] and later by Brown [3; 4; 5] that the slip lines in the bands had a more or less even depth of about 2000 Å. The results obtained by the authors in a previous investigation [6; 7; 8] and in the present one do not show any such effect, and indeed it is difficult to see, even if slip took place by "quanta" of definite size, why this should lead to surface steps of even height in a polycrystal or a number of differently oriented single crystals. Since, in aluminium, slip lines do not usually extend right through whole crystals, this could only happen if all slip lines originated at the surface, or alternately at one and the same depth below the surface, unless one believed there were no obstacles hindering the motion of dislocations in slip bands. Also there would have to be a very complicated relationship between the arbitrary surface orientation and the slip on each line, otherwise one would get steps from zero height to the maximum value. Again it is quite possible that the observed slip lines of greatly varying depth found side by side on brass crystallites in truth belonged to sources all of which had acted by the same amount, but were situated at different distances from the surface. Of course this is highly unlikely, but the consideration shows that in fact it would be difficult to find this effect, even if slip avalanches of uniform size were the general rule. In aluminium, however, the presence of slip lines greatly varying in depth even within single bands, together with the dependence of lamella-thickness on surface orientation, proves that no definite slip distance exists.

The highly interesting theory of slip band formation suggested by Brown [42] and worked out in greater detail by Mott [5] has the following great weakness besides the above point: If softening should take place in the immediate neighbourhood of a slip line, as maintained in this theory, then all metals should show slip bands, and we would have to find a new explanation why brass in particular has none. Also this idea does not take into account the presence of the elementary structure on the metals investigated which do form slip bands. Finally, the mechanism by which slip lamellae should form, proposed by Fisher, Hart, and Pry [36] and independently by Cottrell [43], does in fact exist, but it is rare and obviously has no influence on the formation of the bands. Instead it leads to the so-called "cross-over" of slip bands in double glide [6]. In any case, this idea has the serious disadvantage that with it substantial band formation could only start after multiple slip had commenced, which quite definitely is not the case.

4. *Work-hardening and Some Final Remarks*

Work-hardening has recently been investigated theoretically by Seitz [44] who believes vacant lattice sites, created through moving dislocations, are mainly responsible for work-hardening, and by Mott [35; 37], Lomer [45], and Cottrell [46] who see the main reason for work-hardening in the formation of sessile dislocations. Although the ideas put forward by these investigators are very attractive, they do not solve all the problems. We are now faced with the question of how in detail the interaction and mutual blocking of dislocations, thought to take place in the

pure metals examined, progresses. Only a few of the many problems which must be solved will be given. First, what prevents the dislocations from moving and returning to their sources after the stress is relieved? It will be admitted that it is comparatively easy to think of mechanisms which would lock the dislocations, but it is more difficult to account for the slight change of the elastic constants during cold work in, say aluminium, taking into account the vast numbers of dislocations present in the elementary structure and in the slip bands. Secondly, by what processes are the number of slip bands and the number of lamellae in them determined? Finally, can it be understood why in slip bands, which at most are 0.1 mm. long and about 1.2 microns wide, there may be as many as 15,000 dislocations while in a single slip line of the same length only about 300 dislocation loops could be accommodated?

In brass, on the other hand, conditions seem to be comparatively simple. In this metal, we argued, the sequences of dislocations usually expand unhindered until they meet a powerful obstacle, as for instance a grain boundary. Work-hardening in it is mainly due to the exhaustion of "easy" sources, and we only need a mechanism which prevents the dislocations in the slip lines from returning to their sources when the stress is relieved. The formation of sessile dislocations, in the manner proposed by Lomer, by Cottrell, and by Mott, is such a mechanism.

A few final remarks may be allowed on the question of how far the results obtained with aluminium, copper, and silver on the one hand, and with brass on the other hand, will be applicable to other metals. This question can ultimately be decided only by further experiments. The authors believe, first, that more forms of plastic deformation besides the two investigated exist, and secondly, that a number of other metals will behave according to the two forms described in this paper. For instance, it was shown in Figure 31 that a remarkable similarity exists between the stress-strain curves of $AuCu_3$ crystals and those of brass single crystals. Therefore we expect copper-gold crystals to deform like brass, namely with no elementary structure and no slip bands. In support of this contention we mention a recent investigation by Blewitt and Koehler [40]. These scientists found practically no change in the resistivity of $AuCu_3$ crystals at shears up to 30 per cent, and a sharp increase beyond about 40 per cent shear. From this they deduced that up to about 30 per cent shear slip in the crystals took place in rather big steps on widely spaced planes, a result which agrees well with the idea that no elementary structure forms on these crystals.

This paper is published by permission of the South African Council for Scientific and Industrial Research.

References

1. Heidenreich, R. D. and Shockley, W. J. Appl. Physics, **18** (1947) 1029.
2. Heidenreich, R. D. and Shockley, W. The Strength of Solids (London, Physical Society, 1948) p. 57.
3. Brown, A. F. Nature (London), **163** (1949) 961.
4. Brown, A. F. Metallurg. Applications of the Electron Microscope. (London, The Institute of Metals, 1950) p. 103.
5. Brown, A. F. Advances in Physics, **1** (1952) 427.
6. Wilsdorf, H. and Kuhlmann-Wilsdorf, D. Z. angew. Phys., **4** (1952) 361.
7. Wilsdorf, H. and Kuhlmann-Wilsdorf, D. Z. angew. Phys. **4** (1952) 409.
8. Wilsdorf, H. and Kuhlmann-Wilsdorf, D. Z. angew. Phys., **4** (1952) 418.
9. Kuhlmann-Wilsdorf, D., van der Merwe, J. H. and Wilsdorf, H. Phil. Mag., **43** (1952) 632.
10. Hanson, D. and Wheeler, M. A. J. Inst. Metals, **45** (1931) 229.
11. Trotter, J. J. Inst. Metals, **80** (1952) 521.
12. Wilsdorf, H. and Kuhlmann-Wilsdorf, D. J. Metals, **4** (1952) 527.
13. Leibfrifd, G. Z. Phys. **130** (1951) 214.
14. Cahn, R. W. J. Inst. Metals, **79** (1951) 129.
15. Barrett, C. S. Symposium on Plastic Deformation (Amer. Soc. Metals, 1948).
16. Nabarro, F. R. N. Some Recent Developments in Rheology (London, The Brit. Rheologists' Club, 1950), p. 38.
17. Hollomon, J. H. See N. F. Mott [35, p. 1161].
18. Frank, F. C. and Read, W. T. Phys. Rev., **79** (1950) 722.
19. Kuhlmann, D. Z. Metallk., **41** (1950) 129.
20. Burke, J. E. and Barrett, C. S. Trans. A.I.M.E., **175** (1948) 106.
21. McLean, D. J. Inst. Metals, **74** (1947) 95.
22. Jacquet, P. A. Comptes Rendus, **228** (1949) 1439.
23. Treuting, R. G. and Brick, R. M. Trans. A.I.M.E., **147** (1942) 128.
24. Burghoff, H. L. and Mathewson, C. H. Trans. A.I.M.E., **143** (1941) 45.
25. Haasen, P. and Leibfried, G. Z. Phys. **131** (1952) 538.
26. Maddin, R., Mathewson, C. H., and Hibbard, W. R. Trans. A.I.M.E., **175** (1948) 86.
27. Maddin, R., Mathewson, C. H., and Hibbard, W. R. Trans. A.I.M.E., **185** (1949) 527.
28. Barrett, C. S. and Levenson, L. H. Trans A.I.M.E., **137** (1940) 112.
29. Honeycombe, R. W. K. J. Inst. Metals., **80** (1951) 45.
30. Kuhlmann, D. Proc. Phys. Soc. (London), **A64** (1951) 140.

31. ESHELBY, J. D., FRANK, F. C., and NABARRO, F. R. N. Phil. Mag., **42** (1951) 351.
32. SCHMID, E. and BOAS, W. Kristallplastizität mit besonderer Berücksichtigung der Metalle. (Berlin, Springer, 1935).
33. Göler, VON and SACHS, G. Z. Phys., **55** (1929) 581.
34. BURGHOFF, H. L. Trans. A.I.M.E., **137** (1940) 214.
35. MOTT, N. F. Phil. Mag., **43** (1952) 1151.
36. FISHER, J. C., HART, E. W., and PRY, R. H. Phys. Rev., **87** (1952) 958.
37. MOTT, N. F. Proc. Phys. Soc. (London), **B64** (1951) 729.
38. COTTRELL, A. H. The Strength of Solids (London, Physical Society, 1948), p. 30.
39. MASIMA, M. and SACHS, G. Z. Phys., **50** (1928) 161.
40. BLEWITT, T. H. and KOEHLER, J. S. Pittsburgh Conference on the Plastic Deformation of Cryst. Solids (1950), p. 77.
41. SACHS, G. and WEERTS, J. Z. Phys., **67** (1931) 507.
42. BROWN, A. F. J. Inst. Metals, **80** (1951) 115.
43. COTTRELL, A. H. Private Communication, (1951).
44. SEITZ, F. Advances in Physics, **1** (1952) 43.
45. LOMER, W. M. Phil. Mag., **42** (1951) 1327.
46. COTTRELL, A. H. Phil. Mag., **43** (1952) 645.

PREYIELD PLASTIC AND ANELASTIC MICROSTRAIN IN LOW-CARBON STEEL*

T. VREELAND, Jr., D. S. WOOD, and D. S. CLARK†

This paper presents the results of an experimental investigation of the behavior of an annealed low-carbon steel subjected to rapidly applied constant stresses less than the static upper yield stress. Sensitive measurements of plastic and anelastic microstrain were made, and the relationship between stress and equilibrium microstrain determined.

The experimentally observed microstrain is quantitatively explained by a dislocation-generating mechanism. The equilibrium number of dislocation loops produced by a Frank-Read source is estimated as a function of the applied stress and the dislocation source length. Comparison of the theory and the experimental data leads to the determination of a characteristic length of dislocation which agrees with previous concepts of a mosaic block structure.

LA MICRO-DÉFORMATION NON-ÉLASTIQUE ET PLASTIQUE AVANT LA LIMITE D'ÉCOULEMENT, DANS UN ACIER À BAS CARBONE

Cet article présente les résultats d'une investigation expérimentale du comportement d'un acier à bas carbone, recuit, auquel on applique très rapidement des tensions constantes, inférieures à la tension correspondant à la limite d'écoulement statique, supérieure. La micro-déformation plastique et non-élastique a été mesurée avec précision, et la relation entre la tension et la micro-déformation correspondant à l'équilibre a été déterminée.

La micro-déformation observée expérimentalement est expliquée d'une manière quantitative par un mécanisme générateur de dislocations. Le nombre, correspondant à l'équilibre, de boucles de dislocations produites par une source de Frank-Read est estimé en fonction de la tension appliquée et de la longueur de la source de dislocations. La comparaison entre la théorie et les données expérimentales conduit à la détermination d'une longueur caractéristique de diclocation, qui s'accorde bien avec les concepts antérieurs d'un bloc de structure mosaïque.

PLASTIZITÄT VOR DEM FLIESSEN UND UNELASTISCHE MIKRODEHNUNGEN IN STAHL MIT NIEDRIGEM KOHLENSTOFFGEHALT

Die vorliegende Arbeit beschreibt die Resultate einer experimentellen Untersuchung des Verhaltens von geglühtem Stahl mit niedrigem Kohlenstoffgehalt, der schnellen angelegten, konstanten, äusseren Spannungen unterhalb der Elektrizitätsgrenze unterworfen wurde. Empfindliche Messungen der plastischen und unelastischen Mikrodehnungen wurden durchgeführt, und die Beziehung zwischen Spannung und Mikrodehnung im Gleichgewicht wurde bestimmt.

Ein Versetzungen produzierender Elementarvorgang kann die experimentell beobachtete Mikrodehnung quantitativ erklären. Die Anzahl der Versetzungsschlingen im Gleichgewicht, die von einer Frank-Read Quelle erzeugt wurden, wird als Funktion der angelegten Spannung und der Länge der Versetzungsquelle abgeschätzt. Der Vergleich der Theorie und der experimentellen Daten führt zu der Bestimmung einer charakteristischen Versetzungslänge, die mit früheren Ideen einer Mosaikblockstruktur im Einklang steht.

Introduction

The existence of a definite delay time for the initiation of yielding in an annealed low-carbon steel when subjected to a rapidly applied stress greater than the static upper yield stress has been shown by previous investigations in this laboratory [1; 2; 3]. Plastic and anelastic microstrain of the order of 30×10^{-6} in/in. has been observed during the period of delay prior to yielding [4].

This microstrain has been qualitatively described by Cottrell [5] as the result of the release of a few dislocations, the movement of which is obstructed by other nearby anchored dislocations or grain boundaries. When the resistance to the movement of dislocations is overcome, then yielding is initiated.

The purpose of this paper is to present the results of an investigation in which data have been secured concerning the plastic and anelastic microstrain that occurs as a result of rapidly applied constant stresses which are less than the static upper yield stress. These data provide a basis for a quantitative evaluation of a theory of the mechanism of yielding.

Material and Test Specimens

The material used in this investigation is the same as that employed for the study of stress-pulses and aging effects presented in a previous paper [4]. This material was of the following analysis:

Carbon	0.12%	Silicon	0.27%
Manganese	0.43%	Copper	0.23%
Phosphorus	0.019%	Tin	0.037%
Sulfur	0.042%		

The specimens were of the same design as used previously; namely, with a gage section of $\frac{1}{2}$ in. $\times$ 0.100 in. and $\frac{1}{2}$ in. long. These specimens were annealed at a temperature of 1680°F. (915°C.) for $2\frac{1}{2}$ hr. in dry hydrogen followed by a homogenizing treatment at 1300°F. (704°C.) for 22 hr. It has been

*Received March 6, 1953.
†California Institute of Technology, Pasadena, California, U.S.A.

shown that there is essentially no change in the carbon content of the specimens during these treatments.

Equipment and Test Procedure

The tests were made with the rapid-load testing machine described in a previous paper [1]. The load acting on the specimen was measured by means of a dynamometer employing type AB-14, SR-4 strain gages with suitable temperature compensation.

The plastic and anelastic microstrain was determined by means of the system described in a previous paper [4]. This consists of a strain bar connected in series with the specimen and is constructed such that the elastic strains in it are nominally the same as the elastic strains in the test specimen. The strain gages on the bar and the specimen are arranged so that the elastic strains in the strain bar are subtracted from the total strain in the specimen. The signals from the strain-gage bridge circuits which indicate the plastic and anelastic microstrain in the specimen are recorded on photographic paper by a galvanometer-type oscillograph. The strain-recording sensitivity of the recording system is within 0.5×10^{-6} in/in.

The test specimens were subjected to a rapidly applied constant load. A continuous record of load and microstrain was made for approximately 3.5 sec. after the application of the load. Records of load and microstrain were made at intervals after the initial 3.5 sec. until the microstrain reached an equilibrium value within approximately 5 min.

Experimental Results

The static properties of the material tested were determined in a previous study [4] and are given in Table I. The results of a series of tests in which the

TABLE I

STATIC PROPERTIES OF THE MATERIAL TESTED

ASTM grain size	Hardness Rockwell B	Specimen number	Upper yield stress (10^3 lb/in^2)	Lower yield stress (10^3 lb/in^2)	Yield strain (%)
6.7	54	134	42.5	30.0	>1.6
		181	41.3	28.0	1.7

plastic and anelastic microstrain have been investigated under rapidly applied constant stresses exceeding the static upper yield stress have been previously reported [4]. When the stress to which the specimen is subjected is less than the static upper yield stress, microstrain is also observed. Plastic and anelastic microstrain vs. time for a series of constant stresses is plotted in Figure 1. The microstrain rate decreases with time when the test stress is less than the static upper yield stress. When the test stress ex-

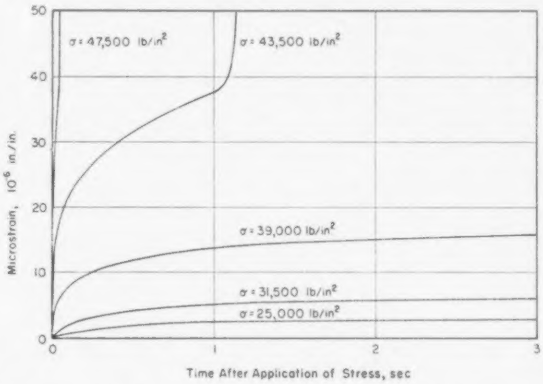

FIGURE 1. Microstrain vs. time for a series of constant stresses.

ceeds the yield stress, the strain rate decreases with time until the initiation of yielding which is characterized by an increase in strain rate. The final values of microstrain, or equilibrium microstrain, for various stresses below the static upper yield stress are plotted as small circles in Figure 2.

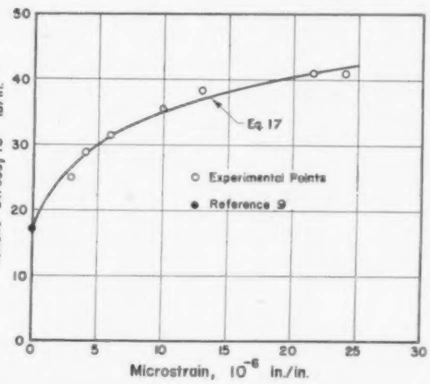

FIGURE 2. Applied tensile stress vs. equilibrium microstrain.

Discussion of Experimental Results

The experimental results presented above will be discussed in terms of a specific application of some general concepts which have been advanced by other investigators in the theory of dislocations. The theory of Cottrell [5] appears to provide a suitable explanation of the present experimental observations; therefore, the following discussion will be concerned with the mechanism of the release of dislocations prior to the initiation of yielding.

A recent theory by Holden [6] attributes the yield behavior of single crystals of iron to a dislocation-

collision process wherein moving dislocations release stationary dislocations by an interchange of energy. For the fine-grained material of this investigation, it seems probable that the dislocation-collision process is not responsible for the microstrain because the mean free path for dislocation travel is comparable to the grain size. Also, the result of such a process would be a strain rate which increases with time. This is contrary to the experimental observations of this investigation (Figure 1.)

The decreasing strain rate observed in this investigation might be attributed to a depletion of the reservoir of dislocations which can be moved by the applied stress. The strain rate would decrease linearly with increasing strain by this mechanism, which is contrary to the experimental results of this investigation. This indicates that some other mechanism gives rise to the observed strain rate vs. strain relations.

A mechanism has been proposed by Frank and Read [7] that may aid in an explanation of the observed microstrain. They have postulated a multiplication process for slow-moving dislocations which in effect constitutes a dislocation source. A segment of a dislocation, with firmly anchored ends, acts as the source. A suitable applied shear stress causes the segment to curve and generate dislocation loops. The stress required to form a new dislocation loop without the aid of thermal fluctuations is given by Frank and Read to be

$$\tau_c = G\lambda\alpha/l \tag{1}$$

where τ_c is the critical resolved shear stress; G is the shear modulus; λ is the magnitude of the Burger's vector; α is a constant of the order of unity; and l is the original length of the segment.

It may be assumed that initially the dislocations in annealed low-carbon steel all have complete atmospheres of carbon and/or nitrogen atoms [8] which prevent their free movement. As each successive loop is formed under the action of an applied stress, the original dislocation line is reformed and must again escape from its atmosphere to form another loop.

The growth of the loops which have been formed will be stopped by obstructions, such as grain boundaries. The rate at which dislocations are generated by the Frank-Read source is a function of the local stress at the dislocation source. The local stress at the dislocation source is the sum of the applied stress and the stress field of opposite sign due to the array of previously released dislocation loops. Thus the rate of generation of new dislocation loops will decrease as the number of previously generated loops increases; hence, the rate of strain should decrease with increasing strain at constant stress. This condition is observed in the present investigation. If the applied stress is low enough, the generation of new dislocation loops will be stopped completely before a sufficient number have been formed to break through the grain boundaries or other obstructions. The equilibrium microstrain observed in this study would then correspond to the total strain produced by the dislocation sources when the generation of new dislocation loops is stopped.

The experimental data indicate that no appreciable microstrain is produced by a tensile stress of less than approximately 17×10^3 lb/in^2. This value agrees with the elastic limit obtained by interpolation of the data presented by Roberts, Carruthers, and Averbach [9].

The maximum resolved shear stress corresponding to a tensile stress of 17×10^3 lb/in^2 is 8.5×10^3 lb/in^2. Thus, by equation (1), the length of the longest dislocation source which contributes to the microstrain is approximately

$$l_m = G\lambda\alpha/\tau = 1.34 \times 10^{-5}\text{ in.},$$

where G is taken as 11.6×10^6 lb/in^2; λ is taken as 0.985×10^{-8} in.; and α is taken as 1.

This value of l_m is approximately 1.2×10^3 times the lattice parameter of alpha iron. A mosaic block size of approximately 10^3 lattice parameters is believed to result from arrays of dislocations within metallic crystals [10]. Thus, it appears that the mosaic block size represents the upper limit of the length of dislocation sources within the material.

The equilibrium microstrain produced by Frank-Read dislocation sources distributed throughout the material will now be calculated. The properties of an individual dislocation source will first be determined, and then the microstrain produced by a distribution of sources throughout the material will be considered.

A Frank-Read source which has formed a number of dislocation loops in a particular slip plane is schematically illustrated in Figure 3. To find the equilibrium microstrain contributed by such a source, it is necessary to determine the equilibrium number and configuration of the dislocation loops that have been formed. The equilibrium number and configuration are determined by the applied stress and interaction of the stress fields associated with the dislocation loops, the source, and the obstruction. The stress field associated with a short segment of a dislocation loop is very complex. However, with a straight dislocation line of infinite length, the stress field, given by Koehler [11], is relatively simple.

Thus, the mathematical development of the properties of a dislocation source is considerably simplified if the interaction between opposite sides of dislocation loops is neglected, and an equilibrium array of straight, parallel, dislocation lines of infinite length is considered. The radial spacings between the dislocation loops and the source are assumed to be equal to the equilibrium spacings between infinite,

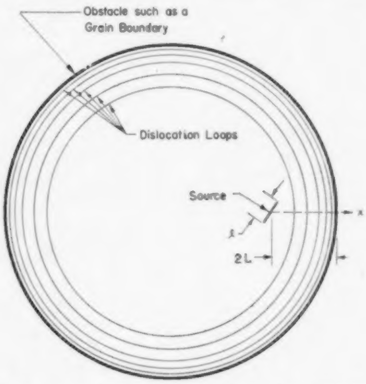

FIGURE 3. Schematic representation of a dislocation source and dislocation loops on a slip plane.

straight dislocation lines and a single dislocation line which represents the source. The minimum distance between the source and obstruction along the slip plane is designated as $2L$. The approximate dislocation model is shown in Figure 4, where x is a distance in units of L along the shortest line between the source and obstruction in the slip plane. The interaction between a dislocation and an obstruction, such as a grain boundary, is not known. It will be assumed that the obstruction cannot move and that it may be represented as a single dislocation line.

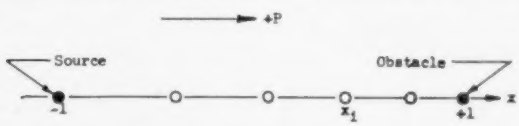

FIGURE 4. Approximate dislocation model with infinite linear dislocations.

The simplifying assumptions mentioned above cannot be rigorously justified. However, there is reason to believe that they will not introduce appreciable error into the calculations. The main contributions to the stress at a point between the dislocation source and the obstruction are the applied stress and the stress due to the nearest dislocations, since the stress due to a straight dislocation line is inversely proportional to the distance from the dislocation. The stresses due to dislocation segments on the opposite side of the source, Figure 3, are comparatively small and may be neglected since those segments are relatively far away.

The equilibrium number of dislocation loops produced by a source when a given shear stress is applied will now be estimated. We begin by considering the stress at any point, x, associated with an infinite dislocation line at x_i, Figure 4, which is given by Koehler [11] as

$$\tau = \frac{B}{L(x - x_i)} \tag{2}$$

where τ is the shear stress at point x, $B = G\lambda/2\pi$ for a screw dislocation, or $B = G\lambda/2\pi\,(1 - \nu)$ for an edge dislocation; and ν is Poisson's ratio.

The value of the constant, $B = G\lambda/2\pi$ for a screw dislocation, will be used in the calculations. The equilibrium equation for the jth dislocation of Figure 4 is found by the use of equation (2), and is

$$\sum_{\substack{i=1 \\ i \neq j}}^{n} \frac{1}{x_j - x_i} + P + \frac{1}{x_j + 1} + \frac{1}{x_j - 1} = 0 \tag{3}$$

$$(j = 1, 2, 3, \ldots, n)$$

where n is the number of dislocations between the source, at $x = -1$, and the obstruction, at $x = +1$; x_i is the equilibrium position of the ith dislocation; P is the applied shear stress ratio, $\tau_r L/B$; and τ_r is the applied, resolved shear stress.

The minimum stress ratio which can form dislocation loops may be estimated by the use of equation (1), as

$$P_{\min} = \frac{G\lambda\alpha L}{l_m B} = 2\pi\alpha \frac{L}{l_m}.$$

For $L < l_m$, the obstacle interferes with the formation of dislocation loops such that their formation is very improbable. Therefore, the minimum value of P which need be considered is approximately 6.

Eshelby, Frank, and Nabarro [12] have developed a mathematical method for determining the equilibrium positions of dislocations in linear arrays. They discuss the dislocation model of Figure 4 for the case with no applied stress. A general solution is not given for the equilibrium positions of the dislocations when there is an applied stress. The treatment of this case by the method of Eshelby, Frank, and Nabarro is not practical when such a general solution is desired.

A mathematical method for determining the desired properties of the dislocation model of Figure 4 will be developed in which it is not necessary to determine the exact equilibrium positions of the individual dislocations. Thus, the difficulties en-

countered in the method of Eshelby, Frank, and Nabarro may be circumvented.

The equilibrium number of dislocations produced by a given dislocation source will be that number of dislocations which makes the local stress at the source less than or equal to the critical stress given by equation (1). For convenience, the local stress τ_s at the source is expressed as the stress ratio $S = \tau_s L/B$; thus, $S_c = \tau_c L/B$ is the critical stress ratio. The stress ratio, S, exclusive of the stress from the dislocation representing the source, is given by

$$S = P - \tfrac{1}{2} - \sum_{j=1}^{n} \frac{1}{x_j + 1};$$

thus,

$$\sum_{j=1}^{n} \frac{1}{x_j + 1} = P - S - \tfrac{1}{2}. \tag{4}$$

Equations (3) and (4) will be used to find the relationship between S, P, and n. We begin by squaring both sides of equation (4) which gives

$$\sum_{j=1}^{n} \left(\frac{1}{x_j + 1}\right)^2 + \sum_{\substack{i=1 \\ i \neq j}}^{n} \sum_{j=1}^{n} \left(\frac{1}{x_j + 1}\right)\left(\frac{1}{x_i + 1}\right) = (P - S - \tfrac{1}{2})^2$$

or

$$\sum_{j=1}^{n} \left(\frac{1}{x_i + 1}\right)^2 + \sum_{\substack{i=1 \\ i \neq j}}^{n} \sum_{j=1}^{n} \left(\frac{1}{x_i + 1} - \frac{1}{x_j + 1}\right)\frac{1}{x_j - x_i} = (P - S - \tfrac{1}{2})^2.$$

Using equation (3), this becomes

$$3\sum_{j=1}^{n} \left(\frac{1}{x_j + 1}\right)^2 + 2P\sum_{j=1}^{n} \frac{1}{x_j + 1} + 2\sum_{j=1}^{n} \left(\frac{1}{x_j^2 - 1}\right) = (P - S - \tfrac{1}{2})^2. \tag{5}$$

The term $2\sum_{j=1}^{n} \left(\frac{1}{x_j^2 - 1}\right)$ may be written in the form

$$2\sum_{j=1}^{n} \frac{1}{x_j^2 - 1} = \sum_{j=1}^{n} \frac{1}{x_j - 1} - \sum_{j=1}^{n} \frac{1}{x_j + 1}. \tag{6}$$

Summing equation (3) over j gives

$$nP + \sum_{j=1}^{n} \frac{1}{x_j + 1} + \sum_{j=1}^{n} \frac{1}{x_j - 1} = 0$$

or

$$\sum_{j=1}^{n} \frac{1}{x_j - 1} = -nP - \sum_{j=1}^{n} \frac{1}{x_j + 1}. \tag{7}$$

Using equations (6) and (7) in equation (5) gives

$$n = P\frac{S^2}{P} + \frac{3}{P}\sum_{j=1}^{n} \left(\frac{1}{x_j + 1}\right)^2 - 2 + \frac{S}{P} + \frac{3}{4P}$$

or

$$n = P - \frac{S^2}{P} + \Delta \tag{8}$$

where

$$\Delta = \frac{3}{P}\sum_{j=1}^{n} \left(\frac{1}{x_j + 1}\right)^2 - 2 + \frac{S}{P} + \frac{3}{4P}.$$

The magnitude of term Δ is estimated in the appendix of this paper, where it is shown that

$$-2 \leqslant \Delta \leqslant 1 \text{ for } 0 \leqslant n \leqslant P_0, 0 \leqslant S$$

and

$$-2 \leqslant \Delta \leqslant 1.04(\tfrac{1}{2}n)^{\frac{1}{3}} - 1 \text{ for } 6 \leqslant P_0 \leqslant n, 0 \leqslant S$$

where P_0 is the value of the stress ratio P, which makes $S = 0$ for the particular value of n.

Thus, a good approximation to the equilibrium number of dislocations produced by a dislocation source is given by

$$n = P - \frac{S_c^2}{P} \qquad \text{for } 0 \leqslant S_c \leqslant P,$$

and

$$n = 0 \qquad \text{for } 0 \leqslant P \leqslant S_c. \tag{9}$$

Since the majority of strain is produced by dislocation sources for which the equilibrium value of n is much greater than unity, the value of n given by equation (9), while not necessarily an integer, may be used in the calculations without introducing appreciable error.

The above equations may now be used to estimate the equilibrium microstrain as a function of tensile stress for a distribution of Frank-Read sources in polycrystalline material. The distribution of dislocation sources is assumed to be uniform throughout the material, and the total number per unit volume will be designated by ρ_s. The fraction of the total number of dislocation sources with lengths between l and $l + dl$ will be denoted by $N(l)dl$. For a fine-grained, polycrystalline material, such as that used in this investigation, the slip planes and slip directions may be assumed to be uniformly distributed over all possible angles. The resolved shear stress ratio on a slip plane is given by

$$P = \frac{\tau_r L}{B} = \frac{\sigma L}{2B}\sin 2\beta \cos\phi \tag{10}$$

where σ is the tensile stress; β is the angle between the normal to the slip plane and the direction of tensile stress; and ϕ is the angle between the maximum shear stress direction on the slip plane and the slip direction.

The number of sources per unit volume with lengths between l and $l + dl$, that will produce dislocation loops on slip planes which lie between β and $\beta + d\beta$, with slip directions between ϕ and $\phi + d\phi$, is given by

$$\frac{\rho_s N(l)}{4\pi^2}\, d\beta\, d\phi\, dl. \tag{11}$$

The generation of one dislocation loop from a given source causes a relative displacement, λ, of the material above the area over which the dislocation loop has passed with respect to the material below. The displacement is in the slip direction. The mean displacement over a slip plane of area A_s is then

$$\lambda A/A_s$$

where A is the area swept out by the loop. The mean displacement when n loops are formed is

$$n\lambda A_m/A_s \tag{12}$$

where A_m is the mean loop area.

The strain in the direction of the tensile stress produced by the mean displacement over one slip plane containing one dislocation source may be obtained from equations (9) and (12) (considering a specimen of unit area such that $A_s = 1/\cos\beta$), and is given by

$$\lambda A_m(P - S_c^2/P)\cos\beta\sin\beta\cos\phi. \tag{13}$$

The equilibrium strain due to all dislocation sources on all slip planes is obtained from equations (11) and (13) and is given by

$$\epsilon_x = \frac{\lambda\rho_s}{8\pi^2}\int_\beta\int_\phi\int_l A_m N(l)(P - S_c^2/P) \cdot \sin 2\beta\cos\phi\, d\beta\, d\phi\, dl \tag{14}$$

where ϵ_x is the microstrain in the direction of the tensile stress, and the integration is carried out over all dislocation sources for which $P \geqslant S_c$.

The mean loop area for a given source is within the following limits:

$$\pi(D - 2L)^2/4 < A_m < \pi D^2/4,$$

where circular loops are considered as shown in Figure 2, and D is the diameter of the obstruction. For a uniform distribution of dislocation sources over a given slip plane, the mean value of $2L$ is approximately $0.15D$, and the above limits on the mean A_m become

$$0.73D^2/4 < A_m < D^2/4.$$

Thus, the mean loop area cannot vary over a wide range, and its mean value may be considered a constant without introducing appreciable error. The length L appears as a linear factor in the term $(P - S_c^2/P)$, and may be taken out of the integration over β, ϕ, and l, and replaced by its mean value L'. The angle β, may be considered to vary in the interval 0 to $\pi/4$, since the integrand of equation (14) contains the variable in the form $\sin 2\beta$. Similarly, the range of ϕ may be restricted to 0 to $\pi/2$. Equation (14) then becomes

$$\epsilon_x = \frac{4\lambda\rho_s A'_m}{\pi^2}\int_\beta\int_\phi\int_l N(l)(P - S_c^2/P) \cdot \sin 2\beta\cos\phi\, d\beta\, d\phi\, dl \tag{15}$$

where A'_m is the mean dislocation loop area of all loops on all slip planes. The limits of integration are

$$\frac{l_c}{\sin 2\beta\cos\phi} \leqslant l \leqslant l_m, \quad 0 \leqslant \phi \leqslant \cos^{-1}\left(\frac{l_c}{l_m\sin 2\beta}\right),$$

$$\tfrac{1}{2}\sin^{-1}\frac{l_c}{l_m} \leqslant \beta \leqslant \frac{\pi}{4}$$

where $l_c = 2G\lambda\alpha/\sigma$. The quantity l_c, is the length of the shortest dislocation source which generates new loops under the action of the applied tensile stress, σ.

The exact configuration of dislocations in alpha iron is not known. Therefore, the distribution of dislocation source lengths, $N(l)$, is not known. A distribution is assumed for which all sources have lengths less than some limiting value, l_m, as is indicated by the experimental data discussed above. The distribution is assumed to be of the form

$$N(l) = c(1 - l^2/l_m^2) \quad \text{for } l \text{ less than } l_m, \text{ and}$$
$$N(l) = 0 \quad \text{for } l \text{ greater than } l_m, \tag{16}$$

where c is a normalizing constant.

Combining equations (15) and (16) and performing the integrations over l and ϕ, gives

$$\epsilon_x = \frac{4\lambda}{\pi}\rho_s A'_m cL'\alpha\frac{l_m}{l_c}\int_{l_c/l_m}^{1}\left[\left\{\frac{\xi^2}{3} + 2\left(\frac{l_c}{l_m}\right)^2\right\} \cdot \cos^{-1}\left(\frac{l_c}{l_m\xi}\right) - \frac{5}{3}\frac{l_c}{l_m}\sqrt{\xi^2 - \left(\frac{l_c}{l_m}\right)^2} - \frac{2}{3}\left(\frac{l_c}{l_m}\right)^3\xi^{-1}\cosh^{-1}\left(\frac{l_m\xi}{l_c}\right)\right]\frac{d\xi}{\sqrt{(1-\xi^2)}} \tag{17}$$

where $\sin 2\beta = \xi$.

The integration over ξ is performed numerically, and the resulting stress vs. microstrain relation is fitted to the experimental data by choosing a suitable value of the constant, $\rho_s A'_m cL'\alpha$, and using the previously determined value of l_m. The value of $\rho_s A'_m cL'\alpha$ which has been taken to fit the data is

$$\rho_s A'_m cL'\alpha = 1.58 \times 10^2\ \text{in}^{-1}.$$

The relationship between applied tensile stress and the equilibrium microstrain given by equation (17) is shown in Figure 2 in which the experimental points are also plotted. Equation (17) follows the experimental data within the limits of the experimental accuracy.

The assumed distribution of dislocation source lengths is plotted as a solid line in Figure 5. The quantity, l_y, corresponding to the shortest dislocation source which is active at the upper yield stress, is indicated in the figure.

The actual distribution of dislocation source lengths may be somewhat different than the assumed distribution. It is reasonable to assume that the actual distribution has a limiting dislocation source length corresponding to the mosaic block size, and

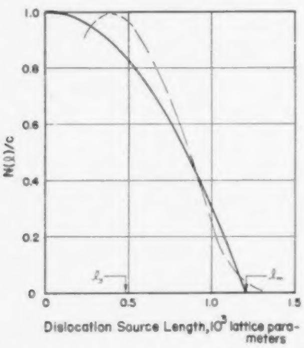

FIGURE 5. Distribution of dislocation source lengths.

that $N(l)$ increases near this limiting length as l decreases. It is not clear whether or not $N(l)$ reaches a maximum value for l greater than zero, as is indicated by the dashed line in Figure 5, or decreases continuously as l increases from zero. However, these two distributions will produce essentially the same form of stress vs. microstrain relation, since the sources with lengths less than l_y do not contribute to the microstrain.

Because of the uncertainties in the actual form of the distribution of dislocation source lengths in alpha iron, and the difficulties in making a reliable estimate of the value of the constants ρ_s, A'_m, and L', the significance of the value of the constant, $\rho_s A'_m c L' \alpha$, cannot be determined. However, it is clear from the above analysis that the generation of dislocation loops from Frank-Read sources distributed throughout the crystals of the material can adequately explain the experimental stress vs. equilibrium microstrain relation as shown in Figure 2. Further correlations with experimental results will be required to establish the reality of the mechanism described and to refine the various assumptions made in this analysis.

Summary and Conclusions

Sensitive strain measurements under conditions of rapid loading indicate that a plastic and anelastic microstrain of approximately 30×10^{-6} in/in. precedes the yield strain in the mild steel employed in this investigation. The total microstrain produced by stresses less than the yield stress is a function of stress and increases from zero at a stress approximately equal to 0.4 times the yield stress to approximately 30×10^{-6} in/in. at the yield stress.

The experimentally observed microstrain may be quantitatively explained by a dislocation-generating mechanism in which the motion at the generated dislocations is stopped by obstructions, such as grain boundaries. Comparison of the theory and the experimental data leads to the determination of a characteristic length of dislocation which agrees with previous concepts of a mosaic block structure. A more complete description of the stress vs. microstrain relation may be made by the techniques employed in this paper when the configuration of the obstructions to dislocation motion and the distribution of dislocation source lengths are more definitely established.

Acknowledgments

The authors wish to express their appreciation to Professor H. F. Bohnenblust of the California Institute of Technology for invaluable aid in developing the mathematical treatment of the properties of the dislocation model presented in this paper. This investigation was conducted under the sponsorship of the Office of Naval Research. The rapid-load testing machine used in this investigation was constructed by the California Institute of Technology under a contract with the United States Air Force. Appreciation is expressed to the U.S. Air Force for permission to use the machine.

Appendix: Estimation of the Term Δ

It is desired to estimate the term

$$\Delta = \frac{3}{P}\sum_{j=1}^{n}\left(\frac{1}{x_j + 1}\right)^2 - 2 + \frac{S}{P} + \frac{3}{4P}.$$

For $P, S > 0$, $-2 \leqslant \Delta$, since $(1 + x_j) > 0$. Two theorems which are easily verified by equations (3) and (4) will be useful in estimating Δ. They are:

(A) x_j increases as P increases with n fixed.

(B) S increases as P increases with n fixed.

It may be verified by equation (4) and theorem (B) that there exists a P_0 such that $S(P_0, n) = 0$. Then $P \geqslant P_0$ for $S \geqslant 0$, and by theorem (A),

$$x_j(P, n) \geqslant x_j(P_0, n),$$

or

$$3\sum_{j=1}^{n}\left(\frac{1}{1 + x_j(P, n)}\right)^2 \leqslant 3\sum_{j=1}^{n}\left(\frac{1}{1 + x_j(P_0, n)}\right)^2$$

Using equation (8),

$$3\sum_{j=1}^{n}\left(\frac{1}{1+x_j(P_0,n)}\right)^2 = nP_0 + 2P_0 - \tfrac{3}{4} - P_0^{\,2} \geqslant 3\sum_{j=1}^{n}\left(\frac{1}{1+x_j}\right)^2.$$

Then

$$-2 \leqslant \Delta \leqslant \frac{P_0}{P}(n - P_0 + 2) - 2 + \frac{S}{P}. \tag{18}$$

For the case $(0 \leqslant n \leqslant P_0;\ 0 \leqslant S)$, $-2 \leqslant \Delta \leqslant 1$, since $P \geqslant P_0$ and $P \geqslant S$ from equation (4), for $n \geqslant 0$, and it remains to estimate $(n)_{\max}$ as a function of P_0. This estimate is carried out by representing a large number of dislocations between the dislocation source and obstruction as a continuous distribution of dislocations from a point $x = a$, where $-1 < a$, to a point $x = b$, where $b < +1$ (Fig. 4). The equilibrium equation, equation (3), for the distributed dislocations is

$$\int_a^b \frac{\phi(x)\,dx}{y - x} + P + \frac{1}{y+1} + \frac{1}{y-1} = 0 \tag{19}$$

where $a < y < b$; $\phi(x)$ is the dislocation density at point x; $\int_a^b \phi(x)dx = n$; $\phi(a) = \phi(b) = 0$; and the Cauchy principal value of the integral is understood. The solution for $\phi(x)$ in this equation is obtained by the method of Tricomi [13] and may be written in the form

$$\frac{\phi(x)}{1+x} = \frac{(b-x)(x-a)\,G(x)}{(x+1)^2(x-1)} \tag{20}$$

where $G(x)$ is a polynomial of the first degree.

The stress ratio at the dislocation source is given by equation (4), which for the distributed dislocation model may be written as

$$S = P - \tfrac{1}{2} - \int_a^b \frac{\phi(x)\,dx}{x+1}. \tag{21}$$

Equations (19), (20), and (21) may be combined to give the following relations between P, n, and S:

$$2P(n+2) - P^2(2+\epsilon) - \frac{1}{2+\epsilon} + \frac{2}{\epsilon^2} + \frac{4S-1}{\epsilon} = 0 \tag{22}$$

and

$$P^2 = \frac{1}{(2+\epsilon)^2} + \frac{4}{\epsilon^3} - \frac{4S-1}{\epsilon^2} \tag{23}$$

where $x = -(1+\epsilon)$ is the zero of the polynomial $G(x)$.

Equations (22) and (23) may be combined to show that

$$n \leqslant P_0 + \gamma(\tfrac{1}{2}P_0)^{\frac{1}{3}} - 2$$

where γ is an absolute constant. For the case $P_0 > 6$,

$$n \leqslant P_0 + 1.04(\tfrac{1}{2}P_0)^{\frac{1}{3}} - 2. \tag{24}$$

Using equation (24) in equation (18) gives

$$-2 \leqslant \Delta \leqslant 1.04(\tfrac{1}{2}P_0)^{\frac{1}{3}} - 1 \quad \text{for } P_0 \geqslant 6,\ S \geqslant 0$$

or

$$-2 \leqslant \Delta \leqslant 1.04(\tfrac{1}{2}n)^{\frac{1}{3}} - 1 \quad \text{for } n \geqslant P_0 \geqslant 6,\ S \geqslant 0,$$

and the estimation of the term Δ is complete.

References

1. CLARK, D. S. and WOOD, D. S. Proc. Amer. Soc. Testing Materials, **49** (1949) 717.
2. WOOD, D. S. and CLARK, D. S. Trans. Amer. Soc. Metals, **43** (1951) 571.
3. WOOD, D. S. and CLARK, D. S. Trans. Amer. Soc. Metals, **44** (1952) 726.
4. VREELAND, T., JR., WOOD, D. S., and CLARK, D. S. Trans. Amer. Soc. Metals, **45** (1953) 620.
5. COTTRELL, A. H. Symposium on the Plastic Deformation of Crystalline Solids, Mellon Institute, 1950.
6. HOLDEN, A. N. Trans. A.I.M.E. **194** (1952) 182.
7. FRANK, F. C. and READ, W. T. Phys. Rev., **79** (1950) 722.
8. COTTRELL, A. H. and BILBY, B. A. Proc. Phys. Soc. London, ***A62*** (1949) 48.
9. ROBERTS, C. S., CARRUTHERS, R. C. and AVERBACH, B. L. Trans. Amer. Soc. Metals, **44** (1952) 1150.
10. TAYLOR, G. I. Proc. Roy. Soc., **145** (1934) 362.
11. KOEHLER, J. S. Phys. Rev. **60** (1941) 397.
12. ESHELBY, J. D., FRANK, F. C., and NABARRO, F. R. N. Phil. Mag., **42** (1951) 351.
13. TRICOMI, F. G. Quart. J. Math. (Oxford second series), **2**, no. 7 (1951) 199.

NOTES ON WORK HARDENING AND RECOVERY*

P. A. BECK†

Although the available data are not conclusive, they suggest that the annealing processes in cold worked metals may be subdivided into at least three distinct stages, which occur successively with increasing annealing time or temperature (apart from overlapping) in the following order: (1) recovery (without interface migration), (2) sub-boundary migration (gradual subgrain growth essentially without reorientation), and (3) grain boundary migration ("recrystallization" with local reorientation, i.e., the discontinuous growth of some crystal fragments with strongly deviating orientations). It appears that most of the stored energy of cold work and a minor component of the work hardening is released in recovery, while subgrain growth is capable of releasing the remaining larger portion of work hardening, which is connected with the sub-boundaries. However, the third stage of annealing ("recrystallization") often sets in prematurely and then it takes over from subgrain growth the function of relieving a large fraction of the work hardening.

NOTES SUR L'ÉCROUISSAGE ET LA RESTAURATION

Malgré que les données disponibles dans ce domaine ne soient pas encore conclusives, elles suggèrent que les processus de recuit dans les métaux écrouis peuvent être divisés en au moins trois phases distinctes, qui se succèdent en fonction du temps de recuit ou de l'accroissement de la température (les enchevauchures mises à part) dans l'ordre suivant: (1) restauration (sans migration des interfaces), (2) migration des sous-joints (croissance graduelle des sous-grains sans réorientation), (3) migration des joints intercristallins (recristallisation avec réorientation locale, c.-à-d. la croissance discontinue de certains fragments cristallins avec forte déviation des orientations). Il apparaît que la plus grande partie de l'énergie accumulée par le travail à froid et une faible partie de l'écrouissage sont libérées lors de la restauration, alors que la croissance des sous-grains est capable d'éliminer le reste de l'écrouissage lié aux sous-joints. En réalité, il arrive souvent que la troisième phase de recuit ("recristallisation") commence prématurément, et c'est alors qu'une fraction importante de l'écrouissage est éliminée, au lieu de l'être lors de la croissance des sous-grains.

BEMERKUNGEN ZUR HÄRTUNG UND ERHOLUNG

Obwohl die vorhandenen Daten nicht völlig schlüssig sind, deuten sie doch darauf hin, dass sich die Glühvorgänge in kaltbearbeiteten Metallen in wenigstens drei Stadien unterteilen lassen, die in der folgenden Weise aufeinander folgen, wenn die Glühzeit oder die Glühtemperatur zunimmt (abgesehen von Überschneidungen): (1) Erholung (ohne Korngrenzenbewegung), (2) Feinkorngrenzenbewegung (langsames Feinkornwachstum ohne Änderung der Orientierung), und (3) Korngrenzenbewegung ("Rekristallisation" mit örtlicher Reorientierung d.h. diskontinuierliches Wachstum einiger Kristallfragmente sehr verschiedener Orientierung). Es scheint, als werde der grösste Teil der in der Kaltbearbeitung aufgespeicherten Energie und ein kleiner Teil der Härtung in dem Erholungsvorgang frei, während das Feinkornwachstum den verbleibenden, grösseren Anteil der Härte, der mit den Feinkorngrenzen verbunden ist, frei machen kann. Das dritte Glühstadium ("Rekristallisation") setzt jedoch oft verfrüht ein, und es übernimmt dann vom Feinkornwachstum die Funktion, einen grossen Teil der Härte zu befreien.

Since the original investigations of Polanyi and Schmid [1], it has been known that zinc single crystals can be extended with only one glide system operating and that a large portion of the work hardening connected with this process can be recovered at room temperature, without recrystallization. Haase and Schmid [2] and, more recently, Li, Washburn, and Parker [3] found that after deformation in pure shear on a single glide system *complete* recovery can be attained on annealing and that the cycle of strain and recovery can be carried out repeatedly, each time returning to the original mechanical properties, corresponding to the well-annealed condition of the single crystal. As shown by Honeycombe [4], it is a characteristic feature of plastic extension by pure shear on one glide system ("easy glide") that it does not involve local disorientations (Laue asterism) even after 100 per cent extension. The calorimetric work of G. Borelius and his associates [6; 7] gives accurate data for the instantaneous rate of the isothermal release of stored energy of cold work at relatively low annealing temperatures (60° and 100°C for Cu). Data of this kind may eventually allow a definite conclusion as to the atomic mechanism of recovery. Even now, however, it is clear that, at least in three cases investigated, by far the largest portion of the stored energy of cold work is released in the early stages of annealing [8; 9; 9*a*].

In all cases of plastic deformation other than "easy glide" the extent of work hardening is much greater than that resulting from pure shear on a single glide system; furthermore, only a fraction of this work hardening can be eliminated by recovery (without interface migration). The conditions described suggest the importance of another, non-recoverable type of work hardening in addition to

*Received February 26, 1953.
†Department of Mining and Metallurgical Engineering, University of Illinois, Urbana, Illinois, U.S.A.

the recoverable type encountered in the case of pure shear. In the following, it will be shown that information is now available which sheds some light on the physical nature of non-recoverable work hardening and from which its relative magnitude can be estimated.

W. L. Bragg proposed a theory of the strength of metals [11], according to which the resistance to shear is inversely proportional to the average linear size of the "mosaic fragments," i.e. subgrains into which the crystals of a metal break down on cold working. In the intervening years the idea of "fragmentation" by plastic deformation has not gained universal acceptance. The formation of subgrains has been rather attributed to "polygonization" [12], a process defined as the thermally activated migration of individual dislocations from their isolated positions, attained in plastic deformation, to the "dislocation walls" or sub-boundaries observed after annealing. Thus, the postulated polygonization mechanism leads to the formation of subgrains on annealing of a crystal continuously bent in plastic deformation, and it leads to the sectionwise straightening of the bent crystal. However, recent investigations by Heidenreich [13] and by Kellar, Hirsch, and Thorp [14; 5] indicate that the cold working of polycrystalline metals results directly in the formation of subgrains within the individual grains of the metal [15], similar to but much finer than the "cells" previously found by Wood and his associates [16; 17] as a result of creep deformation. Subgrains of the order of 0.5 to 2 microns were shown to form on severe cold working at room temperature, not only in Zn and Al, but even in higher melting metals, such as Au, Fe, and Ni [18]. Furthermore, subgrains are also formed when Zn is deformed at liquid nitrogen temperature [19]. This suggests that thermal activation may not be necessary for the formation of subgrains (although it is essential for subgrain growth.) The mechanism of the formation of subgrains in plastic deformation is most likely closely related to kinking, as described by Orowan [20], Barrett and Hess [21], and Washburn and Parker [22].* It is a result of the tendency of line dislocations to arrange themselves in stable arrays or "dislocation walls" in the course of the deformation process, rather than to "get stuck" in isolated positions in the deformed crystal. However this may be, the availability of direct experimental evidence for the formation of subgrains on plastic deformation of a type connected with large non-recoverable work hardening suggests that sub-boundaries do play an important role in this type of work hardening. Unfortunately, no correlated data are at present available for reliable quantitative comparison with Bragg's formula. Using Heidenreich's estimate of the subgrain size of his pure aluminum after "pounding" at 78°K (1 micron), Bragg's formula gives a shear stress of about 960 psi. This value is about 3.7 times smaller than the shear stress calculated from the tensile yield stress, reported by Sherby, Goldberg, and Dorn [28] for a pure Al specimen, prestrained 15 per cent in tension at 78°K, and annealed two hours at 530°K to eliminate the recoverable component of work hardening. In view of the uncertainties of the data, this may perhaps be considered as agreement within an order of magnitude.

Heidenreich showed by means of electron transmission microscopy [13] that in the cold worked condition the subgrains themselves are considerably strained, so that their electron diffraction characteristics are different from those of well-annealed metal. The distortion of the subgrains formed in cold working was also indicated in the micro-beam X-ray diffraction patterns of Kellar, Hirsch, and Thorp. The first effect of annealing, as observed by Heidenreich, was the recovery of the strain-free condition within the subgrains, at relatively low annealing temperatures (20°-150°C for Al) and apparently without sub-boundary migration. This effect is analogous to the behavior of single crystals deformed in pure shear: the finely dispersed imperfections inside the subgrains are easily removed by annealing. As shown also by the sharpening of the micro-beam Laue spots, in the first stage of annealing of cold worked metal the fine, slightly disoriented subgrains are restored to a reasonably high degree of crystalline perfection. Subgrains or domains of this type, but large enough for visual observation at low magnification, have been produced by Li, Washburn, and Parker [3] by means of inhomogeneous deformation of Zn single crystals at 350°C. These authors found in subsequent shear tests that the yield stress of their crystals was greatly increased by the introduction of the substructure. It is quite apparent from these experiments that the formation of sub-boundaries is connected with work hardening, large as compared with that resulting from pure shear, even if the subgrains themselves are essentially strain free [23]. This effect might be interpreted as a result of the trapping of dislocations by the stationary, interlocking dislocation walls which

*See also Jillson [34].

constitute the network of sub-boundaries ("interaction hardening"), a mechanism fundamentally related to that originally proposed by G. I. Taylor [24] and recently modified by N. F. Mott [25]; presumably the sub-boundaries assume the role of the "barriers" discussed by Mott. Whether or not this interpretation of the work-hardening by subgrain formation is satisfactory will have to be decided when more quantitative data become available.

In the experiments of Li, Washburn, and Parker, annealing only 20°C below the melting point removed neither the coarse substructure nor the corresponding work hardening from inhomogeneously deformed Zn crystals. Also, Heidenreich observed very little, if any, change in the fine substructure in cold worked Al up to 200°C, at which temperature the subgrain structure was wiped out by recrystallization. Although subgrain growth does occur at higher annealing temperatures when the subgrains are initially small and when, in spite of this, recrystallization does not interfere [26], it appears that annealing of cold worked pure aluminum at temperatures at least up to about 200°C does not affect the sub-boundaries, or the component of work hardening connected with them. Tietz, Anderson, and Dorn [27] prepared a series of polycrystalline pure aluminum specimens, pre-strained at various temperatures to the flow stress of 12,300 psi (measured at 78°K). Yield stresses were then determined for these specimens at 78°K, after various periods of recovery at 305°K. Assuming that most of the recoverable work hardening inside the subgrains is removed by annealing for eight hours at 305°K, the decrease in yield stress for specimens pre-strained at different temperatures indicates the extent of the work hardening originally present in these specimens in the form of the recoverable component. From the data it appears that the yield stress of the specimen pre-strained at 78°K decreased by 1700 psi, or approximately 14 per cent of the total work hardening. For the specimen prestrained at 194°K the decrease was 1200 psi, or approximately 10 per cent of the total work hardening, and for the specimens prestrained at 273°K and at room temperature, the decrease was 700 psi, or approximately 5.7 per cent of the total work hardening. Although the relative magnitude of the recoverable component of work hardening may be actually somewhat higher than the above figures indicate (because of the possibly incomplete removal of recoverable work hardening by 8 hours of annealing at 305°K), nevertheless, it is a minor fraction of the total work hardening in strained, polycrystalline high-purity aluminum. The data also show that the relative magnitude of this component rapidly decreases as the temperature of cold working is increased. It may be expected that the work hardening in pure polycrystalline aluminum, deformed in the temperature range between approximately 310°K and 570°K (depending on the strain rate) is practically entirely of the non-recoverable type, connected with the sub-boundaries. Under such conditions, work hardening should not be associated with any line broadening. At still higher temperatures, recrystallization accompanies plastic deformation and no work hardening results.

In view of Bragg's and Mott's theories, the extent of work hardening connected with the sub-boundaries may be expected to depend on the average subgrain size. In a very interesting recent investigation by Sherby, Goldberg, and Dorn [28], data were obtained which may be interpreted to show the dependence of the non-recoverable component of work hardening on variations in the subgrain size. In this work, pure aluminum specimens were prestrained under varying conditions, in order to produce substructures of varying fineness. The recoverable component of the work hardening was eliminated either by carrying out the pre-straining at temperatures above 422°K or by annealing the specimens for 2 hours at 530°K after pre-straining at lower temperatures. Consequently, the work hardening in these specimens must have been entirely of the type connected with sub-boundaries. The observed increase of yield stress in tension tests at 78°K from about 1300 psi to 7400 psi may be ascribed to a progressive decrease in subgrain size. Starting with fully annealed material, decreasing subgrain sizes were produced in one experiment by increasing the amount of pre-strain, and in another experiment by decreasing the temperature of pre-strain. Two series of specimens with progressively increasing subgrain size (and with correspondingly decreasing yield strength) were prepared by first prestraining at 78°K, thus setting up a very fine substructure, and subsequently annealing for various periods of time at 530°K with, and without, simultaneous straining in slow creep. In accordance with previous investigations [17; 19], the combined effect of annealing and of simultaneous creep strain was found to increase greatly the rate of subgrain growth on annealing. For instance, the subgrain size giving a yield stress of about 5800 psi was obtained on annealing at 530°K for 170 hr. without straining, or alternatively, for about 1.5 hr. with the simultaneous application of a creep strain of about 0.004.

The second stage of the annealing process, where the work hardening associated with sub-boundaries decreases as a result of sub-boundary migration, was originally isolated by Crussard [33] in extended Al single crystals, and designated by him as "recrystallization *in situ*." More recently [26], it proved to be an important annealing mechanism even in highly deformed polycrystalline metals. Apparently, subgrain growth requires higher temperatures and/or longer periods of annealing than the first (recovery) stage, and it is often quite distinct from the latter. In some cases, as in rolled Mo [30; 10], the increase in strength above the value for well-annealed polycrystalline material can be completely eliminated on annealing by the mechanism of subgrain growth (without recrystallization involving reorientation). In this case subgrain growth is clearly separated from the third stage of annealing, where reorientation takes place by the migration of ordinary high energy grain boundaries (recrystallization). More often the third stage begins before complete softening is attained by subgrain growth, so that the two phenomena partially overlap. For instance, in cold rolled polycrystalline Zr, when annealed at 400°C, only approximately 50 per cent softening is achieved by subgrain growth before recrystallization sets in [31]. For a cold rolled Ni-Fe alloy, 85 per cent softening was reported [32] to correspond to 50 per cent reorientation, suggesting that, here too, subgrain growth contributes to softening.

It is now apparent that the annealing of cold worked metals can be dissociated into at least three distinct stages, which occur successively with increasing annealing temperature or time (apart from possible overlapping) in the following order: (1) recovery (without interface migration), (2) sub-boundary migration (gradual subgrain growth, essentially without reorientation), and (3) grain boundary migration ("recrystallization" with local reorientation, i.e., the discontinuous growth of some crystal fragments with strongly deviating orientations). Present evidence indicates that only a minor component of the work hardening is released in recovery, while subgrain growth is capable of releasing the remaining larger portion which is connected with the sub-boundaries. In practice, however, the third stage of annealing ("recrystallization") often sets in prematurely and then it takes over from subgrain growth the function of relieving much of the work hardening.

References

1. Polanyi, M. and Schmid, E. Verh. Deutsch. phys. Ges., **4** (1923) 27.
2. Haase, O. and Schmid, E. Z. Phys., **33** (1925) 413.
3. Li, C. H., Washburn, J., and Parker, E. R. Fourth Technical Report to ONR (1952).
4. Honeycombe, R. W. K., J. Inst. Metals, **80** (1951–52) 45–56.
5. Hirsch, P. B. Acta Cryst., **5** (1952) 172–175.
6. Borelius, G. L'Etat Solide. 9th Solvay Conference (Bruxelles, R. Stoops, 1952), p. 427.
7. Borelius, G., Berglund, S., and Sjoberg, S. Ark. Fys., **5** (1952) 1–7.
8. Suzuki, T. Sci. Rep. Research Institutes, Tôhoku Univ., **1** (1949) 55.
9. Kanzaki, H. J. Phys. Soc. Jap., **6** (1951) 456.

9*a*. Stansbury, E. E. U.S.Atomic Energy Commission Report ORO–86, 1953.

10. Chen, N. K. and Maddin, R. Trans. A.I.M.E., **197** (1953) 300.
11. Bragg, W. L. Nature, **49** (1942) 511.
12. Cahn, R. W. J. Inst. Metals, **76** (1949) 121.
13. Heidenreich, R. D. Bell System Tech. J., **30** (1951) 867.
14. Kellar, J. N., Hirsch, P. B., and Thorp, J. S. Nature, **165** (1950) 554.
15. Beck, P. A. ASM Symposium on Metal Interfaces (Cleveland, 1952), p. 208–246.
16. Wilms, G. R. and Wood, W. A. J. Inst. Metals, **75** (1949) 693–706.
    Wood, W. A. and Rachinger, W. A. J. Inst. Metals, **76** (1949) 237–253.
17. Wood, W. A. and Scrutton, R. F. J. Inst. Metals, **77** (1950) 423–434.
18. Hirsch, P. B. Private communication.
19. Cohen, M. Private communication.
20. Crowan, E. Nature, **149** (1942) 643.
21. Hess, J. B. and Barrett, C. S. Trans. A.I.M.E., **185** (1949) 599–606.
22. Washburn, J. and Parker, E. R. Trans. A.I.M.E., **194** (1952) 1076–1078.
23. Beck, P. A. Trans. A.I.M.E., **194** (1952) 979–980.
24. Taylor, G. E. Proc. Roy. Soc., **A145** (1934) 362.
25. Mott, N. F. Phil. Mag., **43** (1952) 1151–1178.
26. Beck, P. A. and Hu, Hsun. Trans. A.I.M.E., **194** (1952) 83.
27. Tietz, T. E., Anderson, R. A., and Dorn, J. E. Trans. A.I.M.E., **185** (1949) 921–926.
28. Sherby, O. D., Goldberg, A., and Dorn, J. E. Twenty-First Technical Report to ONR (1952).
29. Hino, J., Shewmon, P. G., and Beck, P. A. Trans. A.I.M.E., **194** (1952) 873–874.
30. Semchyshen, M. and Timmons, G. A. Trans. A.I.M.E. **194** (1952) 279. See discussion of this paper by P. A. Beck, Trans. A.I.M.E., **194** (1952) 1197.
31. McGeary, R. K. and Lustman, B. Trans. A.I.M.E., **197** (1953) 284–291.
32. Seymour, W. E. and Harker, D. Trans. A.I.M.E., **188** (1950) 1001.
33. Crussard, C. Rev. Métall., **41** (1944) 140.
34. Jillson, D. C. Trans. A.I.M.E., **188** (1950) 1009.

DEFORMATION OF SYMMETRIC ZINC BICRYSTALS*

J. J. GILMAN†

Stress-strain data are presented for a symmetric zinc bicrystal with a longitudinal boundary. It is shown that the bicrystal deforms as if it were a monocrystal. The observations are discussed in terms of dislocation theory.

LA DÉFORMATION DES BICRISTAUX SYMÉTRIQUES DE ZINC

Les données concernant la relation tension-déformation sont présentées pour un bicristal symétrique de zinc avec un joint longitudinal. Il est montré, que le bicristal se déforme comme s'il était un monocristal. Les observations sont discutées en termes de la théorie des dislocations.

DIE VERFORMUNG SYMMETRISCHER ZINK-BIKRISTALLE

Es wurden die Spannung-Dehnungsdaten für einen symmetrischen Zink-Bikristall mit longitudinaler Korngrenze angegeben. Es wird gezeigt, dass sich der Bikristall wie ein Einkristall verformt, und diese Beobachtungen werden im Rahmen der Versetzungstheorie diskutiert.

During an investigation of the plastic properties of longitudinal zinc bicrystals, it was observed that a symmetric zinc bicrystal deformed plastically as though it were a monocrystal. This phenomenon has been reported previously by Kawada [1]. The present note presents data confirming Kawada's rather unexpected result and interprets the phenomenon in terms of a simple dislocation model. Also, the general behavior of zinc bicrystals is briefly discussed.

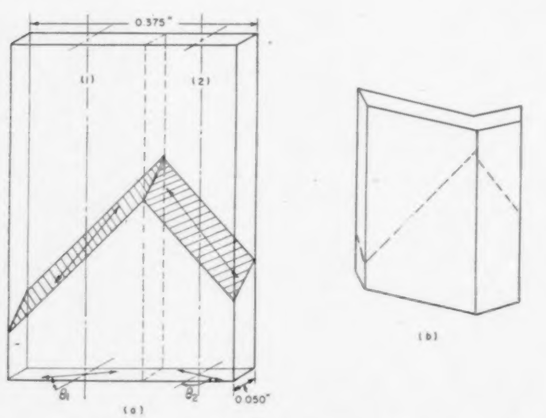

FIGURE 1. Bicrystal A. (*a*) Schematic scale drawing of the bicrystal prior to deformation. (*b*) Schematic drawing of the bicrystal after about 23 per cent elongation.

Before it was deformed, Bicrystal A had the configuration shown in Figure 1*a*. The orientation angles were χ_1, λ_1, θ_1 equal to 32, 38, 76 degrees respectively, and χ_2, λ_2, θ_2 equal to 30, 42, 88 degrees, respectively. χ is the angle between the slip plane and the specimen axis, λ is the angle between the slip direction and the specimen axis, and θ is the angle between the slip-direction, specimen-axis plane, and the normal to the wide side. The specimen's mirror symmetry across the grain boundary is clear from Figure 1*a*.

Figure 2 shows the stress-strain curve of Bicrystal A and, for comparison, the stress-strain curve of a monocrystal that had the same shape and approximately the same orientation as Bicrystal A. The two curves are almost coincident. The close agreement between the stress values for the two specimens may be partly fortuitous, but it is certainly significant that the shapes of the curves are identical. This means that the symmetric bicrystal behaved like two separate monocrystals tested in parallel.

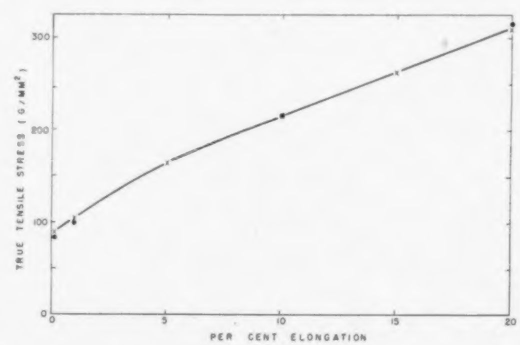

FIGURE 2. Stress-strain curve of Bicrystal A compared with points from curve for a monocrystal of similar orientation angles. ×——× Bicrystal A. ● monocrystal: $\chi_0 = 31°$, $\lambda_0 = 31°$, $\theta = 58°$.

The shape of Bicrystal A after deformation is shown schematically in Figure 1*b*. In addition to the reorientation rotation of the slip planes, Figure 1*b* shows that the two crystals rotated somewhat about the tension axis. This latter rotation was caused by the shape changes of the individual crystals and would not have occurred if θ_1 and θ_2 had been equal to 90 degrees.

*Received February 16, 1953.
†General Electric Research Laboratory, The Knolls, Schenectady, New York, U.S.A.

The grain boundary of Bicrystal A was examined after deformation at 500X, but nothing unusual was observed. The slip bands in each crystal simply extended up to the boundary and then either stopped or suffered a discontinuity in direction.

When a bicrystal is plastically deformed, the lattices of its individual crystals rotate by certain amounts relative to the grain boundary. These incremental rotation angles may be resolved into components about orthogonal axes. The orthogonal axes X, Y, and Z are chosen so that ω_Z is an increment in rotation about the tension axis of the bicrystal, ω_X is an increment in rotation about an axis normal to the grain boundary, and ω_Y is an increment in rotation about an axis which lies in the plane of the grain boundary, but is perpendicular to the tension axis.

It is proposed that ω_Z and ω_Y have a small effect on the stress-strain curves of zinc bicrystals. $\Delta\omega_X = \omega_{X1} - \omega_{X2}$ is the factor which results in the greater hardness of bicrystals compared to monocrystals. If $\Delta\omega_X$ is zero, a bicrystal has a stress-strain curve which is similar to that of a monocrystal.

The rotations about the tension axis, ω_Z are caused by shape changes of the individual crystals in a bicrystal. If the slip directions of the individual crystals lie in the same plane or in mutually perpendicular planes, $\omega_{Z1} = \omega_{Z2} = 0$. Kawada [1] has discussed in detail some typical cases when $\omega_Z \neq 0$, and he shows how the final shape of a deformed bicrystal may be predicted. On the basis of the test of Bicrystal A and tests of other bicrystals, it is believed that ω_Z has little effect on the strength of bicrystals.

ω_X and ω_Y result from the reorientation of the individual crystals as they deform by slip. For symmetric bicrystals, in general, $\omega_Y \neq \omega_X \neq 0$ but $\omega_{X1} = \omega_{X2}$ so $\Delta\omega_X = 0$. Both Kawada [1] and the author have found that symmetric bicrystals approach monocrystals in their softness. This is the justification for the proposal that ω_Y has a very small effect on the strength of a zinc bicrystal. Dislocation theory explains this quite simply.

Consider a symmetric bicrystal. According to the dislocation theory of grain boundaries [2], the disorientation angle, ϕ, is given by $\tan^{-1} b/h$ where b is the magnitude of Burger's vector and h is the dislocation spacing. The number of dislocations per unit length of boundary is

$$M = \frac{\tan\phi}{b}.$$

The number of positive dislocations per unit length of crystal contributing to a plastic shear, ν, is

$$m = \nu/b.$$

The shear is $\nu = \Delta \tan\phi/2$, so, for small ϕ, $m = \frac{1}{2}\Delta n$. Since there are two crystals, the number of dislocations required in the boundary to form the proper disorientation angle after deformation is just equal to the number of dislocations which flow into the boundary because of the shear strain in the crystals. Thus it is easy to understand why symmetric grain boundaries offer little resistance to tensile deformation.

On the other hand, it is difficult to see how dislocations of either edge or screw type can flow into a grain boundary to cause a rotation of the type ω_X. At low strain rates or at high temperatures, the stresses caused by $\Delta\omega_X$ might relax sufficiently by viscous flow to make the grain boundary's contribution to the deformation resistance negligible, but for ordinary strain-rates and temperatures this would not be the case.

Since the rotations normal to the grain boundary, ω_X, cannot be accommodated by simple slip, other mechanisms, such as local twinning and bend-plane formation, operate. These require more energy for their operation than simple slip and hence lead to increased strength.

It has been observed that even when $\Delta\omega_X$ is large, there seems to be no interaction between the two crystals or a zinc bicrystal at distances greater than a few microns from the grain boundary. Each crystal reacts with the boundary independently. The affected regions of the individual crystals extend to definite and relatively absolute distances from the boundary, which depend on the orientation and to some extent on the area of the grain boundary. This means that longitudinal bicrystals should not show geometric correspondence. Dimensionally large ones should contain less inhomogeneous strain per unit volume than small ones and, therefore, have lower yield stresses than geometrically similar, but dimensionally small bicrystals.

Acknowledgments

The bicrystals were grown at Columbia University while the author was employed on a contract with the Office of Naval Research; Contract N6 onr 27128. All other experimental work was performed at the General Electric Research Laboratory.

References

1. Kawada, T. Proc. First World Met. Congress (1951), p. 591, ASM; J. Phys. Soc. Jap., **6** (1951) 362.
2. Read, W. T. and Shockley, W. Phys. Rev., **78** (1950) 275.

THE REDISTRIBUTION OF SOLUTE ATOMS DURING THE SOLIDIFICATION OF METALS*

W. A. TILLER, K. A. JACKSON, J. W. RUTTER, and B. CHALMERS†

A quantitative analysis is made of the redistribution of solute resulting from solidification in the absence of convection of a binary solution for transient and steady state conditions. Diffusion in the liquid is taken into account and shown to be of importance in determining the solute distribution in both the liquid and the solid. It is shown that the distribution for both normal freezing and zone-melting depends on the rate of solidification. When the speed of solidification is increased abruptly, a band of high solute concentration is formed in the solid; the reverse occurs when the speed is decreased abruptly. Values for the length of the constitutionally supercooled zone of liquid adjacent to a growing solid-liquid interface are calculated.

LA DISTRIBUTION DES ATOMES D'UN CORPS DISSOUS LORS DE LA SOLIDIFICATION DES MÉTAUX

Une analyse quantitative est faite de la distribution du corps dissous résultant de la solidification' en absence de convection, d'une solution binaire, dans les cas des régimes transitoires et permanents· Il est montré que la diffusion dans le liquide, dont il est tenu compte, joue un rôle important dans la détermination de la distribution du corps dissous dans le liquide et dans le solide. Il est aussi montré que cette distribution dépend de la vitesse de solidification, aussi bien dans le cas de la solidification normale que dans celui de la fusion en zones ("zone-melting"). Quand la vitesse de solidification est brusquement augmentée, une bande de haute teneur en corps dissous est formée dans le solide; l'inverse se produit quand la vitesse est brusquement diminuée. Des valeurs de la longueur de la zone de surfusion de constitution ("constitutional supercooling") dans le liquide adjacent à la surface de séparation entre le solide en croissance et le liquide ont été calculées.

DIE WÄHREND DES KRISTALLISATIONSVORGANGS IN METALLEN AUFTRETENDE VERÄNDERUNG IN DER VERTEILUNG DER GELÖSTEN PHASE

Die in Abwesenheit von Konvektionsströmen während der Kristallisation erfolgende Veränderung in der Verteilung der gelösten Phase in Zwischenstoffsystemen wird für stationäre und nicht-stationäre Bedingungen quantitativ diskutiert. Die Diffusion in der flüssigen Phase wird in Rechnung gestellt, und es wird gezeigt, dass sie sowohl für die Einstellung der gelösten Phase in der Flüssigkeit als auch im Kristall von Bedeutung ist. Es wird gezeigt, dass die Verteilung sowohl im Fall der normalen Kristallisation als auch im Fall der "Zone-Melting" von der Kristallisationsgeschwindigkeit abhängt. Wenn die Kristallisationsgeschwindigkeit plötzlich ansteigt, bildet sich ein Band erhöhter Konzentration im Kristall. Das Umgekehrte tritt bei einer plötzlichen Verringerung der Kristallisationsgeschwindigkeit auf. Die Ausdehnung der auf Grund des Konstitutionsunterschiedes unterkühlten, der Grenzfläche flüssig-fest im wachsenden Kristall unmittelbar benachbarten Flüssigkeitsschicht wird berechnet.

Introduction

It is well known that redistribution of the solute occurs as a crystal solidifies from a melt of impure metal or alloy. For the case in which a single phase solid is formed, the equilibrium concentration of solute in the solid at the interface between solid and liquid is different from the equilibrium concentration of solute in the liquid adjacent to it, the ratio of the former to the latter being denoted by "k". This ratio is called the distribution coefficient and is expressed diagrammatically by Figure 1.

The resulting segregation has been studied and treated mathematically by a number of investigators. Notable among these studies has been the recent work of Pfann on zone-melting [1]. In his work, he has extended the treatment of normal freezing by Gulliver [2], Scheuer [3], and by Hayes and Chipman [4], to the treatment of the results of traversing a relatively long charge of solid alloy by a small molten zone (i.e. small with respect to the length of the charge). He showed that it is possible to eliminate or enhance the segregation of the solute by suitable variation of the growth conditions.

These treatments of segregation, whether they apply to ordinary freezing or zone-melting, are incomplete. The above-mentioned authors have expressed, in one form or another, the concentration

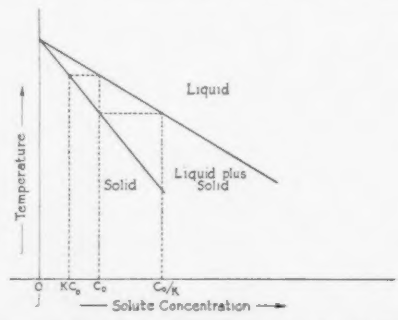

FIGURE 1. Portion of binary constitutional diagram for a solute which lowers the freezing point of the solvent.

*Received March 16, 1953.

†Department of Metallurgical Engineering, University of Toronto, Canada.

in the solid as a function of g, the fraction solidified, and have derived, for freezing, an equation of the form

$$C = kC_0(1 - g)^{k-1} \tag{1}$$

where C_0 is the initial concentration of solute in the melt, and k is the ratio of the solute concentration in the solid to the concentration in the liquid. Equation (1) has been based on the following assumptions:

1. Diffusion in the solid is negligible.
2. Diffusion in the liquid is complete (i.e., concentration in the liquid is uniform at all times).
3. k is constant.

The present paper shows that the second assumption is not valid. According to Frenkel [5] and to Jost [6], the diffusion coefficient is 1–10 cm²/day for all liquid metals thus far studied. It will be shown that the rate of diffusion of solute in the liquid, calculated from this value of the diffusion coefficient, is not large enough for the assumption of complete liquid diffusion to be even approximately valid under the conditions used for the production of single crystals or for zone-melting.

VOL. 1 1953

Mixing of the solute due to convection will tend to level the solute concentration in the liquid. However, convection can be eliminated by growth in a vertical tube so that the variation of the liquid density with temperature along the specimen will result in the least dense part of the liquid being at the top. Mixing due to natural convection will then be absent; incomplete mixing will also occur for horizontal growth under a low temperature gradient, since natural convection will be reduced by a decrease in temperature gradient. For specimens of small cross-section there will be little convection because of the small space available. For specimens of large cross-section, convection must be relatively rapid to remove completely the layer of high solute concentration formed adjacent to the growing interface, before that layer solidifies. Experimentally, it has been observed, for crystals grown horizontally, that a change in the rate of growth produces a marked change in the solute concentration of the solid. If mixing were complete, the solute concentration of the solid would be independent of the speed.

If complete mixing could be obtained, by either forced or natural convection, equation (1) would be valid. Experimentally, complete mixing will be approached most closely by the use of high frequency induction heating, which causes stirring of the liquid, and by growth at a slow speed.

Normal Freezing

The present paper examines the segregation of solute in both normal freezing and zone-melting. The following assumptions are made:

1. Diffusion in the solid is negligible.
2. The value of k (as defined in the first paragraph) is constant.
3. Convection in the liquid is negligible.

Since the solidus and liquidus lines in most equilibrium diagrams are slightly curved, k will vary; however, an average k can be found for the concentration range considered. Attention will be directed to the case of $k < 1$; this occurs when the solubility of solute in the solid is less than in the liquid; this corresponds to "rejection" of solute atoms by the solid as it forms, and therefore to a progressively increasing concentration of solute in the remaining liquid.

Let the solute concentration in the liquid be C_0; then the initial layer of the solid to freeze will have a solute concentration of kC_0. As the crystal grows the liquid concentration will rise because of the solute rejected from the interface; this will cause the solid concentration to rise also. This increase of concentration will continue until a steady state condition is attained. At this point the solid concentration adjacent to the interface will have reached a steady value and the distribution of solute in the liquid near the interface will be constant also.

Let the form of the liquid distribution C_L be as shown in Figure 2, C_0 being the initial concentration in the liquid. Two factors influence the form of C_L, and they are: (1) diffusion in the liquid tending to spread the solute uniformly throughout the melt at a rate governed by the diffusion coefficient D cm²/sec; (2) the process of freezing which acts as a source of solute at the interface between solid and liquid—the rate of freezing is measured by the advance of the interface, R cm/sec.

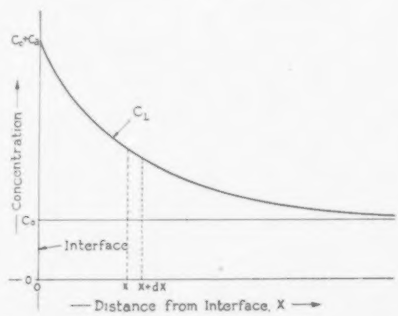

FIGURE 2. Steady state distribution, C_L, of solute in the liquid ahead of the freezing solid-liquid interface.

By consideration of Figure 2, the amount of solute diffusing into unit area of face x is $D(dc/dx)_x$, the amount diffusing out at face $x + dx$ is $D(dc/dx)_{x+dx}$; therefore, the net flow into a volume element is $D(d^2c/dx^2)$ per unit volume. If the solid-liquid interface is considered as the origin, and freezing is represented by moving the liquid distribution past it at the rate R cm/sec, then the net flow out of the same volume element due to freezing is $R\ dc/dx$. Therefore, the differential equation describing a stationary distribution with respect to this coordinate system is

$$D\frac{d^2c}{dx^2} + R\frac{dc}{dx} = 0 \tag{2}$$

which yields a solution

$$C_L = C_a \exp\left(-\frac{R}{D}x'\right) + C_0 \tag{3}$$

where C_a is the solute concentration in the liquid at the interface, and the variable x' denotes distance in front of the interface.

Equation (3) shows that the liquid distribution is exponential and that its "decay constant" is determined by the ratio of the rate of growth to the diffusion coefficient. The value of D as given by Frenkel [5] is approximately 1–10 cm²/day for all liquid metals, whereas R can be varied. A measure of the "characteristic distance" of the redistribution, i.e. where C_L has fallen to $C_0 + C_a/e$ of its value at the interface, is plotted in Figure 3, for various values of R.

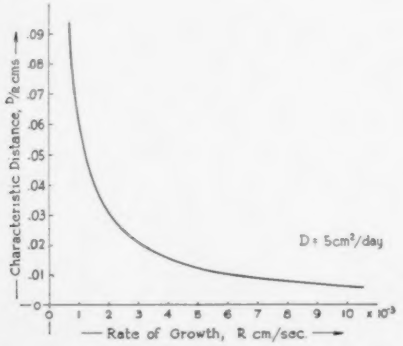

FIGURE 3. "Characteristic distance," D/R, of the solute distribution in the liquid, C_L, (equation 5) as a function of the rate of growth, R.

The influence of convection on the solute distribution in the liquid will depend both on the temperature differences in the liquid and on the rate of growth of the crystal. Natural convection is caused by the presence of temperature differences in the liquid. This convection will tend to lower the solute distribution C_L, especially if the distribution extends far into the liquid. An increasing rate of growth, however, will serve to decrease the effect of the convection on two counts: (i) For rapid rates of growth the exponential solute distribution has a large decay constant and does not extend very far ahead of the interface, but falls rapidly to C_0. This distribution may lie entirely within the "stagnant" layer adjacent to the interface which would not be affected appreciably by convection. (ii) Since the growth is rapid, there will be little time for convection to alter the distribution C_L.

The concentration in the solid C_s, rises from its initial value of kC_0 to its equilibrium value and maintains this concentration as solidification continues. When the steady state has been reached, the amount of solute in the region just ahead of the interface must be constant; therefore, the amount of solute leaving the liquid while the interface is advancing by unit distance must be equal to the amount of solute entering the region concerned. Therefore, the concentration of the solid must equal the concentration of the undisturbed liquid, i.e. C_0. If $C_s < C_0$, there would be an unbalance in the system such that the excess solute would build up the exponential distribution in C_L which would in turn build C_s up to C_0. If $C_s > C_0$, then the solid would be absorbing more than the source is supplying, and would thus tend to lower the exponential in C_L, which in turn drives C_s back to C_0.

From a consideration of Figure 2, steady state conditions yield $C_s = C_0$, and $C_a = C_0/k - C_0$ at the interface. Therefore, equation (3) becomes

$$C_L = C_0\left\{1 + \frac{1-k}{k}\exp\left(-\frac{R}{D}x'\right)\right\}. \tag{4}$$

From equation (4), the form of the solid distribution C_s up to the equilibrium level may be calculated. The curve of solute concentration in the solid at the beginning of the specimen must satisfy the following conditions:

1. It must rise from kC_0 at the beginning of the crystal.
2. It must tend asymptotically to C_0 with distance along the crystal.
3. It must rise continuously from kC_0 to C_0.
4. From consideration of Figure 4, the area between C_0 and C_s must be equal to the area between C_L and C_0 for "conservation of solute."

If it is assumed that the rate of approach of C_s to C_0 with distance along the specimen is proportional to $(C_0 - C_s)$ at any distance x measured from the beginning of the specimen, it follows that C_s is of exponen-

tial form. The justification for this assumption is that it appears plausible and is the simplest possible assumption which fits the four boundary conditions. Using this assumption and the four conditions noted above, C_s is derived in Appendix I, and is given by

$$(5)\quad C_s = C_0\left\{(1-k)\left[1-\exp\left(-k\frac{R}{D}x\right)\right]+k\right\}$$

where x is the distance measured from the beginning of the crystal. The rise of C_s is illustrated in Figure 4, and similarly the "characteristic distance" of the distribution is found to be $x = D/kR$ cm, at which point $C_s = C_0\{(1-k)(1-1/e)+k\}$.

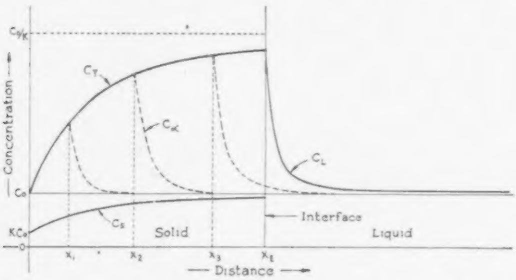

FIGURE 4. Distribution of solute in the liquid, C_α, and in the solid, C_S, in the first part of the specimen to solidify. C_T shows the solute concentration at the growing interface.

The region before equilibrium conditions are reached may be termed the transient region. In this region the shape of the solute distribution in the liquid can be determined from C_s since $C_T = C_s/k$ for any point x as shown in Figure 4. As the solid-liquid interface moves from $x = 0$ to $x = x_E$, the area under the liquid distribution $C_\alpha - C_0$ at any value of x is equal to the area $C_0 - C_s$ from 0 to x; this must be so in order to conserve solute. The form of C_T is given by

$$(6)\quad C_T = \frac{C_s}{k} = C_0\left\{\frac{1-k}{k}\left[1-\exp\left(-k\frac{R}{D}x\right)\right]+1\right\}.$$

It may also be seen that the transient liquid distribution curve C_α is exponential with a "decay constant" identical to that which prevails under equilibrium conditions (see Appendix II). The distribution C_α is given by

$$(7)\quad C_\alpha = C_0\left\{\frac{1-k}{k}\left[1-\exp\left(-k\frac{R^2}{D}t\right)\right]\exp\left(-\frac{R}{D}(x-Rt)\right)+1\right\}$$

where t represents time and $x > Rt$.

For a complete solution of the solute distribution in the solid, the last part of the specimen to solidify must also be considered. The analysis of this region is complicated by the fact that a finite liquid region, in which the concentration changes at all points, must be considered. No attempt will be made to derive quantitatively the solute concentrations in this region. However, the qualitative form of the solute distribution in the solid will be derived.

Let: x' = distance measured from the interface into the liquid,
x = distance measured from the beginning of the specimen,
L = length of specimen,
x_1 = distance from interface to end of specimen.

Assume that L is large compared to D/kR so that the steady state solute distribution in the liquid C_L is established over an appreciable length of the specimen. The transient solute distribution in the solid at the end of the specimen can then be considered independently from that at the beginning.

As the interface approaches the end of the specimen, the concentration at any $x' \leqslant x_1$ must increase. Assume that the concentration at any $x' \leqslant x_1$ remains constant, as shown in Figure 5. Then, since the steady state distribution C_L has been established, the amount of solute in excess of C_0 which would

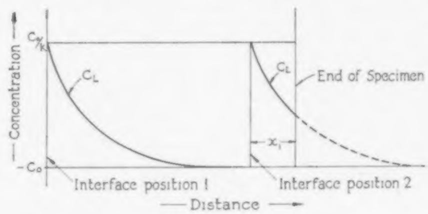

FIGURE 5. Assumed solute concentration, C_L, in last portion of specimen to solidify, used in derivation of equation (8).

have appeared in the solid as the interface moved to $x = (L - x_1)$ is given by the integral of C_L from $x' = x_1$ to $x' = \infty$, and is:

$$(8)\qquad C_0\frac{1-k}{k}\frac{D}{R}\exp\left(-\frac{R}{D}x_1\right).$$

This quantity of solute is represented by the area under the dotted portion of C_L for interface position 2 in Figure 5. If this quantity of solute had come out in the solid by the time the interface reached the point $x = (L - x_1)$, the solute concentration in the liquid at any $x' \leqslant x_1$ would not have changed. Since a change in solute concentration in the liquid is necessary to cause a change in solute concentration in the solid, the amount of solute above C_0 which has appeared in the solid by the time the interface has reached $x = (L - x_1)$ must be less than the value

given by (8). By comparing (8) to the similar expression giving the integrated solute deficiency below C_0 at the beginning of the specimen, the shape of the distribution in the solid at the end of the specimen can be compared to that at the beginning. The solute deficiency at the beginning, from a point $x = x_2$ to a point where the steady state distribution C_L is established, is found from equation (5) by integration, and is given by

$$C_0 \frac{1-k}{k} \frac{D}{R} \exp\left(-k\frac{R}{D}x_2\right). \tag{9}$$

Expressions (8) and (9) are equal when $x_2 = x_1/k$. Therefore, when the interface is at a distance x_2 from the beginning of the specimen, a fraction

$$\left[1 - \exp\left(-k\frac{R}{D}x_2\right)\right]$$

of the solute represented by the area under the steady state distribution C_L is being carried ahead of the interface and when the interface reaches a distance $x_1 = kx_2$ from the end of the specimen, more than this fraction of the solute is still being carried ahead of the interface. If the concentration in the solid is insignificantly different from C_0 at a distance x_2 from the beginning of the specimen, it will still be insignificantly different from C_0 at a distance less than kx_2 from the end. For values of k less than unity, the rise at the end is more rapid than that at the beginning.

If no increase in concentration occurred at any $x' \leqslant x_1$, as postulated previously, then the concentration in the solid would finally reach C_0/k at the

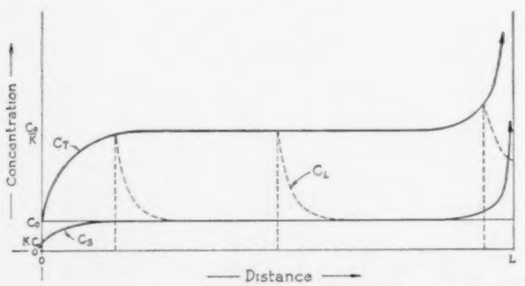

FIGURE 6. Solute distribution in the solid, C_S, and solute concentration in the liquid at the growing interface, C_T, for the complete crystal. The dotted lines, C_L, indicate the solute distribution in the liquid for various interface positions.

end of the specimen. Hence, the concentration in the solid at the end must reach a value greater than C_0/k. If C_0 is large enough, this will result in production of a second phase in a suitable alloy system. For example, let C_V be the limit of solid solubility at the eutectic temperature of a binary eutectic system. When the second phase is formed, the solute concentration in the liquid must be greater than the eutectic composition C_E. Since $C_s > C_0/k$ at the end of the crystal, then the solute concentration in the last liquid to freeze is greater than C_0/k^2. If $C_0/k^2 > C_E$, that is, $C_0 > k^2C_E$, then the second phase will form provided that the necessary nucleation occurs. Therefore, if the initial solute concentration C_0 is greater than kC_V, then the second phase will appear. If the solute is a gas, then the second phase will be gaseous and bubbles of gas will be nucleated.

The form of the solute distribution in the solid for the entire specimen is illustrated by Figure 6.

The Effect of Changing R

Knowing the characteristics of the solute distributions in both the liquid and the solid, it will be shown that increasing or decreasing the speed of growth produces transverse bands of higher or lower concentration. C_L is given by equation (4) for any growth rate R. If the growth rate is increased, then the exponential must become steeper, as shown in Figure 7. When the distribution comes again to a

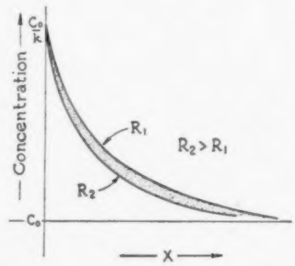

FIGURE 7. Steady state solute distributions in the liquid ahead of the interface for rates of growth R_1 and R_2.

steady state for the new growth rate, the concentration at the interface must once again be C_0/k. From Figure 7, the areas under the two curves are now different and this difference in area is exactly what has been added to the solid distribution due to the changed rate of freezing. If R decreases, the amount of solute entering the solid is temporarily reduced (see Figure 8).

In practice, though the rate of freezing, R, can be changed very rapidly, the solute distribution in the liquid cannot change instantaneously from the distribution characteristic of R_1 to that characteristic of R_2. If $R_2 > R_1$, then the freezing interface rejects more solute than can diffuse down the concentration gradient characteristic of R_1 in the time allowed, and thus the concentration at the interface must increase. The concentration gradient then

becomes steeper, and as the solute distribution changes, the amount of solute diffusing down the gradient will increase until it becomes equal to the amount being supplied as a result of growth, which is governed by R_2. The rate of loss of solute, due to diffusion, will ultimately exceed the rate of supply due to growth and the solute concentration will then decrease to the value characteristic of R_2.

Between the two steady state conditions, C_L must rise (at the interface) by an amount which depends

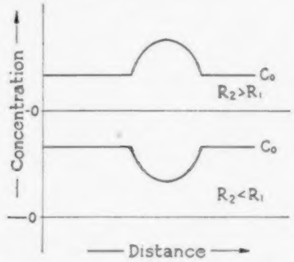

FIGURE 8. Change in solute concentration in the solid, C_S, as a result of a change in growth rate, R.

on the change in R and the values of R_1 and R_2. If R_1 is large, then the distribution C_L is essentially confined to a narrow region adjacent to the interface and the change to the distribution characteristic of R_2 will be accomplished by moving the interface only a very short distance. In this case, the solute concentration in the solid, C_s, will rise and fall steeply.

The amount of solute that appears in the solid as a result of the change in speed can be found by integration of equation (4) for the two values of R, and is given by

$$\Delta C_s = C_0 \frac{1-k}{k} D\left(\frac{1}{R_1} - \frac{1}{R_2}\right). \tag{10}$$

The rate of change of R is controlled by the thermal conductivity of the crystal and the latent heat

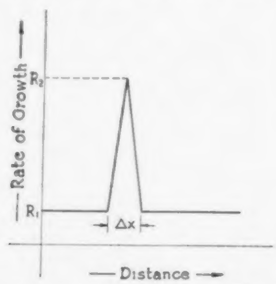

FIGURE 9. Assumed change in growth rate, R, as a function of distance.

of fusion, i.e., how fast the latent heat is conducted away, and on the imposed change in the rate of supply and extraction of heat.

It is thus apparent that the presence of transverse bands [8] differing in concentration from the equilibrium value of C_0 may be created by rapid changes in the growth conditions of the crystal.

If the heat flow conditions for the system are disturbed abruptly by lowering the heat input, an amount ΔQ for a time Δt and back again, then the crystal will react to this sudden discontinuity and a band will result. The crystal will grow rapidly for a very short distance in an accelerating fashion, first positive and then negative, until once again it returns to its initial growth rate when the heat flow conditions are stabilized at their original value. The resulting distribution is represented in Figure 10.

If the distance $\frac{1}{2}\Delta x$ (Figure 9) is less than the distance to the maximum in the curve, then the solid distribution will travel up ΔC_B (the steepness being determined by $R_2 - R_1$), and at the distance $\frac{1}{2}\Delta x$ will start down again since the driving force has been reversed. If the rate of rise is the same as the rate

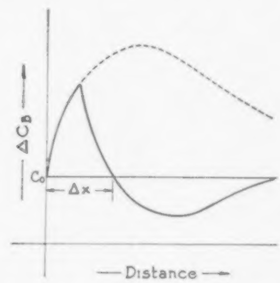

FIGURE 10. Change in solute concentration in the solid caused by the assumed change in growth rate shown in Fig. 9.

of fall, the decay constant for ΔC_B will be the same on both sides (see Figure 10). The value of ΔC_B will fall below C_0 since the acceleration is now negative and the total area under $(\Delta C_B - C_0)$ must be zero to conserve solute. If the rate of growth is once again reversed at Δx, then ΔC_B will start to rise again.

Supercooling

The liquid ahead of an advancing interface may supercool for two different reasons. The interface must be at a temperature below that at which the solid and liquid would be in equilibrium and, therefore, the adjacent liquid is also supercooled.

The second cause of supercooling arises only in impure metals and alloys, and is related to the distribution of solute in the liquid. It was described and discussed qualitatively by Rutter and Chalmers [7] who describe it as "constitutional supercooling."

For an alloy, the distribution of solute in the liquid will be given by equation (4). Thus, every point in the liquid ahead of the interface has a definite concentration of solute atoms, and thus a definite liquidus temperature as given by the equilibrium diagram for the alloy under consideration (see Figure 1). There is also a definite temperature gradient in the liquid metal imposed by the growth conditions. If the temperature at a certain point as maintained by the gradient in the liquid is lower than the liquidus temperature at that point as predicted by the equilibrium diagram, then the liquid at that point will be constitutionally supercooled.

If only constitutional supercooling is considered, then the length of the constitutionally supercooled zone may be calculated. The solute distribution is given by equation (4), and from the equilibrium diagram the equilibrium temperature is given by

$$T_E = T_0 - mC_L \tag{11}$$

where T_0 is the melting point of the pure metal, and m is the slope of the liquidus line (see Figure 1); m is assumed to be constant for simplicity. Thus, the equilibrium temperature for any point in front of the interface is given by

$$T_E = T_0 - mC_0\left[1 + \frac{1-k}{k}\exp\left(-\frac{R}{D}x'\right)\right]. \tag{12}$$

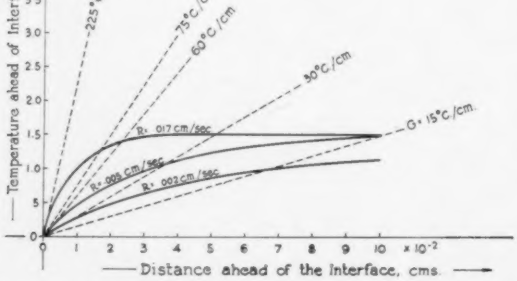

FIGURE 11. Equilibrium liquidus temperature (solid lines), calculated from equation (12), and specimen temperature (dashed lines) calculated from equation (13), as functions of distance ahead of the interface.

The temperature gradient in front of the interface may be expressed as

$$T = T_0 - m\frac{C_0}{k} + Gx' \tag{13}$$

where $T_0 - mC_0/k$ is the temperature at the interface, and G is the temperature gradient in the liquid. If the above two equations are plotted, the point of intersection other than $x' = 0$ will give the length of the supercooled zone. Thus, for $T = T_E$ it is found that

$$1 - \exp\left(-\frac{R}{D}x'\right) = \frac{G}{mC_0(1-k)/k}\,x'. \tag{14}$$

Equation (12) and equation (13) are plotted in Figure 11. The graph gives the length of the supercooled zone for different growth rates. From equations (12) and (13), the critical growth rate and temperature gradient for no supercooling can be calculated by equating the slopes of the two curves at the interface. These critical values are found from a solution of

$$\frac{G}{R} = \frac{mC_0}{D}\,\frac{1-k}{k}. \tag{15}$$

Incubation Distance for Cellular Substructure

A substructure of a cellular nature has been observed and studied in single crystals by Rutter and Chalmers [7]. They are columnar in the direction of growth, and hexagonal in cross-section. Their presence is attributed to the existence of a constitutionally supercooled zone of the melt just ahead of the interface.

As the crystal grows, the liquid concentration at the interface builds up from its initial value C_0 to its equilibrium value C_0/k in a manner given by equation (7). Thus, the crystal must grow for some distance before the liquid concentration is large enough to produce any constitutional supercooling. This incubation distance Z can be calculated by equating the slope of the temperature gradient in the liquid to the slope of the equilibrium temperature in front of the interface as given by equation (11), where the concentration is given by equation (7). The incubation distance is then

$$Z = -\frac{D}{kR}\log_e\left\{1 - \frac{GD}{C_0Rm(1-k)/k}\right\}. \tag{16}$$

For tin containing 0.016 per cent lead ($C_0 = .016$ per cent, $m = 100\text{C}^\circ/40$ per cent, $k = 0.1$, $R = .005$ cm/sec, $G = 75\text{C}^\circ$/cm, and $D = 3 \times 10^{-5}\text{cm}^2/\text{sec}$), it is found that Z is of the order of 0.2 cm.

Zone-Melting

Single Pass

Consider a charge of binary alloy of constant cross-section whose composition C_0 is constant. Let a molten zone of length l traverse the charge, as shown in Figure 12. In the light of the preceding

theory, the segregation of the solute will depend on the zone-length l. By varying the size of the zone-length, two cases may arise.

Case 1. $l > L_c$, the characteristic length of the distribution in the liquid, i.e. where the concentration has fallen close to the value C_0. In this case the

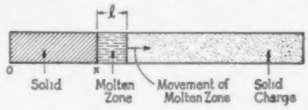

FIGURE 12. Solidification by zone-melting.

liquid distribution will be identical to that for normal freezing, and thus the theory already developed will apply to the segregation of solute for zone-melting.

Case 2. $l < L_c$. Under equilibrium conditions the liquid distribution must satisfy equation (2), and therefore must be of exponential form. At the interface the concentration must be C_0/k as usual, and the concentration must fall off as R/D; thus the distribution must be as shown in Figure 13. At a

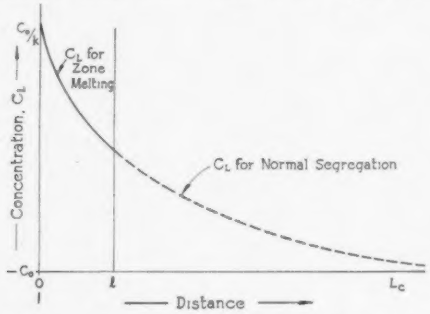

FIGURE 13. Steady state solute distribution in molten zone.

distance l ahead of the interface, the concentration has not fallen to the value C_0, but to a value greater than this, consistent with the exponential decay.

Since the area contained under this distribution must be smaller than the area for the zone-length

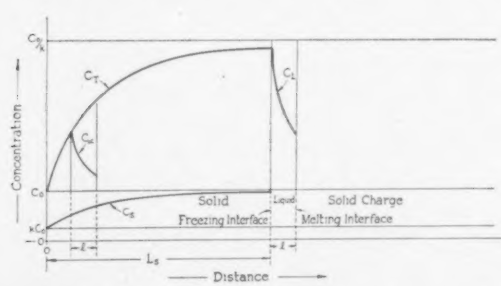

FIGURE 14. Solute distributions in solid, C_S, and in liquid, C_α, in initial transient region for the case of zone-melting. C_T gives the concentration at the growing interface as a function of distance from the beginning of the specimen.

required for normal freezing, C_s must rise more rapidly. Thus, the smaller l is, the more rapid must be the rise of the solute concentration in the solid. This deviation from normal freezing is illustrated in Figure 14. By the use of a treatment similar to that of Appendix I for finding the decay constant in the solid, the distribution C_s may be expressed as

$$C_s = C_0\{(1-k)(1-e^{-\beta x}) + k\} \tag{17}$$

where

$$\beta = k\frac{R}{D}\left[1 - \exp\left(-\frac{R}{D}l\right)\right]^{-1}.$$

Purification

From consideration of equation (17), it may be seen that, since the distribution of solute in the solid rises more sharply than for normal segregation, less purification results.

It is now clear that the smaller l is, the smaller will be the quantity of impurity transferred from the first part of the crystal to the last part in one pass. Therefore, the amount of purification per pass will decrease as l decreases below the characteristic length L_c of the solute distribution in the liquid; hence, one limit on the zone-length should be $l > L_c$.

However, in repeated pass zone-melting, if the zone-length l becomes larger than the characteristic length L_s of the solute distribution in the solid, the average concentration in the first zone-length to be melted will be increased. When this happens, the average concentration may not be much less than the initial C_0 of the first pass; then the amount of purification per succeeding pass will be decreased. With the view to increasing the efficiency of this method of purification then we should make $l < L_s$.

The conclusions from the above work provide the optimum conditions for purification, and they are:

$$L_c < l < L_s. \tag{18}$$

Equation (18) illustrates the importance of R, the rate of growth for a given zone-length l; R determines L_c and L_s, the characteristic lengths of the solute distribution in the liquid and in the solid.

Comparison with Experimental Observations

Banding

The technique of autoradiography as applied by Stewart et al [8] has made observable a form of banding. It was observed that crystals containing

small concentrations of solute sometimes tend to grow with the solute segregating out into alternate bands of large and small concentrations transverse to the direction of growth. One of these autoradiographs showing banding was placed on the densitometer, and there was found to be a periodic rise and fall about a mean value as shown in Figure 10. Thus, in the light of the preceding analysis, the phenomenon can be explained as a result of fluctuations in the heat input to the liquid.

Cellular Substructure

The existence of a zone of supercooling is not in itself the cause of the cellular substructure; it has been pointed out by Winegard and Chalmers [9] that a positive value of dS/dx', where S is the amount of supercooling, is the criterion for the formation of the substructure. This condition arises as soon as constitutional supercooling occurs.

The theory developed considers the distribution of solute ahead of the interface for diffusion in one direction only. This is complete only if the interface is plane; however, for an irregularly-shaped interface, the treatment would require extension to include lateral diffusion. The presence of the cellular substructure would alter the preceding picture, since the centres of the cells extend further into the melt than the bases, thus altering the equilibrium distribution of solute in a direction perpendicular to the direction of growth. Rutter and Chalmers [7], in their study of the substructure, observed this transverse segregation of impurities.

Zone-Melting

Though the distribution of solute as given by equation (17) differs from that of Pfann [1], it predicts the same qualitative results; in addition, however, it shows that the rate of freezing is a factor which influences the redistribution of solute. The more rapid the rate of growth, the steeper will be the rise of the solute concentration in the solid. The zone-length also appears as a factor in the redistribution process; the smaller the zone-length, the steeper will be the rise of the solute concentration in the solid. It may be seen from consideration of equation (17) that any result which may be achieved by changing l can equally well be brought about by changing R, the rate of growth. The optimum conditions of operation in the purification process by the repeated pass method have been evaluated. Finally, from the point of view of the redistribution of solute, it is also seen that, when the zone-length is greater than L_c, there is no difference between zone-melting and normal freezing.

Acknowledgments

The authors are indebted to the National Research Council, Ottawa, and the University of Toronto, for financial assistance during the course of this work.

APPENDIX I

Refer to Figure 4.

Let: C_0 = solute concentration in the melt before solidification begins.

x = distance measured from the beginning of the specimen.

C_s = solute concentration as a function of x.

k = distribution coefficient.

Assume that the rate of approach of C_s to C_0 with x is proportional to $(C_0 - C_s)$ at any x. Then:

$$\frac{d(C_0 - C_s)}{dx} = -\alpha(C_0 - C_s)$$

where α = a constant. The solution of this equation is:

$$C_0 - C_s = Ae^{-\alpha x} + B$$

where A and B are constants. Since $(C_0 - C_s) \to 0$ as $x \to \infty$, therefore $B = 0$, and

$$C_s = C_0 - Ae^{-\alpha x}.$$

Applying condition 1 noted in the text (p. 430),

$$C_s = kC_0 \text{ when } x = 0,$$

$$kC_0 = C_0 - A,$$

$$A = C_0(1 - k).$$

Therefore,

$$C_s = C_0 - C_0(1 - k)e^{-\alpha x}$$

$$= C_0\{(1 - k)(1 - e^{-\alpha x}) + k\}.$$

It will be seen that this equation satisfies conditions 2 and 3.

Condition 4 is satisfied by proper choice of α, as follows: The area A_1 between C_L and C_0 is

$$A_1 = C_0\frac{1 - k}{k}\frac{D}{R}.$$

The area A_2 between C_0 and C_s is

$$A_2 = \frac{1}{\alpha}C_0(1 - k).$$

The condition $A_1 = A_2$ yields

$$\alpha = \frac{kR}{D}.$$

Hence

$$(5)\quad C_s = C_0\left\{(1 - k)\left[1 - \exp\left(-k\frac{R}{D}x\right)\right] + k\right\}.$$

APPENDIX II

Derivation of Equation (7)

Refer to Figure 4.

The notation used will be the same as that in Appendix I; in addition, let:

C_T = the solute concentration in the liquid at the interface, expressed as a function of distance x from the beginning of the crystal.

C_α = solute distribution in the liquid when the interface is at any particular distance $x = x_i$ from the beginning of the crystal.

x_E = value of x for which the steady state is essentially established, i.e., $C_s = C_0$ and $C_T = C_0/k$.

x' = distance in liquid measured from interface as origin.

For any position, x_i, of the interface between 0 and x_E conservation of solute must be maintained. Therefore, the area A_1 between C_s and C_0 up to the point x_i must be equal to the area A_2, between C_α and C_0.

C_T is given by

$$C_T = \frac{C_s}{k} = C_0\left\{\frac{1-k}{k}\left[1 - \exp\left(-k\frac{R}{D}x\right)\right] + 1\right\}.$$

Assuming C_α to be of exponential form, it may be written as

$$C_\alpha = \{C_T(x_i) - C_0\}e^{-\alpha x'} + C_0,$$

where $C_T(x_i)$ denotes C_T evaluated at x_i. Then

$$A_1 = \int_0^{x_i} (C_0 - C_s)\,dx$$
$$= C_0(1-k)\frac{D}{kR}\left[1 - \exp\left(-k\frac{R}{D}x_i\right)\right]$$

$$A_2 = \int_0^\infty \{C_T(x_i) - C_0\}e^{-\alpha x'}dx'$$
$$= \frac{C_0}{\alpha}\frac{1-k}{k}\left[1 - \exp\left(-k\frac{R}{D}x_i\right)\right].$$

Therefore,

$$\alpha = \frac{R}{D}$$

and

$$C_\alpha = C_0\left\{\frac{1-k}{k}\left[1 - \exp\left(-k\frac{R}{D}x_i\right)\right]\exp\left(-\frac{R}{D}x'\right) + 1\right\}.$$

If the interface moves from $x = 0$ to $x = x_i$ in time t at rate R, then C_α may be expressed as

$$C_\alpha = C_0\left\{\frac{1-k}{k}\left[1 - \exp\left(-k\frac{R^2}{D}t\right)\right]\exp\left(-\frac{R}{D}x'\right) + 1\right\}. \quad (7)$$

References

1. Pfann, W. G. J. Metals, **4** (1952) 747.
2. Gulliver, G. H. Metallic Alloys (London, Chas. Griffin and Co., 1922), Appendix.
3. Scheuer, E. Z. Metallk., **23** (1931) 237.
4. Hayes, A. and Chipman, J. Trans. A.I.M.E., **135** (1939) 85.
5. Frenkel, J. Kinetic Theory of Liquids (Oxford, Oxford University Press, 1946), p. 201.
6. Jost, W. Diffusion (New York, Academy Press, 1952), p. 479.
7. Rutter, J. W. and Chalmers, B. Can. J. Phys., **31** (1953) 15.
8. Stewart, M. T., Thomas, R., Wauchope, K., Winegard, W. C., and Chalmers, B. Phys. Rev., **83** (1951) 657.
9. Winegard, W. C. and Chalmers, B. To be published.

VOL. 1 1953

THE THEORY OF D_0 IN THE ARRHENIUS EQUATION FOR SELF-DIFFUSION IN CUBIC METALS*

A. D. Le CLAIRE†

Zener's theory of D_0 is extended. By assuming correlations between the various quantities occurring in the theoretical expressions for the self-diffusion coefficient appropriate to the various current mechanisms of diffusion, and other properties of the lattice to which such quantities are most closely related, it is shown that the experimentally observed values of D_0 and Q (in the equation $D = D_0 \exp(-Q/RT)$) are consistent only with the supposition of a vacancy mechanism in face-centred metals and with a ring mechanism in body-centred cubic metals.

Theoretical relations obtained for D, which include Zener's relation for D_0 as an approximate case, may be used to estimate values of D for those metals whose self-diffusion coefficients have yet to be measured.

LA THÉORIE DU D_0 DANS L'ÉQUATION D'ARRHENIUS POUR L'AUTO-DIFFUSION DANS LES MÉTAUX CUBIQUES

La théorie de Zener du D_0 est étendue. En supposant l'existence de corrélations entre les diverses quantités qui apparaissent dans les expressions théoriques du coefficient d'auto-diffusion relatives aux divers mécanismes de diffusion, et d'autres propriétés du réseau auxquelles ces quantités sont liées, il est montré que les valeurs expérimentales de D_0 et Q (dans l'équation $D = D_0 \exp(-Q/RT)$) ne sont compatibles qu'avec l'hypothèse du mécanisme des lacunes dans les métaux cubiques à faces centrées et le mécanisme des anneaux dans les métaux cubiques centrés.

Les relations théoriques obtenues pour D, qui englobent la relation de Zener comme une approximation, peuvent être utilisées dans l'estimation des valeurs de D pour les métaux, dont les coefficients d'auto-diffusion n'ont pas encore été mesurés.

DIE THEORIE DES D_0 IN DER ARRHENIUS'SCHEN GLEICHUNG FÜR DIE SELBSTDIFFUSION IN KUBISCHEN METALLEN

Zener's Theorie des D_0 ist ausgedehnt. Wenn man Beziehungen zwischen den verschiedenen Variablen in den theoretischen Ausdrücken für den Selbstdiffusionskoeffizienten annimmt, und diese Beziehungen mit den verschiedenen Diffusionsmechanismen und Gittereigenschaften mit denen diese Variablen am engsten in Beziehung stehen in Verbindung setzt, dann kann gezeigt werden, dass die experimentell beobachteten Werte von D_0 und Q (in der Gleichung $D = D_0 \exp(-Q/RT)$) in flächenzentriert kubischen Metallen nur mit einem Leerstellenmechanismus, in raumzentriert kubischen Metallen nur mit einem Ringmechanismus erklärt werden können.

Die theoretische Beziehung für D, die Zeners Beziehung für D_0 als Grenzfall enthält, kann zum Abschätzen der D-Werte für Metalle, deren Selbstdiffusionskoeffizienten noch nicht gemessen sind, benutzt werden.

1. Introduction

The diffusion coefficients for metallic self-diffusion or for diffusion between two dissimilar metals are well known to vary with temperature through the Arrhenius type equation

$$D = D_0 \exp(-Q/RT), \tag{1}$$

where D_0 and Q are temperature independent constants. The "activation energy," Q, generally has a value lying between 20 and 70 kcal/mol (1–3 e.v.). The many values of D_0 which have been reported for binary interdiffusing systems cover the range 10^{-9} to 10 cm^2/sec. For self-diffusion however, D_0 lies in the more restricted range 10^{-1} to 10 cm^2/sec.

Various dynamic models have been proposed in the past (see for example [1]) as representing the fundamental lattice diffusion process and all lead to an equation for D similar to (1). However, the quantities entering into D_0 and Q vary from model to model, and so by comparing the measured and calculated values of these terms a choice may, in principle, be made between the proposed models. The three most discussed probable mechanisms of diffusion are (1) vacancy diffusion, (2) interstitial diffusion, and (3) ring diffusion [2], this latter including as the simplest case diffusion by the mutual exchange of position of two neighbouring atoms.

Direct quantum mechanical calculations of Q have been made [2; 3] for self-diffusion in copper by each of these three mechanisms. The value of Q obtained for the vacancy mechanism turns out to be not only less than the values obtained for the other mechanisms but it is also closest to the experimentally determined self-diffusion activation energy. Thus it is concluded that the vacancy mechanism best represents the actual process giving rise to self-diffusion in copper. It is usually inferred from this result that the same mechanism operates, for both self- and inter-diffusion, in all close-packed structures. This is generally confirmed by observations of several experimental phenomena connected

*Received February 24, 1953.

†Atomic Energy Research Establishment, Harwell, England.

with diffusion in close-packed alloys, particularly of the Kirkendall effect which would certainly not occur if diffusion took place by a ring mechanism. Such observations are most readily interpretable in terms of a vacancy model (see for example [4]). However, for the other than close-packed metals there is comparatively much less evidence of a similar nature from which to draw conclusions as to their mechanism of diffusion. Calculations, similar to those for copper, have been made of Q for self-diffusion in the alkali metals [5]. These calculations suggest that diffusion is by a type of interstitial mechanism, but they are not valid for other body-centred cubic metals. It is particularly unfortunate that no Kirkendall effect experiments have yet been performed on non-close-packed metals.

Very little attention has been given to a comparison of theoretical and experimental values of D_0 with a view to selecting the most likely self-diffusion mechanism. Order of magnitude calculations have from time to time been made and these show agreement with experimental values of D_0 for self-diffusion, but such methods are insufficiently sensitive to discriminate between the proposed models. The first serious attempt in this direction was that of Zener [6] whose analysis indicated that the mechanism of self-diffusion in face-centred cubic metals differs from that in body-centred cubic metals. If, largely on other evidence, a vacancy mechanism is assumed for the face-centred cubic metals, then his calculations suggest a 4-ring diffusion process to be most likely for the body-centred cubic metals.

It is the purpose of this paper to follow up and extend these calculations of Zener and to show that the observed values of D_0 for self-diffusion in face-centred cubic lattices may be given a satisfactory interpretation only on the supposition of a vacancy mechanism of diffusion, while those for body-centred cubic metals are shown to be consistent only with the supposition of a 4-ring diffusion process.

2. The Expression for *D*

The observed diffusion in a crystal lattice is the net result of a large number of random jumps of each atom between successive equilibrium positions. The diffusion coefficient is clearly proportional to the average number n of such jumps made in unit time by each atom. It can be shown that in cubic crystals, when each atom is equally likely to migrate in one direction as in any of the other crystallographically equivalent directions, D is given by

$$D = g \cdot na^2, \tag{2}$$

where a is the lattice constant and g is a geometrical factor depending upon the disposition around any one atom of neighbouring positions into which that atom may jump.

When the migration is from one normal lattice site to another as in vacancy diffusion or ring diffusion, $g = 1/12$ for face-centred cubic lattices and $1/8$ for body-centred cubic lattices. (The calculation of g for the face-centred cubic case is given in [7].) The interstitial positions in the face-centred cubic lattice are at the body centres of unit cells and at the mid-points of their sides. The disposition of nearest neighbour interstitial positions is therefore congruent with that of nearest neighbour lattice positions and so again $g = 1/12$. The same is not true of interstitial positions in the body-centred cubic lattice and in this case g turns out to be $1/24$.

(a) *Self-diffusion by the Vacancy Mechanism*

An atom may move only when there is a vacancy on one of the neighbouring sites. Since the vacancies are distributed at random in the lattice of a pure metal, if α is the fractional concentration of vacant sites, and z the co-ordination number, $z\alpha$ is the probability that a particular atom has a vacancy as neighbour. If p is the probability that in unit time any one atom will move onto a vacant site to which it is adjacent, then n in equation (2) is given by

$$n = z\alpha p. \tag{3}$$

For both body-centred cubic and face-centred cubic lattices then D is given by

$$D = \alpha p a^2. \tag{4}$$

In deriving (2) the assumption is made that successive moves of an atom are independent of one another. It has been pointed out [8] that such is not the case in vacancy diffusion, for an atom that has just made a move in one direction by exchange with a vacancy is clearly more likely to make its next move in the opposite direction rather than in any other direction. An analysis of this situation shows equation (4) to be in error by about 2 per cent but experimental values of D are not at present sufficiently accurate to warrant inclusion of this refinement in (4).

Let ΔF_1 be the change in free energy on forming a vacancy at constant temperature, apart from that contributed by changes in mixing entropy. The total free energy, including the latter contribution, is then found [9] to be a minimum when α is given by

$$\alpha = \exp\left(-\Delta F_1/RT\right), \tag{5}$$

VOL. 1 1953

which therefore represents the equilibrium fraction of vacant sites at temperature T.

In order that an atom may diffuse onto a neighbouring vacant lattice site, it must possess a certain amount of energy in excess of its average to enable it to "squeeze" between the nearest neighbours barring its way to the vacant site, or in other words, to surmount the potential barrier separating it from the vacant site. The probability that it possesses such an excess of energy is given by the Boltzmann factor; p is then the product of this and the number of times per second the atom is moving in the direction towards the vacant site, i.e. ν, its frequency of vibration on a lattice site. Now the excess energy required will vary with temperature because of the thermal expansion of the lattice and the temperature variation of its elastic properties. The energy in the Boltzmann factor must then be the change in free energy, rather than in total energy [10], when an atom is moved from a normal lattice site to the top of the potential barrier separating it from the next and, in this case, vacant site. Denoting this free energy change by ΔF_2 we have

$$p = \nu \exp\left(-\Delta F_2/RT \right). \tag{6}$$

This simple kinetic derivation of p, employing the correct form of the Boltzmann factor, is confirmed by a more rigorous derivation from reaction-rate theory [11].

From (4), (5), and (6) we find for D,

$$D = \nu a^2 \exp\left[-(\Delta F_1 + \Delta F_2)/RT \right]. \tag{7}$$

With each ΔF there is associated a change in entropy ΔS and of heat content or enthalpy ΔH,

$$\Delta F_i = \Delta H_i - T\Delta S_i.$$

ΔS_i and ΔH_i are referred to as the entropy and heat of activation respectively, corresponding to the free energy of activation F_i. D may be rewritten

$$D = \nu a^2 \exp\left[(\Delta S_1 + \Delta S_2)/R \right] \cdot \exp\left[-(\Delta H_1 + \Delta H_2)/RT \right]. \tag{8}$$

On account of the relation $T \cdot \partial(\Delta S)/\partial T = (\partial \Delta H)/\partial T$, we find that

$$-R\frac{\partial \log D}{\partial(1/T)} = \Delta H_1 + \Delta H_2, \tag{9}$$

so that the experimental activation energy Q, which is defined by the left-hand side of (9), is

$$Q = \Delta H_1 + \Delta H_2. \tag{10}$$

From (1) and (8) we find that for both face-centred cubic and body-centred cubic lattices

$$D_0 = a^2 \nu \exp\left[(\Delta S_1 + \Delta S_2)/R \right]. \tag{11}$$

The same expressions for D_0 and Q are derived by Zener [6].

We have already mentioned that a direct calculation of Q has been made for copper and has shown fair agreement with experiment. A corresponding calculation of ΔS_1 and ΔS_2 has not been made for any metal and might indeed be difficult and lengthy. Instead, we shall seek a correlation between the various quantities occurring in the expression for D (equation (8)) and those other physical properties of the lattice to which we might expect them to be most closely related. In this way we express D_0 and Q in terms of these latter quantities and certain correlation coefficients. Comparison with experiment enables the correlation coefficients to be calculated separately for each of the metals for which D has been measured.

If the same values of the constants appear for each metal then we may say that the experimental results are consistent, within the assumptions made, with the type of model assumed in deriving the expressions for D_0 and Q.

ΔF_2, being a change in free energy, is equal to the isothermal work required to move an atom from one lattice position to the top of the potential barrier separating it from the next. Such a movement will produce a local shear strain in the lattice around the diffusing atom and we may equate ΔF_2 to the resulting elastic strain energy. If ϵ represents the strain and if μ is the appropriate shear modulus, then the elastic energy is $\frac{1}{2}\mu\epsilon^2$ per unit volume. For geometrically similar lattices we shall assume the distortions to be geometrically similar and thus localised in volumes proportional to the atomic volume of the lattice in which they occur. ϵ is then the same for each metal of one structure and we therefore write

$$\Delta F_2 = k_2\, \mu (M/\rho), \tag{12}$$

where M is the atomic weight, ρ the density, and k_2 a correlation coefficient which is constant for any one structure type.

Making use of the thermodynamic relation $\Delta S = -\partial(\Delta F)/\partial T$ we then have

$$\Delta S_2 = -k_2 M\, \partial(\mu/\rho)/\partial T. \tag{13}$$

The variation with temperature of the shear moduli of single crystals of metals, or of that part of the experimental shear moduli of polycrystalline metals which is associated only with lattice elasticity and does not contain a contribution from grain

boundary relaxation processes, is found to be quite closely linear [12]. Also, to a sufficient approximation, ρ varies linearly with temperature. Thus we write

$$\mu = \mu_0 + \mu' T, \quad \rho = \rho_0 + \rho' T, \tag{14}$$

where μ' and ρ' denote μ and ρ differented with respect to temperature and μ_0 and ρ_0 are the values of μ and ρ, respectively, extrapolated to 0°K from the temperature range in which we are interested. Since the second terms in (14) are small compared with the first, we obtain

$$\Delta S_2 = -k_2 \frac{M\mu_0}{\rho_0}\left(\frac{\mu'}{\mu_0} - \frac{\rho'}{\rho_0}\right) \tag{15}$$

and thus

$$\Delta H_2 = k_2 \frac{M\mu_0}{\rho_0}. \tag{16}$$

Both μ' and ρ' are negative and since μ'/μ_0 is generally appreciably greater numerically than ρ'/ρ_0, ΔS_2 is essentially positive. This is an example of a general result of Zener [13] to the effect that with any lattice strain there is always associated a positive change of entropy.

Turning now to ΔF_1, let us write it as $\Delta F_1 = \Delta H_1 - T\,\Delta S_1$. ΔH_1 is the change in internal energy on forming a vacancy, and we assume, as has often in the past been suggested, that this is proportional to the latent heat of sublimation L_s of the lattice. Thus we put

$$\Delta H_1 = k_1 L_s, \tag{17}$$

where k_1 is a correlation coefficient which we may expect will be constant for metals of one structure.

The change in entropy ΔS_1 will arise because of the greater freedom of movement of the atoms neighbouring a vacant site, or to put it another way, because of what will be their reduced average vibrational frequency. We see then that ΔS_1 also is positive. As Zener points out [6], the total entropy of activation $\Delta S = \Delta S_1 + \Delta S_2$, as determined from equation (11) using experimental values of D_0 from self-diffusion measurements on cubic metals, is in fact always positive, in conformity with these predictions (see Table I).

ΔS_1 is best discussed further in terms of the final expressions for D_0 and Q. From equation (10), (11), (15), (16), and (17) we find

$$Q = k_1 L_s + k_2 M \mu_0/\rho_0, \tag{18}$$

$$D_0 = a^2 \nu \exp\left[\Delta S_1 - k_2 \frac{M\mu_0}{\rho_0}\left(\frac{\mu'}{\mu_0} - \frac{\rho'}{\rho_0}\right)\right] \Big/ R. \tag{19}$$

The latter we can also write as

$$D_0 = a^2 \nu \exp\left[\Delta S_1 - (Q - k_1 L_s)\left(\frac{\mu'}{\mu_0} - \frac{\rho'}{\rho_0}\right)\right] \Big/ R. \tag{20}$$

Equations (19) and (20) respectively can be used to calculate values of k_2 and k_1. We note that (19) requires a knowledge of μ_0 as well as of μ'/μ_0, whereas (20) requires only μ'/μ_0. It is not immediately obvious exactly what the appropriate modulus should be, but the value of μ'/μ_0 is likely to vary much less with choice of the form of the modulus than is μ alone. For example, for an isotropic solid the shear modulus μ, Young's Modulus E, and Poisson's ratio σ are related by $\mu = E/2(1+\sigma)$, so that neglecting the comparatively small temperature variation of σ, $\mu'/\mu_0 = E'/E_0$, whereas with $\sigma \sim \frac{1}{3}$, $E = (8/3)\mu$. We shall therefore first devote our attention to equation (20) and employ it to calculate k_1.

We are in any case limited in our choice of μ and μ' by the dearth of experimental measurements on the temperature variation of elastic properties. The most extensive are those of Köster [14] on the temperature variation of the Young's moduli of a large number of polycrystalline metals. In view of the foregoing remarks we shall assume that the values of E'/E_0 derived from his measurements are an adequate representation of the true values of μ'/μ_0. The low temperature linear portions of his curves are used to calculate E', these representing most closely true lattice behaviour, as mentioned above.

To return now to ΔS_1. The decrease in the vibrational frequency of the atoms neighbouring a vacant site, which is responsible for the positive entropy change ΔS_1, will also lead to a local change in the elastic properties and we should strictly use the local values of (μ'/μ_0) in calculating k_1. The local values of μ and of (μ'/μ_0) will be numerically less than the bulk values. Now k_1, calculated from (20), increases with increasing numerical value of (μ'/μ_0) and decreases with decreasing ΔS_1. An order of magnitude calculation, given in the appendix, suggests that ΔS_1 and the change in elastic properties locally are so related that, if we ignore ΔS_1 and use in the calculations the ordinary bulk values of (μ'/μ_0), the resulting values of k_1 will be unaffected. We assume as valid this considerable simplification and put $\Delta S_1 = 0$ in (20).

Values of a and L_s are taken from tables and for ν we use the Debye frequency. The results of the

calculation of k_1 for all those cubic metals for which all the relevant data exist, are given in Table I.

TABLE I
THE VALUES OF k_1

	Pb [15]	Ag [16]	Au [17]	Cu [18]	γ-Fe [19]	Co [20]	α-Fe [19]	W [21]
D_0 (cm^2/sec.)	4.016	0.895	0.157	0.178	0.58	0.37	5.8	11.5
Q (kcal/mol)	27.4	45.9	53.0	46.5	67.9	67.0	59.7	142.0
ν ($sec^{-1} \times 10^{-12}$)	1.85	4.5	3.8	6.6	8.8	8.1	8.8	6.4
a (Å)	4.94	4.08	4.07	3.61	3.65	3.545	2.86	3.16
ΔS (cal/mol/deg.)	13.49	9.49	6.40	6.01	7.80	7.13	13.30	14.85
μ'/μ_0	-8.57	-3.62	-2.24	-2.65	(-1.98)	(-1.83)	-2.34	-0.98
ρ'/ρ_0	-0.88	-0.55	-0.42	-0.53	-0.37	0.37	-0.37	-0.14
L_s (kcal/mol)	46.4	67.6	88.7	79.75	91.0	85.0	91.0	194.0
k_1	0.214	0.217	0.201	0.228	—	—	-0.085	-0.180
	Average k_1 = .215 R.M.S. error 4.5%							

Values of D for cobalt and γ-iron are not included in full because the necessary elastic properties are not known. The self-diffusion coefficient of tungsten has not been measured directly. The values given in Table I refer to the diffusion rate in tungsten of iron at very low concentration (~ 0.04 per cent), which van Liempt [21] considers represents the self-diffusion coefficient of tungsten. That this is in fact so has not yet been justified so that the tungsten figures are to be treated with reserve.

The significant feature of Table I is the very appreciable constancy of the values of k_1 for the face-centred cubic metals. (Using the mean value of $k_1 = 0.215$, values of μ/μ_0, shown in brackets, may be calculated for cobalt and iron and these, appear to be quite reasonable.) For copper, $k_1 L_s$, the energy required to form a vacancy is about 0.4 of the total activation energy and may be compared with Huntington and Seitz's estimate [3] of about 0.6. In view of the many approximations in both methods of analysis, this discrepancy is not objectionable. It is interesting in this connection that Nowick [27] has reported that the energy to form a vacancy in a 30 per cent AgZn alloy is about 0.4 of the total activation energy for diffusion in the same alloy.

It would appear then that the values of D_0 for self-diffusion in the face-centred cubic metals are consistent with the supposition of a vacancy mechanism of diffusion. This is further confirmed by the constancy found also for the values of k_2, which may be calculated from equation (18) using the now known mean value of k_1.

In calculating k_2 it is necessary to look more closely into the precise form of the "appropriate modulus" μ. Figure 1 shows the unit cell of a face-centred cubic lattice. An atom at "a" diffusing to a nearest neighbour position at "b" along the dotted line joining "a" and "b" must pass through the centre of a rectangle formed by four nearest neighbours atoms, shown in the diagram by open circles. These atoms will in consequence be displaced along

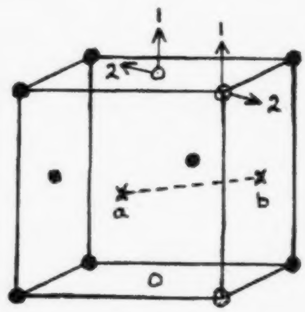

FIGURE 1

directions lying in the plane of the rectangle and it is the elastic energy associated with these displacements and the smaller displacements of outer-lying atoms which is given by the term $\Delta F_2 = M\mu/\rho$. The movement of each displaced atom may be resolved into components 1 and 2 as shown in the figure. The movement in direction 2 is closely related to the atomic movements occurring in a (110) [110] shear for which the appropriate modulus is well-known to be $\frac{1}{2}(c_{11} - c_{12})$. Similarly, movement in direction 1 is related to a shear (110) [001] for which it may be shown that the appropriate modulus is c_{44}. We therefore make the simple assumption that the appropriate modulus equals $c_{44} + \frac{1}{2}(c_{11} - c_{12})$. In view of this approximation it is sufficient to use the room temperature values of μ, thus dropping the distinction between μ and μ_0.

TABLE II
THE VALUES OF k_2

Metal	Q (kcal/mol)	.215 L_s (kcal/mol)	M	ρ (gm/cm^3)	$c_{44} + \frac{1}{2}(c_{11} - c_{12})$ ($kcal/cm^3$)	k_2
Pb	27.4	9.98	207	11.3	4.32	0.221
Ag	45.9	14.5	108	10.5	14.00	0.218
Au	53.0	19.1	197	19.3	13.51	0.245
Cu	46.5	17.1	63.5	8.9	23.55	0.176

Average k_2 = 0.215; R.M.S. error 11.5%.

The values of k_2 are given in Table II. Attempts were made to refine the expression for μ by looking more carefully into the motion of the open circle atoms in Figure 1 relative to their neighbours. These led to expressions for μ more complicated than the simple sum of the two shear moduli c_{44} and $\frac{1}{2}(c_{11} - c_{12})$, but the values of k_2 resulting were not so appreciably more constant than in Table II as to warrant any further discussion of them.

The approximate constancy of k_2 and k_1 for all the face-centred cubic metals indicates that the observed values of D_0 and Q are quite consistent with the supposition of a vacancy mechanism of diffusion. But we note that for the body-centred cubic metals α-iron and tungsten, the values of k_1 are not only far from constant but also both negative. A negative value of k_1 is quite meaningless so we are led to suspect that in these metals some diffusion mechanism other than by vacancies is operating. It may of course be that the experimental values of D_0 and Q are unreliable. The case of tungsten we have already mentioned and the values used for α-iron, which differ very considerably from earlier measurements, have yet to be confirmed. However, we proceed to examine the possibility of the other mechanisms of diffusion for α-iron and tungsten, at the same time demonstrating that the experimental measurements for the face-centred cubic metals are *not* consistent with these other mechanisms.

VOL. 1 1953

(b) *Self-diffusion by a Ring Diffusion Mechanism*

"Ring diffusion" occurs by the synchronous rotation of a number r of atoms lying in a ring, each being the nearest neighbour of the one before and the one after it. The simplest case of $r = 2$ is the familiar exchange process.

The number of jumps made per second by any one atom is then

$$n = p' \cdot N_r z, \tag{21}$$

where z is the coordination number, representing the number of possible positions to which an atom may migrate by rotation of a ring, and N_r is the number of distinct rings, each of r atoms, whose rotation can effect a migration of the atom in any one direction. p' is the probability that in unit time a particular ring rotates, by an angular distance $(1/r)2\pi$, so as to move each atom into the next nearest neighbour position. p' may be derived in exactly the same manner as before, to give

$$p' = \nu \exp\left(-\Delta F'_2/RT\right). \tag{22}$$

$\Delta F'_2$ is now the free energy change, or the minimum isothermal work done, in rotating a ring from one equilibrium position to the top of the potential barrier separating it from the next. ν is the frequency of vibration of the four atoms as a ring. For r small, this may not differ much from the Debye frequency, the value of which we shall use again for ν.

From (2), (21), and (22) we find for ring diffusion in both body-centred cubic and face-centred cubic lattices

$$D = N_r a^2 \nu \exp\left(-F'_2/RT\right). \tag{23}$$

If we again equate $\Delta F'_2$ to the shear strain energy associated with the rotation of a ring to the saddle point, so that $\Delta F'_2 = k'_2 M\mu/\rho$, we readily find, using $\Delta S'_2 = -\partial(F'_2)/\partial T$ that

$$Q = \Delta H'_2 = k'_2 M\mu_0/\rho_0 \tag{24}$$

and

$$\Delta S' = \Delta S'_2 = -Q\left(\frac{\mu'}{\mu_0} - \frac{\rho'}{\rho_0}\right) = R \log \frac{D_0}{N_r a^2 \nu}. \tag{25}$$

Thus

$$R \log N_r = R \log \frac{D_0}{a^2 \nu} + Q\left(\frac{\mu'}{\mu_0} - \frac{\rho'}{\rho_0}\right). \tag{26}$$

If then diffusion occurs by a ring mechanism we may find N_r and hence information on the type of ring operating, by inserting the experimental values of D_0 and Q in (26). The results of the calculation of N_r are given in Table III.

TABLE III
THE VALUES OF N_r

	Face-centred cubic				Body-centred cubic	
	Pb	Ag	Au	Cu	α-Fe	W
N_r	0.022	0.10	0.20	0.13	2.25	4.5
k'_2	—	—	—	—	0.215	0.206

The striking feature of the table is again the sharp distinction between the behaviour of the face-centred cubic and body-centred cubic metals. The experimental values of D_0 and Q for the face-centred cubic metals are clearly quite inconsistent with any ring mechanism of diffusion, for their values of N_r, apart from not being even roughly equal as they should be for a common mechanism, are all small fractions, and a fractional N_r is meaningless. The values of N_r for the body-centred cubic metals are larger by an order of magnitude, and are roughly equal and both greater than one. For a 2-ring process $N_r = 1$ and for the next higher value of $r = 4$, $N_r = 6$. For example, for a migration from $(\frac{1}{2}\frac{1}{2}\frac{1}{2})$ to (000), there are two distinct rings lying on each of

the planes (101), (0$\bar{1}$1), and (1$\bar{1}$0). The experimental values of N_r lie roughly midway between these two theoretically possible values so that while we may say the experimental results are consistent with a ring mechanism it is not possible, most probably because of the crudity of the theory, to decide on these grounds alone on the type of ring. Considerations of Q alone would most likely favour a 4-ring mechanism.

The values of k'_2 for α-iron and tungsten calculated from equation (24) are also given in Table III and are seen to agree quite closely, as is required.

(c) *Self-diffusion by an Interstitial Mechanism*

Although an interstitial mechanism appears to be most improbable from consideration of Q alone, it is interesting to find confirmation of this conclusion through the present methods.

We suppose that each atom has a certain probability β of occupying an interstitial position and that diffusion is effected by the migration of atoms so placed from one interstitial position to another. n is then given by

$$n = p'' z \beta \tag{27}$$

where p'' is the probability that in unit time an atom migrates from one position to another, and z is the number of nearest neighbour interstitial positions to which an interstitial atom may diffuse. For a face-centred cubic lattice $z = 12$, and for a body-centred cubic lattice $z = 4$.

It is readily shown that

$$\beta = 3 \exp(-F''_1/RT) \tag{28}$$

for body-centred cubic lattices, and

$$\beta = \exp(-F''_1/RT). \tag{29}$$

for face-centred cubic lattices.

$\Delta F''_1$ is the free energy increment associated with an atom in an interstitial position. The factor 3 arises because, although the total number of interstitial positions in the face-centred cubic case is equal to that of normal lattice positions, in the body-centred cubic case it is three times the latter number.

From equations (2), (27), (28), and (29), we find, employing an expression for p'' analogous to equation (22), that D is given by

$$D = \nu a^2 \exp[(-\Delta F''_1 - \Delta F''_2)/RT)] \quad \text{(f.c.c.)}, \tag{30}$$

$$D = \tfrac{1}{2}\nu a^2 \exp[(-\Delta F''_1 - \Delta F''_2)/RT)] \quad \text{(b.c.c.)}. \tag{31}$$

$\Delta F''_2$ is the free energy of activation for the interstitial diffusion process.

As before, $\Delta F''_2$ may be equated to the lattice strain energy around a diffusing atom when at the top of the potential barrier. But also in this case $\Delta F''_1$ may be equated to a lattice strain energy, namely that associated with the strain around an atom occupying an interstitial site. We may write each as proportional to $M\mu/\rho$, with proportionality constants k''_2 and k''_1 respectively, and so find eventually that

$$Q = \Delta H'' = k'' M\mu_0/\rho_0 \qquad (k'' = k''_1 + k''_2)$$

and

$$\Delta S'' = -Q\left(\frac{\mu'}{\mu_0} - \frac{\rho'}{\rho_0}\right).$$

These expressions are, in form, identical with those obtained for the ring diffusion mechanism. Thus from equation (30) and (31) it is clear that an interstitial mechanism would be indicated had N_r in Table III appeared as equal to 1 for each of the face-centred cubic metals and 0.5 for each of the body-centred cubic metals. Such requirements are clearly very much further from being fulfilled than are those for the vacancy mechanism in face-centred cubic metals or the ring mechanism in body-centred cubic metals, which we have already considered.

3. Discussion

The results obtained provide a confirmation that in face-centred cubic metals self-diffusion occurs by a vacancy mechanism, and in body-centred cubic metals by a ring mechanism. The equations developed for D_0 and Q, together with the mean values of the constants k_1, k_2, etc. that they contain, derived by comparison with existing measured values of D_0 and Q, may also be used to provide estimates of D_0 and Q for metals whose self-diffusion coefficients have not yet been measured.

Thus from equations (18) and (19), using the mean values of $k_1 = 0.215$ and $k_2 = 0.215$, we find that for aluminium

$$D = 0.72 \exp(-42{,}600/RT) \text{ cm /sec.},$$

and similarly for molybdenum, using $N_r = 2.65$ and $k'_2 = 0.210$, we find

$$D = 16 \exp(-120{,}000/RT) \text{ cm}^2/\text{sec.}$$

By making further approximation in the analysis some of the relations we have derived may be reduced to simpler forms, some of which have already appeared in the literature. For example, Johnson [16] some time ago pointed out that the Q for many metals were roughly proportional to their latent

heats of sublimation L. The values of Q/L are shown in Table IV and all lie quite close to a mean value of 0.66. Inserting the values $L = Q/0.66$ and $k_1 = 0.215$ in equation (20) (with $\Delta S_1 = 0$), we find, for the face-centred cubic metals,

$$D_0 = a^2 \nu \exp\left[-0.67\, Q \left(\frac{\mu'}{\mu_0} - \frac{\rho'}{\rho_0}\right) \Big/ R\right]. \tag{32}$$

This may be compared with the corresponding expression for body-centred cubic metals

$$D_0 = 2.65\, a^2 \nu \exp\left[-Q \left(\frac{\mu'}{\mu_0} - \frac{\rho'}{\rho_0}\right) \Big/ R\right]. \tag{33}$$

If further we choose to ignore ρ'/ρ_0 in equation (20) as being small compared with μ'/μ_0, and recalculate the several values of k_1, we find a mean value of $k_1 = .273$ (the separate values of k_1 are more scattered about the mean in this case), and in place of (32) obtain

TABLE IV

THE RATIOS Q/T_M, Q/L_S AND $T_M \left(\frac{\mu'}{\mu_0} - \frac{\rho'}{\rho_0}\right)$

Metal	T_M	Q/T_M	Q/L_s	$T_M\left(\frac{\mu'}{\mu_0} - \frac{\rho'}{\rho_0}\right)$
Pb	600	45.5	0.591	0.461
Ag	1234	37.2	0.679	0.378
Au	1336	39.7	0.597	0.244
Cu	1357	34.3	0.583	0.288
γ-Fe	1803	37.6	0.746	—
Co	1753	38.2	0.788	—
		Mean ~ 39	Mean ~ 0.66	Mean ~ 0.33

$$D_0 = a^2 \nu \exp\left[-0.57\, Q\, (\mu'/\mu_0)/R\right]. \tag{34}$$

This is exactly the result obtained by Zener, although he gives no clear indication of the significance of the numerical term.

The observed relation between Q and L_s, upon which (32) and (34) are based, can have no such simple or direct relation to the diffusion mechanism, as have the correlations employed in equations (18) and (19). One might expect it to lead to values for ΔS of $Q(L'/L_0)$ which are very much less than the observed values, L'/L_0 being very much less than μ'/μ_0.

The ratio T/T_M has frequently been suggested as a "reduced temperature" for the discussion of elastic properties. Accordingly, we find that the product $T_M(\mu'/\mu_0 - \rho'/\rho_0)$ is very roughly constant and of mean value $-$ 0.33. Substituting in equation (32) (face-centred cubic metals) we obtain

$$\log (D_0/a^2\nu) = 0.22\, Q/RT_M. \tag{35}$$

This is very similar to a relation obtained by Dienes [22], although his actual equation may only be obtained in a rather artificial manner. Rewriting (35) as

$$\log (D_0/a^2\nu) = Q/RT_M - 0.78\, Q/RT_M \tag{36}$$

we make use of the fact, also noted by Johnson [16], that the ratio Q/T_M is roughly constant and of mean value 39. Substituting in the second term only of (36) we obtain

$$\log (D_0/a^2\nu) = Q/RT_M - 15.5, \tag{37}$$

which does not differ significantly from Dienes' relation.

When the selected experimental values of log $(D_0/a^2\nu)$ employed in Table I are plotted against Q/RT_M, the points are very little better disposed about the straight line of slope 0.22 passing through the origin (equation 35) than they are about the line of slope 1 intercepting the log $(D_0/a^2\nu)$ axis at $-$ 15.5 (equation 37), so very considerable are the approximations in both these equations. An important feature of (37) however is that if the experimental values of D_0 and Q differ even by large amounts from the true lattice values, then provided only that the errors Δ log D_0 and ΔQ are related by

$$\Delta \log (D_0/a^2\nu) = \Delta Q/RT_M, \tag{38}$$

the experimental values of log $(D_0/a^2\nu)$ and Q/RT_M will continue to be near the line of equation (37).

Errors in determining the true lattice diffusion coefficient will arise if there is any appreciable grain boundary contribution to the total observed diffusion flow. Furthermore, phenomena associated with the Kirkendall effect in chemical diffusion may also lead to values of D which differ from those for lattice diffusion in the absence of the disturbing features associated with this effect. We may assume that in each such case experimental values of D are more likely to represent true lattice diffusion behaviour the higher the temperature (they certainly do so at or near the melting point), while they depart more from the lattice value the lower the temperature. The straight line drawn through the experimental values of log D and $1/T$ for both high and low temperature measurements (from which the values of Q and D_0 are deduced), may be regarded as having been obtained from the corresponding true straight line by a rotation about the point where it passes through the melting point. If such is in fact the case, then the errors in D_0 and Q will be related by equation (38).

Now Dienes found by an empirical analysis of

experimental results that equation (37) was roughly obeyed by the values of D_0 and Q derived from nearly every self-diffusion coefficient made, as well as by those from a large number of dilute solution chemical diffusion measurements. (The latter we might expect to be roughly covered by equation (20) or (35) and any departure there from to be certainly masked by the approximation in (37).) The large range of values of D_0 considered by Dienes, including many which correspond to negative values of ΔS, is so very much larger than the departures of individual values of D_0 from the line of equation (37), that those latter seem relatively insignificant compared with the general trend expressed by equation (37).

The remarkable agreement found by Dienes between the experimental results and equation (37) does not then necessarily mean that this equation is a true representation of lattice behaviour. It is suspect on account of the negative values of ΔS which it allows, values which are inadmissible if the present theory of D_0 is at all valid. But more important, it may be only a demonstration that many measurements of D_0 and Q are in error, and that the errors are related at least approximately by equation (38). Undue significance is not then to be ascribed to Dienes' result in the absence of more careful experimental results.

Zener [6], and to a greater extent Nowick [23], both make use of the approximate equation (34) for discussing the diffusion coefficient of the solute in dilute alloys, assuming for μ'/μ_0 the value appropriate to the pure solvent. However, in the present state of our knowledge of vacancy diffusion in alloys, it is difficult to see to what extent this use of (34) is justified.

For example, any considerable correlation between successive moves of a solute atom will modify equation (4), upon which all other expressions for D and D_0 depend. Zener has analysed the case where diffusion occurs by the Johnson [24] "solute atom–vacancy molecule" mechanism, and maintains that (4) is unaffected. But this is not the only possibility. If vacancies, distributed at random in the lattice, exchange much more readily with solute than with solvent atoms, then as Johnson himself showed, D for solute atoms is given by (4) multiplied by a factor of the order z. Johnson rejected this mechanism on the grounds that Q for solute diffusion appeared always to be less than Q for self-diffusion of the solvent, but recent experiments [25] in extremely dilute solution show that this inequality may not be universally valid. It may only be a consequence of Kirkendall effects, significant even in quite dilute solid solution, producing abnormally low values of D_0 and Q. These effects are only absent at the extremely low concentrations employed in the experiments referred to.

Furthermore, returning to equation (20) from which (34) is derived, it is difficult to know what value of L_s to employ for an alloy. The choice will depend upon a more detailed knowledge of the mechanism of formation of vacancies in alloys than we possess at present and will influence the constant term in the exponential of (34), even if a corresponding proportionality between Q and L_s exists in this case, so that an equation of the same form as (34) may be derived.

Finally, it does not seem justifiable to use the solvent value of the elastic properties in (34), for the local elastic properties near a solute atom will differ markedly from the bulk average value, although this itself may not depart greatly from the solvent value.

Appendix I

It does not seem possible without elaborate calculation fully to justify the assumption made on p. 441, that the value of k_1 is unaffected if we put $\Delta S_1 = 0$ and then employ the bulk values rather than the local values of the elastic properties. Rough values of ΔS_1 can, however, be estimated on the basis of the same assumption and shown to be of the same order of magnitude as independent estimates of ΔS_1.

If the assumption is to be valid, then we must have

$$\Delta S_1 - (Q - k_1 L_s)\left(\frac{\mu'}{\mu_0} - \frac{\rho'}{\rho_0}\right) = -(Q - k_1 L_s)\left(\left(\frac{\mu'}{\mu_0}\right)^* - \frac{\rho'}{\rho_0}\right),$$

where the asterisk refers to the normal bulk values, i.e.,

$$\Delta S_1 = (Q - k_1 L_s)\,\frac{\partial \Delta \log \mu}{\partial T}. \tag{1a}$$

Now the free energy change ΔF_1 on forming a vacancy is

$$\Delta F_1 = \Delta H_1 + zRT \log \frac{\nu}{\nu^*},$$

where ν^* is the vibrational frequency of an atom in a normal lattice position and ν is the reduced frequency of vibration in the radial direction of each of the z neighbours of a vacancy. The change in entropy ΔS_1 is given by

$$\Delta S_1 = - zR \log \frac{\nu}{\nu^*}. \tag{2a}$$

But also $\Delta S_1 = - \partial \Delta F_1 / \partial T$. Therefore we must have

$$\frac{\partial \Delta H_1}{\partial T} = - zRT \frac{\partial \Delta \log \nu}{\partial T}$$

The frequency of vibration in one direction is related to the modulus for shear in that direction by $\nu \sim \mu^{\frac{1}{2}}$. Thus $\Delta \log \nu = \frac{1}{2}\Delta \log \mu$. Remembering that $\Delta H_1 = k_1 L_s$ we obtain

$$k_1 \frac{\partial L_s}{\partial T} = - \tfrac{1}{2} zRT \frac{\partial \Delta \log \mu}{\partial T}$$

and therefore

$$\Delta S_1 = - \frac{(Q - k_1 L_s) 2k_1}{zRT} \frac{\partial L_s}{\partial T}.$$

Rough values of $\partial L_s / \partial T$ are available and for each of the face-centred cubic metals ($z = 12$) give $\Delta S_1 \sim + 1$ cal/mol/deg., since $\partial L_s / \partial T$ is always negative. The necessary conditions that ΔS_1 should be positive and less than the experimental total entropy of activation ΔS_1 are therefore satisfied, and our initial assumption justified at least to this extent.

An independent estimate of ΔS_1 may be obtained by supposing that, when a vacancy is formed, the volume previously occupied by 13 atoms is now available for 12 atoms (for face-centred cubic lattices where $z = 12$). If V is the volume per atom there is then a change in log V of log (13/12). But the vibration frequency ν is related to V by

$$\frac{\partial \log \nu}{\partial \log V} = - \gamma$$

where γ = Gruneisan's constant, so that we find for ΔS_1, using equation (2a),

$$\Delta S_1 \sim zR\gamma \log (13/12).$$

This leads to values for ΔS_1 of $\sim$ 4–5 cal/mol/deg. These are a little larger than the previous estimate, but the results are sufficiently close to constitute at least an order of magnitude justification for our initial assumption.

McKenzie [26] has studied the effect of spherical holes in a solid on the bulk elastic properties of the solid. Since the characteristic frequency of a solid is determined by its elastic properties, the change in entropy ΔS_1 occasioned by the presence of vacancies may be estimated. The results of a calculation of ΔS_1 by this method give $\Delta S_1 \sim$ 3–4 cal/mol/deg.

References

1. Le Claire, A. D. Progress in Metal Physics, **1** (1949) 307–380.
2. Zener, C. Acta Cryst., **3** (1950) 346-54.
3. Huntington, H. B., and Seitz, F. Phys. Rev., **61** (1942) 315–25, 325–38.
4. Le Claire, A. D. Progress in Metal Physics, **4** (1953) 265–332.
5. Paneth, H. R. Phys. Rev., **80** (1950) 708–11.
6. Zener, C. J. Appl. Phys., **22** (1951) 372–5.
7. Le Claire, A. D. Phil. Mag., **42** (1951) 673–88.
8. Bardeen, J., and Herring, C. Atom Movements (Seminar of the Amer. Soc. Metals, 1951).
9. Mott, N. F. and Gurney, R. W. Electronic Processes in Ionic Crystals (O.U.P., 1951) Chap. **2**.
10. Rushbrooke, G. S. Trans. Faraday Soc., **36** (1940) 1055–62.
11. Wert, C. A. Phys. Rev., **79** (1950) 601–5.
12. Kê, T. S. Phys. Rev., **72** (1947) 41–46.
13. Zener, C. Acta Cryst., **2** (1949) 163–166.
14. Köster, W. Z. Metallk., **39** (1948) 1–9.
15. Seith, W. and Kiel, A. Z. Metallk., **24** (1933) 104–6. The values of D_0 and Q in Table I were obtained by a recalculation from the data given in this paper.
16. Johnson, W. A. Trans. A.I.M.E., **143** (1941) 107.
17. Zagrubskij, A. M. Bull. Acad. Sci. U.R.S.S. (Phys.), **6** (1937) 90.
18. Kubaschewski, O. Trans. Faraday Soc., **46** (1950) 713–22.
19. Buffington, F. S., Bakalar, I. D., and Cohen, M. Physics of Powder Metallurgy (New York, McGraw-Hill, 1951), chap. 6.
20. Nix, F. C. and Jaumot, F. E. Phys. Rev., **82** (1951) 72–4.
21. Liempt, J. A. M. van Rec. Trav. chim. Pays-Bas., **64** (1945) 239–49.
22. Dienes, G. J. J. Appl. Phys., **21** (1950) 1189–92.
23. Nowick, A. S. J. Appl. Phys., **22** (1951) 1182–6.
24. Johnson, R. P. Phys. Rev., **56** (1939) 814.
25. Martin, A. B. and Asaro, F. Phys. Rev., **80** (1950) 123.
26. McKenzie, J. K. Proc. Phys. Soc., **B63** (1950) 1.
27. Nowick, A. S. Phys. Rev., **82** (1951) 551.

THERMODYNAMIC ACTIVITIES IN IRON-NICKEL ALLOYS*

R. A. ORIANI†

The activity of Fe in iron-nickel alloys was studied in a differential apparatus by equilibrating mixtures of H_2O/H_2 gases over pure iron and over the alloys. Errors due to thermal diffusion are minimized in this design, and the measured activity of iron is corrected for the variation of the activity of wüstite with ambient gas composition. Formation of magnetite prevents the investigation of nickel-rich alloys. In the iron-rich face-centered cubic alloys the solid solution is very nearly ideal; the activity coefficients are generally only slightly smaller than unity, the entropies of mixing are slightly larger than the ideal values, and the heats of mixing are small positive numbers.

LES ACTIVITÉS THERMODYNAMIQUES DANS DES ALLIAGES FER-NICKEL

L'activité du fer dans les alliages fer-nickel a été étudiée dans un appareil différentiel, en équilibrant des mélanges gaseux H_2O/H_2 au-dessus du fer pur et au-dessus des alliages. Dans ce projet, les erreurs dues à la diffusion thermique sont réduites au minimum et l'activité mesurée du fer est corrigée pour la variation de l'activité de la wüstite avec la variation de la composition de l'atmosphère gaseuse. La formation de la magnetite empêche l'investigation des alliages riches en nickel. Dans les alliages riches en fer, de structure cubique à faces centrées, la solution solide est presque idéale; les coefficients d'activité sont, en général, légèrement plus grands que les valeurs idéales, et les chaleurs des mélanges sont faibles et positives.

THERMODYNAMISCHE AKTIVITÄTEN IN EISEN-NICKEL LEGIERUNGEN

Die Aktivität von Eisen in Eisen-Nickel Legierungen wurde mit Hilfe einer differenziellen Apparatur untersucht, in der die Gleichgewichtsdaten von H_2O/H_2 Gasmischungen über reinem Eisen und über den Legierungen bestimmt wurde. Die auf Grund der thermischen Diffusion auftretenden Fehler werden in dieser Anordnung klein gehalten, und die gemessene Aktivität des Eisens wurde für die Variation der Aktivität des Wüstits mit der ihn umgebenden Gasatmosphäre korrigiert. Wegen der Bildung von Magnetit ist es nicht möglich, die nickelreichen Legierungen zu untersuchen. In den eisen-reichen flächenzentriert-kubischen Legierungen ist die feste Lösung beinah ideal. Die Aktivitätskoeffizienten sind im allgemeinen nur wenig kleiner als eins, die Mischungsentropien sind etwas grösser als die idealen Werte, und die Mischungswärmen sind kleine, positive Zahlen.

The alloys of iron and nickel are of interest not only because of their commercial importance but also because they apparently form nearly ideal solid solutions in the iron-rich concentration range and exhibit a superlattice about the $FeNi_3$ composition. Since ideality in solid solutions is a great rarity, it is of interest to establish in detail the degree of approach to that condition, as well as the gradation from near ideality to the conditions characteristic of configurational order.

Experimental Details

Because the galvanic cell method cannot be used to study the activity of iron in iron-nickel alloys, the more difficult technique of gas equilibration was adopted. The reaction employed was

$$H_2O_{(g)} + Fe_{(s)} = FeO_{(s)} + H_{2(g)} \tag{1}$$

and is the same one used by Kubaschewski and Goldbeck [1]. The present apparatus (Figure 1) is differential in character, having two complete subsystems connected through a differential manometer and coupled to the same vacuum line. One subsystem contains pure iron in its reaction vessel, the other contains the iron-nickel alloy under investigation, and each subsystem has its own vessel of liquid water maintained at 0°C. An absolute manometer measures the pressure of hydrogen over the pure iron sample; the water vapor pressure in that subsystem is exactly cancelled by the pressure

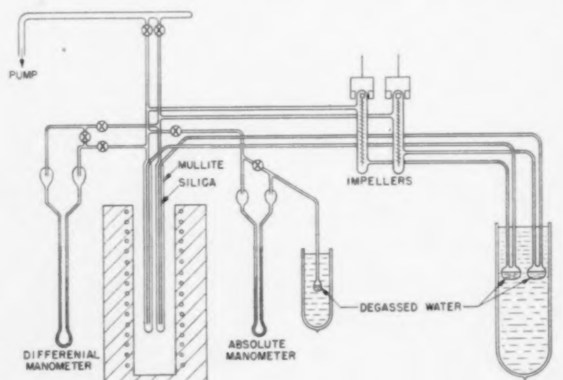

FIGURE 1. Differential equilibration apparatus.

of 0°C water in the manometer bulb. Each subsystem provides for closed-loop circulation which is aided by magnetically driven impellers.

The success of this kind of experiment depends to a large extent on avoiding the accumulation of any

*Received March 18, 1953.
†General Electric Research Laboratory, The Knolls, Schenectady, New York, U.S.A.

gases other than water and hydrogen. In order to avoid loss of hydrogen through the walls of the reaction chambers, heat-stabilized mullite* was used in preference to silica. The mullite tubes were freed of occluded gases prior to use by heating in a vacuum at 1200°C until no further gas evolution was observed. The alloys were made of carbonyl nickel and decarburized electrolytic iron, melted under vacuum in silica crucibles by induction heating. The alloys were homogenized at 1150°C for ten days in quartz ampoules sealed under argon. They were then rolled to strip or drawn to wire and thoroughly cleaned prior to placing within the mullite tube. The water in the reservoirs of the two subsystems and in the reference ampoule of the absolute manometer was thoroughly degassed by repeated alternate freezing and melting under vacuum until the vapor pressure of the water at 0°C was a constant 4.58 mm. Hg [3]. The manometers were filled with Octoil-S under vacuum; the oil was degassed prior to the filling operation by causing the oil to flow in a very thin film along the inside surface of a large glass bulb while a sticking vacuum was maintained. The density of the Octoil-S was measured at three temperatures within 10°C about the average room temperature.

The manometers were read by means of a cathetometer with a precision of 0.01 cm. The furnace employed was nichrome-wound and controlled within 5°C by a Brown Pyrometer Controller. The temperature was measured by means of a chromel-alumel thermocouple placed in contact with the two mullite tubes within the furnace. The calibration of the thermocouple was checked at the aluminum point by Mr. W. K. Murphy. The uncertainty in the temperature measurements in this work is estimated as 5°C.

In carrying out an experiment, the reservoir waters were frozen and kept at dry-ice temperature while the metal samples were introduced; the apparatus was then evacuated. As the furnace temperature was raised, the apparatus was checked for vacuum tightness. The reservoir waters were then warmed and maintained at 0°C within a large dewar filled with cracked ice and water. The reaction was followed for several days at constant temperature until constancy of manometer readings was assured, whereupon the furnace temperature was increased or decreased, the choice being usually made at random. Two experimental criteria were employed to judge whether or not any artifact vitiated any one determination; constancy with time of the pressures over both metals, and linearity of the plot of log of the pressure over the pure iron against reciprocal temperature (see Figure 2). After the runs the alloys were analyzed both for iron and for nickel, the precision being within 0.2 per cent.

Because oxidation rate data for iron-nickel alloys would be of interest in connection with testing the pertinent theories of oxidation, an attempt was made to obtain such information incidentally to the main purpose of the present study.

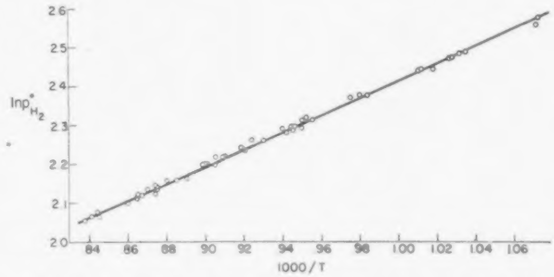

FIGURE 2. Manometer reading of hydrogen pressure over pure iron vs. reciprocal absolute temperature.

The results of such efforts are shown in Figures 3*a* and 3*b*, and indicate that since the rates of reaction were independent of temperature, both for the pure iron and for the alloy, it must be concluded that the controlling process in our apparatus is the transport of water vapor from the reservoirs to the furnace. However, the relatively high values of diffusivity of H_2O through H_2 measured by Schwertz and Brow [4] point to the vaporization from the water surface as the limiting factor, particularly since heat transfer to the free surface is greatly impeded by the absence of convection currents in water at 0°C.

Experimental Results

Assuming that only the iron in the alloys oxidizes in the H_2O/H_2 mixture, that wüstite of identical composition is formed on both the pure iron and on the alloys, and that the thermal diffusion effect in the vapor phase is negligible, then at equilibrium,

$$K(T) = \frac{(p'_{H_2})(a'_{FeO})}{(p'_{H_2O})(a'_{Fe})} = \frac{(p^0_{H_2})(a^0_{FeO})}{(p^0_{H_2O})},$$

where $K(T)$ is the equilibrium constant at temperature T for reaction (1), p is the observed pressure, a is the thermodynamic activity; superscripts ^{0} and $'$ refer to the pure iron and the alloy subsystems respectively. Since by hypothesis $a^0_{FeO} = a'_{FeO}$,

*Measurements by Dr. F. Norton [2] of this Laboratory show that at 665°C the permeability of silica to H_2 is about 1.8×10^{-9}, and that of mullite is 1.8×10^{-11} cm³ (at N.T.P.) /cm²/mm/cm. Hg/sec.

and by design $p^0_{H_2O} = p'_{H_2O}$, the activity of iron in the alloy can at once be computed from the readings of the two manometers,

$$(2) \qquad a'_{Fe} \equiv a^*_{Fe} = \frac{p_{H_2}}{p^0_{H_2}} = 1 - \frac{\Delta p}{p^0_{H_2}}$$

where Δp is the reading of the differential manometer.

The assumption that NiO does not form is given credence by the results of Hickmann and Gulbransen [5] on oxidation of iron alloys with nickel contents

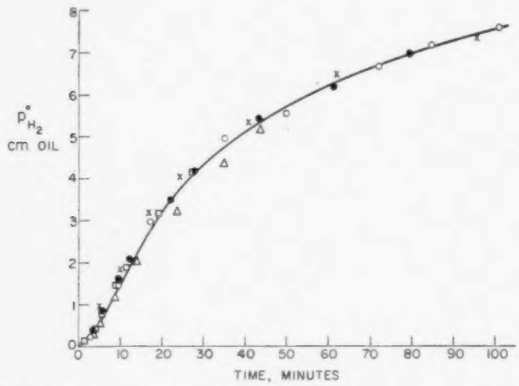

FIGURE 3*a*. Rate of production of hydrogen over pure iron. □ 777°C; ● 835°C; Δ 860°C; ○ 869°C; + 903°C.

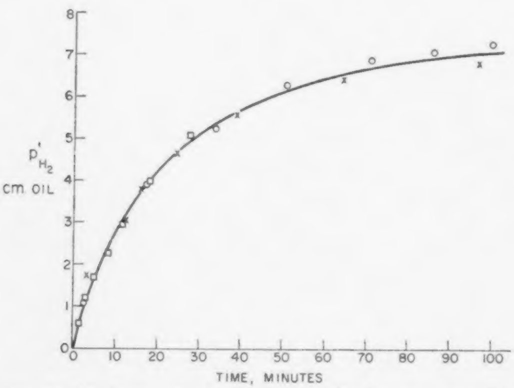

FIGURE 3*b*. Rate of production of hydrogen over Fe-Ni alloy, $x_{Fe} = 0.930$. □ 777°C; ○ 869°C; + 903°C.

as high as 80 per cent. Furthermore, examination by X-ray diffraction (by Mrs. Beulah Decker of this Laboratory) of the oxide formed on an alloy of 10 per cent Ni failed to reveal the presence of NiO; an electron diffraction study of the oxide on an alloy of $x_{Fe} = 0.441$ (by Miss E. Alessandrini of this Laboratory) also failed to show the presence of NiO. However, this study proved the presence of Fe_3O_4 on this alloy, and explained the anomalously high values obtained for this composition. The data are entered in Table I. The formation of

TABLE I

IDENTIFICATION OF Fe_3O_4 ON ALLOY OF $x_{Fe} = 0.441$

Observed spacings (Å)	Tabulated spacings from Fe_3O_4 (Å)
2.467	2.42
2.062	2.10
1.773	1.72
1.609	1.61
1.457	1.48
1.297	1.279
1.091	1.092
0.962	0.966
0.830	0.825

the higher oxide destroys the differential feature of the present apparatus. On the other hand, our data cannot be combined with literature data on the free energy of formation of Fe_3O_4 in order to evaluate the activity of iron in the alloy because the literature data [6] would predict that the alloy of $x_{Fe} = 0.441$ ought not to form Fe_3O_4 at 827°C:

$$(3) \qquad Fe_3O_4 + \gamma Fe = 4FeO, \qquad \Delta G^0 = -3196 \text{ cal. at } 827°C.$$

Hence,

$$\Delta G = \Delta G^0 + RT \ln (0.441)^{-1} = -3196 + 1790 = -1406 \text{ cal.}$$

The ΔG^0 for the above reaction must be calculated by subtraction of the ΔG^0 for $3Fe(\gamma) + 2O_2 = Fe_3O_4$ from the ΔG^0 for $4Fe(\gamma) + 2O_2 = 4FeO$, so that the error in the difference may be large. It is interesting to note that at 627°C, the same literature data yield $\Delta G^0 \approx 0$ for reaction (3) for the alloy $x_{Fe} = 0.441$ so that lower temperatures favor the formation of magnetite. This temperature coefficient probably explains our observation that if the alloy of $x_{Fe} = 0.441$ was maintained at temperatures higher than 850°C, the pressure of hydrogen reached a steady value which yielded a reasonable value of a^*_{Fe} for the alloy. However, when the alloy was cooled to a lower temperature, the p'_{H_2} rose to anomalously high values which persisted if the temperature were subsequently increased. This is the reason why only one high-temperature value is listed in Table II for this high-nickel alloy; it represents a measurement of dubious value upon a metastable system, and the temperature variation could not be obtained. The measurements therefore had to be discontinued at $x_{Fe} = 0.441$, despite the interest attaching to alloys near the $FeNi_3$ composition.

Emmet and Schulz [7] discuss the serious error introduced in measurements on static systems

TABLE II

EXPERIMENTAL RESULTS

	t°C	a^*_{Fe}	a^α_{Fe}	a^γ_{Fe}
$x_{Fe} = 0.930$				
	710	0.968	0.950	0.90_7
	714	.965	.946	$.90_5$
	746	.961	.945	$.91_7$
	777	.952	.936	$.91_7$
	839	.932	.919	$.91_2$
	837	.936	.921	$.91_3$
	869	.926	.910	$.90_6$
	891	.922	.909	$.90_8$
	903	.920	.905	$.90_5$
$x_{Fe} = 0.854$				
	700	.889	.870	$.82_7$
	744	.870	.855	$.82_9$
	787	.865	.850	$.83_5$
	824	.847	.833	$.82_4$
	837	.849	.834	$.82_7$
	876	.841	.826	$.82_3$
$x_{Fe} = 0.808$				
	696	.856	.835	$.79_2$
	749	.842	.824	$.80_0$
	790	.829	.813	$.80_0$
	839	.821	.796	$.79_0$
$x_{Fe} = 0.721$				
	714	.780	.761	$.72_8$
	772	.766	.746	$.73_0$
	836	.748	.729	$.72_3$
	872	.738	.721	$.71_8$
	896	.735	.717	$.71_6$
	908	.729	.711	$.71_1$
$x_{Fe} = 0.598$				
	657	.692	.675	$.62_5$
	700	.680	.662	$.62_9$
	751	.660	.643	$.62_5$
	808	.648	.628	$.62_0$
	879	.620	.603	$.60_1$
$x_{Fe} = 0.441$				
	840	(.45)	(.43)	(.43)

a^*_{Fe} is the uncorrected quantity computed by equation (2).
a^α_{Fe} is the activity of Fe relative to α-Fe, after correction for the non-unity activity of the wüstite.
a^γ_{Fe} is the activity of Fe relative to γ-Fe.

when the effect of thermal diffusion is neglected. In the present apparatus, the differential character of the measurement would be expected greatly to diminish the error. Kubaschewski and Goldbeck [1] have derived the relation

$$(4)\ \log\left(\frac{p_{H_2O}}{p_{H_2}}\right)_{T_2} = 1.035 \log\left(\frac{p_{H_2O}}{p_{H_2}}\right)_{T_1} - 0.21 \times 10^{-3}(T_2 - T_1)$$

from the experimental data of Shibata and Kitagawa [8] for thermal diffusion in H_2O/H_2 vapors between the higher temperature T_2 and the lower temperature T_1. Using this equation one finds that if the gas impellers were not at all effective in overcoming the effect of thermal diffusion, the error in $a^*_{Fe} = 0.60$ as computed by equation (2) would be a positive one of 0.8 per cent at 1020°C. This error would decrease for lower temperatures and for values of a^*_{Fe} nearer unity. Furthermore, that the stirrers are partially effective in overcoming the effect of thermal diffusion is shown by the slope of the ln $p^0_{H_2}$ vs. $1/T$ of Figure 2 in which the $p^0_{H_2}$ is the pressure of hydrogen over the pure iron as measured by the oil manometer (density corrected to that at 27°C) which is at room temperature. The present slope is 2.14×10^3, to be compared with the value of 1.93×10^3 obtained from the combined data of Emmet and Schulz [9] and of Austin and Day [10], a disparity of about 11 per cent; however, if the effect of thermal diffusion were not at all counteracted, the disparity would be in the same direction and 40 per cent [7]. Hence, it may be concluded that the error in a^*_{Fe} due to residual thermal diffusion in both subsystems is certainly less than 0.5 per cent.

The assumption that the wüstite on the alloy has the same composition and hence the same activity as does the wüstite on the pure iron cannot be quite correct, since the gas composition at equilibrium over the alloy differs from that over the pure iron. The composition of the alloy at any one temperature fixes the H_2O/H_2 ratio in the gas phase, and the latter determines the composition and activity of the wüstite on that alloy. The data in the paper by Darken and Gurry [11] make possible by interpolation the calculation of the activity of the wüstite that corresponds to the observed H_2O/H_2 ratio over the alloy. The activity of that wüstite varies from 0.97 to 0.985, referred to unit activity for wüstite in contact with pure iron at corresponding temperatures. These numbers multiply the a^*_{Fe} to yield the values tabulated in the third column of Table II, and graphed in Figure 4. This quantity, a^α_{Fe}, is the activity of iron in the alloy with respect to α-Fe as the reference state, since that is the allotropic form of pure iron actually existing at the experimental temperatures.

Since the structure of the alloys in the temperature range investigated is that of γ-iron, the supercooled γ-Fe would be a more relevant reference state for the activity of Fe in the alloys. The values of a^α_{Fe} were reduced to a^γ_{Fe} by the use of the data for the temperature dependence of the free energy difference between α-Fe and γ-Fe collated by

Fisher [12]. The $a^{\gamma}{}_{\mathrm{Fe}}$ are tabulated in the fourth column of Table II.

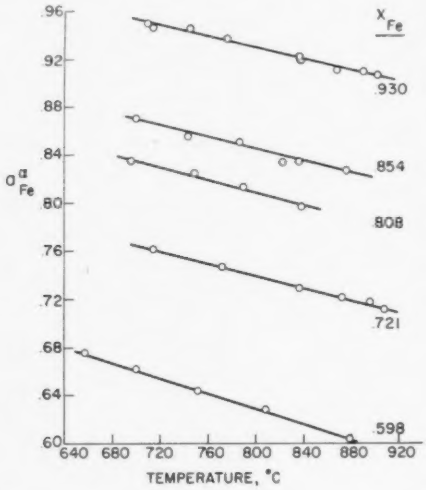

FIGURE 4. Activity of Fe in Fe-Ni alloys relative to α-iron.

Discussion of Results

These data have been used to calculate the deviation at 840°C from ideality of the γ-Fe-Ni solid solutions, by using the relevant thermodynamic equations in the following form [13]:

$$(5)\quad \overline{\Delta G}^{(x)}_{\mathrm{Fe}} \equiv \overline{\Delta G}_{\mathrm{Fe}} - \overline{\Delta G}_{\mathrm{Fe}}(\text{ideal}) = RT \ln (a/x),$$

$$(6)\quad \overline{\Delta G}^{(x)}_{\mathrm{Ni}} \equiv \overline{\Delta G}_{\mathrm{Ni}} - \overline{\Delta G}_{\mathrm{Ni}}\,(\text{ideal})$$

$$= \int_0^x \frac{\overline{\Delta G}^{(x)}_{\mathrm{Fe}}\, dx}{(1-x)^2} - \frac{\overline{\Delta G}^{(x)}_{\mathrm{Fe}}\, xy}{(1-x)^2},$$

$$(7)\qquad \Delta G^{(x)} = x\overline{\Delta G}^{(x)}_{\mathrm{Fe}} + y\overline{\Delta G}^{(x)}_{\mathrm{Ni}},$$

$$(8)\quad \overline{\Delta S}^{(x)}_{\mathrm{Fe}} \equiv \overline{\Delta S}_{\mathrm{Fe}} - \overline{\Delta S}_{\mathrm{Fe}}(\text{ideal})$$

$$= -R\left[T\frac{\partial \ln a}{\partial T} + \ln\frac{a}{x}\right],$$

$$(9)\quad \overline{\Delta S}^{(x)}_{\mathrm{Ni}} \equiv \overline{\Delta S}_{\mathrm{Ni}} - \overline{\Delta S}_{\mathrm{Ni}}\,(\text{ideal})$$

$$= \int_0^x \frac{\overline{\Delta S}^{(x)}_{\mathrm{Fe}}\, dx}{(1-x)^2} - \frac{\overline{\Delta S}^{(x)}_{\mathrm{Fe}}\, xy}{(1-x)^2},$$

$$(10)\qquad \Delta S^{(x)} = x\overline{\Delta S}^{(x)}_{\mathrm{Fe}} + y\,\overline{\Delta S}^{(x)}_{\mathrm{Ni}},$$

$$(11)\qquad \Delta H = \Delta G^{(x)} + T\Delta S^{(x)},$$

$$(12)\qquad \ln a_{\mathrm{Ni}} = \frac{\overline{\Delta G}^{(x)}_{\mathrm{Ni}}}{RT} + \ln y.$$

In these equations, $\overline{\Delta G}_i^{(x)}$ is the partial molar excess free energy of solution of component i, $\overline{\Delta S}_i^{(x)}$ is the partial molar excess entropy of solution of i; $\Delta G^{(x)}$, $\Delta S^{(x)}$, and ΔH are the corresponding total free energy, entropy, and enthalpy of solution in excess over the ideal values. R is the gas constant, $a \equiv a^{\gamma}{}_{\mathrm{Fe}}$, a_{Ni} is the activity of nickel in the alloy; $x \equiv x_{\mathrm{Fe}}$ and y is the atom fraction of nickel in the alloy. In carrying out the graphical integration in equation (6) the point at $x_{\mathrm{Fe}} = 0.441$ was included; furthermore, in extrapolating the integrand to $x_{\mathrm{Fe}} = 0$ (the region which is experimentally inaccessible) the assumption was made that the sign of the $\overline{\Delta G}^{(x)}_{\mathrm{Fe}}$ would remain negative from $x_{\mathrm{Fe}} = 0.441$ to 0. This is compatible with the normal expectation of short-range order in the region of the phase diagram above and about a superlattice structure. Unfortunately, this extrapolation (see Figure 5) supplies

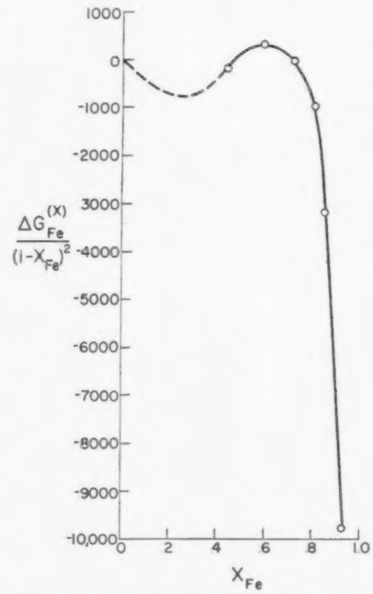

FIGURE 5. Curve for the graphical integration of equation (6).

the chief contribution to the integral in the range from $x_{\mathrm{Fe}} = 0.441$ to 0.721, so that the course of the curve of a_{Ni} vs. x_{Fe} of Figure 6 is relatively poorly known in that composition range. The integrand in equation (9) must be extrapolated even farther since there is no point at $x_{\mathrm{Fe}} = 0.441$, but the shape of the curve is such that the extrapolated section contributes relatively less to the integral of equation (9) than does the corresponding extrapolation of Figure 5 to equation (6). For these reasons more reliance may be placed on the derived data corresponding to the alloys of higher iron content than on those of lower x_{Fe}.

TABLE III

CALCULATED THERMODYNAMIC QUANTITIES AT 840°C*

x_{Fe}	a^{γ}_{Fe}	$\overline{\Delta G}^{(x)}_{\mathrm{Fe}}$	$\Delta G^{(x)}_{\mathrm{Ni}}$	$\Delta G^{(x)}$	a_{Ni}	$\overline{\Delta S}^{(x)}_{\mathrm{Fe}}$	$\overline{\Delta S}^{(x)}_{\mathrm{Ni}}$	$\Delta S^{(x)}$	ΔH
0.930	0.91_0	− 48.0	− 732	− 96	0.05	0.04	0.74	0.09	6
0.854	0.82_8	$-67._5$	79	− 46	0.15	0.06	0.54	0.13	99
0.808	0.79_5	$-35._8$	− 82	− 44	0.18	0.03	0.68	0.15	130
0.721	0.72_0	$-3._1$	− 187	− 54	0.25	0.31	− 0.17	0.17	139
0.598	0.61_2	$51._1$	− 294	− 88	0.35	0.28	− 0.14	0.11	37
0.441	(0.43)	$-56._0$	− 193	− 132	0.51	—	—	—	—

*Units of free energy and enthalpy quantities are cal/mol; units of the entropy quantities are cal/mol/deg.

The present results (Table III) agree qualitatively with those of Kubaschewski and Goldbeck [1] in that the deviations of all the thermodynamic quantities from those corresponding to an ideal solution are very small. Because the quantities of Table III are excess molar quantities of very small magnitude the relative uncertainties are large. Nevertheless, the trends appear significant. The

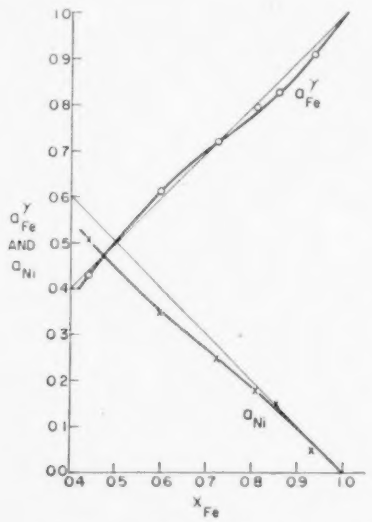

FIGURE 6. Activities of Fe and of Ni in iron-nickel alloys at 840°C.

present measurements indicate a slightly larger than ideal entropy of mixing and very small positive heats of mixing. Kubaschewski and Goldbeck calculated a series of small negative heats of mixing using mainly their data in the range of nickel concentration where the present results indicate that magnetite is the stable oxide; in subsequent calculations they employ the ideal entropy of mixing rather than the quantity calculable from their measurements.

The changes in the thermodynamic quantities consequent on mixing one component in another can be divided into two portions, the configurational and the thermal [14]; thus,

$$\Delta S = \Delta S\text{ (configurational)} + \Delta S\text{ (thermal)},$$
$$\Delta H = \Delta H\text{ (configurational)} + \Delta H\text{ (thermal)}.$$

The configurational terms refer to the mixing process at 0°K; the ΔS(configurational) will be smaller than the ideal value if the configuration represents any deviation from perfect randomness, and the ΔH(configurational) can be expressed, according to the usual nearest-neighbor approximation [15], by $-n_{12}[\epsilon_{12} - \frac{1}{2}(\epsilon_{11} + \epsilon_{22})]$, where n_{12} is the number of nearest-neighbor pairs of atoms of dissimilar species, and the ϵ_{ij} are pairwise interaction energies between nearest neighbors of kind i, j.

The "thermal" quantities may be approximated by

$$\Delta S(\text{thermal}) = \int_0^T \Delta C_p \, d \ln T$$

and

$$\Delta H(\text{thermal}) = \int_0^T \Delta C_p \, dT$$

where ΔC_p is the change in heat capacity associated with the reaction

$$x_1 M_1 + x_2 M_2 = [(M_1)_{x_1}(M_2)_{x_2}].$$

Hence, a very small, positive value of ΔC_p is sufficient to explain the slightly larger than ideal, measured entropy and heat of mixing. However, the calorimetric measurements of Zuithoff [16] indicate a very small, negative ΔC_p for iron-nickel alloys. Since the technique of drop calorimetry employed is apt to lead to error in cases such as the present when the low-temperature reference state is not an equilibrium state, it is believed that it is more likely that these alloys are characterized by a very small positive deviation from the Kopp-Neumann rule of additivity of heat capacity as indicated by the present results.* This in turn implies that the

*Another reason why the accuracy of Zuithoff's heat capacity data is doubtful is that no correction was made for the loss of heat by radiation and convection from the capsule during its descent from furnace to calorimeter.

configurational ΔS is probably very close indeed to the ideal value, and that the configurational $\Delta H \approx 0$, so that the atomic distribution is essentially random in the alloys of lower nickel content. The increase in the $-\Delta G^{(x)}$ and the decrease in $\Delta S^{(x)}$ and ΔH as the atom fraction of nickel increases, as shown in Table III, seem to indicate the trend to be expected if short-range order is to exist in alloys of the composition about $FeNi_3$ but at temperatures above the critical temperature of ordering [17]. If the contribution from the thermal terms remains small, the quasi-chemical theory of order would require that ΔH and $\Delta S^{(x)}$ become negative, and that $a^{\gamma}_{Fe} < x_{Fe}$.

Zener [18], Oelsen [19], and Jones and Pumphrey [20] have used practically identical approaches to calculate the $\alpha/(\alpha + \gamma)$ and the $(\alpha + \gamma)/\gamma$ boundaries in the Fe-Ni system. Assuming the Kopp-Neumann rule for both phases, that the entropy of mixing is ideal for both phases, and that a quantity δH is independent of concentration and of temperature, they are able to calculate the phase boundaries with good precision. The δH is the difference between the heats of solution of one component in the α and the γ phases, and is treated as a parameter to be evaluated from the experimental phase diagram. Oelsen obtains 1100 cal/mol for this quantity, Zener obtains 1600, and Jones and Pumphrey 2500; they all obtain equally good matching with the experimental phase diagram. In view of this lack of sensitivity and of the fact that the present data do not supply any knowledge concerning the α-phase, it is not worthwhile to try to improve these authors' calculations on the basis of the present results.

This research was supported by AEC Contract No. W-31-109-Eng.-52.

References

1. KUBASCHEWSKI, O. and GOLDBECK, O. VON. Trans. Faraday Soc., **45** (1949), 958.
2. NORTON, F. J. J. Ceramic Soc., **36** (1953) 90.
3. Handbook of Chemistry and Physics, 32nd ed. (Chemical Rubber Publishing Co., 1951).
4. SCHWERTZ, F. A., BROW, J. E. J. Chem. Phys., **19** (1951) 640.
5. HICKMANN, J. W. and GULBRANSEN, E. A. Trans. A.I.M.E., **171** (1947) 344.
6. THOMPSON, M. DEKAY. The Total and Free Energies of Formation of the Oxides of Thirty-two Metals (The Electrochemical Soc., 1942).
7. EMMET, P. H. and SCHULZ, J. F. J. Amer. Chem. Soc., **55** (1933) 1376.
8. SHIBATA, Z. and KITAGAWA, H. J. Fac. Sci., Hokkaido Imp. Univ., Sec. III, **2** (1938) 223.
9. EMMET, P. H. and SCHULZ, J. F. J. Amer. Chem. Soc., **52** (1930) 4268.
10. AUSTIN, J. B. and DAY, M. J. Ind. Eng. Chem., **33** (1941) 23.
11. DARKEN, L. S. and GURRY, R. W. J. Amer. Chem. Soc., **67** (1945) 1398.
12. FISHER, J. C. Trans. A.I.M.E., **187** (1949) 688.
13. WAGNER, C. Thermodynamics of Alloys (Addison-Wesley Press, 1952).
14. LUMSDEN, J. Thermodynamics of Alloys (London, The Institute of Metals, 1952).
15. FOWLER, R. and GUGGENHEIM, E. A. Statistical Thermodynamics (Cambridge Univ. Press, 1949).
16. ZUITHOFF, A. J. Rec. Trav. chim. Pays-Bas, **59** (1940) 131.
17. ORIANI, R. A. Acta Met., **1** (1953) 144.
18. ZENER, C. Trans. A.I.M.E., **167** (1946) 513.
19. OELSEN, W. Stahl u. Eisen, Düsseldorf, **69** (1949) 468.
20. JONES, F. W. and PUMPHREY, W. I. J. Iron Steel Inst., **163** (1949) 121.

The Plasticity and Fracture of Irradiated AgCl Single Crystals*

This letter will discuss the changes produced in the plastic and fracture properties of AgCl when it is irradiated with X-rays or with ultraviolet light. Stepanow [1] has obtained stress-strain curves for AgCl single crystals. Nye [2] working with polycrystals found the glide direction to be $\langle 110 \rangle$ but that the orientations of the slip planes are not quite definite. Podaschewsky [3] found that volume coloration of rock salt single crystals by either X-rays or ultraviolet light increases the yield stress and the tensile strength of the material. When the absorption constant in the F band reached 5.5×10^{-3} mm^{-1}, both the yield stress and tensile strength were about doubled.

Flat tensile specimens were cut from a large single crystal of AgCl produced by the Harshaw Chemical Company. They were shaped, polished, etched, and then thoroughly annealed according to the procedure of J. R. Hanes [4]. The dimensions of the specimens between the grips of the tensile machine were $10 \times 4 \times 1$ mm^3. The upper half of the specimen was then irradiated, the specimen being turned over during the irradiation so that both faces of large area were colored. The ultraviolet light from a G. E. 4H lamp produces only surface darkening. The exposure times were several minutes. The X-rays were the unfiltered radiation from a molybdenum target (50 K.V. and 18 m.a.). Volume-coloration (not uniform throughout) is produced by X-ray exposures of a day or so. Spectrophotometric analysis of the colored crystals showed a very broad absorption band ranging from 4000Å to 7000Å, the maximum absorption was at 5200Å.

The specimen was then stressed and observed with a microscope focussed on the boundary separating the colored and the uncolored portions of the crystal. The commencement of plastic deformations in surface-colored specimens can be detected either by the onset of birefringence or by the appearance of glide steps on the surface of the specimen. In the case of volume-coloration only the second method can be used. Observations on 20 specimens lead to the following conclusions:

1. Surface coloration produces little if any hardening relative to the uncolored crystal, i.e., slip lines appear in the surface colored region at essentially the same stress as that required for slip in the uncolored region. Furthermore, slip lines are observed to cross the boundary between the two regions without any noticeable change in them. This may indicate that in AgCl slip is initiated *not* necessarily at the surface of the specimen.

2. Volume-coloration hardens the crystal relative to the uncolored crystal. In certain crystals in which the slip lines in the uncolored region run approximately parallel to the coloration boundary, a large increase in stress is required to produce slip lines of the same system in the colored region. Observations on crystals having slip lines which meet the coloration boundary show that the slip lines terminate in the colored region. Increasing the stress will extend the slip line further into the colored region.

3. The fracture strength of a volume-colored crystal is larger than that of an uncolored crystal. This is similar to the results found on NaCl with and without impurities [5].

4. In volume-colored polycrystals brittle fracture often occurs along the grain boundaries with little or no prior deformation. Whether the break (without necking) runs completely along grain boundaries or partly through one or more grains depends on the geometrical arrangement of the grains and probably also on their orientation. In the former case the fracture strength is remarkably low, often only little higher than the uncolored yield stress. It has been observed that the grain boundaries darken more rapidly than the remainder of the grains during X-ray irradiation. For instance, after X-ray exposure of one-half hour the grain boundaries of a AgCl thin plate, whose crystallites are of millimeter size, become visible against the only slightly darkened background.

Quantitative observations are not carried out because of the following difficulties: The absorption of the volume-colored specimens is so great that the absorption constant cannot be measured, and consequently the rate of coloration has not been determined. Secondly, the coloration is not uniform even in single crystals. Thirdly, the increases in yield stress and fracture strength while observable are not as large as those produced by F-centers in NaCl [3]. This last difference may arise because impurities in atomic distribution are more effective in hardening than precipitates in this case.

*Received March 2, 1953.

In a very recent note, Frankl and Read [6] report that they measured the changes of the internal friction of NaCl when F-centers were introduced and removed. Their result leads to the same conclusion as can be drawn from that of Podaschewsky's experiment, i.e., the mobility of dislocations is greatly decreased by the formation of F-centers and does not recover when the F-centers are bleached at room temperature. Frankl and Read proposed the hypothesis that the dislocations are pinned down by the attachment of positive-ion vacancies, which are freed by the formation of F-centers from vacancy-pairs.

Hardness tests by the author show that Knopp hardness number increases remarkably by the introduction of F-centers from 17 for annealed NaCl crystal plates to 31 for the same specimens irradiated by X-rays. (The longitudinal axis of the diamond indentor is set in parallel with the crystal cubic edges.)

This work was carried out at the University of Illinois. The author wishes to thank Professors J. S. Koehler and F. Seitz for their helpful interest. The material cost of this research was financed through Contract Nonr–177(00).

Yin-Yuan Li

Metals Research Laboratory
Carnegie Institute of Technology
Pittsburgh, Pennsylvania

References

1. Stepanow, A. W. Phys. Z. Sowjet., **8** (1936) 23.
2. Nye, J. F. Proc. Roy. Soc., **198A** (1949) 190; **200A** (1949) 47.
3. Podaschewsky, M. N. Phys. Z. Sowjet., **8** (1936) 79.
4. Haynes, J. R. Rev. Sci. Inst., **11** (1948) 51.
5. Metag, W. Z. Phys., **78** (1932) 363; Edner, A. Z. Phys., **73** (1932) 623.
6. Read and Frankl Phys. Rev., **89** (1953) 663.

High Temperature Hexagonal Phase of Cobalt*

It has occasionally been proposed that pure cobalt transforms from a face-centered cubic to a hexagonal close-packed structure when it is heated to temperatures higher than about 1100°C [1; 2; 3; 4]. The idea has probably stemmed from the known similarity of this element with its closely related neighbor, iron. The iron lattice is body-centered cubic at low temperatures, transforms to a face-centered cubic structure at 910°C and then back to body-centered cubic at about 1400°C. By analogy it was thought that cobalt, which is known to have a hexagonal close-packed lattice at low temperatures and a face-centered cubic lattice above about 450°C, might transform back to a hexagonal lattice at a high temperature. Numerous observed effects have been offered in support of this hypothesis, all of which have been indirect in nature. The observations prior to 1948 have been summarized by Troiano and Tokich [5]. Their data for X-ray diffraction studies of quenched samples show that below 400–500°C the hexagonal form is stable; from this temperature to about 700°C the cubic form can be retained alone on quenching, from still higher temperatures results in the reappearance of the hexagonal form. They attributed the reappearance of the hexagonal form to a grain coarsening effect of the thermal treatment on the transformation rate in the normal 400–500°C range during quenching rather than to a second transformation. High temperature X-ray diffraction results which had been obtained up to the time of the work of Troiano and Tokich had failed to indicate a second transformation at any temperature up to 1187°C. More recently Metcalfe [2; 4] has interpreted dilatometric data as evidence for second transformation at a temperature in the range near the upper limit of previous observation by high temperature X-ray diffraction studies. Thus, it would seem desirable to extend high temperature X-ray diffraction studies to even higher temperatures.

In the present extension of the work, two high-temperature Debye-Scherrer photographs of high-purity cobalt wires were made. The photographs were obtained through the courtesy of Dr. Gordon Skinner, who used the camera described by Johnston and co-workers [6].

Before they were mounted in the X-ray camera, the wires were sealed in argon-flushed and evacuated quartz tubes. They were then held for two hours at 1150°C and 1220°C, respectively, and quenched into water. During the subsequent X-ray exposures, the wires were held at 1147° and $1223° \pm 10°C$, respectively. The air pressure in the camera was less than 10^{-5} mm. of mercury throughout the exposure, except for a few minutes after the heating current was turned on, when it rose to 5×10^{-5} mm. Room temperature Debye-Scherrer patterns were also made before and after the wires were heated in the high-temperature camera. Filtered chromium radiation was used for all pictures.

*Received April 3, 1953.

The results of the experiments are listed in Table I, together with the lattice parameters. Before being heated in the X-ray camera, the wires contained roughly equal amounts of cubic and hexagonal phases; after the high-temperature pattern was made, the proportion of cubic cobalt was less. Presumably this is due to the grain size coarsening of the wire in the high-temperature X-ray camera.

TABLE I

Treatment	Phases	Lattice constants *a*	*c*
(*a*) 1150°C, 2 hrs, W.Q. Room temp. photo	Equal amounts of hex. and cubic	2.505 3.544	4.06 —
(*b*) Spec. (*a*) at 1147°C. High-temp. photo	Single f.c.c. only	3.626	—
(*c*) Spec. (*b*) after cooling. Room temp. photo.	Hex. + cubic. More cubic than in (*a*)	Same as (*a*)	
(*d*) 1220°C, 2 hrs, W.Q. Room temp. photo	Equal amounts of hex. + cubic	Same as (*a*)	
(*e*) Spec. (*d*) at 1223°C. High-temp. photo.	Single f.c.c. only	3.631	—
(*f*) Spec. (*e*) after cooling. Room temp. photo.	Hex. + cubic; Larger grains; lines slightly more diffuse	Same as (*a*)	

Specimens held at 1147°C and 1223°C during the X-ray exposure produced a strong face-centered cubic diffraction pattern with no other lines present. The high-intensity $10.1_{\text{hex.}}$ line is predominant in the patterns made at room temperature, a portion of which is shown diagrammatically in Figure 1*a*. On the other hand, the patterns made at high temperatures (Figure 1*b*)

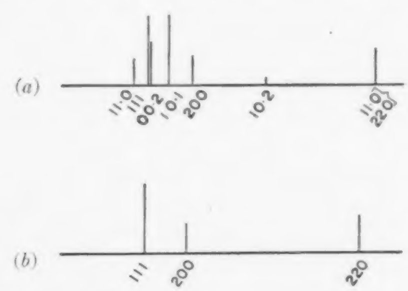

FIGURE 1. Diagrammatic representations of corresponding portions of Debye-Scherrer patterns of cobalt wire. During the exposures the specimen was held at (*a*) room temperature and (*b*) 1147°C or 1223°C.

show no trace of this line, indicating that the hexagonal phase was absent during the exposure. The increase in lattice parameter of the cubic phase for the high temperature over room temperature measurements is such as to be reasonably accounted for by normal thermal expansion. Therefore when the results are added to previous observations, it may be concluded that the face-centered cubic phase is stable from about 450°C up to at least 1223°C.

J. B. NEWKIRK and A. H. GEISLER

General Electric Research Laboratory
The Knolls
Schenectady, New York, U.S.A.

References

1. SYKES, W. P. and GRAFF, H. F. Trans. A.S.M. **23** (1935) 249–283.
2. METCALFE, A. G. Proc. First World Met. Congr., A.S.M. (1952) 717–731.
3. SEYBOLT, A. U. and MATHEWSON, C. H. Trans. A.I.M.E., **117** (1935) 156–172.
4. METCALFE, A. G. J. Metals, **5** (1953) 357–364.
5. TROIANO, A. R. and TOKICH, J. L. Trans. A.I.M.E., **175** (1948) 728–739.
6. EDWARDS, J. W., SPEISER, R., and JOHNSTON, H. L. Rev. Sci. Inst., **20** (1949) 343–347.

Mercury Whiskers*

Volmer and Estermann [1] have described the formation of thin mercury platelets by the condensation of mercury vapor on a glass surface cooled below the freezing point of mercury. In the course of experiments aimed at characterizing the details of the growth mechanism for these platelets it has been discovered that whiskers of solid mercury can be grown on a cold glass substrate. The whiskers are of the order of 1 mm. in length and 0.01 micron in radius. The evidence obtained so far can be interpreted if it is assumed that the whiskers are crystals of mercury whose sole imperfection is an axial screw dislocation.

If a glass surface cooled to -63.5°C is placed in contact with mercury vapor at 6×10^{-6} mm. Hg pressure and -50°C, fine mercury whiskers grow out from the glass surface. They demonstrate no preferred orientation with respect to the normal to the substrate surface. If the mercury pressure is increased, the number of whiskers per unit area of glass substrate increases. The whiskers can be seen to oscillate about their point of attachment

*Received April 15, 1953.

to the glass surface in Brownian motion. They grow with great rapidity in the sense that the growing end of the fiber advances approximately five thousand times more rapidly than can be accounted for by the impingement rate of mercury atoms upon the whisker end from the vapor phase.

The concept of screw dislocations [2] suggests a simple rationalization of the mechanism of whisker growth. Ignoring temporarily how the dislocation is introduced into a mercury nucleus, once the dislocation is present the crystal may grow in the direction of the screw axis by the familiar winding-up process. To account for the extreme rapidity of growth it is necessary to make two additional assumptions: that the whisker is bounded parallel to its axis by low index or close-packed planes which present no growth sites for the condensation of atoms, and that there exists an adsorbed film of mercury on the crystal surface in which the atoms may readily migrate. These assumptions provide a mechanism by which mercury atoms strike the sides of the whiskers, are adsorbed, and migrate to the advancing end where the atoms are incorporated into the crystal.

Returning to the problem of the introduction of a screw dislocation into a mercury nucleus we are faced with two alternatives. Either the nucleus forms with a screw dislocation built in or a perfect nucleus forms and subsequently undergoes a catastrophe giving rise to a screw dislocation. It was possible to resolve this problem by the application of the concepts of nucleation. The supersaturation needed to grow whiskers is approximately two hundred. The supersaturation necessary to nucleate an atomic layer of mercury on a low index plane of mercury is 4×10^6. This value was calculated from the theory of surface nucleation [3] with the assumption that the surface free energy of solid mercury is equal to the surface tension of liquid mercury. It would require an even greater supersaturation to surface-nucleate mercury uniformly on a vitreous glass surface, where we use the term "uniform" to indicate that all surface elements are alike. We are forced to conclude that uniform surface nucleation plays no role in the growth of whiskers. Further evidence for this conclusion is furnished by two observations. The concentration of whiskers per unit area of surface is not as steep a function of supersaturation as required by a uniform nucleation process. The whiskers in succeeding experiments within limits of observation form at the same sites. Uniform nucleation would require them to be randomly formed over the surface.

Since uniform surface nucleation plays no role in whisker growth, we must postulate a step in the glass surface. A vitreous surface, which is only a frozen liquid surface, would not be expected to present any such steps. We are relieved of this difficulty if small crystalline regions are scattered in the sea of vitreous glass, and some of these patches present a step. The step catalyzes the formation of a small monolayer patch of mercury. For the mercury to grow away from the glass substrate, mercury layers must build on the underlying mercury layers. Previous calculations on the supersaturation necessary to uniformly nucleate a new layer of mercury on a face of a mercury crystal indicate that this can occur only if abetted by a step. We must assume a regenerative step which is more commonly called a screw dislocation.

Our picture now includes crystallites of "ordered" glass presenting screw dislocation ends to the mercury vapor. Other crystallites would be inactive. The glass screw dislocation is replicated or transposed to a screw dislocation in mercury, which may have a different Burger's vector than its parent screw. The idea of glass crystallites is not novel and such regions have been observed electron microscopically [4].

When a whisker gets to a length of the order of 1 mm. it ceases to grow with extraordinary rapidity in the axis direction and grows in all directions with equal velocity, governed by the impingement rate of atoms from the vapor. The first evidence is given by cessation of Brownian motion and is followed sometime later by the cyclic appearance of interference colors, blue through red. The assumptions already made are sufficient to explain this behavior. As the whisker increases in length the concentration of mercury ad-atoms at the base of the whiskers increases to the value which allows new layers to nucleate on the low index bounding planes by the intermediation of the mercury-glass edge.

The glass crystallites have varying radii, r_g, which is of significance in the nature of the heterogeneity of the surface with regard to nucleation of solid. If r_c is the critical size of a nucleus for spiraling upward in a whisker, all patches such that

$$r_g < r_c$$

will be ineffective in growing whiskers. By increasing the supersaturation, r_c may be diminished and a new set of patches become available for crystal growth. If

$$r_g > r_c$$

then the whisker will be entirely based on "crystalline" glass and can more easily grow sideways because a crystalline glass-mercury edge would be more effective in nucleating a new low index layer than a vitreous glass-mercury edge. Whiskers, which are based on "crystalline" glass, should be significantly shorter than whiskers which have a vitreous glass-mercury edge at their bases.

G. W. SEARS

General Electric Research Laboratory
The Knolls
Schenectady, New York, U.S.A.

References

1. VOLMER, M. and ESTERMANN, I. Z. Phys., **7** (1921) 13.
2. See BURTON, W., CABRERA, N., and FRANK, F. Phil. Trans. Roy. Soc., **243** (1951) 299.
3. BECKER, R. and DÖRING, W. Ann. Phys., **24** (1935) 719.
4. BEYERSDORF, K. Glas und Hochvakuum Technik, **2** (1952) 8.

On the Debye Model and Low Temperature Phase Transformation in Lithium*

Metallic lithium has often been cited as an example of a simple (isotropic) solid whose specific heat deviates markedly from the Debye curve. Simon and Swain [1], in their publication of the specific-heat data of lithium in the range 15° to 300°K, have discussed the possible existence of an anomaly which could account for the deviation. Their interpretation of this anomaly, attributed to a single electronic transition, has been rejected by Fowler [2] and Lord [3]. The elastic constants of lithium have been computed by Fuchs [4], who has calculated the specific heat of lithium using Born's modification of the Debye theory. Fuchs' analysis gave better agreement with the experimental data than the Debye theory. However, Seitz [5] has pointed out that the agreement is far from being satisfactory.

Some recent publications by Barrett [6] on the low temperature transformations in lithium and studies [7] on the apparent temperature trend in the Debye θ for some highly anisotropic simple solids give another possible clue of reconciling the Debye type of continuum model with the low temperature specific heat of lithium.

Lithium has been reported [8; 9] to have a body-centered cubic structure from ordinary temperatures down to liquid air temperature. However, below this latter temperature, Barrett [6] has discovered a phase transformation from body-centered cubic to close-packed hexagonal. In addition to this, he has discussed another partial transformation that can be induced by cold working the metal. The structure of the induced phase appears to be face-centered cubic. In the close-packed hexagonal phase, the close-packed layers are reported to be in an imperfect stacking sequence. This type of disorder has been described as due to irregularities in the geometric array of successive layers of atoms as they are stacked one above the other in the new phase. Hence, this condition may offer a possible explanation for the discrepancy between the Debye model and the specific heat data below liquid air temperatures.

It is found that below liquid air temperatures the data can be described by an anisotropic continuum model which depends on two characteristic temperatures [7; 10]. This model has been summarized by the following equation:

*Received April 19, 1953.

TABLE I

SPECIFIC HEAT OF LITHIUM AND THE DEBYE MODEL

T°K	C_v (obs) [1]	C_v(calc) Isotropic model	C_v(calc) Anisotropic model
15	0.045	0.024	0.033
20	.095	.056	.080
25	.17	.11	.15
30	.27	.19	.23
35	.41	.30	.37
40	.57	.44	.56
45	.77	.61	.78
50	1.00	.76	1.02
60	1.42	1.24	1.45
70	1.87	1.70	1.93
80	2.31	2.15	2.39
90	2.67	2.58	2.80
100	3.02	2.95	3.17
110	3.32	3.29	
120	3.59	3.59	
130	3.81	3.84	
140	4.01	4.06	
150	4.18	4.25	
160	4.34	4.41	
180	4.57	4.69	
200	4.78	4.89	
220	4.94	5.06	
240	5.09	5.19	
260	5.22	5.30	
280	5.31	5.38	
300	5.39	5.45	

$$C_{2(3)} = 6R\frac{T^2}{\theta_2^3}\int_0^{\theta_2/T}\frac{x^3e^x}{(e^x-1)^2}dx - \left(\frac{\theta_3}{\theta_2}\right)^2\left[6R\frac{T^2}{\theta_3^2}\int_0^{\theta_3/T}\frac{x^3e^x}{(e^x-1)^2}dx - 9R\frac{T^3}{\theta_3^3}\int_0^{\theta_3/T}\frac{x^4e^x}{(e^x-1)^2}dx\right].$$

Using $\theta_2 = 415°$ and $\theta_3 = 280°$, we obtain the results shown in Table I (fourth column). Good agreement is shown to exist from 15° to about 80°K. The latter temperature being approximately the temperature below which Barrett has shown the spontaneous phase transformation to exist in lithium. Above this temperature the data have been described by Debye's model using an "average" θ_D value of 405° obtained from the experimental data above liquid nitrogen temperatures.* The influence of the partially transformed lithium, from body-centered cubic to face-centered cubic induced by cold work, on the specific heat has as yet not been studied experimentally. Barrett has reported significant induced partial phase transformation up to approximately 150°K.

W. DeSorbo

General Electric Research Laboratory
The Knolls
Schenectady, New York, U.S.A.

References

1. Simon, F. and Swain, R. C. Z. phys. Chem., **B28** (1935) 189.
2. Fowler, R. H. Statistical Mechanics, second edition (Cambridge University Press, 1936), pp. 131–2.
3. Lord, R. C. J. Chem. Phys., **9** (1941) 700.
4. Fuchs, K. Proc. Roy. Soc., **A153** (1936) 622; **A157** (1936) 444.
5. Seitz, F. The Modern Theory of Solids, first edition (New York, McGraw-Hill, 1940), p. 116.
6. Barrett, C. S. Phys. Rev., **72**, 245 (1947); Barrett, C. S. and Trautz, O. R. Metals Technol., April 1948, T.P. 2346; Barrett, C. S. Symposium on Phase Transformations in Solids, National Research Council Committee on Solids, Cornell (1948).
7. DeSorbo, W. Eighth Conference on Cryogenics, General Electric Co., Schenectady, New York, October 6–7, 1952.
8. Simon, F. and Vohsen, E. Z. phys. Chem., **133** (1928) 165.
9. Posnjak, E. J. Phys. Chem., **32** (1928) 354.
10. DeSorbo, W. To be published.
11. Baughn, E. C. Trans. Faraday Soc., **48** (1952) 121.

*Baughn [11] reports a θ_D value of 418° for lithium calculated by the Lindemann formula and a value of 420° obtained by the Guggenheimer formula, which relates the force constant, the interatomic distance, and the number of outer electrons.

Shear along Glide Planes in Aluminum†

Based upon the displacement of a scratch by slip lines on an alpha brass single crystal, Treuting and Brick [1] suggested that a shear on the order of 700 atom diameters occurred per active micrographically resolved slip plane. Once this shear had occurred, further slip took place elsewhere. A more direct measurement of shear along glide planes in aluminum single crystals was made by Heidenreich and Shockley [2] using the electron microscope. They found that each lamella composing a slip zone had slipped over its neighbor a distance of 2000Å. These experiments have been repeated by Brown [3] who found that the amount of shear on glide planes in aluminum was 2000Å at room temperature. At −180°C the shear was 1600Å and increased to 2200Å at 250°C.

More recently, Wilsdorf and Kuhlmann-Wilsdorf [4] have calculated shear along glide planes from electron microscope measurements of very well documented aluminum crystals. They found that the number of glide lamellae per glide zone increased with increasing amount of deformation but that the amount of shear along each glide lamella increased only slightly and in some cases remained essentially constant. Their values of shear along individual lamellae ranged from as low as 70Å to as high as 1200Å.

The more direct method of multiple beam interferometry [5] was employed by Tolansky and Holden [6]. Using aluminum specimens cast against special optical flats, they were able to measure shears of about 900Å in the deformed specimens. The earlier work of Holden [7] using slow strain rate established values of the order of 2000Å for aluminum deformed at room temperature. In the experiments of Holden, and Tolansky and Holden, no correction was made as to the true shear along the planes since they did not determine the orientations of the crystals. Nor was it known how many glide lamellae contributed to the total shear of the "slip zone." A slip line refers to slip along one plane (a glide lamella) whereas a slip band or slip zone refers to a group of glide lamellae which have not been resolved into their component lamellae. Although multiple beam interferometry is capable of resolving slip heights down to 5Å [5], its resolution in the plane of the surface is no better than obtained with the ordinary light microscope.

†Received April 20, 1953.

In the experiments reported here, a cylindrical tri-crystal one-half inch in diameter by six inches long of high-purity aluminum (99.9975) was grown by the strain-anneal method. The surface was prepared by alternate etching and polishing (mechanically) followed by electrolytic polishing in a solution of CH_3OH and HNO_3 (2:1) at high current density (1000 amperes/dm²). The final surface preparation included a 30 minute immersion in a bright-dip solution.* The condition of the surface as judged from an interferogram taken at a grain boundary may be seen in Figure 1.

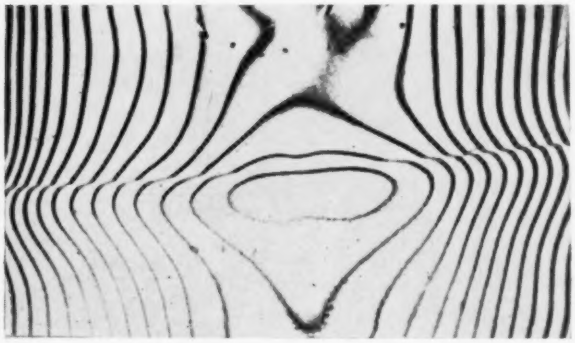

FIGURE 1. Interferogram of grain boundary. Orientation difference of the grains are shown in projection in Fig. 8. 935 ×, reduced to 6/7 in reproduction.

Gentle undulations in the fringes are due to slight depressions or hills in the specimen surface. Sharp jogs in the fringes can be seen at points where they cross the boundary. Such patterns are of particular interest, for they indicate the boundary to be a ledge rather than the customarily visualized groove which would be expected to produce a V-shaped discontinuity in the fringe. It is realized that the profile of a grain boundary should be a function of the specimen preparation and should vary with chemical attack. Consequently, a preliminary survey of the effect of various etchants was conducted. A 30 second etch in aqua regia at room temperature had no effect on the ledge shape appearance nor did a five second etch in 10 per cent NaOH at 70°C.

The interferometer used the Hg green line (5460Å) passing through a Cooke microscope and through a half-silvered microscope cover glass. Initial magnification used was 200 ×.

Since this technique measures the perpendicular or Z height only, a correction is needed in order to determine the true shear, D. Consider the schematic drawing in Figure 2. The shear, D, is

$$D = \frac{Z}{\sin \chi} \cos \alpha$$

where χ is the angle between the slip plane and the specimen axis and α is the angle between

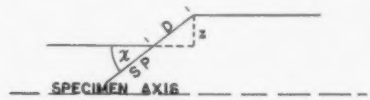

FIGURE 2. Relation of measure step height, Z, to calculated shear, D, on slip plane. χ is the angle between the specimen axis and the slip plane.

the slip direction and the normal to the mean surface projected on the slip plane. The angles χ and λ (the angle between the slip direction and the specimen axis) are determined from the initial and final orientations of the crystal. The angle α is determined by noting the angle between the position of observation and a reference scratch on the grip ends of the specimen (the angle between the reference scratch and the slip direction is known).

To insure that the slip system of highest resolved shear stress was the one to act, the glide plane was determined stereographically from the traces and the slip direction from the longitudinal axis rotation.

The appearance of the specimen after about 5 per cent elongation (the stress was 1000 g/mm²) is shown in Figures 3 and 4. The shear along segments of the zones, calculated from the measured displacements, are shown in Figures 5, 6, and 7. The orientation difference between the two grains is given in Figure 8. Measurements were made on the grain whose orientation is shown by the filled sections of great circles in Figure 8.

The curves shown in Figures 5, 6, 7, and 10 are plotted in two ways. The solid lines are the best fit curves through the data and the dashed curves are drawn through all the points. It is not known which of these curves is the "correct" one. However, since the resolution as determined from the ratio of the width of a fringe to the distance between the fringes ranges from 90Å (Figure 9) to about 150Å (Figures 5, 6, 7) and the circles are about 80Å units in diameter, the dashed curves are probably the more accurate representation of the true amount of shear along the slip zones concerned.

If it is assumed that the amount of shear on a

*Alcoa Bright-Dip Solution (R-5).

plane or group of planes constituting a slip zone is a function of the time that the line is active, it can be said that when the curves of shear versus distance along the line have maxima, these maxima are the points where the slip planes have first intersected the surface. The directions of propagation of the slip lines in these cases would be in both the positive and negative directions from these points. This is in keeping with the model of slip line formation recently discussed by Chen and Pond [8]. In the cases where no maxima appear, it can be said that the direction of propagation is towards the direction of lowest shear along any one line.

Values of shear as much as 5000Å and as little as 150Å have been observed. Along any one line a gradient of shear from as much as 4000Å to almost 100Å was measured.

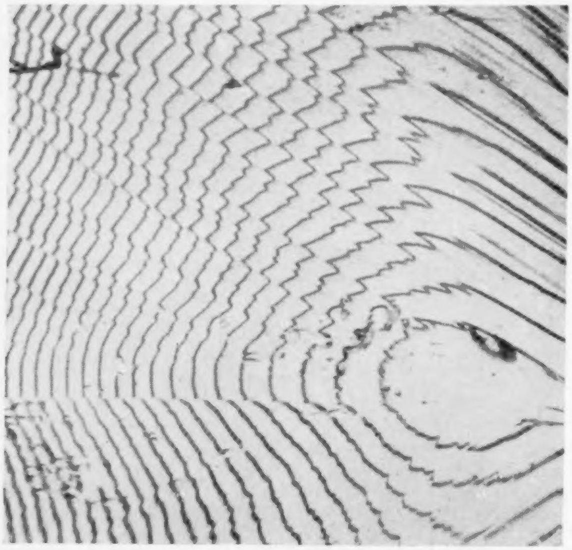

FIGURE 3. Interferogram of the grain boundary (approximately) shown in Fig. 1, but after about 5 per cent elongation. Note short zone which has greatest amount of shear near the boundary (curve 5 in Fig. 5). Position of the boundary is at position 0 microns. 1350 ×, reduced to 5/6 in reproduction.

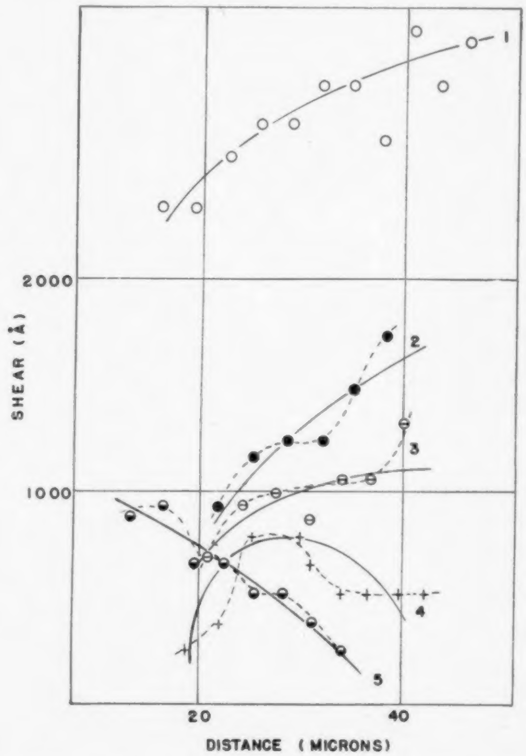

FIGURE 5. Shear, D, versus distance along slip zones away from the grain boundary (at position 0) shown in Fig. 3. Note curve 5 when shear is greatest near the boundary.

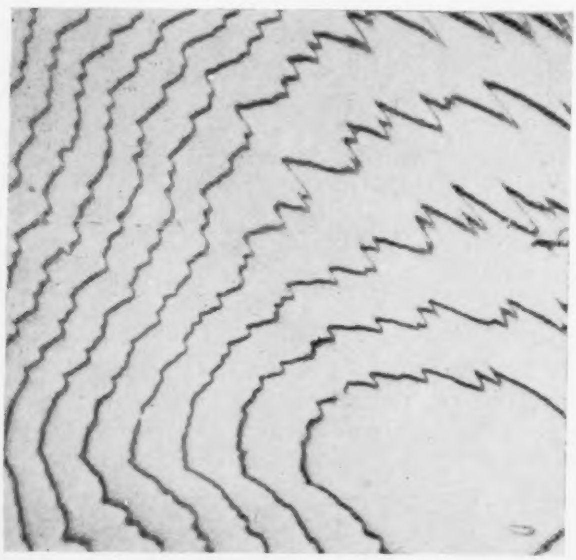

FIGURE 4. Interferogram showing shear along slip zones. The curves of shear versus distance are shown in Fig. 6. Note steep shear gradient in some of the lines. 1600 ×, reduced to 5/6 in reproduction.

Close examination of Figure 3 will show not only that bands exist for a very short distance but that, in one case, the amount of shear along glide planes reaches a maximum near the grain boundary. This latter observation is contrary to the expected behavior of a glide plane in the immediate vicinity of the grain boundary.

It is interesting to note that for the orientation difference shown in Figure 8 and for the amount of deformation, the slip bands stop at from 4 to 10 microns from the boundary.

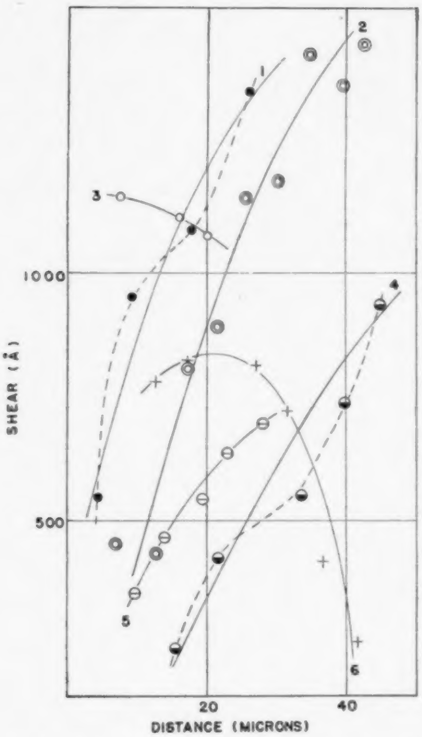

FIGURE 6. Shear, D, versus distance along slip zones, corresponding with interferogram of Fig. 4. Note steep shear gradient.

To observe the amount of shear on glide planes in just a few slip zones, another aluminum crystal prepared in the same manner was pulled in tension until just two bands were visible. The appearance of the fringes and a plot of the shear, D, versus distance along the band are shown in Figures 9, 10, and 11. Here, the shear is shown to decrease to below 150Å near the boundary and varies from 150Å to more than 1800Å away from the boundary.

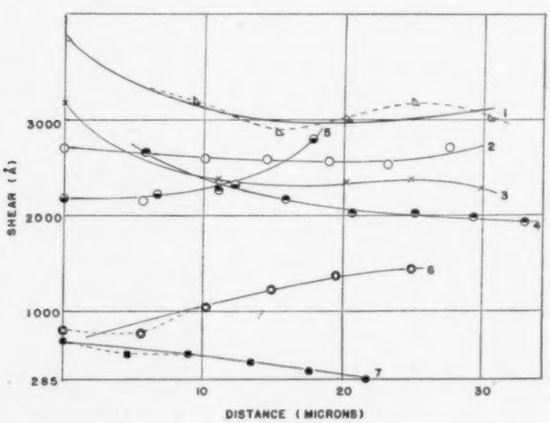

FIGURE 7. Shear, D, versus distance along slip zones at position remote from the grain boundary. Here, a constancy of shear is apparent.

Curve 2 in Figure 11 (the slip zone shown in Figure 10) shows an interesting effect. The bands are in slightly displaced regions presenting the stopped or overlapped appearance so common on deformed aluminum crystals. The plot shows the same amount of shear on both bands at the meeting point and the same amount of increase in shear away from the meeting points. Curve 3 in Figure 11 (shown in Figure 9) gives minimum value of shear of about 150Å near the boundary.

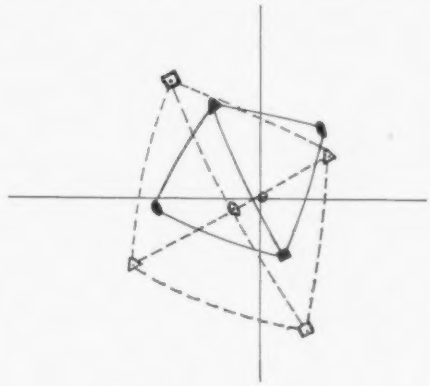

FIGURE 8. Orientation difference of grains shown in Figs. 1 and 3.

Attempts are now being made to incorporate cinematography with the multiple beam interferometry in order to measure the shear along the glide planes as a function of time.

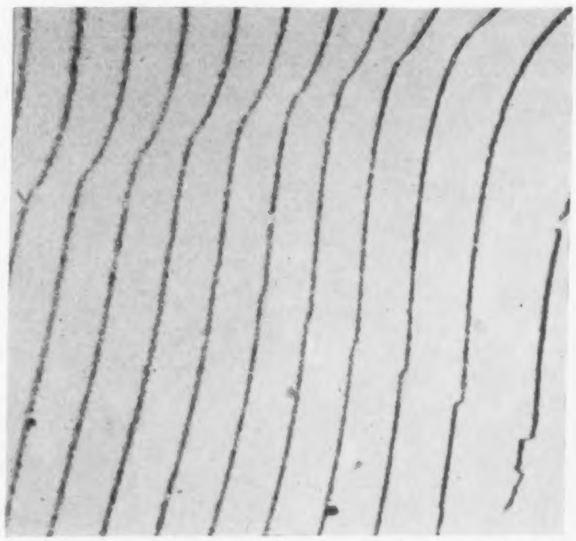

FIGURE 9. Interferogram showing the stopping of a slip zone. The boundary is at the left. 3200 ×, reduced to 6/7 in reproduction.

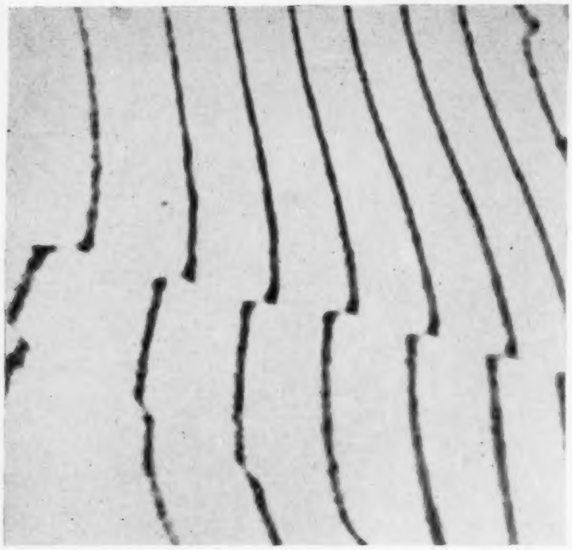

FIGURE 10. Interferogram of the same slip zone as shown in Fig. 9, but at a position remote from the grain boundary. Note that the "zone" splits into two "zones." Shear curves for these zones are shown as curve 2 in Fig. 11. 3500 ×, reduced to 5/6 in reproduction.

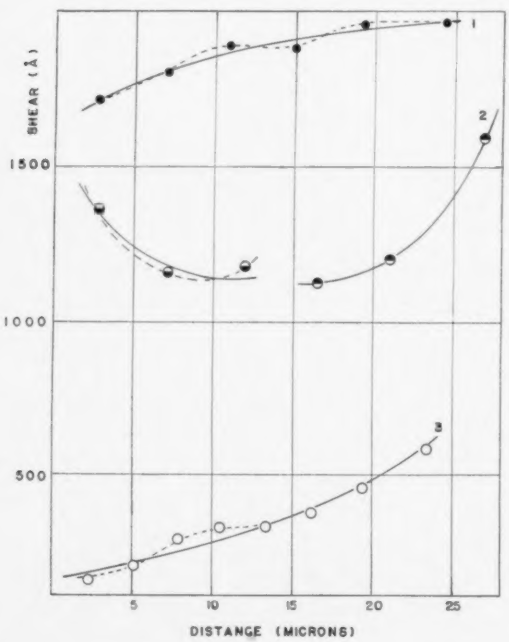

FIGURE 11. Shear, *D*, versus distance along slip zones. Curve 2 represents the split in the zones shown in Fig. 10.

Acknowledgement

The authors would like to thank the Aluminum Company of America for supplying the high-purity aluminum and for the use of their R–5 Bright Dip solution. This work was sponsored by the Office of Naval Research under Contract Nonr 248(35).

R. MADDIN, E. H. HARRISON, and R. W. GELINAS

School of Engineering
The Johns Hopkins University
Baltimore, Maryland

References

1. TREUTING, R. G. and BRICK, R. M. Trans. A.I.M.E., **147** (1952) 128.
2. HEIDENREICH, R. D. and SHOCKLEY, W. Report on a Conference on the Strength of Solids, Bristol, 1947 (London, The Physical Society).
3. BROWN, A. F. Nature, **163** (1949) 961.
4. WILSDORF, H. and KUHLMANN-WILSDORF, D. Z. angew. Phys., **4** (1952) 361; 409; 418.
5. TOLANSKY, S. Multiple Beam Interferometry of Surfaces and Films (Oxford, 1948).
6. TOLANSKY, S. and HOLDEN, J. Nature, **164** (1949) 754.
7. HOLDEN, J. M.Sc. Thesis, University of Manchester (1948).
8. CHEN, N. K. and POND, R. B. J. Metals, October (1952) 1085.

The Formation of Lattice Defects during Slip*

Recent observations [1] have brought to light the existence of an elementary structure on the surface of a slightly deformed aluminum crystal. It consists of a large number of lines, with an average length of a few times 10^{-3} cm., and spaced some hundreds of atomic distances apart. Each line represents a slip distance between 10 and 50 atomic distances. The elementary structure should be clearly distinguished from the usual slip lines, these being much longer, more widely spaced, and showing more slip.

The formation of an elementary structure may be explained in the following way. An activated Frank-Read source emits a number of dislocation rings. These rings expand and cross the ever present, randomly distributed dislocations. Jogs are formed and, as in face-centered cubic crystals, each dislocation probably has some screw character [2], further expansion of the jogged rings produces trails of vacancies or interstitial atoms. Additional expansions of a ring of radius R over a distance equal to the Burgers vector b produces

$$n_s \approx \tfrac{1}{6}\,\pi\sigma R$$

defects per unit length, where σ is the density of

*Received April 27, 1953.

random dislocations, viz. about 10^8 cm^{-2}. The energy involved in the creation of a defect being E_v (between 1 and 2 times 10^{-12} ergs in the case of a vacancy [2]), the energy needed to make this expansion possible increases with increasing R as

$$P_v \approx \tfrac{1}{6}\, \pi\sigma R\, E_v.$$

per unit of dislocation. The energy gained by moving a dislocation of unit length over a distance b in the field of applied stress τ being τb^2, it is seen that for applied stresses of the order of 1 kg/mm^2 expansion of the rings around an activated source will only occur to a limited amount, viz. somewhere between 1 and 2 times 10^{-3} cm.

Also the number of rings emitted by the source is limited by action of the back stress exerted by the rings on the source. Following the lines given by Fisher *et al.* in a recent paper [3], it is found that, in the region of stress mentioned above, the number of emitted rings per source does not exceed 50.

At low stress levels therefore slip in metal crystals will be distributed rather inhomogeneously through the lattice; it is concentrated around activated Frank-Read sources. It is proposed that the intersections of the ring systems with the surface of the crystal are observed as the elementary lines. Length and step height observed are in good agreement with this theory.

The density of activated Frank-Read sources may be estimated from the observed stress-strain curves. In the case of copper or aluminum, the density is found to be about 6×10^9 cm^{-3}. The average spacing perpendicular to the slip planes is then 5×10^{-6} cm, in good agreement with the observations on the elementary structure.

The total number of defects formed at the above mentioned stress level is about 10^{19} cm^{-3}; the strain produced by the dislocations is 3 per cent. Good agreement exists with the density of vacancies estimated from observed resistivity changes at liquid air temperature, viz. $\Delta\rho/\rho$ equals ca. 1 per cent at a strain of 5 per cent [4; 5], when the result of a recent computation by Jongenburger [6] is used. According to this work, the resistance increase by vacancies in copper is 1.3 $\mu\,\Omega$/per cent vacancies.

Raising the stress above a value of about a kg/mm^2 will not appreciably increase the number of rings emitted per source. Formation of new rings is greatly inhibited by the stress field produced by the other activated sources. Only further expansion of the rings takes place. As the strain is proportional to the area swept by the rings and the radius of the rings is to a first approximation directly proportional to the shear stress applied, a quadratic stress-strain relation should be valid. Furthermore, the density of defects should increase proportionally to the 3/2-power of the strain.

When the density of activated Frank-Read sources on a particular slip plane is appreciably higher than the average density (about 10^4 cm^{-2}), expansion of the rings leads to mutual attraction followed by annihilation of a considerable part of the dislocation length. The back stress on the sources drops rapidly, and many new dislocation rings are emitted. Thus a slip zone with slip distance of many hundreds of atomic spacings is propelled through the crystal and on arriving at the surface produces a slip line. The total number of dislocations forming the slip line is again limited, and depends on the density of crossing dislocations, as the number of defects created cannot become higher than the atomic density. The slip plane then collapses. An upper limit is found to be 2000.

At low temperatures the density of defects is very high near to a slipped plane. The stress field produced by this "layer" of defects inhibits expansion of rings on other planes, and the slip lines appear widely spaced. The influence on the electrical resistivity of such layers may be appreciable (internal size effect [7]) and the first recovery step in the resistivity [5] may be attributed to dissolution of the layers. At higher temperatures the vacancies diffuse away, and the slipped plane now contains neither vacancies nor activated sources. As a result, activation of sources on neighbouring planes is favoured and clustering of slip lines will occur, as observed.

A more detailed account of the investigation will be published in due time.

H. G. VAN BUEREN

Philips Research Laboratories
N.V. Philips' Gloeilampenfabrieken
Eindhoven, Netherlands

References

1. WILSDORF, H. and KUHLMANN-WILSDORF, D. Z. angew. Phys., **4** (1952) 361, 409, and 418.
2. Compare e.g. SEITZ, F. Advances in Physics, **1** (1952) 43.
3. FISHER, J. C., HART, E. W., and PRY, R. H. Phys. Rev., **87** (1952) 958.
4. MOLENAAR, J. and AARTS, W. H. Nature, **166** (1950) 690.
5. DRUYVESTEYN, M. J. and MANINTVELD, J. A. Nature, **168** (1951) 868; MANINTVELD, J. A. Nature, **169** (1952) 623.
6. JONGENBURGER, P. Phys. Rev., to be published.
7. MCDONALD, D. K. C. Phil. Mag., **42** (1951) 756.

Thermal Stabilization of Austenite in Nickel Steels*

It is known that in certain steels the amount of martensite obtained on quenching specimens to a fixed reference temperature is dependent on the rate of cooling from the austenitizing temperature.

Morgan and Ko [1] showed that, in an 1.1% C, 5.4% Ni steel, the difference in the martensite contents of specimens quenched into brine and oil was due to thermal stabilization occurring in the region of 300°–400°C. Stabilization of the austenite occurred on isothermal holding at temperatures lower than this, both above and below *Ms*, but it was too slow at these temperatures to reach a detectable amount even during oil quenching.

The experiments have been repeated in order to obtain more data. The specimens used were cut, after a time lapse of one year, from the bars forged from the same ingot. Austenitization at 1100°C was carried out in the same neutral bath used before, and also in vacuo, the results being independent of the method of austenitization. All the other experimental details were identical with those described previously [1].

The present results, shown in Figure 1, were as follows:

(i) *Effect of cooling rate.* The amounts of martensite in the specimens were independent of the quenching medium, whether brine, mercury, or oil. In other words, within this range, the cooling rate had no effect on the progress of transformation.

(ii) *Ageing above Ms* (87°C) Holding at 178°C and 214°C for various periods up to 32 hours had no effect on the amount of martensite at temperatures between *Ms* and 15°C.

(iii) *Ageing below Ms.* Stabilization was observed on ageing below *Ms*. Holding for 24 hours at 52°C (31 per cent martensite) caused a temperature lag (θ) of 16°C and a loss of 15 per cent martensite when the transformation resumed.

These results are consistent with the previous finding [1] that any difference in the amount of retained austenite in this type of steel is associated with stabilization above *Ms*. But it is obvious that some factors were in operation which prevented the occurrence of stabilization above *Ms* in the present specimens.

In order to ascertain the effect of any possible variation in chemical composition, specimens from the two batches were analyzed with the following results:

Element	Analysis	Morgan & Ko's specimens	Present specimens
C	Chemical	1.08%	1.08%
Ni	Chemical	5.4%	5.4%
N_2	Chemical	0.005%	0.005%
B	Spectrographic	Faint trace	Nil
Pb	Spectrographic	Trace	Trace
Al, Bi, Co, Cr, Cu, Mo, Sb, Sn, Te, Ti, V, W, Zn	Spectrographic	Not detected	Not detected

As hydrogen is the only element likely to have been lost during the period between the previous and the present investigations, a possible aftereffect from this element was investigated using specimens cathodically impregnated with hydrogen. About two weeks were allowed to lapse between the hydrogen impregnation and austenitization, a period comparable to that between machining and austenitization in the previous experiments [1]. No stabilization effect above *Ms* was found after isothermal holding at 183°C for periods up to 24 hours.

Scrutiny of the literature shows that similar anomalous results have been reported before. Klier and Troiano [2] found stabilization above *Ms* in a 0.7% C, 15% Cr steel, while Das Gupta and Lament [3] (using specimens from the same melt) and Bogacheva and Sadovskii [4] (using a 0.79% C, 15.2% Cr steel) reported that no such effect

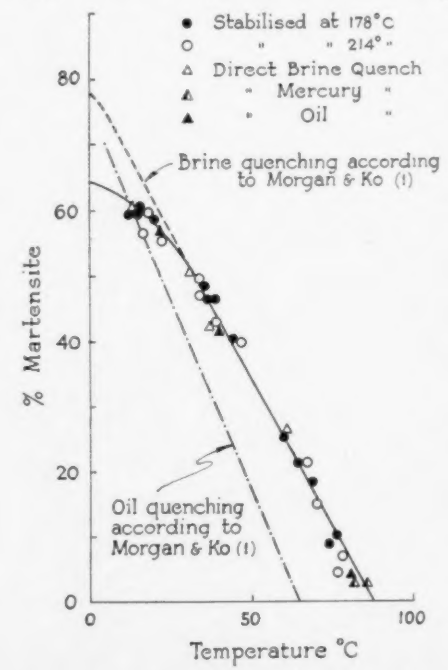

FIGURE 1. Martensite transformation curves.

*Received May 19, 1953.

could be observed. In a 1.1% C, 5.36% Ni steel, a composition similar to that used in the present investigation, Harris and Cohen [5] found no stabilizaion above room temperature (25°C). These authors also reported that their steel showed no difference in the amounts of retained austenite at 25°C after cooling at different rates, although in a previous paper from the same laboratory, Howard and Cohen [6], using apparently the same steel, recorded a difference of 12 to 14 per cent in retained austenite between specimens quenched in oil and 10 per cent NaOH to room temperature (unspecified, probably 25°C according to the given data). Cohen and his co-workers [7] also found that the austenite content of a 1.0% C, 4.82% Ni steel oil quenched to room temperature was dependent on the specimen size.

It must be concluded that there are some unknown factors which determine whether or not stabilization will take place above *Ms*. No suggestion can be made at present as to the nature of these. The effect of boron on stabilization is now being studied.

Thanks are due to Mr. H. Morrogh of The British Cast Iron Research Association for the spectrographic analyses and Dr. E. Marks of Messrs. Richards Thomas Baldwins, Ltd., for the nitrogen analyses.

T. Ko and B. Edmondson

Department of Metallurgy
University of Birmingham
Birmingham, England

References

1. Morgan, E. R. and Ko, T. Acta Met., **1** (1953) 36.
2. Klier, E. P. and Troiano, A. R. Trans. A.I.M.E., **162** (1945) 175.
3. Das Gupta, S. C. and Lament, B. S. Trans. A.I.M.E., **191** (1951) 727.
4. Bogacheva, G. N. and Sadovskii, V. D. Dok. Akad. Nauk, SSSR., **83** (1952) 569.
5. Harris, W. J., Jr. and Cohen, M. Trans. A.I.M.E., **180** (1949) 447.
6. Howard, R. T., Jr. and Cohen, M. Trans. A.I.M.E., **176** (1948) 384.
7. Antia, D. P., Fletcher, S. G. and Cohen, M. Trans. Amer. Soc. Metals, **32** (1944) 290.

Spin-Orbit Coupling Effects in Ferromagnetic Metals*

The remarks made in a recent note by Argyres and Kittel [1] on the ferromagnetic ground state are relevant to some theoretical work on ferromagnetism recently completed by the author. The folowing comments on this note and on the author's work may therefore be appropriate.

The criticism in paragaph (A) of the assumption of 2.22 effective magnetic electrons per atom for iron and 0.6 for nickel appears at first sight to be valid. Such values have been deduced from saturation magnetization data, assuming the effects to be due entirely to electron spin and unaffected by the orbital motion of the electrons. Owing to spin-orbit coupling, this assumption is not entirely correct, coupling effects being demonstrated by the deviations from two of the values of the gyromagnetic ratio g' and the spectroscopic splitting factor g. The only treatment giving a clear physical picture of spin-orbit coupling effects, on the basis of the collective electron theory, is that due to Brooks [2]. A quantitative investigation of this treatment has recently been carried out by the author for nickel, using the results of the d band calculations for that metal by Fletcher and Wohlfarth [3] and Fletcher [4]. Brooks' treatment has now been extended to include the effects of all five atomic d functions, but the additional computational complexities introduced thereby have necessitated the consideration of only three for quantitative purposes, as in Brooks' original paper and in [3]. On this basis theoretical values of 2.22 and 1.82 have been obtained for g and g' respectively. The calculations have also been extended to include second order terms.

The value 2.22 for the g factor of nickel gives 0.54 for the number of effective magnetic electrons per atom, in agreement with Argyres and Kittel's estimate based, presumably, on an experimental value of g. This change would have the effect of increasing the value of the low temperature electronic heat coefficient γ calculated by Fletcher [4] to about 1.9×10^{-3} cal mol^{-1} deg^{-2}, now slightly larger than the experimental value for nickel. The calculated degeneracy temperature would be reduced correspondingly. A direct comparison of the calculated g factor with values deduced from ferromagnetic resonance experiments is not at present possible, since the experimental values derived in different cases vary over a considerable range, e.g. 2.19–2.42 for nickel. The calculated value of g' for nickel is in disagreement with observation; it is not clear, incidentally, why the correction to the effective number of electrons should not rather be made using g' in place of g.

It may be pointed out, in commenting on the more fundamental aspects of the theory, that the

*Received May 22, 1953.

author's d-band calculation is based on a theoretical model which neglects spin-orbit coupling entirely, a fact which has been re-emphasized by Wohlfarth [5]. The use of values of effective electron numbers corrected for this effect to estimate such quantities as specific heats thus appears to be in a way inconsistent with the author's calculation; ideally, attempts should rather be made to include spin-orbit coupling effects *ab initio* in band calculations.

Regarding the remarks on Brooks' paper [2] in paragraph (C) of Argyres and Kittel's note, it may be mentioned that Brooks purports to calculate g', but his method of calculation actually leads to a value for g. The value given by Brooks is less than 2 but Van Vleck [6] has suggested that this is due to assuming erroneously a positive value for the spin-orbit parameter A when summing over the unoccupied d states. Brooks' procedure is quite legitimate, however, since, as he points out quite clearly, the parameter A used is that for a single electron and not that for the atom as a whole. The discrepancy actually appears to arise simply from an algebraic error in sign in Brooks' expression for ΔE (equation (20)). Further, the factor $\frac{2}{3}$ in his expression (21) for g should be $\frac{4}{3}$, so that his value for g should be about 2.05. As Argyres and Kittel point out, this value is too low, owing to Brooks' use of a "mean band width" having the value 20,000 cm^{-1}, slightly less than half the width of the d band calculated by Slater [7]. Even allowing for the possibility that Slater's value may be too large [4], the use of a fraction as large as $\frac{1}{2}$ seems unjustifiable. In the present calculation the comparable "mean band width" would be $20{,}000 \times 0.03/0.22$, i.e. about 3000 cm^{-1}, which is in fact quite close to the depth of the "ferromagnetic Fermi limit" below the top of the d band on which the calculations are based, viz. about 3600 cm^{-1}. These values are considerably larger than those suggested by Argyres and Kittel [1].

Spin-orbit coupling effects also lead to the occurrence of the phenomenon of ferromagnetic anisotropy [2]. A calculation of the anisotropy coefficient K_1 for nickel has also been carried out by the author, the calculation being again based on Brooks' theory and on the author's d-band calculation. Full details and results of these calculations will be reported at a later stage.

I should like to express my gratitude to Dr. E. P. Wohlfarth for his helpful advice, and to Professor H. Brooks for making available to me a copy of his Ph.D. Thesis.

G. C. Fletcher

Department of Mathematics
University College
Exeter, England

References

1. Argyres, P. and Kittel, C. Acta Met., **1** (1953) 241.
2. Brooks, H. Phys. Rev., **58** (1940) 909.
3. Fletcher, G. C. and Wohlfarth, E. P. Phil. Mag., **42** (1951) 106.
4. Fletcher, G. C. Proc. Phys. Soc. (London), **A65** (1952) 192.
5. Wohlfarth, E. P. Proc. Phys. Soc. (London), **A65** (1952) 1053.
6. Van Vleck, J. H. Phys. Rev., **78** (1950) 266 (Reference 21).
7. Slater, J. C. Phys. Rev., **49** (1936) 537.

Erratum

Vol. 1, no. 3, p. 376. Thermal Stabilization of Austenite Iron-Carbon-Nickel Alloys. By Samuel J. Rosenberg. The last sentence of the penultimate paragraph should read:

"It was established that these differences were actually associated with the austenite grain size and not with the temperatures from which the various samples were quenched."

SOME CURRENT PAPERS IN OTHER JOURNALS

Acta Crystallographica, Vol. 6

Part 5, May, 1953 (Partial Contents)

Crystal chemical studies of the 5f-series of elements. XIX. The crystal structure of the higher thorium hydride, Th_4H_{15}. W. H. ZACHARIASEN.

The antiferromagnetic structure deformations in CoO and MnTe. SELMA GREENWALD.

Die Berechnung der Q_0-Funktion aus dem experimentell gewonnenen Intensitätsverlauf eines begrenzten Kristalles. R. HOSEMANN and S. N. BAGCHI.

The structures of the plagioclase felspars. II. H. SORUM.

On the X-ray diffraction patterns of polymer films. C. H. BAMFORD and H. TOMPA.

On the crystal structure of guanidinium bromate. J. DRENTH, W. DRENTH, AAFJE VOS and E. H. WIEBENGA.

Crystal structure and antiferromagnetism of CrSb. B. T. M. WILLIS.

Enumeration of physical constants of crystals. A. RAHMAN.

Three-dimensional Fourier summations on a high-speed digital computer. S. W. MAYER and K. N. TRUEBLOOD.

The thermal expansion of afwillite. ROSEMARY SHAW.

The structure of oxamide. C. ROMERS.

The double Patterson function. DAVID SAYRE.

Part 6, June, 1953 (Partial Contents)

The probability distribution of X-ray intensities. V. A note on some hypersymmetric distributions. D. ROGERS and A. J. C. WILSON.

Determination of elastic constants of crystals from diffuse reflexions of X-rays. III. Diamond. E. PRINCE and W. A. WOOSTER.

An extension of the "Difference Patterson" to facilitate the solution of order-disorder problems. ALFRED J. FRUEH, JR.

Optimum geometric conditions in the design and use of X-ray diffraction tubes and cameras. H. E. HUXLEY.

A method for the estimation of transmission factors in crystals of uniform cross section. N. JOEL, R. VERA, and I. GARAYCOCHEA.

Locating the principal maxima of a Fourier series. H. HAUPTMAN and J. KARLE.

Structures of the ReO_3-type with recurrent dislocations of atoms: "Homologous Series" of molybdenum and tungsten oxides. ARNE MAGNELL.

The structure of crystalline chromous acetate revealing paired chromium atoms. J. N. VANNIEKERK, F. R. L. SCHOENING, and J. F. DEWET.

Structure analysis of single crystals by electron diffraction. I. Techniques. J. M. COWLEY.

Structure analysis of single crystals by electron diffraction. II. Disordered boric acid structure. J. M. COWLEY.

The crystallography of the titanium transformation. CARL J. MCHARGUE.

The interpretation of diffuse X-ray reflexions from single crystals. II. J. HOERNI and W. A. WOOSTER.

Traitement Statistique des Erreurs dans le Cas d'une Structure Pseudo-Centrosymetrique. V. LUZZATI.

A contribution to the determination of signs in the Fourier analysis of crystals. O. A. TESCHE.

The low-temperature crystal structure of magnetite. H. P. ROOKSBY and B. T. M. WILLIS.

Reversible single-crystal rocking-curve broadening. L. C. CHANG, T. A. READ, and M. S. WECHLER.

Die Struktur dünner Aluminium-Silber-Schichten. H. GÖTTSCHE und H. RAETHER.

A remark on some new methods of phase determinations. J. KROGH-MOE.

Some observations on the crystallography of deformation twins. E. O. HALL.

Surface layer on crystalline quartz. O. S. HEAVENS.

Journal of the Institute of Metals, Vol. 81

Part 10, June, 1953

43rd annual May lecture: The present and future metallurgical requirements of the chemical engineer. SIR CHRISTOPHER HINTON.

The use of diamond abrasives for a universal system of metallographic polishing. L. E. SAMUELS.

The solubility of indium in copper. E. A. OWEN and E. A. O'DONNELL ROBERTS.

Priming paints for light alloys. J. G. RIGG and E. W. SKERREY.

The continuity of slip lines across a grain boundary. G. J. OGILVIE.

Part 11, July, 1953

Hydrogen blisters in brass sheet. R. EBORALL and A. J. SWAIN.

Critical-strain effects in cold-worked wrought aluminium and its alloys. W. M. WILLIAMS and R. EBORALL.

The application of grain refinement to cast copper-aluminium alloys containing the beta phase. J. P. DENNISON and E. V. TULL.

The structure of titanium-tin alloys in the range 0–25 At.-% Tin. H. W. WORNER.

Some observations on creep and fracture from investigations on lead cable-sheath alloys. A. LATIN.

Simultaneous determination of the surface tension of tin and its contact angle with silica by the use of conical capillaries. D. V. AYYERTON and T. P. HOAR.

A theoretical investigation of the deformation textures of titanium. D. N. WILLIAMS and D. S. EPPELSHEIMER.

The influence of composition on the incidence of strain markings in aluminium alloys. W. H. L. HOOPER.

Journal of Metals, Vol. 5

No. 5, May, 1953

Asarco rehabilitates copper refinery. G. H. WEIS, D. A. BUSCH, H. K. SPAULDING, and G. B. PAULDING.

Air force heavy press program moves from planning board into fabrication. A. S. COHAN.

Atlantic steel using cold metal charge finds costs in favor of electric furnace. J. E. WILBANKS.

Sinter sampling technique developed by U.S. Steel Corp. R. L. STEPHENSON and D. J. CARNEY.

Deep drawing steel sheet surface quality. R. J. Walter.

Thermal conductivity data presented for various metals and alloys up to 900°C. L. SILVERMAN.

Operations at New Cornelia copper smelter of Phelps Dodge Corporation. J. W. BYRKIT.

Effect of dissolved sulphur on the surface tension of liquid copper. C. E. BAES, JR. and H. H. KELLOGG.

Metallic oxidation in chromium in steel melting. D. C. Hilty, G. W. Healy, and Walter Crafts.
Free energy of vaporization of metals from 0° to 2000°C. J. W. Evans.
Electron microscope study of the effect of cold work on the subgrain structure of copper. Laurence Delisle.
Martensite habit plane in quenched Ti–Mn alloys. Y. C. Liu and Harold Margolin.
Recrystallization of a cold-rolled copper single crystal. Y. C. Liu and W. R. Hibbard, Jr.
Note on contamination of silicon ingots. G. Sandóz and H. E. Stauss.
Notes on the plastic critical temperature in strain-induced martensite reactions. C. Dean Starr.
Simple devices for approximating constant stress during tensile creep tests. R. L. Fullman, R. P. Carreker, Jr., and J. C. Fisher.
Observations on the phase Ti–Ag. R. J. Van Thyne, W. Rostoker, and H. D. Kessler.
On the distribution of sodium in modified Al–Si Alloys. A. B. Michael and M. B. Bever.

No. 6, June, 1953
Hydrometallurgical process yields pure metal powders from sulphides.
Reduction-oxidation process for the treatment of taconites. F. M. Stephens, Jr., Benny Langston, and A. C. Richardson.
Mechanization program results in savings at Laredo antimony smelter. R. L. Kulpaca and J. C. Archibald, Jr.
Chihuahua slag fuming plant to process 19,000 tons per month. V. R. MacDonald.
Lorain cuts banked blast furnace blowing-in time from 72 to 30 hours. W. W. Durfee.
Steam jets efficiently remove dust from open hearth furnace flues. John Peterson.
Open hearth screw steels replacing bessemer. S. Feigenbaum.
Influence of the rate of deformation on the tensile properties of some plain carbon sheet steels. Joseph Winlock.
Vapor pressure of zinc in the reduction of ZnS by Cu and Fe. A. W. Bethune and L. M. Pidgeon.
Recrystallization and Stored Energy. H. P. Leighly, H. L. Walker, and J. W. Marx.
Magnetic annealing of a Co–Fe alloy. A. H. Geisler, J. P. Martin, E. Both, and J. H. Crede.
Order-disorder transformation in Cu–Au alloys near the composition CuAu. J. B. Newkirk.
Self-diffusion of iron in iron oxides and the Wagner theory of oxidation. L. Himmel, R. F. Mehl, and C. E. Birchenall.
Kinetics of galvanizing. D. J. Blickwede.
Concentration gradients associated with growing pearlite. R. E. Grace.
Importance of the iron content of high-purity aluminum. M. Metzger and J. Intrater.
High temperature corrosion in nickel-chromium alloys. Norman Spooner, J. M. Thomas, and L. Thomassen.

Revue de Métallurgie, 50e Année

Numéro 4, avril, 1953
Théorie et pratique du doublage automatique dans les laminoirs. Abel Beneteau.
Étude sur une interprétation statistique des essais de fatigue. R. Girschig.
L'emploi du méthane dans la sidérurgie italienne. A. Scortecci.
Dosage et identification des inclusions dans l'acier. Jean Massinon.
Contribution à l'étude de la structure de bandes dans l'acier forgé. Influence conjugée de la ségrégation mineure, de la migration du carbone et du traitement thermique. P. Cattier, Ch. Dubois, J. Bleton et P. Bastien.
Contribution à l'étude statistique de la dispersion dans les essais de flexion rotative. R. Cazaud.

Numéro 5, mai, 1953
Le problème des soudures fragiles dans les récipients en ferblanc. W. E. Hoare et J. P. Gustin.
Influence des conditions d'élaboration et de traitement thermique sur les caractéristiques des alliages légers résistants à chaud. R. Syre.
Méthodes d'essais pour l'appréciation du "brillant" des laminés d'aluminium. J. Hérenguel et J. Boghen.
Contribution à l'étude des alliages Al–Mg–Si. Marcel Tournaire et Martial Renouard.
Étude expérimentale de l'écrouissage des métaux par la diffraction des microfaisceaux de rayons X. P. B. Hirsch.
L'analyse spectrographique de l'acier au cours de l'élaboration et au laboratoire de contrôle. M. Michonsniky.
Les cahiers des charges et leur application aux tôles épaisses. J. Bernard.
Affinage d'une fonte phosphoreuse par l'oxygène au four Martin. G. Husson et P. Bettembourg.

Zeitschrift für Metallkunde, Band 44

Heft 1, Januar, 1953
Wissenschaft und Technik der Metalle. Paul Brenner.
Bedeutung und Leistungsfähigkeit der Nichtmetallindustrie des Bundesgebiets. H. Sennekamp und A. Väth.
Die technischen und wirtschaftlichen Grundlagen von NE-Schwermetall-Verbundguss. Günther Schwietzke.
Zur Metallographie der Leichtmetalle. VI. Hans Kostron, Elfriede Höffler und Werner Sautter.
Die Feinwanderung an Kontakten aus Legierungen mit Überstruktur. Albert Keil und Carl-Ludwig Meyer.
Über die Kinetik der Wüstitbildung bei der Oxydation von Eisen. Karl Hauffe und Harald Pfeiffer.
Hans Kostron. Paul Brenner.

Heft 2, Februar, 1953
Praktisches und Grundsätzliches zur Korrosion in einem chemischen Betriebe. Max Werner.
Über die Härte. Heribert Moser.
Die Änderung des elektrischen Widerstandes durch Kaltverformung. Hermann Weyerer.
Zur Kenntnis des Systems Kupfer-Mangan-Zinn. Siegfried Valentiner.
Über die Anwendung des Zählrohr-Röntgen-Spektrometers für die direkte Bestimmung von Umwandlungsgeschwindigkeiten. Ilrich Rösler und Wolfram Ruff.
Bemerkung zu der Arbeit von J. Gurland und J. T. Norton: Über die Gerüstbildung in Hartmetallen. Walter Dawihl.
Über die Eigenschaften einer technisch verwendbaren Kupfer-Chrom-Legierung. Gerhard Bunge, Eduard R. Honak und Walter Nielsch.
Gesellschaftsnachrichten.

Heft 3, März, 1953

Über die Passivität des Eisens. Karl Friedrich Bonhoeffer.

Zur Passivität vom Eisen. T. G. Owe Berg.

Korrosion von Aluminiumgeschirr. Paul Melchior.

Spannungskorrosion bei Aluminium-Legierungen. Paul Brenner.

Fremdstromschutz erdverlegter Kabel u. Leitungen durch isolierende Schutzschichten. Fritz und Wilhelm Glander.

Zur Kristallchemie der B-Metalle. I. Konrad Schubert.

Polarisation und Passivierung in der Metallkorrosion. Walter Katz.

Plastische Verformbarkeit des Germaniums bei höheren Temperaturen. Ludwig Graf, Hans-Reiner Lacour und Karl Seiler.

Gesellschaftsnachrichten.

Bücherschau.

Heft 4, April, 1953

Blei im modernen Apparatebau. H. H. Hörger.

Beobachtung über die Verkratzung von Bleilegierungen beim Durchleiten eines Luftstroms durch die Schmelze. H. Hartmann, W. Hofmann und W. Stahl.

Die Dreistoffsysteme Blei-Kadium-Wismut und Blei-Zinn-Wismut. T. H. Ho, W. Hofmann und H. Hannemann.

Messungen der Dauerstandfestigkeit vom Hartblei zwischen 25 und 75°. G. Hillen und W. Hofmann.

Beobachtungen über die Erschütterungsfestigkeit von homogen verbleitem Stahlblech. G. Hillen und W. Hofmann.

Untersuchungen an einem Hartbleirohr aus dem Jahre 1935. W. Hofmann und R. Engel.

Über das System Blei-Silber-Schwefel. R. Vogel.

Vergleich zwischen röntgenographisch und ferromagnetisch bestimmten inneren Spannungen. U. Dehlinger und H. Scholl.

Über den Ablauf der Diffusionsvorgänge in Substitutionsmischkristallen. Th. Heumann und A. Kottmann.

Reaktionen von festem Eisen mit Schmelzen aus Aluminium und Aluminiumlegierungen. E. Hebhardt und W. Obrowski.

Untersuchungen an den Amalgamen der Metalle Mangan, Eisen Kobalt, Nickel und Kupfer. F. Lihl.

Über die Technologie der Werkstoffe für elektrische Kontakte. K. Keil.

Gesellschaftsnachrichten.

Bücherschau.

Heft 5, Mai, 1953

Zur Korngrössenverteilung bei der Rekristallisation von Reinstaluminium. Werner Dickenscheid und Hugo Josef Seemann.

Periodische Steigerungen bei Reinaluminium-Strangguss. Gustav Siebel, Dietrich Altenpohl und H. Cohen.

Untersuchungen im Dreistoffsystem Aluminium-Eisen-Zink. Erich Gebhardt.

Störungen der Gleitung bei Aluminiumeinkristallen. I. Untersuchung der Verfestigung und des Laue-Asterismus. Hansheinz Lange und Kurt Lucke.

Die Anwendung von Aluminium im Flammspritzverfahren. Harribald Sprenger.

Das Zustandsbild des Systems Aluminium-Magnesium. Eine kritische Übersicht. Klaus Eickhoff und Hugo Vosskühler.

Zur Metallographie der Leichtmetalle. VIII. Auf- und Abbauvorgänge während der Kristallisation. Hans Kostron und Margarete Schippers.

Über die Aushärtung von Aluminium-Silber-Legierungen. VII. Zur Konzentrationsabhängigkeit der Aushärtung. Werner Köster und Franz Sperner.

Werkstoffprüfung mit Ultraschall in der Leichtmetall-Halbzeugindustrie. Josef Krautkrämer und Walter Roth.

THE EFFECT OF TEMPERATURE AND COMPOSITION ON THE DEFORMATION OF SINGLE CRYSTALS OF IRON*

H. W. PAXTON† and A. T. CHURCHMAN‡

An investigation has been made of the types of stress-strain curve which it is possible to produce in single crystals of iron in the range of temperature between −180°C and 213°C, for two different carbon contents. It is found that all the effects which can be produced in polycrystalline iron, i.e. cleavage fracture, mechanical twinning, simple and repeated yielding, and smooth stress-strain curves, can also be observed in single crystals containing 0.003 per cent carbon at approximately the same temperature. Crystals containing about 0.0005 per cent carbon also show all the effects except repeated yielding. The main difference between the single crystals of the two compositions is in the rate and magnitude of strain ageing effects. The temperature dependence of the initial yield stress is discussed for crystals containing 0.003 per cent carbon.

L'EFFET DE LA TEMPÉRATURE ET DE LA COMPOSITION SUR LA DÉFORMATION DE MONOCRISTAUX DE FER

Une investigation a été faite du genre de courbe tension-déformation qu'il est possible de tracer pour des monocristaux de fer dans l'intervalle de températures de −180°C à 213°C, pour deux teneurs en carbone différentes. Il a été constaté que tous les effets qui peuvent être produits dans du fer polycrystallin, c.-à-d. rupture par clivage, maclage mécanique, écoulement simple et répété, ainsi que des courbes tension-déformation uniformes, peuvent aussi être trouvés dans des monocristaux contenant 0.003 pour cent de carbone, à la même température approximativement. Des cristaux contenant environ 0.0005 pour cent de carbone montrent aussi tous ces effets, à l'exception de l'écoulement répété. La différence principale entre les monocristaux des deux compositions consiste en la grandeur et la vitesse des effets de vieillissement de déformation (strain ageing). La dépendance de la tension initiale d'écoulement, de la température, est discutée pour le cas des cristaux contenant 0.003 pour cent de carbone.

DER EFFEKT VON TEMPERATUR UND ZUSAMMENSETZUNG AUF DIE VERFORMUNG VON EISENEINKRISTALLEN

Die verschiedenen Typen der Spannungs-Verzerrungskurve, die man von Eiseneinkristallen mit zwei verschiedenen Kohlenstoffgehalten zwischen −180°C und +213°C erhalten kann, werden untersucht. Es zeigte sich, dass alle im polykristallinen Eisen auftretenden Erscheinungen, wie Spaltbarkeit, mechanische Zwillingsbildung, einfaches und wiederholtes Fliessen und glatte Verzerrungs-Spannungskurven, auch an Einkristallen mit 0.003 prozent Kohlenstoff bei ungefähr gleicher Temperatur beobachtet werden können. Einkristalle mit 0.0005 prozent Kohlenstoff zeigen gleichfalls die oben erwähnten Effekte mit Ausnahme des wiederholten Fliessens. Der wesentlichste Unterschied zwischen den Einkristallen verschiedenen Kohlenstoffgehalts ist die Geschwindigkeit und Grösse der spannungsbedingten Alterung. Die Temperaturabhängigkeit der ursprünglichen Fliess-spannung wird für Kristalle mit 0.003 prozent C diskutiert.

Introduction

The effect of temperature on the deformation of polycrystalline iron containing carbon and nitrogen is interesting and complicated. At low temperatures (e.g. − 180°C) deformation twinning and brittle fracture occur. At higher temperatures, up to about 100°C, the yield phenomenon is observed, the yield point itself showing a strong temperature dependence; at temperatures in the range 100–300°C the yield phenomenon changes into that of blue brittleness, or repeated yielding.

The purpose of the present investigation has been to explore the corresponding behaviour of single crystals of iron, since it is now known that these crystals, if they contain a little carbon or nitrogen, show yield phenomena [1; 2].

*Received February 9, 1953.
†Department of Metallurgy, University of Birmingham, England.
‡Now at A.E.I. Research Laboratories, Aldermaston, Berks., England.

Material and Apparatus

The material used for most of the work was Armco iron with an original analysis

C	Si	Mn	S	P	N
0.045%	0.01%	nil	0.005%	0.05%	0.005%

although a small number of confirmatory tests were also done with two different mild steels. All the material was received as hard-drawn wire of diameter 2 mm., and grown into single crystals of length 5 cm. and upwards. These were made by first decarburising the wire in wet hydrogen (bubbled rapidly through water at room temperature giving about 3 per cent water vapour by volume) for 18 hours at 720°C, then straining $2\frac{1}{2}$ to $3\frac{1}{2}$ per cent at room temperature, and finally annealing at 880°C for about four days in a slow stream of wet hydrogen.

The crystals were then subjected to one of two different treatments. In the first, about 0.003 per cent carbon was introduced into them by a treatment

at 700°C for 15 minutes in dry hydrogen, which had been bubbled through n-heptane at room temperature, followed by homogenizing them for 5 days at 670°C, furnace cooling to precipitate excess carbide in particles of reasonably large size and to minimize quench-ageing. Crystals given this treatment will be termed "carburised."

In the second treatment, "as grown" crystals were further decarburised at 720°C for periods up to 240 hours in hydrogen saturated with water vapour at room temperature. The flow rate was about 0.5 cu. ft. per hour. These crystals will be termed "decarburised," although strain ageing experiments described below suggested that very small amounts of carbon or nitrogen were still present.

All the crystals were strained in a hard-beam testing machine of the Polanyi type. For convenience of gripping, the specimens were soft soldered axially into cylindrical mild steel endpieces attached to the straining shackles by flexible Bowden cable (Figure 1). The cables on each grip were of the same length,

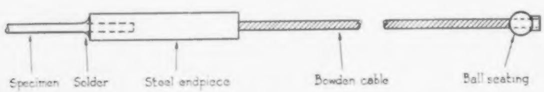

FIGURE 1. Diagram of grips used for tensile experiments on single crystals of iron.

but of opposite twist to prevent torsion of the specimen. The normal plastic strain rate in specimens 5 cm. long was 2×10^{-3} per minute.

Temperatures above room temperature were obtained by immersing the specimen in a bath of liquid paraffin during the experiment. Below room temperature ice and salt, dry ice and alcohol, and liquid air, were used in constant temperature baths.

Carburised Crystals

Several different types of stress-strain curve were obtained on carburised crystals pulled at temperatures in the range $-$ 185°C to 230°C. The effects observed, which are shown in Figures 2 to 8, are qualitatively the same as those in polycrystalline iron and occur roughly at the same temperatures.

The behaviour between $-$185°C and 20°C has already been described by Churchman and Cottrell [2]. At $-$185°C, mechanical twins formed in "bursts" [3] very reminiscent of the martensitic transformation in high nickel steels. A large load drop was observed at each burst (Figure 2), the slope of which is a characteristic of the testing machine. The crystallography of this twinning has been described elsewhere [4]. Cleavage fracture often occurred on a {001} plane after a few per cent extension by twinning.

At $-$70°C, well-marked upper yield points followed by lower yield point extensions up to 3 per

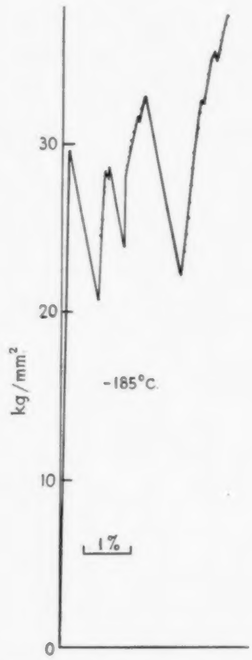

FIGURE 2. Carburised specimen strained at $-$185°C showing large load drops caused by mechanical twinning.

cent were observed (Figure 3). As the temperature of test increased, the magnitude of the stress drop at the yield and the lower yield point extension, during the first experiment on each annealed crystal, fell

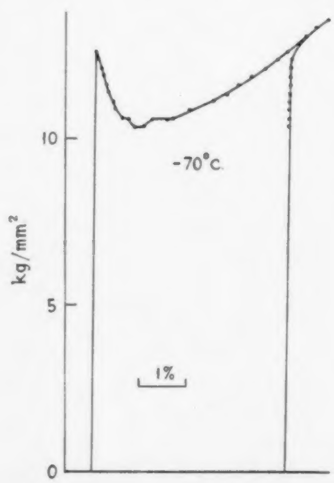

FIGURE 3. Carburised specimen strained at $-$70°C: (*a*) first experiment; (*b*) immediate re-load.

steadily until the temperature range of 50-70°C was reached. Here the character of the curves changed again.

The phenomenon of "blue-brittleness" or repeated yielding was observed above 60°C. The average magnitude of the drops in load increased with temperature up to about 130°C, and above this temperature decreased again until at about 200°C and above, the stress-strain curves were entirely smooth (Figures 5, 6, 7, 8).

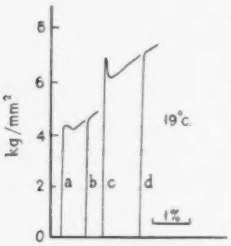

4

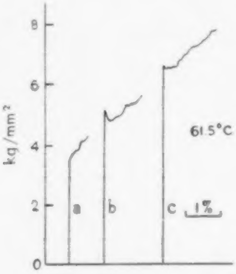

5

FIGURE 4. Carburised specimen strained at 19°C: (*a*) first experiment; (*b*) immediate re-load; (*c*) aged 80 minutes at 60°C; (*d*) immediate re-load.

FIGURE 5. Carburised specimen strained at 61.5°C: (*a*) first experiment, two hours after reaching 61.5°C; (*b*) aged 1 hour at 61.5°C; (*c*) aged 40 hours at 61.5°C.

The upper yield stress measured in the first experiment on each of the carburised crystals is plotted against temperature in Figure 9. The two main features of these results are the very steep temperature dependence of yield stress and the two distinct branches of the curve formed at temperatures above and below about 80°C.

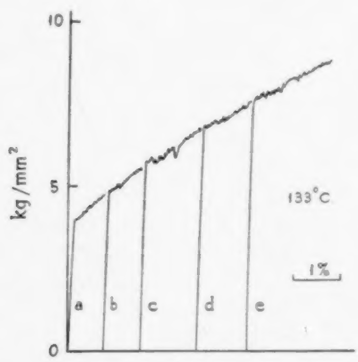

FIGURE 6. Carburised specimen strained at 133°C: (*a*) first experiment; (*b*) aged 2 hours at 133°C; (*c*) aged 18 hours at 133°C; (*d*) aged 2 hours at 133°C; (*e*) aged 40 hours at 133°C.

It is interesting to consider the mathematical form of this curve. Several equations have been proposed for the temperature dependence of yield stress. Andrade [5] has recently shown that the yield stress σ of single crystals of gold, silver, cadmium, zinc and bismuth, over quite wide ranges of temperature, is given by a relation of the form suggested by Orowan [6]

$$\sigma = \sigma_0 - AT^{\frac{1}{2}}$$

where σ_0 and A are constants.

The value of the critical shear stress in aluminium is markedly dependent on purity. The lowest

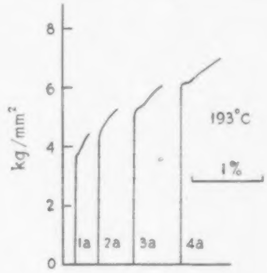

7

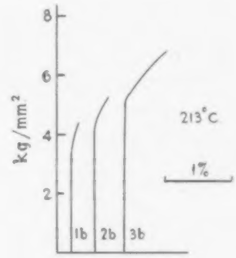

8

FIGURE 7. Carburised specimen strained at 193°C: (*a*) first experiment; (*b*) aged 2 hours at 193°C; (*c*) aged 16½ hours at 193°C; (*d*) aged 4½ hours at 193°C.

FIGURE 8. Carburised specimen strained at 213°C: (*a*) first experiment; (*b*) aged 1 hour at 213°C; (*c*) aged 1 hour at 213°C.

reported values, and thus presumably those for the highest purity of material, are the ones of Rosi and Mathewson [7] on 99.996+ per cent aluminium. They found that the temperature dependence is sufficiently steep to be represented by an equation

$$\sigma = A \exp (Q/RT)$$

where A is a constant and Q is an activation energy.

Cottrell and Bilby [8] have proposed an equation

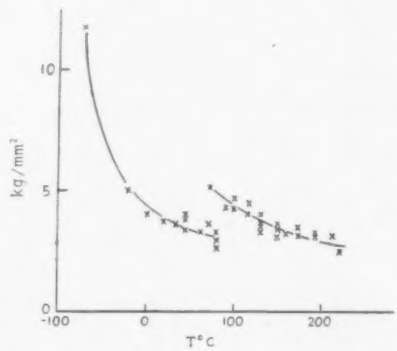

FIGURE 9. Initial yield stress versus temperature of experiment for carburised crystals.

for materials in which the dislocations are anchored by atmospheres of solute atoms. They suggest that at a constant testing rate, yielding should occur

when the quantity U/kT reaches a characteristic fixed value. U (which is a known function of σ/σ_0) is an activation energy for the formation of a stable loop of dislocation, and σ_0 is a constant corresponding to the yield stress at 0°K. The equation U/kT = constant was fitted to the results of McAdam and Mebs [9] for polycrystalline iron, and gave $U/kT = 47$ and $\sigma_0 = 125$ Kg/mm².

The results for the single crystals can be fitted better by the Cottrell-Bilby formula than one of the Orowan or Rosi-Mathewson type, between −185°C and 80°C. The value at −185°C is not known absolutely, but since the material forms mechanical twins here at about 28 Kg/mm², the stress to initiate slip must be larger than this.

The values of the constants, for best fit between theoretical and experimental curves, are

$$\sigma_0 = 117 \text{ Kg/mm}^2$$
$$U/kT = 90$$

Thus σ_0 is approximately equal to that for polycrystalline iron, but U/kT is appreciably larger. These results are summarized in Figure 10. The Orowan curve is fitted so that σ remains positive in

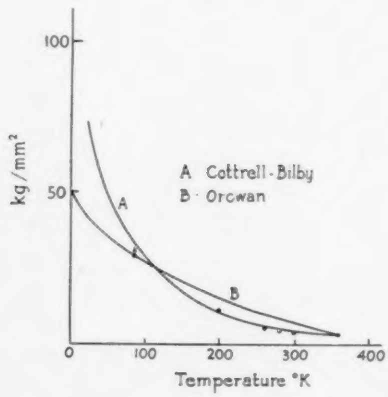

FIGURE 10. Comparison of experimental results (●) on carburised crystals with theoretical curves (full lines) for Cottrell-Bilby and Orowan hypotheses.

the range considered, and is equal to the twinning stress at −180°C.

A further analogy with polycrystals is seen in the rise in initial yield stress which occurs at about 80°C. This temperature coincides closely with that at which repeated yielding begins, i.e. ageing is sufficiently rapid to occur significantly during the time of the experiment. It seems likely that the two phenomena are closely connected, particularly since Holden and Kunz [10] and Paxton [11] have shown that ageing during the initial stressing of a specimen causes the initial yield point to be raised above its normal value.

Decarburised Crystals

These crystals, which have been subjected to anneals up to 240 hours in wet hydrogen at 720°C, showed much less pronounced yield phenomena, too small to be detected by routine testing procedures. However, a small upper yield point could be produced by straining and ageing (*in situ*, and without ever fully unloading the specimen, so that the axiality was undisturbed). The rate of strain ageing was also slowed down very markedly relative to that of carburised crystals. A load drop such as could be produced by ageing for about 1 hour at room temperature in carburised crystals was only produced in decarburised crystals after some 10 to 20 hours at 100°C. The increase in upper yield stress over the final previous applied stress, even after ageing for these long periods, was also much less than that usual for the crystals containing about 0.003 per cent carbon (see Figures 4(*c*), 12(*d*)).

The types of stress-strain curve which were obtained with the decarburised crystals are as follow:

At −185°C, it was possible with fully annealed specimens to produce mechanical twinning just as with carburised crystals, a result different from that obtained earlier [2].

At −70°C, a small upper yield point was obtained in the first experiment on an annealed crystal. The lower yield stress was comparable with that for a crystal containing 0.003 per cent carbon but the lower yield extension was much less—about 0.4 per cent as against 3 per cent (Figure 11).

At room temperature, small load drops were produced after straining 1 per cent and ageing for

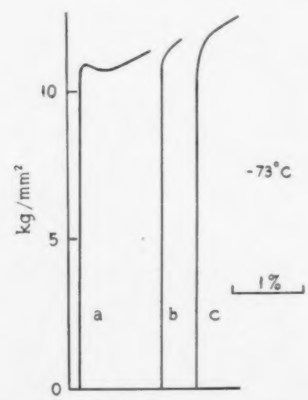

FIGURE 11. Decarburised specimen strained at −73°C: (*a*) first experiment; (*b*) immediate re-load; (*c*) aged 22 hours at 87°C.

18 hours *in situ* at 110°C (Figure 12). After straining approximately 3 per cent, it was no longer possible to produce a yield point even after 24 hours ageing at 110°C.

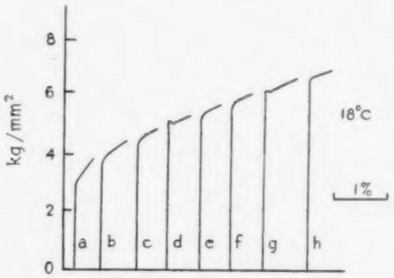

FIGURE 12. Decarburised specimen strained at 18°C: (*a*) first experiment; (*b*) aged $1\frac{1}{2}$ hours at 110°C; (*c*) aged 1 hour at 110°C; (*d*) aged 18 hours at 110°C; (*e*) aged 1 hour at 110°C; (*f*) aged $1\frac{1}{2}$ hours at 110°C; (*g*) aged 24 hours at 110°C; (*h*) aged 18 hours at 110°C.

At 140°C, very small initial yield points were observed after strain ageing, increasing to a maximum after about 100 minutes ageing at this temperature. Repeated yielding was not observed (Figure 13).

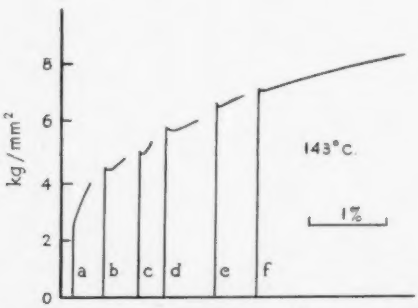

FIGURE 13. Decarburised specimen strained at 143°C: (*a*) first experiment; (*b*) aged 100 minutes at 143°C; (*c*) aged 9 minutes at 143°C; (*d*) aged $17\frac{1}{4}$ hours at 143°C; (*e*) aged 47 minutes at 143°C; (*f*) aged 17 minutes at 143°C.

At 193°C, yield phenomena were almost non-existent. A very slight lower yield extension with small strain age-hardening occurred in one crystal after straining 0.25 per cent and ageing 17 hours at 193°C. The rate of work hardening in this crystal was considerably less than in a carburised crystal at this same temperature.

A chemical analysis of crystals given a decarburising treatment was kindly arranged by Dr. N. P. Allen of the National Physical Laboratory. Three crystals given 18 hours treatment at 720°C in wet hydrogen contained 0.0006 per cent, 0.0003 per cent and 0.0005 per cent C whilst a crystal decarburised for 240 hours contained 0.0004 per cent C. The stated limit of accuracy was 0.0002 to 0.0003 per cent, and these results must be considered as upper limits for the carbon content.

It seems very likely that the results on all the decarburised crystals can be reasonably explained on the grounds that insufficient carbon is present to saturate the dislocations. The theoretical amount needed to provide one carbon atom per atom plane intersected by the dislocation (assuming a density of 10^8 lines/cm^2) is 10^{-6} wt. per cent. The work of Harper [12] indicates that in material which has

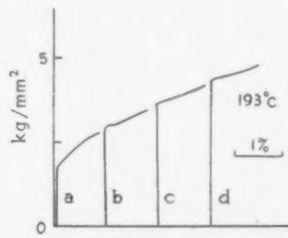

FIGURE 14. Decarburised specimen strained at 193°C: (*a*) first experiment; (*b*) aged 17 hours at 193°C; (*c*) aged $1\frac{1}{2}$ hours at 193°C; (*d*) aged $1\frac{1}{2}$ hours at 193°C.

been strained a few per cent, the dislocation density is about 10^{11} lines/cm^2. Hence, a minimum of about 10^{-3} wt. per cent is necessary to saturate all the dislocations in this case. This amount is certainly not present in the decarburised crystals, and so the dislocation atmospheres are not complete. Yield effects are thus reduced, in much the same way as has been noted recently by Wain [13] using zinc containing 0.0022 per cent nitrogen.

This is illustrated by comparison of Figure 12(*d*) and 12(*h*). A yield point is observed after about 1 per cent strain prior to ageing, but not after about 3 per cent. The number of dislocations has increased so that insufficient solute atoms are present to saturate the whole length of the dislocation lines.

The results of Harper [12] suggest that the density of dislocations ρ is roughly related to the plastic strain ϵ by the formula

$$\rho = 2.5 \times 10^{12} \times \epsilon \text{ cm}^{-2}$$

Hence for 1 per cent plastic strain, $\epsilon = 10^{-2}$ and $\rho = 2.5 \times 10^{10}$ lines/cm^2. The wt. per cent carbon to provide one carbon atom per atom plane intersected by the dislocation is

$$\frac{2.5 \times 10^{10}}{10^8} \times 10^{-6}$$

assuming 10^{-6} wt. per cent C for 10^8 lines/cm^2 [8], i.e. 0.00025 per cent.

A similar calculation for 3 per cent plastic strain

indicates that 0.00075 per cent is necessary for saturation of the dislocations. The analysis of the crystals gave a value of about 0.0005 per cent for the carbon content.

Thus, although the calculation is approximate, it does indicate that the carbon content is in the right range for yielding to disappear with increasing strain.

Repeated yielding does not occur in decarburised crystal since the ageing time is not of the same order as the duration of the experiment.

Repeated Yielding

Consideration of the mechanism of repeated yielding is complicated by the fact that it may occur in different forms depending on the metal, and whether this is in single crystal or polycrystalline form, and on the nature of the testing machine.

The phenomenon of jerky creep was observed in metal single crystals by Becker and Orowan [14] using commercial-purity zinc. Repeated yielding has been observed by Dumbleton [15] in zinc single crystals, and by Ardley and Cottrell [16] in single crystals of α- and β-brass.

The basic feature of the dislocation theory of the effect is that the speed of diffusion of impurity atoms is sufficiently large to anchor the dislocations very quickly once these become held up anywhere in the crystal, but insufficiently large to diffuse so rapidly that a dislocation never effectively breaks away from an atmosphere. There is thus an optimum temperature, for each given strain rate, at which the load drops are a maximum; in the carburised iron crystals this was about 130°C.

The nature of the testing machine is important in determining the form of the phenomenon. In a "soft" machine, or with dead loading, the stress does not relax appreciably during a sudden small extension. Thus one would expect deformation to propagate through the entire length of the specimen. This has been observed by McReynolds [17] in impure polycrystalline aluminium.

On the other hand, in a "hard" testing machine a sudden extension can cause a marked stress drop. This may be sufficient to reduce the average speed of the dislocations substantially, and to enable anchoring to occur before the deformation has occurred throughout the entire specimen. Examples of this have been noted in polycrystalline iron by Hall [18] and Paxton [19]. At temperatures in the region 100-200°C, remarkably regular repeated yielding occurs in the first experiment on an annealed specimen. This occurs in the portion of the stress-strain curve corresponding to the lower yield extension at room temperature. At each fall in stress, the yield front moves a constant distance into the undeformed material quite rapidly. Anchoring occurs and the stress begins to rise again immediately. When the yield front has passed completely along the specimen, a rising stress-strain curve ensues which is accompanied by much more irregular jerky flow.

It would appear that the detailed mechanism in iron single crystals is different from that in other single crystals or in polycrystalline iron. Metallographic study of the initial yield in carburised iron single crystals indicates that a deformation front passes along the specimen in a manner rather similar to that in polycrystals [19]. The lower yield extension in these single crytals decreases with increasing temperature, and it seems probable that at the temperatures at which repeated yielding occurs, it is of the order of 0.1 per cent, which is of the same magnitude as the extension corresponding to each of the load drops. Thus the regular repeated yielding was not observed, since the majority of the specimen has been traversed by the yield front; the second and subsequent load drops are presumably caused by movement of the band front through work hardened material, and as a result occur at successively higher stresses.

Conclusions

In single crystals of iron containing about 0.003 per cent carbon it is possible to produce all the phenomena previously found in polycrystals, i.e. cleavage fracture, mechanical twinning, simple and repeated yielding, and, at sufficiently high temperatures, smooth stress-strain curves.

In crystals with much less than 0.003 per cent carbon most of the same phenomena occur, but to a much less marked degree. Repeated yielding does not occur at all, for the time of ageing is increased by a factor of 10^3 to 10^4.

Acknowledgements

The authors wish to express their gratitude to Professor A. H. Cottrell for many helpful discussions and Professor D. Hanson and the University of Birmingham for the provision of facilities and financial support.

References

1. Schwartzbart, H. and Low, J. R. Trans. A.I.M.E., **185** (1949) 637.
2. Churchman, A. T. and Cottrell, A. H. Nature, **167** (1951) 943.
3. Machlin, E. S. and Cohen, M. J. Metals, **3** (1951) 746.
4. Paxton, H. W. Acta Met., **1** (1953) 141.

5. ANDRADE, E. N. DA C. Phil. Mag., **43** (1952) 1218.
6. OROWAN, E. Z. Phys., **89** (1934) 605.
7. ROSI, F. D. and MATHEWSON, C. H. Trans. A.I.M.E., **188** (1950) 1159.
8. COTTRELL, A. H. and BILBY, B. A. Proc. Phys. Soc. (London), **A62** (1949) 49.
9. MCADAM, D. J. and MEBS, R. W. Trans. A.S.T.M., **43** (1943) 661.
10. HOLDEN, A. N. and KUNZ, F. W. J. App. Phys., **23** (1952) 799.
11. PAXTON, H. W. J. App. Phys., **24** (1953) 104.
12. HARPER, S. Phys. Rev., **83** (1951) 709.
13. WAIN, H. L. Proc. Phys. Soc. (London), **B65** (1952) 886.
14. BECKER, R. and OROWAN, E. Z. Phys., **72** (1932) 566.
15. DUMBLETON, M. J. Ph.D. thesis, Birmingham (1952).
16. ARDLEY, G. W. and COTTRELL, A. H. To be published in Proc. Roy. Soc.
17. MCREYNOLDS, A. W. Trans. A.I.M.E., **185** (1949) 32.
18. HALL, E. O. J. Iron and Steel Inst., **170** (1952) 331.
19. PAXTON, H. W. Ph.D. thesis, Birmingham (1952).

LE CHATELIER'S PRINCIPLE AND STRESS-INDUCED DISPLACIVE TRANSFORMATIONS*

E. S. MACHLIN and S. WEINIG†

An application of Le Chatelier's Principle to stress-induced displacive transformations has been made and illustrated with experimental data on a 9 per cent Mo–Ti alloy. In this case, which involves no measurable change in specific volume between product and parent phases, transformation is induced to occur along plates which on the average are parallel to the planes of maximum shear stress.

LE PRINCIPE DE LE CHATELIER ET LES TRANSFORMATIONS DE DÉPLACEMENT INDUITES PAR DES TENSIONS

Le principe de Le Châtelier a été appliqué aux transformations de déplacement induites par des tensions. Une illustration en a été faite avec les données expérimentales obtenues d'un alliage Mo–Ti à 9 pour cent de Mo. Dans ce cas, qui n'implique pas de modification mesurable du volume spécifique au passage de la phase primaire au produit final, la transformation est induite le long de lamelles parallèles, en moyenne, aux plans de tension de cisaillement maximum.

DAS LE CHATELIER'SCHE PRINZIP UND SPANNUNGSAUSGELÖSTE MODIFIKATIONSUMWANDLUNG MIT ATOMVERSCHIEBUNG

Das Le Chatelier'sche Prinzip wurde auf die spannungsausgelösten Umwandlungen, die von einer Verschiebung der Atome im Gitter begleitet sind, angewandt, und durch experimentelle Resultate an einer 9 prozent Mo–Ti Legierung erläutert. In diesem Falle, in dem keine messbare Änderung des spezifischen Volumens der Ausgangs- und der Endphase auftritt, wird die Umwandlung längs der Kristallebenen ausgelöst, die im Durchschnitt den Ebenen der maximalen Schubspannung parallel sind.

A little known application of Le Chatelier's Principle is involved in the stress-induced displacive (martensitic) transformations. (A displacive transformation is defined in this paper to be any phase transformation that involves a homogeneous deformation.) The purpose of this note is to describe the application of Le Chatelier's Principle to such displacive transformations and to illustrate the validity of the predictions with experimental data obtained using a 9 per cent Mo–Ti alloy.

Certain characteristics of the displacive transformation are important in this analysis. They are as follows:

1. A single crystal of the parent phase can potentially exhibit all the possible permutations‡ of the crystallographic habit planes. A habit plane is the plane of the product plate referred to the parent crystal.

2. The region that transforms also deforms homogeneously. The net total transformation strain observed is usually different from the transformation strains of submicroscopic units of this macroscopic region. Twinning or slip may occur in a product plate on a fine scale relative to the dimensions of the plate. The net strain observed therefore differs from the transformation strain.

3. For a given single crystal of the parent phase, one and only one net total strain is associated with a given permutation of the habit plane indices. Thus, for example, a system yielding an $\{hhl\}$ type habit will in general show twelve different net total strains relative to a given set of coordinates axes in the parent crystal. Hence, for a given size and shape of a product plate (i.e. of a transformed region), there are at most twelve possible length changes of the specimen along any arbitrary direction.

4. The net total strain can be described in terms of the relative motions of parallel invariant planes. For a transformation that involves a volume change there is a component of motion of the invariant planes along their normal direction. In general, there will also be a shear component of motion along a direction in the invariant plane. *The invariant planes are parallel to the habit planes.*

5. The application of stress above the M_s or equivalent temperature activates this displacive transformation in the metastable parent phase for a transformation that occurs on cooling and vice versa.

The problem is to determine whether the application of stress produces transformation products having preferred habit planes. If so, what are the analytic principles determining their choice? Le Chatelier's Principle is the basis for the derivation of these analytic guides. It states, in effect, that the mode of transformation chosen is such that the applied stress does the maximum amount of work.

In applying Le Chatelier's Principle it is necessary to know whether the applied stress acts to nucleate the transformation which then grows out spon-

*Received February 17, 1953; in revised form March 4, 1953.

†School of Mines, Columbia University, New York 27, New York, U.S.A.

‡Two permutations of the habit system $\{225\}$ are $(5\bar{2}2)$ and (522).

taneously, or whether it acts to propagate the "growth" of the product plates. This problem arises because the stress can be assumed to act either on the transformation strain associated with a small volume or on the net total transformation strain associated with a macroscopic region of transformation. As will be shown later, the displacive transformation investigated seems to be of the latter type. Hence, it will be assumed that the stress acts upon the net total transformation strain. If transformations of the former type could be found it appears that this application of Le Chatelier's Principle is capable of providing information as to whether the nucleus comprises a region of net strain or of unit strain of the transformation.

Let the invariant plane strain be the most general type possible, i.e. have a normal as well as tangential component. Let the normal component be ϵ and the tangential component be γ. The work done by the applied stress will be a maximum when the following relation is a maximum

$$\tau_r \gamma + \sigma_r \epsilon \tag{1}$$

where τ_r is the resolved shear stress matching the shear strain component of the net total transformation strain and σ_r is the resolved normal stress matching the corresponding normal strain component.

In a single crystal, for an $\{hhl\}$ type habit there are twelve ways the applied stress must be resolved. The particular permutation of the habit system induced to appear by the applied stress is that for which the above relation is a maximum.

In a polycrystal, the probability is high that potential habit planes will be found such that the above relation will assume its maximum possible value. The situation for a uniaxial stress will be examined as follows. If α is the angle between the normal to the invariant plane and the direction of the applied stress then

$$\tau_r = \sigma_0 \cos\alpha \sin\alpha,$$
$$\sigma_r = \sigma_0 \cos^2\alpha$$

where σ_0 is the applied stress. Substituting and differentiating to determine the value of α at which equation (1) will be maximized, it is found that

$$\tan 2\alpha = \frac{\gamma}{\epsilon}. \tag{2}$$

For the case where $\epsilon = 0$, equation (1) will be a maximum when the invariant plane lies along the plane of maximum shear stress, i.e. the solution of (2) is $\alpha = 45°$.

An experimental investigation to check the proposed application of Le Chatelier's Principle was made using a 9 per cent Mo–Ti alloy. The diffusionless transformation in this system is from a β body-centered cubic lattice to an α' close-packed hexagonal lattice. This transformation occurs with an extremely small volume change. For the purposes of this investigation the normal strain ϵ can therefore be taken equal to zero. In this case, it would be expected that the first plates induced by stress in a polycrystal would form with their habit planes parallel to the planes of maximum shear stress.

The specimens were cut from an 150 gram double arc melted ingot composed of commercial process A titanium and high-purity molybdenum. They were cold rolled and then cut to $\frac{3}{4}'' \times \frac{1}{16}'' \times \frac{1}{4}''$, homogenized in evacuated vycor at 0.1 microns for 24 hours at 1000°C. They were then step-quenched in liquid lead at 700°C for 1–3 seconds followed by a direct quench into water. This treatment resulted in an apparently all-β matrix at room temperature and thereby facilitated the investigation.

Stress was applied in bending, torsion, pure shear, and tension to vary the orientation of the maximum shear stress plane. A distribution curve, showing the number of plates, the normals to which have angles between α and $\alpha + d\alpha$ to the neutral axis, is given in Figure 1 for plates induced by bending stress.

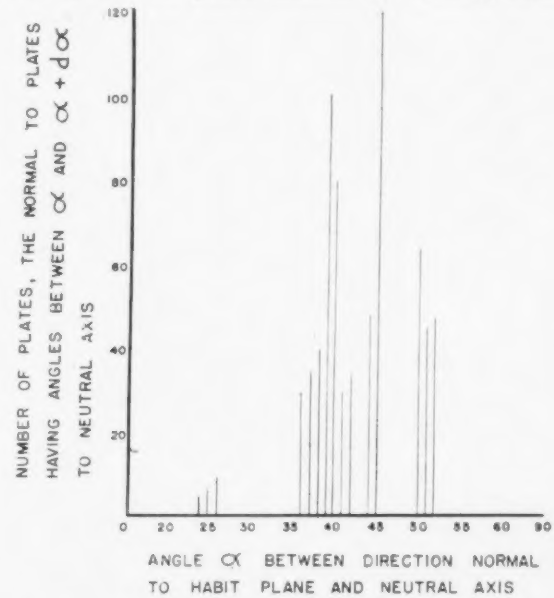

FIGURE 1. Habit distribution of alpha prime plates in bending. (Stabilized 9 per cent Mo–Ti alloy.)

A two-surface analysis was used to determine this angle [1]. In this case the plane of maximum shear stress at the extreme fiber is at 45° to the neutral axis. As shown in Figure 1, the distribution has a maximum about 45°. A random distribution in this case would correspond to a horizontal line. Thus, the

distribution obtained is evidence for the operation of Le Chatelier's Principle in a stress-induced displacive transformation. Further evidence for the applicability of this principle is given in Figure 2 which shows the habit plane traces in a specimen subjected to a torsional twist about the vertical axis. In this case the planes of maximum shear stress lie normal to and parallel to the axis of twist. As shown, the habit planes are parallel to these planes of maximum shear stress. Further investigation for the cases of uniaxial tension and pure shear showed this same correlation between habit planes and planes of maximum shear stress. Thus, the application of Le Chatelier's Principle to stress-induced displacive transformations is consistent with experimental results.

An interesting illustration of point 3 of the introduction is presented in Figure 3. Here a single crystal occupies the entire cross-section over part of the specimen length. According to point 3, one would expect that because the sense of shear in a given plane reverses on crossing from the tension to the compression side of the neutral axis, plates of

FIGURE 2. Alpha prime plates produced in torsion. Torsion axis parallel to bottom of page. (250×, reduced by $\frac{1}{3}$ in reproduction.)

different permutation of the habit system would be induced on the compression side as compared to the tension side. Both however would probably be as close to the maximum shear stress plane as possible. As shown in Figure 3, the habit plane traces do differ comparing both sides of the neutral axis. Because of the sensitivity of the habit induced by the applied stress to the plane of maximum shear stress, direction of maximum shear stress, and magnitude of maxi-

FIGURE 3. Strain-induced alpha prime plates in a beta matrix; specimen bent. *Top*, compression; *bottom*, tension. (35×, reduced by $\frac{1}{3}$ in reproduction.)

mum shear stress [2], it appears that this phenomenon has potential use in three-dimensional stress analysis studies.

Another interesting point is that the plate thickness seems to be a function of the magnitude of the stress, disappearing to zero thickness on approaching the neutral axis. The latter point suggests that in this alloy the applied stress controls the extent of transformation of a single plate. This observation supports the assumption previously made in the analysis concerning the role of applied stress on the diffusionless transformation in this alloy system.

Summarizing, the stress-induced displacive transformation in a stabilized 9 per cent Mo–Ti alloy forms in the manner described by Le Chatelier's Principle. It is suggested that this phenomenon can be useful in studying the nature of the nuclei of stress-induced displacive transformations that propagate without being affected by the applied stress field. Further, it is suggested that this phenomenon has potential use in three-dimensional stress analysis.

Acknowledgement

The authors gratefully acknowledge the financial support of the Watertown Arsenal, Ordnance Corps, U.S. Army.

References

1. BARRETT, C. S. Structure of Metals (New York, McGraw-Hill, 1943), p. 39.
2. Unpublished research, Columbia University.

INTERNAL FRICTION OF IRON AND MOLYBDENUM AT LOW TEMPERATURES*

LO-CHING CHANG and M. GENSAMER†

An internal friction peak has been found in iron at about 100°K, and possibly in molybdenum at about 300°K. These internal friction peaks occur at temperatures corresponding to the ductile to brittle transition of these materials in slow tension tests. The possible role of hydrogen in causing the 100°K peak in iron is briefly discussed.

LE FROTTEMENT INTERNE DU FER ET DU MOLYBDÈNE AUX BASSES TEMPÉRATURES

Une bosse a été trouvée aux courbes de frottement interne du fer aux environs de 100°K et probablement du molybdène aux environs de 300°K. Ces bosses se présentent aux températures correspondant à la transition de l'état ductile à l'état fragile de ces matériaux dans des essais lents d'extension. Le rôle possible de l'hydrogène dans la production de cette bosse à 100°K dans le fer est brièvement discutée.

INNERE REIBUNG BEI EISEN UND MOLYBDEN BEI TIEFEN TEMPERATUREN

Ein Dämpfungsmaximum wurde für Eisen bei etwa 100°K und möglicherweise für Molybden bei etwa 300°K gefunden. Diese Maxima treten bei Temperaturen auf, die dem Übergang formbarspröde in langsamen Zugversuchen mit diesen Metallen entsprechen. Der Einfluss, den Wasserstoff möglicherweise auf das Entstehen des 100°K Maximum im Eisen hat, wird kurz diskutiert.

The internal friction of iron and molybdenum above room temperature has been studied by a number of investigators. Internal friction peaks (at frequencies of about one cycle per second) have been reported by Kê [1] for iron: (*a*) at 300°K, associated with the stress-induced preferential distribution of nitrogen atoms (the corresponding peak due to carbon atoms takes place at a slightly higher temperature); (*b*) at 500°K, due to "stress-induced diffusion of nitrogen atoms within some peculiar type of stress regions created in the specimen after it was subjected to cold work"; and (*c*) at 750°K, due to grain-boundary relaxation. Maringer and Muehlenkamp [2] have found an internal friction peak in molybdenum at about 1000°K, which is believed by them to be associated with the stress-induced diffusion of nitrogen atoms in solid solution. Little is known of the internal friction of these metals below room temperature. In the course of a study of the mechanism of low temperature brittleness in metals and alloys in this laboratory, an internal friction peak has been found in iron at about 100°K, and possibly in molybdenum at about 300°K.

A low frequency, direct recording, internal friction apparatus has been constructed for the study of internal friction of metals at low temperatures, in which the specimen is strained in bending rather than torsion. This arrangement permits the use of short specimens easily machinable from cylindrical rods, at frequencies near one cycle per second. A schematic diagram of the apparatus is shown in Figure 1. The specimen D is mounted upright in collets; the top collet is integral with the mass B, made of

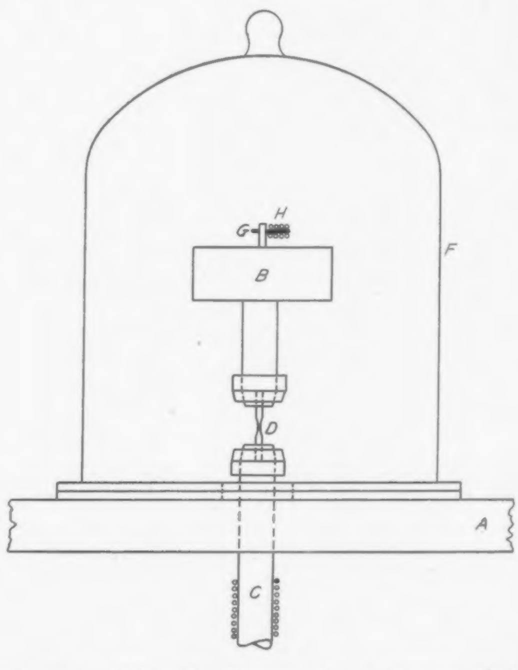

FIGURE 1. Schematic diagram of the internal friction apparatus.

brass, and the bottom collet is part of a solid copper rod C mounted rigidly in the table top A. A small cylindrical soft iron rod G, attached to the mass B, acts as the core of a Schaewitz differential transformer

*Received April 10, 1953.

†School of Mines, Columbia University, New York 27, New York, U.S.A.

coil H. The whole unit is enclosed in a glass bell jar F. The mass is set into oscillation by a pusher which is not shown in Figure 1. The motion of the iron rod G, which for small vibrations varies linearly with the strain amplitude in the specimen, is continuously recorded by a Sanborn hot-wire recording oscillograph.

A detailed drawing of the specimen is shown in Figure 2. A copper-constantan thermocouple is

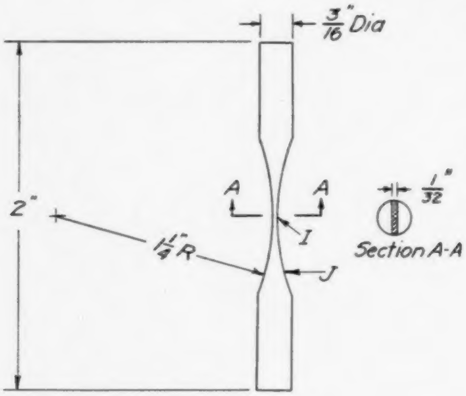

FIGURE 2. Specimen.

inserted into a small hole drilled into the specimen at a point J about 9 mm. from the center point I. Temperature differences between I and J at various cooling rates are predetermined by simultaneous measurement at both points with two thermocouples. During a damping experiment only the temperature at point J is measured.

Heating of the specimen is provided by passing a current through nichrome wires wound around the copper rod C. Cooling of the specimen is provided by flushing liquid nitrogen directly at the lower collet. This has proved very successful in avoiding any condensation on the specimen. The internal

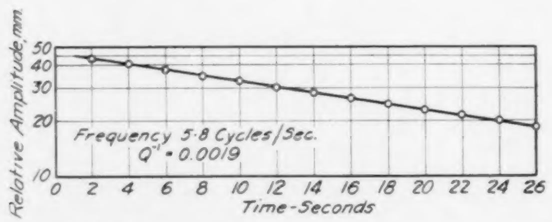

FIGURE 3. A typical logarithmic amplitude versus time curve.

friction of a given specimen under atmospheric pressure and under a pressure of a few microns is negligibly different. The lowest observed internal friction of the present apparatus with iron specimens is about 0.0004, which is about half of that observed by Kê [1] with his torsion apparatus. This shows that the total background due to air damping, apparatus losses, and magneto-mechanical damping in the case of iron specimens, is considerably less than 0.0004. The maximum amplitude of vibration

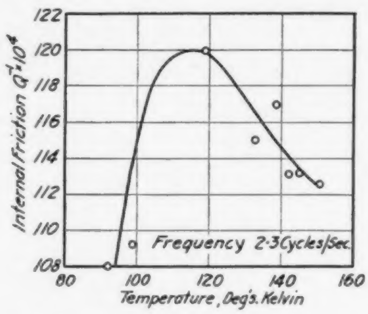

FIGURE 4. Internal friction versus temperature, electrolytic iron.

of the specimen corresponds to a maximum tensile or compressive stress of about 10^8 dynes per sq. cm. (not over 2,000 psi). A typical amplitude versus time curve is shown in Figure 3.

Typical internal friction versus temperature

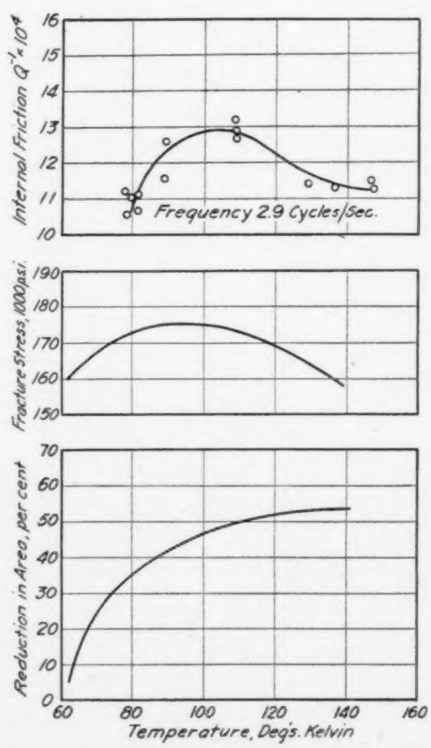

FIGURE 5. Internal friction and mechanical properties versus temperature, 0.20 per cent carbon steel (tensile data from [3]).

curves for polycrystalline electrolytic iron, plain carbon steel containing 0.20 per cent carbon, and Westinghouse arc-cast molybdenum specimens are shown, respectively, in Figures 4, 5, and 6 (upper portion of Figures 5 and 6), each showing a broad peak followed by a fairly rapid drop of internal friction at lower temperatures. The internal friction peak for iron and steel specimens occurs at about 100°K and that for molybdenum at about 300°K. It is interesting to note that these peaks coincide closely with the onset of the ductile to brittle

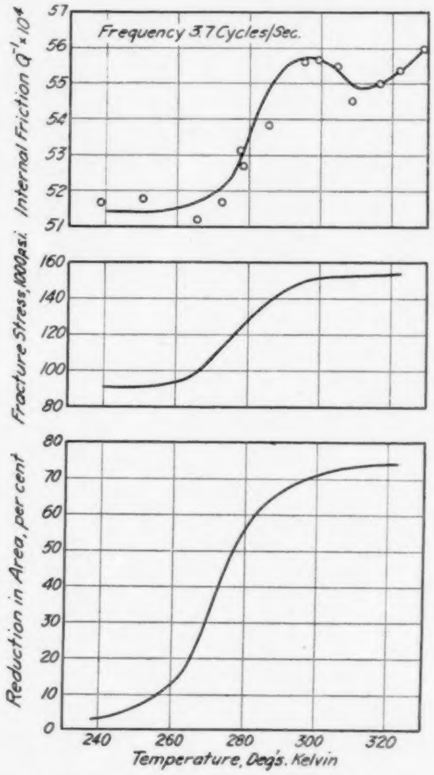

FIGURE 6. Internal friction and mechanical properties versus temperature, Westinghouse arc-cast molybdenum (tensile data from [4]).

transition of these materials in slow tension tests. For purposes of comparison, the fracture stress-temperature and the ductility-temperature curves of similar materials are incorporated in Figures 5 and 6 (lower portion of each figure) [3; 4].

The 100°K internal friction peak in the 0.20 per cent carbon steel is probably associated with the presence of hydrogen in alpha iron. The internal friction-temperature curve for the 0.20 per cent carbon steel after annealing at 975°K for 40 hours under a pressure of about 10^{-5} mm. of mercury is shown in Figure 7(a). The curve for the same specimen immediately after pickling in 50 per cent hydrochloric acid for 4 hours at room temperature is shown in Figure 7(b). The specimen, after pickling, was again annealed at about 775°K for 4 hours under a pressure of about 5×10^{-8} mm. of mercury, and its internal friction-temperature curve is shown in Figure 7(c). The background internal friction, as measured for example at 180°K, is difficult to reproduce; but there seems no doubt that the magnitude of the internal friction peak at 100°K is greater in acid-pickled specimens than in vacuum-annealed specimens. The role of hydrogen in alpha

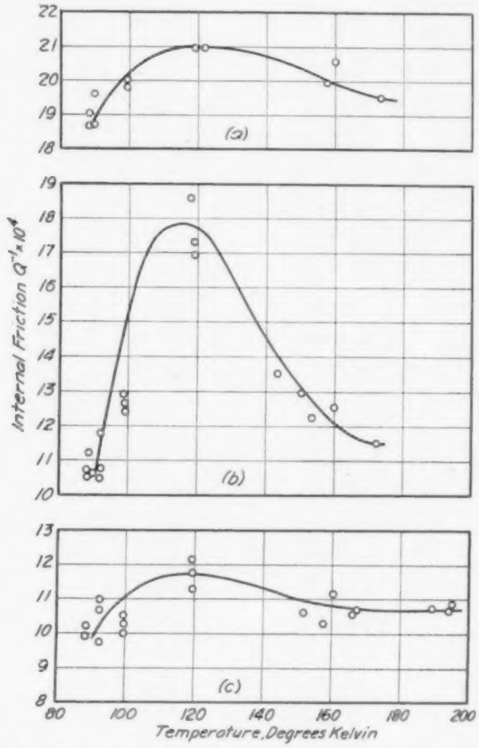

FIGURE 7. Internal friction versus temperature of a 0.20 per cent carbon steel: (*a*) annealed (975°K, 40 hours, 10^{-5} mm. Hg); (*b*) hydrochloric acid pickled; (*c*) annealed again (775°K, 4 hours, 5×10^{-8} mm. Hg).

iron is probably similar to that of carbon and nitrogen at higher temperatures. Further investigation of the nature of these internal friction peaks is in progress in this laboratory.

*Note Added in Proof**

Recent experiments on 0.20 per cent carbon steel specimens show that annealing in hydrogen (at about 875°K under a pressure of 60 atmospheres) results in a more pronounced increase of the 100°K internal friction peak than acid pickling.

*July 24, 1953.

Acknowledgement

This work is supported by the United States Navy under contract Nonr-266(07). The authors wish to thank Mr. Bechtold of the Westinghouse Research Laboratories, East Pittsburgh, Pa., for the supply of molybdenum specimens.

References

1. Kê, T. S. Trans. A.I.M.E., **176** (1948) 448.
2. Maringer, R. and Muehlenkamp, G. T. J. Metals, **4** (1952) 149.
3. Eldin, A. S. and Collins, S. C. J. Appl. Phys., **22** (1951) 1296.
4. Bechtold, J. H. and Scott, H. Metal Progress, **61** (1952) 85.

THE GROWTH OF STRAIN-ANNEAL CRYSTALS OF PREDETERMINED ORIENTATION*

G. K. WILLIAMSON and R. E. SMALLMAN†

The principles involved in the growth of metallic single crystals by recrystallisation methods are discussed, with particular reference to the effects of the temperature gradients and velocity of the furnace, annealing textures, shape and preparation of the specimen. A furnace, designed in accordance with these principles, is described, and with it, long lamellar crystals of any required orientation can be reproducibly grown in superpure (> 99.99 per cent) aluminium and many of its alloys.

LA PRODUCTION DE CRISTAUX D'UNE ORIENTATION PRÉDÉTERMINÉE PAR LA MÉTHODE ÉCROUISSAGE-RECUIT

Les principes impliqués dans la production de monocristaux métalliques par la méthode de recristallisation sont discuté, en s'arrêtant plus particulièrement aux effets du gradient de température, de la vitesse du four, des textures de recuit et de la forme et préparation de l'échantillon. Une description est donnée d'un four conçu suivant ces principes. Ce four permet de préparer, avec reproductibilité, des cristaux oblongs de forme lamellaire et de toutes les orientations voulues, en aluminium très pur (> 99,99 pour cent) et en plusieurs de ses alliages.

DIE ZÜCHTUNG VON EINKRISTALLEN MIT VORBESTIMMTER ORIENTIERUNG NACH DER GLÜHVERFORMUNGSMETHODE

Die grundsätzlichen Erscheinungen beim Züchten von Metalleinkristallen nach Rekristallisationsverfahren werden diskutiert und zwar mit besonderer Betonung des Einflusses von Temperaturabfall, Ofengeschwindigkeit, Glühtexturen und Form und Vorbehandlung der Proben. Ein Ofen, der nach diesen Regeln gebaut wurde, wird beschrieben. In diesem Ofen können lange flache Kristalle jeder gewünschten Orientierung aus Reinst (> 99.99 prozent) Aluminium und vielen seiner Legierungen gezüchtet werden.

1. Introduction

Metallic single crystals grown by "melt" methods (see [1] for review) usually possess lineage structures [2] and uneven surfaces. Recrystallisation methods however are superior in these respects and have the additional advantage that they can be used for growing single crystals in metals having phase transformations below the solidus, as in iron. Two recrystallisation methods are possible; in the first, the crystal is grown by secondary recrystallisation into a matrix with a very pronounced annealing texture, the matrix being either strained [3] or unstrained [4]; and in the other, the crystal is grown into a strained matrix having only slight preferred orientation. In both methods the specimen is usually first annealed to a fine recrystallised grain size, slightly strained (1–3 per cent tensile strain) and then annealed at a gradually increasing temperature [5]. This last anneal is usually given in a stationary furnace, but a travelling furnace is preferable since simultaneous nucleation at many points is prevented, and the temperature gradients are more readily controlled. For the production of a single crystal, all growth must originate from a single nucleus, and one purpose of this paper is to discuss factors which may affect, directly or indirectly, the formation of other active nuclei.

*Received April 22, 1953.
†Department of Metallurgy, University of Birmingham, England.

2. General Factors Influencing the Growth of Single Crystals by Recrystallisation

Suppose that a travelling furnace moves over the specimen with a speed $v = dl/dt$ and has a temperature gradient $S = dT/dl$ where l is measured along the specimen length. The temperature T_g of the interface where the crystal growth is taking place is related to the velocity of steady state growth, which equals v, and if growth is an activated process with activation energy Q_g then

$$v = B \exp(-Q_g/kT_g) \tag{1}$$

The value of B is discussed in section 3. Thus

$$T_g = Q_g/k \ln(B/v) \tag{2}$$

Let the probability of forming a nucleus in unit volume at a temperature T during an increment of time dt be $p(T)\,dt$. Then, assuming for simplicity that S is a constant from $T = 0$ to $T = T_g$, a small element of volume $A dl$, which at time $t = 0$ is at the lowest point of the temperature gradient will have a probability of nucleation given by

$$A\,dl \int_{T=0}^{T=T_g} p(T)\,dt = A\,dl \int_{t=0}^{t=T_g/Sv} p(tSv)\,dt \tag{3}$$

and the total probability of nucleation in the entire sample will be

$$P = \int_0^L A\,dl \int_0^{T_g/Sv} p(tSv)\,dt \tag{4}$$
$$= V \int_0^{T_g/Sv} p(tSv)\,dt$$

where V is the volume of the specimen. If nucleation is also considered to be an activated process, only those regions having the lowest activation energy Q_n need be considered, and if the probability of finding such regions in unit volume is C, then

$$p(T) = C \exp(-Q_n/kT) \tag{5}$$

In this case $p(T)$ is such a steep function of temperature that the integral in equation (4) is reasonable even if S is constant only at temperatures just below T_g, as in most experimental arrangements. Equation (4) has an asymptotic solution if Q_n/kT_g is large (as it must be if the probability of nucleation is to be small); thus*

$$P = \frac{T_g^2 \exp(-Q_n/kT_g)\, CVk}{SvQ_n} \tag{6}$$
$$= \frac{(v/B)^{Q_n/Q_g}\, CVQ_g^2}{Sv(\ln(B/v))^2\, k\, Q_n}$$

For the growth of single crystals, conditions must be maintained so that the value of P is vanishingly small.

The importance of some of the factors in equation (6) has been known for some time, e.g. Schmid and Boas [5] recommend temperature gradients (i.e. $S \neq 0$); furthermore crystals of large volume V are known to be more difficult to produce than small ones. An interesting feature disclosed by equation (6) is the strong influence which the activation energy ratio Q_n/Q_g exerts on the importance of the velocity v. If the preparation of the specimen is such that Q_n/Q_g is appreciably greater than unity (as both intuitive arguments and equation (6) show to be desirable), then P is reduced by a reduction in v, if this latter is smaller than B. This result contradicts the intuitive notion that a slow furnace speed would make P larger by allowing more time for nucleation at each temperature. Although such an effect exists ($1/v$ in equation (6)), it is generally outweighed by the remaining factors in equation (6) which reflect the strong dependence of P upon T_g, which is also reduced by a reduction in velocity (equation (2)).

Some experimental separation of these variables is possible. Suppose that the specimen has a Q_n/Q_g value appreciably greater than unity, then a furnace with either too small a temperature gradient or too great a velocity may fail to produce a single crystal, and this defect can be remedied by a practicable reduction in the velocity. If however Q_n/Q_g is equal to or less than unity, no practicable reduction in the velocity will produce an appreciable reduction in the probability of nucleation, and attention must be directed towards improvement of the preparation of specimens so that Q_n/Q_g is raised.

3. Annealing Textures and Their Effect on *B*

The factor B in equation (1) represents a limiting growth velocity, and, in practice, no single crystal can be grown if v approaches B since the term $(\ln(B/v))^{-2}$ in equation (6) approaches infinity. Studies of secondary recrystallisation by Beck [6; 7] have shown that the value of B is very sensitive to the crystal orientation if there is a pronounced preferred orientation in the samples, the rate of growth being greatest when the orientation of the crystal is rotated from 30 to 40° with respect to the original orientation or texture. In cases where such orientation relationships hold, single crystals are readily grown because of the great increase in the permissible velocity v. Physically this corresponds to a reduction in T_g for a given value of v, so that the probability of nucleation is decreased. On the other hand, for crystals with orientations near to that of the texture or its twin, the factor B appears to be very small, and the growth of such crystals is difficult.

The relative differences in P (v constant) or v (P constant) for these two extreme cases may be estimated if it is assumed that B depends on the degree of disorder at the crystal boundary. A high angle boundary (30 to 40° rotation) may be thought of as a continuous (monatomic) layer of disordered atoms. Each atom in the boundary is near to an irregularity analogous to a vacant site so that atomic migration in the boundary layer is rapid. The effective density of vacant sites in this layer is about 10^{-1}. It is unlikely that a low angle boundary contains any such disordered layer since it may be considered as a wall of dislocations. The only effective vacant sites available for atomic migration are those in thermal equilibrium, and, until the melting point is reached, their density usually does not exceed about 10^{-5}.

The limiting velocity B should be proportional to the density of vacant sites on the boundary and thus vary by a factor of about 10^4 with changes in crystal orientation. If all the other factors in equation (6) are kept constant then P would increase by a factor

*Whittaker and Watson [14].

of more than 10^8 on going from a high to a low angle boundary, when $Q_n/Q_g = 2$ (an approximate value extrapolated from results of Anderson and Mehl [8]). Alternatively, the velocity v would have to be reduced by a factor of more than 10^8 in order to keep P constant in these circumstances. In practice, such a range of furnace velocities is too large to be practicable and it is not surprising that it has been reported that crystals cannot be grown into "low angle" orientations [3]. This is the great disadvantage of the secondary recrystallisation method.

In the alternative method where a crystal is grown into a material with little preferred orientation the value of B varies as the interface moves from grain to grain. The effective value of B will be intermediate between the two extremes discussed above and corresponds to the formation of a single crystal network surrounding, and capable of slowly absorbing, grains with low B values. The value of B is no longer dependent on orientation, and all orientations may be grown under a standard set of conditions. These are, however, more critical than those required for "high angle" crystals grown by secondary recrystallisation. In fact, these latter crystals grow readily in the experimental conditions described in section 4, where the effects of specimen shape prevent growth in the absence of texture. All such crystals are within 2° of a constant orientation and renucleate to the original orientation if any attempt is made to change it (section 6). These results demonstrate the steep orientation dependence of B in this case, and they cannot be explained by an "oriented nucleation" theory alone.

VOL. 1 1953

4. Nucleation and the Effect of Specimen Shape

Recent theories suggest that nucleation is the polygonisation of regions of severe lattice bending [9;10] which are formed to accommodate the different modes and degrees of slip in adjacent grains. The activation energy Q_n in equation (5) depends on the radius of curvature of bending, and the factor C represents the probability of finding a region of such curvature. Although equation (5) ought to be generalised to include a whole range of C and Q_n values, the present simple form is adequate here since the regions of lowest Q_n produce the nucleation most difficult to avoid.

In a polycrystal every grain is constrained to a certain extent to deform equally with its neighbours, this constraint being exerted through the boundary where it joins these neighbours. At places in the grain which are remote from this boundary the deformation is unconstrained until the strain gradient, which is set up near the grain boundary, reaches back to them. The smaller the area of grain boundary and the greater the free surface, for a given grain size, the more intense is this gradient expected to be, i.e. the more inhomogeneous is the deformation near the boundary. Grains totally enclosed in the specimen have boundaries over a solid angle 4π, those at the surface are enclosed over 2π, and those at a free edge over π. Hence, we expect most heterogenity in the latter grains and least in the interior ones. Nucleation is thus most probable at the edges, and least probable inside the specimen.

No theoretical prediction of the relative importance of these sources of nucleation appears to be possible. To investigate this point practically, strained commercially-pure aluminium specimens $1 \times 13 \times 500$ mm. were carried on a nickel strip through an open-ended furnace $8'' \times 1''$ dia. having a maximum temperature of 630°C. No attempt was made to produce a high gradient S. A coarse polycrystalline structure (Figure 1*a*) was obtained over ranges of strain from 1 to 3 per cent and of v from 6 to 1 cm/hr. The form taken by the crystal boundaries is consistent with growth being in the direction of steepest descent through the furnace gradients (Figure 1*b*). Nucleation appears

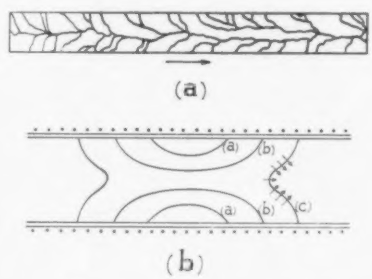

FIGURE 1. (*a*) Typical grain boundaries on a strip specimen pulled through a cylindrical furnace; the arrow gives the direction of furnace travel. (*b*) The form of the temperature isotherms in a cylindrical furnace; temperature $a > b > c$; the arrows represent direction of crystal growth if $c = T_g$.

to be entirely at the edges. It may thus be concluded that specimens having only one surface (rods etc.) should be convertible to single crystals with least difficulty. The use of square rod or strip presents more difficulty since no direct way of suppressing the greater scatter of the deformation at the edges is possible. The difficulty is, however, avoided in the secondary recrystallisation method because growth can proceed at temperatures too low for further nucleation.

A practical way of preventing the edge nuclei from becoming active is to keep the edges cool until the adjoining specimen has grown into a crystal capable of slowly absorbing any nuclei, but not of supporting their growth. A furnace whose gradients satisfy these conditions for specimens $\frac{1}{2}''$ wide and 1 mm. thick is described in section 6 and with it long crystals may be grown consistently in, for example, aluminium and its alloys.

5. Preparation of Specimens

The factors Q_n and C are both sensitive to the preparation of the specimen. The presence of a grain-refining element, as in commercially-pure aluminium, raises C, and stress concentrations at defects produced during rolling or casting lead to low values of Q_n. Apart from such obvious difficulties, the annealing treatment prior to straining is responsible in a great many cases for failure of the strain recrystallisation method; in fact, it appears to be the most critical part of the process. Any recovered, but unrecrystallised, regions remaining in the specimen after annealing will almost certainly serve as active nuclei during the subsequent attempt to grow a single crystal. Work on annealing textures has shown (see Barrett [11] for summary) that low-temperature annealing of aluminium ($<500°C$) generally produces no change in texture, which is suggestive of extensive recovery. Annealing at slightly higher temperatures suggests that the recovered material is relatively stable, even in the presence of recrystallised grains. Since the growth of single crystals appears to be so sensitive to the presence of recovered regions, every possible precaution must be taken to ensure that the specimen is completely recrystallised.* One method of achieving this, which can be often employed, is to retard the dislocation movements necessary for large scale recovery by introducing 0.1 per cent impurity or more; the conditions for complete recrystallisation are then less stringent. In this sense the factors C and Q_n are sensitive to purity, high C/Q_n values tending to be obtained with high-purity materials. For the latter, the growth of large recovered areas must be prevented, and this is best achieved by reducing the time available for recovery at a temperature too low for grain growth and by inducing the finest possible recrystallised grain size so that only slight grain growth will absorb the recovered areas. In terms of equation (6) (which may still hold approximately), P must be large, which is most easily obtained by having a large velocity v, and S must be large in the regions which have not yet started to recrystallise.

A convenient and completely successful method of annealing long aluminium strips of all purities is to lower them, after reducing their reflectivity by coating with lamp-black, through a tubular furnace of high heat capacity at a speed of about 10 cm. per minute, the temperature of the furnace being just below that which would cause a *moving* specimen to melt (about 750°C for aluminium).

A completely recrystallised specimen produces single crystals if given a strain in the range 1 to 3 per cent extension. The smaller strains usually lead to a large number of included grains, and the upper limit is fixed by the rapid decrease of the ratio Q_n/Q_g with increasing strain [8]. The range could probably be extended if slower furnace velocities could be tolerated or a greater gradient S obtained.

6. Furnace Designs and Control of Orientation

As already discussed (section 4), rod specimens need no special furnace design; any cylindrical furnace with open ends will normally suffice, though a gradient furnace such as that used by Andrade and Roscoe [12] is preferable.

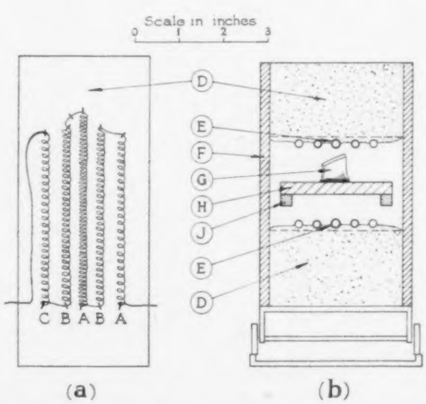

FIGURE 2. A furnace suitable for the growth of crystals by strain recrystallisation in strip $\frac{1}{2}''$ wide and 1 mm. thick.

(*a*) A scale drawing of the heater made from 22 gauge "Brightray C" resistance wire coiled on a $^3/_{16}''$ dia. mandrel. The coils A, B, and C are pinned in tension to the diatomacious brick D prior to fixing in position by a thin layer of alundum cement. Coil A-68 turns, coils B-40 turns, coils C-28 turns.

(*b*) A scale drawing of a section of the assembled furnace D—diatomacious brick supporting heaters, E—heaters partially embedded in cement, F—Sindanyo asbestos board furnace supports, G—specimen with twist and bend, H—asbestos board table, clamped to J in square sections to avoid warping, J—$\frac{1}{4}''$ square mild steel supports for H. The supports J accentuate the gradients produced by the heaters E because of their conduction.

Note added in proof. (Received August 3, 1953.) The difficulty of getting complete recrystallisation has been discussed more fully by Beck [15] and additional experimental evidence of the importance of this effect in the growth of single crystals has been reported by Talbot *et al.* [16] for superpure iron.

A furnace design suitable for use with strip 1 mm. thick and $\frac{1}{2}''$ wide is shown in Figure 2. The necessary difference in temperature between the centre and the edges is obtained by heating the centre more strongly by radiation, and removing heat from the edges by conduction. The large furnace gap above the specimen table enables the specimen to be twisted and bent [3; 13] to control the orientation. The stereogram (Figure 3) demonstrates the method of

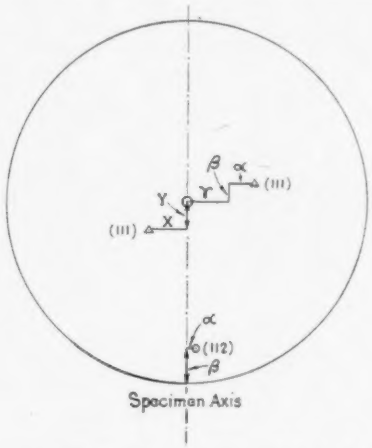

FIGURE 3. Stereogram demonstrating the control of crystal orientation; the primitive of the stereogram is in the plane of the strip.

(*a*) The production of a (111) plane parallel to the surface; a crystal with the orientation shown requires a twist X about the specimen axis, and a bend Y about a perpendicular axis in the plane of the sheet.

(*b*) The production of a crystal with a (111) [112] orientation requires a twist α followed by a bend β, when the [112] direction coincides with the specimen axis and is unaffected by a further twist γ which gives a (111) plane parallel to the surface.

obtaining a partial control (e.g. a crystallographic plane parallel to the sheet surface) and a complete control of the orientation. In the latter, since a bend about an axis perpendicular to the surface of the strip is not possible without introducing further nucleation, it is necessary to get the required crystallographic axis parallel to the specimen axis before twisting the plane into the parallel position. Bends of up to 20° and twists of 30° may be carried out simultaneously.

The furnace is adjusted to a temperature about 10° below that at which a small portion of the specimen melts, the temperature of the windings being about 1000°C. The lower heater is not essential but it compensates for some of the heat losses and thereby allows a reasonable working temperature for, and increases the life of, the upper heater. Generally, it should dissipate about half the wattage of the upper heater.

With the precautions discussed above, long single crystals (two feet long or more) 1 mm. thick and $\frac{1}{2}''$ wide have been grown in high purity (99.992 per cent), commercial purity (99.7 per cent), and in alloys of aluminium containing small additions (less than 2 per cent) of either copper, zinc, or silver.

7. Acknowledgements

We wish to thank Professor D. Hanson for providing facilities and financial support and Professor A. H. Cottrell for numerous valuable discussions. We are also indebted to Mr. T. J. Dennis of Messrs. Richard Thomas and Baldwins Ltd. and Mr. E. E. Spillett of British Aluminium Co. Ltd. for their assistance in the preparation of the aluminium sheet.

References

1. HOLDEN, A. N. Trans. Amer. Soc. Met., **42** (1950) 319.
2. TEGHTSOONIAN, E. and CHALMERS, B. Can. J. Phys., **29** (1951) 370.
3. TIEDEMA, T. J. Acta Cryst., **2** (1949) 261.
4. FUJIWARA, T. J. Sci. Hiroshima Univ., **9** (1939) 227.
5. SCHMID, E. and BOAS, W. Plasticity of Crystals (London, Hughes, 1950), p. 25.
6. BECK, P. A. and HU, H. Trans. A.I.M.E., **194** (1952) 83.
7. BECK, P. A., SPERRY, P. R., and HU, H. J. App. Phys., **21** (1950) 420.
8. ANDERSON, W. A. and MEHL, R. F. Metals Technology, Publication No. 1805 (1945).
9. BECK, P. A. J. App. Phys., **20** (1949) 633.
10. CAHN, R. W. Proc. Phys. Soc. (London), **A63** (1950) 323.
11. BARRETT, C. S. Structure of Metals, 2nd ed. (New York, McGraw-Hill, 1952), p. 492.
12. ANDRADE, E. N. DA C. and ROSCOE, R. Proc. Phys. Soc. (London), **49** (1937) 152.
13. HÄGG, G. and KARLSSON, N. Acta Cryst., **5** (1952) 728.
14. WHITTAKER, E. T. and WATSON, G. N. A Course of Modern Analysis (London, Cambridge University Press, 1950), p. 159.
15. BECK, P. A. J. Metals, **4** (1952) 979.
16. TALBOT, J., BEAULIEU, C. de, and CHAUDRON, G. C. R. Acad. Sci., Paris, **236** (1953) 818.

ZUR REAKTIONSKINETIK VON AuCu UND $AuCu_3$*

U. DEHLINGER†

Nach früheren Versuchen ist die Geschwindigkeit der Umwandlung regellos-regelmässig und die Kerndichte des Zwischenzustands in gestörten Kristallen kleiner als in ungestörten. Dies wird darauf zurückgeführt, dass sich an die Keimbildung eine Kettenreaktion (wandernde Versetzungen) anschliesst, die an Störungsstellen abbricht. Dann ist die Zahl der Atome eines thermodynamisch stabilen Keims im ungestörten Kristall sehr viel grösser als die Reaktionsordnung der Keimbildung. In stark gestörtem Material sind die Verhältnisse der normalen Keimbildung zu erwarten.

ON THE KINETICS OF AuCu AND $AuCu_3$

According to previous experiments the rate of transformation disorder-order and the density of nuclei are smaller in deformed crystals than in undeformed crystals. This is explained by the fact that the nucleation is followed by a chain reaction which stops at the point of deformation. The number of atoms in a thermodynamically stable nucleus in an undeformed crystal is then much larger than the order of reaction for nucleation. In strongly deformed material, normal conditions of nucleation can be expected.

SUR LA CINÉTIQUE DE AuCu ET $AuCu_3$

D'après des expériences antérieures, la vitesse de transformation désordre-ordre et la densité des germes sont plus petites dans des cristaux déformés que dans ceux qui ne le sont pas. Ceci est expliqué par le fait que la germination est suivie d'une réaction en chaîne qui s'arrête au point de la déformation. Le nombre d'atomes, dans un germe thermodynamiquement stable, est alors beaucoup plus grand que l'ordre de la réaction pour la germination. Dans de la matière fortement déformée on peut s'attendre à des conditions normales de germination.

Die 1930 begonnenen Untersuchungen über die Kinetik des Übergangs einer regellosen in eine regelmässige Atomverteilung bei AuCu und $AuCu_3$ gehören zu den frühesten Hinweisen darauf, dass bei den Umwandlungen im festen Zustand der Metalle neuartige und von dem hergebrachten Schema der Keimbildungsvorgänge wesentlich verschiedene Mechanismen vorkommen können. Trotzdem sind bis heute diese Vorgänge noch nicht hinreichend aufgeklärt. Zwar ist durch die vergleichenden Messungen der Röntgenlinienbreite, der Wärmetönung und des Widerstands durch Sykes und Jones [1] die atomistische Deutung des für die Vorgänge besonders kennzeichnenden Zwischenzustands wohl gesichert, aber die bei einem Vergleich der experimentellen Arbeiten auffallende Abhängigkeit der zu diesem Zustand führenden Vorgänge von der Gefügeausbildung hat noch keine Erklärung gefunden. Sykes und Jones erwähnen in dieser Richtung, dass bei $AuCu_3$ die Umwandlungsgeschwindigkeit eines verformten, also stark gestörten Materials wesentlich kleiner ist als die des von ihnen sonst benützten grobkörnigen vielkristallinen Zustands. Feinere und besonders auffallende Unterschiede zeigten sich bei den Untersuchungen an Einkristallen von AuCu: Die Röntgeninterferenzaufnahmen von Dehlinger und Graf [2] stammen von Kristallen, die unmittelbar aus der Schmelze gezüchtet waren und die Umwandlung zum erstenmal mitmachten, während Oshima und Sachs [3] Einkristalle und vielkristallines Material benützten, die durch vorhergegangene Umwandlungen Gitterstörungen erhalten hatten. Infolgedessen finden Dehlinger und Graf einen nahezu "stetigen" Übergang aus der regellosen Verteilung in den Zwischenzustand, d.h. es ist an jedem Zeitpunkt nur ein einziges Achsenverhältnis c/a vorhanden, dessen Wert sich im Lauf der Zeit stetig ändert, während Oshima und Sachs Werte von c/a in der Nähe des Anfangswerts und des Endwerts nebeneinander finden (sogen. zweiphasige Umwandlung). Ausserdem finden Dehlinger und Graf im Zwischenzustand wesentlich breitere Überstrukturlinien als Oshima und Sachs und auch als Sykes und Jones.

Wenn man nach Sykes und Jones den Zwischenzustand als dasjenige Stadium der Umwandlung ansieht, in dem die im Innern angelegten "Kerne" der regelmässigen Verteilung zusammenstossen, wobei sie sich in der "Phase" der Verteilung und bei AuCu auch in der Orientierung der tetragonalen Achse unterscheiden, und wenn die Breite der Überstrukturlinien umgekehrt proportional der Ausdehnung dieser Kerne ist, dann bedeutet der erwähnte Befund, dass die Kerndichte im ungestörten Einkristall grösser ist als im gestörten Einkristall und im vielkristallinen Material.

Dieses experimentelle Ergebnis ebenso wie die kleinere Umwandlungsgeschwindigkeit des vielkristallinen und verformten Materials zeigt unmittelbar, dass die "Kerne" der Überstruktur sich durch einen

*Received April 23, 1953.
†Max-Planck-Institut für Metallforschung und Institut für theoretische und angewandte Physik der Technischen Hochschule Stuttgart.

andern Mechanismus bilden müssen als die Keime bei der Erstarrung von Schmelzen oder der Kondensation von Dämpfen, wo bekanntlich Störstellen die Reaktionsgeschwindigkeit und die Keimzahl erhöhen. Ganz allgemein ist ja die Keimbildung eine Reaktion n-ter Ordnung, d.h. eine Kombination von n statistisch unabhängigen atomistischen Ereignissen, durch die ein thermodynamisch im Gleichgewicht befindliches Gebilde entsteht. Dabei ist n von der Grössenordnung zehn. Wenn nun, was bei der üblichen Keimbildung als selbstverständlich angesehen wird, die Zahl der beteiligten Atome gleich oder nahezu gleich der Reaktionsordnung ist, ist der thermodynamisch stabile Keim ein aus wenigen Atomen zusammengesetztes Gebilde, für dessen Stabilität die Oberflächenenergie und damit auch die lokalen Störstellen entscheidend sind. Anders liegen die Verhältnisse, wenn wir annehmen, dass eine Reaktion niederer Ordnung infolge mechanischer Kopplung der Atombewegung eine sehr grosse Zahl von Atomen erfasst, also eine Kettenreaktion eintritt. Ein solcher Vorgang wird an den Gitterstörungen unterbrochen. Da aber jetzt das ganze, durch die Kettenreaktion entstandene und mindestens in einer Dimension makroskopische Gebilde als Keim zu betrachten ist und auf thermodynamische Stabilität geprüft wird, und da die Oberflächen- und Spannungsenergie umso weniger in Frage kommt, je grösser dieser Keim ist, wird jetzt der Vorgang durch Gitterstörungen gehemmt und mit kleinerer Geschwindigkeit verlaufen.

So kommen wir zu folgendem Bild für die Vorgänge in einem unter die Gleichgewichtstemperatur regelmässig-regellos abgeschreckten, zunächst als ideal, aber endlich betrachteten Kristall der Zusammensetzung AuCu oder $AuCu_3$ mit regelloser Verteilung: An einzelnen Stellen im Innern des Kristalls bilden sich kleine geordnete Bereiche. Auf die Atome an ihren Grenzen werden dann Spannungen ausgeübt, die sie in die geordnete Lage zu ziehen versuchen. Die gesamte Energie der Bereiche nimmt trotzdem zunächst mit zunehmender Bereichsgrösse zu, da der geordnete Zustand ein andres Eigenvolumen, bei AuCu auch ein andres Achsenverhältnis hat als der ungeordnete. Wenn aber die Grenzen des Bereichs in die Nähe der Kristallgrenzen kommen oder wenn verschiedene geordnete Bereiche sich nahe kommen, nimmt diese Energie wider ab. Daher ist für den Beginn des Wachstums die Aufeinanderfolge einer Reihe von statistischen Schwankungen nötig; sie leiten die Kettenreaktion ein, die dann bis zur Ausbildung der Kerne des von Sykes und Jones beschriebenen Zwischenzustands ohne neue Schwankungen weiterschreitet. Die Geschwindigkeit dieses Vorgangs ist wesentlich grösser als wenn die Umsetzung von Gold- und Kupferatomen wie bei der normalen Diffusion bei jedem Atompaar durch neue Schwankungen eingeleitet würde.

Da wandernde Versetzungen, bei denen die zum Überschreiten der jeweiligen Potentialberge notwendige Schwellenenergie durch mechanische Kopplung weitergegeben wird, stets eine solche Kettenreaktion darstellen, wird es wohl möglich sein, auch hier das Fortschreiten der Umsetzung durch Kombination geeigneter Versetzungen geometrisch darzustellen. Vermutlich wird damit eine fortschreitende Reihe von Gitterlöchern verbunden sein müssen, die den diffusionsartigen Vorgang im Substitutionsmischkristall ermöglichen. Auch die Stufenversetzungen des plastischen Gleitens sind erst stabil und können sich spontan ausbreiten, wenn sie eine bestimmte Minimalausdehnung überschritten haben [4].

Nach den Gesetzen des thermodynamischen Gleichgewichts kann selbstverständlich der durch die Kettenreaktion gebildete Zwischenzustand nur dann beständig sein, wenn seine freie Energie kleiner ist als die des regellosen Ausgangszustands. Wenn also der Zwischenzustand frei von Spannungen wäre, könnten die beschriebenen Reaktionen unmittelbar nach Überschreiten der Gleichgewichtstemperatur regelmässig-regellos einsetzen, während die bei der Entstehung der Kerne überschrittenen Energieschwellen nicht die Einsatztemperatur, sondern nur die Geschwindigkeit des Vorgangs beeinflusst. Hat der Zwischenzustand, wie es in Wirklichkeit bei $AuCu_3$ und besonders bei AuCu der Fall ist, Spannungen, dann ergibt sich eine Herabsetzung der Einsatztemperatur gegenüber der wahren Gleichgewichtstemperatur um einen Betrag, der gleich der Spannungsenergie dividiert durch die Entropieänderung ist. Wenn aber die Kettenreaktionen der Thermodynamik unterworfen, also voneinander unabhängige Elemente der thermodynamischen Statistik sind, ist zu schliessen, dass sie nicht nur in einer, sondern auch in entgegengesetzter Richtung gehen können. Es muss also vorkommen können, dass ausgebildete Kerne, deren freie Energie nicht klein genug ist, unter dem Einfluss erneuter Temperaturschwankungen wieder zurückgebildet werden. Auf den oben erwähnten Fall der plastischen Verformung übertragen, heisst das, dass auch plastische Versetzungen während des Gleitvorgangs mit einer gewissen Wahrscheinlichkeit zurückgebildet werden können; ein solcher Vorgang kommt in der "dyna-

mischen Erholung" zu Tage, die nach Kochendörfer notwendig ist, um die Temperatur- und Zeitabhängigkeit der kritischen Schubspannung zu erklären.

Welche Folgerungen sind nun aus dem Vorhergehenden zu ziehen für ein Material, das Störungen enthält, in dem daher die Kettenreaktionen abbrechen, ehe die Kerne zusammenstossen? Sie enthalten in diesem Augenblick wesentlich mehr Spannungsenergie als die ganz ausgebildeten Kerne des ungestörten Gitters und müssen daher aus thermodynamischen Gründen je nach der Temperatur zu einem mehr oder weniger grossen Teil zurückgebildet werden. Wir erhalten also weniger stabile Kerne als im ungestörten Kristall, ausserdem ist ihre zeitliche und räumliche Verteilung stark von der Verteilung der Gitterstörungen abhängig. Mit wachsender Zahl der Gitterstörungen ergeben sich immer ausgeprägter diejenigen Erscheinungen, die für die normale Keimbildung charakteristisch sind. Sind die Störungen gleichmässig verteilt, wie es offenbar bei dem sorgfältig vorbehandelten vielkristallinen Material von Sykes und Jones [1] der Fall war, so erhalten wir eine überall nahezu gleiche Kerndichte, die aber kleiner ist als im ungestörten Einkristall. In weniger gleichartigem Material können nebeneinander Stellen mit voll ausgebildeten Kernen und ohne solche auftreten, also ein "zweiphasiger Zustand," wie er bei Oshima und Sachs [3] sowie besonders bei Gorsky [5] beschrieben ist [6].

Die durch die abgebrochenen Kettenreaktionen gebildeten thermodynamisch stabilen Kerne wachsen durch weniger Atome umfassende Zusatzreaktionen weiter. Im Grenzfall sehr grosser Gitterstörungen, wie er bei verformtem Material vorliegt, wird es sich dabei um diffusionsartige Umsetzungen einzelner Atome handeln. In diesem Fall erhalten wir also die kleinste Geschwindigkeit, wie es den Beobachtungen entspricht.

Literatur

1. Jones, F. W. und Sykes, C. Proc. Roy. Soc., **A161** (1937) 440; **A166** (1938) 376.
2. Dehlinger, U. und Graf, L. Z. Phys., **64** (1930) 359. Herrn Prof. L. Graf danke ich für eine genaue Beschreibung der damaligen Befunde.
3. Oshima, K. und Sachs, G. Z. Phys., **63** (1930) 210.
4. Vgl. Frank, F. C. Symposium on Plastic Deformation (Pittsburgh, 1950), S. 90.
5. Gorsky, W. Z. Phys., **50** (1928) 64.
6. Vgl. auch Siegel, S und Smoluchowski, R. Phase Transformation in Solids (New York, London, 1951).

DIMENSION AND ORIENTATION EFFECTS IN THE YIELDING OF CARBURIZED IRON SHEET CRYSTALS*

A. N. HOLDEN and F. W. KUNZ†

Several annealed and carburized iron single crystals in the form of sheet tensile specimens were tested. Orientations were such that all regions of the standard stereographic triangle were represented by the tensile axes of the specimens. A good correlation between yielding behavior and the maximum dimension of the crystal in the direction of slip was found for all crystals except those having a tensile axis within 10° of a [111] direction. Crystals in which this slip dimension exceeded 0.200 inch showed preferentially a sharp yield point and drop in load.

Crystals that had tensile axes within 10° of [111] were found to deform by the formation of tensile kink bands. Concomitant with the kink band formation, the crystals showed a sharp yield and drop in load irrespective of specimen dimensions or carbon content.

The deformation process in crystals showing a drop in load but not forming kink bands produced deep macroscopic surface grooves.

LES EFFETS DES DIMENSIONS ET DES ORIENTATIONS SUR L'ÉCOULEMENT DES CRISTAUX DE TÔLE DE FER CARBURÉ

Des essais ont été effectués sur plusieurs éprouvettes de tension plates, constituées par des monocristaux de fer recuit et carburé. Les orientations en étaient telles que toutes les régions du triangle stéréographique standard étaient représentées par l'axe d'extension des éprouvettes. Une bonne corrélation a été trouvée entre les caractéristiques d'écoulement et la dimension maximum du cristal dans la direction de glissement, à l'exception des cristaux dont l'axe d'extension était dans l'espace de 10° de la direction [111]. Les cristaux, dans lesquels cette dimension excédait 0,200 de pouce, montraient plutôt une limite d'écoulement bien définie et un abaissement de la charge.

Les cristaux qui avaient l'axe d'extension dans l'espace de 10° de la direction [111] se déformaient par la formation de bandes de pliage (kink bands). Ces cristaux montraient, en plus, une limite d'écoulement bien définie et un abaissement de la charge, indépendamment des dimensions de l'éprouvette et de la teneur en carbone.

Dans les cristaux qui présentaient un abaissement de la charge, mais ne formaient pas de bandes de pliage, la déformation produisait de profondes rainures, à l'échelle macroscopique, sur la surface.

DER EINFLUSS DER GRÖSSE UND DER ORIENTIERUNG AUF DAS FLIESSEN VON KRISTALLEN IN KARBONISIERTEN EISENBLECHEN

Eine Anzahl geglühter und karbonisierter Eisenkristalle wurden in der Form von flachen Zugversuchproben untersucht. Die kristallographische Orientierung der Zugachsen war so, dass alle Bereiche des Normaldreiecks der stereographischen Projektion repräsentiert waren. Für alle Kristalle-mit Ausnahme der Proben, deren Zugachse 10° oder weniger von einer [111] Richtung entfernt war-bestand gute Übereinstimmung von Fliessverhalten und maximaler Abmessung des Kristalls in der Gleitrichtung. Kristalle, bei denen die Grösse in der Gleichrichtung grösser war als 0.200 inch, zeigten bevorzugt einen scharfen Fliesspunkt und eine Verminderung der Last.

Es zeigte sich, dass sich Kristalle deren Zugachse innerhalb von 10° einer [111] Richtung parallel war, under Bildung von Knickbändern ("kinkbands") verformten. Zusammen mit der Ausbildung der Knickbänder ("kinkbands") zeigen diese Kristalle scharfe Fliesspunkte und Lastverminderung unabhängig von der Grösse der Probe und ihrem Kohlenstoffgehalt.

Kristalle, die bei der Verformung eine Verminderung der Last zeigen aber keine Knickbänder ("kinkbands") bilden, zeigen auf ihrer Oberfläche tiefe makroscopische Rillen.

Introduction

There have been several attempts recently to explain the yield point in iron. The most satisfying of these, namely Cottrell's [1] theory concerning the behavior of dislocations anchored by solute atoms, requires that single crystals containing carbon yield in the discontinuous fashion common to polycrystals. That such yielding has been observed sometimes, but not always, with single crystals has been a point of contention [2; 3; 4]. In a recent paper [5] the discrepancies among the several single crystal experiments were rationalized on the basis that the densities of dislocations in the crystals tested could have been sufficiently different to permit serious differences in their yielding behavior. It was postulated [5] that the greater the density of dislocations the greater the opportunity for interaction and cataclysmic propagation and the greater the extent of yield point deformation. As a direct consequence of this postulate, it was suggested that at any given dislocation density a large crystal with a longer total slip path would have a greater yield point elongation than a small crystal with a shorter slip path. An experiment consistent with such a size effect actually was reported, although only a single dimension of the cross section of the crystal was changed to test the concept.

Certain questions remained to be answered, however:

1. Is there any effect of crystal orientation on the yield point phenomenon?
2. What is the nature of strain propagation and

*Received April 2, 1953; in revised form May 15, 1953.
†Knolls Atomic Power Laboratory, General Electric Company, Schenectady, New York, U.S.A.

the deformation markings in those instances where yield points are found in single crystals of iron?

3. Why was it possible to bring about a yield point by increasing only a single dimension (the width) of the iron crystal? Recent evidence [6] obtained with aluminum crystals in the form of sheet specimens showed that slip occurred preferentially in the thin direction irrespective of the classical resolved sear stress analysis. If such a situation also prevails in iron, one would expect the slip path in either a narrow or a wide iron sheet crystal to be approximately of the order of the sheet thickness and there should be little difference in their yielding behavior.

This study of the metallography of deformation and the mechanical behavior of iron single crystals of known orientation was undertaken primarily to answer the foregoing questions.

Experimental Work

It was found impractical to grow crystals of identical orientation in a range of sizes in order to test the previously reported size effect. However, the size of the crystal in the slip direction is probably the important variable, and it was felt that a great variety of dimensions in the slip direction would be available in an assortment of crystals of random orientation in the form of sheet tensile specimens. Consequently, a large number of crystals were grown by a strain-anneal technique from 0.037 inch thick strips of both aluminum-killed deep-drawing sheet and sheet rolled from high-purity iron supplied by National Research Corporation. Excellent crystals several square inches in area were grown in strips from both materials, and no essential difference in mechanical behavior of crystals grown from the two materials was detected in the course of the study.

Tensile specimens were machined with the crystal supported between $\frac{1}{8}$-inch-thick flat plates by milling through the entire sandwich of support plate and crystal. Dimensions of the test pieces were a 1-inch or longer gauge length and approximately $\frac{1}{4}$ inch by 0.030 inch cross section. No attempt was made to reproduce dimensions precisely, but each specimen was carefully measured.

The tensile specimens were abraded on two faces and on each edge on papers through no. 600 grit. They were polished electrolytically to a good metallographic surface. An orientation determination was made of each crystal by a back-reflection Laue method with the incident beam normal to a face of the specimen.

After the crystals had been oriented they were given a treatment that simultaneously carburized and annealed them. This treatment was accomplished by making wax pencil marks on the grip ends of each crystal, sealing it in an evacuated quartz tube, and heating it at 720°C for three hours to diffuse the carbon from the wax into the crystal. The polished surfaces remained excellent during the annealing treatment, but the crystals nevertheless were repolished electrolytically after annealing. Chemical analyses were not made for the carbon content of the particular crystals used for these experiments, but experience with similar crystals has indicated carbon contents of 0.01 to 0.02 per cent should be obtained by this technique. A few specimens were not carburized, as noted later in this paper, but were specifically decarburized.

Tensile tests were made on the crystals in a screw-loading tensile machine with automatic recording of load and extension. Strain rates of the order of 0.001 sec^{-1} were used for all tests.

Whenever drop-in-load yielding was observed with a crystal, the tensile test was stopped immediately before any strain-hardening flow had begun, and the crystal was examined microscopically. Frequently, additional extension would be applied to such a crystal and further microscopic examination would be made.

Results of Tensile Tests

The crystals tested exhibited three types of initial yielding behavior as evidenced by load-elongation curves, namely,

1. A sharp yield point with a pronounced drop in load.

2. A flat portion in the early yielding followed by a change in slope to a more steeply rising curve.

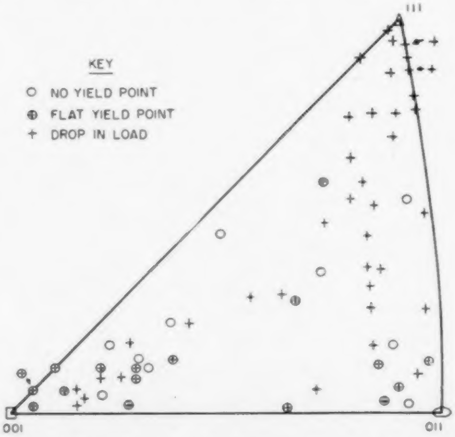

FIGURE 1. Type of yielding for crystals tested.

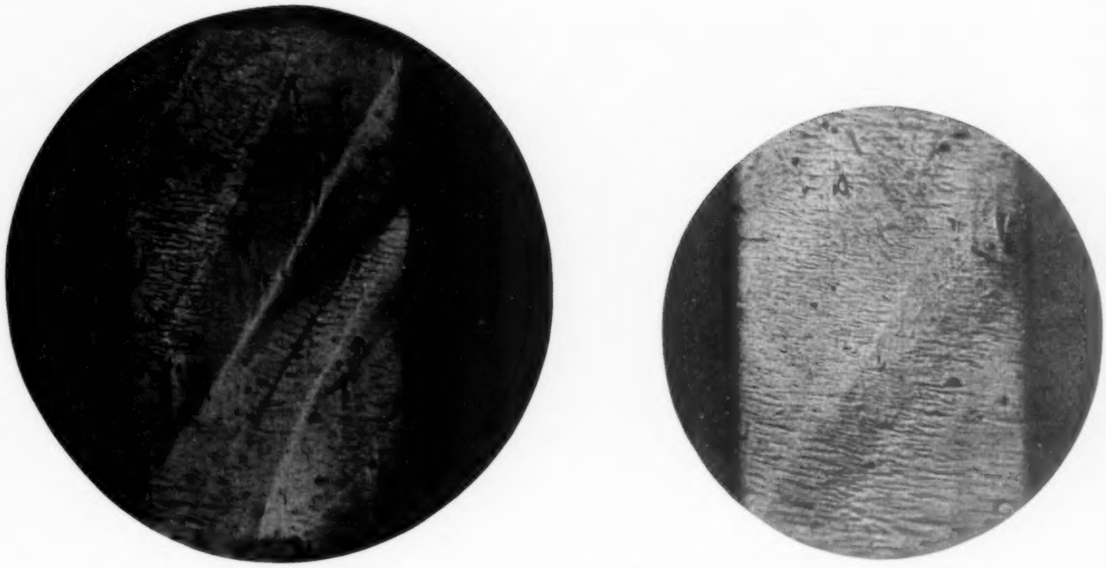

FIGURE. 2. Typical tensile kink bands (12×).

FIGURE 3. Deformation grooves on a crystal edge after drop-in-load yielding (50 ×).

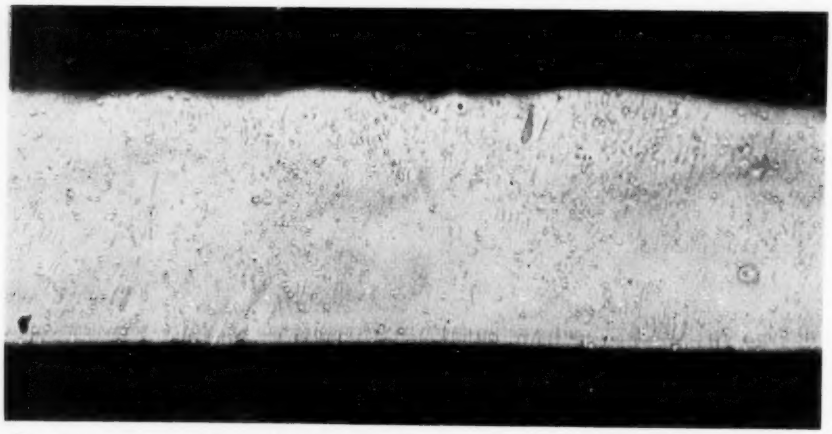

FIGURE 4. The same crystal as shown in figure 3 after further extension (50 ×).

(*a*)

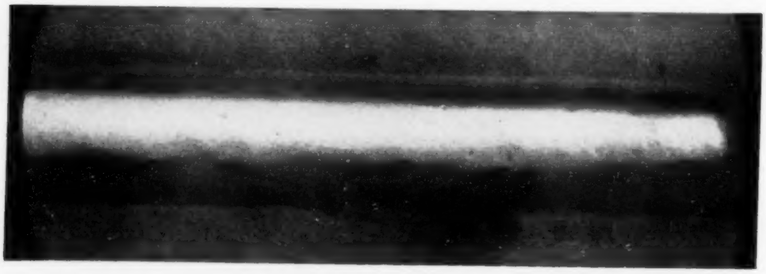

(*b*)

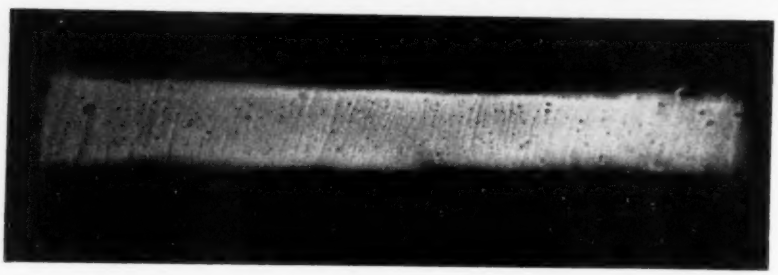

FIGURE 5. Strain-aged crystal after (*a*) repolishing and (*b*) deforming in tension through the yield point (25 ×).

3. No yield point whatsoever.

The appropriate yielding symbol for each of the crystals tested is plotted in Figure 1 in the position in the stereographic triangle that indicates its tensile axis. The striking feature of Figure 1 is that all the specimens having tensile axes near [111] yield with a definite drop in load. In all other regions there seems to be a mixture of the possible kinds of behavior on yielding.

Metallographic Examination

Several different kinds of surface markings were found after small amounts of plastic deformation.

Those crystals with a tensile axis near [111] (within 10°) always showed a drop in load, and their surfaces were kinked. Within and without the kink band there were fine slip markings. Photographs of the appearance of kink bands are shown in Figure 2.

Crystals that had a drop in load upon yielding, but were not of the type having approximately a [111] tensile axis, showed no sign of kinking. The surface of these non-kinked crystals contained shallow macroscopic grooves within which fine slip was not resolved. The grooves were irregular in shape with tributaries, and from the focusing adjustment required with a high-power objective were judged to be 0.001 to 0.003 inches deep. A photograph of a typical crystal edge after drop-in-load yielding is shown in Figure 3.

Crystals which yielded with a flat yield point also had grooves, although they were not as coarse in nature. Crystals which yielded without any sharp yield point did so with the fine wavy slip characteristic of iron, and the use of oblique illumination at greater magnification (250 × or greater) was required to reveal the slip.

It was observed that immediate further extension of crystals which had deformation grooves after initial yielding used up the undeformed material between grooves and obliterated the relief between groove and surroundings, and the coarse grooves were replaced by finer wavy slip. Such a result of additional deformation is shown in Figure 4, a photomicrograph of the crystal of Figure 3 after further extension.

If a crystal had been deformed well into the homogeneous flow region and was then repolished and aged, the resulting yield after such strain aging was again of the drop-in-load type, and again deep grooves were formed on the specimen surface. Photographs, Figure 5, of a crystal that was repolished after strain aging and then deformed in tension show the grooves that form during yielding of a strain-aged crystal.

Experiments on the Nature of Kinking

As a consequence of the coincidence of drop-in-load yielding with apparent kink-band formation for those crystals with axes within 10° of [111], several additional experiments were performed. A few crystals of [111] tensile axis were specifically

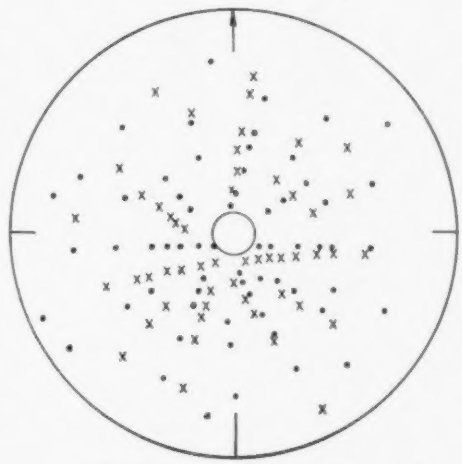

FIGURE 6. Trace of Laue pattern showing kink band and matrix orientations after drop-in-load yielding of 4 per cent: X—kink band, ●—matrix.

decarburized in wet hydrogen for 16 hours at 720°C. Tensile tests on these crystals also produced a drop in load on yielding and apparent kink bands were again formed. Several other crystals with tensile

FIGURE 7. Trace of Laue pattern showing kink band and matrix orientations after deforming the same crystal as in figure 6 an additional 6 per cent: X—kink band, ●—matrix.

axes outside the [111] region were also decarburized and deformed in tension. No drop-in-load yielding occurred when the latter were tested and instead a characteristic smoothly varying curve of stress versus strain was observed.

A careful study of the kink bands revealed that the boundary between kink and matrix was usually crystallographic, and on analysis it was found most often to be a (111) plane when referred to the original orientation. Several boundaries were sufficiently removed from a (111) plane, however, to make suspect two additional conditions: that rotation of the kink boundary occurs during continued deformation producing slight variations from (111); and that infrequently some orientation of boundary other than (111) originally forms.

X-ray Laue photograms were taken both of the region wholly within the band and that completely outside it, and also of the boundary itself with the beam overlapping both the matrix and the kink band. In all of this X-ray work the beam was normal to the wide face of the sheet crystal. Figure 6 presents the trace of a Laue pattern for a kink-band boundary region showing the relative rotation of matrix and kink band after an initial extension of 4 per cent under a continuously dropping load. An analysis of Figure 6 shows that the crystal lattice on either side of the kink band has rotated 8° about a [110] axis in a [111] direction. Traces of the slip observed in the matrix could be accounted for by slip on the appropriate (112) plane although the slip traces were characteristically wavy. Figure 7 shows the result on the Laue pattern of extending the same crystal used for Figure 6 an additional 6 per cent. This additional extension has increased the relative rotations of kink band and parent.

The amount of rotation of the lattice within the kink band itself has been less than the sensitivity of our stereographic analysis, although there is some indication that it is rotating in the opposite sense from the matrix.

Analysis of the Size Effect

An analysis of the effect of the dimension of the crystal in the known slip direction on the type of yielding was made. For this analysis the maximum vector parallel to the slip direction and cut by the surfaces of the crystal was used as the dimension of the crystal. A variety of dimensions in the slip direction ranging from 0.020 inch for slip in the thickness direction of a very thin crystal to over 0.500 inch for slip in the width direction of a wide crystal were obtained. While the plane on which slip occurred was assumed to be that given by Opinsky and Smoluchowski [7], the nature of the slip as previously described (fine wavy or macroscopic grooves) did not permit confirmation of this assumption. The slip direction, however, seemed unambiguous, since the most pronounced offset (whether fine wavy slip or macroscopic grooves) appeared in surfaces normal to the predicted slip direction.

All of the crystals with tensile axes within 10° of [111] had short dimensions in the slip direction. However, none of these crystals of [111] orientation was included in the size effect analysis because their behavior was different from all other crystals, i.e., they deformed by kinking, and carbon was not required to produce drop-in-load yielding.

A chart, Figure 8, was constructed showing the distribution of the three kinds of yielding behavior

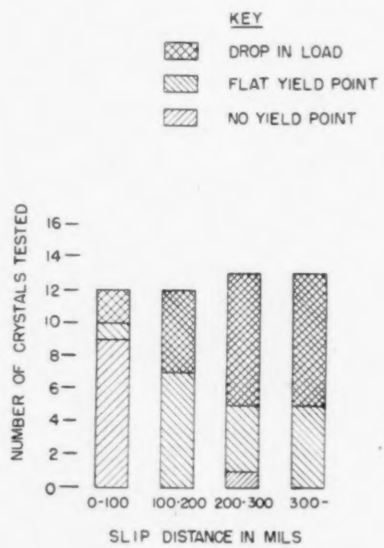

FIGURE 8. Correlation of yielding behavior with slip distance.

for dimensions in the slip direction of 0–0.100 inch, 0.100–0.200 inch, 0.200–0.300 inch, and for 0.300 inch and greater. It can be seen from Figure 8 that there is a clustering of crystals without a trace of yield point in the specimens with 0–0.100 inch slip-direction dimension. There was only one crystal, in fact, with a slip-direction dimension greater than 0.100 inch that had no yield point. Sharp yield points were observed most often with crystals having a slip-direction dimension greater than 0.200 inch. While the correlation depends on data from only fifty crystals, it seems too consistent to be mere coincidence.

Discussion

Except for crystals with tensile axes within 10° of [111], no effect of orientation of the tensile axis upon yield behavior seems to exist. The crystal dimension in the slip direction is an important variable in yield behavior, although variations in crystal perfection and any accidental deformation may offset the effect of size.

This effect of the dimension of the crystal in the slip direction can be understood in terms of the dislocation picture previously presented [5], namely that, at a given dislocation density, the longer the slip path the more probable the collision interaction of a moving dislocation with other anchored dislocations and the greater the deformation cataclysm. It was observed in the previous work [5] that an increase in only the width of a sheet crystal specimen was necessary to enhance the yield point. Because of the orientations commonly found in sheet crystals grown by recrystallization, the probability is very good that an increase in crystal width also increases the dimension in the slip direction. Furthermore, our evidence indicates that the direction of slip for sheet crystals obeys the classical resolved shear stress criteria, slipping in the thickness dimension only when that is required by these criteria.

A feature of the yielding of iron crystals which has become increasingly clear is that the flat type of initial flow curve is quite common. In this type of initial flow, sharp yielding is not observed. For example, a crystal may have a low strain magnification stress-strain curve as shown schematically in Figure 9*a* and a high magnification initial yielding

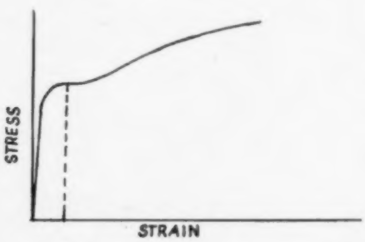

FIGURE 9*a*. Low magnification of strain showing flat type of initial yielding.

curve such as shown schematically in Figure 9*b*. Certainly Figure 9*a* is one degree of manifestation of a yield point, but it appears homogeneous in Figure 9*b*. Such yielding is most common in annealed crystals where total slip distances are intermediate in length, that is, 0.100 inch to 0.300 inch.

It is most interesting that, of the crystals tested by Holden and Hollomon [2], at least those for which orientations were determined seem to fall in this intermediate region. These crystals of Holden and Hollomon were sheet crystals and in the neighborhood of 0.050 inch thick. They were oriented by optical reflection from etch pits and plotted on a stereographic projection of the sheet face with the

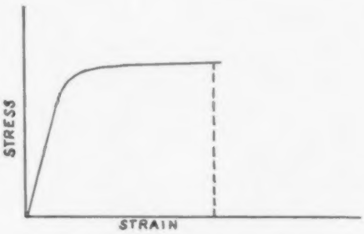

FIGURE 9*b*. High magnification of strain for initial portion of curve shown in figure 9*a*, giving impression of homogeneous yielding.

tensile axis vertical. The slip paths as calculated from their orientations should have been 0.100 inch to 0.150 inch. These crystals therefore should have yielded very much as shown in Figures 9*a* and 9*b*, although in the work cited only the high magnification curve as shown in Figure 9*a* was observed. It is unlikely that Holden and Hollomon tested a variety of orientations since all their crystals were recrystallized from the same 0.080-inch-thick aluminum-killed sheet and were cut out with tensile axis in the same direction. Even those not examined for orientation were probably closely related to those with intermediate slip paths.

The deformation grooves formed during the yielding must be the result of large amounts of localized flow which, from the observed depths of the grooves, might be as much as 1 per cent strain. These grooves are equivalent in single crystals to the Lüders bands in polycrystalline steel. The grooves are consistent with the notion that the release and migration of a single dislocation from its anchoring solute atoms causes the release and migration of perhaps thousands of others by collision interaction. Since the moving dislocations must pass very close to anchored dislocations to effect their release, the flow is localized in thin regions. The deformation grooves are definitely associated with the presence of carbon, since a decarburized iron crystal deforms homogeneously with characteristic fine wavy slip markings. The sudden yielding of a strain-aged crystal containing carbon seems to be by the same mechanism as that which operates for the initial yield point of a carburized annealed crystal, since

the same deformation grooves are produced in either instance.

Since the [111] slip direction is preserved in the deformation process, it is believed that the grooves although not straight are the result of crystallographic slip on a fine scale that need not follow the groove for long distances. During a local cataclysm of plastic flow, the contribution of each Frank-Read dislocation source need not extend across the crystal. If the crystal slips using one dislocation source for a short distance and that dislocation becomes blocked, the glide may be transferred to adjacent sources in nearby parallel planes. The wavy macroscopic appearance of the local flow is then explained by stepwise meandering from one source to another.

It should be pointed out that the effect of crystal shape has not been separated from the size effect reported here, and these dimension effects should be considered an exclusive property of sheet crystals until they are either observed or not observed for other shapes.

The kink band formed in iron strictly obeys the crystallographic requirements set down by Hess and Barrett [8], that the reorientation is about an axis parallel to the glide plane. Furthermore, the kink boundary when initially formed should be a plane that is normal to the glide direction, and it is. The (111) boundary observed in this work also agrees with the boundary observed by Barrett and Levinson [9] for "deformation bands" produced in iron by drawing and by tensile straining. It seems proper to consider tensile kink bands observed here and Barrett's deformation bands to be the same phenomenon.

A particularly important feature of kink band formation in iron is that it contributes to our knowledge of the slip mechanism in iron. If a kink band is to form with the definite boundary or "bend plane" initially normal to the [111] slip direction, and if a planar boundary is maintained through continued slip, slip must occur on a single system in the matrix crystal—in this case on the (211) plane. If two slip systems can operate, local lattice rotations can be accommodated by alternate use of the two planes, and a bend plane and consequent kink band will not form. It seems unlikely that (211) slip in these kinked crystals can be accounted for by a composite of two or more {110} slip planes as has been proposed [10] for body-centered cubic metals. Experimental evidence exists [11], in fact, that indicates kink bands form in aluminum crystals only under conditions of single slip.

It is of interest to note that Orowan [12] once suggested that the yield point or drop-in-load behavior was connected with the formation of "deformation bands" in iron crystals; and for those crystals with tensile axes near [111] this indeed seems to be so. However, the Cottrell mechanism is still required to explain the drop in load in the more common orientations.

Conclusion

One may conclude from this study that the initial yielding behavior of iron crystals containing carbon depends, in part at least, on the crystal dimensions in the slip direction. Sharper yield points and more spectacular load drops are observed for the longer total slip path, a result in agreement with the collision interaction mechanism proposed previously. As long as the tensile axis of the crystal is 10° or more from a [111] direction, the foregoing results appear independent of crystal orientation. However, crystals with tensile axes nearer than 10° to a [111] direction yield by another mechanism, kinking on a (111) plane about a [110] axis, and "drop-in-load" yielding is produced with short total slip paths, with or without the presence of carbon.

For those orientations outside the [111] region, the counterpart of the Lüders band observed in polycrystalline iron seems to be the highly localized region of flow that appears as a wavy groove on the surface of the crystal.

References

1. Cottrell, A. H. Report of Conf. on Strength of Solids (London, The Physical Soc., 1948), p. 30.
2. Holden, A. N. and Hollomon, J. H. Trans. A.I.M.E., **185** (1949) 179.
3. Schwartzbart, H. and Low, J. R., Jr. Trans. A.I.M.E., **185** (1949) 637.
4. Cottrell, A. H. and Churchman, A. T. Trans. A.I.M.E., **185** (1949) 877.
5. Holden, A. N. Trans. A.I.M.E., **194** (1952) 182.
6. Wu, T. L. and Smoluchowski, R. Phys. Rev., **75** (1949) 345.
7. Opinsky, A. and Smoluchowski, R. A Symposium on the Plastic Deformation of Crystalline Solids (Pittsburgh, Mellon Institute, 1950), p. 216.
8. Hess, J. B. and Barrett, C. S. Trans. A.I.M.E., **185** (1949) 599.
9. Barrett, C. S. and Levinson, L. H. Trans. A.I.M.E., **135** (1939) 327.
10. Chen, N. K. and Maddin, R. Trans. A.I.M.E., **191** (1951) 937.
11. Honeycombe, R. W. K. J. Inst. of Metals, **80** (1951) 45.
12. Orowan, E. Nature, **149** (1942) 643.

THE LOW TEMPERATURE SPECIFIC HEAT OF ANTIMONY*

W. DeSORBO†

The specific heat of antimony has been measured in the temperature region 13° to 70°K. The data are compared with a calculation based on an anisotropic continuum model which distinguishes between "soft" and "hard" modes of vibrations in anisotropic lattices resembling "layer-like" structures. Satisfactory agreement exists between the data and the predictions of this model in the temperature region 13° to 300°K. The entropy of antimony at 298.1°K is 10.92 cal/g-atom deg., of which 0.115 was obtained by extrapolating below 13.2°K. For this extrapolation the anisotropic-continuum model was used.

LA CHALEUR SPÉCIFIQUE DE L'ANTIMOINE À BASSE TEMPÉRATURE

La chaleur spécifique de l'antimoine a été mesurée aux températures allant de 13° à 70°K. Les données sont comparées aux résultats d'un calcul basé sur un modèle de continu anisotrope, qui distingue entre les modes de vibration "doux" et "durs" dans des réseaux anisotropes ressemblant à une structure "en couches." Dans la région des températures de 13° à 300°K, les données expérimentales s'accordent d'une manière satisfaisante avec les prédictions basées sur ce modèle. L'entropie de l'antimoine à 298,1°K est de 10,92 cal/atome-g/deg., dont 0,115 ont été obtenus par extrapolation en dessous de 13,2°K. Le modèle du continu anisotrope a servi à cette extrapolation.

DIE SPEZIFISCHE WÄRME DES ANTIMONS BEI TIEFEN TEMPERATUREN

Die spezifische Wärme des Antimons wurde im Temperaturbereich zwischen 13°K und 70°K gemessen. Diese Daten werden mit einer Berechnung verglichen, der ein Modell, das anisotropes Kontinuum voraussetzt, zu Grunde liegt. Dieses Modell unterscheidet zwischen "weichen" und "harten" Schwingungen in anisotropen Gittern, ähnlich den "Schichtstrukturen." Im Temperaturgebiet zwischen 13°K und 300°K besteht zufriedenstellende Übereinstimmung zwischen den experimentellen Ergebnissen und den Voraussagen dieses Modells. Die Entropie des Antimons bei 298,1°K ist 10,92 cal/g-atom Grad, davon wurden 0,115 durch Extrapolieren unterhalb von 13,2°K ermittelt. Das Modell des anisotropen Kontinuums wurde für diese Extrapolation benutzt.

Introduction

Tarassov [1–3] has discussed the application to specific heat data of one- and two-dimensional frequency-distribution functions based on a Debye type of continuum model. This model has been used by him to describe some of the earlier low temperature specific heat data of highly anisotropic monatomic lattices. In his analysis, Tarassov has used one characteristic temperature and in most cases the data available to him extended down to liquid nitrogen temperatures only.

In case of the "chain" structure elements, selenium and tellurium, it has been shown [4; 5] that a simple anisotropic continuum model describes the data satisfactorily. This model which distinguishes between the "soft" and "hard" modes of vibration predicts a T^3 dependence of the specific heat at sufficiently low temperatures. Tarassov had previously derived and applied this anisotropic model to the specific heat data of some molecular lattices.

Recently, the T^2 dependence of the specific heat of "layer" structures graphite [6] and gallium [7] have been verified in the temperature regions 13° to 54°K and 15° to 34°K, respectively. Krumhansl and Brooks [8] have shown that the T^2 dependence may be an intrinsic property of the graphite lattice and predict that at sufficiently low temperatures the specific heat of graphite should vary as T^3.

The lattice anisotropy of antimony is of a "lesser" degree than graphite. The distance between nearest neighbors in graphite is 1.42Å while the distance of next nearest neighbors or between atoms in adjacent layers is 3.40Å [9]. The "layers" in antimony are "puckered" with the distance between nearest neighbors equal to 2.87Å, while the distance between next nearest atoms in "adjacent layers" is 3.37Å [10]. For this reason it was considered important to extend the specific heat studies of antimony to lower temperatures in order to determine in detail the temperature dependence. In this investigation the specific heat of antimony has been extended to 13°K. Previous determinations were those of Gunther [11] (80–98°K), Simon [12] (71–82°K), and Anderson [13] (66–293°K).

Experimental

The sample of antimony used in this investigation is one of the "spectroscopically standardized substance" obtained from Johnson, Matthey and Co., Limited, London, and referred to by them as "H.S." antimony (Laboratory No. 2696). The specimen consisted of granules having an average "diameter" of about 2 to 3 mm. The purity of the sample has been reported to be 99.90 per cent. The

*Received March 25, 1953.
†General Electric Research Laboratory, The Knolls, Schenectady, New York, U.S.A.

following were listed as impurities, (values given in per cent): 0.03 As, 0.01 Pb, 0.015 Fe, 0.015 S. Approximately one and one-half gram-atoms of antimony were used in the experiment.

The cryostat, copper calorimeter, and accessory apparatus used in this investigation have been used previously and are described elsewhere [14].

Results

The specific-heat data, extending from 13° to 70°K, are presented in Table I. The C_v values have been calculated from the C_p data with the aid of the Nernst-Lindemann formula [15].

TABLE I

Specific Heat of Antimony
Atomic Wt. = 121.76; 1.4956 gram-atoms

Mean temp. (°K)	ΔT	C_p (cal/g-atom deg.)	C_v (cal/g-atom deg.)
13.21	2.729		0.246
13.44	0.990		0.248
14.44	0.937		0.321
15.32	0.798		0.378
16.19	0.695		0.433
17.10	1.612		0.521
17.26	1.260		0.522
18.49	1.061		0.616
18.86	1.851		0.672
20.57	1.508		0.824
22.18	1.713		0.929
24.06	2.043	1.089	1.088
26.26	2.394	1.276	1.275
28.78	2.675	1.474	1.472
31.73	3.258	1.726	1.724
34.92	3.097	2.012	2.009
39.55	2.558	2.363	2.358
42.64	2.922	2.602	2.595
47.09	2.606	2.890	2.881
51.70	2.659	3.200	3.187
56.58	2.735	3.524	3.507
58.95	2.615	3.677	3.658
64.33	2.446	3.818	3.796
69.76	2.864	4.065	4.038

Table II lists the value of entropy obtained from a smooth curve of a large graph of specific heats vs. log T for the temperature region 13.2° to 56.2°K. Simpson's rule was used to evaluate the function. The increment of entropy between 56.2 to 298.1°K was that previously obtained by Anderson [13]. The entropy of antimony at 298.1°K is 10.92 ± 0.05 cal/g-atom deg. The extrapolated portion below 13°K amounts to 0.115.

TABLE II

Entropy of Antimony at 298.1°K
(cal/g-atom deg.)

C. T. Anderson		This research	
Extrap. (0–56.2)°K	=1.91	Extrap. (0–13.2)°K	=0.115
Graph. (56.2–298.1)°K	=8.59	Graph. (13.2–56.2)°K	=2.215
$S^0_{298.1}$	=10.50	$S^0_{56.2}$	=2.330

$S^0_{56.2}$	=2.33	This research
Graph. (56.2–298.1)°K	=8.59	Anderson's data
$S^0_{298.1}$	=10.92	

Discussion

A plot of the log C_v vs. log T for antimony is presented in Figure 1. In the low temperature region ($T < 20$°K approx.), where one might expect the Debye type of approximations to be more valid, it is seen that neither the T^2 nor the T^3 dependence is followed. The exponential of T has a value greater than 2 and is increasing continuously with decreasing temperatures approaching a value of 3 at approximately 14°K.

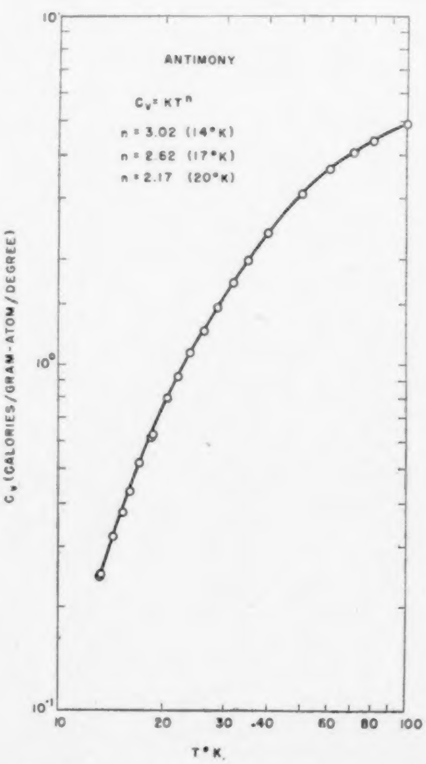

Figure 1. Log C_v as a function of log T for antimony at low temperatures.

In Figure 2 the characteristic temperatures, θ_2 and θ_3, are presented as a function of temperature. The temperature θ_2 has been computed by graphical interpolation of the specific heat integral based on a two-dimensional continuum model.* The characteristic temperature, θ_3, has been computed from the three-dimensional Debye integrals where in one case the experimental C_v data have been used and

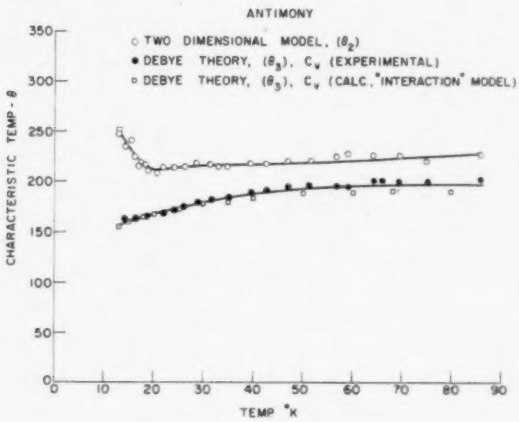

FIGURE 2. Characteristic temperatures as a function of absolute temperature.

in the other C_v has been calculated from an "interaction" continuum model discussed below. The experimental data above 70°K are those of Anderson [13]. The temperature θ_2 can be considered effectively constant above approximately 20°K. Hence the data of this research show that the two-dimensional continuum model could describe the data satisfactorily down to approximately 20°K (see column C_2, Table III). Tarassov [1; 3] had previously discussed the correlation, above the liquid nitrogen temperature, between Anderson's specific heat data on antimony and the two-dimensional model.

Below 20°K, the characteristic temperatures, θ_2 and θ_3, show definite deviations from a constant value. The characteristic temperature θ_2 increases rather abruptly in value while θ_3 is decreasing in value with decreasing temperature. These deviations from a constant value reflect the deviation of the distribution function assumed in the continuum spectrum. Above liquid hydrogen temperatures, it appears that either the two-dimensional continuum integral or the Debye theory could describe the data to a satisfactory degree of approximation. However, it would be difficult to use these continuum ideas at these higher temperatures to distinguish between a "layer" structure or a three-dimensional structure. This lack of sensitivity at the higher temperatures results from the fact that the specific heat is proportional only to the total integral of the distribution function. The distribution between these models based on continuum ideas is more apparent at low temperatures where the exact form of the distribution function is important.

A possible explanation for the increase in θ_2 and decrease in θ_3 at the low temperatures may be that the frequency-distribution function following for the most part a two-dimensional form at the higher temperatures is going over into a three-dimensional form with decreasing temperature. The structure of antimony may be considered roughly a "layer" structure. Each atom is at a slightly closer distance to three of its six nearest neighbors. The main valences occur in the "two-dimensional plane." The bonding perpendicular to the planes is of a weaker character. The main valence forces may be considered to be associated with the higher frequencies in the lattice. As the temperature is decreased the higher frequencies become less highly excited and leave waves of longer and longer wave lengths as the only ones excited. At a temperature sufficiently low, the waves remaining are of sufficient length that they are no longer influenced by the individual atoms in the lattice. For these waves the isotropic-three-dimensional continuum model is more nearly correct. It would seem significant then to apply to an anisotropic monatomic lattice such as antimony a Debye type of continuum model that differentiates between the "soft" and the "hard" modes of vibration.

A simplified "interaction" model accounting for these two types of modes and based on the Debye type of approximations has recently been proposed by Tarassov [3] but, as yet, has not been applied to the problem of "interacting" layers of a monatomic lattice. Tarassov had applied the model to molecular lattices having "chain" and "layer" structures. For the layer type structure, it is supposed that, of the 3N modes of vibration of the lattice, only those modes whose frequencies are less than some limiting frequency ν_1 are distributed like a Debye three-dimensional continuum with a frequency density proportional to ν^2. For those modes with frequencies greater than ν_1 (i.e., shorter wave

---

*From [3],

$$C_2 = 18R\left(\frac{T}{\theta_2}\right)^2 \int_0^{\theta_2/T} \frac{x^2dx}{e^x - 1} - 6R\left(\frac{\theta_2}{T}\right)\left[\exp\frac{\theta_2}{T} - 1\right]^{-1}$$

lengths) the layer character of the lattice predominates and these modes have a frequency density characteristic of a two-dimensional continuum and so proportional to ν. Thus for $\nu < \nu_1$,

$$(1) \qquad N_3(\nu) = C_3\,\nu^2,$$

and for $\nu_1 < \nu < \nu_{\max}$,

$$(2) \qquad N_2(\nu) = C_2\,\nu.$$

It is further assumed* that

$$(3) \qquad \int_0^{\nu_1} C_3\nu^2 d\nu = \int_0^{\nu_1} C_2\nu\, d\nu.$$

Then, since

$$(4) \qquad \int_0^{\nu_1} C_3\nu^2 d\nu + \int_{\nu_1}^{\nu_m} C_2\nu\, d\nu = 3N,$$

we have

$$(5) \qquad C_2 = \frac{6N}{\nu_{\max}^2}, \quad C_3 = \frac{9N}{\nu_{\max}^2\nu_1}$$

and

$$N_3(\nu_1)/N_2(\nu_1) = 1.5.$$

Hence

$$(6) \qquad \int_0^{\nu_1} C_3\nu^2 d\nu = 3N\frac{\nu_1^2}{\nu_{\max}^2}$$

and

$$(7) \qquad \int_{\nu_1}^{\nu(\max)} C_2\nu\, d\nu = 3N\left(1 - \frac{\nu_1^2}{\nu_{\max}^2}\right).$$

The internal energy for the "interacting" layers then has the following form:

$$(8) \quad U_{2(3)} = \frac{9N}{\nu_1\nu_{\max}^2}\int_0^{\nu_1}\frac{h\nu^3}{e^{h\nu/kt} - 1}d\nu + \frac{6N}{\nu_{\max}^2}\int_{\nu_1}^{\nu(\max)}\frac{h\nu^2}{e^{h\nu/kt} - 1}d\nu.$$

*This assumption, made by Tarassov, is arbitrary. Because of the Brillouin zone geometry, one might more reasonable assume, as suggested by Krumhansl [16], that the distribution function be continuous at ν_1, i.e., $N_3(\nu_1) = N_2(\nu_1)$. The expression obtained for the specific heat is then

$$C_{2(3)} = \frac{\theta_2^2}{(\theta_2^2 - \frac{1}{3}\theta_3^2)}\left\{6R\left(\frac{T}{\theta_2}\right)^2\int_0^{\theta_2/T}\frac{x^3e^x}{(e^x-1)^2}dx - \left(\frac{\theta_3}{\theta_2}\right)^2\left[6R\left(\frac{T}{\theta_3}\right)^2\int_0^{\theta_3/T}\frac{x^3e^x}{(e^x-1)^2}dx - \frac{2}{3}(9R)\left(\frac{T}{\theta_3}\right)^3\int_0^{\theta_3/T}\frac{x^4e^x}{(e^x-1)^2}dx\right]\right\}$$

which describes the data equally well with $\theta_2 = 210°$ and $\theta_3 = 50°$. Since so many detailed effects are neglected in this continuum treatment one is not really justified, in this case, in choosing one over the other of these expressions as a closer approximation.

Letting $x = h\nu/kT$, $\theta_2 = h\nu_{\max}/k$ and $\theta_3 = h\nu_1/k$, one can readily derive the following expression for the specific heat of "interacting" layer structures.

$$(9) \quad C_{2(3)} = 6R\frac{T^2}{\theta_2^2}\int_0^{\theta_2/T}\frac{x^3e^x}{(e^x-1)^2}dx - \left(\frac{\theta_3}{\theta_2}\right)^2\left[6R\frac{T^2}{\theta_3^2}\int_0^{\theta_3/T}\frac{x^3e^x}{(e^x-1)^2}dx - 9R\frac{T^3}{\theta_3^3}\int_0^{\theta_3/T}\frac{x^4e^x}{(e^x-1)^2}dx\right].$$

As $T \to 0$, equation (9) reduces to a T^3 expression: i.e.,

$$(10) \qquad C_{2(3)} = \frac{12}{5}\pi^4 R\frac{T^3}{\theta_3\cdot\theta_2^2}.$$

In Table III are summarized the results of the comparison of the experimental specific heats of antimony with equation (9) (column $C_{2(3)}$). In this calculation, θ_2 has been assigned a value of 210° and θ_3 has been given a value of 70°. The table also shows

TABLE III

SPECIFIC HEAT OF ANTIMONY CALCULATED FROM THE TWO-DIMENSIONAL AND "INTERACTION" CONTINUUM MODELS (cal/g-atom deg.)

T(°K)	C_p (expt'l)	C_v		$C_{2(3)}$ (calc.)	C_2 (calc.)
13		0.240		0.274	0.328
15		0.356		0.379	0.430
18		0.592		0.574	0.618
20		0.742		0.733	0.772
25		1.172		1.188	1.218
30		1.592		1.604	1.630
35	2.000		1.997	2.072	2.090
40	2.380		2.375	2.501	2.518
50	3.095		3.084	3.238	3.250
60	3.675		3.656	3.804	3.815
70	4.110		4.082	4.231	4.240
80	4.440		4.403	4.570	4.578
100	4.928		4.870	5.010	5.015
150	5.538		5.429	5.508	5.510
200	5.820		5.660	5.771	5.772
250	5.930		5.772	5.819	5.820
300	6.050		5.790	5.859	5.860

the comparison of the experimental data with the specific heats calculated from the two-dimensional integral in which the characteristic temperature θ_2 also equals 210°. The agreement between the experimental data and equation (9) is satisfactory in the temperature range 13° to 300°K. The results are presented graphically in Figure 3.

Equations (6) and (7) give effectively the number

of "soft" and "hard" modes of vibration, respectively. With the value of $\theta_2 = 210°$ and $\theta_3 = 70°$, approximately 90 per cent of the frequencies are "hard" and 10 per cent "soft."

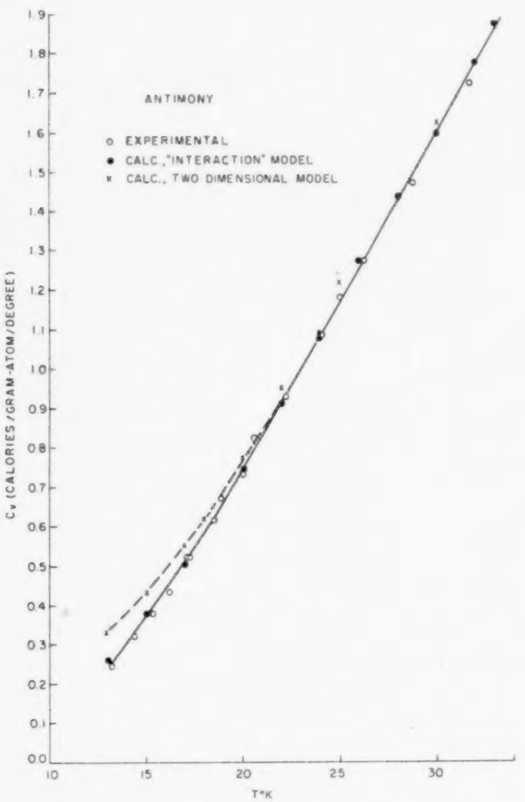

FIGURE 3. Specific heat of antimony calculated from a two-dimensional and an "interaction" models compared with experimental data.

For the purpose of calculating entropy in the region where the T^3 law is valid, the following equation is derived from equation (10):

$$S_0^T = \frac{4}{5}\pi^4 \frac{RT^3}{\theta_3 \cdot \theta_2^2}. \tag{11}$$

From Figure 1 it appears that the T^3 region has been reached at $T \simeq 14°K$. The entropy increment between 0°K and the lowest experimental point, 13.21°K, can be calculated by using equation (11), provided one assumes the third law and neglects any contribution from electronic specific heat.* The characteristic temperatures, θ_2 and θ_3, have the same values cited previously. The entropy increment, $S_0^{13.2°K} = 0.115$ cal/g-atom deg.

Acknowledgements

The author wishes to thank Mrs. E. L. Fontanella for her assistance in the experimental work and in the data computation. Computational assistance was also rendered by Mrs. Elizabeth Morse. Many discussions with R. H. Pry and his criticism of the manuscript are gratefully acknowledged.

This paper was presented in part before the Eighth Conference on Cryogenics, General Electric Company, Schenectady, New York, October 6–7, 1952.

References

1. TARASSOV, V. V. C. R. Acad. Sci. U.R.S.S., **46** (1945), no. 1 and no. 3; **54** (1946), no. 9.
2. TARASSOV, V. V. Doklady Akad. Nauk., **58** (1947), no. 4.
3. TARASSOV, V. V. Zhur. Fiz. Khim., **24** (1950) 111.
4. DESORBO, W. "The Specific Heat of Crystalline Selenium at Low Temperatures," to be published in J. Chem. Phys.
5. DESORBO, W. J. Chem. Phys., **21** (1953) 764.
6. DESORBO, W. and TYLER, W. W. "The Specific Heat of Graphite from 13° to 300°K," to be published (Phys. Rev., **83** 1951, 878).
7. DESORBO, W. J. Chem. Phys., **21** (1953) 168.
8. KRUMHANSL, J. A. and BROOKS, H. "Lattice Vibration Specific Heat in Graphite," to be published in J. Chem. Phys.
9. BERNAL, J. D. Proc. Roy. Soc. (London), **A106** (1924) 749.
10. Strukturbericht, vol. 1, p. 738.
11. GUNTHER, P. Ann. Physik (4), **63** (1920) 476.
12. SIMON, F. and RUHEMANN, M. Z. phys. Chem., **129** (1927) 321.
13. ANDERSON, C. T. J. Amer. Chem. Soc., **52** (1930) 2712.
14. DESORBO, W. J. Amer. Chem. Soc., **75** (1953) 1825.
15. NERNST, W. and LINDEMANN, F. Z. Elektrochem., **17** (1911) 817.
16. KRUMHANSL, J. A. Knolls Atomic Power Laboratory, Report no. 730.

*The data have not been determined at low enough temperatures to permit an evaluation of the electronic specific heat. For Antimony, the Sommerfeld free electron model (q assumed equal to 3) gives $Ce \simeq 3 \times 10^{-4}$T cal/g-atom deg. This probably represents an upper limit to the actual value.

WORK HARDENING IN FACE-CENTERED SUBSTITUTIONAL ALLOYS*

J. S. KOEHLER†

The existing experimental data on the mechanical properties of single crystals of the face-centered cubic substitutional alloys are reviewed. It is shown that the data can be understood by supposing that source hardening and impurity hardening are important whereas interaction hardening is not. The free length distribution of dislocations is found to be essentially independent of concentration. A process which is shown to be important for alloys is that by which a new slip band reduces the impurity stresses in its neighbourhood. It is suggested that vacancy and interstitial production can explain the results. Several experiments are suggested.

L'ÉCROUISSAGE DANS LES ALLIAGES CUBIQUES À FACES CENTRÉES DE SUBSTITUTION

Une revision est faite des données expérimentales sur les propriétés mécaniques de monocristaux des alliages cubiques à faces centrées de substitution. Il est montré que ces données peuvent être comprises, si on suppose que l'écrouissage dû à l'épuisement des sources et l'écrouissage dû aux impuretés sont importants, alors que l'écrouissage d'interaction ne l'est pas. Il est constaté que la longueur libre de distribution des dislocations est essentiellement indépendante de la concentration. L'importance du processus par lequel une nouvelle bande de glissement réduit, dans son voisinage, la tension due aux impuretés, est montrée pour le cas des alliages. Il est suggéré que la production des lacunes et d'atomes interstitiels peut expliquer les résultats. Quelques expériences sont suggérées.

VERFESTIGUNG VON FLÄCHENZENTRIERTEN SUBSTITUTIONS-LEGIERUNGEN

Es wird eine kritische Übersicht der experimentellen Angaben über die mechanischen Eigenschaften von Einkristallen mit flächenzentrierten Substitutionslegierungen gegeben. Die experimentellen Angaben erscheinen verständlich, wenn man annimmt, dass Verfestigung durch Versetzungsquellen und Verunreinigungen ins Gewicht fallen, Verfestigung durch Wechselwirkung der Versetzungen jedoch nicht. Die Verteilung der "freien Weglängen" der Versetzungen erwiess sich praktisch unabhängig von der Konzentration. Es wird gezeigt, dass ein Prozess, in dem ein neues Gleitband die Spannungen der Verunreinigungen in seiner Umgebung vermindert, im Fall der Legierungen von Wichtigkeit ist. Es wird die Annahme zur Diskussion gestellt, dass das Entstehen von Leer- und Fehlstellen die Resultate erklären kann, und verschiedene neue Experimente werden vorgeschlagen.

Experiment

Stress-strain data exist for single crystals of α brass [1], silver-gold [2], and copper-nickel alloys [3] over a range of concentrations. The curves obtained by Sachs and Weerts [2] for the silver-gold system are shown in Figure 1. The stress-strain curves appropriate for the other alloys mentioned are similar.

There are several other pieces of experimental evidence which are available: Goler and Sachs [4] and later Treuting and Brick [5] have shown that slip lines cluster in α-brass, i.e. that additional deformation is accomplished by glide on slip bands which are near previously formed slip bands. Figure 2 shows this behavior according to Treuting and Brick.

There are also data on asterism [6] which reveal that in alloys, in contrast to pure metals, very little asterism occurs until slip on a second slip system begins.

The change in the orientation of a tensile specimen during glide is such that it reduces the resolved shearing stress on the initial slip system so that eventually the resolved shearing stresses on two slip systems become equal. In pure metals further deformation occurs simultaneously by equal amounts of glide on the two slip systems [7]. The alloys, on the other hand, glide on only one slip system at a time [7]. There is also in alloys the phenomenon of "overshooting," i.e. the alloys continue to deform on the initial slip system past the orientation where the two resolved shearing stresses are equal [6]. In fact, a careful examination of the data indicates that *the deformation continues on the initial slip system until the resolved shearing stress on the second slip system exceeds that on the first by the yield stress of the alloy.*

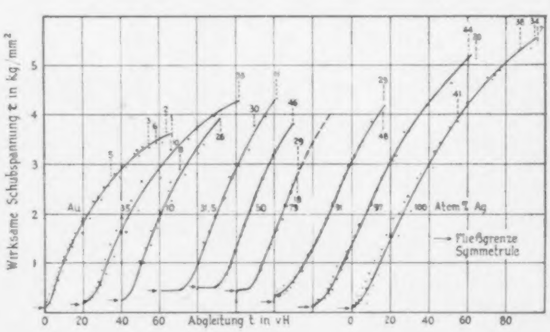

FIGURE 1. Resolved stress-strain curves of gold-silver single crystals of various given compositions. The resolved shearing strain is given in per cent (after Sachs and Weerts).

*Received March 11, 1953.
†Department of Physics, University of Illinois, Urbana, Illinois, U.S.A.

This conclusion is illustrated in Figure 3 by data on α-brass showing the discontinuous increases in the resolved shearing stress which accompany the transition of slip from the initial slip system to the second system.

Theory

The research of Miller and Milligan [8], Rosi and Mathewson [9], Andrade and Henderson [10], Masing and Raffelsieper [11], and Lange and Lucke [12] on the dependence of the stress-strain curves of pure face-centered metals on orientation shows clearly that there are two kinds of work hardening. At small strains one has the phenomenon of "easy glide"; the stress-strain curve is linear and the work hardening is small during easy glide. At larger strains the rate of work hardening increases and the stress-strain curve becomes parabolic. The last two papers cited above give data showing that:

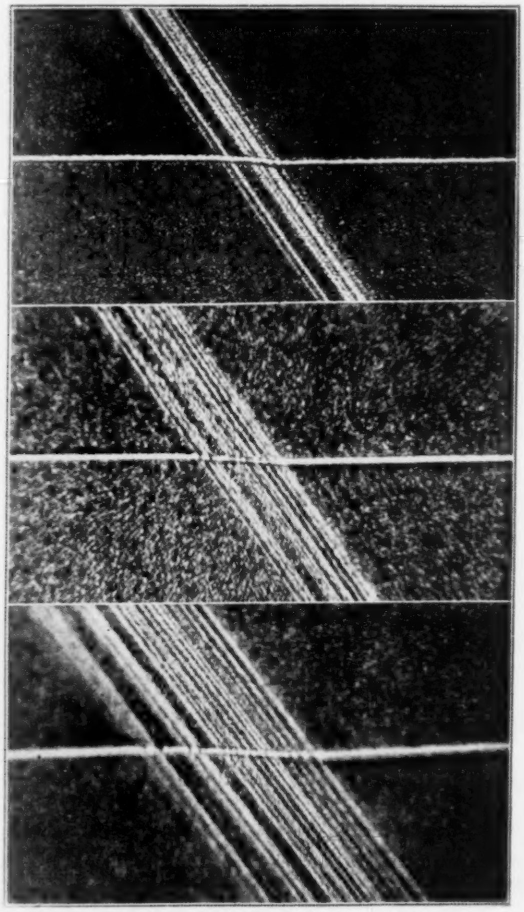

FIGURE 2. Slip steps in a single crystal of 72 per cent α-brass. (*a*) Shearing strain = 0.002; (*b*) shearing strain = 0.004; (*c*) shearing strain = 0.015. Horizontal line is a scratch (after Treuting and Brick).

(*a*) The strain at which the second type of hardening becomes dominant decreases as the initial orientation approaches an orientation giving multiple slip. (*b*) The rate of hardening by the second mechanism increases as one approaches orientations giving multiple slip, i.e. simultaneous slip on several slip systems.

In an earlier paper [13] the two kinds of hardening were interpreted as source hardening and interaction hardening. In the region of small strain, source hardening occurs, i.e. the longest free lengths of dislocations generate and become locked. An increase in stress is then necessary to produce Frank-Read [14] generation at the shorter dislocations. The second kind of hardening was termed interaction hardening. It was first discussed by G. I. Taylor [15]. The essential point is that the larger the dislocation density the more stress will be required to drive the dislocations of opposite sign past one another because they interact.

The experimental data on pure metals indicate strongly that some glide does occur on the inactive slip systems and that the dislocation structure which results is not transparent to dislocations gliding on the initial slip system. Hence interaction hardening occurs. Consider next the situation in an alloy. In

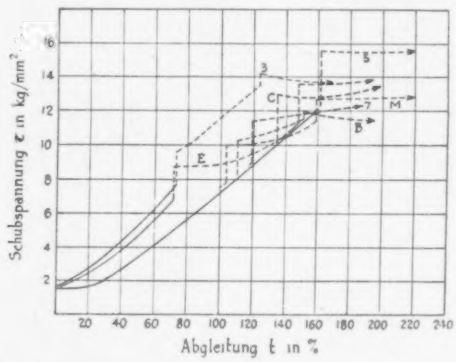

FIGURE 3. Resolved stress-strain curves of various single crystals of 72 per cent α-brass. The discontinuous increases in shearing stress occur when slip stops on the initial slip system and begins on a second slip system (after Masima and Sachs)

this case, the overshooting data show that glide on the initial slip system softens it so that further glide prefers to occur on the initial rather than on an inactive slip system. For this reason it is believed that source hardening and not interaction hardening is important over the major portion of the stress-strain curve of an alloy. This conclusion is in accord with the fact that the ascending portions of the stress-strain curves of silver-gold alloys are linear over large strain increments, particularly for large

impurity concentrations. It is also in accord with the observations that, whereas asterism appears at small strains in pure face-centered metals, little or no asterism is encountered in alloys until slip on a second slip system occurs.

The Treuting and Brick pictures show that source hardening occurs in α-brass at small strains. This is evident because only finite glide occurs at each slip band. Their pictures also show that some process occurs near a slip band which makes it easier for a second slip band to be produced in the vicinity of the first. It will be proposed here that this process reduces the impurity hardening in the vicinity of the original slip band. It will be seen later that this hypothesis explains the phenomena which take place when a change of slip system occurs.

The applied stress σ necessary for deformation is therefore

$$\sigma = \sigma_i + \sigma_s$$

where σ_i is the portion of the applied stress necessary to overcome the influence of the impurities and σ_s is the portion of the applied stress needed for Frank-Read generation.

At this point a second assumption will be made. In Figure 1 the slopes of the ascending straight-line portions of the stress-strain curves agree to within 20 per cent of their value. It will therefore be assumed that the dislocation free length distribution is independent of impurity concentration. The data on α-brass indicate that there the source hardening may be slightly decreased by increasing the impurity concentration.

There is still a point which has not been taken care of: experimentally, the data show that the linear portion of the stress-strain curve does not extrapolate back to zero strain when the stress is zero. Two possible explanations can be offered. It is possible that the presence of impurities alters the locking of sources in such a way that the average glide per slip band is larger in the flat portion of the stress-strain curve than it is in the ascending portion where the impurity stresses cease to be important for glide on the initial slip system. If this is the case, it can be checked by direct observation of the glide at the slip bands in the first and second stages of deformation. Another possibility is that the dislocations, which move through the lattice at yielding, sweep some of the shorter dislocations along with them. This alternative would predict that the transition from the flat to the ascending curve would not be sharp, but that the initial portion of the ascending curve would require larger stresses than otherwise anticipated because some of the short dislocation lengths have already been used. The data given in Figure 1 do show a transition region of the sort suggested by the second alternative. It should be mentioned however that inhomogeneities in concentration could also cause such a transition region.

In the theoretical paper [13] on source hardening in pure metals, an expression for the free length distribution was obtained by fitting experimental data valid for aluminum. Such a fit is not illuminating in the case of the alloys since there are more constants to be determined than there are pieces of experimental information. However, by just blindly using the dislocation distribution found for aluminum, the slope calculated for silver-gold is too small by a factor of three. Thus the distribution must be nearly the same as that found for pure aluminum.

There is still the transition from one glide system to another to be considered. According to the picture presented here, glide on the first slip system eventually completely erases the impurity stresses for further glide on that slip system. The experimental findings on overshooting mentioned earlier show that the glide on the second slip system must still overcome the impurity stress as well as the source stress. This result indicates that the nullification of impurity stresses occurs only in the vicinity of existing slip bands. Thus, in Figure 4 the effect can aid slip on the initial slip system, but since glide on a new slip system must cut through material far from any existing slip band, no aid can be expected. R. Jamison and T. H. Blewitt [16] have found that the distance over which nullification acts in irradiated copper increases with increasing temperature. Thus, at liquid nitrogen temperature after a given strain they found that a slip band cluster occupied a smaller portion of the specimen length than a cluster produced in a similar specimen at room temperature. This suggests that a

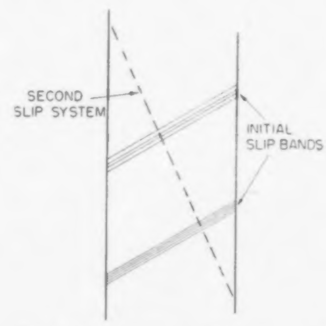

FIGURE 4. Showing that nullification will lower the impurity stresses for the initial but not for the second slip system.

diffusion process plays a role in the effect. Seitz [17] has proposed that glide on a slip band generates vacancies and interstitials in the vicinity. The data on alloys just presented could be understood if one assumed that at least a portion of these vacancies and interstitials moved about a bit and then settled down in such a way as to erase the local impurity stresses. They prefer to erase impurity stresses because in doing so they lower the potential energy of the system. The decrease in the size of the cluster occurs because at low temperature thermal fluctuations are not able to assist their motion away from the slip bands where they are produced. Even at low temperature they may be able to move a little because of the excess local vibrational energy in the vicinity of the glide band. If enough reduction in the range of this softening effect can be produced by lowering the temperature so that new slip lines will not form near the old ones because of the large local dislocation stresses (i.e. if the range drops below a few hundred Angstroms), two changes will occur. First, there will be no flat portion of the stress-strain curve. Second, there will be no overshooting.

The theory presented here and in the earlier paper implies that the slope of the ascending straight-line portion of the stress-strain curve should be dependent on temperature for an alloy having slip bands which are made up of several fine parallel lamellae. Certain aluminum alloys may well have stress-strain curves of this kind.

There are to points concerning the change in slip systems which should be mentioned:

First, if the specimen is so oriented that double slip would occur in a pure metal at a strain which is within the flat portion of the stress-strain curve of the alloy then, since nullification on the initial slip system is incomplete, one would not expect the differences in the resolved shearing stresses to be as large as the yield stress when slip changes from one system to another.

Secondly, it can be seen why slip continues to use only the second slip system once it has begun there. To begin with, the dislocation sources on all slip systems are gradually used as glide proceeds [13]. It is only those on the initial slip system which produce an appreciable amount of glide and which generate large numbers of vacancies and interstitials. In the initial slip system the distribution is used until, at the strain associated with the change in slip system, the longest length l_1 available is given by

$$\sigma_1 = \frac{G_b}{l_1}$$

where G is the modulus of rigidity, b is the Burgers vector of the dislocation, and σ_1 is the resolved shearing stress in the initial system. Similarly for the second system:

$$\sigma_2 = \sigma_1 + \sigma_y = \frac{G_b}{l_2} + \sigma_y.$$

Thus $l_2 = l_1$ so that the dislocation distributions are used to the same extent when the change occurs. But when slip occurs on the second system the purification process begins there. In addition, some of the vacancies and interstitials generated by the glide on the second slip system will be deposited in the region where additional slip would occur on the first slip system. This acts just as an impurity would and hardens the initial slip system where complete nullification has previously occurred. The vacancy interstitial processes thus simultaneously soften the second slip system and add impurities to the initial slip system. This implies that when the orientation changes until slip again takes place on the initial slip system, the resolved shearing stress on the initial slip system will be larger than that on the second, but that the difference will be determined by vacancy interstitial stresses not by impurity stresses (see Figure 3 for data).

The principal conclusions of this discussion are: (1) Some process occurs during glide in face-centered cubic alloys which is able to erase the impurity stresses in the vicinity of the active slip bands. It is suggested that this process may be the production, the motion, and the settling down of vacancies and interstitials in such a way as to nullify impurity stresses. (2) It is suggested that source hardening and impurity hardening play major roles in these alloys whereas interaction hardening has little influence on their mechanical properties. (3) It is found that the free length dislocation distribution is independent of concentration and in fact does not seem to vary much from one metal to another. (4) It is felt that much basic information can be gained from further study of these alloys and to this end a number of experiments are suggested.

This work is supported by the O.N.R.

References

1. MASIMA, M. and SACHS, G. Z. Phys., **50** (1928) 161.
2. SACHS, G. and WEERTS, J. Z. Phys., **62** (1930) 473.
3. OSSWALD, E. Z. Phys., **83** (1933) 55.
4. GOLER, V. and SACHS, G. Z. Phys., **55** (1929) 581.
5. TREUTING, R. G. and BRICK, R. M. Trans. A.I.M.E., **147** (1942) 142.

6. GOLER, V. and SACHS, G. Z. Phys., **55** (1929) 586 and 591; also MADDIN, R., MATHEWSON, C. H., and HIBBARD, W. R. Trans. A.I.M.E., **175** (1948) 190.
7. SCHMID, E and BOAS, W. Plasticity of Crystals (London, Hughes, 1950), p. 142; see also Figure 112 on p. 143.
8. MILLER, R. F. and MILLIGAN, W. E. Trans. A.I.M.E., **124** (1937) 229.
9. ROSI, F. D. and MATHEWSON, C. H. J. Metals, **188** (1950) 1159.
10. ANDRADE, E. N. DA C. and HENDERSON, C. Phil. Trans. Roy. Soc., **A224** (1951) 177.
11. MASING, G. and RAFFELSIEPER, J. Z. Metallk., **41** (1950) 65.
12. LUCKE, K. and LANGE, H. Z. Metallk., **43** (1952) 55.
13. KOEHLER, J. Phys. Rev., **86** (1952) 52.
14. FRANK, F. C. and READ, W. T. Phys. Rev., **79** (1950) 722.
15. TAYLOR, G. I. Proc. Roy. Soc., **A145** (1934) 362.
16. JAMISON, R. and BLEWITT, T. H. Bull. Amer. Phys. Soc., **28**, no. 2 (Durham Meeting, March 1952) 39.
17. SEITZ, F. Advances in Physics, **1** (1952) 43.

SELF-DIFFUSION IN ZINC*

G. A. SHIRN, E. S. WAJDA, and H. B. HUNTINGTON†

The self-diffusion of single crystal, high-purity zinc has been measured from 240°C to the melting point with the use of Zn^{65} as a tracer and the usual lathe sectioning technique. For diffusion parallel to the hexagonal axis the data were well fitted by an activation energy of $Q = 21.8$ kcal/mol and a $D_0 = 0.13$ cm²/sec, and for diffusion perpendicular to the hexagonal axis $Q = 24.3$ kcal/mol and $D_0 = 0.58$ cm²/sec. Several possible mechanisms for the diffusion are discussed and it is apparent that for zinc at least two are involved. It can be deduced that one of these is a vacancy mechanism and it is possible to explain the data on the basis of two vacancy mechanisms.

L'AUTO-DIFFUSION DANS LE ZINC

L'auto-diffusion dans de monocristaux de zinc de haute pureté a été mesurée de 240°C jusqu'au point de fusion, en employant du Zn^{65} comme indicateur et en se servant de la méthode usuelle des sections au tour. Pour la diffusion parallèlement à l'axe hexagonal les données étaient en accord avec une énergie d'activation $Q = 21{,}8$ kcal/mol et $D_0 = 0{,}13$ cm²/sec; et pour la diffusion perpendiculairement à l'axe hexagonal $Q = 24{,}3$ kcal/mol et $D_0 = 0{,}58$ cm²/sec. Quelques mécanismes possibles pour la diffusion sont discutés; il apparaît, que dans le cas du zinc, au moins deux de ces mécanismes sont impliqués. Il peut en être déduit, qu'un de ceux-là est un mécanisme lacunaire et il est possible d'expliquer les données en se basant sur deux mécanismes lacunaires.

SELBSTDIFFUSION IN ZINK

Die Selbstdiffusion von einkristallinem Reinstzink wurde zwischen 240°C und dem Schmelzpunkt mit Hilfe von radioaktivem Zn^{65} und der üblichen Schnitt-Technik untersucht. Die Resultate für Diffusion parallel zur hexagonalen Achse lassen sich gut durch eine Aktivierungsenergie von $Q = 21{,}8$ kcal/mol und $D_0 = 0{,}13$ cm²/sec darstellen, während für Diffusion senkrecht zur hexagonalen Achse $Q = 24{,}3$ kcal/mol und $D_0 = 0{,}58$ cm²/sec gilt. Mehrere mögliche Diffusionsmechanismen werden diskutiert, und es zeigt sich, dass für die Diffusion im Zink mindestens zwei Prozesse verantwortlich sind. Es kann aus diesem Material geschlossen werden, dass einer der Prozesse ein Leerstellenmechanismus ist, und es ist möglich die vorhandenen Daten mit zwei Leerstellenprozessen zu erklären.

1. Introduction

It is the primary purpose of this project to investigate diffusion in those materials where the effect is anisotropic. In single crystals of such materials, the diffusivity is described as a function of orientation by two, or at most three constants, at any given temperature. The study of the variation of these quantities with temperature then promises an avenue of information about the atomic mechanisms by which microscopic mobility is obtained.

In a medium where diffusion is anisotropic, the diffusion constant is actually a second order tensor relating the vectors, concentration gradient, and diffusion flux, which may not be mutually parallel. In any arbitrary system of coordinates such a tensor has nine components of which the six "non-diagonal" components are equal in pairs. For a particular coordinate system (which may or may not be unique) the "non-diagonal" components will vanish. For the concentration gradient in a particular direction which has direction cosines γ_1, γ_2, γ_3 with the axes of this coordinate system, the diffusivity can be expressed as

$$(1) \qquad D(\gamma_1\gamma_2\gamma_3) = D_1\gamma_1^2 + D_2\gamma_2^2 + D_3\gamma_3^2,$$

where D_1, D_2, and D_3 are the three remaining diagonal components of the diffusivity tensor. If now the material possesses an axis of symmetry threefold or higher, the diffusivity becomes isotropic in the plane perpendicular to the axis and equation (1) is replaced by

$$(2) \qquad D(\theta) = D_{\parallel} \cos^2\theta + D_{\perp} \sin^2\theta,$$

where $D(\theta)$ is the diffusivity of the material in a direction making an angle θ with the symmetry axis, and $D_{\parallel}$ and $D_{\perp}$ are respectively the diffusivity parallel and perpendicular to the axis.

For any particular atomic mechanism there is a finite number (one in vacancy and interstitial processes, more in the ring processes) of atoms which undergo permanent displacements, which shall be designated ξ_i, where i denotes the atoms involved. For any particular mechanism the three principal diffusion constants, D_j, where j numbers the principal axes, are in the following proportion:

$$(3) \qquad D_j \sim \sum_i \xi_i^2 \cos^2 \gamma_{ij}$$

where γ_{ij} is the angle between the displacement of the ith atom and the jth principal axis. For the particular case of a symmetry axis, corresponding to equation (2) one has

*Received March 20, 1953.
†Physics Department, Rensselaer Polytechnic Institute, Troy, New York, U.S.A.

$$
\begin{aligned}
D_\parallel &\sim \sum_i \xi_i^2 \cos^2 \theta_i\,, \\
D_\perp &\sim \tfrac{1}{2} \sum_i \xi_i^2 \sin^2 \theta_i\,,
\end{aligned}
\tag{4}
$$

where θ_i is the angle ξ_i makes with the symmetry axis and the factor $\frac{1}{2}$ in the second equation is the average value of $\sin^2 \phi_i$, where ϕ_i is the azimuthal angle for ξ_i.

For the particular application of these ideas to a hexagonal lattice such as zinc, one depends first on picking a sufficiently comprehensive catalogue of possible mechanisms. Five are listed in Table I below:

TABLE I

RATIO OF $D_\perp/D_\parallel$

	hcp	$c/a = 1.86$
1 Ring 4	1	0.78
2 Interstitial	1	.78
3 Vacancy (non-basal)	0.25	.19
4 Vacancy (basal)	∞	∞
5 Ring 3 (basal)	∞	∞
6 Ring 3 (non-basal)	.625	.49

1. Ring [1] of four, composed of two atoms from each of two adjacent basal planes arranged in a rectangle. (For a hexagonal close-packed lattice the atoms would form a square.)

2. Interstitial mechanism. The interstitial atom is assumed to sit in a position displaced by a vector $\sqrt{3}\,a/3,\ 0,\ c/4$ from a regular atom site. Diffusion would take place most probably by a process wherein the interstitial atom replaces the atom at the regular site and this atom in turn moves to a new interstitial site at $-\sqrt{3}\,a/6,\ a/2,\ -c/4$.

3. Vacancy diffusion (non-basal). A vacancy in the lattice is filled by a nearest-neighbour atom coming from an adjacent basal plane.

4. Vacancy diffusion (basal). The vacancy is filled by an atom from the same basal plane.

5. Ring of three (basal). The atoms concerned form an equilateral triangle in the basal plane.

6. Ring of three (non-basal), composed of two atoms in one basal plane and one in an adjoining plane in what would be an equilateral triangle for a hexagonal close-packed lattice.

The first column of Table I gives the ratio of $D_\perp/D_\parallel$ for a hexagonal close-packed lattice, the second column the same ratio for $c/a = 1.86$ corresponding to zinc. The ratios of diffusivities are calculated from equations (4), as for example for the interstitial mechanism 2, $D_\perp/D_\parallel = \frac{1}{2}\,(\sqrt{3}\,a/3)^2/(c/4)^2$ which reduces to unity for $c/a = (8/3)^{\frac{1}{2}}$.

It is apparent that mechanisms 1 and 2 give isotropic diffusion for hexagonal, close-packed crystals. Reference will be made to Table I in evaluating our experimental results in Section IV.

II. Experimental Procedure

The diffusion data was obtained by a standard tracer-sectioning technique. Single crystals of zinc were grown from 99.999 per cent pure zinc, as obtained from the New Jersey Zinc Company. The zinc was sealed at reduced pressure in aquadag-coated pyrex tubes, and lowered through a temperature gradient. The resulting single crystals were cylinders about 4 in. long and $\frac{3}{8}$ in. in diameter. The crystal orientation of the cylinders were determined by cleaving the tip at liquid nitrogen temperature. Those with basal planes within 10° of being either parallel or perpendicular to the specimen axis were retained and usually oriented more precisely by X-rays at a later time.

The suitable crystals were then mounted in wax and carefully cut with a fine jeweler's saw into approximately one inch lengths. These small cylinders were remounted in wax and faced square in a lathe. The lathe smear was next removed by etching. After a pre-anneal the specimens were checked for recrystallization, but the rejection rate was low. The crystals were then electropolished and plated with radioactive zinc.

The following plating solution was found by trial to be the most satisfactory for this purpose:

0.1 gm. $AlCl_3$
0.375 gm. Na_2SO_4
5 cc. H_2O
3 cc. active Zn^{65} solution

The active Zn^{65} solution consisted of 2.2 gm. of Zn^{65} dissolved in 11 ml. of 6 N H_2SO_4 and diluted with water to a total of 15 ml. of solution. A rotary cathode (200 rpm) and a reverse plating cycle were employed. The anode was a pure zinc disc $\frac{3}{8}$ inch in diameter. The overall plating efficiency was low (about 6 per cent). The thickness of the plating was estimated from activity measurements to run about 10^{-4} cm.

The specimens were allowed to diffuse at temperatures ranging from 410°C down to 240°C. with the corresponding diffusion time varying from overnight to several weeks. During the diffusion anneal the specimens were sealed off in small pyrex capsules at reduced pressure. Evaporization and condensation

of the active zinc does not seem to have been a problem as indicated by the following evidence. The fragments of the pyrex capsule never gave any evidence of radioactivity. The activity of the lateral surface of the specimen decreased with distance from the plated surface and did not appear stronger than would be expected from surface diffusion. Lastly, the concentration of the radioactive isotope was found to be higher at the surface than would be expected from the solution of the thin film diffusion problem. The effect of evaporation would be to lower this part of the curve.

After the diffusion period, 20 mils were removed from the cylindrical surface of the crystal to eliminate possible effects of surface diffusion. Sections of approximately 2 mils thickness were then turned off and the chips from each section were carefully collected and weighed to determine the thickness more precisely. They were then dissolved in 50 per cent HCl and sealed in glass tubes to facilitate the determination of their activity, which was done with an automatic G. M. counter [2].

III. Results

The solution of the diffusion equation

$$\frac{\partial c}{\partial t} = D\,\frac{\partial^2 c}{\partial x^2} \tag{5}$$

for the thin film boundary conditions with no appreciable blocking or evaporation from the surface, is

$$c(x, t) = C_0\,(Dt)^{-\frac{1}{2}} \exp\,(-\,x^2/4Dt) \tag{6}$$

where C_0 is the total activity deposited on surface; x, penetration distance into the crystal; t, time for diffusion anneal; D, diffusion coefficient; c, concentration of Zn^{65}. If ln c is plotted against $(\bar{x})^2$, which represents the square of the average penetration distance, and a straight line is drawn through the resulting points, the line intercept is ln $(C_0(Dt)^{-\frac{1}{2}})$ while the slope gives $(-\,4Dt)^{-1}$. The diffusion coefficient is readily calculated from the individual slope for each temperature run.

Sample data for perpendicular and parallel diffusion are shown in Figures 1 and 2 respectively. From the figures it can be seen that the first point lies well above the straight line through the data. This is probably due to departure from the thin film condition, though the possibility of blocking at the surface has not been ruled out.

The measured values for the self-diffusion for the

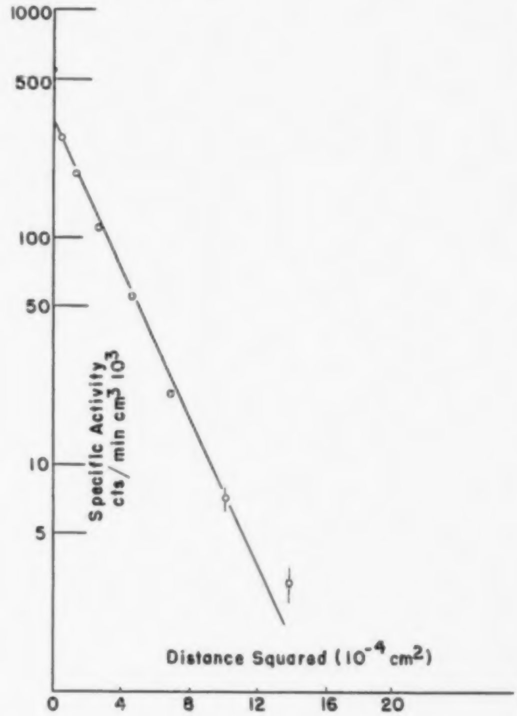

FIGURE 1. Perpendicular diffusion: $T = 268°C$, $t = 169$ hours, crystal no. 24.

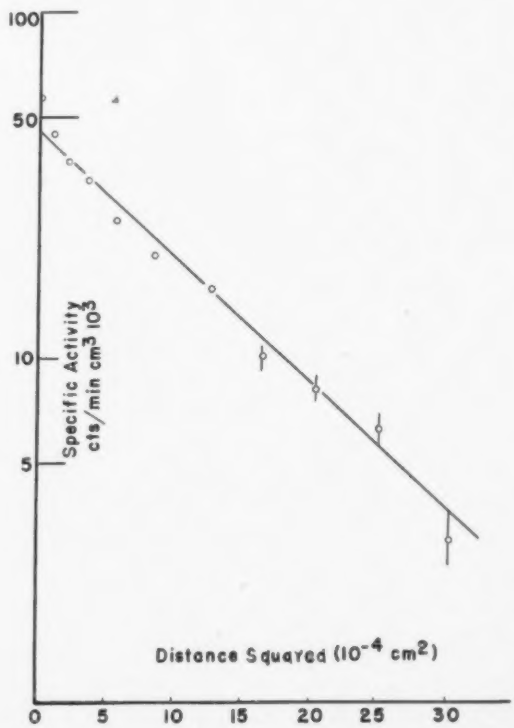

FIGURE 2. Parallel diffusion: $T = 374°C$, $t = 17$ hours, crystal no. 10.

two crystallographic orientations in the temperature range from 240°C to 410°C are shown in Table II.

TABLE II

Crystal no.	D (cm²/sec)	$1/T$ (°K)$^{-1}$	Crystal orientation	Probable error (%)
10	5.015×10^{-9}	1.538×10^{-3}	*	12.3
13	2.815	1.553	88°	16.5
14	1.540	1.624	89	16.7
15	1.783	1.642	*	9.2
16	11.92	1.464	*	11.5
17	11.95	1.466	*	7.0
18	9.20	1.465	84	6.5
19	5.95	1.504	89	3.2
20	.3695	1.724	84½	8.1
21	.668	1.658	84	7.9
22	1.407	1.627	86	5.0
23	2.180	1.585	87	3.4
24	.106	1.8484	88	3.0
25	.1743	1.8484	*	3.8
26	1.192	1.641	86	7.4
27	4.20	1.546	86	9.0
28	.561	1.675	85	10.0
29	.0584	1.949	*	3.0
30	.0266	1.949	87	2.5
31	6.75	1.478	89	1.2
32	8.27	1.478	89	1.3

*All of the crystals used in the parallel runs were under 10°.

The probable error involved in the individual diffusion coefficient measurements (see Table II) arises from many sources and is discussed below.

Error in weighing of sections was not more than 1 per cent. The time of diffusion measurement varied from 1 per cent for the latter runs to about 5 per cent for the earlier runs. (This uncertainty in the early runs has been greatly reduced by a furnace redesign which brought about a reduction of time for attaining equilibrium.) The counting error varied considerably depending on the activity plated on each sample and also on the counting time. With a 1 hr. counting time and an initial activity of about 10,000 c/min. on the sample surface, the counting error was about 2 per cent. The finite thickness of the lathe sections and their misalignment from the perpendicular to the diffusion direction have been estimated to cause an error of 1.5 per cent. (A treatment of these considerations is given in the appendix, since it does not appear to be readily available elsewhere.)

The diffusivities of zinc as given in Table II are based on the room temperature lattice dimensions. The correction to take into account the lattice expansion at higher temperature affects mainly $D_{\parallel}$. The corresponding D_0 is increased by about 2 per cent and the value of Q is increased by (0.004) kcal/mol. These changes are less than observed experimental uncertainty. Also of the same order of magnitude are the corrections arising from the fact that the actual diffusion directions are never exactly parallel or perpendicular to the specimen axis.

If we assume that the diffusion coefficient obeys the exponential relation,

$$D = D_0 e^{-Q/RT} \tag{7}$$

we can plot ln D vs $1/T$. The best straight line drawn through this plot gives a slope which is the activation energy (Q) and an intercept which is the logarithm of the frequency factor (D_0). The data are plotted in Figure 3 for the two diffusion directions. The data were fitted with a least square fit and gave the following values for Q and D_0:

Parallel	*Perpendicular*
$Q = 21.8$ kcal/mol	$Q = 24.3 \pm 0.5$ kcal/mol
$D_0 = 0.1_3$ cm²/sec.	$D_0 = 0.5_8$ cm²/sec.

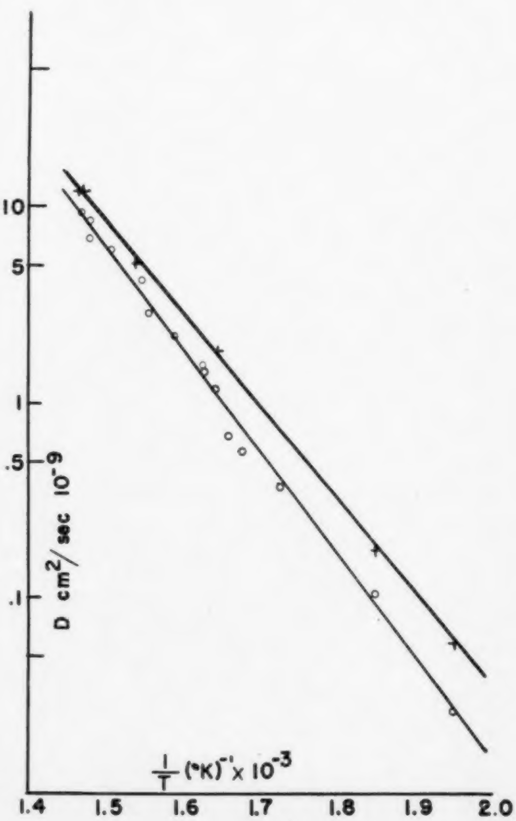

FIGURE 3. Log D vs. $1/T$: +, $D_{\parallel}$; ○, $D_{\perp}$.

IV. Conclusions

The values for diffusivity both parallel and perpendicular to the hexagonal axis lie along straight lines over $2\frac{1}{2}$ decades when plotted on semi-log paper against the reciprocal of the absolute temperature. For the parallel diffusion the fit is very good, fortuitously so perhaps, in view of the calculated probable error. On the other hand, while there is no apparent trend to the deviations for the diffusion perpendicular to the hexagonal axis, the random scatter is somewhat greater than would be expected. We are tempted to speculate that this may be a real effect and that submicroscopic cracks, or mosaic structures, may make diffusion in the basal plane less reproducible than in the direction parallel to the axis. There appears, however, no evidence that this effect is relatively more pronounced at lower temperatures.

An earlier investigation of self-diffusion in zinc was carried out by Miller and Banks [3] about ten years ago. With them our values for Q and D_0 in parallel diffusion are in good agreement but for $D_\perp$ our value of Q is lower by 25 per cent with corresponding changes in D_0. This discrepancy is not too surprising since Miller and Banks had only one single-crystal specimen with figure axis at an angle greater than 45° with the hexagonal axis and they relied largely on polycrystalline units to give information on perpendicular diffusion. While some experiments in our laboratory indicate that grain boundary diffusion should not be important in the temperature range at which Miller and Banks worked, we have found that preferred orientations and grain growth are extremely difficult to eliminate in polycrystalline experiments. It is of interest to point out that in our data the two values of D_0 are within a factor of five of each other and both are of the order of a few tenths cm^2/sec which agrees with recent findings in other diffusion investigations [4] and theoretical concepts [5] on the calculation of the entropy of activation.

When one comes to apply the considerations discussed in the introduction to a determination of what mechanisms may be operative in bulk self-diffusion of zinc, it is apparent that, since the two experimental lines have a difference in slope outside the experimental error, there must be at least two mechanisms involved. In order to explain the fact fact that $D_\parallel$ is of the order of twice $D_\perp$ in the lower temperature range of the measurements, the non-basal mechanism 3 (see Table I) must play a role. (Mechanism 6 is inadequate at the higher temperature.) One can indeed go further if one is willing to make the following assumptions: only two mechanisms make appreciable contributions to the diffusion in this range; the list of mechanisms given in the introduction is sufficiently inclusive; and the data can be relied upon within the quoted experimental error. Upon these assumptions it can be deduced that either of the basal mechanisms 4 or 5 cooperate with 3 in giving the observed behavior of the diffusivity.

The general line of argument by elimination can be illustrated from the following treatment of the possibility that mechanisms 3 plus 1 or 2 are predominate. It would follow then that the diffusivities can be expressed as:

$$\begin{aligned} D_\parallel &= A_3 e^{-Q_3/RT} + A_1 e^{-Q_1/RT} \\ D_\perp &= 0.19\, A_3 e^{-Q_3/RT} + 0.78\, A_1 e^{-Q_1/RT} \end{aligned} \tag{8}$$

where subscripts 1 and 3 refer to the contributions of mechanisms 1 and 3 respectively to $D_\parallel$. Solving one obtains

$$\begin{aligned} A_1 e^{-Q_1/RT} &= (D_\perp - 0.19 D_\parallel)/0.59, \\ A_3 e^{-Q_3/RT} &= (0.78 D_\parallel - D_\perp)/0.59. \end{aligned} \tag{9}$$

The substitution of experimental data in the right-hand sides of these equations gives a reasonable set of values for A_1 and Q_1 but values for $(0.78 D_\parallel - D_\perp)$ turn out to be negative at the high end of our temperature range which indicates that this assumed combination of mechanisms will not explain the data. It should be pointed out, however, that an error of 10 per cent in the ratio of $D_\parallel/D_\perp$ at high temperatures would be sufficient to vitiate the argument. The value of $D_\parallel$ at $t = 410$°C has been measured twice with excellent agreement. Three values of $D_\perp$ have also been measured in this temperature region and lie quite satisfactorily on the plot as as shown in Figure 3. This leads one to believe that an error of 10 per cent in the ratio of $D_\parallel/D_\perp$ at the high temperature end is unlikely, and consequently a combination of mechanism 3 with either 1 or 2 can not explain the data.

In general, similar analyses can be used to disprove other pairs of mechanisms more decisively. If one is willing to postulate three or more mechanisms contributing appreciably, then the problem is insufficiently determined to eliminate these more complex possibilities. The previous arguments, however, suggest strongly that two mechanisms only are operative and that they are quite likely both of the vacancy type.

This particular combination can be analyzed by equations analogous to (8) and (9).

$$D_{\parallel} = A_3\, e^{-Q_3/RT}$$
$$D_{\perp} = 0.19\, A_3\, e^{-Q_3/RT} + A_b\, e^{-Q_b/RT} \tag{10}$$

where A_b and Q_b refer to a purely basal mechanism such as 4 or 5. Solving one obtains

$$A_b\, e^{-Q_b/RT} = D_{\perp} - .19\, D_{\parallel}.$$

The best fit to the experimental data for A_b and Q_b gives $Q_b = 24.9$ kcal/mol and $A_b = 0.7$ cm^2/sec. with a marked scatter at the lower temperatures.

It is apparent from equation (10) that the combination of mechanisms 3 plus either 4 or 5, will never permit $D_{\perp} < 0.19 D_{\parallel}$. Presumably, if the data could be extended to sufficiently low temperatures, the line for $\ln D_{\perp}$ vs $1/T$ would swing parallel to $\ln D_{\parallel}$ and lie lower by a displacement of approximately ln 5. Our data does not extend into the region where this change should be readily apparent.

We wish to express our thanks to Dr. Herbert Clark for his very valuable assistance in handling the radioactive zinc and in preparing the electrolytic plating bath.

This work was supported by an AEC Contract.

APPENDIX A

Derivation of Formula for Error Resulting from Finite Thickness of Slice and Misalignment

Assume that the sections cut on the lathe have a thickness d and that the surfaces of the cuts make a small angle α with the planes of equal radioactive intensity. If the concentration of such activity is represented by $c(x, t)$, then the average concentration in a section with mid-point x, is given by

$$\overline{c(x,t)} = \frac{1}{d}\int c(x,t)\, f(x)\, dx, \tag{A1}$$

where the form of $f(x)$ depends on d, α, and the shape of the specimen. For a specimen of rectangular cross section and misaligned in only one direction, one has for $f(x)$:

$$\begin{aligned} &f(x) = \tfrac{1}{2}(1 + (2(x - x_1) + d)/s) \\ &\qquad \text{for } -\tfrac{1}{2}(d + s) < x - x_1 < -\tfrac{1}{2}(d - s) \\ \text{(A2)}\quad &f(x) = 1 \\ &\qquad \text{for } -\tfrac{1}{2}(d - s) < x - x_1 < \tfrac{1}{2}(d - s) \\ &f(x) = \tfrac{1}{2}(1 - (2(x - x_1) - d)/s) \\ &\qquad \text{for } \tfrac{1}{2}(d - s) < x - x_1 < \tfrac{1}{2}(d + s), \end{aligned}$$

where s is the misalignment distance, i.e. α times the specimen width.

One expands $c(x, t)$ in a power series about x_1,

$$c(x,t) = c(x_1,t) + (x - x_1)\left[\frac{\partial c(x,t)}{\partial x}\right]_{x_1} + \tfrac{1}{2}(x - x_1)^2\left[\frac{\partial^2 c(x,t)}{\partial t^2}\right]_{x_1} \tag{A3}$$

Since $f(x)$ is an even function with respect to $(x - x_1)$, the linear term makes no contribution to (A1). One obtains

$$\text{(A4)}\quad \overline{c(x,t)} = c(x_1,t) + d^{-1}\int_0^{\frac{1}{2}(d+s)} f(x + x_1)\, x^2\, dx\left[\frac{\partial^2 c(x,t)}{\partial x^2}\right]_{x_1}$$

where

$$d^{-1}\int_0^{\frac{1}{2}(d-s)} x^2\, dx = (3d)^{-1}\left(\frac{d+s}{2}\right)^3 \tag{A5}$$

and

$$(2d)^{-1}\int_{\frac{1}{2}(d-s)}^{\frac{1}{2}(d+s)} (1 - (2x - d)/s)x^2 dx = \frac{3d^2 s + s^3 - 2sd^2}{24d} \tag{A6}$$

On substitution and simplifying

$$\overline{c(x,t)} = c(x_1,t) + \frac{d^2 + s^2}{24}\left[\frac{\partial^2 c(x,t)}{\partial x^2}\right]_{x_1} \tag{A7}$$

If one takes the form of $c(x)$ to be $Ke^{-(x/\rho)^2}$ where $\rho = 2(Dt)^{\frac{1}{2}}$, the diffusion distance, it follows that

$$-\frac{d \ln \overline{c(x,t)}}{d(x^2)} \sim \rho^{-2}\left[1 - \frac{d^2 + s^2}{6\rho^2}\right], \tag{A8}$$

to terms in first order in $(d/\rho)^2$ and $(s/\rho)^2$. This shows clearly how the errors from misalignment and thickness of section tend to make experimentally measured diffusivities too large by quantities proportional to the squares of these errors. It is of interest to observe that these results are approximately independent of x_1.

A similar calculation has been carried out for a specimen of circular cross section with the result

$$-\frac{d \ln \overline{c(x,t)}}{d(x^2)} \sim \rho^{-2}\left[1 - \frac{d^2 + 3s^2/4}{6\rho^2}\right]$$

References

1. For detailed discussion of ring mechanisms in diffusion of face-centered cubic metals see ZENER, C. Acta Cryst., **3** (1950) 346.
2. SHIRN, G. A. and WAJDA, E. S. Nucleonics, **10** (1952) 30.
3. MILLER, P. H. and BANKS, F. L. Phys. Rev., **61** (1942) 648.
4. See for example WERT, C. A. J. Appl. Phys., **21** (1950) 1196; or SLIFKIN, L., LAZARUS, D., and TOMIZUKA, T. Phys. Rev., **86** (1952) 656.
5. WERT, C. and ZENER, C. Phys. Rev., **76** (1949) 1169; ZENER, C. J. Appl. Phys., **22** (1951) 372.

DIE AUFSPALTUNG VON VERSETZUNGEN IN METALLEN DICHTESTER KUGELPACKUNG*

A. SEEGER† und G. SCHÖCK‡

Die vorliegende Arbeit behandelt zwei Probleme aus der Theorie der Versetzungen: (1) die elastischen Eigenschaften von geraden Versetzungslinien in Kristallen beliebiger Symmetrie; (2) die Aufspaltung in Halbversetzungen in dichtest gepackten Gleitebenen.

Es ergibt sich, dass die übliche Zerlegung in "reine" Stufen und Schraubenversetzungen dann und nur dann möglich ist, wenn die Richtung der Versetzungslinie geradzählige Symmetrieachse ist. Eine andere Vereinfachung gegenüber dem allgemeinsten Fall tritt dann ein, wenn die Versetzungslinie in eine Spiegelebene (nicht Drehspiegelebene) fällt. Die Aufspaltung in Halbversetzungen wird mit Hilfe des Begriffs der spezifischen Stapelfehlerenergie und unter voller Berücksichtigung der Anisotropie mit dem von Leibfried und Dietze zuerst verwendeten Variationsverfahren für Stufen- und Schraubenversetzungen durchgeführt. Numerische Resultate werden für Cu, Al, Co, angegeben. Die Ergebnisse weichen zum Teil stark von denjenigen ab, bei denen nur Stapelfehlerenergie und isotrope Elastizitätstheorie berücksichtigt werden.

THE SPLITTING OF DISLOCATIONS IN METALS WITH CLOSE-PACKED LATTICES

The present paper deals with two problems in the theory of dislocations: (1) the elastic properties of straight dislocation lines in crystals of arbitrary symmetry; (2) the splitting of half-dislocations in closest-packed lattice planes.

It turns out that the usual splitting into pure edge dislocations and pure screw dislocations is only possible if the direction of the dislocation line is an even symmetry axis. Another simplification with respect to the most general case occurs when the dislocation line is situated in a reflection plane (but not rotation-reflection plane). The splitting of the half dislocations is treated for both edge and screw dislocations by means of the variation method first used by Leibfried and Dietze, using the concept of a specific stacking fault energy and taking the anisotropy fully into account. Numerical results are given for Cu, Al, Co. Some of the results deviate considerably from those based on the stacking fault energy and isotropic elasticity.

LA DIVISION DE DISLOCATIONS DANS LES MÉTAUX À RÉSEAU COMPACT

Le présent article traite de deux problèmes dans la théorie des dislocations : (1) les propriétés élastiques de lignes droites de dislocations dans des cristaux à symétrie arbitraire; (2) la division des demi-dislocations dans les plans de la plus grande densité atomique.

Il apparaît que la division habituelle en pures dislocations-coin et pures dislocations-vis n'est possible que quand la ligne des dislocations est un axe de symétrie pair. Une autre simplification par rapport au cas le plus général se présente quand la ligne des dislocations est située dans un plan de réflexion (mais pas un plan de rotation-réflexion). La division des demi-dislocations est traitée pour les cas des dislocations-coin et des dislocations-vis au moyen de la méthode des variations, dont Leibfried et Dietze se sont servi pour la première fois, employant le concept d'une énergie spécifique des défauts d'empilage et tenant compte de l'anisotropie. Des résultats numériques sont donnés pour le Cu, Al, Co. Certains de ces résultats diffèrent considérablement de ceux qui sont basés sur l'énergie des défauts d'empilage et l'élasticité isotrope.

1. Einleitung

Versetzungen in Kristallen verschiedener Struktur haben im allgemeinen verschiedene Eigenschaften. Die Verschiedenheit beruht zum Teil auf der Anisotropie der Kristalle und zum Teil auf den Potentialverhältnissen in der jeweiligen Gleitebene. Mit der anisotropen Elastizitätstheorie der Versetzungen haben sich Burgers [1] und Eshelby [2] befasst. Da Burgers den Fall einer beliebig verlaufenden Versetzungslinie in kubischen Kristallen im Auge hat, muss er sich auf ein Näherungsverfahren beschränken. Eshelby behandelt nur gerade Versetzungslinien von Stufenversetzungen und findet streng gültige Resultate, doch macht er über die Symmetrieelemente Annahmen, die gerade die Behandlung des praktisch wichtigen Falles, nämlich der Gleitebene {111} in kubisch-flächenzentrierten Kristallen ausschliessen. Wir besprechen in Abschnitt 2 eine Methode, die auch diesen Fall zu behandeln gestattet.

Die Potentialverhältnisse in der Gleitebene sind massgebend für die Frage, ob und wie stark sich vollständige Versetzungen (damit sind solche gemeint, deren Burgersvektor Gittervektoren im Bravaisgitter des betreffenden Kristalls sind) in die zuerst von Heidenreich und Shockley [3] betrachteten unvollständigen Versetzungen oder Halbversetzungen aufspalten können. Diese Aufspaltungsmöglichkeiten sind nach heutiger Ansicht wesentlich für das plastische Verhalten der Metallkristalle, ausserdem kommt ihnen vermutlich eine gewisse Bedeutung für Zwillingsbildung [4] und allotrope Umwandlungen [5] zu.

*Received April 23, 1953.

†Institut für theoretische und angewandte Physik der Technischen Hochschule Stuttgart.
‡Max-Planck-Institut für Metallforschung Stuttgart.

Leibfried und Dietze [6] haben geeignete Ansätze für die theoretische Behandlung dieser Aufspaltung in der {111}-Ebene des kubisch-flächenzentrierten Gitters bzw. in der hexagonalen Basisebene angegeben, aber wegen mathematischer Schwierigkeiten nicht vollständig durchgeführt. Wir werden in Abschnitt 3 zeigen, wie man alle wesentlichen Züge des Problems, einschliesslich der Anisotropie, berücksichtigen und dennoch zu auswertbaren Formeln kommen kann. In Abschnitt 4 werden praktische Beispiele diskutiert.

2. Verallgemeinerte ebene Verzerrungszustände in anisotropen Medien

Das Spannungs-u. Verschiebungsfeld einer geraden Versetzungslinie lässt sich aus einem sog. verallgemeinerten ebenen Verzerrungszustand ableiten. Wir denken uns dabei ein kartesisches Koordinaten system x, y, z so eingeführt, dass Spannungen und Verschiebungen von der z-Koordinate unabhängig werden. Die Versetzungslinie ist dann parallel zur z-Achse. Man kann die Gleichgewichtsbedingungen für die Spannungen mit Hilfe von zwei Funktionen $F(x, y)$ und $\phi\ (x, y)$ befriedigen. Im isotropen Falle geht F in die Airysche Spannungsfunktion, ϕ in die bei der Torsion prismatischer Stäbe benützte Schubspannungsfunktion über [7]. Aus diesen beiden Funktionen leiten sich die Komponenten des Spannungstensors folgendermassen ab:

$$(1)\qquad \sigma_{xx} = \frac{\partial^2 F(x, y)}{\partial y^2}, \quad \sigma_{xy} = -\frac{\partial^2 F(x, y)}{\partial x \partial y}, \quad \sigma_{yy} = \frac{\partial^2 F(x, y)}{\partial x^2}$$

$$(2)\qquad \sigma_{yz} = -\frac{\partial \phi}{\partial x}, \quad \sigma_{xz} = \frac{\partial \phi}{\partial y}$$

Die Funktionen F und ϕ haben dem folgenden System partieller Differentialgleichungen zu genügen [8], das aus den nicht identisch befriedigten Kompatibilitätsbedingungen hervorgeht:

$$(3a)\qquad S_{22}F_{xxxx} + S_{11}F_{yyyy} + (2S_{12} + S_{66})\, F_{xxyy} - 2S_{26}F_{xxxy} - 2S_{16}F_{xyyy} - S_{24}\phi_{xxx} + S_{15}\, \phi_{yyy} + (S_{25} + S_{46})\phi_{xxy} - (S_{14} + S_{56})\phi_{xyy} = 0$$

$$(3b)\qquad S_{24}F_{xxx} - S_{15}F_{yyy} - (S_{25} + S_{46})\, F_{xxy} + (S_{14} + S_{56})\, F_{yyx} - S_{44}\phi_{xx} - S_{55}\phi_{yy} + 2S_{45}\ \phi_{xy} = \text{const.}$$

Die S_{hi} hängen mit den elastischen Koeffizienten s_{ki} durch die Gleichungen

$$(4)\qquad S_{hi} = s_{hi}\, s_{33} - s_{h3}\, s_{i3}$$

zusammen. Für die elastischen Koeffizienten wurde, um in Übereinstimmung mit Boas und Mackenzie [9], Voigt [10] und Maehli [11] zu bleiben, die folgende Definition gewählt

$$(5a)\qquad \begin{pmatrix} e_{xx} \\ e_{yy} \\ e_{zz} \\ e_{yz} \\ e_{zx} \\ e_{xy} \end{pmatrix} = (s_{ik}) \begin{pmatrix} \sigma_{xx} \\ \sigma_{yy} \\ \sigma_{zz} \\ \sigma_{yz} \\ \sigma_{zx} \\ \sigma_{xy} \end{pmatrix}$$

$$(5b)\qquad \begin{aligned} e_{xx} &= \epsilon_{xx} &&= \frac{\partial u}{\partial x} \\ e_{yy} &= \epsilon_{yy} &&= \frac{\partial v}{\partial y} \\ e_{zz} &= \epsilon_{zz} &&= \frac{\partial w}{\partial z} \\ e_{yz} &= 2\,.\,\epsilon_{yz} &&= \frac{\partial v}{\partial z} + \frac{\partial w}{\partial y} \\ e_{zx} &= 2\,.\,\epsilon_{zx} &&= \frac{\partial w}{\partial x} + \frac{\partial u}{\partial z} \\ e_{xy} &= 2\,.\,\epsilon_{xy} &&= \frac{\partial u}{\partial y} + \frac{\partial w}{\partial x} \end{aligned}$$

Die Tensorkomponenten des Verzerrungstensors sind die ϵ_{ik}.

Die Konstante auf der rechten Seite von Gl. (3b) ist nur dann von Null verschieden, wenn an dem betreffenden elastischen Körper Torsionsmomente angreifen. Bei den hier interessierenden Problemen von Versetzungen in Kristallen muss sie Null gesetzt werden.

Für die späteren Anwendungen benötigen wir diejenigen Lösungen, die Einzelkräften in x oder z-Richtung entsprechen, welche am Halbraum $y > 0$ an der Stelle $x = 0$, $y = 0$, $z = 0$ angreifen.

Sucht man die Gl. (3) mit dem Ansatz

$$(6a)\qquad F = A(\alpha)\ \exp\ (i\alpha x + i\alpha\kappa y)$$

$$(6b)\qquad \phi = i\alpha B(\alpha) \exp\ (i\alpha x + i\alpha\kappa y)$$

zu lösen, so bekommt man als Lösbarkeitsbedingung für die Gl. (3a) und (3b) eine Gleichung 6. Grades für κ. Es gibt im wesentlichen zwei durch die Kristallsymmetrie bedingte Möglichkeiten für deren Reduktion auf einen geringeren Grad:

1. Gleichung (3) zerfällt in eine Gleichung 4. Grades für F allein und in eine Gleichung 2. Grades für ϕ allein.

2. Gleichungen (3) ergeben eine Gleichung 3. Grades für κ^2.

Der erste Fall tritt ein, wenn

$$S_{24} = S_{15} = S_{25} + S_{46} = S_{14} + S_{56} = 0 \tag{7}$$

ist.

Nach Voigt ist dies gerade die Bedingung dafür, dass die z-Achse in eine geradzählige (nicht jedoch dreizählige) Symmetrieachse fällt, oder, was damit gleichwertig ist, dass die z-Achse auf einer Spiegelebene (nicht auf einer Drehspiegelebene) senkrecht steht.

Für das Eintreten des 2. Falles gibt es drei verschiedene Möglichkeiten:

$$S_{45} = S_{16} = S_{26} = S_{15} = S_{25} + S_{46} = 0 \tag{8a}$$

$$S_{45} = S_{16} = S_{26} = S_{24} = S_{14} + S_{56} = 0 \tag{8b}$$

$$S_{45} = S_{16} = S_{26} = S_{15} = S_{24} = 0 \tag{8c}$$

Gl. (8a) und (8b) entsprechen den Fällen, dass die x-Achse bzw. die y-Achse zweizählige Achsen sind. Liegt die z-Achse also in einer Spiegelebene, so kann man durch eine Drehung des Koordinatensystems um die z-Achse stets erreichen, dass einer der Fälle (8a) oder (8b) eintritt. Fall (8c) entspricht ohne zusätzliche Bedingung für die S_{ik} keiner kristallographisch deutbaren Eigenschaft. Beispiele aus dem kubischen System stellen für den Fall (7) Versetzungslinien in Richtung $\langle 110\rangle$, für den Fall (8a, b) Versetzungslinien in Richtung $\langle 211\rangle$ dar.

Die Bedingung (7) für das Zerfallen von Gl. (3) in zwei getrennte Gln. für F und ϕ legt diejenigen Richtungen von geraden Versetzungslinien fest, in denen "reine" Stufenversetzungen und "reine" Schraubenversetzungen möglich sind. Unter einer "reinen" Stufenversetzung verstehen wir eine solche, bei der nicht nur der Burgersvektor, sondern alle Verschiebungen senkrecht zur Versetzungslinie sind. Entsprechend treten bei einer "reinen" Schraubenversetzung nur Verschiebungen in Richtung der Versetzungslinie auf.

Für Versetzungslinien in kubischen Kristallen mit einer $\{111\}$-Ebene als Gleitebene stellt die $\langle 110\rangle$-Richtung also die einzige Möglichkeit für das von isotropen Medien her vertraute Auftreten reiner Stufen- und Schraubenversetzungen dar. Dagegen liegen die Verhältnisse für Versetzungen mit der Basisebene des hexagonalen Systems als Gleitebene viel einfacher, da dabei die Bedingungen (7) und (8) für alle Richtungen gleichzeitig erfüllt sind, sodass sich die oben erwähnte Gl. für κ in eine in κ^2 lineare und eine in κ^2 quadratische Gleichung zerspaltet.

Für die folgende Diskussion beschränken wir uns der praktischen Bedeutung wegen auf geradlinige Versetzungen mit der kubischen $\{111\}$-Ebene oder der hexagonalen Basisebene als Gleitebene. Die Normale auf diesen Ebenen sei stets die y-Richtung. Ausserdem behandeln wir nur diejenigen Fälle, in denen eine der oben besprochenen Reduktionen eintritt.

Die elastischen Koeffizienten kubischer Kristalle werden stets in einem Koordinatensystem mit den kubischen Achsen als Koordinatenachsen angegeben [12; 13; 14]. In dieser Aufstellung I lautet das Schema der elastischen Koeffizienten $\mathbf{s}_{ik}$

$$(\mathbf{s}_{ik}) = \begin{pmatrix} \mathbf{s}_{11} & \mathbf{s}_{12} & \mathbf{s}_{12} & 0 & 0 & 0 \\ & \mathbf{s}_{11} & \mathbf{s}_{12} & 0 & 0 & 0 \\ & & \mathbf{s}_{11} & 0 & 0 & 0 \\ & & & \mathbf{s}_{44} & 0 & 0 \\ & & & & \mathbf{s}_{44} & 0 \\ & & & & & \mathbf{s}_{44} \end{pmatrix} \tag{9a}$$

Als Aufstellung I beim hexagonalen System bezeichnen wir ebenfalls die übliche [12; 13; 14], bei der die z-Achse in der hexagonalen Achse liegt. (Die Lage der x- und y-Achse ist wegen der Rotationssymmetrie der elastischen Eigenschaften um die hexagonale Achse belanglos.) Das Schema der $\mathbf{s}_{ik}$ lautet:

$$(\mathbf{s}_{ik}) = \begin{pmatrix} \mathbf{s}_{11} & \mathbf{s}_{12} & \mathbf{s}_{13} & 0 & 0 & 0 \\ & \mathbf{s}_{11} & \mathbf{s}_{13} & 0 & 0 & 0 \\ & & \mathbf{s}_{33} & 0 & 0 & 0 \\ & & & \mathbf{s}_{44} & 0 & 0 \\ & & & & \mathbf{s}_{44} & 0 \\ & & & & & 2(\mathbf{s}_{11}-\mathbf{s}_{12}) \end{pmatrix} \tag{9b}$$

Als Aufstellung II, in der die elastischen Koeffizienten mit s_{ik} bezeichnet werden, wählen wir eine solche, bei der die y-Richtung in eine $\langle 111\rangle$-Richtung bzw. in die Basisnormale fällt. Dann sind hexagonales und kubisches Gitter beides Spezialfälle des trigonalen Gitters mit der y-Achse als dreizählige Symmetrieachse. Es gibt dabei noch verschiedene Möglichkeiten, die x-, z-Achsen zu orientieren. Als (II′) bezeichnen wir diejenige, in der die z-Richtung einer $\langle 110\rangle$-Richtung im kubischen Gitter parallel ist. Die andere von uns zu benützende Orientierungsmöglichkeit (II″) geht aus (II′) durch Vertauschen von x- und z-Koordinate hervor. In diesem Falle ist die z-Richtung parallel zu $\langle 211\rangle$.

Das Schema der elastischen Koeffizienten im trigonalen System lautet in Aufstellung (II′)

$$\begin{pmatrix} s_{11} & s_{12} & s_{13} & 0 & 0 & -s_{36} \\ & s_{22} & s_{12} & 0 & 0 & 0 \\ & & s_{11} & 0 & 0 & s_{36} \\ & & & s_{44} & 2s_{36} & 0 \\ & & & & s_{55} & 0 \\ & & & & & s_{44} \end{pmatrix} \tag{10a}$$

in Aufstellung (II''):

$$
(10\text{b}) \qquad \begin{pmatrix} s_{11} & s_{12} & s_{13} & s_{14} & 0 & 0 \\ & s_{22} & s_{12} & 0 & 0 & 0 \\ & & s_{11} & -s_{14} & 0 & 0 \\ & & & s_{44} & 0 & 0 \\ & & & & s_{55} & 2s_{14} \\ & & & & & s_{44} \end{pmatrix}
$$

Im Spezialfall des kubischen Gitters gilt für das Schema (10a)

$$
(11\text{a}) \qquad \begin{aligned}
s_{11} &= \tfrac{1}{2}\mathbf{s}_{11} + \tfrac{1}{2}\mathbf{s}_{12} + \tfrac{1}{4}\mathbf{s}_{44} \\
s_{22} &= \tfrac{1}{3}\mathbf{s}_{11} + \tfrac{2}{3}\mathbf{s}_{12} + \tfrac{1}{3}\mathbf{s}_{44} \\
s_{12} &= \tfrac{1}{3}\mathbf{s}_{11} + \tfrac{2}{3}\mathbf{s}_{12} - \tfrac{1}{6}\mathbf{s}_{44} \\
s_{13} &= \tfrac{1}{6}\mathbf{s}_{11} + \tfrac{5}{6}\mathbf{s}_{12} - \tfrac{1}{12}\mathbf{s}_{44} \\
s_{44} &= \tfrac{4}{3}\mathbf{s}_{11} - \tfrac{4}{3}\mathbf{s}_{12} + \tfrac{1}{3}\mathbf{s}_{44} \\
s_{55} &= \tfrac{2}{3}\mathbf{s}_{11} - \tfrac{2}{3}\mathbf{s}_{12} + \tfrac{2}{3}\mathbf{s}_{44} \\
s_{36} &= \tfrac{\sqrt{2}}{3}\mathbf{s}_{11} - \tfrac{\sqrt{2}}{3}\mathbf{s}_{12} - \tfrac{\sqrt{2}}{6}\mathbf{s}_{44}
\end{aligned}
$$

Im Schema (10b) tritt an Stelle der letzten Gleichung für s_{36} die Gl.

$$
(11\text{b}) \qquad s_{14} = \tfrac{\sqrt{2}}{3}\mathbf{s}_{11} - \tfrac{\sqrt{3}}{3}\mathbf{s}_{12} - \tfrac{\sqrt{2}}{6}\mathbf{s}_{44}
$$

Im hexagonalen Gitter, bei dem die Fälle (II') und (II'') zusammenfallen, gilt

$$
(11\text{c}) \qquad \begin{aligned}
s_{11} &= \mathbf{s}_{11} \\
s_{12} &= \mathbf{s}_{13} \\
s_{13} &= \mathbf{s}_{12} \\
s_{22} &= \mathbf{s}_{33} \\
s_{44} &= \mathbf{s}_{44} \\
s_{55} &= 2(\mathbf{s}_{11} - \mathbf{s}_{12}) \\
s_{14} &= 0 \\
s_{36} &= 0
\end{aligned}
$$

Wir stellen nunmehr für die oben bezeichneten Spezialfälle diejenigen Lösungen auf, die Tangentialkräften der Stärke 1 entsprechen, welche am Halbraum $y > 0$ im Ursprung angreifen. Dabei bezeichnen wir als Schraubenversetzungsfall denjenigen, in der die Kraft in z-Richtung wirkt und als Stufenversetzungsfall denjenigen, in denen die Kraft in x-Richtung angreift. Für die Anwendung in Abschnitt 3 im Rahmen des Peierls'schen Modells benötigen wir dabei insbesondere die Verschiebungen $u_A(x)$ und $w_A(x)$, die durch diese Beanspruchung in der Grenzfläche $y = 0$ auftreten.

a) *Versetzungslinie in* $\langle 110 \rangle$*-Richtung* (*Aufstellung II'*)

Macht man für das Schema II' den Ansatz (6a), so ergibt sich für κ die Gleichung

$$
(12) \qquad S_{11}\,\kappa^4 - 2S_{16}\,\kappa^3 + (2S_{16} + S_{66})\,\kappa^2 - 2S_{26}\,\kappa + S_{22} = 0
$$

mit

$$
\begin{aligned}
S_{11} &= s_{11}^2 - s_{13}^2 \\
S_{16} &= -\,s_{36}(s_{11} - s_{13}) \\
(13) \qquad 2S_{12} + S_{66} &= 2s_{11}(s_{11} - s_{13}) + s_{11}s_{44} - s_{36}^2 \\
S_{26} &= -\,s_{12}\,s_{36} \\
S_{22} &= s_{11}\,s_{22} - s_{12}^2
\end{aligned}
$$

Die Wurzeln von Gl. (12) seien

$$
(14) \qquad \begin{aligned}
\kappa &= \kappa_1' \pm i\,\kappa_1'' \\
\kappa &= \kappa_2' \pm i\,\kappa_2''
\end{aligned}
$$

mit

$$
\kappa_i', \; \kappa_i'' \text{ reell}, \quad \kappa_i'' > 0.
$$

Die allgemeine, für $y > 0$ brauchbare Lösung von Gl. (3a) ist

$$
(15) \qquad F(x, y) = \int_{-\infty}^{+\infty} \{A_1(\alpha)\exp\,(i\alpha\kappa_1'y - |\alpha|\kappa_1''y) + A_2(\alpha)\exp\,(i\alpha\kappa_2'y - |\alpha|\kappa_2''\;y)\}\exp i\alpha x\,d\alpha
$$

die von uns gesuchte spezielle Lösung mit den Randbedingungen

$$
(16) \qquad \sigma_{yy} = 0, \quad \sigma_{xy} = \tau_{xy}(x) = -\,\delta(x) \qquad \text{für } y = 0
$$

ergibt sich hieraus mit

$$
(17) \qquad \begin{aligned}
A_1(\alpha) &= -\,A_2(\alpha) \\
&= \frac{1}{2\pi i\alpha}\,\frac{1}{i\alpha(\kappa_1' - \kappa_2') - |\alpha|(\kappa_1'' - \kappa_2'')}
\end{aligned}
$$

Aus der Gleichung

$$
(18) \qquad \epsilon_{zz} = \frac{1}{s_{11}}\{S_{11}F_{yy} + S_{12}F_{xx} - S_{16}F_{xy}\}
$$

erhält man unter Berücksichtigung von $\kappa_1' + \kappa_2' = S_{16}/S_{11}$

$$
(19) \qquad \begin{aligned}
u_A'(x) \equiv \epsilon_{xx}|_{y=0} &= -\,\frac{1}{\pi}\,\frac{S_{11}}{s_{11}}(\kappa_1'' + \kappa_2'')\,\frac{1}{x} \\
&\equiv -\,\frac{K_1}{\pi}\,\frac{1}{x}
\end{aligned}
$$

Für eine beliebig vorgegebene Schubspannungsverteilung $\tau_{xy}(x)$ erhält man daraus

$$(20) \qquad u_A'(x) = -\frac{K_1}{\pi}\int_{-\infty}^{+\infty}\frac{\tau_{xy}(\xi)}{x-\xi}\,d\xi$$

Im Schraubenversetzungsfall kann man statt $\phi(x, y)$ die Verschiebung $w(x, y)$ in z-Richtung einführen. Die Kompatibilitätsbedingungen sind dann sämtlich identisch erfüllt, die Gleichgewichtsbedingung

$$(21) \qquad \frac{\partial\sigma_{xz}}{\partial x} + \frac{\partial\sigma_{yz}}{\partial y} = 0$$

geht wegen

$$\epsilon_{xz} = \frac{\partial w}{\partial x}, \quad \epsilon_{yz} = \frac{\partial w}{\partial y}$$

und Gl. (10a) über in

$$(22) \qquad S_{44}\frac{\partial^2 w}{\partial x^2} - 2S_{45}\frac{\partial^2 w}{\partial x\partial y} + S_{55}\frac{\partial^2 w}{\partial y^2} = 0$$

mit

$$(23) \qquad \begin{aligned} S_{44} &= s_{11}\,s_{44} \\ S_{45} &= 2s_{11}\,s_{36} \\ S_{55} &= s_{11}\,s_{55} \end{aligned}$$

Es seien $\kappa = \kappa_3' \pm i\,\kappa_3''$ $(\kappa_3'' > 0)$ die beiden Wurzeln der Gleichung

$$(24) \qquad s_{55}\,\kappa^2 - 4s_{36}\,\kappa + s_{44} = 0$$

Die für den Halbraum $y > 0$ brauchbare allgemeine Lösung von (22) ist

$$(25) \quad w(x, y) = \int_{-\infty}^{+\infty} A(\alpha)\exp\,(i\alpha x + i\,\kappa_3'\alpha y - \kappa_3''|\alpha|y)\,d\alpha$$

Die spezielle Lösung mit der Randbedingung

$$(26) \qquad \sigma_{yz} = \tau_{yz}(x) = -\delta(x) \qquad \text{für } y = 0$$

ergibt wegen $2s_{36} = s_{55}\,\kappa_3'$

$$(27) \quad A(\alpha) = \frac{1}{2\pi|\alpha|}\,(s_{44}\,s_{55} - 4s_{36})^{\frac{1}{2}} \equiv \frac{1}{2\pi|\alpha|}K_2$$

und

$$(28) \qquad w_A'(x) = \frac{\partial w(x, 0)}{\partial x} = -\frac{1}{\pi}K_2\frac{1}{x}$$

Für eine beliebig vorgegebene Schubspannungsverteilung $\tau_{yz}(x)$ erhält man daraus

$$(29) \qquad w_A'(x) = -\frac{K_2}{\pi}\int_{-\infty}^{+\infty}\frac{\tau_{yz}(\xi)}{x-\xi}\,d\xi$$

Die beiden Konstanten

$$(30\text{a}) \qquad K_1 = \frac{s_{11}^2 - s_{13}^2}{s_{11}}\,(\kappa_1'' + \kappa_2'')$$

und

$$(30\text{b}) \qquad K_2 = \kappa_3'' = (s_{44}s_{55} - 4s_{36})^{\frac{1}{2}}$$

reduzieren sich im isotropen Medium auf

$$(31\text{a}) \qquad K_1 = \frac{1-\mu}{G}$$

$$(31\text{b}) \qquad K_2 = \frac{1}{G}$$

wobei G der Schubmodul und μ die Poissonsche Konstante ist. Im hexagonalen Kristallsystem vereinfacht sich ausserdem K_2 zu

$$(32) \qquad K_2 = \sqrt{s_{44}s_{55}}$$

b) *Versetzungslinie in* $\langle 211\rangle$*-Richtung (Aufstellung II'')*

Geht man mit den Gl. (6) in das Simultansystem (3) ein, so erhält man

$$(33\text{a}) \quad A[S_{11}\,\kappa^4 + (2S_{12} + S_{66})\,\kappa^2 + S_{22}] - B[(S_{14} + S_{56})\,\kappa^2 + S_{24}] = 0$$

$$(33\text{b}) \quad A[(S_{14} + S_{56})\,\kappa^2 + S_{24}] - B[S_{55}\,\kappa^2 + S_{44}] = 0$$

Das Verschwinden der Koeffizientendeterminante von (33) liefert für κ die Gleichung

$$(34) \quad \begin{aligned} S_{11}S_{55}\,\kappa^6 &+ [S_{11}S_{44} + S_{55}(2S_{12} + S_{66}) - (S_{14} + S_{56})^2]\,\kappa^4 + [S_{22}S_{55} \\ &+ S_{44}(2S_{12} + S_{66}) - 2S_{24}(S_{14} + S_{56})]\,\kappa^2 + S_{22}S_{44} - S_{24}^2 = 0 \end{aligned}$$

Die drei für den Halbraum $y > 0$ geeigneten Wurzeln haben die Form

$$\begin{aligned} \kappa_1 &= i\,\kappa_1'' \\ \kappa_2 &= \kappa_2' + i\,\kappa_2'' \\ \kappa_3 &= -\kappa_2' + i\,\kappa_2'' \end{aligned}$$

mit κ_i', κ_i'' reell, $\kappa_i'' > 0$. Man erhält drei zugehörige Werte für das Verhältnis A/B:

$$(35) \qquad \frac{B_i}{A_i} = \frac{(S_{14} + S_{56})\,\kappa_i^2 + S_{24}}{S_{55}\,\kappa_i^2 + S_{44}} \equiv \gamma_i$$

Als Lösung für den Halbraum $y > 0$ für Gl. (3a) und (3b) folgt:

$$(36\text{a})\quad F(x,y) = \int_{-\infty}^{+\infty} \alpha\{A_1(\alpha) \exp i\kappa_1|\alpha|y + A_2(\alpha) \exp i\kappa_2|\alpha|y + A_3(\alpha) \exp i\kappa_3|\alpha|y\} \exp i\alpha x \, d\alpha$$

$$(36\text{b})\quad \phi(x,y) = i \int_{-\infty}^{+\infty} \{\gamma_1 A_1(\alpha) \exp i\kappa_1|\alpha|y + \gamma_2 A_2(\alpha) \exp i\kappa_2|\alpha|y + \gamma_3 A_3(\alpha) \exp i\kappa_3|\alpha|y\} \exp i\alpha x \, d\alpha$$

Für die Randbedingungen

$$(37)\quad \sigma_{yy} = \sigma_{yz} = 0, \quad \sigma_{xy} = \tau_{xy} = -\delta(x) \qquad \text{für } y = 0$$

ergibt sich wie oben

$$(38)\quad u_A'(x) = -\frac{K_2}{\pi}\int_{-\infty}^{+\infty} \frac{\tau_{xy}(\xi)}{x-\xi} d\xi$$

mit

$$(39)\quad K_2 = \frac{S_{11}}{s_{11}} \frac{\gamma_1(\kappa_2^2 - \kappa_3^2) + \gamma_2(\kappa_3^2 - \kappa_1^2) + \gamma_3(\kappa_1^2 - \kappa_2^2)}{\gamma_1(\kappa_2 - \kappa_3) + \gamma_2(\kappa_3 - \kappa_1) + \gamma_3(\kappa_1 - \kappa_2)}$$

Für die Randbedingungen

$$(40)\quad \tau_{yy} = \sigma_{zy} = 0, \quad \sigma_{yz} = \tau_{yz} = -\delta(x) \qquad \text{für } y = 0$$

folgt

$$(41)\quad w_A'(x) = -\frac{K_1}{\pi}\int_{-\infty}^{+\infty} \frac{\tau_{yz}(\xi)}{x-\xi} d\xi$$

mit

$$(42)\quad K_1 = i s_{55} \frac{\gamma_1\kappa_1(\kappa_2 - \kappa_3) + \gamma_2\kappa_2(\kappa_3 - \kappa_1) + \gamma_3\kappa_3(\kappa_1 - \kappa_2)}{\gamma_1(\kappa_2 - \kappa_3) + \gamma_2(\kappa_3 - \kappa_1) + \gamma_3(\kappa_1 - \kappa_2)}$$

Im isotropen Fall gilt

$$(43\text{a})\quad K_1 = \frac{1}{g}, \qquad (43\text{b})\quad K_2 = \frac{1-\mu}{g}$$

im hexagonalen Fall

$$K_1 = \sqrt{s_{44}s_{55}}$$

Gegenüber den Gl. (31a, b) erscheinen die Definitionen von K_1 und K_2 gerade vertauscht. Die jetzige Bezeichnung ist jedoch konsequent, wenn man spätere Fallunterscheidungen vermeiden will.

3. Berücksichtigung der periodischen Struktur der Gleitebene

Bei der Behandlung der Verhältnisse in der Gleitebene beschränken wir uns sogleich auf hexagonale Basisebenen, bzw. {111}-Ebenen in flächenzentriert-kubischen Gittern. Das Gemeinsame dieser beiden Fälle ist, dass es für die Atome in einer bestimmten Netzebene zwei Arten von Gleichgewichtslagen gibt, nämlich solche, die zum hexagonalen Gitter führen, und solche, die zum kubischen Gitter gehören. Der Unterschied zwischen diesen beiden Möglichkeiten tritt jedoch erst auf, wenn man mindestens drei aufeinanderfolgende Netzebenen betrachtet und in die Rechnung einbezieht. Würde man dies tun, so würden die entstehenden Gleichungen schwerfällig und keiner strengen Behandlung zugänglich sein. Es ist deshalb zweckmässig, wie Leibfried und Dietze [15] im Rahmen des Peierls'schen Modells weiterhin zwei aufeinanderfolgende Netzebenen zu betrachten und die Grundgleichungen, als Variationsproblem formuliert, mit dem Ritz'schen Verfahren zu lösen.

Da es der Grundgedanke des Variationsverfahrens ist, die Gesamtenergie als Funktion mehrerer Parameter explizit zu berechnen und zu einem Minimum zu machen, kann man den energetischen Unterschied zwischen "kubischer" und "hexagonaler" Gleichgewichtslage hierbei sehr leicht mit Hilfe des Begriffs der spezifischen Oberflächenenergie γ eines Stapelfehlers berücksichtigen. Wenn in einem gewissen endlichen Gebiet eine {111}-Ebene die falsche Gleichgewichtslage besetzt, so ist dieses Gebiet durch Halbversetzungen vom Typus $\frac{1}{6}a < 211 >$ berandet. Man kann deshalb die Fläche F dieses fehlgeordneten Gebietes, das man einen Stapelfehler nennt, als die von der Halbversetzung eingeschlossene Fläche verhältnismässig genau definieren. Für nicht zu kleine F wird der Energieüberschuss E des Stapelfehlers proportional zur Zahl der fehlgeordneten Atome und damit proportional zu F sein:

$$E = \gamma F$$

Über die Bestimmung der spezifischen Oberflächenenergie γ werden wir unten noch einiges sagen. Hier sei der Fall besonders erwähnt, dass der Stapelfehler durch zwei gerade Versetzungslinien mit dem Abstand 2η begrenzt wird.
Die Oberflächenenergie pro Längeneinheit (von der wir in Zukunft allein sprechen werden) wird dann

$$E = 2\eta\gamma$$

Derartige Stapelfehler werden sich im allgemeinen immer bei vollständigen Versetzungen mit dichtest gepackter Netzebene als Gleitebene ausbilden. Es stellt sich hier ein Gleichgewicht ein zwischen der im wesentlichen η^{-1} proportionalen Abstossung der beiden Halbversetzungen und der

Oberflächenspannung des Stapelfehlers. Dieses Auseinanderspreizen einer Versetzungslinie in ein in einer $\{111\}$-Ebene liegendes Stapelfehlerband ist verantwortlich für den Umstand, dass auch Schraubenversetzungen im kubisch-flächenzentrierten Gitter eine definierte Gleitebene haben. Die Breite dieses Bandes bestimmt dabei die Aktivierungsenergie für cross-slip.

Wir werden als Beispiel für die qualitative Behandlung der Aufspaltung die Schrauben- und Stufenversetzungen wählen. Durchgeführt wird die Rechnung für die Schraubenversetzung, doch wurden die Bezeichnungen so gewählt, dass die Ergebnisse ab Gl. (57) für beide Fälle gelten. Mit denselben mathematischen Methoden kann man jedoch auch die Fälle behandeln, in denen der Burgersvektor mit der Richtung der Versetzungslinie einen Winkel von 30° oder von 60° bildet.

Die Gesamtenergie pro Längeneinheit im Peierls'schen Modell setzt sich aus der elastischen Energie E_{el}, aus der Wechselwirkungsenergie E_{AB} und aus der Stapelfehlerenergie $2\eta\gamma$ zusammen. Es gilt im vorliegenden Fall

$$E = E_{el} + E_{AB} + 2\eta\gamma \tag{44}$$

mit

$$E_{el} = -\int_{-\infty}^{+\infty} [\tau_{yz}(x)w_A(x) + \tau_{zy}(x)u_A(x)]\,dx \tag{45}$$

und

$$E_{AB} = \frac{G}{4\pi^2}\frac{b^2}{c}\int_{-\infty}^{+\infty}\left[\frac{3}{2} + 2\cos 4\pi\,\frac{w_A(x)}{b}\right. \tag{46}$$
$$\left.\cos 4\pi\left(\frac{u_A(x)}{h} + \frac{1}{12}\right) + \cos 8\pi\left(\frac{u_A(x)}{h} + \frac{1}{12}\right)\right]dx$$

Wegen der Ableitung der Beziehungen für E_{el} und E_{AB} sei auf die Arbeit von Leibfried und Dietze verwiesen. Die Konstanten b, h und c hängen mit der Würfellänge a im kubischen Gitter folgendermassen zusammen.

$$\begin{aligned} b &= \tfrac{1}{2}\sqrt{2}\,a \\ h &= \tfrac{1}{2}\sqrt{6}\,a \\ c &= \tfrac{1}{3}\sqrt{3}\,a \end{aligned} \tag{47}$$

Im hexagonalen Fall ist $2c$ die Gitterkonstante in Richtung der hexagonalen Achse und $b = \frac{1}{3}\sqrt{3}\,h$ die Gitterkonstante in der Basisebene.

Für den Schubmodul G hat man im hexagonalen und kubischen Fall $G = 1/s_{44}$ zu setzen. Die Nullpunkte für die Verschiebungen werden so gewählt, dass die gegenseitigen Verschiebungen der beiden in die Rechnung einbezogenen Netzebenen

$$\begin{aligned} u_{AB} &= 2u_A \\ w_{AB} &= 2w_A \end{aligned} \tag{48}$$

sind.

Aus den Gl. (20) und (29) folgt

$$\tau_{zy}(x) = \frac{1}{\pi K_1}\int_{-\infty}^{+\infty}\frac{u_A'(\xi)}{\xi - x}\,d\xi \tag{49a}$$

$$\tau_{yz}(x) = \frac{1}{\pi K_2}\int_{-\infty}^{+\infty}\frac{w_A'(\xi)}{\xi - x}\,d\xi \tag{49b}$$

Einsetzen von Gl. (49a, b) in (45) gibt

$$\begin{aligned} E_{el} = &-\frac{1}{\pi K_2}\iint_{-\infty}^{+\infty}\frac{w_A(x)\,w_A'(\xi)}{\xi - x}\,dx d\xi \\ &-\frac{1}{\pi K_1}\iint_{-\infty}^{+\infty}\frac{u_A(x)u_A'(\xi)}{\xi - x}\,dx d\xi \end{aligned} \tag{50}$$

Die Hauptschwierigkeit bei der Berechnung der Gesamtenergie durch das Ritz'sche Verfahren bietet der Anteil E_{AB}. Ein zweckmässiger Ansatz ist

(51)

$$w_A(x) = \frac{b}{4\pi}\operatorname{arc\,tg}\frac{x+\eta}{\sigma} + \frac{b}{4\pi}\operatorname{arc\,tg}\frac{x-\eta}{\sigma} + \frac{b}{4}$$

$$u_A(x) = \frac{h}{12\pi}\operatorname{arc\,tg}\frac{x+\eta}{\sigma} - \frac{h}{12\pi}\operatorname{arc\,tg}\frac{x-\eta}{\sigma}$$

Er stellt zwei Halbversetzungen im Abstand 2η dar, entspricht also dem oben geschilderten Fall. Die Versetzungslänge σ, die ebenso wie η ein freier Parameter ist, wäre eigentlich für die u-Verschiebung und die w-Verschiebung verschieden zu wählen. Die Annahme gleicher Versetzungslängen in den Gl. (51) ist jedoch für die Berechnung von E_{AB} wesentlich, da sie die Gültigkeit der einfachen Gleichung

$$\cos\frac{4\pi w_A}{b} = -\cos\frac{12\pi u_A}{h} + \frac{1}{\rho}\sin\frac{12\pi u_A}{h} \tag{52}$$

mit

$$\rho = \frac{\eta}{\sigma} \tag{53}$$

zur Folge hat. Im Anhang werden wir mit dem Ansatz (51) E_{AB} in der Form

$$E_{AB} = \frac{b^2}{4\pi^2 s_{44}}\,\frac{\sigma}{c}\,A(\rho) \tag{54}$$

berechnen.

Bei der Berechnung von E_{el} treten die Integrale

(55)

$$\int_{-\infty}^{+\infty}\int_{-\infty}^{+\infty}\frac{u_A(x)\,u_A'(\xi)}{\xi - x}\,dx d\xi = -\left(\frac{h}{12}\right)^2\ln\,(1+\rho^2)$$

und

$$(56)\quad \int_{\xi=-\infty}^{+\infty}\int_{x=-L}^{L}\frac{w_A(x)w_A'(\xi)}{\xi - x}\,dx d\xi = \left(\frac{b}{4}\right)^2\left[\ln\,(1+\rho^2) - 4\ln\frac{L}{2\sigma}\right]$$

auf. Bei dem Integral Gl. (56) hat man, um Konvergenz zu erreichen, endliche Integrationsgrenzen $\pm L$ einzusetzen.

Die Gesamtenergie lautet unter Berücksichtigung von Gl. (54, 55 und 56)

$$(57)\quad E = \frac{b^2}{4\pi}\frac{1}{K_2}\left[\ln\frac{L}{2\sigma} - \frac{3-\chi}{12}\ln\,(1+\rho^2)\right] + \frac{b^2}{4\pi^2 s_{44}}\frac{\sigma}{c}A(\rho) + 2\gamma\sigma\rho$$

mit

$$\chi = \frac{K_2}{K_1}$$

Die Bedingungsgleichungen des Ritz'schen Variationsprinzips

$$(58)\quad \left.\frac{\partial E}{\partial\sigma}\right/_{\eta=\mathrm{const}} = 0,\quad \left.\frac{\partial E}{\partial\eta}\right/_{\sigma=\mathrm{const}} = 0$$

ergeben

$$(59)\quad \frac{\sigma}{c} = \frac{s_{44}}{K_2}\,\frac{\pi}{A(\rho) - \rho A'(\rho)}\,\frac{\rho^2(\chi+3)+6}{6(\rho^2+1)}$$

und

$$(60)\quad \gamma = \frac{b^2}{8\pi^2}\frac{1}{s_{44}}\frac{1}{c} \cdot\left[\{A(\rho) - \rho A'(\rho)\}\frac{(3-\chi)\rho}{(3+\chi)\rho^2+6} - A'(\rho)\right]$$

In Abb. 2 ist $A(\rho)$, nach Gl. (A4) des Anhangs berechnet, aufgetragen. Daraus erhält man die in Abb. 3 dargestellte Abhängigkeit der Grösse ρ von der spezifischen Oberflächenenergie γ des Stapelfehlers mit χ als Parameter. Mit dem so gefundenen ρ_0 kann man aus Abb. 4 die zu den betreffenden χ gehörige Versetzungslänge σ_0 entnehmen, und dann aus Gl. (57) mit einem plausiblen Wert von L die Versetzungsenergie pro Längeneinheit berechnen.

Da sich für gewisse Werte von χ und γ der Parameter ρ nach Abb. 3 mehrdeutig ergibt, kann es bei Änderung von γ (etwa mit der Temperatur) Bereiche von η und σ geben, die übersprungen werden und sich nicht realisieren lassen.

Eine weitere bemerkenswerte Eigenschaft der Darstellung der Lösung mit Hilfe der Abb. 3 und 4 ist, dass die auftretenden Kurvenscharen die

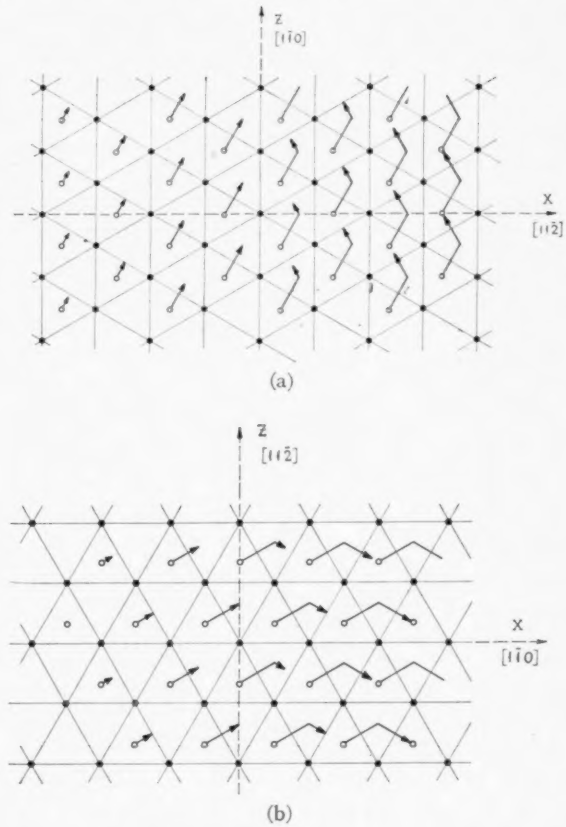

Abb. 1. Schematische Darstellung der Aufspaltung von Versetzungen in einer (111)-Ebene in Halbversetzungen. Versetzungslinie z-Achse: (a) Schraubenversetzung, (b) Stufenversetzung.

eine Grösse χ enthalten, also im anisotropen Fall dieselbe Mannigfaltigkeit wie im isotropen Fall aufweisen. Hat man ein isotropes Medium, so ist bei der Orientierung II' (Abb. 1a)

$$\chi = 1/(1-\mu)$$

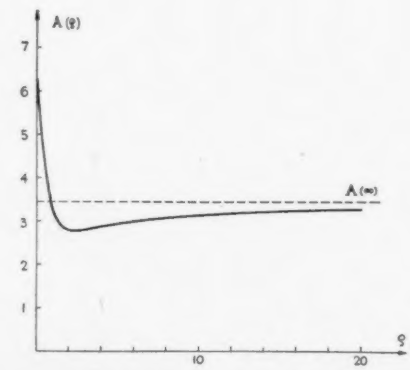

Abb. 2. $A(\rho)$ nach Gl. (A4). Die Kurve nähert sich asymptotisch $A(\infty) = 2\sqrt{3}$.

bei der Orientierung II″ (Abb. 1b)

$$\chi = 1 - \mu$$

wobei μ die Poissonsche Konstante ist.

4. Anwendungen und Beispiele

Um mit den in Abb. 3 gegebenen Formeln die Aufspaltung einer Versetzung in Halbversetzungen quantitativ behandeln zu können, benötigt man die elastischen Konstanten des betreffenden Kristalls sowie die Kenntnis der spezifischen Oberflächen-

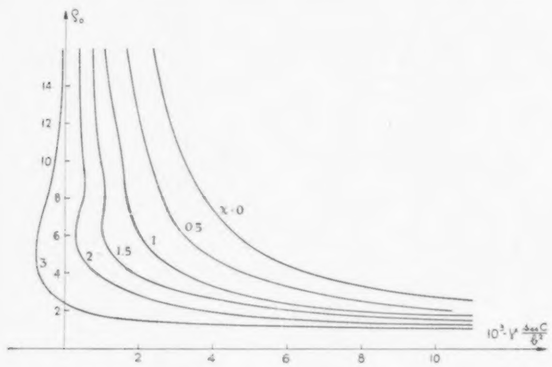

ABB. 3. Abhängigkeit der Grösse $\rho = \eta_0/\sigma_0$ von der Stapelfehlerenergie γ. Parameter für die Kurvenschar ist χ.

energie γ. Die elastischen Konstanten sind für die meisten im Zusammenhang mit der plastischen Verformung interessierenden Metalle gemessen und von Boas und Mackenzie [13] sowie von Schmid [14] zusammengestellt.

Dagegen kann γ nicht direkt gemessen werden. Für Kobalt, das bei ungefähr 420°C eine Umwandlung von hexagonal-dichtester Kugelpackung in das kubisch-flächenzentrierte Gitter aufweist, haben Heidenreich und Shockley [3] eine Umwandlungswärme von 100 cal/g atom zugrundegelegt und

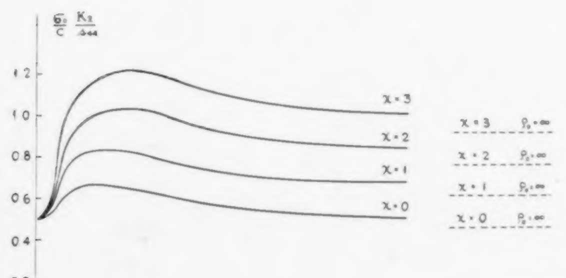

ABB. 4. Abhängigkeit der Länge σ_0 der Halbversetzungen von ρ_0. Im rechten Teil der Abbildung sind die Asymptoten für grosse ρ_0 angegeben.

daraus $\gamma = 20$ erg/cm² abgeschätzt. Nach Christian [16] ist jedoch die Umwandlungswärme nur etwa 60 cal/g atom. Wir werden für die Verhältnisse bei Zimmertemperatur den Wert $\gamma = 20$ erg/cm² benützen. Der Wert von γ ist proportional dem Unterschied der Freien Energie der beiden Modifikationen und damit temperaturabhängig. Am Umwandlungspunkt wird $\gamma = 0$, was zur Folge hat, dass sich die Halbversetzungen unter der Wirkung ihrer elastischen Abstossung auseinanderspreizen. Legt man einen geeigneten Mechanismus für die Bewegung dieser Halbversetzungen zugrunde [5], so kann damit die Umwandlung eines grösseren Gebietes in die neue Modifikation erklärt werden.

Eine andere Möglichkeit zur Abschätzung von γ ergibt sich aus der Messung über Grenzflächenenergie von Orientierungszwillingen. Ein Stapelfehler kann aufgefasst werden als Aufeinanderfolge dreier Orientierungszwillinge, von denen der mittlere nur eine einzige Netzebene umfasst. Man kann deshalb annehmen, dass γ grössenordnungsmässig doppelt so gross wie die Grenzflächenenergie zwischen Orientierungszwillingen ist. Nach der zusammenfassenden Darstellung von Fisher und Dunn [17] sowie einer Diskussionsbemerkung von Shockley hierzu, ergibt sich auf diese Weise für Cu $\gamma = 40$ erg/cm² und für Al $\gamma \approx 200$ erg/cm².

Aus der numerischen Auswertung mit Hilfe von Abb. 2 und 3 ergibt sich folgendes charakteristisches Verhalten:

1. Die Breite des Stapelfehlerbandes ist für Stufenversetzungen ($\chi < 1$ ungefähr) stets grösser als für Schraubenversetzungen ($\chi > 1$ ungefähr).

2. Für eine Stapelfehlerenergie

$$\gamma > 10^{-2} \frac{b^2}{s_{44}C} \text{ ungefähr}$$

ist die Breite des Stapelfehlerbandes von der Grössenordnung 1 bis 2 Atomabstände und nur noch sehr schwach von γ selbst abhängig. Ein Beispiel hierzu ist Aluminium. Genauere Aussagen sind jedoch nicht mehr möglich, da die Annahme gleicher Versetzungslängen für Stufen und Schraubenkomponente in diesem Gebiet keine gute Annäherung mehr ist.

3. Für ein

$$\gamma < 2 \,.\, 10^{-3} \frac{b^2}{s_{44}C} \text{ ungefähr}$$

ist die Breite des Stapelfehlerbandes sehr stark von γ abhängig und nimmt mit fallendem γ sehr rasch zu. Ausserdem besteht ein starker Einfluss der

anisotropen elastischen Eigenschaften. Die Stufenversetzung ist um eine Grössenordnung weiter aufgespalten als die Schraubenversetzung. In diesem Gebiet, für das Kobalt ein Beispiel ist, wirkt sich daher die Unsicherheit von γ besonders stark aus.

Wir haben in Tabelle I die für die Rechnung zugrunde gelegten Konstanten und in Tabelle IIa und IIb Zwischenergebnisse und die Resultate zusammengestellt.

TABELLE I

Elastische Koeffizienten (in 10^{-13} cm²/dyn), Stapelfehlerenergie γ und Atomabstand b von Cu, Al, Co

	s_{11}	s_{12}	s_{13}	s_{33}	s_{44}	γ [erg cm^{-2}]	b [Å]
Cu	14,9	−6,2	0	—	13,3	40	2,56
Al	15,9	−5,8	0	—	35,2	200	2,86
Co	$6{,}2_2$	$-2{,}7_2$	$-1{,}6_3$	$5{,}0_8$	$19{,}2_8$	20	2,51

TABELLE IIa

Numerische Werte für die Wurzeln $\kappa_n = \kappa_i' + i\kappa''$

	z-Achse in $\langle 110\rangle$ Richtung			z-Achse in $\langle 211\rangle$ Richtung		
	κ_1''	κ_2''	κ_3''	κ_1'	κ_2'	κ_2''
Cu	1,85	0,44	1,03	0,38	0,55	1,46
Al	2,09	0,47	1,03	0,7	≈0	1,2
Co	1,59	0,60	1,05	—	—	—

TABELLE IIb

Zwischenergebnisse (siehe Text), Versetzungslänge σ_0 und Abstand $2\eta_0$ der Halbversetzungen

	Versetzungslinie in Richtung	K_1 10^{-13} $\left[\frac{cm^2}{dyn}\right]$	K_2 10^{-13} $\left[\frac{cm^2}{dyn}\right]$	$\frac{s_{44}}{K_2}$	χ	ρ_0	$\frac{\sigma_0}{b}$	$\frac{2\eta_0}{b}$
Cu	$\langle 110\rangle$	13,1	23,6	1,37	1,8	2,2	1,03	5
	$\langle 211\rangle$	21,7	13,1	2,46	0,6	4,0	1,50	12
Al	$\langle 110\rangle$	30,8	39,0	1,04	1,27	≈1	≈0,5	≈1
	$\langle 211\rangle$	39,0	25,0	1,63	0,64	≈1	≈0,8	≈1,6
Co	$\langle 110\rangle$	11,0	18,6	1,04	1,69	4,3	0,8	7
	$\langle 211\rangle$	18,6	11,0	1,75	0,59	≈20	1,3	≈50

Berücksichtigt man wie Heidenreich und Shockley [3] neben γ nur die (isotrop gerechnete) Abstossung der Halbversetzungen, so ergibt sich für die Aufspaltung der Schraubenversetzung bei Kobalt $2\eta_0 = 1.10^{-6}$cm, während die genauere Rechnung in diesem Falle $2\eta_0 = 1{,}8.10^{-7}$cm ergibt.

Leibfried und Dietze haben die Vermutung geäussert, dass sich auch für $\gamma = 0$ eine stabile Gleichgewichtslage mit einem Gleichgewichtsabstand von der Grössenordnung der Versetzungslänge ergeben könnte. Dies ist nach Abb. 2 nur der Fall für $\chi > 2{,}3$. Im Falle der Aufspaltung einer Schraubenversetzung, die am ehesten die vermutete Erscheinung zeigen könnte, entspricht dies bei isotropen Medien $\mu = 0{,}57$. Während ein solches μ bei isotropen Medien nicht möglich ist, könnte χ bei stark anisotropen Metallen einen derartig grossen Wert event. annehmen. Doch haben wir bis jetzt noch kein Beispiel gefunden, bei denen die Leibfried—Dietze'sche Vermutung zutreffen würde.

Die vorstehenden Ergebnisse sollen auf die Berechnung der Aktivierungsenergie für "cross-slip" angewendet werden. Dabei werden wir auch die hier nicht gegebene explizite Darstellung der Energie als Funktion von η bringen.

Die Verfasser danken Herrn Professor U. Dehlinger für seine fördernde Unterstützung, Herrn Kröner für Diskussionen zur anisotropen Elastizitätstheorie.

ANHANG

Berechnung des Integrals

$$A(\rho) = 2\int_0^\infty \left[\frac{3}{2} + 2\cos\frac{4\pi w}{b}\cos 4\pi \cdot\left(\frac{u}{h} + \frac{1}{12}\right) + \cos 8\pi\left(\frac{u}{h} + \frac{1}{12}\right)\right] d\xi \tag{A1}$$

mit

$$w(\xi) = \frac{b}{4\pi}[\operatorname{arc\,tg}(\xi + \rho) + \operatorname{arc\,tg}(\xi - \rho) + \pi]$$

$$= \frac{b}{4\pi}\left[\operatorname{arc\,tg}\frac{2\xi}{1 + \rho^2 - \xi^2} + \pi\right]$$

$$u(\xi) = \frac{h}{12\pi}[\operatorname{arc\,tg}(\xi + \rho) - \operatorname{arc\,tg}(\xi - \rho)]$$

$$= \frac{h}{12\pi}\operatorname{arc\,tg}\frac{2\rho}{1 + \rho^2 + \xi^2}$$

Mit Gl. (52) und der neuen Integrationsvariablen

$$s = \operatorname{tg}\frac{4\pi u}{h}$$

geht (A1) über in

$$A(\rho) = \frac{6\rho}{(\rho^2 - 1)^{\frac{1}{2}}} \times \tag{A2}$$

$$\int_0^{s_0} \frac{(2 + \sqrt{3}/\rho)s^2 - (\sqrt{3} - 1/\rho)s - \sqrt{3}/\rho}{(s + 3^{\frac{1}{2}})\left[s(s^2 - 3)\left(s^3 + \frac{6\rho}{\rho^2 - 1}s^2 - 3s - \frac{2\rho}{\rho^2 - 1}\right)\right]^{\frac{1}{2}}}\, ds$$

Die Nullstellen s_i des Polynoms 6. Grades im Radikanden sind

$$\begin{aligned} s_1 &= -\operatorname{tg}(\omega + \tfrac{1}{3}\pi) \\ s_2 &= -\operatorname{tg}\tfrac{1}{3}\pi = -\sqrt{3} \\ s_3 &= -\operatorname{tg}\omega \\ s_4 &= \ \ 0 \\ s_5 &= +\operatorname{tg}\tfrac{1}{3}\pi = +\sqrt{3} \\ s_6 &= -\operatorname{tg}(\omega - \tfrac{1}{3}\pi) \end{aligned}$$

mit

$$\omega = \tfrac{2}{3}\operatorname{arc\,ctg}\rho \qquad (0 \leqslant \operatorname{arc\,ctg}\rho < \tfrac{1}{2}\pi)$$

Für $\omega \neq 0, \frac{1}{3}\pi$ ist (A2) ein hyperelliptisches Integral vom Geschlecht 2; jedoch besteht zwischen den Doppelverhältnissen der s_i die Beziehung

$$[s_1\, s_2\, s_3\, s_4] = [s_1\, s_2\, s_5\, s_6]$$

die nach Legendre [18] hinreichend ist für die Reduzierbarkeit auf elliptische Integrale.

Mit der Substitution

$$s = \frac{y\,(s_4 - s_2)\,s_1 - (s_4 - s_1)\,s_2}{(s_4 - s_2)\,y - (s_4 - s_1)}$$

lässt sich (A2) als Linearkombination folgender Integrale darstellen:

$$\int \frac{dy}{[y(y-1)(y-\alpha)(y-\beta)(y-\alpha\beta)]^{1/2}} = \frac{1}{[(1-\alpha)(1-\beta)]^{1/2}}\,\frac{1}{2}\,\frac{1}{(\alpha\beta)^{1/2}}\,[G_1 - G_2]$$

$$\int \frac{y\,dy}{[y(y-1)(y-\alpha)(y-\beta)(y-\alpha\beta)]^{1/2}} = \frac{-1}{[(1-\alpha)(1-\beta)]}\,\frac{1}{2}\,[G_1 + G_2]$$

$$\begin{aligned}\int \frac{dy}{y[y(y-1)(y-\alpha)(y-\beta)(y-\alpha\beta)]^{1/2}} &= \frac{[(1-\alpha)(1-\beta)]^{1/2}}{(\alpha\beta)^{3/2}}\,\frac{1}{2}\,[H_1 - H_2] \\ &\quad + \frac{1}{2}\,\frac{1}{\alpha\beta}\,\frac{1}{[(1-\alpha)(1-\beta)]^{1/2}} \\ &\quad \cdot\left[\left(\frac{\alpha+\beta}{(\alpha\beta)^{1/2}} + 1\right)G_1 - \left(\frac{\alpha+\beta}{(\alpha\beta)^{1/2}} - 1\right)G_2\right]\end{aligned}$$

Dabei ist

$$G_i = \int \frac{dz}{[z(1-z)(1-c_i^2 z)]^{1/2}} \qquad (i = 1, 2)$$

$$H_i = \int \frac{dz}{z[z(1-z)(1-c_i^2 z)]^{1/2}} \qquad (i = 1, 2)$$

mit

$$c_1^2 = -\frac{(\sqrt{\alpha} + \sqrt{\beta})^2}{(1-\alpha)(1-\beta)}$$

$$c_2^2 = -\frac{(\sqrt{\alpha} - \sqrt{\beta})^2}{(1-\alpha)(1-\beta)}$$

und

$$\text{(A3)} \qquad z = \frac{(1-\alpha)(1-\beta)\,y}{(y-\alpha)(y-\beta)}$$

Wenn man $s_4 = 0$ sogleich berücksichtigt, so gilt

$$\alpha = \frac{s_1(s_3 - s_2)}{s_2(s_3 - s_1)} \qquad \beta = \frac{s_1(s_5 - s_2)}{s_2(s_5 - s_1)}$$

während sich die Integrationsgrenzen nach folgendem Schema transformieren.

ξ	s	y	z
0	0	1	1
∞	s_6	$\alpha\beta$	1

Die Substitution (A3) transformiert die ursprüngliche ξ-Ebene in zwei Riemann'sche Blätter der z-Ebene. Der Integrationsweg tritt an dem einen Verzweigungspunkt $z = c_2^{-2}$ von einem Blatt in das andere über. Deshalb sind G_2 und H_2 vollständige, G_1 und H_1 unvollständige elliptische Integrale. Im einzelnen gilt in der Legendreschen Schreibweise der elliptischen Integrale

$$G_1 = -\frac{4i}{c_1}\,F(k_1, \phi)$$

$$G_2 = -\frac{4i}{c_2}\,\mathbf{K}(k_2)$$

$$H_1 = -4ic_1\,E(k_1, \phi) + 4i[k_2^2(c_1^2 - c_2^2)]^{1/2}$$

$$H_2 = -4ic_2\,\mathbf{E}(k_2)$$

mit

$$k_i^2 = \frac{c_i^{\,2} - 1}{c_i^2}, \qquad \sin\phi = \frac{k_2}{k_1}$$

Das Endergebnis lautet

$$\text{(A4)} \quad A(\rho) = \frac{6\rho}{(\rho^2 - 1)^{1/2}}\,R^{1/2}\left[\frac{g_1}{c_1}F(k_1,\phi) + \frac{g_2}{c_2}\mathbf{K}(k_2) - h\left(k_2\,(c_1^{\,2} - c_2^{\,2})^{1/2} + c_2\,\mathbf{E}\,(k_2) - c_1\,E\,(k_1, \gamma)\right)\right]$$

mit

$$R = \frac{\cos\omega\,\sin(\omega + \frac{1}{3}\pi)\,\cos(\omega + \frac{1}{3}\pi)[\frac{1}{2}\sqrt{3} + \sin 2\omega]}{\sqrt{3}\,\sin^3\omega}$$

$$g_1 = \frac{2\sin\omega\,[\sin\omega - \frac{1}{2}\sqrt{3}]}{\sin(\omega + \frac{1}{3}\pi)\,\sin(\omega - \frac{1}{3}\pi)} - \frac{2}{\rho}\,\frac{1 + \cos\omega}{\sin(\omega + \frac{1}{3}\pi)}$$

$$g_2 = \frac{2\sin\omega\,[\sin\omega + \frac{1}{2}\sqrt{3}]}{\sin(\omega + \frac{1}{3}\pi)\,\sin(\omega - \frac{1}{3}\pi)} + \frac{2}{\rho}\,\frac{1 - \cos\omega}{\sin(\omega + \frac{1}{3}\pi)}$$

$$h = \frac{\sqrt{3}\,\sin^2\omega}{\sin^2(\omega + \frac{1}{3}\pi)\,\sin(\omega - \frac{1}{3}\pi)}$$

$$c_1^2 = \frac{\sin(\omega + \frac{1}{3}\pi)[\frac{1}{2}\sqrt{3} - \sin(\omega - \frac{1}{3}\pi)]^2}{\sin^3\omega}$$

$$c_2^2 = \frac{\sin(\omega + \frac{1}{3}\pi)[\frac{1}{2}\sqrt{3} + \sin(\omega - \frac{1}{3}\pi)]^2}{\sin^3\omega}$$

Literatur

1. Burgers, J. W. Proc. Ned. Acad. Wet., **42** (1939) 293, 378.
2. Eshelby, J. D. Phil. Mag., **40** (1949) 903.
3. Heidenreich, R. D. und Shockley, W. Report on a Conference on Strength of Solids (London, 1948), S. 57.
4. Cottrell, A. H. und Bilby, B. A. Phil. Mag., **42** (1951) 573.
5. Seeger, A. Z. Metallk., im Druck.
6. Leibfried, G. und Dietze, H. D. Z. Physik, **131** (1952) 113.
7. Biezeno, C. B. und Grammell, R. Technische Dynamik (Berlin, 1939).
8. Siehe Voigt, W. Lehrbuch der Kristallphysik (Leipzig und Berlin, 1910), VII. Kapitel. Gl. (3a) ist bei Voigt mit Vorzeichenfehlern behaftet.
9. Chalmers, B. Progress in Metal Physics, **2** (1950) 90.
10. Voigt, W. Lehrbuch der Kristallphysik (Berlin und Leipzig, 1910).
11. Maehli, Ergebn. exakt. Naturw., **24** (1951) 402.
12. Schmid, E. und Boas, W. Kristallplastizität (Berlin, 1935).
13. Boas, W. und Mackenzie, J. K. Progress in Metal Physics, **2** (1950).
14. Schmid, E. Straumann-Festschrift (Stuttgart, 1952), S. 25.
15. Leibfried, G. und Dietze, H. D. Z. Phys., **131** (1952) 113.
16. Christian, J. W. Proc. Roy. Soc., *A***206** (1951) 51.
17. Fisher, J. C. und Dunn, C. G. Imperfections in Nearly Perfect Crystals (New York, 1952), S. 317.
18. Siehe Kratzer, A. Lehrbuch der Thetafunktionen (Leipzig, 1903).

CRITERION FOR THE ACTION OF APPLIED STRESS IN THE MARTENSITIC TRANSFORMATION*

J. R. PATEL and M. COHEN†

The martensitic reaction is treated as a strain transformation with shear and dilatational displacements, respectively parallel and normal to the habit plane. When external forces are acting, the resulting effect on the M_s temperature is calculated from the mechanical work done on or by the transforming region as the resolved shear and normal components of the applied stress are carried through the corresponding transformation strains. This energy term is added algebraically to the chemical free energy change of the reaction, to compute the alteration in temperature at which the critical value of the thermodynamic driving force is attained to initiate the transformation. The transformation is aided by shear stresses, but may be aided or opposed by the normal stress component depending on whether the latter is tensile or compressive.

The above criterion for the action of applied stress has successfully predicted the quantitative change in the M_s temperature of iron-nickel and iron-nickel-carbon alloys under uniaxial tension, uniaxial compression and hydrostatic pressure. M_s is raised by tension, less so by compression, and is lowered by hydrostatic pressure.

UN CRITERIUM DE L'ACTION D'UNE TENSION APPLIQUÉE SUR LA TRANSFORMATION MARTENSITIQUE

La réaction martensitique est considérée comme une transformation de déformation avec des déplacements induits par un cisaillement et une dilatation, respectivement parallèle et normale au plan limite. Quand des efforts extérieurs agissent, leur effet sur la température M_s est calculé d'après le travail effectué sur ou par la région en transformation quand les deux composantes, de cisaillement et normale, de la tension appliquée sont reliées aux déformations correspondantes de la transformation. Cette énergie est ajoutée algébriquement au changement de l'énergie libre de la réaction, ce qui permet de calculer la modification de la température pour laquelle on atteint la valeur critique de la "force motrice" thermodynamique, pour initier la transformation. La transformation est aidée par les tensions de cisaillement, mais peut être aidée ou contrariée par la composante normale de la tension, suivant que c'est une composante d'extension ou de compression.

Ce criterium de l'action d'une tension appliquée a prédit quantitativement, d'une manière satisfaisante, le changement de la température M_s des alliages fer-nickel et fer-nickel-carbone sous extension et compression uniaxiales et sous une pression hydrostatique. M_s est élevée par l'extension, un peu moins par la compression, et est abaissée par la pression hydrostatique.

KRITERION FÜR DIE WIRKUNG ÄUSSERER SPANNUNGEN AUF DIE MARTENSITBILDUNG

Die Martensitreaktion wird als eine Verzerrungsumwandlung mit Scherungs- und Dehnungsverschiebungen parallel und senkrecht zur Habitusebene behandelt. Im Falle der Einwirkung äusserer Krafte wird der Gesamteffekt auf die M_s-Temperatur aus der geleisteten mechanischen Arbeit auf oder durch die transformierten Bereiche berechnet; dabei werden die Scherungs- und Normalkomponenten der äusseren Spannung mit den entsprechenden Umwandlungsverzerrungen zusammengefasst. Dieser Energiefaktor wird algebraisch zu der Änderung der freien chemischen Reaktionsenergie addiert um die Änderung der Temperatur, bei der der kritische Wert der thermodynamischen Kraft die die Transformation auslöst erreicht ist, zu berechnen. Scherspannungen können die Transformation unterstützen; jedoch kann die Normalkomponente entweder eine unterstützende oder eine hindernde Wirkung haben, je nachdem ob es sich um eine Zug- oder Druckkomponente handelt.

Dies Kriterion für die Wirkung der äusseren Spannungen hat zu einer richtigen Voraussage der quantitativen Änderung der M_s Temperatur in Eisen-Nickel- und Eisen-Nickel-Kohlenstoff Legierungen unter einachsigem Zug, einachsiger Kompression und hydrostatischem Druck geführt. M_s wird durch Zug erhöht, in geringerm Masse auch durch Kompression und durch hydrostatischen Druck vermindert.

1. Martensite Formation as a Strain Transformation

The martensitic transformation is characterized by its displacive shear-like nature. Consequently, it may be regarded as a strain transformation or as a mode of deformation which competes with slip when external stresses are applied to the parent phase. According to Scheil [1], the shear stress required to activate the martensitic transformation decreases with decreasing temperature (becoming nil at the M_s temperature where the reaction starts spontaneously on cooling), whereas the shear stress required to initiate yielding by slip increases with decreasing temperature. Thus, at temperatures near M_s, applied stresses should induce plastic deformation by the martensitic mode rather than by slip. On the other hand, when stresses are applied at temperatures sufficiently high above M_s, the slip mechanism should supersede the transformation in the deformation process. In a general way, these postulated trends have been confirmed by experiment.

Scheil's concept leads to a shear-stress criterion for

*Received April 1, 1953.

†Department of Metallurgy, Massachusetts Institute of Technology, Cambridge, Massachusetts, U.S.A.

the effectiveness of applied stress in promoting the martensitic transformation. In other words, if yielding by slip does not intervene, the applied stress will activate the transformation when the shear-stress component, resolved along a potential habit plane, reaches a critical value. This critical shear stress will depend on temperature and on the nature of the alloy system. However, the validity of this criterion may be questioned because shear strain is not the only displacement accompanying the martensitic transformation. In steels and iron-base alloys, for example, the volume change is of the order of +4 per cent—an expansion which must certainly interact with the applied stresses.

In fact, the macrostrains attending the formation of individual plates of martensite in single crystals of a 70 per cent iron–30 per cent nickel alloy have been measured directly by Machlin [2], using fiducial marks inscribed on various crystallographic faces of the specimens. His results showed a homogeneous displacement* for the transformation, involving a shear strain (γ_0) of 0.20 along the habit plane and a dilational strain (ϵ_0) of 0.05 normal to the habit plane. The magnitude of these transformation strains are well beyond the elastic range of the parent phase, and indicate that the martensitic reaction should be sensitive to both the shear and normal components of the applied stress. The measured strains do not actually account for the over-all conversion of the austenite lattice to that of martensite; further atomic movements are necessary in order to complete the change in structure. Whether the latter movements occur simultaneously with, or in sequence with, the observed macrodisplacement is still a controversial matter [3; 4; 2; 5], but for the present purposes, we are only concerned with the macrostrain of the transformation because this is what interacts with the applied stress in the treatment to be discussed here.

More recently, the importance of the dilational component of the transformation strain was demonstrated by Kulin [6]. A bar of 0.5 per cent carbon–20 per cent nickel steel in the austenitic state was subjected to uniform elastic bending, and was cooled until martensite started to form. Subsequent metallographic examination disclosed that the transformation had occurred exclusively in the portion of the bar where the tensile stresses existed. No transformation took place in the portion of the bar sustaining compressive stresses, the latter being symmetrically equal in magnitude, but opposite in sign, to the aforementioned tensile stresses.

When the acting stresses in the elastically bent bar are resolved into their normal and shear components, it is noted that they are symmetrical in magnitude about the neutral axis. Since the sign of the shear component is immaterial from the standpoint of the martensitic reaction, because of the many potential habit orientations, the striking selectivity of the transformation in the bar can only be attributed to the difference in sign of the *normal* stresses.

This finding invalidates the shear-stress criterion, along with other possible criteria based on shear strain or shear-strain energy, because the demonstrated effect of the normal component is neglected in such considerations. Moreover, if any of these criteria were appropriate, hydrostatic pressure should have no influence on the transformation since no shear stresses would then be applied. In a similar sense, uniaxial compression and tension should have the same effect on M_s when the resolved shear stresses are the same. Experimental evidence is presented in the next section to show that this is not the case.

2. Experimental Results on the Effect of Applied Stress

Figure 1 summarizes the changes in M_s temperature due to applied uniaxial tension, uniaxial com-

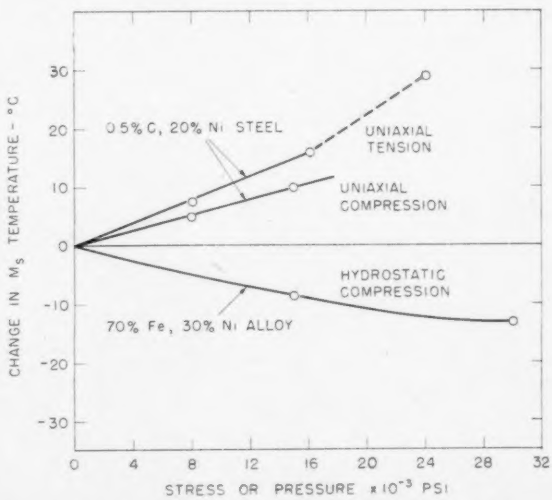

FIGURE 1. Change in M_s temperature as a function of loading condition.

*This kind of displacement is termed a Bowles-type strain [4] or an invariant-plane strain [2]. It can be described by the motion of a plane of no rotation and no distortion (the invariant plane) in a direction not necessarily contained in the plane. The invariant plane is found to lie parallel to the habit plane of the martensitic plate. In the case cited above, the invariant planes slide past one another to provide a component of shear strain (γ_0) parallel to the habit plane, and also move apart to provide a component of dilational strain (ϵ_0) normal to the habit plane.

pression and hydrostatic pressure. The tension and compression experiments were performed on $\frac{1}{16}$-inch- and $\frac{1}{4}$-inch-diameter rods (respectively) of a 0.5 per cent carbon–20 per cent nickel steel, whereas the pressure experiments were carried out on $\frac{1}{16}$-inch-diameter rods of a 70 per cent iron–30 per cent nickel alloy. Both materials were austenitized at 1095°C and oil quenched to room temperature. The $\frac{1}{4}$-inch-diameter specimens were stress relieved at 425°C; this treatment was not found to be essential for the smaller size specimens. The M_s temperature for the nickel-carbon steel was about -40°C, and that of the iron-nickel alloy was about -20°C.

The M_s temperatures were determined by electrical resistance measurements while the austenitic specimens were being subcooled in the stress-free and variously loaded conditions. The procedures for the tensile and compressive runs have been described previously [6]. The hydrostatic pressure runs were made in Professor P. W. Bridgman's laboratory at Harvard University; the details will be presented elsewhere.

It is evident from Figure 1 that the three methods of stressing produced virtually linear changes in the M_s temperature, at least up to about 15,000 psi. The corresponding slopes are $+1.0$, $+0.65$ and -0.57°C/1000 psi, respectively, for the cases of tension, compression and pressure. Thus, there is an appreciable difference between the effects of uniaxial tension and uniaxial compression, despite the identical shear components in these two instances. The influence of hydrostatic pressure is also noteworthy, not only because of its magnitude but because of its sign which differs from that of the other two methods of loading. Clearly, any criterion based on shear alone cannot account for these results.

3. Criterion for the Effectiveness of Applied Stress

3.1 *Free Energy Change in the Martensitic Reaction*

The criterion to be proposed here is a thermodynamic one (*a*) based on the assumption that the M_s temperature of a given alloy occurs at a certain value of the driving force ($-\Delta F$), and (*b*) taking in account the mechanical work performed on or by the transforming region as the resolved normal and shear forces are carried through the respective transformation displacements.

It has been shown that iron-carbon alloys start to transform spontaneously to martensite at temperatures corresponding to a constant driving force of $-\Delta F = 290$ cal/mol [7; 8]. (This means that for a wide range of carbon contents the change in chemical free energy accompanying the transformation of one mol of austenite to one mol of martensite at the M_s temperature is $F^M - F^A = -290$ cal/mol.) In the iron-nickel system, M_s occurs at $F^M - F^A = -200$ cal/mol over the range of compositions under consideration here [9].

In the present study, the thermodynamic work of Jones and Pumphrey [9] is used for the iron-nickel system, and this is extended to the iron-nickel-carbon case. The method of calculation is described in Appendix I. Figure 2 depicts the change in free

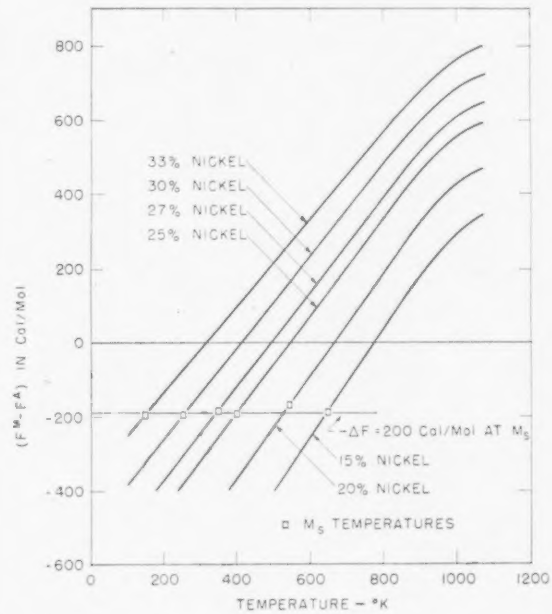

FIGURE 2. Change in free energy attending the austenite-to-martensite reaction in iron-nickel alloys. Plotted from the equation of Jones and Pumphrey [9].

energy as a function of temperature and composition, attending the martensitic transformation in iron-nickel alloys. Figure 3 gives similar information for the iron-nickel-carbon system. In both graphs, the particular compositions were chosen because fairly accurate data were available for their M_s temperatures, and because they straddle the two alloys employed in this investigation. It will be noted that in each series the M_s temperature occurs at a fixed value of the chemical free energy change, the latter being about -200 cal/mol in the iron-nickel alloys and -370 cal/mol in the iron-nickel-carbon alloys. These values signify that the martensitic reaction does not take place at the temperature (T_0) of thermodynamic equilibrium between the austenite and martensite, but only after supercooling sufficiently to achieve the required driving force for the

transformation. Inasmuch as the free energy of nucleation decreases as the driving force increases, this is tantamount to saying that M_s occurs on cooling at the temperature where the free energy of nucleation drops to a critical level [11; 12].

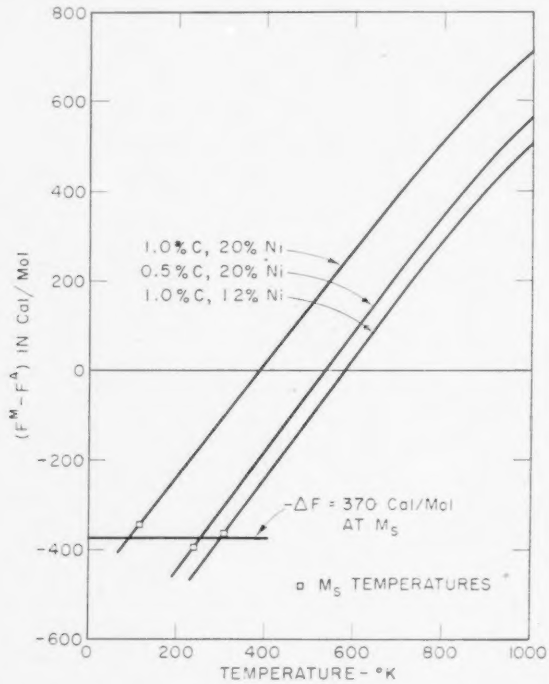

FIGURE 3. Change in free energy attending the austenite-to-martensite reaction in iron-nickel-carbon alloys.

3.2 *Role of Applied Stress*

The work (U) done on or by the transformation due to the action of applied stress is comprised of two terms: ($\tau\gamma_0$) the shear stress resolved along a potential habit plane times the transformation shear strain, and ($\sigma\epsilon_0$) the normal stress resolved perpendicular to the habit plane times the normal component of the transformation strain. Thus

$$U = \tau\gamma_0 + \sigma\epsilon_0. \tag{1}$$

σ is numerically positive when the normal stress is tensile, and negative when this component is compressive. τ is always taken to be positive because the many habit permutations ($\pm\{259\}$ in these alloys) virtually permit shearing in either sense. Hence, in effect, shear stresses will stimulate the transformation, but normal stresses may aid or oppose it depending upon whether σ is tensile or compressive. The units of U in equation (1) are stress times transformation strain or mechanical work per unit volume of austenite reacted to martensite. Values of U can readily be converted to calories per mol, to match the units of $F^M - F^A$.

For uniaxial tension or compression, a consideration of Mohr's circle in Figure 4 shows that the resolved shear and normal stresses are

$$\tau = \tfrac{1}{2}\,\sigma_1 \sin 2\theta, \tag{2}$$

$$\sigma = \pm\,\tfrac{1}{2}\,\sigma_1\,(1 + \cos 2\theta), \tag{3}$$

where σ_1 = absolute value of the applied stress (tension or compression) and θ = angle between the specimen axis and the normal to any potential habit plane.

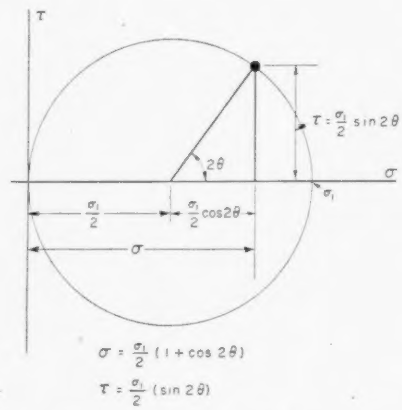

FIGURE 4. Mohr's circle for tension showing the shear (τ) and normal (σ) components of stress as a function of the applied stress (σ_1) and the orientation (θ) between the stress axis and the normal to the potential habit plane.

U may now be expressed as a function of the orientation of a transforming martensitic plate:

$$U = \tfrac{1}{2}\,\gamma_0\,\sigma_1 \sin 2\theta \pm \tfrac{1}{2}\,\epsilon_0\,\sigma_1(1 + \cos 2\theta) \tag{4}$$

Since we are concerned with the plates that form first (at M_s) under the influence of applied stress, it is necessary to find the particular orientation which yields a maximum value of U:

$$\frac{dU}{d\theta} = \gamma_0\sigma_1 \cos 2\theta \pm \epsilon_0\sigma_1(-\sin 2\theta) = 0 \tag{5}$$

$$\frac{\sin 2\theta}{\cos 2\theta} = \tan 2\theta = \pm\,\frac{\gamma_0}{\epsilon_0} \tag{6}$$

Substituting the known components of the transformation strain into equation (6) and then into equation (4), it is now possible to obtain $U_{\max}$. It is then assumed that $U_{\max}$ contributes to (or detracts from) the chemical free energy change to aid (or oppose) the start of the transformation. As illustrated in Figure 5, if $U_{\max}$ is positive, the degree of

supercooling required to reach the appropriate driving force for initiating the reaction is reduced, and the M_s temperature is thereby raised to M_s' by

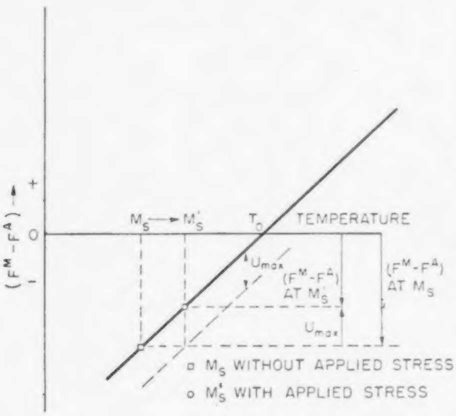

FIGURE 5. Schematic diagram showing how the mechanical energy U_{max} due to the applied stress system changes the M_s temperature by contributing to the thermodynamic driving force of the martensitic transformation. In this case the driving force to start the transformation does not vary with the M_s temperature.

the applied stress. Thus M_s' is the temperature defined by the following relationship, and can be calculated therefrom through the known temperature-dependence of $F^M - F^A$:

(7)* $(F^M - F^A)$ at $M_s' = (F^M - F^A)$ at $M_s + U_{max}$

The calculation will now be carried through for the conditions of 1000 psi tension. In the iron-nickel alloys,

$$\frac{\gamma_0}{\epsilon_0} = \frac{0.20}{0.04} = 5.\dagger$$

From equation (6), $2\theta = 79°$, thus giving the orientation of the first martensitic plates to form on cooling under the applied stress. Substituting in equation (4):

(8) $U_{max} = 122$ in-lbs/in^3 = 1.42 cal/mol.

Using the curve from the 0.5 per cent carbon–20 per cent nickel steel in Figure 3:

(9) $$\frac{d(F^M - F^A)}{dT} = 1.33 \text{ cal/mol-°C}$$

This slope holds for the linear portion of the curve, and prevails for the temperature range of interest.

The increase in M_s due to applied stress of 1000 psi is

(10) $$\frac{dM_s}{d\sigma} = \frac{1.42}{1.33} = +1.07°\text{C}/10^3 \text{ psi (for tension)}$$

In the case of uniaxial compression, a similar analysis gives

(11) $$\frac{dM_s}{d\sigma} = \frac{0.96}{1.33} = +0.72°\text{C}/10^3 \text{ psi (for compression)}$$

With hydrostatic pressure, the same treatment may be employed. In this situation, there are no shear components to aid the reaction. The applied pressure interacts only with the dilatational strain, and opposes the transformation. If σ_1 = the magnitude of the hydrostatic pressure, equation (4) becomes

(12) $$U = -\epsilon_0\sigma_1$$

there being no orientation dependence in this case. For $\sigma_1 = 1000$ psi,

(13) $U = -40$ in-lbs/in^3 = -0.47 cal/mol

Using the curve for the 70 per cent iron–30 per cent nickel alloy in Figure 2 (since experimental results are available on this material for comparison purposes):

(14) $$\frac{d(F^M - F^A)}{dT} = 1.23 \text{ cal/mol-°C}$$

from which

(15) $$\frac{dM_s}{d\sigma} = \frac{-0.47}{1.23} = -0.38°\text{C}/10^3 \text{ psi}$$

(for hydrostatic pressure)‡

Table I summarizes these calculations and the corresponding experimental findings. The agreement is quite good, undoubtedly better than is justified. The criterion proposed here successfully predicts the lowering of M_s by hydrostatic pressure and the raising of M_s by uniaxial tension and compression.

*Equation (7) is not strictly correct unless the driving force to start the transformation is independent of the M_s temperature, as is the case for the alloy systems under consideration here (Figures 2 and 3). Appendix II presents a corresponding treatment for the more general situation in which the driving force for starting the transformation varies with the M_s temperature and therefore with the composition of the alloy.

†According to Machlin's observations [2], ϵ_0 equals 0.05, but more precise dilatometric measurements indicate that the unit bulk expansion is closer to 0.04. This represents a more exact value of ϵ_0 because the latter must correspond to the volume change.

‡Dr. J. C. Fisher kindly suggested a similar calculation for the case of hydrostatic pressure (private communication).

Note added in proof (August 24, 1953). The treatment of Dr. Fisher mentioned here has since appeared in Acta Met., **1** (1953) 310.

TABLE I

EFFECT OF APPLIED STRESS ON THE M_s TEMPERATURE

	Stress System	Uniaxial Tension	Uniaxial Compression	Hydrostatic Pressure
	Material	0.5% C, 20% Ni, bal. Fe	0.5% C, 20% Ni, bal. Fe	70% Fe, 30% Ni
$\frac{dM_s}{d\sigma}$	Calculated	+1.07°C/10³ psi	+0.72°C/10³ psi	−0.38°C/10³ psi
	Experimental	+1.0°C/10³ psi	+0.65°C/10³ psi	−0.57°C/10³ psi
Change in M_s per 15,000 psi	Calculated	+16°C	+10.6°C	−5.7°C
	Experimental	+15°C	+10°C	−8.5°C

The raising of M_s by compression is quantitatively explained on the basis that the resolved shear component of stress aids the transformation more effectively than the compressive normal component opposes it. This is a consequence of the fact that the shear displacement is much larger than the dilatational displacement. Under uniaxial tension, the transformation is aided by both the shear and (positive) normal components of stress, and therefore the M_s is raised even more than in the case of uniaxial compression. Under hydrostatic pressure, the stress system only opposes the transformation, and the M_s is lowered.

4. Conclusions

4.1 The role of applied stress in the martensitic transformation has been quantitatively analyzed for the conditions of uniaxial tension, uniaxial compression and hydrostatic pressure.

4.2 It is assumed that the reaction starts spontaneously on cooling at the temperature (M_s) where the free energy change $F^M - F^A$ reaches a critical negative value. When external stresses are applied, the work done on or by the transformation (as the acting forces are carried through the transformation displacements) contributes algebraically to the free energy change, thus raising or lowering the M_s temperature.

4.3 To calculate this mechanical contribution to the thermodynamic driving force, the normal as well as the shear components of the applied stresses are taken into account, thereby recognizing the interaction with both the dilatational and shear strains of the transformation.

4.4 This treatment predicts that, at least in iron-nickel and iron-nickel-carbon alloys, M_s should be raised by uniaxial compressive stress, should be raised even more by tensile stress, and should be lowered by hydrostatic pressure. These changes in M_s have been confirmed quantitatively by experiment.

Acknowledgments

This work is part of a research program sponsored at the Massachusetts Institute of Technology by the Office of Naval Research.

The authors are indebted to the Office of Naval Reseach for sponsoring this program. They also wish to express their appreciation to Professor P. W. Bridgman of Harvard University for the use of the high pressure facilities in his laboratory and for his helpful advice and interest in this work. William R. Yankee and E. Sudenfield rendered effective aid in various phases of the investigation. Stimulating discussions concerning the significance of the results were held with E. S. Machlin, J. C. Fisher and B. L. Averbach.

APPENDIX I

Free Energy Changes Accompanying the Martensitic Transformation

The thermodynamics of the iron-nickel system have been investigated by Jones and Pumphrey [9], who obtained the following expression for the free energy change accompanying the austenite-to-martensite reaction:

$$F^M - F^A = N_{\mathrm{Ni}}\Delta H_{\mathrm{Ni}} + 1.25 N_{\mathrm{Fe}}\Delta F_{\mathrm{F}} \tag{A1}$$

where N_{Ni} = mol fraction of nickel
N_{Fe} = mol fraction of iron
ΔH_{Ni} = difference between the heat of solution of nickel in ferrite and that in austenite = 2500 cal/mol (adjusted to match the iron-nickel phase diagram).

ΔF_{Fe} = free energy change attending the transfer of one mol of iron from austenite to ferrite.

Values of ΔF_{Fe} have been calculated by Zener [7] from the specific heat data of Austin [13]. For the iron-nickel system, Jones and Pumphrey found that ΔF_{Fe} had to be increased by 25 per cent over the values given by Zener to assure good correlation with the equilibrium diagram. This is the reason for the empirical factor of 1.25 in equation (A1).

To consider the effect of carbon, the method of Fisher [10] was utilized:

$$\text{(A2)}\quad F^M - F^A = N_{N1}\Delta H_{N1} + 1.25 N_{Fe}\Delta F_{Fe} + N_C(10{,}500 - 3{,}425\,T) + \Delta F_*$$

where N_C = mol fraction of carbon

ΔF_* = free energy change due to ordering of carbon atoms in tetragonal martensite

The temperature-dependence indicated by third term on the right side of equation (A2) is obtained from the activities of carbon in austenite and in ferrite, and has been discussed by Fisher [10]. When no carbon is present, equation (A2) reduces to equation (A1).

The results of equations (A1) and (A2) are plotted in Figures 2 and 3.

It is doubtful that ΔH_{N1} is actually constant over the entire temperature range extending down to the subzero levels where the martensitic reaction takes place in these alloys. However, various attempts to use extrapolated values of ΔH_{N1} did not seriously alter the final result. Allowing ΔH_{N1} to change with temperature caused the $(F^M - F^A)$ vs. T curves to become steeper, but this was partially counterbalanced by the fact that the driving force at M_s then varied with the M_s temperature (see Figure 6). The treatment of this case is presented in Appendix II, but in view of the limited data available, the more straightforward calculations given in the text are considered to be sufficiently appropriate for the problem at hand.

APPENDIX II

Effect of Applied Stress When the Driving Force at M_s Depends on M_s

Let the curves 1, 2 and 3 in Figure 6 represent the variation of $F^M - F^A$ with temperature for a series of alloys in a given system. Suppose that the M_s temperatures superimposed on these curves do not lie at a fixed value of $F^M - F^A$. This is shown by curve 4 which indicates how the driving force to start the transformation depends on the M_s temperature (and therefore on composition). It is not necessary to assume linear relationships for these curves.

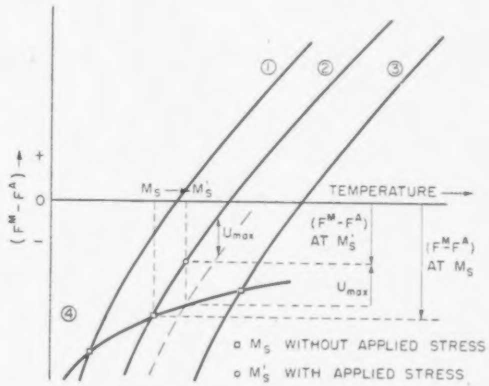

FIGURE 6. Schematic diagram showing how the mechanical energy U_{max} due to the applied stress system changes the M_s temperature of alloy 2 by contributing to the thermodynamic driving force. In this case the driving force to start the transformation varies with the M_s temperature according to curve 4.

Taking alloy 2 as an example, let a stress be applied to the specimen during cooling such that U_{max} is the work (in calories per mol) done on the first-formed plates of martensite as a result of the components of the applied stress being carried through the transformation displacements. In this instance, consider that the transformation is aided by the acting stresses, and M_s is raised. It is now required to find the temperature (M_s') where the combined effects of U_{max} and the chemical free energy change $(F^M - F^A)$ achieve the necessary driving force to start the transformation at M_s'.

The graphical solution to this problem is shown in Figure 6. The dashed curve is drawn parallel to the $F^M - F^A$ curve, but is displaced downward by an amount U_{max}. The intersection of the dashed curve with the M_s temperature line (which designates the driving force necessary to start the transformation as a function of temperature) gives the required temperature M_s'. It is evident that the change of the martensite-start temperature due to applied stress is greater in the case at hand than if the driving force at M_s were independent of M_s (compare with Figure 5).

With hydrostatic pressure, the dashed curve is displaced upwards because U is negative and opposes the transformation. This results in a corresponding lowering of the M_s' temperature.

References

1. SCHEIL, E. Z. anorg. Chem., **207** (1932) 21.
2. MACHLIN, E. S. and COHEN, M. Trans. A.I.M.E., **191** (1951) 1019.
3. GRENINGER, A. B. and TROIANO, A. R. Trans. A.I.M.E., **140** (1940) 307; **185** (1949) 590.
4. BOWLES, J. S. Acta Cryst., **4** (1951) 162.
5. FRANK, F. C. Acta Met., **1** (1953) 15.
6. KULIN, S. A., COHEN, M., and AVERBACH, B. L. J. Metals, **4** (1952) 661.
7. ZENER, C. Trans. A.I.M.E., **167** (1946) 513.
8. COHEN, M., MACHLIN, E. S., and PARANJPE, V. G. Thermodynamics in Physical Metallurgy (American Society for Metals, 1950) p. 242.
9. JONES, F. W. and PUMPHREY, W. I. J. Iron Steel Inst., **163** (1949), Part 2, 121.
10. FISHER, J. C. Trans. A.I.M.E., **185** (1949) 688.
11. FISHER, J. C., HOLLOMON, J. H., and TURNBULL, D. Trans. A.I.M.E., **185** (1949) 691.
12. MACHLIN, E. S. and COHEN, M. J. Metals, **4** (1952) 489.
13. AUSTIN, J. B. J. Industr. Engng Chem., **24** (1932) 1225.

THE EFFECTS OF NEUTRON IRRADIATION IN THE NRX REACTOR ON THE ORDER-DISORDER ALLOY Cu_3Au*

L. G. COOK and R. L. CUSHING†

The irradiation of Cu_3Au with neutrons causes two separable effects. Disordering is caused by fast neutrons, and is negligible with thermal neutrons; the effect is independent of temperature at least up to 100°C. Volume disordering rates of 28.9 per cent/day have been observed with fission spectrum neutrons. A secondary effect, probably ordering, is caused by thermal neutrons; the effect is dependent on temperature even below 100°C. The simultaneous formation of substantial amounts of mercury is probably the direct cause of the effect.

NRX "reactor spectrum" neutron irradiation produces both effects which mutually interfere. Provided the thermal component of the neutron spectrum is screened out, it seems likely that the disordering effect on Cu_3Au can be used as a measure of neutron damage potential to other materials.

LES EFFETS DE L'IRRADIATION AVEC DES NEUTRONS DANS LE RÉACTEUR NRX SUR LA TRANSFORMATION ORDRE-DÉSORDRE DANS L'ALLIAGE Cu_3Au

L'irradiation de Cu_3Au avec des neutrons cause deux effets séparables. Le désordre est causé par des neutrons rapides, mais est négligeable avec des neutrons thermiques; cet effet est indépendant de la température, en tout cas jusqu'à 100°C. Des vitesses de mise en désordre de 28,9 pour cent par jour, en volume, ont été observées avec des neutrons du spectre de fission. Un effet secondaire, probablement une mise en ordre, est causé par des neutrons thermiques; cet effet dépend de la température, même en dessous de 100°C. La formation simultanée de quantités appréciables de mercure est probablement la cause directe de cet effet.

L'irradiation avec des neutrons du "spectre du réacteur" NRX produit tous les deux effets, qui s'entremêlent. Il paraît que, pourvu qu'il soit possible de rendre inopérante la composante thermique du spectre des neutrons, l'effet de mise en désordre sur Cu_3Au puisse être utilisé comme une mesure du potentiel de destruction des neutrons sur d'autres matières.

DIE WIRKUNG VON NEUTRONENBESTRAHLUNG IM NRX "REACTOR" AUF DEN ORDNUNGSGRAD Cu_3Au

Die Bestrahlung von Cu_3Au mit Neutronen ruft zwei verschiedene Effekte hervor. Schnelle Neutronen rufen eine Verminderung der Ordnung hervor, während dieser Effekt bei thermischen Neutronen zu vernachlässigen ist. Diese Effekt ist, zum mindesten bis zu 100°C, unabhängig von der Temperatur. Mit "fission spectrum" Neutronen wurden Ordnungsverminderungsgrade von 28.9 prozent/Tag beobachtet. Ein sekundärer Effekt, wahrscheinlich ein Ordnen, wird von thermischen Neutronen hervorgerufen. Selbst unter 100°C hängt dieser Effekt von der Temperatur ab. Die gleichzeitige Bildung von einer nicht unerheblichen Menge Quecksilbers ist wahrscheinlich eine direkte Ursache dieses Effekts.

Die NRX "reactor spectrum" Neutronen rufen beide Effekte hervor, die sich gegenseitig beeinflussen. Unter der Voraussetzung, dass der thermische Anteil. des Neutronenspectrums ausfiltriert wird, erscheint es möglich, die Verminderung des Ordnungsgrades des Cu_3Au zur Messung des Schädigungspotential der Neutronen für andere Substanzen zu benutzen.

Introduction

When crystals are irradiated with energetic heavy particles, radiation damage may occur in three ways. Atoms may interchange positions on lattice sites more rapidly than usual; they may be removed entirely from lattice sites and located interstitially; or they may be removed from lattice sites and recombine in a different way entirely.

In this paper the first type of damage is considered —the magnitude and mechanism of the interchange of atoms on lattice sites when a solid is irradiated with neutrons. An order-disorder alloy seemed the most promising type of system to study; large changes in observable properties occur when the atoms interchange sites on the lattice, since by this process an initially ordered alloy becomes disordered, or a disordered alloy becomes ordered.

Cu_3Au was selected for the first study because: (1) its thermal behaviour and the mechanism of its transition have been thoroughly studied; (2) the "freezing in" temperature is above 200°C, well above NRX reactor ambient temperature; (3) changes in the unit cell dimensions due to the order-disorder transition are small; (4) the alloy is readily workable, and obtainable in fine wire.

Following the work of Sykes and collaborators [1; 2] it was decided to observe: (i) changes in the electric resistance, since these could be measured during irradiation in the reactor; (ii) changes in the X-ray diffraction pattern, since the behaviour of the superlattice lines would confirm the interpretation of the electric resistance changes; (iii) changes in the specific heat and in subsequent specific heat-temperature curves, since these detect minute and early mechanisms of ordering which leave the

*Received April 2, 1953.

†Chemistry Branch, Atomic Energy of Canada Limited, Chalk River, Ontario, Canada.

electric resistance and superlattice lines relatively unchanged.

This paper presents the results of observations on electric resistance and superlattice lines only, since these give a consistent picture without the support of specific heat data.

During the progress of these experiments, results of somewhat similar experiments carried out at Harwell (U.K.) [3] and Oak Ridge (U.S.A.) [4; 5; 6] have appeared. Most of these appear to refer to "reactor spectrum" neutron irradiations, the effects of thermal and fast neutron irradiation not being separated, nor the effects of temperature studied. These results are referred to and their probable connection with the present results explained.

Experimental Techniques

Cu_3Au wire, 49.1 per cent Cu, 50.9 per cent Au by weight, 0.015 in. dia., was supplied by Johnson, Matthey and Mallory in the cold drawn condition. All samples were annealed at 800°C in vacuo, or in argon, for 30 min. to remove the major effects of the cold drawing operation.

Electric resistance measurements were made by passing a measured current of approximately 50 ma. through a section of wire and measuring the potential drop between two Cu_3Au taps spot welded, or in some instances hard soldered, to the test wire 10 cm. ± 1 mm. apart. The current was measured by the potential drop across a standard resistor. Potential drops were measured with Rubicon precision potentiometers, or with Leeds and Northrup Speedomax recorders and microvolt amplifiers using precision potentiometers to provide a backing potential. In this way small variations in resistance—such as that due to temperature rise on reactor start up—could be amplified and observed.

A laboratory vacuum furnace assembly enabled resistance-temperature curves to be observed for comparison with those of Sykes [2]. In the reactor a special assembly was used, illustrated schematically in Figure 1. The sample assembly could be irradiated with or without the Cd liner or the U cylinder, so that the effects of fission spectrum, reactor epithermal, and thermal neutrons respectively could be separated. Adjustment of the cooling air permitted steady controlled temperatures to be maintained between 25°C and 110°C. Temperature checks were made during the initial reactor start up, using the measured immediate rise in electric resistance and the known initial thermal coefficients to calculate the temperature rise. Further, whenever a shut down

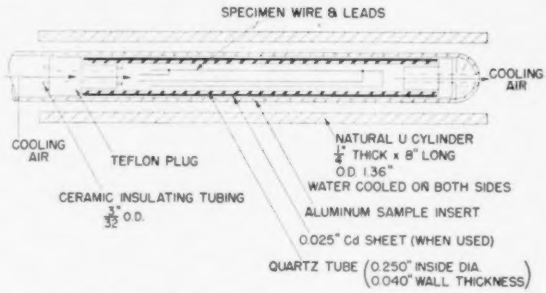

FIGURE 1. Irradiation assembly as used in the NRX reactor.

of the reactor occurred, a new thermal coefficient was obtained (by assuming the temperature rise to be unchanged). Thus not only could the change in electric resistance be observed, but also the concomitant change in the thermal coefficient of electric resistance.

X-ray diffraction Debye-Scherrer pictures were taken on short wire samples with a General Electric XRD unit, before neutron irradiation and again two months afterwards. It was found that very little γ-ray background was developed on the films two months after irradiation, when small samples were used. These X-ray samples were mounted in the reactor in an open holder so that the cooling air could contact the samples themselves, as in the electric resistance experiments. No other direct control of temperature was carried out. It was assumed that the temperatures during neutron irradiation would be close to those of the electric resistance specimens which had similar exposed surface air cooling.

The heat treatment programs used were:

(a) To prepare disordered samples, air quench from 500°C.

(b) To prepare ordered samples,
6 hours at 350°C
16 hours at 340°C
4 hours at 330°C
4 hours at 320°C
16 hours at 300°C
furnace cooled to room temperature.

Results

I. *Resistance-Temperature Curves for* Cu_3Au *Wire*

Samples of Cu_3Au wire in the ordered and disordered states were heated at a rate of 1.75°C/min., and the electric resistance measured (Figure 2, *A* and *B*). A sample cooled slowly from 500°C, down curve *B*, was air quenched at temperature *T*, and the resistance-temperature curve taken (curve

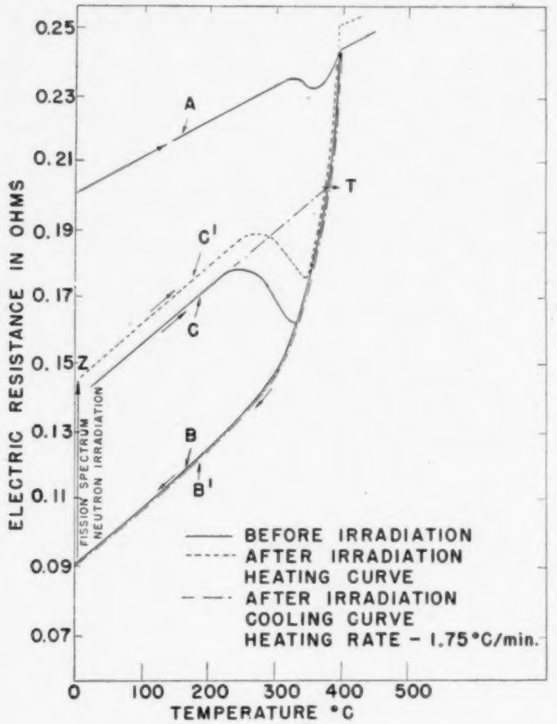

FIGURE 2. Electric resistance versus temperature: unirradiated and irradiated samples.

C). It is evident that the initial rate of relaxation at a temperature of, say 250°C, is much more rapid in a partially disordered sample (curve *C*) than in a fully disordered sample (curve *A*). This effect was found by Sykes [2] and attributed to the fact that in the partially disordered sample there are large "in phase" ordered nuclei which can grow easily, whereas in the fully disordered sample there are no nuclei initially—even when they do form they are "out of phase" and growth is hindered.

As a final check the initial rate of change of resistance at fixed temperature was determined as follows:

	Temperature	Relaxation rate (% of resistance/day)
fully disordered	210°C	<0.01
	260°C	2.4
partially disordered	200°C	<0.01
	220°C	4.2

II. *Temperature Measurement in Reactor*

A typical electric resistance-time curve obtained during a start up and shut down of the reactor is shown in Figure 3. This resistance increase when the reactor begins operation must be due solely to an increase in temperature of the specimen. Two observations confirmed this: first throttling the cooling air increased the resistance; second the difference in resistance increase for ordered and disordered specimens was exactly the expected ratio of the thermal coefficients as measured from Figure 2.

The ice-point resistance of each specimen was determined prior to irradiation, and hence the actual temperature of the sample could be determined

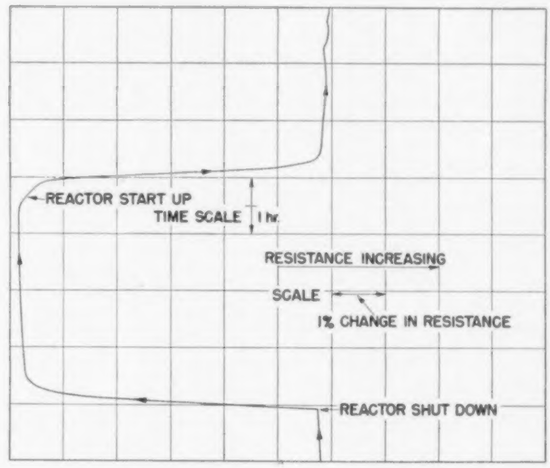

FIGURE 3. Electric resistance change during reactor start up due to temperature rise.

under operating conditions immediately after reactor start up. With the arrangements described, 25–35°C was the usual operating range, although controlled temperatures up to 110°C were also used.

III. *Irradiation in Uranium with Cadmium Shielding (Fission Spectrum Neutrons)*

The general behaviour of the electric resistance of ordered and disordered Cu_3Au when irradiated in uranium with cadmium shielding is shown in Figure 4. The resistance of the ordered sample (curve *A*) rose asymptotically to that of the disordered sample; the resistance of the disordered sample (curve *B*) rose very little, about 0.5 per cent.

X-ray diffraction pictures taken before and after irradiation are shown in Plate I. The disordered alloy remained disordered. The ordered alloy became disordered, shown by the disappearance of the superlattice lines.

As a further check, an ordered sample was irradiated until its resistance (relative to the ordered and disordered values) reached point *Z*, Figure 2. Then the sample was removed to the

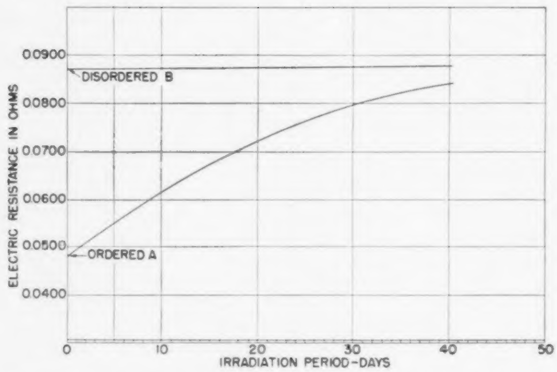

FIGURE 4. Fission spectrum neutron irradiation with Cd shield: temperature 35°C (identical curves obtained at 106°C).

laboratory and an electric resistance-temperature curve taken at ∽1.7°C/min. (curve C' and B'). It is evident that the course of these curves is very close to the course of the curves C and B, and that the sample is in essentially the same state at Z whether prepared by quenching from a temperature T, or by irradiation of a fully ordered specimen with fast neutrons.

Thus, fission spectrum neutrons disorder ordered Cu_3Au but have little effect on disordered Cu_3Au.

IV. *Irradiation with NRX "Reactor Epithermal" Neutrons ("Reactor Spectrum" Neutrons with Cadmium Shielding)*

The general behaviour of the electric resistance of ordered and disordered Cu_3Au in NRX reactor spectrum neutrons with cadmium shielding is shown in Figure 5, curves A and B. The general effects are qualitatively identical to those with fast neutrons, but quantitatively much less pronounced. A slight initial dip in resistance is apparent in both curves.

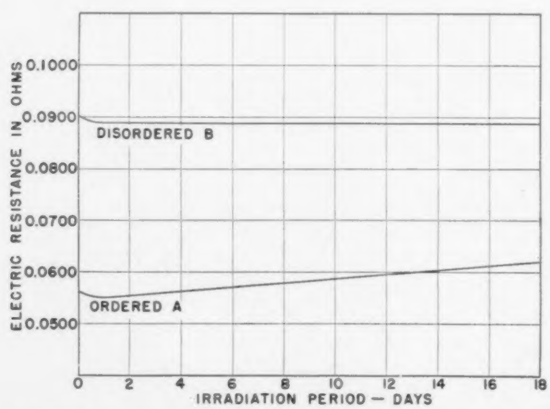

FIGURE 5. Irradiation with "reactor spectrum" neutrons with Cd shield: temperature 44°C.

The fast neutron component normally present in the NRX reactor neutron spectrum disorders ordered Cu_3Au, but has little effect on disordered Cu_3Au.

V. *Irradiation with NRX Reactor Spectrum Neutrons*

The general behaviour of the electric resistance of ordered and disordered Cu_3Au in NRX reactor spectrum neutrons is shown in Figure 6. Since in this example the epithermal (Figure 5) plus thermal neutron components are present, one must look for differences between the curves of Figure 5 and those of Figure 6, and attribute them to the thermal neutron component. The difference is that the initial dips in resistance continue over a longer period

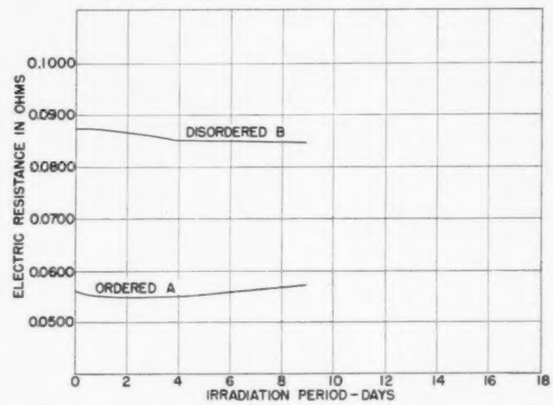

FIGURE 6. Irradiation with "reactor spectrum" neutrons without Cd shield: temperature 28°C.

and become more pronounced before the disordering process takes over; then the curves flatten out and behave like those of Figure 5.

The thermal neutron component of the reactor spectrum has a resistance-lowering effect on both ordered and disordered Cu_3Au.

VI. *Irradiation at Different Temperatures*

An irradiation in uranium with cadmium shielding (fission spectrum) was done at 106°C. The behaviour of the electric resistance was identical with the behaviour at 28°C (Figure 4) and a separate graph is therefore not shown.

An irradiation with "reactor spectrum" neutrons (no cadmium shielding) at 111°C (Figure 7) gave the same general effects as at 28°C (Figure 6), but quantitatively more pronounced and quicker.

VII. *Comparison of Results in Different Fluxes*

Irradiations have been done in three different positions in the NRX reactor and over a relatively

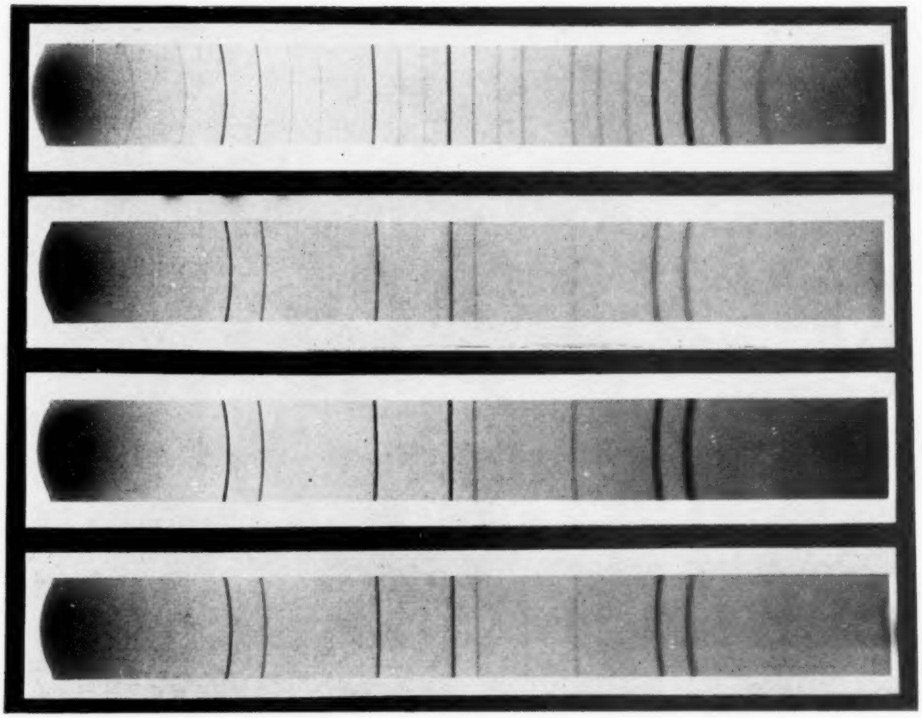

ORDERED
BEFORE
IRRADIATION

ORDERED
AFTER
IRRADIATION

DISORDERED
BEFORE
IRRADIATION

DISORDERED
AFTER
IRRADIATION

PLATE I: X-ray diffraction films.

TABLE I

	Position		
	A	B	C
Position	In graphite shield	Inside callandria near its edge	Near centre of reactor
Nominal thermal neutron flux in that position	4×10^{12} n/cm²/sec.	1.5×10^{13} n/cm²/sec.	6×10^{13} n/cm²/sec.
Type of uranium cylinder used	4″ dia. O.D. ¼″ wall	1.4″ O.D. ¼″ wall	1.4″ O.D. ¼″ wall
Initial rate of increase of electric resistance of ordered Cu_3Au with irradiation time	1.03%/day	2.98%/day	11.7%/day

long period of time. Consequently a precise quantitative comparison of the effects with flux is not possible. However, some quantitative comparison is possible.

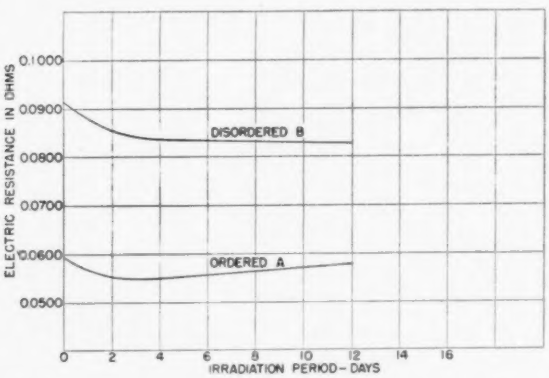

FIGURE 7. Irradiation with "reactor spectrum" neutrons without Cd shield: temperature 111°C.

The three positions used and the initial rates of change of electric resistance of ordered Cu_3Au in them are listed in Table I. The initial rate of change of electric resistance of ordered Cu_3Au increases with the nominal slow neutron flux.

Discussion of Results

There are two distinct and opposed effects of neutron irradiation on Cu_3Au alloy. First, a drop in electric resistance caused mainly by thermal neutrons; second, a rise in electric resistance and a progressive disordering caused by epithermal and fission spectrum neutrons.

The first effect may indicate a limited ordering process. Since the so-called "ordered" alloy possesses in fact a degree of order appropriate to 200°C at least, it is, at room temperature, not in real equilibrium. Hence it is tempting to interpret the resistance decrease observed as an "ordering" of both the ordered and disordered states. However, since Cu_3Au rapidly becomes a mercury amalgam if irradiated by the slow neutron component in the NRX reactor spectrum (with 0.025″ Cd shielding, the formation of Au^{198}, and hence Hg^{198}, was found by activation analysis to be reduced to a little under 10 per cent of the unshielded value) such "ordering" must be attributed in the first instance to the thermal neutrons only through the influence of the mercury formed. Normally one expects an impurity to raise the electric resistance; the fact that introducing mercury produces a decrease in resistance in both alloy states tends to make one think that an ordering process must be taking place.

For comparison, a table of mercury quantities is given (Table II).

A thorough study of the effects of traces of mer-

TABLE II

Irradiation days	Per cent of gold converted to mercury (assuming $\sigma = 95$b., $F = 6 \times 10^{13}$ n/cm²/sec.)	
1	0.005%	
3	0.037%	With Cd shielding the quantities are an order of magnitude lower
5	0.09%	
10	0.26%	
20	0.66%	

cury on the thermal behaviour of Cu_3Au lay outside the scope and objective of this investigation. However, it is of interest that thermal neutron irradiation is probably the ideal method for introducing controlled amounts of mercury atomically dispersed in gold alloys for any such studies.

Blewitt and Coltman [4] reported an increased relaxation rate of disordered Cu_3Au at 200°C when irradiated in the Oak Ridge graphite reactor. Attributing this to the fast neutron component of the flux, they drew conclusions about the formation of Frenkel defects by fast neutron irradiation. It now appears, however, that relaxation of this type is caused by thermal neutrons. Unless screened out (which Blewitt and Coltman did not mention), one would expect a thermal flux to be present approximately equal to the fast flux. If we assume that a thermal flux of $\backsim 10^{12}$ n/cm²/sec. was associated with the fast flux of 1×10^{12} n/cm²/sec., the relaxation effect observed by Blewitt and Coltman could be accounted for by the thermal neutron effect alone.

Adams and Dugdale [3], and Glick *et al.* [5] have reported initial decreases in electric resistivity, followed later by a rise, in "reactor spectrum" neutron irradiations. It is seen from the present work that the use of "reactor spectrum" neutrons produces just this mixture of thermal and epithermal neutron effects. In fact, the only work reported so far in which the thermal neutron component appears to have been negligible was that of Siegel [6]. Since Siegel did not mention thermal neutron screening, it is to be assumed that his samples were irradiated very close to uranium fuel elements, or perhaps actually in a fuel element.

Siegel pointed out that the fast neutron disordering effect seemed larger than was to be expected on the basis of the mechanism proposed by Seitz [7], and suggested that a "thermal spike" mechanism (suggested earlier in another connection by Dessauer [8]) might be useful in explaining the effect. Lark-Horowitz [9] has pointed out that a neutron collision which gave 10^5 e.v. to a recoiling germanium atom (mass $\backsim 72$) would provide enough energy to instantaneously melt a region 10^{-6} cm. in radius, and that in $\backsim 10^{-12}$ sec. the region is quenched. On this picture one would visualise small volumes here and there throughout the ordered alloy suddenly converted to complete disorder. This picture can be quantitatively applied to the results of the present investigation.

Figure 8 illustrates the formation of disordered islands in the ordered matrix, and the fact that as

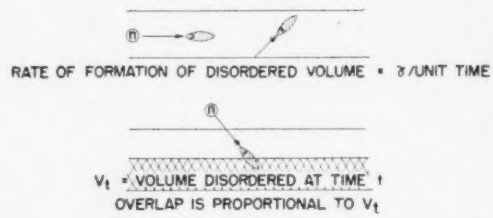

FIGURE 8. Illustration of temperature spike theory.

disordering proceeds by this mechanism, the islands will overlap; in fact, the overlap will be, on the average, proportional to the fraction of total volume already disordered.

$$(1) \qquad \frac{dV_t}{dt} = (1 - V_t)\gamma \text{ or } V_t = 1 - e^{-\gamma t}$$

where V_t is the fractional volume disordered at time t, and γ is the total fractional volume (in islands) produced per unit time.

This is clearly the right shape of curve to reproduce Figure 4.

One must make some assumption connecting V_t and C_t (the conductivity of the alloy). Landauer [10] has considered the problem of the conductivity of a body with spherical islands of another homogeneous material imbedded in it. Using Landauer's notation: if x_1 is the fraction of material of conductivity σ_1 and resistance ρ_1 and x_2 is the fraction of material of conductivity σ_2 and resistance ρ_2 then,

(a) $\rho_m = x_1\rho_1 + x_2\rho_2$ gives an upper limit for ρ_m,

(b) $\sigma_m = x_1\sigma_1 + x_2\sigma_2$ gives an upper limit for σ_m,

(c) $\sigma_m = \frac{1}{4}\{(3x_2 - 1)\,\sigma_2 + (3x_1 - 1)\,\sigma_1 + [((3x_2 - 1)\,\sigma_2 + (3x_1 - 1)\,\sigma_1)^2 + 8\sigma_1\sigma_2]^{\frac{1}{2}}\}$

is the Landauer equation.

If one uses equation (b) to connect the fractional volume disordered with electrical conductivity, one has

$$dx_2 = \frac{d\sigma_m}{\sigma_2 - \sigma_1} \qquad \text{at } x_2 = 0$$

whereas with (c),

$$dx_2 = \left(\frac{\sigma_2 + 2\sigma_1}{3\sigma_1}\right)\frac{d\sigma_m}{\sigma_2 - \sigma_1}.$$

The factor

$$\frac{\sigma_2 + 2\sigma_1}{3\sigma_1}$$

is easily calculated from Figure 9 to be 0.85.

The procedure adopted in this paper has been to use the simple relation (b) throughout, since it

enables an excellent fit to be obtained with the experimental results and enables

$$\left(\frac{d\sigma_m}{dt}\right)_{\substack{t=0\\x_s=0}}$$

to be obtained accurately and easily. It also provides an accurate relative comparison of the fractional volumes disordered in different experiments.

One could, if one wished, reduce all the final results by the Landauer factor (0.85) to obtain the exact fractional volumes disordered. However, this has not been done because it is very doubtful if the interpretation is really valid to this absolute accuracy.

Using our notation,

$$C_t = C_0V_0 + C_dV_d \tag{2}$$

where C_t = conductivity of sample at time t,
C_0 = conductivity in the ordered state,
C_d = conductivity in the disordered state,
V_0 = fractional volume of ordered material at time t,
V_d = fractional volume of disordered material at time t.

Combining equations (1) and (2):

$$C_t = C_0 + \Delta C\left\{1 - \exp\left[-\frac{1}{\Delta C}\left(\frac{\partial C_t}{\partial t}\right)_{t=0} t\right]\right\} \tag{3}$$

where $\Delta C = C_d - C_0$. In this equation C_0 and C_d are fixed; a further measurement of

$$\left(\frac{\partial C_t}{\partial t}\right)_{t=0}$$

or else a normalising at some point C'_t on the experimental curve fixes the equation completely.

To test this equation, curve A, Figure 4, was replotted to conductivity–time co-ordinates (Figure 9). Clearly $\Delta C = C_d - C_0 = 11.46 - 20.82 = -9.36$ mhos. The equation was normalised at the 40-day point requiring

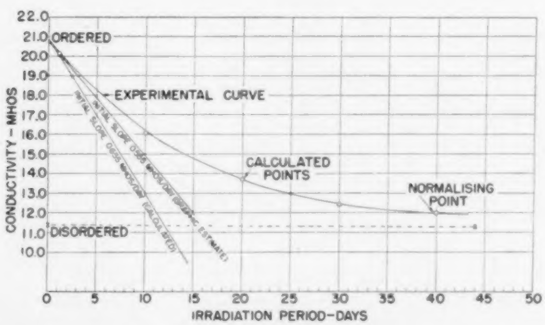

FIGURE 9. Quantitative test of theoretical equation: conductivity curve (Fig. 4 replotted).

$$\left(\frac{\partial C_t}{\partial t}\right)_{t=0} = 0.655 \text{ mhos/day},$$

and other points calculated as follows:

t days	C mhos
0	20.8
1	20.2
10	16.1
20	13.77
30	12.6
40	12.04 (normalisation point)
50	11.75

These points are plotted as circles in Figure 9, along with the calculated initial slope. The equation reproduces the experimental curve within experimental error over the whole course of the experiment.*

Implications of this equation are:

1. The rate of "spiking" was constant throughout the run and equal to the initial rate of disordering which equals

$$\frac{1}{\Delta C}\left(\frac{\partial C_t}{\partial t}\right)_{t=0} = 5.93\%/\text{day}.$$

2. Conductivity (at fixed temperature) is linearly proportional to the volume disordered.

3. The "spiking" rate is linearly proportional to the flux.

These implications will be discussed in detail one by one.

Using implication 1, the initial disordering rates can be calculated from the initial rates of change of resistance (Table I) and are listed in Table III.

Thus one concludes that the fast neutron damage in Position C amounts to the breaking of 28.9 per cent of the nearest neighbour "bonds" per day.

The implication 2 deserves further comment. In view of the fact that irradiation disordering produces a structure behaving identically with one produced by a quench from an appropriate temperature (see Figure 2), one must conclude, with Sykes, that this material, too, contains "in phase" nuclei which can readily grow at temperatures of 220°–250°C. This is, of course, true. The "nuclei" in the present example consist of the ordered walls of the "spiked" islands. The ordered structure can grow inward from the walls easily, being in phase at all points, since the original ordered mass was prepared by slow cooling and was "in phase" throughout.

*The slight increase in electric resistance in curve A, Figure 4, must be interpreted as indicating increased disorder. It is unlikely that the thermal quench used in preparing the disordered specimens was perfect.

TABLE III

Position	Nominal slow neutron flux (n/cm²/sec.)	Initial disordering Rate (%) $= \frac{1}{\Delta C} \cdot \frac{1}{R_0}\left[\frac{1}{R_0}\left(\frac{\partial R}{\partial t}\right)_{t=0}\right]$	
A	4×10^{12}	2.06	different reactor positions with uranium cylinders — fast (fission spectrum) neutrons
B	1.5×10^{13}	6.63*	
C	6×10^{13}	28.9	
Position C without U cylinder, with Cd shielding	6×10^{13}	2.00	Reactor flux, epithermal component

*If one uses, instead of the graphically estimated initial rate of change of resistance, the calculated initial rate of change of resistance using formula (3) fitted to the curve (Figure 9), 7.00 per cent is obtained. In general the rates calculated from the fitted equations are a little higher than one would estimate graphically.

The implication 3 that the initial disordering rates are linearly proportional to the nominal slow neutron flux, while consistent and reasonable, can not be considered strictly proved by the results as the neutron fluxes themselves are not well enough known. Moreover, according to the present picture, the initial disordering rate should, in fact, not be strictly proportional to the neutron flux, but rather to the energy transmitted by neutron collisions to the recoiling atoms.

Rather than try to relate the effects observed too closely to other equally involved flux measurements, it seems best to concentrate experimentally on whether neutron flux as measured by the disordering effect on Cu_3Au bears a direct relation to irradiation damage in other systems; it seems likely that the disordering effect of neutron irradiation on Cu_3Au will be a useful measure of potential damage to other materials.

It is of interest to estimate the average volume of a disordered island. If we put, approximately,

$\sigma = 5$ barns (σ = average total scattering cross-section for fast neutrons in Cu_3Au),

$F = 1.5 \times 10^{13}$ n/cm²/sec.,

the probability of an atom being struck is approximately 6.4×10^{-6}/day. Since the experimental probability of an atom being disordered at this flux is 0.059/day (implication 1), a single temperature spike must contain $\backsim 10^4$ atoms.

Conclusions

The following conclusions may be drawn:

1. Ordered Cu_3Au is rapidly disordered in a $\frac{1}{4}''$ wall uranium cylinder in the NRX reactor. The disordered and partially disordered states are indistinguishable, to a first approximation, from states produced thermally.
2. Disordered Cu_3Au is little affected when irradiated in a uranium cylinder, but the electric resistance drops in a thermal neutron flux. The latter effect is probably due to the formation of mercury as a third component, and consequent changing of the ordering kinetics of the alloy.
3. The neutron irradiation disordering characteristics of Cu_3Au enable it to be used as a type of reactor flux monitor—particularly for epithermal and fast neutrons—or for thermal neutrons if used with a uranium cylinder neutron converter. Its value as a flux monitor probably will be greatest in neutron irradiation damage studies.

Acknowledgment

The continued assistance and co-operation of the Engineering and Operating Branches of Atomic Energy of Canada Limited were essential in building and using the irradiation facilities needed for this work.

References

1. Sykes, C. and Evans, H. J. Inst. Metals, **58** (1936) 255.
2. Sykes, C. and Jones, F. W. J. Inst. Metals, **59** (1936) 257.
3. Adams, J. and Dugdale, R. A. Nature, **168** (1951) 582.
4. Blewitt, T. H. and Coltman, R. R. Phys. Rev., **85** (1952) 582.
5. Glick, H. L., Brooks, F. C., Witzig, W. F., and Johnson, W. E. AECD-3332 (U.S. report), 1952.
6. Siegel, S. Phys. Rev., **75** (1949) 1823.
7. Seitz, F. Discussions of the Faraday Soc., **5** (1949) 271.
8. Dessauer, F. Z. Phys., **12** (1923) 38.
9. Lark-Horowitz, K. Semi-Conducting Materials (London, Butterworth, 1951), p. 55.
10. Landauer, R. J. Appl. Phys., **23** (1952) 779.

THE EFFECTS OF NEUTRON IRRADIATION IN THE NRX REACTOR ON THE ORDER-DISORDER ALLOY CuAu*

L. G. COOK and R. L. CUSHING†

The irradiation of CuAu with neutrons causes two separable effects. Disordering is caused by fast neutrons, and is negligible with thermal neutrons; the rate is approximately 0.7 of the rate for Cu_3Au. A secondary effect, probably ordering, is caused by thermal neutrons, very likely through the agency of the mercury formed, as with Cu_3Au. The effect is much more pronounced with CuAu than with Cu_3Au, probably owing to the fact that the initial "freezing in" temperature is about 80°C instead of 200°C.

LES EFFETS D'IRRADIATION AVEC DES NEUTRONS DANS LE RÉACTEUR NRX SUR LA TRANSFORMATION ORDRE-DÉSORDRE DANS L'ALLIAGE CuAu

L'irradiation de CuAu avec des neutrons cause deux effets séparables. Les neutrons rapides causent une mise en désordre; la vitesse est approximativement 0,7 de la vitesse dans le cas de Cu_3Au. Les neutrons thermiques causent un effet secondaire, probablement une mise en ordre, en toute vraisemblance par l'intermédiaire du mércure formé, comme dans le cas de Cu_3Au. Cet effet est beaucoup plus prononcé dans le cas de CuAu que dans celui de Cu_3Au, probablement à cause du fait que la température de "congélation" est d'environ 80°C au lieu de 200°C.

DIE WIRKUNG VON NEUTRONENBESTRAHLUNG IM NRX REACTOR AUF DEN ORDNUNGSGRAD VON CuAu

Die Bestrahlung von CuAu mit Neutronen führt zu zwei verschiedenen Effekten. Schnelle Neutronen führen eine Verminderung der Ordnung herbei; bei thermischen Neutronen kann dieser Effekt vernachlässigt werden. Die Geschwindigkeit ist etwa 0,7 der Geschwindigkeit der Reaktion Cu_3Au. Ein sekundärer Effekt, wahrscheinlich Ordnen, wird durch thermische Neutronen hervorgerufen, sicher auf dem Umweg über das gebildete Quecksilber wie im Falle Cu_3Au. Dieser Effekt ist im CuAu sehr viel stärker als im Cu_3Au, wahrscheinlich weil die "Einfrierungstemperatur" hier etwa 80°C im Gegensatz zu 200°C ist.

Introduction

The behaviour of Cu_3Au when irradiated with neutrons in the NRX reactor has been described in a previous paper [1]. In this paper the comparable behaviour of CuAu is described.

CuAu was selected as the first example for comparison with Cu_3Au because, although the elements are the same, the mass of the average atom is different.

Experimental Techniques

CuAu wire, 23.6 per cent Cu and 76.4 per cent Au by weight, 0.0157 in. dia., was supplied by Johnson, Matthey and Mallory in the cold drawn condition. All samples were annealed at 800°C in argon for 30 min. to remove the major effects of the cold drawing operation.

The technique of measurement and irradiation was identical with that described for Cu_3Au [1]. The heat treatment programs were:

(a) To prepare disordered samples, air quench from 500°C.

(b) To prepare ordered samples,
16 hours at 425°C,
24 hours at 415°C,
24 hours at 400°C,
72 hours at 375°C,
furnace cooled to room temperature.

*Received April 2, 1953.
†Chemistry Branch, Atomic Energy of Canada Limited, Chalk River, Ontario, Canada.

Results

I. *Resistance-Temperature Curves for* CuAu *Wire*

A sample of CuAu wire in the disordered state was heated at $1.66°C \pm 0.16°C$/min. to 475°C, then slowly cooled and the electric resistance measured (Figure 1, curves *A* and *B*). The sample was then re-heated to 425°C, cooled to temperature *T*, and quenched to point *P*. Then the heating curve *C* was measured.

The temperature at which the metastable disordered alloy "thaws out" is about 80°C, as compared to over 200°C for Cu_3Au. The initiation temperature for "thawing out" is lower for a partially ordered sample (curve *C*) than for a fully disordered sample (curve *A*) (similar to Cu_3Au). The initial rates of change of resistance at fixed temperatures were as follows:

	Temperature	Relaxation rate (% of resistance/day)
fully disordered	100°C	<0.01
	125°C	0.4
partially disordered	75°C	<0.01
	90°C	1.35

II. *Comparison of Irradiation Results for Fast (Fission Spectrum) and "Reactor Spectrum" Neutrons*

A comparison of the behaviour of the electric resistance of the ordered and disordered CuAu wires, in "fission spectrum" and "reactor spectrum" neutrons, is shown in Figure 2.

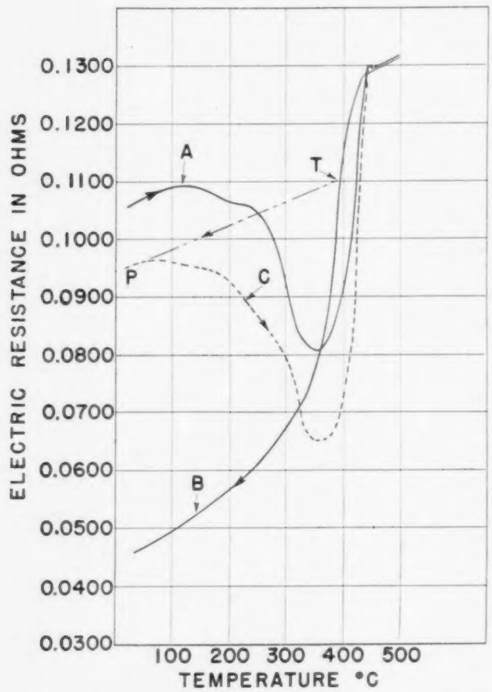

FIGURE 1. Electric resistance versus temperature: heating and cooling rate 1.66 ± 0.16°C/min.

The same general effects occurred as were observed with Cu_3Au. Although the initial dip in resistance is not observed in disordered Cu_3Au irradiated with fission spectrum neutrons with Cd shielding, it does occur with CuAu (curve *A*). In "reactor spectrum" neutron irradiation the dip was much greater (curve *C*) but unfortunately the sample temperature was also higher, so it is uncertain how the increase should be apportioned between the two factors.

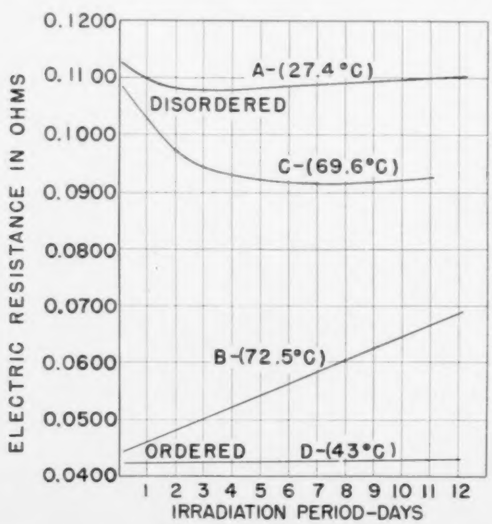

FIGURE 2. CuAu irradiations: A and B, fission spectrum neutrons with Cd shield; C and D, reactor spectrum neutrons without Cd shield.

The ordered sample, in "reactor spectrum" irradiation (curve *D*), does not change its resistance as the irradiation proceeds; the small rise in resistance due to disordering and the dip due to thermal neutrons must just compensate (in Cu_3Au they did not). The ordered sample in "fission spectrum" irradiation (curve *B*) increases its resistance linearly, as with Cu_3Au.

In order to ascertain whether there was any trace of dip in resistance in the very early stages of the "fission spectrum" irradiations, a set of charts was examined in detail over the first 20 hours (Figure 3). No trace of dip is detectable in the ordered samples; the disordering begins at its proper rate the instant irradiation begins. The dip in disordered samples, however, takes 5–6 hours to reach its maximum rate of fall.

III. *Comparison of Rates of Disordering*

The rates of disordering, calculated from graphically estimated initial slopes obtained in various reactor positions, are given in Table I.

Discussion of Results

There are two distinct and opposed effects of neutron irradiation on CuAu alloy, and they are very similar to the effects observed with Cu_3Au.

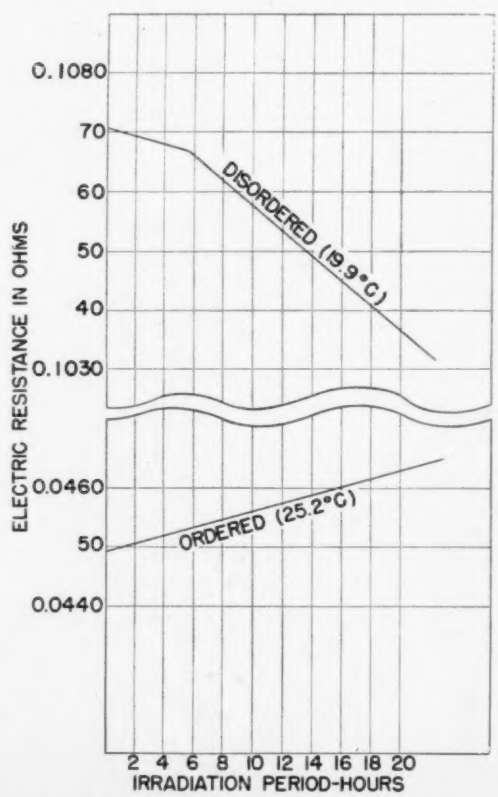

FIGURE 3. Irradiation with fission spectrum neutrons with Cd shield.

TABLE I

	Position		
	A	B	C
Position	Near centre of reactor	Inside callandria near its edge	Near centre of reactor
Nominal thermal neutron flux in that position	6×10^{13} n/cm²/sec.	1.5×10^{13} n/cm²/sec.	6×10^{13} n/cm²/sec.
Type of uranium cylinder used	None	1.4″ O.D. ¼″ wall } Cd shield	1.4″ O.D. ¼″ wall } Cd shield
Initial rate of change of electric resistance of ordered CuAu with irradiation time	0	2.88%/day	4.69%/day
Initial rate of disordering*	0	4.62%/day	7.60%/day

*See Cu_3Au paper [1] for method of calculation.

The initial dip in electric resistance in disordered specimens is more pronounced with CuAu than with Cu_3Au and also sensitive to the presence of thermal neutrons and/or higher sample temperatures during irradiation. The fact that the dip takes a few hours to establish itself (Figure 3) is consistent with the hypothesis that the formation of mercury is the cause—for the mercury is formed through Au^{198} (2.69 days half-life) and it requires several hours for the rate of formation of mercury to become appreciable. It is possible that the slight initial dip in resistance, occurring over the first 6 hours, is due to the formation of traces of Zn from the Cu. Since the Zn is formed through 5 sec. Cu^{66} and 12.8 hour Cu^{64}, it increases more rapidly during the first few hours than the Hg^{198} which comes through 2.69 day Ru^{198}.

The total absence of any detectable dip in resistance in the initial stages of the fast neutron irradiation of ordered wire is also consistent; the disordering process should, in fact, commence immediately the irradiation begins, at which stage no mercury will have been formed and there should be no mutual interference.

It is of special interest to compare the present results quantitatively with those for Cu_3Au. Unfortunately the irradiations described in the present paper and the previous irradiations of Cu_3Au had to be carried out in different positions in the reactor.

In only one set of irradiations were the conditions and locations identical, and for these

Cu_3Au initial disordering rate: 6.63%/day
CuAu initial disordering rate: 4.62%/day

A strict comparison with samples of Cu_3Au and CuAu in the same position at the same time is clearly desirable to confirm this relation; also experiments with other order-disorder systems of widely different atomic weights should be done.

Conclusions

1. Ordered CuAu is rapidly disordered in a ¼″ wall uranium cylinder in the NRX reactor. The rate appears to be approximately 0.7 of the rate for Cu_3Au.

2. Disordered CuAu shows a drop in electric resistance when irradiated in the NRX reactor; the drop is sensitive to the presence of thermal neutrons and does not reach its maximum rate of drop until a few hours after irradiation begins. This effect is probably due to the formation of mercury as a third component, and consequent changing of the ordering kinetics of the alloy.

Acknowledgment

The continued assistance and co-operation of the Engineering and Operating Branches of Atomic Energy of Canada Limited was essential in building and using the irradiation facilities needed for this work.

Reference

1. Cook, L. G. and Cushing, R. L. Acta Met., **1** (1953) 539.

ENERGY ABSORPTION AND X-RAY STUDIES OF KINK FORMATION IN ZINC SINGLE CRYSTALS*

E. I. SALKOVITZ† and J. S. KOEHLER‡

Kink formation in single crystals of zinc was studied dynamically and statically in such a manner that it was possible to measure the energy absorbed during the process. The experiments reveal that two consecutive stages are involved.

(*a*) A uniform bending of the crystal takes place accompanied by an absorption of energy. For the crystals with the pole of the basal plane at about 75° from the specimen axis the energy absorbed was 2.6×10^5 ergs; for 83° crystals the energy absorbed was 4.0×10^5 ergs. Laue patterns taken after the bending had occurred show asterism and a slight rotation of the basal plane.

(*b*) With an absorption of additional energy a sharp kink is produced. For the 75° crystals the additional energy was $.7 \times 10^5$ ergs; for the 83° crystals the additional energy was 1.2×10^5 ergs. After the kink was formed the sections on either side of the kink became straight and relatively parallel. Asterism from these sections *decreased* in going from stage (*a*) to stage (*b*). Severe asterism was obtained from the kink.

X-ray studies show, in agreement with Hess and Barrett, that the basal plane in the kink is rotated relative to the basal plane in the rest of the specimen, about an axis within the basal plane which is perpendicular to the active slip direction. In addition, the plane has bent about this axis. Finally, a qualitative dislocation model is presented which also is quite similar to that of Hess and Barrett.

UNE ÉTUDE AUX RAYONS X ET DE L'ABSORPTION D'ÉNERGIE RELATIVE À LA FORMATION DE PLIS (KINKS) DANS DES MONOCRISTAUX DE ZINC

La formation de plis dans des monocristaux de zinc a été étudiée de façon à pouvoir mesurer l'énergie absorbée pendant le processus. Ces expériences indiquent l'existence de deux étapes consécutives.

(*a*) Une flexion uniforme a lieu, accompagnée d'une absorption d'énergie. Dans le cas des cristaux dont le pôle du plan de base se trouve à une distance d'environ 75° de l'axe de l'éprouvette, l'énergie absorbée était de $2{,}6 \times 10^5$ ergs; pour les cristaux dans lesquels la même distance est de 83°, l'énergie absorbée était de $4{,}0 \times 10^5$ ergs. Des diagrammes de Laue, pris après la flexion, montrent de l'astérisme et une légère rotation du plan de base.

(*b*) Avec l'absorption d'une énergie supplémentaire, un pli très prononcé est produit. Pour les cristaux à 75° l'énergie supplémentaire était de $0{,}7 \times 10^5$ ergs; pour les cristaux à 83° l'énergie supplémentaire était de $1{,}2 \times 10^5$ ergs. Après la formation du pli, les sections des deux côtés du pli devenaient droites et relativement parallèles. L'astérisme de ces sections *diminuait* en allant de l'étape (*a*) à l'étape (*b*). Un fort astérisme a été obtenu du pli.

Des études aux rayons X montrent, en accord avec Hess et Barrett, que le plan de base dans le pli est tourné par rapport au plan de base dans le reste de l'éprouvette, autour d'un axe contenu dans le plan de base et perpendiculaire à la direction active de glissement. En plus, ce plan a fléchi autour de l'axe en question. Finalement un modèle qualitatif de dislocations, similaire à celui de Hess et Barrett, est présenté.

ENERGIEABSORPTION UND RÖNTGENOGRAPHISCHE STUDIEN DER "KNICKBILDUNG" ("KINK FORMATION") IN ZINKEINKRISTALLEN

Knickbildung ("kink formation") in Zinkeinkristallen wurde dynamisch und statisch in einer Weise untersucht, die es gestattete, die während des Vorgangs absorbierte Energie zu messen. Die Versuche zeigten die beiden auf einander folgenden Stadien, die den Vorgang ausmachen.

(*a*) Eine gleichförmige Biegung des Kristalles findet unter Absorption von Energie statt. Für Kristalle, deren Normale zur Basisebene etwa 75° von der Achse der Probe entfernt war, betrug die absorbierte Energie etwa $2{,}6 \times 10^5$ erg. Für 83° Kristalle war die Energie etwa $4{,}0 \times 10^5$ erg. Laue Aufnahmen nach erfolgter Biegung zeigten Asterismus und eine leichte Drehung der Basisebene.

(*b*) Unter weiterer Energieabsorption entsteht ein scharfer Knick ("kink"). Für 75° Kristalle betrug die zusatzliche Energie $0{,}7 \times 10^5$ erg, für 83° Kristalle $1{,}2 \times 10^5$ erg. Nachdem sich der Knick ("kink") gebildet hatte, wurden die Bereiche zu beiden Seiten des Knickes grade und annähernd parallel. Der Asterismus in diesen Gebieten nahm beim Übergang von (*a*) nach (*b*) *ab*. Der Knick selbst zeigt starken Asterismus.

Röntgenuntersuchungen zeigten in Übereinstimmung mit Hess und Barrett, dass die Basisebene des Knickes im Vergleich zu den Basisebenen im übrigen Kristall gedreht sind und zwar um eine Achse, die senkrecht zur wirksamen Gleitrichtung steht. Ausserdem ist die Ebnene um diese Achse gebogen. Ein qualitatives Versetzungsmodell wird beschrieben, das dem von Hess und Barrett ähnlich ist.

I. Introduction

Zinc and cadmium have crystallographic structures which are not quite perfectly close-packed hexagonal because of elongated C axes; this greatly influences the plastic behavior of these two metals. If a compressive stress is exerted parallel to the basal plane, slip is not to be expected to occur readily since the necessary resolved shear stress would be extremely high. Nor is twinning to be expected, for if twinning did occur there would be an elongation of

*Received April 2, 1953.

†Carnegie Institute of Technology, Pittsburgh, Pennsylvania, U.S.A. Now at Naval Research Laboratory, Washington, D.C.

‡Carnegie Institute of Technology. Now at Department of Physics, University of Illinois, Urbana, Illinois.

several per cent in the direction of the compressive stress.

In 1942, Orowan [1] found that single crystals of cadmium whose basal planes were nearly parallel to the specimen axis suddenly collapsed when compressed axially by forming "kinks" in a manner similar to that observed by O. Mügge [2] in cyanite. These kinks were characterized by having sharp ridges and regular curvatures. Orowan suggested that the mechanism of kinking consisted of tilting lamellae, with the amount of glide between neighboring lamellae equal to an integral multiple of the lattice period in the direction of glide, and that the boundary on each side of a kink band consisted of a non-crystallographic plane which bisected the angle between the glide planes on either side of the kink boundary. Presumably then, a concentration of dislocations existed along the boundary plane.

In 1949, Hess and Barrett [3] studied kinking in zinc. They suggested that sudden buckling as described by Orowan was characteristic only when a "soft" machine was used; in a "stiff" machine one should get kinks gradually. They further suggested that the kinking process consists of a progressive rotation of the lattice within a band as deformation proceeds. Hess and Barrett measured rotations from a few degrees to over 80° and concluded that:

1. Rather than being a new type of deformation, kink bands are deformation bands resulting from the ordinary slip process.

2. In a simple kink each boundary is initially a surface containing the direction in the glide plane that is normal to the active glide direction. After severe bending, deviations occur.

3. Kink band formation may be accounted for by assuming that pairs of dislocations are generated between the boundaries by buckling flexures. Dislocations of one sign align themselves in one plane; dislocations of opposite sign in another. The planes of dislocations move apart until stopped by defects or opposing stresses. Successive planes of dislocations follow similar paths and build up continuously increasing angles of bend.

Neither paper gave quantitative data relative to loads applied or time required for formation of kinks. Since a kink band, at least in its initial stage, appears to be a relatively simple phenomenon it may have a relatively simple explanation such as proposed by the authors of these previous papers. Quantitative data, particularly energy data, would be of value in deriving a dislocation model of the phenomenon. The authors' program of research carried out in 1949–50, consisted of three parts: (1) ballistic data gave the energy absorbed during kink formation of zinc single crystals; (2) static compression data gave the necessary load to produce kinks and enabled crude stress-strain curves to be drawn for kink formations; and (3) X-ray studies indicated the nature of the deformation in the kink.

II. Growth and Preparation of Specimens

Single crystals of zinc of 99.999 per cent purity were grown in two ways, both of which were modifications of the Bridgman method. One group was grown in pyrex glass tubing and was given Arabic numerals; the other group grown in graphite crucibles was given Roman numerals. The two groups of crystals behaved similarly in these experiments. As grown the crystals ranged in length from 5 to 20 cm. and were about 6 mm. in diameter.

Orientations of the crystals were determined by taking back-reflection Laue patterns. Those crystals with angle ψ equal to 73° or more were selected for the kinking experiments. (Here ψ is the angle between the specimen axis and the pole of the basal plane.) The selected crystals were placed in wax molds and cut into segments usually about an inch in length using a jeweler's saw with a very fine blade. The ends were then polished on emery papers 2/0, 3/0, and 4/0. Boas and Schmid [4] have shown by X-ray patterns that grinding and polishing produces a worked region 0.30 mm. thick in zinc and 0.46 mm. thick in cadmium. To remove the cold worked region a non-selective etch consisting of 200 g. CrO_3, 15 g. Na_2SO_4 and 1000 cc. water was used which permitted a millimeter of the ends to be etched away, leaving them free of pits and relatively plane.

III. Impact Experiments

The energy absorbed in producing kinks was measured by means of a pair of ballistic pendulums in a manner similar to that described by B. Chalmers [5] for measuring the energy required to twin single crystals of tin. Two cylindrical pendulums were suspended 185 cm. from the ceiling as shown in Figure 1. Each pendulum was supported by four wax-coated nylon fish lines whose lengths could be varied by means of turn-buckles. The pendulum on the right in the photograph, called the holder, had a cylindrical cavity at one end 1 cm. in diameter and 7 cm. deep. Spacers of various lengths could be placed in the cavity so that when a short crystal was inserted, one end of the crystal would still protrude. A neoprene gasket lined the cylindrical wall of the cavity permitting the crystal to be secured axially in place against the end of the cavity by means of three

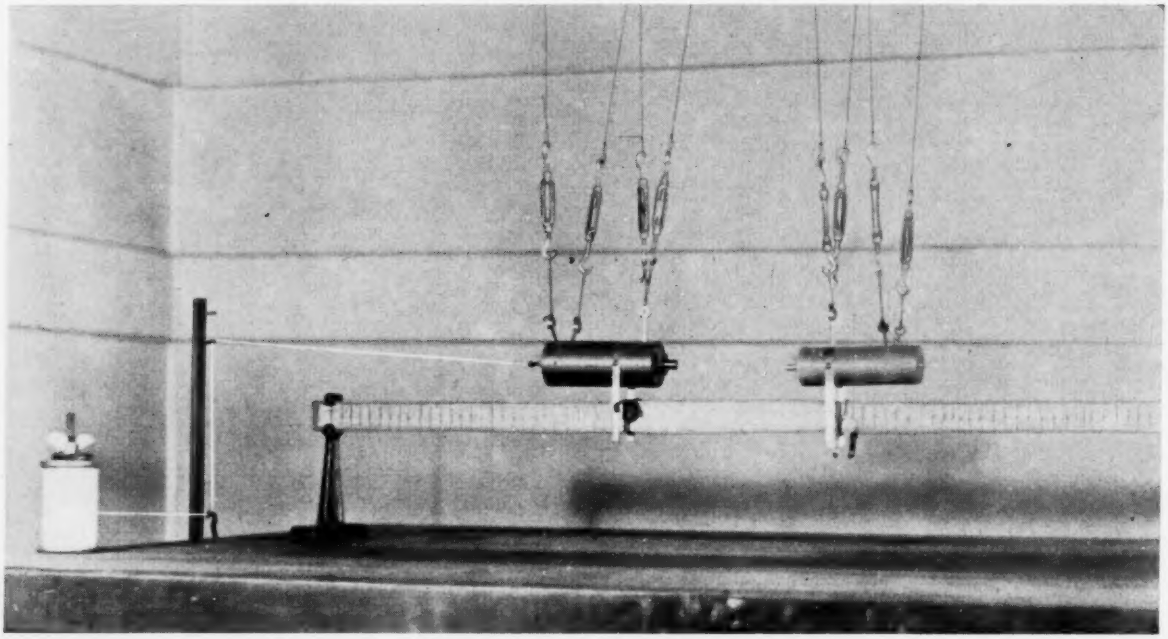

FIGURE 1. Ballistic pendulum.

set screws. The other pendulum, called the striker, had a bolt projecting from its forward end so that the striker pendulum could be effectively lengthened or shortened in the horizontal direction until good contact with the crystal was made in the equilibrium position. As seen in the figure, each pendulum carried a pair of legs which moved position indicators along a meter stick. In all, five different striker pendulums and two different holder pendulums of varying masses were used. The orientation and dimensions of the crystals used in the experiment are given in Table I.

Data were taken in the following manner: After a sample had been centered in the holder and the two pendulums aligned, their equilibrium positions were read on the meter stick. The striker was then drawn back to a predetermined position by means of a thread looped over a hook at the center of the far end of the pendulum (see photograph). The distance between this predetermined position and the equilibrium position was called the initial displacement of the striker. The striker was released by burning the thread and the rebound positions of the striker and holder were recorded after impact giving the corresponding rebound displacements. With a polycrystalline zinc sample in place, striker and holder rebound displacements were recorded for various initial displacements. Calibration curves were then drawn showing that the rebound of the striker as well as the rebound of the holder were proportional to the initial displacement of the striker. Whenever pendulums were changed new calibration curves were made. Frequent checks of these calibrations showed little variation over long periods of time if the pendulums were properly aligned.

In Figure 2 is a typical calibration curve of initial displacement of holder versus rebound displacement of striker for a polycrystalline specimen and typical data taken on a single crystal (Zinc 4–a: the letter *a* indicates the first segment cut from the parent crystal 4). A similar curve was obtained for the re-

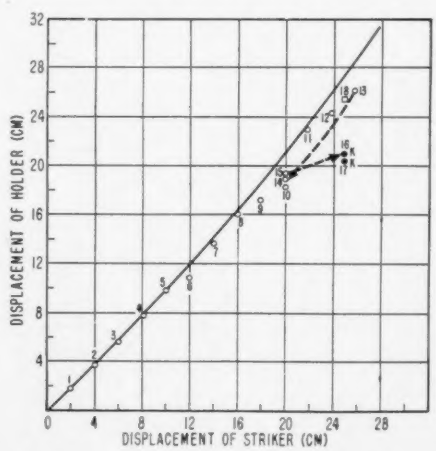

FIGURE 2. Calibration and data on zinc crystal 4–a: mass of striker, 1875 gm.: mass of holder, 306 gm. ○—Before kinking; ● —kinking; □—after kinking. The numbers refer to the order in which the impacts were made.

TABLE I
CRYSTAL ORIENTATION AND DIMENSIONS

Crystal	ψ	Length cm	Diameter cm	Volume cm^3
A-2	73^0	2.61	.39	.432
2-b	75^0	5.01	.55	.730
2-c	75^0	3.04	.55	.552
1-a	75^0	2.66	.57	.652
1-b	75^0	2.15	.57	.539
1-c	75^0	2.66	.57	.652
1-d	75^0	2.54	.56	.621
1-c	75^0	2.54	.55	.596
1-f	75^0	2.51	.53	.561
C-2	86^0	2.53	.40	.426
B-1	83^0	2.52	.41	.433
4-a	83^0	2.41	.52	.511
4-b	83^0	2.55	.52	.541
4-c	83^0	2.48	.51	.526
3-a	82^0	2.58	.46	.433
3-b	82^0	1.90	.51	.403
3-d	82^0	2.50	.51	.531
5-a	83^0	5.06	.51	1.118
5-b	83^0	2.55	.51	.544
Cd-1	80^0	2.09	.50	.410

bound displacement of the striker. The open circles are data taken on 4–a prior to kinking. The solid circles represent readings when kinking occurred; the open square is a reading subsequent to kinking which did not produce further kinking. It will be seen that the first five points lie on the calibration curve, but for striker displacements of 12 cm. or more the points lie below the curve for the polycrystalline sample. This implies an absorption of energy. At a striker displacement of 26 cm., no signs of kinking were found, but the crystal appeared slightly bowed. Two additional impacts were made with a displacement of 20 cm. with no kinking. A third impact with a displacement of 25 cm. however, produced a kink, indicated by the solid circle. A fourth impact of 25 cm. produced a second kink adjacent to the first. A fifth impact, did not produce further kinking, indicated by the open square.

IV. Discussion of Impact Data

Figure 3 shows several kinked crystals, some with secondary and complex kinks similar to those described by previous writers. (The crystals had been handled and etched several times with HCl before photographing, to remove oxide films, and were therefore pitted.)

FIGURE 3. Examples of kinked crystals.

After impact data had been obtained on several crystals it became apparent that before kinking occurred, a certain amount of energy was absorbed which went into plastic deformation. X-ray evidence seemed to indicate that basal slip producing a change in orientation of about 2° took place in the pre-kinking stage. Unfortunately, 2° was about the limit of accuracy of the X-ray orientation process. Macroscopic observation, however, definitely revealed that the crystals were slightly bent or bowed before a kink was produced. In several cases the angle of bend was measured by means of a J & L profile comparator and was found to range from 1° to 4°.

The radius of curvature of the bend in the various crystals ranged from 35 cm. to 76 cm. Using the comparator the kink angle was also measured and

found to range from 6° to 15°. X-ray Laue patterns showed that within the kink the basal plane rotated by amounts comparable to the kink angle measured with the comparator. Additional X-ray results will be discussed below in more detail.

Table II is a compilation of the significant impact data. Columns 2 and 3 give the masses of the striker and holder pendulums used with each crystal. In column 4 are listed the number of impacts delivered to the sample before kinking occurred: for example, crystal 1–c required 14 impacts during which the total energy of impacts calculated for the instant of impact was 2.6×10^6 ergs (column 5). Column 6 gives this energy divided by the volume of the crystal. Columns 7 and 8 show that a total of 1.2×10^5 ergs or 1.8×10^5 ergs/cc. was absorbed by the crystal. For crystal 1–c, velocities ranging from a lowest velocity (l) of 5 cm/sec. to a highest velocity (h) of 60 cm/sec. were imparted to the striker (column 9). The corresponding momenta are shown in column 10. A bowing of 1° was found in this crystal after the 13th impact. The 14th impact made little change; the 15th, at a velocity of 64 cm/sec. (column 9), produced a kink 0.3 cm. long. The energy of the impact divided by the volume of the specimen was 2.0×10^6 ergs/cc. (column 13); the energy absorbed was $.5 \times 10^5$ ergs (column 14). Columns 15 and 16 give the absorbed energy per unit volume of sample, $.8 \times 10^5$ ergs/cc. and the absorbed energy per unit volume of kink, 1.0×10^6 ergs/cc. for this crystal. Finally, the last two columns list respectively the sum total energy required before and during the kinking process, 1.7×10^5 ergs, and this energy per unit volume of sample, 2.6×10^5 ergs/cc.

Crystals with orientations of 73° and 75° were considered jointly. In the discussion of these crystals which follows, A–2, 1–b, and 2–c will be omitted temporarily. With the six remaining 75° crystals it was necessary to first plastically deform the crystals before any kinking could be produced. Plastic deformation, which exhibited itself in a bending of from one to four degrees, was accompanied by an average energy absorption of 2.6×10^5 ergs or 4.0×10^5 ergs/cc. (see Table III). Of the total kinetic energy of impact of the pendulum, only 3.2 per cent was used in producing the bend. The nine 83° crystals absorbed an average of 4.0×10^5 ergs before kinking or 7.4×10^5 ergs per unit volume of specimen. Of the total kinetic energy of the pendulum 3.3 per cent was used in producing the bend in good agreement with the 75° crystals. Table III shows that when the first kink was produced, $.7 \times 10^5$ ergs and 1.2×10^5 ergs were absorbed on the average by the 75° and 83° crystals respectively; in terms of energy per unit volume of sample this was 1.0×10^5 ergs/cc. and 2.2×10^5 ergs/cc., or in terms of energy per unit volume of kink, $.9 \times 10^6$ ergs/cc. and 2.5×10^6 ergs/cc. For the 75° crystals the sum total energy absorbed before and during kinking was 3.3×10^5 ergs, with a spread from 1.4×10^5 ergs to 5.8×10^5 ergs; the corresponding energy per unit volume of sample was 5.0×10^5 ergs/cc., with a spread from 2.6×10^5 to 8.0×10^5 ergs/cc. For the 83° crystals the total energy was 5.4×10^5 ergs with a spread from 1.4×10^5 to 10.2×10^5 ergs/cc.; the energy per unit volume was 9.6×10^5 ergs/cc. with a spread of from 2.2×10^5 ergs/cc. to 18.8×10^5 ergs/cc. The energy absorbed during the two processes is 4.2 per cent of the total kinetic energy of impact for the 75° and 3.8 per cent for the 83° crystals. For 83° orientations there appears to be a larger average energy absorption for the total process than that for the 75° orientations. This is reasonable because the shear stress required for slip in the former case is larger than in the latter. The slenderness ratio (length to diameter), which ranged from 3.1 to 11.6, as well as the crystal length itself, seemed to have no marked influence on the energy absorption.

In order to verify the conclusion that the crystal had to undergo plastic deformation, manifested by bending, before kinking could occur, the following experiment was conducted. An effort was made to give crystal 1–b more than enough energy for the combined processes of bending and kinking. An impact energy of 25.6×10^6 ergs/cc. was delivered and the crystal was found to have a $3\frac{1}{2}$° bend but no kink; the energy absorbed was 37.5×10^5 ergs/cc. or about 14 per cent. The maximum value in column 18 for the other 75° crystals is 8.0×10^5 ergs. Thus, crystal 1–b had absorbed more than four times the energy required to produce bending in the other crystals. A Laue pattern made before the impact showed very sharp spots; a pattern made after the impact showed extreme asterism, indicative of the deformation. Apparently then, two distinct processes occur. First the crystal definitely must bend. Then additional energy must be supplied to produce the kink. The two processes cannot be carried out simultaneously.

It is interesting to examine the behavior of crystals A–2 and B–2. Crystal A–2 (73°) absorbed 1.9×10^5 ergs/cc. in seven impacts and was bowed slightly. Crystal B–2 (83°) absorbed 1.0×10^5 ergs but did not seem to be bowed. In neither case was there any sign of kinking. Apparently, in the case of A–2 energy sufficient only to bend the crystal had been pro-

vided; in the case of B–2, however, the energy provided was insufficient to produce macroscopically detectable bending. For the velocities used in these experiments the fore energy (bending energy) seemed independent of the velocity of impact, but the additional energy required to produce the kink increased as the velocity of impact increased.

Because it is generally stated that zinc has a very rapid recovery rate, the question arose of whether one is justified in simply adding together the energy contributions made during individual impacts. Several experiments were performed to evaluate the effect of recovery upon the impact data. First, 1–b was set aside for 26 days after it had received the impact discussed above. At the end of this period the crystal was given a lighter impact during which only $.8 \times 10^5$ ergs/cc. was absorbed. Upon the next impact a kink was produced with an energy absorption of 0.6×10^5 ergs/cc. of sample, which is within the range of the data for the 75° crystals already considered. If the crystal had recovered completely in this 26 day period, an additional 4.0×10^5 ergs/cc. of energy instead of only $.8 \times 10^5$ ergs/cc., should have been absorbed before kinking occurred. The value in column 18 is large of course because of the large initial impact energy.

Further evidence that recovery was not an important factor in these experiments appears in results obtained with three other crystals. Crystal 2–C had been bent during the polishing process and was set aside for several weeks. When impact tests were finally made on the crystal, a single impact was given with a consequent energy absorption of $.5 \times 10^6$ ergs/cc. accompanied by slightly more bending. The next impact produced a kink, the data for which are in the table. An additional impact produced two additional kinks. The total energy absorbed per unit volume before and during the production of the first kink was 1.7×10^5, an amount smaller than any other similar reading. Apparently some of the necessary plastic deformation preceding kinking was present before the first impact.

Crystals 3–a and B–1 (both 83°) were also tested for evidence of recovery. Crystal 3–a exhibited a 1°45′ bend after having absorbed 1.8×10^5 ergs/cc. It was set aside for 48 hours and then four impacts were applied with a subsequent absorption of $.9 \times 10^5$ ergs/cc. The crystal now had a 4° bend. If complete recovery had occurred in the intervening time, considerably more than $.9 \times 10^5$ ergs/cc. of energy should have been absorbed in the second group of impacts. Similarly crystal B–1 was set aside after it had absorbed 1.8×10^5 ergs/cc. without any sign of bending. Four impacts delivered 48 hours later caused no bending although $.5 \times 10^5$ ergs were absorbed. Three subsequent impacts produced gradual bending of a small amount with an absorption of $.2 \times 10^5$ ergs/cc. The sum of the energies absorbed was 2.5×10^5 ergs/cc. of which 72 per cent had been absorbed during the first series of impacts, again indicating that very little recovery had taken place. It should be noted that the time intervals between successive impacts with several crystals (4–a, 1–d, etc.) was of the order of one or two minutes so that a complete run was made in an hour or two; with others as described above, the elapsed time for a run was 48 hours. The quantitative data for the latter crystals did not differ appreciably from the data for the former.

These recovery experiments seem at variance with the findings of Haase and Schmid [6] who stated that partial recovery occurred in 30 seconds and complete recovery in 24 hours when a tensile load was removed from single crystals of zinc. An examination of their data shows that the crystals studied had orientations near 45°. This indicates that an orientation dependence may exist for recovery of hexagonal metals or that recovery is very strongly dependent upon the nature and amount of deformation.

In Table IV is recorded the angle of bending for several crystals as measured by the comparator. In several cases the bending was observed but not measured. In addition to the comparator measurements, evidence of bending lies in the fact that small surface twins frequently appeared along only one side of a crystal. As stated earlier, a compressive stress applied parallel to the basal plane in a zinc crystal will not cause the crystal to twin. However, if a tensile stress is applied, twinning will occur. The crystals used in these experiments had their basal planes slightly inclined to the specimen axis: therefore, if twinning occurred along only one side of a crystal, that side must have been under tension relative to the other. Consequently the crystal must have been bent.

While measuring the kinking angles on the comparator it was observed that the crystal on either side of the kink was no longer bowed but quite straight. The surfaces of the crystal, however, were tilted relative to each other by a very small angle, although the comparator showed the crystal to be straight initially. For crystal B–1 the tilt angle after kinking was 25′.

Three cadmium crystals were also kinked in the manner described above; data were taken for one, Cd–1 (80°). As expected, cadmium behaved quite

TABLE II IMPACT DATA
Group A 75° Crystals

1 CRYSTAL NUMBER	2 M_S (gm)	3 M_H (gm)	4 No. of Impacts	5 Total Energy of Striker ergs	6 Total E/V of impact ergs/cc	7 Total E' Absorbed ergs	8 Total E'/V Absorbed ergs/cc	9 Vel. of Impact cm/sec	10 Momentum cgs	11 Length cm	12 Volume cc	13 E"/V of Impact ergs/cc	14 E" Energy Absorbed ergs	15 $E"/V_S$ Absorbed ergs/cc	16 $E"/V_k$ Absorbed ergs/cc	17 Total E' + E" ergs	18 $\frac{E' + E"}{V_S}$ ergs/cc
A-2	1035	305	7	1.9×10^6	4.5×10^6	0.8×10^5	1.9×10^5	23	2.4×10^4			Bent					
1-c	322	306	14	2.6×10^6	4.1×10^6	1.2×10^5	1.8×10^5	l 5	0.2×10^4								
								h 60	2.0×10^4		very slight bowing after 13th impact						
								64	2.1×10^4	.3	.074	2.0×10^6	$.5 \times 10^5$	$.8 \times 10^5$	1.0×10^6	1.7×10^5	2.6×10^5
1-d	1035	306	7			$.7 \times 10^5$	1.1×10^5	23	2.4×10^4		very slight bowing after 7th impact						
			2			$.3 \times 10^5$	$.5 \times 10^5$	23	2.4×10^4		lip formed at one end						
			11			2.4×10^5	4.0×10^5	23	2.4×10^4		angle of bow 2 or 3°						
			20	5.5×10^6	8.8×10^6	3.4×10^5	5.6×10^5										
								23	2.4×10^4	.4	.098	$.4 \times 10^6$	$.2 \times 10^5$	$.4 \times 10^5$	$.3 \times 10^6$	3.6×10^5	6.0×10^5
			10	2.7×10^6	4.4×10^6	1.4×10^5	2.2×10^5	23	2.4×10^4								
								23	2.4×10^4	.3	.076	$.4 \times 10^6$	$.2 \times 10^5$	$.3 \times 10^5$	$.2 \times 10^6$	kink grew	
1-f	1035	306	11	3.0×10^6	5.4×10^6	1.1×10^5	2.1×10^5	23	2.4×10^4		slight bend						
			10	2.6×10^6	4.7×10^6	0.9×10^5	1.2×10^5	23	2.4×10^4	.6	.133	$.5 \times 10^6$	$.3 \times 10^5$	$.5 \times 10^5$	$.2 \times 10^6$	1.4×10^5	2.6×10^5
								23	2.4×10^4		no change						
1-e	1035	306	3	3.3×10^6	5.5×10^6	1.5×10^5	2.9×10^5	46	4.8×10^4		slight bend near surface cavity						
								46	4.8×10^4	.4	.093	1.8×10^6	$.4 \times 10^5$	$.6 \times 10^5$	$.4 \times 10^6$	1.9×10^5	3.3×10^5
			2	2.2×10^6	3.7×10^6	$.8 \times 10^5$	1.4×10^5	46	4.8×10^4		kink has bent						
								46	4.8×10^4	.2	.045	1.8×10^6	$.3 \times 10^5$	$.4 \times 10^5$	$.6 \times 10^6$	kink grew	
1-a	5243	306	12	32.6×10^6	46.5×10^6	4.2×10^5	6.0×10^5	l 5	2.4×10^4								
								h 46	24.1×10^4		slight bend after 9 impacts; small lip formed at one end						
								46	24.1×10^4	.3	.063	15.8×10^6	$.9 \times 10^5$	1.3×10^5	1.5×10^6	5.1×10^5	7.3×10^5
1-b	1035	326	1	13.8×10^6	25.6×10^6	20.3×10^5	37.5×10^5	161	16.7×10^4		set aside 26 days						
			1	$.6 \times 10^6$	1.1×10^6	$.3 \times 10^5$	$.8 \times 10^5$	46	4.8×10^4								
								46	4.8×10^4	.3	.059	2.0×10^6	$.3 \times 10^5$	$.6 \times 10^5$	$.6 \times 10^6$	20.9×10^5	38.9×10^5
								46	4.8×10^4	.2	.039	2.0×10^6	$.4 \times 10^5$	$.7 \times 10^5$	1.0×10^6	kink grew	
2-b	1035	309	3	4.5×10^6	6.2×10^6	4.1×10^5	5.7×10^5	l 46	4.8×10^4								
								h 58	6.0×10^4		considerable bending on each impact						
								58	6.0×10^4	{.35 .15}	.079	2.4×10^6	1.7×10^5	2.3×10^5	2.1×10^6	5.8×10^5	8.0×10^5
2-c	1035	309	1	1.1×10^6	2.1×10^6	$.3 \times 10^5$	$.5 \times 10^5$	46	4.8×10^4								
								46	4.8×10^4	{.4 .3 .25}	.072	2.0×10^6	$.7 \times 10^5$	1.2×10^5	$.9 \times 10^6$	$.9 \times 10^5$	1.7×10^5
											.096	2.1×10^6	1.1×10^5	2.0×10^5	1.2×10^6	kink bent	

TABLE II IMPACT DATA
Group B 83° Crystals

1	2	3	4	5	6	7	8	9	10	11	12	13	14	15	16	17	18
3-b	1875	304	4	11.3×10^6	28.0×10^6	2.9×10^5	7.1×10^5	l 46	8.6×10^4								
								h 58	10.8×10^4			Slight bend					
								58	10.8×10^4	.25	.053	7.7×10^6	1.5×10^5	3.7×10^5	2.8×10^6	4.4×10^5	10.8×10^5
3-d	1875	305	5	13.3×10^6	25.0×10^6	7.9×10^5	13.3×10^5	l 46	8.6×10^4			bent					
								h 58	10.8×10^4								
								58	10.8×10^4	.2	.043	5.8×10^6	1.6×10^5	2.9×10^5	3.6×10^6	9.4×10^5	16.2×10^5
								58	10.8×10^4	.1	.021	5.8×10^6	2.1×10^5	3.9×10^5	9.7×10^6	kink grew	
4-a	1875	306	17	21.3×10^6	41.6×10^6	5.8×10^5	11.3×10^5	l 5	$.8 \times 10^4$								
								h 60	11.2×10^4								
								58	10.8×10^4	.19	.043	6.1×10^6	1.1×10^5	2.1×10^5	2.7×10^6	6.9×10^5	13.4×10^5
								58	10.8×10^4	.1	.02	6.1×10^6	1.0×10^5	1.9×10^5	5.0×10^6	secondary kink	
4-b	322	306	19	5.6×10^6	10.3×10^6	4.0×10^5	7.4×10^5	l 5	$.2 \times 10^4$								
								h 58	1.9×10^4								
								58	1.9×10^4	.5	.106	1.0×10^6	$.5 \times 10^5$	$.9 \times 10^5$	$.5 \times 10^6$	4.5×10^5	8.3×10^5
								58	1.9×10^4	.35	.074	1.0×10^6	$.5 \times 10^5$	$.9 \times 10^5$	$.6 \times 10^6$	new kink	
								58	1.9×10^4	.5	.106	1.0×10^6	$.5 \times 10^5$	$.9 \times 10^5$	$.5 \times 10^6$	new kink	
4-c	5243	306	12	33.1×10^6	62.9×10^6	3.8×10^5	7.1×10^5	l 5	2.4×10^4								
								h 48	25.2×10^4								
								51	26.5×10^4	.18	.038	12.7×10^6	1.8×10^5	3.3×10^5	4.6×10^6	5.6×10^5	10.4×10^5
5-a	1221	681	28	3.8×10^6	3.4×10^6	1.1×10^5	1.0×10^5	l 3	$.4 \times 10^4$								
								h 51	6.1×10^4								
								51	6.1×10^4	.38	.084	1.4×10^6	1.3×10^5	1.2×10^5	1.6×10^6	2.4×10^5	2.2×10^5
5-b	1875	326	2	13.6×10^6	25.0×10^6	8.0×10^5	14.5×10^5	85	16.0×10^4								
								85	16.0×10^4	.25	.053	12.5×10^6	2.2×10^5	4.3×10^5	4.2×10^6	10.2×10^5	18.8×10^5
3-a	1035	305	5	3.1×10^6	7.2×10^6	$.8 \times 10^6$	1.8×10^5	35	3.6×10^4			Bend of 1° 45'	Set aside 48 hours				
			4	2.5×10^6	5.7×10^6	$.4 \times 10^6$	$.9 \times 10^5$	35	3.6×10^4			Bend now 4°	R = 37 cm				
								35	3.6×10^4	.10	.017	1.4×10^6	$.3 \times 10^5$	$.7 \times 10^5$	1.7×10^6	1.5×10^5	3.4×10^5
B-1	1035	305	5	$.6 \times 10^6$	1.3×10^6	$.8 \times 10^5$	1.8×10^5	23	2.4×10^4			Set aside 48 hours					
			4	1.9×10^6	4.4×10^6	$.2 \times 10^5$	$.5 \times 10^5$	46	4.8×10^4								
			3	1.4×10^6	3.3×10^6	$.1 \times 10^5$	$.2 \times 10^5$	46	4.8×10^4								
			12	3.9×10^6	9.0×10^6	1.1×10^5	2.5×10^5										
								46	4.8×10^4	.15	.026	1.1×10^6	$.3 \times 10^5$	$.7 \times 10^5$	1.2×10^6	1.4×10^5	3.2×10^5
B-2	1035	305	3	1.0×10^6	2.4×10^6	$.4 \times 10^5$	1.0×10^6	46	4.8×10^4			No bending	Set aside 24 hours				
			25	$.5 \times 10^6$	1.2×10^6			9	1.0×10^4			No bending	No perceptable energy absorption Set aside 24 hours				
			16	$.6 \times 10^6$	1.5×10^6	$<.1 \times 10^5$	$<.1 \times 10^6$	14	1.4×10^4			No bending					
			44	2.1×10^5	5.1×10^6	$.4 \times 10^5$	1.0×10^6										
Cd-1	1035	305	4	7.4×10^6	18.0×10^6	3.1×10^6	7.6×10^5	46	4.8×10^4								
								46	4.8×10^4	.25	.049	2.8×10^6	$.8 \times 10^5$	1.9×10^5	1.6×10^6	3.9×10^5	9.5×10^6
			1	1.1×10^6	2.8×10^6	$.7 \times 10^6$	1.6×10^5	46	4.8×10^4								
								46	4.8×10^4	.38	.068	2.8×10^6	$.8 \times 10^5$	1.9×10^5	1.2×10^6		

TABLE III

AVERAGE VALUES OF IMPACT DATA

			75° *	83° **
Deformation Before Kinking	Total Energy (E') Absorbed		2.6×10^5 ergs	4.0×10^5 ergs
	Total E'/V_{sample}		4.0×10^5 ergs/cc	7.4×10^5 ergs/cc
	Percentage of impact energy absorbed		3.2%	3.3%
Kinking Data	Energy (E") Absorbed		$.7 \times 10^5$ ergs	1.2×10^5 ergs
	E''/V_{sample}		1.0×10^5 ergs	2.2×10^5 ergs
	E''/V_{kink}		$.9 \times 10^6$ ergs	2.5×10^6 ergs
	$E' + E''$	Ave	3.3×10^5 ergs	5.4×10^5 ergs
		Min	1.4×10^5 ergs	1.4×10^5 ergs
		Max	5.8×10^5 ergs	10.2×10^5 ergs
	$\frac{E' + E''}{V_{sample}}$	Ave	5.0×10^5 ergs/cc	9.6×10^5 ergs/cc
		Min	2.6×10^5 ergs/cc	2.2×10^5 ergs/cc
		Max	8.0×10^5 ergs/cc	18.8×10^5 ergs/cc
	of the 9 values of $\frac{E' + E''}{V_{sample}}$ for 83° crystals were definitely higher than the highest 75° crystals.			
	Percentage of total available energy absorbed for both processes		4.2%	3.8%

* Averaged over 6 crystals

** Averaged over 9 crystals

similarly to zinc. The total energy to produce bending plus kinking was 9.5×10^6 ergs/cc.

IV. Compression Tests

In addition to the impact experiments, a series of crude compression tests were run to study kinking under static load. Data were obtained on a hand-operated compression machine. The load was applied by turning a screw which moved the crystal against a spring. This spring had been calibrated by applying dead weight and measuring the resulting compression. During a run the compression of the spring, and therefore in effect the applied load was measured by means of a dial gauge which could be read to .001 in.; (.001 in. = .66 lb. or .31 kg.); the compression of the specimen was measured by means of a dial gauge which could be read to .0001 in.

The data obtained on eight crystals are compiled in Table V. Before the tests were run crystals 6–a and 6–b (86°) were examined in J & L optical comparator and found to be straight. Extremely slow and interrupted rates of compression were applied to these crystals. The total time elapsed for each run was about two hours. Crystal 6–a bowed slightly at a load of 56 kg., the bowing becoming considerable at about 180 kg. Kinks occurred at each end at a load of 303 kg. In crystal 6–b, bowing appeared at a load of 115 kg. Complex kinks, consisting of ridges appeared at a load of 270 kg. The two crystals differed originally only in slenderness ratio, i.e. the ratio of length to diameter. 6–a had a slenderness of 4.8, whereas 6–b had a slenderness of 2.1.

Crystal 7–a (72°), which was also quite straight initially, kinked at a load of only 2.1 kg. when the compression rate was faster and more uniform. The total elapsed time for readings on this crystal was

TABLE IV
ANGULAR MEASUREMENTS

	Crystal	Orientation	Angle of Bowing	Radius* (cm)	Angle of Kink Comparator	X-Ray	Angle of Tilt**
Impact Samples	1-c	75^0	1^0	76			
	1-d	75^0	2^0 or 3^0	48			
	1-a	75^0	2^0	40	$11\frac{1}{2}^0$	11^0	
	1-b	75^0	$3\frac{1}{2}^0$	35			
	3-b	82^0			15^0	11^0	
	3-a	82^0	4^0	37	$5^0 13'$		
	B-1	83^0			$9^0 26'$	10^0	25'
Compression Samples	7-a	72^0			$3^0 41'$	2^0	8'
	D-1	$86\frac{1}{2}^0$			$14^0 41'$	13^0	26'
	4-d	83^0			11^0	11^0	41'

* Radius of curvature

** Tilt between surface above and surface below kink

about fifteen minutes. As soon as the kink was noticed an effort was made to rapidly remove the load. Before this could be done, the kink angle was seen to increase. The kink angle as finally measured on the comparator was 3°41′; as measured by Laue patterns it was about 3°. It was also found that the edges of the crystal above and below the kink were now tilted about 8′ relative to each other as measured on the comparator. During the course of the experiment the load and accompanying strain were recorded. The area under the curve is a measure of the energy absorbed and gave a value of 5×10^5 ergs.

With a fast rate of compression, data was taken next on crystal 4–d (83°). A kink was detected at a load of only 1.2 kg. The kink angle when measured on the comparator was about 11°; the tilt angle was 41′, and the average radius of curvature of the kink surface was 5.2 mm. Because the kink formed so rapidly, stress-strain data were not obtained. In preparing crystal D–1, a very slight bend was introduced about one quarter of the way from one end. Near the middle of the crystal was a growth twin a fraction of a millimeter wide. A compression test was made to see where the kink would form. It formed at the site of the original bend at a load of 9 kg. Again the kink angle increased without any signs of the kink length increasing. The tilt angle and the kink angle, as measured by the comparator, were respectively 26′ and 14°41′. The rotation of the basal plane as measured by Laue patterns was 13°.

Motion picture studies were made of three additional crystals. After determining that each crystal was straight initially, motion pictures were taken of the crystal undergoing compression, while simultaneously another motion picture camera recorded the dial guage data. The primary purpose of these experiments was to establish whether a kink formed abruptly or gradually.

The load was applied rapidly but intermittently to crystal 6–c (86°). At 38.5 kg. the crystal bowed in the shape of a cosine curve; then kinks appeared at top and bottom. Finally a kink occurred at the center. The dial gauges did not follow the motion well, consequently a very erratic stress-strain curve was obtained. This also occurred with the crystal 8 (82.5°), which kinked at 13.5 kg.

TABLE V
COMPRESSION DATA

Crystal Number	ψ	Length (cm)	Diameter (cm)	Load to Kink (kg)	Length of Kink (cm)	Angle of Kink	Remarks
6-a	86^0	2.58	.54	303			Very slow compression rate Slight bow at 56 kg Considerable at 180 kg Kinked at end
6-b	86^0	1.14	.54	270			Very slow compression rate Bowed at 115 kg
7-a	72^0	2.89	.54	2.1	.38	$3^0 41'$** $2-3^0$**	Fast compression rate
4-d	83^0	2.35	.52	1.2	.15	11^0	Fast compression rate Kink angle increased after formation of kinks
D-1	$86\frac{1}{2}^0$	3.59	.46	9	.1	$14^0 41'$* 13^0**	Slight bend initially Fast compression rate
8	$82\frac{1}{2}^0$	2.47	.53	13.5	.2		Fast uniform compression rate Motion pictures taken
E-1	85^0	3.68	.45	9	.15		Fast uniform compression rate Motion pictures taken
6-c	86^0	2.50	.54	>40			Slow compression rate Bowed at 38.5 kg Kinked at top and bottom then in center

* Measurements made on comparator
** Rotation of basal plane measured by X-Rays

Crystal E–1 (85°) kinked at 9 kg. This time it was possible to draw a crude stress-strain curve (see Figure 4). The energy absorbed during the kinking process as calculated from the curve was 3×10^5 ergs.

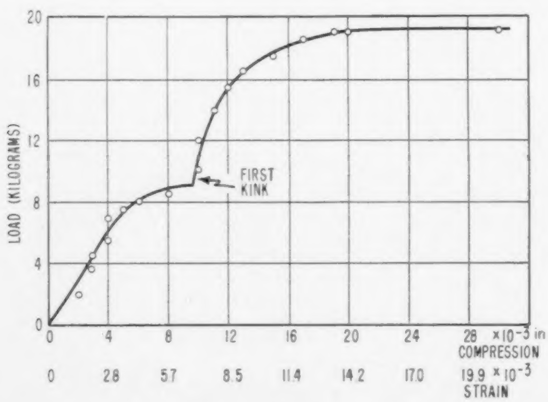

FIGURE 4. Load-strain curve for zinc crystal E–1

When crystal 8 was photographed the 16-mm. camera was run at 16 frames per second. In Figure 5, which is an enlargement of several consecutive frames, the crystal is seen to have no kink in one frame, but in the next frame the kink is present. This indicates that the kink occurred within a time interval of .06 sec. When crystal E–1 was photographed the camera was run at 32 frames per second, and it was possible to see the change occur between consecutive frames, so that the kink occurred probably within .03 sec.

V. X-ray Studies

The discussion in Section III of the energy absorbed in kink formation by impact showed that the kinking process was two fold. The crystal was bowed plastically by the first impact or series of impacts during which a critical amount of energy was absorbed. Additional impacts then produced the kink, with additional energy absorption.

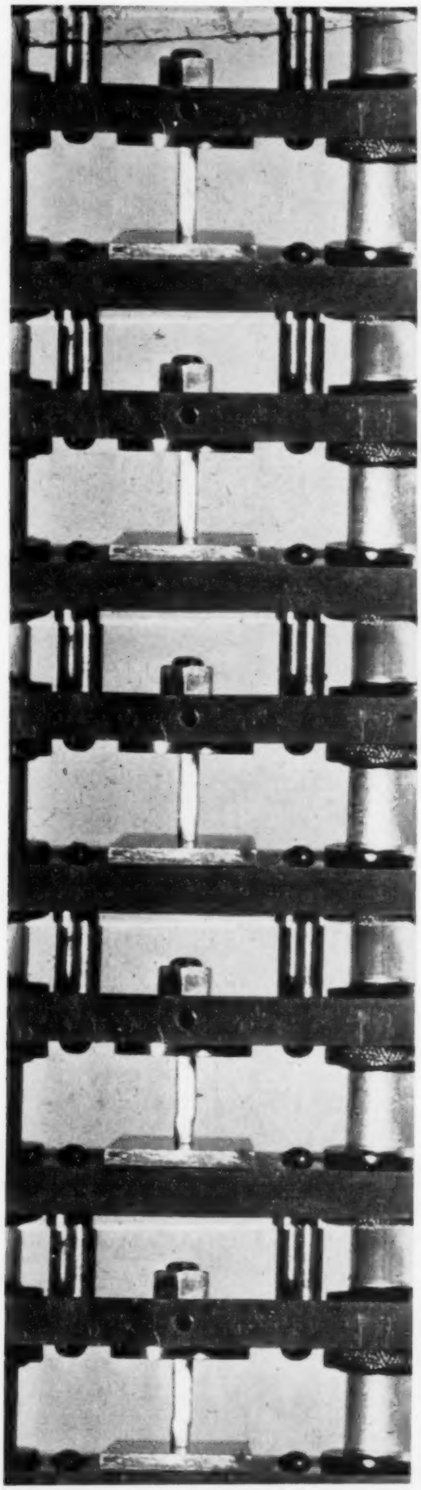

FIGURE 5. Consecutive frames showing formation of kink.

X-ray data were obtained on several of the crystals used in the impact experiments. Figure 6 is a print of a back reflection Laue pattern made of crystal 3–a before it received any impacts. The circular discs are due to circular aluminum shields inserted in the X-ray film holder to reduce the intense diffuse scattering. The Laue spots are seen to be quite sharp. Figure 7 is a Laue pattern made after five impacts, taken near the impact end of the crystal. The pattern is characterized by intense background, diffuse spots and asterism. The crystal itself had experienced a 1°45′ bend. A Laue pattern taken near the opposite end also showed diffuse spots and asterism, but the background intensity was relatively low. After these patterns had been made (a period of 48 hours had elapsed), the crystal was given four more impacts which increased the bending angle to 4°. The next impact produced a kink. A Laue pattern taken above the kink near the impact end still showed high background intensity but much less asterism (Figure 8). A Laue pattern taken on the far side of the kink (Figure 9) was almost devoid of asterism, showing quite sharp spots. Finally, the Laue pattern taken at the kink (Figure 10) showed asterism, diffuse and multiple spots, as well as higher background density than in patterns taken on either side of the kink.

Additional Laue patterns were made of other crystals used in the impact and the compression tests with similar results. In particular, patterns taken of crystal 4–d used in the compression machine, are reproduced here. The original pattern of the crystal showed clear sharp spots. After kinking had occurred Laue patterns were made in the kink and on either side of it with the X-ray beam perpendicular to the kink angle. Figure 11 is a pattern taken below the kink and consists of sharp spots. Figure 12 is one taken within the kink and consists of spots elongated into arcs. When the individual spots were plotted on a stereographic net it was found that the basal plane was nearly parallel to the X-ray beam. Consequently it produced no reflection on the film. Those planes, however, which were slightly inclined to the basal plane and still gave reflections on the outer edge of the film, gave the most curved spots (in stereographic projection); planes nearly perpendicular to the basal gave spots which were relatively sharp. The crystal was next rotated 90° about its axis and Laue patterns obtained from within the kink and from either side of it. In this position the X-ray beam was practically perpendicular to the basal plane. The spots from below the kink were again relatively sharp indicating little distortion. The pattern taken in the kink, Figure 13, revealed very high background scattering and long streaks.

These streaks represent reflections from the basal plane or planes slightly tilted to it.

By analysis of the patterns taken on this and other crystals, it was concluded that within the kink the basal plane had rotated around an axis parallel to or within a few degrees of $(01\bar{1}0)$ in agreement with Hess and Barrett. The nature of the streaks implied that the basal plane had also bent about this axis, or else within the area covered by the X-ray beam the basal plane took on progressively different orientations amounting to a total of 3°. It was argued that if the bending of the basal plane was about a given axis, two transmission glancing angle patterns, one made parallel to and another perpendicular to the bending axis, should give two distinct types of patterns. In the first case, with the X-ray beam parallel to the bending axis, one should get arcs concentric to the X-ray beam; in the second case one should get streaks radial to the X-ray beam. Accordingly the two patterns were made: Figure 14

FIGURE 14. Kink in crystal 4–d: X-ray beam parallel to bending axis.

taken with beam parallel to the bending axis, shows only concentric arcs; Figure 15 taken perpendicular to the bending axis, only radial streaks. These indicate conclusively that the basal plane was bent or assumed progressively different orientations about a single axis.

VI. Summary and Discussion

The experiments show conclusively that the formation of a kink in an originally straight undeformed zinc crystal occurs in two consecutive stages:

(*a*) A uniform permanent bending of the crystal takes place accompanied by an absorption of energy. Laue patterns reveal considerable asterism and indicate the the basal plane has rotated a small

FIGURE 15. Kink in crystal 4–d: X-ray beam perpendicular to bending axis.

amount away from the specimen axis during this first stage.

(*b*) With absorption of additional energy a sharp kink is produced. The kink angle varies from 1° to 14°. The regions on either side of the kink are relatively straight and free from asterism. Severe asterism, however, is obtained from the kink itself. Within the kink the basal plane has rotated and bent further about an axis in its plane normal to the active slip direction. Within the one square millimeter of surface covered by the X-ray beam there is a spread of 1 to 4° in the orientation. Further, the glancing angle X-ray patterns show that the bending within the kink occurs about a single axis. The X-ray reflections consist of maxima and minima intensities indicating that this bending has occurred in lamellar fashion.

In the impact experiments the energy absorbed before kinking was 2.6×10^5 ergs for the 75° crystals and 4.0×10^5 ergs for the 83° crystals. The energy absorbed during kinking was $.7 \times 10^5$ ergs for the 75° crystals and 1.2×10^5 ergs for the 83° crystals. The "fore" energy did not seem to be velocity dependent for the velocities used, but the additional energy required to produce a kink increased as the velocity of impacts increased. In these experiments recovery did not seem to be a significant factor.

In principle the process of kink formation in the static compression experiments was similar to that in the impact experiments. The energy data obtained from the load-elongation curves of a 72° and an 85° crystal are in good agreement with what would be expected from the impact data.

At the 1950 meeting of the American Crystallographic Association, one of us (E.I.S.) proposed an

6


7
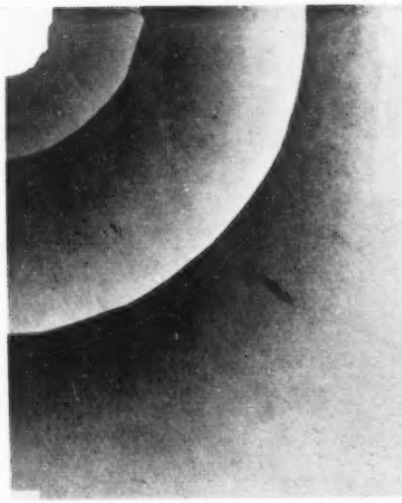

8


9
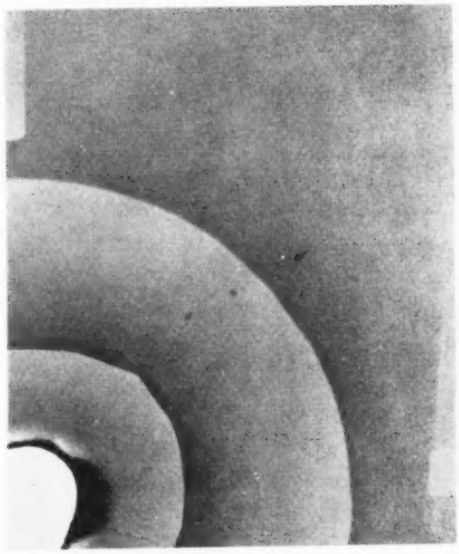

10
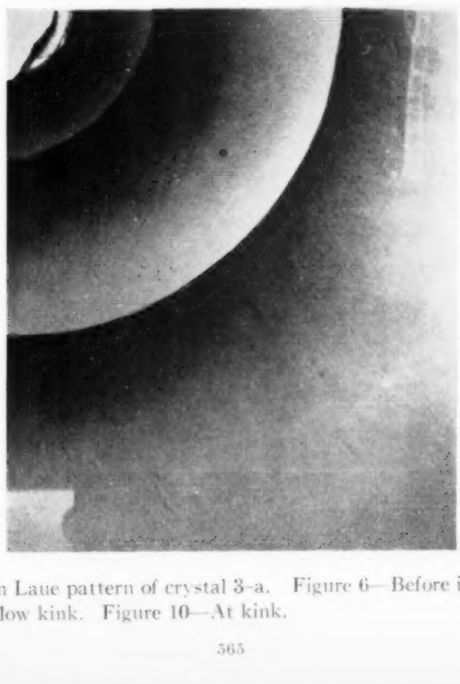

PLATE I. Portion of back-reflection Laue pattern of crystal 3–a. Figure 6—Before impact. Figure 7—After five impacts. Figure 8—Above kink. Figure 9—Below kink. Figure 10—At kink.

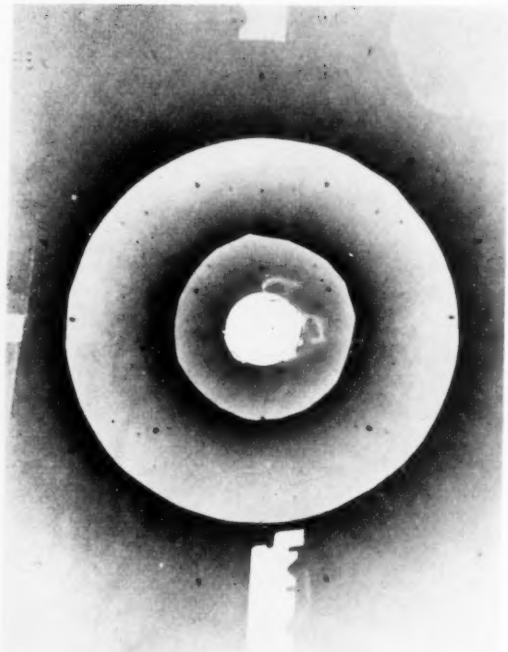

11

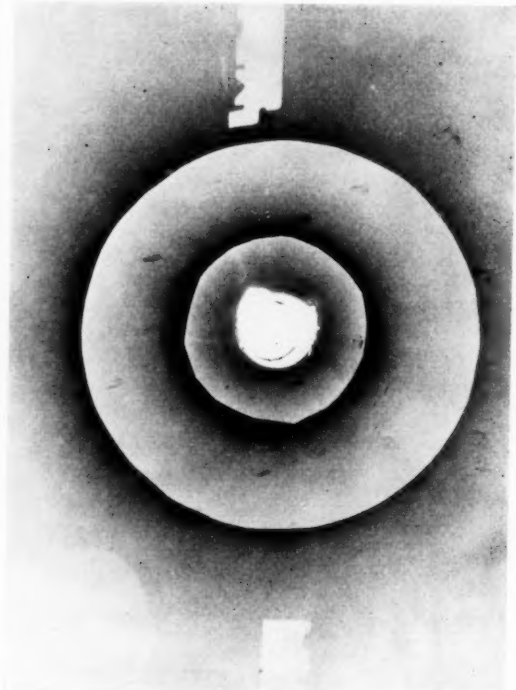

12

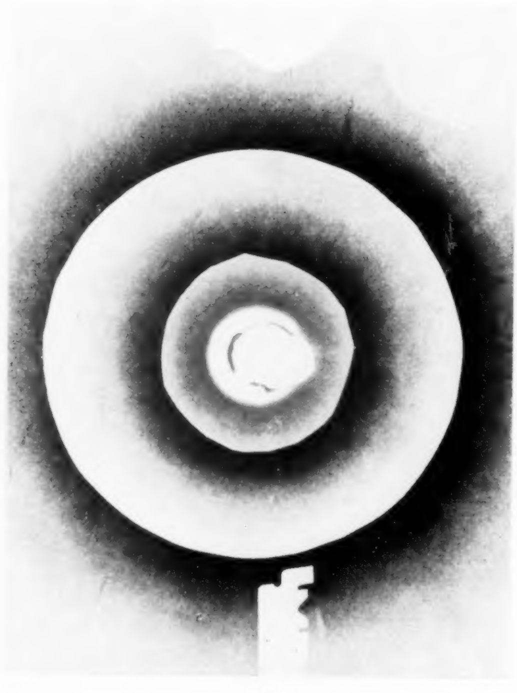

13

PLATE II. Back-reflection pattern of crystal 4-d. Figure 11—Below kink. Figure 12—At kink. Figure 13—At kink (crystal rotated 90° about its axis).

extension to the Hess-Barrett dislocation model for kink formation. This model is not too different from that proposed by subsequent writers.

It will be recalled that the Laue patterns taken after a few impacts had been delivered to the crystal indicated that plastic deformation had occurred. A small amount of rotation of the basal plane away from the specimen axis could be detected. Furthermore a macroscopic bowing of the sample had occurred. Such a bowing should be manifested by the existence of an excess of dislocations of one sign along the extended surface of the crystal relative to the compressed surface; indeed there is an excess of dislocations on the extended surface of each glide lamella. As Cahn [7] showed, if the dislocations move along the glide plane, the radii of curvature of the lamellae increase locally, thereby reducing the strain. The activation energy for the process would be supplied by the several impacts. Dislocations would then pile up along surfaces perpendicular, or nearly so, to the glide plane. The region between these surfaces would consist of badly distorted metal, the material on the opposite sides of these surfaces (the kink boundaries) would be relatively strain free. The X-ray patterns taken within the kink do show this region to be greatly distorted while patterns taken in regions on either side of the kink show them to be relatively strain free. One therefore concludes that the kinked region consists of a disordered array of locked-in dislocations. It is interesting to note that when these samples are heated only the kinked region recrystallizes.

This article is based on a thesis submitted June, 1950 by E. I. Salkovitz in partial fulfillment of the requirements for the degree of Doctor of Science in Physics at the Carnegie Institute of Technology. The investigation was supported by the Office of Naval Research and was reported to the New Hampton meeting of the American Crystallographic Association, August, 1950.

References

1. OROWAN, E. Nature, **149** (1942) 643.
2. MÜGGE, O. Neues Jahrbuch für Mineralogie, **1** (1898) 71.
3. HESS, J. B. and BARRETT, C. S. J. Metals, **1** (1949) 599.
4. BOAS, W. and SCHMID, E. Naturwiss., **20** (1932) 419.
5. CHALMERS, B. Proc. Phys. Soc. London, **47** (1935) 733.
6. HAASE, O. and SCHMID, E. Z. Phys. **33** (1925) 413.
7. CAHN, R. W. J. Inst. Metals, **17** (1949) 121.

AN X-RAY INVESTIGATION OF AGE HARDENING IN AlAg*

C. B. WALKER† and A. GUINIER‡

An AlAg alloy containing 20 per cent Ag by weight has been investigated with both low angle and high angle X-ray scattering techniques. The diffuse scattering from samples quenched from the region of solid solubility has shown that during the quench the majority of the Ag atoms of the alloy have clustered together into small spherical aggregates, each of which is surrounded by regions low in Ag content. With annealing the clusters first grow in size, the atoms continuing to remain on the matrix lattice sites. After sufficient annealing the hexagonal γ' precipitate, of composition Ag_2Al abruptly appears in the form of platelets thin in the (000.1) direction, which exhibit faults in the stacking of the (000.1) planes. On further annealing the platelets grow and become more perfect. The interpretation of the mechanism of precipitation offered by Guinier thus appears to be justified for this alloy.

UNE INVESTIGATION AUX RAYONS X DU VIEILLISSEMENT DANS AlAg

Un alliage contenant 20 pour cent d'Ag en poids a été investigué au moyen des méthodes de dispersion des rayons X à petit angle et à grand angle. La dispersion diffuse donnée par les échantillons trempés à partir de la région de solubilité solide a montré que pendant la trempe, la majorité des atomes d'Ag contenus dans l'alliage se sont groupés en petits amas sphériques, entourés d'une région à faible teneur en Ag. Un recuit provoque, au commencement, une croissance des amas, les atomes continuant à occuper leurs places dans le réseau de la matrice. Après un temps suffisant de recuit, le précipité hexagonal γ', de composition Ag_2Al apparaît subitement sous la forme de lamelles amincies dans la direction [0001] et présentant des défauts d'empilage dans les plans (0001). Si on prolonge le recuit au delà de ce stade, les lamelles continuent à croître et deviennent plus parfaites. Ainsi l'interprétation du mécanisme de précipitation, due à Guinier, est justifiée dans le cas de cet alliage.

RÖNTGENUNTERSUCHUNG DES AUSHÄRTENS EINER Al-Ag LEGIERUNG

Eine Al-Ag Legierung mit 20 Gew. prozent Ag wurde sowohl mit Kleinwinkel- als auch Weitwinkelstreuungsmethoden untersucht. Die diffuse Streuung, die bei Proben gefunden wurde, die aus dem Phasenbereich der festen Lösung abgeschreckt worden waren, zeigte, dass sich die Mehrzahl der Silberatome während des Abschreckens zu kleinen kugelformigen Aggregaten zusammenballen. Jedes dieser Aggregate ist von einem Bereich verminderten Ag-Gehalts umgeben. Beim Glühen wachsen die Aggregate zuerst, und die Atome verbleiben in den Gitterplätzen der Metrix. Nach weiterem Glühen tritt plötzlich das γ' Precipitat der Zusammensetzung Ag_2Al auf. Dies sind Plättchen, deren kurze Achse in der (000.1) Richtung liegt, und die Stapelfehler ("stacking faults") in der (000.1) Ebene aufweisen. Die Plättchen wachsen bei weiterem Glühen und werden gleichförmiger. Im Falle dieser Legierung erscheint die von Guinier gegebene Erklärung des Ausscheidungsmechanismus gerechtfertigt.

Introduction

In studying the course of the age hardening transformation in various alloys X-ray diffraction techniques have provided information otherwise unattainable. This is particularly so in the study of the early stages of age hardening, where, following techniques introduced by Guinier [1] and Preston [2], the investigation is focussed primarily on the diffuse scattering outside of the normal Bragg reflections. While different investigators have agreed on descriptions of the final stages of the phenomenon of precipitation, disagreement still exists concerning the description of the first stages, this disagreement generally being over the manner of interpretation of the diffuse X-ray scattering. Guinier [3], in studying several alloy systems showing precipitation, has interpreted the scattering as showing that the solute atoms in the alloy first cluster together into zones, regions which may show irregularities in terms of interatomic spacings but which are coherent with the parent matrix in that the general disposition of atoms is the same as that for the matrix. On annealing these zones first increase in size, generally showing some modification of internal atomic arrangements tending towards some regular structure, but after further annealing there is an abrupt transition, the zones disappearing and the true precipitate, with its different structure, appearing. Thus this interpretation basically requires the existence of two distinct stages in the precipitation transformation. A different description is offered by Geisler and his associates [4], who maintain that the diffraction patterns "can be interpreted as evidence for precipitation particles which are only a few unit cells in size. Anisotropic growth can be followed until the particles exceed the size in all dimensions necessary for sharp diffraction effects. Interpretation involving pre-precipitation phenomena again can be abandoned." In view of this difference in interpretation, it was thought worthwhile to make a further investigation of some alloy system which

*Received April 13, 1953.
†Department of Physics, Massachusetts Institute of Technology, Cambridge, Mass., U.S.A.
‡Conservatoire Nationale des Arts et Métiers, 292, rue Saint Martin, Paris, France.

had already been studied by both authors in order to determine which interpretation seemed to be justified.

Of the several age hardening alloys which have been studied, the system of aluminum rich AlAg seemed to be one which should give the clearest answer to this problem, since not only does the large difference in atomic scattering factors render the diffuse scattering more easily observable, but also the equal atomic "radii" eliminates possible diffuse scattering due to lattice distortion caused simply by the different sizes of the constituents [5]. Several investigations of this system have been reported, beginning with those of Barrett and Geisler [6] and Guinier [7], with two of the more recent studies being those by Geisler and Hill [4] and Guinier [3]. One fact stands out in a comparison of the experimental results of these investigations: whereas most investigators have found rods of diffuse scattering extending along various matrix (111) directions through reciprocal lattice points, Guinier reported essentially the same phenomenon, but as a characteristic of the second stage of precipitation, since earlier in the annealing history, before the appearance of these rods, a quite different scattering distribution was found. This first type of scattering, found for alloys immediately after sharp quenching from the solid solution and after short anneals at low temperatures, is best described as a distribution of scattering power in the form of spherical shell-like regions surrounding each of the reciprocal lattice points.* To explain this scattering distribution, Guinier [8] offered an interpretation based on an analogy with the scattering from amorphous bodies, describing the Ag atoms as clustered together into spherical zones, with these zones displaying a liquid-like distribution with a marked most probable nearest neighbor distance, and from the positions and breadths of the shells he determined the nearest neighbor separation and the size of the zones. This interpretation met with some difficulties, particularly in the matter of the quantitative determination of cluster size and inter-cluster distances, as was pointed out by Jagodzinski and Laves [9]. To clarify this point, it was felt that the primary objective of this study should be a quantitative study of the intensity distribution in this first type of scattering, which, it was hoped, would make possible a more accurate interpretation of the atomic distribution in this first stage of the precipitation.

Of the several experimental techniques available, the study of small angle scattering was chosen as the basic technique to be employed. This method, though not used in the most recent investigations [10; 11], is particularly powerful for several reasons. First, at low angles not only do the atomic scattering factors have their largest values but also there is a minimum amount of Compton and temperature diffuse scattering present. Again, in the study of single crystals where the sharpest possible Bragg reflections are demanded, the extent of the (000) reflection is determined only by the sharpness of focus of the primary beam, whereas the extent of other Bragg reflections is a function not only of the divergence of the beam but also of the degree of perfection of the single crystal. While single crystals could be grown with a fair degree of perfection, maintenance of this degree of perfection while at the same time reducing the crystal thickness to the optimum thickness for transmission patterns (0.04 mm.) was found extremely difficult. Lastly, for this particular system the diffuse scattering is found in the form of spherical shells surrounding each reciprocal lattice point as will be further discussed below, so that for measurements of the scattering about the (000) reciprocal lattice point, easily preparable polycrystalline foils would give the same scattering as that from single crystals.

Experimental Study of the First Stage of Age Hardening

The alloy studied, of 20 per cent Ag by weight (i.e. 5 per cent atomic), was prepared in ingot form and given homogenizing treatment by the Office National d'Études et Recherches Aéronautiques. By successive annealing and cold rolling this was reduced to strips of 1 mm. thickness. While several of these strips were used in preparing single crystals by strain-anneal processes, the others were reduced by further cold rolling and annealing to polycrystalline foils 0.04 mm. thick. Some of the single crystals were reduced to thicknesses of the order of 0.06 mm. for transmission studies by a combination of polishing and etching, two etches being found suitable: H_2F_2 followed by HNO_3, and a solution of NaOH followed by HNO_3.

Samples of the polycrystalline foil were annealed at 520°C for periods of the order of 24 hours, quenched in water and studied with the small angle scattering equipment developed by Fournet and Guinier [12]. This had as a source of X-rays an

*In this article the term reciprocal lattice point corresponds to each reciprocal lattice intersection having a non-zero scattering power ($F^2 \neq 0$).

electron beam focussed on a rotating Cu anode. The Cu$K\alpha$ radiation was monochromated and focussed by successive diffraction from the $(10\bar{1}1)$ planes of first one, then a second bent and ground quartz crystal, the focus of the first monochromator serving as a source for the second. The beam from the second monochromator was focussed on the flat film, excessive blackening from the direct beam being prevented by the presence of a thin Cu strip as beam stop placed 2 mm. before the film. Sets of slits limited the vertical and horizontal divergence of the beam, and further slits limited the parasitic scattering from the monochromators and from the edges of the first slits, so that with monochromators, slits and film contained in an evacuated chamber, extraneous scattering was reduced to a minimum. Resolution was excellent; with a sample to film distance of approximately 10 cm., scattering at angles down to $2\theta = 24'$ was clearly visible; and with the X-ray tube operating at 45 kv and 45 ma legible patterns were obtained with only two hour exposures.

The typical pattern for a quenched foil showed a diffuse ring surrounding the trace of the direct beam; one such pattern, enlarged three times, is reproduced in Figure 1a. The diameter of the ring depended noticeably on the speed of quenching, slower rates giving rise to smaller ring diameters. When single crystal specimens were given the same anneals and quenched, it was confirmed that their transmission patterns showed this same ring of circularly symmetric scattering, *independent of the orientation of the crystal relative to the X-ray beam.* A description of these results in terms of the matrix reciprocal lattice is then that the (000) reciprocal lattice point is surrounded by a spherically symmetric, shell-like region of scattering power.

When these quenched samples were annealed for various lengths of time at several temperatures between 20°C and 400°C, the diameter of the ring of diffuse scattering diminished and the intensity increased as the anneal progressed as is shown in Figure 1b. The rate of decrease of diameter was greater, the higher the annealing temperature; Figure 2 is a graph of the diameter as a function of time and temperature. For each temperature, as the anneal continued the ring eventually diminished to such an extent that all details were obscured by the beam stop, the pattern showing only a blur of scattering, as is shown in Figure 1c.

Photographic studies of the large angle scattering from single crystals showed that when the (000) reciprocal lattice point was surrounded by its shell of

a

b

c

d

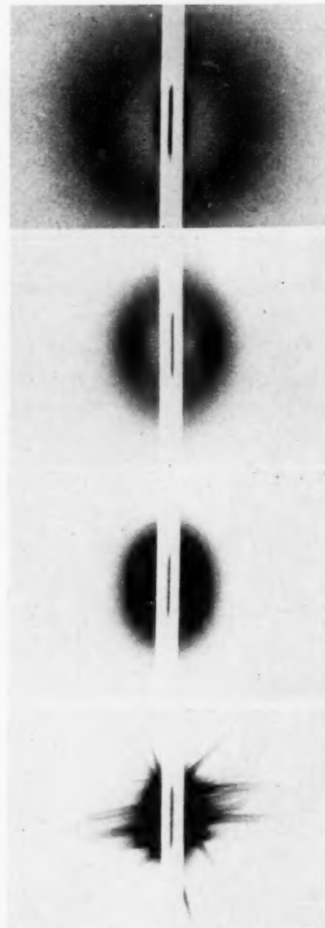

FIGURE 1. Small angle scattering of Cu$K\alpha$ radiation by polycrystalline AlAg in various stages of age hardening; (a) quenched from 520°C; (b) quenched from 520°C, annealed 25 minutes at 205°C; (c) quenched from 520°C, annealed 65 minutes at 205°C; (d) quenched from 520°C, annealed 10 days at 140°C.

scattering power, each of the other reciprocal lattice points was also surrounded by a similar scattering distribution. The Bragg reflections were rather distorted, a result of crystal imperfection and beam divergence, but the shell was clearly evident and its position, relative intensity, and diameter could be determined. The results of those measurements showed that each of these shells of scattering power had the same diameter and scattering power in reciprocal space as that of the shell surrounding the (000) reciprocal lattice point, and *each shell was centered on its respective matrix reciprocal lattice point.* This requires that, whatever the form of the atomic distribution giving rise to this anomalous scattering, the atoms of the alloy must be situated on lattice sites having interatomic spacings and

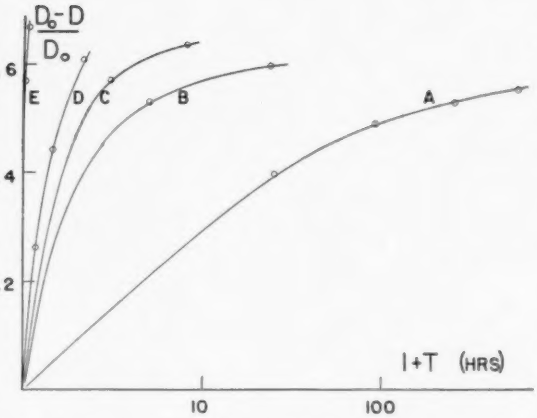

FIGURE 2. Change in diameter of ring of diffuse scattering as a function of time for several annealing temperatures: (A) 100°C; (B) 140°C; (C) 165°C; (D) 205°C; (E) 255°C.

orientations identical to those of the parent matrix, i.e., a most probable supposition, the atoms are located on lattice sites of the parent matrix.

Accurate quantitative determination of the intensity of diffuse scattering with photographic techniques is difficult, given, among others, the problem of subtraction of parasitic and background scattering, whereas this is much more simply done when the detection and enregistry of the scattering is done with a Geiger-Müller counter and associated scaling circuits. Thus for our quantitative measurements of intensity we employed equipment developed by Blin [13] for the particular study of small angle scattering. Radiation from a sealed, Cu target tube was monochromated by the $(10\bar{1}1)$ planes of an asymmetrically cut, bent quartz crystal and focussed at a point on the circle traversed by the counter slits. An evacuable glass chamber with thin polystyrene windows was mounted on the arm supporting the G.M. counter, in between the counter slits and the sample at the center of the table, so that all but 3 or 4 mm. of the beam path between sample and counter could be maintained in vacuum. With this arrangement, by carefully adjusting the monochromator and slits, intensities could be measured down to an angle of $2\theta = 50'$ without the corrections for parasitic scattering becoming too large. The necessary corrections were made from measurements taken without the sample in position, these being corrected for absorption in the sample.

The measured intensity distribution, corrected for parasitic scattering, obtained with this apparatus for a polycrystalline specimen quenched in water after a 24-hour anneal at 520°C is reproduced in Figure 3. This distribution, characteristic of quenched single crystals as well as polycrystalline foils, starts apparently from zero, mounts rapidly to a peak at $2\theta = 2°20'$, then decreases more slowly, reaching zero at an angle of $2\theta = 9°$.

Interpretation of the Diffuse Scattering

The observed periodicity of the diffuse scattering in reciprocal space having shown that the atoms still remained on the matrix lattice sites during this first stage of the transformation, it seemed appropriate to attempt an analysis based on the theory of scattering by binary alloys with local order config-

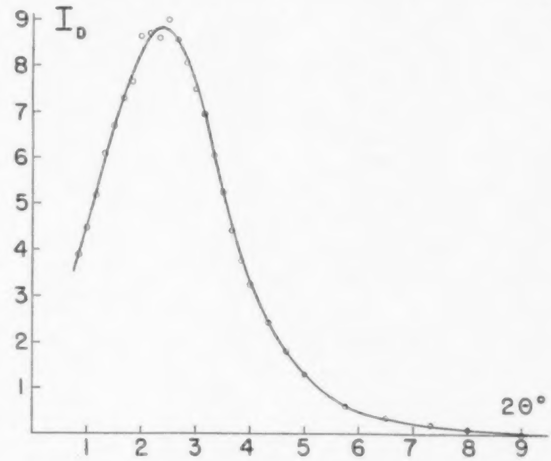

FIGURE. 3. Intensity of diffuse scattering by a polycrystalline sample quenched from 520°C as a function of scattering angle, 2θ. Radiation: CuKα.

uration, best expressed in a recent article by Cowley [14]. Though all applications to date of this theory have been concerned with alloys showing the order-disorder transformation, there is no such limitation contained in the theory. The only serious limitation in the theory is that the atoms remain on the matrix lattice sites. Within this limitation, the diffuse scattering from a binary alloy due to the particular arrangements of its two types of atoms is described by a three-dimensional Fourier series:

$$(1) \quad I_{D_{eu}} = N m_A m_B (f_A - f_B)^2 \left\{ \sum_{n_1} \sum_{n_2} \sum_{n_3} \alpha_{n_1 n_2 n_3} \exp\left[\frac{2\pi i}{\lambda} (\mathbf{S} - \mathbf{S}_0) \cdot (n_1 \mathbf{a}_1' + n_2 \mathbf{a}_2' + n_3 \mathbf{a}_3')\right] \right\}$$

where: $I_{D_{eu}}$ is the scattered intensity in electron units; $N m_A m_B (f_A - f_B)^2$ is the Laue monotonic scattering resulting from a perfectly random distribution of the N atoms of the alloy of m_A atomic per cent A atoms;

$$\alpha_{n_1 n_2 n_3} = 1 - \frac{P(AB_{n_1 n_2 n_3})}{m_B} = 1 - \frac{1 - P(AA_{n_1 n_2 n_3})}{m_B}$$

where $P(AA_{n_1n_2n_3})$ is the probability of finding an atom of type A at a position $n_1\mathbf{a}_1' + n_2\mathbf{a}_2' + n_3\mathbf{a}_3'$ from another A atom, the vectors $\mathbf{a}_1'$, $\mathbf{a}_2'$, and $\mathbf{a}_3'$ being the largest fractions of the unit cell axes such that any atomic position can be described by some combination of the integers n_1, n_2, n_3 (for face-centered cubic lattices, $a_1' = \frac{1}{2}a_1$, $a_2' = \frac{1}{2}a_2$, $a_3' = \frac{1}{2}a_3$) and $\mathbf{S}$ and $\mathbf{S}_0$ are unit vectors in the directions of the diffracted and incident beams, respectively.

Then, by a Fourier transformation:

$$(2)\ \alpha_{n_1n_2n_3} = \int\int\int \frac{I_{D_{eu}}}{Nm_Am_B(f_A - f_B)^2} \exp\left[-\frac{2\pi i}{\lambda}(\mathbf{S} - \mathbf{S}_0) \cdot (n_1\mathbf{a}_1' + n_2\mathbf{a}_2' + n_3\mathbf{a}_3')\right] dv$$

the integration extending over one cell of reciprocal space.

Application of this theory to determine the desired parameters requires a knowledge of $I_{D_{eu}}$ throughout a cell of reciprocal space, and determination of the parameters with reasonable accuracy requires a numerical integration over several thousand points in the cell. A simplification of the technique was possible in this case, since we had determined experimentally that the diffuse scattering was distributed in a spherically symmetric fashion about each reciprocal lattice point, with the intensity in any such "shell" dropping to zero close enough to its reciprocal lattice point so that there was no overlapping of contributions from adjacent "shells." By virtue of this resolution and the symmetry of the reciprocal lattice, not only could the integration be limited to the region surrounding the (000) reciprocal lattice point, but also by expressing the reciprocal lattice vector, $(\mathbf{S} - \mathbf{S}_0)/\lambda$, in spherical coordinates and integrating over the angular variables, equation (2) could be reduced to a simple, one-dimensional integration.

After such manipulation, equation (2) becomes:

$$(3)\ \alpha(R) = \int_0^H \frac{2I_{D_{eu}}(h)}{Nm_Am_B(f_A - f_B)^2}\frac{\sin 2\pi Rh}{2\pi Rh} 4\pi h^2\, dh$$

where

$$R = |a'|\sqrt{n_1^2 + n_2^2 + n_3^2},$$

a radius vector in the crystal lattice;

$$h = |b'|\sqrt{h_1^2 + h_2^2 + h_3^2},$$

a radius vector in reciprocal space, where b' is the length of the reciprocal cell edge and h_1, h_2, and h_3 are the independent variables, fractions of the reciprocal cell edge, which define the point in reciprocal space under consideration; and where when $h = H$, the intensity has dropped to zero. Further, since $\alpha(0) \equiv 1$, and since in the angular region concerned the atomic scattering factors remain essentially constant, this equation becomes finally:

$$(4)\ \alpha(R) = \frac{\dfrac{2}{R}\displaystyle\int_0^H I_D(h)\, h \sin(2\pi Rh)\, dh}{\displaystyle\int_0^H I_D(h)\, 4\pi h^2\, dh}$$

where I_D is now expressed in arbitrary units.

Using the intensity distribution from a quenched sample, that shown in Figure 3, a numerical integration furnished values for $\alpha(R)$, from which the probability distribution of Figure 4 was obtained.

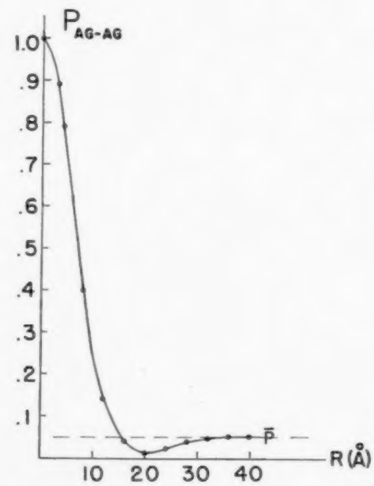

FIGURE 4. Probability distribution characteristic of AlAg quenched from 520°C; P_{AgAg} is the probability that one Ag atom will be at a distance R from another Ag atom.

This probability, $P_{AgAg}(R)$, that of finding one Ag atom on a lattice site a distance R from another Ag atom, decreases from the value 1.0 at $R = 0$, reaching a minimum value well below that for a perfectly random distribution at $R = 20$ Å, and rises again, attaining the average value, $\bar{p} = 0.05$, at about $R = 36$ Å. While this function has meaning only for discrete values of R, those corresponding to actual interatomic distances, the continuous curve is drawn in to make more easily visible the significant variation of this function with increasing atomic separation.

The interpretation of this Patterson-like probability function seems straightforward. The free energy of this system evidently is lowered when Ag atoms surround themselves with other Ag atoms. While

for temperatures above the limiting temperature for solid solubility thermal motion tends to overcome this "ordering," *during the quench this clustering becomes possible* and Ag atoms in regions about certain nuclei assemble into more or less spherical aggregates.* This clustering takes place so rapidly that around each cluster there is left a shell like region with less than average Ag content.† If we consider this phenomenon from a diffusion standpoint, with an "uphill" diffusion of atoms in clustering as opposed to the normal "downhill" diffusion which renders a uniform atomic distribution, then apparently the activation energy for "uphill" diffusion is less than that for "downhill" diffusion, so that the first varies much less quickly with temperature than the second, making possible the clustering during the quench.

Having determined the Patterson-like probability distribution function for the quenched sample, one would like to determine an average cluster size and a measure of the percentage of Ag atoms in the alloy which have formed these clusters. This can be done by assuming different models for the clusters, calculating the probability distributions corresponding to the different models, and comparing these distributions with the distribution determined experimentally. For our calculations we considered a very simple basic model, a homogeneous spherical cluster of high Ag content surrounded by a shell-like region of low Ag content, with variables of cluster composition, cluster size, and percentage of Ag atoms collected in clusters. Calculations of first neighbor Ag-Ag bonds showed quickly that the experimentally determined probability for first neighbors, $\bar{P}_{AgAg}$ (2.8 Å) = 0.89, could only be obtained by considering clusters whose compositions were practically pure Ag, with the added restriction that almost all of the Ag atoms of the alloy be in such clusters. The single model which gave the best fit between calculated and observed distribution functions was that of a spherical cluster of Ag atoms of 8 Å radius, containing 125 Ag atoms, this surrounded by a shell of Al atoms of 28 Å outer radius. A consideration of the departures of this calculated distribution function from the experimental distribution function then described the clusters as being of a range of sizes, with over 50 per cent of the clusters being the size described above and the rest being of somewhat smaller size. The extreme simplicity of our models forbade any attempt to determine a quantitative distribution of cluster sizes.

A check of this calculation can be made by use of the theory of small angle scattering by small particles as developed by Guinier [17]. This predicts the amplitude of radiation scattered by spherical particles as:

$$E_{eu} = N^{\frac{1}{2}} n \exp\left(-\frac{4\pi^2}{10\lambda^2} R_0^2 \epsilon^2\right)$$

where N is the number of particles; n is the number of excess electrons in a particle (excess in the sense of the number of electrons above that for a similar volume of the homogeneous medium surrounding the particle); R_0 is the radius of the particle; and ϵ is the scattering angle measured in radians. The amplitude scattered by a cluster surrounded by a shell, the whole being contained in a homogeneous lattice, can then be calculated by adding the amplitude scattered by the cluster, with a positive excess of electrons, to the amplitude scattered by the shell, with its negative excess of electrons, and the scattered intensity is then given by the square of the amplitude. With a cluster of radius 10 Å surrounded by a shell of outer radius 30 Å, the predicted intensity agreed remarkably well with the observed intensity for all angles above $2\theta = 1.5°$, when the curves are matched at $2\theta = 2°$. The calculations of the percentage of total Ag atoms to be found in clusters then could be made, since the scattered intensity had been determined in electron units; this calculation again resulted in a value of approximately 50 per cent.

The calculations from these simplified models have thus permitted us to determine that during the quench more than 50 per cent of the Ag atoms have clustered into relatively large aggregates, the remaining Ag atoms probably being found in smaller clusters. The average cluster may be described as having a radius of approximately 8 Å and contains on the order of 100 Ag atoms. Around this cluster there is to be found a shell-like region low in Ag content, of an outer radius of the order of 30 Å. Outside of this region *on the average* is found a region of homogeneous atomic distribution, but in

*The actual shape of any one aggregate cannot be determined from the X-ray diffraction data. The diffraction is influenced by a very large number of aggregates so that what is determined is an average shape. Thus if the aggregates actually had the shape of very slightly flattened ellipsoids of revolution, the short axes occurring with equal probability in several directions, such as the various (111) directions, then the diffraction by these aggregates would be practically indistinguishable from that by spherical aggregates. Large departures from spheroidal shapes could of course be remarked, unless more orientations became equally probable.

†The attendant diffraction effect must be classified as a phenomenon which, once seen, becomes obvious. It is the combination of regions with greater than average scattering factor surrounded by shell like regions with less than average scattering factor which produces the shells of scattering power in reciprocal space.

the real crystal randomly distributed Ag atoms are few, so that actually beyond any cluster and its shell of Al atoms one finds primarily other clusters of varying sizes and positions.

When the alloy is quenched and left at room temperature, the clusters formed during the quench do not noticeably change in size, owing to the very slow rates of diffusion at this temperature. The initial size does depend on the speed of quenching, slower rates allowing the formation of larger clusters. When the quenched alloy is annealed at higher temperatures, the decrease in diameter of the shells of scattering power in reciprocal space together with the increase in their intensities indicates that the average size of these clusters is increasing. This growth is probably accomplished by two mechanisms—the absorption by the larger clusters of the remaining "free" Ag atoms brought into their regions of influence by thermal diffusion, and also by coalescence of adjacent large clusters, again as a result of thermal notions.

On continued annealing the Ag clusters grow to such a size that experimentally only a blur of scattering is found around the reciprocal lattice points. During this growth another diffraction phenomenon has been observed at large angles by Geisler and Hill [4] and others. This scattering, weaker in intensity than the spherical shells of scattering power, has been described as having the appearance of a "doubled cross" on transmission Laue patterns. No detailed investigations of the intensity distribution of this scattering has been made, so that any interpretation must be qualitative in nature. Geisler and Hill have interpreted this phenomenon in terms of the formation of "one-dimensional" precipitates. This conclusion does not seem valid, since the existence of such precipitates would in general create intersecting bands of scattering through the (000) reciprocal lattice point, a scattering which has not been found. Instead we offer the interpretation that during the growth of the clusters of Ag atoms some Al atoms have been incorporated into them, and that these exist in some crudely ordered arrangement which might give rise to the observed scattering. More quantitative measurements must be made before this or any other interpretation can be considered as validated. However, since this scattering is much weaker than the "spherical shells" of scattering, it seems reasonable to consider this as a second order effect which may modify slightly the description of the growth of the Ag clusters.

Examination of the Second Stage of Age Hardening

The first stage of age hardening has been characterized by the appearance of shells of scattering power in reciprocal space, which, on annealing, diminish in size and increase in intensity until only a blur of scattering is visible. With still further annealing a completely different type of scattering is observed at small angles—the appearance of short streaks passing through the trace of the direct beam. One such pattern, made from an annealed polycrystalline foil, is reproduced in Figure 1d. The length of anneal necessary for the appearance of these streaks varies with temperature; Table I tabulates some of these values.

TABLE I

ANNEALING TIME TO PRODUCE CENTRAL STREAKS AS A FUNCTION OF TEMPERATURE

T°(C)	t
20	not observed after three months
140	100 hours
165	22 hours
255	18 minutes
300	3 minutes
342	1 minute
405	15 seconds

Two of the dimensions of these streaks were quite sharp, apparently depending only on the dimensions of the crystals and the primary X-ray beam. Examination of a single crystal displaying this scattering showed that the long dimensions of the streaks were directed along the four (111) directions of the matrix reciprocal lattice. The total length of these rods or streaks in reciprocal space was found to be approximately one tenth the distance in reciprocal space from the (000) to the (111) reciprocal lattice point. Investigation of scattering at large angles revealed that further diffuse streaks had appeared around other reciprocal lattice points. These streaks also were directed along matrix (111) directions in reciprocal space and were not symmetric about the matrix reciprocal lattice points to which they were joined. These large angle rods of scattering were generally rather long, having a total length in reciprocal space of approximately four-tenths the distance from the (000) to the (111) reciprocal lattice points. However, certain of these rods were much shorter; these, the rods passing through the (111)-reciprocal lattice point directed towards the origin, had a total length of only one tenth the (000)–(111) distance.

These large angle diffraction effects are similar to those which have been reported by several investigators [4; 10; 11]. Ziegler [11], in the most recent investigation of this phenomenon, shows diffuse rods of two types. Those which pass through the (111) and (222) reciprocal lattice points *directed towards the origin* have a length of roughly one-tenth the (000)–(111) distance. All other rods observed such as that from the $(1\bar{1}\bar{1})$ toward the (200), have lengths of roughly one-half this distance. These results agree quite well with our own, considering the differences in annealing history.

Geisler and Hill have interpreted these diffraction effects as showing the existence of small platelets of the hexagonal close packed γ' precipitating phase, of composition Ag_2Al, having large dimensions in the (000.1) planes, corresponding to the matrix (111) planes, but which are thin in the direction perpendicular to these planes. A full criticism of this interpretation will not be given here, since this has been thoroughly done in two recent papers [3; 11]. These investigators, Guinier and Ziegler, have shown that this by itself is not correct, proposing the modification that the γ' phase is forming as platelets, with these platelets exhibiting faults in the stacking of the (000.1) planes. With this mechanism one can easily obtain qualitative agreement with the experimentally observed scattering, the quantitative agreement depending on the accuracy of assumptions as to the distribution of faults.

The origin of these platelets of the precipitating γ' phase must lie in the clusters of Ag atoms, for it is there that all the Ag atoms have collected. This second stage might well be described as a nucleation and growth phenomenon, the nucleation taking place in a cluster of favorable size and the growth occurring at the expense of the clusters. Barrett and Mehl suggest that the motion of half dislocations along (111) planes may be pictured as one growth mechanism, which would explain the existence of the stacking faults. On further annealing the platelets become more perfect and grow larger, so that the rods in reciprocal space break up and shorten, eventually becoming the reciprocal lattice points of the γ' precipitate. One interesting fact concerning the first appearance of these platelets can be seen in Figure 1d. The streaks corresponding to any one of the crystallites appear as double streaks, indicating that the formation of these platelets takes place more rapidly in the grain boundaries than in the interior of the crystallite.

High Temperature State of the Alloy

In discussing the appearance of the Ag clusters in the quenched alloy, we suggested that the clusters form during the quench, this clustering taking place probably about some nuclei which exist at high temperatures. One of us [7], using high temperature photographic techniques, had previously found no evidence of such nuclei in the temperature range for solid solubility, but we felt that better experimental resolution could be attained with Geiger counter spectrometer techniques. A small furnace was constructed for the spectrometer described in a preceding section, and measurements of the low angle scattering were made at two temperatures within the solid solubility range. The results of this investigation will be mentioned only briefly here, since they do not actually fall within the scope of an article on age hardening, and they will be more completely discussed in a forthcoming article. These measurements showed that the alloy does not exist in a homogeneous state in the solid solubility region, but instead there is a tendency to form small clusters, these probably containing less than six Ag atoms. The results of a recent investigation by Rudman [16], who has been investigating this phenomenon by a study of large angle scattering, agree with this description, though his measurements indicate an even smaller size for the cluster. These clusters serve as the nuclei for the formation of the larger clusters during quenching.

Correlation of X-Ray Data with Measurements of Other Properties

This X-ray investigation has shown the existence of two distinct stages in the age hardening transformation—first the appearance and growth of Ag rich clusters, then the appearance and growth of the hexagonal γ' precipitate. Koster and Braumann's [15] measurements of hardness, elastic limit, thermoelectric force, and conductivity likewise indicate the presence of two stages in this transformation, a cold hardening stage followed by a warm hardening stage. Both our own X-ray measurements and those of Glocker, Koster, Scherb and Ziegler [10] show that the appearance of platelets of the γ' phase is directly correlated to the appearance of the warm hardening stage. The period during which cold hardening exists is just the period in which the clusters are present in the alloy. However, Koster and Braumann show that the AlAg alloy with 38 per cent Ag by weight is capable of a marked

degree of reversion, (retrogression or "Rückbildung"), and their data indicates that for an alloy of 20 per cent Ag the phenomenon, though less marked, may still be possible. A visual examination of the small angle scattering pattern of a sample which had been given thermal treatment to produce reversion did not show any comparable change in the scattering. When the alloy was annealed in the cold hardening region, the clusters increased in size, and when the alloy was heated at the reversion temperature of 200°C, the clusters apparently remained the same or increased in size very slightly, whereas in AlCu, where a similar phenomenon is evidenced, such treatment produces a dissolution of the Guinier Prestor zones. It is possible that the reversion is rather small in this alloy, and that only the small fraction of clusters under a critical size should dissolve. If such were the case, a visual examination of the scattering patterns might not be sufficient to reveal this change. Further examination with the object of quantitatively measuring the intensity distribution after such treatment is now in progress. At the moment, though the warm hardening stage is clearly demonstrated to be the result of the formation of the platelets of the γ' precipitate, the exact relation between the cold hardening stage and the Ag clusters cannot be considered as fully determined.

Summary and Conclusions

Our investigation has shown that the age hardening process in AlAg alloys of high percentage Al takes place in two separate stages. When the alloy is quenched from the region of solid solubility, during the quench Ag atoms cluster into small aggregates of approximate spherical shape, these containing the order of 100 Ag atoms for fast quenches. This clustering takes place so rapidly that there is left a shell-like region surrounding each cluster which is low in Ag content. For the most rapid quenches calculations indicate that at least 50 per cent of the Ag atoms have formed these clusters, with the remaining Ag atoms mostly dispersed in smaller clusters, so that actually in the real lattice outside of any cluster and its associated shell of Al atoms are to be found other clusters of varying sizes and positions. On annealing, these clusters grow in size both by absorption of the Ag atoms not contained in the large clusters and by coalescence of some of the larger clusters, so that as the average size of the clusters increases, the number of clusters decreases. At the same time, there may also be an introduction of some Al atoms into the clusters, these taking up a roughly ordered arrangement. During this first stage the atoms remain on the lattice sites of the parent matrix.

With further annealing the alloy exhibits a new phase, the formation and growth of platelets of the γ' phase, the hexagonal close-packed Ag_2Al precipitate, this occurring at the expense of the Ag clusters. These platelets exhibit stacking faults along the (000.1) planes, so that it is thought that a part of the mechanism of formation may be a motion of half dislocations along the matrix (111) planes. On further annealing, the platelets grow and become more perfect.

Satisfactory correlation of these two stages with the two-stage course of the variation of physical properties has not been accomplished. While the appearance of the platelets of the γ' phase has been correlated with the warm hardening stage of hardening, the cold hardening stage has not been simply linked to the formation of the Ag clusters, since the physical properties exhibit some reversible dependence on temperature which has not been discerned with X-rays.

The definite existence of two stages in the transformation in this alloy, with the atoms in the first stage remaining on the lattice sites of the parent matrix, agrees well with the general interpretation of age hardening transformations offered by Guinier and cannot be explained on the basis of the simplified nucleation and anisotropic growth interpretation offered by Geisler. Though these results cannot be taken as proof of a generalization concerning all alloy systems, at least for this system we believe we have demonstrated that an aggregation of solute atoms into zones precedes the formation of the platelet structure which is the beginning of a true precipitate.

Acknowledgment

Our thanks are extended to M. Jean Blin, whose apparatus was generously loaned for the quantitative measurements, and to the U.S. Fulbright Commission for the grant of a Fulbright scholarship which made possible this dual investigation.

References

1. Guinier, A. Ann. Phys., **12** (1939) 192.
2. Preston, B. D. Proc. Roy. Soc., **A167** (1938) 526.
3. Guinier, A. Acta Cryst., **5** (1952) 212.
4. Geisler, A. H. and Hill, J. K. Acta Cryst., **1** (1948) 238.
5. Warren, B. E., Averbach, B. L., and Roberts, B. W. J. Appl. Phys., **22** (1951) 1493.

6. Barrett, C. S. and Geisler, A. H. J. Appl. Phys., **11** (1940) 733.
7. Guinier, A. Journal de Physique, **8** (1942) 124.
8. Guinier, A. Physica, **15** (1949) 148.
9. Jagodzinski, H. and Laves, F. Z. Metallk., **40**(1949) 296.
10. Glocker, R., Koster, W., Scherb, J., and Ziegler, G. Z. Metallk., **43** (1952) 208.
11. Ziegler, G. Z. Metallk., **43** (1952) 213.
12. Fournet, G. and Guinier, A. Bull. Soc. franç. Min., **74** (1951) 39.
13. Blin, J. C. R. Acad. Sci., Paris, **233** (1951) 1288.
14. Cowley, J. J. Appl. Phys., **21** (1950) 24.
15. Koster, W. and Braumann, F. Z. Metallk., **43** (1952) 193.
16. Rudman, P. S. M.S. thesis, Dept. of Metallurgy, Massachusetts Institute of Technology (January, 1953).
17. Guinier, A. X-Ray Crystallographic Technology (Hilger and Watts Ltd., 1952), pp. 284–286.

THE DIFFUSIVITY OF CARBON IN IRON BY THE STEADY-STATE METHOD*

R. P. SMITH†

From measurements of the rate at which carbon passed through a cylindrical iron shell, the surfaces of which were maintained at different carbon contents, and measurements of the carbon distribution through the cylinder wall, the diffusivity of carbon in austenite and its variation with carbon content were determined for temperatures of 1000, 851 and 802°C. The diffusivities determined by this steady-state method are in good agreement with those reported by others and determined by a non-steady-state method. It is shown that the change in the diffusivity with concentration at 1000°C is in accord with the relation $D = D_{0\gamma}(1 + C\, d \ln \gamma/dC)$ only at low carbon content.

LA DIFFUSIVITÉ DU CARBONE DANS LE FER PAR LA MÉTHODE DE L'ÉTAT PERMANENT

La diffusivité du carbone dans l'austenite et ses variétés a été déterminée pour des températures de 1000, 851 et 802°C, en partant des mesures de la vitesse de passage du carbone à travers d'une douille cylindrique en fer et des mesures de la distribution du carbone dans la paroi du cylindre. Les teneurs en carbone des surfaces de la douille cylindrique étaient maintenues à des valeurs différentes. Les diffusivités déterminées par cette méthode d'état permanent s'accordent bien avec celles qui ont été signalées par d'autres et déterminées par une méthode d'état non-permanent. Il est montré qu'à 1000°C, la variation de la diffusivité avec la concentration est en accord, pour de faibles teneurs en carbone, avec la relation $D = D_{0\gamma}(1 + C\, d \ln \gamma/dC)$.

DIE DIFFUSIONSFÄHIGKEIT VON KOHLENSTOFF IN EISEN NACH DER GLEICHGEWICHTSMETHODE

Die Diffusionsfähigkeit des Kohlenstoffs im Austenit und ihre Abhängigkeit vom Kohlenstoffgehalt wurde bei 1000, 851 und 802°C aus Messungen der Geschwindigkeit mit der Kohlenstoff durch einen Eisenhohlzylinder, dessen Oberflächen auf verschiedenen Kohlenstoffgehalt gehalten wurden, bestimmt. Die Diffusionsfähigkeiten, die mit dieser Gleichgewichts-Methode bestimmt wurden, stimmen zufriedenstellend mit den Daten anderer Authoren, die Nicht-Gleichgewichtsmethoden anwenden, überein. Es wird gezeigt, dass die Konzentrationsabhängigkeit der Diffusionsfähigkeit bei 1000°C nur bei niedrigem Kohlenstoffgehalt der Beziehung $D = D_{0\gamma}(1 + C\, d \ln \gamma/dC)$ folgt.

The diffusivity of carbon in iron, and its variation with carbon content, may be determined by a non-steady-state or a steady-state method [1]. Extensive measurements of the diffusivity of carbon in austenite (face-centered cubic iron) by the former method have been reported by Wells and Mehl [2] and by Wells, Batz and Mehl [3]. The diffusivity determined by this method depends, particularly near the terminal values, on precise measurement of small composition differences [4]. For the steady-state method, the concentration gradient is more nearly uniform, hence the latter method is better adapted to precise determination of the variation of the diffusivity with concentration. This paper deals with the experimental determination of the diffusivity of carbon in iron by a steady-state method involving the passage of carbon through a cylindrical iron shell.

By Fick's first law [5], which serves merely to define the diffusivity D, the flux, J, of carbon is related to the concentration gradient, dC/dx, as follows;

$$J = -D\, dC/dx. \tag{1}$$

If the specimen is a flat plate*, the flux at steady-state is the same through all planes parallel to the surface, that is, J is constant; under this circumstance the diffusivity is seen to be inversely proportional to the slope, dC/dx.

Experimentally it is simpler to use a hollow cylinder (Figure 1) with radial flux. In this case the flux at steady-state is a function of the radial distance r but the quantity, q, of carbon passing through any entire cylindrical area of length l in a given time t is independent of r. The flux, J, through such a cylindrical surface is $q/2\pi rlt$, which is the quantity q divided by the area and by the time. Substituting this value for J into equation (1), it is found that

$$D = -q/2\pi rlt(dC/dr) = -q/2\pi lt(dC/d \ln r) \tag{2}$$

or for a given cylinder

$$D = -K/(dC/d \log r) \tag{3}$$

where K is a constant. The calculation of the

*Received April 16, 1953.

†The Research Laboratory, United States Steel Corporation, Kearny, N.J., U.S.A.

*A single determination of the diffusivity of carbon in iron by this method has been reported by F. Harris, Trans. A.I.M.E., **172** (1947) 531. However, in this case only the mean carbon content of the plate was determined; the surface concentrations were assumed to correspond to equilibrium conditions. Therefore equation (1) was not directly applicable.

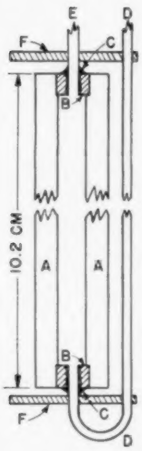

FIGURE 1. Cross section of a diffusion cylinder. A—iron diffusion cylinder, 0.71 or 0.85 cm. i.d., 1.11 cm. o.d.; B—press-fitted copper plugs; C—solder (85 per cent Cu, 15 per cent Ag; D—copper tube, carburizing gas inlet; E—copper tube, carburizing gas outlet; F—alundum (RA 98) centering discs.

diffusivity at a given carbon content requires (by equation (2)) a measurement only of the rate q/t, the cylinder length l, and the slope of the carbon distribution curve (plot of carbon content vs. log r) at the chosen carbon content.

For the temperature range in which austenite is in stable equilibrium with graphite the iron-carbon system is well suited for the steady-state method since, for a given temperature, nearly any gas which will deposit soot on the inside of the iron cylinder will maintain this surface at a carbon content close to its value for equilibrium with graphite [6; 7; 8] while the other surface can easily be held at low carbon content by a decarburizing gas such as wet hydrogen.

Experimental

Diffusion Cylinders

Figure 1 shows a cross-section diagram of a typical diffusion cylinder. The cylinder A made of either a special magnetic grade of ingot iron* or high-purity iron* obtained from the National Research Corporation† was about 10.2 cm. long, 1.11 cm. o.d. and either 0.71 or 0.85 cm. i.d. The ends were closed with press-fitted copper plugs B 0.32 cm. thick with tapped holes in their centers. Threaded copper tubes, 0.12 cm. i.d., were screwed into the copper plugs and welded, in a hydrogen atmosphere, with an alloy of 85 per cent Cu and 15 per cent Ag. To insure proper alignment of the copper plugs, the inside diameter of the iron tube, at the position of the plugs, was increased by about 0.003 cm. The carburizing gas entered the bottom of the cylinder through tube D and vented through tube E. Alundum (RA 98) discs F attached to the copper tubes served to center the diffusion cylinder in the zircon furnace tube.

To establish steady-state, the diffusion cylinder was suspended in a constant-temperature furnace as shown in Figure 2; carburizing gas was passed through the inside of the cylinder and decarburizing gas over its outside surface. The rate of diffusion of carbon through the cylinder wall was determined as indicated in Figure 2 by weighing the carbon (as

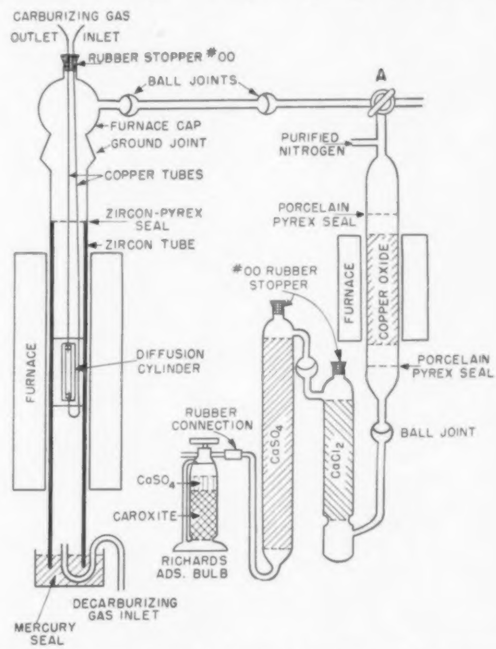

FIGURE 2. Schematic diagram showing sample suspension and analytical train.

CO_2) which had passed in a fixed time through the cylinder into the outgoing decarburizing gas. As steady-state is approached this rate approaches a constant value.

*Analysis (ND = not detected)

	Spectroscopic							
	Al	Cr	Sn	Pt	Mo	Ti	Co	B
Ingot Iron	ND	0.001	ND	ND	0.001	ND	ND	ND
Nat. Res. Iron	ND	ND	ND	ND	0.001	ND	ND	ND

	Quantitative				
	Mn	Cu	Ni	Pb	Si
Ingot Iron	0.032	0.085	0.007	0.001	0.005
Nat. Res. Iron	0.005	0.001	0.005	0.001	0.005

†National Research Corporation, 70 Memorial Drive, Cambridge, Massachusetts.

The carburizing gas was a hydrogen-methane mixture containing 10 per cent methane for measurements at 1000°C and 50 to 60 per cent methane for measurements at 851 and 802°C. The rate of flow was 15 cc. per minute for the 0.71 cm. i.d. cylinders and 30 cc. per minute for the 0.85 cm. i.d. cylinders. The composition of the carburizing gas is not critical, however its methane content and rate of flow must be high enough to maintain a deposit of soot on the cylinder surface and low enough that carbon disintegration of the surface is negligible. The decarburizing gas (tank hydrogen saturated with water vapor at room temperature) entered the bottom of the furnace tube through a mercury seal, passed over the cylinder and was either vented or connected to the analytical train by the three-way stop cock A (Figure 2). The rate of flow of the decarburizing gas was 100 cc. and 200 cc. per minute for the 0.71 and 0.85 cm. i.d. cylinders, respectively.

Analysis of the Outlet Gas

The amount of carbon taken up by the decarburizing gas during a time t was determined by combustion of the gas over copper oxide, removal of water and absorption of the carbon dioxide formed in a weighed absorption bottle as shown schematically in Figure 2. When connected to the analytical train, the decarburizing gas passed through a porcelain tube (2.5 cm. i.d. and 30 cm. long) filled with rolled, oxidized copper gauze held in a furnace at 500 to 550°C. During combustion the temperature inside the combustion tube was somewhat higher than the furnace temperature; in fact, on a few occasions the gauze was found to have melted to a solid mass. The water formed was removed by a tower filled with calcium chloride followed by a tower filled with calcium sulphate. These were connected to each other and to the combustion tube by pyrex ball joints and a porcelain-pyrex seal. The carbon dioxide was absorbed in a weighed Richards bulb [9] attached to the last drying tower by a short piece of rubber tubing. Except for this rubber connection, a number 00 stopper in the top of each drying tower and the furnace cap, the entire system was of pyrex or gas-tight ceramic. Purified nitrogen was introduced into the train just ahead of the combustion tube; this served to flush the train and absorption bottle before and after the combustion period and to carry the products of combustion through the train. After each combustion period the train and weighed absorption bulb were flushed for $\frac{3}{4}$ hour with purified nitrogen. To compensate for the effect of changes of room temperature and pressure on the amount of nitrogen in the absorption bottle an identical absorption bottle, used as a tare, was kept close to the weighed bottle; each bottle was opened to the air momentarily just prior to weighing. The tank hydrogen used for the decarburizing gas was found to contain a small amount of hydrocarbon, which was removed by passing the unsaturated gas through a tube filled with activated charcoal immersed in a dry-ice acetone mixture. With gas thus purified, the blank never amounted to more than 0.5 per cent of the carbon dioxide weighed in a typical analysis. For the diffusion cylinders at 1000°C the combustion period (about 30 and 15 min. for the 0.71 and 0.85 cm. i.d. cylinders respectively) was timed with an electric stop clock. At steady-state the amount of carbon dioxide weighed was of the order of 0.04 grams in each case and for a given cylinder the reproducibility, measured over a period of from 1 to 3 weeks, was of the order of ± 1 per cent of the CO_2 weighed. A few measurements of the rate were made for each cylinder with the pressure of the carburizing gas 10 cm. of Hg above atmospheric pressure; if the rate measured under these conditions was not greater than that determined with the carburizing gas at atmospheric pressure it was assumed that the cylinder was gas tight.

The analytical system was tested by two methods; for the first about 0.1 gm. of reagent grade $CaCO_3$ was weighed into a small platinum crucible and suspended in the furnace cap by a platinum wire; after the furnace had been flushed with purified wet hydrogen, connection was made to the analytical train and the sample lowered into the hot zone (1000°C) of the furnace. After one hour the wet hydrogen was vented, the sample raised into the furnace cap and the analytical train flushed for $\frac{3}{4}$ hour with nitrogen. The carbon dioxide found from the increase in weight of the carbon dioxide absorption bulb was then compared with the theoretical amount corresponding to the initial weight of $CaCO_3$. During the course of the diffusion experiments seven determinations of this type were made, the maximum difference between the CO_2 found and the theoretical amount was 1.0 per cent, the average being 0.5 per cent. Except for one determination, the CO_2 determined by analysis was less than the theoretical. The second method was identical with the first except that a strip of carburized electrolytic iron about 0.1 mm. thick and about 1 gm. in weight was substituted for $CaCO_3$. If the surface of such a strip were maintained fully decarburized, the strip would be 99.9 per cent decarburized in 45 minutes. In this case, the initial

carbon content of the strip was known from its gain in weight on carburization; the loss in carbon on decarburization was determined from the loss in weight of the sample and also by the gain in weight of the Richards bottle; the residual carbon was determined by combustion of the decarburized strip. The results of two measurements by this method are summarized in Table I. The loss in carbon to the

TABLE I

TEST OF APPARATUS FOR DETERMINATION OF THE AMOUNT OF CARBON REMOVED FROM AN IRON-CARBON ALLOY BY THE DECARBURIZING GAS

		Grams of carbon	
Sample number		1	2
Loss from sample	(Initial minus residual)	0.0130	0.0167
	(By weight loss of strip)	0.0125	0.0165
Found in gas		0.0126	0.0164

decarburizing gas, as determined by loss in weight of the sample, is in good agreement with that determined by combustion of the decarburizing gas. The amount of carbon removed as determined from combustion of the decarburizing gas in each case is slightly lower than that determined by the gain in weight on carburization minus the residual. However, the difference is not greater than the possible error in the determination of the residual carbon by the combustion method.

Determination of Cylinder Dimensions

To cool the sample to room temperature without loss of carbon and with as little distortion as possible, it was removed from the furnace and quenched into a salt bath (eutectic mixture of $NaNO_2$ and KNO_3) at 480°C, allowed to cool nearly to the solidification temperature of the salt mixture (150°C) and then quenched in water. Samples thus cooled were slightly too hard to machine well; all samples except number 7 were therefore subsequently sealed in evacuated pyrex tubes and tempered 20 minutes at 600°C. The distance between the copper plugs was determined as follows: (1) The ends were squared by machining and an over-all length measured with a micrometer; (2) The thickness of the copper plugs was determined by microscopic examination of polished sections taken from the ends of the cylinders. Since the carbon flux at the position of the copper plugs will not be normal to the cylinder surface but will bend towards the ends, the effective length, l, to be used in equation (2) will be greater than the distance between the inside surfaces of the copper plugs and less than the over-all length of the cylinder. From steady-state rate measurements for two cylinders, made as nearly identical as possible except that the length of one was half that of the other, the correction for each end effect was found to be equal to one half the wall thickness. The effective length of the diffusion cylinder was therefore assumed to be equal to the distance between the copper plugs plus a distance equal to the wall thickness. This correction amounts to about 2 per cent and 1 per cent in the calculated absolute diffusivity for the 0.71 and 0.85 cm. i.d. cylinders respectively. The outside diameter was determined by micrometer and the inside diameter by microscopic examination of polished sections taken from near the ends of the cylinder. This latter measurement is not as precise as the former since the polished surface may not be exactly normal to the cylinder surface and there may be some error in determining the metal-soot interface. All dimensions of length were corrected from room temperature to the temperature of measurement using the mean coefficient of expansion [10] for this temperature range corresponding to the mean carbon content of the sample.

Determination of Carbon Distribution

The central portion of each cylinder, 7.0 to 7.5 cm. in length, was mounted on a mandrel held in a precision lathe, and successive layers, about 0.12 mm. thick, machined from the cylinders. The diameter of the cylinder was measured with a micrometer before and after each cut, and unless otherwise noted, the mean carbon content of each layer was determined by the usual combustion method [9]. Each layer was machined by a single cut along the length of the cylinder and all turnings from such a cut were used for the determination of the mean carbon content of the layer.

Temperature Measurement and Control

The furnace for the diffusion sample was cylindrical, 20 inches long, wound with Kanthal wire as heating element. The zone of uniform temperature was increased beyond that usually attained in such a furnace by the circuit shown in Figure 3. Variac A controls the power to the furnace; the temperature gradient from top to bottom may be varied by adjustment of variac B and the temperature of the center section may be varied by adjustment of the 500 ohm resistance C. With this arrangement a

temperature zone over 4 inches long could be maintained uniform within ±0.5°C. The temperature of the uniform zone was maintained constant within ±1.0°C with a chromel-alumel control couple and a commercial controller. The temperature of the diffusion sample was determined from measurements at the outside surface of the zircon furnace tube with a platinum-platinum rhodium thermel which was calibrated at the melting point of pure gold and by repeated comparison with a standard couple certified by the Bureau of Standards. Tests with a dummy diffusion cylinder showed that the temperature inside the cylinder was at all points within 0.5°C of the temperature of the outside surface of the furnace tube.

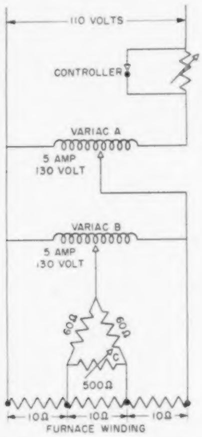

FIGURE 3. Electrical circuit for obtaining a large zone of uniform temperature in a furnace heated by a uniformly spaced helical wire winding.

Experimental Results

Carbon Distribution

The carbon distribution for each cylinder is given in Tables II and III. Here the mean radius $\bar{r}$ is the radius of the center of each machined layer at room temperature and weight per cent $\bar{C}$ is the average weight per cent carbon of the layer. The carbon content found for the final layer was frequently high, probably owing to failure to remove completely the soot from the inside surface. Typical graphs of the carbon distribution for a 0.71 and a 0.85 cm. i.d. cylinder at 1000°C are shown in Figures 4 and 5. The densities used to convert weight per cent carbon to grams per cc. at the diffusion temperature were calculated from the X-ray measurements of Esser and Müller [11]. By equation (3), these graphs would be straight lines if the diffusivity were independent of carbon content. The carbon content of the outside surface of the cylinders varied between 0.10 and 0.15 weight per cent; that at the inside surface was close to that for equilibrium with graphite [6; 7; 8].

TABLE II

CARBON DISTRIBUTION AT 1000°C FOR CYLINDERS 1 TO 6

(The arithmetical mean radius, $\bar{r}$, at room temperature and the average weight per cent carbon, wt. % $\bar{C}$, for each machined layer)

Sample no. 1		2		3		4		5		6	
$\bar{r}$ cm.	Wt. % $\bar{C}$	$\bar{r}$ cm.	Wt. % $\bar{C}$	$\bar{r}$ cm.	Wt. % $\bar{C}$	$\bar{r}$ cm.	Wt. % $\bar{C}$	$\bar{r}$ cm.	Wt. % $\bar{C}$	$\bar{r}$ cm.	Wt. % $\bar{C}$
0.5507	0.175	0.5519	0.139	0.5530	0.228	0.5540	0.187	0.5532	0.277	0.5542	0.206
.5392	.270	.5395	.273	.5428	.294	.5433	.260	.5400	.460	.5431	.412
.5268	.390	.5271	.392	.5306	.407	.5306	.395	.5271	.650	.5296	.621
.5154	.502	.5154	.503	.5187	.516	.5171	.519	.5156	.821	.5171	.804
.5044	.597	.5032	.613	.5060	.633	.5041	.629	.5029	.963	.5047	.948
.4940	.681	.4910	.713	.4920	.729	.4928	.731	.4910	1.087	.4920	1.088
.4836	.746	.4783	.804	.4770	.834	.4808	.822	.4793	1.196	.4785	1.209
.4699	.844	.4656	.894	.4625	.936	.4656	.920	.4663	1.318	.4661	1.319
.4585	.916	.4531	.977	.4493	1.109	.4524	1.020	.4491	1.425	.4501	1.444
.4488	.993	.4394	1.051	.4351	1.108	.4412	1.072				
.4348	1.080	.4275	1.123	.4206	1.177	.4270	1.162				
.4214	1.160	.4181	1.191	.4079	1.254	.4135	1.236				
.4049	1.244	.4059	1.260	.3967	1.315	.4031	1.290				
.3886	1.339	.3924	1.324	.3843	1.378	.3924	1.348				
.3764	1.395	.3777	1.392	.3691	1.441	.3719	1.463				
.3605	1.481	.3647	1.472								

TABLE III

CARBON DISTRIBUTION FOR CYLINDERS 11 AND 12, 851 AND 802°C RESPECTIVELY

(The arithmetic mean radius, $\bar{r}$, at room temperature and the average weight per cent carbon, wt. % $\bar{C}$, for each machined layer)

Temperature	851°C		802°C	
Sample no.	11		12	
	$\bar{r}$ cm.	Wt. % $\bar{C}$	$\bar{r}$ cm.	Wt. % $\bar{C}$
	0.4686	0.45	0.5118	0.250
	.4636	.52	.4999	.439
	.4587	.61	.4867	.643
	.4539	.68	.4745	.777
	.4488	.79	.4618	.896
	.4412	.83	.4493	1.050

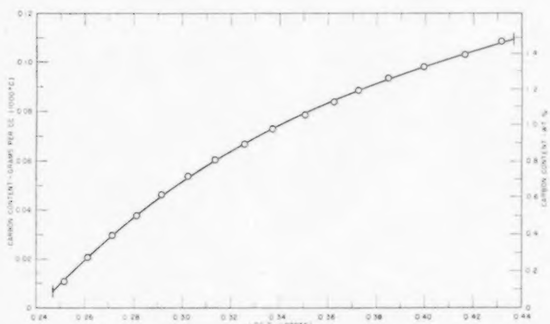

FIGURE 4. A typical carbon distribution curve for a 0.71 cm. i.d. cylinder (sample 2) at 1000°C. At a given carbon content the diffusivity is inversely proportional to the slope of the distribution curve.

For the temperature range 723 to 910°C the solid solution of carbon in iron may be either ferrite (solid solution of carbon in α-iron) or austenite (solid solution of carbon in γ-iron) depending upon the carbon content of the iron. Cylinder 11 (851°C) and 12 (802°C) have an inside shell of austenite and an outside shell of ferrite. Since the flux through the two shells is identical the position of the boundary between the two phases must be such that

$$[D(dc/d \ln r)]_{\text{austenite}} = [D(dc/d \ln r)]_{\text{ferrite}}$$

where the diffusivity D and slope $dc/d \ln r$ for each phase corresponds to the carbon content of the phase at the boundary. The carbon distribution for the austenite portion of these cylinders is given in Table III. The austenite shell of sample 12 was less than 0.4 mm. thick. The machined layers were about half as thick as those for the other samples and the carbon content was determined by the low-pressure combustion method [12].* Extrapolation of the carbon distribution curve to the position of the austenite-ferrite boundary gives a carbon content of the austenite of 0.13 per cent C for sample 11 (851°C) and 0.38 per cent C for sample 12 (802°C). The equilibrium values are reported to be 0.13 and 0.31 per cent C respectively [8; 13]. The discrepancy in the case of sample 12 may be due to errors in the measurement of the position of the austenite-ferrite boundary.†

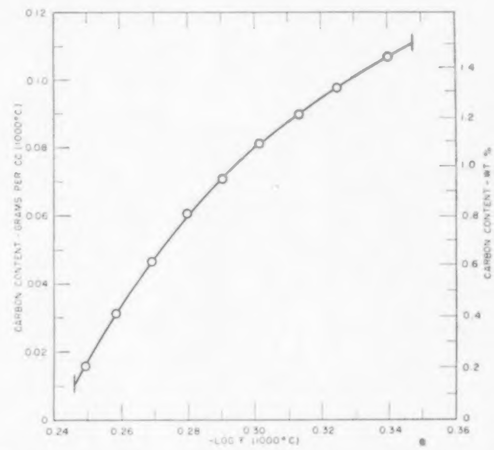

FIGURE 5. A typical carbon distribution curve for a 0.85 i.d. cylinder (sample 6) at 1000°C. At a given carbon content the diffusivity is inversely proportional to the slope of the distribution curve.

The mean carbon content of a few of the cylinders was determined by analysis of samples machined from the ends of the cylinders. The mean carbon content may also be determined graphically from the known carbon distribution in the cylinder by the relation

Mean weight per cent C

$$= \int_{r_1}^{r_2} \text{weight per cent } \bar{C}(d\bar{r}^2)/(r_2 - r_1)$$

where $r_2 - r_1$ is the wall thickness. The mean carbon content determined by either method is not precise; that determined by analysis is subject to sampling error and to the extent of removal of soot from the inside surface, that determined graphically involves integration under extrapolated portions of the curves and the determination of the radius of the inside

*We are indebted to the Analytical Department of Irvin Works, United States Steel Corporation for the low-pressure combustion analysis.

†The boundary position was determined by microscopic examination of polished cross sections cut from the ends of the cylinder. An error of 0.003 cm. in this measurement would account for difference between the extrapolated and equilibrium values of the carbon content.

surface may not be precise. However, the results summarized in Table IV do indicate that the cylinders were carburized uniformly from bottom to top.

TABLE IV

THE AVERAGE CARBON CONTENT OF DIFFUSION CYLINDERS

(As determined by analysis of cross-section samples taken from the ends of the cylinders and from the area under the curve obtained by plotting the mean carbon content of each machined layer against the square of its mean radius)

Sample no.	Analysis Top	Analysis Bottom	Graphical $\int_{r_1}^{r_2}$ wt % $\bar{C}(d\bar{r}^2)/(r_2-r_1)$
2	0.85	0.88	0.84
3	0.86	0.86	0.85
4	0.83	0.86	0.86
5	0.91	0.89	0.92
6	0.87	0.86	0.92

Diffusivity of Carbon in Austenite

The average grams of carbon per second (q/t of equation (2)) passing through each cylinder at steady-state is given in Table V together with the corresponding temperature,* the effective cylinder length, the value of K (equation (3)) and the approximate wall thickness. The diffusivities calculated from the data of Table V and the slope† of each distribution curve corresponding to a number of carbon concentrations are given in Table VI together with the average diffusivity at each concentration and the coefficient of variation (100 times the standard deviation divided by the average) [15] for the determinations at 1000°C. The diffusion coefficients given for samples 11 and 12 (851 and 802°C) are less precise than those for 1000°C since in each case measurements were made on only one cylinder and both the distance over which the carbon distribution was determined and the measured value of q were smaller.

A comparison of these results with those of Wells, Batz and Mehl [3] is shown in Figure 6 where log ($D \times 10^7$) is plotted vs. weight per cent C. The agreement between the two sets of measurements is quite good except at the higher carbon contents at

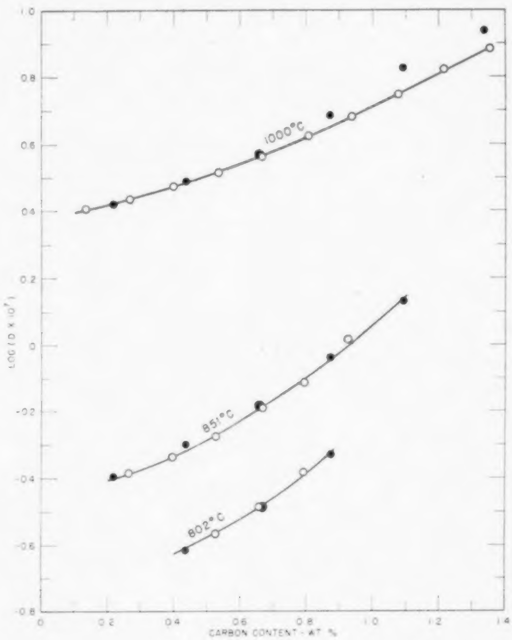

FIGURE 6. Comparison of the diffusion coefficient determined by steady-state and non-steady-state methods; ○ Smith, steady-state; ● Wells, Batz and Mehl, non-steady state.

1000°C where the present results from the steady-state method are somewhat lower than those determined from non-steady-state measurements.*

Since one of the primary objects of the present investigation was to determine the nature of the functional relation of diffusivity to concentration, it seems desirable to determine a measure of the precision with which this has been accomplished. To

*The temperature of the diffusion cylinder measured each day just prior to the analysis of the decarburizing gas was not always 1000, 851 or 802°C. To allow the rate measurements for a given cylinder to be averaged and to express the calculated diffusivities at an even temperature a small correction was made to the measured rates to make them correspond to the temperature given in column 3. This correction (about 1 per cent per degree at 1000°C) was determined from the data of Wells, Batz and Mehl [3] and in no case amounted to more than 3.5 per cent of the measured value.

†The slopes were read with the aid of a glass rod according to the method described by E. Ramsey Wigan [14]. Except at the extreme ends of the curve, the reproducibility of reading the slope was about ±1 per cent.

*A minimum value for the diffusivity of carbon in ferrite at 851 and 802°C may be estimated from the data of Table V, the thickness of the ferrite shell and the assumptions that the carbon content of the ferrite is zero at the outside surface and the value corresponding to equilibrium with austenite [8; 13] at the inside boundary. Since the carbon content is always small it may be assumed that the distribution curve is linear. Under these conditions the calculated diffusivity of carbon in ferrite is 49×10^{-7} at 851°C and 27×10^{-7} at 802°C. These diffusivities are in good agreement with the corresponding values 52×10^{-7} and 26×10^{-7} calculated from the decarburization data of Pennington [16] (760–871°C) by the equation of Darken [17] for diffusion accompanied by phase change. They are not in agreement with the values 29×10^{-7} and 16×10^{-7} calculated from the equation of Stanley [18] (514–786°C) or the values 24×10^{-7} and 16×10^{-7} calculated from the equation of Wert [19]. However, if Stanley's equation were based on his measurements for the temperature range 700 to 786°C the agreement with our estimate would be much better.

TABLE V

DATA RELEVANT TO THE CALCULATION OF THE ABSOLUTE DIFFUSIVITY

Sample no.	Cylinder material	Temp. °C	Rate gm. Carbon per sec. $\times 10^6$	Effective cylinder length cm.	$K \times 10^7$ eq. (3)	Wall thickness cm.
1	Ingot Iron	1000	6.38	9.27	2.52	0.20
2	Ingot Iron	1000	6.66	9.76	2.50	0.20
3	Nat. Res. Corp.	1000	6.40	9.70	2.42	0.20
4	Nat. Res. Corp.	1000	6.67	9.93	2.46	0.20
5	Ingot Iron	1000	12.62	9.85	4.70	0.12
6	Ingot Iron	1000	12.66	9.91	4.69	0.12
11	Ingot Iron	851	1.79	9.88	0.66	0.12
12	Ingot Iron	802	0.94	9.34	0.37	0.12

TABLE VI

ABSOLUTE DIFFUSIVITIES OF CARBON IN IRON

	1000°C								851°C	802°C
Sample no.	1	2	3	4	5	6			11	12
Carbon content gm/cc.	Diffusivity, $D \times 10^7$						Average	Variance* coeff. %	$D \times 10^7$	
0.01	2.59	2.56	2.49	2.46	2.64	2.52	2.54	2.6		
.02	2.80	2.73	2.65	2.65	2.84	2.72	2.73	2.6	0.41	
.03	3.05	2.98	2.92	2.88	3.08	2.98	2.98	1.5	.46	
.04	3.34	3.22	3.23	3.14	3.39	3.32	3.27	2.8	.53	0.27
.05	3.73	3.58	3.66	3.52	3.75	3.67	3.65	2.4	.65	.33
.06	4.33	4.22	4.19	4.04	4.15	4.18	4.19	2.2	.77	.41
.07	4.90	4.86	4.74	4.63	4.73	4.81	4.78	1.9	1.04	
.08	5.77	5.69	5.55	5.44	5.62	5.48	5.59	2.1		
.09	6.74	6.74	6.50	6.61	6.53	6.61	6.63	1.5		
.10	7.64	7.67	7.40	7.66	7.70	7.83	7.65	1.8		
							Av.	2.14		

*The coefficient of variation for a set of numbers is defined as the ratio of their standard deviation to their average, expressed as a percentage.

do this it is necessary to separate errors associated with absolute rate determination from relative errors, i.e. errors in the ratio of the diffusivity at one concentration to that at another concentration; it is only these relative errors, arising in the measurements, analyses and graphical treatment of a diffusion cylinder, which give rise to error in this ratio. This separation of errors and assignment of absolute and relative precision is a more complex problem than it first seems. The method used is to revise Table VI so that the recorded diffusivity does not reflect individual fluctuations in the determination of the absolute rate. This is accomplished by determining for each cylinder a factor f such that division of each diffusivity (for the same cylinder) by this factor minimizes the departure of the diffusivities for this cylinder from the average diffusivities. This factor is, of course, always near unity and its average value is unity. Values of this factor and of the new individual diffusivities, D', obtained therefrom are given in Table VII. The coefficient of variation, v (one hundred times the standard deviation divided by the average), also tabulated, is a convenient way to express the error; it represents approximately the percentage error within which two-thirds of the measurements lie. The coefficient of variation for f (1.8 per cent) reflects the error in the absolute determinations and that for D' (averaging 1.4 per cent) reflects the relative errors; this is consistent with the variance of Table VI (averaging 2.1 per cent) which reflects the total error. The 90 per cent confidence limit [15] of the final values for D reported in Table

TABLE VII

INDIVIDUAL DIFFUSIVITIES AT 1000°C CORRECTED FOR VARIATIONS IN THE DETERMINATION OF THE ABSOLUTE RATE

	Sample no. 1	2	3	4	5	6	Coefficient of variation %
f	1.020	1.003	.986	.973	1.016	1.000	1.8
Carbon content gm/cc.	Individual diffusivities, $D' \times 10^7$						
0.01	2.54	2.55	2.53	2.53	2.60	2.52	1.1
.02	2.73	2.72	2.69	2.72	2.80	2.72	1.3
.03	2.99	2.97	2.96	2.96	3.03	2.98	0.9
.04	3.27	3.21	3.27	3.23	3.34	3.32	1.5
.05	3.66	3.57	3.71	3.62	3.69	3.67	1.4
.06	4.24	4.21	4.25	4.15	4.12	4.18	1.2
.07	4.80	4.84	4.81	4.76	4.66	4.81	1.3
.08	5.66	5.67	5.63	5.59	5.53	5.48	1.3
.09	6.61	6.72	6.59	6.79	6.43	6.61	1.9
.10	7.49	7.65	7.51	7.87	7.58	7.83	2.1
						Average	1.40

VI is 0.901 times the coefficient of variation. Using this 90 per cent limit, the average precision of the reported average diffusivities may be written as ± 1.9 per cent. The corresponding relative precision is 1.2 per cent. It will be noted from Table VII that the precision drops off only slightly at the high carbon limit.*

There are two fundamental methods of approaching the problem of determining the functional relation between diffusivity and concentration. The classical method, as shown for example by Darken [20], leads to the following expression for the case of interstitial diffusion as the present case of carbon in iron

$$D = BkT\,(1 + C\,d \ln \gamma/dC) \tag{4}$$

where k is Boltzmann's constant, T the absolute temperature and B, C and γ are the mobility, concentration and activity coefficient of carbon respectively. This equation evaluates the diffusivity in thermodynamic terms except for B which in general is an unknown function of the concentration. The absolute reaction rate theory as shown by Fisher, Hollomon and Turnbull [21] leads, for interstitial diffusion, to the relation

$$D = A\,\lambda^2\,\gamma\,(1 + C\,d \ln \gamma/dC)/\gamma^* \tag{5}$$

where A is a constant, λ the jump distance and γ^* is the activity coefficient of the activated complex. It will be noted that the two expressions (4) and (5) are nearly identical; the only difference lies in the coefficient of the terms in parenthesis. This coefficient involves an unknown variable in both cases. The simplest hypothesis concerning this coefficient is that it is constant (corresponding to constant mobility or constant ratio of γ to γ^*). In this case, as seen from either equation, $D/(1 + C\,d \ln \gamma/dC)$ would be constant. This quantity is plotted against concentration in Figure 7 (curve B); it is readily seen that it is by no means constant.* For comparison

*The carbon distribution curves for four additional cylinders of ingot iron were determined. These cylinders were not sufficiently gas tight to allow a determination of the absolute rate, however diffusivities for these cylinders may be calculated from the slopes of the distribution curves and the average diffusivities for cylinders 1 to 6 by a method similar to that used to calculate the individual diffusivities of Table VII. The results are given below.

Carbon content gm/cc.	Cylinder 7	8	9	10	Average	Coefficient of Variation %
	Diffusivity, $D' \times 10^7$					
0.01	2.52	2.49	2.59	2.54	2.53	1.3
.02	2.73	2.70	2.77	2.72	2.73	1.1
.03	3.01	2.91	2.98	2.95	2.96	1.0
.04	3.25	3.20	3.30	3.24	3.25	0.8
.05	3.74	3.69	3.70	3.60	3.68	1.6
.06	4.30	4.29	4.22	4.13	4.23	1.8
.07	4.87	4.97	4.80	4.84	4.87	1.4
.08	5.59	5.73	5.57	5.73	5.63	1.2
.09	6.53	6.61	6.45	6.72	6.57	1.2
.10	7.38	7.63	7.38	7.69	7.55	2.4
					Average	1.4

The agreement between the two sets of measurements is quite satisfactory.

*The activity coefficient of carbon in iron was calculated from the activity data of Smith [8]. Within the accuracy of

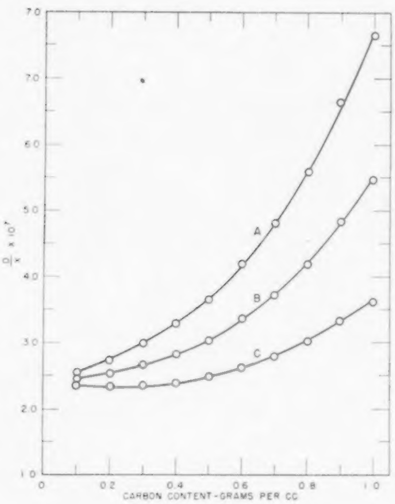

FIGURE 7. Comparison of concentration function of the diffusivity and related quantities. Curve A, $X = 1$; Curve B, $X = 1 + c(d \ln \gamma/dc)$; Curve C, $X = \gamma(1 + d \ln \gamma/dc)$.

the diffusivity is plotted against the concentration in the same figure (curve A).

A second hypothesis concerning the coefficient was made by Birchenall and Mehl [22]; they assume, in effect as pointed out by Fisher, Hollomon and Turnbull, that γ^* is a constant. This assumption simplifies equation (5) to the form

$$D = D_0\gamma(1 + C\, d \ln \gamma/dC)$$

which was believed by Birchenall and Mehl to be consistent with the data then available (D_0 being a constant). If this formulation were correct, $D/[\gamma(1 + d \ln \gamma/dC)]$ would be independent of composition. This quantity is plotted in Figure 7 (curve C); again wide departure from constancy is evidenced in the high concentration range, although there is a short range of constancy at low concentration. The only conclusion that can be drawn at the present time is that neither of the previously suggested postulates is in accord with the present data; the discrepancy is very much greater than the precision limits of the diffusion and activity data.

this data $\log \gamma$ is a linear function of the atom ratio of carbon to iron, n_2/n_1, and is given the equation $\log \gamma = An_2/n_1 + B$, where the value of B depends on the choice of standard state. The value of A determined from equilibrium of iron with mixtures of CO–CO_2 or CH_4–H_2 differs by about 20 per cent, the average value being 2.86. The concentration unit used for the data of Figure 7 is grams carbon per cc. of sample and the standard state is chosen such that γ approaches unity as the concentration approaches zero. Under these conditions $\log \gamma = 1.79C$ and $d \ln a/d \ln C = 1 + C d \ln \gamma/dc = 1 + 4.12C$. If A is a constant for concentrations expressed as atom ratio it will not be constant for concentrations expressed in other units, however, the deviation will amount to only a few per cent which is small compared to the uncertainty in A.

References

1. Methods of determining diffusivity for Metallic systems are described and discussed by C. WELLS, in "Atom Movements" (Cleveland, American Society for Metals, 1951).
2. WELLS, C. and MEHL, R. F. Trans. A.I.M.E., **140** (1940) 279.
3. WELLS, C., BATZ, W., and MEHL, R. F. Trans. A.I.M.E., **188** (1950) 553.
4. For a discussion of methods of calculation of the diffusivity from non-steady-state measurements see [1], also RHINES, F. and MEHL, R. F. Trans. A.I.M.E., **128** (1938) 185.
5. FICK, H. "Über Diffusion," Pogg. Ann., **94** (1855) 59.
6. WELLS, C. Trans. Amer. Soc. Metals, **26** (1938) 289.
7. GURRY, R. Trans. A.I.M.E., **150** (1942) 147.
8. SMITH, R. P. J. Amer. Chem. Soc., **68** (1946) 1163.
9. Sampling and Analysis of Carbon and Alloy Steels (New York, Reinhold Publishing Company, 1938).
10. Alloys of Iron and Carbon, Vol. II (New York, McGraw-Hill Book Company, 1937).
11. ESSER, H. and MÜLLER, G. Arch. Eisenhüttenw. **7** (1933–34) 265.
12. GURRY, R. and TRIGG, H. Industr. Engng. Chem., Anal. ed., **16** (1944) 248.
13. MEHL, R. F. and WELLS, C. Trans. A.I.M.E., **125** (1937) 429.
14. WIGAN, E. RAMSEY. J. Scientific Instruments and Physics in Industry, **26** (1949) 162.
15. ASTM Manual on Quality Control of Materials, (Philadelphia Amer. Soc. Testing Materials, 1951).
16. PENNINGTON, W. A. Trans. Amer. Soc. Metals, **37** (1946) 48.
17. DARKEN, L. S. Trans. A.I.M.E., **150** (1942) 157 (Appendix).
18. STANLEY, J. K. Trans. A.I.M.E., **185** (1949) 752.
19. WERT, C. A. Phys. Rev., **79** (1950) 601.
20. DARKEN, L. S. Trans. A.I.M.E., **175** (1948) 184.
21. FISHER, J., HOLLOMON, J., and TURNBULL, D. Trans. A.I.M.E., **175** (1948) 202.
22. BIRCHENALL, C. E. and MEHL, R. F. Trans. A.I.M.E., **171** (1947) 143.

A STUDY OF DEFORMED AND RECOVERED ALUMINUM CRYSTALS BY A NEW X-RAY TECHNIQUE*

C. A. JULIEN† and B. D. CULLITY‡

By the use of a Soller slit in the primary beam and a line source of X-rays, the focusing Laue method of Guinier and Tennevin has been extended to allow the detection and measurement of torsional strain in a crystal lattice. Focused reflections from planes other than those considered by Guinier and Tennevin may also be obtained under these conditions. In deformed single crystals of aluminum, torsionally strained regions of the lattice are found to occur quite generally. Deformation is found to be highly inhomogeneous when an extended region of a deformed crystal is examined. The reversibility of plastic deformation is shown. Polygonization of bent specimens is confirmed and it is shown that crystals deformed by torsion may recover by partial untwisting rather than by polygonization.

UNE ÉTUDE DE CRUSTAUX DÉFORMÉS ET RESTAURÉS D'ALUMINIUM AU MOYEN D'UNE NOUVELLE MÉTHODE D'APPLICATION DES RAYONS X

La méthode de focalisation de Guinier et Tennevin a été étendue par l'emploi d'une fente de Soller dans le faisceau primaire et d'une source linéaire de rayons X, pour permettre de détecter et de mesurer la déformation de torsion dans un réseau cristallin. Des réflexions focalisées, provenant d'autres plans que ceux qui étaient considérés par Guinier et Tennevin, peuvent aussi être obtenues dans ces conditions. Dans des monocristaux déformés d'aluminium on trouve assez généralement des régions du réseau déformées par torsion. Quand on examine une grande région d'un cristal déformé, il est constaté que la déformation est fortement hétérogène. La réversibilité de la déformation plastique est montrée. La polygonisation des cristaux fléchis est confirmée et il est montré que des cristaux déformés par torsion peuvent subir une restauration par détorsion partielle plutôt que par polygonisation.

EINE UNTERSUCHUNG VON VERFORMTEN UND ERHOLTEN ALUMINIUM-KRISTALLEN MIT EINER NEUEN RÖNTGENMETHODE

Mit Hilfe von Sollerschlitzen im Primärstrahl und einer linearen Röntgenstrahlquelle war es möglich, die fokussierende Laue Methode von Guinier und Tennevin so auszuarbeiten, dass Drehverzerrungen im Kristallgitter aufgefunden und gemessen werden konnten. Ausserdem können unter diesen Bedingungen fokussierte Reflexionen von Ebenen, die Guinier und Tennevin nicht in Betracht zogen, erhalten werden. Durch Verdrehung verzerrte Gitterbereiche treten recht häufig in verformten Aluminium Einkristallen auf. Bei der Untersuchung grosserer Kristallbereiche erwies sich die Verformung als sehr inhomogen. Es wird gezeigt, dass die plastische Verformung reversibel ist. Die Polygonisation gebogener Proben wird bestätigt, und es wird gezeigt, dass sich die durch Drehung verformten Kristalle zu einem Teil durch Zurückdrehen und nicht durch Polygonisation erholen.

Introduction

Guinier and Tennevin [1; 2] have developed a variation of the transmission Laue method which allows them to detect and measure very small angular disorientations in a diffracting crystal lattice. This technique utilizes the fact that a beam of polychromatic X-rays, diverging from a point source, is diffracted into a converging beam which comes to a sharp focus at a fixed point, if the diffracting crystal is undistorted. Any distortion of the crystal broadens the reflection at the focus point and the angular disorientation can be determined from the extent of the broadening. The position of the focus point is readily calculable, its distance from the crystal being of the same order of magnitude as the distance from the crystal to the X-ray source.

Guinier and Tennevin [1] have also pointed out that, by placing the film directly behind the specimen instead of far away at the focus point, "crystal images" can be obtained. In other words, a transmission Laue pattern is recorded in which the individual Laue spots are slightly distorted projections ("images") of the crystal, revealing variations in the diffracting characteristics of different regions of the crystal.

It has been recently shown [3] that both G-T techniques can be usefully extended by placing a *Soller slit* in the primary beam issuing from a *line source* of X-rays. Under these conditions, it is possible (*a*) to measure torsion in the crystal lattice as well as simple disorientation about one axis, and (*b*) to obtain qualitative information regarding the relative perfection of different parts of the crystal. This new technique is applied in the present investigation to a study of the deformation and recovery of aluminum single crystals.

Experimental Methods

The required fine line source of X-rays was provided by the CA-7 tube in a General Electric XRD-3 unit. Pinhole photographs of this source showed that

*Received April 23, 1953.
†Department of Metallurgy, University of Notre Dame, Notre Dame, Indiana, U.S.A. Now at National Research Council, Washington, D.C.
‡Department of Metallurgy, University of Notre Dame.

its projected width, at a target-to-beam angle of 4°, was less than 0.1 mm. and its length about 15 mm. The X-ray tube was positioned by means of a specially made collar so that the window opposite the line source faced the "film side," rather than the spectrometer side, of the XRD-3 unit.

The experimental arrangement is shown schematically in Figure 1 in terms of rectangular coordinates axes XYZ. The line source S is vertical and

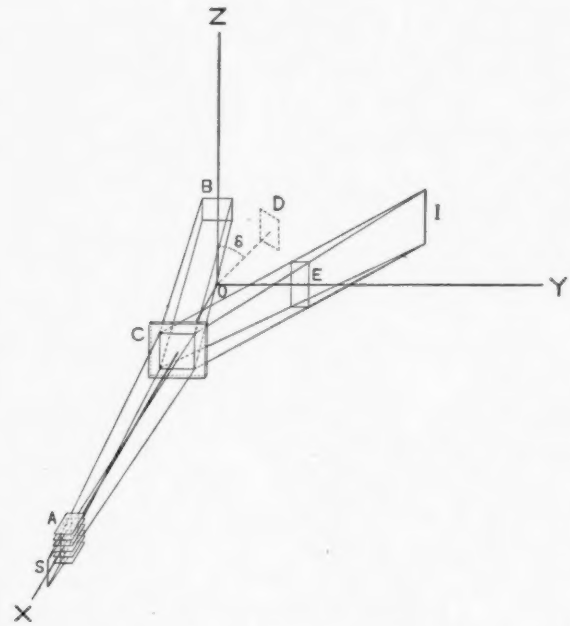

FIGURE 1. Relative position of source, specimen and reflections in a rectangular coordinate system.

parallel to the Z axis while the plates of the Soller slit A are horizontal. The Soller slit minimizes vertical divergence and provides a fixed angle of horizontal divergence, producing a wedge-shaped horizontal beam which is reflected by vertical lattice planes in the crystal C to a sharp line focus at I, if the crystal is perfect. If the crystal is not perfect, but bent or otherwise disoriented about an axis parallel to Z, then the Laue reflection on a film placed at I will be broadened. The distances SC and CI are both of the order of 30–40 cm.

Alternatively, the film is placed a few centimeters behind the crystal and a "crystal image" or "large beam transmission Laue" pattern is recorded. This may or may not be of interest in itself, but it always indicates immediately whether the specimen is correctly oriented for examination by the G-T focusing technique by the presence or absence of a diffraction spot in the same horizontal plane as the primary beam spot. Figure 2(c), discussed below, is an illustration of such a pattern.

As will appear later, it is desirable to have a simple way of designating the diffraction spots on this type of pattern. This may be done satisfactorily by noting the azimuthal angle δ of the spots on the film: thus a spot, such as B in Figure 1, immediately above the primary beam spot, is termed a 0° reflection, while one on the equator line of the film is termed a 90° reflection. In general, the indices of the reflections are of no significance.

Specimen preparation was guided by considerations that the specimen should be (1) a single crystal, (2) as thin as may be conveniently handled without deformation, and (3) of an area approximately equal to the cross-section of the wedge-shaped beam at a convenient distance, i.e., 30–40 cm. from the source. This area is of the order of 1–2 cm^2. Some specimens were prepared by the strain-anneal method, but it was found that specimens of the desired size and shape could be more satisfactorily prepared by growth from the liquid state. The analysis supplied with the stock indicated that the material was 99.9953 per cent Al (by difference). Melting probably reduces this purity.

The apparatus used in the deformation experiments consisted of a bending machine and a torsion machine. The bending machine provided for four-point loading of the plate-shaped specimen in order to produce pure bending in the portion of the crystal between the two inside knife edges, which were one inch apart. These knife edges could be advanced by a micrometer screw, the two outside knife edges being fixed. The torsion machine was designed to produce torsion about the longitudinal axis of a crystal plate measuring about $1\frac{1}{2} \times \frac{3}{4} \times 0.040$ inches. The specimen, with its longitudinal axis vertical, is slipped into a slit in the base of the device and a corresponding slit in a rotatable arm suspended at its center from the top of the machine. The action of a screw bearing against one end of this arm applies torque to the specimen. Both the bending and torsion machines were so designed that diffraction patterns could be made with the specimen under stress.

The annealing experiments were performed in a tubular resistance furnace, $1\frac{1}{2}$ in. in diameter and 3 in. long, the specimen resting in a small refractory cradle. A temperature difference of about 20° C was found to exist between the bottom and top of the specimen and the temperatures given below were obtained by adding 10° C to the temperature indicated by a thermocouple in contact with the bottom

of the specimen. The furnace was positioned horizontally, with the median ray of the primary beam passing along its axis. Mica cover sheets were hung loosely over the open ends of the furnace: they did not noticeably increase X-ray exposure time. With this simple furnace, it was possible to heat a specimen to its melting point in a few minutes with a power input of only about 300 watts.

Experimental Results

General

As previously shown [3], the use of a Soller slit in the primary beam from a line source adds informative detail to all reflections, whatever their azimuthal angle δ, including the 90° reflections studied by Guinier and Tennevin. If the crystal is undistorted, the focused 0° reflection consists of a set of parallel horizontal lines or striations and, as the angular position of the reflection increases, the lines become more and more inclined to the horizontal and more closely spaced until they merge, at $\delta = 90°$, into a single vertical line. Distortion of the crystal causes the originally straight and parallel lines in all but 90° reflections to become curved, broken and/or blurred in a manner dependent on the nature and degree of the deformation. The focused 90° reflection from a distorted crystal is merely broadened if the crystal has been bent but contains fine parallel striations if the crystal has been twisted about a vertical axis. The greater the torsion the greater the inclination of these striations to the vertical and the amount of twist per unit length along the torsion axis can be calculated from this measured angle.

It was found that focused 90° reflections from aluminum crystals deformed by bending or twisting or in some random, accidental manner quite commonly showed evidence of twisted regions in the lattice. These reflections often contained complex multiple sets of striations curving in different directions, indicating that different parts of the crystal were non-uniformly twisted by varying amounts.

However, neither the size nor the location of a twisted region is indicated by the striations in a 90° reflection recorded at the calculated focusing position: to obtain such information it is necessary to record reflections at a *series* of specimen-film distances. An example of this procedure is given in Figure 2, obtained from a crystal accidentally and non-homogenously deformed by a small amount. Figure 2(a) is a 90° reflection recorded on a film 42 cm. from the specimen. Striations indicating torsion appear prominently but are misleading as to the size of the twisted region, as shown by the other photographs of the series. Figure 2(b) is the same 90° reflection recorded at a specimen-film distance of 12 cm. Here very fine, closely spaced striations can be seen (on the original photograph, at least) only in the lower center of the reflection and these may be traced back to the small dark pip (marked with an arrow) at the lower edge of the 90° reflection in Figure 2(c), recorded at 6 cm. from the specimen. This latter photograph is here termed a "large-beam transmission Laue" photograph and shows several Laue spots: the one vertically above the intense spot formed by the primary beam is a 0° reflection and shows that the twisted region is located at the left edge of the specimen. It was concluded from these photographs (and others not reproduced) that the specimen contained a small twisted region located at its lower left-hand corner. This conclusion was confirmed by blocking off all the specimen, about 1 cm. square and 0.5 mm. thick, except for a region about 1 mm. square at the lower left corner and obtaining a 90° reflection at 18 cm. which contained striations just as prominent and extensive as those in Figure 2(a).

Results of Controlled Deformation

A few strip specimens, with a gage length of about 2.5 cm., were investigated after tensile deformation. The 90° reflections from such specimens became enlarged in both dimensions with increasing extension. These reflections were badly blurred and striations due to torsion were either absent or barely visible. The tensile experiments were abandoned as apparatus for inducing small, controlled amounts of pure tensile strain was not available.

With deformation by bending, it is much easier to produce small strains in small thin specimens of the type suitable for the X-ray techniques employed here. Thus, a specimen 1 mm. thick bent to a radius of 30 cm. undergoes a maximum tensile elongation of only 0.16 per cent.

The specimens used for the bending experiments had the form of a thin rectangular plate and were mounted approximately normal to the primary X-ray beam, with their long edges horizontal, and bent about a vertical axis. In this position, the 90° reflections are produced by a plane parallel to the bending axis and approximately normal to the crystal surface, here called the transverse plane. If the crystal and bending machine are rotated 90° around the primary beam axis, then the bending axis becomes horizontal and 90° reflections can be obtained from a plane, here called the longitudinal plane, which is perpendicular to the bending axis and approximately normal to the crystal surface.

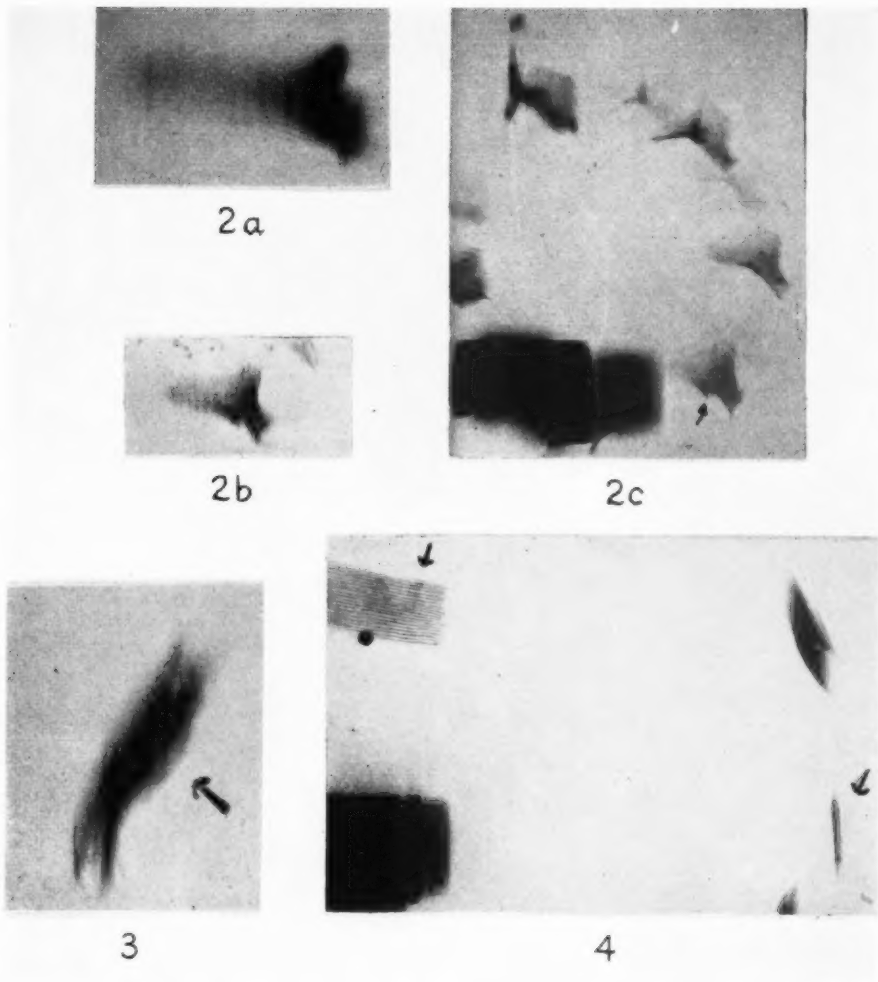

PLATE I. Figure 2—90° reflections from a slightly deformed Al crystal. (*a*) With film at 42 cm. (*b*) At 12 cm. (*c*) At 6 cm, showing entire quadrant of the transmission Laue pattern. Figure 3—Focused 90° reflection from the longitudinal plane of a bent Al crystal. Magnification 2×. Figure 4—Focused reflections from a unstrained Al crystal.

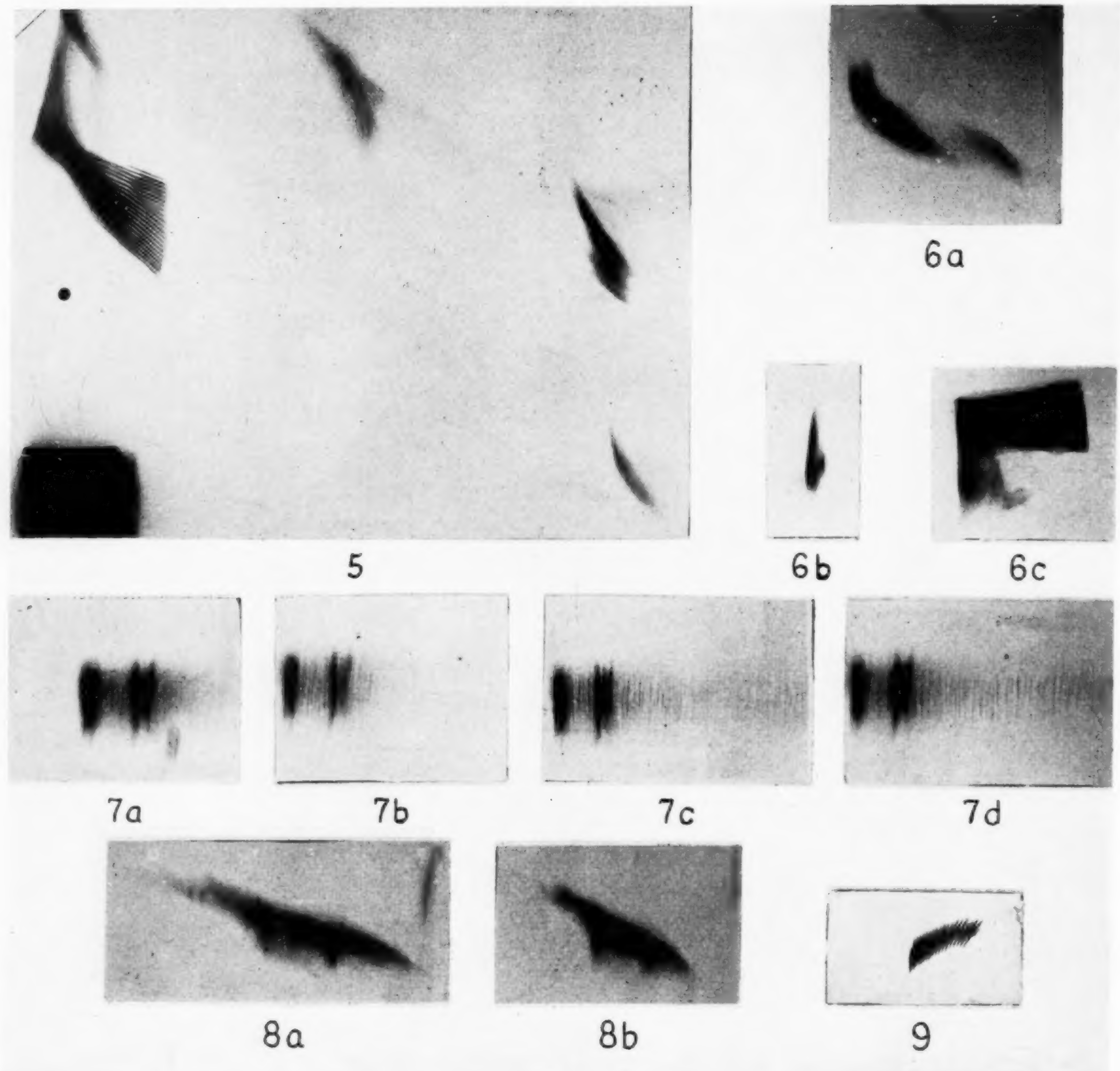

PLATE II. Figure 5—Focused reflections from the crystal of Figure 4, after torsion. Figure 6—Focused reflections from the crystal of Figure 5. (*a*) 90° reflection after twisting. (*b*) Same, after reverse twisting. (*c*) 0° reflection, after reverse twisting. Figure 7—Focused 90° reflections from the transverse plane of a bent crystal. (*a*) Before heating. (*b*) At 590°C. (*c*) At 610°C. (*d*) Long exposure at 610°C. Figure 8—90° reflections from the transverse plane of a twisted crystal. (*a*) Before heating. (*b*) After slow heating to 640°C. Figure 9—75° reflection form bent mica.

It was found that 90° reflections from the transverse plane of bent aluminum specimens broaden as expected, but do not generally show torsional striations. The broadening should be calculable from the radius of curvature of the specimen and the X-ray geometry, and a general equation is developed in the Appendix for this purpose. Experiments on elastically bent quartz crystal plates showed good agreement between the observed broadening of the reflection and that calculated from equation (3) of the Appendix, but such agreement was seldom obtained for plastically bent aluminum crystals. This elementary comparison simply illustrates the non-uniformity of plastic deformation.

Reflections from the longitudinal planes of bent aluminum crystals always show broadening, but usually to a lesser extent than those from a transverse plane. These reflections very frequently contain torsional striations and Figure 3 is a typical example. In this reflection the combination of torsional striations with intense vertical lines (the latter indicating the presence of relatively perfect crystal blocks) suggests a possible function of the twisted portion of the lattice, namely the joining together of more or less perfect crystalline fragments produced by the deformation. This is shown by the fact that the striations curve steeply at one end into an intense vertical line. Actually there are several sets of striations in this reflection, curving into several vertical lines, although only the lower set marked by an arrow shows clearly.

The reflection in Figure 3 was studied by means of multi-position photographs analagous to those shown in Figure 2. This series definitely established the existence of distinct fragments in this specimen and appeared to confirm the role played by the twisted portion of the lattice. In some specimens deformed by controlled bending this "fragmentation" was observed with little or no evidence of twisted lattice regions being present.

Evidence was found for the reversibility of plastic deformation as manifested in X-ray photographs of the type employed here. This is demonstrated for torsional deformation in Figures 4–6. Torsion is a preferable mode of deformation for studying reversibility because the reverse stress could be applied without demounting the specimen.

Figure 4 was made with an unstressed crystal mounted in the torsion machine. Because the respective Bragg angles were quite small, it was possible to record on one film both a 90° reflection and a reflection appearing in approximately the 10° position, with both reflections approximately in focus. They are indicated by arrows in Figure 4 and both show that the crystal contained a sub-structure as prepared, the 90° reflection by the split into two or more lines, and the 10° reflection by the slight ripple indicated by the arrow.

The specimen was then twisted in small increments and its deformation studied by successive pictures of the type of Figure 4. Figure 5 shows its condition after twisting through an angle of about 0.1 radian, or a twist per unit length of about 12 minutes/mm. It is interesting to note that although the specimen has clearly fragmented it has not done so along the lines of the pre-existing substructure disclosed in Figure 4. Torsional striations are faintly visible in the 90° reflection.

At this point the specimen was rotated 10° counterclockwise around the beam axis to bring a more strongly reflecting plane into the 90° position (which of course brought the 10° reflection into the 0° position). The 90° reflection of this new plane, showing both fragmentation and twisting, appears in Figure 6(*a*).

The specimen was then reverse twisted and the reflections, instead of becoming more complex, began to return to the configuration of those from the original undeformed crystal. Figure 6(*b*) shows the 90° reflection after reverse deformation had reduced it to a minimum width, and Figure 6(*c*) is the corresponding 0° reflection. Both show that the crystal has returned to a fairly high degree of perfection, although there is still some residual deformation which apparently cannot be removed by reverse stressing.

Reversibility has also been demonstrated with bending deformation. In some cases, a deformation-broadened 90° reflection can be made, by reverse bending, to return to a width even narrower than that shown in Figure 6(*b*).

Effect of Annealing

The annealing experiments were carried out in the furnace described earlier, which served the very useful purpose of allowing X-ray photographs to be made before, during and after heating without handling of the specimen. Errors due to accidental deformation or changes in orientation were thus avoided.

Figures 7(*a*)–(*d*) show focused 90° reflections from the transverse plane of a specimen bent to a 25 cm. radius. The reflection in (*a*) was recorded at room temperature before heating (some extraneous reflections from the mica cover sheet appear in this picture) and (*b*), (*c*), and (*d*) at elevated tempera-

tures. The exposure time, except for (*d*), was about 5 minutes for each.

The reflection in Figure 7(*a*) from the bent, unannealed specimen shows fragmentation as well as bending. After the room temperature photograph was made, the specimen was heated to 530°C in 10 minutes. X-ray examination during heating from 480° to 530°C revealed no sign of polygonization. Simultaneous X-ray examination and heating (at about 2°C per min.) were continued and between 590° and 600°C the first clear evidence of polygonization was recorded, as shown in Figure 7(*b*). At 610°C polygonization is quite distinct (Figure 7(*c*)).

Another photograph was made at 610°C with a much longer exposure time, 45 minutes. To equalize the X-ray exposure with those of the previous photographs, the X-ray tube current was reduced to a low value. Figure 7(*d*) is the result. Comparison of this reflection with that in Figure 7(*c*) reveals a slight general blurring of the focused lines, indicating that the lattice sub-structure units ("polygons") have undergone a slow change in orientation during the 45 minute exposure.

Annealing experiments were also carried out on twisted specimens. The 90° reflection from the transverse plane of a twisted specimen before heating appears in Figure 8(*a*). This specimen was then slowly heated to about 570°C over a two-hour period with continuous X-ray examination. No change was detected until the range 560–570° was reached; then a slight change in the tilt of the striations and a slight decrease in the spacing of the two principal fragment-reflections were observed. This change continued, with a decrease in the total width of the reflection, with further rise in temperature, as illustrated by Figure 8(*b*) made at 640°C. The inclination of the measurable striations to the vertical has decreased by about 13°, which corresponds to an untwisting of about 6 min/mm. The twisted region of the lattice has thus far undergone recovery by untwisting rather than by polygonization. Elevation of the temperature was continued with a view toward accelerating the recovery but melting of the edges of the specimen began before another photograph could be taken.

Attempts were made to determine whether or not rapid heating would polygonize a twisted lattice. A specimen was heated to 640°C in about 9 minutes without any definite evidence of polygonization appearing. The changes in the general configuration of the 90° reflection were about the same as those resulting from slow heating.

Discussion

Relative to the general role of torsion in plastic deformation, the above results lead quite naturally to the following question. Does the occurrence of torsion depend only on the nature of the applied stresses, i.e. torsion, tension or bending, independently of slip on particular crystallographic planes, or must it of necessity occur in order to accommodate, so to speak, crystallographic slip, whatever the nature of the applied stress? This question cannot be definitely answered here since the effect of crystal orientation relative to the applied stress was scarcely touched on in this investigation.

However, it seems certain in view of the variability of its occurrence, that torsion of the lattice is partly dependent on the orientation of the slip systems relative to the applied forces; on the other hand, it appears to be somewhat related to the applied forces directly in that it was observed in every twisted specimen but not in every bent specimen. In a face-centered cubic metal, there are so many slip systems available that these two relationships are not at all incompatible. Studies with hexagonal close-packed metals might be more suitable for defining the role of torsion.

In this connection it is interesting to note that Heidenreich and Shockley [4] conclude that slip involves not only translation but also relative rotation of the crystal fragments on opposite sides of the slip plane about the normal to that plane. Wilman [5] has also observed rotational slip.

In the present work, evidence was obtained (by diffraction from the transverse planes of a twisted specimen) of untwisting during annealing, which suggests a relaxation of forces which have been holding a portion of the lattice in a state of elastic torsional strain. It may well be that slip is not a simple translation process but that it consists of (i) translation, (ii) rotation, as suggested by Heidenreich and Shockley, and (iii) elastic torsion of the crystal lattice between active slip planes due to unequal rotation of its ends.

The precise condition of the lattice between active slip planes is, however, far from clear. Hsu [6] has used the same X-ray method as the writers in examining reflections from the longitudinal plane (the plane parallel to the axis of applied torsion) of twisted specimens. His observations reveal no untwisting during annealing. Perhaps this longitudinal plane is crossed by so many closely spaced active slip planes that the resultant strain, in the gross sense, is best described as plastic torsion, which

is not relieved by the small readjustments occurring during annealing.

If a twisted specimen deformed by slip, only on widely separated planes, with the material in between still in torsion, the torsional striations would appear broken. The curious reflection shown in Figure 9 appears to be of this kind. It is a 75° reflection, i.e. only 15° away from the G-T orientation, from a bent sheet of mica. The clarity of the striations here is largely due to the fact that the mica was very much thinner than the aluminum specimens. This reflection shows that the lattice is practically untwisted in the lower region but that torsional strain increases toward the upper region until finally "slip" takes place.

Slightly deformed and unannealed aluminum crystals were observed to consist of fragments but one cannot immediately conclude that deformation *caused* fragmentation. If the undeformed crystal was "perfect", then deformation did indeed cause fragmentation; but if the undeformed crystal consisted of fragments all having essentially the same orientation, then deformation has merely disoriented these previously existing fragments. No Laue method of X-ray examination, including the technique used here, can distinguish between these two possibilities.

The fragmentation observed here is relatively coarse in that the whole crystal is divided into a rather small number of fragments. On the other hand, various investigators have concluded that cold-worked aluminum contains subgrains or "domains" about 1 or 2 microns in size. This small scale fragmentation might be called "micro-fragmentation" to distinguish it from the "macro-fragmentation" observed by the present writers in slightly deformed aluminum.

The observation of the reversibility of the macro-fragmentation aspect of deformation appears to clarify a peculiar phenomenon described first many years ago. Thus, Czochralski [7] in 1925 noted that reverse deformation decreased the tendency of a single crystal of aluminum to recrystallize. Interestingly enough, his mode of deformation was torsion. Later Beck [8] found the same result with bending, but also noticed that the hardness continued to increase with reverse bending. It thus appears that the tendency to recrystallize is related to the rotation with respect to one another of macro-fragments while strain hardening is related to something else, perhaps micro-fragmentation. The blurred portion of the reflection in Figure 6(*c*) remaining after reversal could be attributed to micro-fragmentation, but it could equally well be caused by bent macro-fragments.

As regards polygonization, Cahn [9] has advanced the view that the subgrains or "polygons" grow at the expense of one another during annealing. If such growth occurs it must be exceedingly slow. It would be evidenced, in a focused 90° reflection, by an increase in intensity of some lines and a decrease in intensity of others but no change in the position of the lines. Some lines would completely disappear as the subgrains producing them were consumed. On the contrary, the only effect found here, on annealing for 45 min. at 50°C. below the melting point, is a slight blurring of the lines indicating small rotations of the subgrains.

An incidental observation made with respect to the torsional striations is believed to clarify the phenomenon reported by Calnan [10] who found that the asterism in back-reflection Laue patterns sometimes has a varying direction for varying regions of the specimen. This was observed here also in a specimen whose 90° reflections showed multiple complex sets of torsional striations. A back-reflection survey was also carried out on a specimen showing only a single set of striations, and the asterism had a constant configuration.

This observation emphasizes in particular what is indicated in a general way by all the data here, viz., that the deformation of a single crystal is usually very inhomogeneous and that observations on a given small region thereof cannot be considered as representative of the specimen. It is believed that the discrepancies in the conclusions and data on Laue asterism which are found in the literature [11; 12; 13] can be largely accounted for by the fact that most investigators have used a conventional small-beam Laue method. Another point worth mentioning here is that the deformation induced in specimens in the present work was smaller than that used by Guinier and Tennevin, who bent their specimens to radii no larger than 15 cm., and very much smaller than that used by Cahn, who bent to radii of less than 1 cm.

Summary

The utility of the Guinier-Tennevin focusing Laue technique may be substantially extended by employing a Soller slit in the primary beam and a line source of X-rays. Under these conditions, it is possible to detect and measure torsional strain in a crystal lattice. It is also possible to obtain focused reflections from other planes of the crystal, notably the plane

reflecting directly above or below the primary beam. The employment of an unfocused large-beam Laue pattern in conjunction with focused reflections is found to be very useful in studying the state of the lattice of a deformed single crystal.

Examination of aluminum specimens by these methods reveals that deformation is usually very inhomogeneous. One or more regions of twisted lattice are often found.

Both plastic bending and plastic torsion are found to be reversible.

Deformation often appears to be accompanied by a fragmentation of the lattice. Fragmentation is believed to occur on scales of quite different orders of magnitude.

Annealing of bent lattices is found to produce polygonization. Annealing of twisted lattices produces a partial untwisting of the lattice.

Acknowledgements

The writers are grateful for the support given this research by the University of Notre Dame and by the Office of Naval Research, U.S. Navy. They also wish to thank S. S. Hsu and T. F. Conmy for their help in preparing the illustrations.

APPENDIX

The effect of circular bending of a thin crystal plate on a focused Laue reflection is illustrated in Figure 10. The following treatment involves the assumption of the identity of an arc with its chord and thus is valid only for small curvatures.

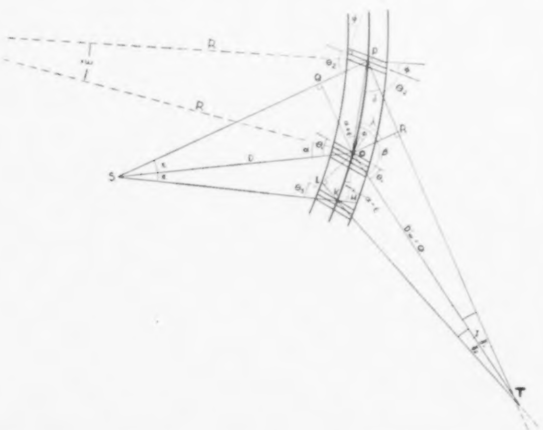

FIGURE 10. Diffraction geometry of a bent crystal.

Consider two rays, the reference ray SO, and the general ray SP which make angles θ_1 and θ_2, respectively, with the diffracting lattice planes which they strike. The general ray diverges from the reference ray by an angle ϵ.

$$\theta_1 = \alpha + \phi$$

where α = the angle between the normal to the crystal at point O and the reference ray SO; ϕ = angle between the normal to the lattice planes and the crystal surface.

$$\theta_2 = \alpha + \phi + \epsilon - \omega$$

where ω = angle of disorientation between the respective lattice planes struck by the rays SO and SP. (It is important to observe a sign convention throughout. Thus,

$$\theta_3 = \alpha + \phi - \epsilon + \omega.)$$

Solving the triangle OTP with the aid of the above relations, we find

$$\gamma_1 = \epsilon - \omega$$

The triangle ORT may then be solved, giving the general equation

$$(1)\quad D' = OT = \frac{OS \sin \epsilon \cos (\alpha + 2\phi + \epsilon - \omega)}{\sin (\epsilon - \omega) \cos (\alpha + \epsilon)}.$$

D' is the distance along the diffracted reference ray at which it is intersected by the diffracted general ray PT. If the crystal is unbent, then $\omega = 0$ and the point of intersection is at I, where

$$(2)\qquad OI = D'_{(\omega=0)} = \frac{OS \cos (\alpha + 2\phi + \epsilon)}{\cos (\alpha + \epsilon)}$$

which is the equation given by Guinier and Tennevin [1].

Similarly, D' may be derived for the general ray SK, but its value will be slightly different (as suggested by the drawing) meaning that, although there may be a position of minimum width for the diffracted beam from a bent crystal, this minimum will never be small enough to be equivalent to the focus (obtained at I) when the crystal is unbent.* Obviously, this minimum will never be at the point I. If bending is convex with respect to the source, the position of minimum width will lie inside of I.

If the bending is sufficient to make $\omega = \epsilon$, D' will be at infinity, i.e. the diffracted reference ray and general ray will be parallel. ω can equal ϵ only for one general ray at a time with circular bending, however.

If the bending is sufficient to make ω greater than

*Even in the unbent crystal the rays will never exactly focus, owing to the fact that OI is a function of ϵ, except in the special case where ϕ is zero. The resulting aberration, however, is exceedingly small when ϵ is small.

ϵ, the diffracted rays diverge and D' is negative, i.e., the intersection lies behind the crystal.

In many cases, one is interested in the broadening of the reflection at the point I, that is, the broadening observed on a film placed at the calculated focusing point for an unbent crystal. If W is the half-width of the beam at the point I, then

$$W = (OT - OI) \tan \gamma_1.$$

If ϵ and ω are assumed to be small, this relation may be written,

$$W = \frac{OS \cos (\alpha + 2\phi) \sin \omega}{\cos (\alpha + \epsilon)}. \quad (3)$$

References

1. GUINIER, A. and TENNEVIN, J. Acta Cryst., **2** (1949) 133.
2. GUINIER, A. and TENNEVIN, J. Progress in Metal Physics, **2** (1950).
3. CULLITY, B. D. and JULIEN, C. A. J. Appl. Phys., **24** (1953) 541.
4. HEIDENREICH, R. D. and SHOCKLEY, W. Conference on Strength of Solids, Bristol, 1947 (London, The Physical Society).
5. WILMAN, H. Proc. Phys. Soc. London, **A64** (1951) 327.
6. HSU, S. S. Private communication.
7. CZOCHRALSKI, J. Z. Metallk., **17** (1925) 1.
8. BECK, P. A. Trans. A.I.M.E., **124** (1937) 351.
9. CAHN, R. W. Progress in Metal Physics, **2** (1950).
10. CALNAN, S. A. Trans. A.I.M.E., **188** (1950), 1040.
11. BURGERS, J. M. Proc. Phys. Soc. London, **52** (1940) 23.
12. YAMAGUCHI, K. Sci. Papers Inst. Phys. Chem. Research (Tokyo), **11**, (1929) 223.
13. KOMAR, A. and MOCHALOV, D. Phys. Z. Sowjet., **9** (1936) 613.

STUDY OF THE ORIGIN OF THE CUBE TEXTURE*

A. MERLINI and P. A. BECK†

In order to test the oriented nucleation and oriented growth theories of annealing textures, a critical experiment was carried out by determining quantitatively the deformation texture and the annealing texture of cross-rolled copper. Even though the cross-rolling texture includes more material in the cube orientation than the straight-rolling texture does, the cross-rolled sheet does not develop the cube texture on annealing. This observation contradicts the prediction of the oriented nucleation theory. The eight main components of the annealing texture in cross-rolled copper may be derived from the two main components of the cross-rolling texture by 30° rotations around [111] axes, in accordance with the expectations of the oriented growth theory.

UNE ÉTUDE DE L'ORIGINE DE LA TEXTURE CUBIQUE

En vue de vérifier les théories sur la germination et la croissance orientées des textures de recuit, une expérience critique a été faite en déterminant les textures de déformation et de recuit du cuivre soumis au laminage croisé. Malgré que la texture du laminage croisé comporte approximativement double proportion de matière ayant l'orientation du cube, que la texture du laminage simple, les tôles soumises au laminage croisé ne développent pas de texture cubique au recuit. Cette observation contredit les prédictions de la théorie de germination orientée. Les huit composantes principales de la texture de recuit, dans du cuivre soumis au laminage croisé, peuvent être dérivées des deux composantes principales de la texture du laminage croisé par des rotations de 30° autour des axes [111], en accord avec les prévisions de la théorie de croissance orientée.

EINE UNTERSUCHUNG DES URSPRUNGS DER WÜRFELTEXTUR

Um die Theorien der orientierten Keimbildung und des orientierten Kristallwachstums zu prüfen, wurden Versuche durchgeführt, um quantitativ die Verformungs- und die Glühtextur von quergewalztem Kupfer zu ermitteln. Obwohl die Textur des quergewalzten Materials Kristalle mit Würfelausrichtung enthält — und zwar mehr als die Textur des grade gewalzten Materials — bildet sich im quergerollten Blech beim Glühen keine Würfeltextur aus. Diese Beobachtung steht im Widerspruch zu den Voraussagen der Theorie der orientierten Keimbildung. Die acht Hauptkomponenten der Glühtextur des quergewalzten Kupfers können von den zwei Hauptkomponenten der Querwalztextur durch Drehungen um [111] Achsen abgeleitet werden. Dies ist im Einklang mit den Voraussagen der Theorie des gerichteten Kristallwachstums.

Introduction

The occurrence of the cube texture is particularly suitable for testing the two contending theories of annealing textures, since it has been given unambiguous interpretation from both points of view. According to the oriented growth theory [1; 2] the formation of the cube texture on annealing of rolled face-centered cubic metals is a consequence of the orientation relationship between this texture and the main components of the rolling texture [3]. The "cube grains" are unique, in that they alone are favorably oriented for nearly maximum boundary mobility with respect to all four (123) [$1\bar{2}1$] type rolling texture components [3; 4]. The theory postulates that the growth of the cube grains is favored over the growth of grains in other orientations only after the new grains have grown large enough to be in contact with matrix material in more than one, and preferably in all four matrix orientations. It is clear that this critical size is smaller and, therefore, that it is attained earlier in the annealing process if the structural units, such as grains and deformation bands, representing the four matrix orientations are smaller, i.e. if the average thickness of the rolled grains is smaller. Decreasing penultimate grain size and increasing rolling reduction both increase that fraction of the annealing period during which the above condition is satisfied. Consequently, on the basis of the oriented growth theory, the percentage of cube texture for a given annealing time and temperature may be expected to increase with decreasing penultimate grain size and with increasing rolling reduction. All these conclusions are in agreement with experience. It has been pointed out [3] that factors promoting grain growth (e.g. increasing annealing time and temperature) tend to increase the percentage of cube texture formed, in accordance with the oriented growth theory. On the other hand, factors inhibiting grain growth (e.g. etching the rolled strip to very small thickness [11] and certain alloy additions forming dispersed particles) tend to suppress the formation of the cube texture, again in accordance with the oriented growth theory. Furthermore, the well-known conspicuous sharpness of the cube texture may be readily interpreted, since selective growth of those grains may be expected to be favored, which are oriented symmetrically with respect to all four matrix texture components and

*Received April 9, 1953.
†Department of Mining and Metallurgical Engineering, University of Illinois, Urbana, Illinois, U.S.A.

have high boundary mobility in contact with all of them.

On the other hand, from the point of view of oriented nucleation [17], the reported occurrence in straight-rolled copper and in certain other face-centered cubic metals of a minor texture component of cube orientation is considered decisive for the formation of the cube texture on annealing [5; 6; 7] In the oriented nucleation theory of annealing textures proposed by Burgers [8] and by Decker and Harker [9], the matrix grains with cube orientation are supposed to be first in attaining the strain-free condition on annealing and in acquiring the capacity to serve as recrystallization nuclei. Burgers, Liu, and Tiedema [10] considered this interpretation confirmed by their finding that, of three orientations investigated, an Al crystal of cube orientation was first to polygonize on annealing at 625°C after 10 per cent extension. However, no interpretation has as yet been given in terms of the oriented nucleation theory of the effects on the formation of the cube texture of any of the various factors discussed above, namely: annealing time and temperature, penultimate grain size, rolling reduction, and etching to small thickness.

A critical test suitable to decide between the two theories could be performed by annealing Cu with a deformation texture consisting of main components different from those in straight rolled Cu, but still including measurable amounts of material in the cube orientation. In such a case, the oriented nucleation theory predicts the formation of the cube texture on annealing, provided that the main deformation texture components are not identical with, or twin-related to the cube texture; it is now generally accepted that, with these two matrix orientations, the cube grains would be unfavorably oriented for growth [8]. On the other hand, the oriented growth theory predicts a completely different annealing texture, whose components are characterized by the most favorable orientation for growth at the expense of the various components of the particular deformation texture considered.

Wassermann [12] found that the texture of cross-rolled face-centered cubic Ni-Fe consists of two symmetrical components of the type $(1\bar{1}0)$ [223] and of a cube texture component. Brick, Martin, and Angier [13], published a (111) pole figure for cross-rolled copper, which they interpreted in terms of two $(1\bar{1}0)$ [223] components and of twin orientations. In view of their results, the cube texture, if present in cross-rolled copper, is likely to represent a minor component. At any rate, although somewhat uncertain, the results described indicate the possibility that cross-rolled copper may be suitable for the above described critical experiment. For this reason, an investigation was undertaken to redetermine both the cross-rolling texture and the corresponding annealing texture by means of the more quantitative methods now available.

Experimental Procedure

For the present work, $1\frac{1}{4}''$ diameter round electrolytic tough pitch copper* rod was used, which was alternately rolled and annealed to the penultimate condition according to the following schedule: (1) rolling from $1\frac{1}{4}''$ dia. to 0.84″ thick, 29.3 per cent R.A.; annealing 20 min. at 400°C, (2) rolling from 0.84″ to 0.56″ thick, 33 per cent R.A.; annealing 20 min. at 350°C; (3) rolling from 0.56″ to 0.425″ thick and cross-rolling from 0.425″ to 0.300″ thick, a total of 46 per cent R.A.; annealing 12 min. at 360°C. Final cross-rolling procedure: the specimen was reversed end to end between first and second pass, between third and fourth pass, etc. The specimen was rotated 90° between second and third pass, between fourth and fifth pass, etc. This procedure was followed during reduction from 0.300″ to 0.128″ thickness. Two reversed passes were also used at each one of the following stages, and 90° rotations were interposed between each two successive stages: (*a*) from 0.128″ to 0.108″, (*b*) from 0.108″ to 0.082″, (*c*) from 0.082″ to 0.070″, (*d*) from 0.070″ to 0.050″, (*e*) from 0.050″ to 0.033″, and (*f*) from 0.033″ to 0.017″. From 0.017″ to 0.010″ the specimen was rolled in many small passes, with progressive 90° rotations between passes. Total reduction in thickness in cross-rolling: 96.5 per cent. For the determination of the annealing texture, the cross-rolled material was annealed for 5 min. at 290°C. As seen in Figure 1, this anneal was sufficient for complete softening.

X-ray specimens were prepared by etching in 30 per cent nitric acid solution both sides of specimens of the 0.010″ thick cross-rolled sheet, and of the cross-rolled and annealed sheet. Care was taken to keep the thickness of the specimen as uniform as possible during etching. In this manner an approximately 0.002″ thick specimen was obtained from the center of each sheet. This specimen was used for the X-diffraction work, both in transmission and in reflection. For the peripherial portion of the (111) and (200) pole figures, at tilting angles of 90° to 40°

*$O_2 \simeq 0.04\%$, Fe 0.0015%, Sb 0.0001%, Pb $<$0.0001%, Sn nil, Ni 0.0005%, Bi 0.00001%.

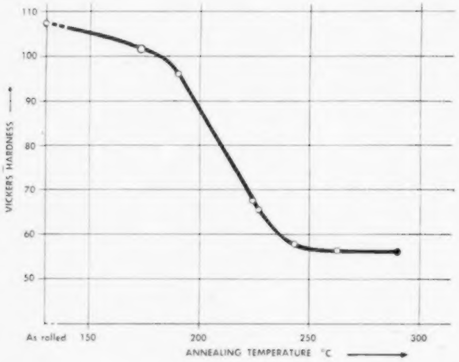

FIGURE 1. Hardness vs. annealing temperature for 96.5 per cent cross-rolled Cu. Annealing time 5 min. in salt bath.

with respect to the rolling plane, the Decker, Asp, and Harker [14] transmission method was used, and data were obtained at 5° tangential and 5° radial intervals. Near maxima, and at other interesting locations, measurements were made at 2° intervals. Corrections were made according to the Decker-Asp-Harker formula for absorption and for variation in effective diffracting path length. For the central portion of the (111) and (200) pole figures, at tilting angles of 0° to 50° from the center, reflection data were obtained by the Schulz method [15] at intervals corresponding to those in the transmission work. By using a main slit 0.020″ wide, and no receiving slit in front of the G.M. counter of the General Electric XRD-3 Spectrometer, the effect of defocusing on the measured X-ray intensity was minimized [16]. In order to eliminate this effect even more quantitatively, in the course of the present work a random sample was prepared from PbS powder, and empirical correction factors were determined for various tilting angles. This correction was used for the pole figures of the annealing texture, but not for those of the deformation texture. The specimen holders for both transmission and reflection were constructed so as to allow "integration" or scanning the specimen surface. This feature is quite necessary for obtaining reliable results in studying annealing textures.

Both methods, when properly used, with all corrections, give relative intensity data to an estimated accuracy of about ±5 per cent. The importance of accurate specimen alignment in the Schulz reflection method was recently discussed in a paper [16], which also gives a brief description of a test for the accuracy of specimen alignment. In the present work, a complete alignment procedure was developed, including the alignment of both the specimen and the main slit with respect to the axis of rotation of the inner ring of the specimen holder. This, and also an alignment procedure for the transmission specimen holder, will be described elsewhere.

The arbitrary units, in which the transmission and reflection intensity data are obtained are, in general, not related to each other. A factor expressing the ratio of the two units has to be established empirically from overlapping data which are determined by both methods. The degree of constancy of this factor for the whole area of overlap gives an indication of the general reliability of the data. By means of the average value of the factor, the data from the two determinations may be fitted together into a single pole figure. Considering the uncertainties involved in this operation, the accuracy of relative intensities in the pole figure as a whole is estimated to about ±10 per cent.

Experimental Results

Cross-Rolling Texture

Figure 2 shows the (111) pole figure and Figure 3 the (200) pole figure obtained in the present work for cross-rolled copper. It is seen that the two main texture components may be described approximately as $(1\bar{1}0)$ [223] type, in accordance with the findings

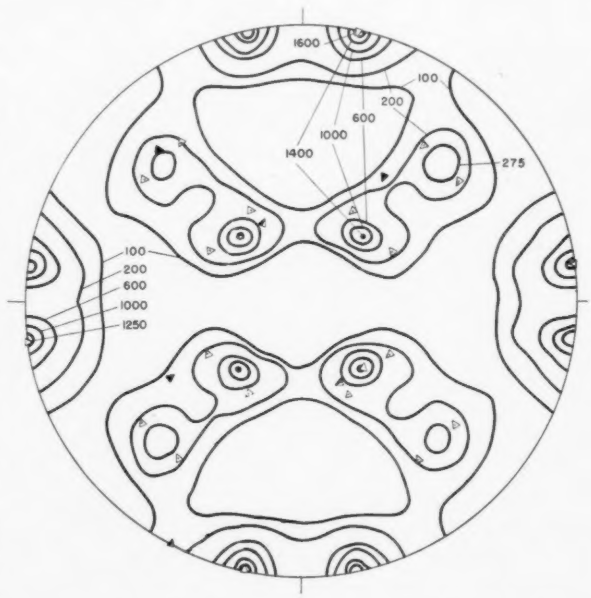

FIGURE 2. (111) pole figure for cross-rolled Cu. Intensities in arbitrary units. Specimen 0.002 in. thick, from center portion of 0.020 in. thick sheet. Open triangles show (111) poles of one of the two main texture components, corresponding approximately to (110) [223]. Half-filled triangles denote (111) poles of a twin orientation derived from a main texture component by rotation around a [111] axis in the rolling plane. Filled triangles locate (111) poles of a twin orientation derived by rotation around a [111] axis near center. Triangles with dot designate (111) poles for minor texture components derived from cube orientation by [100] rotations.

of the previous investigators. There appears a small deviation from this ideal orientation, shown for instance by the angle between the (200) poles of the two components in the rolling plane. This angle was found to be 86.5°, instead of 90°, as expected for the ideal orientations. A corresponding deviation of about 4° is present in the (111) pole figure. These observations indicate that the cross-rolling operation was not perfectly symmetrical with respect to the two rolling directions. The close agreement of the deviations, as seen in the (200) and (111) pole figures, shows the accuracy with which it was possible in the present work to locate intensity maxima.

It is particularly interesting to study the minor texture components, which are important for the purposes of the present work, and which were reported differently by Wassermann [12] for Ni-Fe and by Brick and co-workers [13] for Cu. Of the four twin orientations corresponding to each main component two are obtained by rotation around ⟨111⟩ axes lying in the plane of rolling and two by rotation around the other ⟨111⟩ axes. An orientation each of the first kind (half-filled symbols) and of the second kind (filled symbols) is shown in the pole figures (Figures 2 and 3). It is clear that at least one

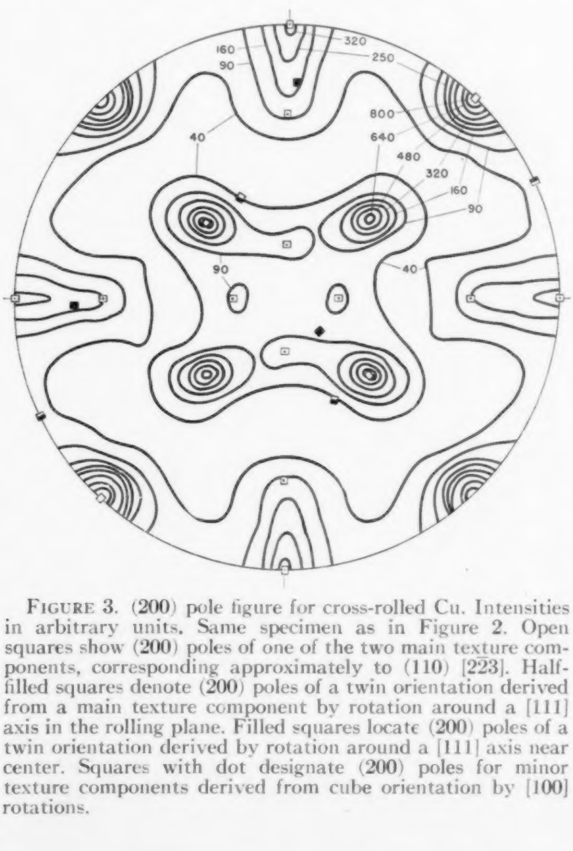

FIGURE 3. (200) pole figure for cross-rolled Cu. Intensities in arbitrary units. Same specimen as in Figure 2. Open squares show (200) poles of one of the two main texture components, corresponding approximately to (110) $[2\bar{2}3]$. Half-filled squares denote (200) poles of a twin orientation derived from a main texture component by rotation around a [111] axis in the rolling plane. Filled squares locate (200) poles of a twin orientation derived by rotation around a [111] axis near center. Squares with dot designate (200) poles for minor texture components derived from cube orientation by [100] rotations.

(111) pole and one (200) pole for each orientation of the first type falls into a low intensity area in the pole figure. Although the case of twin orientations of the second kind is less obvious, it may be observed that the peripherial (200) maxima and the central (200) intensity distribution of the minor textures are not satisfactorily accounted for by these orientations. The presence of sharp (200) maxima in the four rolling directions is strongly suggestive of the presence of the cube texture. This simple interpretation of the peripherial maxima is, however, not sufficient to describe the central (200) pole distribution, which forms a roughly ring shaped broad ridge surrounding the center at a distance of about 22°. Close study of radial and concentric circular sections prepared for the (200) pole figure show that the minor textures may be accounted for by a spread from the cube orientation, corresponding to 22° rotations around all directions in the rolling plane, but predominantly around the rolling directions. As seen in the (200) pole figure, these two principal spreads, which may be described as "partial [100] fiber textures," account reasonably well not only for the central (200) distribution, but also for the radial extensions of the peripherial (200) maxima in the four rolling directions. Figure 2 shows that these orientations are in accord with the (111) pole distribution as well.

The conclusion may be drawn that Wassermann's interpretation of the cross-rolling texture of Fe-Ni is approximately applicable to cross-rolled copper, in that the minor texture components center around the cube texture. That some material is, in fact, exactly in the cube orientation, in spite of the absence of a (200) maximum at the center, is suggested by the quite considerable (200) pole density at that location. The central (200) poles are not associated with the peripherial (200) maxima 45° away from the rolling directions. This is shown by the low (111) pole concentration at 55° from the center towards the four rolling directions. That some of the deformed material is actually aligned in the cube orientation is shown even more clearly in Figure 4, which represents the corrected (111) intensity, measured by the reflection method, for a tilting angle of 55°, as a function of the azimuthal angle. The data were corrected for the measured background intensity of 20 cps. The horizontal line A–A represents the (111) reflection intensity that would theoretically correspond to the (200) reflection intensity of 38 cps. (corrected for background) measured in the direction to the rolling plane normal. It is seen that only the peaks near the azimuthal

angles of 45° and 135°, etc. (see Figure 4), which correspond to the cube orientation, can accommodate the required intensities. It is, of course, clear that these peaks are larger than would be expected from the central (200) intensity alone; they must also represent additional orientations for which the (200) poles do not coincide with the pole of the rolling plane normal.

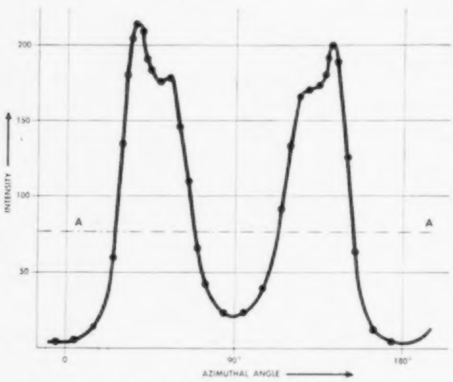

FIGURE 4. X-ray intensity reflected by (111) planes tilted 55° with respect to the rolling plane, as a function of azimuthal angle; 0° and 90° lie toward rolling directions. This figure corresponds to a circular section with 55° radius of the pole figure in Figure 2. Line A–A represents calculated (111) intensity corresponding to (200) intensity measured in center of pole figure.

Straight-Rolling Texture

In view of the occurrence of the two minor "partial fiber textures" in cross-rolled Cu, it was decided to reexamine the minor cube texture component whose presence in straight-rolled face-centered cubic metals was reported by various investigators [5; 6; 7]. Straight-rolled Cu with 92.5 per cent reduction of area was prepared from the same rod that was used for cross-rolling. As seen in Figure 8, the (200) maximum in the rolling direction is much more intense than that in the transverse direction. Figure 9 shows that the (200) maximum expected for the cube texture at the rolling plane normal is missing altogether. This fact is further corroborated by Figure 10 which also indicates low (200) intensities near the normal direction. These findings suggest that the minor texture component in straight-rolled Cu, interpreted by previous investigators as (100) [001], may be instead roughly described as a [100] fiber texture with the fiber axis in the rolling direction. This fiber texture does include the cube orientation; the presence of small but measurable (200) intensities (19 counts per second, corrected for background) in the direction of the rolling plane normal (N.D. in Figures 9 and 10) suggests that there is in fact a small amount of material in the (100) [001] orientation. It appears very likely that the minor "partial fiber texture" components found in cross-rolled Cu are related in their origin to the minor fiber texture component of the straight-rolling texture. As judged from the (200) intensities in the center of the respective pole figures, the fraction of material having the cube orientation was approximately twice as large in the cross-rolled as in the straight-rolled one.

Annealing Texture

As seen in Figures 5 and 6, the eight main components of the annealing texture correspond quite well to the ideal orientations derived from the two main deformation texture components by 30° rotations in either direction around all ⟨111⟩ axes near the center. These eight components may be described by "ideal orientations" of the (519) $[\bar{4}, 11, 1]$ type, and they are consistent with the (111) pole figure published by Brick, Martin, and Angier [13] for recrystallized cross-rolled Cu. The lack of resolution inherent in the photographic method prevented those investigators from identifying the orientations involved. With the present more quan-

FIGURE 5. (111) pole figure for cross-rolled and annealed Cu. Intensities in arbitrary units. Specimen similar to that in Figure 2, from same sheet, after annealing in salt bath for 5 min. at 290°C. Half-filled triangles and triangles with circles give (111) poles of two recrystallization texture components of (510) $[\bar{4}, 11, 1]$ type corresponding to 30° rotations in opposite directions around the same [111] axis of one of the main cross-rolling texture components. The triangles with dots and with crosses represent a similar pair of (510) $[\bar{4}, 11, 1]$ orientations corresponding to rotations around another [111] axis of the same matrix component.

titative methods, the sharpness of the individual texture components turns out to be rather remarkable, considering the complexity of the texture as a whole. Even maxima only about 12° from each other are clearly separated, as seen at the pairs of peaks located about 30° above and below the center of the (200) pole figure (Figure 6). The corresponding pairs

FIGURE 6. (200) pole figure for cross-rolled and annealed Cu. Intensities in arbitrary units. Same specimen as in Figure 5. The square symbols represent (100) poles of the same recrystallization texture components to which the corresponding triangular symbols refer in Figure 5.

right and left of the center are not well separated, however, since their angular distance is apparently smaller. This slight deviation from symmetry in the annealing texture corresponds to that noted above for the rolling texture, and it may be considered as an indirect result of some asymmetry in the rolling operation. In addition, there are several instances in both annealing pole figures of slight irregularities, which in some cases amount to the splitting up of maxima into several individual peaks, somewhat like outstretched fingers of a hand. This apparent fine structure may be real, but at the present time it remains unexplained.

While the results clearly demonstrate that the cube texture component of the deformation texture has not grown to develop the cube texture on annealing, it is interesting to observe in Figure 6 that one of the two minor "partial fiber texture" components observed in the deformation texture in the proximity of the cube orientation remained unabsorbed on annealing for 5 min. at 290°C. The asymmetry apparent from the fact that the other "partial fiber texture" (with the vertical rolling direction as [100] fiber axis) was not retained, may be again a result of the slight asymmetry of the deformation and annealing textures referred to before. Some measurements were made with a specimen annealed for 15 min. at 460°C, and with one annealed for 15 min. at 560°C. The only significant change noted in comparison with the 290°C annealed specimen was a decrease in the relative intensities associated with the retained "partial fiber texture" component near the cube orientation (Figure 7). It is quite apparent that,

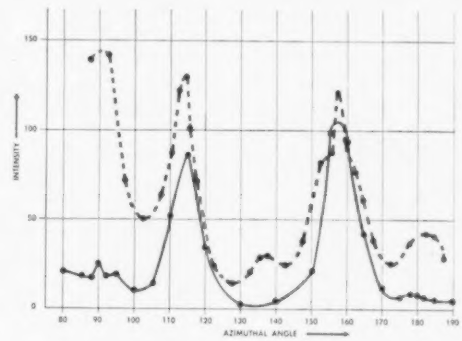

FIGURE 7. X-ray intensity reflected by (200) planes perpendicular to the rolling plane (tilting angle 90°) for cross-rolled and annealed Cu. Maxima appearing at azimuthal angles of 90° and 180° (corresponding to the rolling directions) in the sheet annealed for 5 min. at 290°C (dotted curve) are greatly reduced on annealing for 15 min. at 560°C (solid curve). Intensities in arbitrary units (in the two curves only relative intensities are directly comparable).

with increasing annealing temperature, this component is being progressively absorbed by the main annealing texture components.

Discussion

The fact that in cross-rolled Cu there is some material available in the cube orientation to serve as

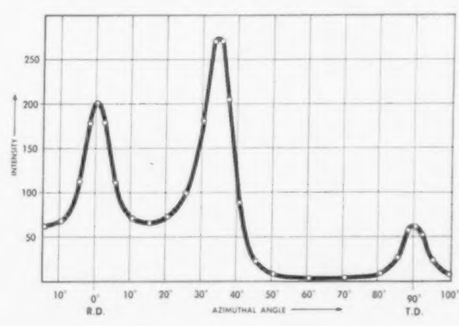

FIGURE 8. X-ray intensity reflected by (200) planes perpendicular to the rolling plane (tilting angle 90°) for straight-rolled Cu. The maximum appearing in the rolling direction (R. D.) is much larger than the one in the transverse direction (T.D.). Intensities in arbitrary units.

nuclei (approximately twice as much as in straight-rolled copper), yet no cube texture forms on annealing, is in disagreement with the prediction of the oriented nucleation theory. Furthermore, since the bulk of the matrix material is in orientations other than (100) [001], or those twin-related to it, the absence of the cube texture after annealing can not be explained on the assumption, suggested by Burgers [17], that the orientation dependence of

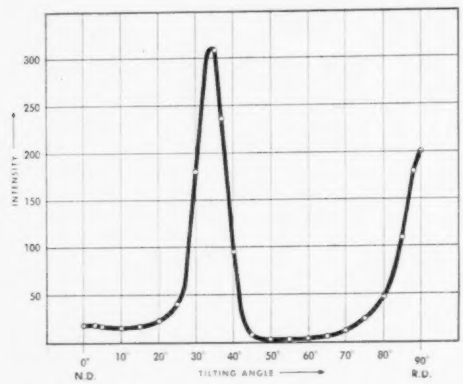

FIGURE 9. X-ray intensity reflected by (200) planes parallel to the transverse direction, as a function of their tilting angle with respect to the rolling plane. Corresponding to the (200) maximum in the rolling direction (R.D.), the cube texture would require a maximum also in the normal direction (N.D.). However, this is in fact missing. Intensities in arbitrary units.

boundary mobility is effective in preventing the formation of the cube texture only when the matrix is very near to those two types of orientations. On the other hand, the absence of the cube texture in the annealed material readily follows if it is accepted, in accordance with the oriented growth theory, that grain boundary mobility is orientation dependent over the whole orientation range, and that annealing textures correspond to orientations with maximum

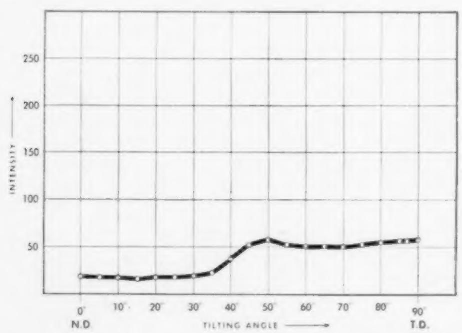

FIGURE 10. X-ray intensity reflected by (200) planes parallel to the rolling direction, as a function of their tilting angle with respect to the rolling plane. The cube texture would require maxima at both the normal direction (N.D.) and the transverse direction (T.D.) which are not observed in this section of the pole figure.

boundary mobility. As pointed out in the Introduction, the cube texture, on this theory, grows only in a matrix with principal components of the (123) [$1\bar{2}1$] type, and there is no reason to expect it to form in a matrix of other orientation. On the basis of the oriented growth theory, one would expect the formation of an annealing texture so oriented with respect to the texture components of the matrix as to possess maximum boundary mobility. It is known from several previous investigations [18; 19; 20; 21] that for copper this orientation relationship corresponds to a 30° rotation around a $\langle 111 \rangle$ axis. The results of the present work show that each component of the major annealing texture has the (519) [$\bar{4}$, 11, 1] type of orientation, and that it is in just the required orientation relationship with one of the main matrix texture components.

It is interesting that not all possible orientations so related to the matrix texture actually do occur. Reorientation takes place only around the $\langle 111 \rangle$ axes near the rolling plane normal. The analoguous lack of completeness in certain other annealing textures has been emphasized particularly by Burke [22], who considered it as a disproof of the oriented growth theory. According to Burke, this theory would require reorientations around all $\langle 111 \rangle$ axes of the matrix, all of which were considered by him equivalent. It has been pointed out [2], however, that not all $\langle 111 \rangle$ axes are necessarily equivalent from the point of view of crystal growth if the matrix is not an ideal single crystal. This is, of course, particularly true if the matrix texture includes more than one major component, as in the present case.* In this connection, it is an important question whether it is possible to account for the absence of the "missing orientations," which are related to the

*Another case in point is the retainment of the [111] fiber texture on annealing of face-centered cubic metals, which was interpreted [23] in terms of the oriented growth theory, as a result of local reorientation corresponding to rotation around the [111] fiber axis. The actual occurrence of such reorientations in extruded Al rod with a [111] fiber texture has been recently reported by Gow and Cahn [24]. It is clear that even an ideal [111] fiber texture corresponds not to one but to an infinite number of crystal orientations, and that the fiber axis is unique among the [111] directions, in that it is the only one common to all these orientations. The equivalence of the fiber axis with other [111] directions, as postulated by Burke, is, of course, out of the question. Similarly, the new grains growing on annealing in straight-rolled copper are surrounded by a matrix comprising 4 major texture components, and in cold rolled cartridge brass they are growing in a matrix having 2 major texture components. In each of these cases the complexity of the matrix texture is such as to destroy the "symmetry" or "equivalence" of the various $\langle 111 \rangle$ directions with regard to the matrix as a whole. Consequently, there is no reason to expect that all orientations derived from a matrix component by a 30° rotation around any [111] axis correspond to equally high boundary mobility.

matrix texture components by 30° rotations around ⟨111⟩ axes parallel to the rolling plane. For each main annealing texture component of the type (519) [$\bar{4}$, 11, 1], derived by [111] rotation from one of the main deformation texture components, the orientation relationship with the other main texture component of the matrix corresponds to a rotation of 49° around an axis 16° away from a ⟨111⟩ direction (Figure 11), as determined by a simple construction in the stereographic projection. For each one of the "missing" annealing texture components, the corresponding orientation relationship may be expressed as a rotation of 35° around an axis 33.5° away from the nearest ⟨111⟩ direction. No relative boundary

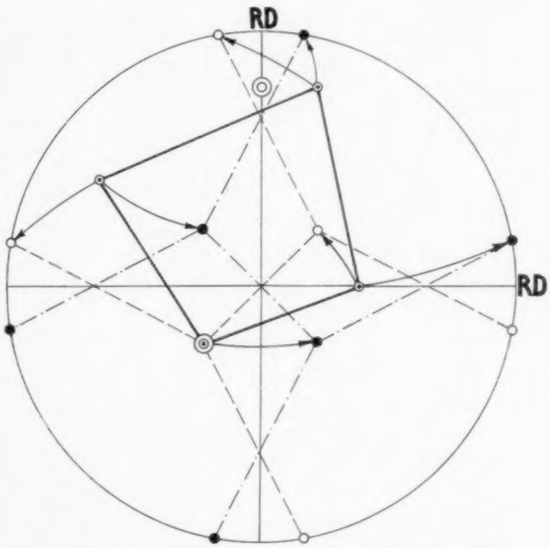

FIGURE 11. One of the eight (519) [$\bar{4}$, 11, 1] annealing texture components of cross-rolled copper (ideal (111) poles indicated by circles with dots, connected by continuous lines) derived from one of the two (110) [$2\bar{2}3$] cross-rolling texture components (ideal (111) poles shown as empty circles, connected by dashed lines) by 30° rotation around common (111) pole (large double circle with dot). The same annealing texture component is related to the other (110) [$2\bar{2}3$] rolling texture component (ideal (111) poles indicated by filled circles, connected by dash-dot lines) by a 49° rotation around an axis (large double circle) 16° away from nearest [111] direction.

mobility data are at present available for these orientation relationships. Nevertheless, it may be significant that the "missing orientations" are very far removed from having a ⟨111⟩ rotational relationship with the second matrix texture component, and that the annealing texture components actually occurring are much closer to such a relationship. The absence of annealing texture components derived from one matrix texture component by rotation around ⟨111⟩ axes parallel to the rolling plane may be rationalized on the basis of the presumably lower mobility of grain boundaries separating this orientation from that of the second matrix texture component, as compared with the corresponding boundary mobility for a (519) [$\bar{4}$, 11, 1] type orientation. This assumption is amenable to direct experimental verification, and it has the advantage of avoiding *ad hoc* hypotheses regarding favored nucleus orientations, which can not be tested experimentally, but which would be necessary in any attempt at an alternative interpretation in terms of oriented nucleation. Careful examination of the intensity data for the cross-rolling texture gives no indication of the presence of minor texture components corresponding to the annealing texture. There appears to be no experimental fact suggesting an explanation of the observed annealing texture, or of the "missing orientations" in terms of oriented nucleation.

Conclusions

1. The texture of cross-rolled Cu consists of two major components of the (110) [$2\bar{2}3$] type and of a minor component, which includes the cube orientation and orientation spreads ("partial fiber textures") derived from the latter mainly by rotations of approximately 22° around the rolling directions.

2. The annealing texture of cross-rolled Cu consists of eight main components of the (519) [$\bar{4}$, 11, 1] type, related to the main cross-rolling texture components by 30° rotations around ⟨111⟩ axes near the rolling plane normal. In the specimen examined there was also a minor texture component corresponding to a retained portion of the minor component of the cross-rolling texture. This retained component progressively decreased in intensity with increasing annealing temperature.

3. The observed reorientation on annealing of cross-rolled Cu decisively contradicts the prediction of the oriented nucleation theory, while it is in excellent agreement with the oriented growth theory of annealing textures.

4. The minor texture component in straight-rolled Cu, which has been assigned the cube orientation by previous authors, can be better described as a [100] fiber texture, with the rolling direction as the fiber axis.

Acknowledgements

The authors wish to express their appreciation to the United States Atomic Energy Commission for sponsorship of this work and financial assistance under Contract No. AT(11–1)–67, Project No. 9, and to Mr. J. S. Smart, Jr. and the American

Smelting and Refining Co. for the chemical analysis of the copper used.

References

1. Beck, P. A., Sperry, P. R., and Hu, H. J. Appl. Phys., **21** (1950) 420.
2. Beck, P. A. Acta Met., **1** (1953) 230.
3. Beck, P. A. Trans. A.I.M.E. **191** (1951) 474.
4. Beck, P. A. and Hu, H. Trans. A.I.M.E. **194** (1952) 83.
5. Sachs, G. and Spretnak, J. Trans. A.I.M.E., **140** (1940) 359.
6. Rathenau, G. W. and Custers, J. F. H. Philips Research Reports, **4** (1949) 241.
7. Coheur, P and Lejeune, J. M. Rev. Mét., **46** (1949) 439.
8. Burgers, W. G. Recrystallization and Grain Growth in Solid Metals, in L'Etat Solide, (Bruxelles, R. Stoops, 1952), 431.
9. Decker, B. F. and Harker, D. J. Appl. Phys., **22** (1951) 900.
10. Burgers, W. G. Liu, Y. H. and Tiedema, T. J. Proc. Koninkl. Nederl. Acad. van Wetenschappen, **94** (1951) 459.
11. Custers, J. F. H. and Rathenau, G. W. Physica VIII, **7** (1941) 759.
12. Wassermann, G. Texturen Metallischer Werkstoffe (Berlin, 1939) 96.
13. Brick, R. M., Martin, D. L. and Angier, R. P. Trans. Amer. Soc. Metals, **31** (1943) 675.
14. Decker, B. F., Asp, E. T. and Harker, D. J. Appl. Phys., **19** (1948) 388.
15. Schulz, L. G. J. Appl. Phys., **20** (1949) 1030.
16. Chernock, W. P. and Beck, P. A. J. Appl. Phys., **23** (1952) 341.
17. Burgers, W. G. and Tiedema, T. J. Acta Met., **1** (1953) 234.
18. Bowles, J. S. and Boas, W. J. Inst. Metals, **24** (1948) 501.
19. Kronberg, M. L. and Wilson, F. H. Trans. A.I.M.E., **185** (1949) 501.
20. Liu, Y. C. and Hibbard, W. R., Jr. Trans. A.I.M.E., **197** (1953)?
21. Beck, P. A. Orientation in Recrystallization and Grain Growth: The Physics of Powder Metallurgy (New York, McGraw-Hill Book Co., Inc., 1951), 40–51.
22. Burke, J. E. Trans. A.I.M.E., **194** (1952) 263.
23. Beck, P. A. and Hu, H. Trans. A.I.M.E., **185** (1949) 627.
24. Gow, K. V. and Cahn, R. W. Acta Met., **1** (1953) 238.

On a Statement by C. S. Smith Concerning an Upper Limit to the Sharing of Corners in Aggregates*

Calculations have been made of the interface area, edge length, and number of vertices (corners) in an aggregate consisting of a large number of crystals which have grown from nuclei distributed at random in space [1]. For the case that all crystals have started to grow simultaneously and isotropically—all interfaces thus being plane—one of the results was that the number of corners is $\frac{24}{35}\pi^2$ ($= 6.77$) times the number of crystals. This is in contradiction to a statement by C. S. Smith [2] that this ratio can never exceed 6, at least in aggregates where in each corner four crystals are meeting, which is also the case in the random aggregate. Now, independently of the calculations in [1], it can be seen that the ratio can indeed be increased over 6. One starts from the stack of truncated octahedra shown in Fig. 19 of [2]. By coalescing two adjacent crystals having a square common interface (and smoothing out the ridge due to the 4 cancelled edges) one gets an aggregate which has 4 corners less for the loss of only one crystal. Thus the initial ratio of 6 can be exceeded.

Recently the writer had the opportunity to discuss this matter with Professor Smith, who told him that he had already submitted a paper to this journal [3], in which his general statement in [2] was retracted, but he maintained it for stacks of (convex) polyhedrons with *plane* faces. Both the procedure sketched above and that indicated by Professor Teller [3] give rise to curved interfaces. As in the random aggregate mentioned all interfaces *are* plane, the writer tried to show that this circumstance does not exclude the possibility of ratios > 6. This was done by a modification of the coalescing process sketched. One starts from nuclei lying on a body-centered cubic lattice. Simultaneous and isotropic growth would yield the stack of truncated octrahedra mentioned above. But now we single out a row of 4 successive nuclei in a [100] direction; the two middle ones are replaced by one nucleus halfway between them and the two outer ones are shifted slightly towards each other. (This double shift is necessary to avoid five-crystal corners.) We let the crystals grow and again obtain an aggregate with 4 corners (and 1 crystal) less than the original regular stack, as detailed inspection shows.

Professor Smith informed the writer that he is in accord with this reasoning; the statement in [2] concerning the maximal ratio of corners and polyhedra is thus retracted also for (convex) plane-faced polyhedra.

The writer's thanks are due to Professor C. S. Smith for sending a copy of his submitted paper [3] and for verifying the procedure sketched above.

J. L. Meijering

Philips Research Laboratories
N. V. Philips' Gloeilampenfabrieken
Eindhoven, Netherlands

References

1. Meijering, J. L. Philips Research Reports (in press).
2. Smith, C. S. In "Metal Interfaces" (Cleveland, A.S.M., 1951) 65.
3. Smith, C. S. Acta Metallurgica, **1** (1953) 295.

*Received June 8, 1953.

Relation between Plastic Strain and Increase of Electrical Resistivity of Metals*

Various experiments, e.g. those of Molenaar and Aarts [1], have shown the increase of electrical resistance on plastic deformation of pure metals at low temperatures. This increase of resistance is usually explained by the formation of lattice defects, such as vacancies, interstitial atoms, and dislocations (cf. Seitz [2]). The author recently discussed in this Journal [3] the mechanism of the formation of lattice defects and the influence of these defects on some characteristic effects of plastic deformation. It was assumed that the vacancies and interstitial atoms are formed in the wake of jogs present in the expanding dislocation rings (emitted in the very first stages of slip) by Frank-Read sources. The jogs originate where the expanding dislocation rings cross the already present, randomly distributed dislocations. On the basis of this theory, the number of jogs formed should be proportional to the area covered by the expanding rings, thus to the strain. The number of vacancies and interstitials increases at a higher rate. Assuming that an expanding ring retains its original shape, the amount of defects will be proportional to the third power of some averaged

*Received June 3, 1953.

distance travelled by the rings (in the case of circular rings to the third power of the radius). Thus the density n_v of vacancies should depend on the strain ϵ as

$$n_v \sim \epsilon^{3/2}, \tag{1}$$

the same being true for the density n_i of interstitial atoms.

By the same argument it can be shown that the total length l_d of dislocation in the metal should increase approximately proportionally to $\epsilon^{\frac{1}{2}}$.

In order to avoid the difficulty that by this mechanism the vacancies or interstitials should be formed in rows next to each other, it is assumed that the space distribution of random dislocations is continuously varying, probably under the influence of the moving dislocation rings.

As Mathiessen's rule should be valid in the case of slight deformations, the extra resistivity on plastic deformation can be expressed in the form:

$$\Delta\rho = n_v\,\Delta\rho_v + n_i\,\Delta\rho_i + l_d\,\Delta\rho_d, \tag{2}$$

where $\Delta\rho_v$, $\Delta\rho_i$ and $\Delta\rho_d$ stand for the increase of resistivity caused respectively by a vacancy, an interstitial atom and a dislocation of unit length. From the above it is concluded that the following formula should apply for the dependence of the extra resistivity on the strain

$$\Delta\rho = A\,\epsilon^{3/2} + B\,\epsilon^{1/2}. \tag{3}$$

Recent experiments by J. A. Manintveld [4] on thin wires of pure copper, silver and gold, annealed for $1\frac{1}{2}$ hour at 550°C and stressed at liquid-air temperature, demonstrate very clearly the existence, for all three metals, of a relation of the form:

$$\Delta\rho/\rho = \sim (\Delta l/l)^{3/2}, \tag{4}$$

where $\Delta l/l$ stands for the elongation of the wire. The proportionality constant is of order unity for all three metals. The results of the measurements are reproduced in the accompanying figure. The agreement between the measured data and formula (4) is almost perfect for elongations between 2 and 11 per cent. Below 2 per cent elongation a small deviation from the 3/2-power relation seems to be present, in the sense that the exponent seems to become somewhat smaller. No accurate determination is possible however.

According to the arguments presented above, this experimental result could be explained by assuming that practically all the extra resistivity is caused by vacancies and interstitial atoms.

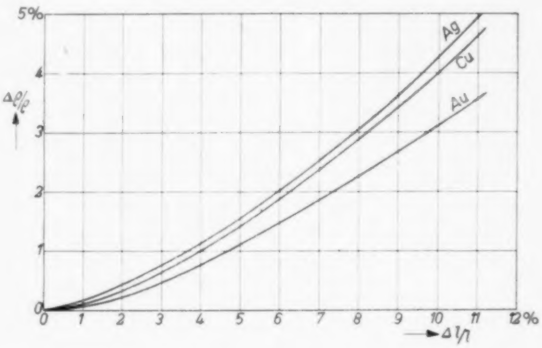

Calculations by the author [3] have shown that in that case indeed a proportionality constant of order unity can be expected. The influence of the dislocations formed at small deformation levels on the resistivity seems thus to be negligible. This conclusion had already become more or less evident from the results of the calculations recently made by Dexter [5]. According to that author, to explain the observed increase of resistivity after straining a metal for a few per cent, the density of dislocations formed should be about 10^{13} cm. This appears to be, on comparison with other estimates, an excessively high dislocation density for a slightly strained metal. The small deviation from the simple 3/2-power relation at very slight extensions may be attributed to the different mechanism of deformation which occurs at this stage [3], viz. the *formation* of new dislocation rings by Frank-Read sources as apposed to the *expansion* of the rings at higher deformations. A more detailed analysis shows that then a relation of the form

$$\Delta\rho \sim \epsilon^{5/4}$$

should describe the actual process more exactly. Also the effect of the jogs on the resistivity should be taken into account, it should be relatively greatest in the first stage of deformation.

A remark may yet be made in connection with the conclusion that dislocations do not appreciably influence the resistivity. Annealing at a temperature of several hundred degrees Centigrade of a metal deformed at low temperature brings about a nearly complete recovery of the extra resistivity, together with an appreciable mechanical softening. About half of the extra resistivity already disappears by annealing at lower temperatures, where no mechanical recovery takes place [6]. The high temperature recovery might be associated with the more or less complete annihilation of dislocations in the crystal. It must be borne in mind, however, that as the dislocations themselves

should have no great effect on the resistivity, it is probably the simultaneous disappearance of the vacancies and interstitials adsorbed on the dislocations (incipient vacancies [2]) that causes the resistance decrease. The room temperature recovery step should then correspond, as has been suggested by Manintveld, to the diffusion of vacancies or interstitials to the dislocations. Their effect on the resistance should not then disappear wholly however, but only for about 50 per cent.

It is a pleasure to express my sincere thanks to Mr. Manintveld for kindly allowing me to make use of his yet unpublished experimental data.

H. G. van Bueren

Philips Research Laboratories
N. V. Philips' Gloeilampenfabrieken
Eindhoven, Netherlands

References

1. Molenaar, J. and Aarts, W. H. Nature, **166** (1950) 690.
2. Seitz, F. Advances in Physics, **1** (1952) 43.
3. Bueren, H. G. van. Acta Met., **1** (1953) 464.
4. Manintveld, J. A. Private communication.
5. Dexter, D. L. Phys. Rev., **85** (1952) 936.
6. Manintveld, J. A. Nature, **169** (1952) 623.

The High Temperature Hexagonal Phase of Cobalt*

The two experiments reported in the letter by Newkirk and Geisler [1] are interesting because of the failure to observe any change in the lattice above 1100°C. There are, however, several instances of differences between these results and previously published results, which make necessary a review of this work. Three sets of high temperature X-ray diffraction observations may be cited, although Meyer's work [2] extended no higher than 1100°C. Marick investigated cobalt wire up to 1187°C [3] and Goldschmidt has made a single observation at 1200°C reported by Metcalfe [4]. At first sight it appears as if Marick's results are in agreement with the observations by Newkirk and Geisler, but further analysis of the data shows a striking disagreement (figure 1). Without entering any discussion of the cause of this variation (see [4]), it is evident that the final conclusion of Newkirk and Geisler may not be true under all circumstances.

Troiano and Tokich [5] concluded that the lower

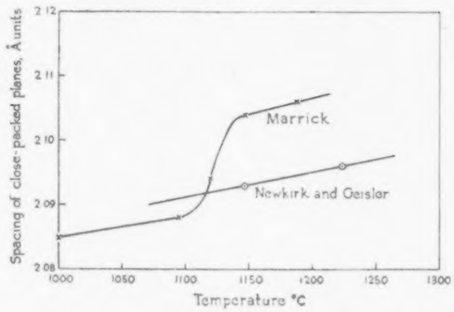

transformation was grain-size dependent, and that the appearance of hexagonal cobalt on cooling was dependent on a sufficiently large grain size. Herein lies one difficulty of the X-ray diffraction method using the Debye-Scherrer type camera. The grain size of the cobalt used in the dilatometric experiments was about 1 mm., whereas it would be reasonable to assume a grain size about 1/100 of this value to obtain smooth diffraction lines. Thermodynamic equilibrium can be approached more closely with the specimen of larger grain size.

Another consideration is the mode of transformation between the two forms of cobalt [6]. This may have two effects. It may give rise to broadening of the lines of the hexagonal close-packed lattice so that detection becomes more difficult, and it may change the transformation temperature by its effect on the entropy.

In the absence of further experimental evidence on these points, it can serve no useful purpose to discuss the mechanism in any more detail. It is felt, however, that these experiments should be repeated, if possible, with a specimen of larger grain size. If this should prove to be impossible, it would be interesting to elongate the wire (preferably a thicker one) when it reached temperature, but before making the exposure. Photometry of the films might also be interesting.

It is noticed that the amount of cubic cobalt in specimen (*c*) in Table I is more than before the high temperature exposure was taken, whereas the earlier explanation in the text applies to a smaller proportion of cubic cobalt.

A. G. Metcalfe

Deloro Smelting and Refining Company
Deloro, Ontario
Canada

References

1. Newkirk, J. B. and Geisler, A. H. Acta Met., **1** (1953) 456.

*Received June 8, 1953.

2. Meyer, W. F. Z. Krist., **97** (1937) 145.
3. Marick, L. Phys. Rev., **49** (1936) 831.
4. Metcalfe, A. G. Proc. World Met. Congress, A.S.M. (1952) 717.
5. Troiano, A. R. and Tokich, J. L. Trans. A.I.M.E., **175** (1948) 728.
6. Edwards, O. S. and Lipson, H. J. Inst. Metals, **69** (1943) 177.

Additional Notes on Textures in Extruded Aluminium*

Further to the letter on "Textures in Extruded Aluminium" [1], it has been noted that the mean rotation of 46° about ⟨111⟩ axes for the "Y" grains, which contained deformation bands, corresponds closely to the 47° rotation obtained upon annealing a compressed single crystal of aluminium which had no deformation bands [2]. Both these results are consistent with the theoretical rotation of 47° (13°) about ⟨111⟩ axes which, according to Kronberg and Wilson [3], gives the third greatest density of coincidence lattice sites. Similar rotations of 38° (22°) and 32° (28°) provide respectively the greatest and second greatest density of coincidence lattice sites [3].

As was pointed out [1], the smaller number and angular range of available nuclei in the less highly deformed "X" grains does not permit selective growth to operate with as great a precision as for the "Y" grains. Thus, the greater scatter in angular rotation for "X" grains may be attributed to the growth of nuclei which have selected coincidence lattice sites corresponding to 13°, 22° and 28° rotations. The mean rotation is, in fact, 22°, as might be expected, since it provides the greatest density of coincidence lattice sites.

The above results seem to provide further evidence that coincidence lattice site considerations are very important in determining the orientation dependence of grain boundary migration rates.

K. V. Gow

Department of Metallurgy
University of Toronto
Toronto, Ontario

References

1. Gow, K. V. and Cahn, R. W. Acta Met., **1** (1953) 238.
2. Beck, P. A. and Hu, H. J. Metals, **1** (1949) 627.
3. Wilson, F. H. J. Metals (1950) 1057.

*Received May 21, 1953.

A "Sub-Regular" Solution Model Applied to the Immiscibility Curve in Liquid Lead-Zinc Alloys*

In a recent paper in this Journal [1], I have examined the properties of an empirical expression in which the heat of solution of a regular solution is allowed to vary linearly with composition. The equation of such a "sub-regular" solution is given by [1]

$$(1) \quad \Delta F = A_1 x^2 y + A_2 x y^2 + RT\,(x \ln x + y \ln y)$$

where x and y are the atomic fractions and the constants A_1 and A_2 are not necessarily independent of temperature. It is a property of a sub-regular solution that the solubility curve is given by

$$(2) \quad \phi \equiv (x_1 + x_2)\, RT \ln \frac{x_1}{x_2} + (y_1 + y_2)\, RT \ln \frac{y_1}{y_2} = -(A_1 - A_2)(x_1 - x_2)^3$$

where x_1 and x_2, y_1 and y_2 are the concentrations co-existing in equilibrium. Consequently the solubility data should give a straight line when the left-hand side of equation (2) (identified as ϕ) is plotted against $(x_1 - x_2)^3$ as long as $(A_1 - A_2)$ is independent of temperature.

It is the purpose of this note to apply the sub-regular solution equations to the immiscibility curve in liquid lead-zinc alloys. As shown by Figure 1, the solubility results of Waring *et al.* [2] fell close to a straight line from the critical temperature down to 500°C when plotted according to

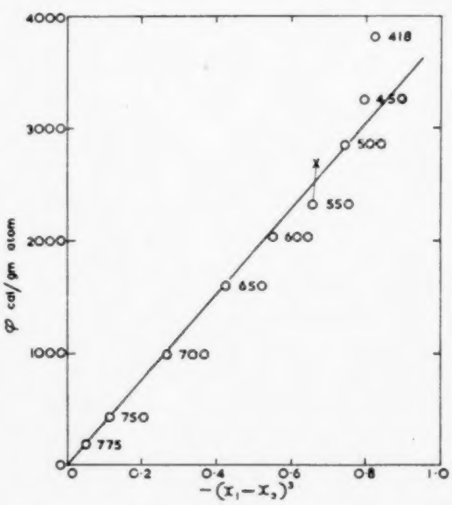

Figure 1. The solubility data for lead zinc alloys at the temperature indicated (°C) plotted according to equation (2).

*Received May 14, 1953.

equation (2). The ratios x_1/x_2 and y_1/y_2 which appear in equation (2) make the plot very sensitive to minor changes in concentration when the solution is very dilute. For example, the point X at 550°C is for $x_2 = 0.010$ compared with the experimental value given as 0.013 and marked by a circle. Therefore, the divergence from the straight line of the points at 450° and 418°C does not necessarily mark the breakdown of the model although different thermodynamic characteristics may be expected from liquids of such different compositions.

The lead-zinc immiscibility curve in the liquid satisfies the predictions of the sub-regular solution model. There is a large temperature dependence of A_1 and A_2 which produces a high heat of solution and correspondingly large additional entropy terms of about 3 cal/gm atom/°C at 800°C and the equiatomic composition. Figure 2 gives the activities of zinc at 1073° and 923°K calculated from the sub-regular solution model.

Lumsden [3] has put forward a four-constant equation which allows the thermodynamic data to be calculated from the miscibility gap. Kleppa [4] has recently published the results of a thermodynamic investigation of the lead-zinc system. He reported that the use of a volume fraction expression for the heat of mixing did not give a very satisfactory agreement with the experimental results, but the activity curves were in good accord with Lumsden's calculations. It will be seen from Figure 2 that the sub-regular solution model predicts lower activities at the lead-rich compositions than those calculated by Lumsden.

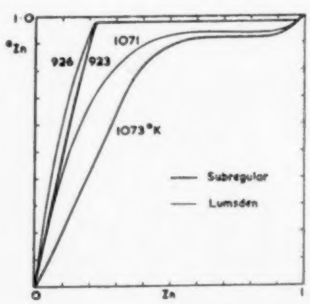

FIGURE 2. Activity composition curves for zinc in its liquid alloys with lead.

The sub-regular solution model appears less accurate than Lumsden's expressions when extrapolated to concentrations away from the solubility curve. It has the advantage of much greater simplicity and allows the solubility curve to be accounted for by only one empirical constant, namely $(A_1 - A_2)$.

H. K. HARDY

Fulmer Research Institute
Stoke Poges, England

References

1. HARDY, H. K. Acta Met., **1** (1953) 202.
2. WARING, R. K., ANDERSON, E. A., SPRINGER, R. D., and WILCOX, R. L. Trans. A.I.M.E., **111** (1934) 255.
3. LUMSDEN, J. Discussions Farad. Soc., **4** (1948) 60.
4. KLEPPA, O. J. J. Amer. Chem. Soc., **74** (1952) 6047, 6052.

Triple η_2 Carbides and the Atomic Size Factor*

In a previous communication [1] the formation of η carbides in general and of η_1 carbides in particular was discussed. Since then, more work has been done on the formation of the triple η_2 carbides and the results are presented here.

The η_2 carbide (A_2B_4C) differs from the η_1 carbide (A_3B_3C) not only in the cube edge but also in the relative intensity of the X-ray diffraction pattern [2], so that these two carbides can easily be distinguished by the X-ray powder method. In the study of triple carbides, where the composition varies within broad limits, the lattice dimension also varies within the range of 0.1 Å. In the following, the identification of the carbide phase is based on the line intensity measurement, while the discussion is based on the change in lattice dimension.

Three genuine triple η_2 carbides were found. The composition of the alloy, the formula of the carbide (to be discussed below), and the lattice dimension found are:

Alloy	Carbide	Cube Edge
$Ti_2Ni_2Ta_2C$	$Ni_2(Ti, Ta)_4C$	$a = 11.52$ Å
$Ti_2Co_2Ta_2C$	$Co_2(Ti, Ta)_4C$	$a = 11.51$ Å
$Ti_2Ni_2Nb_2C$	$Ni_2(Ti, Nb)_4C$	$a = 11.58$ Å

On account of the presence of other phases, e.g., TiC and Ta_2C, the composition of the alloy cannot be used to represent that of the carbide concerned. Otherwise, the formula of the triple carbide would be unambiguously determined as $Ni_2(Ti, Ta)_4C$, etc., (not as $(Ti, Ni)_2\,Ta_4C$, etc.) in conformity with the general formula of the η_2 carbide, A_2B_4C. The function of Ni and Ta in the formation of these

*Received July 16, 1953.

triple carbides is known, and the problem left to be decided is therefore the function of Ti.

It has been shown earlier [1] that the η_2 carbide always has a larger cube edge than the η_1 carbide containing the same metals, owing to the larger amount of the bigger atom B. Moreover, the mixture (Ti, Ni) has a larger mean atomic radius than the mixture (V, Ni) or (Cr, Ni), and consequently the carbide $(Ti, Ni)_3 B_3C$ should have a larger cube edge than $(V, Ni)_3B_3C$ or $(Cr, Ni)_3B_3C$. Therefore, the carbide $(Ti, Ni)_2Ta_4C$ should have a larger cube edge than $(Ti, Ni)_3Ta_3C$, which in turn should have a larger cube edge than $(V, Ni)_3 Ta_3C$ (11.56 Å) or $(Cr, Ni)_3Ta_3C$ (11.44 Å) [1]. The cube edge found for the η_2 carbide in the alloy $Ti_2Ni_2Ta_2C$ is of the same order as that of $(V, Ni)_3 Ta_3C$. This excludes the possibility of Ti being an A component in the carbide A_2B_4C. The same argument applies equally well to the other two triple η_2 carbides mentioned above.

The other alternative is $Ni_2(Ti, Ta)_4C$. This does not seem unreasonable, since the atomic radius of Ti (1.47 Å for coordination number 12) does not differ materially from that of Ta (1.49 Å). For the sake of simplicity, it is assumed when considering the lattice dimension, that Ti is an equivalent of Ta. Of the carbides Ni_2 $(Ti, Ta)_4C$ and $(V, Ni)_3Ta_3$ C, the former has a larger proportion of B, while the latter has an A mixture possessing a larger mean atomic radius. These two factors may compensate each other, and the result is that these two carbides have a similar cube edge.

Thus, in the formation of triple carbides containing Ta and Ni, Cr and V serve as A component and Ti as B component, and both the A and B components can be a mixture of two or more metals. This kind of substitution, Ti or Ta and V or Cr for Ni, is probably governed by the atomic size factor.

It was thought that confirmation of the above reasoning about the effect of the atomic size factor might be obtained from a study of the function of V (radius 1.36 Å) in the formation of the η_2 carbide containing W (1.41 Å) and Ni (1.25 Å). If V replaces Ni, the lattice will be enlarged, and if V replaces W the lattice will be diminished. The η_2 carbide (not a true triple carbide, since the double carbide Ni_2W_4C exists) obtained from a mixture of (VC + 2W + 3 Ni) has a cube edge of 11.5 Å, smaller than that of Ni_2W_4C, 11.25 Å. No VC or V was found to remain (though plenty Ni did not react); therefore, in this case V must be part of the B component, replacing some W.

The fact that V can serve either as an A component when the B component is Ta or Nb, or as a B component when the other B component is W or Mo, further illustrates the importance of the atomic size factor. The observation made earlier [1] that the metal A belongs to period IV and B to period V or VI can no longer be applied to the formation of triple η carbides, though it is still valid in the case of double η carbides.

The relation of Cr to W may be compared with that of V to Ta. Cr might be expected to replace the A component of the carbide A_3W_3C, rather than W, as suggested by earlier workers [3; 4]. However, Chebotarev's statement [4] that V atoms may replace W atoms is in agreement with the present results.

In comparing the carbides $Ni_2(Ti, Ta)_4C$ and Ni_2W_4C, we may consider the mixture (Ti, Ta) to be equivalent to W. This shows that the strength of the metal-carbon bond may be disregarded as an operative factor in the formation of the η carbides, because it is well known that both Ti and Ta have a much stronger affinity for carbon than W has. The question of why neither Ti nor Ta by itself forms an η_2 carbide with Ni still remains unanswered.

The writer wishes to thank Professor G. Hägg for his interest and the Swedish State Council for Technical Research for financial support.

KEHSIN KUO

Institute of Chemistry
University of Uppsala
Uppsala, Sweden

References

1. KUO, K. Acta Met., **1** (1953) 301.
2. KIESSLING, R. Discussion on the paper by P. Rautala and J. Norton. J. Metals, **5** (1953) 745.
3. TAYLOR, A. and SACHS, K. Nature, **169** (1952) 411.
4. CHEBOTAREV, N. T. Izvest. Akad. Nauk. S.S.S.R. Ser. Fiz., **15** (1951) 39.

Erratum

Vol. 1, no. 4, pp. 460–464. Shear along Glide in Aluminum. By R. MADDIN, E. H. HARRISON, and R. W. GELINAS. The magnifications and scale of the abscissae in the illustrations are in error.

The photomicrographs of Figures 1, 3, 4, 9 and 10 should be multiplied by 1/3. The abscissae on the graphs (Figures 5, 6, 7, 8 and 11) should be multiplied by 10/3. The shear measurements on all of the curves are correct as they are.

BOOK REVIEW

Physical Chemistry of Metals. By Lawrence S. Darken and Robert W. Gurry; with a collection of problems by Michael B. Bever. New York: McGraw-Hill Book Company. 1953. Pp. ix+535.

This book will appeal to both the chemist and the metallurgist although it was written expressly for the latter. As a text for students who have completed the usual one-year introductory course in physical chemistry, it should find its place in many metallurgy curricula. It will be a valuable guide to the research workers in this field of applied physical chemistry.

After a brief introductory chapter the next four, approximately one-fourth of the book, are devoted to gases, solids and liquids. The discussion of atomic structure is excessively brief but contains a complete table of arrangement of orbital electrons. Bonding and resonance phenomena are treated briefly but competently. In addition the chapter on solids discusses plastic deformation, Hume-Rothery's classification, atomic radii and crystallography of the elements and imperfections in crystals. It contains a rather full exposition of Pauling's theory of valence and atomic radius in metals.

The chapter on solid solutions and intermetallic compounds includes quantitative discussions of the effect of size factor and electronegativity on extent of solid solubility. Long and short range order and intermediate phases are discussed.

Chapter 5 contains an excellent summary of the structure of liquids as deduced from X-ray diffraction data. The authors make a strong case for ordering in certain liquid metallic solutions. A discussion of the "hole" theory of liquid structure contains the only mention of viscosity.

Chapters 6–10 present the classical approach to thermodynamics with applications to metallic solutions and other systems of especial metallurgical interest. Statistical mechanics is considered beyond the scope of the book but its conclusions are used freely, especially in connection with the third law. This procedure is likely to prove baffling to the student who has not been told about the relation between entropy and randomness.

The treatment of solutions will be especially helpful to research metallurgists. The authors employ the function $\alpha_i = \ln \gamma_i/(1 - N_i)^2$ which is useful in interpolating activity data and in graphical integration of the Gibbs-Duhem equation. This chapter and a later one on free-energy-composition diagrams are especially recommended to the physicist or metallurgist who is unfamiliar with the elegant methods developed by chemists for the thermodynamic treatment of solutions.

Two chapters on the phase rule and heterogeneous equilibria contain the basic principles applicable to one- and two-component systems. Systems of three or more components are not discussed.

Chapter 14 contains summaries of much useful metallurgical data on the free energy of formation of oxides, sulfides, carbides, nitrides and chlorides. In it also is found a brief summary of the authors' own fine work on the system iron-oxygen. The two following chapters are treatises on the two important systems Fe-N and Fe-C. They include extensive and critical reviews of the literature and collations of the quantitative data available.

Chapter 18, "Formal Basis of Diffusion Theory," has already found its honored place in metallurgical literature. This is more than a routine exposition of the mathematical treatment of diffusion data. It includes a full discussion of the "Kirkendall effect," limitations on Fick's law imposed by grain boundaries and lattice defects, and variations of diffusivity with composition or with chemical potential.

The final chapter, "Kinetics of Metallurgical Processes," is an adaptation of a similar chapter in *Basic Open Hearth Steelmaking* (A.I.M.E., 1951). It contains the most compact and understandable exposition of modern rate theory this reviewer has seen. Applications include the few metallurgical reactions on which adequate rate data have been published.

The usefulness of the book could have been enhanced by addition of a section on strain energy and of a chapter on thermodynamics of surfaces.

The book contains a collection of 257 problems which contribute greatly to its usefulness as a classroom text. The problems are chiefly of a quantitative nature, requiring numerical or graphical solution and most of them demand a substantial amount of original thinking on the part of the student. It would have been helpful to many if answers to a few of the problems had been provided. It seems good educational practice in a book of this sort to put the practical applications in the problems. This has been done in an admirable manner.

From the standpoint of the teacher it is not easy

to judge the suitability of a new book until it has been tried in the classroom. The book seems to be a very close approximation to the specialized requirements of a modern curriculum in metallurgy. For a course in thermodynamics Chapters 1, 6 to 14, inclusive, and 17 provide an excellent base. The book will prove stimulating to the advanced student (senior or graduate) and challenging to the teacher. The latter should be prepared to supplement it with respect to several topics which the authors have omitted.

JOHN CHIPMAN

CURRENT PAPERS IN OTHER JOURNALS

Acta Crystallographica, Vol. 6

Part 7, July, 1953 (Partial Contents)

An analysis of the efficiency of convergence of different methods of structure determination. I. The methods of least squares and steepest descents: Centrosymmetric case. M. M. Qurashi.

Calculated powder patterns from very small crystals: body-centered cubic cubes. Chang Morozumi and H. L. Ritter.

The crystal structure of $BaCd_{11}$. M. J. Sanderson and N. C. Baenziger.

X-ray scattering by aggregates of bonded atoms. III. The bond scattering factor: Simple methods of approximation in the general case. R. McWeeny.

Anomalous lattice constants of zinc oxide. G. D. Archard.

The structure of PdO. Jurg. Waser, Henri A. Levy and S. W. Peterson.

A monogram for evaluating the temperature factor. H. J. Grenville-Wells.

The measurement and correction of intensities from single-crystal X-ray photographs. G. Kaan and W. F. Cole.

The structure of β(AlCrSi). Keith Robinson.

A discussion of the Cox and Shaw factor for oblique incidence and the film-to-film factor in multiple-film exposures. M. M. Qurashi.

Archiv für das Eisenhüttenwesen

Heft 5–6, Mai–Juni, 1953

Anwendung von Schall und Ultraschall bei der Gasreinigung. Hermann Schnitzler.

Der Einfluss des Stickstoff-Teildruckes des Blaswindes auf die Aufstickung. Theo Kootz.

Die photometrische Bestimmung des Kupfers in unlegierten und niedriglegierten Stählen mit *o*-Tolidin. Hans Blum.

Der Einfluss der Wasserstoffdiffusion auf den kritischen Reckgrad von weichem unlegierten Stahl. Friedrich Erdmann-Jesnitzer und Hermann Schumann.

Diffusionskornbildung in Eisenlegierungen. Friedrich Erdmann-Jesnitzer, Hermann Schumann und Manfred Beckert.

Überschallprüfung nach dem Durchschallungs- und Impulsecho-Verfahren. Helmut Krainer und Ekkehart Krainer.

Untersuchungen über die Kristallisation des Gusseisens mit Kugelgraphit. Erich Scheil und Leo Hütter.

Umsetzungen der Eisenphosphide mit flüssigem Zink. Rudolf Vogel und Dietrich Horstmann.

Die Beeinflussung der Sintereigenschaften von Metallpulvern durch eine Oberflächenbehandlung. Gerhard Naeser und Hans Burmeister.

Über phosphorlegierten Sinterstahl. Fritz Eisenkolb.

Hartmetall-Legierungen hoher Korrosions-und Oxydationsbeständigkeit. Josef Hinnüber und Otto Rüdiger.

Zur Theorie der Ausscheidungsvorgänge in übersättigten festen Lösungen. Wolfgang Wepner.

Heft 7–8, Juli–August, 1953

Lösungsversuche an Hüttenkalken. Joachim Endell.

Wärmetönungen metallürgischer Reaktionen. Carl V. Schwarz.

Anordnung zur Messung der elektromotorischen Kräfte zwischen Metall-oxyden bei hohen Temperaturen und Untersuchungen im System $FeO\text{-}Al_2O_3$ bei 1500°. Wilhelm Anton Fischer und Rudolf Schafer.

Das Verhalten von Stählen mit verschiedener Kerbschlagzähigkeit bei Verformung unter mehrachsiger Beanspruchung. Hubert Bennek, Eduard Houdremont und Richard Mailänder.

Seigerungserscheinungen an Nickelstählen. Klaus Janssen, Eduard Houdremont und Werner Jellinghaus.

Isothermische Zeit-Temperatur-Umwandlungs-Schaubilder gebräuchlicher Werkzeugstähle. Max Kroneis, Reinhold Gattringer und Helmut Krainer.

Einfluss des Werkstoffzustandes auf die Wasserstoffdiffusion in unlegiertem Stahl. Hermann Schumann und Friedrich Erdmann-Jesnitzer.

Der Einfluss der Umhüllung von Schweisselektroden auf die Fleckenbildung in unlegiertem Schweissgut von Stahl und ihre Entstehung. Friedrich Erdmann-Jesnitzer und Hans Kowalkowski.

Das Zustandsschaubild Eisen-Eisenphosphid-Molybdänphosphid-Molybdän. Rudolf Vogel und Dietrich Horstmann.

Journal of the Institute of Metals, Vol. 81

Part 12, August, 1953

The properties of cast chromium alloys at elevated temperatures. A. H. Sully, E. A. Brandes, and A. G. Provan.

The effect of temperature and purity on the ductility and other properties of chromium. A. H. Sully, E. A. Brandes, and K. W. Mitchell.

The stepped stress/strain curve of some aluminium alloys. N. Krupnik and Hugh Ford.

Discontinuous flow and strain-ageing in a 6% tin phosphor-bronze. N. H. Polakowski.

Yield-point phenomena and stretcher-strain markings in aluminium-magnesium alloys. V. A. Phillips, A. J. Swain, and R. Eborall.

Some methods of measuring surface topography as applied to stretcher- strain markings on metal sheet. W. H. L. Hooper and J. Holden.

Effect of composition and heat-treatment on yield-point phenomena in aluminium alloys. V. A. Phillips.

Growth of sulphide films on copper. T. P. Hoar and A. J. P. Tucker.

Oxidation of copper in the temperature range 200°–800°C. R. F. Tylecote.

Journal of the Mechanics and Physics of Solids, Vol. 1

No. 4, June, 1953

Limit analysis of two and three dimensional soil mechanics problems. D. C. Drucker.

The brittle fracture of metals. E. O. Hall.

A note on a test of the plastic isotropy of metals. H. Ll. D. Pugh.

The yield stress of pure lead in compression. N. Loizou and R. B. Sims.

Experiments with a laboratory extrusion apparatus under conditions of plane strain. N. W. Purchase and S. J. Tupper.

Eine Theorie der Kriechens von Einkristallen. O. G. Folberth and A. Kochendörfer.

On the mechanics of cutting metal strips with knife-edges tools. R. Hill.
A new method for determining the yield criterion and plastic potential of duetill metals. R. Hill.
Experimental investigation of the behaviours of soil under a punch or footing. W. Sylwestrowicz.

Journal of Metals, Vol. 5

No. 7, July, 1953
Monolithic linings in furnace spouts: Working conditions improved at Armco Steel Corp. V. W. Jones. Monolithic linings successful at Crucible Steel Co. G. M. Burrier. Practice adopted at Bethlehem Steel Co. J. C. MacNeill.
Open hearth slag removed economically by blasting. J. O. Dague.
Vancouver Steel Co. Ltd., uses mullite roofs in electric furnaces. G. R. Heffernan.
Huge alloy plant to produce simplex ferrochrome selecting conveyors for handling hot bulk materials. J. W. Snavely.
Phase diagrams play an important role in powder metallurgy. R. Steinitz.
Further studies of the tuyere zone of the blast furnace. J. B. Wagstaff.
Electrical resistance of titanium metal. J. L. Wyatt.
Microscopical examination of tin bronzes in the alpha range. E. C. W. Perryman.
Grain boundary attack on aluminum in hydrochloric acid and sodium hydroxide. E. C. W. Perryman.
Martensite nucleation in substitutional iron alloys. J. C. Fisher.
Calculation of martensite nucleus energy using the reaction-path model. J. C. Fisher and D. Turnbull.
Further progress in the development of Mg-Zr alloys to give good creep and fatigue properties between 500° and 650°F. C. J. P. Ball, A. C. Jessup, P. A. Fisher, D. J. Whitehead, and J. B. Wilson.
Textures of rolled and annealed iodide zirconium. J. H. Keeler, W. R. Hibbard, Jr., and B. F. Decker.
Anelastic behavior of pure gold wire. D. R. Mash, L. D. Hall.
Effect of nickel and molybdenum on stabilization of the austenite-martensite transformation. D. J. Blickwede.

No. 8, August, 1953
Design features of Fairless Works open hearth. H. A. Parker.
British producing germanium from flue dust.
Ion exchange finds wider use in concentration and recovery of metals from dilute solutions. A. B. Mindler, C. F. Paulson.
Deoxidation and degasification practice for basic electric furnace alloy steels. A. L. Ascik.
Vacuum dezincing of desilverized lead bullion. T. R. A. Davey.
Examination of a high sulphur free-machining ingot, bloom, and billet sections. D. J. Carney, E. C. Rudolphy.
Reducing period in stainless steel melting. H. P. Rassbach, E. R. Saunders.
Silicon-oxygen equilibrium in liquid iron—a revision. J. Chipman, N. A. Gokcen.
Thermodynamic properties of molybdenum dioxide. N. A. Gokcen.
Influence of aluminum and silicon deoxidation on the strain agin of low-carbon steels. W. C. Leslie and R. L. Rickett.
Some properties of columbium containing nitrogen. C. Ang and C. Wert.
Isothermal temper embrittlement of SAE 3140 steel. F. L. Carr, M. Goldman, L. D. Jaffee, and D. C. Buffum.
Thermal conductivity of nodular iron. M. J. Sinnott.
Plastic bending of zinc crystals. G. P. Conard II, B. L. Averbach, and M. Cohen.
Modifications of the Schulz technique for the X-ray determination of preferred orientation in rolled metal. M. L. Fuller and G. Vaux.

Revue de Métallurgie, 50e Année

Numéro 6, Juin, 1953
Comment construire les fondations des marteaux-pilons. I. E. Katel.
La fabrication des coussinets autolubrifiants. Le frittage avec apparition de phase liquide. P. Laurent et M. Eudier.
Usure et fatigue des rails de chemins de fer. M. Ros.
Influence de l'azote sur les propriétés de la cémentite. R. Bridelle et A. Michel.
Recherches sur la cristallisation des fontes à graphite sphéroidal. A. Wittmoser.
Etude par diffraction électronique des alliages aluminium-cuivre obtenus par vaporisation sous vide. J.-J. Trillat et Noboru Takahashi.
Etude systématique au moyen du volume-débitgraphe des facteurs déterminant la soufflabilité des charges au convertisseur Thomas (à suivre). P. Leroy, M. Gombert et B. Trentini.

Zeitschrift für Metallkunde, Band 44

Heft 6, Juni, 1953
Die Wirkung von Spannungskonzentrationen auf die Zeitstandfestigkeit der Werkstoffe. G. Sachs, W. F. Brown und D. P. Newmann.
Die physikalischen Vorgänge bei der Wechselbeanspruchung. U. Dehlinger.
Beitrag zum System Tantal-Silizium. R. Kieffer, F. Benesovsky, H. Nowotny und H. Schachner.
Versetzungen und allotrope Umwandlungen. A. Seeger.
Zur Ortskorrelation der Aussenelektronen in der Kristallchemie. K. Schubert.
Zu dem System Mangan-Indium. S. Valentiner.
Thermoelektrische Temperaturmesseinrichtung für hohe Genauigkeitsanforderungen, insbesondere für thermische Analysen. W. Hunsinger.
Ein Beitrag zur Raffination des Magnesiums. K. E. Mann.
Der symmetrierte Induktions-Tiegelofen für Netzfrequenz mit gestampften Tiegel zum Anschluss an ein Drehstromnetz. R. Lethen.
Elektroinduktive Blockheizung mit Netzfrequenz. E. K. L. Haffner.

THE ISOTHERMAL TRANSFORMATION OF METASTABLE BETA-URANIUM SINGLE CRYSTALS*

A. N. HOLDEN†

The transformation of metastable beta-uranium crystals was found to proceed by a martensitic reaction at room temperature. The feature of the transformation of particular interest was that individual uranium martensite plates formed and grew at a slow rate isothermally.

LA TRANSFORMATION ISOTHERME DE MONOCRISTAUX D'URANIUM BÊTA MÉTASTABLE

Il a été constaté que la transformation de cristaux d'uranium bêta métastable s'opérait par une réaction martensitique à la température ambiante. La caractéristique la plus intéressante de cette transformation était, que des lamelles individuelles de martensite de l'uranium se formaient et poussaient isothermiquement à faible vitesse.

DIE ISOTHERME TRANSFORMATION VON METASTABILEN BETA-URAN EINKRISTALLEN

Es wurde gefunden, dass die Umwandlung von metastabilen Beta-Uran Kristallen bei Zimmertemperatur auf Grund einer Martensit Reaktion von statten geht. Es ist von besonderem Interesse, dass in dieser Umwandlung einzelne Uran Martensitplättchen gebildet werden und isotherm mit geringer Geschwindigkeit wachsen.

Introduction

Single crystals of the beta-phase of uranium were first grown and retained in metastable condition at room temperature in material containing 1 atomic per cent of more of chromium. These crystals were stable for months at room temperature and were used by Tucker [1] to determine the beta-phase structure. Crytsals of lower chromium contents down to .3 atomic per cent have been grown recently [2], and these crystals transform to alpha much more rapidly. The results of a study of the transformation in these low chromium alloy crystals, both metallographically and by means of X-ray examination are presented in this paper.

Gross Features of the Transformation

The transformation in these dilute chromium-uranium solid solution alloys was of added interest because the plates of alpha that were formed during room-temperature isothermal transformation had an appearance (see Figure 1) not unlike martensite plates in iron alloys. In fact, a great many of the transformation features were similar to martensite: the plates seemed to prefer only certain habit planes in the parent crystal; the surface of the beta-crystal was distorted by the formation of an alpha-plate; the distortion thus observed frequently appeared feathered very similar to martensite; and deformation of the beta-crystal greatly hastened its transformation.

*Received April 6, 1953.

†Knolls Atomic Power Laboratory, General Electric Company, Schenectady, New York, U.S.A.

Other features of the transformation were unlike martensite of the usual type, however. The transformation of beta-phase crystals to alpha during cooling could be completely suppressed by quenching them from the beta-phase to room temperature, a feature uncommon in the martensite transformation. Furthermore, the growth of the transformation plates occurred without audible clicking and apparently the reaction went to completion isothermally at a slow rate.

The experimental work on this transformation has been concerned with two aspects of the problem; namely, first to classify the transformation as either a martensitic transformation or a nucleation and growth transformation of the standard type, and second to study the crystallography of the transformation.

Classification of the Transformation

In order to classify the transformation as martensitic or non-martensitic, a martensitic transformation will be defined. Martensitic transformations are characterized as follows:

1. The product shall be plate like (lens or needle shaped in two-dimensional section) and form by the cooperative movement of the material within the plate through fractional atom distances.

2. A composition change is not required by the transformation.

Other formerly accepted criteria for a martensite transformation must be considered fallible in the light of recent experimental exceptions to these rules. For example, it was thought that martensite formed only upon cooling; hence the term *athermal*

has been applied to its formation, yet the complete suppression of athermal martensite by rapid quenching has been observed by Kurdjumov et al [3; 4] and recently by Cech and Hollomon [5]. Furthermore, martensite transformations have been reported by Kurdjumov to proceed extensively, isothermally, and this fact has also been corroborated in the recent work cited [5]. Another criterion of the martensite transformation that has persisted until recently is that individual martensite plates grow extremely rapidly. Slow growth of martensite individuals, however, has been reported by Kurdjumov [4] for a copper tin alloy transforming at $-190°C$.

In applying the two remaining criteria; namely, the cooperative movement requirement and the requirement that no composition change occurs, to the transformation at hand, there are certain accepted tests we may make.

The test for a composition change is to measure the rate of growth of the transformation product. If it grows more rapidly than any element will diffuse in the bulk matrix, no composition change must have occurred and a martensite transformation is indicated. Certain transformations, usually known by the generic term *bainite*, have all the characteristics of martensite except that the rate of growth of the transformation plates has been reconciled with bulk diffusion rates, and such a transformation would be indicated by a growth rate consistent with bulk diffusion rates.

The test that can be made for the cooperative movement of the atoms in the transformation product is to observe what happens to parallel scratches on the specimen surface during the transformation. No martensite transformation can fail to shear the scratches wherever a transformation plate occurs, and furthermore the sheared scratches will have the same angle with the matrix throughout the plate.

The rate of isothermal growth of the plates formed on transforming beta-uranium crystals at room temperature was studied by the simple technique of photographing the product at intervals. For this work a polished crystal was studied using polarized light to reveal the transformation. Figure 2 is such a sequence of photographs over an hour period showing the growth to be continuous and at a rate of approximately 0.5 mm increase in length per hour. While this growth is slow for the general class of martensite, it is certainly more rapid than chromium can diffuse, and therefore a composition change seems unlikely and a martensite transformation is indicated.

The question of shearing of scratches was investigated by observing what happened to a finely scratched beta-crystal surface during the transformation. These scratches were applied to the specimen before the crystal was grown because it was found that any scratching subsequent to growth caused immediate transformation of the crystal surface and obscured any shearing effect. A small but definite unidirectional and apparently homogeneous shearing of the scratches was observed upon transformation, and two photographs of this phenomenon are shown in Figure 3.

There seems little doubt that the room-temperature transformation of beta-uranium crystals is by a martensite mechanism. Shearing of the product is accomplished, as can be seen in the shifting of scratches, and there is little chance that composition changes can occur in the time required for plate growth.

The effect of deformation on the transformation seems to be one of introducing critical-size nuclei, for while the rate of growth of the individual plates in strained regions remains slow they begin to form immediately. In a nondeformed region a few hours at room temperature is required to produce any visible plates. Slip bands do not seem to constitute barriers to the migration of the plates.

A question that remains to be answered is why the martensite transformation in uranium proceeds by slow growth of individual plates, while steel martensites grow with velocities approaching that of sound. Some retarding mechanism must operate to slow the uranium growth.

One possibility is that the simultaneous local deformation of the matrix which must occur in rapidly growing steel martensite does not take place readily in uranium. Whereas steel martensites form in a ductile FCC matrix, the beta-phase of uranium deforms by slip at room temperature only on $\{110\}$ type planes and in the [001] direction [2]. It would be highly fortuitous if the two possible systems were oriented so as to relieve the shear stress in beta, and in fact the habit plane* for uranium martensite is 30 degrees from the slip plane.

The alpha-plates, on the other hand, could twin readily [6] so that a large proportion of the trans-

*Habit plane determination is discussed in a succeeding section of this paper.

1

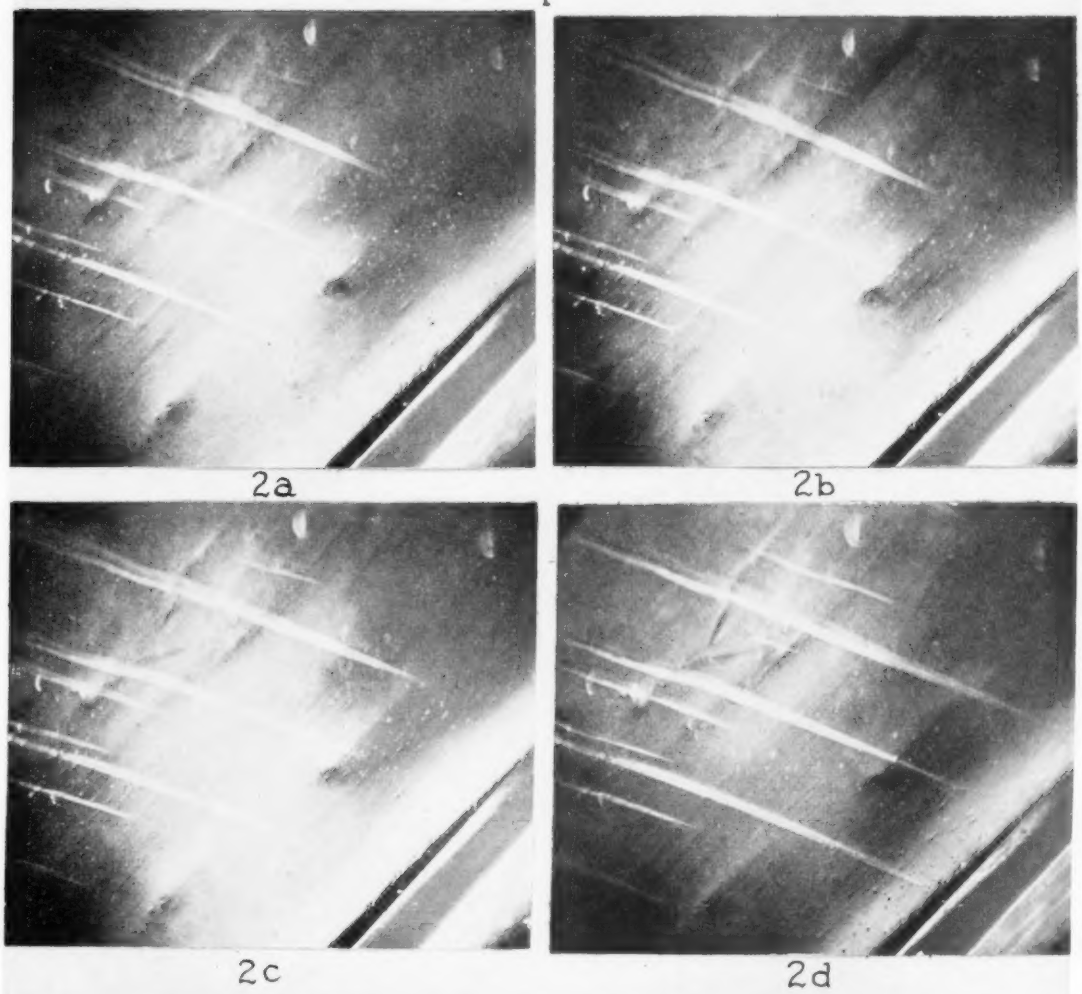

PLATE I. Figure 1—Plates formed by isothermal transformation of beta uranium crystal at room temperature. 100× polarized light. Figure 2—Growth of plates at room temperature (a) 2:50 P.M. (b) 3:05 P.M. (c) 3:20 P.M. (d) 3:53 P.M. Rate of growth approximately .5 mm per hour. Polarized light 40×. All figures reduced to seven-eighths in reproduction.

3a

3b

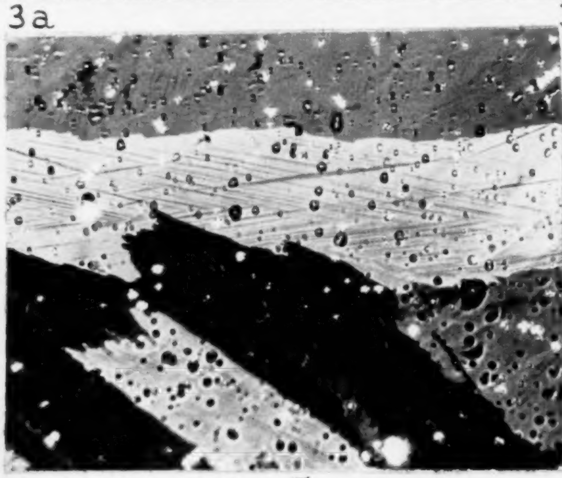

5

6

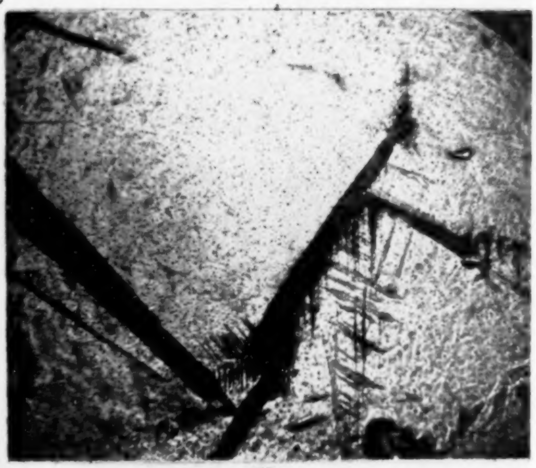

7

PLATE II. Figure 3—Examples of shearing of scratches by the transformation. (a) Polarized light 100× (b) Polarized light 200×. Figure 5—Twins in large alpha-plate. Polarized light 400×. Figure 6—Slip in beta-crystal near junction of two martensite plates. Polarized light 200×. Figure 7—Athermal martensite burst. Polarized light 100×. All figures reduced to seven-eighths in reproduction.

formation stress is relieved by deformation of the uranium martensite plate itself. The growth of the plates would be slowed down by the requirement that twins continually nucleate and relieve the transformation stress. The motion of the plate would be intermittently rapid and slow—immediately after twinning it would move rapidly for a distance and then as the stress increased slow down until another twin formed.

The stresses associated with conventional steel martensite can be relieved by the motion of dislocations in the matrix, since a large number of deformation systems are available for volume adjustment of the matrix, and the growth of conventional martensite is limited only by the velocity of propagation of dislocations which may approach sound velocities. Furthermore, the ductility of FCC material is retained to 4°K.

The relief of strains associated with the growth of conventional and uranium martensites is visualized as shown in Figure 4.

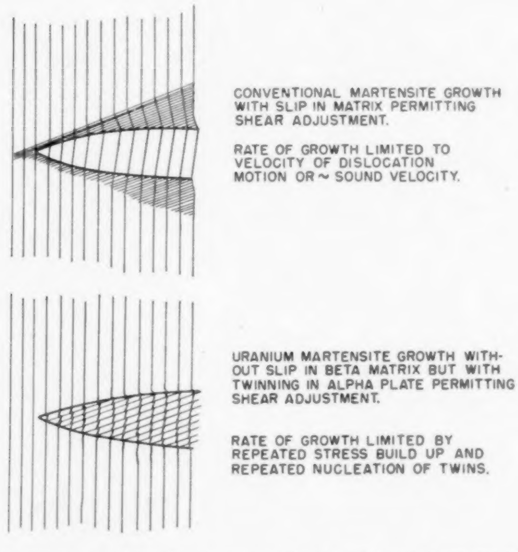

FIGURE 4. Growth of conventional and uranium martensite.

High magnification microscopy has revealed that individual plates of alpha do appear to be twinned, and a photograph of these twin markings at high magnification 400× is presented in Figure 5.

In uranium, slip is often observed on one or both slip systems of the beta-matrix in the stressed region near the junction of two or more large alpha plates. The combination of stresses resolves to cause slip in these regions. Such a region is pictured in Figure 6.

Several, but by no means all, of the beta crystals had a few large martensite plates already formed by the time the first observation was made. In general, less than five minutes from quenching to observation was necessary, so that these could hardly have grown during their sojourn at room temperature unless they grew much faster than any measured rate of growth. It is the preferred explanation that these grew athermally at some higher temperature, perhaps even above 350°C in a region where alpha uranium is known to slip readily and where perhaps the beta-phase also deforms by slip at a reasonable stress and on a greater number of slip systems. Many of these plates appear to be bursts where one plate has triggered another. A photograph of such an athermal burst is shown in Figure 7.

There is another feature common to many martensite reactions; namely, that in the absence of any competing reactions they are reversible upon heating.

A partially transformed beta-crystal was rapidly heated to 625°C, a temperature high in the alpha equilibrium range, by plunging it into a lead pot. It was held for ten minutes, and then quenched. It was found to be a single beta-crystal again with no sign of transformation.

Crystallography of the Transformation

X-ray work has been carried out in several ways, none of which has yielded satisfying results.

The first attempts were to orient large isolated plates by a back-reflection Laue method using a very fine beam. These attempts failed because the plates were evidently strained sufficiently to give distorted patterns that could not be oriented, and, furthermore, the exposure times with the fine beam were so long that excessive oxidation of the crystal occurred.

Attempts were then made to obtain a pole figure of the transformed alpha after the transformation was complete, using cylindrical rather than square crystals, and using standard film techniques. These attempts were not successful because the simple planes (110) and (002) occur in a triple reflection together with the (021) making it very difficult to separate the three on film and almost impossible to correctly assign indices to isolated diffraction spots of the triplet group.

The equipment currently being used is a completely modified Schultz-type goniometer in conjunction wish a Geiger-counter spectrometer [7]. The goniometer was designed to move the speci-

men automatically so that reflection occurs sequentially from all the planes whose normals would trace a spiral path on a stereographic projection. A record of the reflected intensities along this spiral path was made for several planes of interest, and pole figures plotted from this record. Good resolution of the (110) (021) (002) triplet was obtained with this instrument. The results of the X-ray work are presented as a series of typical pole figures. The (002) alpha-pole figure for the transformation is shown in Figure 8, plotted directly over the projection of the beta-crystal matrix. The (040) alpha-planes were found in positions shown in Figure 9, and in Figure 10 the (110) alpha-pole figure for the transformation is shown. Thus far it has not been possible to fit these pole figure data with a single orientation relationship and the work has not progressed to the point where any relationships deduced from the pole figure data are considered positive. It is hoped the results of more thorough orientation study may be the subject of a future paper.

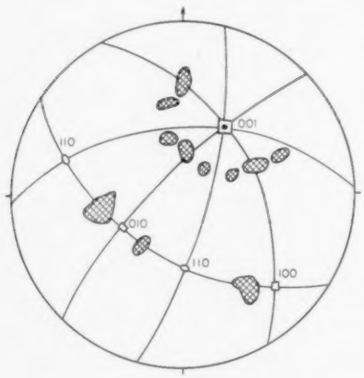

FIGURE 8. (002) alpha pole figure for room temperature martensitic transformation of beta uranium.

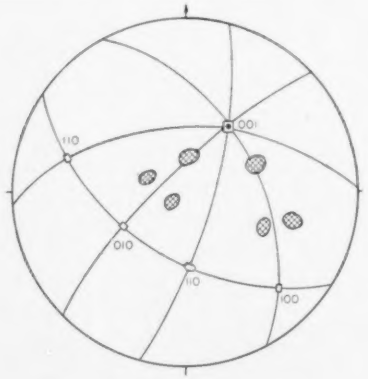

FIGURE 9. (004) alpha pole figure for room temperature martensitic transformation of beta uranium.

The macroscopic habit plane for the martensite transformation of beta-uranium to alpha has been identified by metallographic studies of the traces of plates in adjacent faces of rectangular cross-section crystals. The principal habit plane appears to be approximately a {321} type beta-plane. Figure 11 is a typical plot of the observed poles of the plates on a stereographic projection of the parent beta crystal.

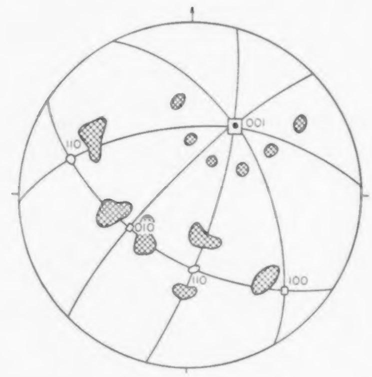

FIGURE 10. (110) alpha pole figure for room temperature martensitic transformation of beta uranium.

The (321) plane according to Tucker's work is an unimportant plane having an extremely low relative intensity value for reflected X-rays. This choice of a crystallographically unimportant habit plane seems characteristic of martensite.

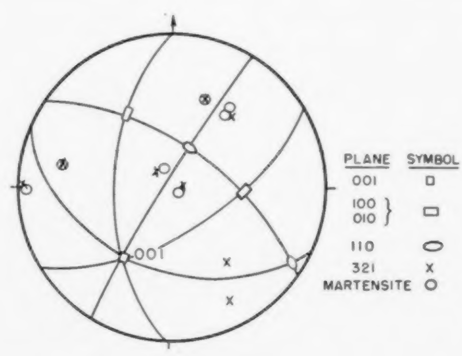

FIGURE 11. Typical coincidence of martensite habit plane with {321} plane in beta matrix.

Geisler [8] has considered that the unimportant crystallographic habit planes for martensite transformations are a consequence of either slip or twinning of the martensite plate itself or of the

matrix, and that the actual lattice matching occurs across smaller segments of boundary that are not parallel to the general plane of the large plate. Since habit planes are usually reported for the macroscopic plate, these planes are not necessarily important.

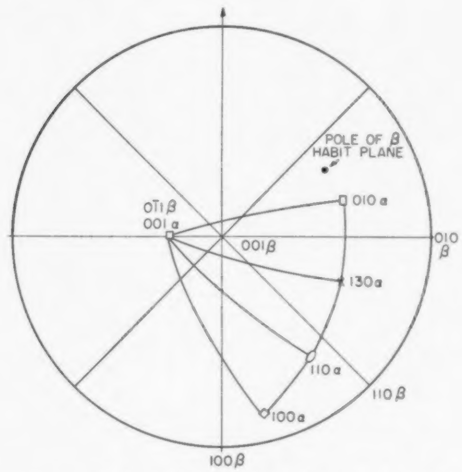

FIGURE 12. Orientation relation in martensite transformation of beta to alpha uranium.

Conclusion

The room-temperature beta-to-alpha transformation of quenched uranium-chromium-alloy crystals is martensitic. The transformation may be suppressed completely by quenching, and occurs isothermally at a slow measurable rate by the relatively slow growth of martensite individuals.

Acknowledgment

I wish to thank J. E. Burke for his interest in this transformation study, and D. W. White and J. C. Fisher who provided much helpful information and discussion. Gratitude is also due the Atomic Energy Commission for permission to publish this work.

Note Added in Proof*

A means has been found recently to ascertain the orientation relationship of the beta to alpha uranium transformation. If the retained beta-crystal is scratched longitudinally prior to any transformation, alpha-plates nucleate and grow with a single habit nearly normal to the scratch. These eventually grow together like touching fingers on a hand and form alpha-crystals perfect enough to give good Laue photograms. From such photograms the relationship shown in Figure 12 was derived. This relationship will account for some but not all the intensities observed in the pole figure work.

*Received Oct. 15, 1953.

References

1. TUCKER, C. W. JR. Acta Cryst. **4** (1951) 425.
2. HOLDEN, A. N. Acta Cryst. **5** (1952) 182.
3. KURDJUMOV, G. V. and NAKSIMOVA, O. P. Doklady Adad. Nauk. SSSR **61** (1948) 83.
4. KURDJUMOV, G. V. and KHANDROS, L. G. J. Tech. Phys. (USSR) **19** (1949) No. 7.
5. CECH, R. E. and HOLLOMAN, J. H. Trans. A.I.M.E. **197** (1953); also J. Metals **5** (1953) 685.
6. CAHN, R. W. Acta Cryst. **4** (1951) 470; also, Acta Met. **1** (1953) 49.
7. HOLDEN, A. N. Rev. Sci. Instr. **24** (1953) 10.
8. GEISLER, A. H. Acta Met. **1** (1953) 260.

SOME PLASTIC PROPERTIES OF NICKEL ALLOYS*

V. F. ZACKAY† and T. H. HAZLETT‡

Several physical and chemical properties of the ferromagnetic elements indicate an equivalence of solid-state bonding for nickel and cobalt. Experimental data on the plastic properties of nickel-base cobalt alloys substantiate this conclusion. Comparable data on nickel-iron alloys show that iron effectively solution-hardens nickel. A sharp discontinuity in the plastic behavior of pure nickel was noted at the Curie temperature.

CERTAINES PROPRIÉTÉS PLASTIQUES DES ALLIAGES DE NICKEL

Plusieurs propriétés physiques et chimiques des éléments ferromagnétiques indiquent l'équivalence des liaisons de l'état solide pour le nickel et le cobalt. Les données expérimentales sur les propriétés élastiques des alliages de cobalt à la base de nickel appuient cette conclusion. Des données comparables sur des alliages nickel-fer montrent que le fer durcit le nickel par dissolution. Une forte discontinuité dans le comportement plastique du nickel pur a été observée au point de Curie.

DIE PLASTISCHEN EIGENSCHAFTEN VON NICKELLEGIERUNGEN

Einige physikalische und chemische Eigenschaften ferromagnetischer Elemente deuten auf eine Equivalenz der Festkörperbindungen von Nickel und Kobalt. Experimentelle Angaben über die plastischen Eigenschaften von nickelreichen Kobalt-Nickellegierungen stützen diese Ansicht. Entsprechende Daten der Nickel-Eisenlegierungen zeigen, dass Eisen Nickel praktisch lösungshärtet. Eine starke Unstätigkeit im plastischen Verhalten des reinen Nickels wurde bei der Curie-temperatur beobachtet.

Introduction

During the past several years much progress has been made in seeking a better understanding of the phenomena involved in the plastic deformation of metals. Advances have been made along a number of lines which must eventually be integrated into a single coherent picture. One phase of this problem is to obtain additional insight into the mechanism of solid solution hardening. Any solute element added to a pure metal strengthens the solvent. It is generally agreed that lattice distortion of the host lattice caused by foreign atoms is one factor producing this effect. Differences in the relative sizes of the two atoms and differences in their interaction are among the causes of such distortion. It has been shown that in aluminum the difference in valence of the solvent and solute atoms, as well as the magnitude of the lattice strains, influences the degree of solid solution hardening. There has been speculation in the case of the transition elements whether d-shell electrons are a significant factor in plastic deformation. This paper presents the preliminary results of a continuing investigation to evaluate the role played by d-level electrons. A critical analysis of these and additional data now being obtained will be reported in a future paper.

Two alloy systems, nickel-iron and nickel-cobalt, are uniquely suited since the strain energy interaction, due to difference in atom size, should be very small. Table I lists some of the physical properties of iron, cobalt and nickel. It may be noted that all three elements have almost identical atomic radii in the elemental state. Each has two 4s electrons in the gaseous state; the crystal structures of each of the three elements are face-

TABLE I

SOME PHYSICAL AND CHEMICAL PROPERTIES OF IRON, COBALT AND NICKEL

Element	Outer electron levels (spectrographic data) 3rd	4s	Atomic radii at 20°C, Angstroms ($\frac{1}{2}$ the distance of closest approach)	Electrode potential (volts)	Work of cohesion (Kcal/mol.)	Compressibility, $\times 10^7$ (kg/cm)	Atomic saturation moment at absolute zero (Bohr magnetons per atom)
Iron	6	2	1.24	0.441	94	5.9	2.22
Cobalt	7	2	1.25	0.278	85	5.3	1.71
Nickel	8	2	1.24	0.231	85	5.4	0.61

*Received May 1, 1953; in revised form, June 1, 1953.
†Assistant Professor of Physical Metallurgy, The Pennsylvania State College, State College, Pennsylvania.
‡Research Engineer, University of California, Berkeley California.

centered-cubic at elevated temperatures. In addition, the magnetic saturation moments of cobalt and iron are nearly equal, but they differ from that of nickel. An analysis of the plastic properties of these two alloy systems based on consideration of their electronic configuration, as revealed by measured physical and magnetic properties, provides useful information.

Materials and Test Conditions

Both nickel-cobalt and nickel-iron alloy systems are characterized by complete solid solubility at elevated temperatures, although their solubilities are restricted at lower temperatures because of phase changes. Three compositions of each of these alloy systems, all within the solid solution range at test temperatures, were selected for this investigation.

The nickel base-metal was prepared by refining Mond pellets by decarburizing, deoxidizing and degassing treatments described previously [1]. This procedure resulted in nickel of 99.95 per cent purity. Relatively high-purity cobalt and iron were added to it to form the alloys, whose chemical compositions are tabulated in Table II.

TABLE II
CHEMICAL ANALYSES OF ALLOYS

Alloying element	Atomic per cent	Weight per cent of residual impurities Cu	Mn	Fe	Si	Co	Mg	S
Nickel	0	....	....	.030	.003	.001	.020	.002
Iron	2.55	....	....	....	.003	.001	.020	.002
	4.94	....	....	....	.003	.001	.020	.002
	9.77	....	....	....	.003	.001	.020	.002
Cobalt	2.43	.001	.001	.034	.005	....	.020	.002
	4.60	.001	.001	.037	.007	....	.020	.002
	8.69	.003	.003	.043	.011	....	.020	.002

The cast ingots were forged and subsequently cold-worked in a series of reductions with intermediate anneals to stabilize the grain size. All specimens were annealed at 1000°C for $1\frac{1}{2}$ hours after final machining.

Pure nickel and the six alloys were creep tested at 700°C and 5750 psi stress, using the tandem-type specimens and equipment previously described [2]. Similar specimens were used for constant strain-rate tensile tests at 700°C. Room temperature stress-strain data, on the other hand, were obtained from specimens using extensometers clamped directly onto the reduced section. All tensile specimens were tested at a constant strain rate of 0.27%/min.

A discontinuity in the elastic modulus occurs at the Curie temperature of pure nickel as illustrated in Figure 1 [3]. Since a break in the curve at this point reflects the influence of the d-shell electrons on the modulus, further information concerning plastic properties in this temperature

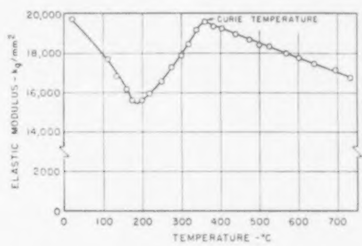

FIGURE 1. Temperature dependence of the elastic modulus of nickel.

range was desired. Therefore, a series of tensile tests emphasizing the 300°C–400°C range was performed.

Precision Lattice Constants

The difference in atomic radii of the host and foreign atoms has been established as one factor which affects the degree of solid solution hardening [4]. Thus the lattice parameters of the alloys under consideration were measured to determine the extent of lattice distortion resulting from alloy additions. These determinations were carried out using the analytical procedure of Nelson and Riley [5].

Electrical Resistivity

Electrical resistivity measurements were secured to assist in the analysis of the electronic configuration of the solid state. Strip specimens, one-half inch wide and one-eighth inch thick were utilized. The potential drop across a six-inch length was measured by means of a Leeds and Northrup Kelvin double bridge. All measurements were corrected to the same temperature, 20°C.

Experimental Results

Stress-strain curves determined for pure nickel and for each of the alloys are shown in Figures 2 and 3 for the 30°C tests, and in Figures 4 and 5 for those performed at 700°C. Examination of Figures 2 and 4 reveals that the tensile properties of the nickel-cobalt alloys are clustered into a relatively narrow band. The high temperature data on these alloys scatter about the pure-nickel curve in a random manner. Stress-strain

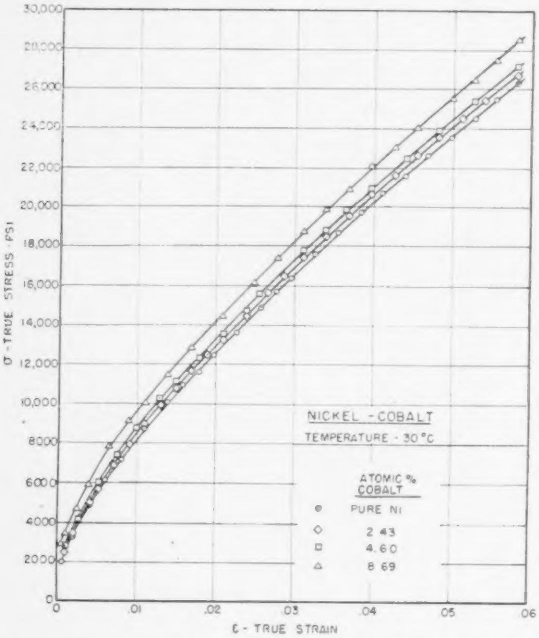

FIGURE 2. Tensile stress-strain curves for nickel-cobalt alloys at 30°C.

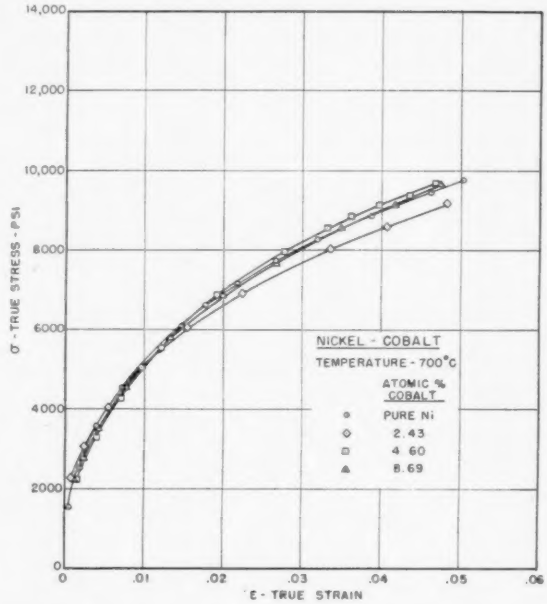

FIGURE 4. Tensile stress-strain curves for nickel-cobalt alloys at 700°C.

curves of the nickel-iron alloys, on the other hand, are influenced markedly at both test temperatures by the iron content as shown in Figures 3 and 5.

Creep curves of each of the alloy systems are shown on logarithmic plots in Figures 6 and 7. The *time-dependent strain only* is used, thereby following the creep-data relationships previously proposed [2]. Again, it is apparent that the addition of cobalt has little effect on the creep resistance

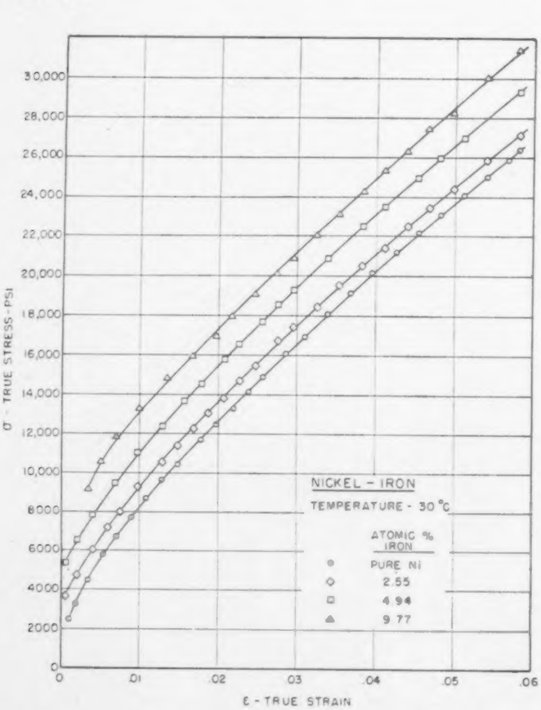

FIGURE 3. Tensile stress-strain curves for nickel-iron alloys at 30°C.

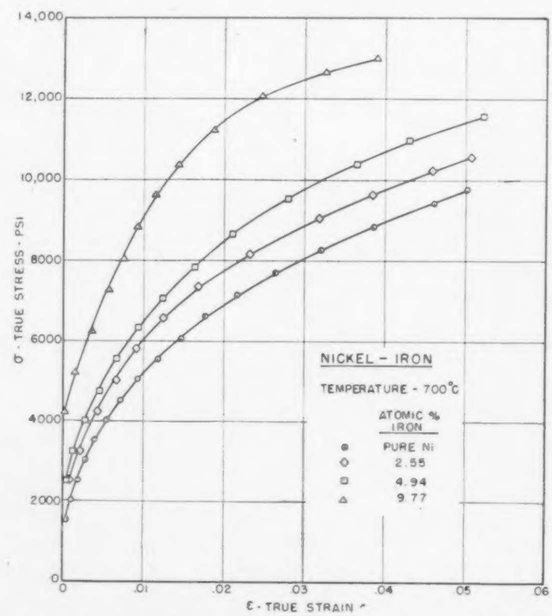

FIGURE 5. Tensile stress-strain curves for nickel-iron alloys at 700°C.

of nickel at 700°C, while iron is an effective strengthening addition.

Variations of the lattice parameters with alloy content are given in Figure 8. The linear relationship between solid-solution alloy content and lattice strains is readily apparent. The addition of cobalt has little effect on the lattice dimensions, while iron increases the parameters by a significant amount.

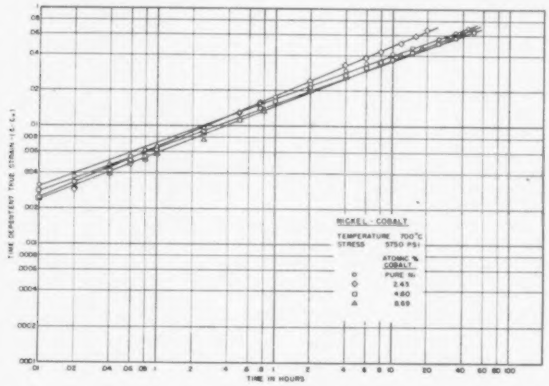

FIGURE 6. Creep curves of nickel-cobalt alloys.

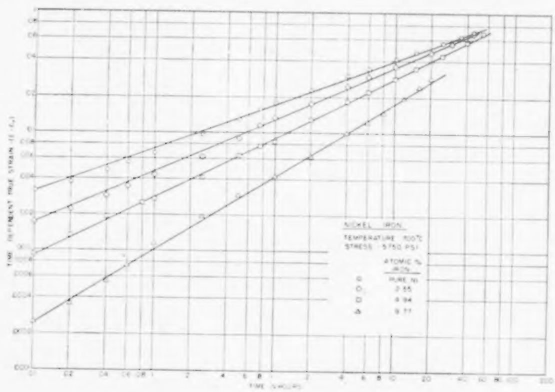

FIGURE 7. Creep curves of nickel-iron alloys.

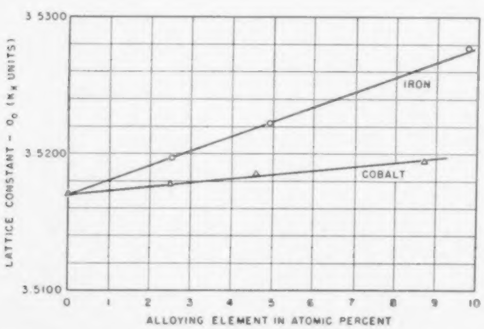

FIGURE 8. Effect of alloying elements on the lattice constant of nickel at 25°C.

Results of the electrical resistivity studies are illustrated in Figure 9. Here, the resistivity of pure nickel at room temperature is considerably increased by the addition of either cobalt or iron; the latter has a more pronounced effect.

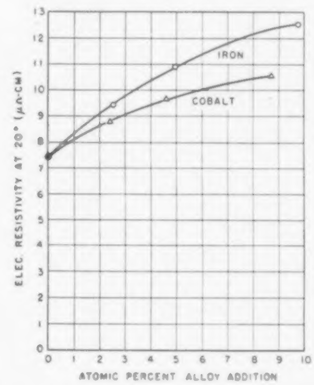

FIGURE 9. Resistivity of Ni-Fe and Ni-Co solid solution system.

Data from the series of tensile tests on pure nickel which were pulled at various temperatures from 30°C to 700°C are summarized in Figure 10 where the flow-stress required to produce a given strain is plotted against the test temperature. Data for four different values of strain are shown. A distinct discontinuity occurs at 350°C, the Curie temperature.

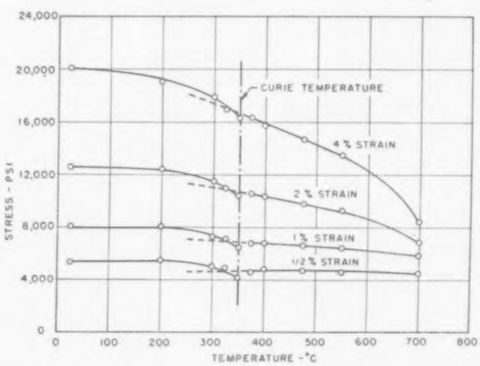

FIGURE 10. Effect of temperature on tensile flow stress at various values of strain.

Discussion

Referring to Table I, the electrode potentials for nickel and cobalt in the same oxidation state are definitely similar, while iron is vastly different. Also the values of work of cohesion and compressibility, which are generally considered indicative of bonding, are approximately the same for

nickel and cobalt but are significantly different for iron. On the basis of the striking similarity of properties it might be inferred that the addition of cobalt should have a small effect on the plastic properties of nickel. This would not be expected for iron as the solute element.

Referring to Figure 8, the addition of cobalt has only a slight effect on the lattice parameter of pure nickel. Iron produces a substantial increase in lattice strain which indicates a possible difference in bonding between the two elements as might be expected from their respective properties.

The addition of cobalt has only a small effect on the plastic properties of nickel. This is indicated by the tensile stress-strain curves at 30°C and at 700°C for the nickel-cobalt alloys in Figures 2 and 4, and in the creep curves of Figure 6 for the same alloys.

Comparable data on the nickel-iron alloys are shown in Figures 3, 5, and 7. In this case the tensile strength and creep resistance are both substantially increased as the iron content is increased.

Nickel is ferromagnetic below, and paramagnetic above, 350°C. Since magnetic properties are associated with d-level electrons, any discontinuity in plastic properties at this temperature would reflect the influence of these electrons. In Figure 10, a discontinuity does occur at 350°C. From elementary magnetic domain considerations only, the change may be interpreted as a weakening above the Curie temperature.

Summary

Several physical and chemical properties of the ferromagnetic elements indicate an equivalence of solid-state bonding for nickel and cobalt. For example, the values of work of cohesion, compressibility, and oxidation potential are practically identical for nickel and cobalt. They are not the same for iron.

Experimental data on the plastic properties of nickel-base cobalt and iron alloys support this conclusion. The addition of cobalt has only a small effect on tensile properties of pure nickel at room temperature and at elevated temperature. A similar behavior is observed in creep tests of the same alloys. As might be expected, cobalt has practically no effect on the lattice parameter of nickel.

Comparable tensile and creep data on nickel-iron alloys show that iron substantially solution-hardens nickel.

In the case of pure nickel, a sharp discontinuity in plastic behavior was noted at the Curie temperature, and may be tentatively explained on the basis of elementary domain theory.

Acknowledgment

The authors wish to thank the U.S. Atomic Energy Commission for sponsoring much of the work on which this paper is based and for permission to publish these data. The authors are indebted to Professor Earl R. Parker for his valuable advise. We are sincerely appreciative of the conscientious work of Mrs. R. Hansen and her valued assistance in all phases of the work; we also want to thank Mr. Paul Langston for his careful work in the preparation of metals used in these tests and Mr. H. Lindgren for his valued assistance in the testing laboratory.

References

1. Zackay, V. F. and Kershaw, F. P. Inst. Eng. Res. Ser. **28**. Issue 4. 1950.
2. Hazlett, T. H. and Parker, E. R. J. Metals **4** (1953) 318.
3. Koster, W. Z. Metallk. **39** (1948) 1.
4. Dorn, J. E., Pietrokowsky, P. and Tietz, T. E. Trans. A.I.M.E. **188** (1950) 933.
5. Nelson, J. B. and Riley, D. P. Proc. Phys. Soc. **62** (1945) 160.

TERNARY ALLOYS FORMED BY ALUMINIUM, TRANSITIONAL METALS AND DIVALENT METALS*

G. V. RAYNOR, C. R. FAULKNER, J. D. NODEN and A. R. HARDING†

A general survey has been made, by metallographic and X-ray methods, and by the examination of extracted crystals, of the constitutions of the alloys of aluminium and zinc with iron, cobalt and nickel, of aluminium and magnesium with cobalt, and of aluminium and beryllium with manganese and iron. In the latter two systems, new ternary compounds $Mn_3Be_2Al_{15}$ and $Fe_3Be_7Al_7$ have been discovered in equilibrium with the aluminium-rich solid solution. No ternary compounds in equilibrium with the aluminium-rich alloys occur in the other systems studied; an unidentified ternary phase separates from zinc-rich alloys in the system Al-Ni-Zn, but does not enter into equilibrium with the zinc-rich solid solution. The outstanding feature of the system Al-Co-Zn is the deposition from zinc-rich melts, at low temperatures, of the high-melting phases CoAl and Co_4Al_{13} in addition to Co_2Al_9; these phases persist in equilibrium with the zinc-rich solid solution. Similarly in the system Al-Ni-Zn, Ni_2Al_3 as well as $NiAl_3$ is found in zinc-rich alloys, while in the system Al-Co-Mg the high-melting phase CoAl enters into equilibrium with the magnesium-rich solid solution. By contrast, only a phase derived from $FeAl_3$, and none of the more iron-rich aluminium-iron compounds, is found in equilibrium with zinc in the system Al-Fe-Zn. The main features of the equilibria are discussed in terms of the free energies of phases present, and the data, taken together with the results of previous work, lead to a better understanding of the factors affecting the formation of aluminium-rich ternary compounds.

ALLIAGES TERNAIRES FORMÉS PAR L'ALUMINIUM, DES MÉTAUX DE TRANSITION ET DES MÉTAUX BIVALENTS

Un examen général des constitutions des alliages d'aluminium et zinc avec le fer, cobalt et nickel, d'aluminium et magnesium avec le cobalt, et d'aluminium et beryllium avec le manganèse et le fer a été fait au moyen de méthodes métallographiques et aux rayons X, ainsi que par l'examen de cristaux extraits. Dans les deux derniers systèmes d'alliages, de nouveaux composés ternaires $Mn_3Be_2Al_{15}$ et $Fe_3Be_7Al_7$ ont été découverts en équilibre avec la solution solide riche en aluminium. Dans les autres systèmes étudiés, aucun composé ternaire n'apparaît en équilibre avec la solution solide riche en aluminium; une phase ternaire non-identifiée se sépare des alliages riches en zinc dans le système Al-Ni-Zn, mais n'entre pas en équilibre avec la solution solide riche en zinc. La caractéristique particulière du système Al-Co-Zn est le dépôt aux basses températures, à partir des liquides riches en zinc, en plus de Co_2Al_9, des phases CoAl et Co_4Al_{13} fondant à une température élevée; ces phases restent en équilibre avec la solution solide riche en zinc. D'une façon semblable, dans le système Al-Ni-Zn, Ni_2Al_3 ainsi que $NiAl_3$ apparaissent dans les alliages riches en zinc, alors que dans le système Al-Co-Mg la phase CoAl, fondant à une température élevée, entre en équilibre avec la solution solide riche en magnesium. Par contre, dans le système Al-Fe-Zn, seulement une phase dérivée de $FeAl_3$, est trouvée en équilibre avec le zinc, sans qu'aucune des phases plus riches en fer dans les composés aluminium-fer, le soit. Les caractéristiques principales des équilibres sont discutées en termes des énergies libres des phases en présence; ces données combinées aux résultats des travaux antérieurs, conduisent à une meilleure compréhension des facteurs affectant la formation des composés ternaires riches en aluminium.

TERNÄRE LEGIERUNGEN VON ALUMINIUM, ÜBERGANGSMETALLEN UND ZWEIWERTIGEN METALLEN

Eine umfasende Untersuchung des Aufbaus von Legierungen des Aluminiums und Zinks mit Eisen, Kobalt und Nickel, des Aluminiums und Magnesiums mit Kobalt und des Aluminiums und Berylliums mit Mangan und Eisen wurde mit Hilfe metallographischer, röntgenographischer und kristallographischer Methoden unternommen. In den beiden letztgenannten Systemen wurden neue ternäre Verbindungen, $Mn_3Be_2Al_{15}$ und $Fe_3Be_7Al_7$, im Gleichgewicht mit der aluminiumreichen festen Lösung gefunden. In den andern hier untersuchten Systemen treten keine ternären Verbindungen im Gleichgewicht mit der aluminiumreichen festen Lösung auf. Eine nicht identifizierte ternäre Phase kann von der zinkreichen Legierung im System Al-Ni-Zn getrennt werden, tritt jedoch nicht im Gleichgewicht mit der zinkreichen festen Lösung auf. Die bemerkenswerteste Eigenschaft des Systems Al-Co-Zn ist die Abscheidung der hochschmelzenden Phasen CoAl und $CoAl_{13}$ zusammen mit Co_2Al_9 bei niedrigen Temperaturen aus der zinkreichen Schmelze. Diese Phasen sind im Gleichgewicht mit den zinkreichen festen Lösungen beständig. Entsprechend bildet sich im System Al-Ni-Zn, Ni_2Al_3 und $NiAl_3$ in den zinkreichen Legierungen, während im System Al-Co-Mg die hochschmelzende Phase CoAl im Gleichgewicht mit der magnesiumreichen festen Lösung auftritt. Im Gegensatz dazu tritt im System Al-FeZn nur eine Phase aus dem $FeAl_3$ und keine weiteren eisenreichen Aluminium-Eisen Verbindungen im Gleichgewicht mit Zink auf. Die wesentlichen Eigenschaften der Gleichgewichte werden vom Standpunkt der freien Energien der anwesenden Phasen diskutiert, und diese Daten zusammen mit den Ergebnissen früherer Arbeiten ermöglichen ein besseres Verständnis der Faktoren, die die Bildung von aluminiumreichen ternären Verbindungen beeinflussen.

I. Introduction

In recent years, a systematic survey of the constitutions of ternary aluminium-rich alloys containing transitional metals of the first long period of the periodic table has been in progress in the authors' laboratory. The main conclusions to be drawn from this work have been discussed by Pratt and Raynor

*Received May 8, 1953

†Department of Metallurgy, University of Birmingham, England.

[1], who point out that the presence of transitional metals effectively prevents some of the valency electrons contributed to the structures of ternary compounds by the other components from contributing to the first Brillouin Zone. This regularity of behaviour is characteristic only of systems where the solvent metal is polyvalent, and is not observed to the same extent for ternary alloys based on zinc. In order to examine the problem further, systematic data are required for alloys of aluminium and a transitional metal with divalent metals, so that the equilibria at both the aluminium-rich and divalent metal-rich corners of the equilibrium model may be defined. Alloy systems of this class previously investigated include:

Al-Cr-Zn [2], Al-Mn-Zn [3], Al-Cr-Mg [4],
Al-Mn-Mg [5] and Al-Fe-Mg [6].

The present paper reports work carried out on the constitutions of the alloys of aluminium and zinc with iron, cobalt and nickel, and of aluminium and magnesium with cobalt. As the work proceeded, it became desirable to include the systems Al-Mn-Be and Al-Fe-Be, the investigation of which is also described.

II. General Experimental Methods

The alloy systems were investigated by metallographic examination of slowly cooled ingots, and of chill-cast specimens which had been quenched after long annealing periods. Interpretations were checked by X-ray examination of annealed alloys and of intermediate phases separated electrolytically or otherwise from both annealed and slowly cooled specimens. Selected samples of extracted crystals were also analysed chemically. In general the methods adopted correspond closely with those described in earlier papers on similar systems [2; 3; 5], and no further discussion will be given here. Any deviation from the standard practice is referred to in the following sections in connection with the particular alloy system involved.

III. Materials Used

The alloys examined in this investigation were prepared from the following materials:

(*a*) Superpure aluminium (99.997%), kindly presented by the British Aluminium Company Ltd.

(*b*) Magnesium, obtained from Magnesium Elektron, Ltd., in which the main impurity was zinc (0.01%); the remaining impurities totalled only 0.029%.

(*c*) Zinc of two grades of purity, kindly presented by the Imperial Smelting Corporation. (*i*) Spectrographically pure metal (Pb, 0.0001%; Cd, 0.00005%; Ca, 0.0001%) which was reserved for zinc-rich alloys intended for annealing and quenching experiments, and for other critical work. (*ii*) "Crown Special" material (Pb, 0.0007%; Cd, 0.001%; Fe, 0.001%; Cu, 0.0002%) which was used for exploratory experiments.

(*d*) Spectrographically standardized iron obtained from Messrs. Johnson, Matthey and Company Ltd., in the form of 1 mm. diameter wire, which was used for the majority of the iron-bearing alloys. For certain exploratory and less critical experiments on alloys containing less than 1.75% of iron, Armco iron wire was used. This contained <0.01% of Si and P; the other impurities were Mn, 0.44%; C, 0.08%; S, 0.04%.

(*e*) Pure nickel, obtained from Messrs. British Timken, Ltd., in the form of shot containing C, 0.03%; Fe, 0.025%; Cu, 0.003%; S, 0.001%.

(*f*) Aluminium-manganese master alloys containing 5.15, 9.8 and 12.95% of Mn. The chief impurities were Cu, 0.001 to 0.0025%; Si, 0.0025 to 0.004%.

(*g*) Aluminium-iron and aluminium-cobalt master alloys with the following compositions:

	Fe %	Mn %	Si %	Cu %	Co %
Al-Fe	5.85	0.01	0.0015	0.01	—
Al-Co	0.014	0.006	0.0065	0.0045	4.85

(*h*) An aluminium-beryllium master alloy, containing 5% of Be, and the following impurities:

Fe, 0.21%; Si, 0.12%; Cu, 0.02%; Mg, 0.004%.

Since the required beryllium additions for critical alloys proved to be small, the impurities introduced into the ternary alloys were correspondingly reduced.

(*i*) Zinc-rich iron-zinc, nickel-zinc and cobalt-zinc master alloys, which were prepared in the authors' laboratory by direct solution of iron, cobalt (electrolytic) or nickel in molten zinc. The methods employed are described below.

IV. The Binary Systems

The aluminium-rich portions of the binary equilibrium diagrams for the alloys of aluminium with manganese, iron, cobalt and nickel have been presented and discussed in previous publications [1; 3; 7; 8], and little further comment is necessary. The binary intermediate phases of interest to the present investigation are as follows:

Al-Mn system:	$MnAl_6$	$MnAl_4$	"δ"	$MnAl_3$	MnAl
Al-Fe system:	$FeAl_3$	Fe_2Al_5	$FeAl_2$*		
Al-Co system:	Co_2Al_9	Co_4Al_{13}	Co_2Al_5	CoAl	
Al-Ni system:	$NiAl_3$	Ni_2Al_3	NiAl		

According to the X-ray investigations of Bradley and Taylor [9], the phase $FeAl_3$ decomposes on cooling into Fe_2Al_5 and Fe_2Al_7; the transformation temperature, though known to be below 600°C and probably in the region of 500°C, is not accurately established.

The equilibrium diagrams of the systems aluminium-zinc [10] and aluminium-magnesium [11] are well established over the whole composition range. No intermediate compounds exist in the former; the latter contains intermediate phases based on Mg_2Al_3 and $Mg_{17}Al_{12}$. The aluminium-beryllium system is less well established, but the region of interest to present work is known accurately [12; 13; 14]. The solid solubility of beryllium in aluminium lies below 0.1 per cent, and a eutectic corresponding to the separation of aluminium and beryllium occurs at 0.87 per cent of beryllium (645°C).

The zinc-rich portions of the iron-zinc, cobalt-zinc and nickel-zinc equilibrium diagrams are of considerable interest, but it is thought to be unnecessary to reproduce them here. The iron-zinc diagram has been recently discussed [15]. In each case a zinc-rich phase with the γ-brass structure is formed (X_5Zn_{21}, where X represents the transitional metal). According to previous work, the equilibrium relationships for the three systems may be summarized as follows:

(*a*) Fe-Zn system [15]: Fe_5Zn_{21} reacts peritectically with the liquid at 668°C to form δ_{FeZn} which transforms to δ'_{FeZn} at lower temperatures. Both δ phases are of unknown crystal structure. δ'_{FeZn} reacts peritectically at 530°C to form the most zinc-rich phase, which is denoted ζ_{FeZn}, is monoclinic and corresponds to a narrow homogeneity range in the region of $FeZn_{13}$.

(*b*) Co-Zn system [16]: Co_5Zn_{21} reacts peritectically to form δ_{CoZn} at 746°C; δ_{CoZn} transforms into δ'_{CoZn}, which reacts with the liquid at 566°C to form ζ_{CoZn}, the most zinc-rich phase, which appears to correspond with $CoZn_{13}$.

(*c*) Ni-Zn system [17]: in this case only one phase (δ_{NiZn}, $NiZn_9$) occurs between the γ-brass structure and the zinc-rich solid solution.

In each case the final eutectic solidification occurs at a very low transitional metal content, and at a temperature almost coincident with the freezing point of zinc.

The magnesium-rich portion of the cobalt-magnesium equilibrium diagram has been investigated by Cramer, Nielson and Schonfield [18] who observed the compound Mg_2Co at 54.8 per cent of cobalt. This phase and magnesium containing very small amounts of cobalt separate as a eutectic at 4.5 per cent of cobalt (632°C).

Since, in the present work, equilibrium relations were not examined in beryllium-rich Al-Mn-Be and Al-Fe-Be alloys, the systems manganese-beryllium and iron-beryllium are not described.

V. The Ternary System Aluminium-Iron-Zinc

(*a*) *Previous Work*

The surfaces of primary separation given by Mondolfo [19], and based upon the work of Fuss [20] are shown in Figure 1. No ternary compounds are reported; a ternary eutectic involving $FeAl_3$, the aluminium-rich solid solution (α) and the zinc-rich solid solution (β) occurs at 380°C and approximately 94 per cent of zinc. Similar conclusions have been reached by Mayer [21]. According to Mondolfo, solid zinc and aluminium enter into equilibrium with Fe_2Al_7, but no isothermal sections are available.

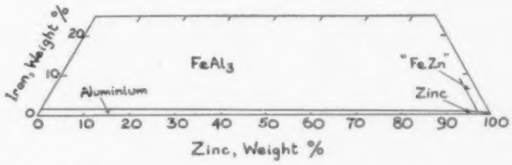

FIGURE 1. Surfaces of primary separation in the system Al-Fe-Zn, according to Mondolfo [19].

(*b*) *Experimental Methods*

Previously described methods were used, except for the preparation of zinc-rich master alloys. These were made by annealing for 7 days with frequent agitation, at a temperature 25°C above the liquidus for the required iron content, quantities of zinc and iron weighed into a hard glass tube which was subsequently evacuated. After rapidly cooling the alloys were examined metallographically; no free iron was observed. Quantities of 250 g. containing up to 3 per cent of iron were readily obtained; the intended compositions were accurately attained, and the method proved superior to that of reducing anhydrous ferric chloride with molten zinc. Master

*The limiting solid solution of aluminium in body-centred cubic iron approximates to the composition FeAl, and should be considered in addition to the intermediate phases.

VOL. 1 1953

alloys prepared by the annealing process were analysed for silicon, because of the possibility of contamination by this element, and in no case was more than 0.01 per cent recorded. As a precaution against inhomogeneity, the alloys were remelted after preparation, stirred, and granulated by pouring into cold water.

Alloys examined metallographically consisted of hard intermetallic compound particles in a matrix of aluminium-rich or zinc-rich solid solution. The compounds encountered were $FeAl_3$ (or a zinc-bearing phase derived from it), δ'_{FeZn} and ζ_{FeZn}; as indicated above, $FeAl_3$ may decompose into Fe_2Al_5 and Fe_2Al_7, but no metallographic evidence of this was obtained. Consequently this phase is referred to throughout as $FeAl_3$, except where there is positive evidence that the equilibrium constituent at low temperatures shows differences from $FeAl_3$. In the course of the work many etching reagents were used, and the recognition of $FeAl_3$ presented no difficulty. The aluminium-rich α solid solution was darkened uniformly by 15 sec. immersion at 20°C in an aqueous mixture of HF (0.5%), HNO_3 (1.5%) and HCl (2.5%). Alloys with more than 30 per cent of zinc traversed the $(\alpha + \alpha')$ region on quenching, and showed a fine decomposition structure; for these alloys, and zinc-rich alloys, the mixed acid reagent was diluted to half strength. The zinc-rich β solid solution was best etched by immersion in, or swabbing with, 10 per cent aqueous sodium or potassium hydroxide. Difficulty was initially experienced in distinguishing δ'_{FeZn} from ζ_{FeZn}, and particularly in revealing the presence (in the latter) of δ'_{FeZn} cores, arising from the $\delta'_{FeZn} + \text{liquid} \rightleftharpoons \zeta_{FeZn}$ reaction. Further work showed this reaction to be rapid, and generally completed on cooling at $\frac{3}{4}$°C/min. Rimming of δ'_{FeZn} by ζ_{FeZn} was, however, observed after rapid cooling, and with experience satisfactory differentiation of the two phases was obtained, using an etching procedure based upon that recommended by Schramm [22].

(c) *Experimental Results*

For the description of the results reported in this and later sections, it is convenient to refer to individual alloys in terms of the percentage (by weight) of transitional metal and divalent metal. Thus, in the present section, "alloy 3/40" refers to material containing 3 per cent of iron and 40 per cent of zinc. Over 150 alloys were examined; approximately half were slowly cooled from the liquid state, and the remainder annealed to equilibrium in the solid state.

(i) *Slowly cooled alloys.* Results for alloys cooled from the liquid at $\frac{3}{4}$°C/min. are summarized in Figures 2 and 3.* Primary crystals with the characteristics of $FeAl_3$ are deposited over most of the composition range investigated. The crystals in several of the alloys were extracted by anodic solution of the matrix and X-ray powder diffraction patterns were obtained, using cobalt or iron K_α radiation. Crystals from alloys containing up to 60 per cent of zinc gave diffraction patterns identical with that obtained from $FeAl_3$ deposited from binary Al-Fe alloys under the same conditions of slow cooling. Further experiments showed that indistinguishable diffraction patterns were obtained from binary compound crystals extracted from alloys which had been (*a*) slowly cooled, (*b*) quenched from above the suspected transformation after annealing for four days at 600°C or overnight at 700°C and (*c*) quenched from below the suspected transformation after annealing for 16 weeks at 470°C. The inference is that under the conditions of the present experiments $FeAl_3$ does not decompose. The diffraction patterns from alloys 0.8/96.5 and 0.75/98.0, however, showed slight but characteristic differences from that of $FeAl_3$. Since it appears that decomposition to Fe_2Al_7 does not occur in the pure binary alloys under our conditions, and since crystals from these zinc-rich alloys have compositions very close to those of crystals from aluminium-rich alloys, the intermetallic compound separating at high zinc contents has been denoted $FeAl_3'$. Analytical evidence, referred to below, suggests that the structural change occurs for zinc contents, in the parent alloy, of 78.5 to 83 per cent; this corresponds with a temperature of approximately 470°C. The differentiation from $FeAl_3$ is so slight that the primary field in Figures 2 and 3 has not been divided by any "reaction line." The $FeAl_3/\alpha$ eutectic valley approaches the Al-Zn

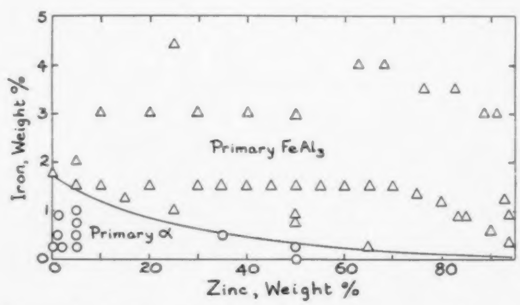

FIGURE 2. Surfaces of primary separation: system Al-Fe-Zn. *Key*: Primary α ○; primary $FeAl_3$ or $FeAl_3'$ △.

*For ternary diagrams in which the scales of the binary axes differ, rectangular axes have been used for simplicity.

VOL. 1 1953

axis with increasing zinc content, and is very close to it at zinc contents exceeding 80 per cent. The composition of the ternary eutectic (liquid $\rightleftharpoons \alpha + \beta + FeAl_3'$) almost coincides with that of the binary reaction, as shown by the presence of primary compound particles in alloy 0.04/95. The primary compound field extends beyond the ternary eutectic point; the secondary depositions of both ($\alpha + FeAl_3$ or $FeAl_3'$) and ($\beta + FeAl_3'$) are therefore observed. The extensive $FeAl_3$-$FeAl_3'$ field is subdivided by a line stretching from the zinc-rich corner of the diagram to the composition of $FeAl_3$. Alloys lying on the aluminium-rich side of this line deposit primary crystals, and the composition of the remaining liquid eventually reaches the boundary between the $FeAl_3$-$FeAl_3'$ and β fields, so that solidification proceeds by the codeposition of $FeAl_3'$ and β and is completed at the ternary eutectic. Alloys lying to the iron-rich side, however, crystallize so that the composition of the remaining liquid reaches the boundary between the $FeAl_3'$ and δ'_{FeZn} or ζ_{FeZn} fields. Here the $FeAl_3'$ reacts peritectically with the liquid, leading to observable rimming. The δ'_{FeZn} and ζ_{FeZn} fields lie close to the iron-zinc axis of the diagram; only alloys 1/98.85 and 0.15/99.75 deposited uncored ζ_{FeZn} crystals. As noted above, the primary δ'_{FeZn} and ζ_{FeZn} fields cannot be distinguished by examining slowly cooled alloys, owing to the high rate of transformation of δ'_{FeZn} into ζ_{FeZn}. The binary iron-zinc alloys represented in Figures 2 and 3 were therefore rapidly cooled to detect the presence of δ'_{FeZn} cores. Diffraction patterns were obtained from extracted ζ_{FeZn} crystals. Thirty-eight lines were measured to facilitate comparison with details given by Schramm [17], and excellent agreement was obtained.

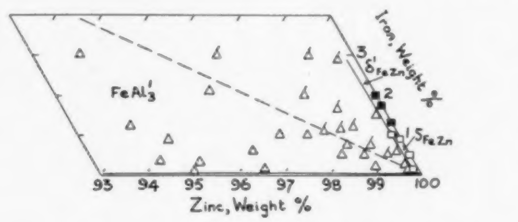

FIGURE 3. Surfaces of primary separation: Zn-rich alloys of system Al-Fe-Zn. *Key*: Primary $FeAl_3'$ △; primary $FeAl_3'$ with reaction rims of δ'_{FeZn} or ζ_{FeZn} △; primary δ'_{FeZn} ■; primary ζ_{FeZn} □.

(ii) *Annealed alloys.* The investigation began with the aluminium-rich alloys whose compositions and annealing treatments are given in Table I.

The microstructures observed after the initial treatment remained unchanged on further annealing. All alloys consisted of α and hard compound crystals indistinguishable from $FeAl_3$. Since crystals extracted from chill-cast binary alloys annealed for 4 days at 600°C, or for 112 days at 470°C and quenched, gave identical diffraction patterns, the microstructures at 600° and 500°C are interpreted as ($\alpha + FeAl_3$). Those at 425°C are most probably to be regarded as ($\alpha + FeAl_3'$).

TABLE I

Alloys	Annealing treatment
2.93/0, 2.64/5, 2.34/10, 5/0, 4/1, 3/2, 2/3, 1/4, 5/5, 3/7, 1/9.	14 + 17 days at 600°C
2.93/0, 2.64/5, 2.34/10, 5/5, 5.23/10, 4.68/20, 4.10/30, 3.5/40	21 + 14 days at 500°C
2.93/0, 2.64/5, 2.34/10, 2.1/15, 1.76/20, 1.46/25, 1.17/30, 0.88/35, 0.59/40, 0.3/45, 0/50.	21 + 28 days at 425°C

More extensive work was carried out at 370°C, at which temperature $FeAl_3'$ is stable. The results are given in Figures 4 and 5, with the exception of those for seven alloys equally spaced between the compositions 5.85/0 and 1.75/70, which showed ($\alpha + FeAl_3'$) microstructures after annealing for 21 to 30 days. The results plotted were obtained from alloys annealed for 30 to 35 days, and further annealing produced no change. The ($\alpha + FeAl_3'$) field persists to 82 per cent of zinc at low iron con-

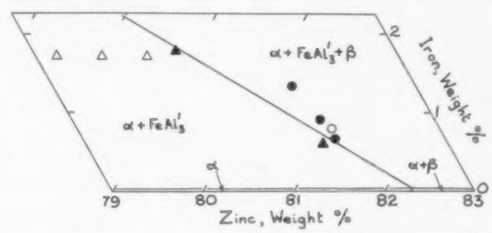

FIGURE 4. System Al-Fe-Zn: ($\alpha + FeAl_3'$)/($\alpha + \beta + FeAl_3'$) boundary at 370°C. In this and subsequent diagrams, full symbols denote analysed alloys. *Key*: $\alpha + FeAl_3'$ △▲; $\alpha + FeAl_3' + \beta$ ○●.

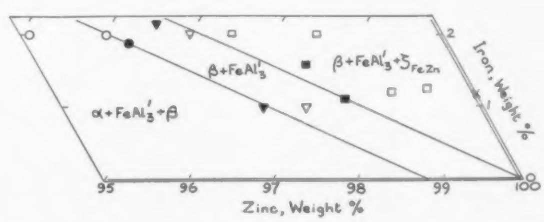

FIGURE 5. System Al-Fe-Zn: equilibria in the Zn-rich corner at 370°C. *Key*: $\alpha + FeAl_3' + \beta$ ○●; $\beta + FeAl_3'$ ▽▼; $\beta + FeAl_3' + \zeta_{FeZn}$ □■; $\beta + \zeta_{FeZn}$ ×.

tents, while the α solid solution field is of negligible width at high zinc contents. The $(\alpha + FeAl_3')/(\alpha + \beta + FeAl_3')$ and $(\alpha + \beta + FeAl_3')/(\beta + FeAl_3')$ boundaries are satisfactorily located, but difficulty arises with the appearance of ζ_{FeZn}, particles of which contained minute traces of iron-aluminium compound which could not be absorbed on protracted annealing. These cores were very small, and since individual particles of iron-aluminium compound were also observed, it is probable that the boundary shown in Figure 5 approximates closely to equilibrium conditions. The boundaries located are consistent with extrapolation to the composition characteristic of $FeAl_3$ on the binary aluminium-iron axis.

The position of the $(\alpha + FeAl_3')/(\alpha + \beta + FeAl_3')$ boundary was also located at 350°C, as shown in Figure 6.

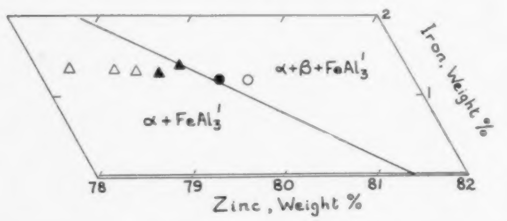

FIGURE 6. System Al-Fe-Zn: $(\alpha + FeAl_3')/(\alpha + \beta + FeAl_3')$ boundary at 350°C. *Key*: as for Figure 5.

(iii) *Compositions of extracted crystals.* Crystals of $FeAl_3$ and $FeAl_3'$ separated from slowly cooled alloys with zinc contents ranging from 10 to 90 per cent were analysed chemically. The results are given in Table II, and plotted in atomic percentages in Figure 7. Figure 8 shows the variation of the zinc and iron contents of the crystals, in terms of the zinc content of the original alloy. The results for alloys 0.9/83.5 and 0.6/90 appear anomalous. It is precisely in this composition range that the diffraction patterns of extracted crystals differ slightly from

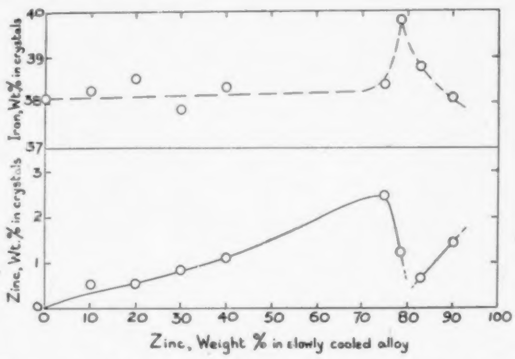

FIGURE 8. Variation of zinc and iron contents of extracted $FeAl_3$ crystals.

that of $FeAl_3$, and it is very probable that the results for alloys 3/10 to 1.3/78.5 represent the solubility of zinc in $FeAl_3$, while those for 0.9/83.5 and 0.6/90 represent the corresponding solubility in $FeAl_3'$. If it

TABLE II

Alloy composition	Alloy no.	Wt % Zn	Wt % Fe	Wt % Al
3/10	1	0.30	38.29	61.41
3/20	2	0.30	38.55	61.15
3/30	3	0.84	37.83	61.33
3/40	4	1.10	38.36	60.54
1.5/75	5	2.47	38.38	59.15
1.3/78.5	6	1.23	39.81	58.96
0.9/83.5	7	0.66	38.79	60.55
0.6/90	8	1.43	38.11	60.46

is assumed that the effect of the structural modification of $FeAl_3$, caused at low temperatures in the presence of zinc, is markedly to contract the homogeneity range of the phase in terms of iron and aluminium (that is, parallel to the aluminium-iron axis), the peculiar form of the results shown in Figure 8 may be interpreted. Figure 9 shows, dia-

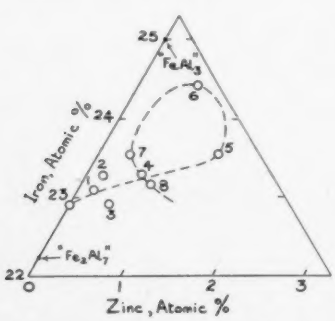

FIGURE 7. Compositions of extracted $FeAl_3$ crystals: system Al-Fe-Zn. The numbers 1 to 8 correspond with those in Table II.

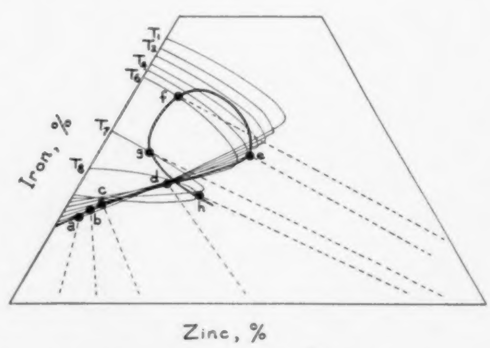

FIGURE 9. Homogeneity range of $FeAl_3$ in the ternary system; diagrammatic. The straight lines attached to plotted points indicate tie-lines.

grammatically, possible forms of the homogeneity range of $FeAl_3$ in the ternary alloys at temperatures T_1 to T_8, decreasing in that order. In drawing this figure, it has been further assumed that at low temperatures zinc dissolves in $FeAl_3$ by the replacement of aluminium, which is reasonable if the slight structural alteration is due to zinc atoms occupying ordered, rather than random, positions in the structure. As the tie lines alter their slopes with increasing zinc content of the parent alloy, at the same time as the homogeneity range of $FeAl_3$ shrinks, it will be possible, as indicated in the Figure, for the composition of the deposited crystals to show first an increase in zinc content (points a, b, c, d, e), followed by a sharp decrease (point f). If, at this stage, there is a marked contraction of the homogeneity range, the regularity is disturbed, and the zinc content of the deposited crystals cannot fall below that corresponding to tangency of the tie line to the boundary. In this way the relatively low iron content for point g, and the high zinc content for point h, may be understood. In view of these considerations, and also because the compositions of the crystals extracted from alloys 0.9/83.5 and 0.6/90 are so close to those of crystals giving the normal $FeAl_3$ diffraction pattern, $FeAl_3'$ is not regarded as a separate phase, but merely as a modification of $FeAl_3$ which is stabilized at low temperatures by the presence of zinc.*

Crystals of ζ_{FeZn} occurring in ternary alloys were unsuitable for analysis, since they contained small $FeAl_3'$ cores. Three samples were extracted from binary Fe-Zn alloys by anodic solution of the matrix in 2.5 per cent aqueous hydrochloric acid; the method suggested by Montoro [23] proved unsuitable. Exposed ζ_{FeZn} crystals were unattacked while in contact with zinc, but suffered corrosion in the electrolyte when detached. Since this led to contamination by magnetic iron-rich material, the dissolving ingot was frequently removed, lightly tapped to remove loose crystals, and the crystals immediately washed and dried. The results given in Table III refer to specially sorted, non-magnetic, bright-surfaced samples. These figures may be compared with the homogeneity ranges reported by Schramm [24] (6.0 to 6.2 per cent of iron) and Montoro [23] (6.0 to 6.5 per cent of iron), and indicate that samples separated from the melt may have iron contents exceeding that of $FeZn_{13}$. $FeZn_{12}$ therefore

*It may be noted that we have been unable to produce diffraction patterns similar to that of $FeAl_3'$ from pure Al-Fe alloys, in spite of repeated attempts involving widely varying heat treatments.

TABLE III

Alloy composition	Wt % Zn	Wt % Fe	"Formula"
0.9/99.1 A	93.23	6.75	$FeZn_{11 \cdot 8}$
0.9/99.1 B	—	6.86	$FeZn_{11 \cdot 6}$
0.45/99.45	—	6.60	$FeZn_{11 \cdot 9}$

appears more appropriate for describing the composition of ζ_{FeZn}, since the extract from alloy 0.45/99.45 would be expected to correspond to the zinc-rich limit of the homogeneity range.

(iv) *Discussion.* The most significant aspect of the results is the persistence of $FeAl_3$, or the $FeAl_3'$ structure derived from it, in equilibrium with zinc-rich material. This behaviour contrasts sharply with that observed in Al-Mn-Zn alloys [3], where $MnAl_6$, $MnAl_4$, δ, $MnAl_3$ and $MnAl$ all enter into equilibrium with the liquid, with increasing zinc content, before the ternary eutectic is reached. The significance of this contrast is discussed below. No ternary compound occurs, in equilibrium with either α or β, in the Al-Fe-Zn system.

VI. The Ternary System Aluminium-Cobalt-Zinc

(*a*) *Previous Work*

No previous work on this system has been noted.

(*b*) *Experimental Methods*

Only the preparation of zinc-rich master alloys requires comment. The reduction of anhydrous cobalt chloride with molten zinc was feasible, but better control of composition was obtained by direct solution of electrolytic cobalt in the molten metal, using the method described for Fe-Zn alloys and an annealing period of 14 days. The alloys contained no free cobalt and were non-magnetic; tests showed silicon contamination to be negligible.

In the metallographic work, Co_2Al_9, Co_4Al_{13}, $CoAl$ and ζ_{CoZn} were observed in addition to α and β. The mixed acid reagent already described was satisfactory for aluminium-rich alloys; 10 per cent aqueous caustic soda was used for zinc-rich material. The Al-Co compounds were difficult to distinguish from one another in etched sections, and greater reliance was placed on examination of unetched sections. Co_2Al_9 was grey to pale violet and in relief; $CoAl$ was deeper violet in colour, was globular in slowly cooled alloys, and was much harder and in greater relief than Co_2Al_9. Co_4Al_{13} was intermediate in both colour and relief. The identification of these phases was checked by X-ray work. ζ_{CoZn} appeared

as a soft pinkish phase in the zinc-rich matrix, which was darkened by caustic soda. In certain alloys, δ'_{CoZn} was recognized as cores in ζ_{CoZn} crystals deposited on slow cooling.

(*c*) *Experimental Results*

(i) *Slowly cooled alloys.* Alloys covering a wide composition range were slowly cooled from the liquid state at $\frac{3}{4}$°C/min. The results are summarized in Figures 10 and 11. The primary α region again

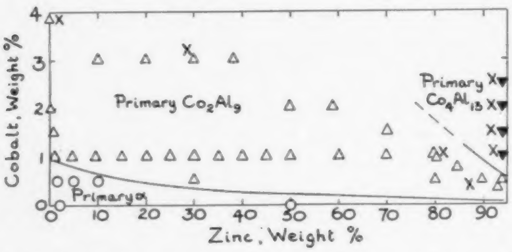

FIGURE 10. Surfaces of primary separation: system Al-Co-Zn. *Key*: primary α ○; primary Co_2Al_9 △; primary Co_4Al_{13} ▼; × denotes alloy from which a diffraction pattern was obtained.

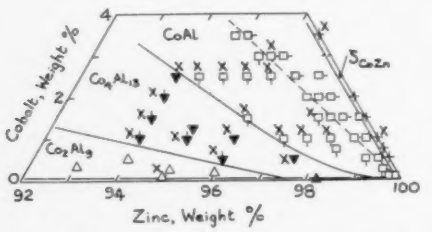

FIGURE 11. Surfaces of primary separation: Zn-rich alloys of system Al-Co-Zn. *Key*: primary Co_2Al_9 △; primary Co_4Al_{13} ▼; primary Co_4Al_{13} with secondary Co_2Al_9; primary CoAl □; primary CoAl with secondary Co_4Al_{13} □ primary CoAl with secondary ζ_{CoZn} □; primary ζ_{CoZn} +; primary β ▲. × denotes an alloy from which a diffraction pattern was obtained.

becomes restricted with increasing zinc content, and the ternary eutectic is very close in composition to the binary Liquid $\rightleftharpoons \alpha + \beta$ eutectic, as indicated by the structure of alloy 0.05/94.95 (primary Co_2Al_9 in ternary eutectic matrix). Because of the complexity of the system, X-ray diffraction patterns were obtained of crystals extracted from many alloys; these are indicated in Figures 10 and 11, and the patterns were in complete agreement with the metallographic work. The primary Co_2Al_9 field extends to a point close to the Al-Zn axis at 97.5 per cent of zinc. The Co_4Al_{13} field also persists at very high zinc contents; alloys 0.1/99.6 and 0.05/99.7 showed, in addition to primary CoAl, secondary Co_4Al_{13} crystals. A primary CoAl field succeeds the Co_4Al_{13} field. The X-ray evidence for the presence of CoAl (ordered body-centred cubic structure) is clear proof of the absence of a primary Co_2Al_5 field in the composition range investigated. The primary CoAl field, like that of $FeAl_3'$ in the Al-Fe-Zn system, is subdivided by a line stretching from the zinc-rich corner of the diagram to the composition of the primary phase. On the aluminium-rich side, CoAl crystals in slowly cooled alloys are rimmed by Co_4Al_{13}; on the cobalt-rich side, CoAl crystals are rimmed by either δ'_{CoZn} or ζ_{CoZn}, the primary fields for which are restricted to a narrow composition region near to the Co-Zn axis. Experiments intended to define the zinc-rich limit of the δ'_{CoZn} field were unsuccessful, owing to the difficulty of recognizing very small δ'_{CoZn} cores in ζ_{CoZn} crystals. It may be noted that alloys 0.5/99.5, 0.75/99.25 and 1.0/99.0 all gave extracts having the ζ_{CoZn} diffraction pattern.

(ii) *Annealed alloys.* Initial experiments are summarized in Table IV. The microstructures of all these alloys were ($\alpha + Co_2Al_9$). Alloys richer in zinc

TABLE IV

Alloys	Annealing treatment
4/1, 3/2, 2/3, 1/4, 0.5/4.5, 4/6, 3/7, 2/8, 1/9, 0.5/9.5, 4.85/0	40 days at 600°C
2.43/0, 2.18/5, 1.94/10, 1.69/15, 0.24/45, 1.45/20, 1.21/25, 0.97/30, 0.73/35, 0.43/40	48 days at 425°C

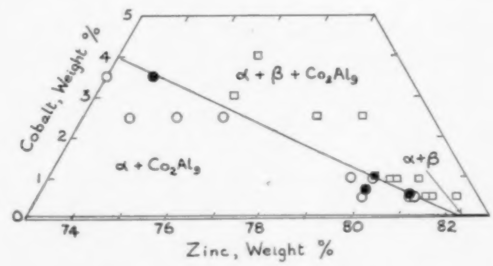

FIGURE 12. System Al-Co-Zn; ($\alpha + Co_2Al_9$)/($\alpha + \beta + Co_2Al_9$) boundary at 370°C. *Key*: $\alpha + Co_2Al_9$ ○●; $\alpha + \beta + Co_2Al_9$ □■.

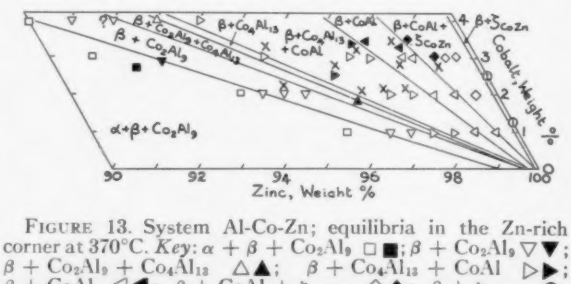

FIGURE 13. System Al-Co-Zn; equilibria in the Zn-rich corner at 370°C. *Key*: $\alpha + \beta + Co_2Al_9$ □■; $\beta + Co_2Al_9$ ▽▼; $\beta + Co_2Al_9 + Co_4Al_{13}$ △▲; $\beta + Co_4Al_{13}$ + CoAl ▷▶; β + CoAl ◁◀; β + CoAl + ζ_{CoZn} ◇◆; $\beta + \zeta_{CoZn}$ ⦶. × denotes alloy from which a diffraction pattern was obtained.

were examined at 370°C; the results are given in Figures 12 and 13, which are based on the examination of alloys annealed for 45 to 78 days. The phase-fields included are in agreement with the slow-cooling experiments. X-ray work on extracts from the alloys indicated in Figure 13 confirmed the metallography, while the presence of ζ_{CoZn} and zinc in alloy 3/96 was confirmed using filings of the alloy. Although no alloy examined lay in the $(\beta + Co_4Al_{13})$ field, a narrow two-phase field must exist as illustrated.

(iii) *Compositions of extracted crystals.* Several samples of extracted Co_2Al_9 crystals were analysed; the results are given in Table V, and plotted in atomic percentages in Figure 14. Figure 15 shows the zinc content of the crystals plotted against that of the parent alloy; the type of discontinuity shown in Figure 7 is absent, in agreement with the fact that no structural modification of the Co_2Al_9 structure by zinc was detected in the X-ray work. Alloys containing more than 60 per cent of zinc gave residues too small for analysis. Since primary Co_2Al_9 is found at zinc contents exceeding that of the ternary eutectic, the maximum zinc content of Co_2Al_9 probably considerably exceeds 3.88 per cent. Though no great reliance can be placed on a long extrapolation, towards the Al-Co axis, of the $(\alpha + Co_2Al_9)/(\alpha + \beta + Co_2Al_9)$ and $(\alpha + \beta + Co_2Al_9)/(\beta + Co_2Al_9)$ boundaries of Figures 12 and 13, this procedure suggests a limiting solubility of approximately 8 per cent of zinc in Co_2Al_9 at 370°C. Using methods similar to that described for the extraction of ζ_{FeZn}, two samples of ζ_{CoZn}, which contained no δ'_{CoZn} cores, were obtained from separate alloys of composition 0.5/99.5. Analysis gave the following results:

TABLE V

Alloy composition	Wt % Zn	Wt % Co	Wt % Al
3/0	—	33.20	66.80
3/10	0.93	32.57	66.50
3/20	1.24	32.45	66.31
3/30	1.55	33.15	65.30
3/38.2	2.26	32.88	64.86
2/50	3.60	31.36	65.04
2/58.8	3.88	31.37	64.75

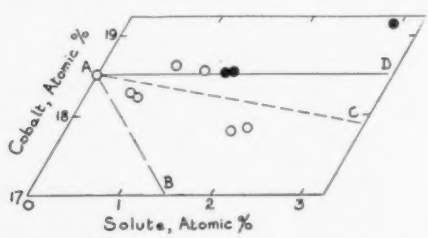

FIGURE 14. Compositions of extracted Co_2Al_9 crystals: systems Al-Co-Zn ○, and Al-Co-Mg ●. *AD*—replacement of Al; *AB*—replacement of Co; *AC*—electron:atom ratio of 1.85 (see text).

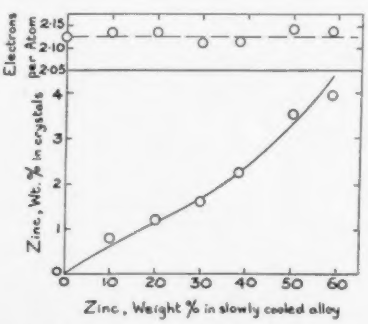

FIGURE 15. Variation of zinc content of extracted Co_2Al_9 crystals.

(1) 7.37% Co; 92.73% Zn.

(2) 7.45% Co; 92.64% Zn.

These compositions lie within the ζ_{CoZn} homogeneity range quoted by Schramm [16] (6.3 to 8.2 per cent of Co) and by Götzl, Halla and Schramm [25] (6.9 to 8.2 per cent of Co). The present results correspond to $CoZn_{11.2}$ and $CoZn_{11.35}$.

(iv) *Discussion.* Unlike $FeAl_3'$ in the Al-Fe-Zn system, Co_2Al_9 does not enter into equilibrium with ζ_{CoZn}. The Co_2Al_9/Co_4Al_{13} reaction line intersects the boundary of the primary β field at 97.5 per cent zinc, while the Co_4Al_{13} field is succeeded by a primary CoAl field extending almost to the Co-Zn axis. Thus CoAl, the highest melting phase in the Al-Co system, comes into equilibrium with the low-melting ζ_{CoZn} phase. In this respect, the system is analogous to the Al-Mn-Zn system. No ternary compound exists in equilibrium with α or β; it is also apparent that Co_2Al_5 does not enter into equilibrium with β.

VII. The Ternary System Aluminium-Nickel-Zinc

Since it was expected that $NiAl_3$, like $FeAl_3$ and Co_2Al_9, would persist at zinc contents exceeding that of the ternary eutectic in the ternary system with zinc, experiments were confined to zinc-rich alloys.

(*a*) *Previous Work*

Restricted work on the ternary system was reported by Fuss [26] who stated that, of the various Al-Ni phases, only $NiAl_3$ enters into equilibrium with β. No ternary compound was reported.

(*b*) *Experimental Methods*

The techniques mentioned above were used for zinc-rich master alloy preparation. The relatively hard aluminium-transitional metal compounds were again best distinguished in unetched alloys, though 10 per cent aqueous caustic soda, and a reagent consisting of 10 g. of potassium hydroxide and 10 g. of potassium ferricyanide in 100 cc. of water proved useful for revealing phases present in addition to α and β. In slowly cooled alloys, a ternary phase T(AlNiZn) was found; when primary, this was always in the form of larger crystals than $NiAl_3$ or Ni_2Al_3, and no difficulty was experienced in its recognition.

(*c*) *Experimental Results*

(i) *Slowly cooled alloys.* Figure 16 summarizes the results of the examination of a limited series of zinc-rich alloys; extracts were obtained from the indi-

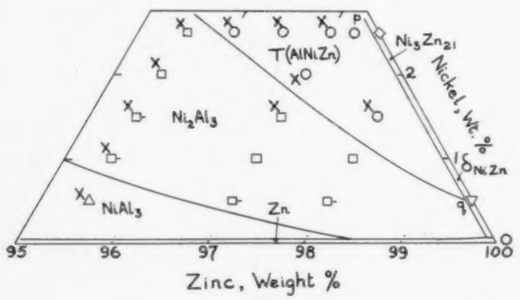

FIGURE 16. Surfaces of primary separation: zinc-rich alloys of system Al-Ni-Zn. *Key*: primary $NiAl_3$ △; primary Ni_2Al_3 □; primary Ni_2Al_3 rimmed by $NiAl_3$ □; primary T(AlNiZn) ○; primary Ni_5Zn_{21} ◇; primary δ_{NiZn} ▽; × denotes alloy from which a diffraction pattern was obtained.

cated alloys, and though these were insufficient for chemical analysis, diffraction patterns were obtained and compared with those of $NiAl_3$, Ni_2Al_3, NiAl, $NiZn_9$ and Ni_5Zn_{21} available from previous work or specially prepared. Extracts from alloy 0.5/95.5 gave a diffraction pattern identical with that of $NiAl_3$. Those from alloys 2.5/95.5, 1.0/95.5, 1.5/95.5, 2.0/95.5 and 1.5/97, however, corresponded with Ni_2Al_3; representative films were measured and indexed, and the diffraction pattern proved to be identical with that given by Bradley and Taylor [27] for this phase. Extracts from alloys 2.5/96, 2.5/96.5, 2.5/97, 2.0/97, 4.0/95.5 and 1.5/98 gave diffraction patterns somewhat similar to that of Ni_2Al_3, but with significant differences. Accurate measurement of the pattern given by crystals from alloy 1.5/98 showed that there was no correspondence with any of the binary Al-Ni phases, or with Ni_5Zn_{21} or $NiZn_9$. The observed pattern was not consistent with a small modification of $NiAl_3$ or Ni_2Al_3, nor with diffraction from a major mixture of phases, though small amounts of Ni_5Zn_{21} and $NiZn_9$ may have been present. The positions and intensities of the lines remained constant throughout the six samples examined; the primary crystals in these alloys were thus identified as a ternary compound T(AlNiZn). Since cores of T(AlNiZn) occurred in secondary $NiZn_9$ crystals, and occasionally in secondary Ni_5Zn_{21} crystals which were in turn rimmed with $NiZn_9$, the boundary *pq* in Figure 16 represents a peritectic reaction. These contaminating effects were present only in small secondary crystals, and not in the larger crystals selected for X-ray work.

(ii) *Annealed Alloys.* From results already described, $NiAl_3$ and Ni_2Al_3 may be expected to enter into equilibrium with β; if, however, the Ni_2Al_3/T(AlNiZn) boundary in Figure 16 intersects *pq* as shown, T(AlNiZn) should not appear in equilibrium with β. To test this conclusion, seven alloys with 2 per cent of nickel and respectively 92, 93, 94, 95, 96, 97 and 97.5 per cent of zinc, together with alloy 3/96.5, were annealed for 45 days at 370°C. In addition to α and β, alloys 2/92, 2/93, and 2/94 contained $NiAl_3$, which was confirmed by X-ray analysis of the extract from alloy 2/92. Alloy 2/95 contained only β and $NiAl_3$, while in alloy 2/96 β, $NiAl_3$ and Ni_2Al_3 were recognized metallographically and confirmed by X-ray diffraction. The remaining alloys showed $(\beta + Ni_2Al_3 + \delta_{NiZn})$ microstructures; diffraction patterns of extracts from alloys 2/97 and 2/97.5 correspond with admixture of Ni_2Al_3 and δ_{NiZn}. A narrow $(\beta + Ni_2Al_3)$ region must exist between the compositions 2/96 and 2/97, but this was not observed experimentally.

(iii) *Discussion.* Although a ternary compound is encountered in these alloys, it does not enter into equilibrium with α or β. The system differs from the Al-Fe-Zn system in that not only the most aluminium-rich aluminium-transitional metal phase appears in equilibrium with β, but Ni_2Al_3 in addition. It also differs from the Al-Co-Zn system since NiAl is not found in equilibrium with β. It is probable that the existence of T(AlNiZn) prevents this equilibrium from being established.

VIII. The Ternary System Aluminium-Cobalt-Magnesium

In the cases described above, equilibrium of high melting aluminium-transitional metal phases with the zinc-rich solid solution is associated with a long eutectic valley extending from the aluminium-transitional metal axis to a point near the Al-Zn axis at 95 per cent of zinc. It was therefore of interest

to examine a system in which the primary α field did not extend to such high concentrations of the divalent component; the sytem Al-Co-Mg was accordingly chosen.

(*a*) *Previous Work*

According to Mondolfo [19], who examined only aluminium-rich alloys, no ternary compound exists in equilibrium with α, which enters into equilibrium with liquid, Co_2Al_9, and Mg_2Al_3 at a ternary eutectic point (33 per cent Mg, 0.5 per cent Co, 448°C).

(*b*) *Experimental Methods*

Techniques employed were again similar to those previously described, except that slow cooling experiments were carried out in a specially designed furnace in a purified argon atmosphere to prevent slow burning-off of magnesium, which proved troublesome in initial experiments. It was possible to prepare slowly cooled ingots differing negligibly in weight from that of the initial materials. In the metallographic work on annealed alloys, the phases encountered were α, Mg_2Al_3, $Mg_{17}Al_{12}$, the Mg-rich solid solution (ϵ), Co_2Al_9 and Co_4Al_{13}; Co_2Al_5 and Co-Al appeared also in slowly cooled specimens. The metallography of the Al-Co phases was similar to that described for the system Al-Co-Zn. For distinguishing the Al-Mg phases the most useful reagent was aqueous sulphuric acid. The optimum concentration and time of etching varied according to alloy composition and type from 20 per cent for 1 min. in the Al-rich range to 5 per cent for 2–5 sec. in the Zn-rich range. Etching characteristics of the Al-Mg phases varied with alloy composition. When present with α, Mg_2Al_3 is coloured brown, but with increase in magnesium content etches less deeply, and appears light when present with $Mg_{17}Al_{12}$, which is coloured slate-blue. Increase in the magnesium content of $Mg_{17}Al_{12}$ again corresponds with lighter etching and ϵ is the darker phase in ($Mg_{17}Al_{12} + \epsilon$) microstructures. Co_2Al_5, which was not encountered in the Al-Co-Zn alloys, appeared in slowly cooled alloys as very hard globular particles in high relief, darker in colour than Co_2Al_9 or Co_4Al_{13}. Primary CoAl was only found in one alloy, and in this case definite identification depended on the diffraction pattern of extracted crystals.

(*c*) *Experimental Results*

(i) *Slowly cooled alloys.* Projected surfaces of primary separation deduced from work on slowly cooled alloys are given in Figure 17. The α/Co_2Al_9 eutectic valley extends to approximately 34 per cent of magnesium; this magnesium content must correspond with <0.5 per cent of cobalt, since primary Co_2Al_9 appears in alloy 0.5/33. The Mg_2Al_3 and $Mg_{17}Al_{12}$ fields are restricted, as shown by the microstructures of alloys 0.5/36 and 0.5/45. At 2 per cent of cobalt the primary Co_2Al_9 field extends to approximately 57 per cent of magnesium, and is then succeeded by a primary Co_4Al_{13} field. Reasonable

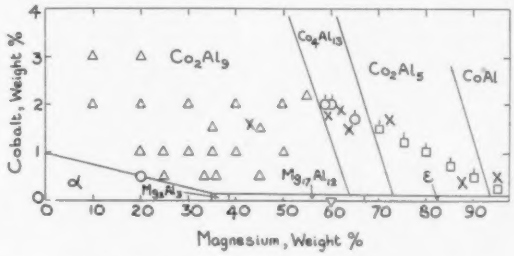

FIGURE 17. Surfaces of primary separation: system Al-Co-Mg. *Key*: Primary α ○; primary Co_2Al_9 △; primary Co_4Al_{13} ♁; primary Co_2Al_5 □; primary CoAl □; × denotes alloy from which a diffraction pattern was obtained.

extrapolation from the binary Al-Co system of the boundary between these two fields suggests that it intersects the boundary of the $Mg_{17}Al_{12}$ field as shown; this is confirmed by annealing experiments described below. The narrow Co_4Al_{13} field is succeeded by a Co_2Al_5 field; the intervening boundary intersects that of the primary ϵ field. The Co_2Al_5 field persists to a composition exceeding 90 per cent of magnesium at low cobalt contents, and then gives way to primary CoAl. The diffraction patterns of crystals extracted from the alloys indicated confirmed the metallographic results. The patterns corresponding to alloys 1.5/70 and 0.5/90, which lie close to the boundaries of the Co_2Al_5 field, were measured and indexed, and the observed reflections were identical with those reported for Co_2Al_5 by Bradley and Cheng [28]. The primary ϵ field is very limited.

(ii) *Annealed alloys.* Alloys were annealed at 400°C for 50 to 245 days, and the results of the metallographic and X-ray work are given in Figures 18, 19 and 20. The $(\alpha + Co_2Al_9)/(\alpha + Co_2Al_9 + Mg_2Al_3)$ boundary is consistent with a line drawn

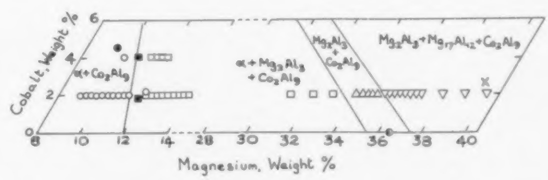

FIGURE 18. System Al-Co-Mg: constitution at 400°C. *Key*: $\alpha + Co_2Al_9$ ○●; $\alpha + Mg_2Al_3 + Co_2Al_9$ □ ■; $Mg_2Al_3 + Co_2Al_9$ △; $Mg_2Al_3 + Mg_{17}Al_{12} + Co_2Al_9$ ▽; Mg_2Al_3 ◐; × denotes alloy from which a diffraction pattern was obtained.

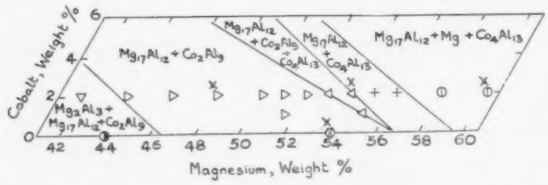

FIGURE 19. System Al-Co-Mg: constitution at 400°C. *Key*: $Mg_2Al_3 + Mg_{17}Al_{12} + Co_2Al_9$ ▽; $Mg_{17}Al_{12} + Co_2Al_9$ ▷; $Mg_{17}Al_{12} + Co_2Al_9 + Co_4Al_{13}$ ◁; $Mg_{17}Al_{12} + Co_4Al_{13}$ +; $Mg_{17}Al_{12} + Mg + Co_4Al_{13}$ ⌽; × denotes alloy from which a diffraction pattern was obtained.

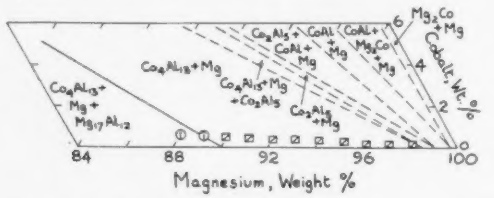

FIGURE 20. System Al-Co-Mg: constitution at 400°C. *Key*: $Co_4Al_{13} + Mg + Mg_{17}Al_{12}$ ⌽; $Co_4Al_{13} + Mg$ ⊠.

from the composition of Co_2Al_9 to that of the solid solubility limit of magnesium in aluminium, and is located by alloy 4.01/10.60, which showed only traces of Mg_2Al_3 after annealing for successive periods of 154 and 58 days.* Metallographic interpretation of alloys in the extensive ($\alpha + Co_2Al_9 + Mg_2Al_3$) field was confirmed by the Co_2Al_9 diffraction pattern obtained from the extract from alloy 2/25. The width of the ($Co_2Al_9 + Mg_2Al_3$) field corresponds to the homogeneity range of Mg_2Al_3, and is succeeded by the ($Co_2Al_9 + Mg_2Al_3 + Mg_{17}Al_{12}$) field; extracts from alloy 2/40 gave the Co_2Al_9 diffraction pattern. The ($Co_2Al_9 + Mg_{17}Al_{12}$) field was similarly confirmed, using alloy 2/48. $Mg_{17}Al_{12}$ also enters into equilibrium with Co_4Al_{13}, and the extract from alloy 2/54 gave a clear mixed diffraction pattern derived from the Co_2Al_9 and Co_4Al_{13} phases. The ($Co_4Al_{13} + Mg_{17}Al_{12} + \epsilon$) field stretches, at low cobalt contents, to 90 per cent of magnesium; in addition to those plotted in Figures 19 and 20, alloys 1.85/62, 1/64, 1/66 and 1/70 also lay in this field. Alloys plotted in Figure 20 all showed ($Co_4Al_{13} + \epsilon$) microstructures, except for the two richest in magnesium. The slow cooling experiments show that Co_2Al_5 and CoAl also appear in equilibrium with the magnesium-rich solution. From Figure 20, the corresponding two- and three-phase fields must make contact with the restricted ϵ field at magnesium contents exceeding 98 per cent.

The solid solubility of cobalt in aluminium and in magnesium is extremely small. Once the phases taking part in the ternary equilibria have been correctly designated, therefore, the various phase boundaries may be represented as straight lines drawn from the compositions of the Al-Co compounds to the critical limiting compositions of the Al-Mg phases. Microstructures observed were entirely consistent with this interpretation, and since the main object of the work was to establish the correct sequence of phase fields, critical alloys were not in general analysed.

(iii) *Compositions of extracted crystals.* Analytical results for four extracts of Co_2Al_9 from ternary alloys are given in Table VI, and included in Figure 14.

TABLE VI

Alloy composition	Wt % Mg	Wt % Co	Wt % Al
2/10	1.03	33.26	65.71
2/20	0.29	31.80	68.01
2/30	1.07	33.28	65.65
2/40	2.16	34.20	63.64

The cobalt content of the crystals from alloy 2/20 is abnormally low, and possibly results from unsuspected contamination with matrix. The remaining analyses are consistent, and indicate a limited solubility of magnesium in Co_2Al_9. The same conclusion results from a study of the phase boundaries at 400°C.

(iv) *Discussion.* The presence of Mg_2Al_3 and $Mg_{17}Al_{12}$ makes the equilibria more complex than in the Al-Co-Zn system. The two systems are, however, analogous in that the high-melting Al-Co compounds separate successively from the melt as the concentration of third metal increases; the cubic CoAl phase enters into equilibrium with the divalent metal in each case. Both systems differ in type from the Al-Fe-Zn system. No ternary compound has been found in the composition range investigated.

IX. The Ternary System Aluminium-Manganese-Beryllium

As the work reported in this paper progressed, it became possible tentatively to define a zone of atomic sizes for third metals alloyed with aluminium and iron or aluminium and manganese, within which ternary compound formation might occur. The closest distance of approach of atoms in metallic beryllium is close to the lower limit of this zone, and it became of interest to examine the Al-Mn-Be system.

(a) *Previous Work*

No previous investigation of Al-Mn-Be alloys has been noted.

*After a similar period of 212 days alloy 1.84/11.86 showed considerably more Mg_2Al_3, but alloy 2.17/11.96 showed none. No explanation of this is available, except for the possibility of an incorrect analysis.

(b) Experimental Methods

Methods employed were similar to those previously described. Since it became necessary to measure the densities of certain extracted crystals, a simple density-bottle technique was developed, which, as estimated from repeated calibrations on material of known density, gave results subject to a total error of less than 1 per cent.

The phases observed were α, Be, $MnAl_6$, $MnAl_4$ and a ternary phase T(AlMnBe). Unetched, distinction between the Al-Mn compounds and traces of Be was difficult; when present in larger amounts, Be occurred as characteristic grey particles. The best etching reagent was 10 per cent aqueous caustic soda containing 10 per cent of carbonate ion added as ammonium carbonate. Used cold for 45 sec., this reagent coloured $MnAl_6$ variable shades of blue, while T(AlMnBe) was coloured uniformly brown and Be almost unattacked.

(c) Experimental Results

The range investigated was 0 to 12 per cent of Mn and 0 to 5 per cent of Be.

(i) *Slowly cooled alloys.* Figure 21 gives the results of an examination of 32 alloys. The α and $MnAl_6$ fields are restricted; alloys 1.8/0.08, 1.8/0.2

FIGURE 21. Surfaces of primary separation; system Al-Mn-Be. *Key*: primary α ●; primary $MnAl_6$ △; primary $MnAl_4$ ○; primary Be ▽; primary T(AlMnBe) □.

and 1.85/0.45 showed primary α, $MnAl_6$ and T(AlMnBe) respectively, and in each case the matrix was almost entirely in the form of a ternary eutectic whose composition is estimated as 0.2 per cent of Be and 1.5 to 1.7 per cent of Mn. The $MnAl_4$ field is also narrow. No evidence was found of $MnAl_6$ or $MnAl_4$ cores in T(AlMnBe) so that AT represents a eutectic valley. The expected rimming of $MnAl_4$ by $MnAl_6$ was, however, observed. The T(AlMnBe) field is approximately parallel to the Al-Mn axis, and is well defined by the results given; the Be-rich boundary represents a peritectic relationship between the ternary compound and Be, since primary Be particles were observed as cores inside secondary T(AlMnBe) crystals.

(ii) *Annealed alloys.* Several alloys were annealed for 28 days at 600°C and examined; microstructures were unchanged after a further 7 days and are summarized in Figure 22. Since the three-

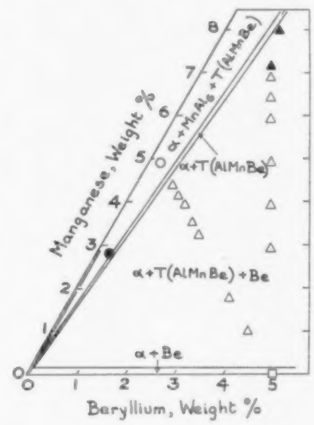

FIGURE 22. System Al-Mn-Be; constitution at 600°C. *Key*: α + $MnAl_6$ ○●; α + T(AlMnBe) + Be △▲; α + Be □.

phase alloy 4.9/0.25 contained an appreciable amount of T(AlMnBe), the (α + $MnAl_6$) field must be very narrow. Only one other alloy (2.82/0.28) contained $MnAl_6$. The remainder all showed (α + T(AlMnBe) + Be) microstructures, and in no case were $MnAl_6$ and Be observed together. A very narrow (α + T(AlMnBe)) field thus exists between the two observed three-phase fields; its direction and extent are defined by alloys 2.82/0.28 and 7.96/1.16.

(iii) *Compositions of extracted crystals.* Analytical results for extracted samples of T(AlMnBe) are given in Table VII. The residues were easy to sort

TABLE VII

Alloy composition	Wt % Be	Wt % Mn	Wt % Al
6.36/1.53	3.34	27.75	68.85
4.9/1.4	2.78	26.05	71.16
3.12/1.25	3.05	32.45	64.50
9.1/1.0	2.35	32.36	65.29
11.0/0.75	3.01	33.54	63.45

because of the characteristically regular habit of the ternary crystals (Figure 23). Optical measurement showed that the angles between the normals to the rectangular faces were in all cases 120° ± 5′, while the semivertical angle of the pyramid formed by the inclined faces was approximately 23.5°.

FIGURE 23. Form of T(AlMnBe) crystals (7×).

The compositions of T(AlMnBe) are plotted in atomic percentages in Figure 24. The beryllium content of the extract from alloy 9.1/1.0 (point *a*) appears incorrect and too low, since the tie-line joining the composition of the extract to that of the parent alloy crosses that for alloy 11.0/0.75, whereas the disposition of the tie-lines for the other alloys is reasonable. Ignoring this analysis, the most prob-

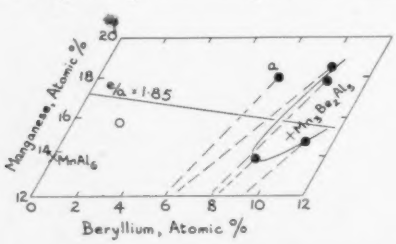

FIGURE 24. Compositions of extracted T(AlMnBe) crystals ● and of a specimen of $MnAl_6$ containing beryllium ○.

able homogeneity range includes the composition $Mn_3Be_2Al_{15}$; it also includes the electron:atom ratio 1.85, assuming that manganese has an effective valency of −3.6 as in previously discussed alloys of this type. The phase may thus be based upon an electron concentration of 1.85 and a ratio of aluminium atoms to total solute atoms of 3:1; this is of interest since the ternary compounds in the systems Al-Mn-Ni, Al-Mn-Cu and Al-Mn-Zn are characterized by the same electron:atom ratio, but a ratio of four aluminium atoms to one of solute.

X-ray diffraction patterns were obtained of extracts from alloys 6.36/1.53, 4.3/0.75, 3.12/1.25 and 11.0/0.75, using CuKα or CoKα radiations, and Table VIII contains the lines observed. The most significant feature is the group of three strong lines, close together, in the range $\theta = 21°$ to $23°$.

TABLE VIII

Line	Visual intensity	θ°. CuKα radiation	Interplanar spacing *d* in kX
1	w	18.68	2.40
2	w	19.75	2.33
3	w	20.50	2.196
4	vs	21.61	2.089
5	s	22.61	2.041
6	vs	22.63	2.000
7	w	32.46	1.425
8	w	35.45	1.326
9	s	36.75	1.286
10	s	37.58	1.261
11	s	38.41	1.238
12	w	38.93	1.224
13	w	39.47	1.210
14	m	45.85	1.073
15	s	46.77	1.056
16	s	47.25	1.047
17	s	60.80	0.881
18	s	61.50	0.876
19	s	72.82	0.807
20	s	73.78	0.800

s = strong; vs = very strong; m = medium; w = weak.

An $MnAl_6$ specimen from alloy 3.85/0.22 contained, by analysis, 2.10 wt. per cent of Be and 15.74 wt. per cent of Mn. This result is included in Figure 24 and it is probable, since the relevant point lies close to a line joining the composition of $MnAl_6$ to the most manganese-rich composition found for T(AlMnBe), that the sample was contaminated with secondary T(AlMnBe) adhering to the primary crystals. Metallographic work showed that such adhesion was common, and no further attempts were made to extract and analyse primary $MnAl_6$, in view of the very small solid solubility of beryllium in $MnAl_6$ indicated by the annealing work.

(iv) *Discussion.* The most interesting feature of the system is the existence of T(AlMnBe) in equilibrium with α. It is also noteworthy that the primary beryllium field occupies a very large composition range. In the solid state, the (α + T(AlMnBe) + Be) field is correspondingly wide, while the (α + T(AlMnBe)) field is very narrow. The boundaries given in Figure 22 are in excellent agreement with the compositions of extracted T(AlMnBe) crystals. From Figure 24, the ternary compound appears to correspond with electron:atom ratios 1.67 to 1.98,

assuming an effective negative valency of -3.6 for manganese, as in previous work [1]. The three intense low angle reflections suggest that the corresponding diffracting planes define the appropriate first Brillouin Zone. The exact form of the zone cannot be discussed until the reflections have been unequivocally indexed. It would be expected, however, if T(AlMnBe) depends upon the electron: atom ratio, that the radius of the Fermi sphere in k-space corresponding to the characteristic number of electrons per atom would be approximately equal to half the reciprocal of the interplanar spacing of the planes defining the zones. Since the density of a sample of mean atomic weight 30.69 was found to be 3.62, the mean volume per atom is 14.2 Å^3. The radius of the Fermi sphere corresponding to 1.98 electrons per atom is thus

$$\left(\frac{3 \times 1.98}{8\pi \times 14.2}\right)^{\frac{1}{3}} \text{ or } 0.255 \text{ Å}^{-1}.$$

The values of half the reciprocal of the relevant interplanar spacings are 0.241, 0.246 and 0.250 Å^{-1} respectively, in good agreement with the Fermi sphere radius. It appears probable that T(AlMnBe) may be considered as a type of electron compound, in common with previously discovered compounds. Since its homogeneity range includes the electron: atom ratio 1.85, it may be classified (on the basis of electronic influences only) with the phases of similar electron:atom ratio in the Al-Mn-Cu, Al-Mn-Ni and Al-Mn-Zn systems. Instead of a ratio of four aluminium atoms to one of solute, however, T(AlMnBe) shows a 3:1 ratio. Its crystal structure does not appear to be closely related to those of the other phases, and is being examined in greater detail.

X. The Ternary System Aluminium-Iron-Beryllium

For comparison with the Al-Mn-Be system, a limited number of Al-Be-Fe alloys was examined. The object was to investigate the possibility of ternary compound formation, and surfaces of primary separation were not examined in detail.

(a) Previous Work

No previous examination of this system has been noted.

(b) Experimental Methods

In alloys annealed to equilibrium, phases observed were α, $FeAl_3$, Be, and a ternary compound T(AlFeBe) which was easily differentiated from $FeAl_3$ by the "mixed acid" reagent referred to above. This, however, attacked the Be constituent very rapidly. The same phases were present in slowly cooled alloys, but the distinction between large primary crystals of $FeAl_3$ and T(AlFeBe) became difficult, and greater reliance was placed on the X-ray diffraction patterns of extracted residues.

(c) Experimental Results

(i) *Slowly cooled alloys.* Twelve alloys, with compositions in the range 0 to 6 per cent of Fe and 0 to 5 per cent of Be, were cooled slowly. Alloys 5.85/0, 5.8/0.08, 5.7/0.15 and 5.56/0.25 deposited plate-like primary $FeAl_3$; secondary and eutectic material was also shown, and the latter contained small Be particles. In alloys 4.7/1, 4.6/1.1, 4.45/1.22 and 4.4/1.25, some well-developed $FeAl_3$ crystals were found, but the bulk of the primary particles appeared as sections of polyhedral crystals. These were difficult to differentiate metallographically from $FeAl_3$, but it was possible to differentiate the two types of crystal in extracted residues by reason of their characteristically different habit. The diffraction pattern of the polyhedral crystals was quite different from that of $FeAl_3$, and confirmed the existence of a new phase. To secure a reliable sample for analysis, selected preparations of polyhedral crystals from alloys 4.7/1.0 and 4.6/1.1 were pooled, and were found to contain 40.97 wt per cent of Fe and 16.00 wt per cent of Be. A sample of $FeAl_3$ from alloy 4.7/1.0 contained 39.52 wt. per cent of Fe and 1.39 wt. per cent of Be. Primary beryllium was deposited from alloys 3.85/2.5, 2.93/2.5, 2.4/3 and 0/5.

(ii) *Annealed alloys.* After annealing for 28 days at 600°C, the results summarized in Table IX were obtained.

TABLE IX

Alloys	Microstructure
5.3/0.5, 4.7/1.0, 4.1/1.5, 3.5/2.0	$\alpha + FeAl_3 +$ T(AlFeBe)
2.95/2.5, 2.4/3.0, 1.8/3.5, 1.2/4.0 0.6/4.5	$\alpha +$ T(AlFeBe) + Be
0/5.0	$\alpha +$ Be

The corresponding isothermal must contain a narrow ($\alpha +$ T(AlFeBe)) field between the compositions of alloys 3.5/2.0 (trace of $FeAl_3$) and 2.95/2.5 (trace of Be). The results confirm the existence of T(AlFeBe) in equilibrium with α, and the approximate phase boundary positions are con-

sistent with the analysed composition of this compound.

(iii) *Discussion.* In contrast to many of the ternary compounds occurring in aluminium-rich alloys, in T(AlFeBe), the amount of aluminium present is relatively small; the compound approximates to $Al_7Fe_3Be_7$. The generalizations applicable to the electron:atom ratios of previously isolated phases would not be expected to apply in this case, owing to the high total solute concentration. No further discussion of this phase is therefore justified at present; it may be noted that its diffraction pattern is different from either $FeAl_3$ or T(AlMnBe) and it cannot be considered as analogous to either structure.

XI. General Discussion

From a comparison of the forms of equilibrium diagrams for the alloys investigated, several interesting points emerge. Some of these are briefly discussed below.

(*a*) *General Forms of the Equilibria*

The constitutional diagrams for ternary alloys of aluminium and zinc with chromium, manganese, cobalt and nickel and of aluminium and magnesium with cobalt, show a distinct analogy in so far as high melting intermediate phases derived from the binary aluminium-transitional metal alloys separate at low temperatures from melts rich in the divalent metal, and may appear in equilibrium with this metal, or a solid solution based on it, in the solid state. The data are summarized in Table X. By contrast, the system Al-Fe-Zn is peculiar in that only a phase derived from the most aluminium-rich binary compound, $FeAl_3'$, is found in equilibrium with zinc. The reason for this difference in behaviour may be sought in terms of the free energies of the various phases, for which heats of formation may be taken as an approximate measure [29]. We may consider a system ABC in which compounds occur as shown in Figure 25. For correspondence with the alloys studied, compounds 1 and 2 are assumed to have low free energies compared with 3. The C-rich solid solution and 3 are in equilibrium, and the third phase entering into equilibrium with these two may be 1 or 2. If compound 1 has a lower free energy than 2, the energy contour diagram of Figure 26*a* is appropriate; the envelope formed by the tangent planes is everywhere convex in the direction of decreasing free energy, and the corresponding equilibrium is as shown in Figure 26*b*. If, however, the free energy of

TABLE X

System	Phases in equilibrium with divalent metal		Remarks
	Phase richest in transitional metal	Other phases	
Al-Cr-Zn	$CrAl_4$	$CrAl_7$	Cr_2Al_{11} is not observed above 50% of Zn.
Al-Mn-Zn	MnAl	$MnAl_3$	Phases less rich in Mn enter into equilibrium with α.
Al-Co-Zn	CoAl	Co_4Al_{13}, Co_2Al_9	Co_2Al_5 does not appear in Zn-rich alloys.
Al-Ni-Zn	Ni_2Al_3	$NiAl_3$	A ternary compound occurs but not in equilibrium with Zn.
Al-Co-Mg	CoAl	Co_2Al_5, Co_4Al_{13}	Co_4Al_{13} and Co_2Al_9 occur in equilibrium with Al-Mg intermediate phases and with α.

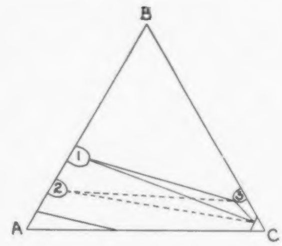

FIGURE 25. Ternary system with compounds between A and B, and C and B.

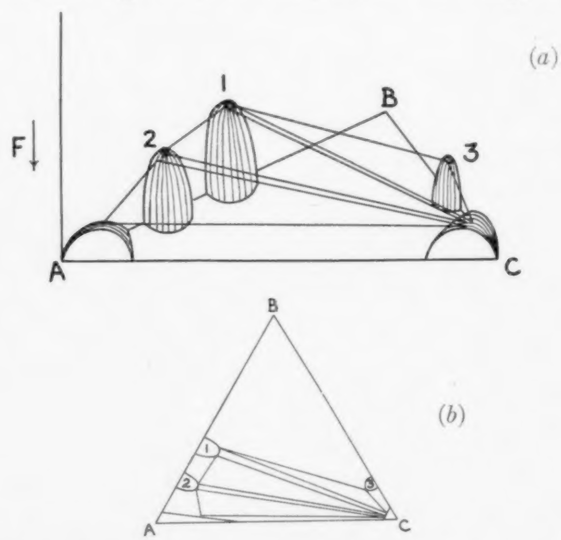

FIGURE 26. (*a*) Free energy diagram; free energy of phase 1 lower than that of phase 2. (*b*) Corresponding isothermal diagram.

compound 2 is markedly lower than that of compound 1, this form of equilibrium is no longer appropriate, since, as shown in Figure 27*a*, a "valley" *ef* may be introduced in the envelope of tangent planes so that it is no longer everywhere convex in the direction of decreasing free energy. Over a large composition range a lower free energy could be achieved by allowing compound 2 to come into equilibrium with 3 and *C*, as shown in Figure 27*b*. In our alloys, therefore, the divalent metal and its neighbouring compound will tend to enter into

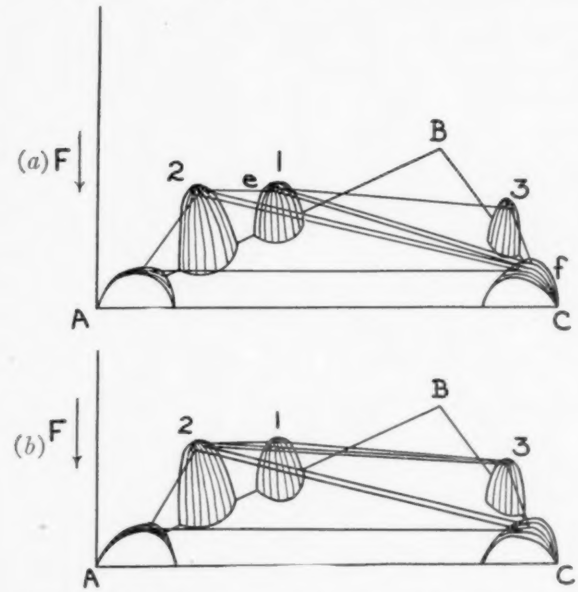

FIGURE 27. (*a*) Inappropriate free energy diagram for free energy of phase 2 less than that of phase 1. (*b*) Appropriate free energy diagram for free energy of phase 2 less than that of phase 1.

equilibrium with the phase of lowest free energy in the aluminium-transitional metal system. As noted above, the heat of formation may be taken as a rough measure of the free energy. Heats of formation are available for the systems Al-Fe, Al-Co and Al-Ni [30] and are shown graphically in Figure 28.* For Al-Co and Al-Ni the heats of formation rise to a maximum at the compositions CoAl and NiAl; by contrast, in the Al-Fe system, $FeAl_3$ has the highest heat of formation. We may thus understand why no phases richer in iron than $FeAl_3$ enter into equilibrium with zinc in the Al-Fe-Zn system, and why CoAl appears in equilibrium with zinc or magnesium in the appropriate ternary systems. Similar considerations probably apply to the systems Al-Cr-Zn

*The phase Co_4Al_{13} is not represented by a point in Figure 28*b*. Its heat of formation may be assumed to be intermediate between those of Co_2Al_9 and Co_2Al_5.

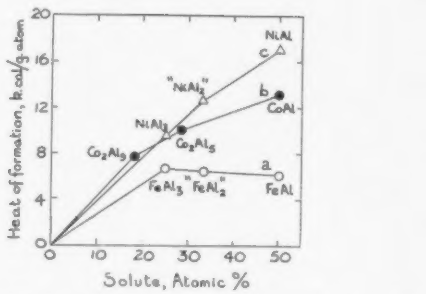

FIGURE 28. Heats of formation in systems (*a*) Al-Fe, (*b*) Al-Co, (*c*) Al-Fe.

and Al-Mn-Zn, but detailed discussion in the absence of thermal data is premature.

In the system Al-Co-Zn, equilibrium between CoAl and zinc implies that Co_2Al_5, Co_4Al_{13} and Co_2Al_9 should also appear in zinc-rich alloys. The non-appearance of Co_2Al_5 in equilibrium with zinc thus requires discussion. Elimination of this phase from the equilibria involving zinc requires equilibrium between Co_4Al_{13} and CoAl, and it is probable that this arises from differing zinc solubilities in the binary Al-Co phases, as indicated in Figure 29.

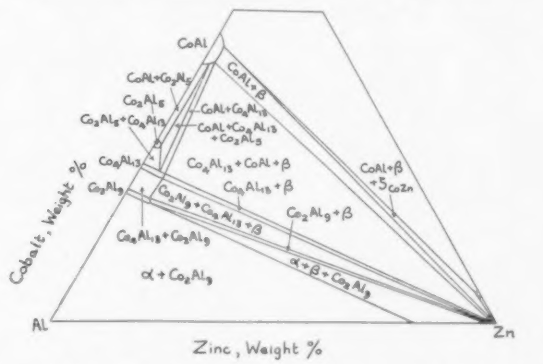

FIGURE 29. Elimination of Co_2Al_5 from Zn-rich equilibria: diagrammatic.

In spite of its maximum heat of formation, NiAl does not appear in equilibrium with zinc. In this case a ternary compound intervenes and the simple free energy considerations outlined above require modification. In the absence of ternary compounds, however, the general form of the constitutional diagrams investigated may be understood.

(*b*) *Conditions for Ternary Compound Formation*

Information from the present and previous work with regard to ternary compounds which exist in equilibrium with α is summarized in Table XI. As previously discussed, extensive solubility of a third metal in the most aluminium-rich phase formed by aluminium and the second solute makes conditions

TABLE XI

Ternary compounds observed		No ternary compounds but extensive solubility in binary compound	No ternary compounds observed	
Al-Cr-Si	Al-Fe-Cu	Al-Co-Si	Al-Cr-Cu	Al-Ni-Si
Al-Cr-Mg	Al-Fe-Si	Al-Co-Ni	Al-Cr-Ni	Al-Ni-Mg
Al-Mn-Cu	Al-Fe-Ni	Al-Fe-Mn	Al-Cr-Zn	Al-Ni-Zn
Al-Mn-Si	Al-Co-Cu	Al-Fe-Co	Al-Fe-Mg	Al-Fe-Ag
Al-Mn-Ni	Al-Ni-Cu	Al-Fe-Cr	Al-Fe-Zn	Al-Fe-Cd
Al-Mn-Mg	Al-Mn-Be		Al-Co-Mg	Al-Mn-Ag
Al-Mn-Zn	Al-Fe-Be		Al-Co-Zn	Al-Mn-Cd

unfavourable for ternary compound formation. Where such solubility does not occur, it is of interest to consider the main factors which may affect the formation of ternary phases.

(i) *Atomic size relationships.* The closest distances of approach of atoms in the crystals of the elements included in Table XI are shown in Figure 30. Con-

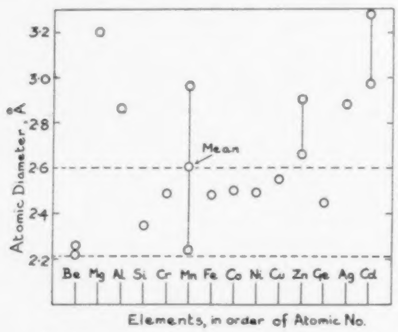

FIGURE 30. Atomic diameters of metals involved in Table XI.

sidering first alloys formed by aluminium, iron and a third metal, the atomic diameters of third metals which give rise to ternary compounds lie within a relatively narrow zone, embracing beryllium at the lower limit of atomic size; the upper limit appears to lie between the atomic diameters of zinc and copper. For ternary alloys containing aluminium and manganese, the upper limit is displaced to include zinc and magnesium, but not cadmium. The fact that silver forms no ternary compound is probably connected with the large size of its ion, which is only slightly less than that of the atom; zinc and cadmium correspond with considerably more "open" structures. According to present data, a similar zone of atomic diameters applies to ternary alloys with aluminium and chromium, except that copper and nickel, for a reason at present obscure, do not lead to ternary compound formation. Passing to alloys containing aluminium and cobalt or nickel, the only elements giving rise to ternary compounds are copper and manganese. No ternary phases occur with silicon or zinc; the range of atomic sizes for the third metal favourable to ternary compound formation thus appears very restricted.

Though exceptions occur, there appears to be a distinct tendency for ternary compound formation in ternary systems of the type considered to be restricted to cases where the atomic diameter of the third element lies within a range of values, which diminishes in extent as the atomic number of the transitional metal increases.

(ii) *Free energy considerations.* The range of favourable atomic sizes for the third metal diminishes for alloys containing cobalt and nickel. In this connection it should be noted that it is in the Al-Co and Al-Ni systems that the highest heats of formation are observed for the binary phases which occur in equilibrium with aluminium:

$FeAl_3$	6.5 kcal/g. atom	
Co_2Al_9	7.7	,,
$NiAl_3$	9.5	,,

Although it is not possible to assess the probable free energy of a hypothetical ternary compound, it is clear that, for a ternary phase of given composition and free energy, the likelihood of its appearance in the equilibrium diagram depends entirely on the relative free energies of the binary phases of comparable solute concentration. Thus, in Figure 31*a* the ternary phase T comes into equilibrium with solvent A; in Figure 31*b* the free energy of A_xB_y

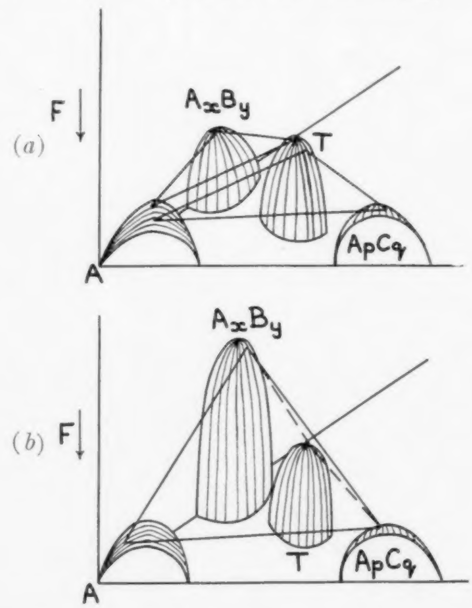

FIGURE 31. Hypothetical free energy diagrams (*a*) for ternary compound formation, (*b*) for no ternary compound formation.

VOL. 1 1953

has been lowered, and T no longer takes part in the equilibria because its free energy is higher than that of a mixture of A_xB_y and A_pC_q. It is probable that the relatively high heats of formation of Co_2Al_9 and $NiAl_3$ are responsible in this way for the small number of aluminium-rich ternary phases observed in systems containing these phases, and hence for the narrowing of the zone of atomic diameters favourable for ternary compound formation. Only ternary phases of very low free energy, such as those formed by third elements of very favourable atomic diameter, would be expected to occur. If it may be assumed that the heats of formation of the most aluminium-rich binary phases continue to fall on passing from the Al-Fe to the Al-Mn system, the relatively large number of ternary phases formed by aluminium, manganese and a third metal may be understood.

In summary, it may be suggested that aluminium-rich ternary compound formation in a system Al-X-Y, where X is a transitional metal of the first long period of the periodic table, depends upon three main factors:

1. The atomic diameter of Y should lie within a comparatively narrow zone of values, the width of which depends on the nature of X.
2. The heats of formation of the aluminium-rich binary phases should not be sufficiently high to prevent the appearance as a stable constituent of any ternary phase which may tend to form.
3. If factors involved in (1) and (2) are favourable, the composition of the ternary compound formed is expected to be controlled mainly by electronic factors, as previously discussed [1].

(c) Solubilities of Third Metals in Co_2Al_9

Characteristic differences in the mode of solution of nickel, silicon, zinc and magnesium in Co_2Al_9 are apparent. Nickel replaces cobalt atoms, and the electron:atom ratio, calculated assuming effective valencies of -0.61 and -1.71 respectively for Ni and Co, rises from 2.125 to 2.285. Silicon up to a solubility of 4.5 at. per cent, behaves similarly. Zinc dissolves in such a way as to preserve an approximately constant electron: atom ratio, and so must replace both cobalt and aluminium. The initial magnesium solubility is such that magnesium replaces only aluminium, and the electron: atom ratio falls (see Figure 14). This behaviour may be correlated with the relative atomic diameters, which are given below in kX units:

Al	Co	Ni	Si	Zn	Mg
2.858	2.499	2.49	2.346	2.659	3.191

Easy replacement of cobalt by nickel, of very similar atomic size, would be expected, as observed. Silicon is also able to replace cobalt without the development of too much strain, but neither nickel nor silicon would be expected to replace the large aluminium atom. Zinc, with an atomic diameter intermediate between those of cobalt and aluminium, will clearly be less easy to substitute for cobalt than is the case for silicon; a compressive distortion will be set up, which may be relieved if at the same time some aluminium atoms are also replaced by zinc. In the case of the large magnesium atom, replacement of the small cobalt atom would be most improbable, and only aluminium can be replaced. As indicated in Table VI, the cobalt content of Co_2Al_9 containing magnesium begins to rise above that corresponding to replacement of aluminium by magnesium; this could be interpreted as due to the development of vacant sites in order to relieve the strain caused by the large magnesium atoms.

(d) Transitional Metals in Zinc-Rich Alloys

New information is available with regard to zinc-rich compounds with transitional metals. As described in sections V and VI, the zinc-rich limits of the Fe-Zn and Co-Zn phases correspond closely with the compositions $FeZn_{12}$ and $CoZn_{11.35}$. Assuming the results of Heumann [31] for Cr-Zn alloys, and of Schramm for Ni-Zn [17] and Mn-Zn [32] alloys, the formulae representing the most zinc-rich phases in the five systems are:

$$CrZn_{15},\quad MnZn_{13},\quad FeZn_{12},\quad CoZn_{11.35}\quad NiZn_9.$$

It is significant that this series shows the same tendency for the number of non-transitional atoms per transitional metal atom to decrease on passing from Cr to Ni as is shown by the corresponding series of Al-rich compounds, with the exception of $FeAl_3$:

$$CrAl_7,\quad MnAl_6,\quad (FeAl_3),\quad Co_2Al_9,\quad NiAl_3.$$

The behaviour is less regular, but the data suggests there may again be a tendency for the transitional metal to act as if it had an effectively negative valency, increasing numerically from Ni to Cr, so that, by a decrease in the number of zinc atoms per transitional metal atom as the effective negative valency of the latter decreases, the electron:atom ratio of the most zinc-rich phase is prevented from rising steeply.

Acknowledgement

This research forms part of a general programme in progress in the Metallurgy Department of the

University of Birmingham, and the authors' thanks are due to the late Professor D. Hanson for his interest. The authors must also acknowledge the careful analytical work of Messrs. Johnson, Matthey and Company, Ltd.

The authors also express their gratitude to the Department of Scientific and Industrial Research, the Royal Society, The Chemical Society and Imperial Chemical Industries, Ltd., for financial assistance which has greatly assisted the work.

References

1. Pratt, J. N. and Raynor, G. V. Proc. Roy. Soc., **A205** (1951) 103.
2. Harding, A. R. and Raynor, G. V. J. Inst. Metals, **80** (1951–52) 435.
3. Raynor, G. V. and Wakeman, D. W. Proc. Roy. Soc., **A190** (1947) 82.
4. Little, K., Axon, H. J. and Hume-Rothery, W. J. Inst. Metals, **75** (1948) 39.
5. Wakeman, D. W. and Raynor, G. V. J. Inst. Metals, **75** (1948) 146.
6. Barrick, M. and Hanemann, H. Aluminium, **20** (1938) 533.
7. Raynor, G. V. and Pfeil, P. C. L. J. Inst. Metals, **73** (1947) 397.
8. Raynor , G. V. and Pfeil, P. C. L. J. Inst. Metals, **73** (1947) 609.
9. Bradley, A. J. and Taylor, A. Proc. Roy. Soc., **A166** (1938) 353.
10. Raynor, G. V. Inst. Metals Annotated Equilibrium Diagram Series, no. 1 (1943).
11. Raynor, G. V. Inst. Metals Annotated Equilibrium Diagram Series, no. 5 (1945).
12. Archer, R. S. and Fink, W. L. Trans. A.I.M.E., Inst. Metals Div. (1928) 616.
13. Losana, L. Alluminio, **9** (1940) 8.
14. Bückle, H. Metallforschung, **1** (1946) 43.
15. Raynor, G. V. Inst. Metals Annotated Equilibrium Diagram Series, no. 8 (1951).
16. Schramm, J. Z. Metallk. **30** (1) (1938) 10.
17. Schramm, J. Z. Metallk., **30** (1) (1938) 122, 327.
18. Cramer, E. M., Nielsen, H. P., and Schonfield, F. W. Light Metal Age, **5** (1947) 6.
19. Mondolfo, L. F. Metallography of Aluminium and Its Alloys (New York, John Wiley and Sons, 1943).
20. Fuss, V. Dissertation, Berlin, 1922.
21. Mayer, A. Gazz. chim. ital., **70** (1944) 55.
22. Schramm, J. Z. Metallk., **29** (7) (1937) 222.
23. Montoro, V. Ricerca Sci., (ii), **8** (1937) 449.
24. Schramm, J. Z. Metallk., **30** (4) (1938) 131.
25. Götzl, F., Halla, F., and Schramm, J. Z. Metallk., **33** (1941) 375.
26. Fuss, V. Z. Metallk., **16** (1924) 24.
27. Bradley, A. J. and Taylor, A. Phil. Mag., **23** (1937) 1049.
28. Bradley, A. J. and Cheng, C. S. Z. Kristallogr. **99** (1938) 480.
29. Raynor, G. V. and Frost, B. R. T. Proc. Roy. Soc., **A203** (1950) 132.
30. Kubaschewski, O. and Evans, E. Ll. Metallurgical Thermochemistry (London, Butterworth-Springer, Ltd., 1951).
31. Heumann, T. Z. Metallk., **39** (1948) 45.
32. Schramm, J. Z. Metallk., **32** (1940) 399.

THE INFLUENCE OF COLD WORK AND RADIATION DAMAGE ON THE DEBYE TEMPERATURE OF COPPER*

D. BOWEN and G. W. RODEBACK†

Copper wires have been cold-worked or subjected to radiation damage. Simultaneous measurements of resistance have been made on a damaged wire and a well-annealed wire. The resistance measurements are made over the temperature range from 4.2°K to 77°K. The differing behavior of the temperature–dependent portions of the resistivities of the two wires has been interpreted as a decrease of Debye temperature in the damaged sample. The maximum change observed is 45°. The thermal annealing of this change has been followed. Some thermodynamic implications of these changes are suggested.

L'INFLUENCE DE L'ÉCROUISSAGE ET DU DÉGÂT DÛ À LA RADIATION SUR LA TEMPÉRATURE DE DEBYE DU CUIVRE

Des fils de cuivre ont été écrouis ou soumis à la destruction par irradiation. Des mesures de résistance, dans un intervalle des températures de 4,2°K à 77°K, ont été effectuées simultanément sur un fil endommagé et un fil bien recuit. Le comportement différent des parties dépendant de la température, de la résistivité des deux fils, a été interprété comme un abaissement de la température de Debye dans l'échantillon endommagé. Le changement maximum observé est de 45°. L'atténuation de ce changement par recuit thermique a été suivi. Certaines implications thermodynamiques relatives à ces changements sont suggérées.

DER EINFLUSS VON KALTBEARBEITUNG UND STRAHLUNGSSCHÄDIGUNG AUF DIE DEBYE-TEMPERATUR DES KUPFERS

Kupferdrähte wurden kalt bearbeitet oder Strahlungsschädigung unterworfen. Der Widerstand eines beschädigten und eines gut ausgeglühten Drahtes wurde gleichzeitig gemessen und zwar in einem Temperaturbereich zwischen 4.2°K und 77°K. Das unterschiedliche Verhalten der temperaturabhängigen Anteile der Widerstände der beiden Drähte wurde als eine Abnahme der Debye Temperatur der beschädigten Probe gedeutet. Der grösste beobachtete Unterschied betrug 45°. Das thermische Ausheilen dieses Unterschiedes wurde verfolgt. Einige thermodynamische Folgerungen dieser Erscheinungen werden angezeigt.

Introduction

The strains in a metal that result from plastic deformation or radiation damage will generally result in a change in the spectrum of lattice oscillations of the solid. Macroscopically this may appear as a change in the elastic moduli. These modal changes will alter the thermodynamic behavior of the material. If the spectrum of lattice oscillations is shifted to lower frequencies, then the specific heat at low temperatures will be larger, and the internal energy and entropy will be altered accordingly. A Debye model can be used as a first approximation to the thermodynamic changes to be expected. For small variations, the change in thermodynamic variables will then be proportional to the change in Debye temperature.

In order to investigate this possibility of Debye temperature change direct comparison of the low temperature resistivities of an annealed copper specimen, and a similar specimen irradiated with alpha particles or cold-worked has been made. By means of this comparison the increment of Debye temperature, $\Delta\theta$, corresponding to the new state of the copper is deduced in terms of the conductivity theory of Gruneisen.

Experimental Procedure

The objective of the experiment is to obtain resistivity measurements as a function of temperature on two samples of the same material, but with differing lattice perfection, with sufficient precision that any difference in their behavior will be easily detectable. This objective is realized by making simultaneous measurements on the two samples while they are maintained at as nearly the same constant temperature as possible. This direct comparison eliminates the necessity of accurate absolute temperature measurements. The resistances are compared by means of a differential resistance bridge, Figure 1. The currents through the samples are maintained constant and equal to 0.02 per cent. When the temperatures of the two are considered equal and unchanging with time the potential across one of them and the difference in potential between the two (terminals A and B in Figure 1) are measured with a potentiometer. By measuring the difference in potential directly the absolute measurement of resistance need not be as accurate for the same precision in the comparison of resistance.

*Received May 22, 1953.

†North American Aviation, Inc., Atomic Energy Research Department, Downey, California.

The specimens are mounted side by side on lavite holders with a platinum resistance thermometer centered between them. The whole assembly is contained in a snug fitting copper box which is suspended in a glass Dewar flask. This flask is partially filled with liquid helium which covers a

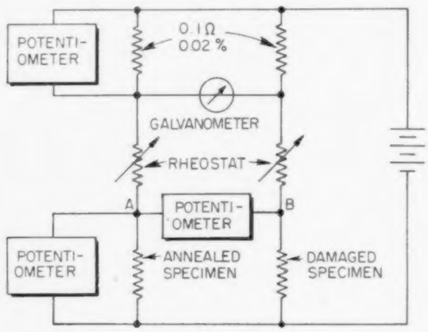

FIGURE 1. Schematic Circuit diagram.

small copper rod suspended from the bottom of the copper box. At the junction of the copper rod and copper box is mounted a 1-watt, 56Ω (room temperature) carbon resistor. Temperatures above 4.2°K are obtained by control of the power dissipated in the carbon resistor, thus maintaining an equilibrium condition between heating and cooling of the copper box. The temperature level can be maintained constant to within 0.01°K.

In all examples to be reported the samples have been wires. In the study of cold work two kinds of wire were used. Johnson Matthey spectroscopically pure copper was cold drawn by hand to 0.0031 inch diameter. In order to insure more nearly uniform cold work, a spool of no. 40 B&S gauge O.F.H.C. copper wire was obtained from the Anaconda Wire and Cable Company. This material was fabricated by continuous cold drawing at a constant rate. The results do not indicate any appreciable differences between the two kinds of samples.

The O.F.H.C. copper was used for the radiation damage studies. In this case the wires were initially annealed for 2 hours at 300°C. After preliminary measurements were made on the two annealed samples one of the samples was irradiated with 15.1μamp hr/cm^2 of 33.6 Mev alpha particles in the 60-inch cyclotron of the University of California at Berkeley. Subsequently, this sample was stored in liquid nitrogen to prevent annealing of the induced radiation damage. A second pair of samples was given as nearly the same treatment as was feasible. These latter results will not be reported in detail. The resistivity measurements for this pair agree with those for the first pair described to the accuracy with which the radiation exposures were equivalent.

The measurements of resistivity were made on the initially damaged materials, and then repeated at successive stages in the thermal annealing of the damage. Since the thermal inertia of the samples is small it is possible to get well-defined thermal histories by annealing them in constant temperature liquid baths. The reference or comparison samples remain unchanged during the anneal. For the cold-worked O.F.H.C. copper the reference was another O.F.H.C. copper wire as drawn. For the cold-worked Johnson Matthey copper wire the reference was another cold-drawn Johnson Matthey wire. For the radiation damage the reference was an annealed (300°C for two hours) O.F.H.C. wire.

The influence of damage on the resistivity is twofold. The most pronounced effect is the increase of residual resistivity. One can attribute this increase to the fixed scattering centers introduced by the damage. A study of the annealing of residual resistivity introduced by cold work has been made [1]. The general shape of the temperature dependent portion of the resistivity curves that we find are in agreement with those found by many previous investigators. A detailed comparison, however, shows that in each case the more heavily damaged sample has a resistivity that increases more rapidly with temperature than the one with which it is being compared.

The Debye Analysis

Let us accept, as suggested in the introduction, that the temperature-dependent portion of the resistivity is altered because of a change in the spectrum of lattice oscillations, perhaps arising from lattice strains. The change in Debye temperature provides a convenient measure of the magnitude of this spectrum change. One may hope that this approximate model will provide an accurate description of the changes that take place. The basis for this hope is the requirement that the Debye theory predict only the difference in resistivity between two nearly equivalent samples, but not the absolute resistivity of either of them. A formula [2] due to Gruneisen provides the connection between resistance and Debye temperature. It is

$$(1)\quad \frac{\rho(T) - \rho(0)}{\rho(\infty)} = \frac{4T^5}{T_\infty \theta^4} \int_0^{\theta/T} \frac{x^5\, dx}{(e^x - 1)(1 - e^{-x})},$$

where θ is the Debye temperature, $\rho(T)$ is the resistance at temperature T, $\rho(\infty)$ is the resistance at temperature T_∞ and $T_\infty \gg \theta$, and $\rho(0)$ is the residual resistance. A more elaborate formula due to Sondheimer [3] has also been used. The results are nearly identical with those obtained with the simpler formula. A suitable combination of resistances to determine the difference in Debye temperature between samples is

$$(2) \quad \frac{[\rho(T_1, \theta_1) - \rho(0, \theta_1)][\rho(T_2, \theta_2) - \rho(0, \theta_2)]}{[\rho(T_2, \theta_1) - \rho(0, \theta_2)][\rho(T_1, \theta_2) - \rho(0, \theta_2)]} = f,$$

where $\rho(T, \theta)$ is the resistance at temperature T for the sample with Debye temperature θ. Using (1) this quantity can be expanded in a Taylor's series in the difference in Debye temperature to give to first order in $\Delta\theta$

$$(3) \quad (f - 1) = \Delta\theta \left[\frac{1}{T_2} D(\theta/T_2) - \frac{1}{T_1} D(\theta/T_1) \right],$$

where

$$(4) \quad D(\theta/T) = \frac{d}{d(\theta/T)} \ln \int_0^{\theta/T} \frac{x^5 \, dx}{(e^x - 1)(1 - e^{-x})}.$$

This function has been plotted in Figure 2.

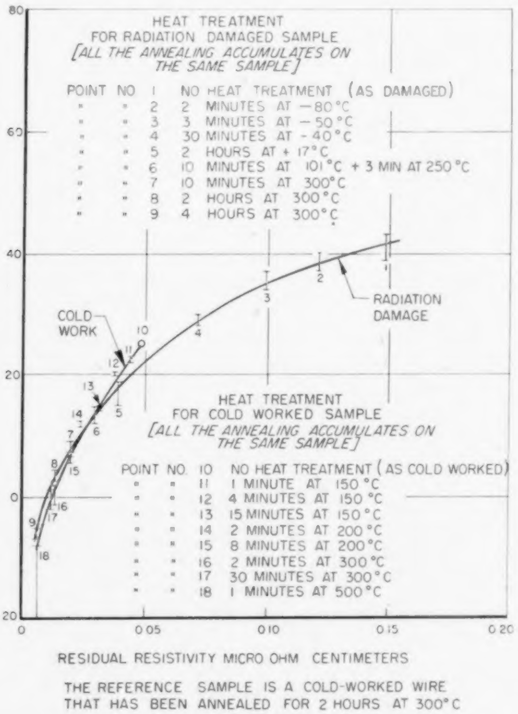

FIGURE 2. Logarithmic derivative of Gruneisen function.

In principle, resistance measurements at any two temperatures and residual resistance will determine the difference in Debye temperature. For maximum accuracy in the determination it is desirable to have the temperatures separated so that the D/T values are appreciably different, and to use as the lower temperature a value such that the resistance there is significantly greater than the residual resistance for each sample. These ideas can be expressed quantitatively in terms of an error equation for $\Delta\theta$. For each determination of $\Delta\theta$ approximately fourteen comparison measurements of resistance are made over the temperature range from 4.2°K to 77.6°K. The $\Delta\theta$ value calculated from each pair of measurements is weighed according to its uncertainty, and an average value, and a standard deviation obtained. The results are shown in Figure 3. The change in theta has

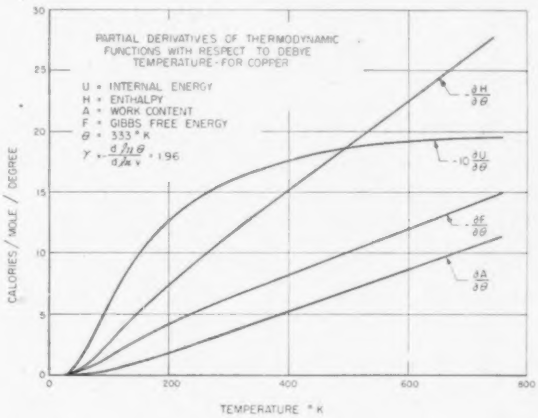

FIGURE 3. Debye temperature change as a function of residual resistivity.

been plotted as a function of the residual resistance with the radiation damage reference sample as an origin for the change. Since the reference samples for the cold work and the radiation damage were different, the origin of the cold work data has been shifted by the difference in Debye temperature between the two reference samples in order to provide easier comparison of the two sets of data. Theta decreases as the damage (residual resistance) increases.

Discussion

It would seem from Figure 3 that the change in Debye temperature is approximately the same function of residual resistivity for both cold work and radiation damage. Through all of this analysis it is assumed that the damage is uniform throughout each sample.

Blackman [4] has emphasized that resistivity depends only on the longitudinal modes, whereas

specific heat depends on both longitudinal and transverse modes. In assuming the damage uniform, one must mean that the lattice defects are distributed at random throughout the entire volume. The resulting strains, however, vary throughout the volume; hence the vibrational pattern undoubtedly also varies throughout the volume. The change in Debye temperature that we derived can at best be a representation of an average modal change. In spite of these reservations it is interesting to compute the thermodynamic implications of the Debye temperature changes. Formulae for the thermodynamic variables as a function of Debye temperature can be found in many texts on statistical mechanics [5]. The derivatives of internal energy, work content, enthalpy and free energy with respect to Debye temperature are shown in Figure 4 as a function

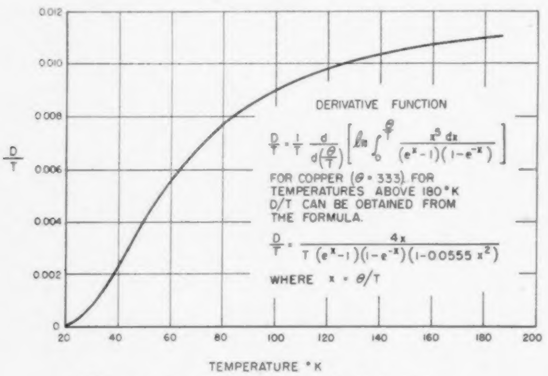

FIGURE 4. Thermodynamic derivatives.

of temperature. The changes in these quantities can be obtained by multiplying the appropriate derivative by the change in Debye temperature. The contribution of zero point oscillations has been ignored.

The Debye temperature changes are negative; hence, the internal energy is larger in the damaged than in the undamaged sample. This additional energy arises because of the larger specific heat in the damaged sample. Attempts have been made to measure the energy stored in cold-worked copper [6]. These measurements have yielded values of about 35 calories per mole when measured at temperatures in the neighborhood of 450°K. At this temperature the energy stored in lattice oscillations for a measured Debye temperature change of 25 degrees (the change attributable to this annealing) is 45 calories per mole. These calculations are crude, but they indicate that a major fraction of the stored energy may be in lattice oscillations.

The calculations on enthalpy and free energy imply a knowledge of the elastic stresses in the material. These are a complex function of position in the damaged material, and the single parameter of Debye temperature change is certainly inadequate to give this complete description. If it were known that the damage produced only a single type of lattice stress (clearly an oversimplification), and the Debye temperature change per unit of this stress were known, then the amount of elastic work for a given Debye temperature change and temperature could be calculated. The enthalpy and free energy were calculated on just this basis. The only stress for which the Debye temperature change is known is a pure compression [7]. The coefficient of Debye temperature change with volume that was used was

$$\gamma = -\frac{d\ln\theta}{d\ln v} = 1.96$$

This value is not measured directly, but is computed from the compressibility, the thermal expansion coefficient, the density, and the specific heat. From the measured Debye temperature change the equivalent pressure-volume change was computed, and this used in the enthalpy, and free energy in lieu of the more detailed stress distribution.

It is interesting to note that the work content decreases on damage, whereas the free energy increases. Thus, the elastic work must be included as an essential part of any thermodynamic treatment that is to predict even as simple a bit of information as the relative thermodynamic stability of two states. The enthalpy change increases with temperature because of an increase of the elastic work. The origin of this latter increase may be found in the nonisotropic thermal expansion around a lattice defect giving rise to temperature-dependent elastic strains. If this concept be valid then the thermal annealing of lattice defects may take place in part when an internal stress has a component in excess of the critical stress in that direction.

Acknowledgments

The authors are indebted to Mr. Haruo Hori and Mr. Desmond McClelland for making the many measurements, to Mrs. Ethel Gould for a variety of computing assistance, and to Mr.

Bert Harwick for planning and supervising the irradiations. This work is based on studies conducted for the Atomic Energy Commission under contract AT-11-1-GEN-8.

References

1. Bowen, D., Eggleston, R. R. and Kropschot, R. H. J. Appl. Phys. **23** (1952) 630.
2. Gruneisen, E. Ann. d. Phys. **16** (1933) 530.
3. Sondheimer, E. H. Proc. Roy. Soc. **A203** (1950) 75.
4. Blackman, M. Proc. Phys. Soc. **A64** (1951) 681.
5. Tolman, R. C. Statistical Mechanics (Oxford, University Press, 1938).
6. Quinney, H. and Taylor, G. I. Proc. Roy. Soc. **A163** (1937) 157.
7. Handb. d. Phys. **24**, 12 (1933) 677.

TENSILE DEFORMATION OF HIGH-PURITY COPPER AS A FUNCTION OF TEMPERATURE, STRAIN RATE, AND GRAIN SIZE*

R. P. CARREKER, Jr. and W. R. HIBBARD, Jr.†

True stress, true strain data are presented for 99.999 per cent copper wire specimens tested over the range 20° to 1223°K (0.015 to 0.905 T/Tm). Five different grain sizes ranging from 0.012 to 0.090 mm diameter were studied. The effect of rate was investigated by rate-change tests over the same ranges of temperature and grain size.

LA DÉFORMATION À L'EXTENSION DU CUIVRE DE HAUTE PURETÉ, EN FONCTION DE LA TEMPÉRATURE, DE LA VITESSE DE DÉFORMATION ET DE L'ÉTENDUE DE DE LA DÉFORMATION

Des données sur les vraies tensions et les vraies déformations sont présentées pour des éprouvettes de fil de cuivre 99,999 pour cent pur, essayées dans l'intervalle des températures de 20°K à 1223°K (le rapport T/Tm variant de 0,015 à 0,905). Cinq dimensions différentes des grains, allant de 0,012 à 0,090 mm de diamètre, ont été étudiées. L'effet de la vitesse a été investigué au moyen d'essais à des vitesses différentes, dans le même intervalle des températures et pour les mêmes dimensions des grains.

DIE ZUGVERFORMUNG VON REINSTKUPFER ALS EINE FUNKTION VON TEMPERATUR, GESCHWINDIGKEIT UND AUSMASS DER DEHNUNG

Wahre Spannung und wahre Dehnungsdaten werden für 99.999 prozent reiner Kupferdrähte in einem Temperaturbereich von 20°K bis 1223°K (0.015 bis 0.905 T/Tm) angegeben. Fünf verschiedene Korngrössen, von 0,012 bis 0,090 mm Durchmesser, wurden untersucht. Der Effekt der Geschwindigkeit wurde durch Versuche mit verschiedener Zuggeschwindigkeit im gleichen Temperaturbereich und mit gleicher Korngrösse untersucht.

Introduction

This paper represents the results of an experimental program designed to establish the effect of temperature, strain rate, and grain size upon the tensile deformation of high-purity copper. It is part of a continuing program whose objective is to document the deformation behavior of pure metals over a range of temperature encompassing, in so far as is feasible, their entire solid range. Additional reports of both creep and tensile properties of pure metals are in preparation. Such information is needed to provide a base point for intelligent alloy design and to establish a phenomenological framework to which deformation theories must conform. Accordingly, the tests and analyses of this investigation extend considerably beyond conventional engineering practice.

Material

Copper, whose purity is reported to be 99.999 per cent, was obtained from the American Smelting and Refining Company. Table I presents the nominal analysis reported by A. S. and R. The copper was swaged and drawn at room temperature from 0.362-inch-diameter rod to 0.030-inch-diameter wire without intermediate annealing. All test samples were cut from the 30-mil wire.

TABLE I
ANALYSIS OF A.S. AND R. COPPER

Element	Maximum percentage	Element	Maximum percentage
Fe	0.00007	As	0.0002
Sb	0.0001	Cr	0.00005
Pb	0.0001	Si	0.00001
Sn	0.0001	Te	0.0002
Ni	0.0001	Se	0.0001
Bi	0.00001	S	0.0001
Ag	0.00003		

Seven-inch lengths of cold-drawn wire were annealed for one hour at selected temperatures: 250°, 350°, 550°, 750°, and 950°C. The 250°C anneals were made in an air atmosphere. All other anneals were made in a hydrogen atmosphere. Figure 1 shows the microstructures produced by these treatments. X-ray analysis showed that all annealing treatments produced a similar texture, a poorly defined combination of [100] and [111] in the wire axis, with a lot of randomness.

Testing Procedure

All tensile tests were made by the use of the Instron tensile-testing machine, Model TT-B, shown in Figure 2. This machine imposes a selected constant rate of head motion and measures the force exerted on the specimen by means of an SR-4 gage attached to an elastic weigh-bar. The

*Received June 4, 1953.
†General Electric Research Laboratory, The Knolls, Schenectady, New York, U.S.A.

(1)

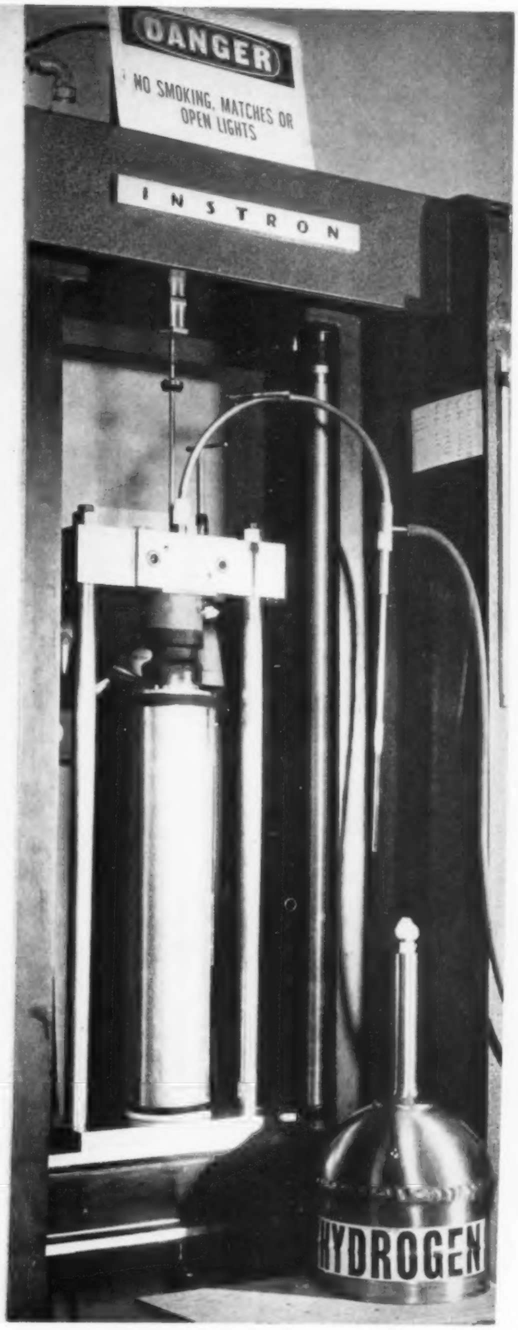

(2)

PLATE I. Figure 1—Micro-structures of high-purity copper developed by annealing one hour at 250°, 350°, 550°, 750° and 950°C after 99.5 per cent cold reduction by swaging and drawing. Average grain diameters, .012, .015, .030, .045 and .090 mm respectively (100×, reduced to three-quarters in reproduction). Figure 2—Instron tensile testing machine, as used for tests in liquid hydrogen bath (−253°C).

use of interchangeable weigh-bars and amplification factors permits a wide choice of sensitivities to be used in automatically recording load as a function of time. The accurate control of head speed and chart speed, characteristic of the Instron machine, and the use of a wire specimen, permits time to be a measure of strain, thus avoiding the use of an extensometer. A mechanical gear shift permits almost instantaneous ten-to-one changes in head speed.

Five-inch gage length specimens were successfully gripped between grooved plates. All tests which were made in baths utilized the compression fixture shown in Figure 3. The fixture is a stainless

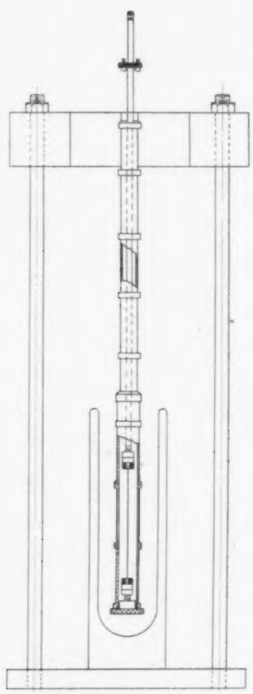

FIGURE 3. Cut-away drawing of compression fixture with specimen and bath in place.

steel tube whose top end is fixed to the moving crosshead through a rigid frame and whose lower end pushes against the bottom specimen grip. The top specimen grip is fastened to a pull rod which extends along the axis of the compression tube and is attached through the weigh-bar to the frame of the machine. Tests made in the furnace utilized the same upper grip and pull-rod arrangement, with the lower pull-rod and furnace attached to the moving lower crosshead.

Temperatures other than atmospheric were achieved by using baths or a furnace. Table II shows the ways in which specific temperatures were obtained. The baths which were not at constant boiling temperatures were mechanically stirred to achieve uniform temperature.

TABLE II

ACHIEVING TEST TEMPERATURES

T°C	T°K	Medium	Temperature measurement
−253	20	Liquid hydrogen	Constant boiling liquid
−195	78	Liquid nitrogen	Constant boiling liquid
−133	140	Freon 11 and 12. Cooled with liquid nitrogen	Cu-constantan thermopile
− 78	195	Dry ice and acetone	Cu-constantan thermopile
0	273	Ice and water	Constant melting solid
27	300	Room	Thermometer
27–127	300–400	Hot silicone oil	Thermometer
>200	>473	Furnace, nitrogen atmosphere	Pt–Pt Rh thermocouple

All test data were reduced to true stress and true plastic strain, assuming constant volume during plastic deformation, so that elongation measurements define instantaneous areas. This assumption precludes the analysis of the present data beyond the necking strain, but for wire specimens the uniform strain is virtually total elongation. The several quantities used in the analysis are defined below:

$l_0, l, \Delta l$ = original length, instantaneous length, change in length;

$A_0, A, \Delta A$ = original area, instantaneous area, change in area;

P, S, σ = applied load, engineering stress, true stress;

e, ϵ = engineering strain or elongation, true strain.

$$S = \frac{P}{A_0} \qquad e = \frac{\Delta l}{l_0}$$

$$\sigma = \frac{P}{A} = \frac{P}{A_0}(1+e) \qquad \epsilon = \int_{l_0}^{l} \frac{dl}{l} = \ln(1+e)$$

Test Results

Effect of Temperature

It was desired to study the effect of temperature on the deformation of copper over its entire solid range. However, the significance of tensile tests made at temperatures greatly exceeding the

previous annealing temperature is open to question. The testing program actually performed is perhaps most easily visualized by reference to Figure 4,

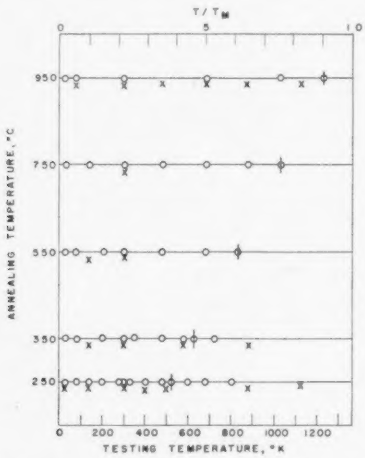

FIGURE 4. Diagram showing the testing program in relation to annealing history, O—standard tensile test, X—change tensile test.

in which each circle represents one or more tests at the temperature indicated and each horizontal row represents specimens having the particular annealing temperatures indicated by the vertical cross-bar. The crosses, displaced slightly downward for clarity, represent tests in which the strain rate was changed during the test in order to determine rate sensitivity.

Figure 5 to 7 show the yield strength (σ at ϵ = .005), tensile strength, and per cent elongation as a

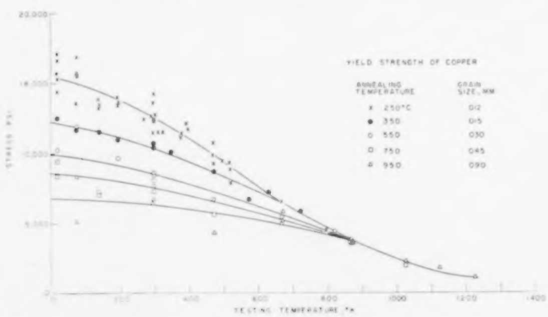

FIGURE 5. Yield strength of copper as a function of temperature for each of several grain sizes.

function of temperature for each of the several grain sizes. Many more tests were made in the 250°C anneal series than in the other series. It offers an indication of the scatter to be expected in a series of nominally identical specimens. The faired curves of Figure 5 are believed to indicate the true effect of grain size on the temperature dependence

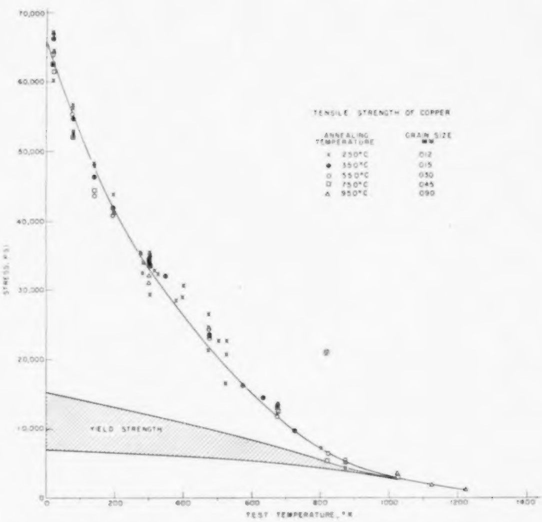

FIGURE 6. Tensile strength of copper as a function of temperature for each of several grain sizes.

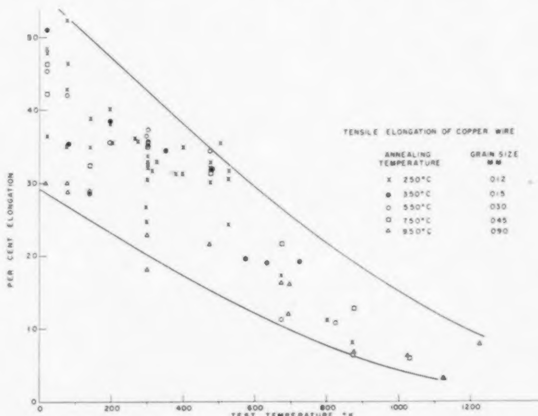

FIGURE 7. Per cent elongation to fracture as a function of temperature for each of several grain sizes.

of the yield stress, despite the very apparent scatter. The effect of grain size on tensile strength, Figure 6, appears to be less than the scatter among specimens of a single grain size. Note that temperature affects the tensile strength to a much greater extent than it does the yield strength, a manifestation of the pronounced effect of temperature on strain hardening. Elongation values, Figure 7, scatter widely, with no apparent effect of grain size. Elongation decreases continuously with temperature, since in these wire specimens the elongation is almost entirely the uniform strain that occurs prior to necking, a quantity directly related to the strain hardening.

Figures 8 to 12 show true stress, true strain curves at several temperatures for each of several grain

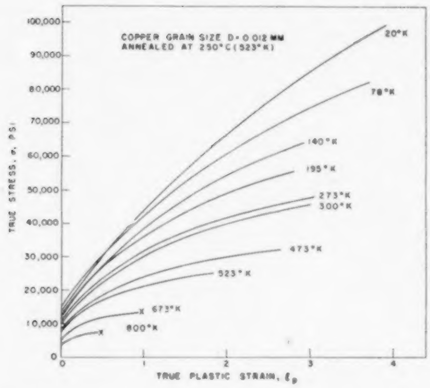

FIGURE 8. True stress, true strain curves at several temperatures for copper annealed at 250°C, grain diameter 0.012 mm.

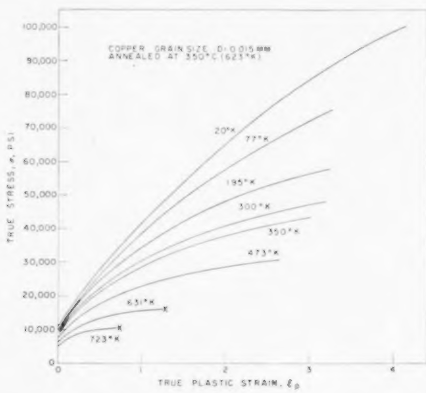

FIGURE 9. True stress, true strain curves at several temperatures for copper annealed at 350°C, grain diameter 0.015 mm.

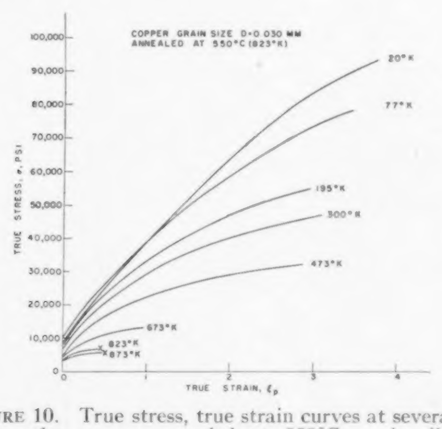

FIGURE 10. True stress, true strain curves at several temperatures for copper annealed at 550°C, grain diameter 0.030 mm.

sizes. Here, again, the great influence of temperature on strain hardening is evident. No evidence of the discontinuous yielding characteristic of impure iron and many other metals was observed at any temperature.

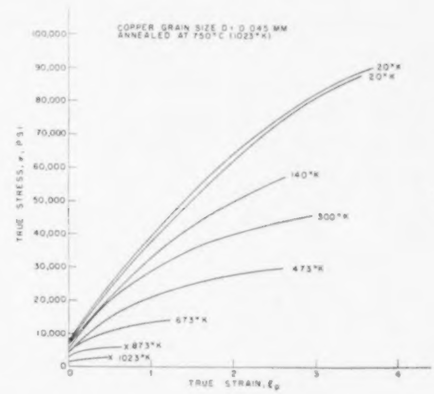

FIGURE 11. True stress, true strain curves at several temperatures for copper annealed at 750°C, grain diameter 0.045 mm.

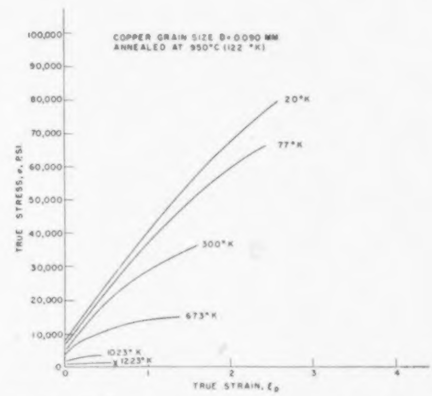

FIGURE 12. True stress, true strain curves at several temperatures for copper annealed at 950°C, grain diameter 0.090 mm.

Figure 13 is a cross-plot of Figure 8, and shows the stress at selected strains as a function of temperature. Note that temperature is more important the larger the strain. Similar graphs may be obtained by cross-plotting the stress-strain curves for other grain sizes.

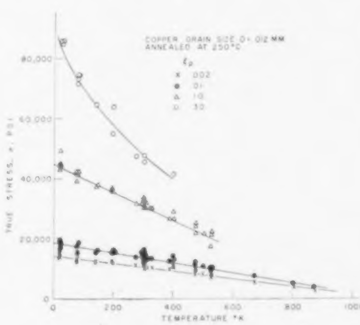

FIGURE 13. Flow stress at selected strains as a function of temperature for copper annealed at 250°C, grain diameter 0.012 mm.

Figure 14 is a logarithmic plot of the true stress, true strain data of Figure 18, selected as typical

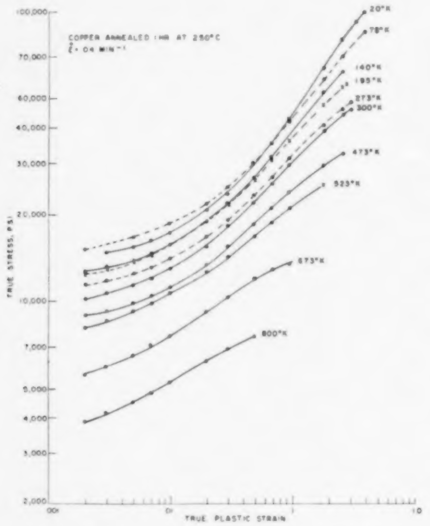

FIGURE 14. Typical logarithmic plot of true stress, true strain (data of Fig. 8).

of the several sets of data when plotted logarithmically. Note that, in general, these curves do not conform to the straight-line relation implied by the equation $\sigma = K\epsilon^m$. However, that relation is a sufficiently good approximation over a limited range of strain to be useful in expressing strain-hardening quantitatively as m, the slope of the log stress, log strain curve. Values of m at the arbitrary strain of 0.1 were determined and plotted in Figure 15 as a function of temperature for each grain size. Both temperature and grain size affect m significantly. A similar plot of m values at a strain of .05 appears virtually the same as Figure 15.

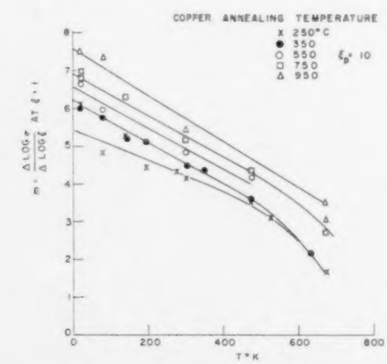

FIGURE 15. Strain-hardening exponent m, from $\sigma = K\epsilon^m$, at $\epsilon = 0.10$, as a function of temperature for several grain sizes.

Effect of Strain Rate

An attempt was made to study the effect of strain rate upon the stress-strain curve of copper as a function of temperature and grain size by straining at selected constant rates covering a factor of one thousand. However, the variation among nominally identical specimens was greater than the effect of strain rate over the range available. This is not to say that the specimens were not reasonably reproducible, but rather that the effect of rate at room temperature and below is very small. This difficulty was circumvented by using a "rate-change" test, in which a rate of .04 min^{-1} was maintained to a strain of approximately .09, where the rate was changed to .004 min^{-1} and the test continued. Thus, a measure of rate sensitivity was obtained using a single specimen. The autographic record allowed very small rate sensitivities to be detected. Rate sensitivity, n, is defined as the ratio of the change in the logarithm of the stress to the change in the logarithm of the strain rate. A detailed analysis of the rate-change test revealed that n is essentially independent of strain, the direction of the rate change, and the absolute values of the rate.

Rate-change tests were made on specimens of each grain size at several temperatures. Typical results, obtained on fine-grained samples, are shown in Figure 16. Fine-grained specimens were

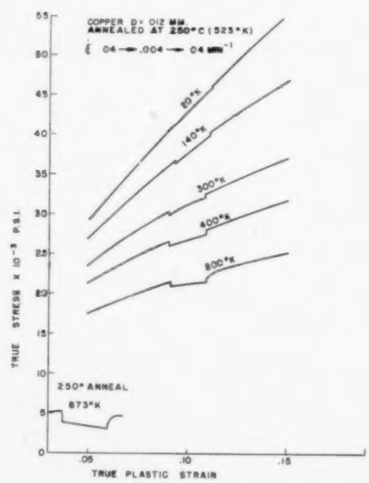

FIGURE 16. Effect of rate changes on the flow curves of copper at several temperatures. Prior anneal at 250°C, grain size 0.012 mm.

more rate-sensitive than coarse-grain specimens, as shown in Figure 17. The strain-rate sensitivity extrapolates to zero at the zero of temperature. The temperature-dependence of the rate sensitivity

is characterized by two regions. At low temperatures, the rate sensitivity is small and increases linearly with the temperature until a critical temperature is reached, above which the rate sensitivity increases markedly with temperature (see Figure 17). This critical temperature corresponds to that above which recovery is apparent in the rate-

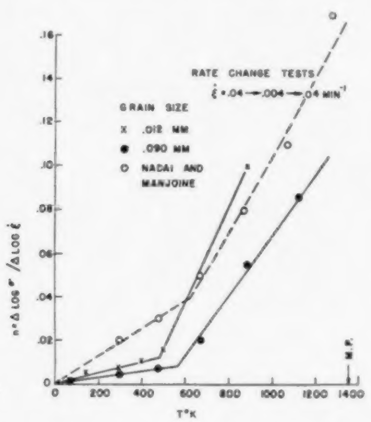

FIGURE 17. Comparison of rate sensitivity determined by rate-change tests with data of Nadai and Manjoine (1) on effect of strain rate on tensile strength.

change test. These results may be compared with those of Nadai and Manjoine [1], who determined the tensile strength of copper (commercially pure, annealed 500°C, five hours) as a function of temperature and strain rate. Qualitatively, the results are similar. The comparatively small quantitative differences are not surprising in view of the differences in material and technique used to evaluate n.

Effect of Grain Size

Some effects of grain size have been presented in the previous sections. Figure 5 effectively demonstrates the influence of grain size on yield strength. The effect is most important at low temperatures and decreases with increasing temperature.

The effect of grain size is most important at small strains, becoming less important with increasing strain. True stress, true strain curves for different grain sizes converge at large strains. Stating the facts more elegantly, the differences in flow stresses are progressively decreased with increasing strain because coarse-grained specimens strain-harden more rapidly than fine-grained specimens. Figure 18 quantitatively demonstrates the effects of grain size on flow stress as a function of strain.

In Figure 18 it is instructive to note some of the details of the dependence of flow stress on strain and grain size at room temperature. The log σ − log d plots for strains of 0.002, 0.01, 0.03, and 0.10 converge to a common point at approximately 1.6×10^{-5}cm. After recognizing the great extrapolation involved, it is interesting that this "convergence diameter" corresponds roughly to Wood's [2] "limiting crystallite size" of 0.7×10^{-5}

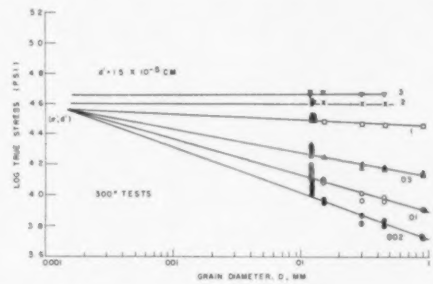

FIGURE 18. Effect of grain size on the flow stress of copper for selected strains at 300°K.

cm for 99.999 per cent copper. At strains larger than 0.10, the flow stress is independent of grain size; the stress level continues to rise with increasing strain, and the plots no longer converge. Wood obtained his "limiting crystallite size" at 8 to 10 per cent reduction by rolling; thereafter, the "crystallite size" alternately decreased and increased as the copper was deformed further.

Consider again the "convergence diameter." Assuming the Frank-Read [3] model of a dislocation generator, it can be shown [4] that the critical stress for the generation of dislocation loops is given by:

$$\tau^* = \frac{Gb}{L} \text{ or, alternatively, } \sigma^* = \frac{Eb}{L},$$

where

σ^* = critical tensile stress,
τ^* = critical shear stress,
E = Young's modulus of elasticity,
G = shear modulus of elasticity,
b = length of Burger's vector,
L = distance between pinning points of dislocation line.

In the present case, E = 16,000,000 psi. Taking b to be one atom spacing, 2.55×10^{-8}cm, and L to be the convergence diameter, 1.6×10^{-5}cm, the critical stress is computed to be 27,500 psi, which agrees with the "convergence stress" of 36,000 psi, within the accuracy of this calculation. The "convergence diameter" and "convergence stress" are consistent with Wood's observations on

"limiting crystallite size" and the "critical stress" defined by a Frank-Read dislocation source of length equal to the "convergence diameter." The authors believe the coincidence to be significant.

Figure 6 shows that variations in grain size have very little effect on the tensile strength of copper. This point is strikingly demonstrated by Figure 19, which plots the tensile strength of

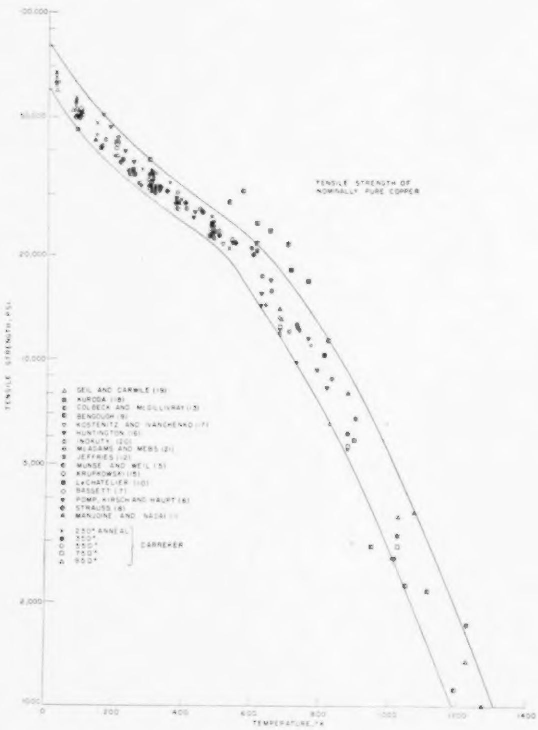

FIGURE 19. Tensile strength vs temperature for nominally pure copper (data from many different sources).

nominally pure copper taken from many literature sources [5–21] as well as from the present investigation. Regardless of minor composition differences and widely different heat treatments and grain sizes, the tensile strength, temperature relation is a narrow band. This results from an inverse relation between yield strength and the strain hardening. Specimens that have low yield strength harden more rapidly than those with high yield strengths, at a given temperature, so that all specimens approach the same flow stress at large strains. The data of Bengough [9] appear to be anomalous in the range from 500° to 750°K probably because of unknown impurities.

Fracture

Figure 7 shows the decrease in per cent elongation to fracture with increasing temperature, a phenomenon closely related to the decrease in strain hardening with increasing temperature. Below a definite high temperature, all fractures were of the typically ductile, necked-down type. Above that temperature, all fractures were of the intergranular type. The maximum temperature for ductile fracture is a function of the grain size (Figure 20). Fine-grained specimens fail inter-

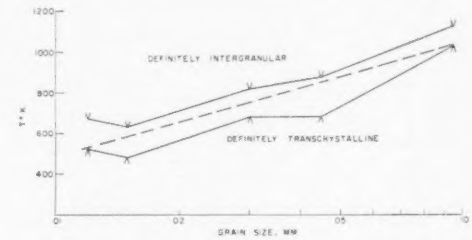

FIGURE 20. Transcrystalline to intergranular fracture transition temperature as a function of grain size.

granularly at a lower temperature than coarse-grained specimens. The crosses terminating some σ-ϵ curves in Figures 8 to 12 indicate intergranular fracture.

Summary

Constant strain-rate tensile tests have been performed on polycrystalline wires of 99.999 per cent copper over a temperature range extending from 20° to 1223°K. Tests were made on five series of specimens, annealed at 250°, 350°, 550°, 750°, and 950°C to produce average grain diameters of .012, .015, .030, .045, and .090 mm. The data are presented as true stress, true strain plots, as well as plots of yield strength, tensile strength, and per cent elongation. These data were analyzed to determine the effect of temperature and grain size on the flow stress at selected strains, the strain hardening, and the fracture characteristics.

Rate-change tests were used to determine the effect of strain rate on the flow stress as a function of temperature and grain size.

It is concluded that:

1. The flow curves (stress-strain) of copper vary regularly over its entire solid range. No discontinuous yielding was noted at any temperature in the range from 0.015 to 0.905 of the absolute melting temperature.

2. The yield strength, tensile strength, and true

flow stress at arbitrary strains extrapolate to finite values at the absolute zero of temperature. There is relatively little dependence of the yield strength on temperature, but there is a marked increase in strain hardening with decreasing temperature, so that the flow stress at large strains and the tensile strength vary markedly with temperature.

3. The effect of grain size on strength is more pronounced at low temperatures. Grain size affects the yield strength markedly, larger grain sizes having lower yield strength. The effect of grain size decreases with increasing strain, so that it exerts little influence on the tensile strength. The tensile strength, temperature relation for nominally pure copper annealed at any temperature that produces recrystallization may be described by a single curve with a 10 per cent scatter band.

4. At 300°K, the flow stress σ at arbitrary small strains is related to the grain diameter d by $\log \sigma = \log B - a \log d$, where "$a$" decreases with increasing strain, so that the straight line plots converge to a common point. The convergence point (σ', d') is consistent with Wood's "limiting crystallite size" for copper and with the critical stress of a Frank-Read dislocation generator of effective length d'.

5. The strain-rate sensitivity n (defined as $n = \Delta\log \text{stress}/\Delta\log \text{strain rate}$) is zero at 0°K, increases linearly with temperature to an inflection point at some critical temperature, and then increases linearly with a much greater slope. The critical temperature corresponds to that temperature where appreciable recovery occurs during the rate-change period. Fine-grained specimens are more rate sensitive than coarse-grained specimens.

6. The uniform elongation that occurs prior to necking increases continuously with decreasing temperature, a logical result of the variation of strain hardening with temperature. The transition temperature from the transgranular, necking type of fracture to the high-temperature, intergranular fracture is a function of grain size. Fine-grained specimens fail intergranularly at lower temperatures than coarse-grained specimens.

Acknowledgments

Many people have contributed in very real ways to this program. The authors wish to acknowledge the help of E. A. Smith, who performed many of the tests; R. W. Powers, who designed the liquid-hydrogen testing arrangement; R. F. Berning, who assisted in developing suitable furnaces, fixtures, and techniques; Miss N. B. Weaver, who performed many calculations and plotted many graphs; and J. H. Hollomon, J. C. Fisher, and J. D. Nisbet, all of whom contributed helpful discussion, criticism, and interest.

The results presented in this paper were obtained in the course of research sponsored by Contract AF 33(038)11773 (Air Force).

References

1. Manjoine, M. J. and Nadai, A. Proc. A.S.T.M. **40** (1940) 822; J. Appl. Mech. **8** (1941) A-77.
2. Wood, W. A. Proc. Roy. Soc. **A172** (1939) 231.
3. Frank, F. C. and Read, W. T., Jr. Carnegie Inst. Tech. and ONR Symposium on Plastic Deformation of Crystalline Solids, Pittsburgh (May 1950) p. 44.
4. Fisher, J. C., Hart, E. W. and Pry, R. H. Phys. Rev. **87** (1952) 958.
5. Munse, W. A. and Weil, N. A. Proc. A.S.T.M. **51** (1951) 996.
6. Pomp, A., Kirsch, A. and Hampt, G. Mitt. Kaiser-Wilhelm Inst. Eisenforsch. Dusseldorf, **21** (1939) 231–241.
7. Bassett, W. H. Discussion to a paper by Price: Symposium on Effect of Temperature on the Properties of Metals. A.S.M.E.-A.S.T.M. joint publication (1931) p. 351.
8. Strauss, Jerome. Trans. Am. Soc. Steel Treating **16** (1929) 191.
9. Bengough, C. D. J. Inst. Metals **17** (1912) 123.
10. Le Chatelier (cited in Reference 9).
11. Bengough, C. D. and Hanson, D. J. Inst. Metals **12** (1914) 57.
12. Jefferies, Zay. Trans. A.I.M.E. **60** (1919) 474.
13. Colbeck, E. W. and MacGillivray, W. E. Trans. Inst. Chem. Engr. (London) **11** (1933) 107.
14. Smith, C. S. Proc. A.S.T.M. (1939) 39.
15. Krupkowski, A. Rev. Metall. **28** (1931) 641; **29** (1932) 74.
16. Huntington, A. K. J. Inst. Metals **8** (1912) 126.
17. Kostenets, V. I. and Ivanchenko, A. M. J. Inst. Techn. Phys. (Russian) **16** (1946) 515.
18. Kuroda, M. Sci. Papers, Inst. Phys. Chem. Research (Tokyo, November 1932) 163.
19. Geil, G. W. and Carwile, N. L. Nat. Bur. Stand. Circ. No. 520 (1952) p. 67.
20. Inokuty, T. Science Reports, Tohoku Imperial University **17** (1928) 817.
21. McAdam, D. J. and Mebs, R. W. Proc. A.S.T.M. **43** (1943) 661.

LOCAL ATOMIC ARRANGEMENTS IN GOLD-NICKEL ALLOYS*

P. A. FLINN†, B. L. AVERBACH‡, and MORRIS COHEN‡

The local atomic arrangements in gold-nickel alloys are determined as a function of composition by observations of diffuse X-ray scattering. Measurements are made at $-190°C$ on alloys quenched from above the solubility gap, there being experimental evidence to show that the high temperature atomic configurations can be retained on quenching. The X-ray data reveal that these alloys exhibit a preference for *unlike* neighbors above the solubility temperature and have short range order analogous to that in copper-gold alloys.

The sizes of the atoms in the solid solutions are also measured from the diffuse scattering. The gold atom in solution is smaller than in the pure metal, but larger than the average atomic dimension calculated from the lattice parameter of the solution. Correspondingly, the nickel atom in solution is larger than in the pure metal, but smaller than the average atomic dimension of the solution. Moreover, the size of each atom varies with the composition of the solution.

LES ARRANGEMENTS ATOMIQUES LOCAUX DANS LES ALLIAGES OR-NICKEL

Les arrangements atomiques locaux dans les alliages or-nickel sont déterminés en fonction de la composition, par l'observation de la dispersion diffuse des rayons X. Des mesures sont effectuées à la température de $-190°C$ sur des alliages trempés en partant d'une region se trouvant au-dessus de la lacune de solubilité, certains résultats expérimentaux indiquant qu'il est possible de retenir par trempe les configurations atomiques qui existent aux températures élevées. Les données obtenues au moyen des rayons X indiquent, qu'au-dessus de la température de solubilité, ces alliages manifestent une préférence pour les voisins dissemblables, et un ordre à petite distance, analogue à celui des alliages cuivre-or.

Les dimensions des atomes dans les solutions solides sont aussi mesurées en partant de la dispersion diffuse. L'atome de l'or est plus petit dans la solution que dans le métal pur, mais plus grand que la valeur moyenne de la dimension calculée à partir du paramètre du réseau de la solution. De même, l'atome de nickel est plus grand dans la solution que dans le métal pur, mais plus petit que la valeur moyenne de la dimension des atomes de la solution. En plus de cela, les dimensions de chaque espèce d'atome varient avec la composition de la solution.

DIE ATOMVERTEILUNG IN GOLD-NICKEL LEGIERUNGEN

Die Nahverteilung der Atome in Gold-Nickel Legierungen wurde als Funktion der Zusammensetzung mit Hilfe von Messungen der diffusen Röntgenstrahlstreuung bestimmt. Die Messungen wurden bei $-190°C$ an Legierungen ausgeführt, die von der Mischungslücke herab abgeschreckt worden waren. Das vorliegende experimentelle Material zeigt, dass die bei hohen Temperaturen vorhandene Atomverteilung beim Abschrecken erhalten bleibt. Die röntgenographischen Daten zeigen, dass diese Legierungen oberhalb der Löslichkeitstemperatur bevorzugt eine Anordnung *ungleicher* Nachbarn bilden und eine den Kupfer-Gold Legierungen entsprechende Näheordnung zeigen.

Ausserdem wurde die Grösse der Atome in den festen Lösungen aus der diffusen Streuung bestimmt. In Lösung ist das Goldatom kleiner als im reinen Metal, aber grösser als die mittleren atomaren Dimensionen, die man mit Hilfe der Gitterkonstanten berechnen kann. Dementsprechend ist das Nickelatom in der Lösung grösser als im reinen Metal aber kleiner als die mittleren atomaren Dimensionen der Lösung. Ausserdem ändert sich die Grösse jedes Atoms mit der Zusammensetzung der Lösung.

1. Introduction

Recent X-ray studies of binary solid solutions have shown that the two types of atoms are seldom arranged in a completely random fashion on the lattice sites [1].§ In alloys which form superlattices, for example Cu_3Au and CuAu, each atom exhibits a preference for unlike nearest neighbors even above the critical disordering temperature. There is also X-ray evidence to indicate that the disordered solid solution in the alloys CuPt and CuAu contains ordered regions which are too small to diffract as a phase, but which have the structure of the lower-temperature superlattice. The order-disorder transformation thus appears rather analogous to a nucleation and growth process in that the ordered phase may grow from ordered nuclei existing in the parent solution. This viewpoint is also consistent with recent observations [2] of two phase regions in alloys on either side of the stoichiometric composition. At the stoichiometric composition, a two-phase region does not appear, such alloys behaving like compounds with metallic binding. The superlattice which develops just below the ordering temperature is, however, imperfectly ordered, even after

*Received June 19, 1953. This work was performed under the sponsorship of the U.S. Atomic Energy Commission under Contract AT(30-1)-1002 and represents a portion of a thesis submitted by P. A. Flinn in partial fulfillment of the requirements for the degree of Sc.D. in Metallurgy at the Massachusetts Institute of Technology, Cambridge, Massachusetts, June 1952.

†Present address: Department of Physics, Wayne University, Detroit, Michigan.

‡Department of Metallurgy, Massachusetts Institute of Technology, Cambridge, Massachusetts.

§Reference [1] contains a summary of the available X-ray data and the experimental techniques used for these measurements.

long periods of heating. This suggests that the ordered nuclei existing above the critical temperature may also be imperfectly ordered. The order-disorder transformation thus seems to combine certain features of both first order and second order transformations.

Relatively few data are available for solutions which do not form superlattices. Recent studies of aluminum-zinc [3] and aluminum-silver [4] solid solutions above the solubility temperature have shown that each atom prefers to surround itself with *like* nearest neighbors. This may be taken as evidence for the presence of nuclei rich in solute atoms existing in equilibrium above the solubility temperature. The gold-nickel system, shown in Figure 1, would seem favorable for a similar study.

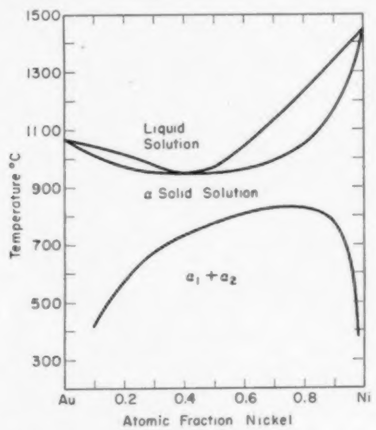

FIGURE 1. Gold-nickel phase diagram.

There is an unbroken series of face-centered cubic solid solutions above 840°C, and on cooling, the alloys decompose into two face-centered cubic solutions, one rich in gold and the other rich in nickel. There is also an adequate difference between the scattering factors of gold and nickel atoms so that the local atomic arrangements can be measured by observations of diffuse X-ray scattering.

Solid solutions may be divided into two classes on the basis of their heats of mixing. Solutions with a negative heat of mixing (heat evolved) usually exhibit a tendency for superlattice or compound formation. Copper-gold alloys, for example, have a negative heat of mixing [5]. Solutions with a positive heat of mixing (heat absorbed) generally display limited solubility, particularly at sufficiently low temperatures, and therefore such systems are useful for studying the nucleation and growth processes leading to observable precipitation [6; 7; 8]. The thermodynamic properties and the local atomic arrangement have been related by means of the quasi-chemical theory [9]* which predicts quantitatively the average preference for like or unlike nearest neighbors depending on whether the heat of mixing is respectively positive or negative. These predictions seem to be borne out in the case of copper-gold alloys where both thermodynamic and X-ray measurements are available [10].

The thermodynamic properties of the gold-nickel system have been determined recently [11]. The heat of mixing is found to be positive and the quasi-chemical theory thus predicts a preference for like nearest neighbors. This atomic configuration can only exist in a solution containing gold-rich and nickel-rich regions, and such a clustered solution is consistent with the miscibility gap in the phase diagram in the sense that gold-rich and nickel-rich solutions precipitate on cooling.

Diffuse X-ray measurements on gold-nickel solutions were undertaken, therefore, in order to ascertain the local atomic arrangements, and thus afford a critical test of the quasi-chemical approach. The X-ray results are described in this paper, from which it becomes evident that the quasi-chemical theory is not generally applicable in its present form.

2. X-ray Measurements of Local Atomic Arrangements

The local atomic arrangements in solid solutions can be determined by observations of the diffuse X-ray scattering; the principal experimental techniques have been summarized in a recent review [1]. In addition to the nearest neighbor identities, it is also possible to obtain information relative to the average sizes of the atoms in the solution, and this proved to be an important aspect of the present investigation. The diffuse scattering due to the local order and size effects in a powder pattern from a binary solution is given by:

$$
(1) \qquad I = N m_A m_B (f_B - f_A)^2
$$

$$
\left\{ 1 + \sum_{i=1}^{\infty}{}' \left[C_i^{\circ} \alpha_i \frac{\sin Sr_i}{Sr_i} + C_i \beta_i \left(\cos Sr_i - \frac{\sin Sr_i}{Sr_i} \right) \right] \right\}
$$

*In this theory, the enthalpy of a solid solution is taken to be the sum of the nearest-neighbor atomic-bond energies. On mixing of the pure components, two unlike pairs are formed at the expense of one like pair of each component: (A–A) + (B–B) = 2(A–B). The heat of mixing per A–B bond formed is assumed to be $E_{AB} - \frac{1}{2}(E_{AA} + E_{BB})$.

where:

I = diffuse intensity in electron units,
N = number of atoms which diffract,
m_A = atom fraction of A atoms,
m_B = atom fraction of B atoms,
f_A = scattering factor for A atoms,
f_B = scattering factor for B atoms,
C_i = number of atoms in the ith shell,

$$S = \frac{4\pi \sin\theta}{\lambda},$$

θ = diffraction angle,
λ = irradiating wavelength,
r_i = distance from a given atom to its ith shell of neighbors,

The local atomic arrangement is described in terms of the coefficients α_i, where:

$$\alpha_i = 1 - \frac{p_i}{m_A} = 1 - \frac{C_i p_i}{C_i m_A} \tag{2}$$

and p_i is the probability of finding an A atom in the ith shell about a B atom at the origin. $C_i p_i$ is thus the number of A atoms in the ith shell about a B atom; while $C_i m_A$ is the random number of A atoms in the ith shell about a B atom.

The average atomic sizes are described by the parameter β_i, where

$$\beta_i = \frac{1}{(\eta-1)}\left[-\left(\frac{m_A}{m_B} + \alpha_i\right)\epsilon_{AA}^{i} + \left(\frac{m_B}{m_A} + \alpha_i\right)\eta\epsilon_{BB}^{i}\right] \tag{3}$$

and

$$\eta = f_B/f_A$$

$$\epsilon_{AA}^{i} = \frac{r_{AA}^{i} - r_i}{r_i} \tag{4}$$

with

r_i = average radius of ith shell calculated from the lattice parameter
r^i_{AA} = distance between an A atom and another in the ith shell around it

The significance of r_i and r^i_{AA} may be seen in Figure 2 in terms of a one-dimensional array of A and B atoms with different sizes. The distance between a large number of atoms is measured over an average number of large and small atoms, providing there are no gross segregations. The distance between an atom and another in its 100th shell is thus sharply defined and independent of the atomic identity. The sharp crystalline reflections arise primarily from the gross average periodicity in the lattice, and hence a solid solution will have a well defined lattice parameter. On the other hand, the distance between nearest neighbors depends on the identity, and three distances r^1_{AA}, r^1_{BB}, r^1_{AB} are possible, (where $i = 1$). Only two of these variables are independent if the average r_1 is fixed. These local deviations from the average lattice site contribute to the diffuse X-ray scattering because they introduce a randomness of position, and this effect is described quantitatively in terms of the parameter β_i.*

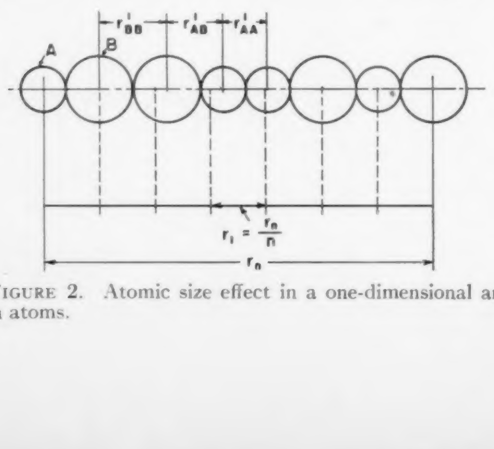

FIGURE 2. Atomic size effect in a one-dimensional array of n atoms.

The shape of the diffuse scattering is largely determined by the sign of the coefficients α_i. For example, if the α_i's are zero, the diffuse intensity described by equation (1) is a smoothly falling function, called the Laue monotonic scattering. If α_1 is negative, and the α_i's for $i > 1$ are negligible, there is a diffuse peak about halfway between the origin and the first lattice reflection. If α_1 is positive, and the α_i's for $i > 1$ are negligible, there is a diffuse peak near the origin (small angle scattering). The coefficients β_i modify these shapes somewhat, but do not usually change their essential character. Measurements of diffuse scattering can thus provide specific information regarding both the average identity and the average sizes of the atoms in solid solution.

3. Experimental Method

Gold-nickel alloy specimens were prepared by a variety of techniques. X-ray transmission samples were made by rolling foils of gold and nickel together and annealing long enough to give a homogeneous alloy. Thicker specimens were prepared by melting high-purity nickel and gold and rolling the ingot to obtain sheet. It was possible to secure randomly oriented fine grain samples by alternate rolling and recrystallisation treatments.

The diffuse X-ray scattering was measured by both photographic and spectrometer methods. The geometry of the photographic transmission

*It should be noted that parameter β is a function of the distance between atoms, and no assumptions concerning the atomic shapes are involved; the spherical atoms shown in Figure 2 are drawn only to illustrate the meaning of the parameter.

(4A)

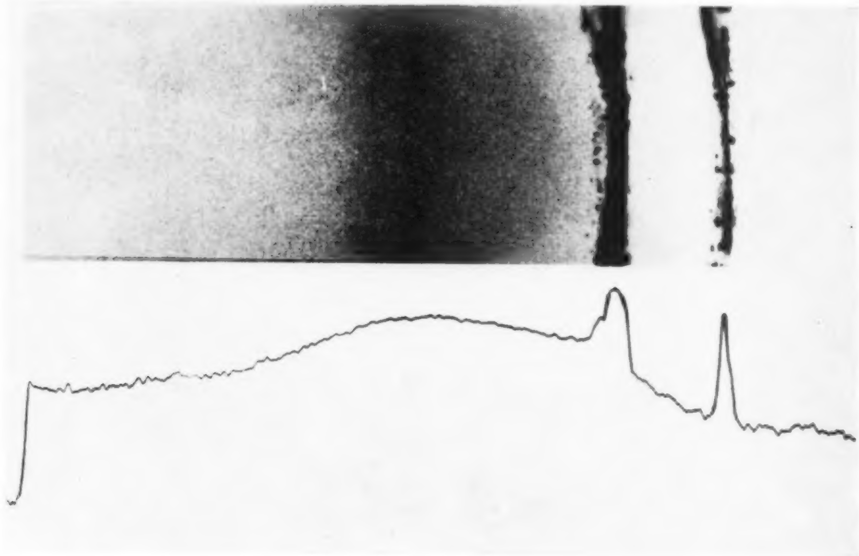

(4B)

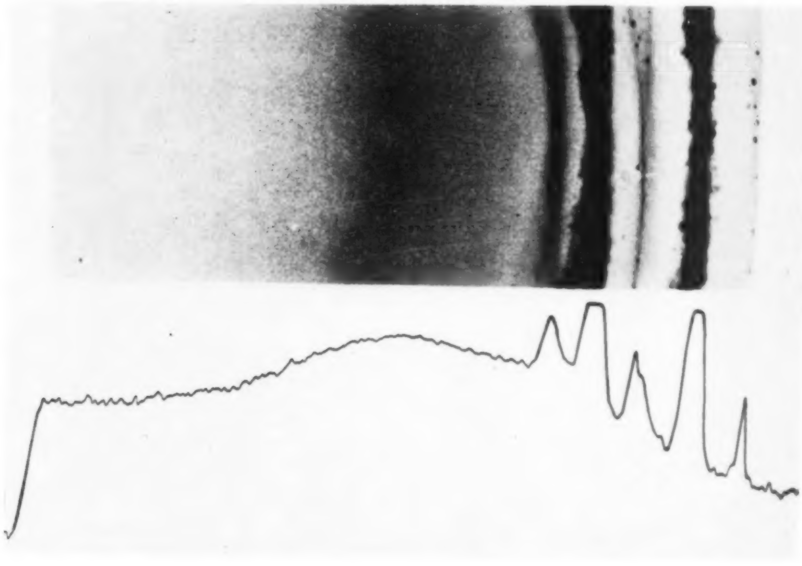

FIGURE 4. Photograms and microphotometer traces showing diffuse scattering from gold-nickel alloys. A. Photogram for 60 per cent nickel–40 per cent gold alloy as quenched from 900°C. B. Photogram of same sample as above, after aging 24 hours at 315°C.

(5A)

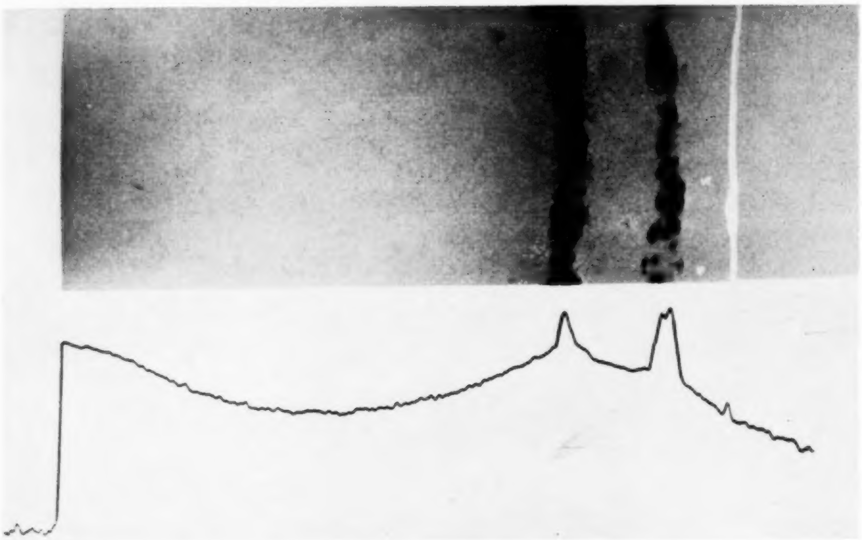

(5B)

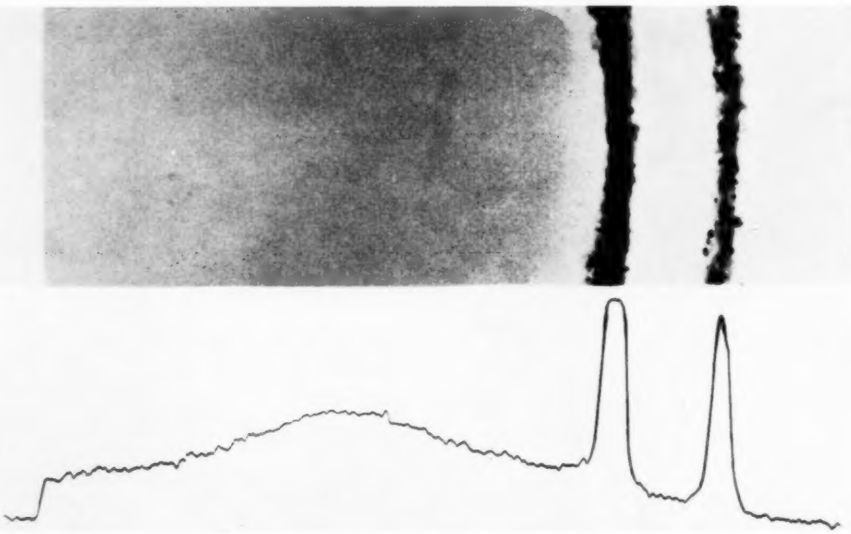

FIGURE 5. Photograms and microphotometer traces from an aluminium-zinc and a gold-copper alloy. A. Photogram of 50 per cent zinc–50 per cent aluminum alloy at 400°C. B. Photogram of 75 per cent copper–25 per cent gold alloy quenched from 900°C.

technique using $CoK\alpha$ radiation, monochromated by reflection from the (111) planes of a bent fluorite crystal, is shown in Figure 3. Since the structure factor for the (222) reflection of fluorite is almost zero, the half-wavelength component of the white radiation was virtually absent. The one-third wavelength component was eliminated by operating the tube at 22 kv, which is the cut-off voltage for this radiation. Air-scattering was eliminated by exposing the specimen in a vacuum or in a helium atmosphere and by introducing suitable slits and baffles. The focusing geometry illustrated in Figure 3 permitted observations down

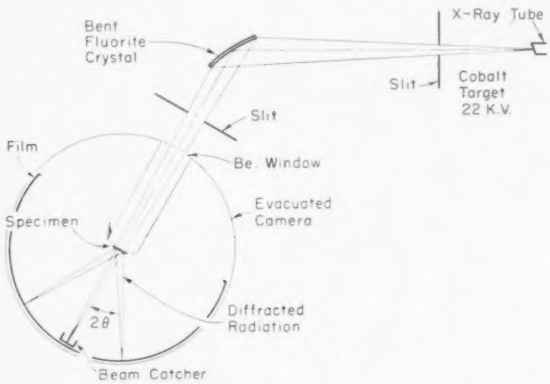

FIGURE 3. Camera arrangement used for photographic method.

to diffraction angles of about one degree. The camera was equipped with a furnace so that diffraction photograms could be taken of specimens at 900°C as well as of samples quenched to room temperature. The diffuse scattering from the quenched samples did not differ significantly in nature from that observed at the high temperature.

A typical diffraction photogram and the corresponding microphotometer trace are shown in Figure 4A. The well at the left edge is the shadow of the beam catcher; the diffraction lines are the (111) and (200) of the face-centered cubic structure. Similar scattering was observed from alloys containing 10 to 90 atomic per cent nickel. The shape of the diffuse intensity curve resembles that of alloys possessing the Cu_3Au type of short range order, i.e., alloys exhibiting a preference for *unlike* nearest neighbors (see Figure 5B). There was no evidence of clustering in any of the gold-nickel alloys, even after precipitation had started on heating within the two-phase region. Figure 4B illustrates the diffuse scattering for an alloy which was aged at 315°C long enough so that the diffraction lines of the gold-rich and nickel-rich precipitate phases as well as those of the matrix phase are clearly visible. Yet the diffuse scattering from the remaining matrix is still characteristic of a solid solution with preference for unlike nearest neighbors.

Figure 5A represents a pattern taken from an aluminum–50 atomic per cent zinc alloy at 400°C by Rudman [3] using the same technique employed here. The small angle scattering, typical of clustering in these alloys, is clearly visible, and indicates that clustering in the gold-nickel alloy, if it had existed, could have been detected by this method. Figure 5B shows the diffuse scattering from a quenched Cu_3Au specimen, from which it is evident that the gold-nickel scattering has a similar form.

In order to calculate values for α_i and β_i from equation (1) it is necessary to determine the intensity in electron units. Although it is possible to obtain the form of the diffuse scattering photographically, it is difficult to standardize the intensity. The diffuse scattering was measured, therefore, with a Geiger-counter spectrometer. A bent fluorite monochromator and $CoK\alpha$ radiation at 22 kv were used here also. To make measurements at low angles and to enhance the intensity, the defocused geometry shown in Figure 6 was

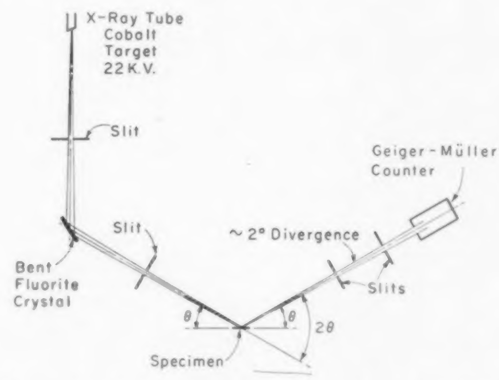

FIGURE 6. Geiger-counter spectrometer arrangement.

adopted. Since there was no sharp fluctuations in the diffuse intensity (Figure 4) the loss of resolution in this procedure was not serious. The intensity in electron units was determined by comparison, under identical conditions, with the scattering from lucite, Pyrex glass, or paraffin. The scattering in electron units from the latter was calculated on the basis of independent scattering by the constituent atoms. The specimens used for the reflection spectrometer technique were

infinitely thick to the X-rays, and the sample was always maintained at equal angles with the incident and diffracted beams.

The spectrometer was equipped with a high-temperature chamber for runs at 900°C, as well as with a low temperature chamber for runs at -190°C. At high temperatures the specimen was bathed in an atmosphere of hydrogen at a few centimeters pressure; at low temperatures an atmosphere of cold dry helium was used. A typical set of measurements made at 900°C at room temperature after quenching from 900°C, and at -190°C on the same alloy is shown in Figure 7.

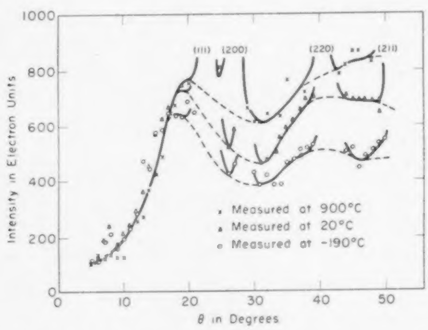

FIGURE 7. Diffuse scattering from a 50 atomic per cent nickel alloy, showing effects of temperature of measurement.

At low diffraction angles the scattering is the same for the three measuring temperatures; at higher angles the curves separate in a manner consistent with the expected increase in the temperature diffuse scattering.

The diffuse scattering in Figure 7 was first converted to electron units by means of the experimental calibration, and then corrected by the Lorentz and polarization factor. The resulting scattering contained, however, contributions due to temperature and Compton modified scattering. The temperature diffuse scattering was calculated on the assumption of independent vibration of the atoms; the details of this calculation as well as those for the Compton scattering are given in reference [1]. The remaining scattering, due to local atomic arrangements, was approximately the same for each of the three curves in Figure 7, thus indicating that the local atomic arrangements at 900°C could be preserved by quenching.

In order to minimize the error introduced by the temperature correction, most of the data reported here were obtained at -190°C. The Fourier transform used for analysis also helped to minimize systematic errors, such as faulty temperature correction. Typical results, in electron units after all corrections and subtractions, are plotted in Figure 8.

4. Analysis of the X-ray Data

The diffuse scattering from the gold-nickel alloys could not be interpreted in terms of the local order coefficients, α_i, alone, but required the intro-

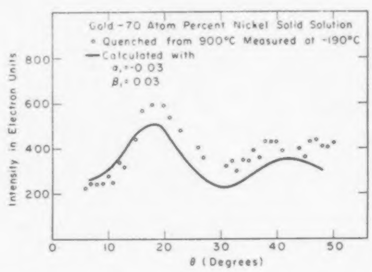

FIGURE 8. Comparison of measured and calculated diffuse intensities.

duction of the parameters, β_i, to account for the differences in atomic sizes. It is possible to determine the values of α_i and β_i from the corrected diffuse scattering, such as that shown in Figure 8, by a least-square fitting of equation (1). A more satisfactory method involves the use of a modified Fourier transform [11]. The resulting transform is given by:

$$(5) \qquad f_a(r) = \int_0^{S_0} S\,K(S) \exp(-a^2S^2) \sin Sr\, dS$$

where:

$$K(S) = \frac{I}{Nm_Am_B(f_B - f_A)^2}$$

S_0 = maximum value of S for which the intensity is measured.

The value of the damping constant a was chosen such that $aS_0 = 1.5$; the exponential weighting function minimizes the effects of an abrupt termination of the data at S_0 where the diffuse intensity due to local atomic arrangements may not yet be negligible. The integration required in equation (5) was carried out as a summation using Lipson-Beevers strips and a typical transform is shown in Figure 9.

The important feature of the transform is the double peak about r_1, the average distance between nearest neighbors as determined from lattice parameter measurements. The negative peak at a distance less than r_1 and the positive peak at a distance greater than r_1 arise from the fact that the

smaller nickel atoms have a scattering power less than the average for the alloy, whereas the larger gold atoms have a greater-than-average scattering. The function $f_a(r)$ would be zero for a perfectly random distribution of atoms of the same size.

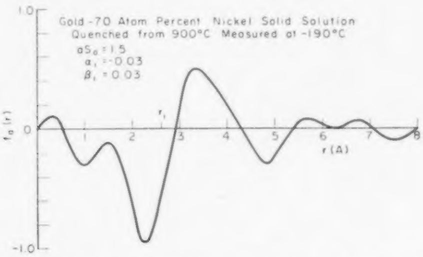

FIGURE 9. Modified Fourier transform of diffuse intensity from a 70 atomic per cent nickel alloy.

$f_a(r)$ is such that the coefficient β_1 can be calculated from the moment of the twin peak about r_1 by the equation [12]:

$$(6) \qquad C_i\beta_i = \frac{2}{\pi\phi(\delta/2a) - \sqrt{\pi}\,(\delta/a)\exp(-\delta^2/4a^2)} \cdot \int_{r_i-\delta}^{r_i+\delta} f_a(r)(r - r_i)\,dr,$$

where:

$$\phi(\delta/2a) = \text{error integral}$$

The interval, 2δ, is chosen large enough to include a representative portion of the function $f_a(r)$ in the vicinity of r_1 and does not have to include the entire peak.

The coefficient α_1 was calculated from the net area under the twin peak within the interval 2δ by the equation [12]:

$$(7) \qquad C_1\gamma_1 = \frac{2r_1}{\pi\phi(\delta/2a)}\int_{r_1-\delta}^{r_1+\delta} f_a(r)\,dr$$

where

$$\gamma_1 = \alpha_1 - \beta_1$$

It is evident that the coefficients beyond the first shell are not well enough resolved by the powder method to be determined here, but their magnitudes appear to be small.

The values obtained for α_1 and β_1 were inserted into equation (1) and the resultant intensity distribution compared with the experimental points in Figure 8. Most of the scattering is well accounted for by considering only nearest neighbor interactions, and the rather small discrepancy at higher diffraction angles may arise from an inadequate temperature correction or from some other source of diffuse intensity such as stray fluorescent scattering. Fortunately, the modified transform discriminates against these systematic errors.

5. X-ray Results

The values of α_1 and β_1 were determined as a function of composition for a series of gold-nickel alloys quenched from 900°C and measured at −190°C (Figure 10). The precision of the β_1

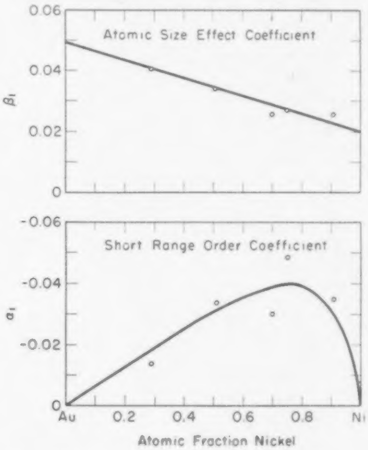

FIGURE 10. Short range order coefficients, α_1, and size effect coefficients, β_1, as functions of composition in gold-nickel alloys.

determination is somewhat better than that of the α_1 because the latter involves the subtraction of two relatively large numbers. In all cases, however, the value of α_1 is negative, indicating a preference for *unlike* nearest neighbors. This short-range order is of the same type and magnitude as that observed in copper-gold alloys, despite the difference in the phase diagrams, and in the sign of the enthalpies of mixing. The average nearest neighbor identities, calculated from the equation (2) and smoothed α_1 values in Figure 10 are summarized in Table I.

The values of β_1 shown in Figure 10 are not consistent with the customary assumption that gold and nickel atoms retain the same size in solid solution that they have in the pure metals. If this were the case, the corresponding values of β_1 would be more than twice those observed. The linear dependence of β_1 on composition suggests that

$$(8) \qquad \begin{aligned} \overset{1}{\epsilon}_{AA} &= a_1 m_B \\ \overset{1}{\epsilon}_{BB} &= b_1 m_A \end{aligned}$$

Introducing these relationships into equation (3)

TABLE I

AVERAGE NEAREST-NEIGHBOR IDENTITIES IN GOLD-NICKEL ALLOYS

Atomic fraction Nickel	α_1	Number of nickel atoms surrounding a gold atom		Number of gold atoms surrounding a nickel atom	
		Random solution	Measured	Random solution	Measured
0.30	−0.020	3.6	3.7	8.4	8.7
0.50	−0.030	6.0	6.2	6.0	6.2
0.70	−0.038	8.4	8.7	3.6	2.7
0.75	−0.040	9.0	9.4	3.0	3.1
0.90	−0.032	10.8	11.2	1.2	1.24

and since α_1 can generally be neglected in comparison to m_A/m_B or m_B/m_A we have:

$$\beta_1 = \frac{1}{(\eta - 1)}\left(-m_A a_1 + \eta m_B b_1\right) \tag{9}$$

This equation represents a linear variation of β_1 with composition and the values of α_1 and β_1 can be obtained from the intercepts at $m_A = 1$ and $m_B = 1$ in Figure 10. This method was used to determine ϵ^1_{AuAu} and ϵ^1_{NiNi} as a function of composition. The average distance between nearest lattice points, r_1, was obtained from the lattice parameters [13; 14], and the average nearest-neighbor distance between gold atoms r^1_{AuAu} and nickel atoms r^1_{NiNi} was then calculated from equation (4) for each composition.

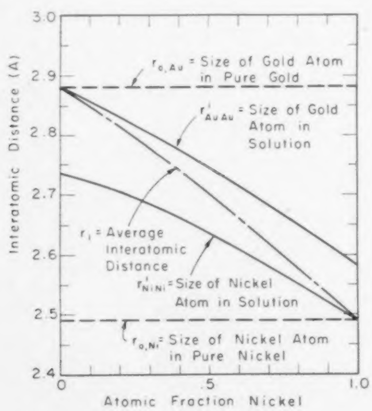

FIGURE 11. Atomic sizes as functions of composition in gold-nickel alloys.

For convenience, the average distance between neighboring like atoms is considered to be the size* of the atom in question. The atomic sizes as a function of composition are given in Figure 11. The size of the gold atom in pure gold, $r_{0,Au}$, and of the nickel atom in pure nickel, $r_{0,Ni}$, as well as the average interatomic distance r_1 determined from the lattice parameter, are aslo shown. The actual atomic sizes, r_{AuAu} and r_{NiNi}, fall in between. The gold atom is larger than the average interatomic spacing, but less than that of pure gold, while the nickel atom is smaller than the average interatomic spacing but larger than that of pure nickel. The size of each atom varies with composition, and is tabulated in convenient form in Table II.

*This could be visualized as the effective diameter of the atom in solution.

TABLE II

AVERAGE SIZES OF GOLD AND NICKEL ATOMS IN SOLUTION

Atomic fraction Nickel	β_1	Average size r_1(Å)	Size of gold atom r_{Au}(Å)	Size of nickel atom r_{Ni}(Å)
0	—	2.88	2.88	—
0.30	0.040	2.78	2.80	2.68
0.50	0.035	2.70	2.75	2.63
0.70	0.028	2.63	2.69	2.59
0.75	0.027	2.60	2.66	2.58
0.90	0.023	2.53	2.62	2.52
1.00	—	2.49	—	2.49

6. Discussion of Results

The X-ray data on local atomic arrangements in gold-nickel alloys cast serious doubts on the generality of the quasi-chemical approach. In this system, both the phase diagram and the measured thermodynamic properties suggest strongly that the solid solution should contain clusters of like atoms, yet the X-ray measurements indicate that the local order is of the opposite kind. Thus, there is no indication that the solution contains embryos of the phases which eventually appear on cooling below the solubility limit.

In addition, the existence of local order with a greater-than-random number of unlike neighbors would imply, according to the quasi-chemical treatment, that the A–B bond is stronger than the average of the A–A and B–B bonds. If this were actually the case, the preference for unlike pairs should also be present in the liquid state. However, Seigle, Cohen and Averbach [11] have shown that the gold-nickel liquid solutions are virtually ideal, which contradicts the hypothesis that

"A likes B" is an explanation of the local order in the solid state.

It seems more likely that both the local order in the gold-nickel solid solutions and their positive heats of mixing are attributable to lattice strain energy resulting from the marked difference in the size of the two atoms. Such elastic energy, of course, would be absent in the liquid state, and would thus account for the difference in thermodynamic behavior between the liquid and solid solutions. On this basis, it is conceivable that the local order achieves a reduction in strain energy because of a somewhat more efficient packing of the large and small atoms.* At lower temperatures, where the randomizing effect of entropy is not so pronounced, it appears that the strain energy can be further reduced by decomposition of the solid solution into a gold-rich and nickel-rich phase.

The conclusion is reached that the quasi-chemical theory in its present form is inadequate to describe the relationship between the observed thermodynamic properties and local atomic configurations. The chemical bonding forces may be controlling in restricted cases, but other factors, such as lattice strain energy, will have to be considered to obtain a more general treatment. This approach may now become more feasible in the light of the measured atomic sizes reported herein.

*An attempt was made to determine whether a superlattice could be formed in this system. Alloys of stoichiometric composition NiAu and Ni_3Au were quenched from 900°C and heated for several months at 200°C where the precipitation reaction is very slow. However, no superlattices were found.

7. Acknowledgments

The authors are grateful to Mr. Mathias Comerford for his assistance with the experimental measurements and to Mr. Peter Rudman for his photogram of the aluminum-silver alloy. The authors also wish to express their appreciation to the Atomic Energy Commission for their support of this program.

References

1. Warren, B. E. and Averbach, B. L. Modern Research Techniques in Physical Metallurgy (American Society for Metals, 1953).
2. Newkirk, J. B. J. Metals **5** (1953) 823.
3. Rudman, P. S., Flinn, P. A. and Averbach, B. L. J. Appl. Phys. **24** (1953) 365.
4. Walker, C. B., Blin, J. and Guinier, A. C. R. Acad. Sci. Paris **235** (1952) 254.
5. Weibke, F. and von Quadt, V. Z. Elektrochem. **45** (1939) 715.
6. Becker, R. Ann. der Physik **32** (1938) 128. Brutcher Translation No. 722.
7. Borelius, G. Ark. Mat. Astr. Fys. **32** (1945) 1.
8. Hobstetter, J. H. Trans. A.I.M.E. **180** (1949) 121.
9. Takagi, Y. Proc. Phys. Math. Soc. Japan **23** (1941) 44.
10. Oriani, R. A. J. Appl. Phys. **21** (1950) 1068.
11. Seigle, L. L., Cohen, M. and Averbach, B. L. J. Metals **4** (1952) 1320.
12. Flinn, P. A., Averbach, B. L. and Rudman, P. S. Submitted to Acta Cryst.
13. Köster, W. and Dannöhl, W. Z. Metallk. **28** (1936) 248.
14. Ellwood, E. C. J. Inst. Met. **80** (1952) 617.

THE INFLUENCE OF OXYGEN CONTENTS ON TRANSFORMATIONS IN A TITANIUM ALLOY CONTAINING 11 PER CENT MOLYBDENUM*

D. J. DELAZARO and W. ROSTOKER†

It has been demonstrated that an approximately quantitative relationship exists between oxygen content and the rate of precipitation of alpha from beta in a Ti + 11% Mo alloy. The presence of oxygen was correlated with the occurrence of sub-grain boundary structures and abnormal variations in precipitation rates from grain to grain. An explanation of the transformation rate effects was suggested in terms of polygonization concepts.

L'INFLUENCE DES TENEURS EN OXYGÈNE SUR DES TRANSFORMATIONS DANS UN ALLIAGE DE TITANE CONTENANT 11 POUR CENT DE MOLYBDÈNE

Il a été démontré qu'il existe une relation approximativement quantitative entre la teneur en oxygène et la vitesse de précipitation de l'alpha à partir du bêta dans un alliage de Ti + 11% Mo. La présence de l'oxygène correspond à l'apparition de structures de sous-joints cristallins et de variations anormales dans la vitesse de précipitation, d'un grain à l'autre. Une explication des effets de la vitesse de transformation en termes des concepts de polygonisation, a été proposée.

DER EINFLUSS DES SAUERSTOFFGEHALTES AUF DIE UMWANDLUNGEN IN EINER TITANLEGIERUNG MIT 11 PROZENT MOLYBDÖN

Es wird gezeigt, dass eine nahezu quantitative Beziehung zwischen dem Sauerstoffgehalt und der Geschwindigkeit der alpha-Ausscheidung von beta Ti in einer Ti + 11% Mo Legierung besteht. Die Gegenwart von Sauerstoff wurde zu dem Auftreten von Sub-Korngrenzenstrukturen und abnormalen Variationen in der Ausscheidungsgeschwindigkeit von Korn zu Korn in Beziehung gesetzt. Eine Erklärung der Transformations-geschwindigkeitseffekte im Rahmen der Polygonisationsvorstellung wird vorgeschlagen.

In the system Ti–Mo [1], the high-temperature (beta) modification of titanium is stabilized to progressively lower temperatures with increasing additions of molybdenum. There are no known intermediate phases. The kinetics of the transformation $\beta \rightarrow \alpha + \beta$ have been discussed in an earlier publication [2]. In this work it was noted that the surfaces of specimens were invariably in a more advanced state of transformation than the interior. The indications were that superficial increases in atmospheric contamination occurring during the solution treatment at 1000°C were responsible. In view of the variability of oxygen contents in commercial and experimental alloys, it was considered that a useful purpose would be served in demonstrating that a relationship existed between oxygen content and transformation rate.

A titanium alloy containing 11 per cent molybdenum was chosen as an alloy base. A 25-gram melt was made from iodide titanium to provide an alloy containing < .02 per cent oxygen. A second melt was made using magnesium-reduced sponge titanium containing about 0.15 per cent oxygen. Two further melts were made using sponge titanium and TiO_2 additions to raise the oxygen levels to about 0.35 and 0.55 per cent oxygen respectively. The latter three alloys were hot forged to $\frac{1}{4}$ inch by $\frac{1}{4}$ inch rods and cut into small specimens for heat treatment. The iodide titanium-base melt was cold rolled to 0.060 inch to provide specimens. At no time was this alloy submitted to any conditions which might permit contamination.

Using lead baths and conventional heat treatment procedures for studying isothermal transformations [2], TTT charts were constructed for the oxygen-bearing alloys. In the case of the iodide titanium-base alloy, the specimens were sealed in evacuated Vycor bulbs for heat treatment. The quenching rates into a lead bath under these conditions were not ideally rapid so that transformation times of less than five minutes could not be accurately estimated. Time periods for this alloy were chosen from five minutes to two hours. The accuracy of the "start of transformation" curve is regarded as somewhat poorer than for the other alloys.

The "start of transformation" curves for the four alloys are plotted in Figure 1. The "finish of transformation" curves are shown in Figure 2. The following points may be noted:

(*a*) Times for visible initiation of transformation are shortened by oxygen additions. The effect is most pronounced above the "knee" of the C curves. At the higher oxygen levels, transformation begins so rapidly that it is difficult to suppress it except by the most rapid quenching.

(*b*) Times for completion of transformation are

*Received June 8, 1953.

†Assistant Metallurgist and Senior Metallurgist, Metals Research Department Armour Research Foundation of Illinois Institute of Technology, Chicago, Illinois.

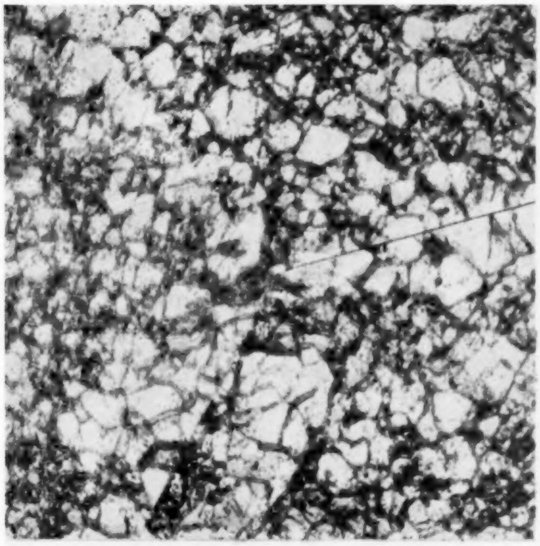

3

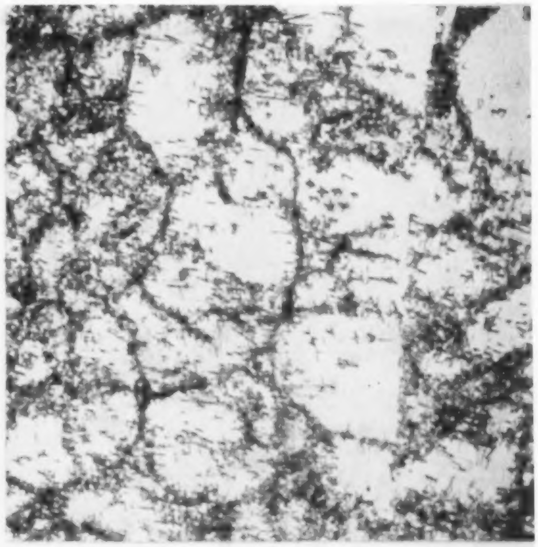

4

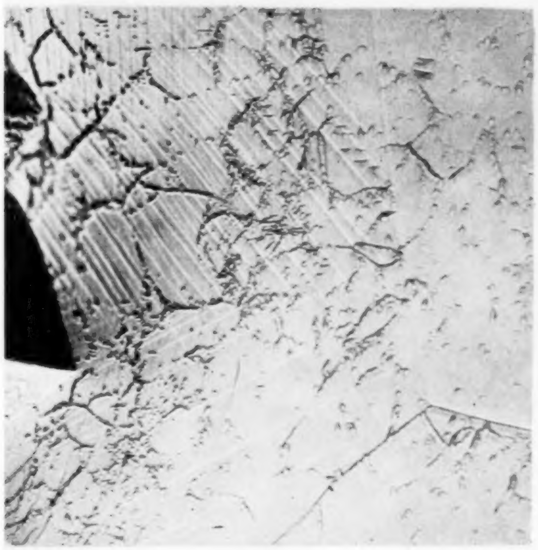

5

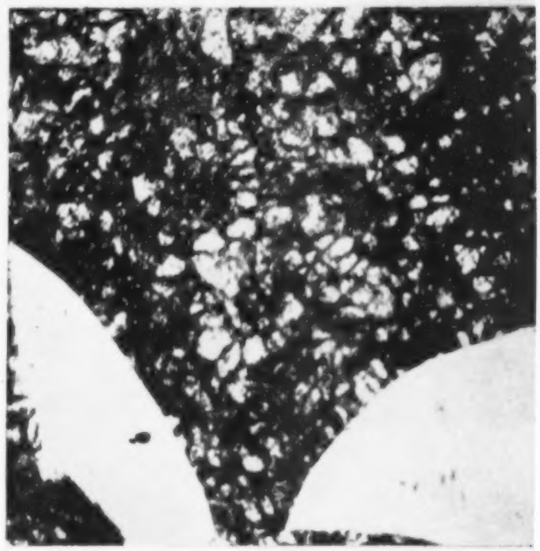

6

PLATE I. Figure 3—11% Mo alloy containing 0.55% oxygen. Heat treatment included solution treating at 1000°C for 20 minutes followed by a quench to 650°C and a hold for 30 seconds prior to final water quenching. The microstructure illustrates the sub-grain boundary configuration within large beta-grains (250×). Figure 4—Same alloy as in Fig. 3. Heat treatment involved an isothermal transformation at 750°C for 60 seconds. The microstructure illustrates the conventional manner of precipitation of alpha about the sub-grain boundaries (1000×). Figure 5—Illustration of the ease with which slip lines originating from a hardness impression traverse sub-grain boundaries without apparent change in direction. Note that the slip lines are stopped by primary beta-grain boundaries (750×). Figure 6—Same alloy and heat treatment as Fig. 4. Microstructure illustrates the radical differences in transformation rates between adjacent beta-grains (250×).

reduced at temperatures above the "knee" of the C curves. In some instances an acceleration factor of 20 is produced.

(*c*) The presence of oxygen appears to have little effect at temperatures below the "knee" of the C curve.

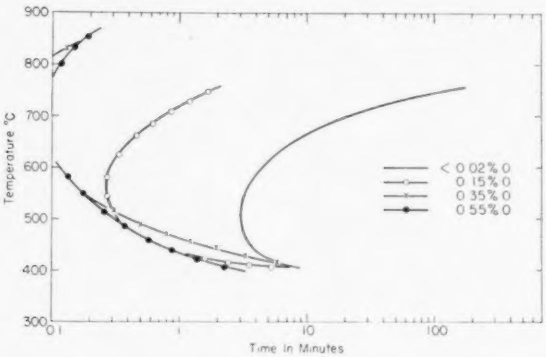

FIGURE 1. Comparison of curves of initiation of visible transformation in Ti + 11% Mo alloys with various oxygen contents.

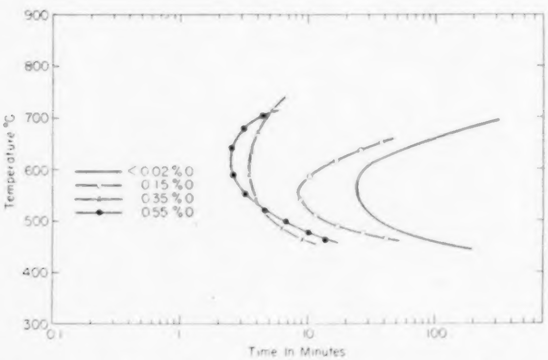

FIGURE 2. Comparison of curves of completion of transformation in Ti + 11% Mo alloys with various oxygen contents.

The configuration of precipitated alpha in the 0.35 and 0.55 per cent oxygen alloys was modified in an unusual manner. Rejected alpha appears predominantly at the beta-grain boundaries in the purer alloys. Only in the advanced stages does alpha appear in the interior of the grains. In the high oxygen alloys, the first signs of precipitated alpha delineate a sub-grain network within the primary beta-grains. This network is not apparent in completely beta structures retained by water quenching. Further transformation defines the network more markedly. Microstructures in Figures 3 and 4 illustrate this effect. In recent years, Guinier [3; 4], Cahn [5] and others have demonstrated that strained crystals can, after thermal treatment, develop aggregates of sub-crystals with orientations varying slightly but randomly about the original crystal orientation. Such "polyganized" structures have been illustrated micrographically on numerous occasions. It seems to have been quite conclusively established that sub-grain networks or "veining" are to be taken as micrographic evidence of polygonization. There would appear to be every reason to expect that the beta sub-grain boundaries would be as favorable for nucleation of precipitating alpha as the primary beta-grain boundaries. One might then reason that if polygonization does occur in the 11 per cent molybdenum alloy it will be clearly in evidence in the early stages of alpha precipitation. The fact that sub-grain boundaries do not appear in the purer alloy would lead to the conclusion that the occurrence of polygonization in these alloys is intimately related to the presence of a minimum amount of oxygen dissolved interstitally in the beta lattice. That the sub-grains are only slightly disoriented can be see from the behaviour of slip lines originating from a hardness indentation shown in Figure 5. The slip lines appear to traverse the sub-grains without change in direction but are stopped by primary beta grain boundaries.

A further phenomenon associated with the presence of oxygen is a pronounced variation in precipitation rates from grain to grain. It is quite common to observe beta-grains which are far advanced in precipitation stages adjacent to grains which apparently have not yet begun to precipitate alpha. Figure 6 illustrates this effect. The distribution of retarded beta grains is completely random, which suggests that the effect is not a result of the geometry of the specimen or the heat treatment to which it was subjected. It seems more likely that the rate of precipitation of alpha in a grain is overwhelmingly dependent on the specific area of sub-grain interface per unit volume and that this quantity varies from grain to grain depending on the prior strain hardening history of each. Attention is directed to the almost complete absence of sub-grain boundaries in the untransformed beta grains of Figure 6.

Acknowledgments

The authors wish to express their appreciation of the sponsorship of this work by the Flight Research Laboratory (under Contract AF33(038)-16347), Wright Patterson Air Force Base, Ohio, and for their permission to publish.

The metallographic preparation and photography were performed by Mr. C. A. Johnson.

References

1. Hansen, M., Kamen, E. L., Kessler, H. D., McPherson, D. J. Trans. A.I.M.E. **191** (1951) 881.
2. DeLazaro, D. J., Hansen, M., Riley, R. E., Rostoker, W. Trans. A.I.M.E. **194** (1952) 265.
3. Guinier, A. and Tenevin, J. Progress in Metal Physics **2** (1950) 177.
4. Guinier, A. Imperfections in Nearly Perfect Crystals (New York, Wiley, 1952).
5. Cahn, R. W. Progress in Metal Physics **2** (1950) 151.

THE ANNEALING OF COPPER AFTER RADIATION DAMAGE AT LOW TEMPERATURES*

R. R. EGGLESTON†

Resistance measurements at the boiling point of liquid helium have been made on copper which was damaged at temperatures below − 150°C by an exposure to 35 Mev alpha particles and then annealed at higher temperatures. The activation energy for the process active at annealing temperatures between − 65°C and − 20°C is 0.717 ev. At temperatures between 250°C and 325°C the activation energy describing the annealing is 2.12 ev. The activation energy obtained at the lower temperatures is in agreement with the value of 0.672 ev for copper cold-worked in liquid helium, and the value of 0.68 ev obtained by Overhauser on copper irradiated in a similar manner and annealed in the same low temperature range.

Cold-work and radiation damage in copper were compared qualitatively by making similar constant time anneals at progressively higher temperatures on specimens irradiated at temperatures below − 150°C and specimens cold-worked in liquid helium. Up to about − 80°C the rate of annealing of the two specimens was similar, but at room temperature about 25 per cent of the radiation damage remained compared to 50 per cent remaining in the cold-worked specimen.

LE RECUIT DU CUIVRE PRÉALABLEMENT ENDOMMAGÉ PAR DES RADIATIONS AUX BASSES TEMPÉRATURES

Des mesures de résistance, au point d'ébullition de l'hélium liquide, ont été effectuées sur du cuivre endommagé à des températures en dessous de − 150°C par des particules alpha de 35Mev et ensuite recuit à des températures plus élevées. L'énergie d'activation du processus de recuit aux températures allant de − 65°C à 20°C est de 0,717 ev. Aux températures variant de 250°C à 325°C l'énergie d'activation du recuit est de 2,12 ev. L'énergie d'activation obtenue aux basses températures est en accord avec les 0.672 ev obtenus pour du cuivre écroui dans l'hélium liquide, et les 0,68 ev obtenus par Overhauser sur du cuivre irradié d'une façon similaire et recuit dans le même intervalle de basses températures. Les dégâts provoqués dans le cuivre par l'écrouissage et par l'irradiation ont été comparés qualitativement, en effectuant des recuits similaires, de même durée, à des températures de plus en plus élevées, sur des échantillons irradiés à des températures inférieures à − 150°C et sur des échantillons écrouis dans l'hélium liquide. Jusqu'environ − 80°C la vitesse de recuit des deux échantillons était similaire, alors qu'à la température ambiante le dégat résiduel était de 25 pour cent dans le cas des échantillons irradiés et de 50 pour cent dans le cas des échantillons écrouis.

AUSGLÜHEN VON KUPFER NACH STRAHLUNGSSCHÄDIGUNG BEI TIEFEN TEMPERATUREN

Der Widerstand von Kupfer, das der Bestrahlung mit 35 MeV Alpha Teilchen bei einer Temperatur unterhalb von − 150°C ausgesetzt und dann ausgeglüht worden war, wurde am Siedepunkt des flüssigen Heliums gemessen. Die Aktivierungsenergie für den bei der Glühtemperatur zwischen − 65°C und − 20°C stattfindenden Vorgang beträgt 0.717 eV. Bei Temperaturen zwischen 250°C und 325°C beträgt die dem Ausglühen zugeschriebene Aktivierungsenergie 2.12 eV. Der bei tieferen Temperaturen erhaltene Wert der Aktivierungsenergie stimmt zufriedenstellend mit dem Wert mit 0,672 eV für in flüssigem Helium kaltbearbeitetem Kupfer überein, ebenso wie mit den 0,68 eV, die Overhauser für Kupfer, das in ähnlicher Weise bestrahlt und in gleichem tiefen Temperaturbereich ausgeglüht wurde, angegeben hat. Kaltbearbeitung und Strahlungsschädigung von Kupfer wurden quantitativ verglichen, indem entsprechende Glühungen (mit konstanter Glühzeit) bei fortschreitend höheren Temperaturen an Proben, die unterhalb von − 150°C bestrahlt oder in flüssigem Helium kalt bearbeitet worden waren, durchgeführt wurden. Bis zu − 80°C war das Verhältnis des Ausheilens bei beiden Proben das gleiche, bei Zimmertemperatur verblieben jedoch 25 prozent der Strahlungsschädigung im Vergleich zu 50 prozent der Kaltbearbeitung.

Introduction

Changes in physical properties take place when metals are exposed either to a neutron flux or to a charged particle bombardment [1, 2]. In the case of a pure metal such as copper, the amount of damage as observed by resistivity measurements is dependent on the thermal history of the bombarded specimen, both during the bombardment and prior to observation.

It is the purpose of this paper to describe measurements of electrical resistance made on copper irradiated at temperatures below − 150°C, then subjected to controlled heat treatments. These treatments were first carried out in the range of temperatures from − 65°C to 0°C and then between 250°C and 300°C. These results will be compared with the annealing behavior of copper which was cold-worked at the liquid helium temperature.

The comparison will be made on the basis of activation energies determined by making the assumption that within each temperature range considered the annealing process can be described by a single, well-defined activation energy. The determination of the energy of activation for annealing active in different temperature ranges

*Received June 6, 1953.

†North American Aviation, Inc., Atomic Energy Research Department, Downey, California.

for material damaged in a variety of ways may aid in the identification of the various possible lattice defects.

The electrical resistance measurements were made at the boiling point of liquid helium, and will be referred to hereafter as residual resistance measurements. Since there is no temperature dependence of the extra resistance due to defects at measurement temperatures below 18°K, it was assumed that Matthiessen's rule holds for measurements made at 4.2°K. Thus the extra resistance measured due to the damage may be assumed proportional to the number of defects. Results of previous work [3] indicate that there is a slight temperature dependence of the resistivity due to defects at other temperatures of measurement. By making measurements of residual resistivity, the possibility of identifying the annealing mechanisms is improved.

Experimental Procedure

The measurement of residual resistivity by standard potentiometric methods was used to detect changes due to thermal treatments in all of the following experiments. The temperature of measurement differed from the thermal treatment temperature; therefore in order to know the time of anneal accurately the specimen had to be taken up to, and lowered from, the thermal treatment temperature rapidly. This method of annealing at a higher temperature and taking measurements at a more desirable or convenient temperature has been called a pulse annealing technique [4]. There are experimental advantages in using residual resistance measurements, in addition to the theoretical advantages discussed above. These advantages are that the temperature coefficient of resistance is small at this temperature, the temperature of measurement is reproducible, and the relative changes arising from the annealing are larger.

In the thermal treatments, the individual specimens were either at a constant temperature or at progressively higher temperatures for a constant time at each temperature. The former treatment will be called an isothermal anneal and the latter a tempering anneal. Constant temperature baths of large heat capacity were used for these anneals.

Commercial O.F.H.C. copper wire of 3-mil diameter was used for these studies; the exact purity was unknown, but from maximum and minimum assays of copper plus silver that were available it is probably safe to assume that the purity was at least 99.9 per cent. For the tempering anneals, a wire about 8.5 cm long was wound on a thin mica strip so that its entire length was evenly bombarded. The isothermal specimens, approximately 0.7 cm long, were mounted similarly, but without a supporting mica strip. The specimen mountings were small enough so that as many as four specimens could be bombarded simultaneously and still receive nearly identical irradiations.

The 60-inch cyclotron of the Crocker Radiation Laboratory at the University of California in Berkeley was used for the alpha-particle irradiations. The energy of the particles at the target was 35 Mev. The range of the particles of this energy in copper is approximately 7 mils so that there should be no inhomogeneities in the samples due to end of range effects in the isothermal samples. The specimens were kept at temperatures below − 150°C during the irradiation by flowing refrigerated helium past the specimen and by limiting the beam current. After the irradiation it was possible to transfer the specimens rapidly, without warming, to liquid nitrogen, in which they were stored before annealing. The exposures of the isothermal samples, tabulated in Table I, varied slightly from sample to sample. These exposures were determined from a beam profile distribution obtained by counting strips from a monitoring foil placed between the specimen and the cyclotron. Before irradiation the specimens were annealed in a vacuum at temperatures of at least 780°C for 10 minutes and above 400°C for 105 minutes.

TABLE I

Annealing temperature	− 65°C	− 50°C	− 35°C	− 20°C
Exposure (μahrs/cm²	13.3	13.0	13.1	13.3
Residual resistance in arbitrary units after irradiation	1570.9_4	1455.0_3	1515.0_0	1433.8_8
After long time at room temperature	460.7_1	464.9_7	473.4_5	451.9_5
Annealing temperature		300°C	275°C	250°C
Residual resistance in arbitary units after anneal 500°C, 2 hr.	Specimen broke	98.2_7	100.7^2	95.7_5
Values of residual resistivity due to defects produced by irradiation	0.0782	0.0777	0.0778	0.0782

Results

An exploratory tempering anneal curve, which

is presented in Figure 1, shows that the most rapid annealing occurs between − 70°C and 0°C. Hence, the temperatures chosen for the isothermal anneals were − 65°C, − 50°C, − 35°C and − 20°C. Between − 70°C and 0°C the tempering curve

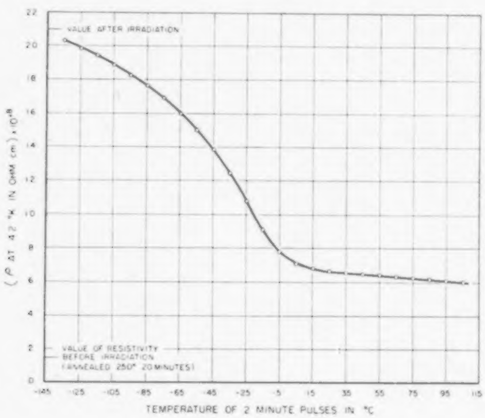

FIGURE 1. Result of tempering anneal on copper irradiated at temperatures below − 150°C to an exposure of 17.2 μahrs/cm^2 with 34.5 Mev alpha particles.

does not exhibit any properties that would indicate more than a single active annealing process. After the isothermal data were taken, each of the four specimens was allowed to stand at ambient room temperature for a period of 12 days. In Table I the data of residual resistance in arbitrary units has been collected at several times during the thermal history together with the exposures and annealing temperatures for each of the specimens.

There are several possible ways to reduce or normalize the data and thus make direct comparisons of the isothermal curves. Since the radiation exposures and lengths of the samples are different, this procedure is of necessity complicated. The normalization procedure to be described was found to yield activation energies that were quite well defined and nearly constant.

The residual resistance values attributed to the defect being annealed were first obtained for each specimen by subtracting from the resistances measured during the annealing a value obtained after a long anneal at room temperature. This value was used since the room temperature anneal resulted in a nearly complete disappearance of the defects under study, leaving relatively undisturbed the defects that anneal at higher temperatures.

Curves of change in resistivity versus exposure under similar irradiation conditions give us information to allow us to make the small relative corrections needed for the normalization, though they are not reliable absolutely. These curves show that at the exposures encountered here, the change of residual resistivity with exposure is 1.71×10^{-3} $\mu\Omega$cm/μahr/cm^2, and at an exposure of 12μahrs/cm^2, the total change of residual resistivity is 0.076$\mu\Omega$cm. In order to get relative values of residual resistivity the above slope was multiplied by the extra exposure given each sample over 12μahrs/cm^2 and then added to the value given above for an exposure of 12μahrs/cm^2. The values of residual resistivity due to the defects introduced by the irradiation are also tabulated in Table I; these values are accurate relatively but not absolutely. The residual resistance data for each specimen were then normalized by multiplying by the ratio of relative residual resistivity values tabulated above to the extra resistance due to the defects after irradiation. Thus it was possible to correct for slight length and exposure differences from specimen to specimen. The normalized annealing curves are displayed in Figure 2. The phenomenological activation

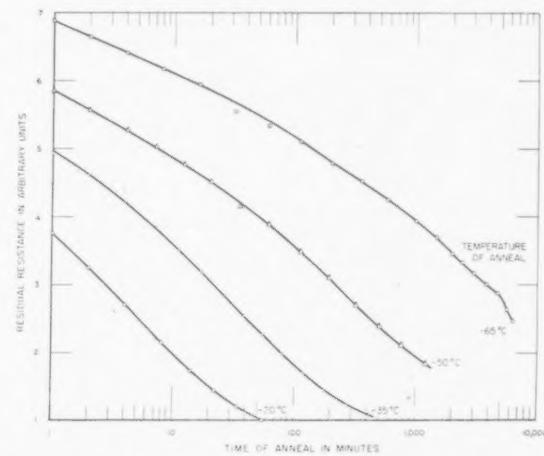

FIGURE 2. Normalized isothermal annealing curves for temperatures of anneal between − 65°C and − 20°C. In order to obtain an approximate value of residual resistivity change in micro ohm cm due to the irradiation, multiply the arbitrary scale by 0.018. Residual resistivity may then be obtained by adding this value to the annealed residual resistivity which is approximately 0.015 $\mu\Omega$cm.

energy can easily be obtained from these curves. When the logarithms of the times to reach equal property values of the helium point resistance along several isothermal curves is plotted against the corresponding reciprocal absolute temperature of the isothermals the points define a line whose slope determines the activation energy. In Figure

3 the results of making several equal property cuts on the curves in Figure 2 are given. The activation energy is seen to be quite well defined. The average energy is 0.717 ev while the spread is from 0.707 ev to 0.742 ev. There is no obvious trend in these values which would indicate that this spread is due to other than experimental uncertainties.

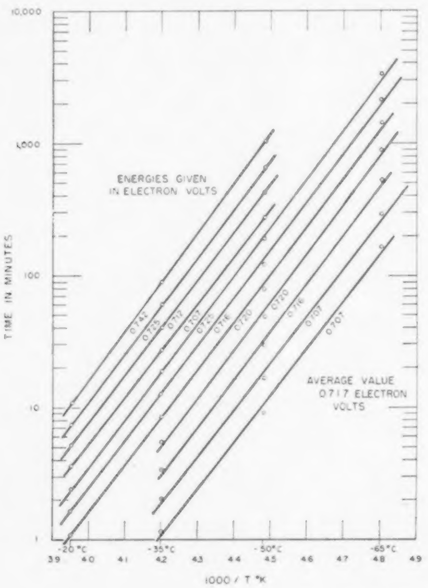

FIGURE 3. Phenomenological determination of activation energy for the annealing process active in the temperature range between $-65°C$ and $-20°C$.

Since both the lengths and the exposure did not vary greatly among the specimens it is possible to use other logical normalization procedures based on the assumption that these slight differences did not exist. Isothermal curves compared after normalization by these assumptions yielded values that differed from the above average value by less than 10 per cent. This is not surprising, since both the lengths and the exposures did not vary greatly among the specimens; thus the normalization corrections should be small as also should be the variation in determined activation energies.

An activation energy of 0.672 ev has been reported previously [5] for copper that had been cold-worked by twisting at liquid helium temperatures and annealed at temperatures between $-50°C$ and $-10°C$. This is not too different from the value found for the irradiated copper. This agreement may indicate that the annealing process is similar in the two cases. Overhauser [6] has irradiated copper at $-180°C$ with 12 Mev deuterons for an exposure of 1.1×10^{17} particles/cm^2 and found an activation energy of 0.68 ev for the annealing occurring above $-50°C$ which is in agreement with both of the above values.

After the above specimens had annealed at room temperature they were then further annealed isothermally at 250°C, 275°C and 300°C, after which they were annealed at 500°C for two hours to completely remove the defects caused by the irradiation. The normalized annealing curves are shown in Figure 4. In this case the normalization was made by assuming that all three of the specimens had identical residual resistivities after the 500°C anneal. The other specimens were normalized to the residual resistance of the specimen annealed at 300°C. The determination of activation energies was made in the same way as for the earlier annealing data. The results of making several equal property cuts on the normalized isothermal curves in Figure 4 are shown in Figure 5. The activation energy is seen to be fairly well defined, the average value being 2.12 ev while the spread is from 2.09 ev to 2.18 ev. The data for this annealing range were not taken over as wide a temperature range as the data at lower temperatures; thus the values of activation energy are less reliable. The activation energy of 2.12 ev is in agreement with values of the copper self-diffusion activation energy, given as 2.1 ev by Seitz [7] and a slightly lower value of 2.02 ev by Mott [8].

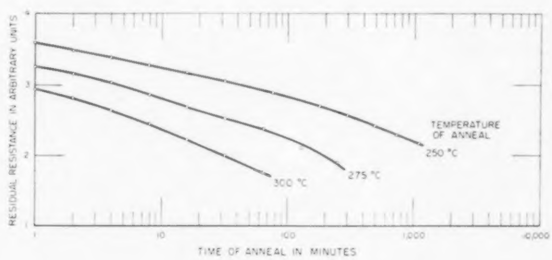

FIGURE 4. Normalized isothermal annealing curves for temperatures of anneal between 250°C and 300°C. In order to obtain an approximate value of residual resistivity change in micro ohm cm due to the irradiation, multiply the arbitrary scale by 0.018. Residual resistivity may then be obtained by adding this value to the annealed residual resistivity which is approximately 0.015 $\mu\Omega$cm.

In Figure 6, tempering curves for irradiated and for cold-worked copper are compared on a percentage basis, allowing several qualitative features of the annealing to be noted. The final resistivities of the damaged specimens were 21.01 and $15.3 \times 10^{-8}\Omega$cm respectively. Initially these specimens had resistivities of 1.56 and $1.37 \times 10^{-8}\Omega$cm respectively.

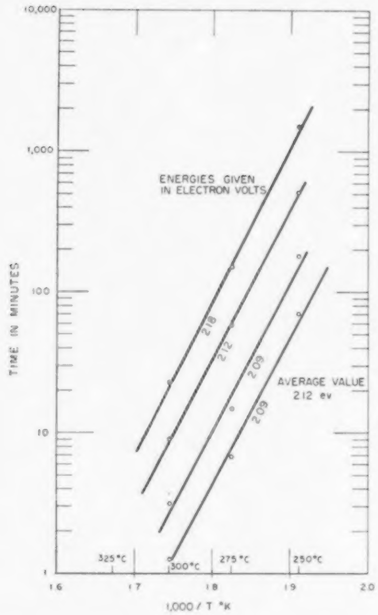

FIGURE 5. Phenomenological determination of activation energy for the annealing process active in the temperature range between 250°C and 300°C.

The irradiated specimen had been exposed at temperatures below − 150°C to 17.2μahr/cm^2 of 34.5 Mev alpha particles, and the cold-worked specimen had been twisted while immersed in liquid helium, after which the specimens were similarly tempered from temperatures near their damage temperature to 100°C. Up to about − 80°C the rate of annealing is nearly equal for the two types of damage; about 75 per cent of the damage still remains. From this temperature to near room temperatures however, the irradiated material anneals to a greater extent than the cold-worked copper so that at room temperature there is only approximately 25 per cent of the radiation damage still present compared

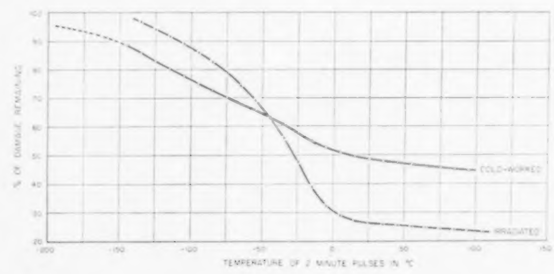

FIGURE 6. Tempering annealing curves for irradiated and for cold-worked copper on a percentage basis. The irradiated specimen received an exposure of 17.2 μahrs/cm^2 with 34.5 Mev alpha particles at temperatures below − 150°C. The cold-worked specimen had been cold-worked by twisting while immersed in liquid helium.

to about 50 per cent for the cold-worked material. As the temperature is raised above 100°C the damage finally anneals completely, that due to the cold-work annealing more rapidly than that due to irradiation. If the agreement in activation energies obtained for the temperature range from − 70°C to 0°C for cold-worked and for irradiated copper is indicative of motion or annihilation of the same defect then the above qualitative features show that this defect is produced in quite different concentrations in the two methods of damage.

The isothermal annealing curves may be described empirically by using a kinetic rate equation,

$$\frac{d(\rho - \rho_0)}{dt} \sim (\rho - \rho_0)^{\alpha} e^{-E/KT} \qquad (1)$$

where

$\rho - \rho_0$ is the resistivity change undergoing annealing,
t is the time,
α is the order of the reaction and is restricted to integer values,
E is the activation energy,
K is the Boltzmann constant
and T is the absolute temperature.

A third order of reaction is needed to fit the isothermal data between − 65°C and − 20°C. For the isothermal annealing between 250°C and 300°C a fourth order of reaction is needed to fit the data.

Acknowledgments

The author wishes to acknowledge the help of C. R. Davidson and Lyle Glasgow of the Irradiation Physics Group at Berkeley for supervising and performing the required irradiations and to thank Miss Sonja Hanjian for patient help in performing the required annealings. This work was based on studies conducted for the Atomic Energy Commission under Contract AT-11-1-GEN-8.

References

1. MARTIN, A. B., *et al.* Phys. Rev. **81** (1951) 664.
2. MARX, J. W., COOPER, H. G., and HENDERSON, J. W. Phys. Rev. **88** (1952) 106.
3. BOWEN, DWAIN, EGGLESTON, R. R., and KROPSCHOT, R. H. J. Appl. Phys. **23** (1952) 630.
4. PARKINS, W. E., DIENES, G. J., and BROWN, F. W. J. Appl. Phys. **22** (1951) 1012.
5. EGGLESTON, R. R. J. Appl. Phys. **23** (1952) 1400.
6. OVERHAUSER, A. W. Bull. Am. Phys. Soc., December 1952.
7. SEITZ, F. Adv. in Physics, Quart. Supp. Phil. Mag. **1** (1952) 43.
8. MOTT, N. F. Phil. Mag. **43** (1952) 1151.

THE KINETICS OF PRECIPITATION OF BARIUM SULFATE FROM AQUEOUS SOLUTION*

D. TURNBULL†

The rate of precipitation of barium sulfate has been investigated using the conductimetric technique. In direct mixing experiments all but a negligible number of precipitation nuclei form during the mixing process, probably in small local volume elements where the supersaturation is larger than it is after complete homogenization. In the earliest stages of precipitation the rate of linear growth of barium sulfate crystals is independent of their size and apparently limited by a process occurring at the crystal-solution interface. After the crystals reach a certain size their growth rate becomes limited by diffusion. It is shown that the assumption of Christiansen and Nielsen [2], that the reciprocal of the time of appearance of turbidity is directly proportional to the homogeneous nucleation frequency, is probably not valid.

LA CINÉTIQUE DE PRÉCIPITATION DU SULFATE DE BARYUM DE SOLUTION AQUEUSE

La vitesse de précipitation du sulfate de baryum a été étudiée en employant la technique conductimétrique. Dans les expériences de mélange direct la plupart des germes de précipitation sont formés pendant la préparation du mélange, probablement dans de petits éléments locaux de volume où la sursaturation est plus grande qu'après l'homogénéisation complète. Pendant les premiers stades de précipitation, la vitesse de croissance linéaire des cristaux de sulfate de baryum est indépendante des dimensions de ces derniers; elle est apparemment limitée par un processus se passant à l'interface cristal-solution. Quand les cristaux atteignent une certaine dimension, la vitesse de croissance devient limitée par la diffusion. Il est montré que la supposition de Christiansen et Nielsen [2], que l'inverse du temps d'apparition du trouble est directement proportionnel à la fréquence de germination homogène, n'est probablement pas valable.

DIE KINETIK DER FÄLLUNG VON BARIUMSULFAT AUS WÄSSRIGER LÖSUNG

Die Fällungsgeschwindigkeit von Bariumsulfat wurde mit Hilfe von Leitfähigkeitsmessungen untersucht. In den direkten Mischungsversuchen bildeten sich alle (mit Ausnahme eines zu vernachlässigenden, kleinen Anteils) Niederschlagskeime während des Mischungsvorganges; wahrscheinlich in kleinen Volumenelementen, in denen die Übersättigung dann grösser ist als nach erfolgtem Mischungsausgleich. In den ersten Stadien der Fällung ist die lineare Wachstumsgeschwindigkeit der Bariumsulfatkristalle unabhängig von ihrer Grösse und anscheinend durch einen an der Grenzfläche Kristall-Lösung stattfindenden Vorgang begrenzt. Wenn die Kristalle eine gewisse Grösse erreicht haben, ist ihre Wachstumsgeschwindigkeit durch die Diffusion begrenzt. Es wird gezeigt, dass die Annahme von Christiansen und Nielsen [2], dass der Reziprokwert der Zeit des ersten Auftretens der Trübung der homogenen Keimbildungsgeschwindigkeit direct proportional ist, wahrscheinlich nicht zu Recht besteht.

Introduction

Recently LaMer and Dinegar [1] and Christiansen and Nielsen [2] have investigated the kinetics of precipitation of barium sulfate from aqueous solutions. These and earlier investigations bearing on the problem have been reviewed briefly by LaMer [3].

Let γ be the mean ionic activity coefficient of barium sulfate, and m_1 and m_2 be the concentration of barium and sulfate ions respectively in moles/cc. The supersaturation ratio S is defined by the equation:

$$S = (m_1 m_2)^{\frac{1}{2}}\gamma/(K)^{\frac{1}{2}} \tag{1}$$

where K ($K = 1.2 \times 10^{-16}$ moles^2 − cm^{-6} at 25°C) is the thermodynamic solubility product. Let the initial supersaturation at time (t) = zero be S_0. Isothermally, S decays to unity following some relationship $S = f(t)$. At constant temperature and ionic strength, the frequency, I, of homogeneous nucleation of barium sulfate crystals per volume is some function of S, $I = f(S)$.

In most of the investigations of the precipitation of barium sulfate an initial supersaturation has been produced by direct mixing of two solutions, one containing sulfate and the other barium ions. In this process there are likely to be produced small volume elements in which $S > S_0$. These regions of "local excess" will persist for only very short periods, but, if dI/dS is large, a significant fraction of the precipitation nuclei may form in them. LaMer and Dinegar used the direct mixing technique in one group of experiments, but in a second group they avoided local excesses by the ingenious technique of generating the sulfate homogeneously in the presence of a barium salt solution by a chemical reaction.

Christiansen-Nielsen and LaMer-Dinegar did not measure $S = f(t)$ but observed that after a time period τ, measured from the instant of mixing, turbidity became apparent. LaMer and Dinegar found that, where S was built up by a chemical

*Received June 10, 1953; in revised form, June 23, 1953.
†General Electric Research Laboratory, The Knolls, Schenectady, New York, U.S.A.

reaction, turbidity became apparent at a fairly well defined value $S = S_0 \approx 22$ that was nearly independent of the time Δt (ranging from 25 to 120 minutes) of build-up of sulfate ion to the critical value (the rate of formation of sulfate was approximately constant).

Christiansen and Nielsen found that their τ-values could be described by the equation $\tau = k'/S_0^7$. They assumed that $\tau \propto 1/(I)_{S=S_0}$; hence, $I = kS_0^7$. To explain these results, Christiansen and Nielsen postulated that the rate determining step in the formation of a $BaSO_4$ nucleus is the reaction:

$$\begin{matrix} Ba_3^{=}(SO_4)_4 & & Ba^{++} & \\ \text{or} & + & \text{or} & \rightarrow Ba_4(SO_4)_4 \\ Ba_4^{++}(SO_4)_3 & & SO_4^{=} & \end{matrix}$$

The basis for this postulate is that the concentration of the 7-ion cluster should be proportional to S^7 (or m^7 where m is the molarity of $BaSO_4$) if a quasi-equilibrium state is assumed. LaMer [3] found that the τ-values of Christiansen-Nielsen and LaMer-Dinegar (from direct mixing experiments) combined were best described by a relation $\tau = k'/S_0^6$. Accepting the Christiansen-Nielsen basic interpretation, although it is inconsistent* with LaMer and Dinegar's results from experiments where S is built up chemically, LaMer [3] proposed that the rate determining step is the addition of an ion to a 6-ion cluster.

This "constant number" theory of Christiansen-Nielsen denies any dependence of nucleus size upon S and is at marked variance with the "classical theory" for nucleation of precipitates in condensed systems as developed, for example, by Becker [4], and Turnbull and Fisher [5]. According to this classical theory, the dependence of I on S is given by [5]:

$$I \approx K_V \exp\left[-a\sigma^3 v^2/k^3T^3(\ln S)^2\right], \tag{2}$$

where

$$K_V \approx n\nu \exp\left[-\Delta G_A/kT\right]; \tag{3}$$

a is a geometrical factor,
σ = interfacial energy per area between nucleus and solution,
v = volume per "molecule" of $BaSO_4$ crystal,
n = number of $Ba^{++} + SO_4^{=}$ ions per volume,
ν = jump frequency,
ΔG_A = free energy of activation for growth of crystals.

*LaMer (private communication) now recognizes this inconsistency.

The classical theory generally predicts that the nucleus size should decrease with increasing S and a much more marked dependence of I on S than is predicted by the Christiansen-Nielsen theory.

The Christiansen-Nielsen assumption of $\tau \propto 1/(I)_{S=S_0}$ is questionable. Turbidity will become perceptible only after considerable growth of particles and τ will be dependent on I, the rate of crystal growth, and the resolving power of the apparatus. There is also the possibility that most of the nuclei in the direct mixing experiments formed in the mixing process due to the local excesses rather than after the solution had become homogeneous. Strong evidence for this mechanism of formation of nuclei in direct mixing experiments is provided by the results of LaMer and Dinegar where the supersaturation is chemically produced. For example, these investigators observed turbidity after five minutes corresponding to $S_0 = 16.0$ in a direct mixing experiment, but in the chemical build-up experiments S increased from 16 to 21 in periods as large as 25 minutes before turbidity became apparent.

Because of these questions on the interpretation of τ, measurements of $S = f(t)$ for various values of S_0 using different direct mixing techniques were undertaken. This paper will describe the results and point out their significance.

Experimental

$S = f(t)$ was measured by a conductimetric technique.† The conductivity cells were of the usual design with lightly platinized platinum electrodes. In some experiments a Brown Impedance Bridge (Model 200B) was used to measure conductivity, but where more precision was required a Shedlovsky [8] bridge was used. The reproducibility of the measured resistances was $\pm \frac{1}{4}$ per cent with the Brown bridge and $\pm$ 0.005 per cent with the Shedlovsky bridge.

Barium sulfate was formed according to one or the other of the following reactions:

$$Ba(OH)_2 + H_2SO_4 \rightarrow 2H_2O + BaSO_4 \tag{4}$$

$$Ba(NO_3)_2 + K_2SO_4 \rightarrow 2KNO_3 + BaSO_4. \tag{5}$$

A supersaturated solution was produced by direct mixing of the appropriate standard solutions

†The author has been informed by private communications [6; 7] that R. A. Johnson [6] of the University of Illinois and F. C. Collins [7] of Brooklyn Polytechnic Institute have undertaken measurements, from a different point of view, on the precipitation of $BaSO_4$ using a conductimetric technique.

by one or the other of the following procedures:

(a) Suppose that the concentration of supersaturated barium sulfate immediately after homogenization is to be m_0. A measured volume, v, of standard barium ion solution of concentration $2m_0$ is poured into a volume, v, of sulfate ion solution of concentration $2m_0$ which is stirred by a motor driven glass propeller.

$(b)_{Ba}$ A volume $v/200$ of barium ion solution of concentration $200m_0$, contained in a calibrated 1 cc Becton-Dickinson tuberculin syringe, is rapidly injected into a volume, v, of sulfate ion solution of concentration m_0 which is simultaneously stirred as in method (a).

$(b)_{SO_4}$ Same as $(b)_{Ba}$ excepting that concentrated sulfate solution is rapidly injected into a more dilute barium ion solution.

After mixing, a part of the resulting solution is added to the conductivity cell and the resistance measured as a function of time. Excepting where otherwise noted, the solutions to be mixed and the conductivity cell were thermostated at 25.00 ± 0.02°.

After each experiment the conductivity cell and all other vessels that had contained supersaturated barium sulfate solutions were cleaned with hot cleaning solution, which dissolves solid barium sulfate. No effect of the freshly platinized electrodes upon the course of the precipitation was noted excepting in a few instances where the initial supersaturation, S_0, was less than 10. However, after about four experiments the electrodes of a particular cell definitely catalyzed precipitation for $S_0 > 10$ even after the cleaning treatment. This catalytic effect was virtually destroyed by replatinizing the electrodes.

The fraction, X, of barium sulfate precipitated in time, t, is defined by:

$$X = \frac{m_0 - m}{m_0 - m_e}, \tag{6}$$

where m is the concentration of $BaSO_4$ at time t; $m = m_0$ at $t = 0$; and $m = m_e$ at $t = \infty$. For reaction (4), m (expressed in moles/cc) was evaluated from the following relationships:

$$m = \frac{(L - L_{H_2O})}{\Lambda_m}, \tag{7}$$

$$\Lambda_m = \Lambda_m{}^0 - a\sqrt{m}, \tag{8}$$

where L is the specific conductivity of the solution; L_{H_2O} the specific conductivity of the water used; and $\Lambda_m{}^0$ the *molar* conductivity at infinite dilution calculated from the ionic equivalent conductivities at infinite dilution tabulated by MacInnes [9]. The constant a in equation (8) was calculated on the assumption that the coefficient $d\ln\Lambda/dm$ is identical for $CaSO_4$ and $BaSO_4$ solutions. $d\ln\Lambda/dm$ for $CaSO_4$ solutions was calculated from data given in I.C.T. [10]. Equation (8) does not describe precisely the variation of Λ_m with m. However, for the very dilute solutions used in our experiments, the variation of Λ_m with m is a second-order effect which, if ignored, would cause an error in X of 2 per cent at most.

When reaction (5) was used to produce a supersaturated solution, the precision of the measurements was reduced somewhat because the other product of the reaction, KNO_3, is a good conductor. For $BaSO_4$, m was calculated from the following relations:

$$m = \frac{(L - L' - L_{H_2O})}{\Lambda_m}, \tag{9}$$

$$L' = \Lambda_m' m', \tag{10}$$

$$\Lambda_m = \Lambda_m{}^0 - a\sqrt{m\left(\frac{\mu}{\mu - \mu'}\right)}, \tag{11}$$

$$\Lambda_m' = \Lambda_m'{}^0 - a'\sqrt{m'\frac{\mu}{\mu'}}, \tag{12}$$

where all the primes refer to KNO_3. The molar conductivity at infinite dilution, $\Lambda_m'{}^0$, for KNO_3 was calculated from MacInnes' table of ionic equivalent conductances. The constant a' was calculated from data given in I.C.T. [10]. μ is the total ionic strength (see MacInnes [9] for definition) and μ' is the contribution to the ionic strength due to KNO_3 only. This correction for the conductivity of $BaSO_4$ in the presence of another electrolyte is approximate. However, if it were assumed that $\Lambda_m/\Lambda_m' = \Lambda_m{}^0/\Lambda_m'{}^0$, the maximum absolute error in X would be only about ten per cent and the maximum relative error about one per cent.

Mean ionic activity coefficients for barium sulfate were evaluated from the relation between γ and μ assumed by LaMer and Dinegar.

Results and Interpretation

Relation of X to t

Controlling the initial supersaturation, S_0, after homogenization, the method of mixing and the temperature, we obtain experimentally X as a function of time, $X = F(t)$. It was discovered that the $X = F(t)$ relations for various values of

S_0 in the range 12 to 20 and for a variety of methods of mixing could all be superposed for $0 \leqslant X \leqslant 0.40$ by multiplying the ordinary time unit for each $X = F(t)$ relation by a suitable relative factor, f ("scale factor"). Figure 1 shows $X = F(t)$ with

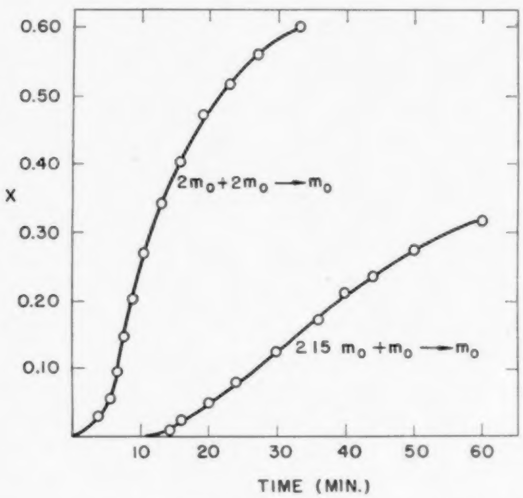

FIGURE 1. Fraction of $BaSO_4$ precipitated with time for two methods of mixing [(a) and $(b)_{Ba}$]. Reaction (4), $S_0 = 16.0$, temp. $= 25.00 \pm 0.02°$, Brown bridge.

S_0 constant (temperature $= 25.00 \pm 0.02°$) for two methods of mixing. Figure 2 shows the superposition of these two curves effected by multiply-

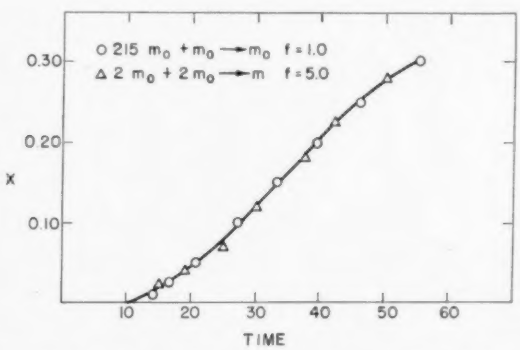

FIGURE 2. Superposition of curves shown in Fig. 1 effected by choice of suitable scale factors, f.

ing t by the indicated factors (the plotted points are readings from the smoothed curves of Figure 1).

Figure 3 shows $X = F(t)$ for the values of S_0 using what proved to be the most reproducible method of mixing, $(b)_{Ba}$. In these particular experiments the temperature was not closely controlled ($27.0 \pm 0.3°$) but it was established that for a constant m_0 the $X = F(t)$ relations for 27° and 25.00° agreed to within the experimental

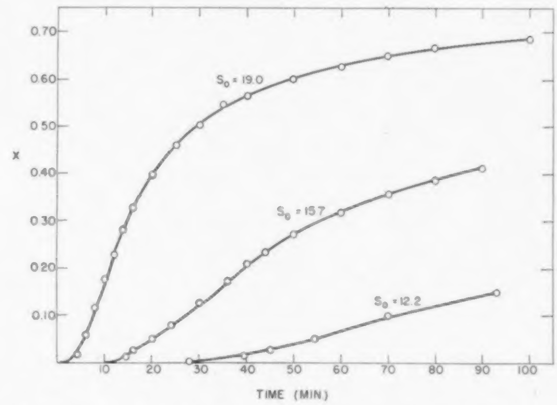

FIGURE 3. Fraction of $BaSO_4$ precipitated with time for three different values of S_0. Reaction (4), mixing method $(b)_{Ba}$, temp. $27.0 \pm 0.3°$, Brown bridge.

uncertainty. Figure 4 shows the superposition of the curves of Figure 3 obtained by applying the indicated scale factors where the plotted points represent readings from the smoothed curves of

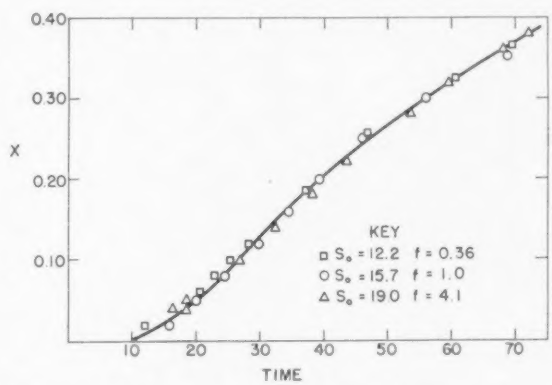

FIGURE 4. Superposition of curves shown in Fig. 3 effected by choice of suitable scale factors.

Figure 3 plus an additional section for $S_0 = 12.2$ not shown in Figure 3. The composite curves of Figures 2 and 4 are also superposable with deviations no greater than the experimental errors. Therefore, the course of the precipitation for all cases investigated can be described by the general relation:

$$X = F(ft), \tag{13}$$

where f is a function of S_0, the method of mixing and the specific solutions used. It was also established that the dependence of X on ft for the earlier stages of precipitation is the same whether the supersaturation is produced by reaction (4) or (5).

As we see from Figure 1, f appears to be markedly

dependent upon the method of mixing of reagents, being a factor of 5 greater for method (a) than for method $(b)_{Ba}$. Table I summarizes the relative scale factors obtained with a variety of mixing methods and reagent solutions for $S_0 = 16.0$ and 15.2 and temperature $= 25.00 \pm 0.02°$.

TABLE I

RELATIVE SCALE FACTORS FOR A VARIETY OF MIXING METHODS AND REAGENT SOLUTIONS
(Temperature $= 25.00 \pm 0.02°$)

Reagents	Method of mixing	S_0	Relative Scale factor (f)
$Ba(OH)_2 + H_2SO_4$	b_{Ba}	16.0	1.0
$Ba(OH)_2 + H_2SO_4$	a	16.0	5.0
$Ba(OH)_2 + H_2SO_4$	a	16.0	3.9
$Ba(OH)_2 + H_2SO_4$	b_{SO_4}	16.0	2.9
$Ba(NO_3)_2 + K_2SO_4$	a	15.1	3.0
$Ba(NO_3)_2 + K_2SO_4$	b_{Ba}	15.2	1.3
$Ba(NO_3)_2 + K_2SO_4$	b_{SO_4}	15.2	3.4
$Ba(OH)_2$* $+ H_2SO_4$	b_{Ba}	16.0	1.6

*A different $Ba(OH)_2$ solution.

For a given S_0, temperature and $Ba(OH)_2$ solution, f was reproducible to within ± 5 per cent for mixing method $(b)_{Ba}$ but only to ± 15 per cent for mixing method (a).

It is surprising that the slowest rate of precipitation (smallest relative value of f) was obtained with method $(b)_{Ba}$ that might be expected to produce the highest local excesses in supersaturation. However, since the f value for method $(b)_{SO_4}$ is about 3 times larger than for $(b)_{Ba}$, it appears that the effect may be associated with the use of a very small volume of a particular solution rather than with the mixing method. With method (a), f was not greatly dependent upon whether the barium salt was added to the sulfate or vice versa.

Interpretation of $X = F(ft)$ Relation

Since the functional relation of X to ft is constant, though f varies greatly for a wide range of S_0 values, method of mixing and different reagent solutions, we conclude that our experiments are best described if it is assumed that: *after homogenization the number of precipitation nuclei that form is negligible in comparison with the number produced in the homogenization process.* According to our picture, a number of precipitation nuclei, n_i, per volume are formed during homogenization. The dependence of X on ft is determined by the rate of growth of these n_i particles. The nuclei probably form in regions of local excess produced during homogenization either by (i) homogeneous nucleation or, more likely, in view of variability of the results with the specific solution, by (ii) heterogeneous nucleation on suspended foreign particles contained in the elements of local excess. In any event, the results imply a very great dependence of I on S. Probably f is primarily a function of n_i.

The over–all shape of the $X = F(ft)$ curve is not simple (see Figure 1). However, analysis of the curves indicated that X becomes proportional to t^3 for values of $X \to 0$. This result possibly implies that for $X \to 0$:

$$X = 1 - \exp[-bt^n] \tag{14}$$

with $n = 3$.

If equation (14) is valid, log ln $[1/(1 - X)]$ plotted against log t should give a straight line of slope n. The tests for this straight line relation are shown in Figures 5, 6, 7 and 8. (The Shedlovsky bridge was used to obtain the points shown in Figures 6, 7, and 8. With this bridge X was measured accurately to values as small as $X = 0.001$.) Within the experimental uncertainty, a straight line relation with $n = 3.0 \pm 0.1$ does obtain in all cases for $X < 0.04$ approx. The relative scale

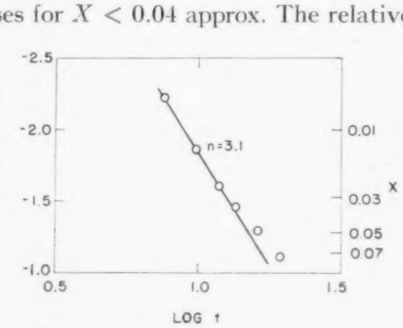

FIGURE 5. Test of equation (14): $S_0 = 16.0$, reaction (4), mixing method $(b)_{Ba}$, temp. $25.00 \pm 0.02°$, Brown bridge.

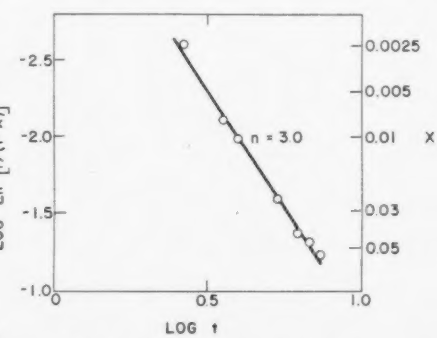

FIGURE 6. Test of equation (14): $S_0 = 15.1$, reaction (5), mixing method (a), temp. $= 25.00 \pm 0.02°$, Shedlovsky bridge.

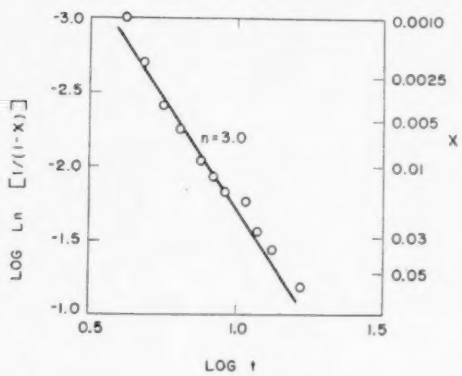

FIGURE 7. Test of equation (14): $S_0 = 15.2$, reaction (5), mixing method (a), temp. = $25.00 \pm 0.02°$, Shedlovsky bridge.

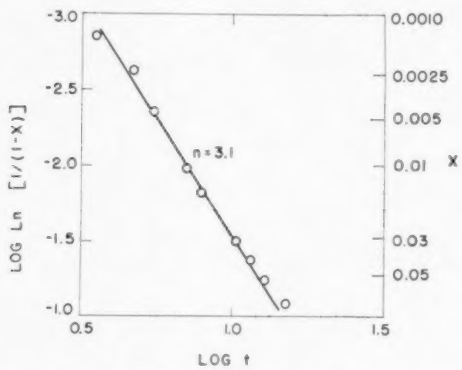

FIGURE 8. Test of equation (14): $S_0 = 16.0$, reaction (4), mixing method $(b)_{Ba}$, temp. = $25.00 \pm 0.02°$, Shedlovsky bridge.

factors corresponding to these results differed by factors as large as $2\frac{1}{2}$.

Wert and Zener [11] have discussed the growth of spherical precipitates from supersaturated solid solutions. Assuming that all the precipitation nuclei are present at $t = 0$ and that the growth is diffusion-limited, they obtain (for small X) an equation of the same form as (14) with $n = 3/2$.

To explain the fact that our results for small X are best described with $n = 3$, we assume that the growth of very small barium sulfate particles *is limited not by diffusion but by a process occurring at the crystal-solution interface.*

As the precipitate crystal grows larger the flux of ions to its surface by diffusional processes decreases. Therefore, when the crystal reaches a certain size its further growth may become limited by the rate of diffusion of ions to the crystal-solution interface rather than by the interface process. Collins [12] has developed the theory for the growth of small precipitate particles as a function of their radius, r. The theory is somewhat analogous to the theory for the thickening of thin oxide films developed by Fischbeck [13] and Grunewald and Wagner [14].

We shall give a simple derivation along the lines suggested by the treatments of Fischbeck [13] and Wert and Zener [11] which leads to a relation $r = f(t)$ similar to that obtained by Collins. The flux, J, per area-time of substance precipitating on the particle may be written:

$$J = K(dr/dt). \tag{15}$$

From Fick's first law

$$J = D(\partial m_x/\partial x)_{x=r}\,, \tag{16}$$

where D is the diffusion coefficient and m_x is the amount of $BaSO_4$ per volume at a distance x from the center of the crystal. Since the solution is very dilute, we make the approximation (see Wert and Zener [11] for comment)

$$(\partial m_x/\partial x)_{x=r} = \frac{m - m_r}{r}$$

giving

$$J = D\frac{m - m_r}{r}, \tag{17}$$

where m is the concentration of $BaSO_4$ at $x = \infty$ and m_r is the actual concentration ($m_r > m_e$) at the crystal solution interface.

J also must satisfy the relation

$$J = (m_r - m_e)G, \tag{18}$$

where G is an interface transfer coefficient independent of m_r.

Eliminating m_r from (17) and (18) and assuming $m_r \gg m_e$, we have

$$K(dr/dt) = \frac{mDG}{Gr + D} \tag{19}$$

which on integration gives

$$r^2/2D + r/G = (mK)t. \tag{20}$$

For $r \to 0$, equation (20) becomes

$$r = (mKG)t \tag{21}$$

and the growth is interface-controlled. When r is very large, (20) becomes

$$r^2 = (2mKDt) \tag{22}$$

and the growth is diffusion-controlled. We conclude that the relative magnitudes of D and G are such that for our experiments the growth of the

$BaSO_4$ crystals is interface-controlled for $X \leqslant 0.04$ approx.

When growth is interface-controlled, $m_r = m$ and, assuming that the crystals are spherical (not a crucial assumption), it follows that

$$(23) \qquad -dm/dt = n_i\,(4\pi r^2)\,(m - m_e)G$$

but

$$(24) \qquad m_0 - m = (n_i/V)\,(4/3)\pi r^3,$$

where V is the molar volume of barium sulfate, hence

$$-dm/dt = (4\pi n_i)^{1/3}(3V)^{2/3}(m_0 - m)^{2/3}(m - m_e)G.$$

From equation (6) we obtain

$$(m_0 - m_e)\,dX/dt = -dm/dt.$$

Therefore

$$(25) \qquad dX/dt = \alpha X^{2/3}(1 - X),$$

where

$$(25a) \qquad \alpha = [36\pi V^2(m_0 - m_e)^2 n_i]^{1/3}G.$$

For X very small, (25) may be integrated to give (14), where $n = 3$ and $b = \alpha/3$.

For $X \geqslant 0.04$ approx., the rate of precipitation becomes less than is predicted by equation (14). Qualitatively we expect from equation (20) that as r increases the growth of the crystals will become diffusion limited and dX/dt will, in agreement with observation, become less than predicted by equation (25). For $X > 0.5$, dX/dt appears to be much smaller than would be expected if the rate were controlled only by diffusion. This effect may be due to the snowing of crystals out of solution by gravity segregation. In agreement with this idea, dX/dt becomes somewhat dependent on cell geometry for $X > 0.5$.

Effect of Supersaturation

The relative scale factors obtained for different S_0 using the most reproducible method of mixing, $(b)_{Ba}$, are shown in Table II (corresponding $X = f(t)$ relations are plotted in Figures 3 and 4). It follows from (14) that for a given value of X, $(dX/dt)_1/(dX/dt)_2 = f_1/f_2$ where subscripts 1 and 2 each denote a particular $X = F(t)$ relation. Hence, from equation (25) we have:

$$(26) \qquad f_1/f_2 = \frac{[(m_0 - m_e)^{2/3} n_i^{1/3}]_1}{[(m_0 - m_e)^{2/3} n_i^{1/3}]_2}.$$

Thus, using (26) relative values of n_i may be calculated from the scale factors. We define β such that

$$\beta(n_i)_{S_0 = 12.2} = 1,$$

where β, but not n_i, is independent of S_0. Table II lists βn_i corresponding to different initial supersaturations. Also shown in the table are LaMer and Dinegar's $1/\tau$ values for the corresponding

TABLE II

f AND βn_i FOR DIFFERENT S_0 VALUES (temperature $27.0 \pm 0.3°$); COMPARISON WITH RESULTS OF LAMER AND DINEGAR

S_0	f	$(1/\tau)$ (min^{-1}) according to LaMer and Dinegar [1]	Our X at t = LaMer-Dinegar τ	$f\tau$	βn_i
12.2	0.36	0.077	0.0006_2	4.7	1.0
15.7	1.0	0.20	0.0007_6	5.0	12.5
19.0	4.1	0.62	0.0011_2	6.6	570.

initial supersaturations corrected for the 2° temperature differential (temperature = $25.00 \pm 0.02°$ in LaMer-Dinegar experiments). In column 4 we list the fraction of barium sulfate precipitated (calculated by extrapolation of the relation $X = bt^3$) in our experiments at t = LaMer-Dinegar's τ.

It is possible, as suggested by Christiansen and Nielsen, that turbidity is perceptible at some constant X independently of the other variables. If so, there should be a correspondence between the relative magnitudes or our scale factors and the $1/\tau$ values. That there is some correspondence is shown by the fact that f changes by a factor of 11 and $1/\tau$ by a factor of 8 between the extremal S_0 values and the rough constancy of $f\tau$ (column 5).

If LaMer and Dinegar's and our results are consistent on the time scale (which is doubtful in view of our findings), their perception of turbidity corresponds to $X = 0.0006$ to 0.001 (see column 4).

On the basis of our results we conclude that Christiansen and Nielsen's assumption that $1/\tau$ is proportional to the frequency of homogeneous nucleation in a homogenized solution is not valid. In fact, the number of nuclei, n_i, produced in the mixing process varies much more with S_0 than does $1/\tau$. Between the extremal values of S_0, n_i changed by a factor of 570 compared to a factor of ~ 10 variation in $1/\tau$ (compare columns 3 and 6, Table II). The interpretation of the dependence of τ upon S_0 in direct mixing experiments must, therefore, be much more complex than assumed by Christiansen-Nielsen and LaMer.

Effect of Heterogeneities

We have noted that the platinized electrodes definitely promoted precipitation after several uses even after treatment with hot cleaning solution. No catalytic effect was observed with

freshly platinized electrodes excepting where $S_0 < 9$ when mixing method (a) was used. We infer from this latter observation that the electrodes promoted nucleation at the higher values of S_0 but the effect was not noticed because the nuclei formed in the body of the solution pumped down the supersaturation much more rapidly than did the electrodes. It was noted that the glass walls of the containing vessels promoted precipitation but again this effect was not relatively important for $S_0 \geqslant 12$. We have pointed out that two possible mechanisms of formation of nuclei in the regions of local excess produced by direct mixing are (1) homogeneous nucleation, and/or (2) nucleation on the surfaces of heterogeneities contained in these regions and activated by the high local supersaturation. Because the rate of precipitation was, unexpectedly, a factor of 5 slower for mixing method $(b)_{Ba}$ than for (a), and because of the dependence of rate upon the reagent solution, we conclude that most of the nuclei were formed in our experiments by the heterogeneous nucleation mechanism (possibly excepting the experiments in which mixing method $(b)_{Ba}$ was used). Schmid and Jetter [15] have demonstrated in more detail the importance of the heterogeneous nucleation mechanism in the normal precipitation of barium sulfate.

Electron Microscopic and Diffraction Examination of Crystals

Mr. Norman Walter of this laboratory separated some of the barium sulfate crystals from a solution in which precipitation was nearly completed and observed them magnified (by a Philips electron microscope) 3000 times. Most of the crystals were approximately 0.1 micron in diameter. Their shape, though not completely resolved, was approximately polyhedral or spherical. A diffraction pattern obtained with the particles *in situ* confirmed the identity of the crystals and that they were single. These results suggest that the growth of the particles becomes diffusion controlled when their diameter is considerably less than 0.1 micron.

Summary of Conclusions

When a supersaturated barium sulfate solution is formed by direct mixing, all but a negligible number of nuclei are formed in the mixing process, probably in small regions where the supersaturation is greater than it is after homogenization is completed.

The assumption of Christiansen and Nielsen that the reciprocal of the time (τ) of appearance of turbidity is directly proportional to the frequency of homogeneous nucleation of barium sulfate crystals probably is not valid. The actual dependence of nucleation frequency on supersaturation is much greater than is predicted by the Christiansen-Nielsen theory.

However, direct mixing experiments can give valuable information on the kinetics of growth of crystals since all nuclei start to grow at the same time and a negligible number form during the course of the experiment.

In the earliest stages of precipitation, $X \leqslant 0.04$, the diameter of barium sulfate crystals increases at a rate independent of time or crystal size. Therefore, in this stage of precipitation the rate of growth is limited by the transfer of ions across the crystal-solution interface and not by diffusion of ions to the interface.

As the crystals become larger and precipitation progresses ($X \geqslant 0.04$), the rate of crystal growth becomes slower and diffusion limited. Finally, the rate of precipitation is further retarded by the snowing of crystals out of solution due to gravity segregation.

Acknowledgment

The author thanks Mr. S. I. Reynolds for the loan of the Shedlovsky bridge, and Mr. N. Walter for examining the crystals with the aid of the electron microscope.

References

1. LaMer, V. K. and Dinegar, R. H. J. Amer. Chem. Soc. **73** (1951) 380.
2. Christiansen, J. A. and Nielsen, A. Acta Chem. Scand. **5** (1951) 673-675.
3. LaMer, V. K. Ind. Eng. Chem. **44** (1952) 1270.
4. Becker, R. Ann. Phys. **32** (1938) 128.
5. Turnbull, D. and Fisher, J. C. J. Chem. Phys. **17** (1949) 71.
6. Johnson, R. A. Private communication.
7. Collins, F. C. Private communication.
8. Shedlovsky, T. J. Amer. Chem. **52** (1930) 1793.
9. MacInnes, D. A. The Principles of Electrochemistry (New York, Reinhold, 1939).
10. Int. Crit. Tables, vol. 6 (New York, McGraw-Hill, 1929) pp. 229-238.
11. Wert, C. A. and Zener, C. J. Appl. Phys. **21** (1950) 5.
12. Collins, F. C. J. Colloid Science, **5** (1950) 499.
13. Fischbeck, K. Z. Elektrochem. **39** (1933) 316.
14. Wagner, C. and Gruenewald, K. Z. Phys. Chem. **40B** (1938) 455.
15. Schmid, G. and Jetter, A. Z. Elektrochem. **56** (1952) 760.

CLEAVAGE DEFORMATION IN ZINC AND SODIUM CHLORIDE*

P. L. PRATT†

Flat surfaces prepared by the cleavage of single crystals show deformation markings associated with the propagation of the cleavage crack. The amount of deformation can be minimised by cleaving thin sections away from the desired specimens, and the technique is useful for cubic materials which cleave on (001). In the case of zinc, intersecting twins are found on the extended side of thin cleavage flakes, together with fine and coarse kinks on the compressed side. Two distinct types of twin intersection were observed in regions of high stress, and their formation, at first sight improbable, is shown to be crystallographically possible.

LA DÉFORMATION PAR CLIVAGE DANS LE ZINC ET DANS LE CHLORURE DE SODIUM

Des marques de déformation, associées à la propagation des fissures de clivage, apparaissent sur des surfaces planes, préparées par le clivage de monocristaux. La quantité de déformation peut être réduite en enlevant de minces sections de l'échantillon par clivage; cette technique est utile dans le cas des matériaux cubiques, dont le plan de clivage est (001). Dans le cas du zinc, on trouve des macles qui s'entrecoupent, du côté soumis à l'extension, et de gros et fins plis du côté soumis à la compression. Deux types distincts d'intersections des macles, furent observés dans les régions de forte tension; il est montré que leur formation est cristallographiquement possible, quoiqu'elle paraisse à première vue improbable.

DIE SPALTVERFORMUNG VON ZINK UND NATRIUMCHLORID

Die flachen Flächen, die man bei der Spaltung von Einkristallen erhält, zeigen Verformungsspuren, die mit der Fortpflanzung von Bruchsprüngen in Beziehung stehen. Das Ausmass der Verformung kann dadurch vermindert werden, dass man dünne Schnitte von den zu bearbeitenden Proben wegbricht, und diese Technik bewährt sich auch bei kubischen Metallen, die in der (001) Ebene spalten. Im Zink wurden sich überschneidende Zwillinge auf der Dehnungsseite von dünnen Spaltschnitten gefunden, während auf der Druckseite feine und gröbere Knicke zu sehen waren. Zwei verschiedene Arten der Überschneidung der Zwillinge wurden im Gebiete grosser Spannungen beobachtet; es wird gezeigt, dass ihre Bildung, die auf den ersten Blick unwahrscheinlich erscheint, kristallographisch möglich ist.

Introduction

Cleavage is often the simplest way of preparing flat surfaces on single crystals, for studying certain of their deformation properties. It is the purpose of this paper to consider the value of this technique, and to interpret some of the markings found on cleaved faces before further deformation.

A highly reflecting surface is easily obtained by cleaving zinc with a chisel at liquid-air temperature, or sodium chloride with a razor blade at room temperature, but the resulting surface is rarely flat and undeformed. In nearly all cases the surface is covered with a system of high and low cleavage steps, radiating from the point of impact, together with markings due to plastic deformation, occurring after cleavage. The best surfaces are obtained by cleaving a relatively thin section away from the desired specimen. In this way most of the deformation is absorbed in the thin flake which curves away from the specimen.

Experimental Techniques

Single crystals of sodium chloride were grown from the melt by passing a platinum crucible containing Analar quality material through a furnace in which a steep temperature gradient was maintained. The crystals were melted out of the inverted crucible before they had cooled much below the melting-point, and then annealed at 600°C for twelve hours. The zinc crystals were of 99.999 per cent purity, and were grown from the melt in the gradient furnace previously described [1].

The cleavage surfaces were examined optically with an opaque stop microscope [2], and with a reflection electron microscope [3].

Experimental Results

1. *Sodium chloride*

Sodium chloride cleaves on the (100) cube plane, and this technique may be used to obtain specimens of any desired size with flat and parallel sides and ends. The cleavage surface of a typical single crystal is shown in Figure 1 with cleavage steps radiating from the top left-hand corner. This surface reveals the mosaic character of the crystal since each element of the mosaic cleaves along its own (100), and the mosaic angle in this case is about 10 minutes of arc. A few horizontal black and white lines can be seen due to slip, induced by the cleavage, on the (110) slip planes at 45° to this surface. The internal stresses due to the slip,

*Received June 11, 1953.

†Atomic Energy Research Establishment Harwell, England. Now at Department of Metallurgy, University of Birmingham, England.

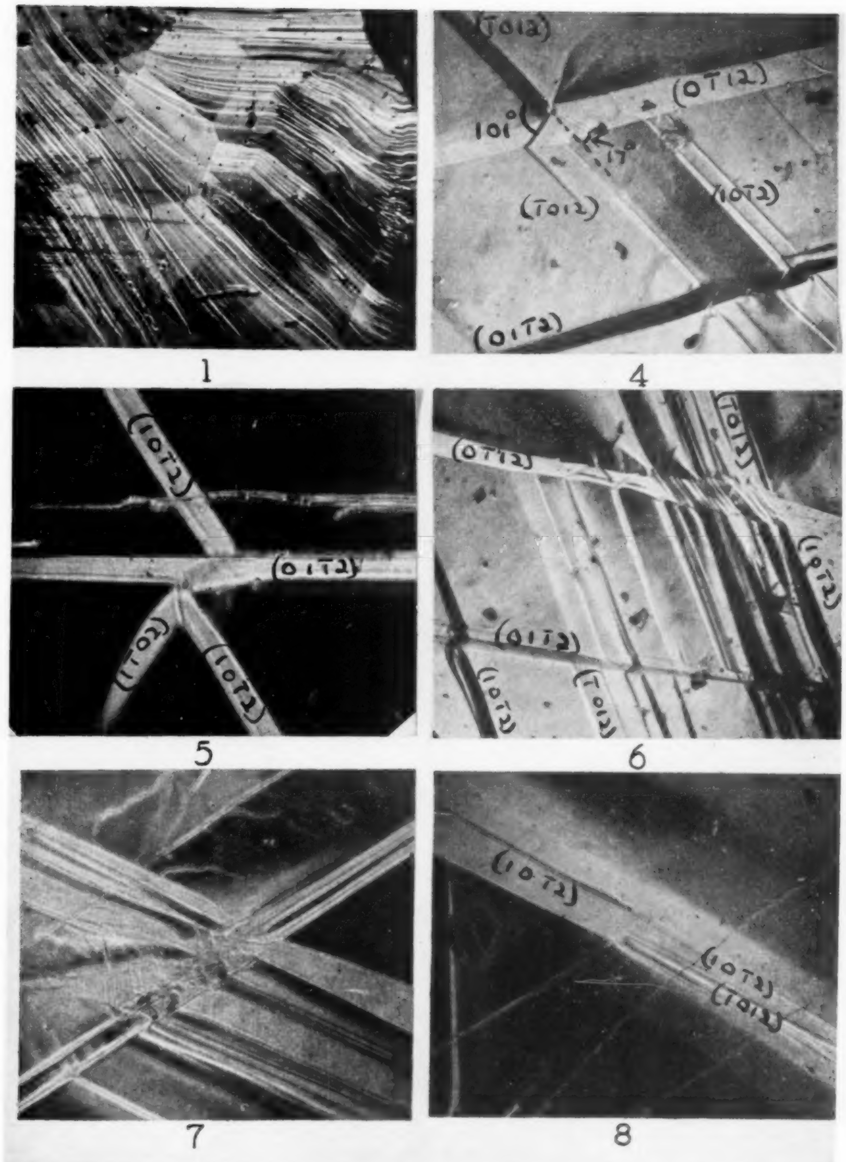

PLATE I. (All figures reduced to three-quarters in reproduction.) Figure 1—Cleavage surface of sodium chloride. 25×. Figure 4—Twin intersections on extended zinc cleavage surface. 145×. Figure 5—Twin intersection of type shown in Fig. 4. 500×. Figure 6—Twin intersections of $(10\bar{1}2)$–$(01\bar{1}2)$, and $(10\bar{1}2)$–$(\bar{0}112)$. 145×. Figure 7—Complex twin intersections. 265×. Figure 8—$(10\bar{1}2)$–$(\bar{1}012)$ transformation at intersection. 145×.

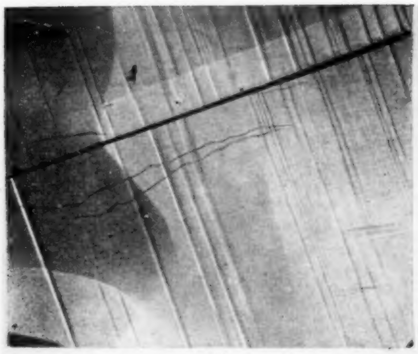

9

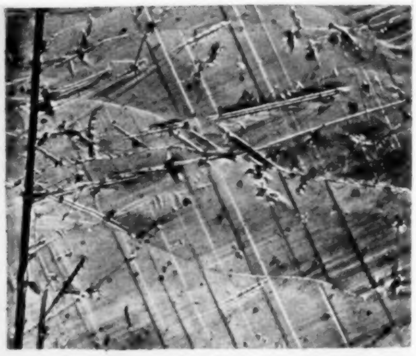

10

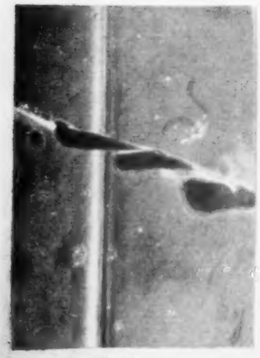

11

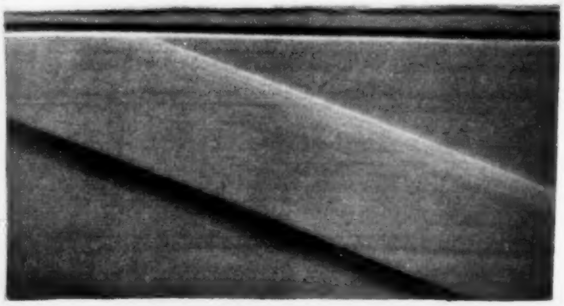

13

14

PLATE II. (All figures reduced to three-quarters in reproduction.) Figure 9—Fine kinks and mosaic walls on zinc surface. 25×. Figure 10—Coarse kinks on compressed zinc cleavage surface. 25×. Figure 11—Kinks at high cleavage step. 150×. Figure 13—Coarse kink. Reflection electron microscope. ↑ ×1,150, →×5,300. Figure 14—Fine kinks. Reflection electron microscope. ↑ ×1,150, →×5,300.

visible as stress-birefringence with transmitted polarized light, may be removed by annealing the crystal at 600°C for twelve hours; recovery within the crystal is then complete.

The surface shown in Figure 1 is by no means the best which can be obtained; with care and patience, specimens can be prepared showing no trace of slip either internally or on the cleavage face.

2. *Zinc*

Zinc cleaves along the basal plane, and hence only two parallel surfaces of the specimen can be prepared by cleavage. As a result, thin discs having the greatest possible area of cleaved surface have been used for most of the recent deformation experiments, [4; 5; 6]. This is unfortunate since the thin sections deform easily during cleavage, and it is difficult to obtain an undistorted specimen. Zinc deforms by slip on the basal plane in the close-packed direction at liquid-air temperature so that, unlike sodium chloride, deformation markings due to slip do not appear on the cleavage face. However, normal slip cannot easily relieve the bending stresses set up during cleavage (Figure 2),

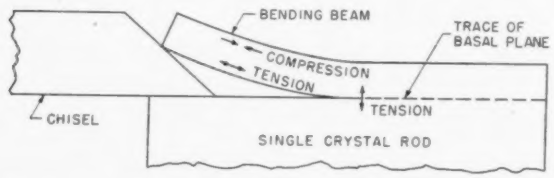

FIGURE 2. Stress system during cleavage of thin flake.

and other surface markings appear both on the upper compressed surface of the thin flake, and also on the lower extended surface. The bending strain is exaggerated in this figure, and it can be seen that the stiffness of the bent beam produces the tensile force across the tip of the crack which is responsible for cleavage.

(*a*) *Lower surface markings.* As Cahn has remarked [7], the tensile stress on the lower surface produces fine twins because the axial ratio of zinc gives rise to a favourable twinning shear for this stress system. The accommodation of these fine twins in the crystal lattice has been studied by different techniques, [1; 8; 9], with good general agreement.

Markings from the six $\{10\bar{1}2\}$ twin systems are found on the cleavage surface, and the relationship between the traces of these systems on the basal plane is shown in Figure 3. In most cases, twins on different $\{10\bar{1}2\}$ systems do not cross because the shear directions are parallel neither to each other, nor to the line of intersection of the twin planes. Intersections have been observed, however, in regions of high stress, as shown on the left and

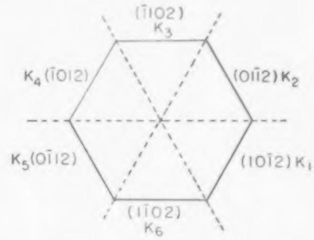

FIGURE 3. Traces of $\{10\bar{1}2\}$ twins on basal plane.

bottom right in Figure 4. The crossing twin frequently splits into two components, with traces on the crossed twin at about 17° and 101° to the original trace as shown on the left in this figure. The broader of these, inclined at 101°, emerges on the far side as a twin of the same system as the the original twin. A similar intersection of $(10\bar{1}2)$ with $(01\bar{1}2)$, is shown at higher magnification in Figure 5. Here the opaque stop has been set to give sensitive dark-field illumination and in the original print two components can be seen in the crossed twin, the broader of which, as before, emerges on the far side. In this case, however, the emergent twin splits into two components, a $(10\bar{1}2)$ parallel to the original twin, with a short $(1\bar{1}02)$ twin giving a trace at 60°. The inclination to the basal plane of the surface of the broader crossing component was determined with the opaque stop microscope and the surface was found to be nearly parallel to that of the crossed twin.

In Figure 6 the opaque stop has been set to distinguish between the parallel traces of the $(10\bar{1}2)$ and $(\bar{1}012)$, and also between those of the $(0\bar{1}12)$ and $(01\bar{1}2)$, twin systems.* Two general types of twin intersection can be seen in the figure; $(10\bar{1}2)$ with $(01\bar{1}2)$ giving a basal plane trace at 101° as before, and $(10\bar{1}2)$ with $(0\bar{1}12)$ giving a trace at 17°. Frequently, the crossing twin fails to emerge on the far side as in the centre of the figure, or it may emerge as a twin of a different system as on the top right of the figure, where $(10\bar{1}2)$ twins have become $(\bar{1}012)$ twins after intersection. In the complex intersection shown in Figure 7, the local stresses have given rise to a series of twins with a trace at 60° to the crossed and crossing twins. A

*The twins in this photograph have been indexed by considering the positions of their parallel accommodation kinks.

unique transformation is shown in Figure 8 in which a broad $(10\bar{1}2)$ twin splits into two at an intersection, and continues as $(10\bar{1}2)$ and $(\bar{1}012)$ with parallel traces. Broad accommodation kinks can be seen above the original twin, and on each side of the pair.

Although common in polycrystalline hexagonal metals, crossing twins are rarely observed in single crystals since they are not true crystallographic intersections and high energies are required for their formation. Their instability is further borne out by the ease with which they split into two components, or even become twins of a different system after the intersection. The crystallography of these twin intersections is described in detail in the Appendix.

(*b*) *Upper surface markings.* The upper compressed surface of thin cleavage sections shows the system of radial steps from the previous parting, together with deformation markings produced by the subsequent compression. In practice, successive cleavages are made from the same side of the single crystal rod, so that the general pattern of the steps is similar from one specimen to another.

While a few twins are found on the upper surface, the most common deformation marking consists of a series of parallel bands or fine lines, at right angles to the twin trace and hence also to the close-packed slip direction. The presence of a twin, an accommodation kink plane, or a mosaic boundary, Figure 9, limits the length of these bands on the cleavage surface. The lines are seen to lie at right angles to the direction of the cleavage run, and therefore parallel to the axis of bending in the cleavage flake. More rarely, Figure 10, these markings appear as black and white bands, indicating that they are narrow areas inclined to the cleavage surface in opposite directions, with the flat central area between the black and the white raised above the level of the surrounding surface. Unlike twin traces, these markings are continuous across a high cleavage step, Figure 11, and this shows that they extend into the material at right angles to the basal plane. If, like twins, they were inclined to the surface, they would be displaced sideways at such a step.

From Figures 9, 10 and 11, it is possible to see how these markings are related to the relaxation of the compressive stresses in the upper part of the bent disc. A section through the surface has been drawn in Figure 12 to show how the buckling spreads into the interior as an array of kink planes, normal to the surface and the slip direction, without crossing the neutral axis into the tensile twinning region.

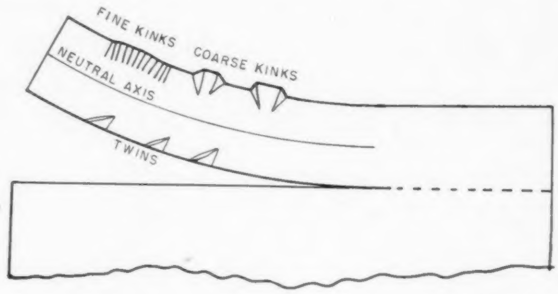

FIGURE 12. Section through thin cleavage flake, showing deformation.

Both the fine kinks shown in Figure 9, and the large bands in Figure 10, have been studied with the reflection electron microscope by Dr. J. W. Menter. The large bands, Figure 13, still show flat surfaces at the higher magnification and this suggests that the lattice tilt is confined to single kink planes, as drawn in Figure 12. The band is made up of two tilted areas of opposite slope, with each area bounded by kink planes containing dislocations of opposite sign in each plane. The fine kinks, Figure 14, are seen to cover large areas of the surface on either side of the principal bands, and they were found in isolated areas, just as in Figure 10, with no simple geometrical buckling of the surface.

Holden [8] has suggested that these markings are kink bands formed by compressive stresses from the impact of the cleaving tool. However, since they were found only on the upper surface of thin cleavages flakes in the above work, it seems probable that they were in fact formed immediately after the propagation of the crack by the bending stresses imposed on the flake. Similar kink markings are produced uniformly over the cleavage face on the compressed side of specimens deformed by bending at room temperature. In this case, as Zappfé has observed [10] the markings may appear at an angle of 76° to the twin traces as well as at right angles to them. These do not appear to be simple kinks although they occur side by side with those normal to twin traces.

Conclusions

The extent of the plastic deformation observed in thin specimens prepared by cleavage renders doubtful their value for further experimental work. So much distortion is introduced during the cleavage process that it is only justifiable to study the

process of cleavage by means of the distortion, or else to develop that distortion further in the subsequent work. In particular cases the latter course may prove useful, but it is barely possible to prepare thin strain-free specimens by cleavage. On the other hand, large undeformed specimens can be obtained by cleaving thin sections away from the desired specimen. This has proved valuable for preparing single crystal specimens of sodium chloride, and should be equally valuable for body-centred cubic crystals, like α-iron, which cleave on the (001).

Twin intersections are found to occur in zinc, where the sense and direction of the twinning shear are not identical in the crossing and secondary twins. This unexpected breakdown of the second basic condition (see Appendix) for twin lamellae to intersect is accompanied by local lattice distortion to relieve the shear discontinuity. Similar intersections have been observed in polycrystalline hexagonal metals, where local regions of high stress may be expected to occur.

Acknowledgements

The author wishes to thank Mr. S. F. Pugh for growing the zinc crystals, Dr. J. W. Menter for his kind assistance in examining the specimens with his reflection electron microscope, Mr. L. Kent for preparing the photographic prints, and the Director, Atomic Energy Research Establishment, Harwell, for permission to publish this paper.

Appendix

Twin Intersections in Zinc

The conditions for two twin lamellae to intersect each other have been considered by Cahn [11], and, following his treatment, the conditions for physical continuity of the crossing twin are, quite simply:

1. The traces of the crossing (A) and secondary (C) twins in the plane of the crossed twin (B) must be parallel.

2. The direction (η_1) and magnitude (s) of shear must be identical in the crossing and secondary twins, and the sense of shear must be the same.

Assuming that the secondary twin (C) has the same indices relative to the lattice of B as the crossing twin A in the parent lattice, the orientations of A and C are related by reflection in the twinning plane of B. In the stereogram, Figure 15, the pole of the twinning plane of B, K_{1B}, is at the centre, with the corresponding poles for A and C at K_{1A} and K_{1C}. The traces of K_{1A} and K_{1C} are both parallel to XY, and the first condition is therefore satisfied. The shear direction of K_{1A}, however, lies at η_{1A} on the great circle, while that of K_{1C} lies at η_{1C} on the opposite great circle. Thus the shear directions in A and C are not parallel, and intersections would not be expected to occur.

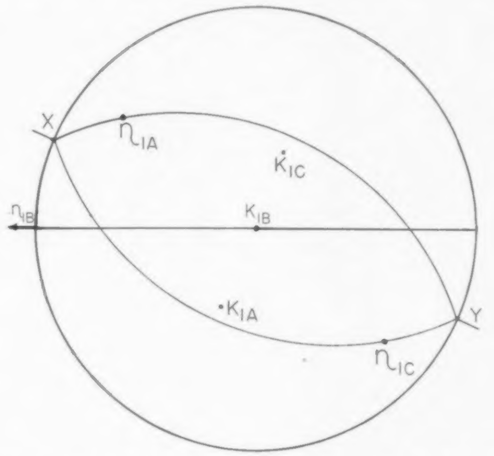

FIGURE 15. Stereogram of twin intersection with pole of K_{1B} at centre.

It is more instructive in the case of zinc to plot a stereographic projection with the basal plane as the primitive circle instead of the twinning plane of the crossed twin, K_{1B}, as above. For this purpose the poles of the six twinning planes have been numbered $K_1 \ldots K_6$ in accordance with Figure 3. The two general types of intersection, observed experimentally, will be considered separately treating $(10\bar{1}2)$ as the crossing twin, previously referred to as A.

$(10\bar{1}2)$–$(01\bar{1}2)$ Intersection

In Figure 16a the c-axis of the parent crystal is at the centre, with the poles of the twinning planes at K_1 and K_2 respectively. The shear direction of the crossing twin, K_1, lies in the twin plane at η_1, and similarly that of K_2 at η_2. These twinning planes, represented by the great circles, intersect along the direction given by X.

The problem now is to see whether any of the six possible twins, relative to the lattice of the crossed twin K_2, also give an intersection with K_2 parallel to the direction X. The poles of these six twins are obtained as before by reflecting the standard projection in the twinning plane of K_2, and the important poles in this case are shown at $\underline{K}_1$ and $\underline{K}_3$ in the stereogram. The plane of $\underline{K}_1$ intersects K_2 at X, and this is the case considered in Figure 15 where the indices of the secondary are the same as those of the crossing twin. From

this plot, however, the angle between the traces of the twins K_1 and $\underline{K}_1$ on the basal plane can be measured as 100°, compared with the figure of 101° measured from the photograph in Figure 4. This makes it clear that in spite of the shear anomaly the twin intersection does take place, and

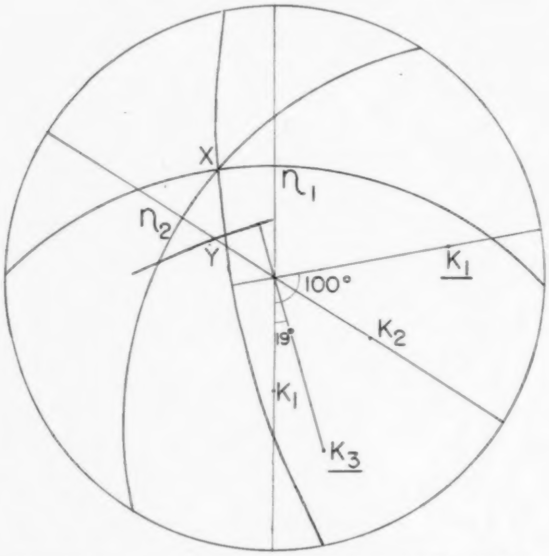

FIGURE 16a. Twin intersection of type $(10\bar{1}2)$–$(01\bar{1}2)$.

the twinning strain of the $(10\bar{1}2)$ twin in the parent is transmitted through the crossed twin as a secondary twin with the same relative indices. The plane of $\underline{K}_3$ intersects K_2 at Y, and the angle between the traces of K_1 and $\underline{K}_3$ on the basal plane is found to be 19°, compared with the experimental value of 17° for the narrower secondary component in Figure 4. $\underline{K}_3$ is the pole of that twinning plane which makes the next nearest intersection with K_2, and the experimental evidence suggests that it too can become a secondary twin in this type of intersection. A perspective view of the intersection is shown in Figure 16b, looking down through the basal plane which lies in the plane of the paper. This is oriented in the same sense as Figures 4 and 5, and shows how the $\underline{K}_1$ secondary twin is preferred to the $\underline{K}_3$ component. The direction of shear in $\underline{K}_1$, indicated by the arrow, is very nearly parallel to the basal plane, in keeping with the experimental observation that the surface of the secondary twin was nearly parallel to the surface of the crossed twin.

$(10\bar{1}2)$–$(0\bar{1}12)$ Intersection

In Figure 17a the *c*-axis of the parent is at the centre, with the poles of the twinning planes at

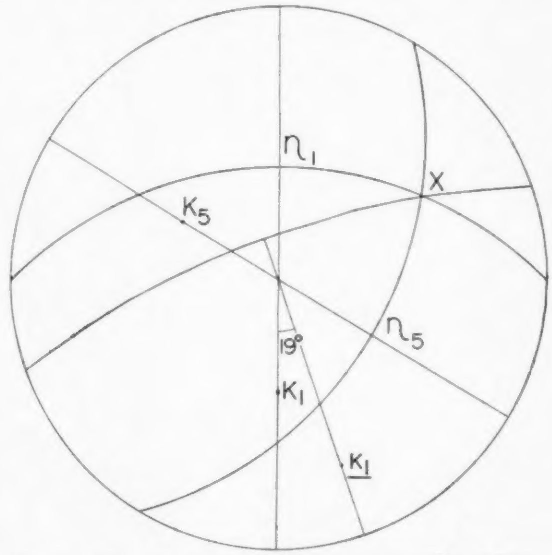

FIGURE 17a. Twin intersection of type $(10\bar{1}2)$–$(0\bar{1}12)$.

K_1 and K_5. The twins intersect along the direction given by the point X. The pole of the secondary twin with the same indices as K_1 appears at $\underline{K}_1$, and this twin plane intersects K_5 at X. The angle

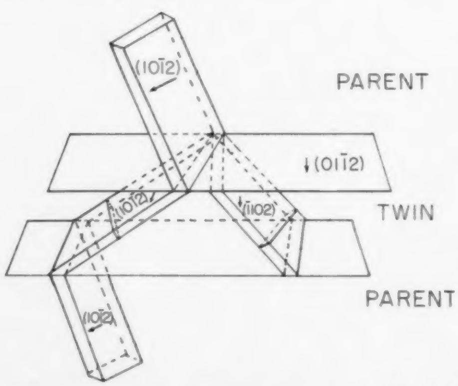

FIGURE 16b. Twin intersection of type $(10\bar{1}2)$–$(01\bar{1}2)$.

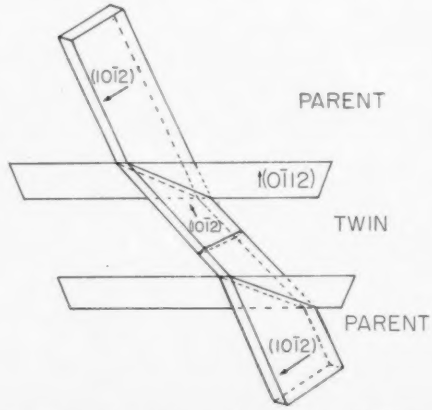

FIGURE 17b. Twin intersection of type $(10\bar{1}2)$–$(0\bar{1}12)$.

between the traces of K_1 and $\underline{K}_1$ is found to be 19° from this figure, compared with the experimental value of about 17° measured from Figure 6. A perspective view of the intersection appears in Figure 17b. As with the $(10\bar{1}2)$–$(01\bar{1}2)$ case, in spite of the shear anomaly, the twin intersection occurs in such a way that the crossing and secondary twins have the same indices in their respective lattices.

References

1. PRATT, P. L. and PUGH, S. F. J. Inst. Metals **80** (1951-52) 653.
2. LOMER, W. M. and PRATT, P. L. J. Inst. Metals **80** (1951–52) 409.
3. MENTER, J. W. J. Inst. Metals **81** (1952–53) 163.
4. JILLSON, D. C. Trans. A.I.M.E. **188** (1950) 1009.
5. WASHBURN, J. and PARKER, E. R. J. Metals **4** (1952) 1076.
6. PRATT, P. L. and PUGH, S. F. Acta. Met. **1** (1953) 218.
7. CAHN, R. W. J. Inst. Metals **80** (1951–52) 723.
8. HOLDEN, J. Phil. Mag. **43** (1952) 976.
9. MOORE, A. J. W. Proc. Phys. Soc. (London) **B65** (1952) 956.
10. ZAPFFE, C. A., WORDEN, C. O., and LANGRAF, F. K. La. met. italiana **3–4** (1951) 1.
11. CAHN, R. W. Acta. Met. **1** (1953) 49.

DEFORMATION MECHANISMS IN TITANIUM AT ELEVATED TEMPERATURES*

C. J. McHARGUE and J. P. HAMMOND†

The deformation mechanisms of titanium have been studied for coarse-grained specimens deformed in tension at 815°C. Slip planes of the types $\{10\bar{1}0\}$ and $\{10\bar{1}1\}$ were observed, and it was noted that $\{10\bar{1}1\}$ slip occurs more frequently than at room temperatures. A decrease in the amount of twinning was observed; however, considerable twinning was observed on $\{11\bar{2}1\}$ and $\{11\bar{2}2\}$ planes. No instances of basal slip or $\{10\bar{1}2\}$ twinning were noted at 815°C.

LES MÉCANISMES DE DÉFORMATION DANS LE TITANE AUX TEMPÉRATURES ÉLEVÉES

Les mécanismes de déformation dans le titane ont été étudiés sur des échantillons à gros grains, déformés par extension, à 815°C. Des plans de glissement des types $\{10\bar{1}0\}$ et $\{10\bar{1}0\}$ ont été observés, il a été remarqué, que le glissement sur $\{10\bar{1}1\}$ était beaucoup plus fréquent qu'à la température ambiante. Il a été constaté, que le maclage était moins fréquent. Du maclage considérable a été, cependant, observé sur les plans des types $\{11\bar{2}1\}$ et $\{11\bar{2}2\}$. Dans aucun cas, du glissement sur le plan de base ou du maclage sur $\{10\bar{1}2\}$ n'a été noté à 815°C.

DER MECHANISMUS DER DEFORMATION DES TITANS BEI HÖHEREN TEMPERATUREN

Der Deformationsvorgang des Titans wurde an grobkörnigen, durch Spannung verformten Proben bei 815°C untersucht. Gleitebenen des Typs $\{10\bar{1}0\}$ und $\{10\bar{1}1\}$ wurden beobachtet, und es zeigte sich, dass $\{10\bar{1}1\}$ Gleitung häufiger als bei Zimmertemperatur auftritt. Es wurde eine Verringerung der Zwillingsbildung beobachtet; jedoch zeigte sich erhebliche Zwillingsbildung auf den $\{11\bar{2}1\}$ und $\{11\bar{2}2\}$ Ebenen. Bei einer Temperatur von 815°C wurde weder Gleitung auf der Basisebene noch $\{10\bar{1}2\}$ Zwillingsbildung beobachtet.

It has been observed that many metals undergo changes in the slip systems when deformed at temperatures other than room temperature. Some of the materials for which alterations in the slip systems have been reported are aluminum, magnesium, β-tin, molybdenum, sodium, potassium, and some iron-silicon alloys [1].

Schmid reported the operation of $\{0001\}$, $\{10\bar{1}1\}$, and $\{10\bar{1}2\}$ slip planes in magnesium deformed above 225°C [2]. Bakarian and Mathewson [3] confirmed the existence of $\{0001\}$ and $\{10\bar{1}1\}$ slip at 330°C but were not able to find evidence of $\{10\bar{1}2\}$ slip.

The slip systems of titanium at room temperatures have peen reported as $\{10\bar{1}0\}$ $\langle 11\bar{2}0\rangle$ plus a slight amount of $\{10\bar{1}1\}$ $\langle 11\bar{2}0\rangle$ slip [4], or $\{0001\}$ $\langle 11\bar{2}0\rangle$ and $\{10\bar{1}0\}$ $\langle 11\bar{2}0\rangle$ slip [5]. The reported presence of $\{10\bar{1}1\}$ $\langle 11\bar{2}0\rangle$ slip in titanium at ambient temperatures suggests that this system may become more active at elevated temperatures, since it is activated at higher temperatures in magnesium.

There have been no instances in which new twin planes were observed at elevated temperatures. The usual experience is to find that twinning becomes less frequent as the temperature of deformation is increased. Cahn [6] reported that somewhere between 300° and 450°C slip almost entirely superseded twinning in *alpha*-uranium. At 300°C, deformation produced many twins, while no twins were observed in specimens deformed above 450°C. Barrett and Haller [7] noted that the amount of twinning occurring in polycrystalline magnesium deformed at 200°C was much less than usually observed at lower temperatures. In these specimens, no twinning was encountered when the deformation was accomplished above 300°C. In polycrystalline beryllium [7] twinning was reported to be common for deformation occurring below 300°C but was absent in the temperature range of 400° to 800°C.

A multiplicity of twinning planes has been reported for titanium [4; 5], whereas only $\{10\bar{1}2\}$ twinning has been noted for the other hexagonal close-packed metals studied [1]. The twin planes of titanium are $\{10\bar{1}2\}$, $\{11\bar{2}1\}$, and $\{11\bar{2}2\}$, the last family of planes being active only rarely at room temperatures.

This paper reports a study of the deformation mechanisms of titanium deformed at 815°C.

Experimental Methods

Iodide titanium obtained from the New Jersey Zinc Company was used throughout this investigation. The reported analysis of this material was:

*Received June 12, 1953.
†Department of Mining and Metallurgical Engineering, University of Kentucky, Lexington, Kentucky.

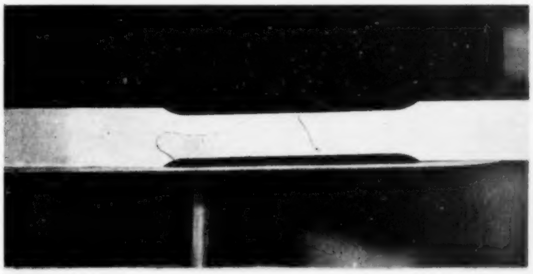

1

4

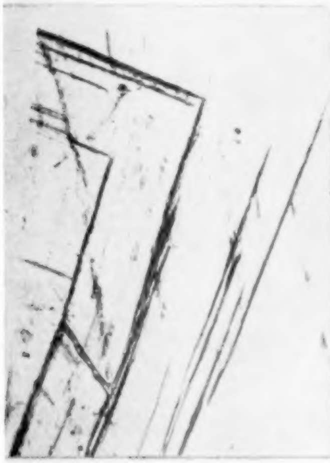

5

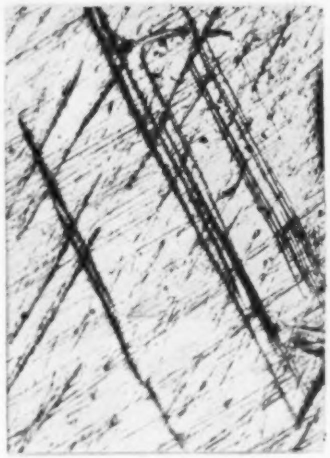

6

7

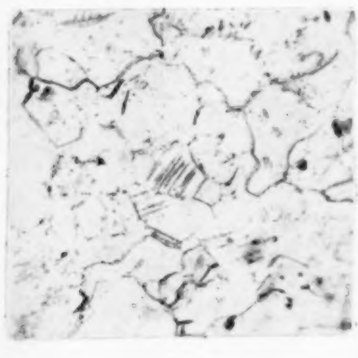

9

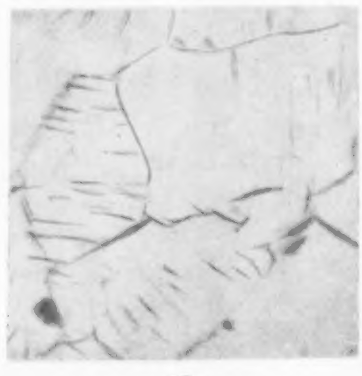

10

PLATE I. Figure 1—Macrograph of large grain produced by cyclic method. Figure 4—$\{10\bar{1}0\}$ slip lines in titanium deformed at 815°C (250×). Figure 5—Twin markings in titanium deformed at 815°C (250×). Figure 6—$\{10\bar{1}0\}$ slip lines and twin markings in titanium deformed at 815°C (250×). Figure 7—Typical photomicrograph of wavy $\{10\bar{1}1\}$ slip lines. (100×). Figure 9—Photomicrograph of iodide titanium rolled 90 per cent at 565°C (500×). Figure 10—Photomicrograph of iodide titanium rolled 90% at 790°C (500×).

N_2, 0.002 per cent; Mn, 0.004 per cent; Fe, 0.0065 per cent; Al, 0.0065 per cent; Pb, 0.0025 per cent; Cu, 0.01 per cent; Sn, 0.002; and Ti, remainder. Ingots were made from the iodide titanium crystal bar by arc-melting on a copper hearth in an argon atmosphere. The 15g ingots were cold-rolled to strips approximately 0.05 inch thick.

Production of Large Grains

While it would have been desirable to have single crystals for the study of deformation mechanisms, no suitable method has been developed for the production of single crystals of titanium large enough to work with. Both the strain anneal method and a cyclic process were used to produce grains large enough for study. The cyclic process gave a better yield of usable grains, and all grains studied except AI and BI were produced in this manner.

Grains AI and BI were obtained from the strain anneal procedure. Cold-rolled strip was vacuum-annealed at 700°C in order to obtain a fine, equiaxed grain structure. Strips of the annealed material 3 inches long were pulled in tension so as to give elongations of approximately 1.5 per cent. The strained strips were annealed in a vacuum, with the temperature being increased from 400°C to 850°C at a rate of approximately approximately 195°C per day. This treatment was followed by a final anneal at 850°C for 48 hours.

Specimens subjected to the cyclic treatment contained grains up to 0.5 inch in size. Pieces of the cold-rolled strip were sealed in evacuated quartz tubes and heated to 850°C. After being held for 24 hours at 850°C, the specimens were held at 1100°C for 4 hours, and returned to 850°C for 24 hours. Several heatings to 1100°C were given, and the treatment ended with a final anneal at 850°C. A typical specimen prepared in this manner is shown in Figure 1.

Before being deformed, all specimens were lightly polished and etched.

Deformation Procedure

A Southwark-Emery 60,000 pounds capacity testing machine was fitted with a furnace for the high temperature tests. The furnace was resistance-wound and input was through two variacs and a Micromax recorder-controller. A thermocouple was placed in contact with the grain under study, and indicated temperature control was ±5° at 815°C. All heating was done in an atmosphere of dried 99.98 per cent argon, and the specimen surfaces remained bright during the heating.

Determination of Slip and Twinning Elements

Identification of the slip and twinning planes was based on the use of a stereographic plot of a back-reflection Laue photogram of the region under study. The X-ray exposures were made with an Unican X-ray camera with goniometer and a telescope for aligning specimens. Tungsten radiation was used. The orientations of the fourteen grains studied are shown in Figure 2.

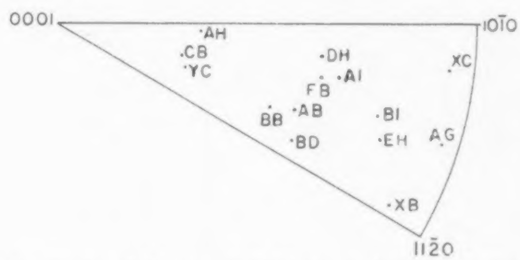

FIGURE 2. Orientations of grains deformed in tension at 815°C.

Most of the grains were analyzed by the pole locus method described by Bowles [9]. In this method, the slip and twin traces from only one surface are necessary. A stereographic projection was first made of the grain. The normal to each visible slip and twinning trace was then drawn on the plot as a great circle passing through the center. A tentative identification of the deformation elements could be made by noting which poles of planes fell on the trace normals. However, in order to obtain an unambiguous solution, the great circles and the stereogram were rotated so that the orientation corresponded to the standard projection. The arcs of the great circles representing trace normals were then rotated into one stereographic triangle. The pole representing the intersection of the arcs identifies the trace. Such a solution of one grain is shown in Figure 3.

The two-surface method of analysis was used in a few cases, but the majority of the determinations were made by the pole locus method.

Discussion of Results

The results of fourteen grains studied are shown in Table I. Two slip planes, $\{10\bar{1}0\}$ and $\{10\bar{1}1\}$, and two twin planes, $\{11\bar{2}1\}$ and $\{11\bar{2}2\}$ were observed to be active at 815°C.

Figures 4–7 show typical appearances of deformation markings in titanium pulled in tension at

815°C. The appearances of $\{10\bar{1}0\}$ slip bands and $\{11\bar{2}1\}$ twins are similar to those present in titanium deformed at room temperature [4]. Typical appearance of $\{10\bar{1}1\}$ slip bands is shown in Figure 7. These slip markings are characterized by being wavy, as were $\{10\bar{1}1\}$ slip bands in magnesium [3].

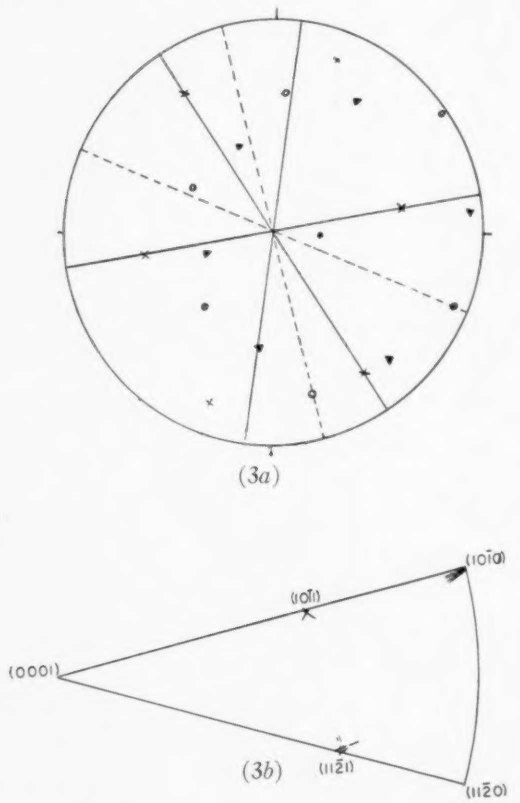

FIGURE 3. Solution of deformation elements. (*a*) Stereographic projection containing normals to traces of slip bands (—) and twins (– –). (*b*) Trace normals rotated into one unit triangle of standard projection. ● = (0001), ▲ = $\{10\bar{1}1\}$, ○ = $\{11\bar{2}1\}$.

Slip on $\{10\bar{1}0\}$ planes apparently dominated at the temperature of testing, but it appeared that $\{10\bar{1}1\}$ slip occurred more frequently than at lower temperatures. Rosi and co-workers [4] reported slip on $\{10\bar{1}1\}$ only in crystals which exhibited a complex slip process, whereas Jillson and Anderson [5] failed to note its occurrence at all. It is significant that all the slip in three grains occurred on $\{10\bar{1}1\}$ planes. No instances of basal slip were observed. Very little, if any, slip of this nature was reported for room temperature deformation [4; 5].

The twinning behavior of titanium at 815°C was interesting. In every hexagonal close-packed metal,

TABLE I

DEFORMATION ELEMENTS OF TITANIUM AT 815°C

Grain	Slip plane	Twin plane
BB	....	$11\bar{2}2$
XC	$10\bar{1}0 + 10\bar{1}1$	$11\bar{2}1$
DH	$10\bar{1}0 + 10\bar{1}1$	$11\bar{2}1$
EH	$10\bar{1}1$	$11\bar{2}1$
CB	$10\bar{1}0$	$11\bar{2}1$
AI	$10\bar{1}0 + 10\bar{1}1$	....
BI	$10\bar{1}1$	$11\bar{2}2 + 11\bar{2}1$
YC	$10\bar{1}0$	$11\bar{2}1$
FB	$10\bar{1}1$	$11\bar{2}1$
AB	$10\bar{1}0$	$11\bar{2}1$
BD	$10\bar{1}0$	....
XB	$10\bar{1}0$	$11\bar{2}2$
AH	$10\bar{1}0$	$11\bar{2}1$
AG	$10\bar{1}0$	....

$\{10\bar{1}2\}$ twinning has been observed, and this type of twinning was observed frequently in titanium by the investigators cited earlier [4; 5]. However, in the present study, no twinning on the $\{10\bar{1}2\}$ family was found, although twins of the $\{11\bar{2}1\}$ and $\{11\bar{2}2\}$ types were observed. Twins were found in all but three grains, but not to the extent found in grains deformed at lower temperatures. In three grains, $\{11\bar{2}2\}$ type twins were observed, and in two of these, grains accounted for all of the twinning. It appeared that the relative amount of $\{11\bar{2}2\}$ twinning was greater at 815°C than at room temperature, although the total amount of twinning seemed to be less.

It is significant that in magnesium [7] and beryllium [8], for which only $\{10\bar{1}2\}$ twinning has been reported, twinning entirely ceases as the deformation temperature is increased. Similar behavior is observed for $\{10\bar{1}2\}$ twinning in titanium, but a different behavior is exhibited by $\{11\bar{2}1\}$ and $\{11\bar{2}2\}$ twinning. While the frequency of twinning seems to be less than in grains deformed at lower temperatures, there is still an appreciable amount of $\{11\bar{2}1\}$ and $\{11\bar{2}2\}$ twinning at 815°C. The reasons for these differences in behavior of twin systems are not apparent.

In instances in which the slip plane changes with temperature, the direction of slip has always remained the same [1]. It has been shown that a $\langle 11\bar{2}0\rangle$ direction serves as slip direction for both $\{0001\}$ and $\{10\bar{1}1\}$ slip in magnesium [3]. Rosi, Dube, and Alexander [4] have reported that the slip direction for $\{10\bar{1}0\}$ slip in titanium at room temperature is of the $\langle 11\bar{2}0\rangle$ type.

In one instance in the present investigation (grain AG), the movement of the specimen axis

during extension was observed by determining the grain orientation at different stages of extension. In this case, the movement was toward a direction of indices $\langle 11\bar{2}0\rangle$, Figure 8. In view of the fact that both $\{10\bar{1}0\}$ and $\{10\bar{1}1\}$ planes contain $\langle 11\bar{2}0\rangle$ directions, and from the above observations, it seems reasonable to assume that the slip direction at 815°C is of the type $\langle 11\bar{2}0\rangle$ for both families of slip planes.

FIGURE 8. Change in orientation of stress axis during deformation of grain AG.

The change in lattice constants has been reported for titanium over the temperature range of 25° to 225°C [9]. These values were reported as $\Delta a_0 = 11.0 \pm 0.3 \times 10^{-6}$ and $\Delta c_0 = 8.8 \pm 0.3 \times 10^{-6}$. Thus, as the temperature is increased, the c/a ratio of titanium decreases. It has been suggested that in the hexagonal close-packed metals, the complexity of the slip systems increases as the c/a ratio decreases [4]. Because of the decrease in c/a ratio, the atomic density of the $\{10\bar{1}0\}$ and $\{10\bar{1}1\}$ planes becomes greater as the temperature is increased. Apparently, the density of packing of the $\{10\bar{1}1\}$ planes reaches a point where slip can take place more readily than on the same planes at lower temperatures.

In Figures 9 and 10, typical microstructures of hot-rolled polycrystalline iodide titanium are shown. Figure 9 shows both $\{10\bar{1}2\}$ and $\{11\bar{2}1\}$ twins in iodide titanium reduced 90 per cent in thickness at 565°C. It will be noted that many of the grains are twin-free. One grain near the center of the photomicrograph contains several $\{10\bar{1}2\}$ twins and the grain just beneath it contains both $\{10\bar{1}2\}$ and $\{11\bar{2}1\}$ twins. Figure 10 is a photomicrograph of similar material reduced 90 per cent at 790°C. This microstructure shows that most of the grains contain no twins, and that the only twins present are of the $\{11\bar{2}1\}$ type. Thus it appears that $\{10\bar{1}2\}$ twinning ceases to be active somewhere in the temperature range of 565° to 790°C.

Conclusions

The slip and twinning elements have been determined in coarse crystals of arc-melted iodide titanium deformed in tension at 815°C. A study of fourteen grains showed that at least two types of slip and two types of twin planes are operative at this temperature. The slip planes were of the types $\{10\bar{1}0\}$ and $\{10\bar{1}1\}$ and the twin planes were of the types $\{11\bar{2}1\}$ and $\{11\bar{2}2\}$. No instance of basal slip or of $\{10\bar{1}2\}$ twinning was noted.

Photomicrographs of iodide titanium rolled at 565° and 790°C indicated that $\{10\bar{1}2\}$ twinning ceases to be operative somewhere between these temperatures.

Acknowledgments

The work reported herein was supported by the Flight Research Laboratory, Wright-Patterson Air Force Base, Contract No. A.F. 33–(038)–19574.

References

1. BARRETT, C. S. Structure of Metals, 2nd ed. (New York, McGraw-Hill, 1953).
2. SCHMID, E. Z. Elektrochem. **37** (1931) 447.
3. BAKARIAN, P. W. and MATHEWSON, C. H. Trans. A.I.M.E. **152** (1943) 226.
4. ROSI, F. D., DUBE, C. A., and ALEXANDER, B. H. J. Metals **5** (1953) 257; Trans. A.I.M.E. **197** (1953) 257.
5. JILLSON, D. C. and ANDERSON, E. A. Final Report to Philadelphia Ordnance District from New Jersey Zinc Company, Contract DA-36-034-ORD-278RD (1952).
6. CAHN, R. W. Acta Met. **1** (1953) 49.
7. BARRETT, C. S. and HALLER, C. T. Trans. A.I.M.E. **171** (1947) 246.
8. KAUFMAN, A. R., GORDON, P., and LILLIE, D. W. Trans. A.S.M. **42** (1950) 785.
9. BROCKLEHURST, R. E. Private communication (1951), Air Materiel Command, Wright-Patterson Air Force Base.

THE DYNAMIC YIELDING OF MILD STEEL*

J. D. CAMPBELL†

Results of dynamic and impact tests on mild steel are reviewed, and a criterion for dynamic yield is proposed, based on Cottrell and Bilby's theory of yielding. The criterion is applied to some of the published experimental data and a comparison is made with theory. The need for further experimental work is emphasized.

L'ÉCOULEMENT DYNAMIQUE DANS L'ACIER DOUX

Une revue est faite des résultats d'essais dynamiques et au choc effectués sur l'acier doux, et un criterium, basé sur la théorie d'écoulement de Cottrell et Bilby, est proposé pour l'écoulement dynamique. Ce criterium est appliqué à certaines des données expérimentales publiées; une comparaison est faite avec la théorie. La nécessité de continuer les travaux expérimentaux est soulignée.

DYNAMISCHES FLIESSEN IN WEICHEM STAHL

Die Ergebnisse von dynamischen Versuchen und von Schlagversuchen werden kritisch zusammengestellt, und ein Kriterion für dynamisches Fliessen wird vorgeschlagen, dem die Theorie des Fliessens von Cottrell und Bilby zu Grunde liegt. Dieses Kriterion wird auf einige experimentelle Daten in der Literatur angewandt, und die Ergebnisse werden mit der Theorie verglichen. Es wird betont, dass weiteres experimentelles Material dringend benötigt wird.

1. Introduction

Two main types of test have been employed in investigations of the behaviour of materials subjected to rapid loading:

(a) tests in which the load is increased at a more or less uniform rate until yield occurs; and

(b) tests in which a load is rapidly applied and removed and the permanent set (if any) measured.

Examples of investigations employing the first of these types of test are those of Morrison [1], Nadai and Manjoine [2], and MacGregor and Fisher [3]. In these investigations the stress-strain curve for mild steel was found to vary with the rate of strain, at any given temperature.

Examples of investigations employing the second type of test are those of Hopkinson [4], Mason [5] and Brown and Edmonds [6]. These investigations have shown that it is possible for mild steel to withstand stresses higher than the "static" yield stress for short periods of time without yielding. Since in tests of this type the rate of strain is not constant, but decreases to zero at maximum stress, it is evident that the yield stress of mild steel is not a simple function of rate of strain.

Recently a third type of test has been employed, in which a constant stress is applied and the time before yielding is measured [7; 8; 9; 10]. The results of these tests have confirmed that the yielding of mild steel occurs at stresses higher than the "static" yield point if the time of loading is small, even though the rate of strain at yield is zero.

*Received June 19, 1953.
†Oxford University, England.

It thus appears that a theory is needed by which the results of dynamic tests of various types may be correlated. In the present paper a method is proposed for effecting this correlation.

2. Theory

It is now well established that the yielding of metals is due to the movement of dislocations within the crystal lattice. This movement is caused by the applied stress aided by the effect of thermal fluctuations of molecular velocity. Cottrell and Bilby [11] have shown that in mild steel the dislocations are anchored by atmospheres of carbon atoms; they have thus explained the existence of an upper and a lower yield point. They have also shown that the mean time before a dislocation is released from its atmosphere is proportional to $\exp[U(\sigma/\sigma_0)/kT]$, where U is the activation energy for the applied stress σ, σ_0 is the yield stress at 0°K, k is Boltzmann's constant and T is the absolute temperature. It follows from this that at time t the total number of dislocations released is proportional to

$$\int_{-\infty}^{t} \exp[-U(\sigma/\sigma_0)/kT]\,dt.$$

It seems reasonable to suppose that yield will occur when the density of released dislocations reaches a certain critical value. With this assumption, yield will occur at a time t_1 given by

$$\int_{-\infty}^{t_1} \exp[-U(\sigma/\sigma_0)/kT]\,dt = \text{constant}.$$

The constant will evidently depend on the particular steel tested, but should be independent of the

stress-time variation corresponding to the test used. If it is assumed that for $t < 0$ the material is unstressed and has no free dislocations, and that for $t > 0$ the stress is given by $\sigma = f(t)$, then the time of yield, t_1, is given by

$$(1) \qquad \int_0^{t_1} \exp\left[-U\{f(t)/\sigma_0\}/kT\right] dt = C,$$

where C is the constant for the material.

Theoretical activation energy curves have been derived by Cottrell and Bilby from a consideration of the mechanism of release of a dislocation. Yokobori [12] has pointed out that these curves may be represented approximately by equations of the type

$$(2) \qquad U = -\frac{1}{n} \log_e (\sigma/\sigma_0),$$

where n is a constant.

Substituting this expression for U into equation (1) gives

$$(3) \qquad \int_0^{t_1} [f(t)/\sigma_0]^\alpha dt = C,$$

where $\alpha \equiv (nkT)^{-1}$, a dimensionless constant.

Thus to determine the yield stress for any given type of dynamic test $\sigma = f(t)$, t_1 is found from (3) and the yield stress Y is then given by

$$(4) \qquad Y = f(t_1).$$

3. Applications

(i) *Constant Strain-rate Tests*

Here the stress is given by

$$(5) \qquad \sigma = f(t) = E\dot{\epsilon}t$$

where $\dot{\epsilon}$ is the strain-rate and E is the modulus of elasticity (the material being assumed to be elastic up to the yield point).

Substitution of (5) into (3) gives

$$(6) \qquad t_1 = [(\alpha + 1)\, C(\sigma_0/E\dot{\epsilon})^\alpha]^{\frac{1}{\alpha+1}}$$

and hence from (4) and (5)

$$(7) \qquad Y = \sigma_0[(\alpha + 1)\, CE\dot{\epsilon}/\sigma_0]^{\frac{1}{\alpha+1}}$$

i.e., $Y \propto \dot{\epsilon}^{\frac{1}{\alpha+1}}$ at constant temperature.

Yokobori has derived an approximation to this relation by somewhat different reasoning. He assumes $nkT \ll 1$ and so obtains the result

$$Y \propto \dot{\epsilon}^{nkT} = \dot{\epsilon}^{\frac{1}{\alpha}}$$

Eliminating $\dot{\epsilon}$ between (6) and (7) gives

$$(8) \qquad t_1 = (\alpha + 1)\, C(Y/\sigma_0)^{-\alpha}.$$

Thus the theory predicts power-law relationships between yield stress and strain-rate and between yield stress and time to yield, at constant temperature.

(ii) *Constant Stress Tests*

If a constant stress Y is applied at time $t = 0$, (3) indicates that the time of yield is

$$(9) \qquad t_1 = C(Y/\sigma_0)^{-\alpha}.$$

It has been found experimentally [7] that there exists a definite delay time before yield occurs in constant stress tests. Equation (9) indicates that this delay time should be a power function of the stress.

Equation (9) may be compared with equation (8): it is seen that for a given yield stress the time to yield in a constant strain-rate test is $(\alpha + 1)$ times that in a constant stress test.

(iii) *Impact Tests*

In many impact tests the stress increases rapidly to a maximum and then decreases to zero. According to (3), yield will take place in a test of this type if, at any time, the value of the integral reaches the critical value C. The maximum value of the integral evidently occurs when the stress returns to zero. Thus, theoretically, yield can occur at any time during loading or unloading. Owing to the form of the activation energy curve, however, very little contribution is made to the value of the integral by the parts of the stress-time curve in which the stress is small. For example, if the stress-time curve is taken as

$$\sigma = \sigma_m \sin \omega t \qquad (0 \leqslant t \leqslant \pi/\omega)$$

the value of the integral at time t is

$$(10) \qquad (\sigma_m/\sigma_0)^\alpha \int_0^t \sin^\alpha (\omega t)\, dt.$$

Since $\alpha \gg 1$, the curve of the integrand is sensibly zero except for values of t near to $\pi/2\omega$; thus with $\alpha = 20$ the value of the integral increases only about 2 per cent as the stress falls from $0.9\sigma_m$ to zero. It is therefore very unlikely that yield would occur during unloading at a stress less than say 90 per cent of the maximum stress.

The maximum value of the integral (10) occurs when $t = \pi/\omega$, and is given by

$$(11) \qquad \sqrt{\frac{\pi}{\omega}} \left(\frac{\sigma_m}{\sigma_0}\right)^\alpha \frac{\Gamma\left(\dfrac{\alpha + 1}{2}\right)}{\Gamma\left(\dfrac{\alpha}{2} + 1\right)}$$

where Γ is the gamma-function.

Since $\alpha \gg 1$, the asymptotic expressions may be used in (11), and the maximum value becomes

$$\frac{1}{\omega}\left(\frac{\sigma_m}{\sigma_0}\right)^{\alpha}\sqrt{\left[\frac{2\pi e}{\alpha}\left(1-\frac{1}{\alpha}\right)^{\alpha}\right]}. \tag{12}$$

Thus in tests of this type we may expect the yield stress to vary as $\omega^{1/\alpha}$.

4. Comparison with Experimental Results

The hypothesis involved in equation (1) leads to the conclusion that there is no "static" yield stress, i.e., that by increasing the time of loading sufficiently the yield stress can be made indefinitely small. This is evidently contrary to experience and it therefore appears that the theory given does not apply for large durations of loading. It is suggested below that the critical time of loading above which the theory fails to hold is of the order of 1 second. Accepting this value, it follows that in order to compare with the theory tests must be carried out at relatively high speed. Owing to experimental difficulties, however, the available data relating to tests of this kind are rather meagre. An attempt is made below to check the theory against some of the published results of tests on mild steel.

(i) *Constant Strain-rate Tests*

Morrison [1] carried out constant strain-rate tests on two annealed steels containing 0.2 and 0.6 per cent carbon respectively. His results are shown in Figure 1, where the logarithm of the

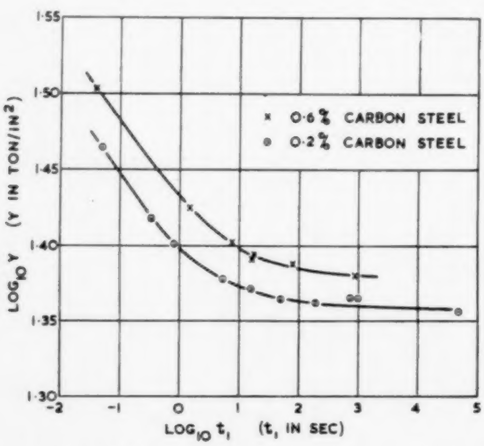

FIGURE 1. Yield stress (Y) versus time to yield (t_1) at constant strain-rate (Morrison).

yield stress is plotted against the logarithm of the time to yield. It will be seen that for each of the steels tested, the curve appears to become approximately straight for times less than about 1 second, but that this cannot be regarded as proved, owing to the small number of points in this range. Accepting the lines drawn, however, a numerical comparison with theory is possible. The slopes of the two curves for $t_1 < 1$ sec. are approximately the same and equal to -0.053. From (8) therefore we have

$$0.053 \simeq 1/\alpha = nkT.$$

Taking $k = 1.38 \times 10^{-16}$ erg/°C and $T = 290$°K, this gives $1/n \simeq 0.48$ eV. Thus the activation energy curve is given by

$$U \simeq -0.48 \log_e (\sigma/\sigma_0) \text{ eV} \tag{13}$$

Cottrell and Bilby give four activation energy curves obtained by taking various values for the parameters involved in their analysis. These curves are reproduced in Figure 2, together with

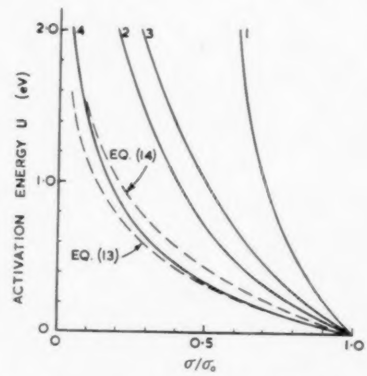

FIGURE 2. Activation energy curves. Curves 1–4: theoretical (Cottrell and Bilby). Dotted curves: derived from dynamic tests.

that represented by equation (13). It will be seen that the latter lies near to Cottrell and Bilby's curve 4, which they state is the most reasonable of their four curves.

It thus appears that for times of loading less than about 1 second the theory is in reasonable agreement with Morrison's experimental results.

(ii) *Constant Stress Tests*

Vreeland, Wood and Clark [10] have published results of constant stress tests carried out on annealed mild steel of 0.12 per cent carbon content. The actual values obtained for the yield stress are not given in Vreeland, Wood and Clark's paper; the points on their stress-delay time graph have been reproduced in Figure 3, which may therefore contain errors due to replotting. There is in any

case a considerable amount of scatter in the results; however, the straight line drawn fits the points reasonably well, for delay times less than about 2 seconds. The slope of this line is -0.040 and hence from (9) $1/\alpha \simeq 0.040$. Taking the same

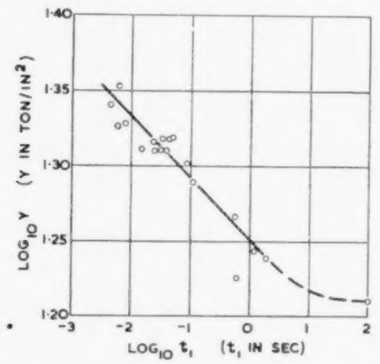

FIGURE 3. Yield stress (Y) versus time to yield (t_1) at constant stress (Vreeland, Wood and Clark).

values as before for k and T, this gives $1/n \simeq 0.63$ eV and hence

(14) $$U \simeq -0.63 \log_e (\sigma/\sigma_0) \text{ eV}.$$

The activation energy curve represented by equation (14) has also been plotted in Figure 2; it may be seen that it lies between Cottrell and Bilby's curves 4 and 2 but is nearest to curve 4. Again, therefore, the experimental results are in reasonable agreement with theory, when yield occurs in less than about 1 second.

It is unfortunately not possible to check the conclusion stated at the end of Sec. 3 (ii) by comparing Vreeland, Clark and Wood's results with those of Morrison, since the materials tested were different.

(iii) *Impact Tests*

Davies [13] has given the results of experiments in which a mild steel plate was subjected to impact loads by means of a bouncing steel ball. The stress necessary to cause yield was measured by determining the minimum height of drop required to cause a permanent indentation of the plate, the stress being calculated from Herz' theory of impact. The ratio of this stress to that obtaining under "static" conditions was found to be 2.04; the time of loading and unloading in the dynamic tests was about 15 microseconds. A difficulty arises in applying the proposed theory to these results, in that "static" conditions are not defined. From the constant strain-rate and constant stress tests, however, it appears that the "static" yield stress is equal to that given by the theory for a time of loading of about 10 seconds. Making this assumption, a value of n may be estimated from Davies' results. Thus, assuming that the loading curve is sinusoidal, (12) indicates that

$$\frac{\text{dynamic yield stress}}{\text{"static" yield stress}} = \left(\frac{\omega}{\omega_s}\right)^{1/\alpha}$$

where ω_s is the value of ω corresponding to "static" conditions. Taking $\pi/2\omega_s = 10$ sec. and $\pi/2\omega = 15 \times 10^{-6}$ seconds we obtain

(15) $$\left(\frac{10}{15 \times 10^{-6}}\right)^{1/\alpha} = 2.04$$

and hence $1/\alpha = 0.053$.

This compares with the values 0.053 and 0.040 obtained from constant strain-rate and constant stress tests respectively. Equation (15) must, however, be regarded as approximate only, in view of the uncertainty in the value of ω_s. However, a tenfold variation of ω_s only changes $1/\alpha$ by about 0.01.

5. Discussion and Conclusions

It is evident that much more experimental work is required in order to test the proposed criterion of dynamic yield of mild steel. Many of the existing results indicate the existence of a static yield stress, independent of rate of strain. This is not accounted for by the proposed criterion, equation (1). It seems, therefore, that when the time of loading is sufficiently great, some mechanism other than that contemplated in equation (1) must come into operation. The critical loading time above which this effect is appreciable appears to be of the order of 1 second, though it probably varies slightly with the type of test. This time is too small for any significant amount of long-range migration of solute atoms to occur, such as that leading to strain ageing. It has, however, been shown by Snoek [14] that in general a redistribution of interstitial solute atoms in α-iron occurs when an external stress is applied; and that the relaxation time for this process is of the order of 1 second at room temperature. The mechanical effects of this redistribution have been discussed by Nabarro [15]. It seems possible that, when the time before yield is 1 second or more, this mechanism causes a change in the dynamic behaviour of the metal. Any comprehensive theory of yielding must therefore include this effect, if comparison is to be

made between the results of static and dynamic tests.

The proposed theory is in reasonable agreement with experimental results when the time of loading is less than about 1 second, though further and more accurate tests are desirable to check this. Unfortunately the experimental difficulties in carrying out high-speed dynamic tests are considerable and much of the existing work has not been sufficiently accurate to allow a comparison with theory to be made. It is hoped that the present paper will be of use in the design of future dynamic and impact tests and in the interpretation of their results.

Acknowledgments

Grateful acknowledgment is made to Professors A. H. Cottrell and J. L. M. Morrison for helpful suggestions made during the course of this work; also to the Physical Society and to the American Society for Metals for permission to reproduce material from their publications.

References

1. Morrison, J. L. M. The Engineer **158** (1934) 183.
2. Nadai, A. and Manjoine, M. J. J. Appl. Mech. **8** (1941) 77.
3. MacGregor, C. W. and Fisher, J. C. J. Appl. Mech. **12** (1945) 217.
4. Hopkinson, B. Proc. Roy. Soc. **A74** (1905) 498.
5. Mason, W. Proc. Inst. Mech. Eng. **128** (1934) 409.
6. Brown, A. F. C. and Edmonds, R. Proc. Inst. Mech. Eng. **159** (1948) 11.
7. Clark, D. S. and Wood, D. S. Proc. Am. Soc. Test. Mat. **49** (1949) 717.
8. Wood, D. S. and Clark, D. S. Trans. Am. Soc. Met. **43** (1951) 571.
9. Wood, D. S. and Clark, D. S. Trans. Am. Soc. Met. **44** (1952) 726.
10. Vreeland, T., Wood, D. S., and Clark, D. S. Trans. Am. Soc. Met. **45** (1953) 620.
11. Cottrell, A. H. and Bilby, B. A. Proc. Phys. Soc. **A62** (1949) 49.
12. Yokobori, T. Phys. Rev. **88** (1952) 1423.
13. Davies, R. M. Proc. Roy. Soc. **A197** (1949) 416.
14. Snoek, J. L. Physica **8** (1941) 711.
15. Nabarro, F. R. N. Report of a Conference on Strength of Solids, Phys. Soc. (1948) 38.

SUR LA MESURE DES DÉSORIENTATIONS RÉTICULAIRES DANS LES MONOCRISTAUX MÉTALLIQUES*

H. LAMBOT†, L. VASSAMILLET‡, J. DEJACE§

L'utilisation d'un faisceau de rayons X convergent obtenu à l'aide d'un monochromateur à quartz courbé permet de déterminer les désorientations angulaires du réseau cristallin. Les monocristaux étudiés sont irradiés suivant une ou deux bandes minces d'environ 50 microns de largeur. L'emploi d'un rayonnement caractéristique permet d'observer les réflexions de Bragg à de grandes distances (1 mètre) avec des temps de pose relativement courts.

Pour des désorientations réticulaires inférieures à l'angle d'ouverture azimuthal du faisceau (1°), l'échantillon est maintenu fixe en position de réflexion. L'imperfection peut alors être suivie aux différents niveaux de la zone irradiée.

La détermination des décalages supérieurs à cette valeur s'effectue en décomposant le domaine angulaire de réflexion en une série discrète de positions fixes (oscillation décomposée).

L'observation des monocristaux en oscillation continue a également permis de mettre en évidence une structure interne des taches de Bragg habituelles, en relation avec les défauts géométriques du réseau.

Dans cet article, la technique est illustrée uniquement par des exemples de mesures de désorientations mais elle permet également de déceler les sous-structures éventuelles qui seront envisagées plus tard.

Il importe de remarquer que le montage proposé permet d'opérer aussi bien par réflexion que par transmission, donc d'examiner des éprouvettes d'épaisseur quelconque.

THE MEASURING OF LATTICE DISTORTIONS IN METAL SINGLE CRYSTALS

The use of a converging X-ray beam obtained by means of a curved quartz monochromator enables one to determine the angular distortions of a crystal lattice. The single crystal to be studied is irradiated along one or two narrow bands, approximately 50 microns in width.

The use of a characteristic radiation makes possible the observation of the Bragg reflection at large distances (1 meter) with relatively short exposure times.

In case of lattice distortions which subtend a smaller angle than the angle of azimuthal divergence of the beam (1°), the specimen is maintained in a fixed position of reflection. The imperfection can then be followed at different levels of the irradiated zone. Larger distortions are investigated by decomposing the angular domain of reflection into a discrete series of fixed positions (decomposed oscillation).

The observation of single crystals in continuous oscillation has revealed an internal structure of the usual Bragg spots in relation to the geometrical imperfections of the lattice.

In this paper, the technique is illustrated only by examples of distortion measurements, but it also allows the observation of eventual substructures that will be considered later. It is important to note that the proposed apparatus mounting provides versatility for operation both in reflection and transmission, and hence permits examination of specimens of any thickness.

DIE MESSUNG VON GITTERSTÖRUNGEN IN METALLEINKRISTALLEN

Mit Hilfe eines konvergenten Röntgenstrahlbündels, das durch einen gekrümmten Quarz Monochromator erhalten wurde, ist es möglich, die Verzerrungen eines Kristallgitters zu bestimmen. Es werden im zu untersuchenden Einkristall ein oder zwei enge Bänder–etwa 50 Mikron breit–belichtet.

Belichten mit Eigenstrahlung ermöglicht es, die Bragg-Reflexionen in grösserer Entfernung (1 Meter) und mit relativ kurzen Belichtungszeiten zu beobachten.

In allen Fällen, in denen die Drehungen des verzerrten Gitters kleiner als der Winkel der azimutalen Divergenz des Röntgenstrahls (1°) ist, wird die Probe in einer festen Reflexionslage gehalten. Die Gitterstörungen können dann auf den verschiedenen Lagen der belichteten Zone beobachtet werden. Zur Untersuchung grösserer Verzerrungen wird der Reflexionskegel in eine Anzahl fester Lagen zerlegt (Zerlegtes Oszillieren).

Die Untersuchung von kontinuierlich oszillierenden Einkristallen zeigte eine innere Struktur der Bragg-Reflexionen, die in Beziehung zu den geometrischen Gitterstörungen steht.

In der vorliegenden Arbeit ist diese Technik nur an Beispielen von Verzerrungsmessungen erläutert; es lassen sich jedoch auch Beobachtungen von Mosaikstrukturen damit durchführen, was für eine spätere Untersuchung geplant ist. Es wird darauf hingewiesen, dass der Kristallhalter in der beschriebenen Apparatur sowohl für Rückstrahlung als auch Durchstrahlung geeignet ist; dies ermöglicht die Untersuchung von Proben jeder Dicke.

1. Introduction

Devant la difficulté d'une description précise de la structure des cristaux réels à partir des "blocs mosaïques", Guinier et Tennevin [1] ont abordé l'étude d'un aspect partiel mais mieux défini du problème des imperfections cristallines. Adoptant un point de vue essentiellement géométrique, ils se sont proposé de déterminer expérimentalement la constitution du faisceau des normales à la famille de plans réticulaires déterminés. Leur technique repose sur la propriété de focalisation des rayons X réfléchis dans la méthode de Laue et elle les a

*Received June 19, 1953.

†Chef de Travaux à l'Université de Liège (Belgique). Actuellement Research Associate à l'Université d'Illinois.

‡Fulbright Fellow à l'Université de Liège (1950–1952).

§Attaché au Centre National Belge de Recherches Métallurgiques (section de Liège).

conduits à mesurer des écarts angulaires extrêmement faibles entre les plans cristallins d'un même groupe dans un volume assez grand de l'échantillon.

L'observation des perturbations locales dans les monocristaux a encore été entreprise, dans des conditions tout à fait différentes, à l'aide de la technique de Barrett [2] utilisant la réflexion d'un rayonnement monochromatique (3). Smoluchowski [4] a également tenté un pareil examen en transmission. Bien que les résultats obtenus présentent un très grand intérêt, ils restent néanmoins purement qualitatifs.

Dans cet article, nous proposons une technique basée sur l'emploi d'un faisceau convergent strictement monochromatique et susceptible de fournir une mesure précise des désorientations réticulaires de Guinier et Tennevin.

2. Dispositif expérimental

Nous utilisons un tube démontable à anticathode de cuivre ou de molybdène. Par concentration électrostatique des électrons, nous réalisons facilement un foyer fin dont les dimensions optiques sont de l'ordre de 0.6×0.08 mm. Le faisceau divergent qui en est issu est envoyé sur un monochromateur à quartz courbé (type Johann ou Johannsson) qui fait converger les rayons incidents sur une petite surface rectangulaire. Le réglage de ce monochromateur est effectué par voie photographique de manière à obtenir la séparation nette de $\kappa\alpha_1$, et $\kappa\alpha_2$. Dans ces conditions, la section minimum du faisceau utilisé se compose de deux bandes minces d'environ 50 microns de largeur sur quelques millimètres de hauteur (celle-ci étant d'ailleurs réglable par la fente F_2). L'élimination de $\kappa\alpha_2$ peut aisément s'effectuer* à l'aide d'un couteau effilé disposé au voisinage du "point" de focalisation (fig. 1). Le monocristal étudié est placé exactement en ce dernier "point".

En diminuant l'ouverture angulaire des rayons sortant du tube (avec la fente F_1), il est possible d'obtenir après le monochromateur un faisceau très homogène. Celui-ci peut être caractérisé de la manière suivante. Dans le plan horizontal, la focalisation s'effectue sur une largeur minimum f fixée par la dimension du foyer sur l'anticathode et la qualité de la lame-monochromatrice. Dans ce plan, un point isolé de f reçoit des rayons de toutes les directions contenues dans l'angle d'ouverture ω du faisceau (environ 1°). Dans le plan vertical passant par le rayon horizontal moyen, le faisceau présente une divergence en hauteur qui peut également être caractérisée par un angle d'ouverture ω' (1 à 2°).

Conçu de cette manière, notre dispositif permet donc d'irradier une tranche de l'échantillon d'une largeur de 50μ seulement. De plus, l'utilisation d'une radiation caractéristique rend possible l'enregistrement des réflexions de Bragg dans des temps relativement courts. Par exemple, pour un régime de 2 mA et 45 Kv, une réflexion normale d'un monocristal d'aluminium d'épaisseur 0.5 mm, fixé en position de Bragg et irradié par le doublet

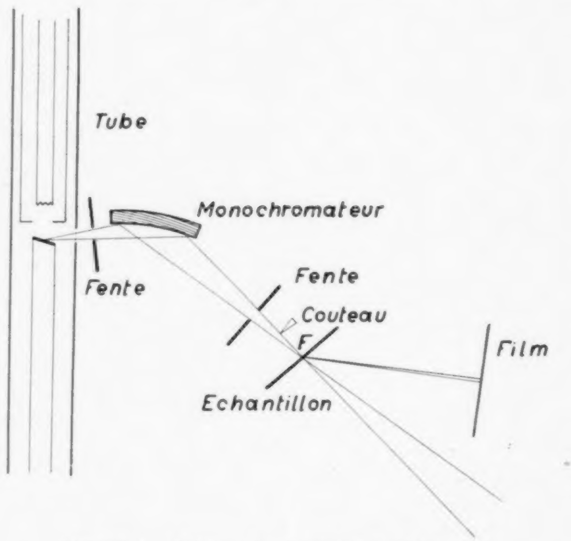

FIGURE 1. Schéma du dispositif expérimental.

séparé Mo $\kappa\alpha_1 - \kappa\alpha_2$ donne une tache intense à une distance d'un mètre en 30 minutes. L'utilisation d'un tube à anticathode tournante (10 à 15 mA et 45 Kv) nous permet même d'observer les réflexions à cette distance sur un écran radioscopique courant (en chambre noire).

Nous avons examiné nos échantillons de trois manières différents:

(1) monocristal fixe en position de Bragg;
(2) succession de telles positions fixes décalées légèrement l'une par rapport à l'autre dans l'intervalle angulaire de réflexion (oscillation décomposée);
(3) cristal en oscillation continue.

3. Cristal fixe en position de réflexion

Envisageons d'abord le cas d'un cristal (en F) fixe en position de Bragg. Pour une famille de plans réflecteurs *verticaux* supposés rigoureusement parallèles, il est facile de calculer la largeur instru-

*On peut également éviter ce réglage supplémentaire en utilisant le rayonnement $WL\alpha$.

mentale de la réflexion obtenue. Celle-ci dépend de la largeur spectrale de la radiation utilisée, de la dimension finie du foyer f, de l'épaisseur E intéressée par le rayonnement dans l'échantillon et de la divergence verticale du faisceau.

Nous illustrerons le calcul général par deux exemples d'examen, l'un en transmission (fig. 2) et l'autre en réflexion (fig. 3).

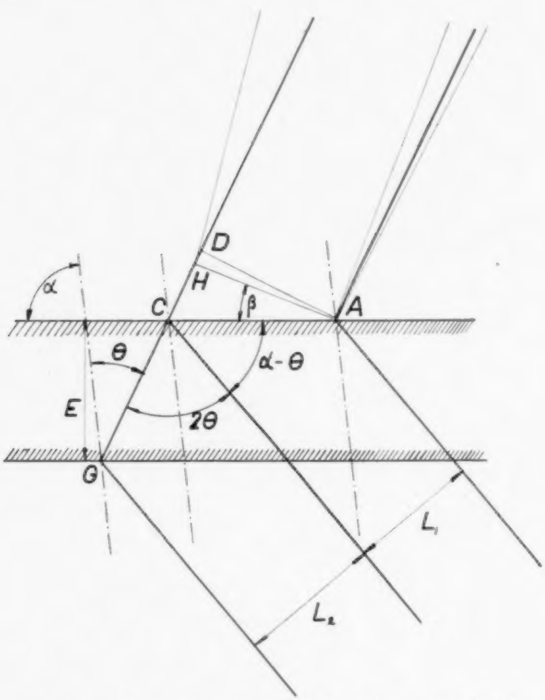

FIGURE 2. Largeur instrumentale d'une tache de Bragg observée en transmission.

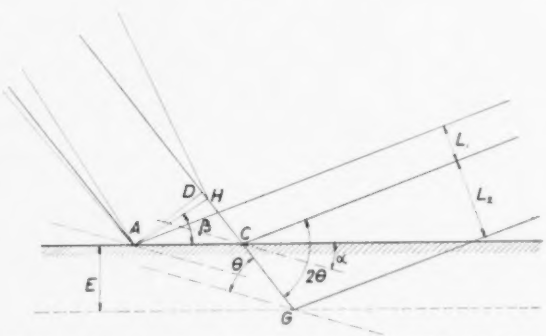

FIGURE 3. Largeur instrumentale d'une tache de Bragg observée en réflexion.

Les notations choisies ont la signification suivante:

θ = angle de Bragg de la réflexion observée,

α = angle aigu du plan réticulaire avec la surface de l'échantillon

β = angle de la surface du cristal avec le plan perpendiculaire au rayon incident moyen.

f = largeur du foyer en F.

E = épaisseur intéressée dans l'échantillon.

D = distance film-échantillon.

ω' = divergence verticale du faisceau.

1. *Largeur due à l'ouverture spectrale de la radiation employée*

Si nous considérons la largeur $\Delta\lambda$ de la bande $\kappa\alpha_1$ nous pouvons écrire que

$$\Delta\theta = \frac{\text{séc}\,\theta}{2d}\,\Delta\lambda$$

La valeur correspondante de l'élargissement à une distance D s'exprime donc par

$$L_0 = \left| D\,\frac{\text{séc}\,\theta}{2d}\,\Delta\lambda \right|$$

2. *Largeur L_1 due à f**

Dans le cas de la transmission (fig. 3):

$$L_1 = |AC \sin(\alpha - \theta)|$$

Or,

$$AC = \left| \frac{AD}{\sin(\alpha_1 + \theta)} \right|$$

et

$$AD = |AH \cdot \sin(\alpha + \theta - \beta)|$$
$$= |f \sin(\alpha + \theta - \beta)|$$

Donc

$$L_1 = \left| f\,\frac{\sin(\alpha - \theta)}{\sin(\alpha + \theta)} \sin(\alpha + \theta - \beta). \right|$$

En réflexion (fig. 3), on obtient de même:

$$L_1 = \left| f\,\frac{\sin(\alpha - \theta)}{\sin(\alpha + \theta)} \sin(\alpha + \theta + \beta) \right|.$$

3. *Largeur L_2 due à E (figs. 2 et 3)*

$$L_2 = |CG \cdot \sin 2\theta|.$$

Or,

$$CG = \left| \frac{E}{\sin(\alpha + \theta)} \right| .$$

*En réalité, la largeur finie f est, au moins en partie, due à la largeur spectrale de la raie utilisée. Comme l'imperfection propre du monochromateur semble au moins égale à cette largeur naturelle, on peut négliger le fait que les différents points du foyer reçoivent des rayons de longueurs d'onde différentes.

Donc

$$L_2 = \left| E \frac{\sin 2\theta}{\sin (\alpha + \theta)} \right|$$

4. *Largeur L_3 due à ω' (fig. 4)*

Soient R_0 et R_0' les pôles des rayons moyens horizontaux incident et réfléchi sur les plans de

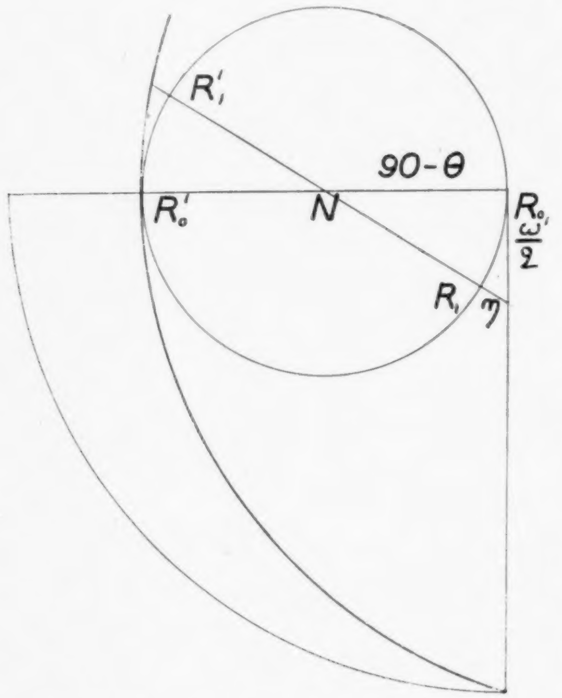

FIGURE 4. Correction due à la divergence verticale du faisceau.

normale N. Le décalage azimuthal d'un rayon R_1 (R_1') subissant la réflexion sur les mêmes plans et faisant avec R_0 (R_0') un angle vertical de $\frac{\omega'}{2}$ peut être représenté par η.

On voit aisément que

$$\sin (\theta - \eta) = \sin \theta \cos \frac{\omega'}{2}$$

d'où

$$\sin \eta \sim \left(1 - \cos \frac{\omega'}{2}\right) tg\, \theta$$

et

$$\eta \sim \frac{\omega'^2}{8}\, tg\, \theta$$

Donc $L_3 = \frac{1}{8} D\omega'^2\, tg\, \theta$.

Dans le but de proposer pour la largeur instrumentale une seule expression valable quelle que soit la disposition relative du plan réflecteur, de la surface de l'échantillon et du rayon incident, nous avons été amenés à adopter les conventions de signes suivantes:

(1) l'angle 2θ mesuré à partir du faisceau réfléchi vers le faisceau direct est compté positivement dans le sens des aiguilles d'une montre.
(2) l'angle aigu α est compté positivement dans le sens des aiguilles d'une montre à partir du plan réflecteur vers la surface du cristal;
(3) l'angle aigu β est mesuré de la même manière à partir du plan perpendiculaire au rayon moyen vers la surface de l'échantillon.

Dans ces conditions on peut écrire:

$$L = \left| D \frac{\text{séc}\, \theta}{2d} \Delta\lambda \right| + \left| f \frac{\sin (\theta + \alpha)}{\sin (\theta - \alpha)} \sin (\theta - \alpha + \beta) \right| + \left| E \frac{\sin 2\theta}{\sin (\theta - \alpha)} \right| + \frac{1}{8} D\, \omega'^2\, tg\, \theta$$

Avec notre montage $(\theta - \alpha + \beta)$est pratiquement égal à 90° et le quatrième terme est extrêmement faible.

Dans le cas de la transmission $(\alpha > \theta)$, les conditions expérimentales conduisant à une largeur instrumentale minimum sont réalisées lorsque α est négatif (avec les conventions adoptées) et a une valeur numérique voisine de $(90 - \theta)$, pour un θ aussi petit que possible.*

En réflexion $(\alpha < \theta)$ α doit être négatif et voisin de θ.

Dans le cristal réel, du fait de l'imperfection éventuelle du réseau, la normale à la famille de plans réflecteurs considérée peut cesser d'être unique pour être remplacée par un véritable faisceau plus ou moins ouvert. Toute désorientation azimuthale conduisant à un pareil cas, donnera évidemment lieu à un élargissement de la tache observée. La mesure de l'angle sous lequel cette largeur L est vue à partir de l'échantillon permettra en principe de trouver l'angle d'ouverture maximum du faisceau des normales. Il y a lieu de remarquer qu'avec notre dispositif, cet angle ϵ vaut L/D tandis qu'avec la méthode de Laue focalisé, ϵ est exprimé $L/2D$. La différence de sensibilité qui en résulte n'est cependant pas très importante car l'utilisation d'une radiation monochromatique conduit à des temps de pose suffisamment courts pour permettre l'adoption de grandes distances D.

En effet, l'existence d'un terme d'élargissement

*On peut éventuellement songer à observer les réflexions $\frac{\lambda}{2}$ moins intenses mais conduisant à des θ plus petits.

5

6

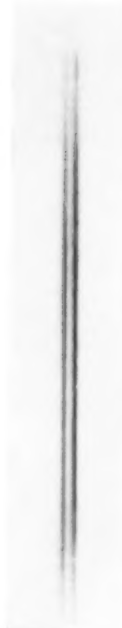

7

8

9

10

11

PLATE I. Figure 5—**Réflexion** ($10\bar{1}0$) d'une lame de quartz rodée optiquement. $E = 0.33$ mm: $\lambda = \mathrm{Mo}_{K\alpha}$; $D = 75$ cm (en transmission). Figure 6—Réflexion (220) d'un monocristal d'aluminium raffiné (99.99%). $\lambda = \mathrm{Cu}_{K\alpha_1}$; $D = 120$ cm (en réflexion). Figure 7—Réflexion (110) d'un monocristal de fer pur (99.85%) $\lambda = \mathrm{Mo}_{K\alpha}$, $D = 138$ cm (en réflexion). Figure 8—Réflexion (111) d'un monocristal d'aluminium à 99.85%. $E = 0.5$ mm. $\lambda = \mathrm{Mo}_{K\alpha}$. $D = 80$ cm (en transmission). Figure 9—Réflexion (111) d'un monocristal d'aluminium à 99.95%; étiré de 3.2%. $E = 0.5$ mm; $D = 80$ cm (en transmission). Figure 10—Réflexion d'un monocristal d'aluminium mince (0.08 mm) ayant subi une déformation accidentelle (en transmission). Figure 11—Réflexion d'un monocristal mince de cuivre pur ayant subi une déformation accidentelle (en transmission).

12a

12b

12c

12d

13

15

14

PLATE II. Figure 12—Réflexion (111) d'un monocristal d'aluminium raffiné (99.99%): (a) étiré de 4%; (b) après revenu de 12 h. à 300°C; (c) après revenu de 12 h. à 400°C; (d) après revenu de 12 h. à 550°C. $D = 87.5$ cm (en transmission). Figure 13—Réflexions (111) d'un monocristal d'aluminium à 99.95% étiré d'environ 3% (oscillation décomposée et en transmission). $D = 20$ cm. Figure 14—Réflexions (111) d'un monocristal d'aluminium raffiné (99.99%) (oscillation decomposée et en transmission). $D = 20$ cm. Figure 15—Structure interne d'une tache de Bragg obtenue avec un monocristal d'aluminium en oscillation continue.

proportionnel à D (largeur L_0) n'exclut nullement la possibilité d'adopter de grandes distances film-échantillon.

La comparaison de la limite de sensibilité obtenue avec notre montage et celle caractérisant la technique de Guinier et Tennevin est en faveur de cette dernière. En fait, nous pouvons déceler une désorientation angulaire de vingt secondes d'arc.

Par contre, notre dispositif permet aussi bien l'examen par réflexion que par transmission rendant ainsi possible l'étude d'éprouvettes d'épaisseur quelconque.

Il est évidemment possible d'objecter qu'une variation de la distance réticulaire d d'une partie à l'autre de la zone irradiée aurait également pour effet d'élargir la tache de Bragg correspondante.

La distinction rigoureuse entre ces deux effets est extrêmement difficile à priori. Néanmoins, il est aisé de montrer qu'avec notre dispositif, ce sont essentiellement les désorientations réticulaires qui sont à l'origine des élargissements observés. L'énergie nécessaire pour modifier d est incomparablement plus grande que celle qui est requise par la déformation géométrique des plans du réseau.*

En vue de raccorder nos observations à celles de Guinier et Tennevin, nous avons examiné un type de cristal extrêmement parfait comme le quartz (fig. 5). La perfection géométrique (désorientation de 20 secondes maximum) se manifeste aussi bien par la finesse et la séparation nette du doublet α_1 et α_2 que par la répartition uniforme de l'intensité sur une assez grande hauteur.

Nous avons également pu constater que les monocristaux préparés par la méthode d'Elam-Carpenter possèdent une perfection très élevée.

La figure 6 reproduit une tache observée en réflexion avec la seule composante $\kappa\alpha_1$, sur un monocristal d'aluminium raffiné (99.99%). Dans le domaine irradié de 50μ de largeur, la désorientation est au maximum de 50 secondes.

Les cristaux de fer pur préparés par la méthode de Lacombe et Moufflard [5] permettent d'enregistrer des raies de réflexion aussi fines et homogènes. L'échantillon de la figure 7, irradié par le doublet $\kappa\alpha_1 - \kappa\alpha_2$ bien séparé† admet une désorientation maximum de 50 secondes.‡

Bien entendu, tous les cristaux préparés par écrouissage critique ne sont pas aussi parfaits. L'exemple de la figure 8 mérite entre autres d'être retenu. Dans les deux régions extrêmes en hauteur, la désorientation ne dépasse pas 2 minutes. Mais ces deux parties du même monocristal sont décalées l'une par rapport à l'autre d'environ 10 minutes d'arc. Ces observations nous semblent devoir être mises en parallèle avec celles de Tiedema sur la nucléation des cristaux d'aluminium obtenus par recristallisation [6]; le décalage angulaire entre les deux parties principales est en accord avec les résultats de cet auteur. Mais grâce à notre technique, il est de plus possible de suivre leur raccordement. Celui-ci s'effectue par une rotation progressive des plans réticulaires. Cette rotation n'est pas continue car l'existence de minces segments dans la tache suggère la présence de petits paquets de plans assez parfaits très faiblement décalés les uns par rapport aux autres (1 à 2 minutes) et constituant de véritables individualités. De tels cas ne sont pas rares dans l'aluminium.

La technique proposée convient particulièrement pour l'étude de la régularité géométrique du réseau en fonction des divers traitements mécaniques et thermiques que l'on peut faire subir aux cristaux.

Dans cet article, nous nous contenterons d'illustrer ces possibilités par quelques exemples.

La figure 9 se rapporte à un monocristal d'aluminium à 99.95% initialement très parfait et soumis à une extension de 3.2%. L'aspect sinueux de la réflexion reflète bien l'hétérogénéité de la déformation réticulaire dans la mince région irradiée. La désorientation moyenne est de 20 minutes d'arc et le décalage entre deux régions différentes peut atteindre 1 degré. La distribution de l'intensité est assez peu uniforme et semble devoir être rapportée à la distribution des normales en dehors du plan horizontal.

Un cas typique à ce dernier égard est reproduit à la figure 10. Il s'agit d'un monocristal d'aluminium mince (1/10 mm) simplement manipulé en vue d'un réglage et en prenant pourtant quelque précaution pour en éviter la déformation. Les normales subissent dans le plan horizontal des vicissitudes très considérables se manifestant par une ouverture angulaire très grande et très irrégulière. Dans le plan vertical, les désorientations de normales conduisent à la formation de zones d'intensités très différentes dans la réflexion de

*Des cristaux faiblement étirés (quelques pour cent) donnent naissance à des élargissements qui conduiraient à des variations de d supérieures au taux d'allongement macroscopique. Pour $D = 1$ mètre et $\theta = 10°$, une variation de largeur de 2 mm, peut être rapportée à une désorientation de 0.002 rad. ou à un $\frac{\Delta d}{d} = 1\%$.

†Dans le cas de cristaux aussi parfaits, il est utile de travailler avec le doublet $\kappa\alpha_1 - \kappa\alpha_2$ dont la nette séparation est un indice de haute perfection géométrique.

‡Nous tenons à remercier M. Lacombe qui a bien voulu mettre à notre disposition quelques échantillons.

Bragg. Nous signalerons encore en passant la fine striation de la tache observée, phénomène sur lequel nous nous réservons de revenir plus tard.

Nous reproduirons encore le cas d'un monocristal de cuivre involontairement déformé au cours des manipulations de réglage sur notre dispositif (fig. 11).

La sensibilité de notre technique est bien mise en évidence par l'exemple suivant.

Un monocristal d'aluminium raffiné initialement bien parfait est soumis à une traction de 4%. Le résultat de la déformation est visible sur la figure 12a. Dans cet état, l'échantillon est soumis à des revenus progressifs. Après 12 heures à 200°C., la tache commence à se décomposer en un grand nombre de stries minces noyées dans un fond encore assez diffus. Au fur et à mesure que la température s'élève, la structure interne de la réflexion devient de plus en plus distincte et la dimension des stries augmente de manière à peu près continue (voir fig. 12).

Cet aspect peut être rattaché au phénomène de polygonisation au sens de Cahn [6], Guinier [7] etc. . . . (formation d'une sous-structure à partir de régions courbées sous l'action de la température) ou de la croissance des "sous-grains" de Wood [8] résultant directement de la déformation.

Nous reviendrons plus tard sur cette question à la suite des remarques de Beck [9].

Nous signalerons simplement que notre technique permet de rendre cette sous-structure nettement visible à 200°C alors que celle de Guinier et Tennevin ne la décèle qu'à 450°C (aluminium raffiné 99.99%).

Ces quelques exemples donnent une idée des imperfections géométriques qui peuvent exister dans les monocristaux métalliques et passent pratiquement inaperçues lorsqu'on s'adresse uniquement aux méthodes de diffraction habituelles.

4. Cristal en oscillation décomposée

L'examen des cristaux en position fixe ne permet évidemment pas de déceler les désorientations dépassant la valeur de ω. Mais il existe un moyen de prolonger la détermination des décalages de normales au delà de ω. Il suffit de décomposer l'oscillation continue de l'échantillon dans le domaine de Bragg en une série de positions discrètes et d'enregistrer séparément les rayons réfléchis pendant les différentes poses. On peut ainsi pointer l'azimuth où la réflexion commence et celui où elle se termine. Cet intervalle rapporté à ω fournit immédiatement la valeur de la désorientation cherchée. Ce procédé peut d'ailleurs être utilisé pour déterminer un décalage inférieur à ω mais néanmoins pas trop petit. Il a de nouveau l'avantage de permettre la recherche de l'imperfection géométrique suivant les différents niveaux de la zone irradiée.

Le cliché de la figure 13 a été obtenu avec un monocristal d'aluminium étiré d'environ 3%. Les différentes taches correspondent à des positions fixes de l'échantillon décalées de 12 en 12 minutes dans le domaine de la réflexion. Les différentes régions du volume irradié ne réfléchissent pas le rayonnement incident pour une même position fixe, ce qui montre que l'orientation des plans n'est pas la même en tout point.

La mesure de l'angle dans lequel la réflexion a lieu a fourni dans le cas présent, la valeur de 2°06′. L'ouverture du faisceau incident étant de 1°10′, nous pouvons en déduire que la désorientation maximum des plans réticulaires observés est de 56′ environ. La valeur obtenue à l'aide de la largeur d'une tache isolée (à grande distance) fournit une valeur de 58′. L'accord entre les deux techniques est donc excellent.

La figure 14 correspond à un cas où la désorientation est supérieure à ω. Il importe à nouveau de remarquer la forme très irrégulière des taches et la répartition très inhomogène de l'intensité diffractée.

Des tractions de l'ordre de 5 à 10% sur l'aluminium donnent généralement naissance à des faisceaux de normales d'angle supérieur à ω. Pour des déformations égales ou supérieures, il importe donc d'utiliser l'oscillation décomposée pour obtenir une mesure de l'imperfection totale.

Sur ces clichés, comme sur ceux obtenus avec le cristal fixe, la répartition de l'intensité diffractée est rarement uniforme et indique ainsi une certaine répartition des normales en dehors du plan horizontal.

5. Cristal en oscillation continue

Dans le cas d'un cristal oscillant en F autour d'un axe vertical, on peut aisément prévoir que la largeur des réflexions de Bragg est fixée par l'ouverture ω du faisceau incident. Elle est insensible aux faibles désorientations géométriques du réseau.

Par contre, la distribution de l'intensité à l'intérieur d'une tache peut être fortement influencée par ces défauts.

Considérons, par exemple, dans le volume irradié une région de plans réflecteurs verticaux rigoureusement parallèles sur une certaine hauteur. Supposons qu'à une autre altitude, certains de ces

plans subissent par rapport au plan moyen des décalages angulaires donnant lieu à un faisceau de normales uniquement horizontales. Au cours d'une oscillation continue d'amplitude suffisamment grande, il n'y a aucun facteur géométrique susceptible d'introduire une différence d'intensité diffractée entre les niveaux de la tache correspondant aux deux régions considérées. Par contre, le facteur physique d'extinction peut conduire à une intensité supérieure à l'altitude du domaine perturbé.

D'autre part, si nous conservons le cas de plans réflecteurs verticaux parfaitement orientés dans une première région I et si nous imaginons à un autre niveau du volume irradié une zone II où ces plans réticulaires ont une normale oblique sur l'horizontale, il est facile de voir que les rayons réfléchis par II pourront venir se superposer à ceux qui sont issus de I. Par conséquent, l'intensité diffractée durant l'oscillation sera nettement différente aux altitudes correspondant à I et II.

On peut d'ailleurs prévoir la forme adoptée par ces zones intenses au sein des différentes taches dans les deux cas envisagés.

Si, dans la zone irradiée, deux régions se distinguent uniquement par des valeurs différentes du facteur d'extinction (avec les normales aux plans réflecteurs contenues dans le plan horizontal), le niveau qui, dans la tache de Bragg, correspond à la zone du pouvoir réflecteur élevé sera marqué par un renforcement de l'intensité. Nous devons donc observer l'apparition d'une strie plus ou moins nette mais rigoureusement horizontale.

Par contre, dans le cas d'une région présentant (à une altitude différente) des normales obliques sur l'horizontale, le renforcement de l'intensité suivra l'hyperbole-intersection du film plan avec le cone des rayons réfléchis par une série de plans également inclinés sur l'axe de rotation.

Il est malheureusement impossible actuellement de distinguer ces aspects différents. D'ailleurs les deux effets peuvent se superposer en pratique.

Pour des plans réflecteurs non verticaux, les deux cas envisagés se distingueront théoriquement par des striations en hyperboles légèrement différentes. Encore une fois, il est impossible de déceler ce faible écart expérimentalement.

Les cristaux métalliques (ainsi d'ailleurs que les cristaux minéraux et organiques) observés au point de focalisation sous une épaisseur de quelques dixièmes de mm, donnent pratiquement toujours naissance à des taches striées. La figure 15 reproduit une réflexion due à l'aluminium. Le nombre et la netteté de ces stries varient fortement suivant les échantillons. Certains cristaux de quartz, par exemple, montrent seulement une ou deux bandes floues très peu contrastées pour un volume irradié de 0.2 mm^3. Par contre, les cristaux métalliques donnent généralement lieu dans les mêmes conditions à des stries nombreuses et assez rares.

Pour un tel échantillon, ce nombre augmente avec le volume irradié et lorsque ce dernier devient suffisamment grand, les stries sont tellement serrées qu'il devient impossible de les distinguer, la tache prenant un aspect uniforme.

L'orientation observée pour les zones de forte intensité est bien celle des hyperboles dont il a été question ci-dessus.

Cette structure fine obtenue même avec des cristaux assez parfaits, indique donc à nouveau la présence d'imperfections dans le réseau. Bien que ne fournissant que des indications qualitatives à ce sujet, le procédé est extrêmement sensible à ce genre de défauts, étant donné le mécanisme de formation des stries mettant en jeu le bilan de l'énergie diffractée par les différentes parties du réseau au cours de l'oscillation.

Remerciements

Nous tenons à exprimer nos remerciements aux Professeurs Beck, Brasseur et Guinier pour l'intérêt qu'ils ont bien voulu nous manifester. A la correction des épreuves, le docteur J. Barraud nous a également signalé ses observations antérieures sur le mica [11].

Bibliographie

1. Guinier, A. et Tennevin, J. Acta Cryst. **2** (1949) 133.
2. Barrett, C. S. Techn. Publ. Amer. Inst. Mech. Eng. n° 1865, 1945.
3. Honeycombe, R. W. K. J. Inst. Met. **80** (1951) 39.
4. Smoluchowski, R. C. R. Acad. Sci., Paris **222** (1946) 1496.
5. Moufflard, M. et Lacombe, P. Rev. Metall. **49** (1952) 140.
6. Tiedema, T. J. Proc. K. Ned. Akad. Wet. **53** (1950) 1422.
7. Cahn, R. W. J. Inst. Met. **76** (1949) 121.
8. Guinier, A. Imperfections in Nearly Perfect Crystals (New York, Wiley), p. 402.
9. Wood, W. A. and Rachinger, W. A. J. Inst. Metals **75** (1949) 571.
10. Beck, P. A. J. Metals (septembre 1952) et Communication personnelle (février 1953).
11. Barraud, J. C. R. Acad. Sci. **214** (1942) 795; **229** (1949) 378.

TERNARY LAVES AND SIGMA-PHASES OF TRANSITION METALS*

KEHSIN KUO†

The B metal of the Laves phase AB_2 can be replaced by a mixture of B′ and B″, thus forming a ternary phase $A(B', B'')_2$. The metals B′, B, and B″, belong to the same period of the Periodic Table and B lies between B′ and B″. This kind of substitution produces many ternary Laves phases of transition metals.

This kind of substitution can also be applied to the formation of the sigma-phase A_aB_b. However, in this case the ratio a/b changes, e.g., σ-$MoCr_2Ni_2$ and σ-WCr_8Ni_5 as compared with σ-MoFe and σ-WFe.

LES PHASES TERNAIRES DE LAVES ET DU TYPE SIGMA DANS LES MÉTAUX DE TRANSITION

Le métal B de la phase AB_2 de Laves peut être remplacé par un mélange de B′ et B″, formant ainsi une phase ternaire $A(B', B'')_2$. Les métaux B′ et B″ appartiennent à la même période de la classification périodique et se trouvent de part et d'autre de B. Ce genre de substitution produit de nombreuses phases ternaires de Laves dans les métaux de transition.

Une substitution similaire peut aussi être appliquée à la formation de la phase sigma A_aB_b. Dans ce cas, cependant, le rapport a/b change, par exemple σ-$MoCr_2Ni_2$ et σ-WCr_8Ni_5 comparés à σ-MoFe et σ-WFe.

TERNÄRE LAVES UND SIGMA-PHASEN DER ÜBERGANGSMETALLE

Das B Metall der Laves Phase AB_2 kann durch eine Mischung von B′ und B″ ersetzt werden und so eine ternäre Phase $A(B', B'')_2$ bilden. Die Metalle B′, B und B″ gehören derselben Gruppe des periodischen Systems an, und B steht zwischen B′ und B″. Diese Art Substitution erzeugt zahlreiche ternäre Laves-Phasen der Übergangsmetalle.

Eine derartige Substitution kann auch auf die Bildung der Sigma-Phase A_a B_b angewandt werden. In diesem Falle ändert sich jedoch das Verhältnis a/b, d. h. σ-Mo Cr_2Ni_2 und σ-WCr_8 Ni_5 werden mit σ-MoFe und σ-WFe verglichen.

Introduction

The most common intermediate phase in binary systems of transition metals is the Laves phase AB_2 [1], which may have any one of the three closely related structures characterized by the compounds $MgNi_2$, $MgCu_2$, and $MgZn_2$ [2]. Though the atomic size factor was considered of primary importance for the stability of these Laves phases [3; 4], the electronic factor ought also to be taken into account [5]. By studying a great number of ternary systems containing magnesium Laves and Witte [6] established the importance of the electron/atom ratio and found many ternary Laves phases with Mg as the component A.

The recognition of the general occurrence of the sigma-phase of transition metals is a quite recent matter. This phase is isostructural with β-uranium [7]. Only a few sigma-phases occur at the composition AB and no general formula can be derived to denote composition of the phase. On account of this, several authors have considered the sigma-phase as an electron compound [8–10], but no definite conclusion could be arrived at owing to the uncertainty about the electron configuration of the transition metals.

It has been shown in a previous publication [11] that the A metal of the η_1 carbide A_3B_3C can be replaced by a mixture of metals A′ and A″, all these three metals belonging to the same period in the periodic table and A lying between A′ and A″; e.g., Cr_3Nb_3C and $(V, Ni)_3Nb_3C$. The ternary phase Al_9FeNi is siostructural with the binary one Al_9Co_2 [12], and this provides another example of this sort of substitution. The formation of ternary Laves and sigma-phases of transition metals has been investigated by applying this principle and the results are presented in this paper.

Alloys were either melted in a vacuum induction furnace and then heated at 1000°C for 24 hours or heated directly at this temperature for 50 hours in evacuated silica tubes. The phases were later determined by an X-ray powder method. The experimental details have been published elsewhere [11].

Laves Phases

Binary Phases

The binary Laves phases with Ti, Nb, Ta, or Zr as A and the transition metals belonging to period IV as B are shown in Table I.

Geometrical consideration of these three types of

*Received June 25, 1953.

†Institute of Chemistry, University of Uppsala, Sweden.

TABLE I

BINARY LAVES PHASES OF TRANSITION METALS, AB_2

A \ B		V	Cr	Mn	Fe	Co	Ni	Cu
Ti	d_A/d_B	1.08	1.13	1.16	1.17	1.18	1.18	1.15
	Structure-Type	—	$MgCu_2$, $MgZn$*	$MgZn_2$	$MgZn_2$	$MgCu_2$†	—	—
Nb	d_A/d_B	1.08	1.13	1.16	1.17	1.18	1.18	1.15
	Structure-Type	—	$MgCu_2$	$MgZn_2$	$MgZn_2$	$MgCu_2$	—	—
Ta	d_A/d_B	1.10	1.14	1.17	1.18	1.19	1.19	1.16
	Structure-Type	—	$MgCu_2$, $MgZn_2$*	$MgZn_2$	$MgZn_2$	$MgCu_2$†	—	—
Zr	d_A/d_B	1.18	1.23	1.26	1.27	1.28	1.28	1.25
	Structure-Type	$MgZn$	$MgZn_2$, $MgCu_2$*	$MgZn_2$	$MgCu_2$†	$MgCu_2$	—	—

*High-temperature phase. The transition temperature range is 1000–1100°C for $TiCr_2$ [13], 1375–1590°C for $TaCr_2$ [14], and 900–994°C for $ZrCr_2$ [15].

†If the B metal is slightly in excess (7.4%) the $MgNi_2$ type of structure will occur instead of the $MgCu_2$ [1].

structure of the Laves phases shows that the ideal atomic size ratio of the components A and B, d_A/d_B, is $\sqrt{3/2} = 1.225$ [2;3]. This condition is necessary, but not sufficient, and it cannot be used to predict the formation of these phases. An obvious example is the inability of Ni, serving as the component B, to form any Laves phase with Ti, Nb, Ta, or Zr.

Berry and Raynor [4] considered that as the deviation of d_A/d_B from its ideal value becomes larger, the Laves phase changes its structure from the $MgZn_2$ type to the $MgCu_2$ type. On the other hand, Laves and Witte [7] found that as the electron/atom ratio increases from 0.66 to 2.0, the sequence of structure types of the ternary Laves phase containing Mg appeared to be: $MgNi_2$ (0.66–0.9), $MgCu_2$ (1.1–1.7), $MgNi_2$ (1.8–1.9), and $MgZn_2$ (2.0). The reappearance of the $MgNi_2$ type of structure at an electron/atom ratio around 1.8 was explained by Witte [16; 17] as the result of the filling of the second Brillouin zone of the $MgNi_2$ lattice. But neither of these two hypotheses can explain the formation of the different Laves phases of transition metals, owing to the following two facts. First, as the atomic number of B increases, the structure type of the Laves phase changes from $MgCu_2$ to $MgZn_2$ and then back to $MgCu_2$. Secondly, both types of structure may exist for the same phase, but at different temperatures; e.g., $TaCr_2$.

Ternary Phases

As stated above, the ternary Laves phases of magnesium have been studied extensively by Laves and coworkers. However, only three ternary Laves phases containing *one* transition metal are known, and they are: $Mg(Ni, Zn)_2$, $Mg(Co, Zn)_2$, and $Mg(Ni, Si)_2$, all having the $MgCu_2$ type of structure [6].

The ternary Laves phases with Ta as metal A, and the transition metals of the IV period as B metals (B′ and B″) are shown in Table II. In the case of B′ = V or Cr, all possible ternary phases are obtained except $Ta(V, Fe)_2$ and $Ta(V, Ni)_2$. These two phases should have the $MgCu_2$ type of structure. They may exist, and could perhaps be found by thorough investigation of various compositions of the B mixture.

It seems that the occurrence of a ternary Laves phase is a general phenomenon, and a survey of the collected data presented in Table II (and Table I) gives us the following observations:

TABLE II

LAVES PHASES WITH TANTALUM AS METAL A AT 1000°C

Structure Type	Binary phase AB_2	Ternary phase*, $A(B', B'')_2$			
		$B' = Ti$	$B' = V$	$B' = Cr$	$B' = Fe$
$MgCu_2$ cubic	$TaCr_2$, $a = 6.979$ Å	—	$TaV_{1.5}Mn_{0.5}$, $a = 7.008$ Å	—	—
$MgZn_2$ hexagonal	$TaMn_2$, $a = 4.806$ Å, $c = 7.952$ Å	$TaTiCo$, $a = 4.982$ Å, $c = 8.140$ Å	$TaVCo$, $a = 4.893$ Å, $c = 7.909$ Å	$TaCrCo$, $a = 4.856$ Å, $c = 7.952$ Å	—
			$TaVNi$, $a = 4.848$ Å, $c = 7.909$ Å	$TaCrNi$, $a = 4.856$ Å, $c = 7.888$ Å	—
	$TaFe_2$, $a = 4.816$ Å, $c = 7.868$ Å	—	$TaV_{1.5}Cu_{0.5}$, $a = 5.032$ Å, $c = 8.206$ Å	$TaCr_{1.5}Cu_{0.5}$, $a = 4.885$ Å, $c = 7.927$ Å	—
$MgCu_2$ cubic	$TaCo_2$, $a = 6.735$ Å	—	$TaVCu$, $a = 7.115$ Å	—	$TaFeNi$, $a = 6.717$ Å

*The composition given for the various ternary Laves phases is the composition of the alloy as weighed beforehand. Owing to the presence of other intermediate phases or metallic oxides, this composition can only be accepted as approximate. Nor can the lattice constants be considered as typical, since they vary within broad limits as the proportion of B′ and B″ varies; e.g., for $Ta(Cr, Co)_2$, $a = 4.856$–4.915 Å, $c = 7.888$–8.037 Å.

1. The general formula of the ternary phase is $A(B', B'')_2$ and it has the same type of structure as AB_2, where B lies between B′ and B″. In other words, the mixture of B′ and B″ has average properties essentially very similar to those of B.

2. There are three cases of *genuine, ternary* (i.e., existing separately from binary Laves phases) Laves phases $A(B', B'')_2$ according to their relations to the corresponding binary phases AB_2' and AB_2''.

(i) None of the phases AB_2' or AB_2'' exists; e.g., $Ta(V, Ni)_2$.

(ii) One of the phases AB_2' or AB_2'' exists, but the ternary phase has a different type of structure; e.g., $Ta(Fe, Ni)_2$ and $Ta(V, Co)_2$.

(iii) Both phases AB_2' and AB_2'' exist, but the ternary phase has a different type of structure; e.g., $Ta(Cr, Co)_2$.

3. If the B′ component is vanadium, the ternary Laves phase also changes its type of structure from $MgCu_2$ to $MgZn_2$ and then back to $MgCu_2$ as the atomic number of B″ increases, in a similar manner to the structural changes in the binary phases in Table I. This may perhaps imply that the mixtures (V, Mn), (V, Co), (V, Ni), or (V, Cu) have average properties similar to those of Cr, Mn, Fe, or Co, respectively.

4. The same phase $A(B', B'')_2$ can have either the $MgZn_2$ type or the $MgCu_2$ type of structure, depending upon the proportion of B′ to B″ in the B mixtures, e.g., $Ta(V, Cu)_2$. As the proportion of Cu in the mixture (V, Cu) increases, the average properties of this mixture vary from those of Cr to Mn and Fe, and then to Co. The resulting structure of the ternary Laves phase would change from $MgCu_2$ to $MgZn_2$ type and then back to $MgCu_2$. The change from $MgCu_2$ to $MgZn_2$ has not been discovered yet, but it may occur at the vanadium end of the (V, Cu) mixture.

5. Titanium can serve as the component A in forming binary Laves phases, but it can also serve as one of the B components of the ternary phases, e.g., $Ta(Ti, Co)_2$.

Experiments have also been made to investigate the possibility of using Ti, Nb, or Zr as the A component to form the ternary Laves phases. Nb, like Ta, forms a great number of ternary Laves phases with different mixtures of B components. No ternary phase containing Ti as the A

component has been found (in experiments with the compositions: TiVNi, TiCrCo, TiFeNi, and TiVCo). However, the author's work has not been extensive enough to exclude definitely the possibility of Ti forming ternary Laves phases.

Zr has only been investigated in a few isolated cases. Both $ZrFe_2$ [1] and $ZrMo_2$ [18] are known to have the $MgCu_2$ type of structure, but the ternary phase $Zr(Mo, Fe)_2$, like $ZrMn_2$, is isomorphous with $MgZn_2$. This indicates that the B component, at least in the case of A = Zr, is not necessarily an element of period IV.

The above-mentioned experimental work seems to favour the electron compound hypothesis, since a mixture of V (atomic radius 1.36 Å for coordination number 12) and Cu (1.28 Å) cannot have the mean radius of Mn (1.27 Å), Fe (1.26 Å), of Co (1.25 Å). The fact that the Laves phase $Ta(V, Cu)_2$ exists and has a structure isomorphous with $TaMn_2$ ($TaFe_2$) or $TaCo_2$ may be regarded as evidence for the electron compound character of the Laves phases.

At the beginning of this investigation it was hoped to obtain some idea about the electron configuration of the transition metals by studying the composition limits of the $MgCu_2$ and $MgZn_2$ types of structure in the various ternary Laves phases. However, owing to the presence of other phases, it is impossible to obtain exact composition data for these ternary phases. The main impurity is the metallic oxides of the general formula A_3B_3O, A being Ti, Nb, Ta, and B being Mn, Fe, Co, or Ni [19 ; 20], formed by the reaction between the metal powder and the refractory crucible or the silica tube.

Sigma-Phases

The binary sigma phases of the transition metals are summarized in Table III. Owing to the variation in composition, this phase is denoted as A_aB_b. The sigma-phase is a low-temperature phase if one component is Cr or V, and a high-temperature phase if one component is Mo or W. (σ-CrFe is stable below 810°C and σ-VFe below 1240°C while σ-MoFe only is stable above 1180°C.)

Despite the great interest recently devoted to the formation of sigma-phases, only one *genuine* ternary phase, σ-$MoCr_2Ni_2$, (this formula has no other significance than to show the approximate composition of this phase) has been reported [22; 23]. It has a narrow composition range and a wide temperature range of stability.

Owing to the similarity in chemical behaviour

TABLE III

BINARY SYSTEMS CONTAINING SIGMA-PHASES, INDICATED BY LINES JOINING THE TWO METALS*

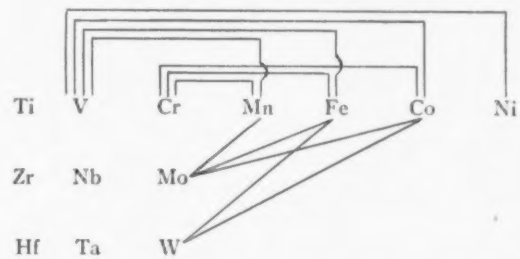

*Apart from the two σ-phases reported recently in the W-Co and W-Fe systems [21], all the σ-phases have been reviewed by Sully [8].

of Mo and W, it was suspected that a ternary sigma-phase may also exist in the system W-Cr-Ni. This led to the confirmation of the existence of the σ-WCr_8Ni_5. It also has a narrow composition range and a wide temperature range of stability. All the observed lines of the X-ray powder photograph can be indexed on a tetragonal lattice with a = 8.901–8.945 Å and c = 4.599–4.621Å. These dimensions are larger than those of the σ-CrFe lattice (8.799 and 4.546 Å) but smaller than those of the σ-$MoCr_2Ni_2$ (9.101 and 4.722 Å). This latter fact is due to the smaller percentage of W relative to Mo in the respective ternary sigma-phases. Some weak small angle reflections not noticed before, such as 110, 301, and 310, were observed.

It may perhaps be concluded from the existence of these two ternary sigma-phases that a mixture of Cr and Ni has mean properties similar to those of Fe or Co, a phenomenon analogous to that of the formation of the ternary Laves phases. However, in the latter case the ternary phase thus obtained has a constant general formula AB_2. In the formation of sigma-phase, the substitution of (Cr, Ni) for Fe or Co changes the composition from AB to AB_4 (with Mo as A) or AB_{13} (with W as A).

Efforts were made to use Ti, Zr, Nb, or Ta as the component A, but no binary or ternary sigma-phase was obtained. It is perhaps of interest to note that with the exception of W, no single A component forms both Laves and sigma-phases. According to Arnfelt and Westgren [24] WFe_2 is isostructural with $MgZn_2$, but is only stable below 1040°C while the σ-WFe is only stable above this temperature [21]. This gives the impression that the formation of one of these kinds of phases excludes the possibility of the other's formation. Together, they

form the two largest families of intermediate phases of transition metals.

Acknowledgment

The author wishes to thank Professor Gunnar Hägg for his never-failing support and advice, and the Swedish State Research Council for Technical Research for financial aid.

References

1. Wallbaum, H. J. Z. Kristallogr. Mineral. petrogr. Abt. **A103** (1941) 391.
2. Laves, F. and Witte, H. Metallwirtschaft **14** (1935) 645.
3. Laves, F. and Wallbaum, H. J. Z. anorg. Chem. **250** (1942) 110.
4. Berry, R. L. and Raynor, G. V. Acta Cryst. **6** (1953) 178.
5. Laves, F. and Löhberg, K. Nachr. Ges. Wiss. Göttingen, Neue Folge **1** (1934) 59.
6. Laves, F. and Witte, H. Metallwirtschaft **15** (1936) 840.
7. Dickins, G. J., Douglas, A. M. G. and Taylor, W. H. J. Iron Steel Inst. **167** (1951) 27.
8. Sully, A. H. J. Inst. Metals **80** (1951) 173.
9. Das, D. K., Rideout, S. P., and Beck, P. A. J. Metals **4** (1952) 1071.
10. Bloom, D. S. and Grant, N. J. J. Metals **5** (1953) 88.
11. Kuo, K. Acta Met. **1** (1953) 301.
12. Bradley, A. J. and Taylor, A. J. Inst. Metals **66** (1940) 53.
13. Levinger, B. W. J. Metals **5** (1953) 196.
14. Duwez, O. and Martens, H. J. Metals **4** (1952) 72.
15. Rostoker, W. J. Metals **5** (1953) 304.
16. Witte, H. Zur Struktur und Materie der Festkörper (Berlin, Springer-Verlag, 1952), p. 272.
17. Lieser, K. H. and Witte, H. Z. Metall. **43** (1952) 396.
18. Duwez, P. J. Amer. Chem. Soc. **73** (1951) 5509.
19. Karlsson, N. Nature **168** (1951) 558.
20. Karlsson, N. Private communication.
21. Goldschmidt, H. J. Research **4** (1951) 343.
22. Putman, J. W., Grant, N. J., and Bloom, D. S. "Symposium on the Nature, Occurrence, and Effects of Sigma Phase" (Baltimore, Amer. Soc. Test. Mat., Special Tech. Pub. No. 110, 1951) p. 61.
23. Beck, P. A. Reference 22, p. 69.
24. Arnfelt, H. and Westgren, A. Jernkont. Ann. **119** (1935) 185.

ORDER-DISORDER IN Cu-Au ALLOYS. I. SHORT-RANGE ORDER IN AN ALLOY CONTAINING 23 ATOMIC PER CENT Au*

C. H. SUTCLIFFE† and F. E. JAUMOT, Jr.‡

Short-range order parameters have been measured by X-ray diffraction methods for a single crystal of a Cu-Au alloy containing 23 atomic per cent Au. Measurements of the diffuse background intensity have been made throughout the reciprocal lattice unit cell and analyzed by means of a three-dimensional Fourier analysis. Short-range order parameters are given for the first ten shells surrounding a given atom for three temperatures above the critical temperature. Interaction energies are computed from a relation given by Cowley. These results are compared with the results previously reported for the alloy Cu_3Au.

LA TRANSFORMATION ORDRE-DÉSORDRE DANS LES ALLIAGES Cu-Au. I. L'ORDRE À PETITE DISTANCE DANS UN ALLIAGE CONTENANT 23 POUR-CENT d'Au EN ATOMES

Les paramètres de l'ordre à petite distance, pour un monocristal d'un alliage Cu-Au contenant 23 pour-cent d'Au en atomes, ont été mesurés au moyen de la diffraction des rayons X. Des mesures de l'intensité du fond diffus ont été faites sur toute l'étendue de la maille du réseau réciproque, et étudiées au moyen d'une analyse de Fourier à trois dimensions. Les paramètres de l'ordre à petite distance sont donnés pour les dix premières couches entourant un atome donné, pour trois températures différentes, au-dessus de la température critique. Des énergies d'interaction sont calculées d'après la relation donnée par Cowley. Ces résultats sont comparés aux résultats rapportés antérieurement pour l'alliage Cu_3Au.

DER ORDNUNGSGRAD IN Cu-Au LEGIERUNGEN. I. NAHEORDNUNG IN EINER LEGIERUNG MIT 23 ATOMPROZENT Au

Die Naheordnungskoeffizienten wurden röntgenographisch an einem Einkristall einer Cu-Au Legierung mit 23 Atomprozent Au gemessen. Die Intensität des diffusen Untergrundes wurde in der gesamten Elementarzelle des reziproken Gitters gemessen und mit Hilfe einer dreidimensionalen Fourieranalyse analysiert. Die Parameter der Naheordnung werden für drei Temperaturen oberhalb der kritischen Temperatur und für die ersten zehn Schalen um ein gegebenes Atom angegeben. Die Wechselwirkungsenergien werden nach einer von Cowley gegebenen Beziehung berechnet. Die Resultate werden mit den früher für Cu_3Au veröffentlichten Ergebnissen verglichen.

Introduction

X-ray measurements of short-range order in the alloy Cu_3Au have been made previously, using powder samples and film techniques [1] and Geiger-counter spectrometer techniques [2]. A recent theory of short-range order [3] predicts that the short-range order parameters defined have maximum values at the 50–50 atomic per cent composition. Thus, considerable interest is attached to measurement of this short-range order parameter for compositions other than the stoichiometric composition. As an integral part of a study of order-disorder in alloys, we have measured the short-range order present at temperatures above the critical temperature, in a single crystal of Cu-Au alloy containing 23 atomic per cent Au.

The Experiment

It has been shown [4] that the X-ray diffuse-scattering due to short-range order can be written as:

$$(1)\quad I_D' = \frac{I_D}{N m_A m_B (F_A - F_B)^2} = \sum_l \sum_m \sum_n \alpha_{lmn} e^{2\pi i (lh_1 + mh_2 + nh_3)}$$

The short-range order parameter is defined by:

$$(2)\qquad \alpha_{lmn} = 1 - P_{lmn}/m_A.$$

Here, P_{lmn} is the probability that an atom with coordinates l, m, n with respect to a B atom is an A atom; m_A and m_B are the fractions of atoms A and B; f_A and f_B are the respective atomic scattering factors; N is the total number of atoms; h_1, h_2, h_3 are continuous coordinates in reciprocal space.

Thus, from equation (1), the corrected short-range order intensity, I_D', can be represented by a three-dimensional Fourier series, and is a periodic function with periods which are double the reciprocal vector lengths. The α_{lmn} are coefficients of the Fourier series and can be evaluated by the usual integration over a unit cell. In practice, instead of an integration, a summation over a large number of points throughout the reciprocal unit cell is considered a satisfactory approximation. Because the unit cell has a center of symmetry in

*Received June 28, 1953.

†Randal Morgan Laboratory of Physics, University of Pennsylvania; present address: The Philco Corporation, Philadelphia, Pennsylvania.

‡Randal Morgan Laboratory of Physics, University of Pennsylvania.

the case under consideration, the exponential may be replaced by a cosine function. Thus we can express the short-range order parameters as:

$$\alpha_{lmn}=K\sum_{h_1}\sum_{h_2}\sum_{h_3} I_D'\cos 2\pi(lh_1+mh_2+nh_3), \tag{3}$$

where K is a normalizing constant given by:

$$\alpha_{0,0,0} = K\sum_{h_1}\sum_{h_2}\sum_{h_3} I_D' = 1.$$

The coefficients, α_{lmn}, provide us with convenient short-range order parameters, as has been discussed in detail by Cowley [2; 3].

A single crystal of Cu-Au, $\frac{1}{2}$ inch in diameter and 1 inch long, containing 23 atomic per cent Au, was grown *in vacuo*, in a Bridgeman-type furnace [5]. The crystal was oriented with a specially designed mount and cut parallel to the (100) plane. Final orientation was made by means of back-reflection Laue patterns. After polishing and etching, the crystal was annealed for 48 hours at 875°C, 24 hours at 600°C, 24 hours at 400°C, 200 hours at 360°C, and 300 hours at 300°C.

The experimental technique used was essentially that described by Cowley [2]. Copper K_α radiation, monochromated by a bent quartz crystal fell on a (100) face of the crystal and the diffracted radiation was measured with a Geiger counter. The divergence of the primary and secondary beams was about 2.3 degrees. The crystal was mounted in a combined furnace and sample mount so that three degrees of freedom in the motion of the crystal permitted scanning through any desired portion of reciprocal space, while the primary and diffracted beams maintained equal angles with the face of the crystal. The nichrome winding of the furnace was immediately behind the crystal, allowing all measurements to be made at temperature. A continuous flow of hydrogen was maintained through the cavity formed by the nickel shield which surrounded the sample.

The diffuse-intensities were measured at 900 points contained within 1/32 of the unit cell, and the entire unit cell built up from these intensities by use of the center of symmetry and the planes of symmetry in the unit cell of a face-centered cubic material. The final result was a cubic net of intensity values containing 8000 points, with cube axes h_1, h_2, and h_3.

In general the observed diffracted intensity contains, in addition to the short-range order diffuse intensity, sharp crystalline reflections due to scattering of the half-wavelength radiation by the quartz monochromator, as well as the normal Bragg reflections, Compton-modified scattering, fluorescence radiation, temperature diffuse scattering, and fluctuations in the background radiation due to a "size-effect."* All but the last three of these were corrected for in the manner described by Cowley [2].

An attempt was made to eliminate air-scattering by placing one $\frac{1}{16}$-inch lead sheet perpendicular to the sample face with its edge less than $\frac{1}{8}$ inch from the sample. Another lead sheet was fixed to the side of the counter-holder nearest the X-ray tube and extended toward the sample. The remaining air-scattering, which was small, was measured by removing the crystal.

In order to correct for the temperature-diffuse scattering, measurements of the scattered intensity were made at temperatures above room temperature (300°C), at room temperature (25°C), and below room temperature (−150°C). These measurements were made at the same points as the actual data except that they were taken at every other position instead of every one. In order to make these measurements as independent of short-range order as possible, the crystal was "ordered" by maintaining it at a temperature of 375°C for 100 hours and then cooling it slowly to approximately 300°C. Then the amount of long-range order was large, but the contribution of the short-range order small. After measurements were completed at the higher temperature, the sample was cooled quickly to room temperature by passing hydrogen, in large quantities, through the furnace so that the short-range order contribution would not be changed appreciably, but the temperature-diffuse scattering would be considerably reduced. Finally, the low temperature was achieved by passing liquid air over the rear of the furnace while simultaneously forcing cold dry nitrogen over the nickel foil shield surrounding the sample to prevent formation of ice. The hydrogen flow through the furnace was kept constant for all measurements. Using these measurements and assuming a linear dependence for the temperature scattering, the effect was extrapolated out.

The distribution of the intensities, I_D', was found to be similar to that reported by Cowley [2]. Figure 1 is a contour plot of the scattering power

*A difference in atomic sizes of the constituent atoms in an alloy has been shown [6] to make an additional contribution to the diffuse scattered radiation. The presence of a "size-effect" can be detected by a difference in the depths of the valleys on either side of a principal reflection (see [6]).

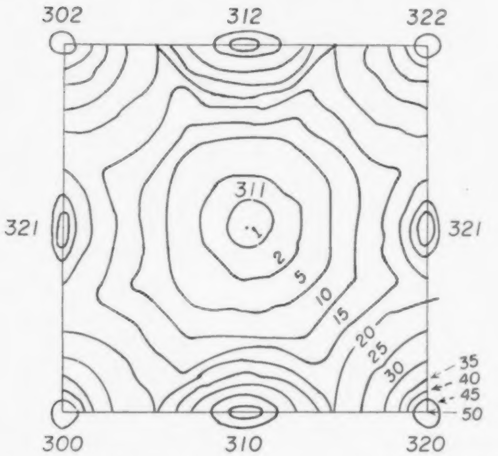

FIGURE 1. Contour plot of the scattering power due to short-range order in the $(3,k,l)$ plane, in arbitrary units.

due to short-range order, in arbitrary units, in a plane bisecting the reciprocal lattice unit cell. The indices given in the figure are the usual indices h, k, l. The disk-like character of the diffuse maxima, previously reported [2], is clearly indicated.

Results

The symmetry of the cosine function in equation (3) was not the same as the symmetry of I_D' throughout the unit cell, but the summation of the product was equal in two halves of the unit cell. Consequently, it was necessary to sum the function only over the 4000 points contained in half the unit cell.

One would expect that the distribution of I_D' would be symmetrical throughout the unit cell with respect to h_1, h_2, h_3. However, it turned out that this symmetry was not realized. That is, values of α_{lmn} for various permutations of the l, m, and n were not equal. This asymmetry probably arose from experimental errors, most probably in the correction for temperature-diffuse scattering. The asymmetry could have been caused by failing to correct for a "size effect," which appeared experimentally to be negligible. If the latter were the case, a weighted average of values of α_{lmn} for various permutations of the l, m, n would correct for it. In any case, such an average would tend to reduce the error, and was made for all α_{lmn}. The absolute differences in the α_{lmn} were small, although for the higher values of l, m, n the percentage differences became as high as 20 per cent.

From the number of experimental intensities available for the calculations, the α could have been obtained for values of l, m, n as high as (7, 7, 7). However, since the relative error becomes quite large for large values of l, m, n and consequently the α become meaningless, the values are being reported only to α_{420}.

Table I gives the values for the α_i for values of i from one to ten, for the three temperatures 404°C, 450°C, and 525°C. Here, i is the number of the shell of atoms surrounding the origin atom. Also included in the table are the coordination numbers c_i, the values of α_i for the case of perfect order, and the coordinates of representative points in the ith shell, referred to half of the length of the face-centered cubic cell as unit distance.

TABLE I

VALUES OF SHORT-RANGE ORDER PARAMETERS FOR THE Cu-Au ALLOY CONTAINING 23 ATOMIC PER CENT Au

				α_i		
i	c_i	Coordinates	Perfect order	404°C	450°C	525°C
1	12	1, 1, 0	−0.299	−0.137	−0.115	−0.104
2	6	2, 0, 0	+0.896	+0.179	+0.118	+0.089
3	24	2, 1, 1	−0.299	−0.019	−0.012	−0.007
4	12	2, 2, 0	+0.896	+0.074	+0.037	+0.022
5	24	3, 1, 0	−0.299	−0.041	−0.023	−0.018
6	8	2, 2, 2	+0.896	+0.036	+0.014	+0.002
7	48	3, 2, 1	−0.299	−0.014	−0.008	−0.006
8	6	4, 0, 0	+0.896	+0.093	+0.070	+0.072
9	12	3, 3, 0	−0.299	−0.020	−0.002	−0.001
	24	4, 1, 1	−0.299	−0.005	−0.000	−0.003
10	24	4, 2, 0	+0.896	+0.039	+0.012	+0.008

Discussion of Results

The short-range order parameters decrease with temperature in all cases, as expected. Also, in general, the tendency is for α to decrease with increasing distance from the origin. Further, in all cases except the 6th and 9th shells at the higher temperature, all have the same sign as for the case of perfect order. The departures from expected behavior will be discussed presently.

The absolute values of the α_i are less for the 23 atomic per cent Au alloy than for the 25 per cent Au alloy [2], as predicted by the theory [3].

Errors in this work are potentially large and somewhat uncertain. Certainly, the major source of error was the corrections for scattering due to factors other than short-range order—in particular, the correction for temperature-diffuse scattering. A rough estimate of the error involved, based partly on the asymmetry of the α_i and on the calculable error in the experimental procedure, leads us to believe that the error in the α_i probably does not exceed 10 per cent for the inner shells,

and possibly 30 per cent for the more distant shells, which have smaller values of α_i.

It was mentioned above that, although the general tendency is for the α to behave as if short-range order were the predominating mechanism, there are deviations from this behavior. For example, α_8 is larger than α_6, and for i odd, α_5 is larger than α_3. Furthermore, while the α_i have, for the most part, the same sign at the experimental temperatures as for perfect order, we have α_6 and α_9 with reversed signs at 525°C. Both types of deviations were explained by Cowley [2] in terms of a "liquid-like" arrangement of atoms about the origin atom. By plotting the radial distribution of atoms in a monatomic liquid on the same plot as the defect of copper atoms in a given shell, he was able to show comparatively good agreement with his experimental data on a 25 per cent Au alloy. The data we obtained for a 23 atomic per cent Au alloy do not show the effect nearly so strongly as Cowley's. This is evident in Figures 2 and 3 where we have

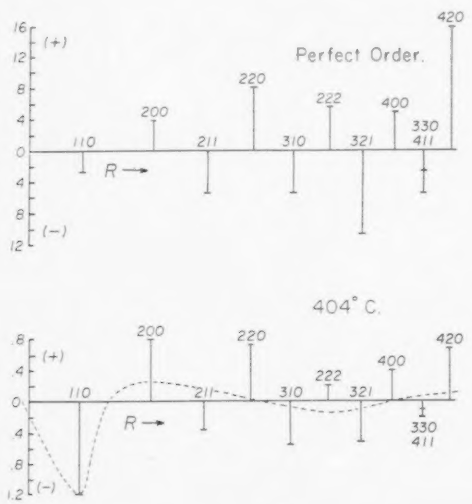

FIGURE 2

plotted the copper atoms in defect in a given shell as a function of the distance from the origin ($D_{Cu} = 0.77\ c_i\alpha_i$). We have also included (dotted curve) the radial distribution function fitted at the first shell. There is some tendency to a "liquid-like" behavior, particularly at the higher temperatures. However, compared with the data on a sample of stoichiometric composition [2], the 23 per cent Au sample shows a tendency toward what one would expect if what might be called "medium-range" order were present.

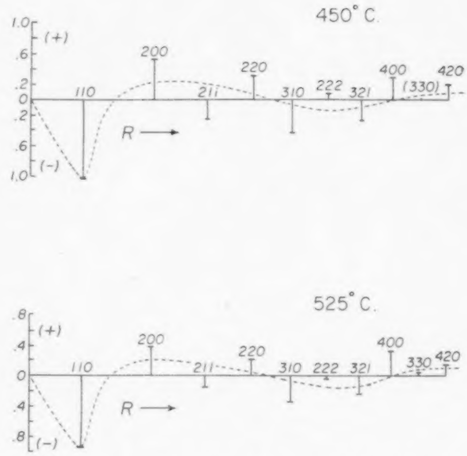

FIGURES 2 and 3. Defect of Cu atoms about an Au atom as a function of distance from the Au atom.

Cowley [3] has related the α_i and the interaction energy, V_{IJ}, between an atom in the Ith shell and one in the Jth shell, through the expression:

$$(4)\quad 2\sum_J V_{IJ}\alpha_J + kT \ln\left\{\left(\frac{m_A}{m_B} + \alpha_i\right)\left(\frac{m_B}{m_A} + \alpha_i\right) \Big/ (1 - \alpha_i)^2\right\} = 0.$$

T is the absolute temperature, k is Boltzmann's constant and the other quantities have been defined above.

Thus, knowing the α_i, the V_{IJ} can be calculated. If we choose a given atom (say a gold atom) as origin atom, we can put $V_{IJ} \rightarrow V_i$, where i is the number of the shell in which the Jth atom appears. The interaction energies have been calculated for the first three shells, assuming that only V_1, V_2, and V_3 are appreciable. The values obtained are $V_1 = 394k$, $V_2 = 43k$, and $V_3 = 65k$, in units of energy per atom.

The value of V_3 should be considered more uncertain than V_1 or V_2, since its magnitude is very sensitive to the values of α_i, and the coefficient of V_3 in equation (4) contains a predominance of α_i with i large, and it is these α_i which probably have the greatest error.

The magnitudes and signs of the V_i are of some interest. In general, a positive sign would indicate a tendency to unlike pairs of atoms and a negative sign would indicate segregation of like atoms

$$\left(V_{IJ} = \frac{V_{AA,IJ} + V_{BB,IJ}}{2} - V_{AB,IJ}\right).$$

However, when one considers shells beyond the first nearest neighbors, the relative values of the

TABLE II

COMPARISON OF THE NUMBER OF Cu ATOMS, AND THE NUMBER OF Cu ATOMS IN DEFECT IN A GIVEN SHELL ABOUT AN Au ATOM

		n_i				Copper atoms in defect			Percentage of perfect order	
i	c_i	Disorder	Perfect order	404°C	525°C	Perfect order	404°C	525°C	404°C	525°C
1	12	9.24	12	10.50	10.20	−2.76	−1.34	−0.96	48.5%	34.8%
2	6	4.62	0.48	3.79	4.21	+4.14	+0.83	+0.41	20.0	9.9
3	24	18.48	24	18.83	18.61	−5.52	−0.35	−0.13	6.3	2.4
4	12	9.24	0.96	8.56	9.04	+8.28	+0.68	+0.20	8.2	2.4
5	24	18.48	24	19.24	18.81	−5.52	−0.76	−0.33	13.8	6
6	8	6.16	0.64	5.94	6.17	+5.52	+0.22	−0.01	4	0

interaction energies of like pairs (V_{AA}, V_{BB}), as well as unlike pairs (V_{AB}), must be considered. Also the variation of the interactions with distance becomes important. Thus, it is not obvious that one should expect a particular sign for V_2 in spite of the fact that a tendency to order leads to the first shell about an Au atom at the origin being Cu-rich, the second Au-rich, and the third Cu-rich. Certainly, one would expect V_1 to be positive and large compared to V_2 and V_3. At the same time, lacking detailed information on the individual interactions, a positive value for V_2 is not unreasonable, nor is the fact that V_3 apparently has a larger magnitude than V_2.

The average number of copper atoms in a given shell about an origin atom can be calculated from $n_i = m_{Cu}c_i(1 - \alpha_i)$. The value of n_i for the first six shells are given in Table II for the cases of disorder, perfect order, 404°C, and 525°C. Also included are the number of copper atoms in defect at perfect order, 404°C, and 525°C. The last two columns, labeled *percentage of perfect order*, are simply the percentage ratios of the copper atoms in defect at the temperatures given, to the defect at perfect order.

It is obvious from the table that there is considerable tendency to short-range order even at the higher temperature. Also, we see evidence of a tendency to a "liquid-like" distribution. That is, shell 3 shows an inconsistently small amount of order, while shell 5 shows an abnormally large amount. Shell 6 at 525°C actually shows the liquid-like tendency to such an extent it exhibits less than zero order, or a negative order. It should be repeated, however, that this tendency is less than that found in a 25 atomic per cent Au sample [2].

For more specific comparison with the results on the 25 per cent alloy, we have reproduced Cowley's data in Table III [2]. Notice in particular that although the difference in magnitudes of the

TABLE III

EXPERIMENTAL VALUES OF SHORT-RANGE ORDER PARAMETERS FOR Cu_3Au AT TEMPERATURES ABOVE THE CRITICAL TEMPERATURE*

i	c_i	Coordinates	Perfect order	405°C	460°C	550°C
1	12	1, 1, 0	−0.333	−0.152	−0.148	−0.131
2	6	2, 0, 0	1.00	0.186	0.172	0.105
3	24	2, 1, 1	−0.333	0.009	0.019	0.026
4	12	2, 2, 0	1.00	0.095	0.068	0.045
5	24	3, 1, 0	−0.333	−0.053	−0.049	−0.032
6	8	2, 2, 2	1.00	0.025	0.007	−0.009
7	48	3, 2, 1	−0.333	−0.016	−0.008	−0.003
8	6	4, 0, 0	1.00	0.048	0.042	0.019
9	{12	3, 3, 0	−0.333	−0.026	−0.022	−0.011
	24	4, 1, 1	−0.333	0.011	0.020	0.007
10	24	4, 2. 0	1.00	0.026	0.025	0.007

*Permission has been obtained from J. M. Cowley to reproduce this table.

α_3 for the 23 and 25 atomic per cent Au samples is not large, there is a change of sign.

From the data in Table III, Cowley [3] computed values of the V_i and found $V_1 = 358k$, $V_2 = -34k$ and $V_3 = -19k$. Although we have relative agreement in magnitude, V_2 and V_3 are of opposite sign from that found in the present work.

Cowley [3] relates the V_i to the critical temperature, T_c, for the stoichiometric alloy through the relation

$$T_c = \frac{3}{2k}\left(V_1 - \tfrac{3}{2}V_2 + 2V_3 - \ldots\right).$$

Using this relation we have calculated T_c using values of the V_i obtained from Cowley's data and the present data. We find $T_c = 284°C$ and 417°C respectively. The experimental value is generally given as 390°C to 396°C. Using a somewhat different formula for T_c for the case of Cu-rich alloys [3], we find for the 23 per cent alloy: $T_c =$

149°C from Cowley's data and 311°C from the present data. The experimental value appears to be approximately 386°C [7].

Acknowledgment

The authors would like to express their appreciation to Professor Foster C. Nix for his interest and advice during the course of this work, which was supported by the Flight Research Laboratory, U.S.A.F.

References

1. Wilchinsky, Z. W. J. Appl. Phys. **15** (1944) 806.
2. Cowley, J. M. J. Appl. Phys. **21** (1950) 24.
3. Cowley, J. M. Phys. Rev. **77** (1950) 669.
4. Norman, W. and Warren, B. E. J. Appl. Phys. **22** (1951) 483.
5. Nix, F. C. Rev. Sci. Inst. **2** (1938) 426.
6. Warren, B. E., Averbach, B. L. and Roberts, B. W. J. Appl. Phys. **22** (1951) 1493.
7. Jaumot, F. E., Jr., and Sutcliffe, C. H. To be published.

ON THE NUCLEAR MAGNETIC RESONANCE IN METALS AND ALLOYS*

N. BLOEMBERGEN and T. J. ROWLAND†

The shift of the nuclear resonance and the line width has been measured in α- and β-tin, thallium, lead and several alloys. While gray tin has no shift relative to the resonance in insulating compounds, white tin has an anisotropic shift of 0.79 per cent along the tetragonal axis and 0.74 per cent perpendicular to it. A theory for the anisotropy and asymmetry of the observed line is given.

Thallium has an anomalously broad resonance line with a shift of 1.54 per cent. In thallium alloys the shift varies continuously with composition in each phase and has discontinuities when phase transitions occur. A maximum shift of 2.1 per cent has been found in a TlMg-alloy, while the NaTl structure exhibits a negative shift of -1.0 per cent.

Quadrupolar effects are important when the nuclear spin $I > \frac{1}{2}$. The intensity of the copper resonance in pure copper can be increased by annealing and decreased by cold work. In alloys like α-brass and copper-silver the intensity decreases rapidly with increasing zinc or silver content. At 25 per cent zinc the copper resonance becomes unobservable. These effects are explained in terms of quadrupole interaction and can give information about the state of order or disorder on an atomic scale in the alloy.

SUR LA RÉSONANCE NUCLÉAIRE MAGNÉTIQUE DANS DES MÉTAUX ET ALLIAGES

Le déplacement de la résonance et l'élargissement des raies ont été mesurés dans l'étain α et β, le thallium, le plomb et dans quelques alliages. L' étain gris n'a pas de déplacement par rapport à la résonance dans des composés isolants, alors que l'étain blanc a un déplacement anisotrope de 0,79 pour cent le long de l'axe tétragonal et de 0,74 pour cent perpendiculairement à cet axe. Une théorie de l'anisotropie et de l'asymétrie de la raie observée est donnée.

Le thallium a une raie de résonance anormalement large et un déplacement de 1,54 pour cent. Dans les alliages de thallium le déplacement varie d'une façon continue avec la composition dans chaque phase et subit des discontinuités aux points de transition entre phases. Un déplacement maximum de 2,1 pour cent fut trouvé dans un alliage Tl-Mg, alors qu'un déplacement négatif de 1,0 pour cent caractérise la structure de NaTl.

Les effets quadrupolaires sont importants quand le "spin" nucléaire $I > 1/2$. L'intensité de la résonance du cuivre pur peut être augmentée par recuit et diminuée par écrouissage. Dans des alliages comme le laiton α et cuivre-argent, l'intensité diminue rapidement quand la teneur en zinc ou en argent augmente. A 25 pour cent de zinc, la résonance devient inobservable. Ces effets sont expliqués en termes d'interaction de quadrupôles et peuvent renseigner sur l'état d'ordre ou désordre dans l'alliage, à l'échelle atomique.

ZUR KERNMAGNETISCHEN RESONANZ IN METALLEN UND LEGIERUNGEN

Die Verschiebung der Kernresonanz und die Linienbreite wurde an α und β Zinn, Thallium, Blei und einigen Legierungen gemessen. Während graues Zinn im Vergleich zur Resonanz von isolierenden Verbindungen keine Verschiebung zeigt, hat weisses Zinn eine anisotrope Verschiebung von 0,79 prozent längs der tetragonalen Achse und 0,74 prozent senkrecht dazu. Es wird eine Theorie der Anisotropie und Asymmetrie der beobachteten Linie entwickelt.

Thallium zeigte eine anomal breite Resonanzlinie und eine Verschiebung von 1.54 prozent. In Thalliumlegierungen ändert sich die Verschiebung kontinuierlich mit der Zusammensetzung in jeder einzelnen Phase, und zeigt Unstätigkeiten wenn Phasenumwandlungen auftreten. Eine maximale Verschiebung von 2,1 prozent wurde in einer Thallium-Magnesium Legierung gefunden, während die NaTl Struktur eine negative Verschiebung von $-1{,}0$ prozent aufweist.

Wenn der Kernspin $I > 1/2$ ist, fallen die Quadropoleffekte stark ins Gewicht. Die Intensität der Kupferresonanz in reinem Kupfer kann durch Glühen verstärkt und durch Kaltbearbeitung vermindert werden. In Legierungen wie α-Messing und Kupfer-Silber nimmt die Intensität mit wachsendem Zink- oder Silbergehalt stark ab. Bei 25 prozent Zink ist die Kupferresonanz nicht mehr zu beobachten. Diese Erscheinungen lassen sich durch Quadropol-Wechselwirkung erklären, und sie ermöglichen Rückschlüsse auf den Ordnungsgrad einer Legierung in atomaren Dimensionen.

1. Introduction

Nuclear magnetic resonance experiments have already yielded some interesting information on the electronic structure and self-diffusion in metals. The three main sources of information from nuclear resonance about the structure of matter are the position of the resonance line, the width and shape and the spin-lattice relaxation time.

It was discovered by Knight [1] that the resonance frequency in metals is higher than for nuclei of the same isotope in an insulating material in the same magnetic field. The effect is caused by the local field produced by the conduction electrons as was first shown by Townes [2]. The internal field produced at the position of the nuclei is much larger than might be anticipated from the electronic paramagnetic susceptibility, because of the partial

*The research was supported jointly by the ONR, Signal Corps and U.S. Air Force.
*Received August 17, 1953.
†Harvard University, Cambridge, Massachusetts.

S-wave character of the wave function. Let the expectation value for an electron with a wave vector **k** near the Fermi level, to be at the nucleus in the metal, be given by

$$(1)\qquad |\psi_{\bar{k}\ \mathrm{met}}(0)|^2 = C_k|\psi_{\mathrm{atom}}(0)|^2$$

Here ψ_{met} is the metallic wave function normalized to unity over one atomic volume V_0, ψ_{atom} (0) is the atomic wave function where the conduction electron is supposed to be in an S-state outside a closed shell. The hyperfine interaction in the free atom in an S-state [3] is given by

$$A\,\mathbf{I}\cdot\mathbf{S}$$

where the hyperfine structure constant is proportional to $|\psi_{\mathrm{atom}}(0)|^2$. In the metal only $2\beta H_0 V_0 N(E_F)$ conduction electrons per atom have unbalanced spins, with magnetic moments parallel to H_0. Here $\beta = \mu_{\mathrm{el}}$ is the Bohr magneton and $N(E_F)$ is the density of states, the number of states per unit volume and per unit energy interval, at the Fermi level. For a free-electron gas

$$V_0 N(E) = \tfrac{3}{4} E_F^{-1}.$$

In the metal the nuclear spin and the electron spin will always be decoupled due to the strong interaction between conduction electrons. For a nuclear spin transition $\Delta M_I = \pm 1$, the interaction energy with the electron spins changes by an amount

$$(2)\qquad \gamma\,\hbar\,\Delta H = h\Delta\nu = \beta H_0 V_0 N(E) CA.$$

Here C is a suitable average of C_k over the Fermi surface, γ is the nuclear gyromagnetic ratio, $\gamma\hbar I = \mu_N$ is the maximum value of the z-component of the nuclear magnetic moment. The relative Knight shift can thus be written in the form

$$(3)\qquad \frac{\Delta H}{H_0} = \frac{\Delta\nu}{\nu_0} = \frac{\beta I}{\mu_N} CA\,V_0 N(E).$$

If $N(E)$ is known from electronic specific heat or magnetic susceptibility measurements, the value of C can be determined experimentally from the observed Knight shift and compared with theoretical values. One would expect the values of C to be of the order of unity, as the metallic wave function near the Fermi level will usually still have a large percentage of S-wave character and the renormalization factor should not change the order of magnitude [4]. The observed values of $\Delta\nu/\nu_0$ are in agreement with the expectation and range from 0.026 per cent for Li to 1.54 per cent for thallium, the largest value reported so far for any element. This is, of course, directly related with the large value of atomic hyperfine splitting for this heavy element.

The relaxation time in metals has been discussed theoretically by Heitler and Teller [5], Korringa [6] and Overhauser [7], and has been studied experimentally by Bloembergen [8], Poulis [9] and Rollin [10]. It is determined by the off-diagonal components of the nuclear spin-electron spin interaction. In the fundamental process these spins flip simultaneously $\Delta m_I = -\Delta m_s = \pm 1$. The balance of energy $\pm\hbar\,(\gamma_{\mathrm{el}} - \gamma_N)H_0$ is taken up by a change in wave number of the conduction electron. Only electrons near the Fermi level can take up such a small amount of energy. The probability for the process is therefore proportional to kT and the complete theoretical expression for the relaxation time T_1 is

$$(4)\qquad \frac{1}{T_1} = \frac{\pi kT}{\hbar} V_0^2 N^2(E) C^2 A^2.$$

From equations (3) and (4) follows Korringa's relation between the line shift and the relaxation time

$$(5)\qquad T_1\left(\frac{\Delta H}{H}\right)^2 = \frac{\hbar}{\pi kT}\left(\frac{\beta I}{\mu_N}\right)^2.$$

The relation equation (5) is only approximately fulfilled. Another term should be added to the right-hand side of equation (4) describing the interaction of the nuclear spin with the nonspherically symmetrical part of the electronic motion. The complete Hamiltonian for the nuclear spin interaction with the conduction electrons is

$$(6)\qquad \mathscr{H} = \frac{8\pi}{3}\beta\gamma_N\hbar\,\mathbf{I}\cdot\mathbf{S}(\mathbf{r})\,\delta(\mathbf{r}) - \beta\gamma_N\hbar\,\mathbf{I}\cdot\left(\frac{\mathbf{S}}{r^3} - \frac{3\mathbf{r}(\mathbf{S}\cdot\mathbf{r})}{r^5}\right) - \gamma_N\hbar\frac{e}{mc}\left(\mathbf{I}\cdot\frac{[\mathbf{r}\times\mathbf{p}]}{r^3}\right) + \frac{e^2Q}{r^3}(3\mathbf{II} - \epsilon\mathbf{I}^2)\cdot(3\mathbf{rr} - \epsilon\mathbf{r}^2).$$

Here $\mathbf{r}$ is the radius vector of the electron with the nucleus at the origin.

The first term is the point interaction discussed before. The second term represents the interaction of the nuclear spin with the electron spin, the third term with the electron orbit, the last term is the quadrupole interaction, not included in Korringa's paper. To find the matrix elements the terms of the Hamiltonian must be integrated over the multi-electron wave function of the metal. In our approxi-

mation we integrate over a one-electron wave function ψ_k and then sum over all wave numbers k. The orbital angular momentum $\mathbf{p}$ in the metal is quenched. There is no preference for a left- or right-handed motion of the electrons, and this interaction will not contribute to the Knight shift in a first approximation. The spin-spin interaction, the second term on the right side of equation (6), will make a contribution in a noncubic crystal. The effect will depend on the angle of the crystalline axes and the external field, and the average for a polycrystalline specimen will be zero. This anistropy of the Knight shift will be discussed in detail in section 5 below. It leads to a spurious broadening and asymmetry of the line in polycrystalline material, which is proportional to the external magnetic field. If the crystal is noncubic and if the nuclear spin $I \geqslant 1$, the last term does not vanish. In polycrystalline material the quadrupole interaction will give rise to a broadening of the line which will be discussed more fully in section 2. Clearly the complete quadrupole interaction also includes the effect of nuclear charges and nonconduction electrons. All these contributions to the inhomogeneous electric field can be lumped together in discussing the line position and broadening.

The contribution of the Hamiltonian equation (6) to the relaxation time has a different character. For the Bloch-type one-electron wave functions $\psi_{\bar{k}}$ and $\psi_{\bar{k}'}$, non-diagonal elements of the type $\mathscr{H}_{\bar{k}\bar{k}'}$ must be squared, averaged over the Fermi distribution and multiplied by the density of final states to obtain the total transition probability. The contribution of the last three terms is now nonvanishing even in cubic crystals, since the individual wave function $\psi_{\bar{k}}$ does not have this symmetry. This result has to be added to the right-hand side of equation (4), and the relaxation time should be shorter than that calculated from equation (5). This has been found generally to be the case [11]. Since only electrons near the tail of the Fermi distribution will be able to take up the small amount of energy of the processes involved, the transition probability will remain proportional to the absolute temperature and independent of the external field, even if the complete Hamiltonian is used. The Korringa relation should be more closely obeyed, the more dominant the S-wave character of the one-electron wave functions near the Fermi level.

The inverse proportionality between T_1 and T has been established rather satisfactorily in a number of cases, although a notable exception is presented by Cesium at high temperatures [11]. There is no confirmation that T_1 is independent of H_0. In fact, a few results by Poulis indicate otherwise. More data on the H_0-dependence of T_1 are desirable. Deviations from the theoretical behavior [equations (4) and (5)] could be attributed to correlation and exchange effects, omitted in the one-electron approximation. It is not clear how the effective density of "one-electron states" could depend very strongly on H or T, even if the interaction between electrons is taken into account.

The experimentally observed shifts ΔH are indeed proportional to H and seem to be independent of T, except for a small and rather trivial volume effect.

The line width is determined by the nuclear dipolar interaction and by the finite life-time T_1 caused by the relaxation mechanism. The second moment of the absorption line due to dipolar interaction in a polycrystalline powder is given by

$$(7)\quad \frac{1}{\gamma^2 T_2^{\,2}} = \left\{(\Delta H^2)_{av}\right\} = \frac{3}{5}\, I\,(I+1)\,\gamma^2 \hbar^2 \sum_j r_{0j}^{-6} + \frac{4}{15}\sum_f I_f(I_f+1)\,\gamma_f^{\,2}\,\hbar^2\, r_{0f}^{-6}.$$

The summation j extends over identical nuclei in the crystal, the summation f includes all different nuclei. Gutowski [11] has shown that in metals at higher temperatures the contribution of the relaxation mechanism to the width amounting to $(\frac{1}{2}T_1)$ is important. In that case the width will increase proportionally with the temperature. The relaxation mechanism will nearly always be the width-determining factor above the melting point. In the liquid state the dipolar interaction of the nuclei has to be averaged over the Brownian motion and is reduced to a very small value. A decrease in the dipolar width has been observed with increasing temperature in the solid metals lithium and sodium, when the self-diffusion becomes sufficiently rapid [11; 12; 13]. This phenomenon is entirely analogous to the motional narrowing occurring in liquids and could be expected to occur in other metals just below the melting point. It gives information about the self-diffusion as a function of temperature when the elementary jumping process of the diffusion has a frequency larger than T_2^{*-1}.

It seems profitable to extend the observations of the shift, width and relaxation time to alloys, in order to gather information about the density of states and electronic structure in these systems. In the next section we shall discuss the importance of quadrupole interaction in alloy systems and the difficulties presented by it.

The equipment consisted of a Pound-Knight-Watkins type of radiofrequency spectrometer [14; 15] and a permanent magnet with a field near 6000 gauss in a $1\frac{1}{4}$-inch gap, the diameter of the pole faces being 4 inches. The field was calibrated by the proton or Li^7 resonance in an aqueous solution of LiCl. The inhomogeneity in the volume occupied by the samples was less than 0.4 gauss, or negligible compared to the width of most resonances described in this paper. The field in the gap was found to vary with temperature, about -1.3 gauss per °C, probably due to the expansion of the magnet yoke. The temperature of the magnet was always recorded and a correction to the magnetic field was applied. A few measurements were made at fields between 2000 and 5500 gauss with an electromagnet. This magnetic field was less homogeneous and drifted with time. Further measurements at other field strengths will be carried out with an improved electromagnet. The frequency of the oscillator was compared with the frequency of a standard frequency meter with an estimated error of less than 100 cps.

The magnetic field was modulated sinusoidally at 280 cps with amplitudes ranging between 0.2 and 20 gauss. To detect the weak broad lines the larger modulation amplitudes are necessary. The frequency of the oscillator was slowly swept through the resonance and its output fed into a phase-sensitive detector with a time constant of 8 sec (effective bandwidth about $\frac{1}{8}$ cps). The derivative of the absorption in the sample as a function of frequency was recorded on an Esterline-Angus recording instrument.

Due care should be taken that the experimentally observed quantities really correspond only to nuclear absorption. This will be true only when the metallic particle size is small compared to the skin depth [16]. If this condition is not fulfilled, part of the observed signal may be due to eddy-current losses and corrections should be applied in order to evaluate the correct line shift and relaxation time. The metallic samples are always used in a finely divided polycrystalline form to increase the effective volume as the radiofrequency field cannot penetrate further than a few skin depths. Although experiments on single crystals would be desirable it would be difficult to make the effective volume of the sample sufficiently large.

The samples were made from powdered metals suspended in mineral oil. Oxygen-free electrolytic copper, thallium, lead, tin (c.p. grade), mercury (triply distilled), and zinc (s.p.) were obtained commercially. Alloys were made by melting weighed ratios of the constituents in an evacuated quartz or glass tube. They were allowed to cool slowly and were held at appropriate annealing temperatures to bring about equilibrium in the phases under consideration. The metals were then filed and sieved through a 200-mesh sieve. The particle size was smaller than the skin depth in all cases, and it could be assumed that the whole weight of the powdered sample contributed equally to the absorption signal. Insulation between the particles was achieved either by a very thin oxide coating or by the oil in which they were suspended. In some instances the powders were annealed in an inert atmosphere. In the oil suspension, particles could even be heated above their melting point without agglomeration. The glass tube containing the suspension was inserted in a shielded radiofrequency coil. The assembly could be inserted in a Dewar flask with a tail of 10 mm inside and 18 mm outside diameter for measurements at 77°K. In another assembly a heater wire was wrapped around the shield of the coil. A thermal insulating layer on the outside made it a miniature oven. The temperature could be raised to 350°C. The modulation coils were outside the Dewar or oven. The coil was connected to the oscillator by a coaxial cable 20 inches long.

2. Quadrupole Effects

When it was attempted to detect the magnetic resonance of the copper isotopes in brass (80% Cu and 20% Zn), the signal was unobservable, although a similar volume of pure copper gave a signal to noise ratio of over one hundred. This rather unexpected result can be explained by considering quadrupole interaction [17]. Although the crystallographic structure of α-brass as determined by X-rays has cubic symmetry, the environment of individual copper nuclei in the solid solution will not have this symmetry. If a few of the nearest neighbors are Zn-atoms the cubic symmetry has certainly disappeared on a submicroscopic scale. There may then exist gradients of the electric field which will vary in direction and magnitude at the position of the various copper nuclei. If a copper atom happens to have twelve other copper atoms as nearest neighbors, there may still be a deviation from cubic symmetry arising from Zn atoms among the next nearest or further neighbors, although in this case the magnitude of the gradient can be expected to be smaller. Even in pure copper a certain inhomogeneity of the internal electric field will exist due to strains around dislocations or other imperfections in the

lattice. It has been shown by Pound and Watkins [15; 18] that these strains in single crystals of the alkali halides are sufficient to wipe out the satellite transitions, i.e., the resonance of bromine and iodine nuclei in KBr and KI crystals is due solely to transitions between the levels with $m_I = \frac{1}{2}$ and $m_I = -\frac{1}{2}$. The reason is that the energy difference between these two levels is unaffected by the quadrupole interaction as the first-order approximation quite generally depends on m_I^2 only. There is a first-order perturbation of the other energy differences, and these transitions are spread out over such a large frequency interval as to become unobservable. It is possible that in pure and well-annealed metals the quadrupole broadening is considerably less and that the satellite transitions also contribute to the signal. Evidence for this will be presented below. It is true that the metals will have at least the same density of dislocations as the alkali halide crystals. But the electron orbits in the metal ions are probably deformed less under the influence of strains than of the Br^- and I^- ions. Furthermore, the quadrupole moments of the Cu isotopes are a factor 2 smaller than that of Br^{79}. Finally, the effect of strains in metals on the electric field gradient at a nucleus a few interatomic distances away will be smaller because atoms are displaced rather than positive or negative ions carrying a net charge.

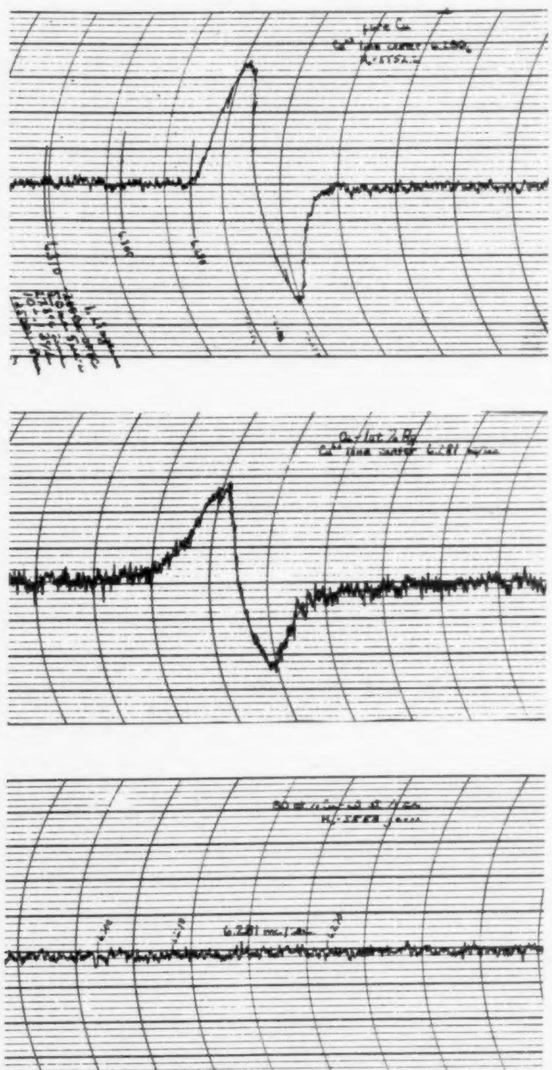

FIGURE 1. A recording of the derivative of the absorption of the Cu^{63} resonance at room temperature in Upper: Pure annealed copper. Middle: 99% Cu and 1% Ag. Note the appearance of weak tails, absent in pure copper. Lower: 80% Cu – 20% Zn. An extremely weak resonance with an intensity less than 1% of that in pure copper has been observed at 77°K in this alloy.

The disappearance of the resonance line in alloys with a spin $I = \frac{3}{2}, \frac{5}{2}$, etc., will then occur in two steps. At first the quadrupole interaction will wipe out all transitions except the $m = \frac{1}{2} \rightarrow -\frac{1}{2}$ transition by a first-order perturbation process. We shall write down the formulas for the case of axial symmetry of the inhomogeneous field. This will be correct if one solute atom is in particular responsible for the field. For somewhat higher solute concentrations in the solid solutions it is by no means correct. Nevertheless, the right order of magnitude of the line displacement and broadening will be obtained in this case. Let θ be the angle between the external magnetic field and the axial electric field. The first-order quadrupole perturbation gives for the frequency of the transition

$$(8)\quad \Delta W_{m\rightarrow m-1} = h\nu_0 - (2m-1)(1-3\cos^2\theta)\frac{3e^2qQ}{8I(2I-1)}.$$

It is seen that the frequency of the transition $m = \frac{1}{2} \rightarrow -\frac{1}{2}$ is not changed in this approximation. The satellite lines are broadened since all angles θ will occur in the polycrystalline sample. Summing over all angles we find that each satellite line has a second moment in a polycrystalline powder

$$(9)\qquad \overline{(\Delta\nu)^2} = (2m-1)^2\frac{9}{64}\frac{e^4q^2Q^2}{I^2(2I-1)^2h^2}\frac{4}{5}.$$

On the average these lines are not displaced since $\langle 1 - 3\cos^2\theta\rangle_{av} = 0$. The line shape is quite characteristic and has been described in other papers. Often the broadening, of which equation (9) gives

the magnitude, will make the lines unobservable. The transition $m = \frac{1}{2} \rightarrow -\frac{1}{2}$ will only be broadened in a second approximation according to the equation

$$\text{(10)} \quad \Delta W_{\frac{1}{2}\rightarrow-\frac{1}{2}} = h\nu_0 + A(1 - 9\cos^2\theta)(1 - \cos^2\theta)$$

$$\text{(11)} \quad A = \frac{9}{64}\,\frac{2I+3}{4I^2(2I-1)}\,\frac{e^4Q^2q^2}{h\nu_0}$$

The center of gravity of the line will be displaced toward lower frequencies by an amount

$$\text{(12)} \quad \overline{\delta\nu} = Ah^{-1}\int_0^{\pi/2}(1 - 9\cos^2\theta)(1 - \cos^2\theta)\sin\theta\, d\theta = -\frac{8}{15}Ah^{-1}$$

while the second moment of line averaged over all angles is

$$\text{(13)} \quad \overline{\left(\delta\nu + \frac{A}{h}\,\frac{8}{15}\right)^2} = 0.93\,A^2h^{-2}.$$

The experiment in brass (20% Zn) was carried out at a frequency $\nu_0 = 6.3$ Mc/s. The line should have been at least 50 kc wide in order to escape observation. This enables us to calculate a lower limit for q or grad E in the alloy. Substituting the values [19] $Q^{63} = -0.157 \times 10^{-24}\text{cm}^2$ (or $Q^{65} = -0.145 \times 10^{-24}\text{cm}^2$) and $\Delta\nu = 50$ kc in equation (9), we find that

$$\frac{e^2Qq}{h} > 0.17 \times 10^6\text{cps}$$

is necessary for the satellites to disappear. A more stringent requirement is obtained from equation (13). The condition that the line $m = \frac{1}{2} \rightarrow -\frac{1}{2}$ disappear gives

$$\frac{e^2Qq}{h} > 2.6 \times 10^6\text{cps}$$

or

$$q = 4.8 \times 10^{23}\text{cm}^{-3}$$

The simplest picture one can form about the origin of the internal electric field is that the Zn atoms have a different charge. The bivalent Zn atoms will produce one extra positive electronic charge at their lattice sites compared to the monovalent Cu-atoms. The electrons around the Zn atom are redistributed —either by the formation of a bound state or a distribution of conduction electrons—to produce a screened Coulomb potential of the form [20; 21]

$$\text{(14)} \quad V = \frac{e}{r}e^{-Kr}$$

where a reasonable value for K is 10^8 cm^{-1}. Differentiating this expression twice, we obtain for the gradient

$$\text{(15)} \quad eq = \frac{\partial E_r}{\partial r} = \frac{2e}{r^3}e^{-Kr}(1 + Kr + \tfrac{1}{2}K^2r^2)$$

One Zn atom would produce a gradient at the nearest Cu atom ($r = 2.55 \times 10^{-8}$cm) of $q = 6.4 \times 10^{22}$ cm^{-3}. This is much smaller than the experimental limiting value. The effect should, moreover, depend strongly on the effective valency of the alloying agent. Actually, it is observed that silver produces at least as large a quadrupole broadening as zinc. Although Huang [22] has shown that considerable polarization effects may occur even if the solvent and solute atom have the same valency, a description in terms of distorted electron orbitals is more appropriate, as will be discussed below.

It is of interest to investigate how the apparent line intensity decreases as the concentration of Zn or Ag increases. In Figure 2 the maximum absorption, corrected for the effective number of copper nuclei in the sample, is plotted as a function of the solute concentration C.

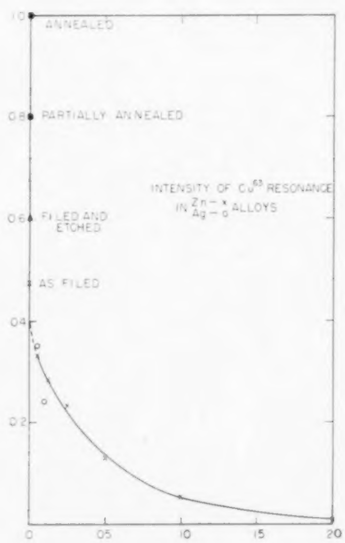

FIGURE 2. The intensity of the Cu^{63} magnetic resonance in annealed and cold worked copper and in alloys with zinc and silver. By cold work the contribution of the transitions $m_I = \frac{3}{2} \rightarrow \frac{1}{2}$ $m_I = -\frac{1}{2} \rightarrow -\frac{3}{2}$ is washed out. Annealing restores the total intensity of the nuclear resonance.

In pure copper samples the intensity varies between 0.4 and 1.0. The unit intensity was assigned to a well-annealed pure electrolytic copper sample. Cold worked copper filings then had an intensity between 0.4 and 0.5 with respect to this reference point. The intensity could be increased by a factor

of nearly two when the cold worked powder was annealed. The strains connected with dislocations in the worked material produce electric field gradients which wipe out the transitions $m_I = \frac{3}{2} \rightarrow \frac{1}{2}$ and $m_I = -\frac{1}{2} \rightarrow -\frac{3}{2}$ by first-order quadrupole perturbation. The intensity ratio of these satellites to the central line $m = \frac{1}{2} \rightarrow -\frac{1}{2}$ is 3: 4: 3. The remaining intensity of 0.4 is thus ascribed to the $m_I = \frac{1}{2} \rightarrow -\frac{1}{2}$ transition.

In the cold-worked powdered alloys the intensity then decreases further by second-order quadrupole perturbation of the central line. However, the line does not broaden gradually nor does it show a shift toward lower frequencies, as could be expected from equations (12) and (13). Only a vestige of a broadened tail is apparent in the recording for a Cu-Ag alloy. We assume, therefore, that the electric field gradient is very large and makes the line unobservable, when a Zn or Ag atom is very close to a copper atom, but is rather small and does not affect the central line, when the Zn or Ag atoms are further away. Let the Zn atom in n neighboring positions around a copper nucleus make its resonance unobservable, and let the effect of the Zn atom be zero, if it is not in one of these n positions. We calculate the probability that a copper atom has no Zn atom in its n neighboring lattice sites. If the relative concentration of the solute is C, each lattice site in the random solid solution of α-brass has a probability $1 - C$ to be occupied by a Cu atom. The desired probability is therefore $(1 - C)^n$. In this case the copper atom is surrounded only by copper atoms. The immediate neighborhood has cubic symmetry and the copper nucleus will contribute to the resonance signal. There are of course a few other configurations with cubic symmetry (e.g. all neighbors are Zn atoms) but for low Zn concentrations these have a much smaller probability and need not be considered here. We therefore find for the apparent intensity

$$\ln \mathscr{I} = n \ln (1 - C).$$

In Figure 3 we have plotted $\mathscr{I}$ versus the composition on a double logarithmic scale. It is seen that the experimental points fall surprisingly well on a straight line. Its slope determines $n = 18$. If this number came out much larger our theory would be incorrect as the underlying assumption was that only relatively few neighbors produce an appreciable gradient. The face-centered cubic lattice of copper has 12 nearest neighbors at a distance of 2.55 Å and six next nearest neighbors at a distance 3.61 Å. The number of these positions agrees well with the experimental value. The quadrupole interaction in one of these 18 positions should then be at least 2.6×10^6 cps as derived from equation (13). This corresponds to an asymmetry in the wave function around the Cu atom equivalent to 4 per cent of an atomic $3d^9\,4s^2\,{}^2D_{3/2}$ state or 20 per cent of the atomic

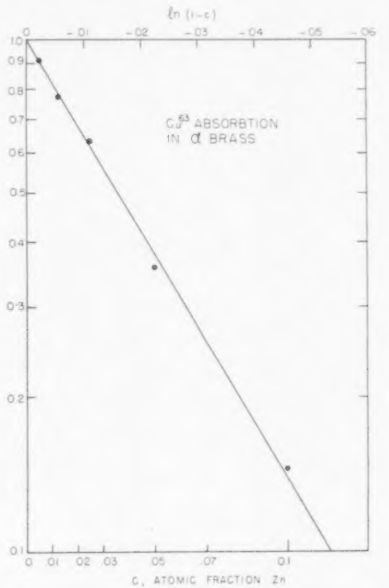

FIGURE 3. A doubly logarithmic plot of the intensity of the central transition line $m_I = \frac{1}{2} \rightarrow -\frac{1}{2}$ of Cu^{63} versus zinc concentration C in α-brass. The intensity is normalized to unity for no zinc content. The drawn line $(1 - C)^n$ has a slope corresponding to $n = 18$ with surprisingly good precision. This can be considered as a proof that a Zn atom shares an unsaturated covalent bond with the twelve nearest and six next nearest copper atoms only.

$3d^{10}\,4p\,{}^2P_{3/2}$ state [23]. In the case of a neighboring silver atom such a distortion is probably not unreasonable. In the case of a neighboring Zn atom the extra electron may be shared by the surrounding copper atoms, each taking part with an unsaturated covalent bond [24]. An excess of a 20% $4p$ bond in the direction of the Zn atom may not be unreasonable. Townes and Dailey [25] have shown that covalent bonding can satisfactorily describe quadrupole coupling in molecules. We leave the question open of what description of distorted orbits will be most appropriate for the metals. Orbital distortion, however, seems to be the dominant origin for quadrupole effects even in alkali halide crystals, strained by the presence of dislocations. Watkins has shown that a calculation based on a distribution of point charges deviating from cubic symmetry does not give the correct answer. A phenomenological multiplication factor β, larger than unity, has to

be introduced to obtain results in agreement with the experimental quadrupole coupling.

It can be expected that the shells of the alkali ions will be much less susceptible to deformation than the shells of the transition elements or heavier elements on the right-hand side of the periodic system. In general, the quadrupole interaction provides a serious handicap in the investigation of alloy systems with nuclear spin $I > \frac{1}{2}$. The line broadening may, however, not be prohibitive for isotopes with small values of the quadrupole interaction like Li^6 and Li^7. In Li-systems the quadrupole effect could perhaps be studied in detail as the resonance lines may not disappear. The intensity of the nuclear resonance in alloys, if $I > \frac{1}{2}$, gives information about the amount of order in the immediate neighborhood around nuclei with spin $I > \frac{1}{2}$. Tendencies of solute atoms to stay away from each other, the first stages of precipitation and deviations from perfect solid solution or perfect order could be studied in this fashion.

In ordered structures with cubic symmetry the quadrupole broadening should be absent. Attempts to detect the resonance in β-brass near the 50%–50% composition have failed, presumably because the ordering is not complete. Also liquid structures should be accessible to investigation as in this case the quadrupole interaction has to be averaged over the rapidly changing configurations and effectively cancels, although there will remain a contribution to the relaxation process. A small quadrupole contribution to the relaxation process is possibly responsible for the fact that the relaxation times for the pairs of isotopes Ga^{69}–Ga^{71} and Rb^{85}–Rb^{87} have a somewhat smaller ratio than the inverse ratio of the squares of the gyromagnetic ratios for these isotopes [11]. It so happens that the isotope with the smaller magnetic moment has the larger quadrupole moment in both cases. For gallium we have

$$\frac{T_1^{69}}{T_1^{71}} = 1.25, \quad \left(\frac{\mu^{71}}{\mu^{69}}\right)^2 = 1.61, \quad \left(\frac{Q^{71}}{Q^{69}}\right)^2 = 0.4.$$

The experimental result is explained if the quadrupole interaction contributes 9% to the relaxation mechanism for Ga^{71} and consequently 35% for Ga^{69}. Since the two rubidium isotopes have different total spin, the comparison is not so straightforward, and detailed investigation of transitions between the various m-levels would have to be made, not warranted by the experimental uncertainties.

The use of isotopes with spin $I = \frac{1}{2}$, however, avoids all complications of the quadrupole effect. The fact that the intensity of the resonance is not drastically reduced, as in the case of thallium alloys as discussed in a later paragraph, provides perhaps the most convincing proof of the assumption of quadrupole interaction in brass.

3. Nuclear Resonance in Tin, Thallium and Lead

During the first attempts no resonance was found in metallic thallium. If the line width were determined by nuclear dipolar interaction the second moment of the line equation (7) would be 4.6 kc/s, and the resonance easily observable. The hypothesis was made that the spin-lattice relaxation time would be extremely short and the line correspondingly broader, on account of the very large hyperfine splitting in this element. A broad resonance of 33 kc/s between points of maximum slope (equivalent to 14 gauss) was then found at liquid-air temperature. Subsequent investigations showed that the line width was independent of temperature in the range from 77°K–400°K. This seems to rule out the relaxation mechanism as the line broadening agent. If the conduction electrons are responsible for the relaxation, the line width should be proportional to the absolute temperature. For a Raman scattering process of vibrational lattice phonons a T^2-dependence would be expected.

It has been suggested by Gutowski [12] that an anisotropy of the Knight shift could be responsible for the width in metals. It will be shown in the next paragraph that the anisotropy, which would have to be about 20% in this case, produces an asymmetrical line with a width proportional to the resonance frequency. Experiments in external fields ranging from 2000 to 6200 gauss revealed no change in the width. Furthermore, the line should become narrow in the cubic phase of thallium, which is stable above 232°C. No resonance was observable above 150°C. If the line had the dipolar width of 4.6 kc/s, it would have been observed. Even more striking is the failure to detect the resonance in the liquid phase, the melting point being at 302°C.

Although the width makes the determination of the line position somewhat inaccurate, the relative Knight shift is so large that it can be measured with fair precision. Figure 4 shows a record of line derivatives of the Tl^{203} and Tl^{205} resonance in fields of 3000 gauss and 5600 gauss respectively. These resonances were compared with the narrow lines in a saturated aqueous solution of thallium acetate. To what extent these lines can really serve as standards is open to criticism in view of the concentration-dependent chemical shift occurring in solutions of thallium salts [26]. For Tl^{205} a Knight shift $\Delta\nu/\nu_0 = 1.54\% \pm .05\%$ has been found, the

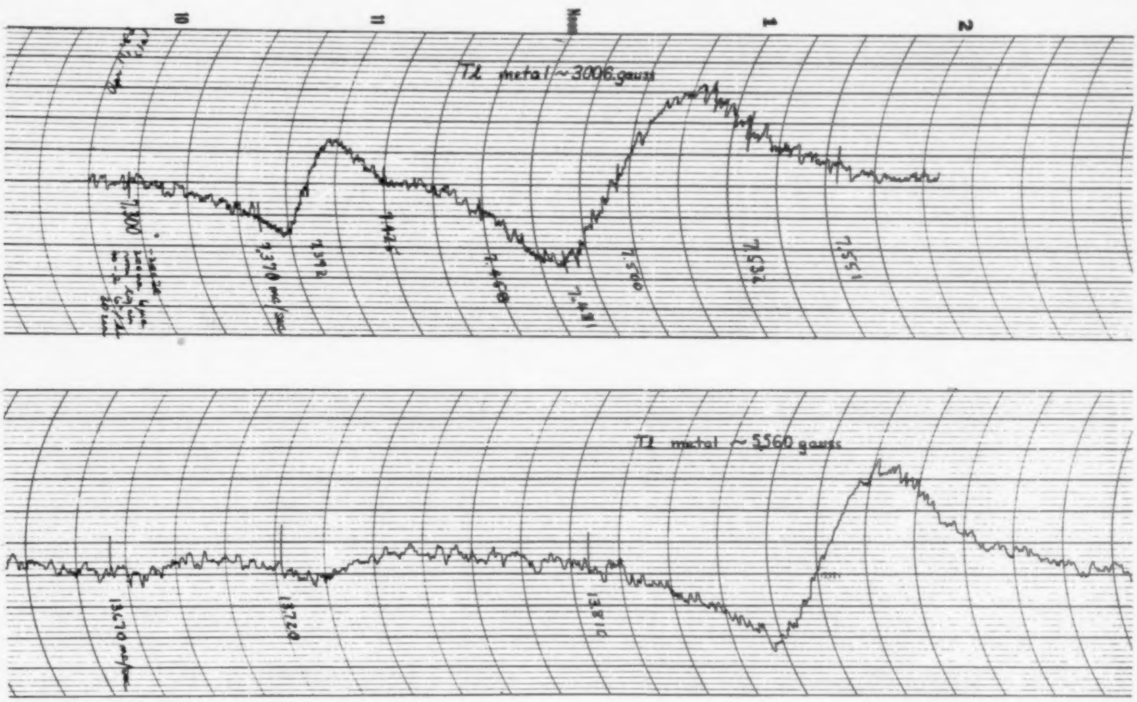

FIGURE 4. The derivatives of the magnetic absorption in metallic thallium lower curve at 5560 gauss; upper curve at 3006 gauss. The peak at the high-frequency side belongs tothe Tl^{205} isotope (relative abundance 70%). The anomalous behavior of the Tl^{203} isotope (relative abundance 30%), which has a magnetic moment only 1.0% smaller than Tl^{205}, remains unexplained.

largest so far reported for an element. The behavior of the Tl^{203} resonance is baffling. In going from 2000 to 6000 oersted, the Knight shift changes from 1 to 1.5 per cent, the width changes from 17 kc/s, to 33 kc/s, and the intensity decreases by a factor three. No such anomalies are observed for the Tl^{205} resonance.

The two isotopes have magnetic moments differing only by one per cent and it is not clear how they could behave so differently, if our interpretation of the recordings is at all correct. The preliminary experimental data are mentioned here only for the sake of completeness. Some numerical values are compiled in Table I.

For Pb^{207} in metallic lead a Knight shift of 1.24% ± 0.04% has been found. A preliminary value was previously reported by Knight.

The Knight shifts for the resonances of Sn^{117} and Sn^{119} in white tin are 0.74 per cent and 0.72 per cent, which can be considered equal within the experimental error. No values for tin and thallium had been reported previously, a fact undoubtedly due to the unexpected broadness of the lines.

The resonances of Sn^{117} and Sn^{119} in grey tin reveal no Knight shift. It has been shown that the diamond structure of grey tin is semiconducting.

TABLE I

Sample	Isotope	External field strength (Gauss)	Resonance freq. Mc/s	% Knight shift*	Line width (kc/s) obs†	Line width (kc/s) calc‡
β-Sn	Sn^{119}	6102	9.761	0.79 ∥		
	Sn^{117}	6102	9.323	0.77 ∥		
	Sn^{119}	6102	9.756	0.74 ⊥	3–5	.71
	Sn^{117}	6102	9.319	0.72 ⊥	3–5	
α-Sn	Sn^{119}	6100.2	9.6786	0.00	5	.75
	Sn^{117}	6100.2	9.245	0.00	5	
Tl	Tl^{205}	1993	4.968	1.43±.10	30±3	4.6
		3007	7.500	1.50	34±2	
		3665	9.140	1.54	33	
		4890	12.200	1.61	33	
		5563	13.876	1.55	33	
		6108	15.238	1.53	33	
		6495	16.231	1.70	33	
	Tl^{203}	1993	4.899	.99	17	3.9
		3050	7.500	1.04	22	
		3720	9.140	1.0±.1	28	
		4960	12.200	1.07	35±5	
		5563	13.686	1.11	31	
		6490	16.007	1.33	33	
Pb	Pb^{207}	5553.4	5.0026	1.24	<2	.28

*∥, H_0 parallel to tetragonal axis; ⊥, H_0 perpendicular to tetragonal axis.
†Between points of maximum slope.
‡Second moment.

The conduction electrons contribute little or nothing to the magnetic susceptibility in this α-phase, $\chi_{\alpha-\mathrm{Sn}} = -0.025 \times 10^{-6}$ and $\chi_{\beta-\mathrm{Sn}} = +0.025 \times 10^{-6}$ c.g.s. units per gram. The contribution to the Knight shift is correspondingly negligible in α-Sn. The number of electrons and holes with unbalanced spin is very small, and furthermore the wave function has predominantly p-character near the top of the valence band and the bottom of the conduction band in the diamond structure. The intensity of the lines for the two isotopes in both modifications is about equal, in agreement with their abundance ratio of 1.08. The lines in α-Sn have a normal shape, but the width is about six times as large as the dipolar broadening. This can clearly not be blamed on the conduction electrons in this semiconducting material.

In the β-modification, however, both resonances have a marked asymmetry. This may be understood as the anisotropy of the Knight shift in the markedly tetragonal white tin structure. A striking confirmation for the correctness of this hypothesis would be to check the proportionality of this asymmetric broadening with the external field. The integrated line, assuming that the recording in Figure 5 gives the derivative, is sketched in Figure 6. This line

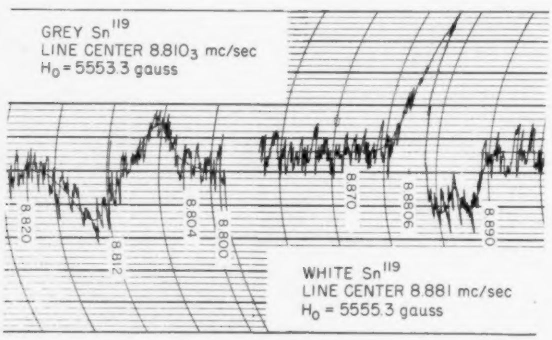

FIGURE 5. The derivative of the absorption of Sn^{119} in grey tin (diamond cubic) and white tin (tetragonal). The latter curve shows a pronounced asymmetry.

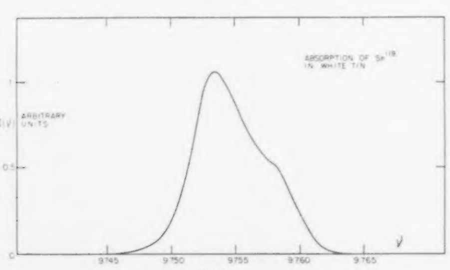

FIGURE 6. The integrated line shape in tetragonal tin, derived from the recording in Fig. 5.

will be interpreted in the next paragraph. The result is that the figures quoted for the Knight shift above are valid, if the field is perpendicular to the tetragonal axis. For fields parallel to the axis the Knight shifts are 0.79 and 0.77 per cent or 7 per cent higher.

4. Anisotropy of the Knight Shift

The first term in the Hamiltonian equation (6) does not depend on the direction of the external field. The second term produces a shift of the nuclear resonance which depends on the orientation of the external field H_0 with respect to the crystallographic axes. It vanishes only for cubic symmetry. The third term in equation (6) can be neglected as the orbital momentum is frozen in. In the first-order perturbation calculation we are only interested in elements diagonal in the nuclear and electron spin. If we denote the angle between H_0 and the radius vector between electron and nucleus by α we retain only the following part of the Hamiltonian

$$(16) \quad \mathscr{H}_{\mathrm{anis}} = \mp \gamma_N \hbar \; \beta m_I (1 - 3\cos^2\alpha) r^{-3}.$$

The $-$ or $+$ sign depends on whether the electron moment is parallel or antiparallel to H_0 respectively. To calculate the shift we determine the energy difference due to equation (16) between two nuclear spin orientations for which $\Delta m_I = 1$. We have to integrate equation (16) over the electron wave function ψ_k and then sum over all states k, taking the contributions of electrons of opposite spin with opposite sign. Per unit volume only $2\beta H_0 N(E_F)$ electrons near the Fermi level with unbalanced spin will therefore contribute. If V_0 is the atomic volume we find for the energy difference

$$(17) \quad \Delta W = \gamma_N \hbar \, \beta 2\beta H_0 V_0 N(E_F) \left\langle \int \psi_k^* \, (3\cos^2\alpha_k - 1) r_k^{-3} \, \psi_k \right\rangle$$

Average over Fermi surface

If we introduce an average wave function ψ, so that $\psi^*\psi$ represents the average electron density in space of the conduction electrons near the Fermi level, we find from equation (17) for the relative Knight shift

$$(18) \quad \frac{\Delta H_{\mathrm{anis}}}{H_0} \, 2\beta^2 V_0 N(E_F) \int \psi^* (3\cos^2\alpha - 1) r^{-3} \psi \, dx\,dy\,dz.$$

the field H_0 makes the polar angles θ and ϕ with respect to the x,y,z-coordinate system. The radius vector $\mathbf{r}$ has polar angles Θ and Φ. We can now express $(1 - 3\cos^2\alpha)$ by means of a well-known

addition theorem in terms of tesseral harmonics in the angles θ and ψ and Θ and Φ respectively.

$$(19)\quad \tfrac{1}{2}(3\cos^2\alpha - 1) = \sum_{m=-2}^{2} (-1)^m P_2^m(\cos\Theta)\, P_2^{-m}(\cos\theta)\, e^{im(\Phi-\phi)}$$

We shall first discuss the case of axial symmetry. It is probably a good approximation to assume that ψ consists of a mixture of p-type wave functions of the form

$$\psi_0,\ \frac{1}{\sqrt{2}}(\psi_{+1} + \psi_{-1}) \text{ and } \frac{1}{\sqrt{2}}(\psi_{+1} - \psi_{-1}).$$

These wave functions are real and represent the quenching of the p-orbits by the crystalline field. In the case of axial symmetry the electron density can then be written as

$$(20)\quad \psi\psi^* = g(r)\{A(x^2+y^2) + Cz^2\} = r^2 g(r)[A + (C-A)\cos^2\Theta]$$

Here $g(r)$ is a radial function, whose form is unimportant for our purposes. Clearly equation (20) could be extended to higher-order terms with axial symmetry, and the following integrations could easily be carried through, if d — or higher orbital states were included. Substituting equations (19) and (20) into (18) we find after carrying out the integration over Φ, that only the term with $m = 0$ in equation (19) contributes, and obtain

$$(21)\quad \frac{\Delta\nu_{\text{anis}}}{\nu_0} = \frac{\Delta H_{\text{anis}}}{H_0} = \beta^2 V_0 N(E_F)\, q(3\cos^2\theta - 1)$$

where

$$(22)\quad q = \int \psi(3\cos^2\Theta - 1)r^{-3}\psi\, dV = \frac{16\pi}{15}(C-A)\int_0^\infty r g(r)\, dr$$

is the quadrupole moment of the electrons near the Fermi level. The interaction with a nuclear quadrupole moment would involve a different quantity q^1, in which the charges of all electrons and nuclei are involved and not just the charges of the conduction electrons near the Fermi level.

The shift equation (21), which averages to zero for a polycrystalline material, is, of course, superimposed on the isotropic shift $\Delta\nu_{\text{is}}$ given by equation (3).

It is to be noted that the angular dependence of equation (21) is the same, as could be inferred in a purely phenomenological way, if one assumes that a linear tensor relation exists between the internal field $\Delta\mathbf{H}$ and the external field H_0. Since in first-order approximation only the component of $\Delta\mathbf{H}$ parallel to H_0 will alter the resonance frequency we can write down immediately

$$(23)\quad \Delta\nu = \Delta\nu_\parallel \cos^2\theta + \Delta\nu_\perp \sin^2\theta$$

The phenomenological quantities $\Delta\nu_\parallel$ and $\Delta\nu_\perp$ can be identified as

$$\Delta\nu_\parallel = \Delta\nu_{\text{is}} + 2\beta^2 V_0 N(E_F) q\nu_0$$
$$\Delta\nu_\perp = \Delta\nu_{\text{is}} - \beta^2 V_0 N(E_F) q\nu_0$$

The number of nuclei in the powdered specimen, for which the magnetic field makes an angle θ with the crystallographic z-axis is, of course, proportional to $\sin\theta$. This distribution over angles must be transformed into a distribution function over resonance frequencies. The straight-forward procedure is the same as used, e.g., by Pake [27] for the shape of the resonance of the two-proton systems in powders. Using equation (23) we find for the line intensity

$$\mathscr{I}(\nu) \propto \sin\theta\left(\frac{d\nu}{d\theta}\right)^{-1} \propto (\nu - \nu_0 - \Delta\nu_\perp)^{-\frac{1}{2}} \quad \text{if } \Delta\nu_\parallel > \nu - \nu_0 > \Delta\nu_\perp$$

or

$$\mathscr{I}(\nu) \propto (\Delta\nu_\perp + \nu_0 - \nu)^{-\frac{1}{2}} \text{ if } \Delta\nu_\perp > \nu - \nu_0 > \Delta\nu_\parallel$$

$$(24)\quad \mathscr{I}(\nu) = 0 \text{ outside this interval.}$$

The line shape $\mathscr{I}(\nu)$ is given by the dotted line in Figure 7 for the case $\Delta\nu_\parallel > \Delta\nu_\perp$, corresponding to a positive value of q. Dipolar broadening and finite life-time will change the distribution to one indicated by the solid line. This is in excellent agreement with

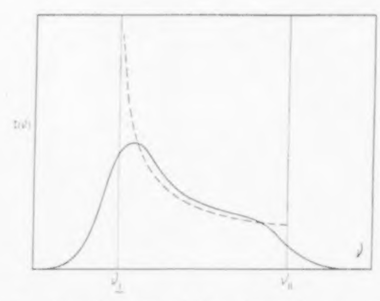

FIGURE 7. The theoretical line shape in a polycrystalline powder due to the anisotropy of the Knight shift in an axially symmetric conductor (dotted curve). The drawn curve gives the experimental line shape, if dipolar interaction and other causes of symmetric line broadening are superimposed.

the line shape observed in tetragonal tin. We conclude therefore that q is positive. The dominant contribution to the gradient of the electric field at the nucleus comes from electrons along the tetragonal axis. This agrees with the crystal structure [28] where the four nearest neighbors form a tetrahedron, squashed in the direction of the tetragonal axis, while the two next nearest neighbors are in the direction of the tetragonal axis. If one assumes a uniform charge distribution around each nucleus, it is elongated along the tetragonal axis. The experiment gives for the anisotropy

$$\frac{\Delta\nu_{\parallel} - \Delta\nu_{\perp}}{\nu_0} = 0.05\%$$

We calculate $N(E_F)$ from the electronic specific heat data [21; 29] with the result that $V_0\, N(E_F) = 0.19 \times 10^{12}\ \text{erg}^{-1}$. Substituting these values into equation (23), we obtain $q = +\,8.8 \times 10^{24}\text{cm}^{-3}$. The relative anisotropy of the shift $(\Delta\nu_{\parallel} - \Delta\nu_{\perp})/\Delta\nu_{\text{is}}$ amounts to 7 per cent. This should be considered as large. The p-character of the wave function must be appreciable. The hyperfine interaction in the p-state is smaller than in the s-state, and furthermore we detect only the anisotropy in the p-wave functions. The total amount of p-character should well exceed 50 per cent near the Fermi level in white tin.

In hexagonal structures where the nearest neighbors have a nearly cubic arrangement, much smaller anisotropies should be expected, and in fact no other asymmetric lines have been reported. The asymmetry should become more pronounced in higher fields. The problem treated here is somewhat similar to the dipolar interaction in solid hydrogen treated by Reif [30]. For the proton spin pair a symmetric line always results because the spin of the proton has equal probability for parallel or antiparallel orientation. In our problem of the nuclear spin-electron spin pair interaction, we have to take the average value of the electron spin moment, as the motion of the electrons is much more rapid than the nuclear precession frequency. The net moment is always oriented parallel to H_0. This leads to an asymmetric broadening, proportional to the value of H_0. These two features enable us to distinguish the anisotropic Knight shift from quadrupole interactions, in case the nuclear spin $I > \frac{1}{2}$. It is interesting that a value q for the upper conduction electrons can be derived from this effect, but this is of no direct avail in the absolute determination of nuclear quadrupole moments. As pointed out before, another q involving the total charge distribution is effective in that case.

The derivation for the anisotropy of the Knight shift showed no relation with the anisotropy in the observed magnetic susceptibility. The latter is mostly due to diamagnetic effects of the orbital motion. It is possible that some anisotropy in the Pauli spin paramagnetism occurs because of an anisotropic g-factor. If the spin-orbit coupling due to the partial "non-s character" in the wave function is appreciable compared to crystalline field splittings in the conduction band, one will have a g-factor different from 2, and in a tetragonal crystal one has to distinguish between $g_{\parallel}$ and $g_{\perp}$. The partial s-character of the wave function then leads, according to equation (3), to an anisotropy in the Knight shift

$$(24a)\qquad \frac{\Delta\nu_{\parallel} - \Delta\nu_{\perp}}{\nu_0} = \frac{(g_{\parallel} - g_{\perp})\beta I}{2\mu_N}\, CA\, V_0 N(E)$$

This anisotropy effect should be added algebraically to that given by equation (21). Phenomenologically the two effects are indistinguishable. It will be very difficult to obtain experimental information about $g_{\parallel}$ and $g_{\perp}$. In the absence of a theoretical evaluation we have used equation (21) only to obtain a value for q. This will be incorrect, if the anisotropy in g is several percent. This would still require a sizeable amount of "non-s character" of the wave function, but perhaps less than the use of equation (21) would indicate. The anisotropic diamagnetic susceptibility will of course give rise to an anisotropic magnetic shielding of the nuclei. But the order of magnitude of this effect is much smaller, perhaps a few parts in a million [31].

We finally extend the preceding considerations to the general case when there is no axis of symmetry. Instead of equation (20) we now have for the average density of the conduction electrons near the Fermi level

$$(25)\qquad \psi\psi^* = g(r)(Ax^2 + By^2 + Cz^2)$$

Substituting equations (19) and (25) into equation (18) one finds that $\Delta\nu_{\text{anis}}$ is now not only a function of θ, but also of ϕ.

$$(26)\quad \frac{\Delta\nu_{\text{anis}}}{\nu_0} = 2\beta^2 V_0 N(E_F) \left\{ (C - \tfrac{1}{2}A - \tfrac{1}{2}B)\,\frac{8}{15}\,\pi(3\cos^2\theta - 1) + \frac{4}{5}\,\pi(A - B)\sin^2\theta\cos 2\phi \right\} \int_0^\infty rg(r)dr$$

This expression reduces properly to equation (21) for $A = B$.

In order to calculate the line shape we introduce three frequencies ν_1, ν_2 and ν_3, at which the resonance

occurs, if H_0 points along one of the axes. We assume without loss of generality that $\nu_3 > \nu_2 > \nu_1$. The resonance frequency for the direction θ, ϕ is then given by

$$(27)\quad \nu = \nu_1 \sin^2\theta \sin^2\phi + \nu_2 \sin^2\theta \cos^2\phi + \nu_3 \cos^2\theta$$

A comparison with equation (26) readily relates these phenomenological quantities with the A, B and C and with the isotropic shift $\Delta\nu_{\mathrm{is}}$. We first calculate from equation (27) what the line shape would be if θ were held fixed

$$\mathscr{I}'(\nu, \theta) \propto \left(\frac{\partial\nu}{\partial\phi}\right)^{-1} \propto (\nu - \nu_3\cos^2\theta - \nu_1\sin^2\theta)^{-\frac{1}{2}} (-\nu + \nu_3\cos^2\theta + \nu_2\sin^2\theta)^{-\frac{1}{2}}$$

for

$$\frac{\nu - \nu_1}{\nu_3 - \nu_1} > \cos^2\theta > \frac{\nu - \nu_2}{\nu_3 - \nu_2} \text{ if } \nu_2 < \nu < \nu_3$$

and

$$\frac{\nu - \nu_1}{\nu_3 - \nu_1} > \cos^2\theta > 0 \text{ if } \nu_1 < \nu < \nu_2$$

and zero outside these intervals for θ. To find the actual shape we have to integrate over the permissible range of θ values.

$$\mathscr{I}(\nu) = \int \mathscr{I}'(\nu, \theta) \sin\theta d\theta$$

and find after some manipulation that $\mathscr{I}(\nu)$ can be brought into the form of the complete elliptic integrals.

$$(28)\quad \mathscr{I}(\nu) \propto \sqrt{\frac{\nu_3 - \nu_1}{\nu - \nu_1}} \int_0^{\pi/2} \left\{1 - \frac{(\nu_2 - \nu_1)(\nu_3 - \nu)}{(\nu_3 - \nu_2)(\nu - \nu_1)} \sin^2\gamma\right\}^{-\frac{1}{2}} d\gamma \quad \text{for } \nu_2 < \nu < \nu_3$$

$$\mathscr{I}(\nu) \propto \sqrt{\frac{(\nu_3 - \nu_1)(\nu_3 - \nu_2)}{(\nu_3 - \nu)(\nu_2 - \nu_1)}} \int_0^{\pi/2} \left\{1 - \frac{(\nu - \nu_1)(\nu_3 - \nu_2)}{(\nu_3 - \nu)(\nu_2 - \nu_1)} \sin^2\gamma\right\}^{-\frac{1}{2}} d\gamma \quad \text{for } \nu_1 < \nu < \nu_2$$

$$\mathscr{I}(\nu) = 0 \qquad \text{for} \quad \begin{matrix}\nu < \nu_1 \\ \nu > \nu_3\end{matrix}$$

The line shape has been plotted in Figure 8, for the case $\nu_3 - \nu_2 = \frac{1}{2}(\nu_2 - \nu_1)$. The values of the elliptic integrals can be found in the tables of Jahnke and Emde [32]. There is a logarithmic divergence at the frequency ν_2. Further broadening of the line by dipolar interaction will smooth this out almost completely, and the real line shape is indicated by the drawn line. Note that the line would be symmetrical, if $\nu_3 - \nu_2 = \nu_2 - \nu_1$. No observations on a metal with less than axial symmetry have been made. It would be interesting if such a line shape could be identified.

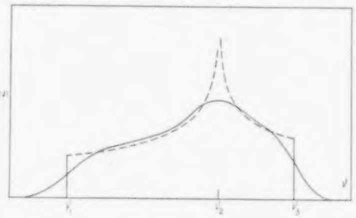

FIGURE 8. The theoretical line shape in a polycrystalline powder due to anisotropy of the Knight shift in a conductor with less than axial symmetry. The drawn curve includes the symmetric broadening by dipolar interaction and finite relaxation time.

5. The Nuclear Resonance in Thallium Alloys

After the line in metallic thallium had been found, experiments on thallium alloys were immediately successful. The lines retained their intensity, as quadrupole effects are absent. The width varied somewhat in the different alloys, but not by spectacular amounts. An exception is perhaps formed by the thallium-bismuth alloys where the line width

TABLE II

System	Phase or composition	Isotope	Knight shift	Line width (Kc/s) experim.*	calc†
Na-Tl	pure Tl	Tl^{205}	1.54±.05	33	4.6
	NaTl	Tl^{205}	−1.03	50	
	Na_2Tl	Tl^{205}	.68	38	
	NaTl	Na^{23}	−.016	2.4	2.0
Mg–Tl	MgTl	Tl^{205}	2.12	40	
In-Tl	50 At.% In-Tl	Tl^{205}	1.68	38	
Sn-Tl	0–25 At.% Sn-Tl	Tl^{205}	1.54 to 1.97	33–64	
(See detailed shift vs. composition data, Figure 9)					
	25 At.%Sn-Tl	Sn^{119}	.67	5	
	pure β-Sn	Sn^{119}	.74	5	0.71
	pure α-Sn	Sn^{119}	0.0	5	0.76
Hg-Tl	13 At.%Hg-Tl	Tl^{205}	1.71	34	
	60 At.%Hg-Tl (liquid)	Tl^{205}	1.49	20	
	72 At.%Hg-Tl	Tl^{205}	1.01	33	
	92 At.%Hg-Tl (liquid)	Tl^{205}	1.18	(30)	
Pb-Tl	34 At.%Pb-Tl	Tl^{205}	1.39	34	
	90 At.%Pb-Tl	Tl^{205}	1.90	33	
	pure Pb	Pb^{207}	1.24	< 2	0.28
Bi-Tl	6 At.%Bi-Tl	Tl^{205}	1.71	75	
	19 At.%Bi-Tl	Tl^{205}	1.74	110	
	59 At.%Bi-Tl	Tl^{205}	1.1	110	

*Between points of maximum slope.
†Second moment.

increased by a factor 3 to 110 kc/s. A remarkable result was obtained in a liquid alloy (90% Hg, 10% Tl) at room temperature. The width has the same order of magnitude as in the solid phases and is apparently not narrowed by the rapid motion in the liquid. This is all the more remarkable as a spin lattice relaxation mechanism is again ruled out by the lack of variation with temperature.

Data on the width and Knight shift are assembled in Table II. The Knight shift exhibits appreciable variations on alloying. In each phase it changes continuously with composition. This behavior is illustrated for the thallium-tin system in Figure 9.

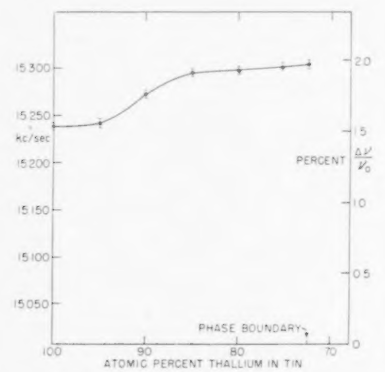

FIGURE 9. The shift of the Tl^{205} resonance in solid solutions of tin in thallium. The fact that tin concentrations less than 3% have no effect on the Knight shift can be considered as proof of Friedel's theory of impurity levels in metals, which leave the Fermi level unaffected. For higher concentrations the curve represents the filling up of the conduction band and gives the density of electron states $N(E)$.

The solubility of thallium in tin is too small to obtain data at the other end of the phase diagram. The relative shift increases from 1.54 per cent in pure thallium to 1.97 per cent at the phase boundary. The Knight shift of tin in the alloy (20% Sn–80% Tl) on the other hand is smaller (0.67%) than in pure tin (0.74%). According to equation (3) the variation can be caused by a change in the quantities C, V_0 and $N(E)$. In a first approximation it is probably correct to assume that CV_0 is constant, as the hyperfine interaction normalized per atom is inversely proportional to the atomic volume V_0. Then the plot of the Knight shift is also a plot of density of states near the Fermi level $N(E_F)$. For a free electron gas this quantity is proportional to $E_F^{1/2}$. It is plausible that the addition of tin to thallium raises the number of conduction electrons per unit volume and consequently E_F and $N(E_F)$. There are some data on the magnetic susceptibility which also indicate an increase of $N(E)$. The specific susceptibility increases from a value -0.22×10^{-6} for pure thallium to -0.11×10^{-6} for an alloy of 80% thallium and 20% tin. The density $N(E)$ levels off near the phase boundary; a decrease which might be expected according to Jones's explanation [33] of the Hume-Rothery rules is not observed. Additions of less than 3 per cent tin do not change the Knight shift. The density of states $N(E_F)$ remains constant at first and increases only when more than 3 per cent tin is added. This is in agreement* with Friedel's theory of impurities in metals [34]. The tin atoms in small concentration act like impurities, which have either a bound electron or a compressed Fermi gas of conduction electrons around them. In either case the maximum momentum k_M, and therefore $N(E_F)$ are unchanged. For higher concentrations the impurities interact and $N(E_F)$ increases.

The line width increases by a factor two if 10 per cent tin is added. Data are given in Figure 10.

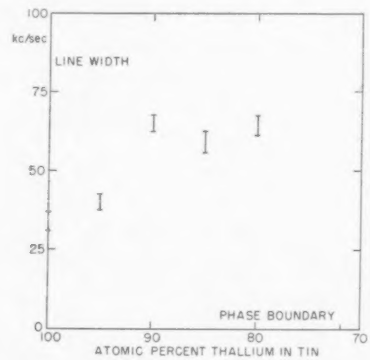

FIGURE 10. The line width, measured between points of maximum slope, in solid solutions of tin in thallium.

The thallium nuclei in the solid solution do not all have the same environment. There will be a certain distribution in the values of $|\psi(0)|^2$, depending on the presence of tin atoms in the immediate neighborhood. This will lead to a distribution of Knight shifts. Although one would expect an asymmetric distribution for small tin concentrations, an asymmetric broadening has not been observed.

Discontinuities in the Knight shift occur when phase transitions take place. In the two-phase regions of the phase diagram the resonance will therefore be double. This is illustrated in Figure 11, where the Knight shift is plotted versus composition of thallium-mercury alloys. The relative change in

*Professor H. Brooks first suggested this explanation to the authors.

the Knight shift is more than 70% in going from the β- to the γ-phase. The change is partly caused by volume effects but mostly by the electronic structure. Another example of the effect of phase change on the Knight shift is the melting of Tl–Hg alloys. A pure increase in volume would presumably lower the Knight shift according to equation (3). Actually, an increase of 20 per cent is observed on melting, indicating a change in the electronic structure.

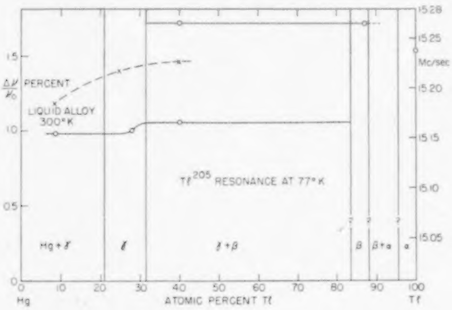

FIGURE 11. The shift of the Tl^{205} resonance in thallium mercury alloys. In the two-phase regions two resonance lines occur. In the β- and α-phase region an unresolved line, presumably consisting of two components, was observed but is not indicated in the figure. The dotted line refers to the resonance at 24°C in liquid alloys. Discontinuities occur in the transition from one solid phase to another and to the liquid phase. The indicated phase boundaries do not apply to the liquid phase.

The behavior of the Knight shift over the phase diagram is roughly what could be expected. The knowledge of the electronic structure of these alloys is, however, insufficient to attempt a quantitative explanation.

A thallium-magnesium alloy exhibits the largest Knight shift of 2.1 per cent.

A most remarkable result was obtained in the ordered NaTl structure. This intermetallic compound shows a negative Knight shift (−1.03%) for thallium. Since it is an ordered structure with cubic symmetry, the Na^{23} resonance could also be observed and it shows a small shift towards lower frequencies. A shift of −0.016 per cent was found compared to a solution of NaI. In metallic sodium an ordinary positive shift of 0.11 per cent occurs. We have not yet performed experiments at other frequencies and do not know whether the shift is really proportional to ν_0, although it seems unlikely that a chemical shift would be this large. Experiments on other alloys with the NaTl structure are also planned.

A possible explanation of the negative shift might perhaps be found along the following lines. Abragam and Pryce [35] have shown that Mn^{++} ions, and other ions of the iron group, exhibit configurational interaction, in which a 3s-electron is promoted to the 4-s orbital. The total spin or the magnetic moment of the ion is not changed by this promotion, but the interaction with the nucleus is changed. The electron spin interacts more strongly in the 3-s orbit than in the 4-s orbit. The effective spin density at the nucleus due to the unpaired s-electrons is determined by overlap integrals of radial wave functions. This configurational interaction accounts for the hyperfine structure of the Mn^{++}-ion. Abragam and Pryce* [36] show that it is proportional to the amplitude of the admixed wave function and not to its square. It is an interference effect which actually gives a negative sign for the $A\,\mathbf{I}\cdot\mathbf{S}$ interaction in the Mn^{++} ion. The question is whether configurational interaction in a metal might cause some mixing with a state in which an inner s-electron is promoted to higher orbits in the conduction band with s-wave character, and whether this effect would yield a particularly large negative value for NaTl. Clearly much theoretical work and more experimental data are needed to confirm this hypothesis. The width of the Na^{23} resonance in NaTl is normal. It should be remembered that the tabulated experimental and theoretical values are not directly comparable. The width of the thallium resonance is, however, of the same order of magnitude as found in all other samples. This is another argument that the anomalously large width is a characteristic of the atomic configuration of the heavy elements, rather than of the electronic structure of the conduction band.

Unfortunately, we have no data on the spin-lattice relaxation time for any of the observed resonances. No check on the validity of the Korringa relation is therefore possible.

Acknowledgement

The authors wish to express their indebtedness to Professors H. Brooks, J. Friedel and H. Jones and Dr. C. Herring for several valuable discussions. One of us (T.J.R.) acknowledges a stipend from the California Research Corporation. The research was made possible through support extended to Cruft Laboratory, Harvard University, jointly by the Office of Naval Research, the Signal Corps of the U.S. Army, and the U.S. Air Force, under ONR Contract N5ori-76, T. O. 1.

*The authors are indebted to Dr. Abragam for calling their attention to this effect and for making the manuscript available before publication.

References

1. KNIGHT, W. D. Phys. Rev. **76** (1949). 1259.
2. TOWNES, C. H., HERRING, C. and KNIGHT, W. D. Phys. Rev. **77** (1950) 852.
3. FERMI, E. Z. Phys. **60** (1930) 320.
4. KOHN, W. and BLOEMBERGEN, N. Phys. Rev. **80** (1950) 913; **82** (1951) 283.
5. HEITLER, W. and TELLER, E. Proc. Roy. Soc. **A155** (1936) 637.
6. KORRINGA, J. Physica **16** (1950) 601.
7. OVERHAUSER, A. W. Phys. Rev. **89** (1953) 1316.
8. BLOEMBERGEN, N. Physica **15** (1949) 588.
9. POULIS, N. J. Physica **16** (1950) 373.
10. HATTON, J. and ROLLIN, B. V. Proc. Roy. Soc. **A199** (1949) 222.
11. GUTOWSKI, H. S. and MCGARVEY, B. R. J. Chem. Phys. **20** (1952) 1472.
12. GUTOWSKI, H. S. Phys. Rev. **83** (1951) 1073.
13. NORBERG, R. E. and SLICHTER, C. P. Phys. Rev. **83** (1951) 1075.
14. POUND, R. V. and KNIGHT, W. D. Rev. Sci. Inst. **21** (1951) 219.
15. WATKINS, G. Thesis, Harvard University (1952).
16. BLOEMBERGEN, N. J. App. Phys. **23** (1952) 1383.
17. POUND, R. V. Phys. Rev. **79** (1950) 685.
18. POUND, R. V. J. Phys. Chem. (to be published).
19. BLEANEY, B., BOWERS, K. D. and TRENAM, R. S. Proc. Phys. Soc. **66**A (1953) 410.
20. MOTT, N. F. and JONES, H. The Theory of the Properties of Metals and Alloys (Oxford University Press, 1936), pp. 86–88.
21. MOTT, N. F. Prog. in Metal Phys. **3** (1952) 76.
22. HUANG, K. Proc. Phys. Soc. **60** (1948) 161.
23. BRIX, P. and KOPFERMANN, H. Landolt-Bornstein, Zahlenwerte und Funktionen I.5
24. PAULING, L. Proc. Roy. Soc. **A196** (1949) 343.
25. DAILEY, B. P. and TOWNES, C. H. J. Chem. Phys. **17** (1949) 782.
26. GUTOWSKI, H. S. and MCGARVEY, B. R. Phys. Rev. **91** (1953) 81.
27. PAKE, G. E. J. Chem. Phys. **16** (1948) 327.
28. WYCKOFF, Crystal Structures (New York, Interscience Publishers).
29. KEESOM, W. H. and VAN DER LAER, P. H. Physica **5** (1938) 193.
30. REIF, F. Thesis, Harvard University (1953).
31. RAMSEY, N. F. Phys. Rev. **86** (1952) 243.
32. JAHNKE E. and EMDE, F. Tables of Functions (New York, Dover Publications, 1945).
33. MOTT, N. F. and JONES, H. op. cit., pp. 170–173.
34. FRIEDEL, J. Phil. Mag. **43** (1952) 153.
35. ABRAGAM, A. and PRYCE, M. H. L. Proc. Roy. Soc. **A205** (1951) 135.
36. ABRAGAM, A. and PRYCE, M. H. L. To be published.

HEAT CAPACITY AND RESISTANCE MEASUREMENTS FOR ALUMINUM AND LEAD WIRES*

T. E. POCHAPSKY†

Heat capacity and electrical resistance measurements are reported for aluminum and lead at temperatures ranging from room temperature to near the melting point of each metal. A pulse heating method is used. The results show that both the heat capacities and temperature coefficients of resistance increase with temperature in such a way as to suggest that they are influenced by a single activated process rather than by impurities. Although this behavior may possibly be explained by a more complete theory of anharmonic lattice vibrations, evidence is presented to suggest a possible relationship between the anomalies and the presence of vacancies. Interpreting the excess heat capacity in terms of the heat of formation of vacancies, however, requires more vacancies than would be expected on the basis of self-diffusion experiments.

MESURES DE LA CAPACITÉ CALORIFIQUE ET DE LA RÉSISTANCE DE FILS D'ALUMINIUM ET DE PLOMB

Des mesures de capacité calorifique et de résistance électrique sont rapportées pour l'aluminium et le plomb, aux températures allant de la température ambiante jusqu'au voisinage du point de fusion de chacun des métaux. Une méthode de chauffage par pulsation a été utilisée. Ces résultats montrent que les capacités calorifiques et les coefficients de température de la résistance augmentent avec la température d'une manière qui fait croire, que tous les deux sont influencés par un processus activé, simple, plutôt que par des impuretés. Malgré que ce comportement puisse être expliqué par une théorie plus complète de vibrations anharmoniques du réseau, il est suggéré, en s'appuyant sur les faits présentés, qu'il peut y avoir une relation entre les anomalies et la présence de lacunes. L'interprétation de l'excès de capacité calorifique en termes de chaleur de formation des lacunes, nécessite un plus grand nombre de lacunes que celui auquel on s'attendait d'après les expériences d'autodiffusion.

MESSUNGEN DER WÄRMEKAPAZITÄT UND DES ELEKTRISCHEN WIDERSTANDES AN ALUMINIUM UND BLEI-DRÄHTEN

Es wird über Messungen der Wärmekapazität und des elektrischen Widerstandes von Aluminium und Blei im Temperaturbereich, das sich von Zimmertemperatur bis fast zum Schmelzpunkt des betreffenden Metalls erstreckte, berichtet. Es wurde eine "*pulse heating*" Technik angewandt. Die Ergebnisse zeigen, dass sowohl die Wärmekapazität als auch die Temperaturkoeffizienten des Widerstandes in einer Weise zunehmen, die vermuten lässt, dass sie durch einen einzigen aktiven Vorgang beeinflusst werden und nicht durch Verunreinigungen. Obwohl dieses Verhalten möglicherweise durch eine weiter ausgebaute Theorie der anharmonischen Gitter-Schwingungen erklärt werden könnte, wird an Hand der dargestellten Resultate eine eventuelle Beziehung zwischen den Anomalien und dem Vorhandensein von Leerstellen angenommen. Die Deutung der zusätzlichen Wärmekapazität als Bildungswärme von Leerstellen würde jedoch mehr Leerstellen erfordern als auf Grund der Selbstdiffusionsversuche zu erwarten ist.

1. Introduction

Above the Debye temperature, the heat capacity of a metal at constant volume is expected to change with temperature because of electronic contributions and because of anharmonicity of the lattice [1]. Existing theories, at least as far as they have been developed, show that both these influences should produce a linear change with temperature. Consequently, if actual measurements of the heat capacity do not exhibit this behavior, it may be suspected either that the theoretical development is incomplete or that additional mechanisms are involved.

Among metals melting at low temperatures, the alkali metals stand out as having a behavior contrary to that expected. Recent careful work shows that the heat capacity of sodium [2] increases unusually rapidly as the melting point is approached. The present measurements were performed, in part, to determine whether similar increases occur for lead and aluminum. In addition, individual measurements were made during times of the order of a millisecond by using a pulse heating technique in order to investigate the possibility that the heat capacity depends on diffusion processes such as might be associated with premelting or with vacancy formation. Resistance measurements are an essential part of the method and these offer an additional means of interpreting the results.

*Received June 6, 1953.
†Institute for the Study of Metals, The University of Chicago, Chicago, Illinois.

2. Experimental Procedure

When a fine wire is included in one arm of a balanced Wheatstone bridge and a pulse of current is introduced in the battery circuit, the wire heats up and unbalances the bridge. The heat capacity of the wire can be calculated [3] from the deflection of a ballistic galvanometer detector, provided that

the current and constants of the circuit are known. An accurate initial balance of the bridge is not necessary if two equal and opposite current pulses are used consecutively. Furthermore, if the pulse separation is made variable, the cooling of the wire can be studied and so any variation of heat capacity can be determined over the time range used.

This double-pulse method is used in the present measurements. In a description of details to be published elsewhere [4], it is shown that the specific heat capacity of the metal used in a wire specimen can be written

$$(1) \qquad c_p = \left(\frac{RR'}{mG_0}\right)_{\text{spec}} \left(\frac{mG_0}{RR'}\right)_{\text{plat}} (c_p)_{\text{plat}} + \Delta.$$

In the parenthesis, R is the specimen resistance, R' the temperature coefficient of resistance, m the mass and G_0 the galvanometer deflection extrapolated to zero pulse separation. Corresponding quantities for a platinum calibrating specimen appear in the second parenthesis. The quantity Δ is the error made in assuming that various terms remain constant during each pulse; it represents an error of less than 1 per cent.

Specimens, in the form of wires approximately 5 mils in diameter, are tested in a vacuum furnace. They are supported on a frame of slender quartz rods to minimize plastic flow at high temperatures. An oil diffusion pump is used without a cold trap.

Readings were taken during heating and cooling for aluminum and for lead. Each specimen was tested twice and additional data were obtained for a second wire of each metal. Cooling curves only were obtained for extruded wires of distilled sodium; tests on this metal were made during the development of the apparatus and were not carried to the point of obtaining heat capacity measurements. Spectroscopic analysis after testing shows the aluminum to have been 99.9 per cent pure, with .05 per cent silicon and .03 per cent boron as the principal impurities. The presence of boron is questionable because it was detected in only one of three wires. The lead was 99.99 per cent pure and had a remainder of aluminum, silver and silicon. A film noticed on the aluminum after testing was apparently carbon; no progressive contaminating effect was noticed during the course of the measurements.

The temperature rise per double pulse rose with the furnace temperature, and, near the melting point, was about 2°C for the lead and 5°C for the aluminum.

Resistances determined during the tests are considered accurate to a fraction of 1 per cent and temperature coefficients are probably correct to 2 per cent or better. Wire temperatures, obtained with a calibrated platinum–platinum $+10\%$ rhodium couple, are considered known to ± 1°C. The cooling curves show heat losses to be trivial. Variation in the individual heat capacity determinations, using smoothed temperature coefficients, was approximately $\pm 1\%$ for a given wire. Consideration of all sources of error suggests a maximum error for the absolute heat capacity of less than 5 per cent.

3. Results

Smoothed values obtained at various temperatures for the resistance, the temperature coefficient of resistance, and the molar heat capacity of aluminum and lead are shown in Tables I and II. The molar heat capacities at constant volume shown there, C_v, are derived from the relation

$$\frac{C_p}{C_v} = 1 + \alpha A T$$

which is based on the assumption that Grüneisen's constant is independent of temperature T. The constant A is determined by evaluating the exact thermodynamic relationship between the heat capacities at room temperature where the experimental quantities are known. Thermal expansion coefficients, α, are based on the results of Uffelmann [5] and of Stokes and Wilson [6] for lead and the work of Wilson [7] and Hidnert [8] for aluminum.

Experimental points for the heat capacities obtained from smoothed values of the temperature coefficients of resistance are shown in Figure 1 for the two lead specimens and in Figure 2 for two runs on a single aluminum wire. The solid curves represent the best fit for all measurements and are compared with the results of other observers in Figures 3 and 4.

After introducing the first pulse, the metal wires cool with a time constant of a few seconds. The initial cooling rate is practically independent of temperature, presumably because the most important initial thermal loss is caused by conduction at the ends of the wire. For an aluminum specimen of the size used, the decrease in galvanometer deflection after .02 seconds is $2 \pm \frac{1}{2}\%$ at all temperatures. Similar constancy is obtained for lead, aluminum, platinum, and sodium after .02 second and 0.1 second.

An attempt was made to find possible gross

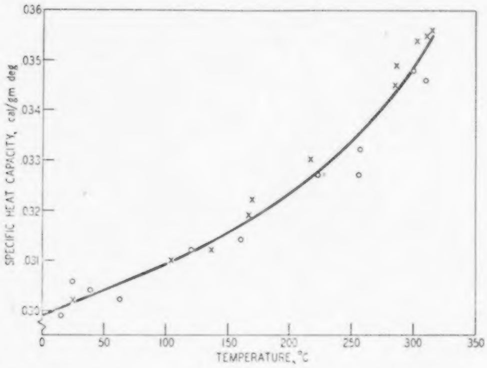

FIGURE 1. Experimental points for heat capacities of two lead specimens.

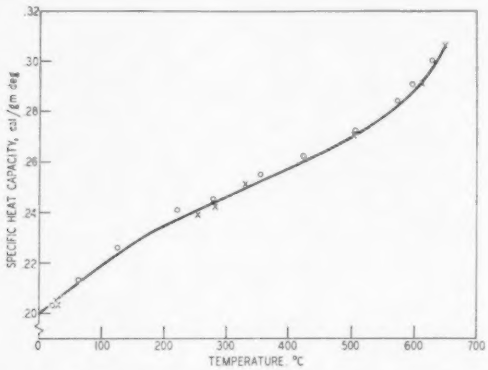

FIGURE 2. Experimental points for heat capacity during two runs on one aluminum specimen.

changes in the galvanometer deflection near the melting temperature of lead. A 5-mil lead wire, held at a temperature a few degrees below the melting point, was pulsed with enough current to raise the temperature of normal lead approximately 5 degrees per double pulse. Although the resistance at low currents remained at the expected value,

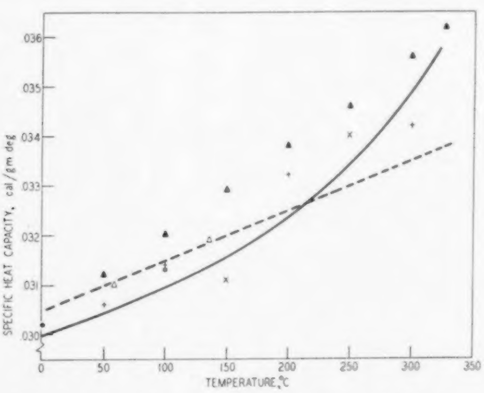

FIGURE 3. Heat capacity of lead compared with results of observers noted in Reference 9. Solid curve, present results; dashed curve, Kelley; ▲ Klinkhardt • Griffiths and Griffiths; + Schübel; × Awbery and Griffiths; △ Magnus.

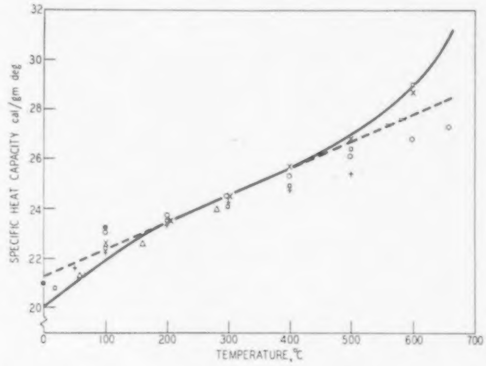

FIGURE 4. Heat capacity of aluminum compared with results of observers noted in Reference 9. Solid curve, present results; dashed curve, Kelley; □ Seekamp; × Awbery and Griffiths; ○ Wüst, M. and D.; + Schübel; ▲ Magnus.

the galvanometer deflection was 10 per cent higher than expected at small separation times and 6 per cent higher for pulses separated by more than 0.1 second. When the ambient temperature was then increased slowly, however, it was found that each pulse produced a permanent increase in the resistance of the specimen.

4. Discussion

Although an absolute uncertainty of nearly 5 per cent might be expected in the results for the heat capacities, a comparison with the measurements of other investigators [9] shows that the actual error is much smaller. This comparison is illustrated in Figures 3 and 4 where the values reported by Kelley [9] should be given additional weight because they represent an expert evaluation of all work prior to 1948. He does, however, bias his results to obtain a linear dependence on temperature. A more rapid increase at high temperatures is evident in the present as well as past determinations.

The results for aluminum agree with those obtained by Awbery and Griffiths [9], except at the lower temperatures. Mesasurements for lead are over 1 per cent lower than might be expected, probably because of erroneous calibration with respect to platinum. It is believed that the accuracy of the measurements is sufficient to establish the general shapes of the heat capacity curves shown.

A plot of c_v against T yields curves that have the same general features as similar curves for c_p. The rise above a linear increase persists at high temperatures, and overestimates of the $c_p - c_v$ correction suggest that the similarity is not a consequence of using the Grüneisen relation.

Examination of the values of the temperature coefficient of resistance shows that they increase with temperature in a manner similar to the heat capacity. An accurate correlation between these two quantities is not necessarily to be expected because the resistance depends on the electronic structure as well as on changes in the lattice produced by heating. A change in the thermal expansion coefficient with temperature, for instance, would be expected to be accompanied by a change in the temperature derivative of the resistance coefficient.

The increases in the heat capacities and the resistance coefficients are such that they do not seem to be attributable to contamination. Aluminum of the purity used might have a much larger anomaly than observed within 50°C of the melting temperature, provided that the foreign material is soluble in liquid aluminum and not in the solid, but the dependence of the heat capacity on temperature would then be appreciably different from that observed. Such impurity melting should produce an excess heat capacity that varies as $(T_m - T)^{-2}$ at a temperature T below the melting temperature T_m. There is sufficient scatter in the individual measurements for lead to make it difficult to exclude impurity melting on the basis of the shape of the heat capacity curve. Such a process is doubtful because the resistance measurements, carried closer to the melting point than was possible with the heat capacity measurements, showed no evidence of a rise due to impurities. The large galvanometer deflections obtained with the fine lead wire near the melting temperature are interpreted to be the result of an increase in resistance associated with partial melting very close to the melting point.

It is believed that the results obtained are characteristic of pure lead and aluminum and that these two metals behave in a manner similar to high-purity sodium [2]. The increases may be explainable in terms of anharmonicity of the lattice vibrations. On the other hand, an analysis of the results shows that the anomalies may be caused by an activated process.

If an activated process is assumed, the heat capacity anomaly for aluminum is such as to require an activation energy of 27,000 cal/mole while that for lead requires about 11,000 cal/mole. Corresponding values for the excess temperature coefficient of resistance are 18,000 cal/mole and 15,000 cal/mole. The heat capacity at constant pressure was used in these determinations. Similar values are obtained if C_v is used, but the accuracy of the $C_p - C_v$ correction is probably not sufficient to give the latter calculation any more significance than that obtained from C_p. The energy obtained from the heat capacity of lead cannot be considered very accurate because that value is sensitive to the manner of drawing a curve through the scattered points shown in Figure 1. The data are such that the energy could just as well be that obtained from the resistance coefficients.

From the total excess heat and the activation energies, the number of activated units was computed to be about 2×10^{-3} per atom at the melting point. Calculations based on the published heat capacity of sodium [2] suggest an activation energy of about 10,000 cal/mole and a number of activated units of 1.7×10^{-3} at the melting point.

A comparison of these energies with those found in self-diffusion experiments [10] suggests that one might attempt to relate the excess heat capacities to the processes responsible for self-diffusion—in particular, to the formation of vacancies. For many cubic metals, a 10^{-3} fraction of vacancies per atom at the melting point is not unreasonable provided that half the free energy of the diffusion process is assigned to the formation of vacancies. On the other hand, from the heats of formation obtained in the present work and half the entropies obtained from self-diffusion measurements a fraction of 10^{-4}, or less, seems more likely. It can be argued that the values of the energies determined here suffer because of experimental errors and because they are obtained from the heat capacity at constant pressure. Then, because the concentration of vacancies is highly sensitive to the heat of formation, a 10^{-3} fraction cannot be definitely excluded on the basis of the second estimate. It should be noted, however, that the fraction of vacancies calculated from the total excess heat is relatively insensitive to the errors mentioned.

It was originally hoped that the speed of measurements would be sufficient to permit measuring the heat capacity before vacancy equilibrium is established in the lattice by diffusion from mosaic boundaries or dislocations. Then, generation of vacancies would cause abnormally fast cooling of the wires after the initial pulse. For an equilibrium concentration of only 10^{-4} vacancies per atom at the melting temperature, the cooling curves should show a detectable anomaly in the time range .001 to .100 sec, provided that the ratio R'/C_p is changed by the production of vacancies. This latter condition is apparently not satisfied by lead within experimental error. The cooling anomaly which might be expected for a 10^{-3}

fraction of vacancies in the case of aluminum, and, possibly, sodium was not observed. Nevertheless, the method of attaining equilibrium is not understood well enough to set an accurate time limit for the equilibration of vacancies and a time shorter than a millisecond is not unreasonable.

If anomalies exist in the metals considered here, it is reasonable to expect that they should also be present in other materials. As shown by the work of Carpenter [11], they do not occur in mercury, bismuth and iodine. Then, the increases in heat capacity found for the cubic metals investigated may be caused by a mechanism sensitive to crystal structure.

The results described in this report are unusual enough to suggest that further studies be made of the three metals investigated. One merit of the procedure is that verification of the heat capacity results can be made by means of independent resistance measurements. Such measurements on pure materials should give results that are in substantial agreement with the data in Tables I and II. Inasmuch as the excess heat capacity is associated with an excess resistance of a few per cent, it should be possible to quench in that additional resistance if vacancies are responsible. Quenching experiments of this kind have already been reported for gold by Kauffman and Koehler [12]. By extending them to the metals studied here, it should be possible to determine whether vacancy equilibrium is achieved in a time less than the millisecond interval used in the present experiments.

TABLE I

HEAT CAPACITY AND ELECTRICAL RESISTANCE OF ALUMINUM

Temperature °C	Resistance R/R_0	Resistance according to Holborn* R/R_0	Temp. coefficient of resistance $\frac{dR}{dT}/R_0 \times 10^3$	Heat capacity cal/mole deg	
				C_p	C_v
0	1.000	1.000	4.38	5.40	5.16
100	1.448	1.442	4.55	5.90	5.54
200	1.911	1.890	4.77	6.35	5.86
300	2.400	2.346	4.96	6.64	6.00
400	2.915		5.20	6.94	6.13
500	3.453		5.55	7.29	6.30
550	3.739		5.81	7.50	6.41
600	4.036		6.15	7.80	6.61
625	4.195		6.38	8.00	6.76
650	4.361		6.65	8.23	6.94

*Obtained from the Landolt-Börnstein Tables.

TABLE II

HEAT CAPACITY AND ELECTRICAL RESISTANCE OF LEAD

Temperature °C	Resistance R/R_0	Resistance according to Holborn* R/R_0	Temp. coefficient of resistance $\frac{dR}{dT}/R_0 \times 10^3$	Heat capacity cal/mole deg	
				C_p	C_v
0	1.000	1.000	4.08	6.20	5.82
50	1.206		4.21	6.30	5.85
100	1.419	1.422	4.35	6.40	5.86
150	1.642		4.53	6.52	5.90
200	1.874	1.877	4.70	6.70	5.98
250	2.112		4.92	6.93	6.10
275	2.239		5.04	7.06	6.16
300	2.369	2.379	5.21	7.21	6.25
315	2.448		5.39	7.35	6.33
325	2.502		5.50		

*Obtained from the Landolt-Börnstein Tables.

Acknowledgments

The author wishes to acknowledge helpful conversations with various members of the staff at the Institute for the Study of Metals, particularly with M. H. Cohen and J. W. Stout, during the course of this investigation. He also wishes to thank the sponsors of the Institute for the support that made the work possible. The work was supported in part by the office of Ordnance Research, U.S. Army[Contract No. Da-11-022-ORD-834].

References

1. BORN, M. and BRODY, E. Z. Physik **6** (1921) 132.
2. GINNINGS, D. C., DOUGLAS, T. B. and BALL, A. F. J. Res. Nat. Bur. Standards, **45** (1950) 23.
3. See, for example, KURRELMEYER, B., MAIS, W. H. and GREEN, E. H. Rev. Sci. Instr. **14** (1943) 349.
4. Submitted to Rev. Sci. Instr. by author.
5. UFFELMAN, F. L. Phil. Mag. **10** (1930) 633.
6. STOKES, A. R. and WILSON, A. J. C. Proc. Phys. Soc. (London) **53** (1941) 658.
7. WILSON, A. J. C. Proc. Phys. Soc. (London) **53** (1941) 235.
8. HIDNERT, P. Bur. Standards Sci. Paper No. **497** (1925) 697.
9. Data were obtained from the following sources: KELLEY K. K., U.S. Bur. Mines. Bull. No. **476** (1949); SEEKAMP, H., Z. anorg. Chem. **195** (1931) 345; KLINKHARDT, H., Ann. Physik (4) **84** (1927) 182; AWBERY, J. H. and GRIFFITHS, E., Proc. Phys. Soc. (London) **38** (1926) 378; WÜST, MEUTHEN and DURRER, Forshung a. d. Geb. d. Ingenieurw. **204** (1918) 1; SCHÜBEL, P., Z. anorg. Chem. **87** (1914) 81; GRIFFITHS, E. H. and GRIFFITHS, E., Proc. Roy. Soc. (London) **A88** (1913) 549; MAGNUS, A., Ann. Physik, ser. 4, **31** (1910) 597.
10. NACHTRIEB, WEIL, CATALANO and LAWSON. J. Chem. Phys. **20** (1952) 1189.
11. CARPENTER, L. G., HARLE, T. F., and STEWARD, C. J. Nature **141**, June 4, 1938.

The Nucleation Problem in Deformation Twinning*

A number of investigators have in recent years accumulated results pointing to the existence of a critical shear stress, resolved in the twinning plane and direction, which determines at what applied stress a twin will appear and spread. Most of this evidence has been listed by Barrett [1]. We were perturbed to note that quite different values for this critical stress were obtained by three research groups [2, 4], each using cadmium crystals of comparable purity. Room temperature values were 140 ± 40 [2], 420 ± 50 [3] and 50 ± 25† [4] gm/mm^2. Experiments were accordingly undertaken with crystals oriented so that there could be no slip, to see how such divergence could be accounted for. Zinc, which has a twinning crystallography similar to that of cadmium, was used. Electrolytically polished crystal wires 1.5 mm in diameter were tested in tension on a Polanyi machine, the relaxation of the stiff beam being used as twinning indicator. This was found to be very sensitive.

From the published critical stress values for zinc [5; 6], we expected twinning at a resolved shear stress of about 500 gm/mm^2, or an applied load of some 1500 gm. No trace of twinning was to be found, however, at loads up to 8–10 kg, and the specimen eventually fractured in this range. Twins were seen in the immediate vicinity of the fracture, but since crystals examined in the machine at stresses only slightly below the fracture stresses were entirely devoid of twins, we attribute this localised twinning to the stress concentration arising at the instant of fracture.

A few specimens twinned readily at loads of 4–7 kg. These were specimens which had been slightly bent in handling and were seen to contain some small twin wedges before testing. Once a specimen contained full-size twin lamellae, further twinning occurred at loads of only 1–3 kg. In another series of tests small indentations were made in the crystal while it was under load. If the load exceeded about 6 kg, a violent burst of twinning—reminiscent of burst of martensite transformation—was the invariable result of indenting the crystal. It is noteworthy that the indentations were so small that if a crystal was indented *before* loading, no twins were formed at loads as high as 9 kg.

*Received July 21, 1953
†Our estimate of the experimental scatter.

We believe that these preliminary results indicate that there are three characteristic stages in twinning: (1) The creation of an initial wedge-shaped twin, (2) the spread of this twin across the crystal, (3) the thickening of the twin lamella, generally accompanied by the creation of new twins. These three processes require stresses decreasing in the same order. The stress for process (1), or nucleation, cannot be measured, since it requires a mode of loading that provides local stress concentrations (pinpricks, bending). Perhaps the recent experiments of Ancker [7] give a rough indication of this stress. She found that internally strained zinc crystals having locally a strain $\delta a/a \sim 0.003$, spontaneously twinned some weeks after they were made, thereby dispelling the lattice strain. This strain corresponds to a local tensile stress, parallel to an a-axis, of about 100 kg/mm^2. If we assume that the shear stress in the twinning plane is of the same order, this is about 40 times the highest stress at which we found the sudden load drop that accompanies the spread of a twin nucleus, and some 100 times the highest applied stress required to create fresh twins. The easy nucleation of later twins must no doubt be attributed to the stress concentration which is known to exist at the interface between the parent crystal and the original twin; similarly the ease with which an existing twin can spread across the crystal can be put down to the stress concentration at the apex of the spreading wedge.

Thus it appears that in tensile experiments one never measures the true stress needed to nucleate a new twin. If a crystal twins at all before it breaks, this must be because it contains twin nuclei already. The stress at which a nucleus will spread is variable, and this gives us an explanation for the great variety of published mean values for the "twinning stress" of cadmium. It is of course eminently reasonable that the spread of an existing twin should to a first approximation be subject to a critical shear stress law. It remains to explain why each research group has obtained values for this stress in quite a narrow range. One way to explain this is to postulate a dependence of the critical stress on lattice perfection, which has been shown to have a powerful influence on the spread of twins in calcite [8]. The above views make it necessary also to postulate that a wedge-shaped twin, as it spreads, becomes suddenly unstable and thereafter offers a greatly reduced resistance to spreading. There is good precedent for this in the behaviour

of calcite [9]. The effectiveness of indenting a loaded crystal in producing a burst of twinning (see above) suggests that the kinetic energy of a rapidly spreading twin is an important variable.

Work is being continued, with special emphasis on attempts to study separately the various stages of twinning. This note is published by kind permission of the Director, Atomic Energy Research Establishment.

R. L. Bell and R. W. Cahn

Department of Metallurgy
University of Birmingham
Birmingham 15, England

References

1. Barrett, C. S. Structure of Metals (New York, McGraw Hill, 1952), p. 382.
2. Thompson, N. and Millard, D. J. Phil. Mag., **43** (1952) 421.
3. King, R., Gumbell, S. W., and Makin, M. J. To be published.
4. Jakovleva, E. S. and Jakutovich, M. V. Zh. Eksper. Teor. Fiz., **10** (1940) 1146.
5. Miller, R. F. Trans. A.I.M.E., **122** (1936) 176.
6. Davidenkov, N. N., Kolesnikov, A. F., and Fedorov, K. N. Zh. Eksper, Teor. Fiz. **3** (1933) 350.
7. Ancker, B. Ann.d.Physik, **12** (1953) 145.
8. Garber, R. I., Zalidvadny, S. Ya., and Startsev, V. I. Dokl. Akad. Nauk. USSR, **58** (1947) 571.
9. Garber, R. I., J Physics USSR, **11** (1947) 55 (in English).

Thermodynamics of Surface Adsorption*

In a recent paper entitled "Mechanism of Temper Brittleness", Spretnak and Speiser [1] considered the thermodynamics of surface adsorption and derive the equation

$$\mu_2(d\Gamma_2/dT) = d\gamma/dT \tag{1}$$

where γ is the surface tension, T the absolute temperature, μ_2 the chemical potential (or partial molal free energy) of the solute, and Γ_2 is the surface concentration (moles per unit area) of the solute. The above authors state that μ_2 is negative and consequently "the temperature coefficient of Γ_2 is positive when the temperature coefficient of surface tension is negative." It is the purpose of this note to point out that equation (1) is in error, to derive the correct expression for the temperature variation of surface concentration, and to show the particularly simple form taken by this equation in dilute solutions. It is apparent that equation (1) is a very unusual type of thermodynamic equation since it implies that one can assign a definite magnitude and sign to the partial molal free energy μ_2, whereas in conventional thermodynamics only changes in free energy are measurable and μ itself is undefined to within an arbitrary additive constant. One does not expect, therefore, to be able to draw conclusions based on the sign of μ. The error lies in Spretnak and Speiser's equation (9) where they equate the entropy to the total derivative with respect to temperature of the Gibbs free-energy function of the surface layer, rather than the partial derivative at constant pressure, surface tension, and surface concentration.

The correct expression for the temperature variation of surface concentration may readily be obtained. To do so we shall follow the approach used by Guggenheim [2]. For a two-component system Guggenheim shows (p. 215) that

$$-d\gamma = (S^\sigma - \Gamma_1 \bar{S}_1 - \Gamma_2 \bar{S}_2)\, dT + [\Gamma_2 - \Gamma_1 x/(1-x)]\, (\partial\mu_2/\partial x)\, dx \tag{2}$$

where S^σ is the surface entropy per unit area, $\bar{S}_1$ and $\bar{S}_2$ are partial molal entropies of solvent and solute respectively in the bulk phase and x is the mole fraction of solute. The Γ's are the number of moles per unit area in the surface layer and will depend therefore on the arbitrary boundary which is chosen to separate the surface layer from the bulk material. However, as Guggenheim shows, the quantities $\Gamma_2 - \Gamma_1 x/(1-x)$, which we shall abbreviate by Γ, and $S^\sigma - \Gamma_1 \bar{S}_1 - \Gamma_2 \bar{S}_2$ are invariant to the position of this dividing surface provided it is outside the region of concentration gradients. In equation (2) constancy of pressure is assumed so terms involving dP have been dropped. There remain two independent variables which are chosen as T and x. If the surface is the boundary between two grains of the same solid phase, then, if the relative orientation of the grains is held constant, two independent variables are needed to specify the system. Furthermore, because of the identity of composition in two grains of the same phase, Γ is independent of the positions of the two dividing surfaces as long as they are in the region of constant composition. The treatment given here also applies to a surface between a solid (or liquid)phase and an attenuated vapor [2, pp. 214–216]. If, however, the boundary is between two different solid phases, such as alpha- and gamma-iron, there is one less degree of freedom and only one independent variable may be chosen. In this case the equations become more complicated and will not be discussed here.

*Received June 18, 1953; in revised form September 20, 1953.

At constant temperature equation (2) becomes

$$(3) \qquad -(\partial\gamma/\partial x)_T = \Gamma(\partial\mu_2/\partial x)_T$$

which is the Gibbs adsorption isotherm. By differentiating equation (3) with respect to temperature at constant x one obtains

$$(4) \quad -\partial^2\gamma/\partial x\partial T = (\partial\Gamma/\partial T)_x (\partial\mu_2/\partial x)_T + \Gamma\partial^2\mu_2/\partial x\partial T.$$

$(\partial\mu_2/\partial x)_T$ and $\partial^2\mu_2/\partial x\partial T$ are obtainable from a knowledge of the thermodynamic properties of the bulk phase so that from a measurement of surface tension as a function of x and T one can obtain the surface concentration and its temperature derivative.

In order to use equation (3) and (4) it is necessary to have information about the activity of the solute in the condensed phase. There is an important simplification of these equations that may be made in the range of dilute solutions. In this range Henry's law [3] is valid for the solute and the variation with composition of the chemical potential of the solute is a colligative property, depending only on the mole fraction. Then

$$(\partial\mu_2/\partial x)_T = RT/x \text{ and } \partial^2\mu_2/\partial x\partial T = R/x.$$

Equations (3) and (4) become

$$(5) \qquad -(\partial\gamma/\partial x)_T = RT\Gamma/x$$

$$(6) \quad RT^2(\partial[\Gamma/x]/\partial T)_x = (\partial\gamma/\partial x)_T - T(\partial^2\gamma/\partial x\partial T).$$

It should be emphasized that the validity of equations (5) and (6) does not depend on an assumption of ideal solutions laws, but is valid for any solution in the dilute range where the activity of the solute is proportional to its mole fraction. It is the analogue for surface adsorption effects of the familiar van't Hoff law of freezing point lowering. In the dilute solution range one would also expect Γ/x to be a constant independent of composition since it is the distribution coefficient between the surface and bulk phases. If the surface tension is found to be a linear function of x, then the assumption of dilute solutions and Henry's law is experimentally verified. In this range Γ/x is a function of temperature only and so one may drop the requirement of constancy of x in the temperature derivatives of equation (6) and may therefore use data where the composition is different at different temperatures.

Ordinarily the amount of solute in the surface will be negligible in comparison to that in the bulk material and one may set x equal to an experimentally measured mole fraction of solute which includes surface as well as bulk material. If, however, an appreciable amount of the total solute is in the surface phase, then care must be taken to identify x with the composition of the bulk phase. In such a case the observed value of γ at constant temperature and over-all composition will be found to be a function of the surface-to-volume ratio.

J. W. Stout

Institute for the Study of Metals
The University of Chicago
Chicago, Illinois

References

1. Spretnak, J. W. and Speiser, R. Trans. Am. Soc. Metals **43** (1951) 734.
2. Guggenheim, E. A. Thermodynamics (New York, Interscience, 1950).
3. See Lewis, G. N. and Randall, M. Thermodynamics (New York, McGraw-Hill, 1923) p. 232.

The Structure of Gamma-Manganese*

We should like to make the following brief comments on Dr. Morgan's suggestion [1] that pure γ-manganese may have a face-centred-tetragonal structure at all temperatures.

1. Since publication of our work on manganese-copper alloys, we have obtained several X-ray photographs of pure manganese at temperatures above 1100°C. These all show a f.c.c. structure. We hope soon to publish details of this work and of the high temperature camera designed to investigate the structures of γ and δ-manganese.

2. The argument for a high-temperature tetragonal form of manganese is based on Zener's suggestion that the tetragonal form is an antiferromagnetic superlattice, and Isobe's observations of an increase in susceptibility with temperature. Although experiment disproves the suggestion, it is worth while briefly examining the basis for this argument which we believe to be invalid.

Néel's estimate of 1720°K for the antiferromagnetic Curie point in manganese was an early one and is not substantiated by later evidence. Its validity may be judged from the corresponding estimate for chromium (4150°K) where no structural complications arise. The neutron diffraction results of Schull and Wilkinson [2] show that the actual antiferromagnetic Curie points of α-manganese and chromium are $\backsim$100°K and 475°K respectively. It is possible that some or all of the

*Received August 13, 1953.

other manganese structures may be ordered antiferromagnetic arrays at temperatures above the Curie point for the α-phase, but this seems most improbable. Certainly Isobe's results constitute no proof, since the susceptibility of chromium continues to increase with temperature to at least 1400°C. As discussed by Kriessman [3], it does not seem possible to explain the sign of the temperature coefficient of susceptibility purely in terms of antiferromagnetism or paramagnetism.

3. Even if γ-manganese is antiferromagnetic, we do not believe that this is responsible for the tetragonal structure. The postulated magnetic forces would be very weak in comparison with normal electronic interactions, and would seem to be incapable of producing the observed change in axial ratio. This remark also applies to Zener's explanation of the b.c.c. structures in V, Cr, W, and Mo, and the neutron diffraction results do not support his interpretation. More direct evidence comes from the crystallographic mechanism of the cubic $\rightarrow$ tetragonal change. This is identical with that observed in indium-thallium alloys [4], but in the latter case a tetragonal structure with $c/a > 1$ is found. Since this cannot reasonably be attributed to a magnetic superlattice, some other explanation (e.g., the nonspherical field of the indium ion) must be sought. Any such explanation could also be applied *a fortiori* to manganese alloys, since the other crystal structures show clearly that manganese is an unusual element.

Z. S. BASINSKI and J. W. CHRISTIAN

Inorganic Chemistry Laboratory
Oxford University, England

References

1. MORGAN, E. R. Acta Met. **1** (1953) 377.
2. SCHULL, C. G. and WILKINSON, M. K. Rev. Mod. Phys. **25** (1953) 100.
3. KRIESSMAN, C. J. Rev. Mod. Phys. **25** (1953) 122.
4. BOWLES, J. S. and BARRETT, C. S. and GUTTMAN, L. Trans. A.I.M.E. **188** (1950) 1472.

Thermal Annealing of Radiation-Induced Hardness Changes in Alkali Halides*

Vaughan, Leivo, and Smoluchowski recently have reported that proton irradiation increases the hardness of sodium and potassium chloride [1]. The hardness change resulted indirectly from ionization produced by the bombardment rather than from direct ionic displacements, since the number of the latter was negligible.

Similar effects of energetic particle bombardment have been observed in this laboratory, as well as large increases in hardness induced by comparatively low energy X-irradiation.† It has been found in addition that hardness changes occurring under conditions where a large number of displacements may be expected differ markedly in their thermal annealing characteristics from those where damage is largely due to ionization. During the course of annealing experiments on bombarded crystals, which are described below, it has been possible to isolate several distinct hardness annealing states, certain of which are associated with specific optical absorption bands and have been correlated with the thermal annealing of optical effects of radiation damage. The results obtained in cases where ionization is the primary effect of bombardment (particularly those in the case of low-energy, X-ray-induced hardness changes) demonstrate the significant role of excitons and photoelectrons in causing large changes in the physical properties of insulators, in contrast to radiation effects in other solid materials in which direct displacements or thermal spikes are chiefly responsible for lattice disorder and radiation damage. These effects of electronic excitation, which include the generation of isolated vacancies by dissociation from clusters and dislocations, processes discussed extensively by Seitz [2] and Markham [3], greatly complicate the problem of direct experimental determination of the number of displacements in alkali halides through their influence, for example, on such crystal properties as the ionic conductivity. Electronic effects such as these unfortunately must be considered to be among the primary causes of radiation damage in the alkali halides.

The materials studied in these experiments were Harshaw Chemical Company NaCl and KCl. Hardness measurements reported below were made with a Tukon tester, using the 136° indenter with a 50-gram load. Depth of indentation was 6.7×10^{-3} mm per filar unit of diagonal length. Since the diagonals averaged one to two filar units, the depths usually were greater than 10^{-2} mm. The indentation diagonals were oriented approximately in the [110] direction. Values of DPH given were

*Received August 21, 1953.

†The effect of low-energy X rays on hardness has just been reported by Y. Li in another letter to this journal (**1**, 1953) 455), who refers to a much earlier report of this effect in the Russian literature.

obtained from the averaged results of at least five widely spaced indentations, the variation among indentations being between one and two per cent, comparable to the limit imposed by the filar eyepiece. Indentations were rejected whose diagonals were not equal, which occurred near steps, cracks, or other inhomogeneities, and near the crystal edges.

The crystals were annealed on a massive copper block in a manually controlled oven, whose temperature, determined with an iron-constantan thermo-couple, was held constant within ±2°C. They subsequently were cooled on an aluminum slab at room temperature.

The diamond-point hardness of the unirradiated KCl used in these experiments is 9.4. The effects of X-ray and electron bombardment are shown in Figures 1 and 2: hardness increased due to both

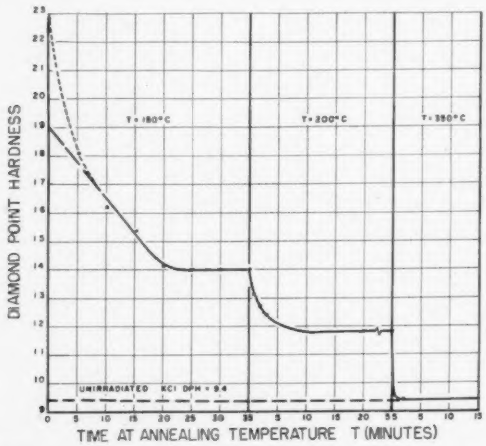

FIGURE 1. Thermal annealing of radiation-induced hardness in electron-bombarded KCl (1 Mev, $2\mu ah$ at 20°C).

irradiations by over 100 per cent. The early parts of the annealing curves, however, indicate a qualitative difference between the effects of the two kinds of irradiation.

Figure 1 illustrates the thermal annealing of KCl after bombardment at room temperature with approximately $2\mu ah$ of one Mev electrons. DPH is plotted *versus* time at 150° and subsequently at 200° and 350°C. An initial sharp drop at 150° is followed by an approximately linear decrease to a DPH of 14, after which no further perceptible annealing takes place at this temperature. The linear portion of the curve may be extrapolated back to a DPH in the neighborhood of 19.0 at zero time. The significance of this value is indicated by the curve for X-rayed KCl in Figure 2. (The X-ray source was North American Phillips type-32066 copper target tube operated at 50 kv and 20 ma, with the crystal immediately adjacent to the mica window.) After a half-day or less of X-irradiation under these conditions, both the F-center density and the associated hardness changes saturate, no further increases being observed. The crystal illustrated in Figure 2 was

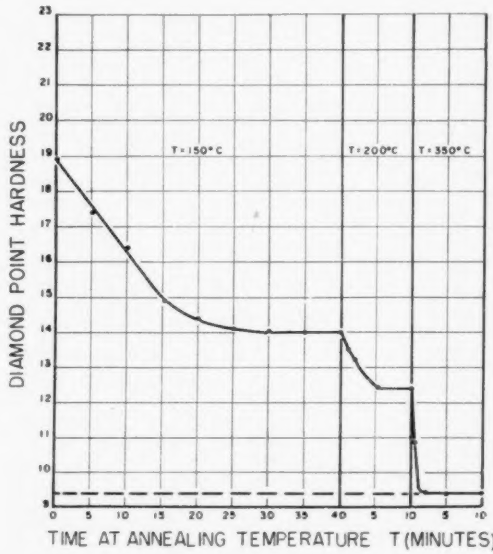

FIGURE 2. Thermal annealing of radiation-induced hardness in X-rayed KCl (50 kv, 20 ma, 16 hours).

exposed for 16 hours; one exposed for two days also yielded a maximum DPH of about 19.0, from which it may be inferred that this is a saturation value for the lattice defect configuration associated with the 150° annealing state. Exposure to light for one hour after the irradiation, which induced formation of M, R, N, and K centers in the colored crystal, had no observable effect on the hardness.

While direct ion displacements do not occur in the X-irradiated crystal, an appreciable number should be produced by one Mev electrons. Whether the defects thus produced remain frozen in the lattice at room temperature is not yet clear; it is evident, however, from the curve in Figure 1 that a relatively unstable configuration exists in electron-bombarded crystals which is not present in those damaged by X-rays. Thus far the only absorption peaks found to be present in electron-bombarded crystals which are absent in those X-rayed at room temperature are the V_1, N, and K bands [4]. One or more of these may be associated with the first annealing state in electron-bombarded crystals; experiments to determine this are planned.

The behavior of NaCl is similar to that of KCl, as indicated by Figure 3, which is the annealing curve for an electron-bombarded crystal. The point at zero annealing time and DPH 33.4 is the hardness of another crystal after 12 hours' exposure to the X-ray source. It lies on an extrapolation of the curve corresponding to the second annealing state in electron-bombarded NaCl, confirming the observations on KCl. The saturation value of the hardness in X-rayed crystals is approximately twice the original value, in both KCl and NaCl.

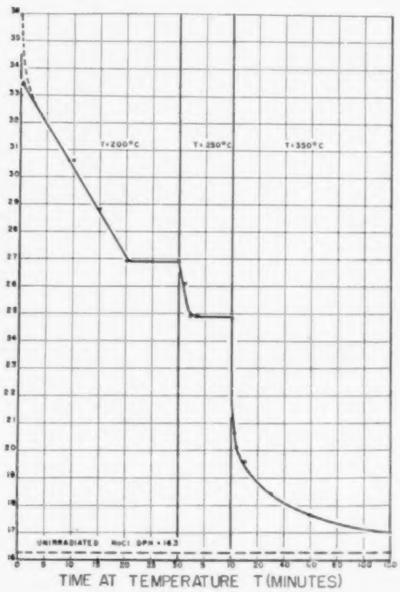

FIGURE 3. Thermal annealing of radiation-induced hardness in electron-bombarded KCl (1 Mev, 5*μah*, at 20°C).

The hardness change during the 150° anneal in KCl occurs simultaneously with complete disappearance of the F-band. The only absorption peak remaining both in X-rayed and electron-bombarded crystals is a previously discussed [4] temperature-insensitive band in the neighborhood of 750 *mμ*. This band is observed during thermal annealing of crystals colored by any of the presently known chemical or photochemical methods provided the initial density of F-centers is substantially greater than about $10^{17}/cm^3$; it has been variously attributed to subultramicroscopic colloidal particles [5] and to a new type of center [4] (Zwischenzentren). That the initial high hardness is not directly related to the presence of the F-band, however, is demonstrated by measurements on additively colored KCl, in which relatively high concentrations of F-centers due to additive coloring cause no hardness change whatever.

The hardness of the irradiated KCl crystals undergoing no further change at 150°C, the temperature was raised to 200°. A rapid decrease in hardness at this temperature, to a value still somewhat above that of the unirradiated crystals, was accompanied in both the electron-bombarded and X-rayed cases by disappearance of the remaining absorption bands; at the end of the 200° anneal the crystals were entirely clear. That this hardness change is directly related to the change in absorption is demonstrated by a hardness increase in additively colored crystals during thermal conversion at 150°C of the F-centers to the colloidal or Z-band. While the F-centers themselves produce no increase in hardness, thermal conversion of F-centers to the Z-band does so, to a degree proportional to the initial concentration of excess alkali metal. This procedure is entirely reversible; the hardness of an additively colored KCl crystal originally containing 2×10^{17} F-centers cm^{-3}, which is 9.8 when the absorption strength lies in the Z-band, returns to 9.4 in 15 seconds at 330°, together with complete reconversion to the F-band. The conversion $Z \rightarrow F$ takes 90 seconds in a crystal containing 6×10^{17} cm^{-3}, at the same temperature, the hardness changing from 10.9 to 9.4. It may be noted that while the reaction $Z \rightarrow F$ at 330° and the associated hardness change occur in a few seconds, even in the dark, the process $F \rightarrow Z$ at 150° requires about 10 minutes, in daylight, to reach equilibrium, after which no further changes in hardness is observed. The hardness change accompanying the transformation $F \rightarrow Z$ in daylight is a surface effect, the interior of the crystal which is not penetrated by an appreciable intensity of F-light, being unaffected. Furthermore, 40 minutes at 150°C had no observable effect either on the hardness or the optical absorption of a KCl crystal containing 2×10^{17} F-centers cm^{-3}, when the crystal was heated in the dark. The process does occur in the dark at this temperature but requires a much greater time as is demonstrated by the curves in Figure 4, obtained by inserting a furnace into the specimen compartment of a Beckman DU Spectrophotometer and taking absorption curves as the conversion progressed. (Thus far no evidence has been obtained of any difference between the final results of annealing in the light and in the dark, but further experiments are in progress to check this very important point.) The rapidity of the same process in the presence of light suggests that the thermally activated step in the transformation $F \rightarrow Z$ is

the ejection of an electron from the F-center trap,* a process relatively improbable at this temperature from the unexcited state but highly probable when the electron is in the excited level close to the conduction band.

A 10-minute anneal is sufficient to remove the 200° annealing state in KCl. The corresponding process was complete in two minutes at 250° in NaCl; no further change occurring in an additional

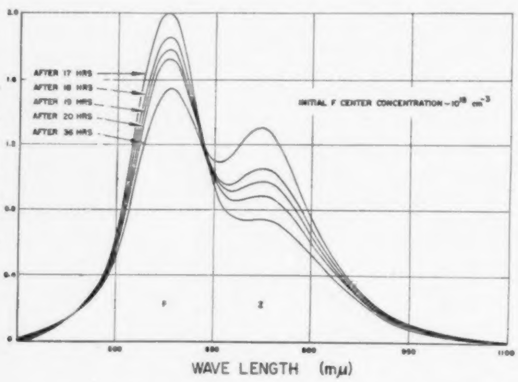

FIGURE 4. Thermal conversion of F-centers to Z-centers at 140°C (measured at 140°C).

eight minutes at 250°. No attempt was made to isolate further structure in the hardness annealing curves; both the NaCl and KCl crystals were given a final heat treatment at 350°C, whose results are shown in Figures 1, 2, and 3. Two minutes at 350° is sufficient to return the electron-bombarded KCl to its original hardness of 9.4 while two hours at this temperature brings the hardness of electron-bombarded NaCl to a value of 17.0, only slightly above the unirradiated value, 16.3.

There may be little lattice damage in all of the above cases. Much more severe damage may be expected in a rock salt crystal bombarded at liquid nitrogen temperature with a beam of 40 Mev alpha-particles. Fragments of such a crystal, bombarded in July, 1951 with 9.8 μah of 40 Mev alpha-particles in the Crocker Laboratory 60-inch cyclotron, were available for hardness measurements. These crystals had been stored at room temperature since the irradiation took place. Figure 5 shows the results of thermally annealing one fragment at 330°C. While the general shape of the curve is similar to those described above, the annealing process is quite different. The bombarded crystal, which was completely opaque to visible light originally, became completely clear during the first 15 seconds of the annealing period, during which there was no change in hardness. Thus all of the damage which annealed subsequently corresponds to that present in electron-bombarded

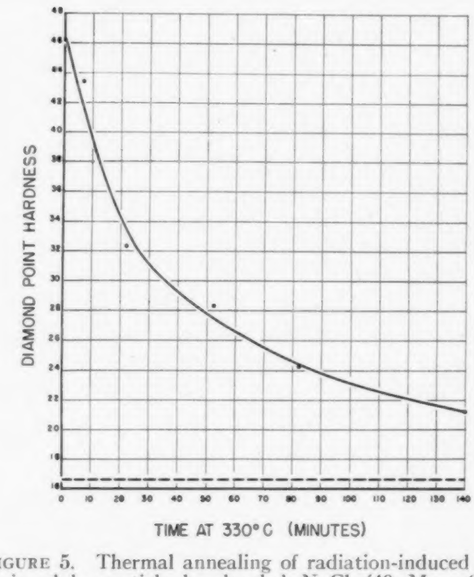

FIGURE 5. Thermal annealing of radiation-induced hardness in alpha-particle bombarded NaCl (40 Mev, 9.8μah at −170°C).

NaCl after complete removal of the 200° and 250° annealing states. Points taken after the first 40 minutes at 330° fit a (time)[1] curve, suggesting a diffusion-limited annealing process. Further experiments are necessary to verify this interpretation.

This work was done under the Atomic Energy Commission Contract AT-11-1-GEN-8.

D. R. WESTERVELT

North American Aviation, Inc.
Atomic Energy Research Department
Downey, California

*This observation has been reported by Scott, Smith, and Thompson at the Symposium on Impurity Phenomena at the Knolls Laboratory, June 18–20, 1953. An additional possibility is that the thermally activated step involves the excited state rather than the ionized or dissociated state of the F-center. Some early work by Mollwo on coagulation of color centers in an electrical field makes this seem less probable, however.

References

1. VAUGHAN, W. H., LEIVO, W. J. and SMOLUCHOWSKI, R. Phys. Rev. **91** (1953) 245.
2. SEITZ, F. Rev. Mod. Phys. **18** (1946) 384; Phys. Rev. **80** (1950) 239; Rev. Mod. Phys. **23** (1951) 328; Adv. in Phys. **1** (1952) 43.
3. MARKHAM, J. J. Phys. Rev. **88** (1952) 500.
4. WESTERVELT, D. R. NAA-SR-221, 117 (1952); Phys. Rev. **91** (1953) 218.
5. SCOTT, A. B. and SMITH, W. A. Phys. Rev. **83** (1951) 982.

Notes on Geisler's Theory of Phase Transformations, with Special Reference to Indium-Thallium Alloys*

Geisler [1] has recently proposed that martensitic transformations should be regarded as accompanied by strains, rather than generated by them. In discussing the validity of this concept, we shall refer especially to the indium-thallium transformation, which he uses as one example. According to the previously accepted two-shear theory [2], there are eight possible tetragonal orientations in a given set of main bands, four for each direction of the "first" shear.† These eight orientations are all different from those in a set of main bands at 90 degrees to the first set, but main bands at 60 degrees contain one common orientation. There are thus 36 different tetragonal orientations which may be produced from one cubic crystal: in 12 of these orientations the "second" shear† has magnitude 2ϵ, and the remaining 24, 4ϵ.

The relation between cubic and tetragonal lattices may be represented as a single homogeneous deformation for each tetragonal crystal. The positions of the atoms in the cubic lattice may be specified by,

$$\mathbf{r} = \tfrac{1}{2}m_i\mathbf{e}_i \ \ (i = 1,2,3)$$

where the vectors $\mathbf{e}_i$ are of length a, and define the cubic unit cell, and m_i are integers such that $\sum_i m$ is even. The summation convention is used. After transformation the atoms lie at points

$$\mathbf{r}' = \tfrac{1}{2}m_i\mathbf{e}'_i$$

where the tetragonal cell is defined by the vectors $\mathbf{e}_i'$. The relation between $\mathbf{e}_i'$ and $\mathbf{e}_i$ may be written

$$\mathbf{e}_i' = \mathbf{M}\mathbf{e}_i.$$

If we use the two shear mechanism, the matrix $\mathbf{M}$ for a transformation $(101)\ [10\bar{1}]\ 2\epsilon$, $(110)\ [1\bar{1}0]\ 2\epsilon$ was shown by Bowles and coworkers [2] to be

$$\mathbf{M} = \begin{pmatrix} 1 + 2\epsilon + 2\epsilon^2 & -\epsilon - \epsilon^2 & -\epsilon - \epsilon^2 \\ \epsilon + 2\epsilon^2 & 1 - \epsilon - \epsilon^2 & -\epsilon^2 \\ \epsilon & 0 & 1 - \epsilon \end{pmatrix}$$

From this matrix it follows (a) that the $[1\bar{1}\bar{1}]$ direction is unrotated and undistorted, (b) that the $[01\bar{1}]$ $[2\bar{1}\bar{1}]$ directions are unrotated if ϵ^2 is neglected in comparison with ϵ. Since $\epsilon \simeq 0.01$, this is justified. These three directions then define three unrotated planes, which are (111), $(01\bar{1})$ and (211).

Geisler begins with the assumption that the coherent nuclei form on (111) planes according to the relation $(111)_C \parallel (111)_T$, $(1\bar{1}0)_C \parallel (1\bar{1}0)_T$. This relation is obviously consistent with that derived above. The 4 $\{111\}$ planes each contain 3 $\langle 110\rangle$ directions giving 12 parent orientations. These correspond to the 12 orientations obtained by a second shear of 2ϵ. The remaining tetragonal orientations are obtained by twinning the parent orientations. In order to explain the experimental pole figure, Geisler assumes that only two of the four possible twins of each parent are formed. Although he does not state so explicitly, these are twins on the two $\{101\}$ planes which have a $\langle 101\rangle$ direction in common with the $\{111\}$ conjugate plane. Thus for the parent orientation used above, the two possible twinning planes are $(101)_T$ and $(011)_T$. With these assumptions, the 36 possible tetragonal orientations correspond exactly with the two shear mechanism. The more detailed description of Geisler's theory, however, contains some errors and inconsistencies.

Geisler states that a set of main bands contains 4 parent orientations and 8 twins, giving 12 orientations in all. This is incorrect. Although each parent may form two twins, only one twin is present in each of the two sets of main bands which may contain the parent. Thus with the orientations above, the parent and the (101) twin are present in main bands parallel to (011), and the parent and the (011) twin in the main bands parallel to (101). That this must be so follows (a) from the experimental work of Bowles *et al* [2], who plotted the pole figure from a single set of main bands, (b) from the observation that if two sets of sub-bands are present in one main band they are on $\{101\}$ planes at 90 degrees to each other, whereas the two possible twinning planes of any parent orientation are at 60 degrees to each other, (c) from strain energy considerations. It may be readily shown, and is indeed physically obvious, that the parent orientation above and its (110) twin will give zero macroscopic strain on the (011) plane, but not on any other $\{101\}$ plane.

The error in Geisler's presentation may be circumvented, but the whole theory then becomes much less plausible. In his Figure 4, the top portion of the diagram, showing main bands containing single sets of sub-bands, is still correct: we also wish to emphasise that the macroscopic tilt between

---

*Received August 27, 1953.

†We use the terms "first" and "second" purely for convenience: they are not meant to imply any physical resolution of the atom movements into two components.

the cubic surface and the main band *P*-1, *T*-1 is identical with that between the surface and the main band *P*-3, *T*-3, and similarly for the other two main bands. The part of the diagram showing two sets of sub-bands in one main band is incorrect. The figure implies that *one* main band contains only three distinct orientations, and that there are four such main bands possible. The correct description is that one main band may contain orientations *P*-1, *T*-1, *P*-3, *T*-3, and the other *P*-2, *T*-2, *P*-4, *T*-4. A main band containing *P*-1, *T*-1, *T*-5 (or *P*-3, *T*-7, *T*-3) would have a macroscopic tilt about the intersection of the sub-bands, which is both energetically very unlikely and experimentally unobserved. Such a set of orientations would form, in fact two interpenetrating main bands.

If we reject the inconsistencies of the original description, we are left with a possible mechanism for growth of the tetragonal phase, but this now requires that a main band containing two sets of sub-bands should result from the chance amalgamation of two different parent nuclei and one each of their twins. Although single sets of sub-bands are observed more readily than double sets, this process is obviously implausible, especially when the occurrence of parallel colonies of such main bands is considered.

Geisler ascribes little crystallographic significance to the main bands. In experiments on single and double interface transformation in indium-thallium alloys [3], however, we have observed that the interface always maintains a highly crystallographic character, and is plane, except possibly on an atomic scale. The reason for this is that the strain energy can then be made quite small, if the twins have thickness ratio 2:1. In order to minimise the strain energy in this way, it is clear that the tetragonal lattice must be finely twinned near to the interface: the observable twins in fact result from a coarsening of the original twin structure [3]. In discussing his theory, Geisler proposes that motion of the main band perpendicular to its plane results from the simultaneous growth of parent and twin. If by this he implies that the parent and twin both extend to the interface, we agree that this provides a valid description of the growth. The atom movements, however, are then identical with those in the two shear process, since they must be coordinated one after another to give the observed surface tilts. We do not think that it is then meaningful to distinguish growth by atom jumps from growth by shear process: since the atom jumps constitute a system of shears it is perfectly valid to regard the structure as *generated* by shear.

We believe that this criticism also applies to Geisler's general theory, and to related theories such as the atom-by-atom growth mechanism of Fisher, Hollomon and Turnbull [4]. Once a macroscopic region of marensite product has formed, the surface tilts must be produced by some pattern of deformation. If the agents of this deformation (slip dislocations, twin boundaries, etc.) lie in the transformation interface, there is minimum strain energy, but the description of the growth of the phase by coherent atom movements is exactly equivalent to a double strain or similar mechanism. If the deformation pattern does not extend to the interface, the experimental results are not fully explained. There will be large strains at the interface: in addition, phenomena such as the reversibility reported by many workers (most recently by Newkirk and Geisler [5]) would not be expected, since plastic deformation is generally irreversible.

We may summarize our views by stating that Geisler's growth mechanism for indium-thallium is incorrect; by suitable modification it may be made to agree with experiment, but it then becomes indistinguishable from the two shear mechanism. This criticism in no way invalidates the possibility that nucleation of the tetragonal phase may result from the formation of coherent platelets on {111} planes. The growth of such nuclei and their twins might originally require thermal activation energy for individual atomic movements, but would degenerate into a shear process as soon as a critical size was reached. Nuclei retained athermally by cooling from a higher temperature would grow spontaneously as soon as they became supercritical.

Analogies between martensitic reactions and crystal growth from the vapour have often been made. In martensitic reactions with rational habit planes, and in most examples of mechanical twinning, the edge of an incompletely formed plane is a transformation or twinning dislocation, and may be compared with the atomic step in a crystal growing from the vapour. When the incomplete plane reaches a certain size, the transformation dislocation will glide with little or no thermal activation, spreading the martensite structure over the whole atomic plane. There is thus a formal analogy with the crystal growth problem, the main difference arising from the elastic coupling between the

phases in the martensitic reaction. The atom by atom theories (if they are at all distinguishable from the dislocation theories) must require the formation of a new two-dimensional nucleus on each succeeding atomic plane. The kinetics of the transformations do not support this interpretation, and in particular the formation of macroscopic regions of homogeneous strain would not be expected. Thus in the transformation in cobalt, the very large strain energy due to the homogenous shear could be reduced by shearing randomly in the three equivalent $\langle 112 \rangle$ directions of a $\{111\}$ plane [6], and this would be expected since the two-dimensional nucleus for each of these movements has identical energy of formation. Similarly, the transformation in indium-thallium could proceed by much more frequent reversal of the first shear. The existence of macroscopic surface tilts is strong evidence that the characteristic of martensitic reactions is the growth *mechanism* and not the energetics of growth. This is the opposite conclusion to that reached by Geisler. The dislocation node theory of twinning and transformations, developed by Cottrell and Bilby [7] and by Bilby [8] is the analogue of Frank's theory of crystal growth, and allows growth at much smaller degrees of super-cooling. Finally, if the habit plane is irrational, the crystal can advance rapidly into the matrix without the need for a generating node. In the crystal growth problem, the irrational planes are rapidly removed, but if the parent phase is solid, the elastic energy forces the interface to remain irrational, and growth is by motion of the whole dislocation array.

Z. S. Basinski and J. W. Christian

The Inorganic Chemistry Laboratory
Oxford University, England

References

1. Geisler, A. H. Acta Met. **1** (1953), 260.
2. Bowles, J. S., Barrett, C. S. and Guttman, L. Trans. A.I.M.E. **188** (1950), 1478.
3. Basinski, Z. S. and Christian, J. W. Submitted to Acta Met.
4. Fisher, J. C., Hollomon, J. H. and Turnbull, D. Trans. A.I.M.E. **185** (1949) 691.
5. Newkirk, J. B. and Geisler, A. H. Acta Met. **1** (1953) 370.
6. Anantharaman, T. R. and Christian, J. W. Phil. Mag. **43** (1952) 1338.
7. Cottrell, A. H. and Bilby, B. A. Phil. Mag. **42** (1951) 573.
8. Bilby, B. A. Phil. Mag. **44** (1953) 782.

Magnetic and Crystallographic Studies on the Higher Antimonies of Iron, Cobalt and Nickel*

As a continuation of a previous investigation on the system chromium-antimony [1] the higher antimonides of iron, cobalt and nickel were studied by magnetic, X-ray, and optical goniometer methods.

The alloys were prepared by heating and annealing a calculated mixture of the two components in evacuated and sealed quartz tubes. In the range 50–100 atomic per cent antimony the following intermediate phases were found: $FeSb_2$, $CoSb_{2-x}$, $CoSb_3$ and $NiSb_{2+x}$ ($x = 0.1$–0.2). Of these $CoSb_3$ has not been reported previously.

The diantimonides all have the marcasite structure (space group V_h^{12} — Pnnm). From X-ray diffraction diagrams taken on single crystals, and, in the case of $NiSb_{2+x}$, from powder diagrams, the unit cell dimensions and independent atomic parameters u and v were determined (see Table I).

TABLE I

Crystallographic Properties of the Investigated Compounds

Compound	**a***	**b***	**c***	**u**	**v**	Me-Sb*	Sb-Sb*	Density
$FeSb_2$	5.83	6.55	3.204	0.188	0.355	2.59	2.90	—
$CoSb_{2-x}$	5.596	6.373	3.370	0.195	0.360	2.55	2.82	8.24
$NiSb_{2+x}$	5.180	6.314	3.838	0.22	0.36	2.56	2.87	7.85
$CoSb_3$ (cubic)	9.036	—	—	0.343	0.157	2.56	2.85	7.62
CoSb (hexagonal)	3.880	—	5.185	—	—	2.58	—	—

*Lattice constants and interatomic distances are given in metric A-units.

The axial ratios of $FeSb_2$ and of $CoSb_{2-x}$ were confirmed by optical goniometer measurements on single crystals.

Cobalt triantimonide has the cubic skutterudite structure (space group T_h^5 — I m3) with the unit cell edge and parameter values as given in Table I. From the lattice constants and parameter values the interatomic distances in all compounds were determined.

The density of three of the compounds was measured by a vacuum pyknometric method,

*Received August 31, 1953.

see Table I. By comparing the observed and the calculated densities it seems most likely that $CoSb_{2-x}$ is a substitutional solid solution where cobalt replaces antimony in the crystal structure. $NiSb_{2+x}$ has probably a structure with vacant nickel positions.

The magnetic susceptibilities were measured by the Gouy cylinder method. The magnetic properties of iron diantimonide are shown in Figure 1. They

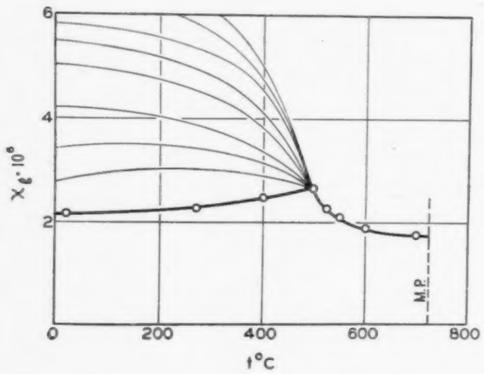

FIGURE 1. Magnetic susceptibility of $FeSb_2$. Heavy curve: quenched from 7000°C (paramagnetic) Fine curves: cooled slowly (ferromagnetic).

may be described as an antiferromagnetism superimposed by a weak and variable ferromagnetism. The ferromagnetic Curie point coincides with the antiferromagnetic transition point, 500°C. The heavy curve in Figure 1, which describes the antiferromagnetic state, was obtained for samples quenched from 700°C. The fine curves which describe the superimposed ferromagnetism were obtained for slowly cooled samples.

Between -183°C and 450°C the other compounds all showed weak, temperature-independent para- or diamagnetism as follows: $CoSb_{2-x}$: $\chi_g = +0.1 \cdot 10^{-6}$; $CoSb_3$: $\chi_g = +0.1 \cdot 10^{-6}$; $NiSb_{2+x}$: $\chi_g = -0.1 \cdot 10^{-6}$. The same was found to be the case for cobalt mono-antimonide, CoSb: $\chi_g = 1.0\text{–}1.1 \cdot 10^{-6}$.

The magnetic values were corrected for induced diamagnetism by the following amounts: Sb: $\chi_{mol} = -0.95 \cdot 10^{-4}$; Fe: $\chi_{mol} = -10 \cdot 10^{-4}$, Co: $\chi_{mol} = -0.15 \cdot 10^{-4}$ and Ni: $\chi_{mol} = -0.20 \cdot 10^{-4}$. From the corrected values for the molar susceptibilities the effective magnetic moments, μ_{eff} in Bohr magnetons, were calculated by the equation $\mu_{eff} = 2.84 \sqrt{\chi_{mol} \cdot T}$. The results obtained are shown in Figure 2.

The magnetic measurements were undertaken in order to find out whether the interatomic bonds in these compounds are mainly ionic, and derived from an ideal scheme Me^{4+}, $(Sb_2)^{4-}$, or whether the bonds are covalent, and formed by the d^2sp^3 orbitals of the metal atoms and the sp^3 orbitals of the antimony atoms. The latter bond model has

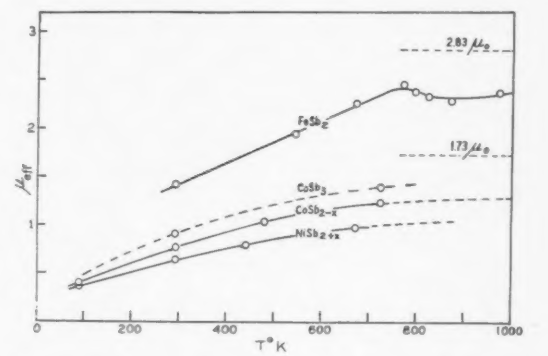

FIGURE 2. Effective magnetic moments of the iron, cobalt and nickel diantimonides (in Bohr magnetons).

been suggested by Pauling and Huggins [3] for compounds with pyrite, marcasite and skutterudite structures.

In Table II are listed theoretical values for the magnetic moments and the interatomic distances which are to be expected for the ionic as well as the covalent bond model. With the exceptions of the distances between neighbouring antimony

TABLE II

THEORETICAL MAGNETIC MOMENTS AND INTERATOMIC DISTANCES FOR IONIC AND COVALENT BONDS

Compound	Magnetic moment		Interatomic distances			
			ionic		covalent	
	ionic	covalent	Me-Sb	Sb-Sb	Me-Sb	Sb-Sb
$FeSb_2$	4.90	2.83	≃3.0	2.82	2.56	2.72
$CoSb_2$	5.92	1.73	"	"	2.57	"
$NiSb_2$	4.90	0.00	"	"	2.57	"
$CoSb_3$	4.90	0.00	"	"	2.57	"

atoms, the experimental results are best fitted by the covalent bond model. The small deviations between observed and theoretical magnetic moments and between observed and calculated values for the Sb-Sb distance are regarded as a result of a transition towards metallic binding, whereby some of the valency electrons are promoted to an electron gas or conduction band.

By decreasing temperature the unsaturated electron spins in the iron and cobalt diantimonides

interact antiparallel, and, in the case of iron diantimonide a pronounced antiferromagnetic state exists below 500°C. High-temperature X-ray studies on this compound showed that the thermal expansion coefficient along the *c*-axis is about $2.5 \cdot 10^{-5}$, whereas it is about $0.2 \cdot 10^{-5}$ along the *a*- and *b*-axis. This is regarded as a result of the loosening of the antiferromagnetic interaction in the *c*-direction with increasing temperature. It has not been possible to decide, however, whether the antiferromagnetic interaction occurs directly between neighbouring iron atoms in the *c*-direction, or whether the neighbours in the *c*-direction form ferromagnetic rows, which again are coupled antiparallel with each other. In the latter case the small superimposed ferromagnetism might be regarded as a result of a slight disorder in the stacking of ferromagnetic rows. It may also be the result of an ordered arrangement of lattice defects in the way Nèel has suggested for hematite and pyrrhotite [3].

The interaction between uncompensated electron spins are regarded as mainly responsible for the length of the *c*-axis. The increase of this unit cell edge in the sequence $FeSb_2$ to $NiSb_2$ corresponds to a decrease in the number of uncompensated electron spins from about two to about zero. Surveying all known compounds with marcasite structure it is found that a short *c*-axis (loellingite group with $c/b \approx 0.50$) is found for compounds with one or two uncompensated electron spins, whereas a long *c*-axis (marcasite group with $c/b \approx 0{\cdot}62$) is found for compounds with no, or practically no, uncompensated electron spins.

According to Körber and Oelsen [4] the heat of formation of the diantimonides increases in the sequence $FeSb_2$ to $NiSb_2$. The higher stability of the nickel compound may be regarded as a result of the closely filled electron orbitals as compared to the cobalt and iron compounds which have incompletely filled electron orbitals. Similarly, the fact that cobalt is the only one of the three metals which forms a triantimonide is regarded as a result of this compound being the only triantimonide with closely filled electronic orbitals.

A detailed communication on this investigation is in print at "N.T.H.-Trykk," Trondheim, Norway, and will be supplied from The Department of Metallurgy on request.

Acknowledgement

This investigation was carried out partly in the laboratories of Professor H. Haraldsen, Department of Chemistry, University of Oslo, and partly at the Institute for the Study of Metals, University of Chicago. Financial support has been received from The Norsk Hydro's Fond.

TERKEL ROSENQVIST

Department of Metallurgy, N.T.H.
Trondheim
Norway

References

1. HARALDSEN, H., ROSENQVIST, T. and GRÖNVOLD, F. Archiv Math. og Naturvidensk. B. L. No. 4 (1948).
2. PAULING, L. and HUGGINS, M. L. Z. Krist. **87** (1934) 205.
3. NÈEL, L. Proc. Phys. Soc. **65**(**A**) (1952) 869.
4. KÖRBER, F. and OELSEN, W. Mitt. Kaiser Wilh. Inst. Eisenforsch. **19** (1937) 209.

Comment on Paper by Tiller, Jackson, Rutter and Chalmers*

In a recent paper in this Journal [1], W. A. Tiller, K. A. Jackson, J. W. Rutter and B. Chalmers discussed solute segregation during solidification from the melt, for the case where diffusion is the only mixing process in the liquid. They have made a valuable addition to the mathematics of segregation by treating the opposite extreme from the case of complete mixing in the liquid, previously considered by others. The purposes of this note are to indicate the nature of the equations which govern in the intermediate range, where mixing in the liquid is incomplete but nevertheless greater than attained by diffusion alone, which range encompasses nearly all situations met in actual practice, and also to discuss certain assumptions in the above paper.

The parameter of chief interest is the effective distribution coefficient, k_{eff}, defined as the ratio of solute concentration in the just-freezing solid to that in the main body of the liquid. For the diffusion-limited case, as solidification proceeds, k_{eff}, rises (for $k < 1$) steadily from its equilibrium value, denoted simply as k, and asymptotically approaches unity. For complete mixing (no enriched layer), k_{eff} remains at the value k. It can be readily shown that in the presence of partial mixing, caused by convection or stirring, k_{eff} approaches a constant value between k and unity. Hence, as has been indicated [2], the normal freezing and zone-melting equations derived for

*Received September 26, 1953.

the case of complete mixing are equally valid in the case of partial mixing, except for a short transition region at the beginning of the ingot, provided that the appropriate value of k_{eff} be used. It is not, as the authors imply, necessary that complete mixing be achieved for such equations to be valid. Theory and experiment for k_{eff} are described by Burton, Slichter and Prim [3], and by McFee [4]. In this connection the work of Hall [5] on solutes in germanium suggests that transport processes at the solid-liquid interface as well as those in the liquid influence the value of k_{eff}.

With respect to single-pass zone-melting, the liquid distribution C_L of Figure 14 appears to neglect diffusion at the leading interface of the molten zone as C_L should have the value C_0 at this point. With respect to zone-refining, we question the statement that the optimum zone length for purification is given by conditions (18), for the reason that these conditions were derived for the poorest possible experimental situation for doing zone-refining, namely, the absence of convection or stirring.

P. Pfann

Bell Telephone Laboratories, Inc.
Murray Hill
New Jersey

References

1. Tiller, W. A., Jackson, K. A., Rutter, J. W. and Chalmers, B. Acta Met. **1** (1953) 428.
2. Pfann, W. G. Trans. A.I.M.E. **194** (1952) 747.
3. Burton, J. A., Slichter, W. P., and Prim, R. C. "Distribution of Solutes in Crystals Grown from the Melt," J. Chem. Phys. (November, 1953).
4. McFee, R. H. J. Chem. Phys. **15** (1947) 856.
5. Hall, R. N. Phys. Rev. **88** (1952) 139.

Strain Markings in Alpha-Brass*

In a recent paper, D. K. and H. Wilsdorf [1] suggest that the possibility of producing strain markings on a deformed crystal depends on whether or not the original slip markings had an "elementary structure." They argue that strain markings cannot be etched out on pure metals because the existence of the elementary structure makes the slip-line density so high that the etch is non-selective. Alpha-brass does not exhibit an elementary structure and therefore its relatively widely spaced slip-bands can be selectively etched.

The above explanation of strain-markings assumes that the material at slip planes in both pure metals and alpha-brass is somehow different from the unslipped matrix. However, this assumption does not seem to be entirely justified in the case of pure metals. On the other hand it does seem to be justified in the case of alpha-brass and thus explains why etching produces strain markings in this and probably other alloy crystals.

As Fisher [2] has pointed out, the act of slip in an alloy crystal changes the short-range order pattern across the slip plane. This accounts for part of the strength of alloy crystals and, since it would be expected to change the chemical potential at a slipped plane. it may account for the appearance of strain markings upon etching.

J. J. Gilman

Metallurgy Research Department
General Electric Company
Schenectady, New York

References

1. Wilsdorf, D. K. and Wilsdorf, H. Acta Met. **1** (1953) 394.
2. Fisher, J. C. Acta Met. **2** (1954).

Nuclear Composition—A Factor of Interest in Nucleation*

Nucleation in the solid state is a very complicated process. Therefore, theoretical investigations in this field deal with simplified models. Some factors are examined while other factors are neglected. A factor that is usually neglected is the uncertainty of the nucleus composition. It is not necessarily true that the nuclei which form most readily have the composition appropriate for the precipitate, when equilibrium has been established. In the present note this point will be examined, on the assumption that many other factors can be neglected.

Gerlach [1] has found that the precipitate in an Au-rich Au-Ni-alloy has a higher Au-content at the beginning of precipitation than later. Scheil [2] has explained this by starting from the assumption that the surface tension of a nucleus depends on its composition in a specified manner. A thermodynamic treatment could be carried out, which showed that the probability should be greatest for formation of nuclei with higher Au-content than that of the equilibrium precipitate. Thus, under this assumption about the surface

*Received October 1, 1953.

*Received August 31, 1953.

tension the nucleus should exhibit a composition between that of the parent phase and that of the equilibrium precipitate. In the present paper a thermodynamic treatment will be carried out under the assumption that the surface tension of the nuclei is independent of composition.

Figure 1 shows curves of the Gibbs free energy per mole for two phases (I and II) in a binary system. A and B are the two components. Suppose that a homogeneous specimen of phase I has the composition x_0. Its free energy per mole is represented by the point o. The tangent in the point o gives, by its two intercepts at A and B, the values of the chemical potentials μ_A° and μ_B° for this composition. The chemical potential is defined by $\mu_A = \frac{\partial G}{\partial n_A}$, where G is the Gibbs free energy of the specimen and n_A is the number moles A. Absolute chemical activity, λ, can be obtained by the definition $\mu_A = RT \ln \lambda_A$.

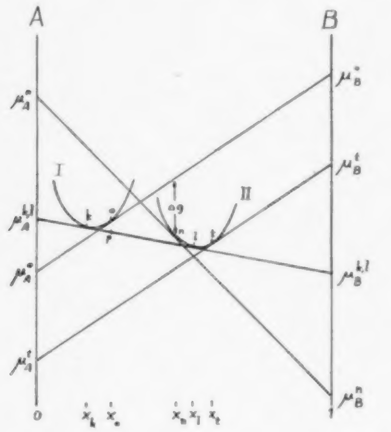

FIGURE 1. Free-energy diagram. The point o represents the parent phase. x_t is the thermodynamically most favourable nuclear composition.

The free energy of the specimen can be lowered as far as the point p, if the homogeneous specimen is split into one part of composition x_k and structure I and another part of composition x_l and structure II. Thus it is evident that a precipitation of phase II should be expected on thermodynamic grounds. Before the precipitation can take place, the nucleation troubles must be overcome. For this reason the precipitation process is very slow at the beginning. One is therefore justified in assuming that the nucleus at the beginning of precipitation is surrounded by parent phase of unchanged composition. Then the formation of a nucleus with the composition x_n involves transferring of the mole fraction x_n B-atoms from a state with the chemical potential for B equal to μ_B° to a state with the value μ_B^n. The mole fraction $(1 - x_n)$ A-atoms are transferrred from μ_A° to μ_A°. The free energy decrease per mole nucleus is consequently $(1 - x_n)(\mu_A^\circ - \mu_A^n) + x_n(\mu_B^\circ - \mu_B^n)$. From the geometry of Figure 1 it is easy to see that this free-energy decrease is represented by the vertical distance Δg if the point n represents the free energy of the nucleus.

Unfortunately, the point n does not represent the free energy of the nucleus. The curves in Figure 1 hold only for large units of the phases. Because of the additional contribution to the free energy from the surface tension, a small nucleus of phase II, surrounded by phase I will have higher free energy per mole than curve II shows. Thus, formation of the nucleus n will not involve the free-energy decrease Δg. (Stresses, if present, will also contribute to the free energy, but are neglected in this paper.) This is indeed the reason why the precipitation is very slow at the beginning. Under our assumption that the surface tension is independent of the composition, its counteracting effect is overcome most easily at that composition, which gives the largest Δg. This thermodynamically most favourable nucleus composition, x_t, can be obtained by drawing a tangent to curve II parallel with the tangent through the point o, representing the parent phase. Hence for this composition, x_t, one has

$$\overset{\circ}{\mu}_A - \mu_A^t = \overset{\circ}{\mu}_B - \mu_B^t$$

$$\frac{\overset{\circ}{\lambda}_A}{\lambda_A^t} = \frac{\overset{\circ}{\lambda}_B}{\lambda_B^t}$$

It should be noted that the creation of the most favourable composition for phase II nucleation involves a larger composition change from the parent phase than the creation of the equilibrium phase II composition. The more supersaturated the parent phase is, the more far away lies the most favourable composition.

In a ternary system the thermodynamically most favourable nuclear composition x_t isobtained by means of two parallel tangent planes. In systems of more than three components a corresponding treatment is possible, although it is not easily illustrated geometrically. The same relationships as in a binary system will still hold.

$$\frac{\overset{\circ}{\lambda}_A}{\lambda_A^t} = \frac{\overset{\circ}{\lambda}_B}{\lambda_B^t} = ---- = \frac{\overset{\circ}{\lambda}_K}{\lambda_K^t}$$

Figure 1 shows that the equilibrium state

$(k + l)$ has lower chemical potential for $B(\mu^{k,l})$ than the original specimen (μ_B°). However, the equilibrium state has higher chemical potential for $A(\mu^{k,l})$ than the original specimen (μ_A°). If the growth of phase II takes place successively, atom by atom, which is not necessary, one can wonder how phase II has been able to receive A-atoms at all. These atoms have not, by themselves, moved from a state with low potential to a state with higher. By means of the thermodynamically most favourable nuclear composition one can give a satisfactory description of the process. When a nucleus of the favourable composition has become large enough, passed the critical size, it has lower potential for both of the components than the parent phase. Thus it can grow by receiving both kinds of atoms. Gradually the decrease of B-content in the parent phase becomes appreciable and its composition is displaced to the left and finally reaches x_k. During this process the chemical potential for A in the parent phase is raised to $\mu_A{}^{k,l}$). The nuclear composition is displaced at the same time and this finally reaches x_l. This shift takes place in such a way that all the time both potentials are lower than in the parent phase, surrounding the new phase.

We have found that an increased supersaturation in the parent phase favours nuclear compositions which lie far from that of the parent phase. In the same way an increased supersaturation in the parent phase will also favour the nucleation of phases, the compositions of which lie far from that of the parent phase (Figure 2). A sample that from the beginning consists of phase I of composition x_0 will in equilibrium contain a separated phase II of composition x_l and phase I will have adjusted its composition to x_k. Before the separation has had time to change the composition x_0 of the parent phase, however, the formation of another phase (III) will cause a greater decrease of the free energy per mole of separated phase. The figure shows that the further to the right phase III lies, the more it will be favoured by supersaturation of the parent phase.

A carbon-rich carbide can be formed in the first stage of separation both from martensite [3] and from supersaturated ferrite [4]. The cementite does not come until later, and the carbon-rich carbide is then dissolved. Since the carbon content of this carbide is higher than that of the cementite, the reason for its formation may very well be that outlined above. It is probable that graphite nuclei can be formed much more easily from martensite than from ferrite which is in equilibrium with cementite. This may also be taken as an example of the fact that increased supersaturation increases the tendency to formation of phases with "distant" composition.

On cooling of an unalloyed cast-iron melt either cementite or graphite may be formed. Then according to the above argument, an increased supersaturation of carbon in the melt should at every temperature favour the formation of graphite more than of cementite and thus increase the tendency to grey solidification. That is the case, too. This can, however, be explained in other ways [5].

Let the curves I, II and III of Figure 2 represent the free energy of melted cast iron, cementite, and graphite. It is quite evident that if the free-energy curve of the melt had lain further to the left, an increased supersaturation of carbon in the melt would not have misfavoured the formation of cementite compared with that of graphite to so high a degree as is now the case. It is therefore conceivable that an alloying element which has this effect of displacing the free-energy curve of the melt can thereby increase the tendency to white solidification. It is not altogether inconceivable that this may be a reason why so-called phosphide-eutetic, steadite, solidifies white.

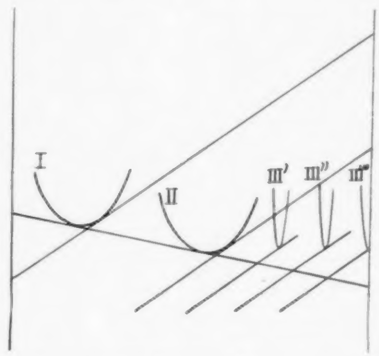

FIGURE 2. Free-energy diagram. The point o represents the parent phase. Phase III becomes more favored the more to the right it lies.

MATS HILLERT

Metallografiska Institutet
Stockholm, Sweden

References

1. GERLACH, W. Z. Metallk. **40** (1949) 281.
2. SCHEIL, E. Z. Metallk. **43** (1952) 40.
3. JACK, K. H. J. Iron and Steel Inst. **169** (1951) 26.
4. TSOU, A. L., NUTTING, J. and MENTER, J. W. J. Iron and Steel Inst. **172** (1952) 163.
5. HILLERT, M. Carbon activity in alloyed iron-carbon systems (to be published).

BOOK REVIEW

Modern Research Techniques in Physical Metallurgy. Cleveland, Ohio: American Society for Metals. Pp. 335.

Science advances by the perception of new theoretical ideas and the discovery of new facts. Both these ways helped to develop physical metallurgy from a merely descriptive to a quantitative science during the fifteen years from about 1920 to 1935. During that period the electron theory provided an explanation of the electrical and magnetic properties of metals, and the dislocation hypothesis gave the clue to the explanation of their mechanical properties, whilst the application of X-ray diffraction methods and the use of large single crystals yielded results of physical significance. The last fifteen years or so have seen a refinement both in theory and in experimental techniques leading to consolidation and detailed extension of the basic structure. Usually prominence is given to theoretical developments and not sufficient attention is paid to the introduction of new techniques, although these are particularly important during the present phase in which more accurate measurements are required in many fields.

The volume under review contains papers and discussions of the annual seminar of the American Society for Metals held in Philadelphia during October 1952. The papers deal with research methods but emphasis is placed on the kinds of information that can be obtained.

Kehl, in his article on Optical Microscopy treats phase contrast microscopy and the reflecting-type objective thoroughly and critically. He is doubtful about the wide applicability of the former technique but stresses its usefulness for investigations of surface irregularities such as those caused by surface finishing, relief polishing and plastic deformation.

Field Emission Microscopy is described by Müller. In this method magnifications up to 500,000 times are obtained by placing the specimen in the form of a fine needle in an evacuated tube pointing to a fluorescent screen and applying a high voltage between the needle point and an anode. Electrons are emitted from the specimen and an image is obtained on the screen. Migration of crystal boundaries, condensation and adsorption phenomena are those to which the method has been applied; the building up of mono-molecular layers which cannot be observed with the conventional electron microscope has been shown by the new technique.

Heidenreich discusses Electron Diffraction and Microscopy of Metals. The techniques used are briefly summarized as they are well known, but the collection of examples is of great metallurgical interest.

Barrett restricts his review of X-ray Diffraction Techniques to improvements in the design of X-ray tubes (to produce beams of high intensity), in monochromatization and in the various types of counting tubes. It has been recognized in recent years that many problems, particularly those connected with the deformation of metals, can be solved only if X-ray intensities are measured accurately, and for this purpose the use of counters and strictly monochromatic radiation is indispensable. The author's recent stay in England has left a noticeable mark in his frequent references to English practice. The advantages of the various methods are set out in the clear manner we have become used to expect from Barrett.

A major contribution to the method of evaluating measurements of the Diffuse Scattering of X-rays has been made by Warren and Averbach. Any deviation from the ideal crystal structure gives rise to diffuse scattering in addition to the sharp Bragg reflections. This is an outstanding article and the discussion of the effects of temperature, plastic deformation and short range order should be mentioned as of particular importance.

Five years have gone since Zener in his book explained the basis of anelasticity and indicated its uses. At that time many people did not have the confidence in the method and theory which Zener himself showed. However, we can now say that without doubt the method has proven itself, and promises wider application in the future. "The Metallurgical Use of Anelasticity" was written by Wert, who participated in the early development of the subject and has continued working actively in this field. The author is careful in stating the limitations of the method and discourages exaggerated hopes for successful solution of many problems by its use. However, the method has been successful in obtaining information on the rates of diffusion, ordering and phase changes in substitutional alloys, and on the solid solubility of interstitial atoms.

It is evident that Chalmers' article, "Crystal Growth and Crystal Boundary Techniques," has

been written by someone who has contributed a great deal to our knowledge in this field and can speak about it with authority. One would wish the author had more space at his disposal, though one realizes that a whole volume could well be written on the subject.

Geisler describes recent improvements in the techniques of determining Crystal Orientations and Pole Figures which have made these determinations more quantitative; Bever summarizes the use of Radioactive Tracers in Physical Metallurgy Research, and Parker and Washburn deal with techniques recently developed for studying the Deformation of Single Crystals, in particular the use of shear strain instead of tensile strain. These papers are interesting, though in no way exciting. They treat selected examples and it is obvious that many others could be added.

There are four most welcome papers dealing either with subjects about which little information has been published (Siegel on Radiation Damage as a Metallurgical Research Technique) or in which the publications are not readily available (Irwin on High Speed Strain Measurements) or in which papers are not usually written for the metallurgist from his point of view (Shull on Techniques and Applications of Neutron Diffraction and Williams on Ferromagnetic Domains). They provide a valuable source of information in fields which will become increasingly important to the metallurgist within the next few years. Even if the book contained only these four papers and that by Warren and Averbach, it would be compulsory reading for all those engaged, on the experimental side, in furthering the science of metallurgy.

W. Boas

SOME CURRENT PAPERS IN OTHER JOURNALS

Acta Crystallographica, Vol. 6

Part 8–9, September, 1953 (Partial Contents)

Electron-density errors at special positions. D. W. J. Cruickshank and J. S. Rollett.

A simple but versatile strip technique for calculating structure factors. Leroy Alexander.

The meaning of the average of $|\mathbf{F}|^2$ for large values of the interplanar spacing. David Harker.

Neutron-diffraction study of the structure of the A-form of the rare earth sesquioxides. W. C. Koehler and E. O. Wollan.

A preliminary examination of the structure of α-$Ca_3(PO_4)_2$. A. L. Mackay.

The direct use of three-dimensional X-ray data in crystal-structure determination. P. A. Kenyon and C. A. Taylor.

A contribution to the vector-algebraic method for the interpretation of the Patterson synthesis. A. Bezjak.

Part 10, October, 1953 (Partial Contents)

An improved determination of the crystal structure of β-uranium. Charles W. Tucker, Jr. and Peter Senio.

Crystallographic calculations on the Manchester University Electric Digital Computer (Mark II). F. R. Ahmed and D. W. J. Cruickshank.

Photo-elastic behaviour of barium nitrate and lead nitrate crystals. S. Bhagavantam and K. V. Krishna Rao.

Temperature diffuse scattering for cubic powder patterns. B. E. Warren.

Preliminary X-ray investigation of pseudo-wollastonite. J. W. Jeffery and L. Heller.

Sayre's equation and Zachariasen's method. W. Cochran.

A defect of the James and Brindley atomic scattering factors. W. Cochran.

The crystal structure of aluminium titanate. A. E. Austin and C. M. Schwartz.

A computional procedure for determining lattice parameters from powder photographs. G. D. Archard.

Journal of the Chemistry Society

September, 1953 (Partial Contents)

The anodic behaviour of copper in neutral and alkaline chloride solutions. H. Lal and H. R. Thirsk.

Journal of the Institute of Metals, Vol. 81

Part 12, September, 1953

The mechanism of residual-stress formation in sand castings. R. N. Parkins and A. Cowan.

The constitution of aluminium-copper-silicon alloys. H. W. L. Phillips.

The structure and mechanical properties of copper-manganese-tin alloys. J. C. Blade and J. W. Cuthbertson.

The preparation and properties of magnesium alloy sheets of controlled impurity content. H. G. Cole, A. E. L. Tate, and B. Walters.

The behaviour of the crystal boundaries of aluminium at temperatures near the melting point. W. I. Pumphrey and J. V. Lyons.

A slide-rule for the interconversion of atomic and weight percentages for any binary alloy system. W. A. Rachinger.

Structural studies of the creep of lead. R. C. Gifkins.

The re-investigation of a nickel-titanium alloy and observations on $\beta/(\alpha + \beta)$ boundaries in titanium systems. A. D. McQuillan.

Part 13, October, 1953

An investigation of thickening and metal entrapment in a light alloy melting flux. A. H. Sully, H. K. Hardy, and T. J. Heal.

Constitution of the copper-rich copper-aluminium-germanium alloys. G. V. Raynor and P. Greenfield.

Some observations of the mechanism of pitting corrosion. R. May.

The effect of iron, manganese, and chromium on the properties in sheet form of aluminium alloys containing 0.7% magnesium and 1.0% silicon. R. Chadwick, N. B. Muir, and H. B. Grainger.

The copper-indium eutectoid at 31.36 wt.-% indium. Chester W. Spencer and David J. Mack.

The free-energy diagram of the system titanium-oxygen. O. Kubaschewski and W. A. Dench.

The effect of cold working on an iron-manganese alloy. J. Gordon Parr.

Part 14, November, 1953

Twenty-fourth Autumn Lecture: The new metal titanium. Maurice Cook.

The oxidation of aluminium-magnesium alloys by steam: A contribution to research on mould reaction. Marjorie Whitaker. With an Appendix by A. R. Heath.

Some creep characteristics of a group of precipitation-hardening alloys based on the alpha-copper-aluminium phase. J. P. Dennison.

The computation of loads in metal strip rolling by methods involving the use of dimensional analysis. Maurice Cook and R. J. Parker.

A survey of the uranium-nickel system. J. D. Grogan and R. J. Pleasance. With an Appendix by Betty E. Williams.

La Metallurgia Italiana

Luglio, 1953

Criteri preliminari per lo studio del campo plastico. R. Zingale.

Attualità nel campo della produzione dell'alluminio. R. Carmina.

Recenti progressi nelle applicazioni delle leghe leggere. C. Panseri.

Augusto, 1953

L'esame radiografico delle saldature: una completa valutazione dei difetti in termini di resistenza statica ed a fatica. O. Masi e A. Erra.

Lo studio di alcuni fenomeni elettrochimici con l'impiego di un dispositivo elettroponderale: Nota V. -Antimonio. P. Spinedi.

Leghe speciali per pistoni. G. Tremolada e E. Gattoni.

Revue de Métallurgie, 50ᵉ Annee

Numéro 7, juillet, 1953

Gaz et soufflures congénitales (ou endogènes) en fonderie. Albert Portevin.

Observations sur le faciès cristallographique de la martensite. ROBERT F. MEHL et D. M. VAN WINKLE.

Quelques aperçus sur les laboratoires des Etats-Unis et les Congrès Métallurgiques de Philadelphie (octobre 1952). MME. A. R. WEILL.

Recherches sur les alliages austénitiques réfractaires à faible teneur en métaux dont l'approvisionnement est difficile. W. SIEGFRIED et F. EISERMANN.

Analyse thermoélastique des transformations des alliages métalliques. R. CABARAT, P. GENCE, L. GUILLET et R. LE ROUX.

Etude systématique au moyen du volume débitgraphe des facteurs déterminant la soufflabilité des charges au convertisseur Thomas (suite) P. LEROY, M. GOMBERT et B. TRENTINI.

Numéro 8, août, 1953

Récentes recherches dans l'industrie sidérurgique américaine. E. C. BAIN.

Anomalies observées dans la recristallisation des tôles et de tubes d'alliages cuivreux contenant de l'aluminium. J. MARÉCHAL et M. DOUCET.

Lacunes des couches d'aluminium de placage de l'alliage AU4G (duralumin) compatibles avec la protection contre la corrosion. G. GAUTIER.

Etude thermo-élastique et décomposition isotherme de l'eutectoïde des bronzes d'aluminium. RENÉ LE ROUX.

Etude systématique au moyen du volume débitgraphe des facteurs déterminant la soufflabilité des charges au convertisseur Thomas (suite). P. LEROY, M. GOMBERT et B. TRENTINI.

Numéro 9, septembre, 1953.

Etude de la pyrolyse de la dolomie dans l'azote et le gaz carbonique secs, en température linéairement croissante. ALBERT RICHER et PIERRE VALLET.

Contribution au dosage de l'oxygène sous forme d'alumine dans les aciers au carbone. F. MEUNIER et P. FLAMENT.

Dosage de l'aluminium et de son nitrure dans les aciers au carbone. M. URBAIN.

Le microanalyseur à sonde électronique. R. CASTAING.

Etude de défauts des pellicules-répliques d'alumine en relation avec la structure de l'aluminium et de ses alliages. P. BUSSY.

Economies par la trempe superficille à la flamme. H. W. GRÖNEGRESS.

Etude systématique au moyen du volume-débitgraphe des facteurs déterminant la soufflabilité des charges au convertisseur Thomas (fin). P. LEROY, M. GOMBERT et B. TRENTINI.

Zeitschrift für Metallkunde, Band 44

Heft 8, August, 1953

Schmelzen von Metallen ohne Tiegelreaktion. OTTO WINKLER.

Produktionsplanung in amerikanischen Werken der NE'-Metallhalbzeugindustrie und in der Stahlindustrie. BERHARD TRAUTMANN.

Wirtschaftliche Gesichtspunkte bei der zerstörungsfreien Werkstoffprüfung. FRITZ FÖRSTER.

Struktur und chemische Eigenschaften der Boride der Übergangsmetalle der 4., 5. and 6. Gruppe. PAUL SCHWARZKOPF und FRANK W. GLASER.

Die Struktur von $NiHg_4$. FRANZ LIHL und HANS NOWOTNY.

Die Rekristallisationstexturen des Titans. D. N. WILLIAMS und D. S. EPPELSHEIMER.

Die Beschleunigung des Fliessens von Metallen in Paraffinöl durch polare Zusätze. WERNER KLINKENBERG, KURT LÜCKE und GEORG MASING.

Wesen und Eigenschaften der Korngrenzen polykristalliner Metallkörper (1. Teil). KURT LÜCKE.

Über die Eigenschaften metallischer Schmelzen. VI. Die innere Reibung flüssiger Silber-Zinn-Legierungen. ERICH GEBHARDT, MANFRED BECKER und ERICH TRÄGNER.

Nomogramm zur Bestimmung des Spannungsverlaufes bei reiner Biegung für Werkstoffe mit linearer Verfestigung. RUDOLF BÖKLEN.

Zur Kenntnis des Systems Nickel-Kohlenstoff-Magnesium. ERICH SCHEIL und LEO HÜTTER.

Arbeitsverfahren zur Bestimmung von Chrom in Kupfer-Chrom-Legierungen. HUGO WIEDMANN und HANS NUFER.

Zum Existenzbereich der $Delta_1$-Phase im Eisen-Zink-System. HEINZ BABLIK, FRANZ GOTZL und RUDOLF KUKACZKA.

Zur Frage der Existenz der $Delta_1$-Phase im System Zinc-Eisen. FRANZ LIHL.

Bemerkung zur Arbeit von Th. Heumann und A. Kottmann: Über den Ablauf der Diffusionsvorgänge. HELMUT BUCKLE.

Heft 9, September, 1953

Untersuchungen des Bruchfeingefüges im System Wismut-Antimon. CARL A. ZAPFFE.

Über den Zerfall des hexagonalen Aluminiumborids AlB_2. FRANZ LIHL und PETER JENITSCHEK.

Wesen und Eigenschaften der Korngrenzen polykristalliner Metallkörper (Fortsetzung und Schluss). KURT LÜCKE.

Lösungskalorimeter zur genauen Bestimmung von Lösungs- und Bildungswärmen. FRANZ EBERHARD WITTIG.

Zur Frage der Bildungswärmen im System Aluminium-Magnesium. FRANZ EBERHARD WITTIG und GEORG PILLER.

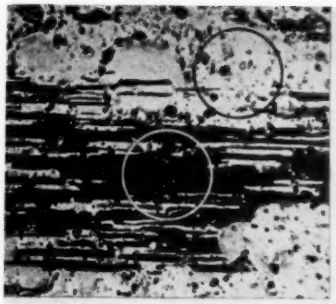

29a

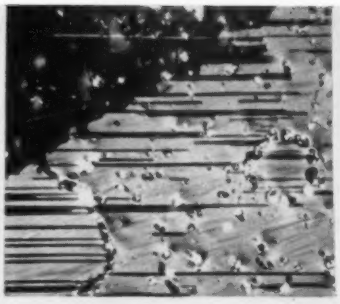

30a

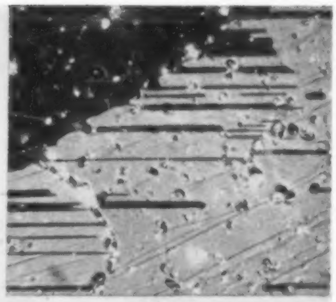

30b

31

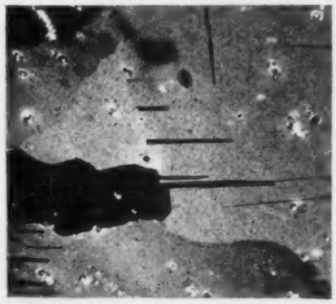

32

33

34

PLATE V. Figure 29*a*—Annealed twin configuration. (172) type. 140×. Figure 30*a*—Annealed deformation twins. (172) type. 16 hrs. at 630°C. 220×. Figure 30*b*—The same, repolished, after a further anneal of 6 hrs. at 645°C. 220×. Figure 31—Annealed (130) and (130) twins. (24 hrs. at 635°C.) 200×. Figure 32—Specimen annealed 24 hrs. at 635°C. Region of incipient recrystallization, showing swelling of twin tip. 200×. Figure 33—Thermal etching grooves along twins (annealed 24 hrs. at 635°C). 100×. Figure 34—Parting at (172) twin. 300×.